中国石油大学（华东）
CHINA UNIVERSITY OF PETROLEUM

声学测井实验室

声波测井论文集

Proceedings of acoustic logging

2026版

苏远大　唐晓明　等



前　言

声波测井是地球物理测井的重要分支，也是认识井周地层岩石物理性质与地下结构特征的核心技术手段。20 世纪中叶以来，声波测井经历了从模拟信号到时测量到全波列数字采集、从单极子速度评价到多极子各向异性分析、从井壁附近参数提取到井旁远探测成像的发展历程。声波在井筒、井壁及地层中的传播过程蕴含着丰富的地层信息，通过研究不同模式波的传播规律，分析到时、速度、振幅、频率、相位和衰减等响应特征，可以提取地层纵横波速度、弹性参数、渗透率及各向异性等信息，开展井周裂缝与构造识别、储层评价和固井质量评价，为油气勘探开发与井筒工程提供依据。

本论文集整理了作者团队二十余年来在测井声学理论、方法及应用方面公开发表的代表性研究成果，按研究内容和应用场景分为随钻声波测井、远探测声波测井、套管井声波测井、声波测井处理方法及现场应用五个专题。各专题既呈现相应方向的研究进展，也体现波场理论、数值模拟、物理实验与现场资料解释之间的联系。

随钻声波测井是在钻井过程中实时获取地层声学信息的技术方向。随钻条件下钻铤波强烈干扰地层信号，如何压制仪器直达波、提取可靠的地层参数，是这一方向的核心问题。围绕这一问题，本部分研究了钻铤波的传播、衰减与阻带特征，讨论了刻槽式隔声体、不同厚度管柱组合以及仪器尺寸的优化，为压制仪器直达波提供了理论和实验依据；在此基础上，发展了慢速地层单极子横波测量、多极子联合反演、四极子波频散处理及钻铤偏心影响校正等方法，实现了地层纵横波速度、横波速度变化和横向各向同性参数的提取。进一步地，本部分还分析了各向异性与含裂隙孔隙地层中的随钻声场，介绍了利用斯通利波反演地层渗透率的方法，并探讨了随钻震电测井中井外界面的电磁响应。

远探测声波测井将声波探测范围由井壁附近延伸至井旁地质体，是声波测井从单井参数测量向空间探测的重要拓展。本部分以井外反射体和井旁地质结构的距离、方位识别为主线，针对偶极横波反射成像中方位 180°不确定性，研究了方位响应及其消除方法，并介绍了方位纵波远探测与低频偶极横波远探测的理论、实验和现场应用。通过多裂缝体系波场模拟、角谱法以及井孔与弹性波相互作用分析，讨论了声波辐射、反射和井中接收的物理过程，考察了仪器偏心、地层性质及裸眼与套管条件对响应的影响。相关应用涵盖邻井探测与多井声学测距、海洋钻探井旁断层识别、斜井周围地质构造成像，以及利用四分量偶极横波资料快速反演构造走向。

套管井条件下，套管波的强能量掩盖了携带地层信息的地层波，同时水泥胶结状态直接影

响声波在套管—水泥—地层界面的传播。本部分从两个方面展开：一是针对套管波干扰地层波的问题，介绍了双源反激测井方法、激励参数优化及仪器研制，讨论了通过调节双源延迟时间与幅度比压制套管波的机理和效果；同时发展了多重滤波与相关处理、波干涉以及超级混合虚折射干涉等阵列处理方法，提高了地层波的可识别性。二是针对固井质量评价，利用黏弹性滑移边界描述套管、水泥与地层之间的耦合，结合理论计算和物理实验分析了不同胶结条件下套管波的速度、衰减和频散特征，并讨论了过油管偶极声波及随钻声波固井评价方法。

在资料处理与工程应用方面，本部分侧重复杂井孔条件下的地层参数提取与工程解释。等效仪器理论及其模型频散处理方法用简化模型描述仪器与井孔导波的相互作用，为现场资料处理提供了计算基础；深度学习方法则用于随钻模式波慢度快速反演和横波横向各向同性参数估计。相关研究还讨论了大井眼超慢速地层的偏心偶极横波测量、弯曲波频散反演及方位横波各向异性的物理模拟验证。工程应用涵盖水力压裂效果的弹性波评价、利用井周波速径向变化评价岩石脆裂性，以及射孔对声波测井响应的影响。

此外，本论文集还收录了与上述专题相关的基础方法研究，包括利用圆周时移和相位差提取频散波相慢度、慢速地层随钻多极子声源传播特性的数值分析，以及正交偶极资料在地层各向异性评价中的应用；固井评价方面，讨论了将裸眼声波时差与变密度测井地层波能量相结合的方法，分析了地层声速对固井质量评价的影响及其消除途径，改进了对水泥胶结状态的识别。这些研究补充了频散波处理、声源传播机理和测井解释方法，也为理解前述专题中的相关问题提供了参考。

将这些已发表成果按专题重新整理，旨在帮助读者把握不同研究问题之间的联系：仪器与井孔的耦合影响波场形成，波场传播特征决定信息提取方式，而可靠的处理与反演又是地层评价和工程应用的基础。希望本论文集能够为从事声波测井相关研究的读者提供参考，也为青年学生了解研究思路、比较理论方法和开展后续工作提供帮助。

本论文集以电子版形式发布，所收录内容为作者团队前期公开发表成果的整理与汇编，仅供学术交流、科研学习与研究参考使用。衷心感谢各位合作者在相关研究中的付出，诚挚欢迎专家、学者、工程技术人员和青年学生提出意见与建议，共同探讨测井声学领域的科学问题与技术发展。

全体作者

2026 年

目录 CONTENTS

01 随钻声波测井

理论、方法及应用 / 15 篇论文

专题首页 1

1.1 一种刻槽式随钻声波测井隔声体的理论与实验研究 2

Theoretical and experimentation of a carved collar isolator for logging-while-drilling acoustic tool

1.2 组合管柱固有隔声阻带的随钻单极隔声方法 10

Acoustic isolation of a monopole logging while drilling tool by combining natural stopbands of pipe extensional waves

1.3 利用不同厚度管柱组合拓宽钻铤波隔声阻带 17

Extensional-wave stopband broadening across the joint of pipes of different thickness

1.4 随钻声波测井钻铤模式波衰减规律研究与隔声体设计 22

LWD acoustic color mode wave attenuation character research and isolator design

1.5 随钻单极子声波测量慢速地层横波慢度 32

Measurement of the shear slowness of slow formations from monopole logging-while-drilling sonic logs

1.6 随钻多极子声波数据联合反演疏松慢速地层纵、横波速度 40

Joint inversion of logging-while-drilling multipole acoustic data to determine P- and S-wave velocities in unconsolidated slow formations

1.7 随钻四极子横波测井钻铤尺寸优化设计的理论研究 48

Theoretical analysis of the optimal collar size for a logging while drilling quadrupole tool

1.8 钻铤偏心对随钻四极子横波测井影响：理论与实例分析 58

Influence of drill collar eccentricity on quadrupole shear-wave logging while drilling: theory and field case

目录 CONTENTS

01 随钻声波测井

理论、方法及应用 / 15 篇论文

专题首页 1

1.9 随钻四极横波测量的数据驱动频散处理方法 **69**

A data-driven dispersive processing of LWD quadrupole wave data

1.10 利用随钻四极波频散反演地层横波速度径向剖面 **76**

Mapping formation shear-velocity variation by inverting logging-while-drilling quadrupole-wave dispersion data

1.11 随钻多极子声波测井联合反演地层各向异性 **84**

Joint inversion of logging-while-drilling multipole acoustic data to determine formation shear-wave transverse isotropy

1.12 横向各向同性地层随钻多极子测井声场的分波分析与特性研究 **96**

Theoretical calculation and mechanism analysis for component waves of acoustic logging while drilling in transversely isotropic formations

1.13 含孔隙、裂隙地层随钻多极子声波测井理论 **111**

Numerical study on the characteristics of multipole acoustic logging while drilling in cracked porous medium

1.14 随钻斯通利波测井反演地层渗透率的理论、方法及应用 **125**

Formation permeability estimation using Stoneley waves from logging while drilling: theory, method, and application

1.15 随钻条件下井旁界面声电效应的辐射电磁波响应特征 **136**

Characteristics of radiating electromagnetic waves induced by the interface outside the borehole during seismoelectric logging while drilling

目录 CONTENTS

02 远探测声波测井

理论、方法及应用 / 15 篇论文

专题首页 147

2.1 井中偶极横波远探测方位180°不确定性问题的求解：理论、方法和实验 中 148

Solving the azimuthal 180°-ambiguity problem in borehole dipole shear wave reflection imaging: Theory, method and experiment 英 164

2.2 井中方位纵波远探测：理论、实验与现场应用 180

Azimuthal reflected P-wave imaging: theory, experiment and field application

2.3 利用井中低频偶极横波进行声波远探测的新方法 191

A new acoustic remote sensing method utilizing borehole low-frequency dipole shear wave

2.4 多裂缝体系下的偶极SH横波远探测声场模拟方法 200

SH wavefield simulation of dipole acoustic reflection survey for multi-fracture system

2.5 钻挺偏心对随钻声波远探测反射声场方位响应特性的影响 212

Effects of collar eccentricity on azimuthal response characteristics for acoustic reflection measurement while drilling

2.6 偏心偶极横波方位远探测的井孔辐射和接收响应 225

Borehole radiation and reception responses for azimuthal shear-wave reflection imaging with an off-centred dipole acoustic tool

2.7 基于远井眼弹性波的邻井探测 241

Detecting a fluid-filled borehole using elastic waves from a remote borehole

2.8 井孔与弹性波的相互作用：理论、方法和应用 248

The interaction between borehole and elastic waves: theory, method and application

目录 CONTENTS

02 远探测声波测井

理论、方法及应用 / 15篇论文

专题首页 147

2.9 基于角谱法的偶极SH横波远探测声场模拟方法 260

Simulation method of the SH wavefield for dipole acoustic reflection imaging based on the angular spectrum method

2.10 偶极横波远探测在裸眼井及套管井中接收波场的方位响应特征 272

Azimuthal response of the received wavefield in open and cased boreholes for dipole shear-wave reflection imaging

2.11 利用邻井偶极声波数据探测超软地层中的套管井 291

Delineating a cased borehole in unconsolidated formations using dipole acoustic data from a nearby well

2.12 基于偶极四分量数据的多井声法测距 300

Acoustic ranging of multiple nearby wells using dipole acoustic logging

2.13 利用剪切波成像定位大洋钻探中的近井断层 305

Shear wave imaging to determine near-borehole faults for ocean drilling exploration

2.14 基于四分量偶极横波远探测的斜井地质构造解释 311

Application of four-component dipole shear reflection imaging to interpret the geological structure around a deviated well

2.15 基于四分量偶极横波远探测的井周构造走向快速反演方法研究 322

Research on a fast inversion method for structural strike around a borehole based on four-component dipole shear wave reflection imaging

目录 CONTENTS

03 套管井声波测井

理论、方法及应用 / 10 篇论文

专题首页 332

3.1 过套管声波测井的双源反激参数优化实验研究 333
Experimental studies on parameter optimization of dual source transmitters excitation in through casing acoustic logging

3.2 一种过套管双源反激声波测井仪器 347
A Through-Casing Acoustic Logging Tool Using Dual-Source Transmitters

3.3 一种过套管双源反激声波测井方法 356
A cased-hole acoustic logging technique using the dual source of opposite polarity

3.4 套管井声波测井多重滤波与阵列相关信号处理方法及应用 364
A multiple filtering and correlation array signal processing technique for cased-hole acoustic logging and applications

3.5 基于波干涉原理的套管井阵列声波处理方法及其应用 372
An interference-based array signal processing technique for cased-hole acoustic logging and applications

3.6 基于超级混合虚折射干涉法的阵列声波处理方法及其在套管井中的应用 383
A super-mixing-virtual interferometric array signal processing technique and its applications to cased-hole acoustic logging

3.7 用黏弹滑移界面表征的固井声波测井理论 392
An acoustic-wave theory for casing bond evaluation using viscoelastic slip boundary modeling

3.8 套管井不同胶结条件下的声波传播特性理论与实验研究 400
Cased borehole acoustic-wave propagation with varying bonding conditions: Theoretical and experimental modeling

3.9 过油管偶极声波测井固井质量评价方法研究 409
Evaluating the cementing quality of cased well through tubing by dipole acoustic logging method

3.10 随钻声波测井固井质量评价理论与数值模拟研究 420
Theoretical and numerical simulation of LWD acoustic cement logging

目录 CONTENTS

04 声波测井处理方法及现场应用

10 篇论文

专题首页 432

4.1 用弹性波评价井下水力压裂：数值模拟与现场应用 433
Elastic-wave evaluation of downhole hydraulic fracturing: Modeling and field applications

4.2 一种声波测井的等效仪器理论及其应用 441
An equivalent-tool theory for acoustic logging and applications

4.3 基于深度学习的随钻多极子模式波慢度快速反演方法 451
Fast inversion of formation slowness from LWD acoustic wave modes using deep learning

4.4 基于CNN-LSTM网络的随钻声学测井横波横向各向同性反演 466
Inversion of S-wave transverse isotropy from acoustic logging-while-drilling data using a CNN-LSTM network

4.5 偏心偶极子测量大井眼超软地层横波慢度 483
Ultraslow formation shear slowness estimation in a large borehole using an eccentric dipole tool

4.6 基于等效仪器理论的模型驱动井中偶极声波数据频散校正 495
Model-based dispersive processing of borehole dipole wave data using an equivalent-tool theory

4.7 利用井孔弯曲波频散数据确定地层横波横向各向异性 504
Determining formation S-wave transverse isotropy from borehole flexural-wave dispersion data

4.8 基于弹性波速径向变化的岩石脆裂性定量评价 513
Quantitative evaluation of rock brittleness and fracability based on elastic-wave velocity variation around borehole

4.9 射孔对井中声波测井的影响：数值模拟与现场应用 521
Effect of perforation on borehole acoustic wave logging: Modeling and application

4.10 井中方位横波各向异性测量：物理模型与偶极声波验证 528
Azimuthal shear-wave anisotropy measurement in a borehole: Physical modeling and dipole acoustic verification

目录 CONTENTS

05 其他

5 篇论文 专题首页 534

5.1 一种提取声波测井频散波相慢度的方法 535
A Method to Extract Phase Slowness of Dispersive Wave from Sonic Logging Data

5.2 基于软地层随钻多极子声源传播特性的数值研究 541
On Numerical Study of the LWD Multipole Source Propagation Characteristics in Slow Formation

5.3 正交偶极声波测井资料在评价地层各向异性中的应用 544
Evaluating formation shear-wave anisotropy by using cross-dipole acoustic logging data

5.4 裸眼时差与变密度测井地层波能量相结合改进固井 II 界面评价 548
Improved second interface cementing evaluation using open hole slowness and formation wave energy of variable density log

5.5 地层声速对固井质量评价的影响及消除方法 552
Effects of Formation Velocity on Cementing Evaluation and Its Elimination

06 苏远大简历

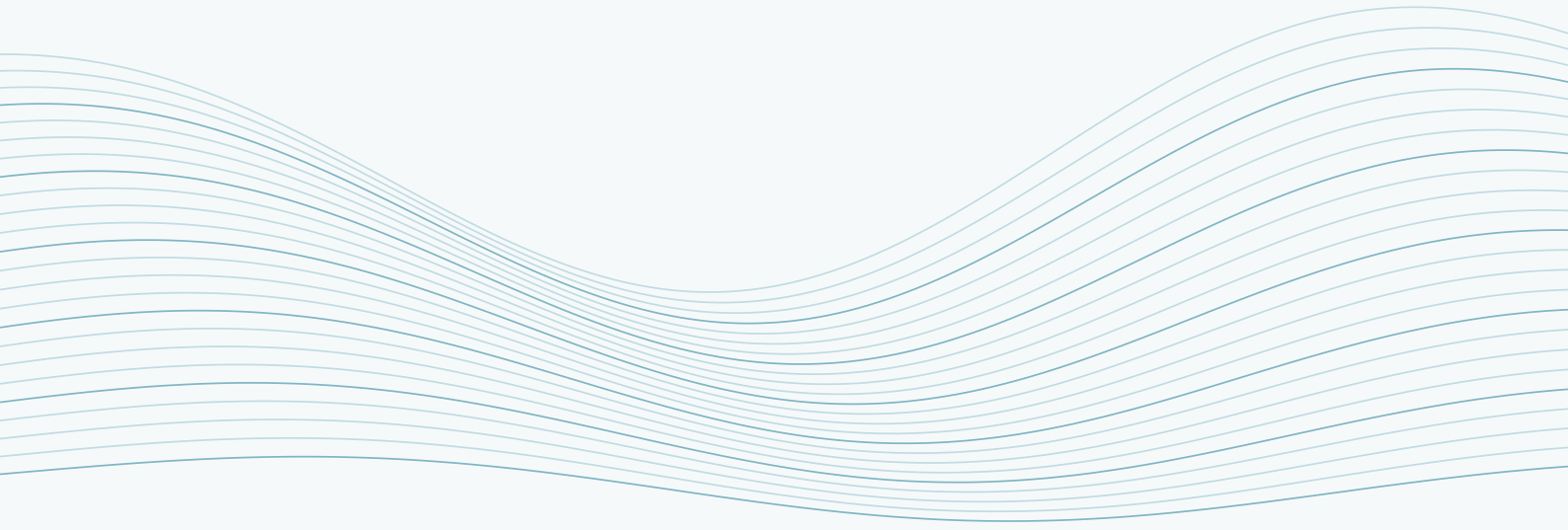
01

专 题 / 01

随钻声波测井

理论、方法及应用

LOGGING-WHILE-DRILLING ACOUSTIC LOGGING



收录 15 篇论文

苏远大，庄春喜，唐晓明等. 2016. 一种刻槽式随钻声波测井隔声体的理论与实验研究. 地球物理学报，59(12)：4521-4528，doi：10.6038/cjg20161215.

Su Y D, Zhuang C X, Tang X M, et al. 2016. Theoretical and experimentation of a carved collar isolator for logging-while-drilling acoustic tool. *Chinese J. Geophys.* (in Chinese), 59(12): 4521-4528, doi: 10.6038/cjg20161215.

一种刻槽式随钻声波测井隔声体的理论与实验研究

苏远大，庄春喜，唐晓明*，黑创，许松，李振，杨喜龙

中国石油大学(华东)地球科学与技术学院，青岛 266580

摘要 隔声体的设计与效果评价对随钻声波测井仪器的研发至关重要.针对刻槽式隔声体结构，利用数值模拟的方法分析了钻铤波在其传播过程中隔声阻带形成、拓宽并达到稳定的物理过程.在此基础上优化设计并加工了一种可用于随钻声波测井实验样机的刻槽式隔声体.在实验室内利用声波频率扫描方法测量了该隔声体的钻铤波声衰减，并进一步在实验井中测试验证了隔声体在井孔中工作时的隔声效果.最后，开展了随钻测井环境下的现场实验，测到了高质量的地层波信号和对应的纵波时差.理论分析和实验对比研究结果表明，刻槽隔声体有效地降低了钻铤直达波的干扰.本文的工作为随钻声波测井刻槽式隔声体的设计及评价测试提供了一套系统的理论及实验方法.

关键词 随钻声波测井；隔声体；钻铤波；阻带；刻槽

doi：10.6038/cjg20161215 **中图分类号** P631 **收稿日期** 2016-03-18；2016-10-10 **收修定稿**

Theoretical and experimentation of a carved collar isolator for logging-while-drilling acoustic tool

SU Yuan-Da, ZHUANG Chun-Xi, TANG Xiao-Ming*, HEI Chuang, XU Song, LI Zhen, YANG Xi-Long

School of Geosciences, China University of Petroleum, Qingdao 266580, *China*

Abstract The design of logging-while-drilling (LWD) isolator is crucial for suppressing tool waves propagating along the drill collar under LWD conditions. This study simulates and analyses the physical process of stopband forming, evolution, and stabilization of a carved collar. Based on the simulation results, we have designed and manufactured an optimal LWD prototype isolator. We measured the collar wave attenuation of the carved isolator using the frequency-sweep technique, and tested the performance of the isolator in two experimental wells in the laboratory condition. Finally, we did a field test of the tool in the LWD environment which shows that formation acoustic signals with good quality and high SNR are measured in the designated isolation stopband. The theoretical and experimental results indicate the cutting groove isolator in this study can effectively suppress the drill collar wave which provide a standard method for the design and evaluation of an LWD acoustic isolator on a carved drill collar.

Keywords Acoustic logging-while-drilling; Isolator; Collar wave; Stopband; Grooved collar

基金项目 国家自然科学基金(41474092，41604109)资助.

作者简介 苏远大，男，1978 年生，副教授，博士，主要从事声波测井的方法和资料处理等方面研究工作. E-mail：syuanda@sina.com

*通讯作者 唐晓明，男，1955 年生，教授，博导，国家“千人计划”科学家，主要从事声波测井研究工作. E-mail：tangxiam@aliyun.com

(C)1994-2023 China Academic Journal Electronic Publishing House. All rights reserved. http://www.cnki.net

1 引言

近年来,随钻声波测井技术被广泛用于大斜度井、水平井以及深水井中地层纵、横波速度测量(Tang et al., 2003; Mohammed et al., 2011; Nazlan et al., 2015).尤其是在深水钻井中,随钻声波测井可用来实时预测地层孔隙压力和岩石力学参数等,进而对指导安全钻井具有重要意义(Asadi et al., 2015; Brown et al., 2015).与电缆测井相比,随钻声波测井中会激发出一种沿着钻铤传播的导波,若不作隔声处理,这一钻铤波将会在测量的波形中占主导地位,从而会严重妨碍地层波的测量(Tang and Cheng, 2004).因此,隔声体的设计与隔声效果评价是随钻声波测井的核心技术.

国内、外学者针对随钻声波中钻铤波传播规律及其隔声技术开展了较多研究工作(Tang and Cheng, 2004; Sinha et al., 2009; 王华等,2009; 苏远大等,2011).Tang 和 Cheng(2004)指出钻铤波在频率域上存在一个固有阻带,具体的频率位置由钻铤尺寸所决定.这个固有阻带的带宽较窄(大约有 2～3 kHz 的带宽),难以达到随钻声波的测量要求.Aron 等(1994)和 Joyce 等(2001)提出在发射声源和接收器之间的钻铤上刻槽可以衰减钻铤波,进而来拓宽隔声阻带.苏远大等(2011)和 Matuszyk 和 Torres-Verdín(2014)数值模拟研究了钻铤刻槽前、后的钻铤波衰减规律,给出了钻铤波衰减与刻槽结构和尺寸的关系,并在此基础上设计了一种随钻声波测井隔声体结构.考虑到钻铤刻槽会损害机械强度以及加工成本高等因素,唐晓明等(2012)和苏远大等(2015a,2015b)提出了一种不需要在钻铤上刻槽的变径隔声技术.根据钻铤波存在固有阻带这一声学现象,对长度大于声波波长的不同横截面积的钻铤加以最优化组合来拓宽有效隔声阻带.这一新的变径隔声技术的隔声效果也得到了实验室声衰减测量实验的验证.迄今为止,国外随钻声波测井仪器大都采用钻铤刻槽结构的隔声技术(Aron et al., 1994; Joyce et al., 2001; Kinoshita et al., 2010),国内也正在开发类似的技术.从现场实际应用效果来看,现有的刻槽式隔声体在中、高速压实地层中应用效果较好(Tang et al., 2007; Market, 2007; Murray et al., 2014),但在钻遇的疏松软地层中,普遍存在隔声效果较差的情况,进而导致地层波信噪比低,不利于地层波速度的测量(Sollie, 1999; Izuhara et al., 2013; Blyth et al., 2013).因此,进一步深入研究这种刻槽式隔声体的隔声阻带形成机理以及实验室隔声效果评价方法,这对优化和改进隔声体设计具有重要意义.

本文针对这一问题,利用数值模拟方法研究了一种周期性刻槽钻铤中的声场特性,分析了钻铤波在其传播过程中隔声阻带的形成机理与拓宽过程.基于上述刻槽结构的隔声机理,综合考虑隔声效果和钻井机械强度等因素,优化设计并加工了一种刻槽式隔声体的随钻声波测井实验样机.利用声衰减测量验证了其隔声效果,将其进一步置于实验井中,在设计的最佳有效阻带内激发并测量声波,验证了该隔声体在井孔中的隔声效果.最后,开展了实际随钻测井环境的现场实验验证,实验结果测量得到了信噪比较高地层波信号,处理后得到的地层波时差与电缆测井吻合较好.详细的理论与实验研究表明,该刻槽隔声体可以推广应用于随钻声波测井的生产实际.本文的工作为随钻刻槽式隔声体的设计提供了理论依据,同时也为隔声体的测试提供了一套全面的实验验证方法.

2 刻槽钻铤隔声阻带形成过程和机理

苏远大等(2011)利用有限差分数值模拟了刻槽前、后钻铤波的衰减特征,结果表明钻铤刻槽后可有效地拓宽钻铤波的隔声阻带.这里重点模拟分析声波在周期刻槽钻铤中由近及远传播时有效隔声阻带形成并拓宽的物理过程.建立刻槽结构钻铤的有限差分模型,在钻铤外壁加载环状声源和接收器分别用来激发和记录钻铤波.数值模拟记录不同时刻的声场分布及距离声源不同位置处钻铤波的波形和振幅谱,进而分析刻槽钻铤的隔声阻带形成过程.

图 1 给出一种周期性刻槽结构的钻铤示意图.钻铤外径 176 mm,内径为 60 mm;槽宽 25 mm,槽深 15 mm,内、外槽间距均为 85 mm.刻槽结构的起始和终止位置到源的距离分别为 0.45 m 和 2.715 m.数值模拟时将钻铤置于液体(水)中,环状声源放置于刻槽的左侧(如图所示),声源选取主频为 15 kHz 的宽带激发函数.

图 2 给出了某一时刻刻槽隔声体的声场模拟快照,作为对比,我们也模拟了光滑钻铤情况的声场(如上部图所示).从模拟结果可以看出,声场快照中存在钻铤中和水中传播的两种声波模式,且钻铤中传播的模式要明显快于水中传播模式.通过与光滑

(C)1994-2023 China Academic Journal Electronic Publishing House. All rights reserved. http://www.cnki.net

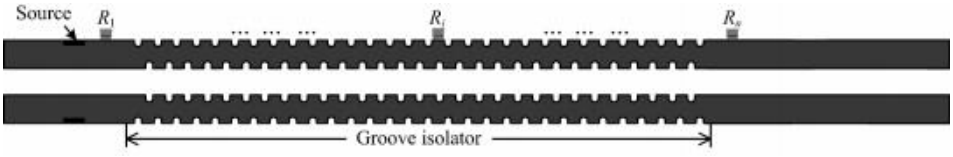


图 1　周期刻槽结构的钻铤示意图

Fig. 1　The schematic diagram of carved drill collar

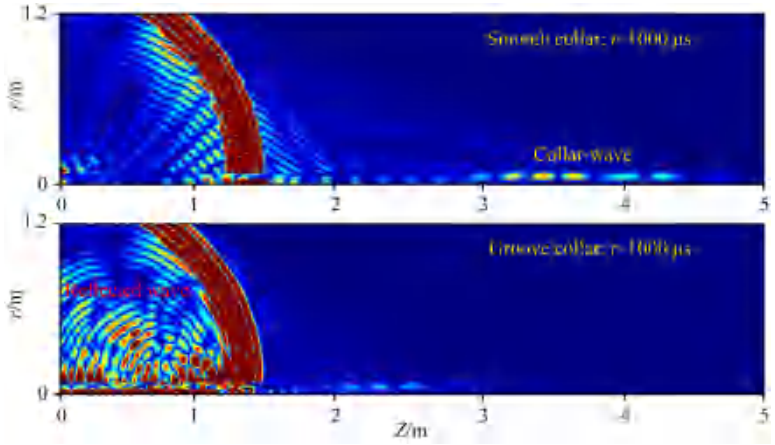


图 2　刻槽(下)与光滑(上)钻铤的声场快照图

Fig. 2　Wavefield snapshots of the smooth collar (upper) and carved collar (lower)

钻铤声场分布的对比可以看出,刻槽钻铤中的钻铤波幅度相对于光滑钻铤情况发生了明显的衰减. 主要原因在于,刻槽钻铤中存在很多声阻抗不连续界面,声波遇到刻槽会发生一系列反射、散射和透射现象,如图 2b 中观察到明显的向后传播的反射波. 因此,沿着刻槽钻铤传播的声波经过多次反射和透射波叠加,会使大部分频率成分的钻铤波衰减,从而导致沿刻槽隔声体透射过去的钻铤波幅度很弱,实现隔声的目的.

分析表明,钻铤波在刻槽钻铤中传播时有一个隔声阻带逐步形成、拓宽并达到稳定的物理过程. 为了说明这一过程,我们将一系列接收器放置于钻铤表面来考察刻槽钻铤中不同位置处的钻铤波频谱特征. 图 3 给出了不同位置接收器记录的钻铤波振幅谱,其中声源到第一个接收器的距离为 0.25 m,两个接收器间距为 0.15 m. 下面我们详细分析声波经过刻槽钻铤的振幅谱变化特征. 靠近声源时(TR=0.25 m)接收的钻铤波振幅谱与声源频谱基本保持一致. 随着距离增加,出现了不同频率成分的钻铤波幅度衰减现象. 当进入刻槽位置之前(TR<0.45 m)逐渐形成了均匀钻铤的固有阻带(Su et al., 2015a);声波进入刻槽钻铤后,固有阻带以外频率成分的钻铤波开始衰减,并且幅度衰减得很明显,但由于刻槽位置的钻铤波发生反射、散射和透射,使刚进入刻槽钻铤时振幅衰减特征比较复杂,具体表现在 TR=0.55～1.75 m 之间的钻铤波振幅变化;跨过刻槽构造(TR>2.0 m)后形成了稳定的阻带,且随着距离增加这一阻带基本保持不变,该阻带即为刻槽隔声体的有效隔声阻带,如图中红色方框所示. 上述数值模拟结果证明:刻槽可以使钻铤波的隔声阻带明显拓宽并最终稳定,进而达到隔声的要求.

3　隔声效果的实验室测量

基于上述刻槽结构钻铤的隔声机理,并综合考虑隔声效果和钻井机械强度等因素,我们利用有限差分数值模拟方法(Wang and Tang, 2003;苏远大等, 2011)优化设计了一种刻槽式的随钻声波隔声体. 图 4 给出了该刻槽式隔声体结构的随钻声波测井实验样机. 该样机的声系部分主要包括:发射声源、刻槽结构隔声体和接收器阵列. 其中隔声体部分钻铤外径 178 mm,内径 84 mm,刻槽长度约 2.2 m,槽宽 26 mm,槽深 13 mm,两种交替变换的槽间距分别为 84 mm 和 104 mm. 发射声源和接收器均采用瓦片状宽频带的压电陶瓷换能器. 下面我们首先对实验样机隔声性能进行实验室内的实验验证.

3.1　隔声阻带的声衰减测量

为了测量和分析刻槽隔声体的有效隔声阻带,

(C)1994-2023 China Academic Journal Electronic Publishing House. All rights reserved.　http://www.cnki.net

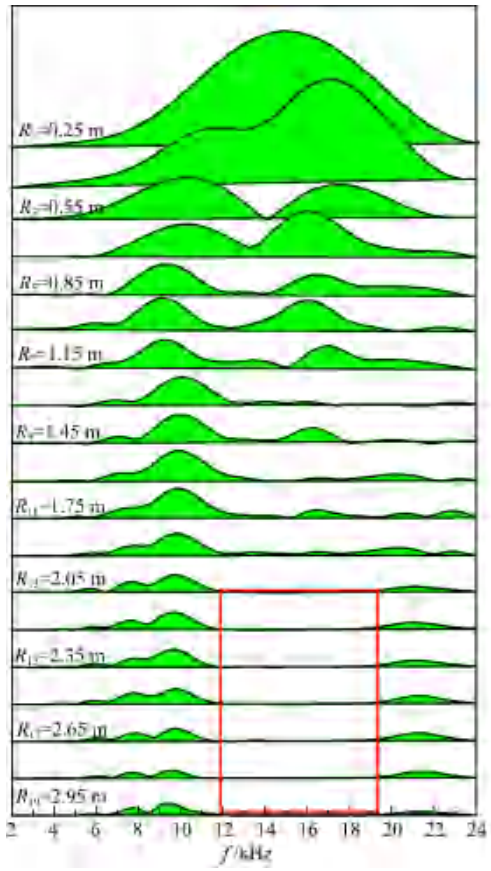


图 3 刻槽钻铤中钻铤波隔声阻带的形成过程
红框所示频段为刻槽隔声体最终形成的隔声阻带.

Fig. 3 Variation of collar wave amplitude spectrum across carved collar
The red rectangular marks the collar wave stopband after its propagating across the carved collar



图 4 刻槽隔声体结构的随钻声波测井实验样机

Fig. 4 The LWD prototype model with a carved collar isolator

我们利用扫频技术来测量钻铤波声衰减随频率的变化(苏远大等,2010;Su et al.,2015b).用窄带 Chirp 信号源来激励发射声源产生沿钻铤传播的声波信号.将声源的中心频率从 2 kHz 变到 24 kHz 进行扫频测量,扫频间隔 1 kHz.两个声波接收换能器分别安装在隔声体两侧的钻铤外表面,如图 4 中 R_n 和 R_f 所示.对比声源扫频激励下经过刻槽隔声体前、后所记录的钻铤波信号.图 5(a,b)分别给出靠近声源的接收器 R_n 记录的声源主频从 6 kHz 到 20 kHz 的波形和对应的频谱.图 5(c,d)是经过隔声体后接收器 R_f 所记录的波形和频谱.从图中可以看出,近接收器 R_n 记录的波形振幅较大,且其频率和幅度主要由声源主频所决定;然而,远接收器 R_f 记录的波形在 10~18 kHz 频带范围内振幅大幅度降低.

根据以上两组频谱数据,钻铤波经过隔声体前、后的声衰减量或系数可由下式计算得到(乔文孝等,2002;苏远大等,2010):

$$AT = 20\log\left(\frac{A_f}{A_n}\right), \tag{1}$$

其中 A_n 和 A_f 分别表示近、远接收器记录的不同频率的钻铤波振幅.

图 6 给出了实验测量的随频率变化的钻铤波声衰减曲线(点线).作为对比,也给出了理论计算的钻铤波振幅谱曲线(实线).从结果中可以看出,实验测量的钻铤波最大衰减达到 60 dB,其中钻铤波衰减较大(大于 30 dB)的频率范围与理论设计的有效阻带(10~18 kHz,如图中实线振幅谱能量几乎为 0 的频段)对应得很好.这说明我们所设计的刻槽隔声体的实验结果与理论设计吻合,达到了隔声体设计的要求.接下来,将刻槽隔声体置于井孔中来进一步测试其在地层条件下的隔声性能.

3.2 实验井中的地层波测量

选取两口有代表性的软、硬地层的实验井来测试刻槽式隔声体的隔声效果,同时考察该仪器所测地层信号的有效性.实验时选取在有效隔声阻带 10~18 kHz的频率范围内激发和接收声波信号.发射声源选用主频 13 kHz 的 3 个周期幅度锥化正弦波作为激励信号源;接收信号采集电路的滤波范围也选择在有效阻带范围.图 7 为凝灰岩硬地层实验井中测量的结果,其中图(a,b)分别为测量波形和速度分析结果.从波形图中可看出,波列中主要存在地层纵、横波振型,钻铤波基本被压制,地层声波信号的相关性很好.采用时差-时间相关法(STC)处理得到的相干图存在两个明显的相关性极大值,分别对应于地层纵、横波时差.图 8 给出了疏松砂岩地层实验井中测量的波形和速度分析结果.从图中可看出软地层井孔中也测量到了质量较高、相关性较好的地层纵波信号.实验井的测试结果表明:我们所设计的刻槽隔声体在软、硬地层中的隔声性能良好.

(C)1994-2023 China Academic Journal Electronic Publishing House. All rights reserved. http://www.cnki.net

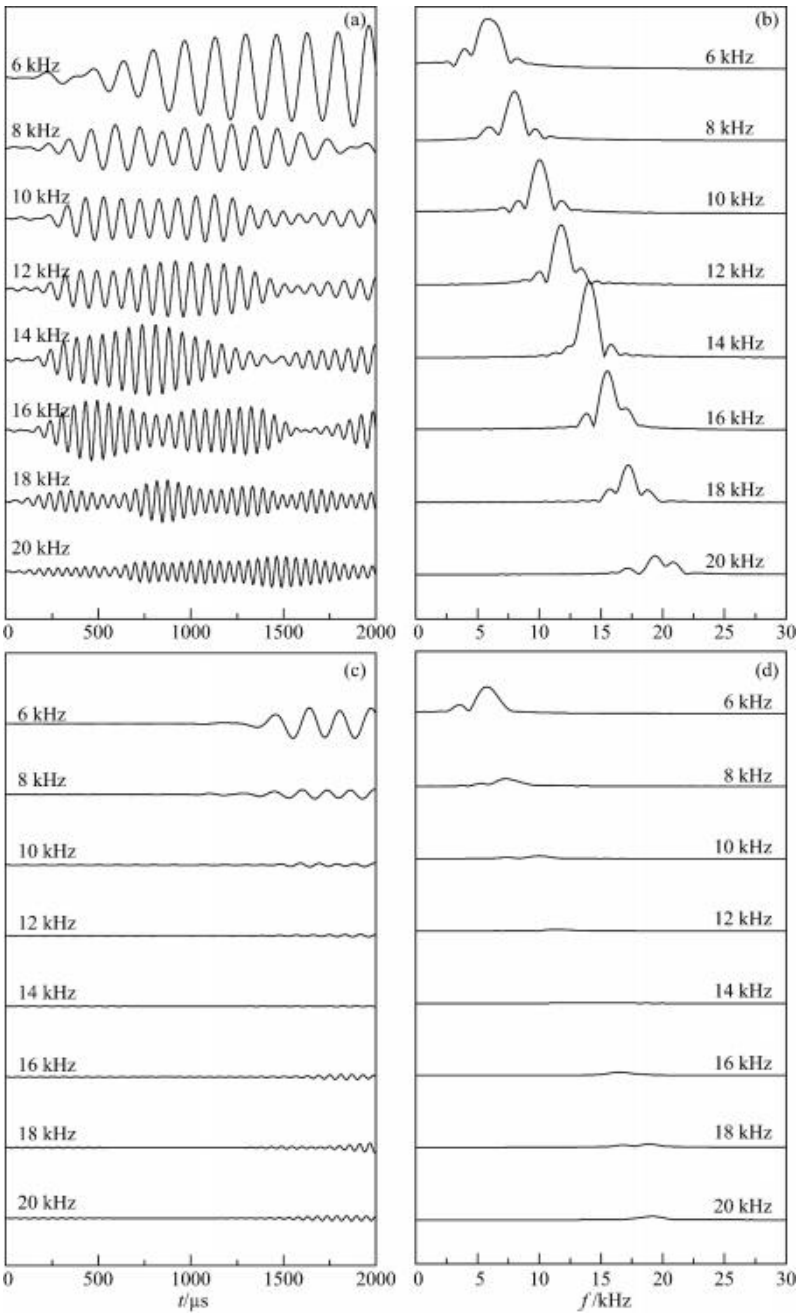


图 5　隔声体两侧远、近接收器记录的波形和对应的频谱

Fig. 5　Sweep acoutic signals (left) and spectra (right) before (a,b) and after (c,d) transmission across the carved collar isolator

4　随钻环境的现场测量结果

上述实验室的测量结果初步验证了刻槽隔声体的有效隔声阻带及其井孔中隔声效果. 实际钻井环境与实验室相比非常恶劣,钻铤的扭曲、振动以及与井壁的撞击及泥浆循环等都会产生声波测井中的环境噪声. 有必要进一步对刻槽隔声体的声波测井仪器在实际钻井过程中进行实验,以考察其在随钻测井环境下的工作性能及应用效果.

利用所研制的随钻测井仪器,在新疆进行了现场随钻测井环境下的野外试验. 该井井深 1900 m,井斜 27°,钻井用 PDC 钻头,ROP 在 65～85 m/h,泥浆排量 20000 方左右,井内压力约 60 MPa,温度 100 ℃. 图 9 给出了随钻测井环境下现场实测的原始波形及其处理分析结果. 图中第 1 道是随钻测井时井下存储记录的原始波形. 从原始波形的变密度图中可看到明显的到时和幅度随深度变化的地层波信号,同时也观察到了直达钻铤波的干扰. 为了分析测量原始波形的频率成分,图中第2道给出了原始

(C)1994-2023 China Academic Journal Electronic Publishing House. All rights reserved.　http://www.cnki.net

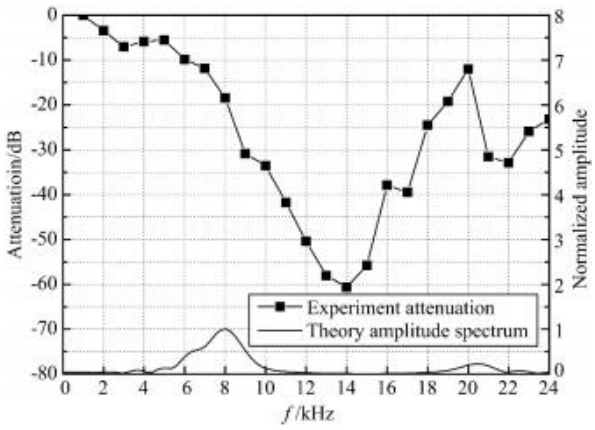


图 6 实验测量的钻铤波声衰减(点线)和理论振幅谱(实线)

Fig. 6 Comparison of experimental attenuation curve (dotted curve) and theoretical amplitude spectrum (solid curve)

波形的频谱图. 从频谱的分布可看出,原始谱中包含了两个主要能量频段,即 10 kHz 以上的幅度较大的高频成分和 10 kHz 以下的低频成分,对 10 kHz 以下低频滤波后的波形由图中第 3 道给出,此时可见在所设计隔声阻带以外频率成分的波主要是直条状的低频钻铤直达波和钻井噪声. 前述理论设计和实验结果表明,该实验样机的隔声体有效隔声阻带为 10～18 kHz,因此我们对原始波形进行 10～18 kHz的带通滤波,滤波后波形由图中第 4 道给出. 从变密度波形可看出滤波后的波形基本没有直条状的钻铤波的干扰,信号的到时随深度的变化而变化,表明实钻环境下的确测量到了井下地层的声波信号. 对此声波数据所作的速度相关分析(第 5 道)可见地层波的信号质量和相关性都较好,从相干图中提取的地层纵波时差由图中第 6 道红线给出. 为了证明该随钻测量地层时差的可靠性,图中第 6 道给出了该井段随钻纵波时差(红线)和电缆纵波时差(黑线)的对比. 对比结果表明随钻与电缆测井的纵波时差符合很好. 现场随钻实验进一步证明我们设计的刻槽式隔声体有效地隔阻了钻铤波的干扰,获得了较高质量的地层声波数据和可靠的地层纵波时差.

5 结论与认识

本文理论模拟并分析了周期性刻槽结构隔声体中钻铤波有效阻带的形成过程和机理. 在此基础上,将优化设计的刻槽式隔声体用于随钻声波测井实验

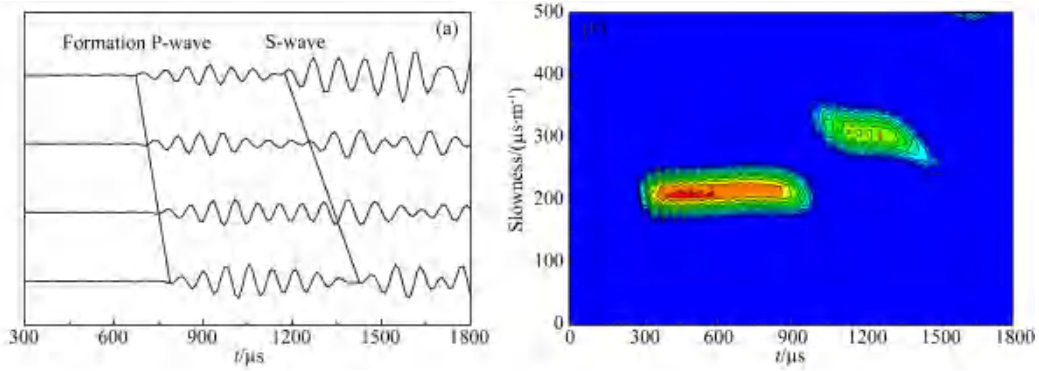


图 7 硬地层实验井测量的波形及速度分析结果

Fig. 7 Measured array waveforms (a) and STC result (b) in experimental well with a fast formation

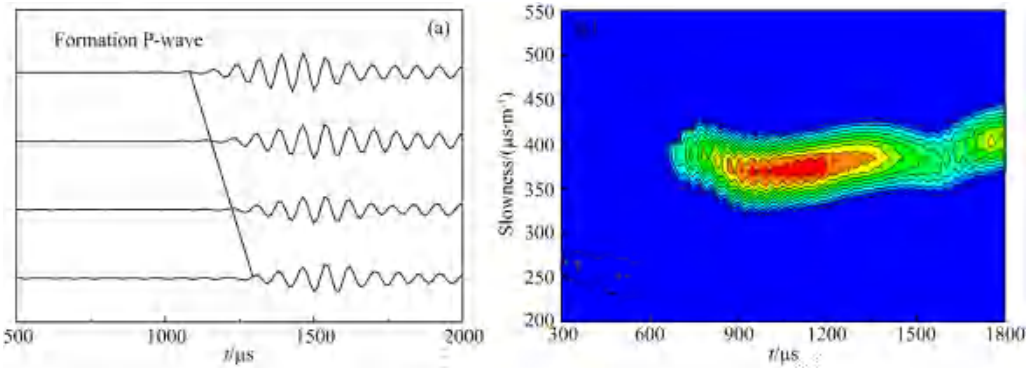


图 8 软地层实验井测量的波形及速度分析结果

Fig. 8 Measured array waveforms (a) and STC result (b) in experimental well with a slow formation

(C)1994-2023 China Academic Journal Electronic Publishing House. All rights reserved. http://www.cnki.net

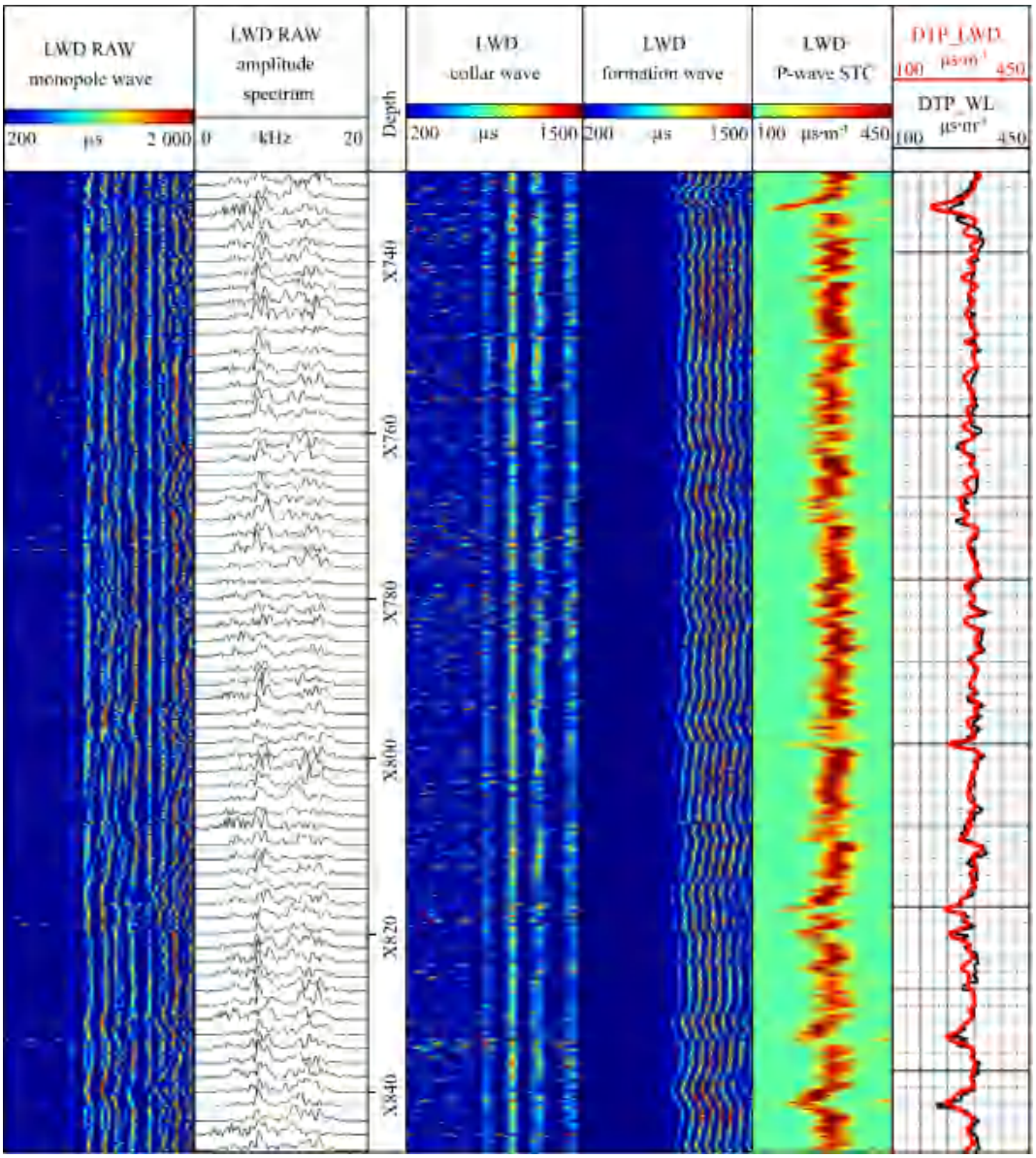


图 9　实钻环境下随钻声波样机的现场测量数据及处理结果.

第 1 道为原始波形,第 2 道为其波谱,第 3 道为 10 kHz 以下滤波后的钻铤波及随钻噪声,第 4 道为 10～18 kHz 带通滤波后的地层波,第 5 道是地层纵波的 STC 相关图,第 6 道为随钻测量时差与电缆测量结果的对比

Fig. 9　Field test result of the LWD acoustic tool in drilling environment

Panel 1 is the raw data. Panel 2 is the raw wave spectrum. Panel 3 shows the collar wave (plus some drilling noise) after filtering the raw data below 10 kHz. Panel 4 shows the formation acoustic wave after band-pass filtering the raw data within 10～18 kHz. Panel 5 is the STC correlogram of formation wave data. Panel 6 is the formation P-wave slowness from the STC correlogram compared with its counterpart from the wireline measurement after drilling

样机. 分别在实验室、典型实验井和随钻测井现场进行了隔声效果的验证. 得到的主要结论和认识如下:

(1) 钻铤波在刻槽隔声体传播过程中,会产生多次反射、散射和透射的声波叠加现象,钻铤波能量衰减形成了隔声阻带,阻带沿钻铤逐渐拓宽并最终达到稳定. 在此阻带中进行随钻声波测量便可达到隔声的目的.

(2) 实验室内利用声波频率扫描方法测量的钻铤波声衰减量最大达到 60 dB,其中衰减量大于 30 dB 的频率范围与理论设计的有效隔声阻带(10～18 kHz)对应良好.

(3) 将实验样机声源的工作频带设计在该阻带之内,在典型的软、硬地层实验中均测量到了信噪比高、相关性好的地层声波信号.

(4) 现场随钻声波测井实验表明:本文设计的刻槽隔声体降低了钻铤直达波的干扰,获得了高质

(C)1994-2023 China Academic Journal Electronic Publishing House. All rights reserved.　http://www.cnki.net

量的地层声波信号和可靠的地层纵波时差,能够满足随钻测井的要求.

致谢 本文工作得到国家自然科学基金和中海油田服务股份有限公司的资助.感谢中海油服刘西恩首席专家、孙志峰高工、仇傲高工、罗瑜林高工、李辉高工、王春艳工程师、李杰工程师、罗博工程师等在现场随钻测井实验方面的支持和帮助.

References

Aron J, Chang S K, Dworak R, et al. 1994. Sonic compressional measurements while drilling. // SPWLA 35th Annual Logging Symposium. Tulsa, Oklahoma: Society of Petrophysicists and Well-Log Analysts.

Asadi M S, Khaksar A, White A, et al. 2015. Wellbore stability analysis in depleted deepwater reservoirs: A case study from Australia. // SPE Annual Technical Conference and Exhibition. Manama, Bahrain: SPE.

Blyth M, Yamamoto H, Pistre V. 2013. Logging while drilling for shallow hazard detection: the challenges of large hole acoustic logging. // SPWLA 19th Formation Evaluation Symposium. Chiba, Japan: Society of Petrophysicists and Well-Log Analysts.

Brown J P, Fox A, Sliz K, et al. 2015. Pre-drill and real-time pore pressure prediction: Lessons from a sub-salt, deep water wildcat well, Red Sea, KSA. // SPE Annual Technical Conference and Exhibition. Manama, Bahrain: SPE.

Izuhara W, Kinoshita T, Yamamoto H. 2013. Dispersion characteristics of leaky compressional mode with LWD sonic tool. // SPWLA 19th Formation Evaluation Symposium of Japan. Chiba, Japan: Society of Petrophysicists and Well-Log Analysts.

Joyce B, Patterson D, Leggett J, et al. 2001. Introduction of a new omni-directional acoustic system for improved real-time LWD sonic logging-tool design and field test results. // SPWLA 42nd Annual Logging Symposium. Houston, Texas: Society of Petrophysicists and Well-Log Analysts.

Kinoshita T, Dumont A, Hori H, et al. 2010. LWD sonic tool design for high-quality logs. // SEG 80nd Annual Meeting. Denver, Colorado: SEG.

Market J. 2007. New broad frequency LWD multipole tool provides high quality compressional and shear data in a wide variety of formations. // SPWLA 48th Annual Logging Symposium. Austin, Texas: Society of Petrophysicists and Well-Log Analysts.

Matuszyk P J, Torres-Verdín C. 2014. Frequency-domain simulation of logging-while-drilling borehole sonic waveforms. *Geophysics*, 79(2): D99-D113.

Mohammed S, Crowe J, Belaud D, et al. 2011. Latest generation logging while drilling sonic tool: Multipole acoustics measurements in horizontal wells from offshore west South Africa. // SPWLA 52th Annual Logging Symposium. Colorado Springs: Society of Petrophysicists and Well-Log Analysts.

Murray D R, Belaud D, Ogawa R, et al. 2014. Deployment of new sonic-while-drilling technology in a large development project in the Middle East: A case study. // Abu Dhabi International Petroleum Exhibition and Conference. Abu Dhabi, UAE: SPE.

Nazlan M F A, Raza T A, Salem S A A, et al. 2015. Azimuthal sonic data enables safe landing in very thin carbonates reservoir of lower cretaceous. // Abu Dhabi International Petroleum Exhibition and Conference. Abu Dhabi, UAE: SPE.

Qiao W X, Chen X L, Du G S, et al. 2002. On performance evaluation of a sound isolator. *Well Logging Technology* (in Chinese), 26(2): 104-106.

Sinha B K, Şimşek E, Asvadurov S. 2009. Influence of a pipe tool on borehole modes. *Geophysics*, 74(3): E111-E123.

Sollie F O. 1999. WL and LWD sonic logging of soft formation—a case study from a deep-water, frontier-area field. // SPWLA 40th Annual Logging Symposium. Oslo, Norway: Society of Petrophysicists and Well-Log Analysts.

Su Y D, Zhuang C X, Tang X M. 2011a. LWD acoustic color mode wave attenuation character research and isolator design. *Chinese J. Geophys.* (in Chinese), 54(9): 2419-2428.

Su Y D, Zhuang C X, Deng L, et al. 2011b. Experimental research on performance evaluation of LWD acoustic isolator. *Well Logging Technology* (in Chinese), 35(5): 402-405.

Su Y D, Tang X M, Liu Y K, et al. 2015a. Extensional—wave stopband broadening across the joint of pipes of different thickness. *The Journal of the Acoustical Society of America*, 138(5): EL447-EL451.

Su Y D, Tang X M, Xu S, et al. 2015b. Acoustic isolation of a monopole logging while drilling tool by combining natural stopbands of pipe extensional waves. *Geophysical Journal International*, 202(1): 439-445.

Tang X M, Dubinsky V, Wang T, et al. 2003. Shear-velocity measurement in the logging-while-drilling environment: Modeling and field evaluations. *Petrophysics*, 44(2): 79-89.

Tang X M, Cheng C H. 2004. Quantitative Borehole Acoustic Methods. Amsterdam: Elsevier.

Tang X M, Lilly D, Petpisit K. 2007. Analysis of LWD acoustic data validates its accuracy. // SPWLA 48th Annual Logging Symposium. Austin, Texas: Society of Petrophysicists and Well-Log Analysts.

Tang X M, Su Y D, Tan B H, et al. 2013. Method and apparatus for a logging while drilling acoustic isolation by using variable thickness drilling collar. Chinese Patent: ZL201110299591.3. 2013-10-30.

Wang H, Tao G, Wang B, et al. 2009. Wave field simulation and data acquisition scheme analysis for LWD acoustic tool. *Chinese J. Geophys.* (in Chinese), 52(9): 2402-2409.

Wang T, Tang X M. 2003. Finite-difference modeling of elastic wave propagation: A nonsplitting perfectly matched layer approach. *Geophysics*, 68(5): 1749-1755.

附中文参考文献

乔文孝, 陈雪莲, 杜光升等. 2002. 隔声体性能评价的方法研究. 测井技术, 26(2): 104-106.

苏远大, 庄春喜, 唐晓明. 2011a. 随钻声波测井钻铤模式波衰减规律研究与隔声体设计. 地球物理学报, 54(9): 2419-2428.

苏远大, 庄春喜, 邓林等. 2011b. 随钻声波测井隔声体性能评价实验研究. 测井技术, 35(5): 402-405.

唐晓明, 苏远大, 谭宝海等. 2013. 一种在钻铤上变径隔声的随钻声波测井方法及装置. 中国发明专利: ZL201110299591.3. 2013-10-30.

王华, 陶果, 王兵等. 2009. 多极子随钻声波测井波场模拟与采集模式分析. 地球物理学报, 52(9): 2402-2409.

(本文编辑 刘少华)

(C)1994-2023 China Academic Journal Electronic Publishing House. All rights reserved. http://www.cnki.net

Geophysical Journal International

Geophys. J. Int. (2015) **202,** 439–445
GJI Marine geosciences and applied geophysics

doi: 10.1093/gji/ggv150

Acoustic isolation of a monopole logging while drilling tool by combining natural stopbands of pipe extensional waves

Yuan-Da Su, Xiao-Ming Tang, Song Xu and Chun-Xi Zhuang

School of Geosciences, China University of Petroleum, Qingdao 266555, *China. E-mail: tangxiam@aliyun.com*

Accepted 2015 April 1. Received 2015 January 15; in original form 2014 November 17

SUMMARY

For extensional wave propagation along a cylindrical pipe, there exists a natural stopband in the frequency range between the first and second modes. This study explores the feasibility and practicality of building a drill collar acoustic extensional-wave isolator by combining the stopbands of pipes of different thicknesses. Numerical modelling shows that this is indeed possible and a stopband of designated width can be obtained using an optimization procedure. Laboratory measurement on an optimized design further verified this concept. The result provides a viable approach for the acoustic isolation design of a logging while drilling acoustic tool.

Key words: Downhole methods; Guided waves; Wave propagation.

1 INTRODUCTION

Acoustic isolation is essential for the design and operation of logging while drilling (LWD) acoustic measurement tools used in oil and gas exploration. In the existing isolation scheme, the drill pipe is periodically cut to create a frequency-domain stopband for the acoustic propagation along the drill pipe (Leggett *et al.* 2001; Kinoshita *et al.* 2010; Su *et al.* 2011). Such scheme, besides its manufacturing cost, can adversely affect the integrity and mechanic strength of the drill collar. Aiming to overcome the shortcoming of the existing isolation techniques, this study proposes a novel approach utilizing the natural stopband of pipe extensional waves and combining the stopbands of pipes of different thicknesses. The result of the combination is a broadened stopband whose width is much larger than that of the individual stopband of each pipe. Making the LWD acoustic measurement within the broadened stopband significantly enhances the acoustic signals for the surrounding formation rocks relative to those from the drill pipe. The new acoustic isolation method not only maintains the mechanic integrity of the drill collar and reduces the manufacture cost, but also obtains an isolation result comparable to that of the existing method.

In what follows, we first describe the natural stopband phenomenon for the pipe extensional waves and its variation characteristics for various pipe thicknesses. We then discuss the concept of forming a broader stopband by combining pipes of different thicknesses. We validate this concept through theoretical analysis and numerical modelling. In the last part, we build a physical model and conduct a laboratory experiment to evaluate the modelling and designated isolation results.

2 THEORY

Elastic wave propagation along cylindrical waveguides such as pipes and rods has been studied by many authors with well-known results (Plona *et al.* 1992; Sinha *et al.* 1992; Hsu *et al.* 1997; Rao & Vandiver 1999). With the rapid development of LWD acoustic technology in the 1990s, there was renewed interest in studying the various pipe wave modes in connection with the LWD measurements, giving rise to many useful LWD applications (Aron *et al.* 1994; Tang *et al.* 2002, 2003; Wang & Tang 2003; Tang & Cheng 2004; Zhu *et al.* 2008; Sinha *et al.* 2009; Guan *et al.* 2013). From these studies it is generally known that the LWD monopole, dipole, and quadrupole measurements will respectively excite the extensional, flexural, and screw wave modes along the drill pipe. In acoustic terminology, the extensional and flexural waves respectively represent the symmetric and antisymmetric particle motion of a cylindrical pipe, and the screw wave exhibits the alternating oblate/prolate motion of the pipe (Ewing *et al.* 1957; Tang & Cheng 2004). Although it has been demonstrated (Tang *et al.* 2002, 2003; Tang & Cheng 2004) that the quadrupole, compared to dipole, is a better technology to measure formation shear velocity and the pipe quadrupole wave can be ignored if the measurement is made below its cut-off frequency, the pipe extensional wave must be suppressed in order to extract formation compressional velocity from the monopole measurement. With this requirement, the groove-cutting technology has been used for the LWD monopole tool (Aron *et al.* 1994; Leggett *et al.* 2001; Kinoshita *et al.* 2010; Su *et al.* 2011; Matuszyk & Torres-Verdín 2014), as described in the literature.

2.1 The natural stopband phenomenon of pipe waves

For a cylindrical pipe, there exist an infinite number of extensional modes along the frequency axis. For the LWD measurement with a steel pipe (see property in Table 1), only the first two or three such modes are encountered in the frequency range of [0–20] kHz. A very important phenomenon is that a stopband exits in the frequency range between the first and second modes. Using the

© The Authors 2015. Published by Oxford University Press on behalf of The Royal Astronomical Society.

Downloaded from http://gji.oxfordjournals.org/ at University of North Dakota on May 23, 2015

Table 1. Parameter values for calculating the stopband phenomenon of pipe waves.

	Vp ($m\,s^{-1}$)	*Vs* ($m\,s^{-1}$)	Density ($g\,cm^{-3}$)	Inner diameter (mm)	Outer diameter (mm)
Pipe	5860	3130	7.85	50	122

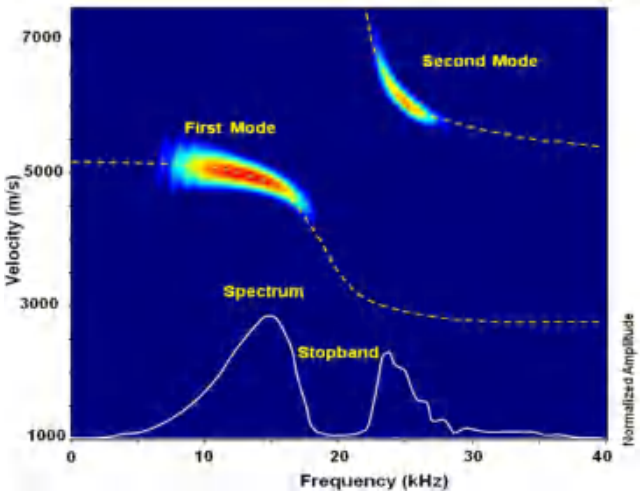


Figure 1. Extensional wave propagation characteristics along a steel pipe immersed in fluid. Wave amplitude spectrum (white line) shows two dominant peaks. The theoretical dispersion curves of the first and second modes (yellow dotted line) are overlain with the VD display of VFC analysis of the array data. A stopband exists in the frequency range between the first and second modes marked by two coherence peaks.

parameters of Table 1. Fig. 1 simulates wave propagation along a steel pipe immersed in fluid. A ring source and an array of receivers are placed around the pipe rim to excite and receive the pipe extensional waves (see Tang & Cheng 2004). The source centre frequency is 18 kHz. The calculated wave amplitude spectrum shows two dominant peaks. A velocity–frequency coherence (VFC) analysis (Tang & Cheng 2004) of the array data reveals the dispersion characteristics of the first and second wave modes, whose peak coherence respectively follows the theoretical dispersion curves of the first and second modes and corresponds to the spectral amplitude peaks very well. The dispersion analysis result shows that the stopband of Fig. 1 occurs in the frequency range between the first and second wave modes.

The location and width of the stopband are controlled by the inner/outer diameter and thickness of the pipe. Fig. 2 illustrates the variation of the stopband as the diameter and thickness change. The wave amplitude spectra were calculated by repeating the calculation of Fig. 1 for a number of source centre frequencies. In fact, the stopband variations are well described by the following formula, obtained by analysing and fitting the data of Fig. 2.

$$f_c = 0.58V_p(d_1 + d_2)$$
$$\Delta f = 0.0318V_p/(d_1 + d_2)^{1.65}, \quad (1)$$

where d_1 and d_2 are inner and outer diameters of the pipe, respectively, and V_p is the compressional velocity. The implication of Fig. 2 is that, if we combine two pipes of different thickness in such a way that their stopbands connect each other, the resulting stopband of the pipe combination will be significantly broadened. Further, by combining pipes of various thicknesses, we may get a stopband of sufficient width. Doing acoustic measurements in this

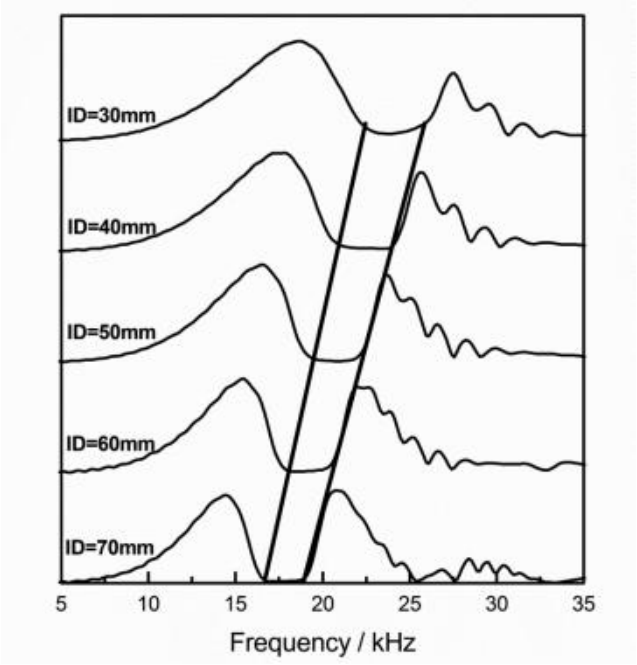


Figure 2. The variation of the stopband as the diameter and thickness change. The centre-frequency and width of the stopband increases with increasing pipe thickness.

band can minimize the pipe wave propagation and obtain the desired formation wave signal.

2.2 Analyses of the combination of pipes of different thickness

We use theoretical analyses and numerical modelling to validate the concept of stopband broadening using the combination of pipes of different thickness. The wave phenomena at the joint of two pipes of different thickness are quite complicated. (Here a welded contact is assumed at the pipe joint.) When a pipe wave impinges onto the joint, wave transmission, reflection, and scattering, etc. will all occur. The benefit of considering only one type of wave mode, that is, the extensional wave, is that the axially symmetric nature of such a joint means that the axially symmetric extensional pipe waves do not mode convert to any non-axially symmetric modes, such as flexural or screw modes. Without going into more detailed theoretical analyses, we simply treat the pipe joint as a linear system because the above-mentioned wave phenomena can all be described by the linear elastic wave theory. For a linear system, if the input wave has a stopband of very low excitation energy, the output from the system, that is, the wave energy transmitted across the pipe joint, will also be low in that frequency band. In other words, the transmitted wave will 'inherit' the stopband of the incident wave. At a sufficient distance away from the joint, which is about one wavelength, the scattering effect of the pipe joint diminishes and the waves are reguided to become extensional waves along the pipe of changed thickness. The inherent stopband across the joint, together with the stopband before the joint, as inherited by the transmitted wave, results in a broadened stopband where the transmitted wave has very low energy.

We substantiate the above analysis using numerical modelling. Still using the same source–receiver parameters for Fig. 1, but with a change of pipe thickness at the middle point between source

Downloaded from http://gji.oxfordjournals.org/ at University of North Dakota on May 23, 2015

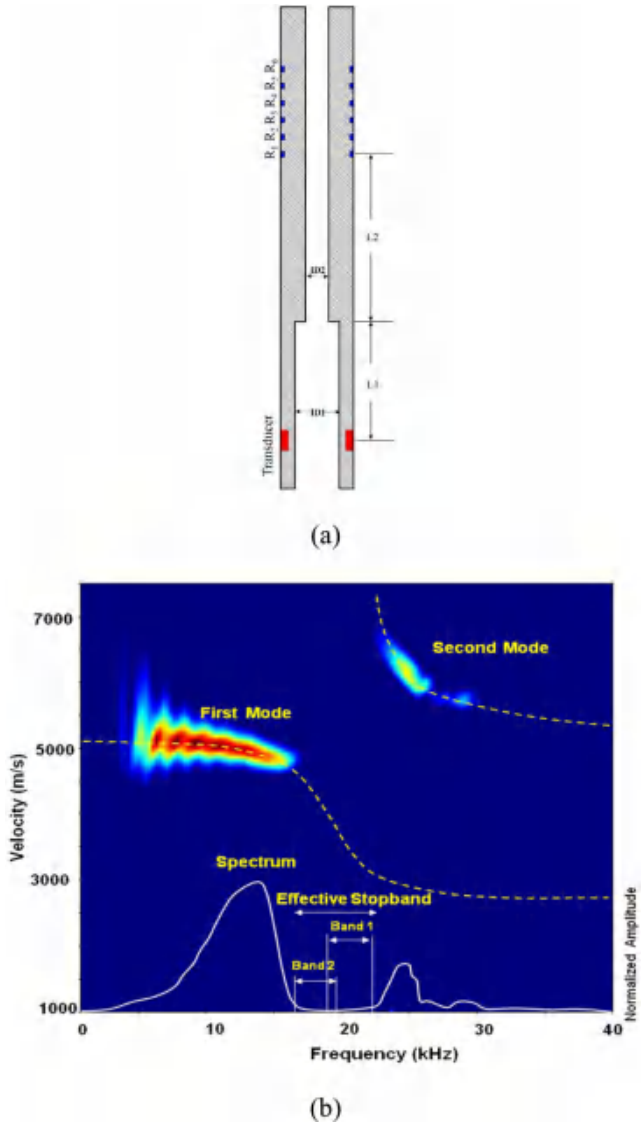


Figure 3. Diagram showing the two-pipe system (a) and the wave propagation simulation result (b). Compared with single pipe result of Fig. 1, the stopband of two-pipe system is indeed broadened.

and receiver one (Fig. 3). Toward the receiver array, the pipe inner diameter remains unchanged (50 mm), towards the source, the inner diameter is changed to 70 mm. A finite difference method (Kessler & Kosloff 1990; Randall *et al.* 1991; He *et al.* 2013) was used for the modelling. The modelling results, after the same analyses as for Fig. 1, are displayed in Fig. 3. The stopband for this two-pipe system, as depicted by the wave amplitude spectrum and VFC coherence peaks, are indeed broadened compared to each individual stopband. In fact, the new stopband width is approximately the sum of the widths of the two bands. The above concept is thus validated for the simple two-pipe system.

Generating the two-pipe system result to a pipe system with multiple joints/intersections of pipes of different thicknesses, one expects that the waves transmitted across these joints/intersections will inherit the stopbands of all these pipes combined. For wave transmission through a linear system, the well-known transmission line analogy can be applied. By this analogy, the transfer function of the pipe combination for the transmitted pipe waves is the product of the transfer function of each individual pipe, as given below:

$$T(f) = \left[\prod_{i=1}^{N} \alpha_i T_i(f)\right] T_{N+1}(f), \tag{2}$$

where α_i is the transmission coefficient at the ith joint of the pipe combination having N joints, T_i is the transfer function of the ith pipe. For a long pipe of sufficient length, the amplitude spectrum of T_i for various pipe thicknesses is shown in Fig. 2, with a well-defined stopband in the spectrum. Our modelling shows that, although the wave characteristics are complicated in the vicinity of the joint, at approximately one wavelength away from it, the pipe extensional wave behaviour dominates. Therefore, the condition for the pipe combination is that the distance from source (receiver) to the first (last) joint, and the length of each pipe in between should be longer than the dominant wavelength.

Eq. (2) suggests that, for the T_i function of each pipe containing a stopband, if we select the pipe parameters in such a way that the high-frequency end of one pipe's stopband overlaps with the low-frequency end of another pipe's stopband, we can form a combined stopband of sufficient width to meet the requirement of the LWD acoustic measurement. The numerical modelling in the following proves this concept and validates the transmission line analogy of eq. (2).

2.3 Pipe parameter selection using optimization

For the pipe wave isolation design of an LWD acoustic system, the pipe parameters are best selected using an optimization procedure. Given source–receiver spacing and frequency range of acoustic measurement, we first select the number of pipe joints. For example, if the source–receiver spacing is 2 m, the measurement frequency range is 10–20 kHz, the longest wavelength would then be about 0.5 m for steel pipes, and the maximum allowable number of joints is then 3. The parameters to be determined are then the thickness of each pipe, source-to-first joint distance, and receiver-to-last joint distance. The optimization is done by minimizing the pipe wave energy, which is proportional to the wave's power spectrum, in the measurement frequency range for entire receiver array.

$$E(d_1, \ldots, d_N, L_1, \ldots, L_N) = \sum_{m=1}^{M} \int_{\omega_1}^{\omega_2} [P(\omega; d_1, \ldots, d_N, L_1, \ldots L_N)]^2 \, \mathrm{d}\omega, \tag{3}$$

where P is the wave power spectrum; ω_1 and ω_2 are the low- and high-frequency end of the designated stopband, respectively; N is number of pipes and M is number of receivers in array; d_n and L_n $(n = 1, \ldots, N)$ are the inner diameter and length of the ith pipe. The parameter could also be constrained to maintain the minimum thickness of the pipe to satisfy the tool strength requirement. These parameters are adjusted to minimize the objective function of eq. (3). The forward modelling for the multiple pipe system is calculated using the finite difference method. For cylindrical symmetry, the modelling can be done efficiently to allow parameter iteration through the optimization process. The parameter values that minimizes eq. (3) are output as the optimum design parameters.

Fig. 4 shows an example of the optimum pipe wave isolation design and the resulting stopband, where the wave modelling parameters are the same as those used for Figs 1 and 2. In fact, the outer diameter of these models is the minimum size of the drill pipe use in the petroleum industry. The optimized pipe shape is shown

Downloaded from http://gji.oxfordjournals.org/ at University of North Dakota on May 23, 2015

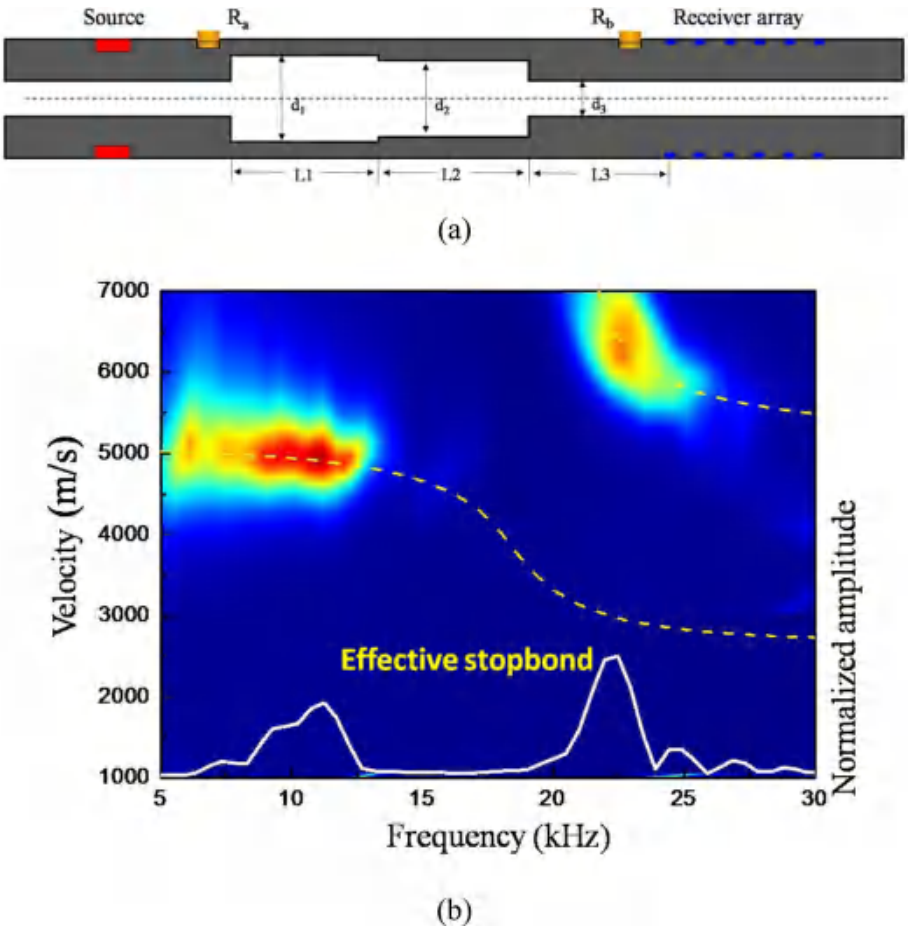


Figure 4. Optimized shape of pipe combination (a) and the resulting stopband (b). The model in (a) has an outer diameter of 128 mm. Other specifications for the model are: $d_1 = 98$ mm, $d_2 = 82$ mm, $d_3 = 48$ mm, $L_1 = 1.12$ m, $L_2 = 0.6$ m, $L_3 = 0.5$ m.

in Fig. 4(a), with the specifications of the model given in the figure caption. Fig. 4(b) shows a well-defined stopband for this optimized system, which is much broadened compared to the stopband of each individual pipe (e.g. see Fig. 2). This theoretical design example validates our concept of LWD acoustic isolation by combining multiple pipes of different thicknesses. A laboratory experiment has also been conducted to verity the practicality of this design principle.

3 LABORATORY EXPERIMENTAL VERIFICATION

To verify the above design principle in the laboratory, we built a physical model using the optimized shape and specifications shown in Fig. 4(a). A cylindrical transmitter and an array of receivers were placed on the rim of the pipe system, with source–receiver spacing of 3 m. To test the transmitted wave characteristics of the pipe combination, we used an impulsive source of centre frequency of 15 kHz and compare the theoretically modelled (upper waveform) and measured (lower waveform) waves of receiver 1 in Fig. 5. The theoretical and experimental waveforms compare very well. Both waveforms show the characteristics of a high frequency wave riding on a low-frequency wave, indicating that the frequency content between the low- and high-wave frequencies is lost after transmission through the system with a stopband. To analyse the stopband of the physical model, we utilized a frequency-swip technique. A narrow-band chirp signal was used to excite the system, by sweeping the signal centre frequency from 4 to 28 kHz, at a 1 kHz increment. For comparison, the signals before and after transmission across the system are recorded for the various sweep frequencies.

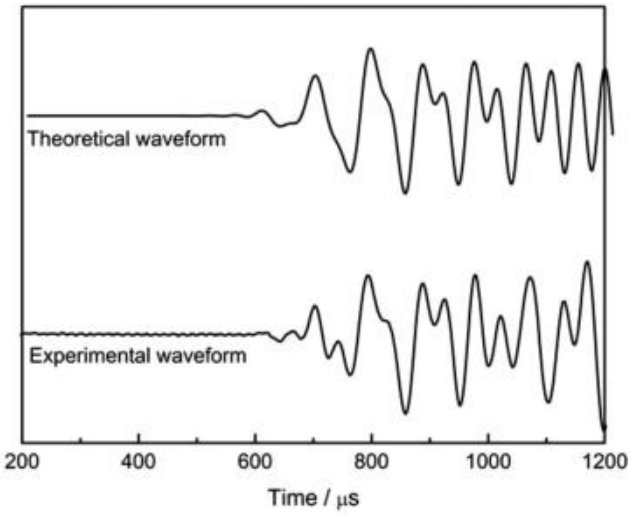


Figure 5. Comparison of modelled (upper waveform) and measured (lower waveform) waves transmitted across the pipe combination system.

Downloaded from http://gji.oxfordjournals.org/ at University of North Dakota on May 23, 2015

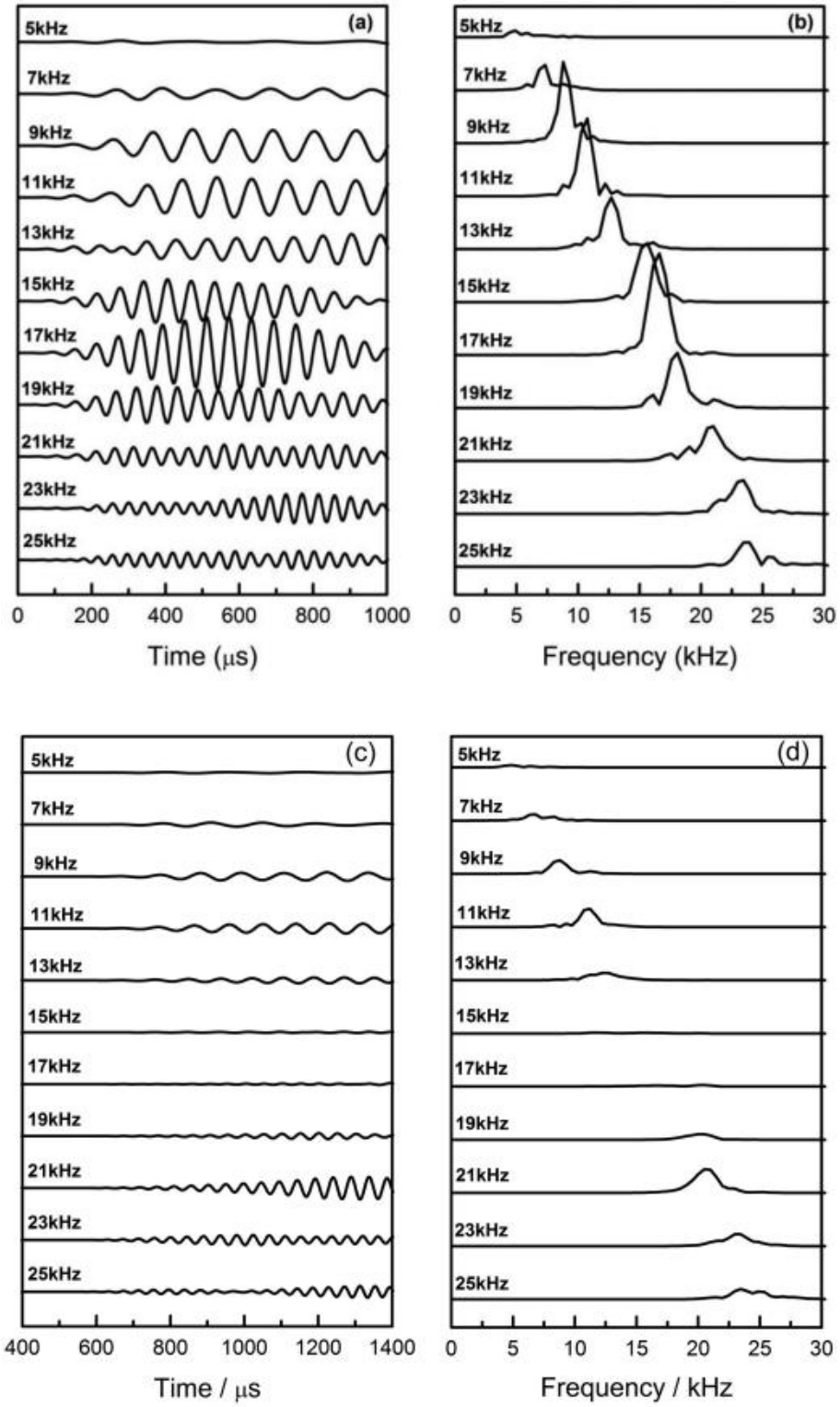


Figure 6. Sweep signals (left-hand panel) and spectra (right-hand panel) before (a and b) and after (c and d) transmission across the pipe combination system.

The receiver locations are respectively marked as R_a and R_b in Fig. 4(a).

Figs 6(a) and (b) show, respectively, the sweep signal and its amplitude spectrum for the sweep frequencies from 5 to 25 kHz for the receiver close to source. Figs 6(c) and (d) are the signals and spectra of the receiver across the pipe system. The pipe wave spectra near the source have significant amplitudes for all frequencies, the amplitude variation being mainly due to the frequency response of the transmitter source. In contrast, the wave spectra across the pipe system shows a marked stopband in the frequency range of

Downloaded from http://gji.oxfordjournals.org/ at University of North Dakota on May 23, 2015

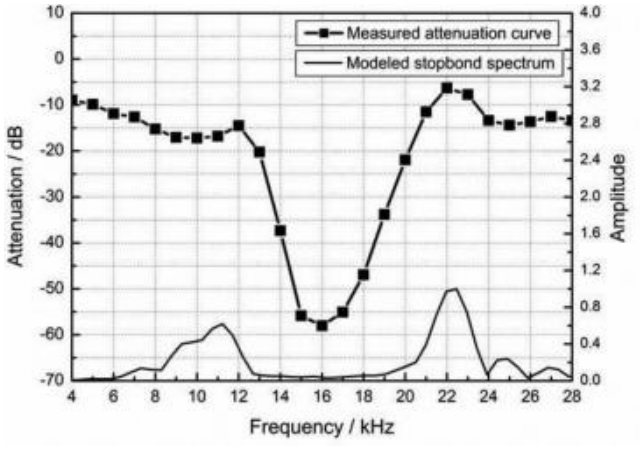


Figure 7. Measured stopband attenuation (upper curve with markers) compared with the modelled stopband spectrum (lower curve) for the pipe combination system.

13–19 kHz. From the two sets of frequency spectra, wave attenuation across the multiple-pipe system can be calculated using

$$Att = 20 \log \left(\frac{A_b}{A_a} \right), \quad (4)$$

where A with subscripts *b* and *a* denotes the wave amplitude before and after transmission across the pipe system, respectively. The experimental attenuation data of the measured frequency points (curve with markers) are plotted in conjunction with the theoretically calculated wave spectrum with the stopband (lower curve) in Fig. 7. The frequency band of high attenuation corresponds with the theoretical stopband quite well, with the high attenuation value of the centre band reaching 60 dB. Theory and experiment are in good agreement.

4 NUMERICAL SIMULATION OF LWD MEASUREMENT

To evaluate the performance of the optimized acoustic isolation design in Fig. 4, we conduct a numerical simulation for the LWD condition. The model is placed in a borehole of 0.18 m diameter, concentric with the borehole axis; the inner chamber and outer annulus are filled with water whose density and acoustic velocity are 1 g cm^{-3} and 1500 m s^{-1}, respectively. The homogeneous, isotropic formation surrounding the borehole has a density of 2.3 g cm^{-3} and compressional (V_p) and shear (V_s) velocities of 3500 and 2000 m s^{-1}, respectively. The finite difference technique, as used in previous modelling, is used for the simulation. To generate signals within the stopband of the isolator, a band-limited acoustic source is used. The source centre frequency is 16 kHz and band width is 3 kHz, corresponding to the stopband shown in Fig. 4.

Fig. 8 shows the simulated waveforms for a receiver array of 0.2 m spacing placed along the rim of the collar (Fig. 4a). Source to receiver distance is 3 m. For comparison, the waveforms with (thick solid curve) and without (thin curve) the isolator were calculated. Without acoustic isolation, the collar extensional wave following its arrival time (line across array) is clearly identified. Trailing the collar wave is the formation compressional wave, as indicated by a line across array. (We purposely choose a moderately slow V_p in order to show the collar wave.) When the isolator is placed between source and the receiver array (Fig. 4a), the collar wave is largely eliminated and the first arrival is the formation compressional wave.

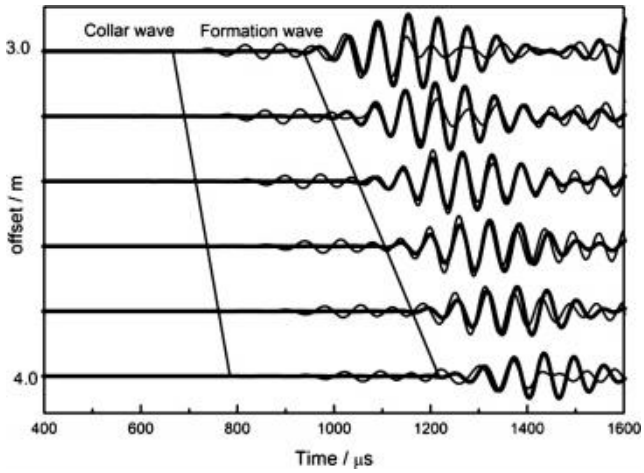


Figure 8. Simulated array waveforms for the LWD configuration. The waveforms were calculated respectively with (thick curve) and without (thin curve) the isolation design. The lack of the collar wave in the former waveforms shows the effectiveness of the design.

The simulation result shows that the optimized isolator design is quite effective in cancelling the collar wave within the designated stopband.

5 CONCLUSION

The low wave amplitude stopband of a pipe extensional wave is a very useful natural phenomenon that can be utilized to design an acoustic isolator for a monopole LWD acoustic tool. We demonstrated that, when a pipe wave incidents onto another pipe of different size, the transmitted pipe wave possesses the stopbands of both pipes. This enables us to design an isolator of designated stopband using a multiple-size pipe system. Further, by using an optimization procedure to select the pipe parameters, an optimum design can be obtained. The acoustic isolation design was verified by a laboratory experiment and by numerical simulation in the LWD condition. The result of this work provides a new approach for LWD acoustic isolation design.

ACKNOWLEDGEMENTS

This work is supported by the National Natural Science Foundation of China (grant nos 41204070, and 41474092).

REFERENCES

Aron, J., Chang, S.K., Dworak, R., Hsu, K., Lau, T., Masson, J.P. & Plona, T.L., 1994. Sonic compressional measurements while drilling, in *Proceedings of the SPWLA 35th Annual Logging Symposium*, Society of Petrophysicists and Well-Log Analysts.

Ewing, W.M., Jardetzky, W.S. & Press, F., 1957. *Elastic Waves in Layered Media*, McGraw-Hill.

Guan, W., Hu, H. & Zheng, X., 2013. Theoretical simulation of the multipole seismoelectric logging while drilling, *Geophys. J. Int.*, **195,** 1239–1250.

He, X., Hu, H. & Wang, X., 2013. Finite difference modelling of dipole acoustic logs in a poroelastic formation with anisotropic permeability, *Geophys. J. Int.*, **192,** 359–374.

Hsu, C., Kostek, S. & Johnson, L., 1997. Tube waves and mandrel modes: experiment and theory, *J. acoust. Soc. Am.*, **102,** 3277–3289.

Kessler, D. & Kosloff, D., 1990. Acoustic wave propagation in 2-D cylindrical coordinates, *Geophys. J. Int.*, **103,** 577–587.

Downloaded from http://gji.oxfordjournals.org/ at University of North Dakota on May 23, 2015

Kinoshita, T., Dumont, A., Hori, H., Sakiyama, N., Morley, J. & Garcia-Osuna, F., 2010. LWD sonic tool design for high-quality logs, in *Proceedings of the SEG Annual Meeting*, Society of Exploration Geophysicists.

Leggett, J.V., Dubinsky, V., Patterson, D. & Bolshakov, A., 2001. Field test results demonstrating improved real-time data quality in an advanced LWD acoustic system, in *Proceedings of the SPE Annual Technical Conference and Exhibition*, Society of Petroleum Engineers, Paper 71732.

Matuszyk, P.J. & Torres-Verdín, C., 2014. Frequency-domain simulation of logging-while-drilling borehole sonic waveforms, *Geophysics*, **79,** D99–D113

Plona, T.J., Sinha, B.K., Kostek, S. & Chang, S.K., 1992. Axisymmetric wave propagation in fluid-loaded cylindrical shells. II: theory versus experiment, *J. acoust. Soc. Am.*, **92,** 1144–1155.

Randall, C.J., Scheibner, D.J. & Wu, P.T., 1991. Multipole borehole acoustic waveforms: synthetic logs with beds and borehole washouts, *Geophysics*, **56,** 1757–1769.

Rao, V.R. & Vandiver, J.K., 1999. Acoustics of fluid-filled boreholes with pipe: guided propagation and radiation, *J. acoust. Soc. Am.*, **105,** 3057–3066.

Sinha, B.K., Plona, T.J., Kostek, S. & Chang, S.K., 1992. Axisymmetric wave propagation in fluid-loaded cylindrical shells. I: theory, *J. acoust. Soc. Am.*, **92,** 1132–1143.

Sinha, B.K., Simsek, E. & Asvadurov, S., 2009. Influence of a pipe tool on borehole modes, *Geophysics*, **74,** E111–E123.

Su, Y.D., Zhuang, C.X. & Tang, X.M., 2011. LWD acoustic collar mode wave attenuation character research and isolator design, *Chin. J. Geophys.*, **54,** 690–701.

Tang, X.M. & Cheng, C.H.A., 2004. *Quantitative Borehole Acoustic Methods*, Elsevier Science Publishing.

Tang, X.M., Dubinsky, V., Wang, T., Bolshakov, A. & Patterson, D., 2002. Shear-velocity measurement in the logging-while-drilling environment: modeling and field evaluations, in *Proceedings of the SPWLA 43th Annual Logging Symposium*, Society of Petrophysicists and Well-Log Analysts.

Tang, X.M., Patterson, D., Dubinsky, V., Harrison, C.W. & Bolshakov, A., 2003. Logging-while-drilling shear and compressional measurements in varying environments, in *Proceedings of the SPWLA 44th Annual Logging Symposium*, Society of Petrophysicists and Well-Log Analysts.

Wang, T. & Tang, X., 2003. Finite-difference modeling of elastic wave propagation: a nonsplitting perfectly matched layer approach, *Geophysics*, **68,** 1749–1755.

Zhu, Z., Toksöz, M.N., Rao, R. & Burns, D.R., 2008. Experimental studies of monopole, dipole, and quadrupole acoustic logging while drilling (LWD) with scaled borehole models, *Geophysics*, **73,** E133–E143.

Downloaded from http://gji.oxfordjournals.org/ at University of North Dakota on May 23, 2015

Extensional-wave stopband broadening across the joint of pipes of different thickness

Yuanda Su, Xiaoming Tang,[a] Yukai Liu, Song Xu, and Chunxi Zhuang
School of Geosciences, China University of Petroleum, Qingdao, China
syuanda@sina.com, tangxiam@aliyun.com, liuyukai.1008@163.com, xusongupc@sina.com, zhuangchunxi@sina.com

Abstract: The stopband of pipe extensional waves is an interesting natural phenomenon. This study demonstrates an important extension of this phenomenon. That is, the stopband can be effectively broadened by transmitting the waves across the joint of pipes of different thickness. The theoretical and experimental results reveal the detailed process of stopband forming along the pipe and the band broadening across the pipe joint. The result can be utilized to provide a method for logging while drilling acoustic isolation design.

© 2015 Acoustical Society of America
[CC]

Date Received: May 22, 2015 Date Accepted: October 22, 2015

1. Introduction

Acoustic logging while drilling (LWD) is used to obtain real-time compressional and shear velocities for oil-gas exploration applications. In the measurement of compressional wave velocity of an earth formation, pipe extensional waves are inevitably excited along the drill pipe, which must be suppressed or isolated in order to properly measure the formation wave signal.[1,2] Although groove-cutting techniques can effectively isolate the pipe waves within a designated stopband,[1,3] cutting grooves on the drill pipe adversely affects the mechanical strength of the drill string. We propose a new concept of pipe wave isolation using the natural stopband of pipe waves and its broadening across the joint of pipes of different thickness.

Elastic wave propagation along cylindrical pipes has been extensively studied by many authors.[4–8] It is well-known that an axisymmetric monopole source excites extensional waves along the pipe and an infinite number of such wave modes exist along the frequency axis.[4,7] For practical applications, only the first two or three such modes are used. A very important phenomenon is that a stopband of very low wave amplitude exists in the frequency range between the first and second modes, and the location and width of the stopband vary with the inner and outer diameter and thickness of the pipe.[2,3] To demonstrate this stopband phenomenon and its variation characteristics, we simulate extensional wave propagation along a steel pipe. The compressional velocity, shear velocity, and density of the pipe are 5860 m/s, 3130 m/s, and 7850 kg/m^3, respectively. The pipe's outer diameter is fixed at 122 mm, and the inner diameter is varied from 20 to 70 mm. An axisymmetric ring source is used to excite the extensional wave propagation and a receiver is placed 3 m away from the source to record the wave signal. We used a Ricker wavelet for the source signal. In the modeling, the source frequency is successively varied from 22 to 18 kHz corresponding to the pipe inner diameter change from 20 to 70 mm. Figure 1 illustrates the simulated wave amplitude spectrum for the varying pipe thickness, with a clearly identified stopband of very low amplitude. The spectral peaks below and above the stopband coincide with the dominant frequency excitation range of the first and second extensional wave modes, respectively. It is clear that the location and width of the stopband are controlled by the thickness of the pipe. The important implication of the result in Fig. 1 is that, if one connects two concentric pipes of different thickness in such a way that their stopbands connects each other, the resulting stopband of the combined system will be significantly broadened. Furthermore, by connecting concentric pipes of various thicknesses, one may get a stopband of sufficient width. This concept can be used to provide a very useful method for acoustic isolation design. The new acoustic isolation method avoids cutting grooves on the pipe and therefore maintains the strength of the drill string.

[a]Author to whom correspondence should be addressed.

08 October 2026 08:25:20

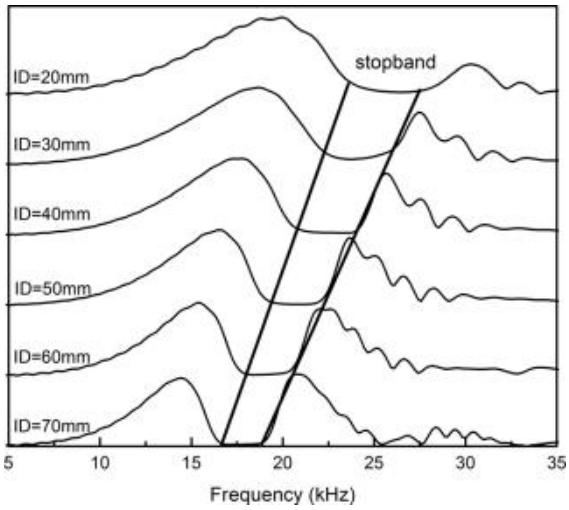


Fig. 1. The variation of extensional-wave stopband with varying inner diameter (ID) of a pipe of fixed outer diameter.

2. An analysis of stopband variation across pipe joint

A theoretical analysis is given here to evaluate the above concept of stopband broadening using the connection of pipes of different thicknesses. (Here, a welded contact is assumed at the joint of two pipes.) When a pipe extensional wave impinges onto the pipe joint, wave reflection, transmission, and scattering, etc., will all occur. Although the wave phenomena at the pipe joint are quite complicated, a simple theoretical analysis using the transmission line analogy of a linear system can be applied to explain the stopband broadening phenomenon. We treat the two-pipe system as a linear system because wave reflection, transmission, and scattering, etc., can all be described by the linear elastic wave theory. For a linear system, if the input (i.e., the incident) wave has a stopband of very low excitation energy, the output from the stopband, i.e., the wave energy transmitted across the pipe joint, will also be low in that frequency band. That is, the transmitted wave will "inherit" the stopband of the incident wave. At some distance away from the joint, the scattering effect of the pipe joint diminishes and the transmitted waves are reguided to become extensional waves along the pipe of changed thickness. The natural stopband for the pipe of changed thickness, together with the stopband before the joint, as inherited by the transmitted wave, result in a broadened stopband where the transmitted wave has very low energy. In terms of the transmission line analogy, the transfer function of the pipe combination for the transmitted pipe wave can be described as follows:

$$A(f) = aA_1(f) \cdot A_2(f), \tag{1}$$

where a is the transmission coefficient at the joint, $A_1(f)$ and $A_2(f)$ are the transfer function of the left pipe and right pipe, respectively. For a single pipe transfer function $A_1(f)$ or $A_2(f)$, its amplitude spectrum is shown in Fig. 1, with a well-defined stopband. The implication of Eq. (1) is that, if the stopbands of the two pipes connect each other, the resulting stopband of the pipe combination will be the superposition of the two stopbands, which is much broader than each individual stopband. A finite difference waveform modeling method[9,10] was used to test this concept by simulating wave propagation in the system.

3. Numerical simulation

We demonstrate the above described stopband broadening phenomenon using numerical modeling. Figure 2 shows a two-pipe system model and the source-receiver configuration. The left and right pipes have an inner diameter of 70 and 50 mm, respectively. They have the same outer diameter of 122 mm. A ring source of 18 kHz center frequency is used to excite wave propagation in the system. The distance from source to the pipe joint is 1.5 m. A receiver array is placed along the pipe system to record the wave signal. The recorded wave amplitude spectrum array is shown in Fig. 3 for the varying transmitter to receiver (TR) distances along the pipe. The wave amplitude spectrum variation across the pipe joint is now elaborated. Close to the source (TR = 0.3 m), the wave spectrum resembles the source wave spectrum. As the TR

08 October 2026 08:25:20

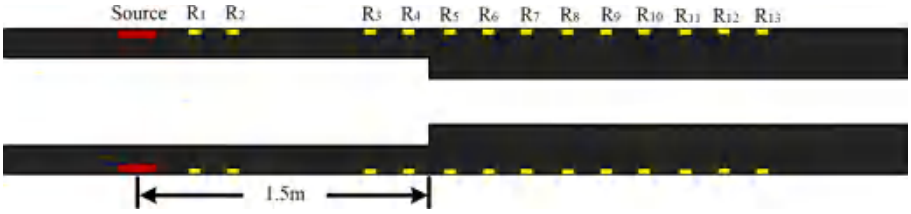


Fig. 2. (Color online) A two-pipe system model and the source-receiver configuration. The left and right pipes have an inner diameter of 70 and 50 mm, respectively, with a common outer diameter of 122 mm.

distance increases, a stopband begins to form. The stopbands denoted by band 1 and band 2, as taken from Fig. 1 for the two different inner diameters, are indicated in the figure. Near the pipe joint, the wave stopband is close to, but appreciably different from, its counterpart in Fig. 1. The difference may be due to the interference from wave reflection and scattering from the pipe joint. After transmission across the joint (TR $>$ 1.5 m), a stopband corresponding to band 1 is formed, but the wave spectrum still contains the wave scattering effect from the joint. As the scattering effect diminishes with increasing distance away from the joint, the stopband corresponding to band 2 begins to take shape. At about 0.5 m away from the joint, a stable stopband is formed. Thereafter, the stopband appears invariant with increasing distance. As expected from the previous theoretical analysis, the width of this stopband is approximated the sum of the widths of band 1 and band 2. The numerical simulation results, together with demonstrated wave phenomenon, validate our concept of stopband broadening using pipes of different thicknesses.

4. Physical experiment verification

A physical model was built to verify the simulated wave phenomenon and further validates the stopband broadening concept. The two-pipe system model, made of two steel pipes, has the same physical dimension specified in Fig. 2. The measurement system in conjunction with the physical model is shown in Fig. 4(a). A cylindrical transmitter in connection with a signal generator is placed at the rim of the model to generate wave signal in the model. An 18 kHz burst signal is used to actuate the transmitter. Four

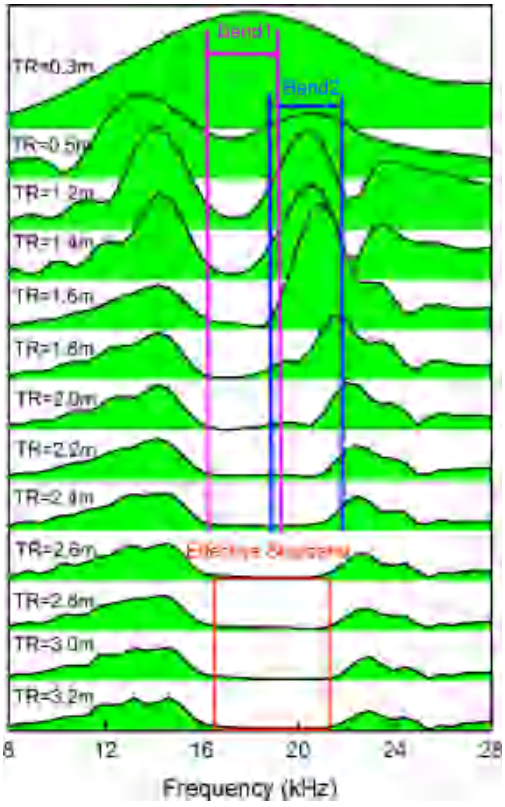


Fig. 3. (Color online) Variation of wave amplitude spectrum across pipe joint illustrating the stopband forming and broadening phenomenon.

08 October 2026 08:25:20

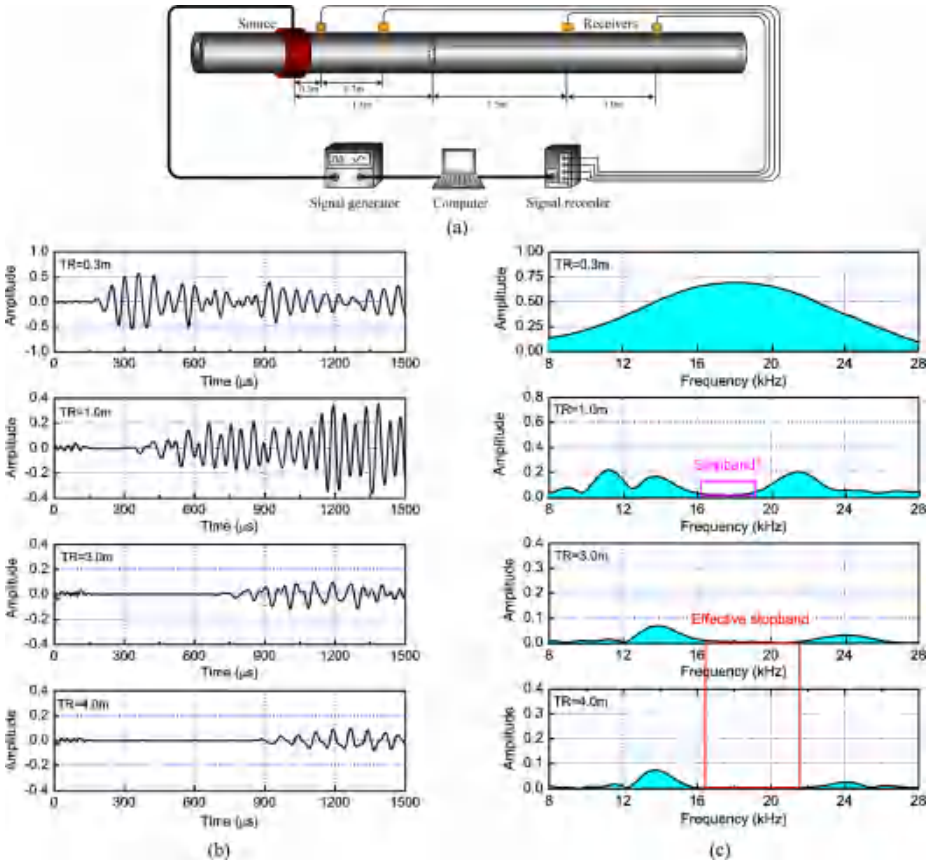


Fig. 4. (Color online) The physical model and measurement system (a) and the measured pipe waves (b) and their amplitude spectra (c) for the four receiver stations.

receivers are successively placed at TR = 0.3, 1, 3, and 4 m away from the source to record the wave signal. The signal is sent to a signal recorder, where the wave data are acquired for further analysis. The measurement system is controlled by a computer.

The recorded wave signal and its amplitude spectrum at the four receiver stations are, respectively, displayed in Figs. 4(b) and 4(c). The experimental result is compared with its simulated counterparts for explanation. For the signal recorded near the transmitter (TR = 0.3 m), the wave signal spectrum is similar to the source signal spectrum, showing a peak around 18 kHz. At TR = 1 m distance, a stopband for the left pipe can be clearly identified. The displayed wave spectrum characteristics are very similar to the numerical modeling results of Fig. 3. Across the pipe joint, at TR = 3 m from the source, a stopband of broadened width is formed. The width of the effective stopband is consistent with the modeling result shown in Fig. 3, which is approximately the sum of the stopband widths of the left and right pipes. At TR = 4 m from the source, the effective stopband characteristics are almost the same as those at TR = 3 m. The experimental results are in good agreement with the modeling results.

5. Discussion and conclusion

The stopband of pipe extensional waves and its broadening across the joint of pipes of different thicknesses are an interesting and important natural phenomenon. We have demonstrated that, when a pipe extensional wave impinges onto another pipe of different thickness, the transmitted wave possesses an effective stopband consisting of the stopbands of both pipes. The stopband broadening phenomenon has a very useful practical application. For example, for a logging while drilling acoustic measurement tool built on drill pipes, the demonstrated natural wave phenomenon can be utilized for designing an acoustic isolator of the measurement system.

Acknowledgments

This work is supported by the National Natural Science Foundation of China (Grant Nos. 41204070 and 41474092).

08 October 2026 08:25:20

References and links

[1]J. Aron, S. K. Chang, R. Dworak, K. Hsu, T. Lau, J-P. Masson, J. Mayes, G. McDaniel, C. Randall, S. Kostek, and T. J. Plona, "Sonic compressional measurements while drilling," in SPWLA 35th Annual Logging Symposium, Tulsa, OK (June 1994), paper SS.

[2]X. M. Tang and A. Cheng, Quantitative Borehole Acoustic Methods (Elsevier Science Publishing, Amsterdam, 2004), Chap. 6.

[3]Y. D. Su, C. X. Zhuang, and X. M. Tang, "LWD acoustic collar mode wave attenuation character research and isolator design," Chin. J. Geophys. 54(5), 690–701 (2011).

[4]T. J. Plona, B. K. Sinha, S. Kostek, and S. K. Chang, "Axisymmetric wave propagation in fluid-loaded cylindrical shells. II: Theory versus experiment," J. Acoust. Soc. Am. 92(2), 1144–1155 (1992).

[5]D. S. Drumheller and S. D. Knudsen, "The propagation of sound waves in drill strings," J. Acoust. Soc. Am. 97(4), 2116–2125 (1995).

[6]V. R. Rao and J. K. Vandiver, "Acoustics of fluid-filled boreholes with pipe: Guided propagation and radiation," J. Acoust. Soc. Am. 105(6), 3057–3066 (1999).

[7]H. T. Pan, K. Koyana, and Y. Usui, "Experimental and numerical investigations of axisymmetric wave propagation in cylindrical pipe filled with fluid," J. Acoust. Soc. Am. 113(6), 3209–3214 (2003).

[8]B. K. Sinha, E. Simsek, and S. Asvadurov, "Influence of a pipe tool on borehole modes," Geophysics 74(3), E111–E123 (2009).

[9]Q. H. Liu, E. Schoen, F. Daube, C. Randall, H. L. Liu, and P. Lee, "A three-dimensional finite difference simulation of sonic logging," J. Acoust. Soc. Am. 100(1), 72–79 (1996).

[10]T. Wang and X. Tang, "Finite-difference modeling of elastic wave propagation: A nonsplitting perfectly matched layer approach," Geophysics 68(5), 1749–1755 (2003).

08 October 2026 08:25:20

苏远大,庄春喜,唐晓明. 随钻声波测井钻铤模式波衰减规律研究与隔声体设计. 地球物理学报,2011,**54**(9):2419～2428,DOI:10.3969/j.issn.0001-5733.2011.09.026

Su Y D, Zhuang C X, Tang X M. LWD acoustic color mode wave attenuation character research and isolator design. *Chinese J. Geophys.* (in Chinese), 2011, **54**(9):2419～2428, DOI:10.3969/j.issn.0001-5733.2011.09.026

随钻声波测井钻铤模式波衰减规律研究与隔声体设计

苏远大,庄春喜,唐晓明

中国石油大学(华东)地球科学与技术学院,青岛 266555

摘 要 随钻声波测井技术近年来发展很快,这门技术的关键技术之一是随钻仪器的隔声设计,以保证在随钻条件下有效地测量地层的声波信号.针对普遍采用的刻槽隔声技术,本文利用三维有限差分弹性波场模拟对钻铤刻槽前、后的声波响应进行了数值模拟和理论研究.通过模拟结果的理论分析给出了钻铤波固有阻带分布规律与钻铤尺寸关系和钻铤波衰减频段与刻槽宽度、深度的关系.在此基础上,设计了一种随钻声波测井隔声体结构,给出了理论声衰减曲线和典型地层井孔中的响应特征.现场实验井测试结果表明,本文设计的隔声体结构有效地消除了钻铤直达波的干扰,能够测量到高质量地层纵波的波形和时差.

关键词 隔声体,钻铤模式波,声衰减,有限差分,随钻声波

DOI:10.3969/j.issn.0001-5733.2011.09.026 **中图分类号** P631 **收稿日期** 2010-11-16,2011-09-01 收修定稿

LWD acoustic color mode wave attenuation character research and isolator design

SU Yuan-Da, ZHUANG Chun-Xi, TANG Xiao-Ming

School of Geosciences & Technology, China University of Petroleum, Qingdao 266555, *China*

Abstract The acoustic logging while drilling (LWD) technology has undergone a rapid development in recent years. A key technology of the LWD acoustic measurement is the design of an acoustic isolator to suppress acoustic propagation along the drill pipe, such that the acoustic signals from formation can be effectively measured under the LWD conditions. In order to optimize the "groove cutting" technique commonly used for the LWD isolator design, we apply a 3D finite-difference elastic-wave modeling technique to simulate and analyse the acoustic response of a drill pipe before and after cutting grooves. Analyses of the simulation results reveal the relationship between in the collar's stopband characteristics (suches as center frequency and width) and collar size, and that between collar wave attenuation and the width and depth of grooves. Based on the results, a new-type LWD acoustic isolator structure is designed, and the theoretical acoustic attenuation curve and the borehole response characteristics for typical soft and hard formation conditions are obtained. The field experiment well test results indicate that an LWD acoustic tool with the new-type acoustic isolator can suppress the interfere of collar wave and measure a high quality formation compressional-wave data and slowness.

基金项目 国家高技术研究发展计划(863)课题(2007AA6Z232),国家油气重大专项(2011ZX05020－002),中国石油大学(华东)"青年教师人才建设工程"资助.

作者简介 苏远大,男,1978 年生,讲师,中国石油大学(华东)博士研究生,主要从事声波测井理论、方法及应用研究. E-mail:syuanda@sina.com

Keywords Isolator, Collar mode wave, Attenuation, Finite difference, LWD acoustic

1 引 言

声波测量为了解地下储层岩性、流体性质和井周地层性质等提供了非常有用的信息.声波测井是用来评价储集层油气存在和指导油田安全生产等的主要测量手段之一[1~6].例如,在岩石力学分析中,声波资料能够提供孔隙压力、岩石强度、地层侵入、地应力方位和大小等信息[5].在岩石物理分析中,声波资料能够用来评价地层岩性、孔隙度和识别孔隙流体类型[6].近年来,为节省钻井架占用时间、实时判断钻井效率和风险管理,随钻测井技术得到快速发展[7].实时的随钻声波测量能够为井壁稳定性分析、最佳钻井、孔隙压力预测和地震标定等提供及时的数据[8].

随钻测井在非常恶劣的环境(扭曲、撞击和震动等)下工作,随钻声波测量装置必须安装在高强度的厚壁钻铤上,为沿着钻铤传播的声波提供了良好的波导.这种波称钻铤模式仪器直达波,它对拟测的地层信号形成极大干扰.因此,随钻声波测井仪器的隔声体设计至关重要.随钻单极子声源激发的钻铤模式波幅度往往大于地层纵波的幅度,且相干性极强,必须经过压制处理才能测量到地层纵波(Tang and Cheng[1],2004).比较幸运的是,钻铤模式波在频域上存在一个阻带(大约有 2~3 kHz 的带宽),这个阻带存在的频率范围大约是在 10~20 kHz,具体频率位置由钻铤尺寸所决定(Sinha and Plona et al[9,10].,1992; Rama Rao and Vandiver[11] 1997; Tang and Cheng[1],2004).回顾电缆声波测井仪器的发展历史,仪器直达波均是通过在发射声源和接收器之间的壳体上加工狭缝和刻槽等手段来消除的.随钻声波测井隔声体设计也可以利用在钻铤上周期性地切割凹槽来有效地衰减钻铤波或拓宽钻铤波的阻带.目前,针对声波测井三维问题的理论研究主要是利用有限元和有限差分等数值模拟方法[12~22].闫向宏等[23]利用二维有限元模拟研究了刻槽尺寸和结构对钻铤波传播规律的影响.杨勇等[24]利用有限差分模拟了三种周期性凹槽结构的随钻声波测井隔声体的隔声效果,并分别计算了不同结构隔声体在井孔中的响应特征.王华等[25]利用有限差分系统研究了随钻多极子波的响应特征,提出了用信号处理的手段消除钻铤波的干扰.以上研究工作均未给出实验室和现场资料的验证结果.Leggett 等[26]和 Tang 等[27]曾报道过一种周期刻槽式隔声体设计可以获得 40 dB 的钻铤波衰减.Tang[28]等和 Kinoshita[29]等分别报道了贝克休斯和斯伦贝谢公司设计的新型随钻声波隔声体的现场测试效果.上述公司的新型随钻声波测井隔声体是在大量有限差分数值模拟和实验测试研究基础上设计的,与原有隔声体相比钻铤模式波基本被衰减掉,地层纵波和斯通利波波形质量都非常好.

本文用三维有限差分程序数值模拟了刻槽前、后随钻声波测井钻铤模式波波形.给出了钻铤波固有阻带分布规律与钻铤尺寸的关系和钻铤波衰减频段与刻槽宽度、深度的关系.设计了一种随钻声波测井隔声体结构,通过数值模拟和现场实验井中隔声体测试结果验证了该隔声体结构有效地消除了钻铤直达波的干扰,能够测量到高质量地层纵波的波形和时差.

2 三维有限差分方法

本文采用直角坐标系下三维非均匀交错网格有限差分[12~22]程序模拟随钻声波测井响应.考虑到井孔和钻铤的圆周边界我们采用更精细的空间步长,空间步长(Δx,Δy,Δz)选择满足:

$$\max(\Delta x,\Delta y,\Delta z) < \frac{V_{\min}}{20 f_0}, \tag{1}$$

其中,$V_{\min}$ 是介质中最小声速,f_0 为声源的中心频率.

对于采样空间四阶交错网格差分,时间二阶差分的情况,时间步长 Δt 满足的稳定条件:

$$\Delta t < \frac{\Delta h}{V_{\min}}\left[\sqrt{3}(\eta_1+\eta_2)\right]^{-1}, \tag{2}$$

其中,Δh 是 Δx、Δy、Δz 中的最小网格步长,$\eta_1 = \frac{9}{8}$,$\eta_2 = -\frac{1}{24}$ 差分算子系数.

为了验证三维有限差分程序,计算了轴对称情况下的随钻声波测井全波波形,并与实轴积分法结果对比,模型示意图如图 1 所示,在紧靠钻铤的应力节点上加载点声源,通过控制点声源的相位来实现多极子声源.计算中地层、钻铤和泥浆参数由表 1 给出.模型尺寸为 2 m×2 m×6 m,空间步长 0.0025 m,时间步长 1×10^{-7} s.图 2 给出了利用有限差分和实轴积分模拟的软地层随钻单极子声波波形,声源为主频 8 kHz 的 Ricker 子波,源距 3.3 m,接收间距

0.15 m,图中红线为有限差分计算结果,黑线为实轴积分计算结果.图中可见,对钻铤模式波和地层纵波来说,有限差分的计算结果和实轴积分结果基本吻合.地层纵波和后续波均略有偏差,但可以验证数值模拟方法的正确性,作为考察随钻声波测井钻铤波传播规律,精度满足要求.

表 1　地层、钻铤、泥浆参数和尺寸

Table 1　Formation collar mud parameter and size

材料	纵波速度 (m/s)	横波速度 (m/s)	密度 (kg/m³)	内半径 (m)	外半径 (m)
泥浆	1500	—	1000	0	0.12
钻铤	5860	3130	7850	0.027	0.089
软地层	2500	1200	2300	0.125	∞
硬地层	4500	2500	2500	0.125	∞

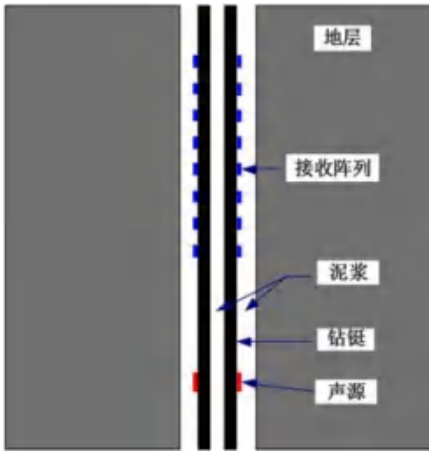


图 1　随钻声波测井理论模型

Fig. 1　LWD acoustic theory model

3　钻铤模式波数值模拟与规律分析

随钻声波测井仪器为了消除沿钻铤传播的直达

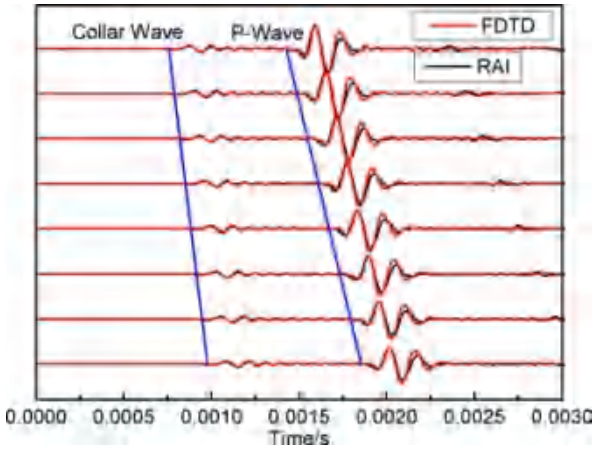


图 2　均匀地层模型三维有限差分(红线)和实轴积分(黑线)计算波形对比

Fig. 2　Waveform comparisons for 3D FDTD (red lines) and RAI (black lines) methods in isotropic formation model

波对地层波测量的干扰,通常在发射声源和接收器之间的钻铤上刻槽,即随钻声波测井的隔声体.本文模拟了随钻声波测井隔声体刻槽前、后钻铤模式波的波形响应特征对比.钻铤内径 0.08 m,外径 0.174 m,声速参数见表 1,为考察钻铤模式波井外地层用泥浆代替.在钻铤外壁周期刻环形槽,槽深 $d_1=0.015$ m,槽宽 $L_1=0.1$ m,槽间距 $L_2=0.1$ m,槽个数 $N=10$.图 3(a)和(b)分别给出了钻铤刻槽前、后钻铤模式波时域波形和对应的频谱图.图中黑线给出发射和接收换能器之间钻铤未刻槽情况的钻铤模式波波形和频谱,红线是刻槽后钻铤波的波形和频谱.可看出未刻槽的钻铤波幅度较大,刻槽后的钻铤波幅度与未刻槽相比明显降低.从频谱图中可看出刻槽前钻铤波在 13 kHz 频率附近存在一个频带较窄(12.5～14.5 kHz)的振幅很小的阻带,这个阻带为该尺寸钻铤的固有阻带.通过对钻铤刻槽使钻铤模式波幅度明显降低,同时将钻铤波阻带变宽(12.3～16.8 kHz),即该刻槽结构基本实现12～17 kHz频率范围内的

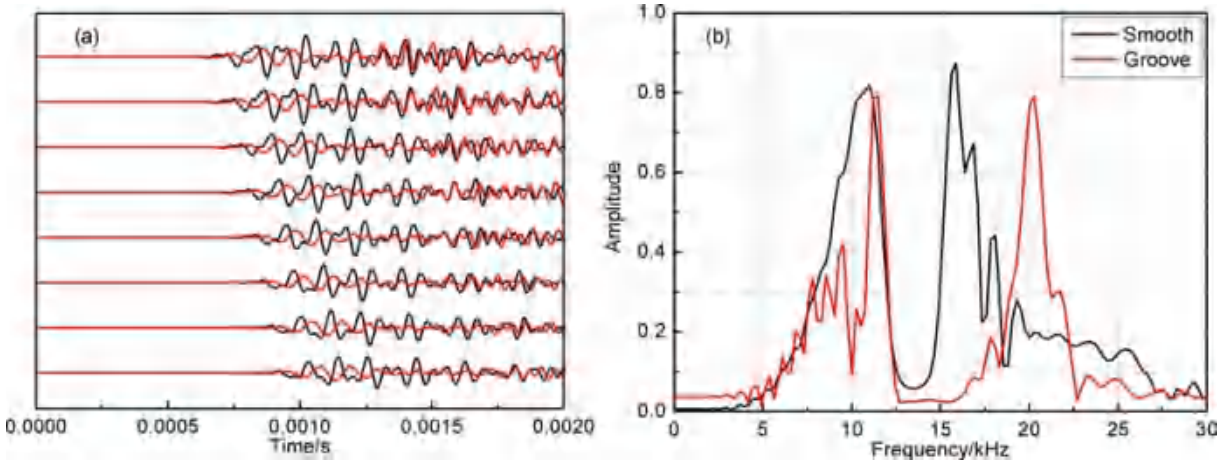


图 3　钻铤刻槽前、后钻铤模式波波形和频谱

Fig. 3　The waveforms and spectrums of collar mode wave with grooves or without

钻铤波完全衰减,其中最大衰减频率为 15.7 kHz.

杨勇等[24]理论研究表明,随钻声波测井隔声体使某一中心频率附近钻铤波达到最佳衰减效果的刻槽结构是槽宽和槽间距约等于该频率处波长的 1/4,即满足以下关系:

$$L_1 = L_2 \sim \frac{1}{4fS} = \frac{1}{4}\lambda, \tag{3}$$

其中,L_1 槽的轴向长度;L_2 两个槽之间的距离;f 预定的中心频率;S 钻铤纵波时差;λ 为波长.本文数值模拟时钻铤纵波速度为 5860 m/s,上述刻槽结构的槽宽 L_1 和槽间距 L_2 为最大衰减频率处波长的 0.268 倍,本文结果与文献[24]中的结论一致.

因此,从刻槽后的钻铤模式波的频谱中可以看出,随钻声波测井隔声体设计的关键在于了解给定尺寸钻铤的固有阻带的中心频率和带宽,通过改变刻槽结构来拓宽该阻带,达到仪器设计要求.

3.1 固有阻带的中心频率、宽度与钻铤尺寸的关系

图 4(a,b)分别给出了实际生产中使用的四种不同规格尺寸钻铤(外径 4.75in,6.75in,8.25in 和 9in 钻铤,1in=2.54 cm,下同)的钻铤模式波的波形和对应的频谱.从频谱图可看出,不同尺寸钻铤的钻铤波均明显存在一个阻带,且随着钻铤外径变小阻带的中心频率升高,阻带宽度增加.

图 5(a,b)分别给出钻铤模式波固有阻带中心频率和阻带宽度与钻铤尺寸的关系.图 5a 横坐标是钻铤内径和外径之和(d_1+d_2),单位英寸,纵坐标是钻铤模式波固有阻带的中心频率 f_c,图中方块为固有阻带的中心频率,图中实线为固有阻带中心频率的拟合曲线.图 5b 横坐标是钻铤内径和外径之和,单位英寸,纵坐标是钻铤模式波固有阻带的宽度 Δf,图中方块为固有阻带的宽度,实线为拟合曲线.

从图中可看出,四种常用尺寸钻铤的拟合结果很好,清楚地反映出外径 4.75in、6.75in、8.25in 和 9in 四种常用尺寸钻铤的钻铤模式波固有阻带的中心频率 f_c 和宽度 Δf 与钻铤内、外径或壁厚的关系,具体关系为:

$$f_c = 0.58V_p/(d_1+d_2), \tag{4}$$

$$\Delta f = 0.0318V_p/(d_1+d_2)^{1.65}, \tag{5}$$

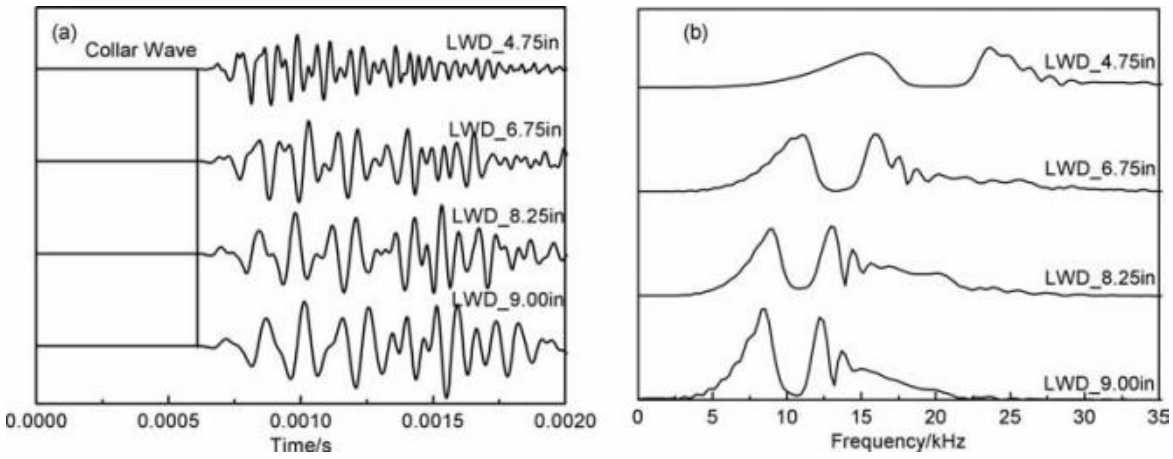


图 4 不同尺寸钻铤的钻铤波波形和对应的频谱

Fig. 4 The waveforms and its spectrum of collar mode wave of different collar sizes

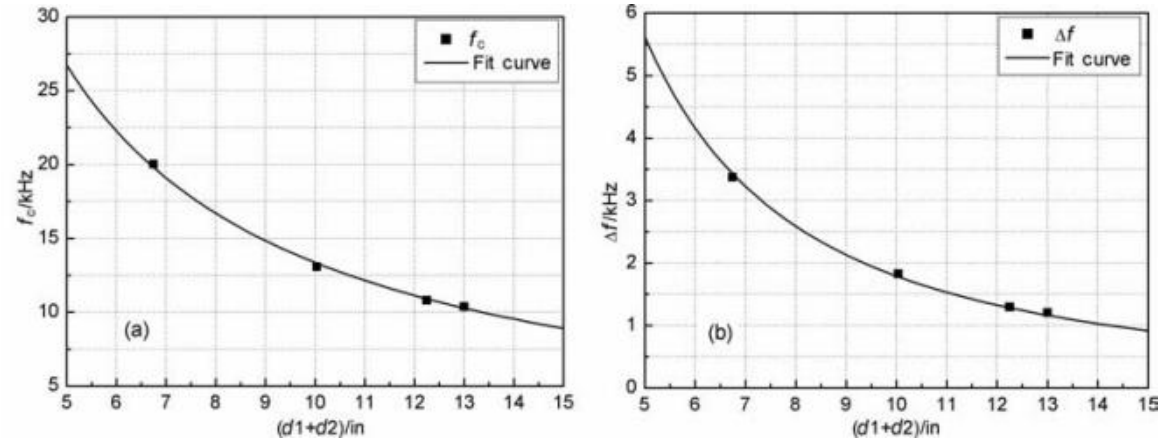


图 5 钻铤模式波固有阻带的中心频率和宽度与钻铤尺寸的关系

Fig. 5 The relationship between the center frequency and band width of the collar mode wave inherent stopband and the collar sizes

其中 V_p—钻铤纵波速度,单位为 m/s; d_1 —钻铤内径,单位为英寸; d_2 —钻铤外径,单位为英寸; d_1+d_2 —实际上反映钻铤的壁厚.

3.2　钻铤波衰减幅度与刻槽深度的关系

图 6a 给出了不同刻槽深度隔声体的钻铤波波形.图中黑线为未刻槽的钻铤波波形,蓝线为刻槽深度 0.015 m 的钻铤波波形,红线为刻槽深度 0.02 m 的钻铤波波形.对比三种情况可看出,刻槽深度增加使钻铤波幅度减小,同时使残余钻铤波的延迟时间增加.图 6b 给出了对应的频谱曲线.对比刻槽深、浅的两种情况的频谱发现,刻槽深度增加可使钻铤波阻带频率范围略有加宽.因此,在满足钻铤强度的前提下,适当增加刻槽深度可提高随钻声波测井隔声体的隔声效果.

3.3　钻铤刻内槽和外槽对钻铤波衰减的影响

图 7 给出了钻铤外壁周期刻槽和内壁周期刻槽的钻铤波频谱对比.图中黑线为未刻槽的钻铤波频谱,蓝线为钻铤外壁周期刻环形槽(槽深 $d_1=0.015$ m,槽宽 $L_1=0.1$ m,槽间距 $L_2=0.1$ m,槽个数 $N=10$)的钻铤波频谱,红线为钻铤内壁周期刻环形槽(槽深

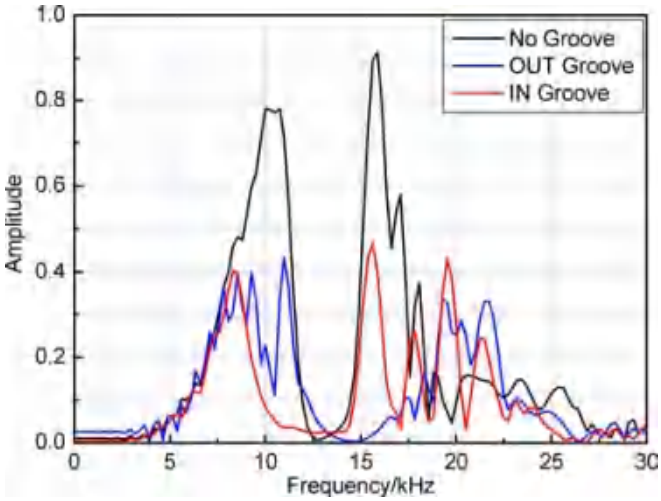


图 7　钻铤内、外壁刻槽钻铤波频谱对比

Fig. 7　The spectrums of collar mode wave with in groove and out groove

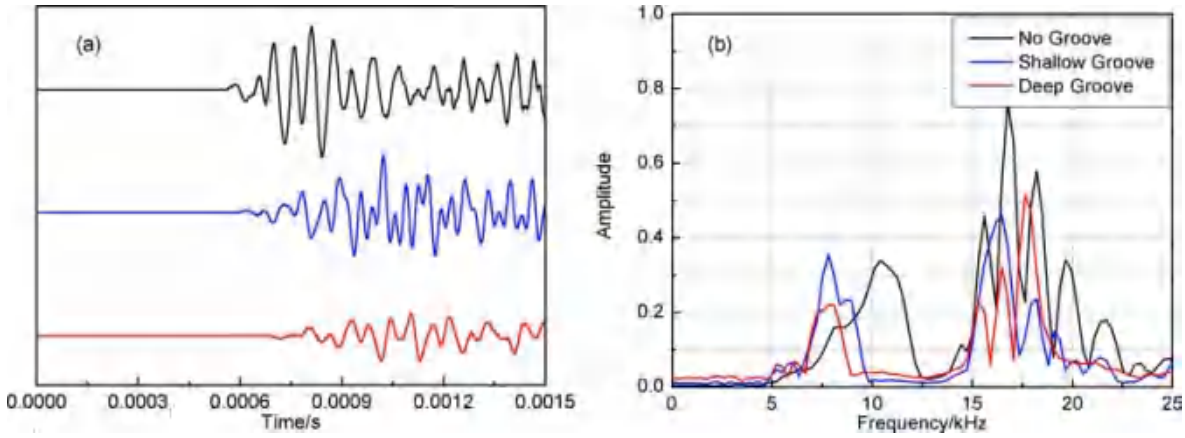


图 6　不同刻槽深度钻铤模式波的时域波形和对应频谱图

Fig. 6　The waveforms and spectrums of collar mode wave with different groove depth

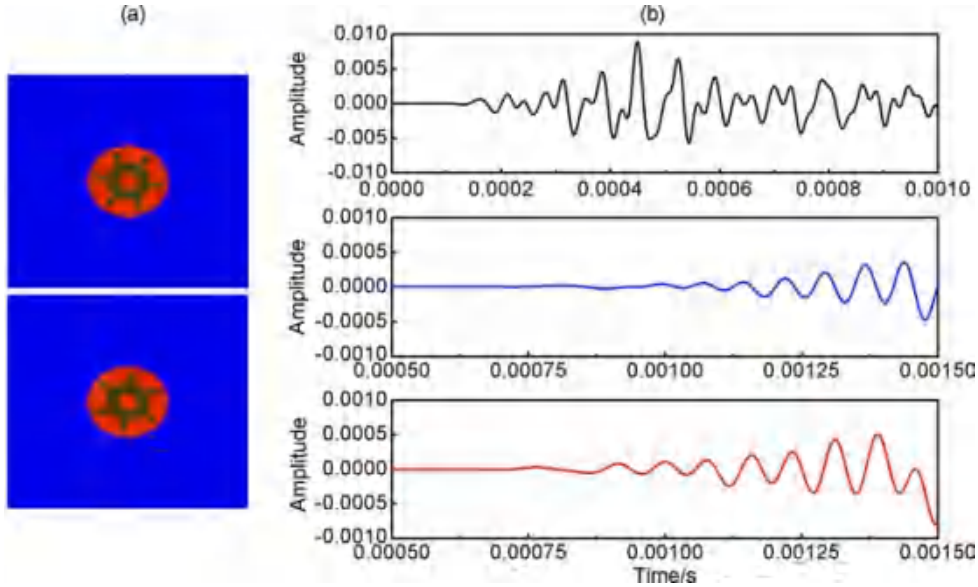


图 8　周向环形通槽与周向 45°铣槽的钻铤波波形对比

Fig. 8　The comparison of colar wave from circle grooves and grooves with 45 degrees interval

d_1=0.015 m,槽宽 L_1=0.1 m,槽间距 L_2=0.1 m,槽个数 N=10)的钻铤波频谱.从图中可看出,同样的刻槽尺寸下,在钻铤外壁周期刻槽主要衰减较高频率成分的二阶钻铤模式波,而钻铤内壁周期刻槽主要衰减低频成分的一阶钻铤模式波.因此,在实际随钻声波测井隔声体设计时,可考虑在钻铤内、外壁同时周期刻槽到达最佳隔声效果.

3.4 周向环形通槽与周向 45°铣槽钻铤波幅度对比

随钻测井在非常恶劣的环境(扭曲、撞击和震动等)下工作,仪器的主体结构必须具有很高的机械强度.随钻声波测井刻槽式隔声体是力学薄弱环节,在实际仪器设计时可以考虑在钻铤周向 360°铣一系列槽孔来代替周向环形通槽来增加仪器强度,但对隔声效果会有所影响.

图 8a 给出了周向间隔 15°铣一系列 45°槽的有限差分网格图,轴向相邻两个槽交错排列,如图上、下所示.图 8b 给出了数值模拟的两种刻槽结构钻铤波对比图,作为对比上图给出隔声体近端未刻槽接收的波形,中间图为经过周向刻环形槽后的钻铤波波形,下图为经过轴向交错排列周向 45°铣槽后的钻铤波波形.对比两种刻槽结构的钻铤波可看出,周向 45°铣槽隔声体对钻铤波的衰减要比周向环形槽隔声体小,但是在幅度上差别并不大.因此,在满足钻铤机械强度和隔声效果的前提下,实际随钻声波测井隔声体设计可以利用较深的交错排列铣槽代替周向环槽结构.

4 随钻声波测井隔声体的设计与实验验证

基于上述钻铤模式波传播规律与刻槽结构关系的理论研究,本文设计了一种钻铤规格 8.25in 随钻声波测井隔声体,如图 9 所示.钻铤外径 8.25in,隔声体部分水眼内径 4in.刻槽的隔声体部分长度 2.2 m,发射声源和接收换能器安装在钻铤外壁的 0.01 m 深度的凹槽内,钻铤两端安装发射和接收电子线路部分的内径 5.5in.隔声体部分主要包含三组刻槽结构,一组刻槽为钻铤外壁轴向 360°车通槽,槽宽 0.03 m,槽深 0.02 m,槽间距0.155 m,共 10 个;另一组为钻铤外壁相差 30°交错排列的 45°铣槽,如 8a 所示结构,槽宽 0.025 m,槽深 0.03 m,槽间距 0.155 m;第一和二组槽的间距为 0.09 m;第三组为钻铤内壁轴向 360°车通槽,如图中隔声体内壁,槽宽0.01 m,槽深0.015 m,槽间距 0.155 m.



图 9 随钻声波测井隔声体结构示意图

Fig. 9 The schematic diagram of LWD acoustic isolator

4.1 隔声体的声衰减特性数值模拟

图 10 分别给出了三维有限差分数值模拟的隔声体在刻槽前、后的阵列时域波形、频谱及其计算的相对声衰减曲线,数值模拟时选用主频 11 kHz 的宽带 Ricker 子波声源函数.图 10a 给出隔声体刻槽前、后的波形,源距 3.05 m,接收间距 0.2 m,黑线为刻槽前的波形,红线刻槽后的波形,可看出声波经过刻槽的隔声体部分幅度明显衰减;图 10b 给出了对应的频谱.从未刻槽的钻铤波频谱可看出,外径 8.25in 的标准钻铤的钻铤波固有阻带的中心频率在10 kHz左右,带宽约 2 kHz;刻槽后的新型隔声体的钻铤波阻带频率范围拓宽到 7.5～15 kHz.图 10c 给出了刻槽后的钻铤波相对于未刻槽情况的相对声衰减曲线,横坐标为频率,纵坐标为相对声衰减.可看出在阻带频率范围内的相对声衰减约－10 dB,计算公式参考文献[30],在固有阻带中心频率 10 kHz 频率附近声衰减值增大是因为在该频段刻槽前后的钻铤波幅度本身很小导致的.该尺寸钻铤的内径变化(水眼部分内径 4in,电路部分内径5.5in)导致的钻铤波衰减约－10 dB,因此,本文设计的新型隔声体在 7.5～15 kHz 频率范围内的声衰减在－20 dB 以上.

4.2 典型地层井孔中响应特征模拟

根据刻槽前、后钻铤波的首波到达时间可以计算得到,隔声效果差时一阶模式钻铤波对地层纵波速度为 4500 m/s 的地层干扰较大,隔声体效果好时二阶模式钻铤波对地层纵波速度为 2570 m/s 的地层干扰较大.本文选取两种典型的软、硬地层模拟井孔中的响应波形,地层、井孔参数如表 1 所示.

根据刻槽后隔声体的频谱和衰减曲线,本文数值模拟时选用主频 11 kHz,频带 7.0 kHz～15 kHz 的高斯声源函数,该声源的频率落在隔声体最佳衰减的阻带范围内.图 11 给出数值模拟的声源函数和对应的频谱曲线,图中黑线为声源时域波形,蓝线为对应的声源频谱曲线.

图 12 给出了本文隔声体在软地层井孔中单极子声源的模拟波形和对应的时差—时间相关分析图.图 12a 给出了模拟的阵列波形,从波形中可看出,该隔声体的随钻声波测井测量的全波列中只有

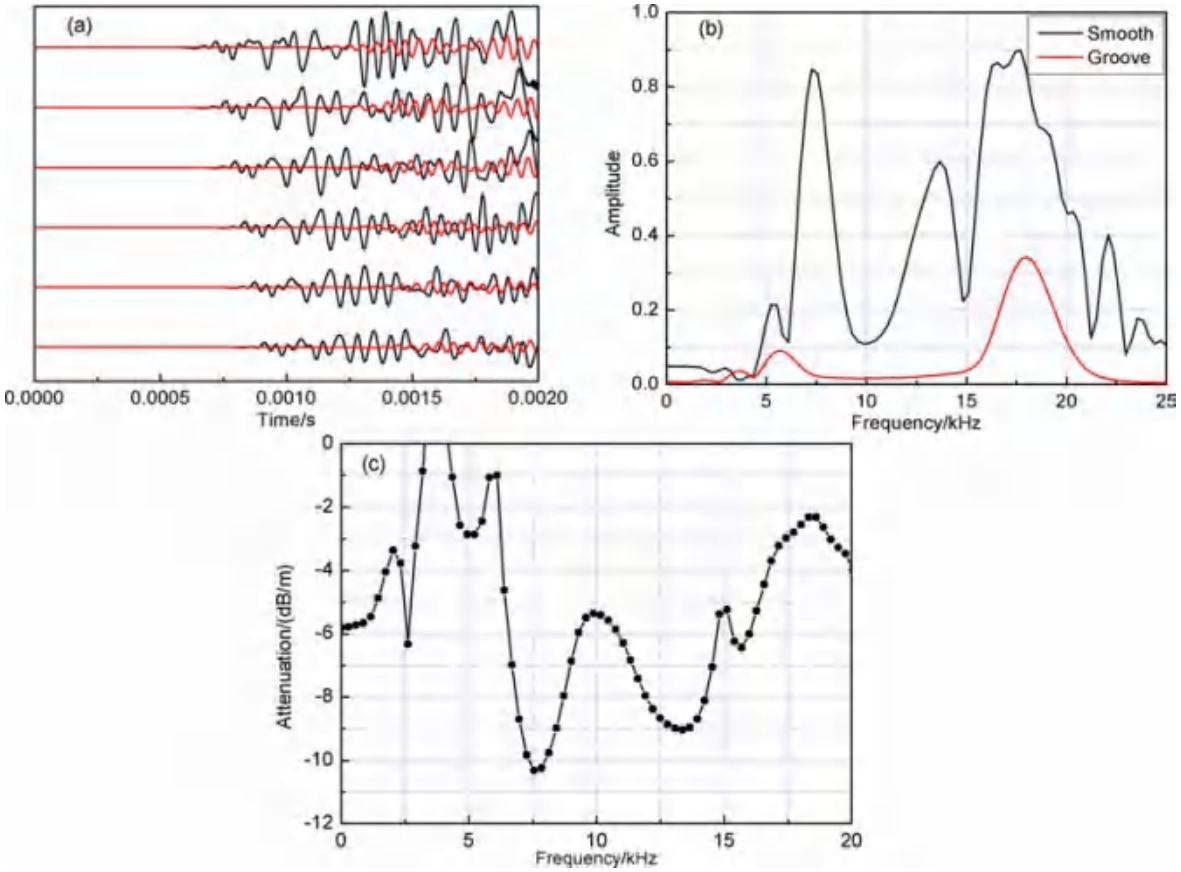


图 10　新型 8.25in 随钻声波测井隔声体数值模拟波形、频谱和相对声衰减曲线

Fig. 10　The simulation waveforms, its spectrum and relative acoustic attenuation curve by new 8.25in LWD acoustic isolator

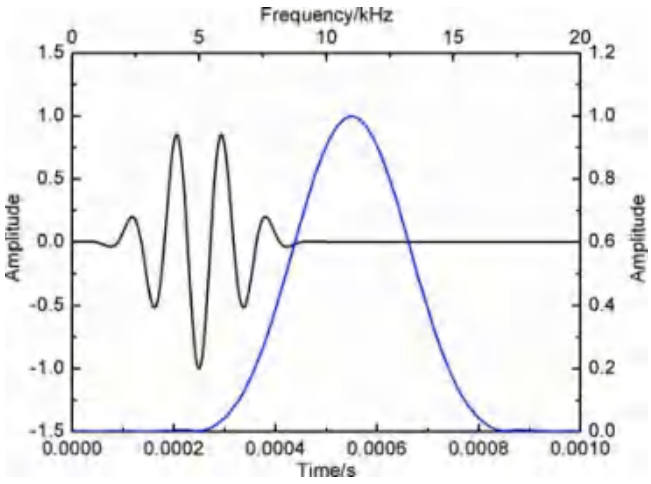


图 11　随钻声波测井井孔响应模拟的声源波形和频谱

Fig. 11　LWD acoustic simulation source waveform and spectrum

幅度较大的地层纵波,钻铤波幅度非常小.波形幅度放大 50 倍后,如图下部的波形,可看到残余的钻铤波,地层波信号与干扰的钻铤波信号的信噪比非常高.图 12b 给出了对理论模拟波形的时差—时间相关分析图,图中横坐标为时间,纵坐标为时差(速度的倒数),颜色代表相关系数.可看出在时差—时间相关系数图上存在两个极大值,分别对应钻铤波时差和地层纵波时差,即钻铤波的速度为 4976 m/s,地层纵波速度为 2490 m/s.用本文设计隔声体的随钻声波测井在软地层测量的地层纵波速度与理论值非常接近.

图 13 给出了本文隔声体在硬地层井孔中单极子声源的模拟波形和对应的时差—时间相关分析图.图 13a 给出了模拟的阵列波形,从波形中可看出,硬地层中测量的全波列中幅度最大的是地层横波,与之相比地层纵波幅度非常弱.波形幅度放大 12.5 倍后,如图中下部的波形,可以看到清晰的地层纵波波形,残余的钻铤波幅度非常小,有效的地层波纵波信号与干扰的钻铤波信号的信噪比也很高.图 13b 给出了对理论模拟波形的时差—时间相关分析图.可看出在时差—时间相关系数图上存在两个明显的极大值,分别对应地层横波时差和地层纵波时差,即地层纵波的速度为 4018 m/s,地层横波速度为 2472 m/s.从图中也可看出在纵波相关系数极大值附近也存在钻铤波的相关系数极大值,但相关系数较小.用本文设计隔声体的随钻声波测井在硬地层测量的地层纵波速度和地层横波速度与理论值非常接近.

因此,本文在理论研究的基础上设计的随钻声波测井隔声体在典型软、硬地层均能测量到高质量的地层纵波.对比两种地层情况发现,随钻声波测量

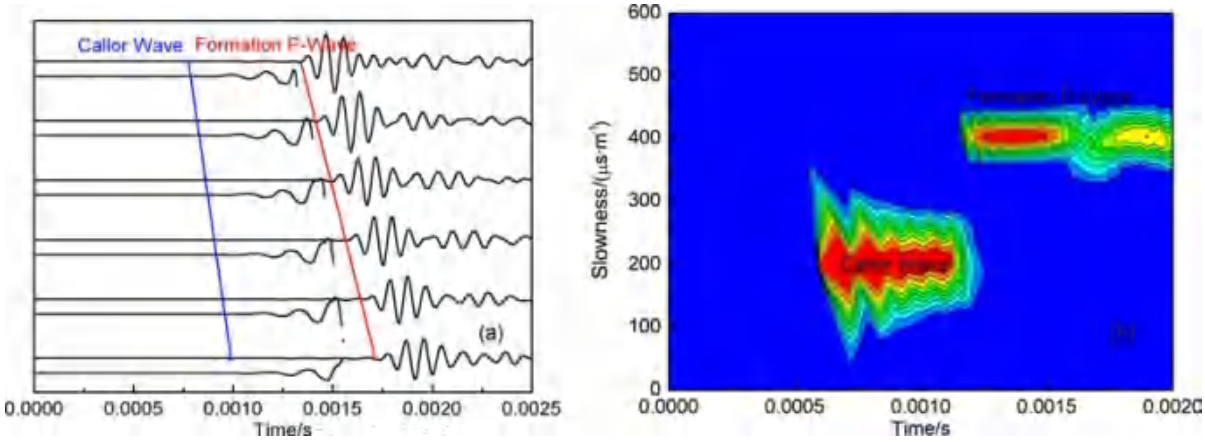


图 12 软地层理论模拟波形和时差—时间相关分析图

Fig. 12 Theoretical simulation waveforms in soft formation and Slowness-Time Coherence analysis

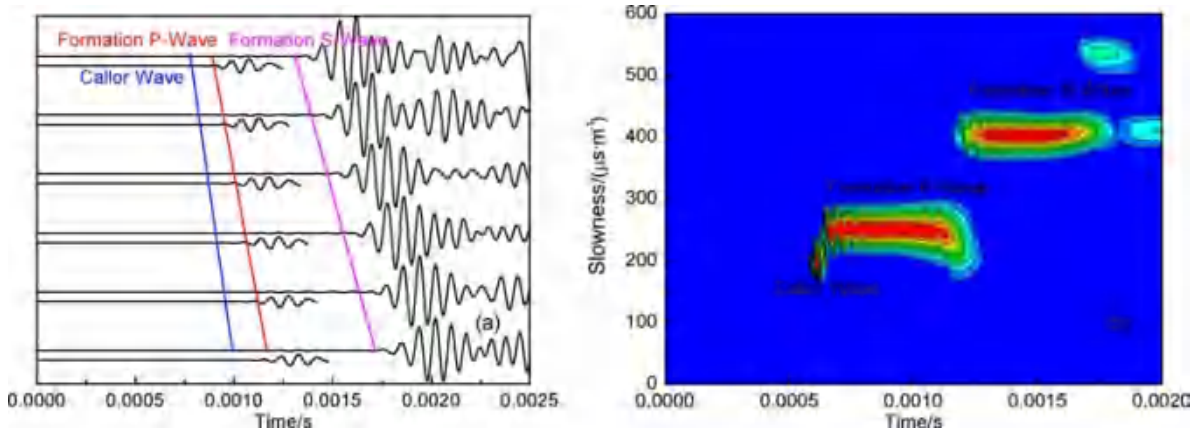


图 13 硬地层理论模拟波形和时差—时间相关分析图

Fig. 13 Theoretical simulation waveforms in fast formation and Slowness-Time Coherence analysis

在软地层测量的全波列中地层纵波幅度最大,地层纵波与钻铤波的信噪比高;硬地层中测量的全波列地层横波幅度非常大,实际应用时要注意地层横波对纵波的干扰.

4.3 现场实验井的隔声效果测试

基于本文隔声体结构的随钻声波测井仪器样机在某油田实验井中进行了隔声效果现场测试,测试井段为 2000～2100 m,该井段地层纵波速度 5000 m/s 左右,属于硬地层.实验过程中是用电缆吊着随钻声波实验样机在目的层进行测试,发射声源采用主频 13 kHz的 3 个周期正弦波激励,随着电缆匀速缓慢上提,等时间间隔存储测量的全波列.图 14 给出了随钻声波测井仪器样机在实验井中的现场测试结果.图中第 1 道给出了测量的随钻单极子声波变密度波形和地层纵波到时曲线;第 2 道给出对应的时差相关系数图;第 3 道给出测量的地层纵波时差曲线.从测量的变密度波形和相关系数图中可看出,本文设计的随钻声波测井隔声体在硬地层实验井中,没有钻井噪声且仪器居中的情况下有效地消除了钻铤直达波的干扰,测量到了高质量的地层纵波波形

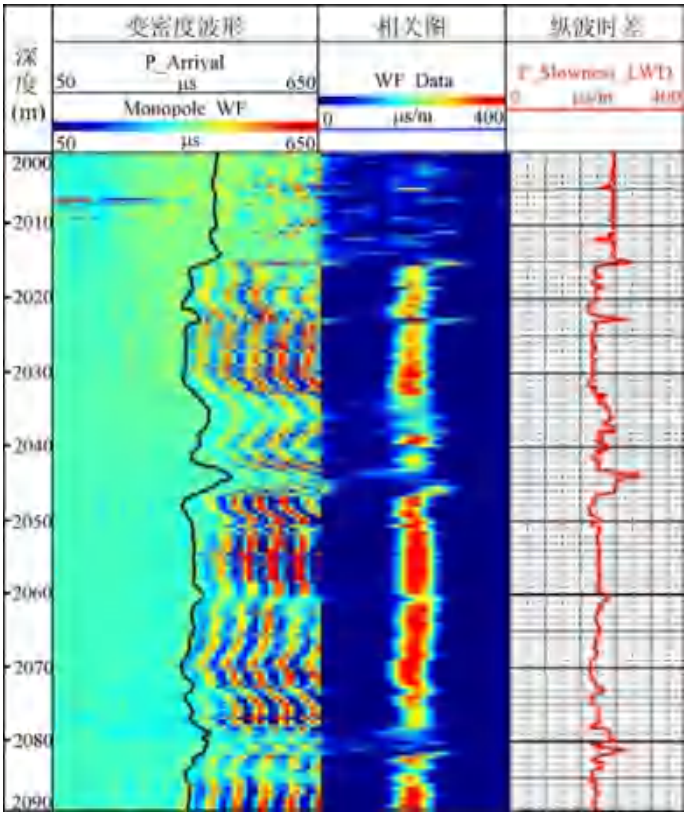


图 14 随钻声波测井仪器样机在实验井中的现场测试结果

Fig. 14 Field experiment hole test results of LWD acoustic logging tool

和时差.

5　结论与认识

本文利用三维有限差分程序模拟了钻铤刻槽前、后的随钻声波测井钻铤模式波响应特征,分析了钻铤模式波的衰减规律,在此基础上设计了随钻声波测井隔声体结构,并得到现场实验井测试数据的验证,从中得出以下认识与结论:

(1)均匀钻铤的钻铤模式波存在一个频带较窄的固有阻带,通过钻铤刻槽可拓宽该阻带的频率范围.

(2)钻铤波固有阻带的中心频率随着钻铤尺寸(钻铤内、外径之和)增加按非线性规律降低,固有阻带的频带宽度随着钻铤尺寸增加按非线性规律减小.

(3)随钻声波测井隔声体使某一中心频率附近钻铤波达到最佳衰减效果的刻槽结构是槽宽和槽间距约等于该频率处波长的 1/4.

(4)钻铤刻槽深度增加使钻铤波幅度减小、延迟时间增加,同时可使钻铤波阻带频率范围略有加宽.在满足钻铤强度的前提下,适当增加刻槽深度可提高随钻声波测井隔声体的隔声效果.

(5)数值模拟研究和现场实验井测试结果表明,利用本文设计的隔声体开发的随钻声波测井仪器样机有效地消除了钻铤波直达波干扰,能够测量到高质量的地层纵波波形和时差.

致　谢　感谢两位匿名审稿专家提出的宝贵意见和建设性建议.

参考文献(References)

[1] 唐晓明,郑传汉. 定量测井声学. 北京:石油工业出版社,2004
Tang X M, Zheng C H. Quantitative acoustic well logging (in Chinese). Beijing: Petroleum Industry Press, 2004

[2] 江玉龙,王祝文,伍　东. 阵列声波处理技术的研究与应用. 地球物理学进展,2009,**24**(1):246～253
Jiang Y L, Wang Z W, Wu D. Research and applications of high resolution array acoustic processing techniques. *Progress in Geophysics* (in Chinese), 2009, **24**(1): 246～253

[3] 李　铭,李艳华,楚泽涵. 声频谱测井方法研究进展. 地球物理学进展,2003,**18**(2):229～233
Li M, Li Y H, Chu Z H. Research evolution of acoustic spectrum logging methods. *Progress in Geophysics* (in Chinese), 2003, **18**(2): 229～233

[4] 张碧星,王克协. 各向异性介质地层中多极源声波测井的现状与发展. 地球物理学进展,1998,**13**(2):1～14
Zhang B X, Wang K X. Status quo and development of the acoustic multipole logging in anisotropic formation. *Progress in Geophysics* (in Chinese), 1998, **13**(2): 1～14

[5] 高　坤,陶　果,马　勇. 多极子阵列声波测井资料在塔河油田酸压设计施工中的应用. 地球物理学进展,2006,**21**(4):1227～1231
Gao K, Tao G, Ma Y, Application of multipole array sonic logging to acid hydralic fracuring. *Progress in Geophysics* (in Chinese), 2006, **21**(4): 1227～1231

[6] Joyce B, Patterson D, Leggett J, et al. Introduction of a new omni-directional acoustic system for improved real-time LWD sonic logging-tool design and field test results. SPWLA 42th Annual Logging Symposium, 2001, paper SS

[7] 张辛耘,郭彦军,王敬农. 随钻测井的昨天、今天和明天. 测井技术,2006,**30**(6):487～492
Zhang X Y, Guo Y J, Wang J N. The logging while drilling: past, present and future. *Well Logging Technology* (in Chinese), 2006, **30**(6): 487～492

[8] Alford J, Goobie R B, Sayers C M, et al. A sound approach to drilling. *Oilfield Review*, 2006, (4): 68～78

[9] Sinha B K, Plona T J, Kostek S, et al. Axisymmetric wave propagation in fluid-loaded cylindrical shells: I-Theory. *J. Acoust. Soc. Am.*, 1992, **92**(2): 1132～1143

[10] Plona T J, Sinha B K, Kostek S, et al. Axisymmetric wave propagation in fluid-loaded cylindrical shells: II-Theory versus experiment. *J. Acoust. Soc. Am.*, 1992, **92**(2): 1144～1155

[11] Rama Rao V N, Vandiver J K. Acoustics of fluid-filled boreholes with pipe: Guided propagation and radiation. *J. Acoust. Soc. Am.*, 1999, **105**(6): 3057～3066

[12] Liu Q H, Daube F, Randall C, et al. A three-dimensional finite-difference simulation of sonic logging. *J. Acoust. Soc. Am.*, 1996, **100**(1): 72～79

[13] Cheng N Y, Cheng C H, Toksoz M N. Borehole wave propagation in three dimensions. *J. Acoust. Soc. Am.*, 1995, **97**(6): 3483～3493

[14] Wang T, Tang X M. Finite-difference modeling of elastic wave propagation: A nonsplitting perfectly matched layer approach. *Geophysics*, 2003, **68**(5):1749～1755

[15] 杨慧珠,张友生,陶　果. 井眼条件下弹性波传播问题的三维有限差分数值模拟. 地球物理学进展,2003,**18**(2):348～352
Yang H Z, Zhang Y S, Tao G. Three dimensional finite difference numerical simulation of elastic wave propagation under borehole conditions. *Progress in Geophysics* (in Chinese), 2003, **18**(2): 348～352

[16] 林伟军,王秀明,张海澜. 倾斜地层中的井孔声场研究. 地球物理学报,2006,**49**(1):284～294
Lin W J, Wang X M, Zhang H L. Acoustic wave propagetion in a borehole penetrating an inclined layered formation. *Chinese J. Geophys.* (in Chinese), 2006, **49**(1): 284～294

[17] 何峰江，陶 果，王锡莉. 贴井壁声波测井仪的有限差分模拟研究. 地球物理学报，2006，**49**(3)：923～928
He F J, Tao G, Wang X L. Finite difference modeling of the acoustic field by sidewall logging devices. *Chinese J. Geophys.* (in Chinese), 2006, **49**(3): 923～928

[18] 王秀明，张海澜，王 东. 利用高阶交错网格有限差分法模拟地震波在非均匀孔隙介质中的传播. 地球物理学报，2003，**46**(6)：842～849
Wang X M, Zhang H L, Wang D. Modelling of seismic wave propagetion in heterogeneous poroelastic media using a high-order staggered finite-difference-method. *Chinese J. Geophys.* (in Chinese), 2003, **46**(6): 842～849

[19] 赵海波，王秀明，王 东等. 完全匹配层吸收边界在孔隙介质弹性波模拟中的应用. 地球物理学报，2007，**50**(2)：581～591
Zhao H B, Wang X M, Wang D, et al. Applications of the boundary absorption using a perfectly matched layer for elastic wave simulation in poroelastic media. *Chinese J. Geophys.* (in Chinese), 2007, **50**(2): 581～591

[20] 乔文孝，车小花，鞠晓东等. 声波测井相控圆弧阵及其辐射指向性. 地球物理学报，2008，**1**(3)：939～946
Qiao W X, Che X H, Ju X D, et al. Acoustic logging phased arc array and its radiation directivity. *Chinese J. Geophys.* (in Chinese), 2008, **51**(3): 939～946

[21] He X, Hu H S, Guan W. Fast and slow flexural waves in a deviated borehole in homogeneous and layered anisotropic formations. *Geophys. J. Int.*, 2010, **181**(1): 417～426

[22] 宋若龙，刘金霞，姚桂锦等. 非轴对称套管井中声场的并行有限差分模拟. 地球物理学报，2010，**53**(11)：2767～2775
Song R L, Liu J X, Yao G J, et al. Parallel finite difference modeling of acoustic fields in nonaxisymmetric cased hole. *Chinese J. Geophys.* (in Chinese), 2010, **53**(11): 2767～2775

[23] 闫向宏，苏远大，孙建孟等. 周期性轴对称凹槽结构隔声特性数值模拟. 计算物理，2010，**27**(6)：869～876
Yan X H, Su Y D, Sun J M, et al. Acoustic Characteristics of Axisymmetric Periodic Groove Structures. *Chinese Journal of Computational Physics* (in Chinese), 2010, **27**(6): 869～876

[24] 杨 勇，车小花，李 俊等. 基于时域有限差分法的随钻声波测井仪隔声体隔声效果的数值模拟. 中国石油大学学报(自然科学版)，2009，**33**(3)：66～70
Yang Y, Che X H, Li J, et al. Sound isolation numercial simulation on isolator of logging while drilling sonic tool using finite difference time-domain method. *Journal of China University of Petroleum* (*Edition of Natural Science*) (in Chinese), 2009, **33**(3): 66～70

[25] 王 华，陶 果，王 兵等. 多极子随钻声波测井波场模拟与采集模式分析. 地球物理学报，2009，**52**(9)：2402～2409
Wang H, Tao G, Wang B, et al. Wave field simulation and data acquisition scheme analysis for LWD acoustic tool. *Chinese J. Geophys.* (in Chinese), 2009, **52**(9): 2402～2409

[26] Leggett J V III, Dubinsky V, Petterson D, et al. Field test results demonstrating improved real-time data quality in an advanced LWD acoustic system. SPE Annual Conference and Exhibition, 2001, paper 71732

[27] Tang X M, Dubinsky V, Harrison C W, et al. Logging-While-Drilling shear and compressional measurements: case histories. SPWLA 44th Annual Logging Symposium Transactions, 2003, paper II

[28] Tang X M, Lilly D, Petpisit K. Analysis of LWD acoustic data validates its accuracy. SPWLA 48th Annual Logging Symposium Transactions, 2007, paper B

[29] Kinoshita T, Dumont A, Hori H, et al. LWD sonic tool design for high-quality logs. 80th Ann. Internat. Mtg., Soc. Explor. Geophys., Expanded Abstracts, 2010. 513～516

[30] 乔文孝，陈雪莲，杜光升等. 隔声体性能评价的方法研究. 测井技术，2002，**26**(2)：104～106
Qiao W W, Chen X L, Du G S, et al. On Performance Evaluation of a Sound Isolator. *Well Logging Technology* (in Chinese), 2002, **26**(2): 104～106

(本文编辑 刘少华)

GEOPHYSICS, VOL. 85, NO. 1 (JANUARY-FEBRUARY 2020); P. D45–D52, 9 FIGS.
10.1190/GEO2019-0236.1

Check for updates

Downloaded 12/23/19 to 218.201.114.137. Redistribution subject to SEG license or copyright; see Terms of Use at http://library.seg.org/

Measurement of the shear slowness of slow formations from monopole logging-while-drilling sonic logs

Yuanda Su[1], Xinding Fang[2], and Xiaoming Tang[1]

ABSTRACT

Acoustic logging-while-drilling (LWD) is used to measure formation velocity/slowness during drilling. In a fast formation, in which the S-wave velocity is higher than the borehole-fluid velocity, monopole logging can be used to obtain P- and S-wave velocities by measuring the corresponding refracted waves. In a slow formation, in which the S-wave velocity is less than the borehole-fluid velocity, because the fully refracted S-wave is missing, quadrupole logging has been developed and used for S-wave slowness measurement. A recent study based on numerical modeling implies that monopole LWD can generate a detectable transmitted S-wave in a slow formation. This nondispersive transmitted S-wave propagates at the formation S-wave velocity and thus can be used for measuring the S-wave slowness of a slow formation. We evaluate a field example to demonstrate the applicability of monopole LWD in determining the S-wave slowness of slow formations. We compare the S-wave slowness extracted from a monopole LWD data set acquired in a slow formation and the result derived from the quadrupole data recorded in the same logging run. The results indicated that the S-wave slowness can be reliably determined from monopole LWD sonic data in fairly slow formations. However, we found that the monopole approach is not applicable to very slow formations because the transmitted S-wave becomes too weak to detect when the formation S-wave slowness is much higher than the borehole-fluid slowness.

INTRODUCTION

Based on the type of acoustic source used in a logging tool, conventional acoustic logging while drilling (LWD) can be categorized into three types: monopole, dipole, and quadrupole (Tang and Cheng, 2004). When the formation S-wave velocity is faster than the borehole-fluid velocity (i.e., a fast formation), P- and S-wave velocities can be measured from the corresponding refracted P- and refracted S-waves that are acquired by using a monopole LWD tool. However, the S-wave velocity cannot be directly obtained from monopole logging when the formation shear velocity is lower than the borehole-fluid velocity (i.e., a slow formation) because the refracted S-waves cannot be generated in such an environment (Tang and Cheng, 2004). The slow-formation phenomenon is commonly encountered when logging is run in shallow unconsolidated sediments or high pore-pressure zones. The need for measuring S-wave slowness in slow formations drives the development of dipole and quadrupole logging tools. The dipole acoustic LWD tool was first developed and tested for S-wave slowness measurements due to its success in wireline logging (Varsamis et al., 1999). However, the application of a dipole acoustic source in an LWD environment was found to have two serious issues caused by the drill collar (Tang et al., 2002). The first drawback is the strong contamination caused by tool modes. The second problem is that the dipole flexural-wave slowness does not converge to the formation S-wave slowness at low frequencies. To overcome these problems, the quadrupole acoustic LWD tool was invented as a substitute for the dipole tool in LWD logging (Tang et al., 2002). Compared to the dipole method, the quadrupole method determines the formation S-wave slowness using the formation quadrupole wave, which is not affected by the tool modes at low frequencies because the tool collar modes exist only above a cut-off frequency that is usually above 10 kHz (Tang et al., 2002). A new type of LWD tool named unipole was developed in recent years (Wang et al., 2011; Syresin et al., 2016). The transmitter and receivers of a unipole tool are all located on a single side of the tool, and so it can be

Manuscript received by the Editor 15 April 2019; revised manuscript received 31 July 2019; published ahead of production 21 October 2019; published online 6 December 2019.
[1]China University of Petroleum, School of Geosciences, Qingdao 266555, China.
[2]Southern University of Science and Technology, Department of Earth and Space Sciences, Shenzhen 518055, China. E-mail: fangxd@sustech.edu.cn.
© 2020 Society of Exploration Geophysicists. All rights reserved.

Downloaded 12/23/19 to 218.201.114.137. Redistribution subject to SEG license or copyright; see Terms of Use at http://library.seg.org/

used to obtain information about the azimuthal variations in the properties of the formation around a borehole.

Theoretically, formation S-wave slowness can be measured from quadrupole LWD but the processing and interpretation of quadrupole logging data is not trivial. The quadrupole wave is dispersive, and its slowness is equal to the formation S-wave slowness only at the cut-off frequency (Chen, 1989; Tang and Cheng, 2004; Jørgensen and Burns, 2013). The quadrupole-wave dispersion near the cut-off frequency is sometimes hard to obtain accurately because of poor signal-to-noise ratio or due to signal distortion caused by the logging environment. Therefore, the extraction of the formation S-wave slowness from quadrupole data often requires the use of a model-based inversion approach to account for the dispersion characteristics of the quadrupole mode (Zhang et al., 2010; Su et al., 2013).

Through numerical modeling, Fang and Cheng (2018) discover that the transmitted S-wave generated by a monopole LWD tool in a slow formation can be detected. Because the slow-formation transmitted S-wave is nondispersive, it can be used for S-wave slowness measurement through time-semblance analysis. This provides a data-based approach for measuring the S-wave slowness in a slow formation and may be used to calibrate the results derived from the model-based quadrupole approach. However, Fang and Cheng (2018) do not provide direct evidence to demonstrate the applicability of their approach in LWD logging except for analyzing modeling data and a wireline field example. In this paper, we study a field LWD logging data set acquired in a slow formation and compare the S-wave slowness measured from the monopole and quadrupole LWD sonic logs.

THEORY

The borehole transmitted S-wave, which is different from the refracted S-wave, detected in a slow-formation environment is an inhomogeneous wave (attenuated rapidly away from the wellbore) propagating along the wellbore induced by the transmitted S-wave propagating in the formation. Figure 1 shows snapshots of the wavefield excited by a monopole source in wireline and LWD models. The only difference between these two models is the presence of a tool in the LWD model. The formation P- and S-wave slownesses are 456 and 892 μs/m, respectively. The borehole-fluid slowness is 679 μs/m. These two numerical examples illustrate that the transmitted S-wave (denoted as "S" in Figure 1) exists in wireline and LWD environments. The transmitted S-wave has similar behavior in these two models indicating that the presence of the LWD tool has little effect on its propagation. However, the Stoneley wave that propagates right after the transmitted S-wave behaves differently in these models. Compared with the wireline case, the Stoneley wave is apparently slower in the LWD model. This difference can be explained through analyzing the characteristics of their Stoneley-wave dispersion, which can be analytically calculated based on the dispersion equations of the models (Rao and Vandiver, 1999). As shown in Figure 2, the dispersion curve of the Stoneley wave in the wireline model (the squares) bends downward toward the formation S-wave slowness at low frequencies. This can result in interference of the low-frequency parts of the transmitted S-wave and the Stoneley wave, making the transmitted S-wave difficult to discern in monopole wireline data. However, the dispersion curve of the Stoneley wave in the LWD model (the triangles) bends toward the opposite direction at low frequencies. This can increase the temporal separation of the transmitted S-wave and the Stoneley wave in the LWD data. It has been demonstrated that the dispersion of the Stoneley wave in wireline and LWD environments follows these variation trends in general situations (Fang and Cheng, 2018). Moreover, an LWD tool has the capability to acquire stronger transmitted S-wave signals because its receivers tend to be closer to the wellbore. Therefore, although the transmitted S-wave can appear in wireline and LWD data, it is easier to distinguish in LWD data. This provides an opportunity to extract the S-wave slowness of slow formations from LWD monopole sonic logs.

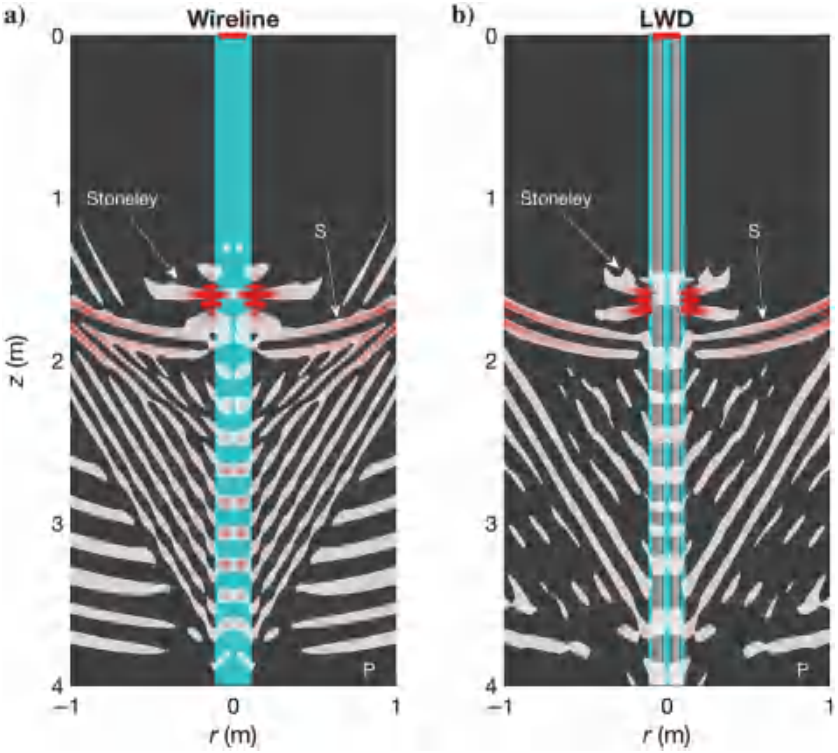


Figure 1. Comparison of the snapshots of the wavefield excited by a monopole source in (a) wireline and (b) LWD environments. The borehole radius is 11.7 cm. The LWD tool's (modeled as a steel pipe) inner and outer radii are 2.7 and 8.4 cm, respectively. P and S denote the P- and transmitted S-waves, respectively. The monopole source is located at z ¼ 0 m. The source signal's center frequency is 8 kHz.

Figure 3 shows the synthetic monopole waveforms for the two models (Figure 3a and 3b) and the corresponding semblance of slowness-time-coherence (STC) (Figure 3d and 3e). The dashed red lines in Figure 3a and 3b indicate the transmitted S-wave recorded in the borehole fluid. It arrives a bit earlier than the Stoneley wave. Although the transmitted S-wave appears relatively weak in the waveform data, its nondispersive nature makes it become prominent in STC after stacking. Compared to the wireline model,

the transmitted S-wave and the Stoneley wave are better separated in LWD STC because the drill collar slows down the Stoneley wave, as explained previously. It can be seen that the formation S-wave slowness (892 μs/m) can be obtained directly from the bright spot that corresponds to the transmitted S-wave in Figure 3e. Figure 3c shows the synthetic waveforms for quadrupole LWD, which is the conventional way for slow-formation S-wave slowness measurement. The quadrupole dispersion shown in the semblance of slowness-frequency-coherence (SFC) in Figure 3f indicates that the quadrupole dispersion curve (the black circles) converges to the formation S-wave slowness at the cut-off frequency (approximately 2 kHz). This dispersion characteristic of the quadrupole wave is the theoretical basis of the quadrupole approach for slow-formation S-wave slowness measurement. The formation S-wave slowness can be either estimated directly from the quadrupole slowness at the cut-off frequency or inverted from the dispersion curve using a model-based inversion approach. The synthetic results shown in Figure 3 demonstrate that the transmitted S-wave and quadrupole wave have the capability for determining the S-wave slowness of a slow formation. We investigate the field applicability of these two approaches in the next section.

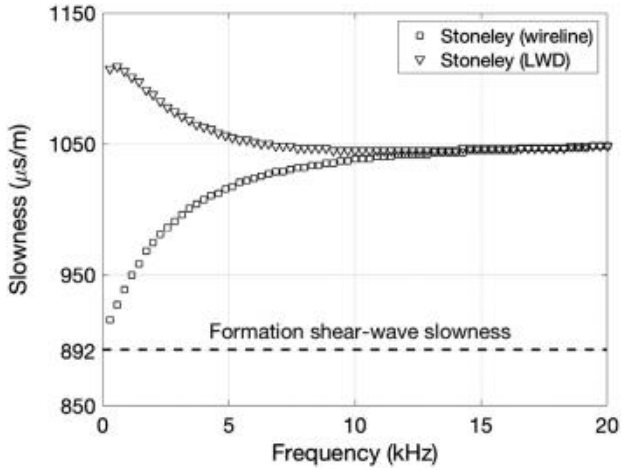


Figure 2. Comparison of the dispersion curves of the Stoneley wave in the wireline (squares) and LWD (triangles) models. The dashed line indicates the formation S-wave slowness.

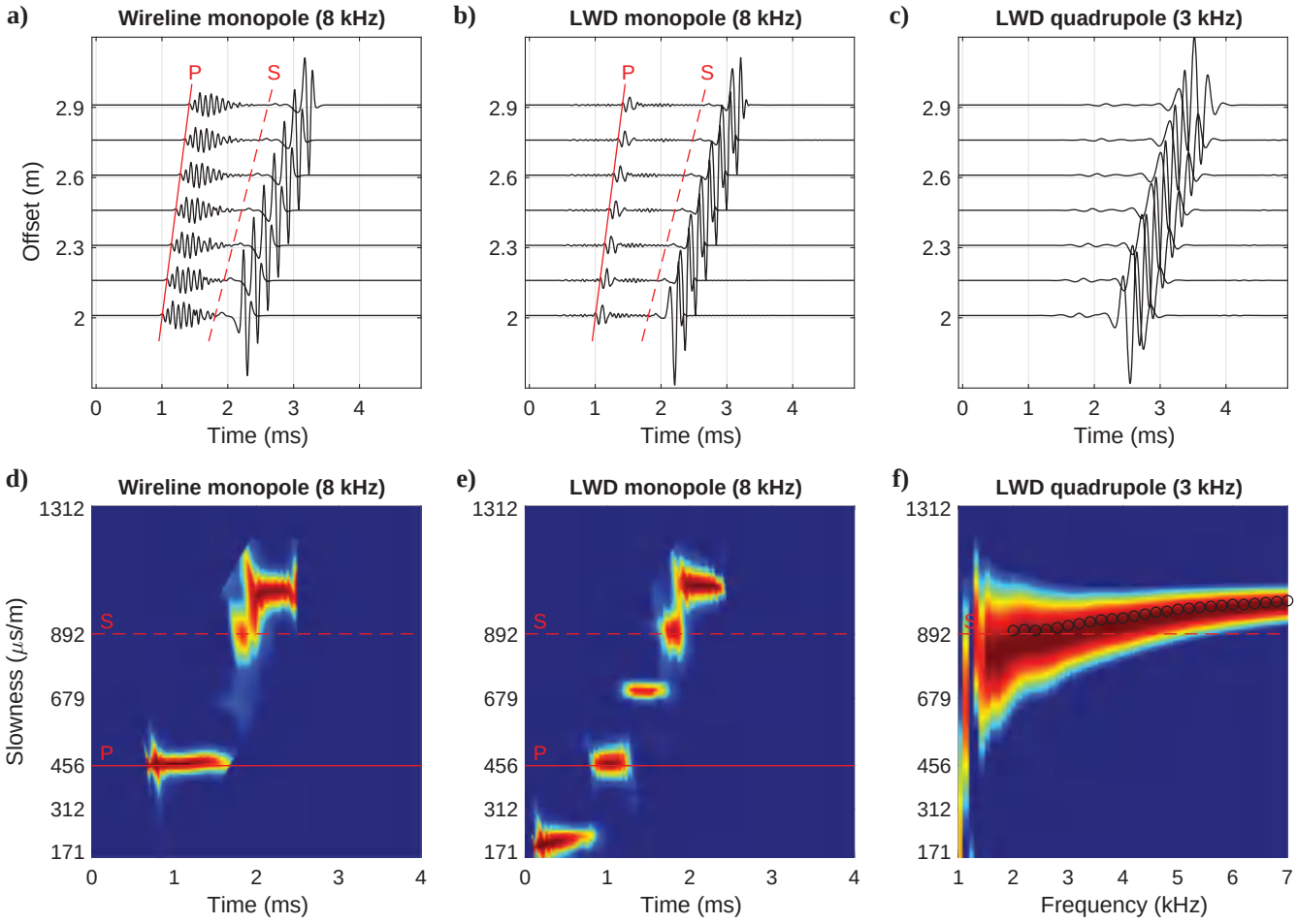


Figure 3. (a and b) Synthetic monopole waveforms for the wireline and LWD models, respectively. The solid and dashed red lines mark the P- and S-wave arrival time, respectively. (d and e) STC calculated from the corresponding waveforms. (c and f) Synthetic quadrupole waveforms and the corresponding SFC for the LWD model, respectively. The black circles in (f) represent the quadrupole dispersion curve. The source signal's center frequencies are 8 and 3 kHz for the monopole and quadrupole sources, respectively.

Downloaded 12/23/19 to 218.201.114.137. Redistribution subject to SEG license or copyright; see Terms of Use at http://library.seg.org/

Downloaded 12/23/19 to 218.201.114.137. Redistribution subject to SEG license or copyright; see Terms of Use at http://library.seg.org/

FIELD DATA ANALYSIS

We have briefly discussed the generation mechanism of the transmitted S-wave in a slow formation. Through numerical modeling, we have shown that monopole and quadrupole LWD can be used to derive the S-wave slowness of a slow formation. In this section, we study the characteristics of the transmitted S-wave observed in a suite of field LWD data acquired in a slow formation and compare the S-wave slowness extracted from the monopole and quadrupole data. Figure 4 shows the logging data recorded in a 150 m long section. The caliper data (Figure 4b) indicate that the wellbore is in an intact condition. The gamma-ray log (Figure 4a) does not change much with depth but the density log (Figure 4c) shows significant variations. The signals with high amplitude (in red) shown in the monopole data (Figure 4d) are the Stoneley wave, and the dominant signals in the quadrupole data (Figure 4e) are the quadrupole wave.

Figure 5 shows a comparison of the monopole and quadrupole waveforms at two different depths. Note that the monopole and quadrupole transmitters are located at different distances to the first receiver. Figure 6 shows the corresponding STC and SFC for the monopole and quadrupole data, respectively. Figure 5a shows a coherent wave arriving ahead of the Stoneley wave. In Figure 6a and 6b, we can see that the slowness of this wave is approximately 760 μs/m, which is the same as the slowness of the quadrupole wave at the cut-off frequency (approximately 2 kHz). This wave is interpreted as the slow-formation transmitted S-wave because its slowness is larger than the estimated mud slowness that is approximately 680 μs/m. The consistency between the slowness of the transmitted S-wave and that of the quadrupole wave at the cut-off frequency demonstrates the detectability of the slow-formation transmitted S-wave in a borehole. However, the transmitted S-wave does not appear in the monopole data acquired at the depth of ×78 m (Figures 5c and 6c). The quadrupole data indicate that the S-wave slowness is more than 800 μs/m at this depth. To understand this phenomenon, we investigate the compressional-to-shear (PS) transmission at a fluid-solid planar interface (Aki and Richards, 1980). Figure 7 shows the value of the PS transmission

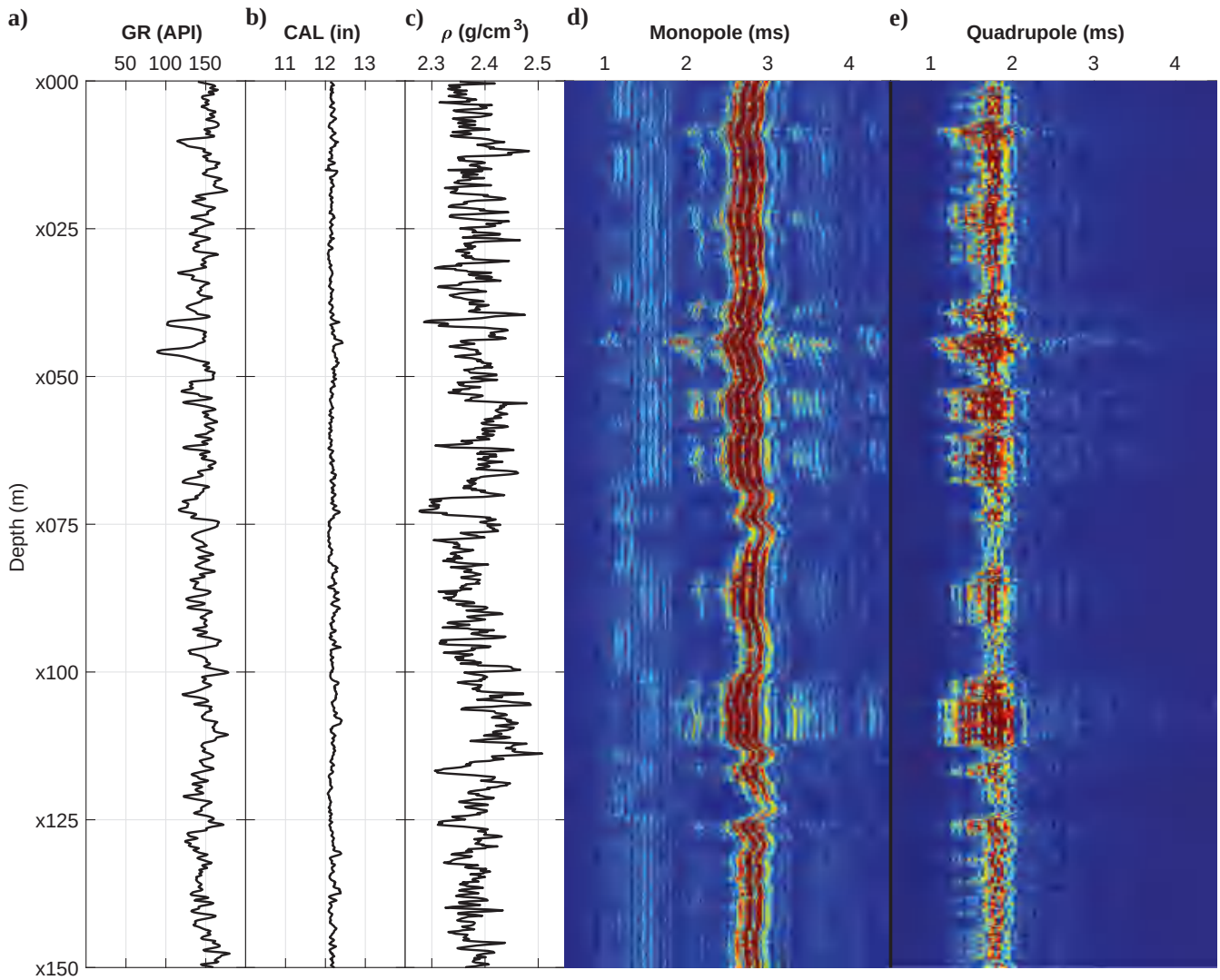


Figure 4. (a) Gamma ray, (b) caliper, (c) density, (d) monopole waveforms recorded at the first receiver, and (e) quadrupole waveforms recorded at the first receiver.

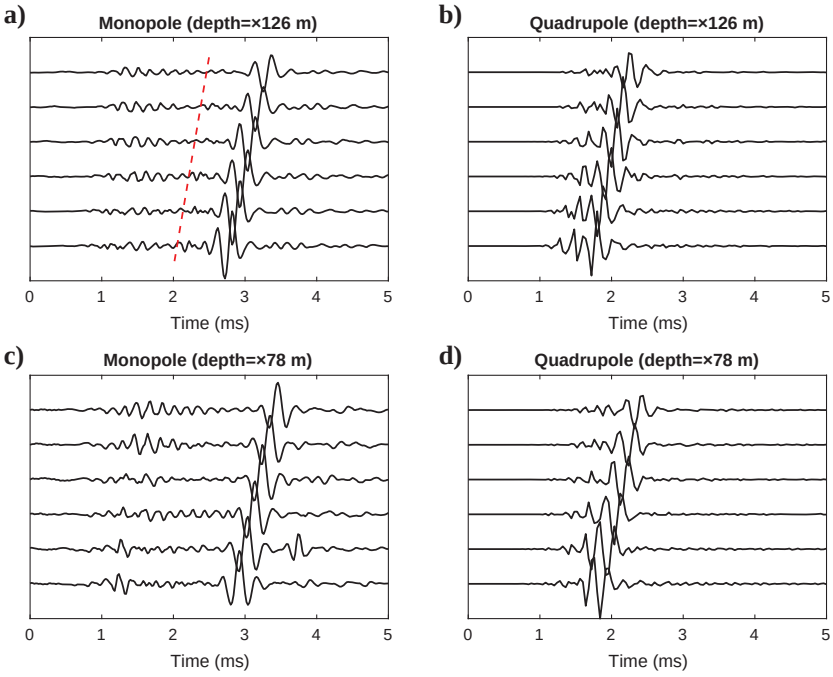


Figure 5. (a and c) Monopole and (b and d) quadrupole waveforms recorded at (a and b) ×126 m and (c and d) ×78 m depth. The dashed red line in (a) indicates the transmitted S-wave.

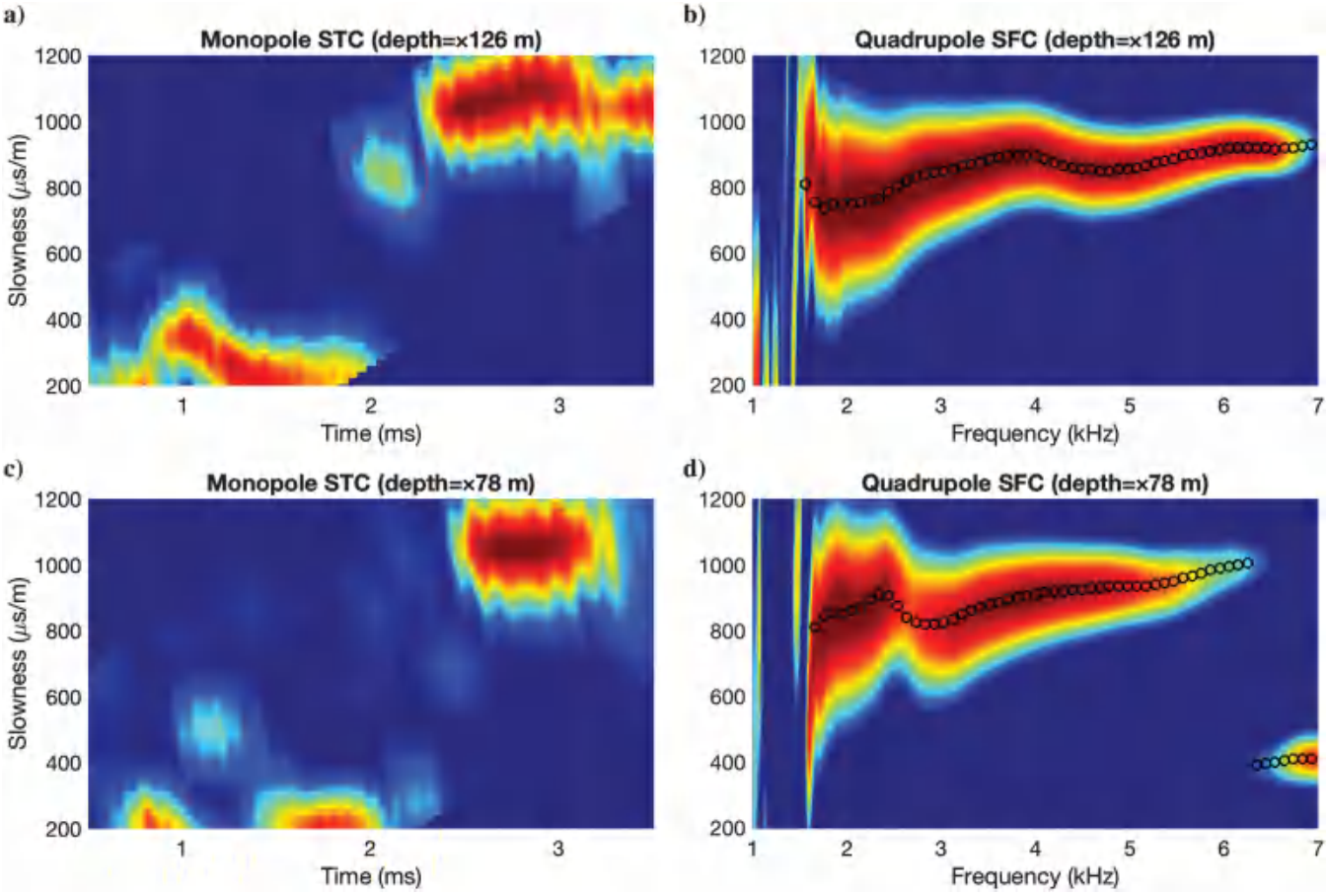


Figure 6. (a and c) STC for the monopole data and (b and d) SFC for the quadrupole data at (a and b) ×126 m and (c and d) ×78 m depth. The red circle in (a) highlights the bright spot that corresponds to the transmitted S-wave. The black circles in (b) and (d) represent the quadrupole dispersion curves.

Downloaded 12/23/19 to 218.201.114.137. Redistribution subject to SEG license or copyright; see Terms of Use at http://library.seg.org/

Downloaded 12/23/19 to 218.201.114.137. Redistribution subject to SEG license or copyright; see Terms of Use at http://library.seg.org/

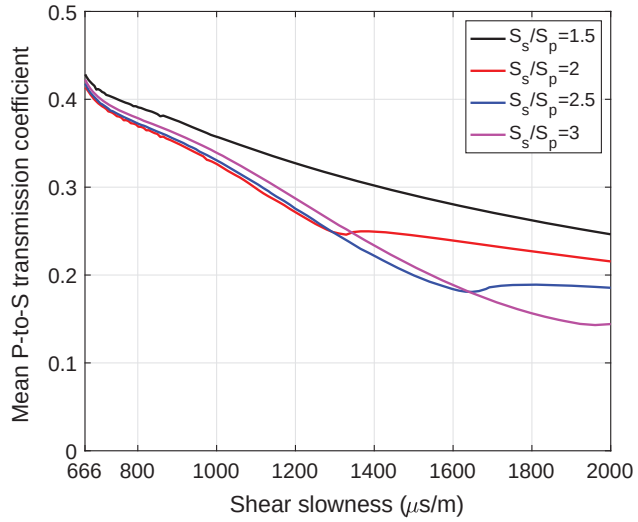


Figure 7. Variation of the compressional-to-shear transmission coefficient (the average of the absolute value over all incident angles) for varying formation P- (S_P) and S-wave (S_S) slownesses at a fluid-solid interface. The fluid slowness is 666 μs/m.

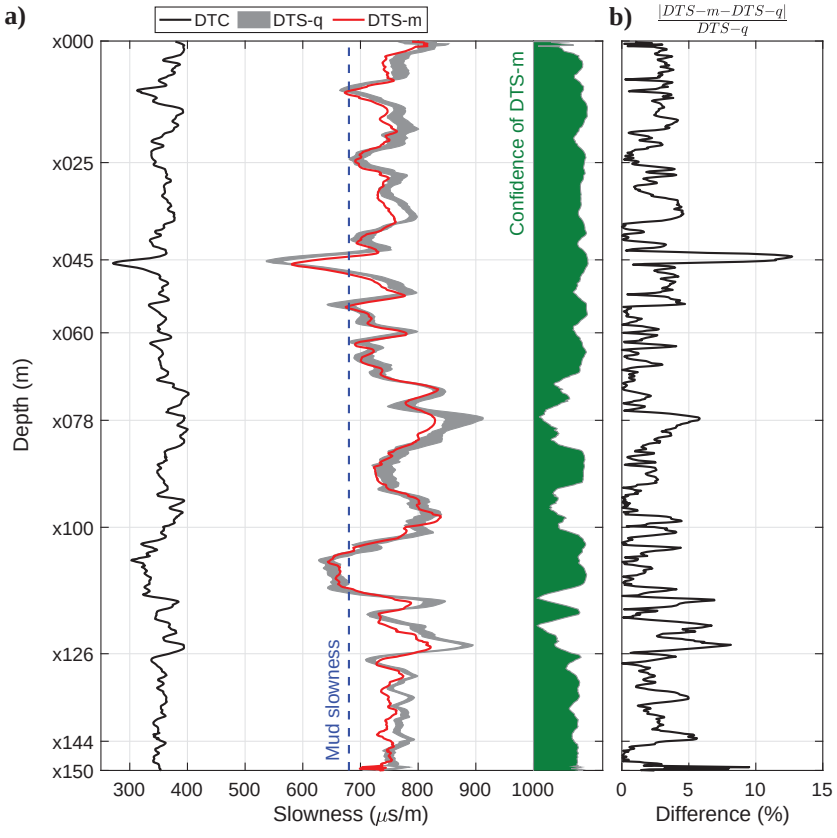


Figure 8. (a) Black compressional slowness (DTC) and red monopole-derived shear slowness (DTS-m) curves in the left panel are the P- and S-wave slownesses extracted from the monopole data, respectively. The gray-shaded curve (DTS-q) is the S-wave slowness determined from the quadrupole data. The gray shading represents the uncertainty of the S-wave slowness measurements. The area chart in green represents the DTS-m confidence, which is defined as the amplitude of the transmitted S-wave relative to that of the Stoneley wave in an STC plot. The black curve in (b) gives the percentage difference between DTS-m and DTS-q.

coefficient at a fluid-solid interface (the average of the absolute value over all of the incident angles) decreases with increasing S-wave slowness of the formation for a wide range of formation shear-to-compressional slowness ratio. Although the effect of wellbore curvature is not considered in the PS transmission calculation, this simple analysis implies that the strength of the borehole transmitted S-wave should decrease with increasing formation S-wave slowness. Thus, the transmitted S-wave is too weak to detect at the depth of ×78 m due to the increase in the formation S-wave slowness.

We calculate the monopole STC at each depth and then manually pick the slowness of the transmitted S-wave from the monopole STC. We also derive the quadrupole dispersion relation from the quadrupole waveforms and estimate the formation shear slowness from the dispersion curves near the cut-off frequencies. In Figure 8, the black compressional slowness (DTC) and red monopole-derived shear slowness (DTS-m) curves are the P- and S-wave slownesses extracted from the monopole data, respectively. Because DTS-m is more reliable when the transmitted S-wave is more prominent in the data, we use the amplitude ratio of the transmitted S-wave and the Stoneley wave, which is shown as the area chart in green, to represent the confidence of DTS-m. By analyzing the quadrupole data, we find that the quadrupole dispersion curves do not always steadily converge to a single slowness value near the cut-off frequencies. To account for the uncertainty in interpreting the dispersion, we estimate a possible range for the S-wave slowness measured from the quadrupole dispersion at each depth. The gray-shaded curve (DTS-q) shows the S-wave slowness estimated from quadrupole dispersion with the width of the gray shading representing the measurement uncertainty. We use a 2 m moving average window to smooth the DTS-m and DTS-q curves to make the variation trends more prominent. The percentage difference between DTS-m and DTS-q (mean values) shown in Figure 8b indicates that the difference between the S-wave slowness determined from the monopole and quadrupole data is generally less than 6%. When considering the confidence of DTS-m (the green area chart), we can see that the DTS-m curve agrees well with the DTS-q curve in the regions of high confidence. The low-confidence regions, such as at the depth of ×078 and ×100 m, are associated with layers with an S-wave slowness greater than approximately 800 μs/m. This is consistent with our previous finding that the magnitude of the transmitted S-wave decreases with the increasing formation S-wave slowness. Note that DTS-q is provided as a reference here, but it is not necessarily the exact formation S-wave slowness because the quadrupole dispersion may be affected by several unknown factors associated with the logging operation and downhole environments.

Figure 8 also indicates that there are several thin layers having their S-wave slowness lower than the mud slowness (the dashed blue line). The monopole formation S-wave detected in

these fast layers is actually the refracted S-wave. This does not affect our analysis as the slow-formation transmitted S-wave and the fast-formation refracted S-wave propagate at the formation S-wave velocity. Thus, the processing procedure for obtaining S-wave slowness can be applied to the fast and slow formations.

Figure 9 shows a comparison of the monopole STC (the left column) and quadrupole SFC (the right column) together with the quadrupole dispersion (the black circles) at five different depth positions. At the depth of ×045 m, the bright spot appearing at approximately 2 ms in Figure 9a should correspond to the refracted S-wave because the monopole STC and quadrupole dispersion indicate that this is a fast formation. The slowness of the low-frequency portion of the quadrupole dispersion curve shown in Figure 9b is a bit lower than that of the refracted S-wave. This discrepancy can be caused by the abrupt velocity change at this depth, as shown in Figure 8. In Figure 9c, 9g, and 9i, the S-wave slowness values extracted from the transmitted S-wave (the dashed red lines) agree well with the slowness of the quadrupole dispersion curves at

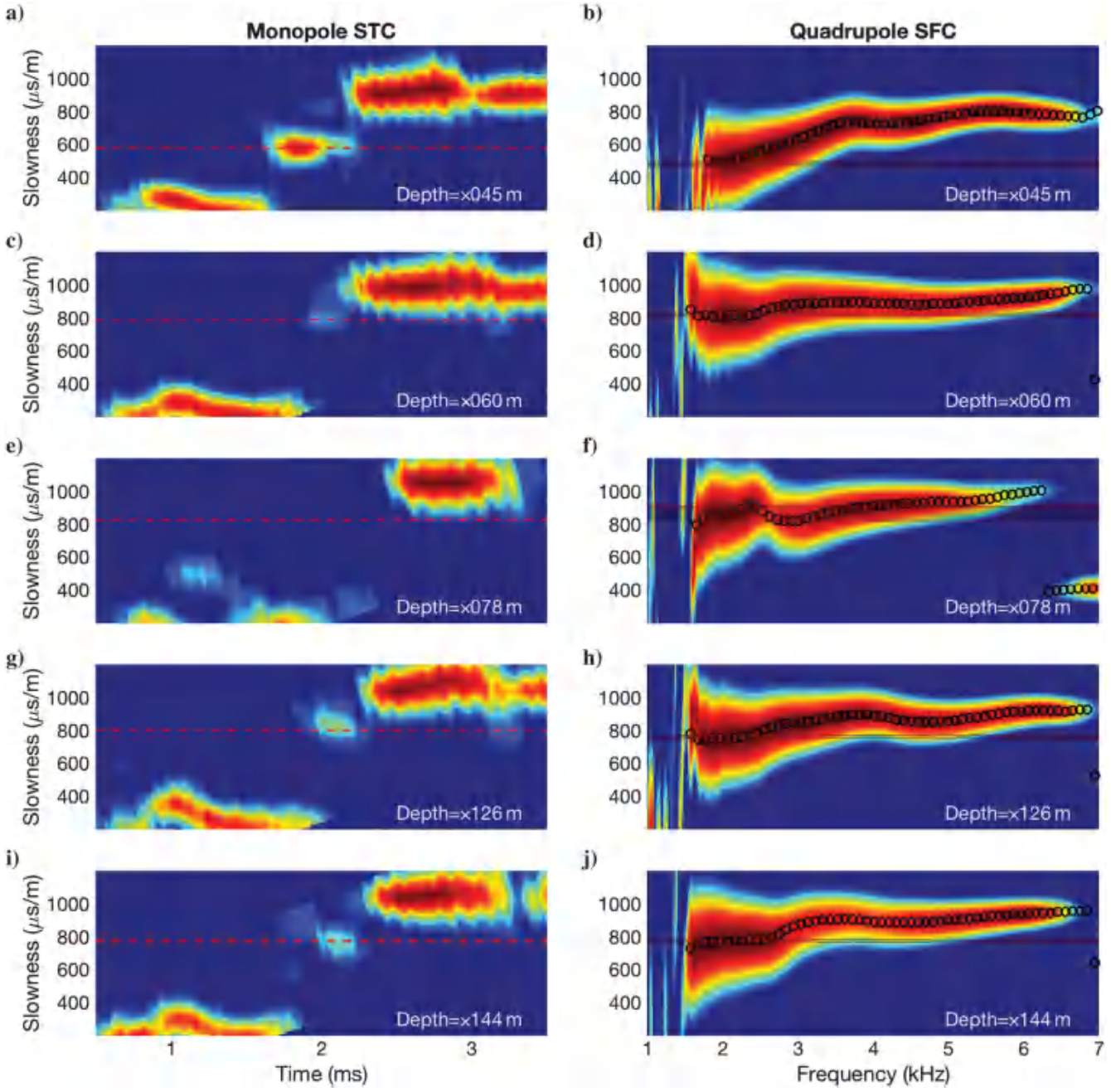


Figure 9. Comparison of monopole STC and quadrupole SFC at five different depths. The dashed red lines in the STC plots indicate the S-wave slowness determined from the monopole transmitted S-wave. The red stripes in the SFC plots represent the S-wave slowness interpreted from the quadrupole dispersion curves, which are shown as black circles. The height of the stripes, which is equivalent to the width of the gray shading of the DTS-q curve in Figure 8, corresponds to the estimated uncertainty.

Downloaded 12/23/19 to 218.201.114.137. Redistribution subject to SEG license or copyright; see Terms of Use at http://library.seg.org/

Downloaded 12/23/19 to 218.201.114.137. Redistribution subject to SEG license or copyright; see Terms of Use at http://library.seg.org/

the cut-off frequencies (approximately 2 kHz). However, the transmitted S-wave in Figure 9e is too faint to discern. The corresponding quadrupole dispersion shown in Figure 9f indicates that the formation S-wave slowness is more than 800 μs/m at this position. Overall, the field data results demonstrate that the transmitted S-wave is detectable in a borehole and can yield formation S-wave slowness in fairly slow formations. When the formation S-wave slowness is higher than a certain value, for example, 800 μs/m in these field data, the transmitted S-wave becomes too faint to detect.

The results for this field data set demonstrate that the S-wave slownesses extracted from monopole and quadrupole data show consistent variation trends. However, the DTS-m and DTS-q curves shown in Figure 8 are not exactly the same. This suggests that the analysis of field data is complicated. The relatively large difference between DTS-m and DTS-q in the regions with low DTS-m confidence could be caused by the uncertainty induced by weak transmitted S-wave signals. In other regions, the deviation of DTS-m from DTS-q may not represent an error in DTS-m because there is no true solution in this study because the exact formation S-wave slowness is unknown. We derive DTS-m and DTS-q based on the formation responses of different waves and then interpret them as formation S-wave slowness. The underlying assumption in the analyses is that the formation at each measured depth is homogeneous and isotropic. However, the actual formations can be heterogeneous, anisotropic, and even inelastic. These complexities can have different effects on the propagation of the transmitted S-wave and the quadrupole wave, resulting in different alterations to DTS-m and DTS-q. Thus, the DTS-m or DTS-q curves are not necessarily identical because they may represent different physical responses of the formations. Therefore, to better understand and interpret the DTS-m and DTS-q measurements, it is necessary to perform a thorough investigation of the influence of different downhole complexity factors to the propagation of the transmitted S-wave and the quadrupole wave in future studies.

CONCLUSION

We have studied an acoustic LWD data set acquired in a slow formation and shown that a monopole source can produce a detectable transmitted S-wave in a fairly slow formation. This phenomenon is consistent with our numerical modeling results. Comparison of the S-wave slowness extracted from the transmitted S-wave and that derived from the quadrupole data demonstrates the applicability of the transmitted S-wave in measuring the S-wave slowness of slow formations. This provides a new technique to measure the S-wave slowness of slow formations during drilling when quadrupole LWD is not available. We have tested this new method on numerical and field data. However, this approach is not applicable to very slow formations because the transmitted S-wave is too weak to detect in such formations.

ACKNOWLEDGMENTS

This work was supported by Science and Technology Foundation of Shenzhen (grant no. KQTD20170810111725321) and National Natural Science Foundation of China (grant nos. 41704112 and 41774138). We thank J. Shragge, J. Blanch, D. Draganov, and three anonymous reviewers for their comments that helped us improve the manuscript.

DATA AND MATERIALS AVAILABILITY

Data associated with this research are confidential and cannot be released.

REFERENCES

Aki, K., and P. Richards, 1980, Quantitative seismology: Theory and methods: Freeman.

Chen, S., 1989, Shear-wave logging with quadrupole sources: Geophysics, 54, 590–597, doi: 10.1190/1.1442686.

Fang, X., and A. Cheng, 2018, Detection of formation S-wave in a slow formation using a monopole acoustic logging-while-drilling tool: Geophysics, 83, no. 1, D9–D16, doi: 10.1190/geo2017-0300.1.

Jørgensen, O., and D. Burns, 2013, Novel finite-element approach applied to borehole quadrupole dispersion analysis in stress-sensitive formations: Geophysics, 78, no. 6, D499–D509, doi: 10.1190/geo2012-0487.1.

Rao, R. V. N., and J. K. Vandiver, 1999, Acoustic of fluid-filled boreholes with pipe: Guided propagation and radiation: Journal of the Acoustical Society of America, 105, 3057–3066, doi: 10.1121/1.424635.

Su, Y. D., X. M. Tang, C. X. Zhuang, S. Xu, and L. Zhao, 2013, Mapping formation shear-velocity variation by inverting logging-while-drilling quadrupole wave dispersion data: Geophysics, 78, no. 6, D491–D498, doi: 10.1190/geo2013-0136.1.

Syresin, D., N. Sakiyama, H. Yamamoto, R. Iritani, and H. Nakajima, 2016, Characterization of azimuthal slowness sensitivity for LWD unipole tools: 57th Annual Logging Symposium, SPWLA, Extended Abstracts, SPWLA-2016–BB.

Tang, X. M., and C. Cheng, 2004, Quantitative borehole acoustic methods: Elsevier.

Tang, X. M., V. Dubinsky, T. Wang, A. Bolshakov, and D. Patterson, 2002, Shear velocity measurement in the logging-while-drilling environment: Modeling and field evaluations: 43rd Annual Logging Symposium, SPWLA, Extended Abstracts, SPWLA-2002–RR.

Varsamis, G. L., L. T. Wisniewski, A. Arain, and G. Althoff, 1999, A new MWD full wave dual mode sonic tool design and case histories: 40th Annual Logging Symposium, SPWLA, Extended Abstracts, SPWLA-1999–F.

Wang, T., M. Dawber, and P. Boonen, 2011, Theory of unipole acoustic logging tools and their relevance to dipole and quadrupole tools for slow formations: Annual Technical Conference and Exhibition, SPE, Extended Abstracts, SPE-145515, doi: 10.2118/145515-MS.

Zhang, Z., M. Mochida, M. Kubota, H. Yamamoto, and T. Endo, 2010, Shear slowness estimation by inversion of LWD borehole quadrupole mode: 80th Annual International Meeting, SEG, Expanded Abstracts, 528–532, doi: 10.1190/1.3513837.

GEOPHYSICS, VOL. 81, NO. 5 (SEPTEMBER-OCTOBER 2016); P. D553–D560, 7 FIGS., 1 TABLE.
10.1190/GEO2016-0133.1

Downloaded 09/03/16 to 218.201.114.139. Redistribution subject to SEG license or copyright; see Terms of Use at http://library.seg.org/

Joint inversion of logging-while-drilling multipole acoustic data to determine P- and S-wave velocities in unconsolidated slow formations

Yuan-Da Su[1], Can Jiang[1], Chun-Xi Zhuang[1], Song Xu[1], and Xiao-Ming Tang[1]

ABSTRACT

We have developed a joint inversion method for logging-while-drilling (LWD) multipole acoustic data processing to simultaneously determine the formation of P- and S-wave velocities. The presence of the LWD tool strongly influences the dispersion characteristics of quadrupole and monopole leaky-P-waves, especially in unconsolidated slow formations. We have verified that an equivalent-tool theory can be adequately used to model the LWD multipole wave dispersion characteristics and can therefore be used to do forward modeling for the inversion. A major advantage of jointly inverting the multipole data sets, as compared with separately inverting each individual data set, is the reduction of uncertainties in the estimated formation of P- and S-wave velocities. We have applied the method to field data processing. The results found that the method not only corrected the dispersion effect in the quadrupole and leaky-P-wave data but also simultaneously obtained the formation of P- and S-wave velocities.

INTRODUCTION

Logging-while-drilling (LWD) acoustic technology has been undergoing rapid development in the past few decades. A significant advancement in LWD acoustic technology is the development of quadrupole S-wave technology (Tang et al., 2002, 2006; Dubinsky et al., 2003; Kinoshita et al., 2010). The advantage of the LWD quadrupole technology is that when the measurement is made in the low-frequency range, the formation quadrupole wave propagates at formation shear velocity and the tool quadrupole wave is not excited. Despite the advancement of the technology, LWD acoustic data processing faces many challenges in acquiring the accurate formation of P- and S-wave velocities. One of the challenges is data processing for shallow, unconsolidated, and acoustically very slow formations frequently encountered in drilling a deepwater reservoir.

A major difficulty in LWD acoustic data processing is the dispersion effect of the waveform data that is caused by borehole waveguide and aggravated by the presence of a large LWD tool. In general, the LWD quadrupole waves are quite dispersive, especially when a heavy drilling mud is used. Adding to the complexity, the LWD P-waves from a monopole source also become dispersive in drilling an unconsolidated, very slow formation. The waves are referred to as leaky-P-waves in the literature (Tang and Cheng, 2004). The P-waves are leaky because they radiate energy into formation by conversion to S-waves. The attenuation caused by the energy loss in turn causes dispersion of the waves propagating along the borehole (Tang and Cheng, 2004). Various methods have been developed to extract the formation of P- and S-wave velocities from the LWD data. Because the waves are dispersive, dispersion correction methods are commonly used. For example, Tang et al. (2006) and Zhang et al. (2010) develop model-based inversion methods to invert S-wave velocity from quadrupole-wave data. Tang et al. (2010) develop a curve-fitting method to acquire the P-wave velocity from the leaky-P-wave data. In the previous methods, the P- and S-wave velocities were obtained separately from the monopole P- and quadrupole-wave data. A major contribution of this work is to obtain the P- and S-wave velocities simultaneously from a joint inversion of the two data sets. This is possible because, in the LWD environment, the dispersion characteristics of leaky-P-waves and quadrupole waves are largely controlled by the LWD tool that occupies a large portion of the borehole. This common controlling factor provides a basis for the joint inversion of the two types of data in the LWD environment.

In what follows, we first describe an equivalent tool method to model the LWD multipole wave dispersion characteristics, which provides forward modeling for the leaky-P- and quadrupole-wave

Manuscript received by the Editor 11 March 2016; revised manuscript received 16 June 2016; published online 11 August 2016.
[1]China University of Petroleum, School of Geosciences, Qingdao, China. E-mail: syuanda@sina.com; jiangcan_upc@sina.com; zhuangchunxi@sina.com; xusongupc@sina.com; tangxiam@aliyun.com.
© 2016 Society of Exploration Geophysicists. All rights reserved.

Downloaded 09/03/16 to 218.201.114.139. Redistribution subject to SEG license or copyright; see Terms of Use at http://library.seg.org/

dispersion. We then use the modeling to formulate a joint inversion method for the leaky-P- and quadrupole-wave data and validate the results using synthetic data. Finally, we apply the inversion method to field data processing and present the processing result.

EQUIVALENT-TOOL THEORY FOR LWD ACOUSTIC WAVES

The forward modeling of the multipole LWD wave dispersion curves needs to include the effects of the LWD tool. The actual logging tool built on the drill collar can be quite complicated, consisting of various compartments for electronics and sensors, etc. Therefore, using an effective model to adequately describe the LWD tool is essential for LWD wave dispersion curve modeling.

The equivalent-tool theory can be used to provide an effective method for LWD modeling. The theory is originally proposed by Tang and Cheng (2004) for modeling the monopole Stoneley wave and later extended by Su et al. (2011) for modeling multipole guided waves. More recently, Lee et al. (2016) successfully applied the theory to model the dispersion of wireline dipole acoustic data. Regardless of the tool's internal structure, the equivalent-tool theory uses only two parameters, tool radius and modulus, to model the tool effects on the multipole wave propagation and dispersion (Su et al., 2011). The dispersion equation for an equivalent tool centered in the borehole surrounded by a homogeneous, isotropic, and elastic formation is given by

$$D(k;\omega;F;B;M_T;a)=0; \tag{1}$$

where k is the axial wavenumber, ω is the angular frequency, F represents the elastic formation parameterized by P- and S-slowness and density, and B is the borehole waveguide containing borehole fluid parameterized by fluid P-slowness and density and borehole radius. The LWD tool is parameterized by tool radius a and tool effective modulus M_T (for a steel LWD collar, $M_T \approx E/(1-\upsilon)$, where E is the Young's modulus and υ is the Poisson's ratio [see Tang and Cheng, 2004]); D is the determinant of a 4×4 matrix $H_{ij}(i;j=1;2;3;4)$, modified from its counterpart without the tool. The mathematical expressions for the latter matrix, i.e., the matrix without the tool, can be found in Lee et al. (2016). For the equivalent-tool theory, the modification consists of replacing the elements H_{11} and H_{12} of the matrix without the tool, with the following expressions:

$$\begin{aligned} H_{11} &= -\left[\frac{n}{R}I_n(fR)+fI_{n+1}(fR)\right] \\ &\quad -E_{tool}\left[\frac{n}{R}K_n(fR)-fK_{n+1}(fR)\right] \\ H_{21} &= \rho_f\omega^2[I_n(fR)+E_{tool}K_n(fR)]; \end{aligned} \tag{2}$$

where ρ_f is the borehole fluid density, $f=\sqrt{k^2-\omega^2/\alpha_f^2}$ is the radial fluid wavenumber, α_f and R are the borehole fluid velocity and radius, respectively, I_n and K_n are the first and second modified Bessel functions of order n, respectively, and n is the order of multipole with $n=0$, 1, 2 denoting the monopole, dipole, and quadrupole, respectively. The tool coefficient in the above expressions is given below:

$$E_{tool}=-\frac{(M_T/a)\left[\frac{n}{a}I_n(fa)+fI_{n+1}(fa)\right]+\rho_f\omega^2 I_n(fa)}{(M_T/a)\left[\frac{n}{a}K_n(fa)-fK_{n+1}(fa)\right]+\rho_f\omega^2 K_n(fa)}: \tag{3}$$

By solving dispersion equation 1 in the frequency range of a given wave model (e.g., monopole $n=0$ or quadrupole $n=2$) to find the wavenumber k, the theoretical phase slowness dispersion curve $S(\omega)$ containing the LWD tool effect is calculated using

$$S(\omega)=\frac{k}{\omega}: \tag{4}$$

To follow the convention used in the logging community, we will use slowness (inverse velocity), instead of velocity, in the rest of the paper.

We use an LWD model to test the validity and effectiveness of the above equivalent-tool theory for modeling the LWD leaky-P- and quadrupole-wave dispersion characteristics. Figure 1 illustrates the cross section of an LWD acoustic tool consisting of a source, a receiver array, and an acoustic isolator with an internally carved drill collar between source and receiver. The elastic parameters of the LWD model are listed in Table 1 with an acoustically slow formation (slow

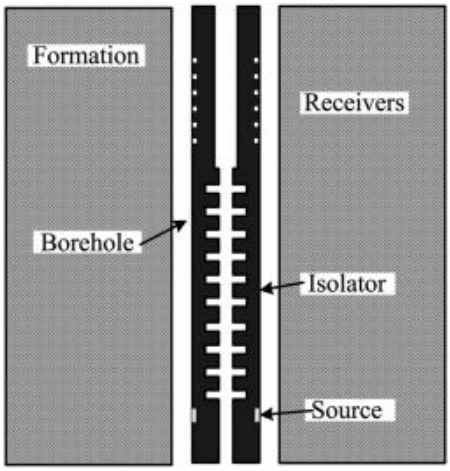


Figure 1. The LWD acoustic tool model to test the equivalent-tool theory.

Table 1. Parameters of drill collar and formation for calculating the LWD multipole waves.

Medium	P-slowness (μs/m)	S-slowness (μs/m)	Density (g/cm^3)	Radial range (m)
Collar	171	319	7.85	0.05–0.108
Mud	667	—	1.00	0–0.05 and 0.108–0.157
Slow formation 1	400	1000	2.198	0.157–∞
Slow formation 2	469	1218	2.172	0.157–∞

Downloaded 09/03/16 to 218.201.114.139. Redistribution subject to SEG license or copyright; see Terms of Use at http://library.seg.org/

formation 1, for which the parameter values are close to those used for the LWD modeling, e.g., Tang et al., 2002). For an LWD acoustic tool, groove cutting or carving is commonly used to isolate tool wave propagation along the tool. Because of the carved structure, numerical methods, such as the finite-difference or finite-element methods, are used to model acoustic wave propagation in the LWD environment. In this paper, a finite-difference method (Liu et al., 1996; Wang and Tang, 2003) is used to model multipole (monopole and quadrupole) wave propagation in the LWD model. Using a slowness-frequency-coherence method (Tang and Cheng, 2004; Lee et al., 2016), the waveforms across the receiver array are processed to obtain the monopole leaky-P- and quadrupole-wave dispersion data (open circles in Figure 2) in the frequency range of 2–7 kHz. The dispersion data for the two LWD wave modes, as calculated from the carved collar model in Figure 1, are simultaneously fitted using the equivalent tool model with tool radius $a = 0.108$ m and modulus $M_T = 269.6$ GPa. The theoretical dispersion curves (solid curve) calculated using the equivalent-tool theory fit the data very well, proving the validity of the theory.

THE JOINT INVERSION METHOD

The joint inversion method described below combines the sensitivity of LWD acoustic leaky-P- and quadrupole-wave modes to the formation of P- and S-wave velocities to invert the velocities and reduce the uncertainties in the inverted velocity values. For this inversion, a sensitivity analysis (Tang and Cheng, 2004; Su et al., 2011) is first performed on the wave modes using the model parameters of slow formation 1. The sensitivity is defined as the normalized partial derivative of the wave mode phase dispersion curve with respect to a model parameter, which indicates the importance of the parameter in affecting the wave's propagation characteristics. The sensitivity analysis result of Figure 3 demonstrates how the LWD tool and the formation elastic parameters affect the multipole wave dispersion characteristics. The leaky-P-wave is most sensitive to the P-velocity of the formation toward the low frequency. With increasing frequency, the P-sensitivity (solid curve) decreases and the wave's sensitivity to S-velocity (dashed curve) and that to the tool radius (dotted curve) systematically increase more than 40% toward high frequencies. This shows that the S-velocity of the formation and the LWD tool must be considered to handle the dispersion effect of the leaky-P-wave. In comparison, the quadrupole wave in this slow formation is mostly (slightly) sensitive to the S-velocity (P-velocity) of the formation and moderately sensitive to the LWD tool radius. The negative tool sensitivity means that the quadrupole velocity decreases (more dispersion) when tool size increases. The joint sensitivity of the LWD multipole waves to the LWD tool and formation (especially the S-velocity) parameters can be used to formulate a joint inversion method to more accurately determine the formation of P- and S-wave velocities.

The inversion consists of minimizing the following objective function constructed as the rms misfit error between theoretical dispersion curves of leaky-P S_m^{LP} and quadrupole S_m^{Q} and their respective dispersion data counterparts S_d^{LP} and S_d^{Q} in the respective measurement frequency ranges Ω_1 (leaky-P) and Ω_2 (quadrupole),

$$E(p;s) = \int_{\Omega_1} |S_m^{LP}(\omega;p;s) - S_d^{LP}(\omega)|^2 d\omega + \lambda \int_{\Omega_2} |S_m^{Q}(\omega;p;s) - S_d^{Q}(\omega)|^2 d\omega; \quad (5)$$

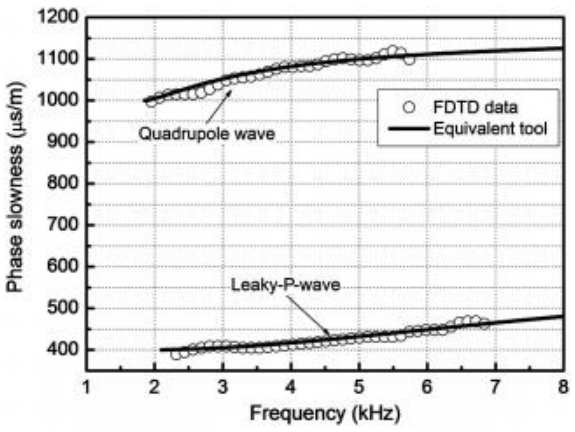


Figure 2. The LWD leaky-P (lower lines) and quadrupole (upper lines) dispersion data from the finite-difference time-domain (FDTD) modeling (open circles) of the model of Figure 1 and from the equivalent-tool theory (curve).

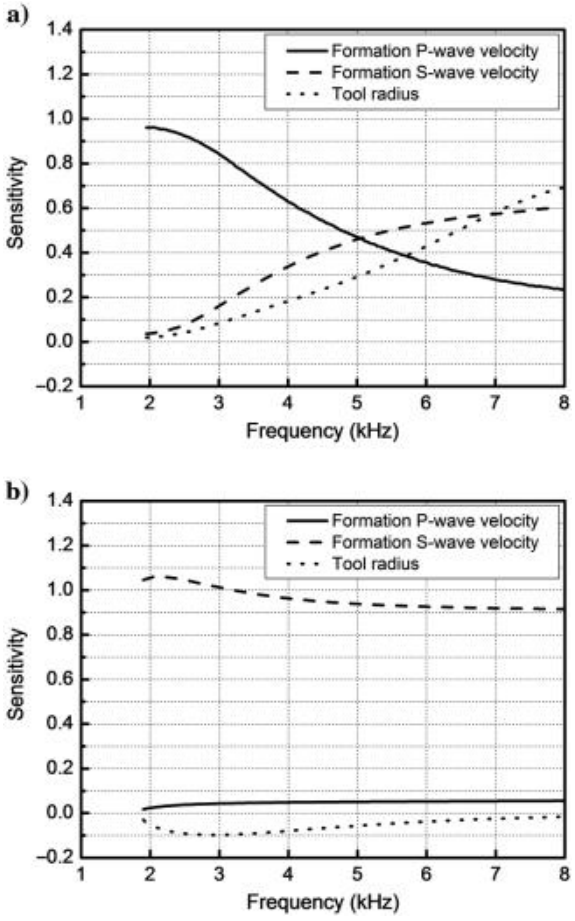


Figure 3. Sensitivity analysis for (a) the leaky-P- and (b) quadrupole-wave modes. The model parameters are listed in Table 1 (slow formation 1). The results show that both wave modes are influenced by the LWD tool and the formation parameters.

where p and s are the formation of P- and S-wave slowness parameters, respectively. The factor λ is a weighting factor to balance the contribution of each term in equation 5. In practice, λ is chosen according to the size of Ω_1 relative to Ω_2. The objective function can be minimized using the downhill simplex method (Press et al., 1992), which does not need to calculate the derivatives of the function with respect to the model parameters and is efficient.

We use the synthetic multipole acoustic data (see Figure 4) calculated using the finite-difference method for the model of Figure 1 with a very slow formation (slow formation 2 in Table 1, for which

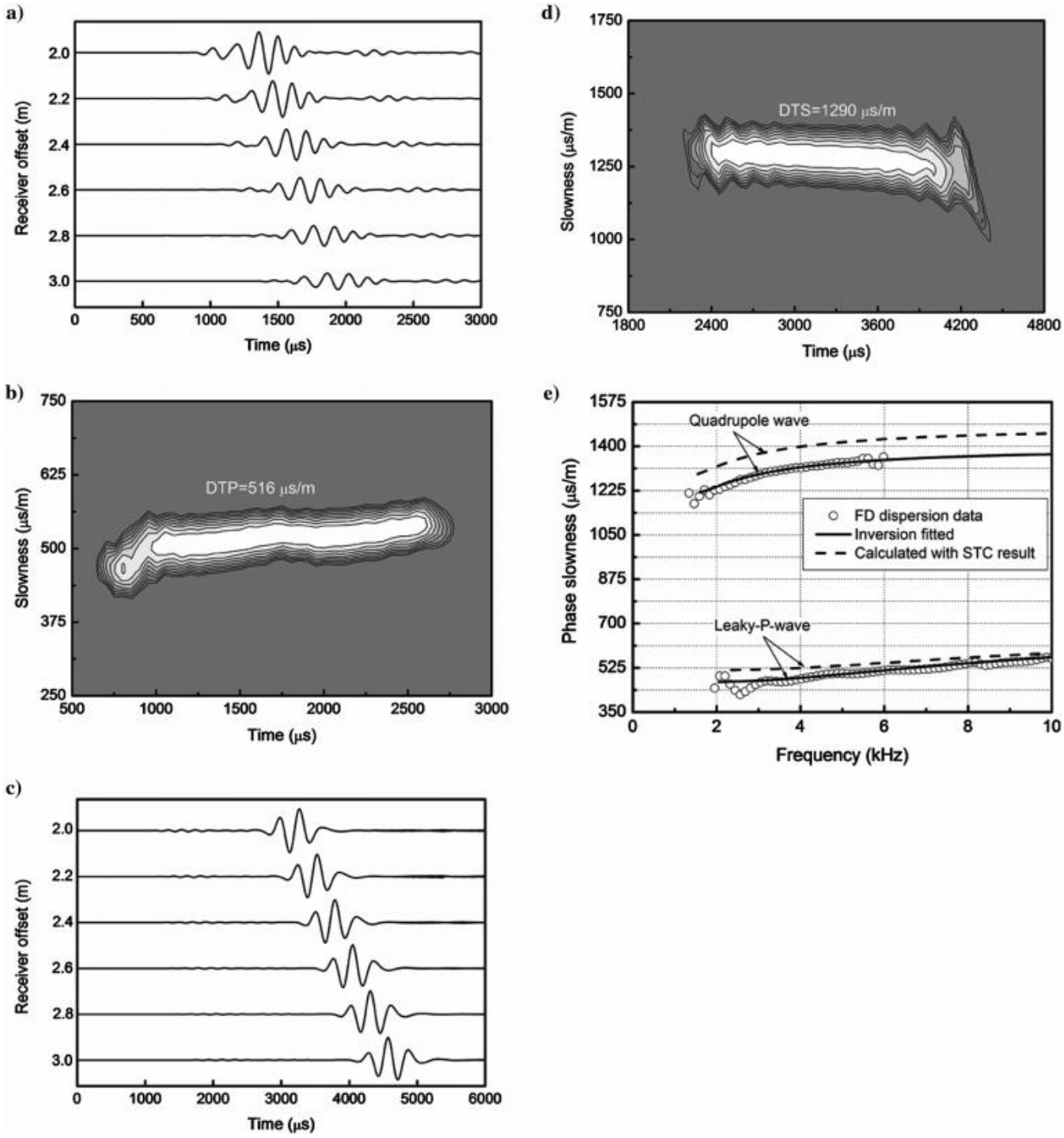


Figure 4. Test of the joint inversion method using (a) synthetic LWD leaky-P and (c) quadrupole waveform data. (e) The dispersion plot shows that the (b and d) leaky-P (lower lines) and quadrupole (upper lines) dispersion curves (solid) calculated using the STC processing results (the picked P- and S-slowness values DTP and DTS, as indicated in the figure) cannot fit the data (open circles). The dispersion curves from the joint inversion (dashed) fit the data quite well.

Downloaded 09/03/16 to 218.201.114.139. Redistribution subject to SEG license or copyright; see Terms of Use at http://library.seg.org/

Downloaded 09/03/16 to 218.201.114.139. Redistribution subject to SEG license or copyright; see Terms of Use at http://library.seg.org/

the parameter values are close to those of the very slow formation example to be discussed) to demonstrate the advantage of the joint inversion used in equation 5. The respective LWD leaky-P (Figure 4a) and quadrupole (Figure 4c) array waveform data are processed using the standard slowness-time-coherence (STC) method (Kimball and Marzetta, 1984), giving the respective STC correlograms in Figure 4b and 4d. The STC processing results, as picked from the high coherence (bright strip) location of the correlogram, are $p = 516$ μs/m and $s = 1290$ μs/m for the P- and S-slowness, respectively. Because the STC method does not handle the dispersion effect of the waveform data, it usually gives a slowness value that is significantly higher than the true formation slowness (Kimball, 1998; Geerits and Tang, 2003; Lee et al., 2016).

Using the respective STC-processed leaky-P and quadrupole results as the formation of P- and S-slowness values in the equivalent-tool theory (same tool parameters $M_T = 269.6$ GPa and $a = 0.157$ m are used), Figure 4e plots the calculated quadrupole and leaky-P-wave dispersion curves (solid curve) against the quadrupole and leaky-P dispersion data (open circles) extracted from the waveforms. The comparison shows that the STC method significantly overestimates the formation of P- and S-slowness values. Then, we use our inversion method to estimate the two slowness values.

The leaky-P and quadrupole dispersion data (open circle) in Figure 4e are used to test the inversion method described in equation 5. The forward modeling for the inversion uses the same equivalent-tool parameters as in Figure 2. To show how the joint inversion of equation 5 can help determine the formation of P- and S-slowness values, we first determine the inversion for each individual wave mode. In the leaky-P data inversion, the second term of equation 5 is dropped. Likewise, in the quadrupole data inversion, the first term is dropped. The resulting objective function in the 2D P- and S-slowness domains for the respective situation is shown in Figure 5a and 5b, respectively. The leaky-P objective function shows a long valley of low function values (white strip in the figure) slantly traversing the 2D plane, showing that the wave mode is indeed sensitive to the P- and S-wave slowness (see sensitivity analysis in Figure 3). However, because the valley is quite long, any pair of the P- and S-slowness values along the valley could be a solution to fit the leaky-P dispersion data. The quadrupole objective function also shows a long valley, varying slowly with the P-wave slowness. This again shows that the quadrupole wave is most sensitive to S-slowness and slightly sensitive to P-slowness. However, if the P-slowness is unknown, the S-slowness value along the valley has some uncertainty.

When the leaky-P and quadrupole objective functions are combined in equation 7, the resulting objective function shows a well-defined minimum (Figure 5c, indicated by an arrow). It is straightforward to find that, if the two valleys of Figure 5a and 5b are overlain, the minimum of Figure 5c occurs at the intersection of the two valleys. From the minimum, the formation of P- and S-slowness values are uniquely determined. The inverted P-slowness of 471.2 μs/m and S-slowness of 1214.5 μs/m are in agreement with their respective model parameter values (see Table 1). The model dispersion curves (dashed curves) calculated with the inverted parameter values fit the data (open circles in Figure 4e) quite well. Thus, combining, or jointly inverting, the leaky-P- and quadrupole-wave data not only simultaneously determines the formation of P- and S-wave slowness but also significantly reduces uncertainties of these two estimated parameters.

APPLICATION TO FIELD DATA

Multipole LWD acoustic data are commonly acquired to determine the formation of P- and S-slowness profiles, especially in the unconsolidated formation of deepwater wells. In the following, we apply our joint inversion method to field data processing and demonstrate the advantage and effectiveness of the method. The inversion is applicable and robust in the absence of strong drilling noises. In this condition, the leaky-P and quadrupole dispersion data can be reliably measured in the respective frequency range. This condition

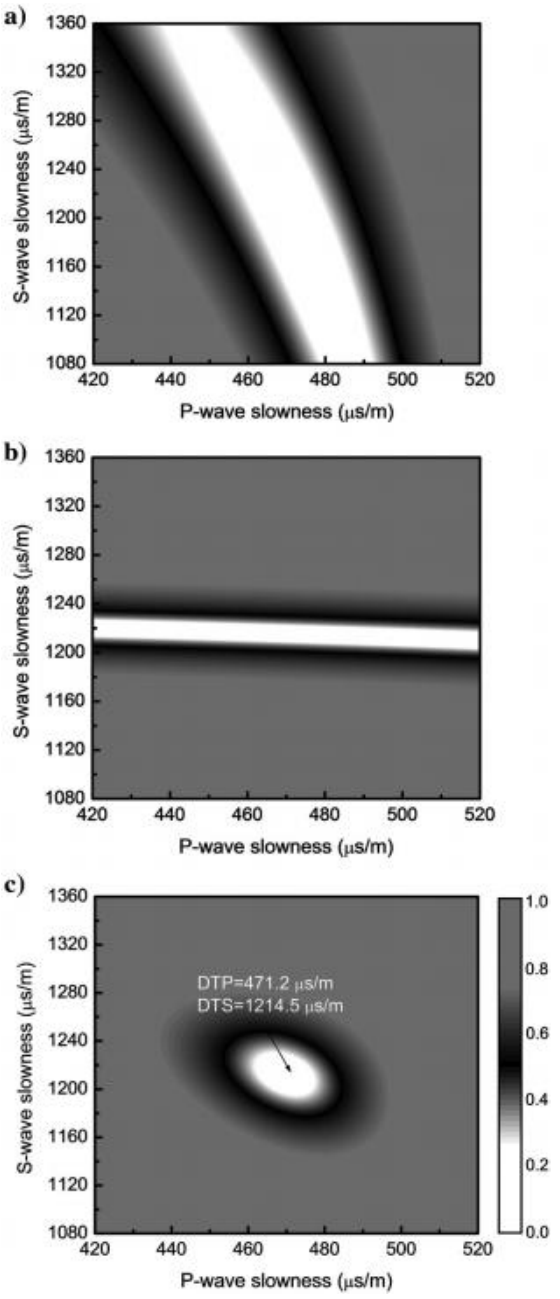


Figure 5. Objective function plots for (a) separately inverting leaky-P and (b) quadrupole data and for (c) the joint inversion of both data. The well-defined solution in panel (c) reduces the solution uncertainty in panels (a and b) cases.

Downloaded 09/03/16 to 218.201.114.139. Redistribution subject to SEG license or copyright; see Terms of Use at http://library.seg.org/

is usually satisfied in unconsolidated soft formations in which drilling is quiet without strong noises. Two data sets will be used. One is the data from a moderately fast formation, and the other is the data from a very slow formation.

Prior to the inversion, the monopole and quadrupole data are first filtered to remove low-frequency drilling noises. The dispersion characteristics of the data are then analyzed for the depth range of interest. This process determines the respective wave's frequency range for the inversion. In this frequency range, the wave's dispersion data are reliably measured.

Moderately fast formation example

Using the joint inversion, Figure 6 shows a moderately fast formation example for a depth interval of 420 m. Panel 1 shows the gamma ray and borehole caliper log curves. Panels 2 and 3 (4 and 5) show the variable density display of the monopole (quadrupole) waveform data and the STC correlogram from the data. Because this is a moderately fast formation, the formation of S-wave can be detected from the monopole data (panel 2) and the formation of S-slowness can be directly picked from the STC correlogram (see the DTS_Monopole curve in panel 3) of the data, which provides a test for our joint inversion method.

As explained before, LWD quadrupole is a dispersive wave and the STC-processed quadrupole slowness (see Panel 5) is slower than the true formation slowness. The joint inversion processing results are shown in panels 6 and 7. The inverted P-slowness is overlain with the STC-processed P-slowness in panel 6. Their percentage difference is the shaded curve in this panel. In this fast formation, the dispersion effect of the P-wave is negligible (except in the upper part where the formation is relatively slower) and the inverted P-slowness agrees well with the STC processed result. Still, the joint inversion is very effective in correcting the dispersion effect in the quadrupole-wave data. Panel 7 shows the processing result for the quadrupole wave. The inverted S-slowness curve (red) is overlain with the monopole S-slowness curve (blue). Because the latter curve is usually dispersion free, the excellent agreement between the two results demonstrates that the joint inversion method can indeed obtain the true formation of S-slowness from the dispersive LWD quadrupole data. There is a systematic difference between the inversion slowness (red) and the STC-processed slowness (black) curves. Their percentage difference is the shaded curve in this panel, showing there is an overall 3%–4% dispersion correction for this formation interval.

Very slow formation example

We now discuss the processing result of Figure 7 for the LWD data acquired for an unconsolidated, very slow formation of roughly 600 m interval. In Figure 7a, panel 1 shows the gamma ray and caliper log curves of this formation. Panels 2 and 3 show the monopole and quadrupole waveform data, respectively. For this very

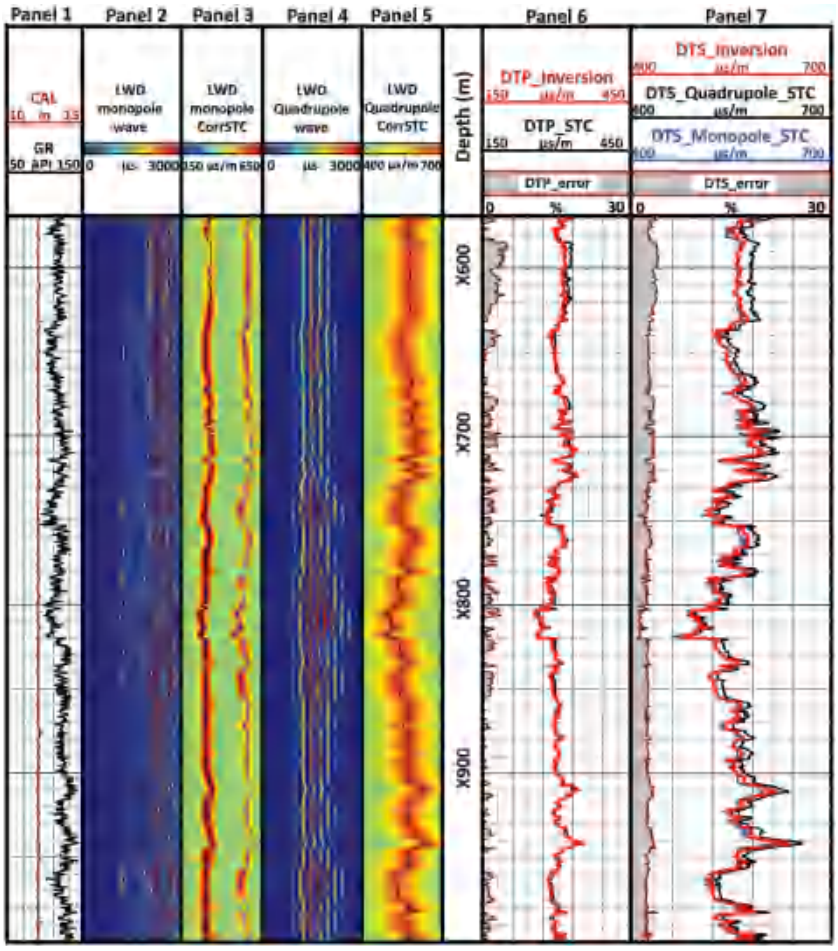


Figure 6. Example of LWD data joint inversion for a moderately fast formation. Panel 1 shows the conventional log curves. Panels 2 and 3 (4 and 5), respectively, show the monopole (quadrupole) wave data and the STC correlogram. Panels 6 and 7, respectively, show the inverted P- and S-slowness curves. In panels 6 and 7, the difference between the STC-processed slowness (black) and the inverted slowness (red) is the shaded curve on the left. In panel 7, the inverted slowness agrees with the monopole-S slowness (blue), validating the inversion results.

slow formation, the monopole data consist of mostly dispersive leaky-P-waves. The P- and S-slowness inversion results are displayed in panels 4 and 5, respectively. The curves in black are the STC-processing results, and the curves in red are the inversion results. The percentage difference between the inversion and STC-slowness curves is the gray-shaded curve in the respective panel. Figure 7b shows the leaky-P and quadrupole dispersion data (open circle) and theoretical dispersion curves calculated using the inversion (red) and STC (black) P- and S-slowness values for three representative depths from the upper (×335 m), middle (×575 m), and lower (×815 m) part of the formation.

There is a substantial dispersion effect in the leaky-P- and quadrupole-wave data, especially in the upper section in which the formation is unconsolidated and acoustically very slow. The dispersion correction is approximately 6%–8% for quadrupole and 10% for leaky-P-wave. With decreasing slowness (especially the S-slowness) in the middle section, the quadrupole dispersion decreases. In the bottom section in which formation becomes fast, the dispersion effects for both waves are much reduced. The validity of the inversion results can be seen from the dispersion data fitting plots in Figure 7b. The dispersion curves (black) from the STC-processed P- and S-slowness values cannot fit the data, whereas the curves (red) from the inverted slowness values fit the data quite well. Thus, the joint inversion collectively corrects the dispersion effect for the two wave data sets and obtains more accurate P- and S-slowness results from the data.

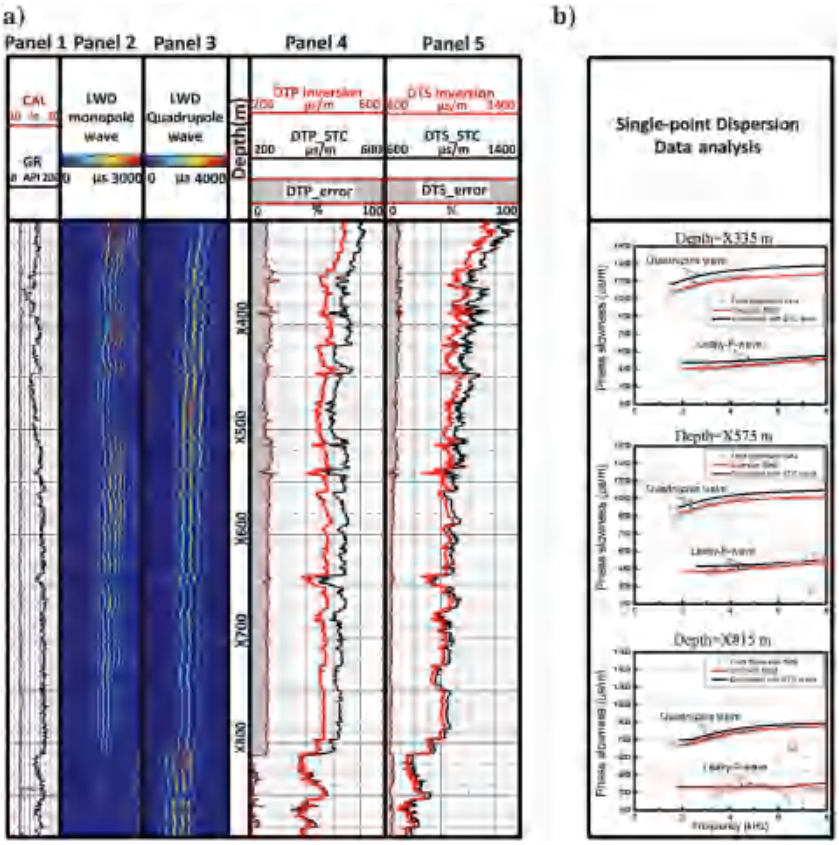


Figure 7. Example of the LWD data joint inversion for an unconsolidated slow formation. In (a), Panel 1 shows the conventional log curves. Panels 2 and 3 show the monopole leaky-P- and quadrupole-wave data, respectively. Panels 4 and 5, respectively, show the inversion (red) and STC-processed (black) leaky-P and quadrupole-S slowness curves and the percentage difference (shaded curve) of the red and black curves. Panel (b) shows details of dispersion data (open circles) fitting from STC (black) and inversion (red) results for three representative depths.

CONCLUSION

The multipole LWD acoustic data acquired in unconsolidated slow formations can be strongly dispersive, resulting in large uncertainties for P- and S-wave slowness measurements from these data. We demonstrated that the LWD model consisting of an elastic formation and an equivalent LWD tool can adequately model the dispersion characteristics of the multipole LWD waves. Furthermore, by using the LWD model to simultaneously fit the monopole and quadrupole dispersion data, we have developed a joint inversion method to simultaneously determine the P- and S-wave slowness profiles from the data. By using the joint inversion, the uncertainties in the formation slowness measurement from the LWD data are significantly reduced. Field data processing results show that the inversion corrects the dispersion effect in the LWD data and obtains the reliable formation of P- and S-wave velocities from the data, supporting the validity and effectiveness of the method.

ACKNOWLEDGMENTS

The authors thank the associate editor and reviewers for their comments and suggestions that helped to improve the manuscript. This work is supported by China Natural Science Foundation (grant no. 41474101 and 41474092).

REFERENCES

Dubinsky, V., X. M. Tang, A. Bolshakov, and D. Patterson, 2003, Engineering aspects of LWD quadrupole measurements and field test results: Presented at the SPE Annual Technical Conference and Exhibition, SPE, 84248.

Geerits, T., and X. M. Tang, 2003, Centroid phase slowness as a tool for dispersion correction of dipole acoustic logging data: Geophysics, 68, 101–107, doi: 10.1190/1.1543197.

Kimball, C. V., 1998, Shear slowness measurement by dispersive processing of borehole flexural mode: Geophysics, 63, 337–344, doi: 10.1190/1.1444333.

Kimball, C. V., and T. L. Marzetta, 1984, Semblance processing of the borehole acoustic array data: Geophysics, 49, 274–281, doi: 10.1190/1.1441659.

Kinoshita, T., A. Dumont, H. Hori, N. Sakiyama, J. Morley, and F. Garcia-Osuna, 2010, LWD sonic tool design for high-quality logs: 80th Annual International Meeting, SEG, Expanded Abstracts, 513–517.

Lee, S. Q., X. M. Tang, Y. D. Su, and C. X. Zhuang, 2016, Model-based dispersive processing of borehole dipole wave data using an equivalent-tool theory: Geophysics, 81, no. 1, D35–D43, doi: 10.1190/geo2015-0210.1.

Liu, Q. H., E. Schoen, F. Daube, C. Randall, H. L. Liu, and P. Lee, 1996, A three-dimensional finite difference simulation of sonic logging: Journal of the Acoustical Society of America, 100, 72–79, doi: 10.1121/1.415869.

Press, W. H., S. A. Teukolsky, W. T. Vetterling, and B. P. Flannery, 1992, Numerical recipes in C: Press Syndicate of the University of Cambridge.

Su, Y. D., X. M. Tang, C. Hei, and C. X. Zhuang, 2011, An equivalent-tool theory for acoustic logging and applications: Applied Geophysics, 8, 69–78, doi: 10.1007/s11770-011-0272-6.

Downloaded 09/03/16 to 218.201.114.139. Redistribution subject to SEG license or copyright; see Terms of Use at http://library.seg.org/

Tang, X. M., and C. H. Cheng, 2004, Quantitative borehole acoustic methods: Elsevier Science Publishing Co.
Tang, X. M., V. Dubinsky, and D. Patterson, 2006, Development of a low-frequency quadrupole shear-wave technology to improve quality of LWD shear velocity measurement: Presented at the SPE Annual Technical Conference and Exhibition, SPE, 102335.
Tang, X. M., V. Dubinsky, T. Wang, A. Bolshakov, and D. Patterson, 2002, Shear-velocity measurement in the logging-while-drilling environment: Modeling and field evaluations: Presented at the SPWLA 43rd Annual Logging Symposium.
Tang, X. M., C. Li, and D. Patterson, 2010, A curve-fitting technique for determining dispersion characteristics of guided elastic waves: Geophysics, 75, no. 3, E153–E160, doi: 10.1190/1.3420736.
Wang, T., and X. M. Tang, 2003, Finite-difference modeling of elastic wave propagation: A nonsplitting perfectly matched layer approach: Geophysics, 68, 1749–1755, doi: 10.1190/1.1620648.
Zhang, Z., M. Mochida, M. Kubota, H. Yamamoto, and T. Endo, 2010, Shear slowness estimation by inversion of LWD borehole quadrupole mode: 80th Annual International Meeting, SEG, Expanded Abstracts, 528–532.

Downloaded 09/03/16 to 218.201.114.139. Redistribution subject to SEG license or copyright; see Terms of Use at http://library.seg.org/

苏远大，许松，江灿等. 2017. 随钻四极子横波测井钻铤尺寸优化设计的理论研究. 地球物理学报，60(4)：1606-1615，doi：10.6038/cjg20170432.

Su Y D, Xu S, Jiang C, et al. 2017. Theoretical analysis of the optimal collar size for a logging while drilling quadrupole tool. *Chinese J. Geophys.* (in Chinese), 60(4): 1606-1615, doi: 10.6038/cjg20170432.

随钻四极子横波测井钻铤尺寸优化设计的理论研究

苏远大，许松，江灿，唐晓明

中国石油大学(华东)地球科学与技术学院，青岛 266580

摘要 随钻声波测井主要是采用四极子技术来测量软地层的横波速度，但在超软地层的横波测量方面仍然面临挑战. 随钻四极子声源会分别激发出沿着钻铤和地层传播的螺旋模式导波，其中四极子钻铤波存在截止频率，即只有在该频率以上才能激发出钻铤波. 当钻铤波截止频率降低到与地层波测量频段接近时，会干扰地层波信号的测量，尤其是在疏松的软地层这一干扰现象相当严重. 数值模拟和现场实测数据分析结果表明：四极子钻铤波的截止频率主要取决于仪器接收器阵列位置的钻铤壁厚，而对声源与接收器之间的刻槽隔声体以及钻铤外地层介质不敏感. 在此基础上，本文利用一种等效的随钻声波测井简化模型来分析与设计钻铤波截止频率与钻铤尺寸关系的理论图版. 该理论图版可用于指导随钻四极子横波测井仪器钻铤尺寸的优化设计和数据处理，进而获得高质量的地层波信号以及准确的横波速度.

关键词 随钻声波测井；横波速度；钻铤四极子波；截止频率；钻铤壁厚

doi：10.6038/cjg20170432 **中图分类号** P631 **收稿日期** 2016-02-14，2016-11-01 收修定稿

Theoretical analysis of the optimal collar size for a logging while drilling quadrupole tool

SU Yuan-Da, XU Song, JIANG Can, TANG Xiao-Ming

School of Geosciences, China University of Petroleum, Qingdao 266580, *China*

Abstract Logging-while-drilling (LWD) shear-wave velocity measurement in slow formation is mainly performed with quadrupole sources. However, this technology still faces many challenges in the ultra-slow formations. The LWD quadrupole waves consist of a formation quadrupole mode propagated along the borehole and a collar quadrupole mode propagated along collar, respectively. The collar quadrupole wave exists only above a certain frequency called the cut-off frequency. However, tool-wave contamination occurs when its cut-off frequency close to the main frequency band during the shear-wave measurement, especially in the slow formation situation. Both numerical simulations and field data analysis results show that the collar-wave cut-off frequency mainly depends on the collar thickness of receiver array section. The cut-off frequency is neither sensitive to the formation properties nor to the groove-isolator between source and receivers. Based on the sensitivity analysis of the LWD tool model, we developed an equivalent simplified approach to produce a theoretical template about the cut-off frequency versus collar sizes. The template can be used to aid the design of the LWD quadrupole tools or to guide the data processing measured by existing LWD tools, so as to obtain accurate formation shear velocity from the LWD quadrupole measurement.

基金项目 国家自然科学基金(41474092，41604109)资助.

第一作者简介 苏远大，男，1978 年生，副教授，博士，主要从事声波测井理论、方法及处理研究. E-mail：syuanda@sina.com

Keywords　Acoustic logging-while-drilling; Shear wave velocity; Collar quadrupole wave; Cut-off frequency; Collar thickness

1　引言

近年来,随钻声波测井技术发展很快,已在大斜度井、水平井以及深水钻井中广泛使用.随钻声波测井可以在钻井过程中确定地层纵波、横波速度,进一步用于实时预测地层孔隙压力、评估井壁稳定性以及评价岩石脆裂性等,这为油气田的勘探和开发提供了重要信息.

随钻纵波速度测量方面已经取得了成功(Aron et al., 1994; Minear et al., 1995; Joyce et al., 2001).在随钻单极子纵波测井中,通常采用在发射声源和接收换能器之间周期性刻槽的方法来阻隔沿着钻铤传播的波,从而有效地测量地层传来的声波(Joyce et al., 2001;Kinoshita et al., 2008;苏远大等, 2011).相对纵波测量而言,随钻横波测井仍然面临挑战,特别是在疏松的软地层(Tang et al., 2006;Scheibner et al., 2010).最初的随钻横波测量采用偶极子技术(Varsamis et al.,2000),但由于钻铤的存在使偶极子声源激发的钻铤弯曲波与地层弯曲波之间干扰严重,且使软地层中弯曲波的速度与地层横波速度差异较大(Tang and Cheng, 2004).因此,偶极子技术在软地层随钻横波测量中的应用受到很大限制.Tang 等(2002)首先提出利用低频四极子技术在随钻测井中测量地层的横波速度.相比偶极子技术,利用四极子测量地层横波具有明显的优势.四极子声源只有在某一截止频率以上才能激发钻铤模式的螺旋导波,而在低于截止频率的频段内只存在地层模式的螺旋波,而且该模式波在低频时以地层的横波速度传播(Tang et al.,2002;Tang and Cheng,2004).根据这些优势,国外制造了随钻四极子声波测井仪器,并在现场中广泛应用(Dubinsky et al.,2003;Market,2007;Kinoshita et al.,2008),国内正在开发类似的技术.

在随钻多极子声波测井仪器研制过程中,人们往往容易忽略钻铤厚度会影响四极子测量数据的质量.现有的随钻四极子仪器大都采用在薄壁钻铤位置安装四极子接收换能器装置(Tang et al.,2005).然而,这种薄壁钻铤必然会使沿着钻铤传播的四极子波的截止频率降低(Tang et al.,2002;Kinoshita et al.,2010),当其与地层四极子波的频率接近时,会严重干扰地层横波的测量.而且,这种低频的钻铤四极子波很难采用类似单极子纵波的隔声技术来消除掉.从随钻四极子实测现场数据来看,在疏松软地层中存在较强的钻铤四极子直达波的干扰,使地层四极子波的信噪比低,甚至有可能被钻铤直达波完全覆盖(苏远大,2014).这些实际问题都不利于随钻四极子准确测量地层横波速度.因此,本文在数值模拟和现场资料处理分析的基础上,考察随钻四极子声波测井仪器的钻铤波截止频率的主控因素,设计四极子钻铤波截止频率与钻铤尺寸的理论图版.将这一理论图版用于指导随钻四极子横波测井仪器的最优化设计以及现有测量数据处理参数的选取.最后,给出超软地层现场随钻四极子测井数据的处理实例.本文的研究工作为随钻四极子仪器设计与数据处理提供了理论依据.

2　钻铤四极子波截止频率的主控因素分析

2.1　钻铤壁厚对四极子波的影响

充液井孔中随钻四极子声源会激发一种沿着钻铤-井孔模型传播的频散模式螺旋导波,这一导波在四极子全波中占主导地位,是四极子测量的主要研究对象(崔志文,2004).由于井孔中钻铤的存在,使四极子螺旋波一部分能量沿着钻铤传播,称之为四极子钻铤模式螺旋波;另一部分沿着地层传播,称之为四极子地层模式螺旋波(Tang et al.,2002; Sinha et al.,2009).为了便于叙述,将其简称为四极子钻铤波和地层波.Tang 等(2002), Tang 和 Cheng(2004)理论模拟分析表明,四极子声源只有在某一特定频率以上才能激发钻铤模式的螺旋波,这一频率称之为钻铤波截止频率,在低于截止频率的频段,只存在以地层横波速度传播的地层模式螺旋波.这为随钻四极子横波测量奠定了理论基础.Tang 等(2002)、崔志文(2004)和 Kinoshita 等(2010)进一步研究发现,四极子钻铤波的传播特征非常敏感于钻铤的壁厚,即钻铤壁厚变薄四极子钻铤波的截止频率会降低,当其与地层波的频率接近时会对横波的测量产生干扰.上述理论研究工作从四极子波的频散特征出发,指出了薄壁钻铤不利于地层横波速度的测量.这里我们分别模拟厚壁钻铤和薄壁钻铤两种情况的

表 1 钻铤尺寸和地层参数

Table 1 Parameter values of collar and formation for calculating LWD quadrupole wave

参数	纵波速度 ($m \cdot s^{-1}$)	横波速度 ($m \cdot s^{-1}$)	密度 ($g \cdot cm^{-3}$)	内半径 (m)	外半径 (m)
钻铤	5860	3130	7.85	0.042/0.062	0.089
泥浆	1500	—	1.00	—	0.117
软地层	2770	1250	2.52	0.117	∞

软地层四极子波形特征,来进一步分析钻铤波对地层横波测量的干扰程度.

参考 Tang 等(2006)文献,随钻波形模拟时四极子声源采用主频 3 kHz 的 Ricker 子波,声源和接收器阵列均加载于均匀钻铤的外壁,其中声源到第 1 个接收器距离为 2.5 m,两个相邻接收器之间距离为 0.15 m. 具体的井孔、钻铤及地层参数由表 1 给出. 图 1 给出厚壁钻铤(壁厚 47 mm)情况的四极子阵列波形及对应的速度—频率二维谱分析结果(Tang and Cheng,2004). 从图 1a 的阵列波形中可看出,波列中只存在一个幅度较明显振型,该振型是以接近地层横波速度(图中红线为横波到时)传播的地层模式四极子波. 为了进一步分析波动模式,对阵列波形作速度—频率相关的二维谱分析(Tang and Cheng,2004),其结果由图 1b 中的变密度图给出. 作为对比,我们也将理论的随钻四极子波频散曲线(白虚线)画在二维谱图上. 从图 1b 中可看出,该频段内只存在一个相关性高峰值区域,恰好对应的是四极子地层模式波. 这是因为该钻铤尺寸(厚壁钻铤)下的四极子钻铤波的截止频率较高(约 7 kHz,见图 1b 中钻铤波频散曲线),远高于声源的有效频带,此时只能激发起沿井孔传播的四极子地层波,激发不出来四极子钻铤波,这也是随钻测井中用四极子技术测量地层横波的优势所在. 模拟分析结果与 Tang 等(2002),Tang 和 Cheng(2004)的结论一致,这也从侧面验证了模拟的正确性.

接下来,我们给出薄壁钻铤(壁厚 27 mm)情况模拟的软地层四极子波形及对应的二维谱分析结果,如图 2 所示. 数值模拟时除了钻铤厚度以外,其他参数与图 1 完全相同. 从图 2a 的波形中可看出,波列中存在两个明显的振型,到时靠后的一个振型是四极子地层波(红线为横波到时),另外一个最先到达的振型为四极子钻铤模式波. 图 2b 给出了阵列波形的二维谱图以及理论频散曲线,可看出在声源主频 3kHz 附近的频段存在两个明显的相关性高峰值区域,其中相速度快和慢的两个高峰值区域分别对应的是四极子波的钻铤模式和地层模式,见图中理论频散曲线(白虚线). 与厚壁钻铤情况相比,钻铤波频散特征发生了较大的变化,其截止频率由 7 kHz降低至 2.5 kHz 左右(见图 2b 钻铤波频散曲线),但地层波的传播特征变化很小. 从理论频散曲线上取声源主频处的钻铤波相速度后计算阵列波形到时曲线,如图 2a 中蓝线所示. 相对于软地层横波,钻铤直达波传播速度较快,其后续波明显干扰了地层波,使地层波到时不清晰,不利于横波信号的拾取.

对比上述两种情况的模拟波形不难发现,厚壁钻铤的四极子地层波信噪比很高,而薄壁情况受钻铤波的干扰较明显,这不利于地层横波的测量. 分析其原因,四极子声源在较低的激发频率下,钻铤波对地层波的干扰程度主要取决于四极子钻铤模式波的截止频率. 因此,钻铤波截止频率对随钻声波仪器的设计至关重要. 这里只讨论的钻铤厚度对截止频率的影响,接下来我们进一步分析考察仪器结构、地层性质变化等对钻铤波截止频率的敏感度.

2.2 仪器结构及地层参数对钻铤波截止频率的影响

图 3 给出了常用的随钻声波测井仪器结构及井孔模型示意图,随钻声波仪器主要包括多极子(单极和四极子)发射声源、隔声体和接收器阵列三部分. 其中,源与接收器之间的隔声体通常采用如图 3 所示的大量周期刻槽结构来消除钻铤波;接收器阵列位置处通常为较均匀的钻铤,其厚度根据仪器实际设计需要可以改变. 接下来,针对该随钻四极子声波仪器结构,结合现场软地层实测数据,利用有限差分数值模拟方法(Wang and Tang,2003)来进一步分析随钻四极子波的传播特征.

图 4 给出了现场实测、数值模拟和理论计算的随钻四极子波频散曲线对比,其中小圆圈是从某软地层实测的随钻四极子阵列波形中提取的频散数据;现场频散数据也显示出软地层中随钻四极子波存在两个模式,即传播速度较高的钻铤波模式和以接近地层横波速度传播的地层模式. 从四极子地层模式波的截止频率附近可以确定出该软地层的横波速度为 1360 $m \cdot s^{-1}$,另外,地层纵波速度、密度和井径等参数由其他测井数据获得,分别为 2683 $m \cdot s^{-1}$,2.512 $g \cdot cm^{-3}$,12.5 in,钻铤及泥浆参数参见表 1. 我们针对图 3 所示的实际仪器结构,用有限差分方法来数值模拟四极子波形,并从模拟阵列波形中提取出四极子波的频散曲线,由图 4 中蓝实线所示. 从

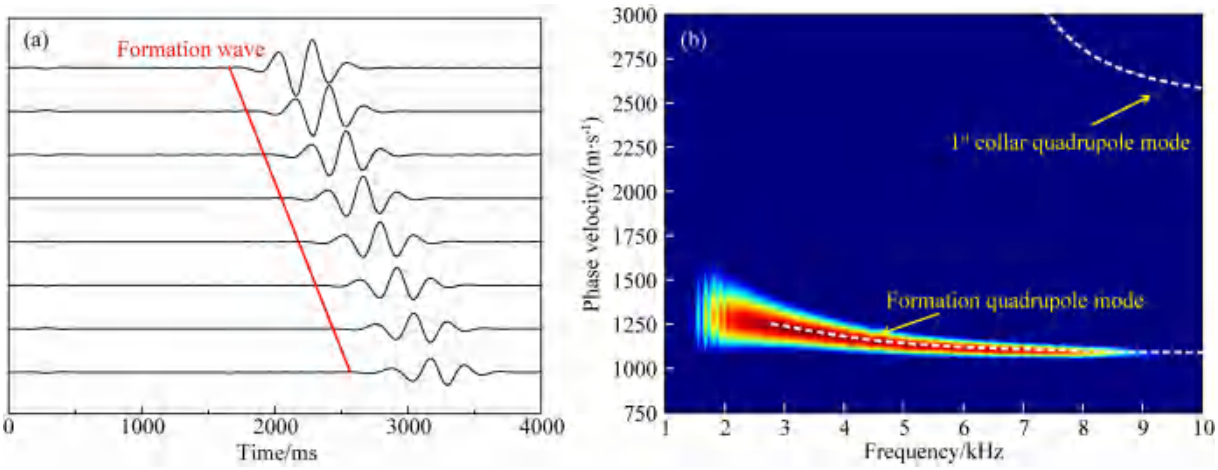


图 1　(a) 软地层厚壁钻铤模拟的低频四极子波形;(b) 软地层厚壁钻铤四极子波的速度-频散分析

Fig. 1　(a) Simulated LWD quadrupole array waveforms with thick collar thickness by low-frequency source in a slow formation; (b) Velocity-frequency analysis for LWD quadrupole with thick collar thickness in a slow formation

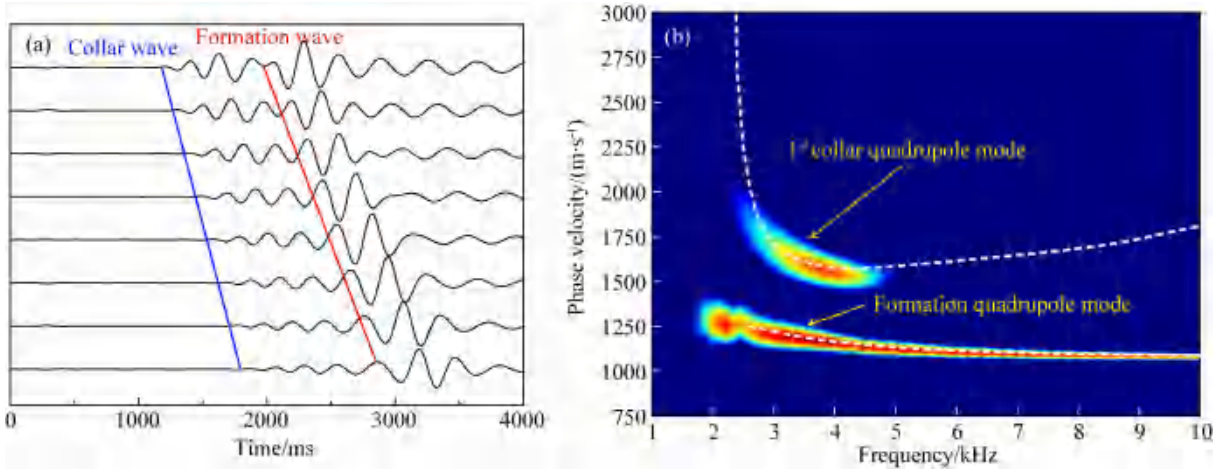


图 2　(a) 软地层中薄壁钻铤模拟的低频四极子波形;(b) 软地层薄壁钻铤四极子波的速度-频散分析

Fig. 2　(a) Simulated LWD quadrupole array waveforms with thin collar thickness by low-frequency source in a slow formation; (b) Velocity-frequency analysis for LWD quadrupole with thin collar thickness in a slow formation

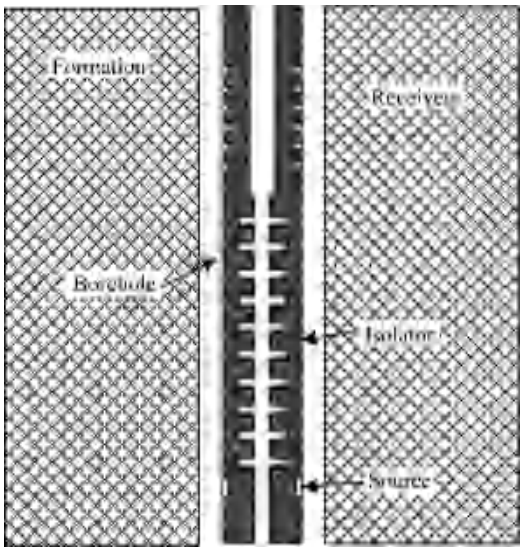


图 3　随钻声波测井模型示意图

Fig. 3　Schematic diagram of LWD acoustic tool with grooved isolator

图 4 中可看出,数值模拟(蓝线)和现场实测(小圆圈)的四极子钻铤模式和地层模式波频散曲线均吻合很好,这也说明了有限差分数值模拟结果的可靠性.

借鉴 Su 等(2011)提出的声波测井等效仪器理论,我们将图 3 中复杂仪器结构等效成均匀的圆管型钻铤,其内、外径与接收器位置的钻铤尺寸一致,即外径为 8.5 in,内径 4.0 in. 用均匀钻铤理论计算的四极子波频散曲线由图 4 中红线给出,结果发现等效的均匀钻铤的频散曲线(红线)与现场(小圆圈)和有限差分数值模拟(蓝线)的结果吻合较好. 这说明了源与接收器之间的刻槽隔声体对四极子钻铤和地层波的影响很小. 也就是说,四极子钻铤模式波的频散特征主要由接收器阵列位置的钻铤尺寸(或壁厚)控制. 为了进一步考察钻铤内、外介质对四极子钻铤波的影响,我们将图 3 所示的充液井孔模型退化为钻铤内外为空气介质的情况,理论计算的四极子钻铤波频散曲线由图 4 中绿线给出. 值得关注的是,这时我们又发现空气模型(相当于钻铤自由边界

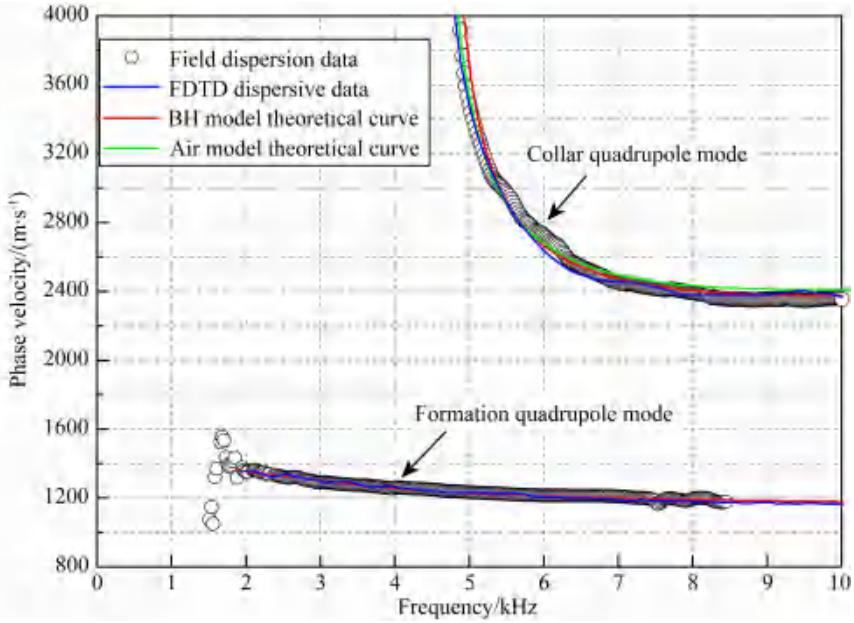


图 4 现场实测、有限差分数值模拟和理论计算的随钻四极子波频散曲线

Fig. 4 LWD quadrupole dispersion results from field data (dark circles), FDTD simulation (blue lines) and theoretical simulation (red and green lines)

模型)的频散曲线(绿线)与上述三种情况的频散数据吻合的也较好,这说明四极子钻铤波的传播特征对钻铤内、外介质的敏感度较低,主要由钻铤本身参数决定.这一理论模型的简化和验证过程为随钻四极子仪器的最优化设计提供了理论基础.

以上分析了钻铤波截止频率是干扰地层波质量的主要因素,且分析了仪器结构对截止频率的影响,下面利用现场四极子实测井段数据来进一步分析仪器内外介质的变化对钻铤波的截止频率的影响.图 5 给出了某软地层井段的随钻四极子实测波形数据及其频散分析结果.图中第 1 道给出井径曲线;第 2 道给出随钻四极子波形以及对应的钻铤波(红线)和地层横波(粉线)的到时曲线,从波形中明显看到钻铤波对地层横波的干扰;第 3 道给出典型深度点的频散分析结果,图中小圆点是利用加权频谱相干法(Tang and Cheng,2004)从现场测量阵列波形中提取的四极子波频散数据,红色和绿色实线分别是用均匀钻铤的井孔模型理论计算的钻铤波和地层波频散曲线.从整个井段来看,地层横波速度(见图中第 2 道粉色到时曲线和第 3 道频散数据中的横波速度值)随着深度增加而升高,井径大小也略有变化(见图中第 1 道井径曲线).但是,值得关注的是,从典型深度点的四极子钻铤波频散数据来看,钻铤波的截止频率变化很小(参考图中粉色箭头),均在5 kHz 左右.

综上所述,对于实际的随钻四极子声波仪器而言,钻铤波对软地层横波测量的干扰程度除了与地层本身衰减大小有关以外,主要由钻铤波截止频率决定,而钻铤波截止频率的大小主要由接收器阵列位置的钻铤尺寸所控制.因此,在四极子仪器最优化设计过程中,钻铤波截止频率与钻铤尺寸的关系至关重要.

3 钻铤尺寸优化设计的理论图版

为了得到四极子钻铤波截止频率与钻铤尺寸之间的一般变化规律,根据上述理论与现场数据的分析研究结果,我们采用简化的自由边界钻铤模型来求解四极子钻铤波截止频率,进而建立钻铤尺寸与截止频率的关系图版.

3.1 理论模型的简化

根据图 4 中钻铤波频散曲线的对比分析结果,我们可以将复杂的随钻仪器模型的数值模拟问题简化为自由边界均匀钻铤模型的频散方程理论求解问题.即只考虑钻铤内、外界面应力为零的边界条件,则四极子钻铤波频散方程为

$$H\big|_{6\times 6}(k,\omega;C)=0, \tag{1}$$

其中,k 是波数,ω 是角频率;C 代表钻铤参数.行列式系数 H 可由充液井孔随钻声波测井模型频散方程行列式系数 D 退化而成,即 $H_{i,j}=\begin{cases}D_{i+1,j+1}(i=1\sim 3)\\ D_{i+2,j+1}(i=4\sim 6)\end{cases}$,行列式系数 D 的具体表达式参考文献(Tang and Cheng, 2004).

这里我们只关心钻铤波截止频率的求解,即波数 $k=0$ 时方程(1)的解,则方程(1)变为

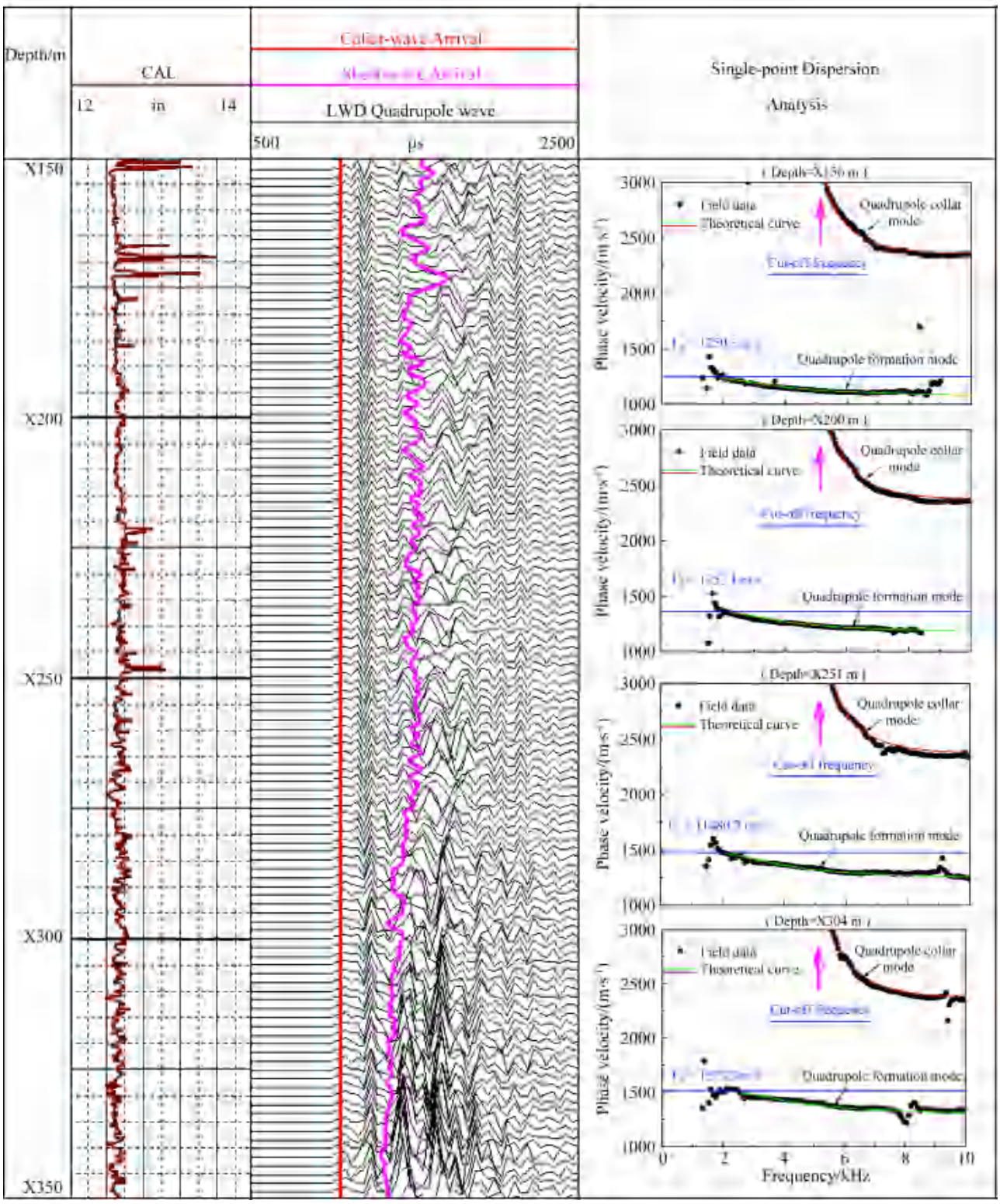


图 5　现场软地层随钻四极子实测波形及频散分析结果

Fig. 5　Field data of LWD quadrupole array waveforms for a slow formation and its dispersion curves in different depths

$$H\big|_{6\times6}(k,\omega_c;C)\big|_{k=0}=\begin{vmatrix} H_{11} & H_{12} & H_{13} & H_{14} & 0 & 0 \\ 0 & 0 & 0 & 0 & H_{25} & H_{26} \\ H_{31} & H_{32} & H_{33} & H_{34} & 0 & 0 \\ H_{41} & H_{42} & H_{43} & H_{44} & 0 & 0 \\ 0 & 0 & 0 & 0 & H_{55} & H_{56} \\ H_{61} & H_{62} & H_{63} & H_{64} & 0 & 0 \end{vmatrix}, \tag{2}$$

进一步,可将方程(2)整理为

$$H\big|_{6\times6}(k,\omega_c;C)\big|_{k=0}=\begin{vmatrix} H_{11} & H_{12} & H_{13} & H_{14} & 0 & 0 \\ H_{31} & H_{32} & H_{33} & H_{34} & 0 & 0 \\ H_{41} & H_{42} & H_{43} & H_{44} & 0 & 0 \\ H_{61} & H_{62} & H_{63} & H_{64} & 0 & 0 \\ 0 & 0 & 0 & 0 & H_{25} & H_{26} \\ 0 & 0 & 0 & 0 & H_{55} & H_{56} \end{vmatrix}, \tag{3}$$

$$H\big|_{6\times6}(k,\omega_c;C)\big|_{k=0}=W\big|_{4\times4}(k,\omega_c;C)\big|_{k=0}\cdot T\big|_{2\times2}(k,\omega_c;C)\big|_{k=0}. \tag{4}$$

数值分析表明,行列式 W 与一阶模式的四极子钻铤波截止频率有关.因此,有关钻铤波截止频率的方程可进一步简化为

$$W\big|_{4\times4}(k,\omega_c;C)\big|_{k=0}=0, \tag{5}$$

其中,ω_c 代表钻铤波的截止频率;C 代表钻铤参数,W 行列式各元素的具体表达式见附录.

3.2 截止频率与钻铤尺寸的关系图版

这里我们利用简化模型的频散方程(5)计算不同尺寸钻铤的四极子波截止频率.图 6 给出了理论计算的四极子钻铤波截止频率与钻铤尺寸的关系图版,其中横坐标为钻铤的壁厚,纵坐标为钻铤波截止频率.图 6 中四条粗实线分别代表四种常用尺寸(外径 OD 为 4.75 in、6.75 in、8.25 in、9.0 in)钻铤的四极子波截止频率与钻铤壁厚变化的关系曲线,虚线反映钻铤内径固定时壁厚变化所对应的截止频率变化趋势.为了进一步验证利用简化模型设计图版的适用性和可靠性,我们将外径 6.75 in 实际仪器结构置于软地层井孔中(如图 3 示意),利用有限差分方法数值模拟计算几种不同壁厚(即接收器位置壁厚 ID 分别为 30 mm、40 mm、50 mm、60 mm、70 mm)的钻铤波截止频率结果,如图 6 中黑色小圆圈给出.结果发现考虑实际仪器结构和地层情况的数值模拟结果与简化模型理论计算结果吻合较好,尤其是在厚壁情况.这里也注意到薄壁(30 mm)时两者差异较明显,其主要原因由于薄壁情况钻铤模式波所受钻铤外影响因素更敏感.实际情况为了保证钻井的机械强度,钻铤的壁厚一般也不宜过薄.因此,对比结果说明简化模型制作的理论图版能够反映实际随钻仪器钻铤波截止频率与壁厚的变化规律.从理论图版中可看出,四种常用尺寸的钻铤波截止频率均随壁厚增加而升高,相对来讲,钻铤外径越小钻铤波截止频率越高,且截止频率随厚度增加升高的越明显.

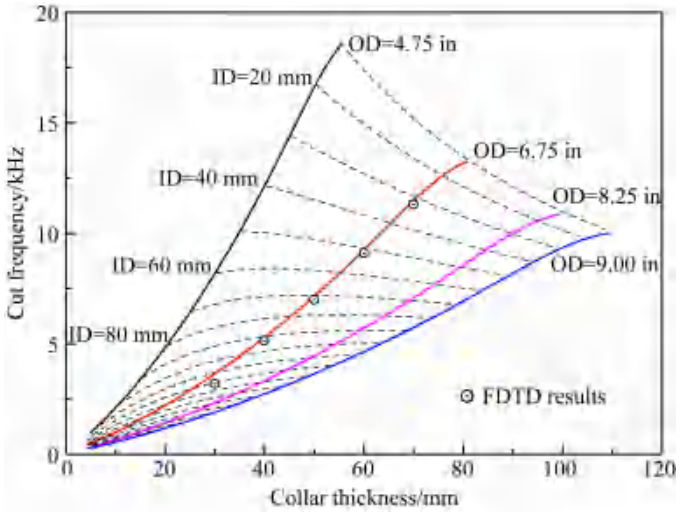


图 6 钻铤波截止频率与钻铤尺寸的理论模板

Fig. 6 Theoretical template of collar-wave cut-off frequency versus collar size

这一理论图版对于随钻四极子横波测井的仪器优化设计与现场测井数据分析都有着重要的指导意义.为了准确测量软地层的横波速度,通常要求四极子声源在较低的频率范围(小于 3 kHz)工作.这样我们设计随钻四极子仪器时,为了有效地消除钻铤波对地层四极子波的干扰,尽量要满足钻铤波截止频率较高(通常大于 7.5 kHz 为宜).因此,针对不同尺寸实际仪器的设计,在保证钻铤强度和泥浆流道的前提下,可以根据图 6 中的理论图版选择四极子接收器阵列位置的最优化壁厚参数.例如,外径 8.25 in 的随钻声波仪器最佳壁厚为 70~80 mm.另一方面的应用是,对现有的随钻四极子声波测井仪器来说,在已知钻铤壁厚情况下,也可参考图版获得钻铤波的截止频率范围,来指导四极子数据的处理,进而有效地消除钻铤波的干扰.接下来我们用一个现场随钻测井实例来验证这一理论图版的实际应用效果.

4 现场应用举例

随钻四极子声波测井技术已经开始大量应用于现场的地层横波速度测量.图 7 给出某软地层井段的随钻四极子测量数据及其处理结果.图 7 中第 1、2 道分别给出原始测量的四极子变密度波形和对应的相干图.由图 7 中可看出整个井段均存在较强的钻铤波,且相干性很强,而四极子地层模式波的幅度

和相干性较弱.底部井段(大于 X090 m)在钻铤波之后可以看到明显的四极子地层波信号;随着深度变浅,地层变疏松对声波衰减增大,导致顶部井段(小于 X090 m)基本看不清地层波信号,且相干性也很差,受钻铤波干扰严重,无法直接提取地层横波速度.本井段测井采用外径 8.25 in 的随钻声波工具,我们根据该仪器接收换能器位置的钻铤尺寸(外径 8.25 in,内径 4 in)可以从图 6 中的理论图版确定该仪器的钻铤波截止频率约为 5 kHz.因此,为了消除钻铤波的干扰而获得高信噪比的地层四极子波信号,我们通过对原始测量四极子波在钻铤波截止频率以下进行滤波,其滤波的频率范围选择 1～4 kHz.滤波处理后的波形如图 7 中第 3 道所示,此时获得了纯净的四极子地层模式波,地层波的信噪比较高,对应的相干性也很好(见图 7 中第 4 道).作为对比验证,第 5 道分别给出了滤波处理后提取的地层横波时差(红线)和电缆测井的横波时差(黑线),两者的横波时差吻合较好.值得关注的是,从现场软地层数据处理结果来看,现有的四极子随钻声波仪器测量波形中普遍存在较强的四极子钻铤波的干扰,一般可以在理论图版的指导下处理出比较准确的地层横波时差.为了进一步提高疏松软地层随钻四极子波数据质量,建议增加现有仪器接收器位置的钻铤厚度,同时降低四极子声源的工作频率.

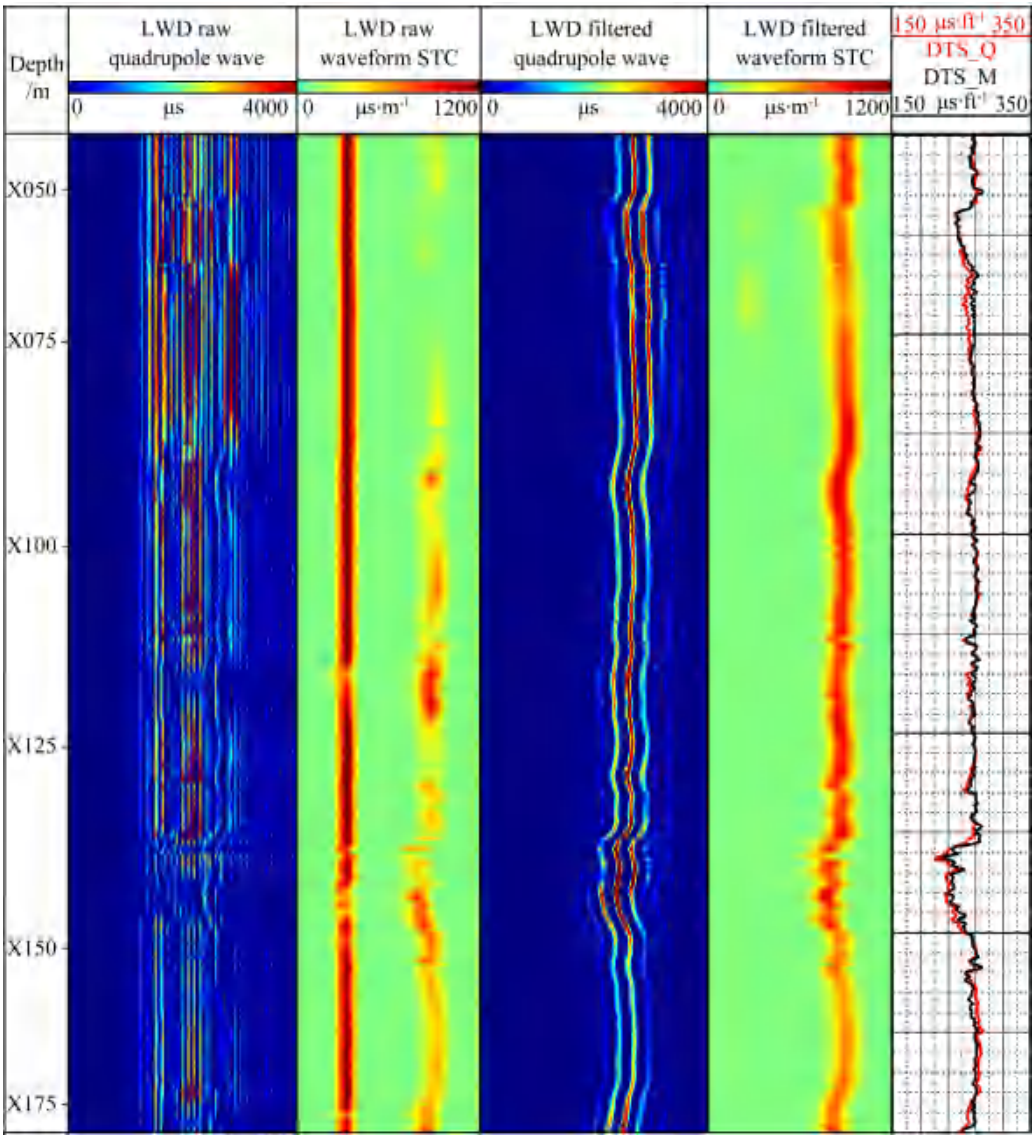


图 7　现场软地层随钻四极子声波测井处理实例

Fig. 7　Field data processing example of LWD quadrupole acoustic tool in a slow formation

5　结论与认识

随钻四极子声源在疏松的软地层通常也会激发出沿着钻铤传播的四极子螺旋导波,这一模式波具有截止频率,当其降低到与地层波测量频段接近时会明显干扰地层波信号,不利于地层横波测量.通过数值模拟和现场实测数据分析证明了四极子钻铤波的截止频率主要取决于接收换能器阵列位置的钻铤壁厚,即随着钻铤壁厚的增加钻铤波截止频率升高.

基于等效的随钻声波测井简化模型进一步分析与设计了钻铤波截止频率与钻铤尺寸的关系图版,并通过现场实测资料的处理效果验证了这一理论图版的适用性.本文的研究结果可以用于指导新的随钻四极子声波测井仪器的最优化设计,进而提高软地层横波测量数据的质量.

附录 自由边界钻铤频散方程行列式系数

自由边界一阶模式的钻铤四极子波截止频率的方程可表达为 4×4 的矩阵 $\boldsymbol{W}$:

$$\boldsymbol{W}\big|_{4\times4}(\boldsymbol{k},\omega_c;\boldsymbol{C})\big|_{k=0}=\begin{vmatrix} W_{1,1} & W_{1,2} & W_{1,3} & W_{1,4} \\ W_{2,1} & W_{2,2} & W_{2,3} & W_{2,4} \\ W_{3,1} & W_{3,2} & W_{3,3} & W_{3,4} \\ W_{4,1} & W_{4,2} & W_{4,3} & W_{4,4} \end{vmatrix}=0, \tag{A1}$$

行列式 $\boldsymbol{W}$ 各元素的具体表达式如下:

$$\begin{aligned}
&W_{1,1}=-(k_s^t)^2I_2(pr_a)+\frac{2p}{r_a}X_2(pr_a);\ W_{1,2}=-(k_s^t)^2K_2(pr_a)+\frac{2p}{r_a}Y_2(pr_a);\\
&W_{1,3}=-\frac{4s}{r_a}X_3(sr_a);\ W_{1,4}=-\frac{4s}{r_a}Y_3(sr_a);\ W_{2,1}=\frac{4p}{r_a}X_3(pr_a);\\
&W_{2,2}=\frac{4p}{r_a}Y_3(pr_a);\ W_{2,3}=-s^2X_4(sr_a);\ W_{2,4}=-s^2Y_4(sr_a);\\
&W_{3,1}=-(k_s^t)^2I_2(pr_b)+\frac{2p}{r_b}X_2(pr_b);\ W_{3,2}=-(k_s^t)^2K_2(pr_b)+\frac{2p}{r_b}Y_2(pr_b);\\
&W_{3,3}=-\frac{4s}{r_b}X_3(sr_b);\ W_{3,4}=-\frac{4s}{r_b}Y_3(sr_b);\ W_{4,1}=\frac{4p}{r_b}X_3(pr_b);\\
&W_{4,2}=\frac{4p}{r_b}Y_3(pr_b);\ W_{4,3}=-s^2X_4(sr_b);\ W_{4,4}=-s^2Y_4(sr_b);
\end{aligned} \tag{A2}$$

$$\begin{cases} X_1(x)=\dfrac{n}{x}I_2(x)+I_3(x) \\ X_2(x)=\dfrac{2}{x}I_2(x)-I_3(x) \\ X_3(x)=-\dfrac{1}{x}I_2(x)-I_3(x) \\ X_4(x)=\left[1+\dfrac{4}{x^2}\right]I_2(x)-\dfrac{2}{x}I_3(x) \end{cases} \quad \begin{cases} Y_1(x)=\dfrac{2}{x}K_2(x)-K_3(x) \\ Y_2(x)=\dfrac{2}{x}K_2(x)+K_3(x) \\ Y_3(x)=-\dfrac{1}{x}K_2(x)+K_3(x) \\ Y_4(x)=\left[1+\dfrac{4}{x^2}\right]K_2(x)+\dfrac{2}{x}K_3(x) \end{cases} \tag{A3}$$

其中 I、K 分别代表第一类、第二类贝塞尔函数;r_a、r_b 分别代表钻铤内径、外径;k_p^t、k_s^t 分别代表钻铤纵波、横波波数,$k_p^t=\dfrac{\omega}{v_p^t}$,$k_s^t=\dfrac{\omega}{v_s^t}$;$p$、$s$ 分别代表钻铤纵波、横波径向波数,$p=\sqrt{k^2-(k_p^t)^2}=\mathrm{i}k_p^t$,$s=\sqrt{k^2-(k_s^t)^2}=\mathrm{i}k_s^t$.

References

Aron J, Chang S K, Dworak R, et al. 1994. Sonic compressional measurements while drilling. // 35th Annual Logging Symposium. Tulsa, Oklahoma: Society of Petrophysicists and Well-Log Analysts.

Cui Z W. 2004. Theoretical and numerical study of modified Biot's models, acoustoelectric well logging and acoustic logging while drilling excited by multipole acoustic sources [Ph. D. thesis] (in Chinese). Changchun: Jilin University.

Dubinsky V, Tang X M, Bolshakov A, et al. 2003. Engineering aspects of LWD quadrupole measurements and field test results. // SPE Annual Technical Conference and Exhibition. Denver, Colorado: Society of Petroleum Engineers.

Joyce B, Patterson D, Leggett J, et al. 2001. Introduction of a new omni-directional acoustic system for improved real-time LWD sonic logging-tool design and field test results. // 42nd Annual Logging Symposium. Houston, Texas: Society of Petrophysicists and Well-Log Analysts.

Kinoshita T, Endo T, Nakajima H, et al. 2008. Next generation LWD sonic tool. // 14th Formation Evaluation Symposium of Japan. 1-7

Kinoshita T, Dumont A, Hori H, et al. 2010. LWD sonic tool design for high-quality logs. // 80th Annual International Meeting. Denver, Colorado: SEG, 513-517.

Market J. 2007. New broad frequency LWD multipole tool provides high quality compressional and shear data in a wide variety of formations. // 48th Annual Logging Symposium. Austin, Texas: Society of Petrophysicists and Well-Log Analysts.

Minear J, Birchak R, Robbins C, et al. 1995. Compressional slowness measurements while drilling. // 36th Annual Logging Symposium. Paris, France: Society of Petrophysicists and Well-Log Analysts.

Scheibner D, Yoneshima S, Zhang Z X, et al. 2010. Slow formation shear from an LWD tool: quadrupole inversion with a gulf of Mexico example. // 51th Annual Logging Symposium. Perth, Australia: Society of Petrophysicists and Well-Log Analysts.

Sinha B K, Şimşek E, Asvadurov S. 2009. Influence of a pipe tool on borehole modes. *Geophysics*, 74(3): E111-E123.

Su Y D, Zhuang C X, Tang X M. 2011. LWD acoustic color mode wave attenuation character research and isolator design. *Chinese J. Geophys.* (in Chinese), 54(9): 2419-2428, doi: 10.3969/j.issn.0001-5733.2011.09.026.

Su Y D, Tang X M, Hei C, et al. 2011. An equivalent-tool theory for acoustic logging and applications. *Applied Geophysics*, 8(1): 69-78.

Su Y D. 2014. Optimized design and field data processing method of acoustic logging-while-drilling tool [Ph. D. thesis](in Chinese). Qingdao: China University of Petroleum (East China).

Tang X M, Dubinsky V, Bolshakov A, et al. 2002. Shear-velocity measurement in the logging-while-drilling environment: modeling and field evaluations. // 43th Annual Logging Symposium. Oiso, Japan: Society of Petrophysicists and Well-Log Analysts.

Tang X M, Cheng A. 2004. Quantitative borehole acoustic methods. UK: Elsevier.

Tang X M, Patterson D J, Wang T, et al. 2005. Method and apparatus for LWD shear velocity measurement: U. S. Patent 6, 850, 168.

Tang X M, Dubinsky V, Patterson D J. 2006. Development of a low-frequency LWD quadrupole shear-wave technology to improve quality of formation shear velocity measurement. // SPE Annual Technical Conference and Exhibition. San Antonio, Texas, USA: SPE.

Varsamis G L, Arian A, Blanch J, et al. 2000. LWD shear velocity logging in slow formations design decisions and case histories. // 41st Annual Logging Symposium. Dallas, Texas: Society of Petrophysicists and Well-Log Analysts.

Wang T, Tang X M. 2003. Finite-difference modeling of elastic wave propagation: a nonsplitting perfectly matched layer approach. *Geophysics*, 68(5): 1749-1755.

附中文参考文献

崔志文. 2004. 多孔介质声学模型与多极源声电效应测井和多极随钻声测井的理论与数值研究 [博士论文]. 长春: 吉林大学.

苏远大, 庄春喜, 唐晓明. 2011. 随钻声波测井钻铤模式波衰减规律研究与隔声体设计. 地球物理学报, 54(9): 2419-2428, doi: 10.3969/j.issn.0001-5733.2011.09.026.

苏远大. 2014. 随钻声波测井仪器最优化设计与数据处理方法 [博士论文]. 青岛: 中国石油大学(华东).

(本文编辑　胡素芳)

饶博,苏远大,李盛清等. 2023. 钻铤偏心对随钻四极子横波测井影响:理论与实例分析. 地球物理学报,66(1):111-121,doi:10.6038/cjg2022Q0477.

Rao B, Su Y D, Li S Q, et al. 2023. Influence of drill collar eccentricity on quadrupole shear-wave logging while drilling: theory and field case. *Chinese J. Geophys.* (in Chinese), 66(1): 111-121, doi: 10.6038/cjg2022Q0477.

钻铤偏心对随钻四极子横波测井影响:理论与实例分析

饶博[1], 苏远大[1,2*], 李盛清[1], 孙云涛[3], 陈文轩[3], 唐晓明[1,2]

1 中国石油大学(华东)深层油气重点实验室, 青岛 266580

2 崂山实验室海洋矿产资源评价与探测技术功能实验室, 青岛 266071

3 中国科学院地质与地球物理研究所, 北京 100029

摘要 随钻四极子声波测井技术主要用于测量地层的横波速度.但在复杂旋转钻进过程中钻具的偏心会对测量的四极子波形质量及横波速度产生不利影响.本文建立以钻铤和井孔分别为基准的双柱坐标系偏心随钻声波测井模型,利用贝塞尔函数的平移加法定理构建边界条件和井中响应函数,数值模拟了钻铤居中和偏心时四极子声源激发的声场.发现偏心后的随钻四极子声场中除地层四极子波外,还有单极斯通利波和偶极弯曲波的多阶模式波共存且相互耦合,尤其是在软地层钻铤严重偏心时四极子模式波受斯通利波模式和弯曲波模式干扰更为严重,不利于地层横波速度的测量.现场随钻四极子声波测井仪器实验样机在居中和偏心的状态下实测的数据表明:当随钻四极子样机居中测井时,可测量到高质量的四极子波形,处理得到相关性较强的地层横波时差,与单极测量横波时差吻合较好;但钻铤偏心测量时采集的波形成分复杂,偏心引起的低频斯通利波模式对地层四极子模式的耦合干扰非常严重,导致地层横波时差的相关性很差,测量值介于横波与斯通利波时差之间,与实测单极横波时差差异很大甚至无法使用,尤其在疏松软地层中影响更为突出.本文从偏心随钻四极子井孔声场理论出发,结合现场实测数据,重点分析钻铤偏心对四极子横波测井的影响,为指导偏心状态下随钻四极子横波时差处理与校正方法提供理论基础.

关键词 随钻声波测井; 四极子; 仪器偏心; 横波速度

doi:10.6038/cjg2022Q0477 **中图分类号** P631 **收稿日期** 2022-06-21, 2022-09-07 收修定稿

Influence of drill collar eccentricity on quadrupole shear-wave logging while drilling: theory and field case

RAO Bo[1], SU YuanDa[1,2*], LI ShengQing[1], SUN YunTao[3], CHEN WenXuan[3], TANG XiaoMing[1,2]

1 *Key Laboratory of Deep Oil and Gas, China University of Petroleum, Qingdao* 266580, *China*

2 *Laboratory for Marine Mineral Resources, Laoshan Laboratory, Qingdao* 266071, *China*

3 *Institute of Geology and Geophysics, Chinese Academy of Sciences, Beijing* 100029, *China*

Abstract The shear-wave velocity of formation is measured by using a acoustic logging-while-drilling (ALWD) quadrupole tool, while the eccentricity of drill collar will seriously influence the quality of the quadrupole waveforms and the shear-velocity measurement during the complicated

基金项目 中国科学院 A 类战略性先导科技专项(XDA14020302),国家自然科学基金(U21B2064,41821002,42074137,42174145),山东省自然科学基金(ZR201911120382)和中央高校基本科研业务费专项基金(20CX06077A)联合资助.

第一作者简介 饶博,男,1995 年生,博士研究生,主要从事随钻声波测井理论研究. E-mail:1004062422@qq.com

***通讯作者** 苏远大,男,1978 年生,博士,教授,主要从事声波测井理论、方法及处理研究. E-mail:syuanda@sina.com

rotary drilling process. In this study, an eccentric ALWD model is established in the dual-cylindrical coordinate systems based on locations of the drill collar and borehole. The translational addition theorem of Bessel functions is utilized to construct the boundary conditions and borehole response functions. Then the wave-field excited by quadrupole sources under the conditions of the centered and eccentric drill collar models is numerically simulated. The results show that an eccentric tool causes multipole wave modes including the formation quadrupole mode, and the Stoneley-wave and the flexural wave coexist and couple with each other. It should be noted that when the drill collar is seriously eccentric in the slow formation, the quadrupole mode is seriously disturbed by Stoneley-wave and the flexural wave modes, which is not conducive for the shear velocity measurement. Field data analysis results show that high quality and pure quadrupole waveforms of the formation can be measured, and accurate shear-wave slowness can be obtained, which is in good agreement with the shear-wave velocity of ALWD monopole mode. However, the waveform has complex components when the ALWD tool is eccentric. The coupling interference of low-frequency Stoneley-wave causes poor correlation of formation quadrupole waveforms and unreliable shear-wave slowness. The measurement of slowness is between the actual shear-wave and Stoneley-wave, which is extremely different from the result of monopole measurement of the ALWD tool. This discrepancy become obvious in the slow formation. Therefore, based on the eccentric quadrupole ALWD theory and combined with the measured data, this study concentrates on the analysis of the influence of drill collar eccentricity on quadrupole-wave data, which provides a theoretical foundation for the processing and correction of quadrupole data of ALWD with an eccentric drill collar.

Keywords Acoustic logging while drilling; Quadrupole; Tool eccentricity; Shear-wave velocity

0 引言

随钻测井可以节省钻井时间、为安全高效钻井提供实时决策以及地质导向等服务,已广泛应用于深水、深层和非常规的油气资源勘探与开发.其中随钻声波测井获得的地层纵波和横波速度可以为井壁稳定性、钻井优化、地层孔隙压力预测和井震结合提供实时的地层声速信息.

随钻条件下测量地层横波速度仍然面临挑战.由于井孔中流体的大部分体积被钻铤所占据,导致在钻后电缆测井中常用的偶极源横波测井技术受到极大地限制(Tang and Cheng,2004).因此,随钻声波测井中主要是采用四极子技术来测量地层的横波速度,理论上低频随钻四极子波以地层横波速度传播,几乎不受钻铤直达波干扰(Tang et al., 2002).但从随钻四极子实测现场数据来看,在硬地层中低阶四极子波频散较强,不利于地层横波速度的测量;此外,在疏松软地层中仍然存在较强的钻铤直达波的干扰,导致目标模式波的信号质量下降,地层四极子波的信噪比低,上述实际问题都对随钻四极子横波测井技术提出了新的挑战(苏远大等,2017).为了解决上述难题,学者们从仪器壁厚设计、声源激发频率优化、声源振动模式、频散校正等方面进行了大量的数值模拟、物理实验和数据处理方面的研究(Tang et al.,2003;Byun and Toksöz,2003;Zhu et al., 2008;王华等,2009;王兵等,2012;王军等,2019).

除此之外,随钻环境下的测量条件苛刻,仪器存在强烈的轴向、环向、径向等方向冲击振动和移动,尤其是仪器的径向移动,这种偏离井中心轴线的测量(偏心测量)使得井中产生复杂的非轴对称声场.受钻铤自重的影响,仪器偏心在水平井或大斜度井中表现更为明显,因此对钻铤偏心状态下的四极子声波测井响应研究具有实际意义.Zheng 等(2004)应用有限元方法计算了仪器偏心对随钻多极子模式波的影响,发现了斯通利波速度降低、弯曲波和螺旋波出现模式分裂等现象;Huang 等(2004)利用有限差分方法研究了随钻偏心声场也得出了相似的结论,并指出仪器偏心引入的多阶模式波会降低目标模式的信号质量.Pardo 等(2013)对比了随钻和电缆条件下偏极子声源激发的声场响应,指出在快速

地层中仪器偏心不影响地层横波速度的提取. Wang 等(2013)进一步考察了随钻多极子声源在大斜度井和水平井中激发的声场,提出了一种可以量化仪器偏心距离与方位的随钻偶极声波测井方法. Wei 等(2018)利用有限差分方法研究了偏极子源偏心时激发的井孔声场,并指出在声源垂直方位上的接收器接收到的波形信号受钻铤偏心的影响最小,随后基于偏心点源在环向各向异性地层模型中激发的声响应规律,提出可利用校正后的快、慢横波波速评价地层的各向异性(卫建清等,2019).

上述针对随钻偏心声波测井的研究大都是采用有限元或者有限差分等数值方法,计算效率低. Haugland 等(2004a,b)首次发表了针对含偏心实心柱的充液井孔的声场解析算法. Ji 等(2021)进一步针对具有一定壁厚的空心钻铤,在钻铤和井孔双柱坐标系下推导了随钻偏心模型的波动方程解析解,并模拟了不同钻铤偏心距下的方位接收单极子波形. 在以上研究基础上,本文重点针对随钻四极子声波测井开展了双柱坐标系下钻铤偏心对横波速度测量的影响研究,并结合现场随钻四极子测井仪器实验样机的实测数据考察了钻铤偏心对四极子横波速度测量的影响. 本文的研究工作为偏心状态下随钻四极子横波时差处理与校正方法提供理论基础.

1　钻铤偏心随钻四极子声波测井理论

图 1a 给出了含偏心钻铤的充液井孔中随钻四极子声波测井模拟所用的双柱坐标系 (r_1,φ_1,z_1) 和 (r_2,φ_2,z_2),分别以钻铤和井孔为坐标基准,其中钻铤轴与井轴相互平行(钻铤在井中平动,未研究钻铤倾斜等复杂模型),因此下文中用 z 表示 z_1 和 z_2. 一个环状四极子源被置于钻铤外壁以实现声场的激发,如图 1b 所示,该四极子源是由 4 个四分之一圆弧状子声源构成,相邻两瓣可以产生振幅相同但相位相反的力. 类似的,在钻铤外壁距离声源上方 3 m 处间隔 45°环向布置 8 个方位接收器(接收站),每个接收站间距为 0.1524 m,接收横截面如图 1c 所示,图中 a,b,c 分别表示钻铤的内、外半径和井眼半径,O_1 和 O_2 分别为两套坐标系的坐标原点,$e=|O_1O_2|$ 表示钻铤偏离井轴的平动距离,其满足 $0\leqslant e\leqslant c-b$. 类似地,定义钻铤偏心率 $E=e/(c-b)$,其满足 $0\%\leqslant E\leqslant 100\%$.

将含钻铤的充液井孔考虑成经典的柱状分层介质,由刚性钻铤及其内外流体层和井外地层四部分组成. 为了推导钻铤偏心时的随钻声场解析解,本文将井内钻铤及其内外流体层中的波势函数在以钻铤为基准的第一套坐标系中表示,将井外地层中的波势函数在以井孔为基准的第二套坐标系中表示. 当源激发出的声波与井眼相互作用时,基于亥姆霍兹分解理论,固体中位移场 $\boldsymbol{u}_s$ 可以用一个无旋势函数 ϕ_s 和两个无散势函数 χ_s 和 Γ_s 表示:

$$\boldsymbol{u}_s=\nabla\phi_s+\nabla\times(\chi_s\hat{\boldsymbol{z}})+\nabla\times\nabla\times(\Gamma_s\hat{\boldsymbol{z}}),\quad(1)$$

式中,$\hat{\boldsymbol{z}}$ 是沿 z 轴方向的单位矢量;ϕ_s,χ_s,Γ_s 分别为钻铤或者地层中 P 波,SH 波和 SV 波的势函数,下文分别用 $\phi^{\text{tool}},\chi^{\text{tool}},\Gamma^{\text{tool}}$ 或者 $\phi^{\text{F}},\chi^{\text{F}},\Gamma^{\text{F}}$ 表示.

井内流体位移场 $\boldsymbol{u}_f$ 可以用一个无旋势函数 ϕ_f 表示:

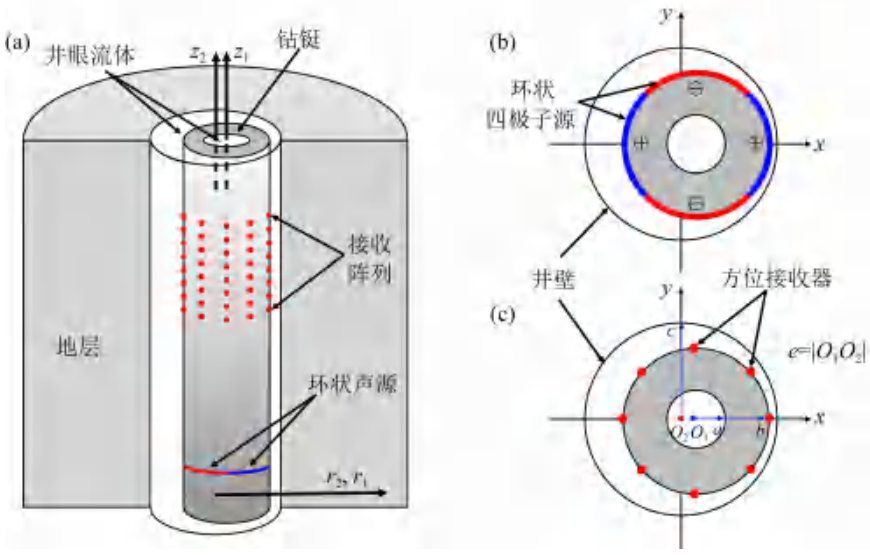


图 1　(a) 随钻偏心声波测井示意图;(b) 随钻环状四极子源截面图;(c) 随钻方位接收器截面图

Fig. 1　(a) Schematic diagram of the ALWD model with the eccentric collar; (b) Configuration of the ring quadrupole source in ALWD; (c) Configuration of the receiver array in ALWD

$$\boldsymbol{u}_{\mathrm{f}} = \nabla\phi_{\mathrm{f}}, \tag{2}$$

式中，ϕ_{f} 为钻铤内、外流体层中 P 波的位移势函数，下文分别用 ϕ^{in}，ϕ^{out} 表示.

针对上述方程，根据柱状分层介质声场理论，钻铤及其内外流体层中的位移场在频率-波数域内具有以下形式的通解：

$$\begin{cases}
\phi^{\mathrm{tool}}(k,\omega,r_1,\varphi_1) = \sum\limits_{n=-\infty}^{\infty}[A_n^{\mathrm{tool}}\mathrm{I}_n(\eta_{\mathrm{p}}^{\mathrm{tool}}r_1) + B_n^{\mathrm{tool}}\mathrm{K}_n(\eta_{\mathrm{p}}^{\mathrm{tool}}r_1)]\cos(n\varphi_1)\mathrm{e}^{\mathrm{i}kz}, \\
\chi^{\mathrm{tool}}(k,\omega,r_1,\varphi_1) = \sum\limits_{n=-\infty}^{\infty}[C_n^{\mathrm{tool}}\mathrm{I}_n(\eta_{\mathrm{s}}^{\mathrm{tool}}r_1) + D_n^{\mathrm{tool}}\mathrm{K}_n(\eta_{\mathrm{s}}^{\mathrm{tool}}r_1)]\sin(n\varphi_1)\mathrm{e}^{\mathrm{i}kz}, \\
\Gamma^{\mathrm{tool}}(k,\omega,r_1,\varphi_1) = \sum\limits_{n=-\infty}^{\infty}[E_n^{\mathrm{tool}}\mathrm{I}_n(\eta_{\mathrm{s}}^{\mathrm{tool}}r_1) + F_n^{\mathrm{tool}}\mathrm{K}_n(\eta_{\mathrm{s}}^{\mathrm{tool}}r_1)]\cos(n\varphi_1)\mathrm{e}^{\mathrm{i}kz}, \\
\phi^{\mathrm{in}}(k,\omega,r_1,\varphi_1) = \sum\limits_{n=-\infty}^{\infty}A_n^{\mathrm{in}}\mathrm{I}_n(\eta_{\mathrm{f}}r_1)\cos(n\varphi_1)\mathrm{e}^{\mathrm{i}kz}, \\
\phi^{\mathrm{out}}(k,\omega,r_1,\varphi_1) = \sum\limits_{n=-\infty}^{\infty}[A_n^{\mathrm{out}}\mathrm{I}_n(\eta_{\mathrm{f}}r_1) + B_n^{\mathrm{out}}\mathrm{K}_n(\eta_{\mathrm{f}}r_1)]\cos(n\varphi_1)\mathrm{e}^{\mathrm{i}kz},
\end{cases} \tag{3}$$

式中，ω 为圆频率；k 为轴向波数；I_n 和 K_n 分别表示第一类和第二类 n 阶变型贝塞尔函数，n 为第一套(钻铤)坐标系中的方位序数；$\eta_{\mathrm{f}} = (k^2 - \omega^2/\alpha_{\mathrm{f}}^2)^{1/2}$ 为钻铤内外流体层中纵波的径向波数；α_{f} 为流体中纵波波速；$\eta_{\mathrm{p}}^{\mathrm{tool}} = (k^2 - \omega^2/\alpha_{\mathrm{tool}}^2)^{1/2}$ 和 $\eta_{\mathrm{s}}^{\mathrm{tool}} = (k^2 - \omega^2/\beta_{\mathrm{tool}}^2)^{1/2}$ 分别为钻铤中纵、横波的径向波数，α_{tool} 和 β_{tool} 分别为钻铤的纵、横波波速；$A_n^{\mathrm{tool}}(B_n^{\mathrm{tool}})$，$C_n^{\mathrm{tool}}(D_n^{\mathrm{tool}})$，$E_n^{\mathrm{tool}}(F_n^{\mathrm{tool}})$ 分别表示钻铤中入射(出射)P 波、SH 波以及 SV 波的振幅系数，A_n^{in}，$A_n^{\mathrm{out}}(B_n^{\mathrm{out}})$ 分别表示钻铤内外流体层纵波的振幅系数.

受辐射条件约束，在无限大地层中只有向外辐射的声波，则井外无限大地层中位移势函数的解析表达式可写为：

$$\begin{cases}
\phi^{\mathrm{F}}(k,\omega,r_2,\varphi_2) = \sum\limits_{m=-\infty}^{\infty}B_m^{\mathrm{F}}\mathrm{K}_m(\eta_{\mathrm{p}}^{\mathrm{F}}r_2)\cos(m\varphi_2)\mathrm{e}^{\mathrm{i}kz}, \\
\chi^{\mathrm{F}}(k,\omega,r_2,\varphi_2) = \sum\limits_{m=-\infty}^{\infty}D_m^{\mathrm{F}}\mathrm{K}_m(\eta_{\mathrm{s}}^{\mathrm{F}}r_2)\sin(m\varphi_2)\mathrm{e}^{\mathrm{i}kz}, \\
\Gamma^{\mathrm{F}}(k,\omega,r_2,\varphi_2) = \sum\limits_{m=-\infty}^{\infty}F_m^{\mathrm{F}}\mathrm{K}_m(\eta_{\mathrm{s}}^{\mathrm{F}}r_2)\cos(m\varphi_2)\mathrm{e}^{\mathrm{i}kz}
\end{cases} \tag{4}$$

式中，m 为第二套(井孔)坐标系中的方位序数；$\eta_{\mathrm{p}}^{\mathrm{F}} = (k^2 - \omega^2/\alpha^2)^{1/2}$ 和 $\eta_{\mathrm{s}}^{\mathrm{F}} = (k^2 - \omega^2/\beta^2)^{1/2}$ 分别为地层中纵、横波的径向波数，α 和 β 分别是地层的纵、横波波速；B_m^{F}，D_m^{F}，F_m^{F} 分别表示井外地层中出射 P 波、SH 波以及 SV 波的振幅系数.

上述势函数中的振幅系数均由模型的边界条件(径向位移和正应力连续，切向应力为零)确定.

钻铤内流体和钻铤界面($r_1 = a$)处：

$$\begin{cases}
u_r^{\mathrm{in}}(a^-) = u_r^{\mathrm{tool}}(a^+), \\
\sigma_{rr}^{\mathrm{in}}(a^-) = \sigma_{rr}^{\mathrm{tool}}(a^+), \\
0 = \sigma_{rz}^{\mathrm{tool}}(a^+), \\
0 = \sigma_{r\varphi}^{\mathrm{tool}}(a^+).
\end{cases} \tag{5}$$

钻铤和钻铤外流体界面($r_1 = b$)处：

$$\begin{cases}
u_r^{\mathrm{tool}}(b^-) = u_r^{\mathrm{out}}(b^+), \\
\sigma_{rr}^{\mathrm{tool}}(b^-) = \sigma_{rr}^{\mathrm{out}}(b^+) + \sigma^{\mathrm{s}}(b^+), \\
\sigma_{rz}^{\mathrm{tool}}(b^-) = 0, \\
\sigma_{r\varphi}^{\mathrm{tool}}(b^-) = 0.
\end{cases} \tag{6}$$

钻铤外流体和地层界面($r_2 = c$)处：

$$\begin{cases}
u_r^{\mathrm{out}}(c^-) = u_r^{\mathrm{F}}(c^+), \\
\sigma_{rr}^{\mathrm{out}}(c^-) = \sigma_{rr}^{\mathrm{F}}(c^+), \\
0 = \sigma_{rz}^{\mathrm{F}}(c^+), \\
0 = \sigma_{r\varphi}^{\mathrm{F}}(c^+),
\end{cases} \tag{7}$$

式中，上标 in，tool，out，F 分别表示钻铤内流体、钻铤、钻铤外流体及井外地层中的波场；$\sigma^{\mathrm{s}} = p_0/\pi$ 为环状四极子源产生的应力分量(崔志文，2004).

如公式(7)所示，钻铤外流体和地层界面处的等式方程建立于井孔坐标系，因此需要将钻铤外流体层中的位移势表达式由钻铤坐标系转化到井孔坐标系中，可应用圆柱贝塞尔函数的平移加法定理(Ji et al., 2021)，具体表达式如下：

$$\begin{cases}
\mathrm{I}_n(\eta_{\mathrm{f}}r_1)\begin{Bmatrix}\cos(n\varphi_1)\\ \sin(n\varphi_1)\end{Bmatrix} = \sum\limits_{m=-\infty}^{\infty}(-1)^{n-m}\mathrm{I}_{n-m}(\eta_{\mathrm{f}}e)\mathrm{I}_m(\eta_{\mathrm{f}}r_2)\begin{Bmatrix}\cos(m\varphi_2)\\ \sin(m\varphi_2)\end{Bmatrix}, \\
\mathrm{K}_n(\eta_{\mathrm{f}}r_1)\begin{Bmatrix}\cos(n\varphi_1)\\ \sin(n\varphi_1)\end{Bmatrix} = \sum\limits_{m=-\infty}^{\infty}\mathrm{I}_{n-m}(\eta_{\mathrm{f}}e)\mathrm{K}_m(\eta_{\mathrm{f}}r_2)\begin{Bmatrix}\cos(m\varphi_2)\\ \sin(m\varphi_2)\end{Bmatrix}.
\end{cases} \tag{8}$$

进而可建立完备有解的平衡方程.由公式(1)—(4)计算出随钻声场中各介质层中的位移及应力分量,代入 3 个边界条件中,令 $\binom{n}{m}=0,\pm1,\cdots,\pm N$,即可推导出随钻偏心井孔声场的特征矩阵方程:

$$\boldsymbol{D}_{(24N+12)\times(24N+12)}\boldsymbol{X}_{(24N+12)\times1}=\boldsymbol{Q}_{(24N+12)\times1}, \tag{9}$$

式中,$\boldsymbol{D}$ 为随钻偏心声场特征矩阵,其元素详细表达式参见文献(Ji et al., 2021);N 控制计算精度(本文 N 取值为 5);向量 $\boldsymbol{X}$ 由各介质层振幅系数组成,向量 $\boldsymbol{Q}$ 为声源向量,具体表达式如下:

$$\boldsymbol{X}_{(24N+12)\times1}=\begin{bmatrix}A_{-N}^{\mathrm{tool}},A_{-N+1}^{\mathrm{tool}},\cdots,A_{N-1}^{\mathrm{tool}},A_{N}^{\mathrm{tool}},B_{-N}^{\mathrm{tool}},B_{-N+1}^{\mathrm{tool}},\cdots,B_{N-1}^{\mathrm{tool}},B_{N}^{\mathrm{tool}},\\ C_{-N}^{\mathrm{tool}},C_{-N+1}^{\mathrm{tool}},\cdots,C_{N-1}^{\mathrm{tool}},C_{N}^{\mathrm{tool}},D_{-N}^{\mathrm{tool}},D_{-N+1}^{\mathrm{tool}},\cdots,D_{N-1}^{\mathrm{tool}},D_{N}^{\mathrm{tool}},\\ E_{-N}^{\mathrm{tool}},E_{-N+1}^{\mathrm{tool}},\cdots,E_{N-1}^{\mathrm{tool}},E_{N}^{\mathrm{tool}},F_{-N}^{\mathrm{tool}},F_{-N+1}^{\mathrm{tool}},\cdots,F_{N-1}^{\mathrm{tool}},F_{N}^{\mathrm{tool}},\\ A_{-N}^{\mathrm{in}},A_{-N+1}^{\mathrm{in}},\cdots,A_{N-1}^{\mathrm{in}},A_{N}^{\mathrm{in}},A_{-N}^{\mathrm{out}},A_{-N+1}^{\mathrm{out}},\cdots,A_{N-1}^{\mathrm{out}},A_{N}^{\mathrm{out}},\\ B_{-N}^{\mathrm{out}},B_{-N+1}^{\mathrm{out}},\cdots,B_{N-1}^{\mathrm{out}},B_{N}^{\mathrm{out}},B_{-N}^{\mathrm{F}},B_{-N+1}^{\mathrm{F}},\cdots,B_{N-1}^{\mathrm{F}},B_{N}^{\mathrm{F}},\\ D_{-N}^{\mathrm{F}},D_{-N+1}^{\mathrm{F}},\cdots,D_{N-1}^{\mathrm{F}},D_{N}^{\mathrm{F}},F_{-N}^{\mathrm{F}},F_{-N+1}^{\mathrm{F}},\cdots,F_{N-1}^{\mathrm{F}},F_{N}^{\mathrm{F}}\end{bmatrix}^{\mathrm{T}}, \tag{10}$$

$$\boldsymbol{Q}_{(24N+12)\times1}=(0,\cdots,0,\sigma^{\mathrm{s}},0,\cdots,0)^{\mathrm{T}}, \tag{11}$$

式中,σ^{s} 是向量 $\boldsymbol{Q}$ 中的第 $11N+8$ 个元素(忽略高阶贡献).

利用求解得到的振幅系数 $\sum_{n=-N}^{N}A_n^{\mathrm{out}}$ 和 $\sum_{n=-N}^{N}B_n^{\mathrm{out}}$ 代入关系式 $p^{\mathrm{out}}=\rho_{\mathrm{f}}\omega^2\phi^{\mathrm{out}}$ 可计算钻铤外流体层中接收到的声压场(唐晓明和郑传汉,2004):

$$p^{\mathrm{out}}(z,t)=\frac{1}{2\pi}\int_{-\infty}^{\infty}\rho_{\mathrm{f}}\omega^2S(\omega)\int_{-\infty}^{\infty}\sum_{n=-N}^{N}\left[A_n^{\mathrm{out}}\mathrm{I}_n(\eta_{\mathrm{f}}b)+B_n^{\mathrm{out}}\mathrm{K}_n(\eta_{\mathrm{f}}b)\right]\cos(n\varphi_0)\mathrm{e}^{-\mathrm{i}\omega t}\mathrm{e}^{\mathrm{i}kz}\,\mathrm{d}k\,\mathrm{d}\omega, \tag{12}$$

式中,ρ_{f}为井内流体密度;$S(\omega)$为声源谱函数;$\varphi_0=0°,90°,180°,270°$为钻铤坐标系中接收器的方位.

2　数值计算结果及分析

本节基于上述随钻偏心声波测井理论,对比分析了在快速和慢速地层模型中,钻铤居中和偏心时随钻四极子声波测井的响应特征.对应于图 1 中建立的模型,钻铤向 x 轴正方向(0°方位)偏心,偏心率设为 90%,即偏心距为 24.3 mm.模型的声学参数详见表 1.声源谱函数采用主频为 3 kHz、脉宽为 0.5 ms的余弦包络脉冲函数(崔志文,2004).

表 1　模型声学参数

Table 1　Acoustic parameters of the model

	纵波波速 (m·s^{-1})	横波波速 (m·s^{-1})	密度 (kg·m^{-3})	外径 (m)
钻铤内流体	1500	—	1000	0.027
钻铤	5860	3130	7850	0.09
钻铤外流体	1500	—	1000	0.117
快速地层	4500	2300	2500	∞
慢速地层	2770	1250	2252	∞

2.1　快速地层

采用表 1 中快速地层参数,图 2a 和 b 分别给出了钻铤居中和偏心时随钻四极子声场的频率-速度二维谱.图中颜色深浅表征模式波的强度.前人研究表明四极子声源在较低频段内不激发钻铤模式的螺旋导波(Tang et al.,2002),因此本文只重点研究携带地层信息的地层模式波.从图 2a 中可以看出,在所给频率、速度范围内,随钻居中四极子声场中仅存在两阶地层四极子模式波,在截止频率处波速均为地层横波速度,如图中黑色箭头所指.仪器偏心后,如图 2b 所示,在流体速度以下,四极子源激发出了多阶流固界面波,主要包括偶极一阶弯曲波和单极斯通利波,二者相互耦合导致频散曲线相较于钻铤居中时都发生了改变,其中单极斯通利波相速度明显降低.除此之外,钻铤偏心后,一阶地层四极子波附近出现多极模式波,从频散特征上看,包括了偶极二阶弯曲波和六极子波,尤其是在 4.16 kHz 处,一阶地层四极子波的频散曲线被二阶弯曲波截断形成两个新的模态,如图中红色圆圈所示.

上述分析表明,钻铤偏心后的非轴对称四极声场中多极模态耦合共存,会对地层横波速度的提取造成不利影响.下面利用公式(12)分别计算钻铤居中和偏心时井中方位接收的全波信号,如图 2c 和 d 所示.由于钻铤偏心后整个声场仍关于 x 轴对称,因此仅给出了 0°～180°范围内五个方位上的模拟波形.在随钻声波测井中,一般采用正交四方位数据组合的形式作为数据输出,如图中红色虚线表示的合成波形所示.一般情况下,随钻四极子接收方式可表示为:

$$\tilde{p}^{\mathrm{out}}=p^{\mathrm{out}}(0°)-p^{\mathrm{out}}(90°)+p^{\mathrm{out}}(180°)-p^{\mathrm{out}}(270°). \tag{13}$$

钻铤居中(图 2c)时,在 45°和 135°方位上接收不到波形信号,这与四极子声源的偏振方式有关;0°和 180°方位接收全波相同,与 90°方位接收波形相位相反,这些波形对应于图 2a 中的一阶地层四极子模式波,落后于横波初至的高振幅波包为四极子波"艾里相".钻铤偏心后,45°和 135°方位上出现波形,其他方位上也接收到除地层四极子波外的多阶模式波.特别地,在 0°方位上,钻铤偏心后该侧与井壁之间的环形水槽厚度减小导致接收波形振幅增大,到时提前.

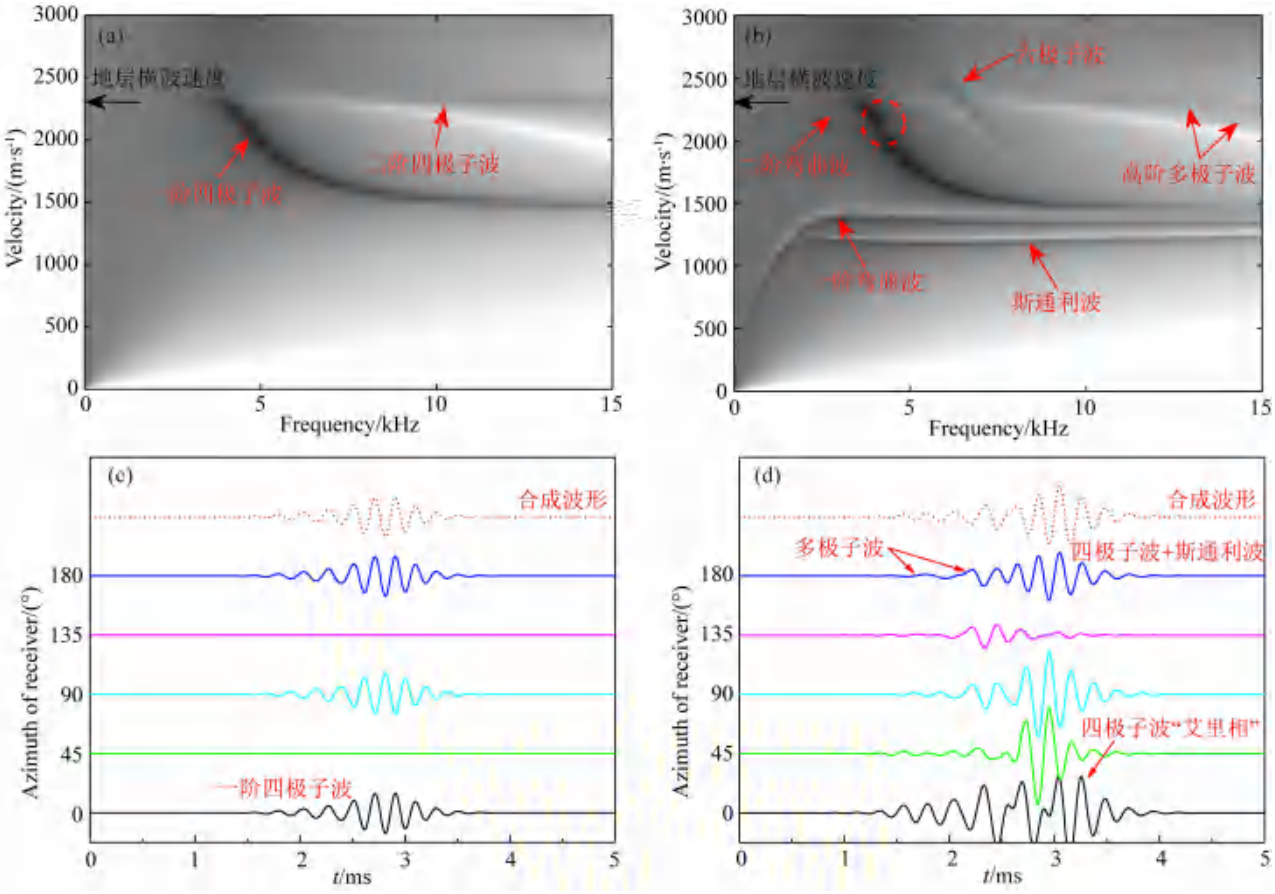


图 2 快速地层随钻四极子声场频散分析和方位接收波形

(a)和(c)钻铤居中;(b)和(d)钻铤偏心.

Fig. 2 The dispersion analysis of ALWD quadrupole acoustic field and azimuth received waveforms in fast formation

(a) and (c) The collar is in centralized case; (b) and (d) The collar is in eccentered case.

图 3 给出了快速地层中,钻铤居中和偏心时井中阵列接收的全波波形以及对应的时间-时差相关分析图(STC 图).图 3a 中蓝色波列为钻铤居中时的四方位合成阵列波形,红色波列为钻铤偏心后的四方位合成阵列波形.如图所示,钻铤居中时接收波形对应于图 2a 中的一阶地层四极子模式波.钻铤偏心后接收波形成分复杂,依次接收到低频一阶地层四极子波和二阶地层弯曲波的叠加波形、一阶地层弯曲波、四极子波"艾里相"以及高振幅的斯通利波,其中四极子波"艾里相"受斯通利波影响较大,波形拖尾明显.钻铤偏心后接收的全波波形中包含有较多除一阶地层四极子波外的多阶模式波,可以应用时间-时差相关法(唐晓明和郑传汉,2004)来有效分析全波中各成分波的到时与时差(速度的倒数).

图 3b 和 c 分别给出了对应于图 3a 中阵列接收波形的时间-时差相关处理结果.如图 3b 所示,钻铤居中时,全波中的主要成分是一阶地层四极子波,频散较强,四极子波"艾里相"清晰可见.首波时差提取值为 438 $\mu s \cdot m^{-1}$,与设置的快速地层横波时差值对应.钻铤偏心后,接收全波成分复杂,首波中包含有一阶地层四极子波和偶极二阶弯曲波成分,提取的首波时差值为 453 $\mu s \cdot m^{-1}$,如图 3c 所示,大于设定的地层横波时差,出现了横波时差测不准的现象.

2.2 慢速地层

采用表 1 中慢速地层参数,图 4a 和 b 分别给出了钻铤居中和偏心时随钻四极子声场的频率-速度二维谱.如图 4a 所示,钻铤居中时,在所给频率、速度范围内井孔中只存在单一模式的地层四极子波,速度频散较弱,在截止频率(2.38 kHz)处波速对应

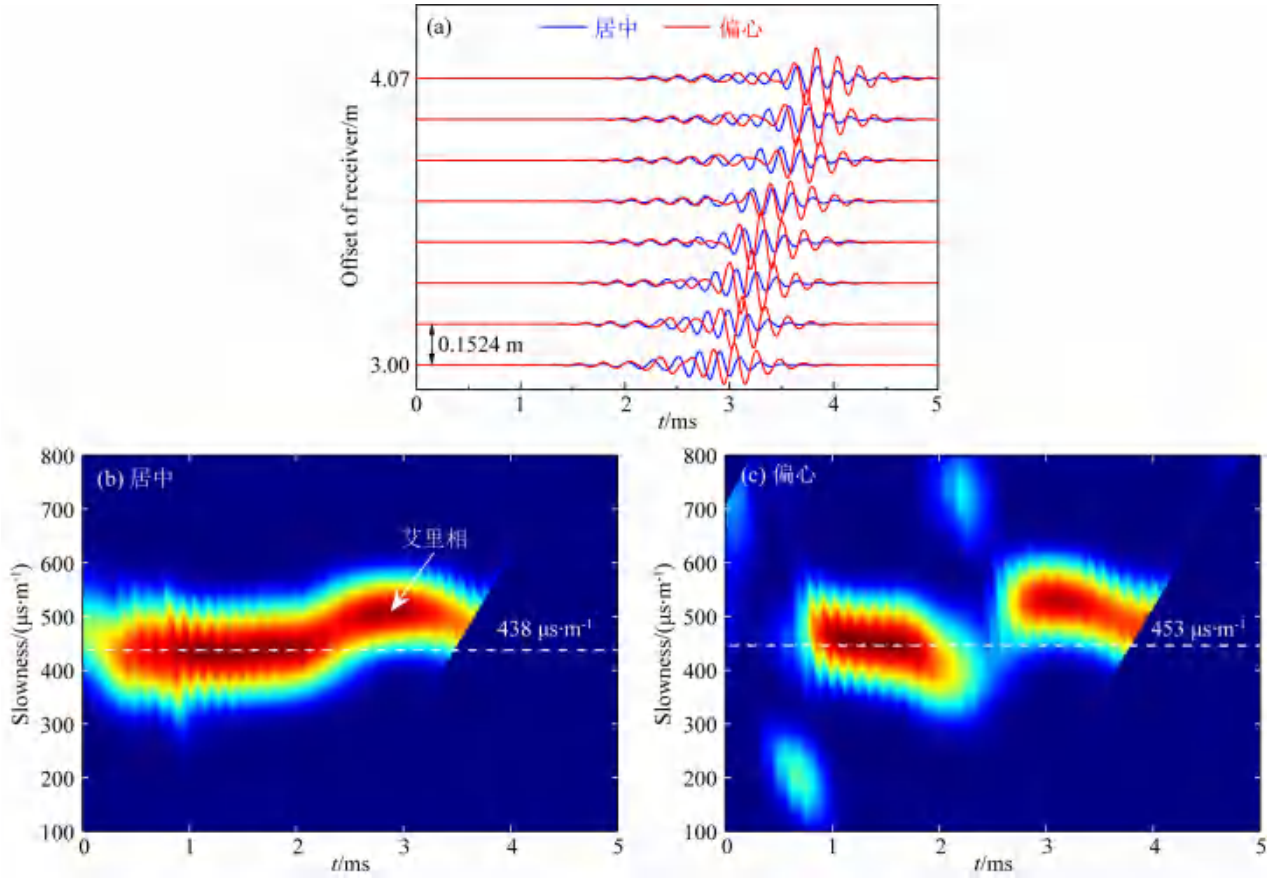


图 3　快速地层中随钻四极子阵列波形及时间-时差相关图

Fig. 3　Array waveforms and Slowness-Time correlogram of ALWD quadrupole in fast formation

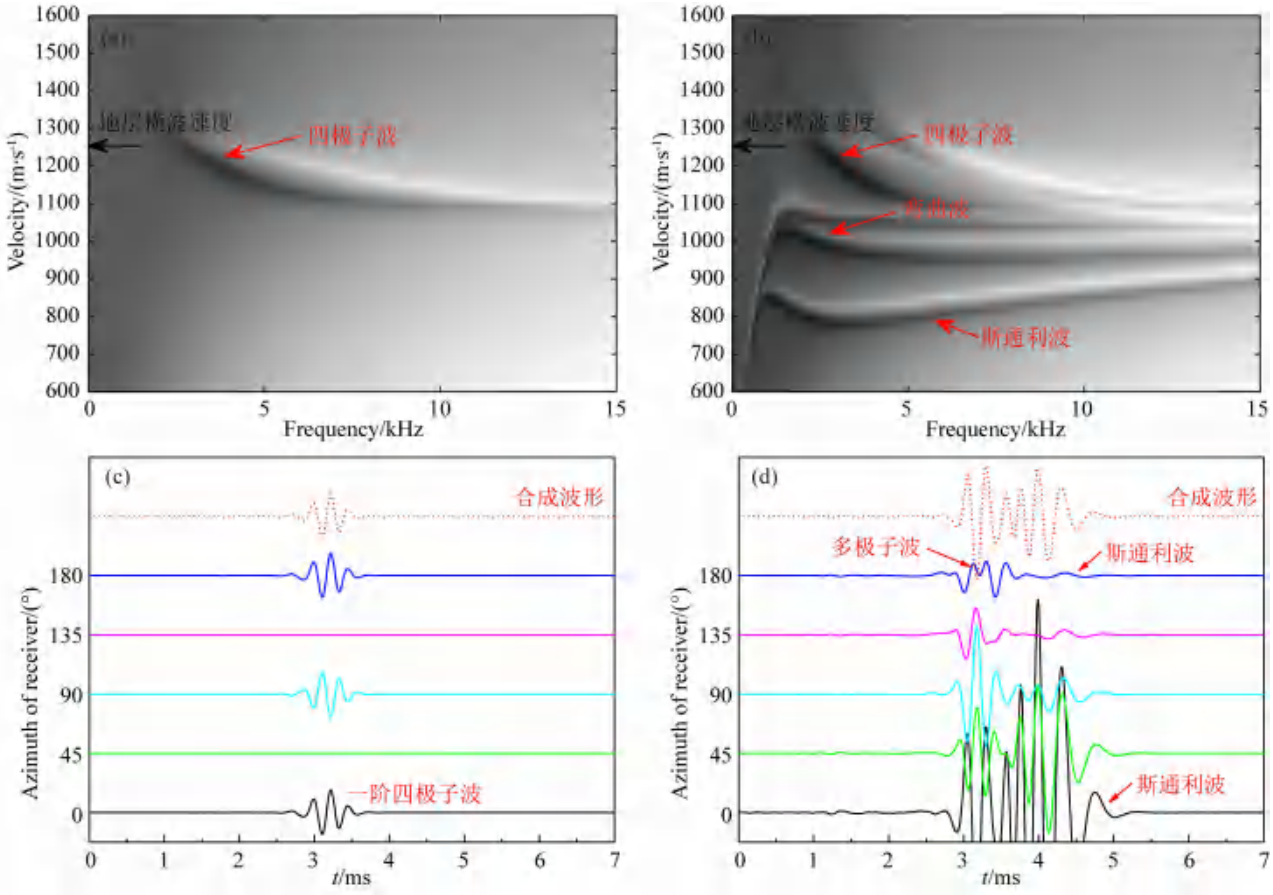


图 4　慢速地层随钻四极子声场频散分析和方位接收波形

(a)和(c)钻铤居中；(b)和(d)钻铤偏心.

Fig. 4　The dispersion analysis of ALWD quadrupole acoustic field and azimuth received waveforms in slow formation

(a) and (c) The collar is in centralized case; (b) and (d) The collar is in eccentered case.

地层横波速度,如图中黑色箭头所指.如图 4b 所示,钻铤偏心后,随钻四极声场中出现了较多振幅与地层四极子波相当的多极模式波,其中单极斯通利波波速较慢,在全波列中到时较晚,偶极弯曲波与地层四极子波波速相近,在时域上易发生波形混叠现象.类似地,计算了在慢速地层中,钻铤居中和偏心时井中方位接收的全波信号,如图 4c 和 d 所示.对比发现:钻铤偏心后各方位接收的地层四极子波均受到了单极和偶极模式波的影响.特别地,在 0°方位上斯通利波振幅极高,将严重影响地层四极子波的相干性.

图 5 进一步给出了慢速地层中,钻铤居中和偏心时井中阵列接收的合成全波波形以及对应的 STC 图.如图 5a 中蓝色波列所示,钻铤居中时,波列中只包含地层四极子波,频率成分单一,频散较弱.钻铤偏心后,阵列接收波形受到单极和偶极模式波的耦合干扰:地层四极子波耦合叠加偶极弯曲波,首波振幅升高;出现斯通利波波群,对应波形振幅较高,拖尾现象严重,源距较短时会严重干扰地层四极子波波形.

类似地,图 5b 和 c 分别给出了对应于图 5a 中阵列接收波形的时间-时差相关处理结果.如图 5b 所示,钻铤居中时处理得到的 STC 图中只有一个相关峰值区域,对应的时差值为 850 $\mu s \cdot m^{-1}$,与设定的慢速地层横波时差值对应.钻铤偏心后,斯通利波相关性突出,同时首波也受到偶极弯曲波的干扰出现了轻微的频散现象,如图 5c 所示,导致提取的首波时差值为 912 $\mu s \cdot m^{-1}$,远大于设定的地层横波时差.测量值相较于快速地层偏离真实值更多.

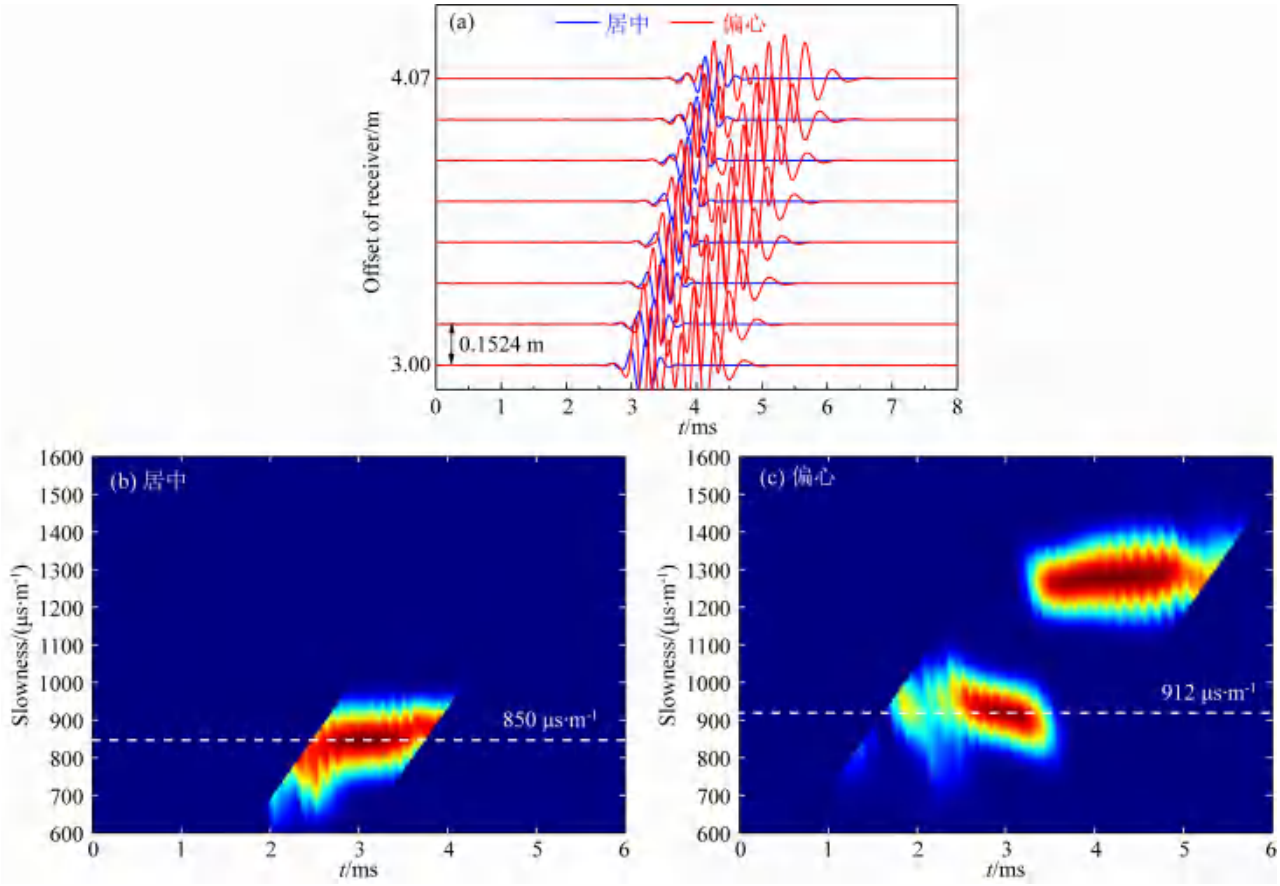


图 5 慢速地层中随钻四极子阵列波形及时间-时差相关图

Fig. 5 Array waveforms and Slowness-Time correlogram of ALWD quadrupole in slow formation

以上数值模拟结果表明,当钻铤偏心时测量的四极子波波形成分复杂,偏心引起的低频斯通利波模式对地层四极子模式耦合干扰非常严重,导致地层横波时差的相关性很差,无法提取到可靠的地层横波时差,该不利影响在疏松软地层中表现更为突出.

3 现场实例分析

随钻四极子声波测井技术已被大量应用于现场的地层横波时差测量.下面结合国内自主研发的随钻四极子声波测井仪器实验样机,进行野外现场资料的实例分析.图 6 给出了包含钻铤居中和偏心测量的两个深度段四极子随钻声波测井现场数据的处理成果图及单点处的阵列波形和对应的频散分析结果.其中上段为加入扶正器钻铤居中测量井段的处理结果,下段为未加扶正器钻铤偏心测量井段的处理结果.

图中第 1 道和第 2 道分别给出了随钻单极子测量的变密度波形和对应的 STC 图.从波形中可以看

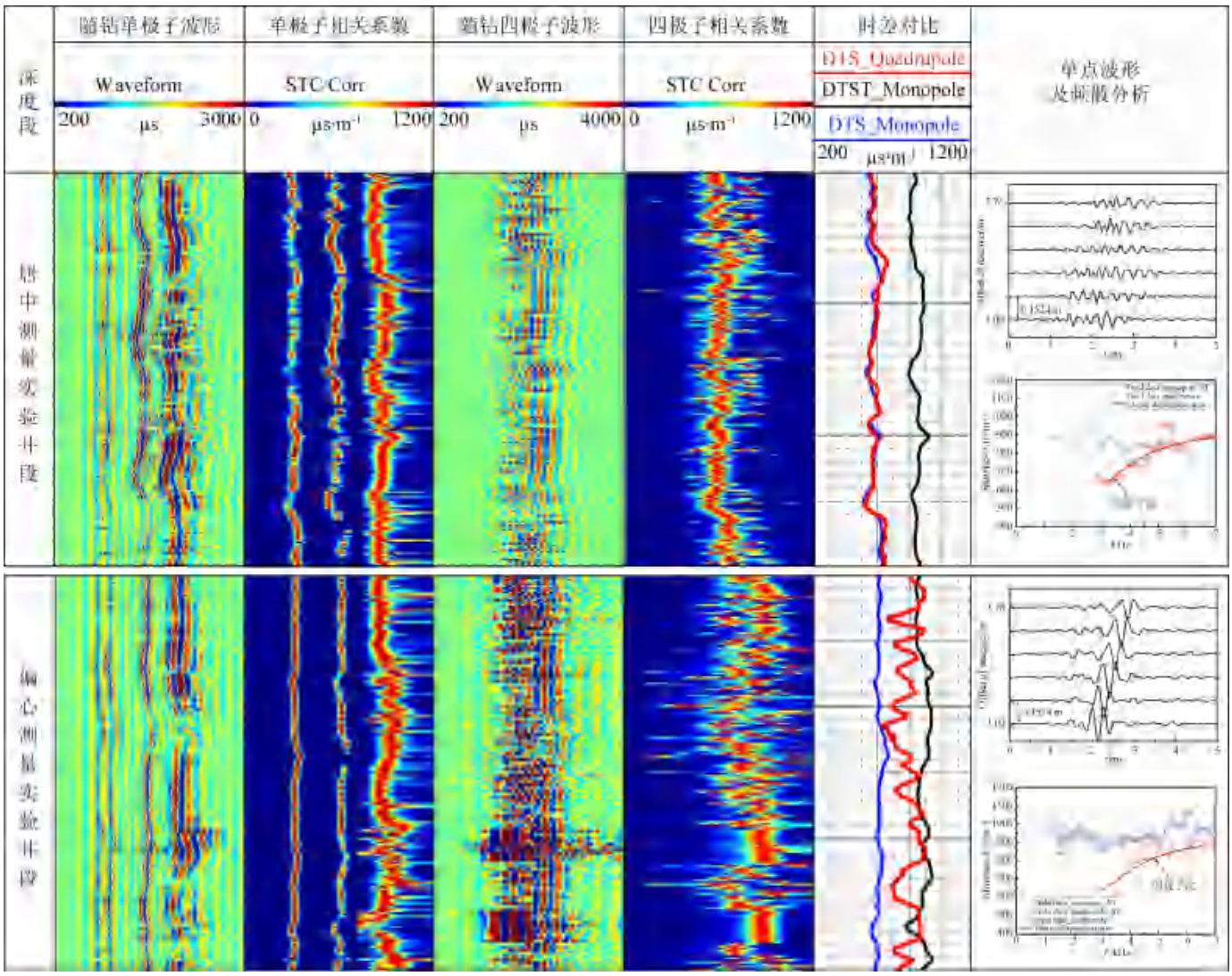


图 6　某实验井随钻四极子声波测井处理实例

Fig. 6　Field data of ALWD quadrupole acoustic tool in an experimental well

出,单极测量的全波波形中主要是地层纵横波以及斯通利波,且地层波的相关性较好(见第 2 道 STC 图). 图中第 3 道和第 4 道分别给出了随钻四极子测量的变密度波形和对应的 STC 图. 第 5 道给出了基于随钻四极子测井数据处理得到的地层横波时差曲线(红线),并与随钻单极子处理结果进行对比,蓝线为单极横波时差曲线,黑线为斯通利波时差曲线. 第 6 道给出了对应井段中某一深度点处的阵列波形和频散分析结果. 从上部加扶正器测量的成果图可以看出,居中测量得到的波形质量较高,单点的阵列波形中能清晰地识别出地层四极子波,并且基于随钻居中模型的理论频散曲线(红线)和从现场实测阵列波形中提取的四极子波频散数据(红色圆圈)吻合良好. 全井段处理得到的横波时差相关性强,连续性好,与单极横波处理结果基本吻合,说明钻铤居中时,四极子横波测量准确可靠(见第 4、5 道).

在未加扶正器的下部井段,仪器偏心测得的四极子波形质量受到斯通利波的干扰. 从单点的阵列波形中可以看出,钻铤偏心后四极子声场中除了地层四极子波外还有高振幅的斯通利波,分别对应频散分析图中的红色和蓝色圆圈,并且四极子声源激发出的斯通利波模式与相同深度点处随钻单极斯通利波频散数据(黑色圆圈)基本重合. 斯通利波的出现降低了地层四极子波的相关性,全井段的横波时差相关性很弱,测量值介于横波与斯通利波时差之间,难以得到准确的地层横波时差(见第 4、5 道). 以上的数值模拟和实测数据表明仪器偏心会对四极子横波速度测量造成极大的影响. 因此在实际测井过程中要尽可能地保证仪器居中,如加扶正器等.

4　结论

本文建立了随钻偏心声波测井模型,针对该非轴对称柱状分层结构,利用双柱坐标系解析算法计算了快速和慢速地层中钻铤居中和偏心时四极子声

源激励的随钻声场,并通过居中和偏心测量的现场实例分析得出如下结论:

(1)通过对比钻铤居中和偏心时的全波波形和速度频散,发现在快速地层中钻铤偏心会使得在地层横波附近出现多极模式波并对其产生干扰.在低频段一阶地层四极子波的频散曲线被偶极二阶弯曲波截断形成两个新的模态,时域上表现为四极子波和偶极弯曲波的叠加,时间-时差相关图(STC 图)也说明了钻铤偏心后在快速地层中横波时差测量值偏大.

(2)在慢速地层中钻铤偏心导致横波时差测不准的现象更为突显.因为钻铤偏心激发出的流固界面波速度与地层四极子波速度相近,偏心率较大时在钻铤偏心一侧流固界面波振幅甚至会超过地层四极子波,进而严重影响地层横波时差的提取.

(3)现场随钻四极子声波测井实验样机在居中和偏心的状态下实测的数据表明:当随钻四极子样机居中测井时,可测量到高质量的波形,处理得到的横波时差相关性强,与单极测量横波时差吻合较好;但钻铤偏心状态下测量的四极子波形成分复杂,偏心引起的低频斯通利波模式对地层四极子模式耦合干扰非常严重,导致地层横波时差的相关性很差,无法提取到可靠的地层横波时差甚至无法使用,尤其在疏松软地层中影响更为突出.因此在实际测井过程中要尽可能地保证仪器居中测量.

References

Byun J, Toksöz M N. 2003. Analysis of the acoustic wavefields excited by the logging-while-drilling (LWD) tool. *Geosystem Engineering*, 6(1): 19-25.

Cui Z W. 2004. Theoretical and numerical study of modified Biot′s models, acoustoelectric well logging and acoustic logging while drilling excited by multipole acoustic sources [Ph. D. thesis] (in Chinese). Changchun: Jilin University.

Haugland S M. 2004a. Mandrel eccentricity effects on acoustic borehole-guided waves. // Proceedings of 2004 SEG Annual Meeting. Denver: SEG, 282-285.

Haugland S M. 2004b. Analytical solution for an eccentric mandrel in a fluid-filled borehole: the acoustic case. // Proceedings of 2004 2004 SEG Annual Meeting. Denver: SEG, 330-333.

Huang X J, Zheng Y B, Toksöz M N. 2004. Effects of tool eccentricity on acoustic logging while drilling (LWD) measurements. // Proceedings of 2004 SEG Annual Meeting. Denver: SEG.

Ji Y J, He X, Chen H, et al. 2021. Acoustic fields for monopole logging while drilling with an eccentric collar. *Geophysics*, 86(2): D43-D63.

Pardo D, Matuszyk P J, Torres-Verdin C, et al. 2013. Influence of borehole-eccentred tools on wireline and logging-while-drilling sonic logging measurements. *Geophysical Prospecting*, 61(S1): 268-283.

Su Y D, Xu S, Jiang C, et al. 2017. Theoretical analysis of the optimal collar size for a logging while drilling quadrupole tool. *Chinese Journal of Geophysics* (in Chinese), 60(4): 1606-1615, doi: 10.6038/cjg20170432.

Tang X M, Dubinsky V, Bolshakov A, et al. 2002. Shear-velocity measurement in the logging-while-drilling environment: modeling and field evaluations. // Proceedings of the SPWLA 43rd Annual Logging Symposium. Oiso: SPWLA.

Tang X M, Dubinsky V, Wang T, et al. 2003. Shear-velocity measurement in the Logging-While-Drilling environment: modeling and field evaluations. *Petrophysics*, 44(2): 79-90.

Tang X M, Cheng C H. 2004. Quantitative borehole acoustic methods. Netherlands: Elsevier Science Publishing Inc.

Wang B, Tao G, Chen T R, et al. 2012. Experimental study of acoustic logging while drilling measurements using an asymmetric source. *Chinese Journal of Geophysics* (in Chinese), 55(1): 327-332, doi: 10.6038/j.issn.0001-5733.2012.01.033.

Wang H, Tao G, Wang B, et al. 2009. Wave field simulation and data acquisition scheme analysis for LWD acoustic tool. *Chinese Journal of Geophysics* (in Chinese), 52(9): 2402-2409, doi: 10.3969/j.issn.0001-5733.2009.09.027.

Wang H, Tao G, Zhang K. 2013. Wavefield simulation and analysis with the finite-element method for acoustic logging while drilling in horizontal and deviated wells. *Geophysics*, 78(6): D525-D543.

Wang J, Li H Y, Guan W, et al. 2019. Experimental studies on the mechanism of monopole acoustic collar wave. *Chinese Journal of Geophysics* (in Chinese), 62(4): 1541-1553, doi: 10.6038/cjg2019M0042.

Wei J Q, He X, Chen H, et al. 2018. Wavefield characteristics of unipole sonic LWD with eccentric tools. // Proceedings of 2018 SEG International Exposition and Annual Meeting. Anaheim: SEG, 734-738.

Wei J Q, He X, Li X Q, et al. 2019. Simulation of acoustic LWD with an eccentric source and inversion of formation anisotropy. *Chinese Journal of Geophysics* (in Chinese), 62(4): 1554-1564, doi: 10.6038/cjg2019L0731.

Zheng Y B, Huang X J, Toksöz M N. 2004. A finite element analysis of the effects of tool eccentricity on wave dispersion properties in borehole acoustic logging while drilling. // Proceedings of 2004 SEG Annual Meeting. Denver: SEG, 294-297.

Zhu Z Y, Toksöz M N, Rao R, et al. 2008. Experimental studies of monopole, dipole, and quadrupole acoustic logging while drilling (LWD) with scaled borehole models. *Geophysics*, 73(4): E133-E143.

附中文参考文献

崔志文. 2004. 多孔介质声学模型与多极源声电效应测井和多极随钻声测井的理论与数值研究[博士论文]. 长春: 吉林大学.

苏远大，许松，江灿等. 2017. 随钻四极子横波测井钻铤尺寸优化设计的理论研究. 地球物理学报，60(4)：1606-1615，doi：10.6038/cjg20170432.

唐晓明，郑传汉. 2004. 定量测井声学. 赵晓敏译. 北京：石油工业出版社.

王兵，陶果，陈天润等. 2012. 非对称声源多极子随钻声波测井实验室测量研究. 地球物理学报，55(1)：327-332，doi：10.6038/j.issn.0001-5733.2012.01.033.

王华，陶果，王兵等. 2009. 多极子随钻声波测井波场模拟与采集模式分析. 地球物理学报，52(9)：2402-2409，doi：10.3969/j.issn.0001-5733.2009.09.027.

王军，李红一，关威等. 2019. 单极源钻铤波传播机制的实验研究. 地球物理学报，62(4)：1541-1553，doi：10.6038/cjg2019M0042.

卫建清，何晓，李希强等. 2019. 含偏心点声源的随钻测井声场模拟和地层各向异性反演研究. 地球物理学报，62(4)：1554-1564，doi：10.6038/cjg2019L0731.

（本文编辑　何燕）

孔凡童，庄春喜，苏远大等. 2017. 随钻四极横波测量的数据驱动频散处理方法. 地球物理学报，60(12)：4938-4944，doi：10.6038/cjg20171232.

Kong F T, Zhuang C X, Su Y D, et al. 2017. A data-driven dispersive processing of LWD quadrupole wave data. *Chinese J. Geophys.* (in Chinese), 60(12): 4938-4944, doi: 10.6038/cjg20171232.

随钻四极横波测量的数据驱动频散处理方法

孔凡童，庄春喜，苏远大，唐晓明*

中国石油大学(华东)地球科学与技术学院，青岛 266580

摘要 针对随钻四极横波测量中的频散效应，本文采用了一种数据驱动的频散处理方法. 根据四极子声波频散数据计算慢度概率密度及其拟合函数，再对该函数寻边确定实际地层的横波慢度. 该方法在对理论模拟数据及现场随钻测井数据处理中均取得了良好的应用效果，为随钻四极子横波测井提供了一种快速有效的处理方法.

关键词 随钻横波测井；四极子声波；频散效应；数据驱动；慢度概率密度

doi：10.6038/cjg20171232 **中图分类号** P631 **收稿日期** 2017-01-16，2017-05-26 收修定稿

A data-driven dispersive processing of LWD quadrupole wave data

KONG Fan-Tong, ZHUANG Chun-Xi, SU Yuan-Da, TANG Xiao-Ming*

School of Geosciences, China University of Petroleum, Qingdao 266580, *China*

Abstract A data-driven dispersive method is developed to process the logging while drilling (LWD) quadrupole waveform data. A Slowness Probability Density (SPD) is first calculated from the LWD wave dispersion data and is subsequently fitted with a proper analytical function. By finding the edge of the function, the true formation shear slowness can be determined. We have applied the method to process synthetic and field LWD quadrupole wave data. The results show that the method corrects the dispersion effect in the waveform data and obtains accurate estimates of formation shear slowness.

Keywords Quadrupole shear logging while drilling; Quadrupole wave; Dispersion effect; Data-driven; Slowness Probability Density

1 引言

随钻声波测井在近年来发展迅速，已经成为了地球物理勘探和油藏工程应用中的重要技术. 四极子波在随钻条件下测量横波速度时具有较好的性质(苏远大，2006；Tang et al.，2002；Dubinsky et al.，2003)，被广泛用作地层横波速度测量. 然而，作为在钻铤存在条件下沿钻井传播的导波，四极子波具有很强的频散效应：四极子声波仅在低频时才以地层横波速度传播，其波速随频率增加大幅下降；在泥浆密度和仪器尺寸较大的情况下，频散效应更为严重(Tang et al.，2003). 其后果是，对随钻四极声波测井数据用常规的时间慢度相关法(STC，为一非频散常规处理方法)(Kimball and Marzetta，1984)处理，得到的慢度大于实际地层慢度(Geerits

基金项目 国家自然基金(41474092，41604109)，山东自然科学基金(ZR2014DL009)资助.

第一作者简介 孔凡童，男，1992 年生，硕士，从事声波测井资料处理与解释的方法研究. E-mail：kft_upc@163.com

* **通讯作者** 唐晓明，男，1955 年生，教授，多年来一直致力于地球物理(特别是声波)测井、岩石物理学、地震波传播及测量等方面的研究和技术开发工作. E-mail：tangxiam@aliyun.com

and Tang, 2003, Kimball,1998).

为了从随钻四极声波数据中得到准确的地层横波慢度,国内外学者开展了大量的相关研究.其中应用比较普遍的是基于理论模型的频散校正方法(Tang et al., 2006; Zhang et al., 2010; Lee et al., 2016; Su et al., 2016),这类方法需要假设均匀地层模型计算理论频散曲线,计算时需要输入较多的模型参数(如地层密度、速度及井径等),当实际地层情况严重偏离理论模型时,难以得到理想结果.另一类方法是数据驱动法.根据导波频散曲线低频截止频率处的慢度为地层慢度这一基本事实(唐晓明和郑传汉,2004),Huang 和 Yin(2005)提出了一种数据驱动的频散校正方法.该方法将频率-慢度域中的二维频散数据向慢度轴投影,得到与慢度相关的统计直方图,再通过确定该直方图的边缘的方法来估算实际地层慢度.然而,当该方法应用于随钻数据时,噪声的严重干扰会导致该方法的失效.为弥补噪声干扰的影响,Tang 等(2010)提出了一种对声波频散数据进行曲线拟合的方法.通过构造解析函数代替理论频散曲线,降低了个别频率点上频散数据出现奇异值的影响.由于拟合所用的解析函数是从实际频散数据来构造的,该方法也是一种数据驱动法.

本文采用的数据驱动频散处理方法是将解析函数拟合的思想用于慢度直方图的拟合.首先通过慢度-频率相干法计算实际频散曲线,然后计算慢度概率密度函数(SPD,相当于上述的慢度直方图),根据概率密度函数形态特征采用与之相适应的拟合函数,再利用统计特征值匹配的方法确定该函数的参数值,最后对该拟合函数寻边来确定地层慢度.对该频散处理方法用有限差分模拟的随钻四极子声波数据进行了验证,并结合现场随钻测井资料的进行了处理.处理结果表明该方法快速有效,能较为准确地确定地层慢度.

2　方法概述

本文所述频散波处理方法需要首先从实际测井资料中提取频率-慢度频散数据(曹正良等, 2005).假设有 N 个接收器的阵列声波测井数据中的导波为 $X_n(t)$,$(n=1,2,\cdots,N)$,其傅里叶变换后的频谱为 $X_n(\omega)$,$(n=1,2,\cdots,N)$.此阵列声波频谱的慢度-频率相关函数为(唐晓明和郑传汉, 2004; Lee et al., 2016)

$$\rho(\omega,s)=\frac{\left|\sum_{n=1}^{N}X_n^*(\omega)\mathrm{e}^{-\mathrm{i}\omega(n-1)sd}\right|}{\sqrt{N\sum_{n-1}^{N}X_n^*(\omega)X_n(\omega)}},\qquad(1)$$

其中 * 为复共轭,接收器间距为 d,ω 为角频率.对每一频率 ω 求取相关函数最大值对应的慢度 s,便得到实际数据的频散数据 $S_d(\omega)$.

通过该频散数据可以计算慢度概率密度函数 SPD(Slowness Probability Density Function, Tang et al., 2010),定义如下:

$$\mathrm{SPD}(s)=\frac{1}{\omega_\mathrm{H}-\omega_\mathrm{L}}\int_{\omega_\mathrm{L}}^{\omega_\mathrm{H}}\exp\left\{-\left[\frac{s-S_\mathrm{d}(\omega)}{\sigma_\mathrm{s}}\right]^2\right\}\mathrm{d}\omega,\qquad(2)$$

其中 ω_H 和 ω_L 分别为频散数据 $S_\mathrm{d}(\omega)$ 的频率上限与下限,σ_s 为 $S_\mathrm{d}(\omega)$ 的均方差开根.与传统的统计直方图(Huang and Yin, 2005)相比较,上述的 SPD 为一连续函数,可以减少频散数据中异常值的影响.随钻四极声波的频散特征是其慢度在低频时趋于地层横波慢度,即该导波慢度在地层横波慢度附近取值的概率密度增加,使得 SPD 函数呈现一明显的峰值.因此,确定该峰值的边缘即可提取地层的慢度.然而在随钻环境下,测井数据中的强噪声干扰有时会严重影响 SPD 函数的形态,使其边缘的确定十分困难.本文采用一种基于函数拟合的计算方法,通过对拟合函数的解析计算来代替对 SPD 函数直接寻边.

对 SPD 数据的拟合函数的考虑是基于上述的导波慢度随频率的单调变化特征,这一特征使得 SPD 函数在峰值边缘处较为陡峭,根据这种形态特征提出一种相适应的拟合函数:

$$f(s)=A(s-s_0)^\beta\mathrm{e}^{-\alpha(s-s_0)},\ s\geqslant s_0,\qquad(3)$$

其中 s 为慢度变量,该拟合参数共包括四个参数:A、α、β、s_0,A 确定了拟合函数的幅度值,α、β 确定了拟合函数的形态,s_0 确定了拟合函数的起始值.该函数有一明显的峰值,且其低慢度一侧甚为陡峭.虽然其它函数或函数组合也能满足这种形态,但(3)式的解析性质可以使以下的统计特征值匹配计算变得十分简便.用上述解析函数直接拟合 SPD 数据,可以确定(3)式中的四个参数.然而这是一个计算量较大的四参数的反演问题,不适合测井数据的快速有效处理.我们采用以下统计特征值匹配的方法来确定这些参数.

根对(2)、(3)式所示的概率密度及其拟合函数,计算二者的期望、均值和方差(蔡德勒等, 2012)等

统计特征值 I_0、s_c、σ_c^2，再令计算的二函数的各统计特征值分别相等，即匹配二者相应的特征值，得到

$$\begin{cases} I_0 \equiv \int_\Omega \mathrm{SPD}(s)\mathrm{d}s = \dfrac{A\Gamma(\beta+1)}{\alpha^{\beta+1}}, \\ s_c \equiv \dfrac{\int_\Omega s \cdot \mathrm{SPD}(s)\mathrm{d}s}{\int_\Omega \mathrm{SPD}(s)\mathrm{d}s} = \dfrac{\beta+1}{\alpha} + s_0, \\ \sigma_c^2 \equiv \dfrac{\int_\Omega (s-s_c)^2 \cdot \mathrm{SPD}(s)\mathrm{d}s}{\int_\Omega \mathrm{SPD}(s)\mathrm{d}s} = \dfrac{\beta+1}{\alpha^2}. \end{cases} \tag{4}$$

上式中右端是根据解析函数(3)式求得的各统计特征值，其中 Γ 为伽马函数；Ω 为慢度区间，可以根据实际数据并参考 STC 处理结果设置合理区间. 令这些特征值分别等于 SPD 数据计算出的相应特征值，便得到确定拟合函数 $f(s)$ 中四个参数的三个方程，仍需的第四个方程由调节 $f(s)$ 中慢度起始值 s_0 得到.

为了确定拟合函数的起始慢度 s_0，以拟合均方差构建如下的目标函数：

$$E(s_0) = \int_\Omega [f(s;s_0) - \mathrm{SPD}(s)]^2 \mathrm{d}s, \tag{5}$$

其中 $f(s;s_0)$ 为式(3)中的拟合函数，现以 s_0 为待求参量. 拟合函数的参数 A、α、β 已经通过特征值匹配方法确定，上式就变成了一维函数极小值优化问题，当 $E(s)$ 最小时，拟合函数与 SPD 函数拟合最好，此时对应的 s_0 就是拟合函数的起始慢度.

拟合函数确定以后，其寻边问题由函数的解析性质很容易解决. SPD 函数在其边缘处增加最快，所以其边缘对应于拟合函数的一阶导函数极值. 由(3)式求取该极值处的慢度值，最终得到实际地层的慢度值 s_e：

$$s_e = \frac{\beta - \sqrt{\beta}}{\alpha} + s_0. \tag{6}$$

上述方法通过求解声波频散数据的慢度概率密度函数的寻边问题，增强了声波数据处理的抗噪性和稳定性，能够快速准确的提取实际地层慢度，适合于现场随钻声波测井资料的快速处理.

3 方法验证

为验证本文方法的正确性和有效性，利用有限差分方法模拟在慢地层中传播的随钻四极子波波形(Liu et al.，1996；Wang and Tang，2003). 随钻声波测井仪器模型的剖面见图 1，其中包括声源、接收阵列、以及放置在它们中间位置的刻槽隔声体，模拟参数见表 1. 模拟所得阵列波形如图 2a 所示，图中突出的振相便是四极声波，其慢度接近于地层横波慢度. 利用常规的慢度-时间相干方法(STC)对该四极子波形数据进行处理，处理结果如图 2b 的相干图所示，据此获得地层横波慢度为 1290 $\mu s \cdot m^{-1}$，由于 STC 方法并没有考虑四极子波的频散效应，获得的慢度值比实际地层横波慢度大不少，所以需要对该波形数据用频散方法处理.

下面利用本文所述方法对模拟波形数据进行处理. 该方法主要利用四极子波的低频信息，所以在提取频散数据时，设置频率区间为 1～3 kHz，慢度区间为 1150～1350 $\mu s \cdot m^{-1}$，所得频散数据(散点)如图 2c 所示. 可以看出，实际频散数据显示出明显的频散效应，慢度随频率增加，低频段平缓趋于地层横波慢度. 根据式(2)计算 SPD 函数(散点)，如图 2d 所示. 由于低频数据较为平坦，在数据在趋于地层慢度时概率密度最大，显示出突出的峰值. 利用式(3)所示的拟合函数采用上述的方法对该 SPD 函数进行拟合，拟合函数(红色)如图 2d 所示，可以看出该函数很好地拟合了 SPD 数据的低慢度部分. 通过式(6)计算获得地层横波慢度为 1215.5 $\mu s \cdot m^{-1}$，与模拟参数符合很好，表明该方法是准确有效的.

表 1 计算随钻多极子波的地层及钻铤参数

Table 1 The parameters of drill collar and formation for calculating the LWD multipole waves

介质	纵波慢度 ($\mu s \cdot m^{-1}$)	横波慢度 ($\mu s \cdot m^{-1}$)	密度 ($g \cdot cm^{-3}$)	半径范围 (m)
钻铤	171	319	7.85	0.05～0.108
泥浆	667	—	1.00	0～0.05 或 0.108～0.157
慢地层	469	1218	2.172	0.157～∞

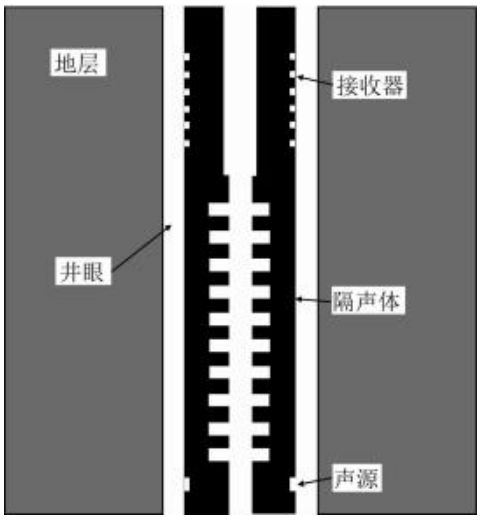


图 1 随钻声波测井仪器模型

Fig. 1 The LWD acoustic tool model

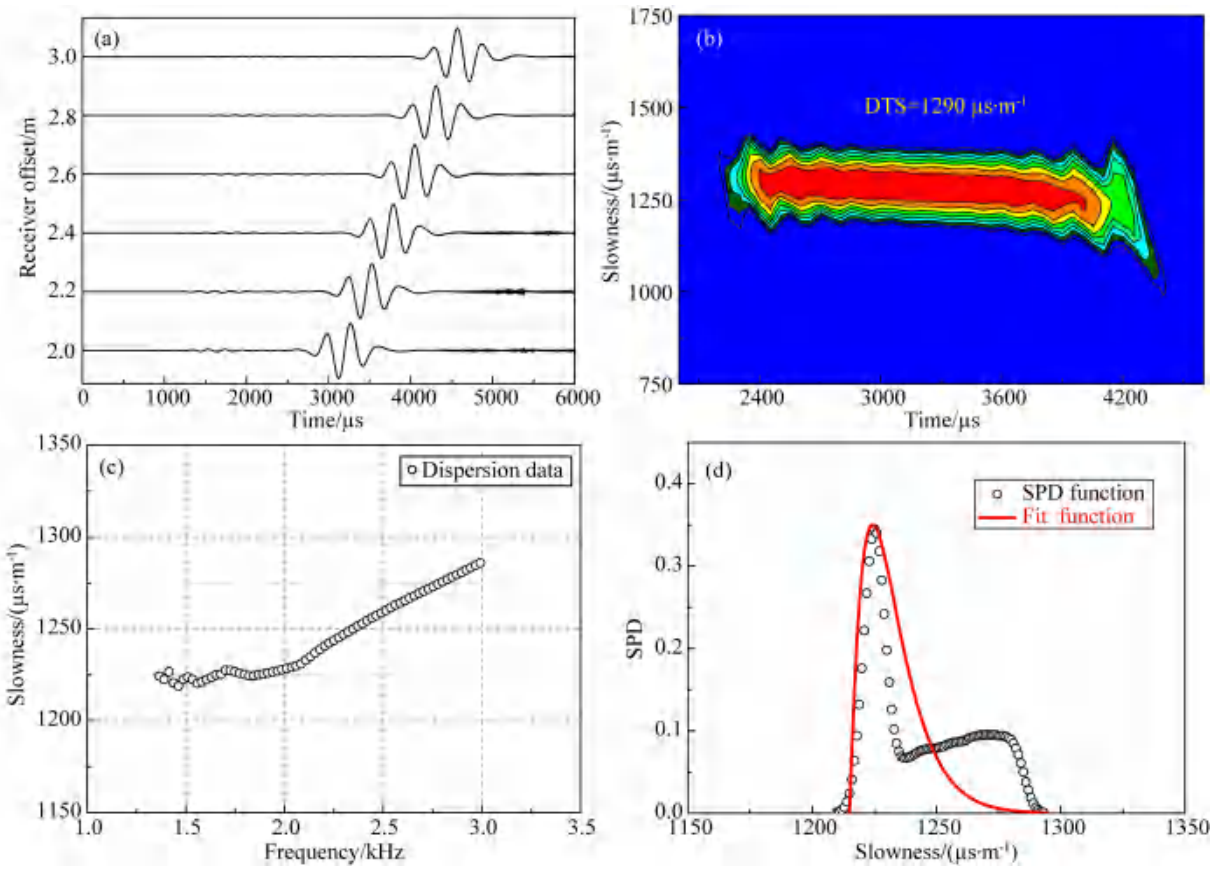


图 2　模拟数据及其处理结果

(a) 四极子波形;(b) 四极子波的 STC 处理结果;(c) 四极子波的频散曲线;(d) SPD 函数(散点)及其拟合函数(红色).

Fig. 2　Synthetic LWD data and processing result

(a) Synthetic LWD quadrupole waveform data; (b) The STC correlogram of the data; (c) Frequency dispersion of the wave data; (d) SPD (markers) of the dispersion data and its fitting function (red curve).

4　实际数据处理

4.1　中速地层处理实例

利用本文方法对一中速地层的随钻四极声波数据进行处理,井段长度为 350 m,处理结果如图 3 所示.图中第一道为岩性曲线,给出了自然伽马、井径曲线.第二道为随钻四极阵列数据第一接收器的变密度波形图.处理结果如图中第三道所示,其中给出了提取的横波慢度(红线)以及拟合函数(变密度图),拟合函数可以作为一种质量监控工具,其边缘对应于实际地层慢度.可以看出,提取的慢度很好地追踪了拟合函数的边缘.图中第四道分别给出了非频散 STC 方法计算的四极横波慢度(蓝线)和用本文方法提取的横波慢度(红线).由于随钻四极子波的频散,频散与非频散两条慢度曲线的差异就反映了波的频散效应,该差异即为常规 STC 提取的地层横波慢度所需的频散校正量,如第四道中灰色填充曲线所示.该层段校正量约为 7%～8%,说明该频散效应影响甚大不容忽略.作为对比,图中同时给出了单极子横波慢度曲线(黑线),可以看出频散处理结果与单极横波慢度符合很好.由单极提取的横波慢度一般不受频散的影响,反映地层的横波慢度.这种符合说明本文的频散处理方法能从频散很强的随钻四极波形数据中有效地获取地层横波慢度.

4.2　超慢地层应用实例

在慢速地层中,单极声波测井无法得到地层横波慢度,四极声波测井成为地层横波慢度随钻测量的主要技术,随钻四极子波的频散处理方法因此变得十分重要.利用本文方法对一 500 m 井段的超慢地层的随钻四极声波数据进行处理,处理结果如图 4a 所示.从第二道波形图中可以看到四极子波的到时随着深度的增加逐渐提前,四极子波受到的频散效应影响逐渐减弱.第三道为频散处理结果,所提取的地层横波慢度可以很好地追踪拟合函数的边缘.第四道分别给出了常规 STC 处理结果(蓝线)和频散校正结果(红线),二者之间的差异为图中的灰色填充曲线所示.在浅部未固结的超慢地层中,四极子波频散效应较强,频散校正量约为 10%左右.随着深度的增加,地层横波慢度逐渐减小,四极子波频散

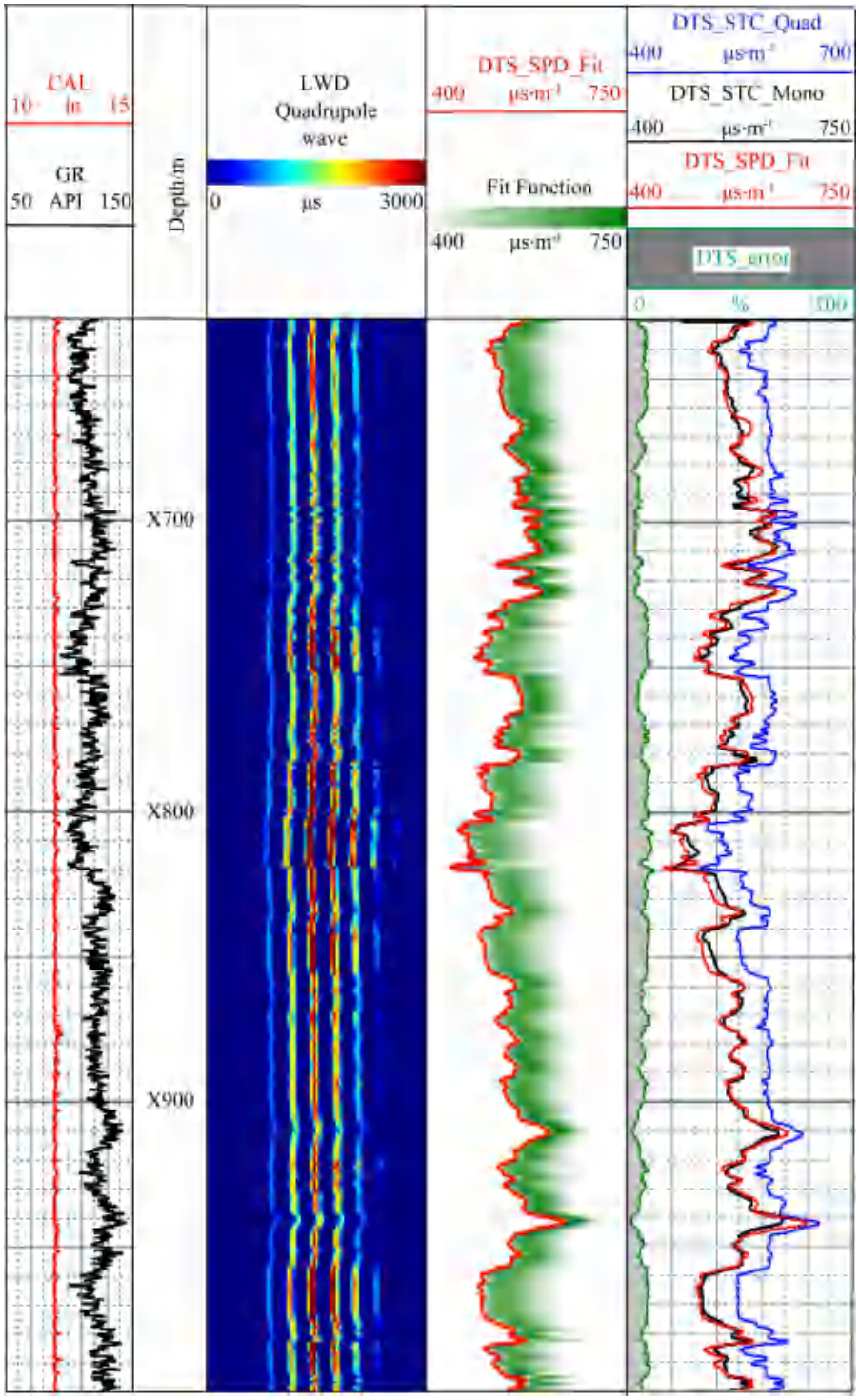


图 3 中速地层随钻声波数据处理实例

Fig. 3 Example of LWD data processing for a moderately fast formation

效应逐渐减弱,在深部快地层处频散校正量降至2%～3%左右.

为进一步验证频散处理结果的正确性,图 4a 第四道还给出根据图 1 的理论模型所做频散校正(Su et al., 2016)得到的横波慢度(黑线). 在这个实例中,基于理论模型的频散处理与数据驱动的频散处理所得结果十分一致. 这两种结果的一致性,除了证明随钻四极声波理论(Tang et al., 2002)与实际数据吻合之处,还说明了本文处理方法的正确性. 图 4b 还分别给出了深层(X827m)、中层(X559m)、浅层(X401m)的三个有代表性的深度点的实际频散数据. 图 4c 给出了相应的 SPD(散点)及其拟合函数(红线). 频散数据的低频部分跳动较大,导致 SPD 的边缘较难确定. 但是本文的拟合函数的方法仍能对 SPD 进行有效寻边,从而获得较为准确的地层横波慢度(三深度点的地层横波慢度由图 4b 中的箭头给出).

5 结论

为了解决随钻四极声波测量地层横波慢度中的

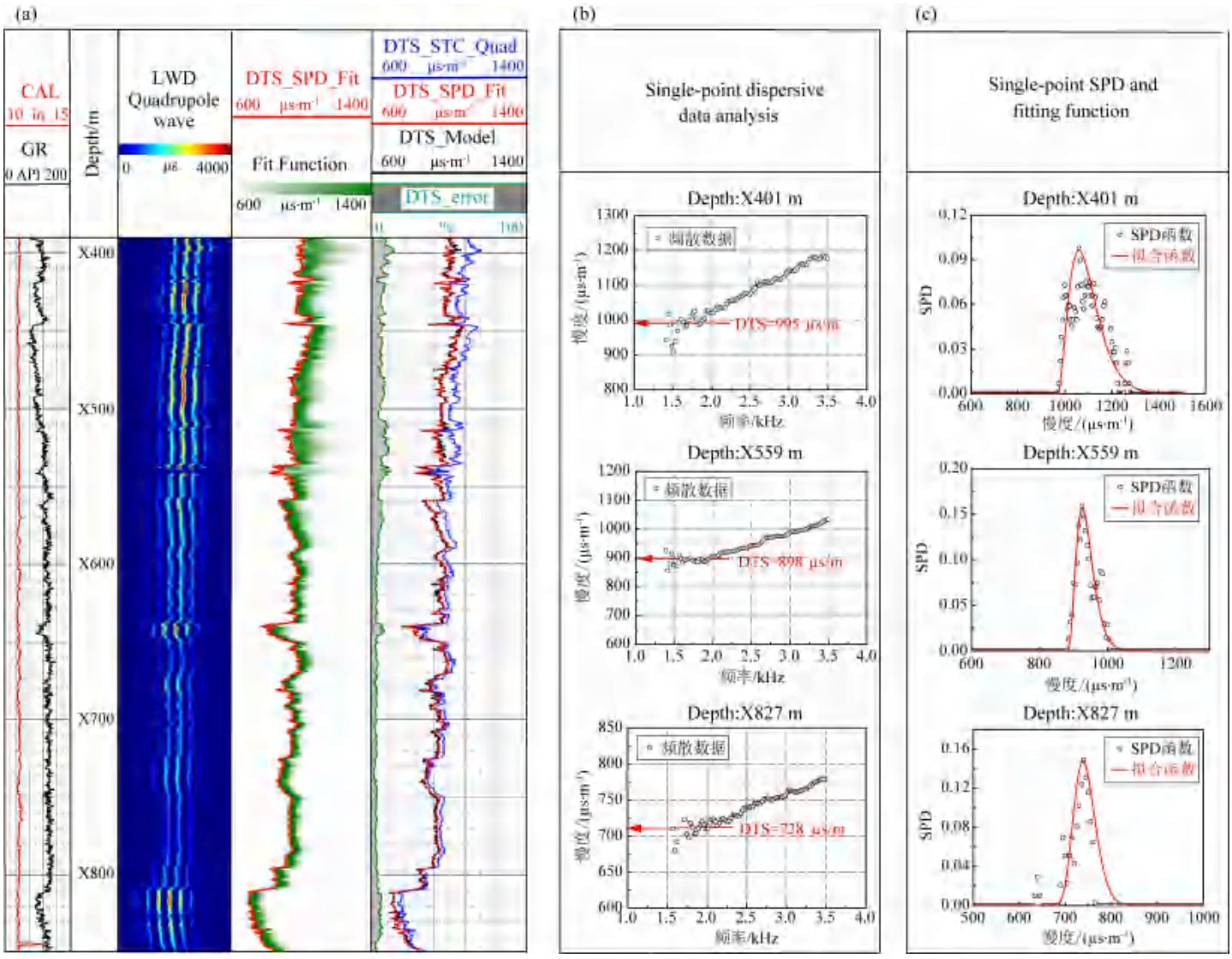


图 4　超慢地层随钻声波数据实例

Fig. 4　Example of LWD data processing for an unconsolidated slow formation

频散问题,本文采用了并实现了一种新的数据驱动的频散处理方法.该方法将四极子声波低频慢度的提取转化为波的慢度概率密度函数的寻边问题,并给出了一种曲线拟合的快速寻边方法.即首先利用慢度-频率相干法对四极子波波形数据进行处理获得其频散数据,通过该频散数据计算 SPD 函数,最后对该 SPD 函数进行寻边获得实际地层慢度.对实际随钻四极声波数据的处理结果表明,该方法可以准确提取地层横波慢度,且不需要复杂的理论模型计算,为随钻四极子横波测井提供了一种快速有效的处理方法.

References

Cao Z L, Wang K X, Xie R H, et al. 2005. A comparative study on application of three dispersion analysis to array sonic logs. *Chinese Journal of Geophysics* (in Chinese), 48(6): 1449-1459.

Dubinsky V, Tang X M, Bolshakov A, et al. 2003. Engineering aspects of LWD quadrupole measurements and field test results. // SPE Annual Technical Conference and Exhibition. Denver, Colorado: Society of Petroleum Engineers, doi: 10.2118/84248-MS.

Geerits T, Tang X M. 2003. Centroid phase slowness as a tool for dispersion correction of dipole acoustic logging data. *Geophysics*, 68(1): 101-107, doi: 10.1190/1.1543197.

Huang X J, Yin H Z. 2005. A data-driven approach to extract shear and compressional slowness from dispersive waveform data. //SEG Technical Program Expanded Abstracts 2005. Society of Exploration Geophysicists, 384-387.

Kimball C V, Marzetta T L. 1984. Semblance processing of borehole acoustic array data. *Geophysics*, 49(3): 274-281, doi: 10.1190/1.1441659.

Kimball C V. 1998. Shear slowness measurement by dispersive processing of the borehole flexural mode. *Geophysics*, 63(2): 337-344, doi: 10.1190/1.1444333.

Lee S Q, Tang X M, Su Y D, et al. 2016. Model-based dispersive processing of borehole dipole wave data using an equivalent-tool theory. *Geophysics*, 81(1): D35-D43, doi: 10.1190/geo2015-0210.1.

Liu Q H, Schoen E, Daube F, et al. 1996. A three-dimensional finite difference simulation of sonic logging. *Journal of the Acoustical Society of America*, 100(1): 72-79, doi: 10.1121/1.415869.

Su Y D, Sun J M, Fan Y R, et al. 2006. On Numerical study of the LWD multipole source propagation characteristics in slow formation. *Well Logging Technology* (in Chinese), 30(3): 205-207, doi: 10.3969/j.issn.1004-1338.2006.03.005.

Su Y D, Jiang C, Zhuang C X, et al. 2016. Joint inversion of logging-while-drilling multipole acoustic data to determine P- and S-wave velocities in unconsolidated slow formations. *Geophysics*, 81(5): D553-D560, doi: 10.1190/geo2016-0133.1.

Tang X M, Dubinsky V, Bolshakov A, et al. 2002. Shear-velocity measurement in the logging-while-drilling environment: Modeling and field evaluations. // Presented at the SPWLA 43rd Annual Logging Symposium. Oiso, Japan: Society of Petrophysicists and Well-Log Analysts.

Tang X M, Patterson D, Dubinsky V, et al. 2003. Logging-While-Drilling shear and compressional measurements in varying environments. // SPWLA 44th Annual Logging Symposium. Galveston, Texas: Society of Petrophysicists and Well-Log Analysts.

Tang X M, Dubinsky V, Patterson D J. 2006. Development of a low-frequency LWD quadrupole shear-wave technology to improve quality of formation shear velocity measurement. // Presented at the SPE Annual Technical Conference and Exhibition. San Antonio, Texas, USA: SPE.

Tang X M, Li C, Patterson D J. 2010. A curve-fitting technique for determining dispersion characteristics of guided elastic waves. *Geophysics*, 75(3): E153-E160, doi: 10.1190/1.3420736.

Wang T, Tang X M. 2003. Finite-difference modeling of elastic wave propagation: A nonsplitting perfectly matched layer approach. *Geophysics*, 68(5): 1749-1755, doi: 10.1190/1.1620648.

Zhang Z X, Mochida M, Kubota M, et al. 2010. Shear slowness estimation by inversion of LWD borehole quadrupole mode. // 80th Annual International Meeting, SEG, Expanded Abstracts. SEG: 528-532.

附中文参考文献

埃伯哈德·蔡德勒等. 2012. 数学指南: 实用数学手册. 李文林译. 北京. 科学出版社.

曹正良, 王克协, 谢荣华等. 2005. 三种阵列声波测井数据频散分析方法的应用与比较. 地球物理学报, 48(6): 1449-1459.

唐晓明, 郑传汉. 2004. 定量测井声学. 赵晓敏译. 北京: 石油工业出版社.

苏远大, 孙建孟, 范宜仁等. 2006. 基于软地层随钻多极子声源传播特性的数值研究. 测井技术, 30(3): 205-207, doi: 10.3969/j.issn.1004-1338.2006.03.005.

(本文编辑 胡素芳)

GEOPHYSICS, VOL. 78, NO. 6 (NOVEMBER-DECEMBER 2013); P. D491–D498, 11 FIGS., 2 TABLES.
10.1190/GEO2013-0136.1

Mapping formation shear-velocity variation by inverting logging-while-drilling quadrupole-wave dispersion data

Yuan-Da Su[1], Xiao-Ming Tang[1], Chun-Xi Zhuang[1], Song Xu[1], and Long Zhao[1]

ABSTRACT

The logging-while-drilling (LWD) quadrupole wave is a dispersive wave mode guided along the borehole with a drill collar. The wave is sensitive to the formation alteration caused by drilling. We inverted LWD quadrupole-wave dispersion data to estimate a radial shear-velocity profile away from the wellbore. We also explored the nonuniqueness of the inverse problem and solved it by using a constrained inversion method. This was done by constraining the high-frequency portion of the model dispersion curve with another curve calculated using the near-borehole velocity. The constraint condition is based on the physical principle that a high-frequency LWD quadrupole wave has a shallow penetration depth and is therefore sensitive to the near-borehole shear velocity. Particularly, we found that a monotonically continuous velocity profile can be well approximated using a one-zone equivalent model, allowing for a drastic simplification of the inversion process. We used theoretical modeling and real data examples to validate the method for the LWD wave data. The quadrupole dispersion data and the inversion results clearly demonstrated that formation alteration can occur even while the well is being drilled.

INTRODUCTION

Logging-while-drilling (LWD) quadrupole shear-wave logging was developed for measuring shear velocity in the LWD environment (Tang et al., 2003; Kinoshita et al., 2010). However, the formation property near the borehole is often altered by instant mechanical damage due to drilling even while the well is being drilled. Su et al. (2011) demonstrate the drilling-induced alteration from LWD leaky-compressional-wave data. This study aims at obtaining the radial velocity changes from LWD quadrupole-wave data. It has long been recognized that the radial velocity changes affect the dispersion characteristics of guided waves propagating along the borehole (Tang and Patterson, 2010). Methodologies have also been developed to identify the radial alteration from the wireline dipole wave dispersion characteristics and to determine the radial velocity profile (Burridge and Sinha, 1996; Tang, 1996; Sinha et al., 2005; Tang and Patterson, 2010; Yang et al., 2012). However, the inversion of the radial velocity profile is a challenging problem due to the nonuniqueness of the inverse problem. Moreover, to the authors' knowledge, using LWD quadrupole-wave data for the velocity-profile inversion has not yet been reported, for which the nonuniqueness problem also needs to be analyzed and solved.

One way to solve the nonuniqueness problem is to apply a priori information to constrain the model solution of the dispersion data inversion problem. From a family of solutions that fit the dispersion data, the constraint information singles out one solution that not only fits the data but also satisfies the constraint condition. Tang and Patterson (2010) derive the constraint information from analyzing the high-frequency asymptotic characteristics of borehole flexural waves and develop a constrained inversion method for the wireline-dipole-logging data. For the LWD quadrupole-wave data, however, it remains to be seen that such constraint information can still be used in the LWD condition, where the guided wave dispersion characteristics are significantly affected by the drill collar, which occupies a large portion of the borehole.

We also demonstrate an improvement on the efficiency of the inversion method. This improvement, based on the observation that the dispersion characteristics from a monotonic, continuous shear-velocity profile, can be equivalently modeled using a two-layer velocity model with appropriate model parameters. Consequently, using the two-layer model in the inversion greatly simplifies the theoretical dispersion calculation and speeds up the inversion process.

In the following, we first analyze the quadrupole-wave dispersion characteristics and develop an appropriate constraint for the

Manuscript received by the Editor 3 April 2013; revised manuscript received 5 June 2013; published online 9 October 2013.
[1]China University of Petroleum, School of Geosciences, Qingdao, China. E-mail: syuanda@sina.com; tangxiam@yahoo.cn; zhuangchunxi@sina.com; xusongupc@sina.com; zhaolong88610@126.com.
© 2013 Society of Exploration Geophysicists. All rights reserved.

inversion. We also demonstrate the equivalence between a monotonic, continuous velocity profile and the two-layer model for the inversion. We then apply the inversion method to the field LWD quadrupole dispersion data.

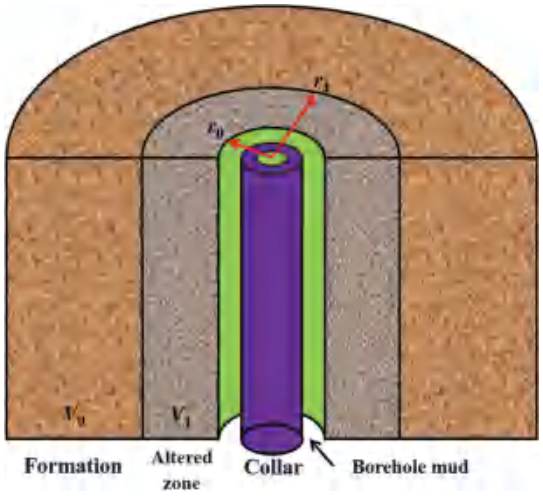


Figure 1. A one-zone alteration model for calculating LWD quadrupole-wave propagation.

Table 1. Parameter values for calculating the alteration model of Figure 1.

	V_P (m/s)	V_S (m/s)	Density (kg/m^3)	Inner radius (m)	Outer radius (m)
Collar	5860	3130	7850	0.27	0.89
Borehole fluid	1500	—	1000	0	0.1
Altered zone	4500	2000	2500	0.1	0.2
Formation	4500	2300	2500	0.2	∞

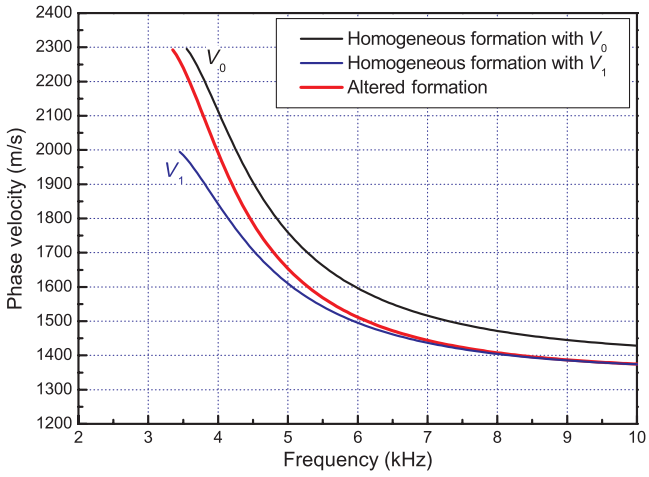


Figure 2. LWD quadrupole-wave dispersion with (red curve) and without (black curve labeled V_0) formation alteration. A homogeneous formation dispersion curve calculated using altered-zone velocity V_1 is also shown (blue curve labeled V_1).

SENSITIVITY ANALYSIS AND CONSTRAINED INVERSION OF LWD QUADRUPOLE DISPERSION DATA

The LWD quadrupole wave is a dispersive wave mode guided along the borehole with a drill collar. In general, the wave-dispersion characteristics are governed by the dispersion equation (Tang et al., 2002),

$$D(k;\omega;B;F(r)) = 0; \tag{1}$$

where k is the wavenumber, ω is the angular frequency, B refers to the borehole portion of the waveguide consisting of borehole fluid and the drill collar, and $F(r)$ refers to an elastic, isotropic formation whose properties (i.e., P- and S-wave velocities and density) can vary with radial distance r. A continuously varying radial profile can be approximated as a multilayered cylindrical structure with staircase variations. For the multilayered structure, the dispersion equation is solved using the Thomson-Haskell propagation matrix method (Schmitt, 1988; Tang and Cheng, 2004). The detailed mathematical expression for the dispersion equation is given in Appendix A.

Solving the dispersion equation for each frequency, we find the wavenumber k for the LWD quadrupole-wave mode, from which the wave phase velocity or slowness (inverse of velocity) is obtained as

$$V(\omega) = \omega/k: \tag{2}$$

Using the above approach, we can calculate the theoretical dispersion curve of the LWD quadrupole wave for various alteration conditions.

We use the simple altered formation model in Figure 1 to analyze LWD quadrupole-wave dispersion characteristics associated with alteration. The model parameters are listed in Table 1. In this simple two-layer model, a cylindrical alteration zone of 0.1-m thickness is placed between a fluid-filled borehole of radius $r_0 = 0.1$ m and the virgin formation, with the altered and virgin formation shear velocities being $V_1 = 2000$ m/s and $V_0 = 2300$ m/s, respectively. An LWD drill collar modeled as a steel pipe is centered at the borehole. Figure 2 shows the quadrupole-wave phase-velocity dispersion curve (red curve). For comparison, we also plot the dispersion curves of a homogeneous formation calculated with V_0 (black curve) and V_1 (blue curve), respectively. At the low-frequency portion of the (red) curve near the cutoff frequency, the wave's velocity reaches the virgin formation shear velocity V_0. As the frequency increases, the wavelength shortens and the wave's sensing volume diminishes to the near-borehole region, such that the wave's velocity is most sensitive to the altered zone velocity V_1.

The sensitivity analysis (Tang and Cheng [2004]; see also the wireline dipole example of Tang and Patterson [2010]) result of Figure 3 further demonstrates how the alteration-zone thickness affects the dispersion characteristics in the low- to medium-frequency range. For comparison, we also calculate the sensitivities of V_0 (black dashed curve) and V_1 (red dashed curve) for the homogeneous formation scenario. The sensitivity to the virgin velocity V_0 (black solid curve) approaches unity toward the cutoff, which shows that the low-frequency quadrupole wave with a deep penetration depth is mostly controlled by the virgin formation property.

As the frequency increases, the sensitivity diminishes and gives way to the sensitivity of V_1. The latter sensitivity increases from the cutoff frequency and approaches its homogeneous formation counterpart toward high frequencies. This means that, with decreasing wavelength at higher frequencies, the wave's sensitivity is mostly controlled by the altered zone property.

Comparing the sensitivity curves of V_1 and r_1 reveals the root cause of nonuniqueness in the inversion of the altered zone parameters from dispersion data. Starting from small values near the cutoff frequency, the two sensitivity curves respectively reach a peak and trough as the frequency increases. In this frequency range with high-magnitude sensitivities, the two sensitivity curves are anticorrelated, indicating that the change of dispersion by increasing the degree of alteration could be offset by reducing the alteration zone thickness. Still using the simple two-layer alteration model, we investigate a constrained inversion analysis to solve the nonuniqueness problem.

The inversion consists of minimizing the following objective function, constructed as the rms misfit error between model dispersion curve V_m and given dispersion data V_d and a constraint term:

$$E(\Delta V;\Delta r) = \sum_{\Omega}[V_m(\Delta V;\Delta r;\omega) - V_d(\omega)]^2 + \lambda\sum_{\Omega'}[V_m(\Delta V;\Delta r;\omega) - V_h(V_1;\omega)]^2; \quad (3)$$

where Δr and ΔV are, respectively, the thickness and velocity change of the altered zone; the misfit error is summed over the frequency range Ω where the dispersion data is given; the model dispersion curve V_m is calculated using equation 2 by solving equation 1; and the second term is a constraint to be described later. We first study the inversion without the constraint by setting $\lambda = 0$.

Figure 4 shows the variable-density (VD) display of the unconstrained $E(\Delta r;\Delta V)(\lambda = 0)$ for the 2D domain of Δr and ΔV. The theoretical (red) curve for the altered formation in Figure 2, for which the frequency range Ω is 3.5–10 kHz, is used as the dispersion data V_d for the calculation. A striking feature is that the objective function shows a long valley that crosses the solution point. Using any $(\Delta r;\Delta V)$ pair along the valley to fit the dispersion curve in Figure 2 will produce a good fit. The display in Figure 4 demonstrates the nonuniqueness of the radial parameter inversion problem. The valley trajectory again shows the anticorrelation of the $(\Delta r;\Delta V)$ parameters. That is, the change of dispersion characteristics could be produced either by a larger altered zone with a smaller velocity change or by a smaller altered zone with a larger velocity change.

We show how the constraint term in equation 3 can solve the nonuniqueness problem. We notice that the altered zone dispersion curve (Figure 2) and its corresponding sensitivity (red solid curve labeled V_1 in Figure 3) asymptotically approach their respective homogeneous formation counterparts computed using the near-wall shear velocity V_1. We use this high-frequency wave characteristic to develop a constraint condition. In the inversion process, we compute not only the altered formation dispersion curve V_m, but also a homogeneous formation dispersion curve V_h computed using the near-wall velocity V_1. The constraint condition is set by matching the high-frequency portion of both curves. This gives the second term in equation 3. The high-frequency range Ω' can be higher than Ω or a high-frequency portion of Ω. The multiplier λ, called the penalty coefficient, acts as a weighting factor for the constraint term such that this term in equation 3 has a significant contribution to the objective function. Under this condition, stable inversion result can be obtained. In practice, λ is chosen according to the size of Ω' relative to Ω.

We now demonstrate the effect of the constraint on the inversion. The constrained objective function in equation 3, for the simple model in Figure 1, is computed in the same way as for the unconstrained case. In computing the constraint term, Ω' is set to 8–10 kHz and $\lambda = 2$. Figure 5 displays the VD image of the new objective function. A dramatic effect to notice is that the long value in the unconstrained objective function is now replaced by a well-defined minimum in the vicinity of the true solution point. This minimum

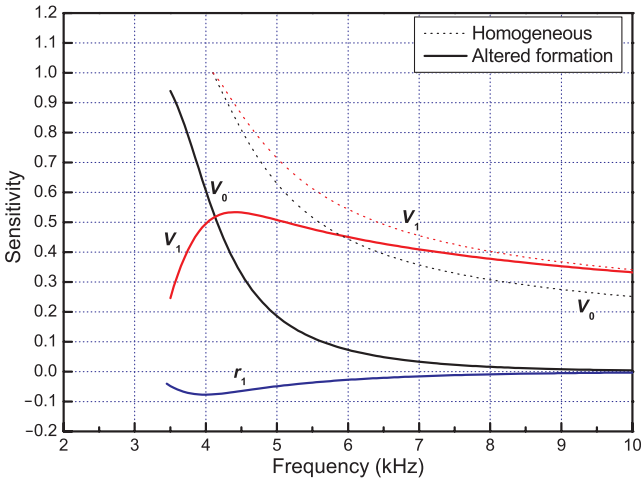


Figure 3. Sensitivity analysis for the alteration model of Figure 1. For comparison, the sensitivity for a homogeneous formation is also calculated for the virgin formation and altered-zone velocity (dashed curves). Curves V_0 and V_1 are, respectively, the sensitivity curves for the virgin and altered formations. Curve r_1 is the sensitivity curve for the outer radius of the altered zone.

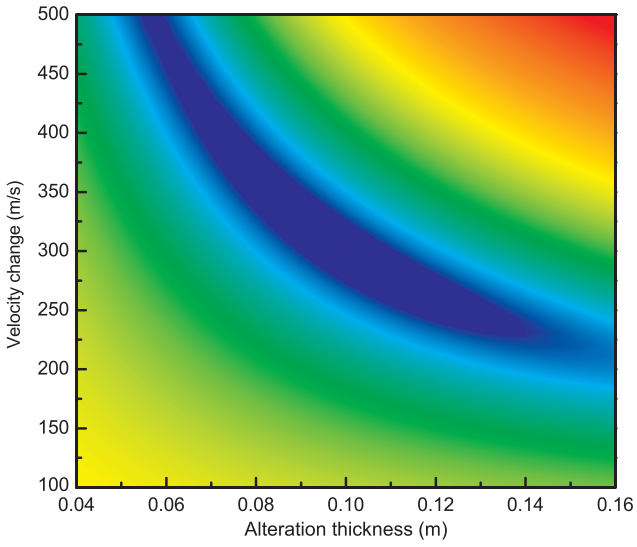


Figure 4. VD display of objective function versus velocity alteration and altered-zone thickness. The long valley trend shows there is no unique solution for the inversion.

gives a unique solution for the inversion. Locating this minimum using a minimization algorithm (e.g., downhill simplex, Levenberg-Marquardt; Press et al., 1989) gives $\Delta V = 280$ m/s and $\Delta r = 0.108$ m. The estimated parameter values are about 8% different from their true values. Considering data error and other uncertainties in field data applications, the constraint scheme and the inversion result are quite satisfactory. This example shows that the constraint given in equation 3 can effectively suppress the nonuniqueness of the inversion.

INVERTING A CONTINUOUS PROFILE USING THE ONE-ZONE ALTERATION MODEL

The constrained inversion scheme for the one-zone alteration model (see Figure 1), as given in equation 3, can be extended to a monotonically continuous shear-velocity variation profile. After drilling through an earth formation, the radial property change near a borehole is most likely to occur close to the borehole wall, as is the case for a stress-induced alteration, drilling damage, or fluid invading the formation, etc. It is also reasonable to assume that the property change is monotonic, increasing or decreasing away from the borehole. For this situation, a simple analytical model is proposed (Tang and Patterson, 2010) to model the radial S-velocity profile:

$$V(r) = V_0 - \left(\frac{\overline{\Delta V}}{1 - e^{-1}}\right) \cdot \exp\left(-\frac{r - r_0}{\Delta r}\right); \quad (r \geq r_0); \tag{4}$$

where r_0 is the borehole radius and V_0 is the virgin formation velocity in the far borehole region and $\overline{\Delta V}$ is the average velocity change within an "equivalent" alteration zone of thickness $\Delta r = r_1 - r_0$. In the equivalent alteration zone, we use the average velocity $\overline{V}_1 = V_0 - \overline{\Delta V}$ to compute the homogeneous formation dispersion curve for the constraint term in equation 3 because this velocity is the average of the volume sensed by the high-frequency wave. We do not use $V_1 = V(r_0)$ because this is the velocity value at the borehole wall, which is not representative of the volume. Note the varying velocity model (equation 4) applies only to the S-velocity. The P-velocity is treated as constant in the inversion because the quadrupole wave is most sensitive to the S-velocity.

We now describe why the inversion of the continuous profile of equation 4 can be treated as the inversion for the one-zone alteration model. A well-known principle for dealing with nonuniqueness in geophysical inverse problems, such as the present radial profile inversion problem, is that one can find linear averages of the unknown profile over a depth range, although it is infeasible to simultaneously determine both the radial location and precise value of the profile. In fact, this is also the principle for the Backus-Gilbert (1970) inversion that Burridge and Sinha (1996) use. Indeed, integrating or averaging, the varying part of the profile (second term of equation 4) from r_0 to ∞ results in

$$\left(\frac{\overline{\Delta V}}{1 - e^{-1}}\right) \cdot \Delta r = (V_0 - V_1) \cdot \Delta r = \Delta V \cdot \Delta r; \tag{5}$$

where $V_1 = V(r_0)$. In terms of the one-zone alteration model, this is the product of the velocity change from borehole to virgin formation and zone thickness. Thus, in the averaging sense, the continuous profile of equation 4 is equivalent to the one-zone alteration model, with ΔV and Δr being, respectively, the overall velocity change and size of the equivalent alteration zone, as obtained from averaging the velocity profile. According to the above-stated inversion principle, these averaged properties can be resolved from the inversion. Applying this equivalence to the dispersion data from a continuous profile, we need only to invert two parameters $\overline{\Delta V}$ (or ΔV) and Δr using equation 3. With the known $\overline{\Delta V}$ and Δr from inversion, a continuous profile can be reconstructed from equation 4. This inversion scheme avoids iteratively solving equation 1 for a continuous velocity profile and greatly speeds up the inversion. We use a numerical example to demonstrate this inversion scheme and verify its accuracy.

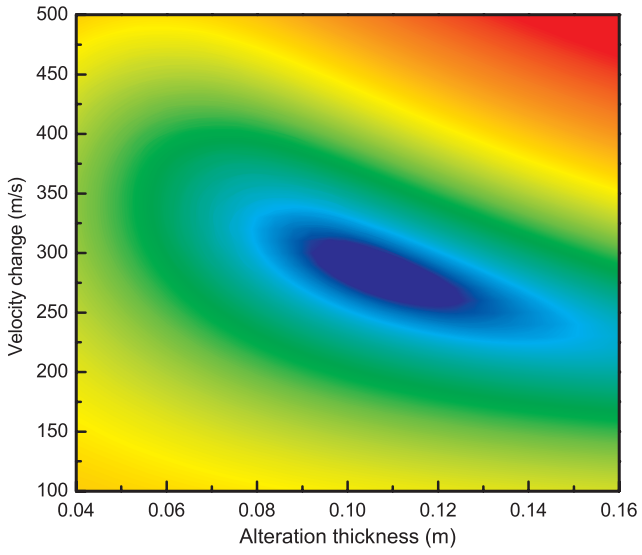


Figure 5. VD display of constrained objective function versus velocity alteration and altered-zone thickness. The well-defined minimum shows that a unique solution is found after constraining the model dispersion curve.

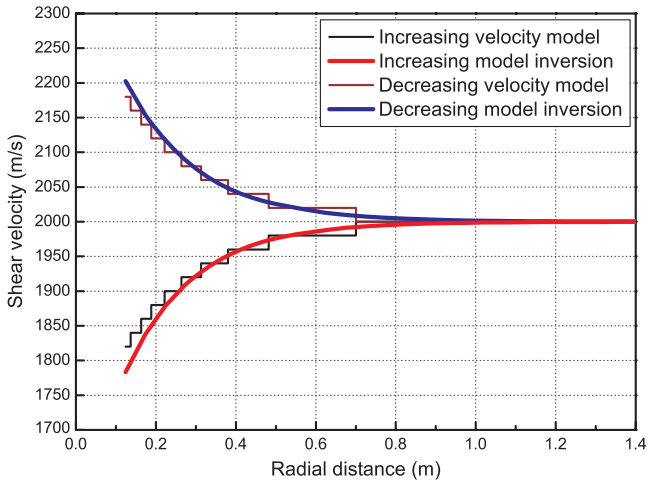


Figure 6. Approximating a continuous radial profile using layered structures with staircase variations, with velocity decreasing (upper curves) or increasing (lower curves) away from the borehole. Continuous curves (red and blue) are the radial profile reconstructed from inversion.

Using equation 4, we calculate two continuous profiles, one with $\overline{\Delta V} = 126$ m/s, increasing from the borehole, and the other with $\overline{\Delta V} = -126$ m/s, decreasing from the borehole, both with $V_0 = 2000$ m/s and $\Delta r = 0.2$ m. We then approximate the profiles using a multilayered cylindrical structure with staircase variations, smaller steps near the borehole and larger steps away from the borehole, as shown in Figure 6. The detailed structure parameter values are given in Table 2. The dispersion data are then calculated by solving equation 1 for the layered structure. Other parameters, such as drill collar and borehole fluid, etc., are the same as those used in the previous examples. For simplicity, we only show the results for the case of decreasing velocity from the borehole in the following.

Table 2. Parameter values for modeling a continuous radial profile in formation.

Layer	Increasing		Decreasing		Density (kg/m^3)	Inner radius (m)	Outer radius (m)
	V_P (m/s)	V_S (m/s)	V_P (m/s)	V_S (m/s)			
1	3258	1820	3942	2180	2500	0.1240	0.1370
2	3296	1840	3904	2160	2500	0.1370	0.1630
3	3334	1860	3866	2140	2500	0.1630	0.1885
4	3372	1880	3828	2120	2500	0.1885	0.2220
5	3410	1900	3790	2100	2500	0.2220	0.2640
6	3448	1920	3752	2080	2500	0.2640	0.3130
7	3486	1940	3714	2060	2500	0.3130	0.3800
8	3524	1960	3676	2040	2500	0.3800	0.4820
9	3562	1980	3638	2020	2500	0.4820	0.7000
Formation	3600	2000	3600	2000	2500	0.7000	∞

Parameters for two profiles are listed: one with the velocity increasing, and the other with the velocity decreasing, away from borehole.

The calculated dispersion data are shown in Figure 7 (markers), which is significantly above the dispersion curve (black curve) for the homogeneous formation with virgin formation parameters, indicating the effects of alteration. Using the dispersion data and the one-zone alteration model to calculate the objective function (equation 3) for the constrained inversion, the resulting function, plotted a VD display for the 2D domain of Δr and $\overline{\Delta V}$ in Figure 8, shows a well-defined minimum at $\overline{\Delta V} = 128$ m/s, $\Delta r = 0.183$ m. The theoretical dispersion curve calculated with these parameters and the one-zone model fits the data very well (red curve in Figure 7). (Although the P-velocity is varied in the profile modeling, the good inversion result with a constant virgin formation P-velocity validates this approximation.) Furthermore, using these values to calculate the profile of equation 4 gives the inverted profile in Figure 6 (blue curve), which fits the original profile (staircases) very well. For the case of increasing velocity from borehole, applying a similar procedure gives the inverted profile (red curve), which fits the original profile quite well. This numerical example therefore supports the use of the one-zone alteration model to invert a monotonically varying velocity profile.

FIELD DATA APPLICATION

The above-described inversion method has been applied to processing LWD quadrupole-wave data to assess the drilling-induced formation alteration. We use a data application example to demonstrate the results of the above inversion method. The results are shown in Figure 9 for

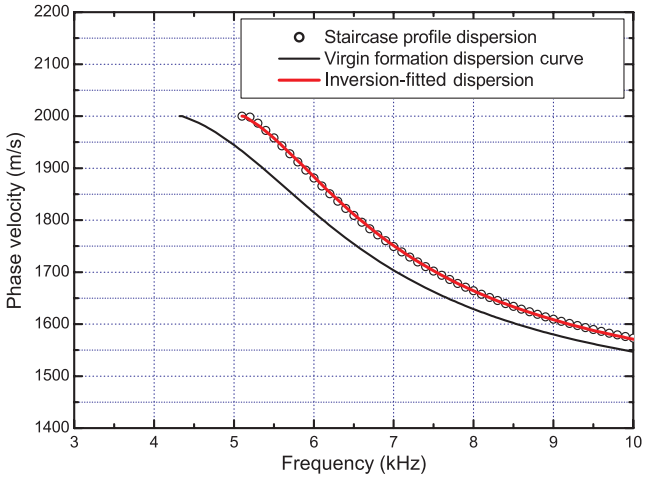


Figure 7. Theoretical LWD quadrupole-wave dispersion data (markers) calculated from the decreasing staircase profile model of Figure 6. Lower black curve is the dispersion for a homogeneous virgin formation. The red dispersion curve overlain with the data is the inversion-fitted dispersion from the one-zone alteration model.

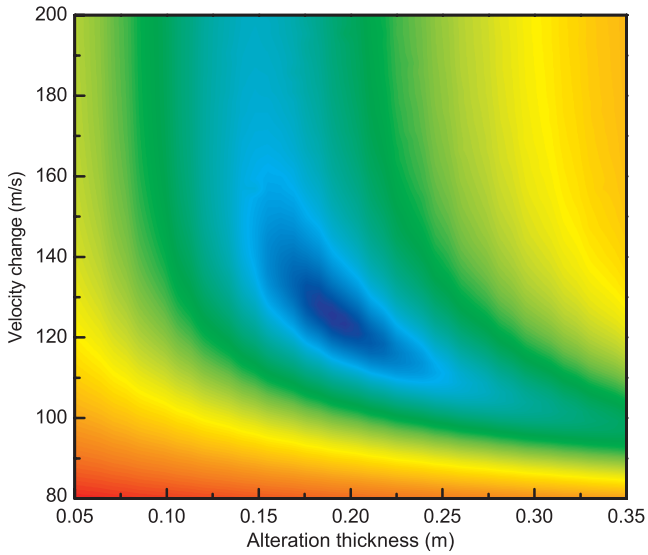


Figure 8. VD display of the constrained objective function versus velocity alteration and altered-zone thickness. The objective function is computed using the dispersion data of the continuous profile and the one-zone alteration model. The well-defined minimum finds a unique solution for the average velocity and size of the alteration zone.

an 80-m depth interval across a fast formation. The gamma ray and caliper log curves are shown in track 1. The borehole of about 6-in diameter was drilled with water-based mud. The monopole and quadrupole acoustic waveform data (VD images) are displayed in tracks 2 and 3, respectively. The data were respectively processed to give the compressional (DTP) and shear (DTS) slowness curves in track 4.

The quadrupole-wave data are inverted to estimate the shear-wave-velocity radial profile. As an example, Figure 10 shows the LWD quadrupole-wave dispersion data (markers in Figure 10b) obtained from processing the array LWD waveform data (Figure 10a) for an unaltered formation at 4130 m. The dispersion data can be well fit by the theoretical dispersion curve (solid curve) computed for a homogeneous formation, and the formation is therefore interpreted as having no radial variation. In contrast, Figure 11 shows the dispersion data (markers in Figure 11b) obtained from processing the array LWD waveform data (Figure 11a) for an altered formation at 4124 m. The alteration is indicated by the excessive dispersion shown in the data (markers) relative to the homogeneous formation dispersion curve (black solid curve). Because the quadrupole-wave amplitude diminishes toward the cutoff frequency (e.g., Tang et al., 2002), the low-frequency ends of the data points are scattered. However, the theoretical dispersion curve can always be calculated for a given virgin formation velocity. For an LWD tool with about a 3-m source-receiver offset, the waves penetrate deep into the formation and the measured velocity (slowness) curves (panel 4 of Figure 9, where DTP and DTS respectively denote P- and S-wave slowness log curves) correspond to the virgin formation velocity (as indicated by an arrow in Figure 11), providing a control for the inversion. After the inversion, the data are fit by the dispersion curve (red solid curve) computed for an altered formation. The shear-wave radial profile used to compute the dispersion curve is taken as the formation shear-velocity profile at that depth.

The inverted shear-wave velocity variation profile image is displayed in an axis-symmetric manner with borehole in the center (track 5). The radial distance of the profile is 1 m. The profile image shows interesting variations. The scale of the color scheme is from −15% (blue) to 15% (red). Significant radial variations can be observed from 4122 to 4128 m. In fact, the dispersion data shown in Figure 11 are from this interval. Besides, several intervals show moderate radial variations, whereas the rest of the formation interval is quite homogeneous. The validity of the velocity profile is analyzed below.

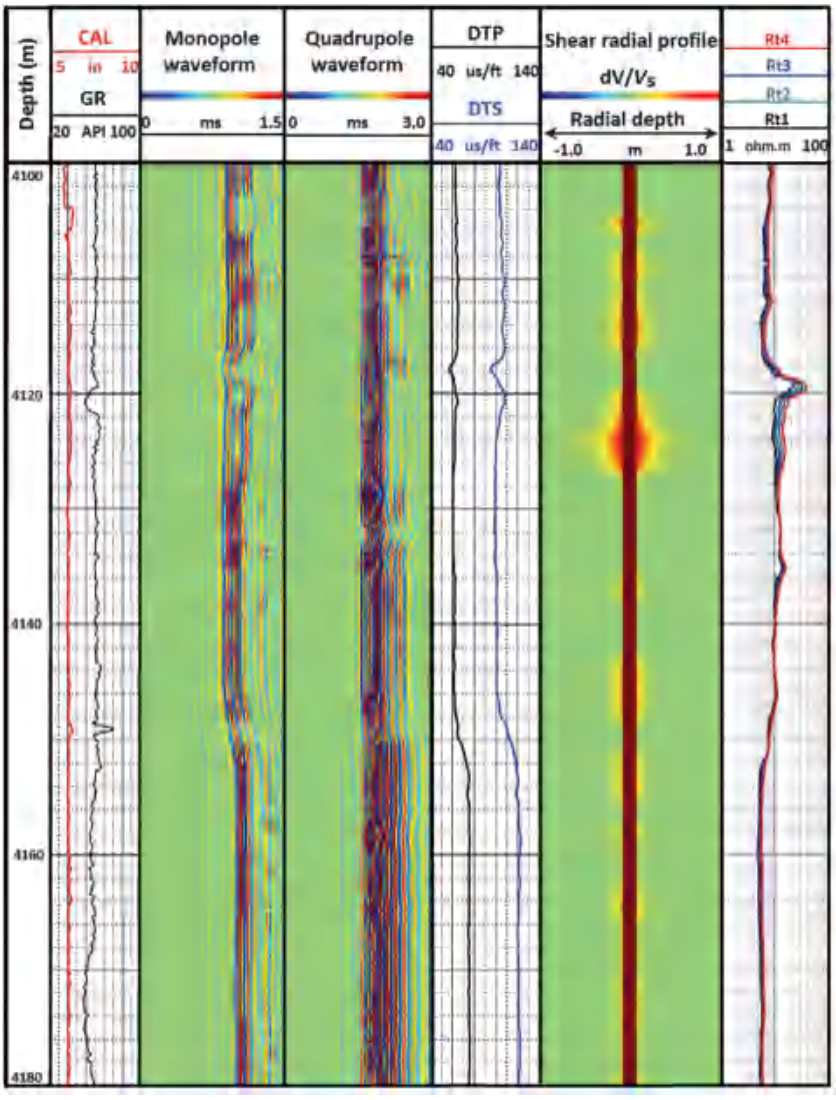


Figure 9. Radial S-velocity variation inversion using LWD quadrupole-wave data (track 3). The radial variation image (track 5) is compared with the shallow-to-deep resistivity log curves in track 6.

The radial profile variations are compared with the available resistivity log data obtained from LWD resistivity logging across the depth interval. Shown in track 6 are the resistivity log curves from shallow (black curve) to deep (red curve), plotted on a logarithmic scale from 0.1 to 100 ohm-m. The shallow and deep resistivity curves show clear differences for the intervals with significant radial variations, with the deep resistivity higher than the shallow resistivity. Because this is a very tight formation, the formation permeability is quite low. However, if the formation is mechanically altered by drilling to instantly generate some microcracks/fissures, the near-borehole formation may become permeable and borehole-fluid invasion into the permeable formation can occur. With the fluid invasion, the shallow resistivity curve, which is sensitive to the near-borehole formation, will show a lower resistivity value due to the invaded low-resistivity borehole fluid (water-based mud) relative to the deep resistivity curve, which is sensitive to the virgin formation. With the above elaboration, one can understand why the radial alteration is correlated with the shallow and deep resistivity separation, while the absence of the separation correlates to an unaltered homogeneous formation. The comparison with the resistivity data thus suggests that the quadrupole-wave inverted radial profile is valid.

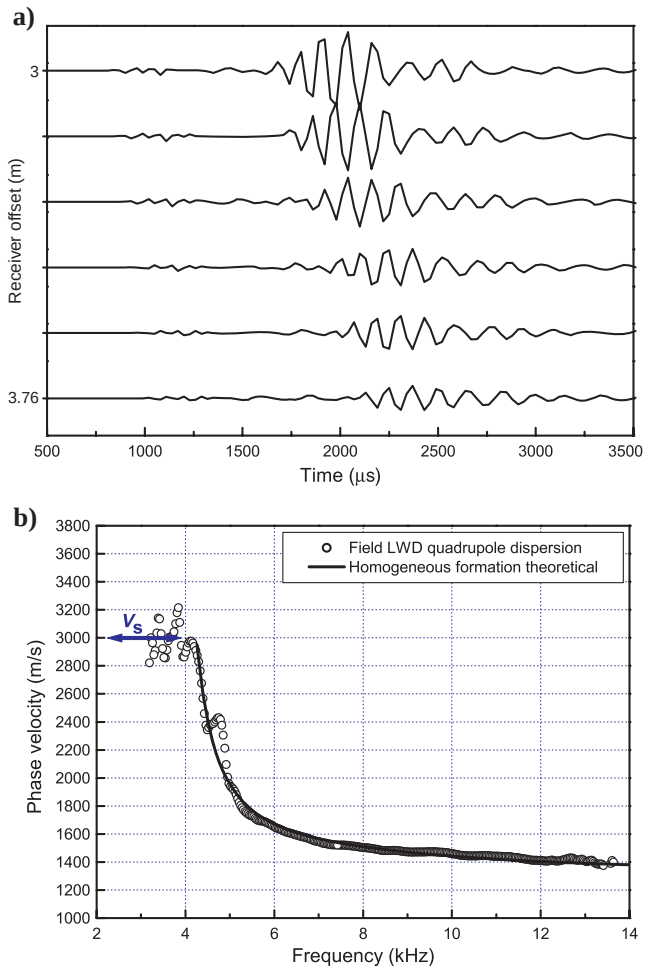


Figure 10. (a) Array quadrupole-wave data and (b) the waveform-processed dispersion data (markers in lower figure). The dispersion data can be fit with a theoretical curve calculated for a homogeneous formation. The arrow indicates formation shear velocity.

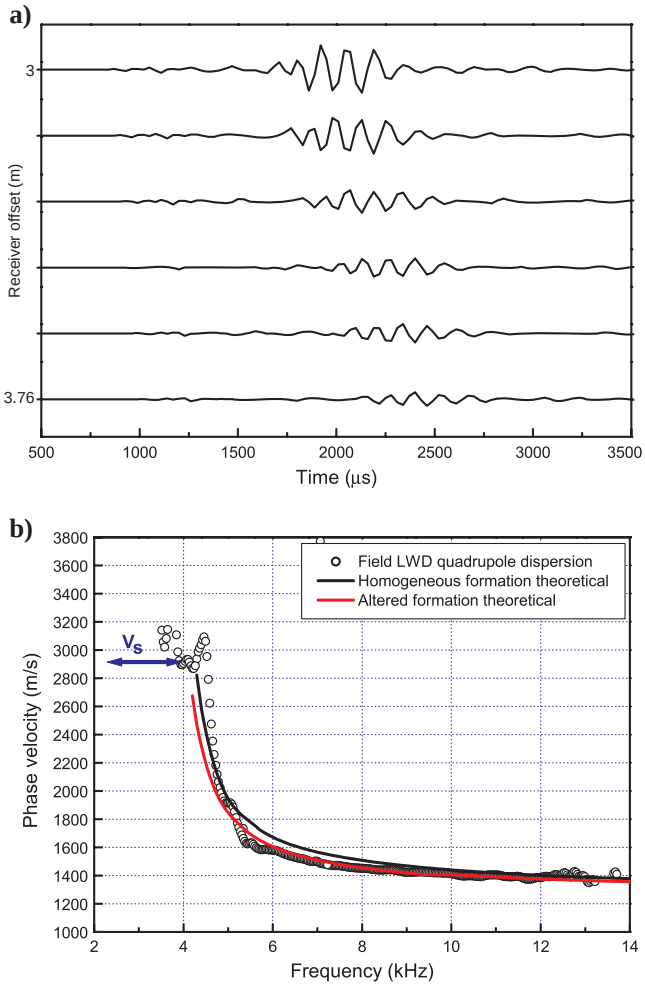


Figure 11. (a) Array quadrupole-wave data and (b) the waveform-processed dispersion data (markers). The dispersion data can be fit by the dispersion curve (red) for an altered formation. The dispersion curve calculated for a homogeneous formation is also plotted (black). The arrow indicates virgin formation shear velocity.

CONCLUSIONS

We have shown that it is possible to invert a S-velocity radial profile from LWD quadrupole-wave dispersion data. We have demonstrated that the nonuniqueness of the inversion can be suppressed using the constrained inversion method. This is done by constraining the high-frequency portion of the model dispersion curve with another curve calculated using the near-borehole velocity. Further, we have demonstrated that a monotonically continuous velocity profile can be inverted using an equivalent one-zone alteration model to find the average velocity variation and size of the alteration zone, from which the continuous profile can be reconstructed. The inversion has been applied successfully to process field LWD quadrupole-wave data with reasonably good results, providing an important application for the LWD quadrupole-wave technology.

ACKNOWLEDGMENTS

This study is supported by the National Natural Science Foundation of China (no. 41204070).

APPENDIX A

DETAILS OF DISPERSION EQUATION 1

The dispersion equation 1 for an altered formation surrounding a borehole occupied by a fluid and a drill collar can be expressed as the determinant of a 12 × 12 matrix H:

$$D(k;\omega;B;F(r)) = \begin{vmatrix} H_{1;1} & H_{1;2} & \cdots & H_{1;12} \\ H_{2;1} & H_{2;2} & \cdots & H_{2;12} \\ \vdots & \vdots & \ddots & \vdots \\ H_{12;1} & H_{12;2} & \cdots & H_{12;12} \end{vmatrix} = 0: \quad \text{(A-1)}$$

The method for deriving the dispersion equation and the H matrix can be found in Tang and Cheng (2004). The elements of the matrix H are given as follows:

$$H_{1;1} = -fX_1(fr_a);\ H_{1;2} = p_1X_1(p_1r_a);\ H_{1;3} = p_1Y_1(p_1r_a);$$
$$H_{1;4} = \frac{n}{r_a}I_n(s_1r_a); H_{1;5} = \frac{n}{r_a}K_n(s_1r_a);\ H_{1;6} = iks_1X_1(s_1r_a);$$
$$H_{1;7} = iks_1Y_1(s_1r_a);\ H_{2;1} = \rho_f\omega^2 I_n(fr_a);$$
$$H_{2;2} = \mu^t\left[(k^2+s_1^2)I_n(p_1r_a) + \frac{2p_1}{r_a}X_2(p_1r_a)\right];$$
$$H_{2;3} = \mu^t\left[(k^2+s_1^2)K_n(p_1r_a) + \frac{2p_1}{r_a}Y_2(p_1r_a)\right]; H_{2;4} = -\frac{2\mu^t n s_1}{r_a}X_3(s_1r_a);$$
$$H_{2;5} = -\frac{2\mu^t n s_1}{r_a}Y_3(s_1r_a);\ H_{2;6} = 2ik\mu^t s_1[s_1I_n(s_1r_a) + \frac{1}{r_a}X_2(s_1r_a)];$$
$$H_{2;7} = 2ik\mu^t s_1[s_1K_n(s_1r_a) + \frac{1}{r_a}Y_2(s_1r_a)];\ H_{3;2} = \frac{2np_1}{r_a}X_3(p_1r_a);$$
$$H_{3;3} = \frac{2np_1}{r_a}Y_3(p_1r_a); H_{3;4} = -s_1^2X_4(s_1r_a);\ H_{3;5} = -s_1^2Y_4(s_1r_a);$$
$$H_{3;6} = \frac{2ikns_1}{r_a}X_3(s_1r_a);\ H_{3;7} = \frac{2ikns_1}{r_a}Y_3(s_1r_a); H_{4;2} = 2ikp_1X_1(p_1r_a);$$
$$H_{4;3} = 2ikp_1Y_1(p_1r_a);\ H_{4;4} = \frac{ikn}{r_a}I_n(s_1r_a);\ H_{4;5} = \frac{ikn}{r_a}K_n(s_1r_a);$$
$$H_{4;6} = -(k^2+s_1^2)s_1X_1(s_1r_a);\ H_{4;7} = -(k^2+s_1^2)s_1Y_1(s_1r_a);$$
$$H_{5;2} = p_1X_1(p_1r_b); H_{5;3} = p_1Y_1(p_1r_b);\ H_{5;4} = \frac{n}{r_b}I_n(s_1r_b);$$
$$H_{5;5} = \frac{n}{r_b}K_n(s_1r_b);\ H_{5;6} = iks_1X_1(s_1r_b); H_{5;7} = iks_1Y_1(s_1r_b);$$
$$H_{5;8} = -fX_1(fr_b);\ H_{5;9} = -fY_1(fr_b);$$
$$H_{6;2} = \mu^t[(k^2+s_1^2)I_n(p_1r_b) + \frac{2p_1}{r_b}X_2(p_1r_b)];$$
$$H_{6;3} = \mu^t[(k^2+s_1^2)K_n(p_1r_b) + \frac{2p_1}{r_b}Y_2(p_1r_b)]; H_{6;4} = -\frac{2\mu^t n s_1}{r_b}X_3(s_1r_b);$$
$$H_{6;5} = -\frac{2\mu^t n s_1}{r_b}Y_3(s_1r_b);\ H_{6;6} = 2ik\mu^t s_1[s_1I_n(s_1r_b) + \frac{1}{r_b}X_2(s_1r_b)];$$
$$H_{6;7} = 2ik\mu^t s_1[s_1K_n(s_1r_b) + \frac{1}{r_b}Y_2(s_1r_b)];\ H_{6;8} = \rho_f\omega^2 I_n(fr_b);$$
$$H_{6;9} = \rho_f\omega^2 K_n(fr_b); H_{7;2} = \frac{2np_1}{r_b}X_3(p_1r_b);\ H_{7;3} = \frac{2np_1}{r_b}Y_3(p_1r_b);$$
$$H_{7;4} = -s_1^2X_4(s_1r_b);\ H_{7;5} = -s_1^2Y_4(s_1r_b); H_{7;6} = \frac{2ikns_1}{r_b}X_3(s_1r_b);$$
$$H_{7;7} = \frac{2ikns_1}{r_b}Y_3(s_1r_b);\ H_{8;2} = 2ikp_1X_1(p_1r_b);\ H_{8;3} = 2ikp_1Y_1(p_1r_b);$$
$$H_{8;4} = \frac{ikn}{r_b}I_n(s_1r_b);\ H_{8;5} = \frac{ikn}{r_b}K_n(s_1r_b);\ H_{8;6} = -(k^2+s_1^2)s_1X_1(s_1r_b);$$
$$H_{8;7} = -(k^2+s_1^2)s_1Y_1(s_1r_b);\ H_{9;8} = -fX_1(fr_0);\ H_{9;9} = -fY_1(fr_0);$$
$$H_{9;10} = G_{1;2}; H_{9;11} = G_{1;4}; H_{9;12} = G_{1;6};\ H_{10;8} = \rho_f\omega^2 I_n(fr_0);$$
$$H_{10;9} = \rho_f\omega^2 K_n(fr_0);\ H_{10;10} = G_{4;2}; H_{10;11} = G_{4;4};\ H_{12;12} = G_{4;6};\ H_{11;10} = G_{5;2};$$
$$H_{11;11} = G_{5;4};\ H_{11;12} = G_{5;6};\ H_{12;10} = G_{6;2}; H_{12;11} = G_{6;4};\ H_{12;12} = G_{6;6}: \quad \text{(A-2)}$$

The other unlisted elements of the H matrix are all zero. In the above expressions, I_n and $K_n(n = 1; 2)$ are, respectively, the modified Bessel functions of the first and second kind of order n (for quadrupole, $n = 2$); r_0, r_a, and r_b are, respectively, the borehole radius, collar inner radius, and collar outer radius; ρ_t and ρ_f are the collar and fluid density; α_t, β_t, and α_f are the collar P- and S-wave velocity and borehole fluid velocity, respectively; and $p_1 = \sqrt{k^2 - \omega^2/\alpha_t^2}$, $s_1 = \sqrt{k^2 - \omega^2/\beta_t^2}$, and $f = \sqrt{k^2 - \omega^2/\alpha_f^2}$ are, respectively, the collar compressional, shear, and borehole acoustic radial wavenumbers. The collar shear modulus is $\mu^t = \rho_t\beta_t^2$. The symbol G is a 6 × 6 matrix to model an altered formation with staircase variations, obtained using the Thomson-Haskell propagator matrix method. All formation property and parameters are contained in G. Expressions for the elements of G can be found in Tang and Cheng (2004). To simplify the expressions for the elements of H, the following combinations of Bessel functions are used:

$$\begin{cases} X_1(x) = \frac{n}{x}I_n(x) + I_{n+1}(x) \\ X_2(x) = \frac{n(n-1)}{x}I_n(x) - I_{n+1}(x) \\ X_3(x) = \frac{1-n}{x}I_n(x) - I_{n+1}(x) \\ X_4(x) = \left[1 + \frac{2n(n-1)}{x^2}\right]I_n(x) - \frac{2}{x}I_{n+1}(x) \end{cases} \quad \begin{cases} Y_1(x) = \frac{n}{x}K_n(x) - K_{n+1}(x) \\ Y_2(x) = \frac{n(n-1)}{x}K_n(x) + K_{n+1}(x) \\ Y_3(x) = \frac{1-n}{x}K_n(x) + K_{n+1}(x) \\ Y_4(x) = \left[1 + \frac{2n(n-1)}{x^2}\right]K_n(x) + \frac{2}{x}K_{n+1}(x) \end{cases} : \quad \text{(A-3)}$$

REFERENCES

Backus, G., and F. Gilbert, 1970, Uniqueness in the inversion of inaccurate gross Earth data: Philosophical Transactions of the Royal Society of London, A, 266, 123–192, doi: 10.1098/rsta.1970.0005.

Burridge, R., and B. K. Sinha, 1996, Inversion for formation shear modulus and radial depth of investigation using borehole flexural waves: 66th Annual International Meeting, SEG, Expanded Abstracts, 158–161.

Kinoshita, T., A. Dumont, H. Hori, N. Sakiyama, J. Morley, and F. Garcia-Osuna, 2010, LWD sonic tool design for high-quality logs: 80th Annual International Meeting, SEG, Expanded Abstracts, 513–517.

Press, W. H., B. P. Flannery, S. A. Teukosky, and W. T. Vetterling, 1989, Numerical recipes: Cambridge University Press.

Schmitt, D. P., 1988, Shear-wave logging in elastic formations: Journal of the Acoustical Society of America, 84, 2215–2229, doi: 10.1121/1.397015.

Sinha, B., B. Vissapragada, S. Kisra, H. Yamamoto, T. Endo, and H. P. Valero, 2005, Optimal well completions using radial profiling of formation shear slownesses: SPE Annual Technical Conference and Exhibition, 95837.

Su, Y. D., X. E. Liu, C. X. Zhuang, Z. F. Sun, and C. Hei, 2011, Estimating radial variation of unconsolidated formations using borehole leaky-P wave dispersion: 52nd Annual Logging Symposium Transactions, Society of Petrophysicists and Well Log Analysts, R1–R14.

Tang, X. M., 1996, Processing dipole waveform logs for formation alteration identification: 66th Annual International Meeting, SEG, Expanded Abstracts, 162–165.

Tang, X. M., and C. H. Cheng, 2004, Quantitative borehole acoustic methods: Elsevier Science Publishing, Inc.

Tang, X. M., V. Dubinsky, T. Wang, A. Bolshakov, and D. Patterson, 2003, Shear-velocity measurement in the logging-while-drilling environment: Modeling and field evaluations: Petrophysics, 44, 79–90.

Tang, X. M., and D. J. Patterson, 2010, Mapping formation radial shear-wave velocity variation by a constrained inversion of borehole flexural-wave dispersion data: Geophysics, 75, no. 6, E183–E190, doi: 10.1190/1.3502664.

Tang, X. M., T. Wang, and D. J. Patterson, 2002, Multipole acoustic logging-while-drilling: 72nd Annual International Meeting, SEG, Expanded Abstracts, 364–368.

Yang, J. Q., B. K. Sinha, and T. M. Hanbashy, 2012, A theoretical study on formation shear radial profiling in well-bonded cased boreholes using sonic dispersion data based on a parameterized perturbation model: Geophysics, 77, no. 3, WA197–WA210, doi: 10.1190/geo2011-0279.1.

GEOPHYSICS, VOL. 85, NO. 4 (JULY-AUGUST 2020); P. D121–D132, 10 FIGS., 2 TABLES.
10.1190/GEO2019-0611.1

Check for updates

Downloaded 08/07/20 to 218.201.114.137. Redistribution subject to SEG license or copyright; see Terms of Use at https://library.seg.org/page/policies/terms
DOI:10.1190/geo2019-0611.1

Joint inversion of logging-while-drilling multipole acoustic data to determine formation shear-wave transverse isotropy

Yang-Hu Li[1], Song Xu[1], Can Jiang[1], Yuan-Da Su[2], and Xiao-Ming Tang[2]

ABSTRACT

Seismic-wave anisotropy has long been an important topic in the exploration and development of unconventional reservoirs, especially in shales, which are commonly characterized as transversely isotropic ([TI] or vertical TI [VTI]) media. At present, the shear-wave (S-wave) TI properties have mainly been determined from monopole Stoneley- or dipole flexural-wave measurements in wireline acoustic logging, but the feasibility of those obtained from logging-while-drilling (LWD) acoustic data needs to be established. We have developed a joint inversion method for simultaneously determining formation S-wave transverse isotropy and vertical velocity from LWD multipole acoustic data. Our theoretical analysis shows that the presence of anisotropy strongly influences LWD Stoneley- and quadrupole-wave dispersion characteristics. Although the monopole Stoneley and quadrupole waves are sensitive to the formation S-wave TI parameters, they suffer from the typical nonuniqueness problem when using the individual-wave data to invert parameters alone. Thus, the respective dispersion data can be jointly used to estimate the formation S-wave TI properties. By the joint inversion, the nonuniqueness problem in the parameter inversion can also be effectively alleviated. The feasibility of the method has been verified by the processing results of theoretical synthetic data and field LWD acoustic-wave data. Therefore, the result offers an effective method for evaluating VTI formation anisotropy from acoustic LWD data.

INTRODUCTION

In the exploration and development of unconventional reservoirs, many sedimentary layers, such as shale, appear as transversely isotropic (TI) media (Tang, 2003; Tang and Cheng, 2004; He and Hu, 2009; He et al., 2010; Wei et al., 2018; Xu et al., 2018a). This problem can be analytically solved when the symmetric axis of the TI medium is parallel to the well axis. The solution can therefore be used as the theoretical foundation for studying the problem of acoustic wireline logging in a vertical borehole surrounded by a vertical TI (VTI) formation (Xu et al., 2017). Theoretical modeling results show that, for a vertical well with a VTI formation, acoustic logging can only directly measure the velocity of a wave propagating along the well (White and Tongtaow, 1981; Schmitt, 1989; Tang and Cheng, 2004). However, for geophysical applications, it is sometimes desirable to determine the velocity of a horizontally propagating wave, for example, the shear wave (S-wave). This study will focus on how to determine VTI properties from the logging-while-drilling (LWD) acoustic data.

LWD acoustic technology has been developed to measure formation P- and S-wave velocities (Tang and Cheng, 2004). A particular feature of LWD technology is that it uses the quadrupole wave to measure the S-wave velocity, as compared to wireline logging in which the dipole wave is commonly used for S-wave measurement (Tang et al., 2003; Xu et al., 2018b). The advantages of LWD S-wave measurement using the quadrupole have been studied by numerous authors using theoretical modeling and laboratory and field measurements (Tang et al., 2003; Cui, 2004; Tang and Cheng, 2004; Briggs, 2006; Tang et al., 2006; Sinha et al., 2009; Wang and Tao, 2011; Lee et al., 2013). The existing studies indicate that the presence of a large LWD tool strongly affects the sensitivity of the quadrupole wave to the formation S-wave and VTI parameters. For example, Sinha and Simsek (2010) discuss the influence of the drill collar on the borehole waveguide in an anisotropic formation. Lee et al. (2013) show the LWD guided-wave

Manuscript received by the Editor 25 September 2019; revised manuscript received 22 December 2019; published ahead of production 29 March 2020; published online 14 May 2020.
[1]China University of Petroleum (East China), School of Geosciences, Qingdao, China. E-mail: lyanghu@outlook.com; xusongupc@sina.com; jiangcan_upc@sina.com; syuanda@sina.com (corresponding author); tangxiam@aliyun.com.
[2]China University of Petroleum (East China), School of Geosciences, Qingdao, China; Key Laboratory of Deep Oil and Gas (China University of Petroleum (East China)), Qingdao, China; and Qingdao National Laboratory for Marine Science and Technology, Qingdao, China. E-mail: syuanda@sina.com; tangxiam@aliyun.com
© 2020 Society of Exploration Geophysicists. All rights reserved.

Downloaded 08/07/20 to 218.201.114.137. Redistribution subject to SEG license or copyright; see Terms of Use at https://library.seg.org/page/policies/terms
DOI:10.1190/geo2019-0611.1

characteristics with a TI formation. Wang and Qiao (2015) study the influence of TI anisotropy on the LWD quadrupole wave and analyze the wave's depth of penetration in the formation. Wei et al. (2018) simulate the wavefield of multipole acoustic LWD in a TI formation using a finite-difference method, and their results show that the quadrupole wave is sensitive to the formation anisotropic parameters.

This paper proposes a joint inversion method to simultaneously determine the formation shear-wave anisotropy parameters using the LWD Stoneley- and quadrupole-wave data and their propagation characteristics. The advantage of the joint inversion, compared with inverting individual-wave data, is suppressing the nonuniqueness problem and improving the result accuracy (Tang and Patterson, 2010; Su et al., 2016; Xu et al., 2018c). We first theoretically analyze the dispersion characteristics of LWD multipole waves and study the effect of formation anisotropy on the acoustic LWD measurements. We then test the applicability of the ANNIE approximation (Schoenberg et al., 1996) to LWD-multipole-dispersion modeling to compensate for the missing TI parameters that are insensitive to the borehole measurements. With theoretical modeling, we develop the joint inversion method to extract the anisotropy parameter from the Stoneley and quadrupole waves. Through joint inversion, we can not only suppress the nonuniqueness of the inversion problem, but we also simultaneously determine the formation S-wave TI parameters. Finally, we apply the method to process a field LWD acoustic data set, demonstrating that the method is capable of determining the formation S-wave anisotropy magnitude and variation along the borehole from the LWD data.

THEORETICAL ANALYSIS

Figure 1 depicts LWD acoustic measurements in a vertical borehole surrounded by a TI formation. The symmetry axis of the TI medium coincides with the borehole axis. The cylindrically stratified acoustic model is shown in Figure 1b, which consists of the inner fluid (water), drill collar, outer fluid (water), and the TI formation, the outer diameters being r_0, r_1, r_2, and infinite, respectively. The drill collar is concentric with the borehole. The parameters of the borehole and TI formation that will be used in the theoretical analysis are shown in Table 1.

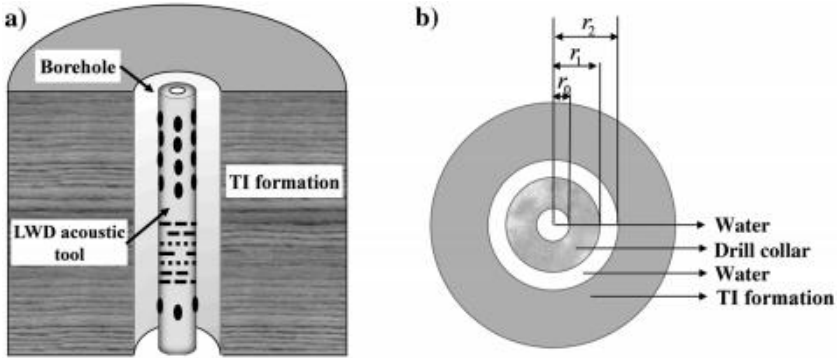


Figure 1. (a) Model for logging in a TI formation with a multipole acoustic LWD tool and (b) cross section of the model.

Table 1. The LWD acoustic model parameters.

	v_P (m/s)	v_S (m/s)	Thomsen γ	Density (kg/m^3)	Outer radius (m)
Inner fluid	1500	—	—	1000	0.027
Drill collar	5860	3130	—	7850	0.090
Outer fluid	1500	—	—	1000	0.117
Fast formation	4800	2300	0.2	2550	∞
Slow formation	2100	1200	0.2	2450	∞

A TI formation is described by five elastic constants (Tang and Cheng, 2004):

$$[C_{11}; C_{13}; C_{33}; C_{44}; C_{66}]: \tag{1}$$

For a vertical borehole surrounded by a VTI formation, C_{11} and C_{33} relate, respectively, to the horizontal and vertical P-wave velocities; C_{44} and C_{66} relate to the vertical and horizontal S-wave velocities, respectively. The Thomsen (1986) S-wave anisotropy parameter γ is defined as

$$\gamma = \frac{C_{66} - C_{44}}{2C_{44}}: \tag{2}$$

For the LWD acoustic model of Figure 1 and the VTI formation, the dispersion equation for the multipole acoustic wave propagation in the model can be analytically derived (see Appendix A), as given by

$$D(n; k; \omega; C_{44}; C_{66}; C_{11}; C_{13}; C_{33}; Bo; Co; Fo) = 0; \tag{3}$$

where n is the order of the multipole, with $n = 0$, 1, 2 denoting monopole, dipole, and quadrupole, respectively; k is the wavenumber of the wave mode, and ω is the angular frequency; and the symbols Bo, Co, and Fo represent the model parameters of the borehole fluid, drill collar, and the formation, respectively. Detailed mathematical descriptions of equation 3 are given in Appendix A.

By solving the dispersion equation 3 in the frequency range of interest, the phase velocity (or slowness) dispersion curves of the Stoneley wave (denoted by ST) and the quadrupole wave (denoted by QD) are calculated using

$$\begin{cases} v_{ST} = \omega/k_{ST} \\ v_{QD} = \omega/k_{QD} \end{cases} \quad \text{or} \quad \begin{cases} S_{ST} = k_{ST}/\omega \\ S_{QD} = k_{QD}/\omega \end{cases}: \tag{4}$$

Figure 2 shows the LWD Stoneley- and quadrupole-wave dispersion curves for the slow (Figure 2a) and fast (Figure 2b) formation parameters of Table 1. The fast (slow) formation is defined as the formation whose S-wave velocity is faster (slower) than the velocity of fluid inside the borehole. For comparison, the anisotropic (solid) and isotropic (dashed, assuming $C_{44} = C_{66}$) dispersion curves are calculated. In the slow formation scenario, the anisotropic Stoneley velocity, which is mostly sensitive to C_{66}, is significantly faster than the isotropic velocity. However, for the fast formation case, the difference is largely reduced because the wave's sensitivity to C_{66} is overrun by its sensitivity to the borehole fluid (Tang and Cheng, 2004). The isotropic and anisotropic quadrupole-wave velocities approach the vertical shear velocity ($v_{SV} = \sqrt{C_{44}/\rho}$) at the cutoff frequency for the fast and slow formation scenarios, which shows

Downloaded 08/07/20 to 218.201.114.137. Redistribution subject to SEG license or copyright; see Terms of Use at https://library.seg.org/page/policies/terms
DOI:10.1190/geo2019-0611.1

that the low-frequency LWD quadrupole measurement obtains only v_{SV}.

Nevertheless, Figure 2 shows that the anisotropic Stoneley- and quadrupole-wave velocity dispersion curves are different from their isotropic counterparts, indicating the sensitivity of these LWD acoustic wave modes to VTI formation anisotropy. The sensitivity can be expressed in terms of the relative difference (RD) between the anisotropic and isotropic dispersion curves as

$$RD(\omega) = \frac{v_{ani}(\omega) - v_{iso}(\omega)}{v_{iso}(\omega)} \times 100\%; \quad (5)$$

where v_{ani} and v_{iso} represent the anisotropic- and isotropic-phase velocity dispersion curves, respectively.

Figure 3 shows the relative difference curves of the Stoneley wave (Figure 3a) and the quadrupole wave (Figure 3b) in the fast (solid) and slow (dashed) VTI formations, respectively. The relative difference for the Stoneley wave decreases with increasing frequency in the fast and slow formations, which indicates that anisotropy affects the Stoneley wave more effectively at low frequencies than at high frequencies. Moreover, the Stoneley-wave relative difference is much higher in the slow formation than that in the fast formation, suggesting that the anisotropy measurement using the Stoneley wave is more suitable in the slow formation than in the fast formation. For the quadrupole wave, the relative difference increases with the increasing frequency in the slow formation and it becomes nearly constant toward high frequencies. This suggests that the anisotropy measurement using the quadrupole wave should be in the middle- to high-frequency range. However, in the fast formation scenario, the relative difference for the quadrupole attains a peak value above the cutoff frequency, suggesting that this is the optimum frequency range for the fast formation anisotropy measurement.

The anisotropy-induced difference shown in Figure 3 is related to all of the parameters of the model shown in Figure 1. The importance of each parameter in affecting the wave propagation can be assessed using a sensitivity analysis. The sensitivity is actually the partial differential of the normalized phase velocity with respect to a model parameter defined as (Tang and Cheng, 2004)

$$Sens^{p}(\omega) = \left(\frac{p}{v_{phase}(\omega)}\right)\frac{\partial v_{phase}(\omega)}{\partial p}; \quad (6)$$

where $Sens^{p}$ represents the sensitivity of the phase velocity v_{phase} to the parameter p. The sensitivity is also called the partition coeffi-

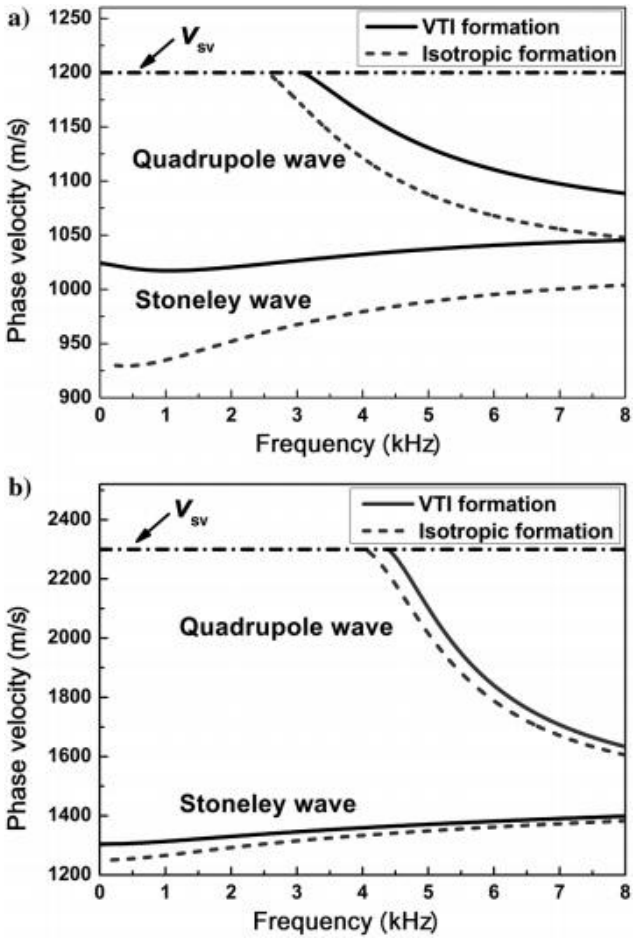


Figure 2. LWD Stoneley- and quadrupole-wave dispersion curves (solid) for the (a) slow and (b) fast VTI formations. For comparison, the isotropic counterpart (dashed) is also plotted.

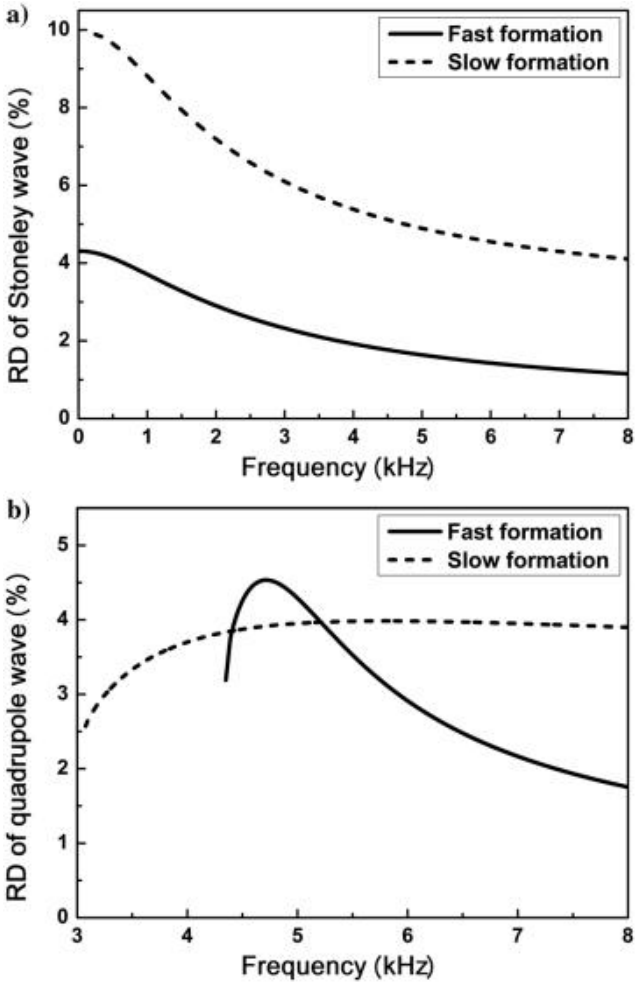


Figure 3. The relative difference (RD) between the anisotropic and isotropic dispersion curves of the LWD (a) Stoneley and (b) quadrupole waves for the fast (solid) and slow (dashed) VTI formations.

Downloaded 08/07/20 to 218.201.114.137. Redistribution subject to SEG license or copyright; see Terms of Use at https://library.seg.org/page/policies/terms
DOI:10.1190/geo2019-0611.1

cient because it describes the proportion of the total strain energy of the wave partitioned to each model parameter. Because of the conservation of energy, the sum of the partition coefficients for all parameters must be equal to 1. Therefore, if the wave model has a high sensitivity to a parameter, it indicates that the parameter can be determined with high confidence or low uncertainty.

Figure 4 shows the LWD Stoneley-wave sensitivities, respectively, to borehole-fluid velocity (v_f, dots), vertical (v_{SV}, dashed), and horizontal (v_{SH}, solid) shear velocities for the slow (Figure 4a) and fast (Figure 4b) VTI formation models. In the slow formation scenario, the Stoneley sensitivity is dominated by v_{SH} (about 50%) at low frequencies, which provides the theoretical basis for inverting v_{SH} from the Stoneley wave. With increasing frequency, the wave's sensitivity to v_{SV} increases. However, in the fast formation case, the Stoneley sensitivities to v_{SH} and v_{SV} are much reduced relative to the slow formation scenario. This sensitivity reduction means that the TI parameter estimation from the Stoneley wave will have difficulty in the fast formation. Moreover, the Stoneley wave is very sensitive to v_f in the slow and fast formations. It is worth noting that the LWD Stoneley-wave sensitivity to v_{SH} is significantly enhanced compared with the wireline logging in the slow and fast formations, which makes the LWD Stoneley wave more favorable for inverting v_{SH}. This conclusion is consistent with that of Lee et al. (2013).

The sensitivity analysis of the quadrupole wave for the same model is shown in Figure 5. As can be seen from Figure 5, the quadrupole wave has a high sensitivity to v_{SV} in the whole frequency range for slow (Figure 5a) and fast (Figure 5b) formations, which is the basis for shear-velocity measurement using the LWD quadrupole. For fast and slow formations, the quadrupole sensitivity to v_{SH} increases from the cutoff frequency to a value above 10%. In particular, the fast formation sensitivity shows a peak around 5 kHz, suggesting that this frequency range is optimum for inventing v_{SH}. In addition, the quadrupole wave is also sensitive to v_f, especially in the fast formation scenario, as compared to the Stoneley wave. The high sensitivity to v_f indicates that the borehole fluid will significantly affect the dispersion characteristics of Stoneley and quadrupole waves. However, the velocity of the borehole fluid in the field condition is usually unknown; therefore, we use the calibration method proposed by Lee et al. (2016) to determine the fluid parameter for the inversion.

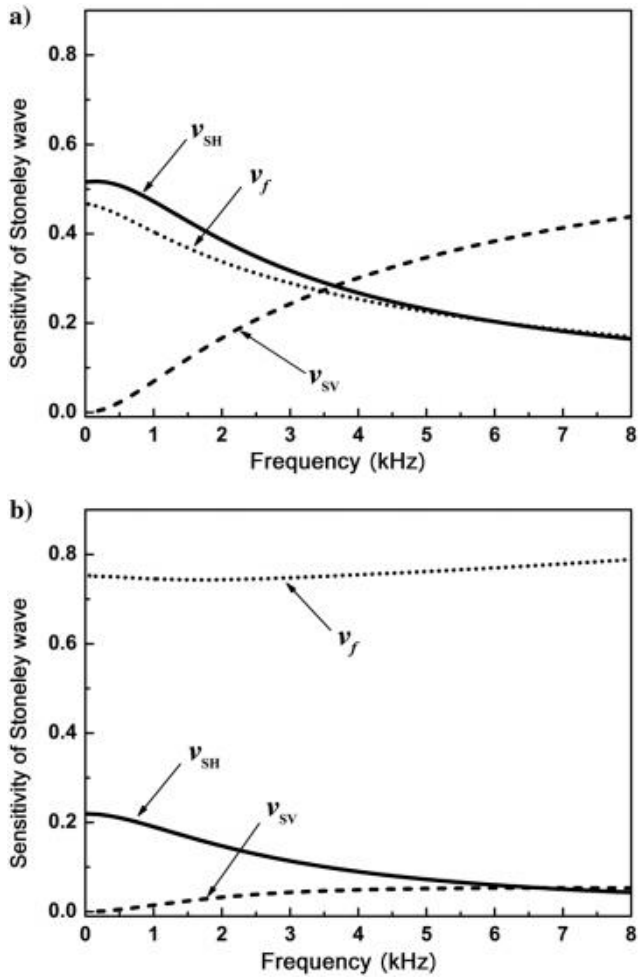


Figure 4. The LWD Stoneley-wave sensitivities to borehole-fluid velocity (the dots labeled v_f), vertical (the dashed curve labeled v_{SV}), and horizontal (the solid curve labeled v_{SH}) shear velocities for the (a) slow and (b) fast VTI formations.

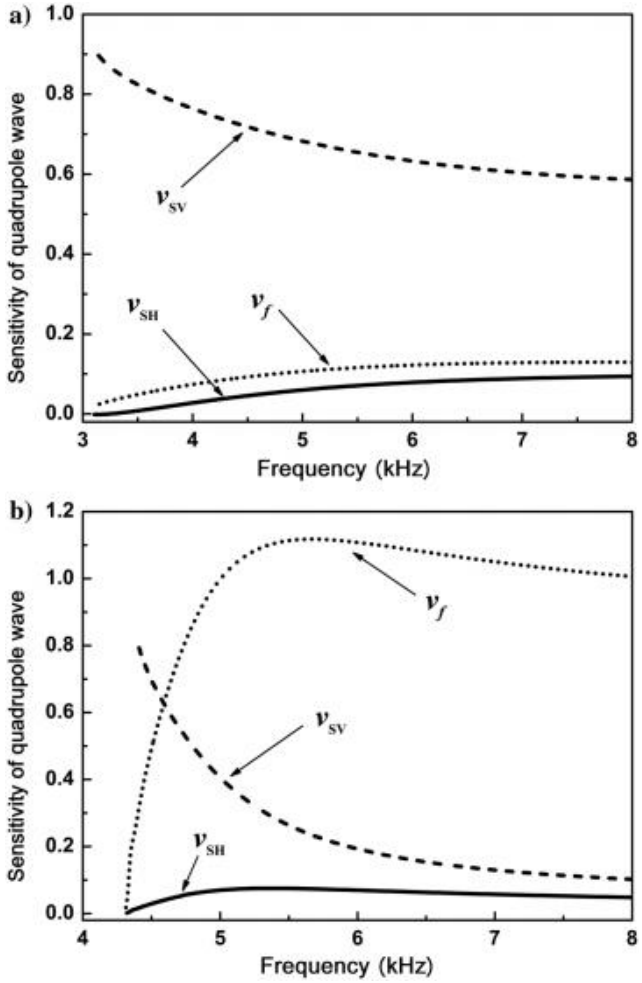


Figure 5. The LWD quadrupole-wave sensitivities to borehole-fluid velocity (the dots labeled v_f), vertical (the dashed curve labeled v_{SV}), and horizontal (the solid curve labeled v_{SH}) shear velocities for the (a) slow and (b) fast VTI formations.

Downloaded 08/07/20 to 218.201.114.137. Redistribution subject to SEG license or copyright; see Terms of Use at https://library.seg.org/page/policies/terms
DOI:10.1190/geo2019-0611.1

The theoretical analysis results show that the Stoneley and quadrupole waves are sensitive to the VTI formation anisotropy after addressing the effect of borehole fluid. However, the inversion for the multiple anisotropy parameters using an individual wave alone may suffer from the typical nonuniqueness problem of inversion. In this regard, the proposed joint inversion method using both wave modes can not only suppress the nonuniqueness problem but also improve the accuracy of the inversion result in fast and slow formation scenarios. As can be seen from the above analysis results, in the slow formation scenario, the high sensitivity of the quadrupole wave to v_{SV} can be used to correct the dispersion effect of the wave on the anisotropic inversion while taking advantage of the high sensitivity of the Stoneley wave to v_{SH}. In the fast formation scenario, the sensitivity of the quadrupole wave to v_{SH} can make up for the sensitivity reduction of the Stoneley wave to v_{SH}. Furthermore, the relative difference curves shown in Figure 3 can be used to guide the selection of the inversion frequency band. According to Figure 3, Stoneley-wave data should be acquired in the low-frequency band for fast and slow formations, whereas the quadrupole-wave data should be used in a higher frequency range.

We focused on determining S-wave TI parameters C_{44} and C_{66} to estimate the S-wave anisotropy parameter γ (equation 2). However, the TI formation represented by equation 1 has five parameters. The parameter C_{33} relates to vertical P-wave velocity that can be mea-

Table 2. The TI parameters of eight sedimentary rocks for testing the ANNIE approximation (data are from Thomsen, 1986).

	v_P (m/s)	v_S (m/s)	ε	δ	γ	Density (kg/m^3)
Fast formation 1	4846	3170	0.063	0.008	0.028	2690
Fast formation 2	4476	2814	0.097	0.091	0.051	2500
Fast formation 3	3749	2621	0.128	0.078	0.100	2920
Fast formation 4	3383	2438	0.065	0.059	0.071	2350
Slow formation 1	3048	1490	0.255	−0.050	0.480	2420
Slow formation 2	2074	869	0.110	0.090	0.165	2257
Slow formation 3	1875	826	0.225	0.100	0.345	2000
Slow formation 4	1409	780	0.022	0.018	0.004	2030

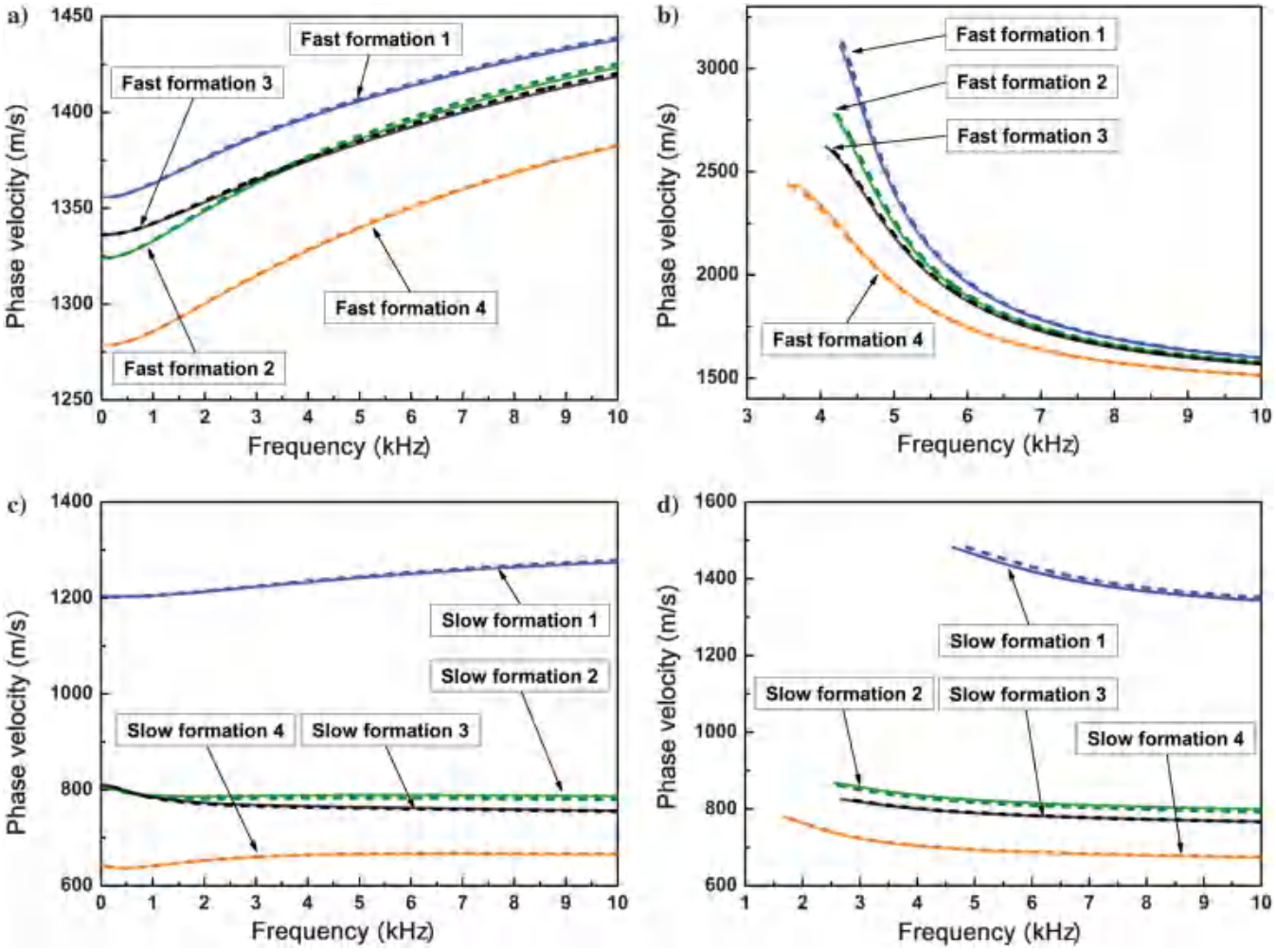


Figure 6. The LWD-wave dispersion curves calculated using the exact TI parameters (dashed) and the ANNIE approximation (solid). (a and b) The Stoneley- and quadrupole-wave dispersion curves for the fast formations, (c and d) the Stoneley- and quadrupole-wave dispersion curves for the slow formations, respectively.

Downloaded 08/07/20 to 218.201.114.137. Redistribution subject to SEG license or copyright; see Terms of Use at https://library.seg.org/page/policies/terms
DOI:10.1190/geo2019-0611.1

sured directly from logging. The remaining two parameters can be expressed using the ANNIE approximation (Schoenberg et al., 1996)

$$\begin{cases} C_{13} = C_{33} - 2C_{44} \\ C_{11} = C_{33} + 2(C_{66} - C_{44}) \end{cases}. \quad (7)$$

The problem is then reduced to the estimation of two unknowns (C_{44} and C_{66}).

Xu et al. (2017) test the accuracy of the ANNIE approximation using core measurement data. For the present LWD acoustic problem, it remains to test the appropriateness of the ANNIE approximation for calculating the guided-wave dispersion curves using the anisotropic model of Figure 1. In the following, we compare the wave dispersion curves with and without the ANNIE approximation for different formations. Eight sets of core data from Thomsen (1986) are used. The relevant formation parameters are shown in Table 2. Two modeling calculations are performed using the data. In the first, the TI formation is modeled using the exact Thomsen parameters ε, δ, and γ in Table 2. In the second, the parameters ε and δ are calculated using the ANNIE approximation (equation 7). As shown in Figure 6, the solid curves from using the ANNIE approximation are almost identical to the dashed curves from using the exact parameter values. In fact, the reason for using the ANNIE approximation is that the LWD Stoneley and quadrupole waves are primarily sensitive to C_{44} and C_{66} and are relatively insensitive to C_{11}, C_{13}, and C_{33}.

THE JOINT INVERSION METHOD

Having established the theoretical modeling approach for the LWD multipole waves, we now discuss the joint inversion method to estimate the TI properties from the wave data. The multipole wave slowness dispersion data are calculated using the slowness-frequency-coherence (SFC) method (Tang and Cheng, 2004). The data are then fitted by their respective theoretical dispersion curves calculated using equations 3 and 4. The inversion is formulated by minimizing the objective function E constructed by a weighted sum of the Stoneley- and quadrupole-wave results calculated by the sum of the least-squares error between the theoretical and measured data for

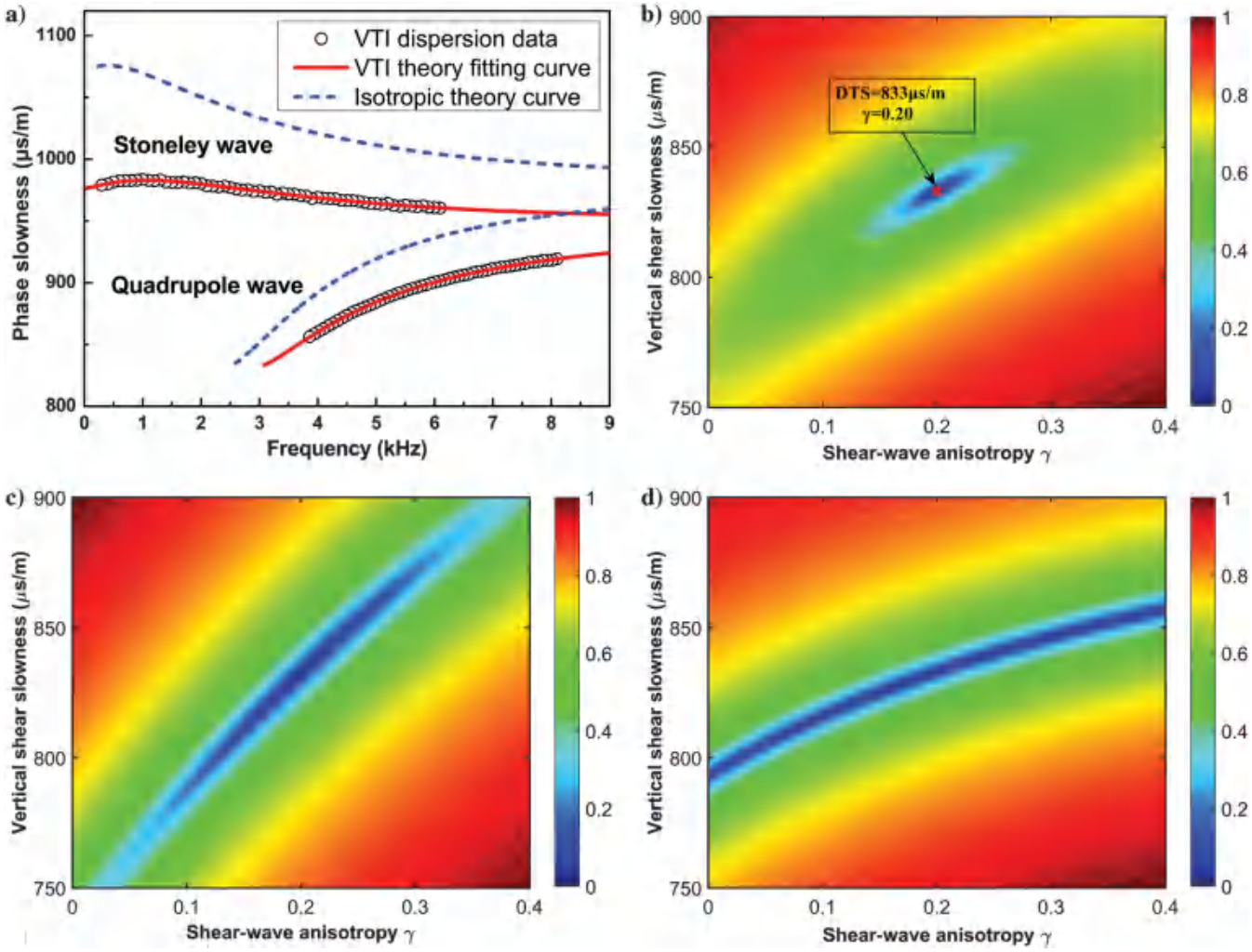


Figure 7. Test of the joint inversion method using synthetic-wave dispersion data in (a) (circles) and (b) VD display of the objective function, showing a well-defined solution minimum. The calculated dispersion curves from the solution (solid) fit the data very well. The VD images in (c and d) are the objective function for the Stoneley and quadrupole, respectively. The elongated valleys of the images indicate the nonuniqueness problem for inverting the individual wave data.

Downloaded 08/07/20 to 218.201.114.137. Redistribution subject to SEG license or copyright; see Terms of Use at https://library.seg.org/page/policies/terms
DOI:10.1190/geo2019-0611.1

the Stoneley and quadrupole waves over their respective frequency ranges, as explained in the following. The inversion is aimed at obtaining the vertical shear slowness S_{SV} and the Thomsen parameter γ:

$$E(S_{SV};\gamma) = (1-\lambda)\sum_{\Omega_{ST}} P_{ST}(\omega)\cdot[S_t^{ST}(S_{SV};\gamma;\omega) - S_d^{ST}(\omega)]^2 + \lambda\sum_{\Omega_{QD}} P_{QD}(\omega)\cdot[S_t^{QD}(S_{SV};\gamma;\omega) - S_d^{QD}(\omega)]^2: \quad (8)$$

In equation 8, for calculating the objective function, S_t and S_d denote the modeled and measured dispersion data, respectively; Ω_{ST} and Ω_{QD} represent the processing frequency ranges for the Stoneley and quadrupole waves, respectively; P_{ST} and P_{QD} are the power spectra for the Stoneley and quadrupole waves, respectively, which are normalized by the maximum in their respective frequency range; λ is the weighting factor, which is used to adjust the relative contribution of the Stoneley and quadrupole terms to the objective function according to the size of the data over Ω_{ST} and Ω_{QD}, respectively, and the value range of λ is between 0 and 0.5. The effectiveness of the inversion formulation is tested first using synthetic waveform data.

We use the slow formation parameters of Table 1 as an example for the numerical testing. The dispersion data (circles in Figure 7a) are extracted using the SFC method from the synthetic array waveform data. The frequency bands Ω_{ST} and Ω_{QD} used for the inversion are 0.5–6.0 kHz and 4.0–8.0 kHz, respectively. The weighting factor λ is 0.1. By using a small value of λ, a bigger weight is given to the Stoneley wave because of its high sensitivity to anisotropy in the slow formation.

Figure 7a shows the synthetic dispersion data (circles) and the inversion-fitted dispersion curves (solid). For comparison, the theoretical isotropic dispersion curves (dashed) are also plotted. Figure 7b shows the variable density (VD) display of the objective function over the 2D parameter domain $(S_{SV};\gamma)$, indicating a well-defined minimum at the solution point ($S_{SV} = 833$ μs/m ($V_{SV} = 1200$ m/s), $\gamma = 0.20$), which gives the inversion-fitted dispersion curves in Figure 7a. The inversion fits the data very well, verifying the effectiveness and accuracy of the method.

To quantity the inversion accuracy, we calculate the quantity indicator (QI) using the following formula:

$$QI = \left[\frac{1}{N_{ST}}\sum_{\Omega_{ST}}\left|S_t^{ST}(S_{SV}^*;\gamma^*;\omega) - S_d^{ST}(\omega)\right| / S_t^{ST}(S_{SV}^*;\gamma^*;\omega) + \frac{1}{N_{QD}}\sum_{\Omega_{QD}}\left|S_t^{QD}(S_{SV}^*;\gamma^*;\omega) - S_d^{QD}(\omega)\right| / S_t^{QD}(S_{SV}^*;\gamma^*;\omega)\right]\cdot 100\%; \quad (9)$$

where N_{ST} and N_{QD} are the numbers of data points within the frequency ranges of Ω_{ST} and Ω_{QD}, respectively, and S_{SV}^* and γ^* denote the inversion result. The QI parameter of equation 9 is basically the average of the relative data fitting error over the inversion frequency ranges. For the inversion result of Figure 7b, the QI parameter value is only 0.32%, indicating an accurate and reliable inversion result.

To demonstrate the advantage of the joint inversion method, the Stoneley- and quadrupole-wave data are inverted separately using the individual term of equation 8. The results are shown in Figure 7c and 7d, respectively. Neither objective function has a well-defined minimum at the solution point ($S_{SV} = 833$ μs/m, $\gamma = 0.20$). Instead, the functions show a long valley over the 2D parameter domain, such that any point $(S_{SV};\gamma)$ along the valley will fit the respective dispersion data (Stoneley or quadrupole) quite well. This again indicates the typical nonuniqueness problem in the guided-wave dispersion data inversion (Tang and Patterson, 2010; Su et al., 2016; Xu et al., 2018c).

It is interesting to note that the valley for the quadrupole is leaning more toward the γ axis, meaning that the quadrupole is mostly sensitive to S_{SV} and less sensitive to γ; whereas the valley for the Stoneley extends at an angle with the S_{SV} and γ axes, meaning that

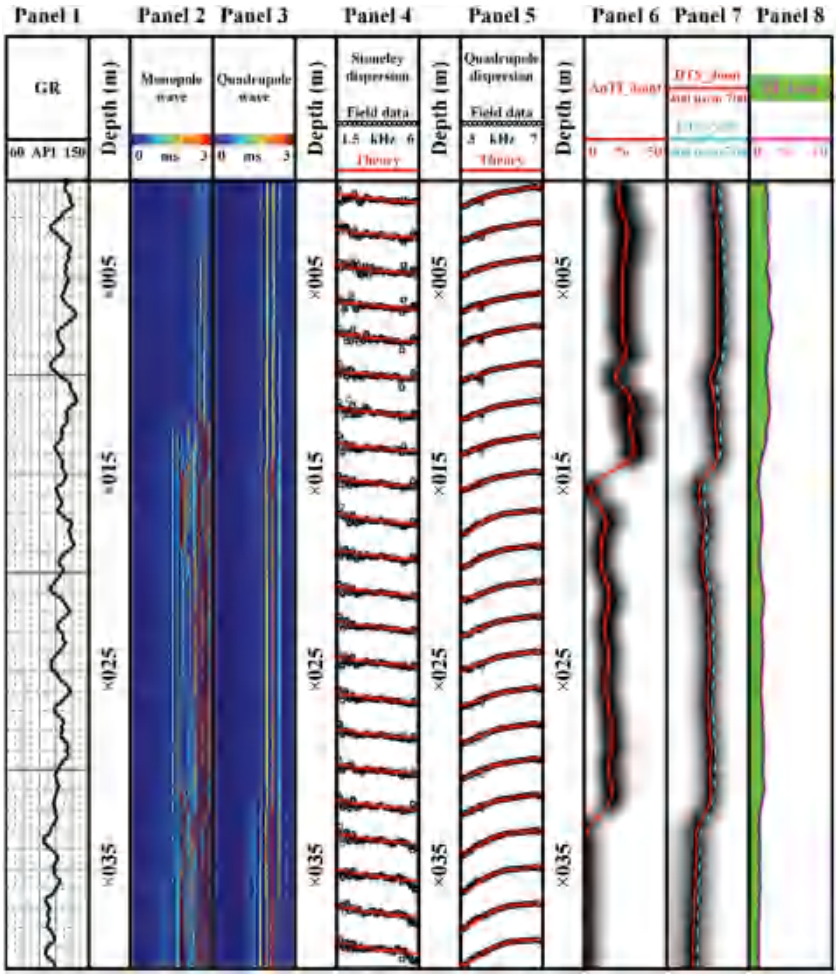


Figure 8. Example of the joint inversion method for a sand-shale formation (see the gamma-ray curve in panel 1) using the LWD monopole (panel 2) and quadrupole (panel 3) wave data. Panels 4 and 5 display the dispersion data fitting of the Stoneley and quadrupole waves, respectively. Panels 6 and 7 show the inversion results. For comparison, the STC-processed result (dashed) is also plotted in panel 7. Panel 8 predicts the quality indicators of the inversion results.

the Stoneley is sensitive to both parameters. By joint inversion, the two valleys cross each other at the solution point, forming the well-defined minimum in Figure 7b.

APPLICATION TO FIELD DATA

Applying the above inversion method to a field LWD data set acquired in a fast formation with a vertical borehole, we obtain

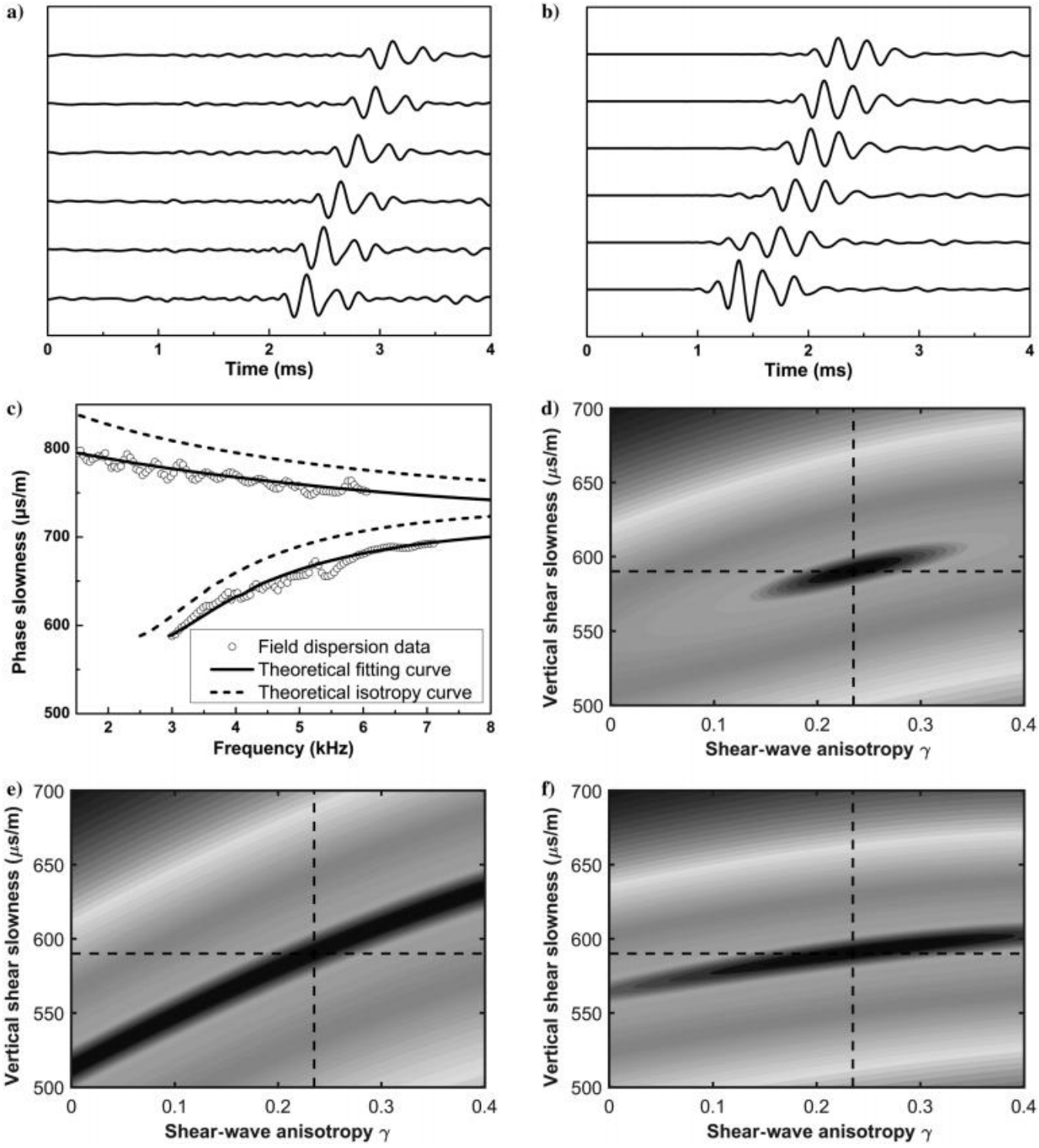


Figure 9. Detailed inversion result for an anisotropic formation depth (X004m). (a and b) The LWD array Stoneley- and quadrupole-wave data, for calculating the dispersion data in (c) (circles). The solution minimum of the joint inversion (d) gives the inversion-fitted dispersion curves (the solid curves in [c]), compared to the dispersion curves for an isotropic formation (the dashed curves). (e and f) show the objective functions for the individual Stoneley- and quadrupole-wave data.

Downloaded 08/07/20 to 218.201.114.137. Redistribution subject to SEG license or copyright; see Terms of Use at https://library.seg.org/page/policies/terms
DOI:10.1190/geo2019-0611.1

the result of Figure 8. For a detailed illustration, only the result of a 40 m depth interval is shown. First of all, we obtained the borehole-fluid velocity of the well interval using the calibration method of Lee et al. (2016). The gamma-ray curve in panel 1 shows that the formation consists mainly of a sand-shale sequence. Panels 2 and 3 show the VD display of the LWD monopole- and quadrupole-waveform data. The Stoneley- and quadrupole-wave dispersion data were extracted from the waveform data are shown in panels 4 and 5

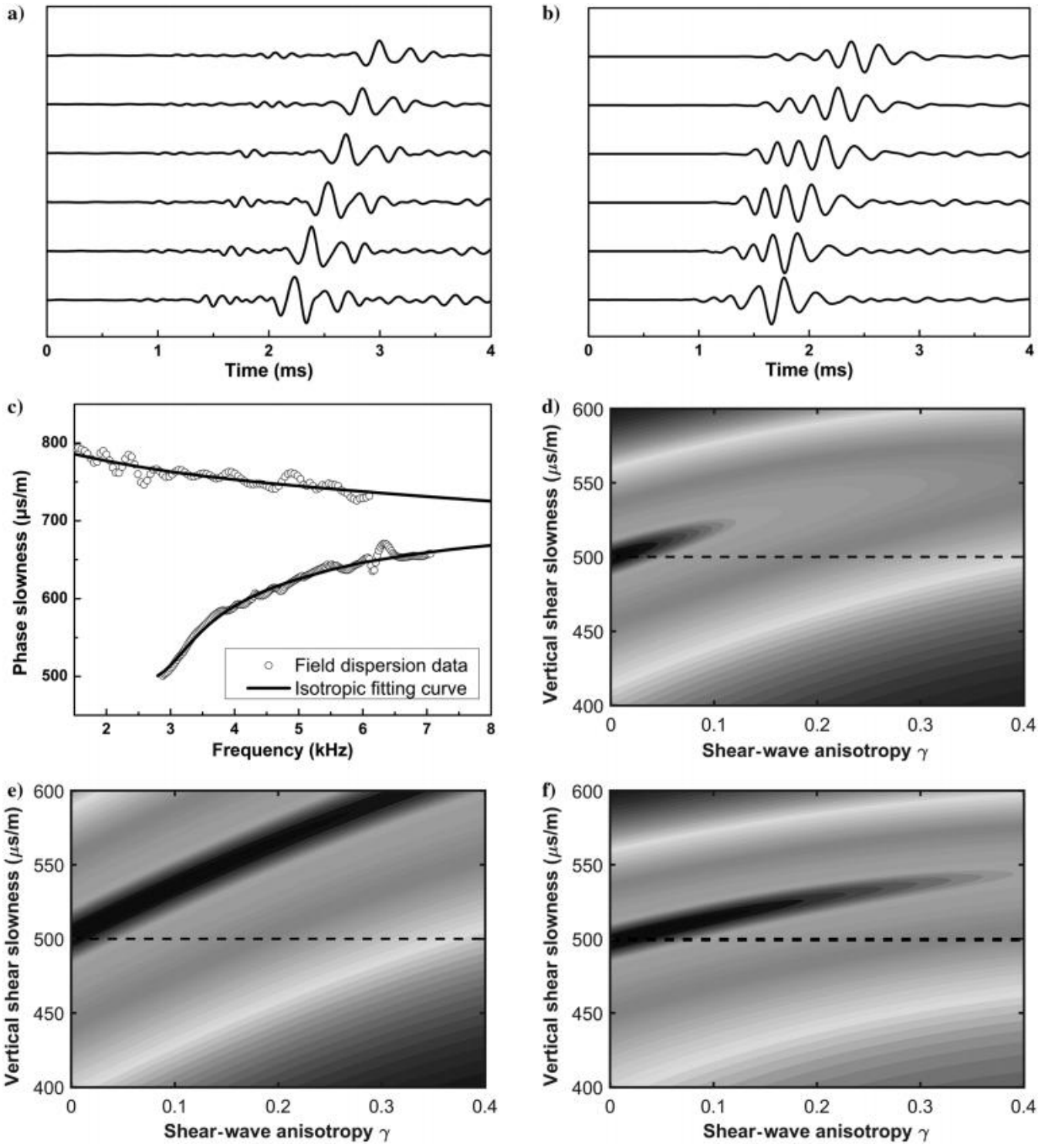


Figure 10. Detailed inversion result for an isotropic formation depth (X037m). (a and b) The LWD array Stoneley- and quadrupole-wave data, for calculating the dispersion data in (c) (circles). The solution minimum of the joint inversion (d) is at zero anisotropy. The isotropic formation dispersion curves (solid) fit with the dispersion data very well. (e and f) The objective functions for the individual Stoneley- and quadrupole-wave data.

Downloaded 08/07/20 to 218.201.114.137. Redistribution subject to SEG license or copyright; see Terms of Use at https://library.seg.org/page/policies/terms
DOI:10.1190/geo2019-0611.1

Downloaded 08/07/20 to 218.201.114.137. Redistribution subject to SEG license or copyright; see Terms of Use at https://library.seg.org/page/policies/terms
DOI:10.1190/geo2019-0611.1

(the black circles displayed at a 2 m increment), respectively. Panels 6 and 7 show the inversion results of anisotropy and vertical S-wave slowness, respectively. In the joint inversion method, the frequency ranges for the Stoneley wave (1.5–6.0 kHz) and quadrupole wave (3.0–7.0 kHz) are used, and the weighting factor λ is 0.15. An interesting result is the anisotropy profile γ for the sand-shale formation. The anisotropy is quite high ($\gamma > 20\%$) in the upper section, it becomes moderate in the middle section ($\gamma \approx 10\%$), and it diminishes in the bottom section. The result obtained using the traditional slowness time coherence (STC) method is also shown in panel 7 (the dashed curve). The comparison shows that the S-wave slowness from STC is larger than the new result due to the dispersion effect of the LWD quadrupole wave (Tang and Cheng, 2004). For quality control of the inversion results, the inversion-calculated theoretical dispersion curves are compared with the respective dispersion data in panels 4 and 5 (the red curves). The theoretical curves fit the data quite well. The goodness of the fit is shown by the QI parameter profile in panel 8, which is calculated from equation 9. The QI value of this well section is between 1% and 3%, indicating that the anisotropy model fits the data well and the inversion result is reliable.

To further validate the inversion result, a detailed inversion analysis is shown in Figure 9 for an anisotropic formation depth of X004m. The LWD array Stoneley- and quadrupole-waveform data are shown in Figure 9a and 9b, respectively, whereas the processed dispersion data are shown in Figure 9c (circles). Figure 9d shows that the VD display of the objective function has a solution minimum over the 2D parameter domain. The theoretical dispersion curves (the solid curves in Figure 9c) calculated from the inversion result fit well with the dispersion data. In comparison, the theoretical curves calculated for an isotropic formation (the dashed curves in Figure 9c) cannot fit the data, showing that the formation is indeed anisotropic. As a comparison, Figure 9e and 9f show the objective function using the individual Stoneley- and quadrupole-wave data, respectively. The features of their individual function are very similar to their synthetic data counterparts in Figure 7c and 7d. The long valleys on the VD images indicate the nonuniqueness of inverting the individual data. By joint inversion of the two data sets, the valley in Figure 9d is shortened to form a minimum at the solution point.

For comparing with this anisotropic example, the results of the same analysis for an isotropic formation depth at X037m are shown in Figure 10. The results are plotted in the same manner as their anisotropic counterparts in Figure 9, showing a marked difference compared to Figure 10. Note that the solution minimum occurs at zero anisotropy (Figure 10d). Correspondingly, the dispersion data are well fitted by the theoretical dispersion curves calculated with the isotropic formation (Figure 10c).

CONCLUSIONS

Geophysical data inversion, as exemplified by the present LWD acoustic data inversion for anisotropy, faces two typical problems. One is the multiple parameter nature of the problem, and the other is the nonuniqueness of the inversion result. Our approach to the first problem is singling out the most important parameter(s) and reducing the size of the problem. The solution to the nonuniqueness problem is combining data from different measurements that have sensitivity to the parameter(s) of interest. Using sensitivity analysis, we identified that the two shear moduli C_{44} and C_{66} are the most sensible parameters for the inversion and, by using ANNIE approximation, we reduced the five-parameter VTI problem into a two-parameter inversion problem. This approach greatly reduces the difficulty of the problem and is efficient for field data processing. In the joint inversion of the LWD Stoneley and quadrupole data sets, each data set provides complementary information that helps to reduce and/or suppress the nonuniqueness of the inversion. Thus, the joint inversion not only obtains more accurate estimates of anisotropy, but it also corrects the dispersion effect in the quadrupole wave data.

The joint inversion method developed in this study for the LWD multipole acoustic-wave data can suppress the nonuniqueness problem and improve the inversion result accuracy. For the LWD situation, the monopole Stoneley and quadrupole waves are sensitive to the formation S-wave anisotropy parameters but are inadequate to resolve the parameters using the individual wave data alone. By combining the two waves in the joint inversion, the ability to resolve the anisotropy parameters is much improved. We have validated the joint inversion method using detailed theoretical analyses and synthetic data testing. Application of the method to field LWD acoustic data processing shows that the joint inversion can simultaneously correct the dispersion effect in the quadrupole S-wave slowness estimation and obtain the formation S-wave anisotropy, thus offering an effective tool for LWD acoustic data processing.

ACKNOWLEDGMENTS

The authors thank the reviewers for their comments and suggestions that helped to improve the manuscript. This work was supported by the National Natural Science Foundation of China (grant nos. 41774138, 41804124, and 41821002), the National Key R&D Program of China (grant no. 2019YFC0605504), and the Natural Science Foundation of Shandong Province (grant no. ZR2019BD039).

DATA AND MATERIALS AVAILABILITY

Data associated with this research are confidential and cannot be released.

APPENDIX A

LWD MULTIPOLE ACOUSTIC-WAVE PROPAGATION WITH A VTI FORMATION

The wavefield for the multiple layered model shown in Figure 1 is connected by the boundary conditions at the model interfaces. An acoustic ring source is placed on the rim of the drill collar to excite the wavefield. Using the radial displacement and stress continuity condition for the solid-liquid boundary, the boundary conditions can be written as follows:

For the interface between the inner fluid annulus and the drill collar ($r = r_0$)

$$\begin{cases} u_f^{in} = u_{tool} \\ \sigma_{rrf}^{in} = \sigma_{rr}^{tool} \\ 0 = \sigma_{rz}^{tool} \\ 0 = \sigma_{r\theta}^{tool} \end{cases}; \tag{A-1}$$

For the interface between the drill collar and the outer fluid annulus ($r = r_1$)

Downloaded 08/07/20 to 218.201.114.137. Redistribution subject to SEG license or copyright; see Terms of Use at https://library.seg.org/page/policies/terms
DOI:10.1190/geo2019-0611.1

$$\begin{cases} u_{tool} = u_f^{out} + u_f^d \\ \sigma_{rr}^{tool} = \sigma_{rrf}^{out} \\ \sigma_{rz}^{tool} = 0 \\ \sigma_{r\theta}^{tool} = 0 \end{cases}; \tag{A-2}$$

For the interface between the outer fluid annulus and the VTI formation ($r = r_2$)

$$\begin{cases} u_f^{out} = u_{fm} \\ \sigma_{rrf}^{out} = \sigma_{rr}^{fm} \\ 0 = \sigma_{rz}^{fm} \\ 0 = \sigma_{r\theta}^{fm} \end{cases}; \tag{A-3}$$

Combining the above 12 equations results in the following matrix equation:

$$\{H_{ij}\}_{12\times12} \cdot \{O_j\}_{12\times1} = \{b_i\}_{12\times1}; \tag{A-4}$$

where

$$\{O_j\}_{12\times1} = \{A_n^{in}; A_n^{tool}; B_n^{tool}; C_n^{tool}; D_n^{tool}; E_n^{tool}; F_n^{tool}; A_n^{out}; B_n^{out}; B_n^{fm}; D_n^{fm}; F_n^{fm}\}^T; \tag{A-5}$$

and

$$\{b_i\}_{12\times1} = \{0; 0; 0; 0; u_f^d; 0; 0; 0; 0; 0; 0; 0\}^T. \tag{A-6}$$

The term u_f^d is the displacement of the ring source, and the specific expression is given by (Tang and Cheng, 2004)

$$u_f^d = \varepsilon_n[nK_n(fr_1)/r_1 - fK_{n+1}(fr_1)]I_n(fr_1); \tag{A-7}$$

where $\varepsilon_n = 1$ for $n = 0$ and $\varepsilon_n = 2$ for $n > 0$. The dispersion equation 3 for computing the LWD multipole wave propagation is obtained setting the determinant of equation A-4 to zero as

$$D(n; k; \omega; C_{44}; C_{66}; C_{11}; C_{13}; C_{33}; B_o; C_o; F_o) = \det(H) = 0; \tag{A-8}$$

where "det" denotes taking the determinant of the matrix H for the VTI formation. We use the following symbols to represent the combination of Bessel functions for brevity:

$$\begin{cases} X_1(x) = \frac{n}{x}I_n(x) + I_{n+1}(x) \\ X_2(x) = \frac{n(n-1)}{x}I_n(x) - I_{n+1}(x) \\ X_3(x) = \frac{1-n}{x}I_n(x) - I_{n+1}(x) \\ X_4(x) = \left[1 + \frac{2n(n-1)}{x^2}\right]I_n(x) - \frac{2}{x}I_{n+1}(x) \end{cases}; \tag{A-9}$$

$$\begin{cases} Y_1(x) = \frac{n}{x}K_n(x) - K_{n+1}(x) \\ Y_2(x) = \frac{n(n-1)}{x}K_n(x) + K_{n+1}(x) \\ Y_3(x) = \frac{1-n}{x}K_n(x) + K_{n+1}(x) \\ Y_4(x) = \left[1 + \frac{2n(n-1)}{x^2}\right]K_n(x) + \frac{2}{x}K_{n+1}(x) \end{cases}; \tag{A-10}$$

Matrix H contains the following elements (all unlisted elements are 0):

$$\begin{aligned}
&H_{1;1} = -fX_1(fr_0);\ H_{1;2} = pX_1(pr_0);\ H_{1;3} = pY_1(pr_0);\ H_{1;4} = \frac{n}{r_0}I_n(sr_0);\\
&H_{1;5} = \frac{n}{r_0}K_n(sr_0);\ H_{1;6} = iksX_1(sr_0);\ H_{1;7} = iksY_1(sr_0);\\
&H_{2;1} = \rho_f\omega^2 I_n(fr_0);\ H_{2;2} = \mu^t[2k^2 - (k_s^t)^2]I_n(pr_0) + \frac{2p\mu^t}{r_0}X_2(pr_0);\\
&H_{2;3} = \mu^t[2k^2 - (k_s^t)^2]K_n(pr_0) + \frac{2p\mu^t}{r_0}Y_2(pr_0);\ H_{2;4} = -\frac{2\mu^t ns}{r_0}X_3(sr_0);\\
&H_{2;5} = -\frac{2\mu^t ns}{r_0}Y_3(sr_0);\ H_{2;6} = 2ik\mu^t s[sI_n(sr_0) + \frac{1}{r_0}X_2(sr_0)];\\
&H_{2;7} = 2ik\mu^t s[sK_n(sr_0) + \frac{1}{r_0}Y_2(sr_0)];\ H_{3;2} = \frac{2pn\mu^t}{r_0}X_3(pr_0);\\
&H_{3;3} = \frac{2pn\mu^t}{r_0}Y_3(pr_0);\ H_{3;4} = -s^2\mu^t X_4(sr_0);\ H_{3;5} = -s^2\mu^t Y_4(sr_0);\\
&H_{3;6} = \frac{2iksn\mu^t}{r_0}X_3(sr_0);\ H_{3;7} = \frac{2iksn\mu^t}{r_0}Y_3(sr_0);\ H_{4;2} = 2ikp\mu^t X_1(pr_0);\\
&H_{4;3} = 2ikp\mu^t Y_1(pr_0);\ H_{4;4} = \frac{ikn\mu^t}{r_0}I_n(sr_0);\ H_{4;5} = \frac{ikn\mu^t}{r_0}K_n(sr_0);\\
&H_{4;6} = -(k^2+s^2)s\mu^t X_1(sr_0);\ H_{4;7} = -(k^2+s^2)s\mu^t Y_1(sr_0);\\
&H_{5;2} = pX_1(pr_1);\ H_{5;3} = pY_1(pr_1);\ H_{5;4} = \frac{n}{r_0}I_n(sr_1);\ H_{5;5} = \frac{n}{r_0}K_n(sr_1);\\
&H_{5;6} = iksX_1(sr_1);\ H_{5;7} = iksY_1(sr_1);\ H_{5;8} = -fX_1(fr_1);\\
&H_{5;9} = -fY_1(fr_1);\ H_{6;2} = \mu^t[2k^2 - (k_s^t)^2]I_n(pr_1) + \frac{2p\mu^t}{r_1}X_2(pr_1);\\
&H_{6;3} = \mu^t[2k^2 - (k_s^t)^2]K_n(pr_1) + \frac{2p\mu^t}{r_1}Y_2(pr_1);\ H_{6;4} = -\frac{2\mu^t ns}{r_0}X_3(sr_1);\\
&H_{6;5} = -\frac{2\mu^t ns}{r_0}Y_3(sr_1);\ H_{6;6} = 2ik\mu^t s\left[sI_n(sr_1) + \frac{1}{r_1}X_2(sr_1)\right];\\
&H_{6;7} = 2ik\mu^t s\left[sK_n(sr_1) + \frac{1}{r_1}Y_2(sr_1)\right];\ H_{6;8} = \rho_f\omega^2 I_n(fr_1);\\
&H_{6;9} = \rho_f\omega^2 K_n(fr_1);\ H_{7;2} = \frac{2pn\mu^t}{r_1}X_3(pr_1);\ H_{7;3} = \frac{2pn\mu^t}{r_1}Y_3(pr_1);\\
&H_{7;4} = -s^2\mu^t X_4(sr_1);\ H_{7;5} = -s^2\mu^t Y_4(sr_1);\ H_{7;6} = \frac{2iksn\mu^t}{r_1}X_3(sr_1);\\
&H_{7;7} = \frac{2iksn\mu^t}{r_1}Y_3(sr_1);\ H_{8;2} = 2ikp\mu^t X_1(pr_1);\ H_{8;3} = 2ikp\mu^t Y_1(pr_1);\\
&H_{8;4} = \frac{ikn\mu^t}{r_1}I_n(sr_1);\ H_{8;5} = \frac{ikn\mu^t}{r_1}K_n(sr_1);\ H_{8;6} = -(k^2+s^2)s\mu^t X_1(sr_1);\\
&H_{8;7} = -(k^2+s^2)s\mu^t Y_1(sr_1);\ H_{9;8} = -fX_1(fr_2);\ H_{9;9} = -fY_1(fr_2);\\
&H_{9;10} = (1+ika')q_P Y_1(q_P r_2);\ H_{9;11} = \frac{n}{r_2}K_n(q_{SH}r_2);\\
&H_{9;12} = (b'+ik)q_{SV}Y_1(q_{SV}r_2);\ H_{10;8} = \rho_f\omega^2 I_n(fr_2);\ H_{10;9} = \rho_f\omega^2 K_n(fr_2);\\
&H_{10;10} = [C_{11}q_P^2 - C_{13}k^2 + (C_{11}-C_{13})ika'q_P^2]K_n(q_P r_2)\\
&\qquad + \frac{2C_{66}q_P}{r_2}(1+ika')Y_2(q_P r_2);\\
&H_{10;11} = -\frac{2C_{66}nq_{SH}}{r_2}Y_3(q_{SH}r_2);\\
&H_{10;12} = [(C_{11}q_{SV}^2 - C_{13}k^2)b' + (C_{11}-C_{13})ikq_{SV}^2]K_n(q_{SV}r_2)\\
&\qquad + \frac{2C_{66}q_{SV}}{r_2}(ik+b')Y_2(q_{SV}r_2);\\
&H_{11;10} = \frac{2C_{66}nq_P}{r_2}(1+ika')Y_3(q_P r_2);\ H_{11;11} = -C_{66}q_{SH}^2 Y_4(q_{SH}r_2);\\
&H_{11;12} = \frac{2C_{66}nq_{SV}}{r_2}(b'+ik)Y_3(q_{SV}r_2);\\
&H_{12;10} = C_{44}q_P[2ik - a'(k^2+q_P^2)]Y_1(q_P r_2);\ H_{12;11} = \frac{iknC_{44}}{r_2}K_n(q_{SH}r_2);\\
&H_{12;12} = -C_{44}q_{SV}[(k^2+q_{SV}^2) - 2ikb']Y_1(q_{SV}r_2);
\end{aligned} \tag{A-11}$$

Downloaded 08/07/20 to 218.201.114.137. Redistribution subject to SEG license or copyright; see Terms of Use at https://library.seg.org/page/policies/terms
DOI:10.1190/geo2019-0611.1

where I and K are the first- and second-kind modified Bessel functions, respectively; v_f is the fluid velocity; v_P^t and v_S^t are the P- and S-wave velocities of the drill collar, respectively; $k_f = \omega/v_f$ is the fluid wavenumber; $k_P^t = \omega/v_P^t$ and $k_S^t = \omega/v_S^t$ are the P- and S-wave wavenumbers of the drill collar, respectively; $f = \sqrt{k^2 - (k_f)^2}$ is the radial wavenumber of the fluid; $p = \sqrt{k^2 - (k_P^t)^2}$ and $s = \sqrt{k^2 - (k_S^t)^2}$ are the P- and S-wave radial wavenumbers of the drill collar, respectively; and $\mu^t = \rho_t \cdot (v_S^t)^2$ and ρ_t are the shear modulus and density of the drill collar, respectively. The radial wavenumbers for the formation quasi-P- and quasi-S-waves are given by

$$\begin{cases} q_P = \omega\sqrt{\frac{-V+\sqrt{V^2-4UW}}{2U}} \\ q_{SV} = \omega\sqrt{\frac{-V-\sqrt{V^2-4UW}}{2U}}; \\ q_{SH} = \sqrt{\frac{c_{44}k^2-\rho\omega^2}{C_{66}}} \end{cases} \tag{A-12}$$

where the symbols U, V, and W are defined as

$$\begin{cases} U = C_{11}C_{44} \\ V = \rho(C_{11}+C_{44}) - (C_{11}C_{33} - C_{13}^2 - 2C_{13}C_{44})(k^2/\omega^2) : \\ W = C_{33}C_{44}(\rho/C_{44} - k^2/\omega^2)(\rho/C_{33} - k^2/\omega^2) \end{cases} \tag{A-13}$$

The S- to P-wave coupling parameter a' and the P- to S-wave coupling parameter b' are given by

$$\begin{cases} a' = -\frac{1}{ik}\frac{(C13+2C44)k^2-C11q_P^2-\rho\omega^2}{C44k^2-(C11-C13-C44)q_P^2-\rho\omega^2} \\ b' = -ik\frac{C44k^2-(C11-C13-C44)q_{SV}^2-\rho\omega^2}{(C13+2C44)k^2-C11q_{SV}^2-\rho\omega^2} : \end{cases} \tag{A-14}$$

REFERENCES

Briggs, V. A., 2006, A comparison of logging while drilling (LWD) and wireline acoustic measurements: Ph.D. thesis, Massachusetts Institute of Technology.

Cui, Z. W., 2004, Theoretical and numerical study of modified Biot's models, acoustoelectric well logging and acoustic logging while drilling excited by multipole acoustic sources: Ph.D. thesis, Jilin University.

He, X., and H. S. Hu, 2009, Borehole flexural modes in transversely isotropic formations: Low-frequency asymptotic velocity: Geophysics, 74, no. 4, E149–E158, doi: 10.1190/1.3141442.

He, X., H. S. Hu, and W. Guan, 2010, Fast and slow flexural waves in a deviated borehole in homogeneous and layered anisotropic formations: Geophysical Journal International, 181, 417–426, doi: 10.1111/j.1365-246X.2010.04503.x.

Lee, S. Q., X. M. Tang, Y. D. Su, and C. X. Zhuang, 2016, Model-based dispersive processing of borehole dipole wave data using an equivalent-tool theory: Geophysics, 81, no. 1, D35–D43, doi: 10.1190/geo2015-0210.1.

Lee, X. Q., H. Chen, X. He, X. M. Wang, and J. S. Cong, 2013, Analyses on mode waves of acoustic logging while drilling in transversely isotropic formations: Chinese Journal of Geophysics, 56, 3212–3222, doi: 10.6038/cjg20130933.

Schmitt, D. P., 1989, Acoustic multipole logging in transversely isotropic poroelastic formations: The Journal of Acoustical Society of America, 86, 2397–2421, doi: 10.1121/1.398448.

Schoenberg, M., F. Muir, and C. M. Sayers, 1996, Introducing ANNIE: A simple three-parameter anisotropic velocity model for shales: Journal of Seismic Exploration, 5, 35–49.

Sinha, B. K., and E. Simsek, 2010, Sonic logging in deviated wellbores in the presence of a drill collar: 80th Annual International Meeting, SEG, Expanded Abstracts, 553–557, doi: 10.1190/1.3513843.

Sinha, B. K., E. Simsek, and S. Asvadurov, 2009, Influence of a pipe tool on borehole modes: Geophysics, 74, no. 3, E111–E123, doi: 10.1190/1.3085644.

Su, Y. D., C. Jiang, C. X. Zhuang, S. Xu, and X. M. Tang, 2016, Joint inversion of logging-while-drilling multipole acoustic data to determine P- and S-wave velocities in unconsolidated slow formations: Geophysics, 81, no. 5, D553–D560, doi: 10.1190/geo2016-0133.1.

Tang, X. M., 2003, Determining formation shear-wave transverse isotropy from borehole Stoneley-wave measurements: Geophysics, 68, 118–126, doi: 10.1190/1.1543199.

Tang, X. M., and C. H. Cheng, 2004, Quantitative borehole acoustic methods: Elsevier Science Publishing Company Inc.

Tang, X. M., V. Dubinsky, and D. J. Patterson, 2006, Development of a low-frequency LWD quadrupole shear-wave technology to improve quality of formation shear velocity measurement: Annual Technical Conference and Exhibition, SPE, Extended Abstracts, doi: 10.2118/102335-MS.

Tang, X. M., V. Dubinsky, T. Wang, A. Bolshakov, and D. Patterson, 2003, Shear-velocity measurement in the logging-while-drilling environment: Modeling and field evaluations: Petrophysics, 44, 79–90.

Tang, X. M., and D. J. Patterson, 2010, Mapping formation radial shear-wave velocity variation by a constrained inversion of borehole flexural-wave dispersion data: Geophysics, 75, no. 6, E183–E190, doi: 10.1190/1.3502664.

Thomsen, L., 1986, Weak elastic anisotropy: Geophysics, 51, 1954–1966, doi: 10.1190/1.1442051.

Wang, H., and G. Tao, 2011, Wave field simulation and data acquisition scheme analysis for LWD acoustic tools in very slow formations: Geophysics, 76, no. 3, E59–E68, doi: 10.1190/1.3552929.

Wang, R. J., and W. X. Qiao, 2015, Numerical study on quadrupole acoustic LWD in VTI formations: Chinese Journal of Geophysics, 58, 2862–2872, doi: 10.6038/cjg20150820.

Wei, J. Q., X. He, H. Chen, and X. M. Wang, 2018, Inversion of anisotropy in a TTI stratum using quadrupole acoustic LWD and multimode acquisition: Chinese Journal of Geophysics, 61, 792–802, doi: 10.6038/cjg2018L0410.

White, J. E., and C. Tongtaow, 1981, Cylindrical waves in transversely isotropic media: The Journal of Acoustical Society of America, 70, 1147–1155, doi: 10.1121/1.386946.

Xu, S., X. M. Tang, Y. D. Su, S. Q. Lee, and C. X. Zhuang, 2017, Determining formation S-wave transverse isotropy from borehole flexural-wave dispersion data: Geophysics, 82, no. 2, D47–D55, doi: 10.1190/geo2016-0223.1.

Xu, S., X. M. Tang, Y. D. Su, and C. X. Zhuang, 2018c, Determining formation shear wave transverse isotropy jointly from borehole Stoneley- and flexural-wave data: Chinese Journal of Geophysics, 61, 5105–5114, doi: 10.6038/cjg2018L0521.

Xu, S., X. M. Tang, C. Torres-Verdín, and Y. D. Su, 2018a, Seismic shear wave anisotropy in cracked rocks and an application to hydraulic fracturing: Geophysical Research Letters, 45, 5390–5397, doi: 10.1029/2018GL077931.

Xu, S., C. X. Zhuang, Y. D. Su, Y. K. Liu, Z. P. Zhang, S. J. Guo, and X. M. Tang, 2018b, Acoustic source characterization for a logging while drilling tool: Theoretical and experimental modeling: The Journal of the Acoustical Society of America, 144, EL178–EL184, doi: 10.1121/1.5053105.

饶博，唐晓明，苏远大. 2022. 横向各向同性地层随钻多极子测井声场的分波分析与特性研究. 地球物理学报，65(8)：3198-3212，doi：10.6038/cjg2022O0423.

Rao B, Tang X M, Su Y D. 2022. Theoretical calculation and mechanism analysis for component waves of acoustic logging while drilling in transversely isotropic formations. *Chinese J. Geophys.* (in Chinese), 65(8): 3198-3212, doi: 10.6038/cjg2022O0423.

横向各向同性地层随钻多极子测井声场的分波分析与特性研究

饶博[1,2]，唐晓明[1,2,3]，苏远大[1,2,3]*

1 中国石油大学(华东)地球科学与技术学院，青岛 266580

2 中国石油大学(华东)深层油气重点实验室，青岛 266580

3 青岛海洋科学与技术试点国家实验室，青岛 266580

摘要 随钻声场在各向异性地层中的传播一直是随钻声波测井的重要课题.该问题中钻铤与井孔和地层的相互作用极大地影响着声场，特别是系统中的模式波的传播特征.因此，本文采用分波计算法来详细地研究在横向各向同性(VTI)地层中随钻多极子声波的传播规律，将声场全波分解成来自波数域中的奇异点(包括支点和极点)的分波的贡献，以此模拟分析了声场中各个分波的传播特征，包括模式波在频域中的频散、激发响应及时域中的分波波形.结果表明：在快速 VTI 地层中，钻铤的存在使得单极伪瑞利波和二阶四极地层螺旋波的频散大为降低，可以此来测量地层垂直向横波速度；慢速 VTI 地层中仅存在单一四极地层螺旋波，其低频速度为地层垂直向横波速度.值得注意的是，在各向异性参数满足 $\delta > \varepsilon + c_{44}/2c_{33}$ 的地层中，上述模式波的低频截止速度均小于地层的垂向横波速度，这一结果与已知的裸眼井情况一致.

关键词 横向各向同性；随钻声波测井；频散；分波；横波速度

doi：10.6038/cjg2022O0423 **中图分类号** P631 **收稿日期** 2020-10-30，2022-06-27 收修定稿

Theoretical calculation and mechanism analysis for component waves of acoustic logging while drilling in transversely isotropic formations

RAO Bo[1,2], TANG XiaoMing[1,2,3], SU YuanDa[1,2,3]*

1 *School of Geosciences, China University of Petroleum (East China), Qingdao* 266580, *China*

2 *Key Laboratory of Deep Oil and Gas, China University of Petroleum (East China), Qingdao* 266580, *China*

3 *Qingdao National Laboratory for Marine Science and Technology, Qingdao* 266580, *China*

Abstract The acoustic wave propagation in the presence of a drill collar and an anisotropic formation has always been an important topic of acoustic Logging While Drilling (LWD). In this subject, the interaction between the drill collar and the borehole and the formation greatly affects the wave propagation characteristics, especially those of the guided wave modes in the system. To tackle the problem, this work uses an analytical wave separation method to calculate the detailed propagation characteristics of each wave component of the multipole LWD wavefield in a Vertical Transversely Isotropic (VTI) formation, analyzing the wave amplitude excitation, velocity dispersion, and the time-domain waveform characteristics. The results show that in a

基金项目 国家自然科学基金(41821002，42074137)，国家重点研发计划(2019YFC0605504)和中国石油重大科技项目(ZD2019-183-004)联合资助.

第一作者简介 饶博，男，1995 年生，博士研究生，主要从事声波测井理论研究. E-mail：1004062422@qq.com

***通讯作者** 苏远大，男，1978 年生，博士，教授，主要从事声波测井理论、方法及处理研究. E-mail：syuanda@sina.com

fast VTI formation, the presence of drill collars greatly reduces the dispersion of monopole pseudo Rayleigh waves and second-order quadrupole screw waves, allowing for measuring the formation vertical shear-wave velocity using these wave modes. In a slow VTI formation, only a single formation quadrupole wave is excited, whose low-frequency velocity is the formation vertical shear-wave velocity. Worthwhile to mention is that, in formations whose anisotropic parameters satisfy the condition $\delta > \varepsilon + c_{44}/2c_{33}$, the low-frequency cut-off velocity of the above-mentioned LWD acoustic wave modes are all lower than the formation vertical shear-wave velocity. This result is consistent with that obtained in an open-hole condition.

Keywords Transversely isotropy; Acoustic logging-while drilling; Dispersion; Component-wave; Shear velocity

0　引言

近年来,深水、深层钻井逐渐增多,水平井及大斜度井的数量明显增加,因此对随钻测井技术的需求更加迫切.在随钻测井过程中,地层纵横波速度的获取对地层参数的反演以及指导水力压裂有着十分重要的作用,对此测井界研发了单极子纵波(Schmitt,1988;Minear et al.,1995)和四极子横波(Tang et al.,2002)的随钻多极子声波测井技术.随着以页岩油气为代表的非常规油气资源勘探开发的深入(吕庆达等,2018),地层各向异性对随钻声波测量的影响变得十分重要.为此胡恒山和何晓(2009)详细推导了横向各向同性介质中的波动方程,求解了 VTI 地层中裸眼井声波的频散方程,研究了伪瑞利波、弯曲波以及螺旋波的频散特征.何晓等(2010)针对 VTI 地层给出了满足辐射条件的井孔声场复数解析函数的单值定义,据此进行了裸眼井多极子声场的分波计算.在随钻声波测井中,李希强等(2013)建立随钻 VTI 声波测井模型,通过模式分析法研究了 TI 地层中随钻井孔内一些模式波的传播特性,指出与裸眼井的情况类似,随钻斯通利波也可以用于反演地层水平向横波速度;许松(2015)在此基础上提出一种同时反演地层水平向和垂直向横波速度的联合反演方法,进而求取地层的各向异性;王瑞甲和乔文孝(2015)进一步研究了 TI 地层中各向异性对随钻四极子声波测井的影响,指出地层各向异性对地层四极子模式波的影响较大,建议在实际数据处理时,考虑采用基于数据驱动的频散校正.

综上所述,研究随钻条件下 VTI 地层的声传播规律具有十分重要的意义.但由于 VTI 地层随钻声场中钻铤模式波与地层模式波耦合复杂,难以从全波波形中直接区分.针对这一问题,本文采用分波计算的方法来深入探究地层模式波的传播特征.为此分别对单极、偶极以及四极子声源激发的随钻声场进行了分波与全波计算;通过与电缆测井的结果比较,考察了钻铤对地层模式波的影响,发现在少数参数满足 $\delta > \varepsilon + c_{44}/2c_{33}$ 的地层中,伪瑞利波、弯曲波及四极子螺旋波的截止频率速度小于真实地层垂向横波速度,应结合其他各向异性参数来确定该横波速度.计算结果为各向异性地层中随钻声波测井解释和地层评价提供了理论依据.

1　横向各向同性地层随钻多极子声场理论

图 1 给出了横向各向同性(VTI)地层中随钻声波测井模型示意图,分别为模型三维图(图 1a)和井孔横截面图(图 1b),由内到外依次是钻铤内流体、钢钻铤、钻铤与地层之间的流体环以及井外 VTI 地层,图中 r_c 代表钻铤内径,r_b 代表钻铤外径,r_a 代表井孔半径.

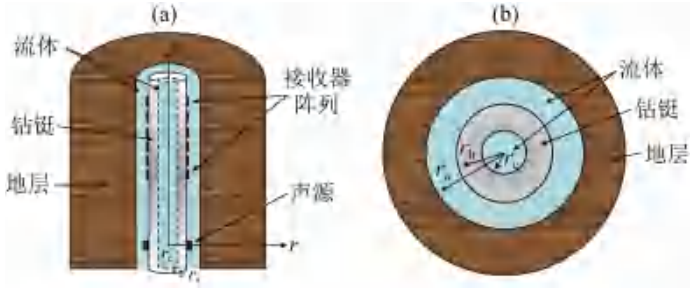


图 1　VTI 地层中随钻声波测井模型(a)及井孔截面图(b)

Fig. 1　Schematic diagram of acoustic model for logging while drilling in a VTI formation (a) and the cross sectional view of the model (b)

1.1　井孔内含钻铤的声场

根据柱状分层介质声场理论(唐晓明和郑传汉,2004;崔志文,2004),钻铤位移势 Φ^{tool}、χ^{tool} 和 Γ^{tool} 及其内外层流体的位移势 Φ^{in}、Φ^{out} 表达式为:

$$\begin{cases}\Phi^{\text{tool}}(k,\omega,r,\theta) = [A_n^{\text{tool}} I_n(p_{\text{tool}} r) + B_n^{\text{tool}} K_n(p_{\text{tool}} r)]\cos[n(\theta-\phi)]\mathrm{e}^{\mathrm{i}kz},\\ \chi^{\text{tool}}(k,\omega,r,\theta) = [C_n^{\text{tool}} I_n(s_{\text{tool}} r) + D_n^{\text{tool}} K_n(s_{\text{tool}} r)]\sin[n(\theta-\phi)]\mathrm{e}^{\mathrm{i}kz},\\ \Gamma^{\text{tool}}(k,\omega,r,\theta) = [E_n^{\text{tool}} I_n(s_{\text{tool}} r) + F_n^{\text{tool}} K_n(s_{\text{tool}} r)]\cos[n(\theta-\phi)]\mathrm{e}^{\mathrm{i}kz},\\ \Phi^{\text{in}}(k,\omega,r,\theta) = A_n^{\text{in}} I_n(fr)\cos[n(\theta-\phi)]\mathrm{e}^{\mathrm{i}kz},\\ \Phi^{\text{out}}(k,\omega,r,\theta) = [A_n^{\text{out}} I_n(fr) + B_n^{\text{out}} K_n(fr)]\cos[n(\theta-\phi)]\mathrm{e}^{\mathrm{i}kz},\end{cases} \tag{1}$$

式中 $A_n^{\text{tool}}(B_n^{\text{tool}})$、$C_n^{\text{tool}}(D_n^{\text{tool}})$、$E_n^{\text{tool}}(F_n^{\text{tool}})$ 分别是钻铤中入射(出射)纵波、SH 横波以及 SV 横波的振幅系数，A_n^{in}、$A_n^{\text{out}}(B_n^{\text{out}})$ 分别为钻铤内外流体层纵波的振幅系数，$f=(k^2-k_{\text{f}}^2)^{1/2}$ 为流体径向波数，k 为轴向波数，$k_{\text{f}}=\omega/v_{\text{f}}$ 为流体波数，ω 是圆频率，v_{f} 是流体速度；$p_{\text{tool}}=(k^2-k_{\text{p}}^2)^{1/2}$ 和 $s_{\text{tool}}=(k^2-k_{\text{s}}^2)^{1/2}$ 分别表示钻铤纵波的径向波数和钻铤横波的径向波数，$k_{\text{p}}=\omega/v_{\text{p}}^{\text{tool}}$ 和 $k_{\text{s}}=\omega/v_{\text{s}}^{\text{tool}}$ 分别表示纵波和横波波数，$v_{\text{p}}^{\text{tool}}$、$v_{\text{s}}^{\text{tool}}$ 分别表示钻铤纵波、横波速度，I_n、K_n 表示第一类和第二类 n 阶变型贝塞尔函数，分别描述了从外向内传播的声波与从内向外传播的声波，n 为多极子阶数，ϕ 为声源激发方向与接收器接收方向的夹角.

根据柱坐标系下位移分量与势函数的关系和应变-位移关系以及胡克定律可推导出钻铤及其内外流体层的位移和应力场表达式 $\boldsymbol{u}^{\text{tool}}$、$\sigma_{rr}^{\text{tool}}$、$\sigma_{rz}^{\text{tool}}$、$\sigma_{r\theta}^{\text{tool}}$、$\boldsymbol{u}_{\text{f}}^{\text{in}}$、$\sigma_{rf}^{\text{in}}$、$\boldsymbol{u}_{\text{f}}^{\text{out}}$、$\sigma_{rf}^{\text{out}}$，具体表达式参考论文(崔志文，2004).

1.2 井孔外 VTI 地层的声场

TI 固体的弹性性质由 c_{11}，c_{13}，c_{33}，c_{44}，c_{66} 五个弹性常数来表达，若 TI 介质对称轴与井轴平行，则柱坐标系下的应力-应变关系为：

$$\begin{pmatrix}\sigma_{rr}\\ \sigma_{\theta\theta}\\ \sigma_{zz}\\ \sigma_{\theta z}\\ \sigma_{rz}\\ \sigma_{r\theta}\end{pmatrix} = \begin{pmatrix} c_{11} & c_{11}-2c_{66} & c_{13} & 0 & 0 & 0\\ c_{11}-2c_{66} & c_{11} & c_{13} & 0 & 0 & 0\\ c_{13} & c_{13} & c_{33} & 0 & 0 & 0\\ 0 & 0 & 0 & c_{44} & 0 & 0\\ 0 & 0 & 0 & 0 & c_{44} & 0\\ 0 & 0 & 0 & 0 & 0 & c_{66}\end{pmatrix}\begin{pmatrix}e_{rr}\\ e_{\theta\theta}\\ e_{zz}\\ e_{\theta z}\\ e_{rz}\\ e_{r\theta}\end{pmatrix}, \tag{2}$$

其中 σ_{ij} 和 $e_{ij}(i,j=r,\theta,z)$ 分别是 TI 固体中的应力和应变.

根据赫姆霍兹弹性位移分解理论，地层中位移场 $\boldsymbol{u}_{\text{s}}^{\text{VTI}}$ 可分别用一个无旋势函数 Φ^{VTI} 和两个无散势函数 χ^{VTI} 和 Γ^{VTI} 来表示，具体表达式为：

$$\boldsymbol{u}_{\text{s}}^{\text{VTI}} = \nabla\Phi^{\text{VTI}} + \nabla\times\chi^{\text{VTI}}\boldsymbol{j}_z + \nabla\times\nabla\times\Gamma^{\text{VTI}}\boldsymbol{j}_z, \tag{3}$$

式中，Φ^{VTI}、χ^{VTI}、Γ^{VTI} 分别表示固体中纵波、SH 横波以及 SV 横波的势函数；$\boldsymbol{j}_z$ 为轴向单位矢量.

将式(3)代入弹性波动方程并且结合位移-应变关系以及上述 TI 介质的本构关系得到对应于三个位移势函数 Φ^{VTI}、χ^{VTI}、Γ^{VTI} 的三个波动方程，具体表达式为：

$$\begin{cases} c_{11}\nabla^2\Phi^{\text{VTI}} + (c_{13}+2c_{44}-c_{11})\dfrac{\partial^2\Phi^{\text{VTI}}}{\partial z^2} + \rho\omega^2\Phi^{\text{VTI}} + \\ \qquad \dfrac{\partial}{\partial z}\left[(c_{11}-c_{13}-c_{44})\nabla^2\Gamma^{\text{VTI}} + (c_{13}+2c_{44}-c_{11})\dfrac{\partial^2\Gamma^{\text{VTI}}}{\partial z^2} + \rho\omega^2\Gamma^{\text{VTI}}\right] = 0,\\ \dfrac{\partial}{\partial z}\left[(c_{13}+2c_{44})\nabla^2\Phi^{\text{VTI}} + (c_{33}-c_{13}-2c_{44})\dfrac{\partial^2\Phi^{\text{VTI}}}{\partial z^2} + \rho\omega^2\Phi^{\text{VTI}}\right] + \\ \qquad \left(\dfrac{\partial^2}{\partial z^2}-\nabla^2\right)\left[c_{44}\nabla^2\Gamma^{\text{VTI}} + (c_{33}-c_{13}-2c_{44})\dfrac{\partial^2\Gamma^{\text{VTI}}}{\partial z^2} + \rho\omega^2\Gamma^{\text{VTI}}\right] = 0,\\ c_{66}\nabla^2\chi^{\text{VTI}} + (c_{44}-c_{66})\dfrac{\partial^2\chi^{\text{VTI}}}{\partial z^2} + \rho\omega^2\chi^{\text{VTI}} = 0,\end{cases} \tag{4}$$

方程组中前两个是 P 波和 SV 横波的耦合波动方程，第三个是纯 SH 横波的波动方程，与 P-SV 波动不耦合.

将式(1)固体介质中 P、SH 和 SV 波势函数的通解代入式(4)中可得到 VTI 地层中以这三个波的振幅系数 $(B_n^{\text{VTI}}, D_n^{\text{VTI}}, F_n^{\text{VTI}})$ 为未知系数的线性方程组.根据该方程组的非零解得到式(5)、(6)，其解给出这三个波的径向波数 q，式(5)、(6)为：

$$c_{66}q^2 - c_{44}k^2 + \rho\omega^2 = 0, \tag{5}$$

$$(q^2 - k^2)(Uq^4 + V\omega^2 q^2 + W\omega^4) = 0, \tag{6}$$

其中:

$$\begin{cases} U = c_{11}c_{44}, \\ V = \rho(c_{11} + c_{44}) - (c_{11}c_{33} - c_{13}^2 - 2c_{13}c_{44})(k^2/\omega^2), \\ W = c_{33}c_{44}(\rho/c_{44} - k^2/\omega^2)(\rho/c_{33} - k^2/\omega^2). \end{cases}$$

式(5)只与 SH 横波有关,其解为:

$$q = q_{\mathrm{SH}} = \sqrt{\frac{c_{44}k^2 - \rho\omega^2}{c_{66}}}. \tag{7}$$

式(6)为两个因式的乘积,第一个因式无意义,其解不代表任何波动;第二个因式代表了 P 波和 SV 横波的耦合,二者的解分别为:

$$\begin{cases} q = q_{\mathrm{P}} = \omega\sqrt{\dfrac{-V + \sqrt{V^2 - 4UW}}{2U}}, \\ q = q_{\mathrm{SV}} = \omega\sqrt{\dfrac{-V - \sqrt{V^2 - 4UW}}{2U}}. \end{cases} \tag{8}$$

将式(7)、(8)代入式(1)地层波势函数的通解,得到其解析表达式:

$$\begin{cases} \Phi^{\mathrm{VTI}}(k,\omega,r,\theta) = \left[B_n^{\mathrm{VTI}}K_n(q_{\mathrm{P}}r) + b'F_n^{\mathrm{VTI}}K_n(q_{\mathrm{SV}}r)\right]\cos[n(\theta-\phi)]\mathrm{e}^{\mathrm{i}kz}, \\ \chi^{\mathrm{VTI}}(k,\omega,r,\theta) = D_n^{\mathrm{VTI}}K_n(q_{\mathrm{SH}}r)\sin[n(\theta-\phi)]\mathrm{e}^{\mathrm{i}kz}, \\ \Gamma^{\mathrm{VTI}}(k,\omega,r,\theta) = \left[a'B_n^{\mathrm{VTI}}K_n(q_{\mathrm{P}}r) + F_n^{\mathrm{VTI}}K_n(q_{\mathrm{SV}}r)\right]\cos[n(\theta-\phi)]\mathrm{e}^{\mathrm{i}kz}, \end{cases} \tag{9}$$

系数 a' 和 b' 由式(10)给出,其中 ρ 为地层密度:

$$\begin{cases} a' = \dfrac{\mathrm{i}}{k}\dfrac{(c_{13}+2c_{44})k^2 - c_{11}q_{\mathrm{p}}^2 - \rho\omega^2}{c_{44}k^2 - (c_{11}-c_{13}-c_{44})q_{\mathrm{p}}^2 - \rho\omega^2}, \\ b' = -\mathrm{i}k\dfrac{c_{44}k^2 - (c_{11}-c_{13}-c_{44})q_{\mathrm{sv}}^2 - \rho\omega^2}{(c_{13}+2c_{44})k^2 - c_{11}q_{\mathrm{sv}}^2 - \rho\omega^2}. \end{cases} \tag{10}$$

在此基础上得到 TI 地层的位移、应变分量,根据式(2)求得应力分量,具体表达式见附录 A.

1.3　边界条件

以上理论推导给出了图 1 所示模型各部分的声场,现将声场由界面处的边界条件衔接;柱坐标下固、液界面的边界条件是径向位移和应力连续和切向应力为零(唐晓明和郑传汉,2004).参考郑晓波(2017)论文,通过径向应力连续的方式将位于钻铤外表面的声压源 p^{s} 引入随钻声场,以实现声场的激发.

钻铤内流体和钻铤界面($r=r_{\mathrm{c}}$)处:

$$\begin{cases} u_{rf}^{\mathrm{in}} = u_r^{\mathrm{tool}}, \\ \sigma_{rrf}^{\mathrm{in}} = \sigma_{rr}^{\mathrm{tool}}, \\ 0 = \sigma_{rz}^{\mathrm{tool}}, \\ 0 = \sigma_{r\theta}^{\mathrm{tool}}. \end{cases} \tag{11}$$

钻铤和钻铤外流体界面($r=r_{\mathrm{b}}$)处:

$$\begin{cases} u_r^{\mathrm{tool}} = u_{rf}^{\mathrm{out}}, \\ \sigma_{rr}^{\mathrm{tool}} = \sigma_{rrf}^{\mathrm{out}} + p^{\mathrm{s}}, \\ \sigma_{rz}^{\mathrm{tool}} = 0, \\ \sigma_{r\theta}^{\mathrm{tool}} = 0. \end{cases} \tag{12}$$

钻铤外流体和地层界面($r=r_{\mathrm{a}}$)处:

$$\begin{cases} u_{rf}^{\mathrm{out}} = u_r^{\mathrm{VTI}}, \\ \sigma_{rrf}^{\mathrm{out}} = \sigma_{rr}^{\mathrm{VTI}}, \\ 0 = \sigma_{rz}^{\mathrm{VTI}}, \\ 0 = \sigma_{r\theta}^{\mathrm{VTI}}. \end{cases} \tag{13}$$

将图 1 模型各部分声场的应力和位移表达式代入以上边界条件,得到矩阵方程:

$$\boldsymbol{H}\cdot\boldsymbol{O} = \boldsymbol{Q}, \tag{14}$$

其中向量 $\boldsymbol{O}$ 和 $\boldsymbol{Q}$ 的具体表达式如下:

$$\boldsymbol{O} = \left\{A_n^{\mathrm{in}}, A_n^{\mathrm{tool}}, B_n^{\mathrm{tool}}, C_n^{\mathrm{tool}}, D_n^{\mathrm{tool}}, E_n^{\mathrm{tool}}, F_n^{\mathrm{tool}}, A_n^{\mathrm{out}}, B_n^{\mathrm{out}}, B_n^{\mathrm{VTI}}, D_n^{\mathrm{VTI}}, F_n^{\mathrm{VTI}}\right\}^{\mathrm{T}},$$

$$\boldsymbol{Q} = \left\{0,0,0,0,0,p^{\mathrm{s}},0,0,0,0,0,0\right\}^{\mathrm{T}}.$$

矩阵 $\boldsymbol{H}$ 中各元素的详细形式见附录 B.随钻声场中模式波的频散特征由 $\boldsymbol{H}$ 确定,令其行列式 $\boldsymbol{G}$ 为零,得到各模式波的频散方程(宋云红等,2020):

$$\boldsymbol{G}(k,\omega) = \det\boldsymbol{H}(k,\omega) = 0, \tag{15}$$

通过求解该方程得到各模式波波数 k 在不同频率下的根,然后利用式(16)计算各模式波的相速度频散曲线.式(16)为:

$$v_{\mathrm{phase}}(\omega) = \frac{\omega}{\mathrm{Re}(k(\omega))}. \tag{16}$$

参考 Tang 和 Cheng(2004)等文献,钻铤外环上的声压波形可由式(17)计算:

$$P(z,t) = \frac{1}{4\pi^2}\int_{-\infty}^{+\infty}\rho_{\mathrm{f}}\omega^2 S(\omega)\mathrm{e}^{-\mathrm{i}\omega t}\int_{-\infty}^{+\infty}\left[A_n^{\mathrm{out}}I_n(fr_{\mathrm{b}}) + B_n^{\mathrm{out}}K_n(fr_{\mathrm{b}})\right]\mathrm{e}^{\mathrm{i}kz}\,\mathrm{d}k\,\mathrm{d}\omega. \tag{17}$$

其中 $S(\omega)$ 为声源函数.

1.4　分波理论基础

由于 VTI 地层随钻声场中钻铤模式波与地层模式波耦合复杂,难以从全波波形中区分,因此采用分波计算的方法来分析钻铤与地层各向异性对地层模式波的影响.分波计算的理论是根据柯西积分定理,将复波数域中沿实轴的积分转化为实质支点的割线积分与极点的留数之和,波数域中这些奇异点

的贡献构成了波场中的各种成分,使其呈现出不同的传播形态.此方法的优点是可以有效地提取全波中的各个成分,有利于分析各成分波的传播特征.相比之下,经典的实轴积分只能计算全波波形,需进一步处理才能分析各成分波的特征;但实轴积分计算的全波可以用来验证分波的计算结果.

计算中会涉及到径向虚波数的平方,使得随钻声场函数产生多值性,径向波数为零的奇异点被称作式(17)中被积函数的支点,其中部分支点对应的径向虚波数的正负值会产生多值性,这样的支点被定义为实质支点,反之被定义为非实质支点.针对随钻声波测井模型,郑晓波(2017)指出当声源不在最内层介质时,有且只有最外层介质的支点才是整个随钻声场的实质支点.针对横向各向同性地层,何晓(2010)证明:井孔声场函数的实质支点的个数和分布受地层各向异性程度的差异的影响,但其中地层的纵横波支点始终是井孔声场函数的实质支点,其具体表达式为:

$$\begin{cases} k_{\mathrm{pt}} = \omega\sqrt{\rho/c_{33}}, \\ k_{\mathrm{st}} = \omega\sqrt{\rho/c_{44}}, \end{cases} \tag{18}$$

另外两个支点的表达式如下:

$$k_{\mathrm{h}} = \omega\sqrt{\frac{(-b-\sqrt{b^2-4ac})\rho}{2c}}, \tag{19}$$

$$k_{\mathrm{l}} = \omega\sqrt{\frac{(-b+\sqrt{b^2-4ac})\rho}{2c}}, \tag{20}$$

式中系数 a、b、c 由弹性常数确定,具体表达式为:

$$\begin{cases} a = (c_{11}-c_{44})^2, \\ b = 2(c_{13}^2+2c_{13}c_{44}-c_{11}c_{33})(c_{11}+c_{44}) \\ \quad\quad +4(c_{33}+c_{44})c_{11}c_{44}, \\ c = (c_{13}^2+2c_{13}c_{44}-c_{11}c_{33})^2-4c_{11}c_{33}c_{44}^2. \end{cases}$$

He 和 Hu(2009)对 VTI 地层各向异性与井孔声场函数的支点数的关系给出了严格的数学证明;支点的个数及分布与 Thomsen(1986)参数有关:

$$\begin{cases} \varepsilon = \dfrac{c_{11}-c_{33}}{2c_{33}}, \\ \delta = \dfrac{(c_{13}+c_{44})^2-(c_{33}-c_{44})^2}{2c_{33}(c_{33}-c_{44})}, \\ \gamma = \dfrac{c_{66}-c_{44}}{2c_{44}}, \end{cases} \tag{21}$$

共分为 3 种情况:当参数满足 $\delta>\varepsilon+c_{44}/2c_{33}$ 时,$\pm k_{\mathrm{h}}$ 和 $\pm k_{\mathrm{l}}$ 均是井孔声场函数的实质支点,此时 VTI 地层的单值定义如图 2 所示;另外两种地层参数情况下井孔声场函数的单值定义参考何晓(2010)的论文.

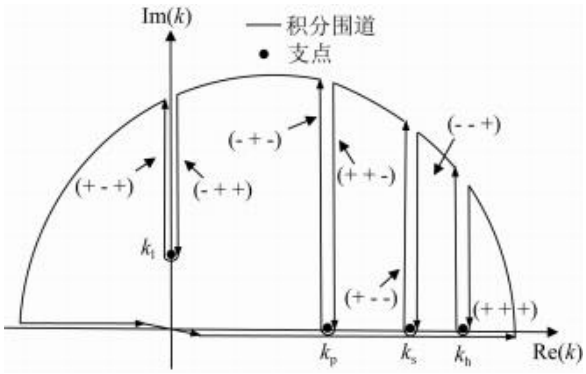


图 2 弹性 TI 地层井孔声场响应函数的单值定义($\delta>\varepsilon+c_{44}/2c_{33}$)

Fig. 2 Singled-value definition of the borehole acoustic response function for a TI elastic formation with $\delta>\varepsilon+c_{44}/2c_{33}$

按图 2 所示,式(17)中计算全波的实轴积分路径可转化为复波数域中(半径很大的)半圆弧与绕过实质支点的路径之和;根据约当引理,圆弧段的贡献为零,只有竖直围道的路径对积分有贡献,对应着沿井壁传播的地层体波.以地层纵波支点为例,地层纵波支点对声场的贡献的表达式为:

$$P_{\text{P-cut}}(\omega,z) = \frac{1}{4\pi^2}\int_{-\infty}^{+\infty} S(\omega)\rho_{\mathrm{f}}\omega^2 \mathrm{e}^{-\mathrm{i}\omega t}\int_{k_{\mathrm{P}}}^{k_{\mathrm{P}}+\mathrm{i}\infty} \left[\begin{array}{l} \left(\dfrac{N_8(k,\omega)}{G(k,\omega)}I_n(fr)+\dfrac{N_9(k,\omega)}{G(k,\omega)}K_n(fr)\right)^{\mathrm{R}} \\ -\left(\dfrac{N_8(k,\omega)}{G(k,\omega)}I_n(fr)+\dfrac{N_9(k,\omega)}{G(k,\omega)}K_n(fr)\right)^{\mathrm{L}} \end{array}\right] \mathrm{e}^{\mathrm{i}kz}\,\mathrm{d}k\mathrm{d}\omega, \tag{22}$$

其中,"R"代表积分路径在支点右侧,"L"代表积分路径在支点左侧,式中对波数 k 的积分则对应着体波的激发强度(本文的激发强度为井中接收声压信号的强度).

复波数域中极点的留数对声场的贡献对应着全波中的模式波,其表达式为:

$$P_{\mathrm{pole}}(\omega,z) = \frac{1}{2\pi}\int_{-\infty}^{+\infty} \mathrm{i}\rho_{\mathrm{f}}\omega^2 S(\omega)\mathrm{e}^{-\mathrm{i}\omega t}\mathrm{e}^{\mathrm{i}kz}\left(\frac{N_8(k,\omega)}{\partial G(k,\omega)/\partial k}I_n(fr)+\frac{N_9(k,\omega)}{\partial G(k,\omega)/\partial k}K_n(fr)\right)\Bigg|_{k=k_{\mathrm{pole}}}\mathrm{d}\omega, \tag{23}$$

其中,$N_i(k,\omega)$ 则是 $\boldsymbol{H}$ 矩阵中第 i 列被声源向量 $\boldsymbol{Q}$ 取代后的矩阵行列式的值,式(23)中极点 k_{pole} 为一阶极点.模式波的激发强度可以表示为:

$$I_{\text{pole}}(\omega,z)=\mathrm{i}\mathrm{e}^{\mathrm{i}kz}\rho_{\mathrm{f}}\omega^{2}\left(\frac{N_{8}(k,\omega)}{\partial G(k,\omega)/\partial k}I_{n}(fr)+\frac{N_{9}(k,\omega)}{\partial G(k,\omega)/\partial k}K_{n}(fr)\right)\Bigg|_{k=k_{pole}}. \tag{24}$$

2　数值计算结果及分析

本节基于上述随钻声场理论及分波计算方法,计算了横向各向同性地层中,随钻单极、偶极和四极子声源激发的各模式波的频散曲线和激发强度曲线,并在此基础上给出各极点和支点对应的时域波形.计算时所选地层及井孔参数由表 1 和表 2 给出,本文计算所用声源为余弦包络脉冲函数(郑晓波,2017).

表 1　地层参数

Table 1　Formation parameters

ρ/(kg·m^{-3})	纵波速度 /(m·s^{-1})	横波速度 /(m·s^{-1})	ε	δ	γ
2000	4243	2739	0.1	0.4	0.1
2500	2476	1053	0.279	0	0.271

表 2　钻铤和流体参数

Table 2　Drill collar and fluid parameters

	纵波速度 /(m·s^{-1})	横波速度 /(m·s^{-1})	ρ/(kg·m^{-3})	外径 /m
钻铤内流体	1500	—	1000	0.027
钻铤	5860	3130	7800	0.09
钻铤外流体	1500	—	1000	0.117

2.1　随钻单极声场中的分波特征

图 3a、b 分别给出了横向各向同性地层随钻单极声场中各模式波的频散和激发强度曲线.图 3a 中实线对应的是随钻情况下的频散曲线,作为对比也给出了(无钻铤)电缆条件下的频散曲线(点划线),图中 V_{p}、V_{sh}、V_{sv}、V_{f} 分别表示地层纵波,地层水平向横波,地层垂向横波以及井孔流体声波的波速.如图所示,标识符号"P-R"表示的地层伪瑞利波的低频截止速度接近地层垂向横波速度 V_{sv},并且,钻铤的引入使声场中增加了钻铤的拉伸型模式波(C1、C2)和内斯通利波(IN-ST).另一个重要现象是钻铤对伪瑞利波和斯通利波(ST)的频散特征产生了较大的影响,使得斯通利波的相速度整体下降;而伪瑞利波的截止频率往高频移动,其频散变化与电缆测井时相比大幅度减弱,有利于地层横波速度的测量.从图 3b 中各极点和支点激发强度曲线中可看出,在随钻声场中,地层体波的信号十分微弱,是因为其对应的支点激发强度(图中虚线)与模式波激发强度(实线)相比,要小 1～2 个数量级.以下重点研究随钻条件下井孔模式波的传播特征.

根据式(22)、(23)可计算出各个极点和支点对随钻声场的贡献,给出各分波的波形.图 4 给出了计算所得的随钻单极子声场中各支点(体波)和极点(模式波)的分波波形,作为对比也给出了实轴积分法计算的全波波形(波形计算的声源主频为 8 kHz,源距为 3 m).图中第 1～7 道给出了这些分波的归一化波形,分波的标识符号(图左端)与图 3 相同,分

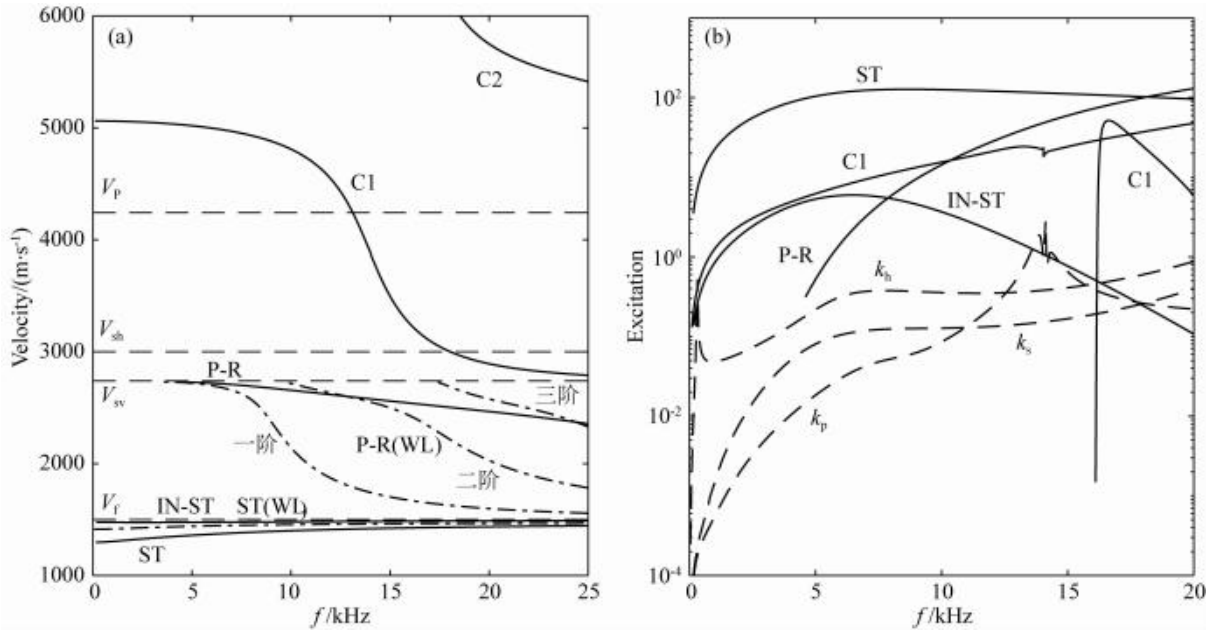


图 3　(a)VTI 地层单极随钻声场模式波频散曲线;(b)声场响应函数中的极点和支点对应的流体声压激发强度

Fig. 3　(a) LWD monopole wave velocity dispersion curves for a VTI formation; (b) Pressure excitation spectra for poles and branch points of the borehole acoustic response function

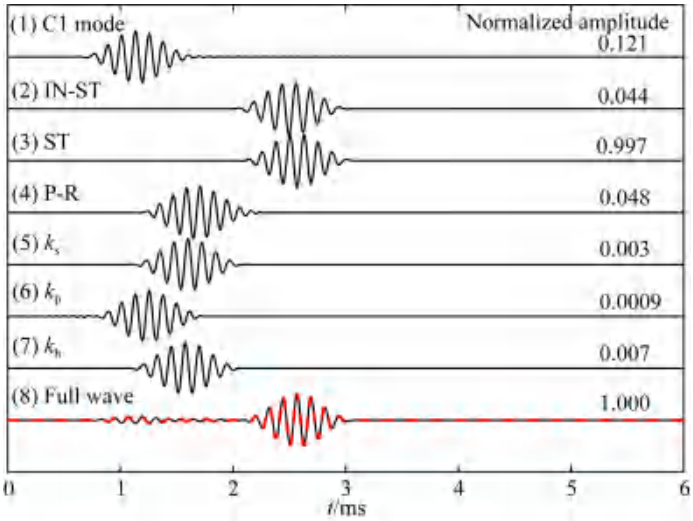


图 4 VTI 地层中单极随钻声场的极点和支点对应的分波

Fig. 4 Component waves from poles and branch points of LWD monopole wavefield in a fast VTI formation

波相对于全波的实际波幅比例在图右端给出. 计算结果表明,全波中的首波是由 C1 钻铤模式波与纵波支点 k_P 贡献的分波组成;由于纵波支点的激发强度远小于 C1 钻铤模式波,如图 3b 所示,地层纵波被钻铤模式波所掩盖;地层横波波群组成复杂,按照到时,包括伪瑞利波和支点 k_s、k_h 的贡献,其中伪瑞利波占主要成分,因此伪瑞利波在提取地层垂向横波速度时影响很大;斯通利波与内斯通利波混叠,组成的波包在全波波形中幅度最大,到达最晚;C2 钻铤模式波截止频率较高,且在 8 kHz 的主频段激发强度小,因此其产生的分波没有给出;图中第 8 道为实轴积分法计算的全波波形(红色虚线)与各分波叠加后的波形(黑色实线)的对比,二者无论在相位还是幅度上均十分吻合,验证了分波计算结果的正确性.

2.2 随钻偶极声场中的分波特征

图 5a 给出了横向各向同性地层随钻偶极声场中各模式波的频散曲线(实线),并与电缆测井中的结果进行对比(点划线). 钻铤的存在使地层弯曲波(标识为 Flexural 的实线)频散曲线产生畸变,高频段随频率增加,但其低频截止仍是地层垂向横波速度;与电缆测井相比,随钻偶极声场中增加了多个模式波,包括频散特征受井外地层影响较大的界面波(Surface)以及钻铤模式波(D1-D4). 由于钻铤与井孔的相互作用,界面波和弯曲波的中高频部分从形态上看像是无钻铤时的地层弯曲波与无井孔时的钻铤弯曲波发生了交换. 钻铤模式波(D1-D4)在高频时相互耦合的现象复杂,但在低频段对偶极声波测井的影响可以忽略.

考察随钻偶极子声场中各个分波的激发响应特征. 如图 5b 所示,3 个支点的分波激发强度远小于各模式波的强度,说明随钻偶极声场中地层体波信号依然十分微弱,常被其他模式波所掩盖. 如图 6 给出了图 5 对应的随钻偶极子声场的分波波形. 分波的标识符号(图左端)与图 5 相同,分波相对于全波的实际波幅比例在图右端给出. 地层纵波最先到达,但因为其幅度极小,无法在全波中观测到;地层横波波群构成复杂,由支点 k_s、k_h 贡献的分波以及地层弯曲波和钻铤模式波(D1-D4)共同组成(D3 和 D4 在主频段幅度太小,未画出),其中地层弯曲波占主

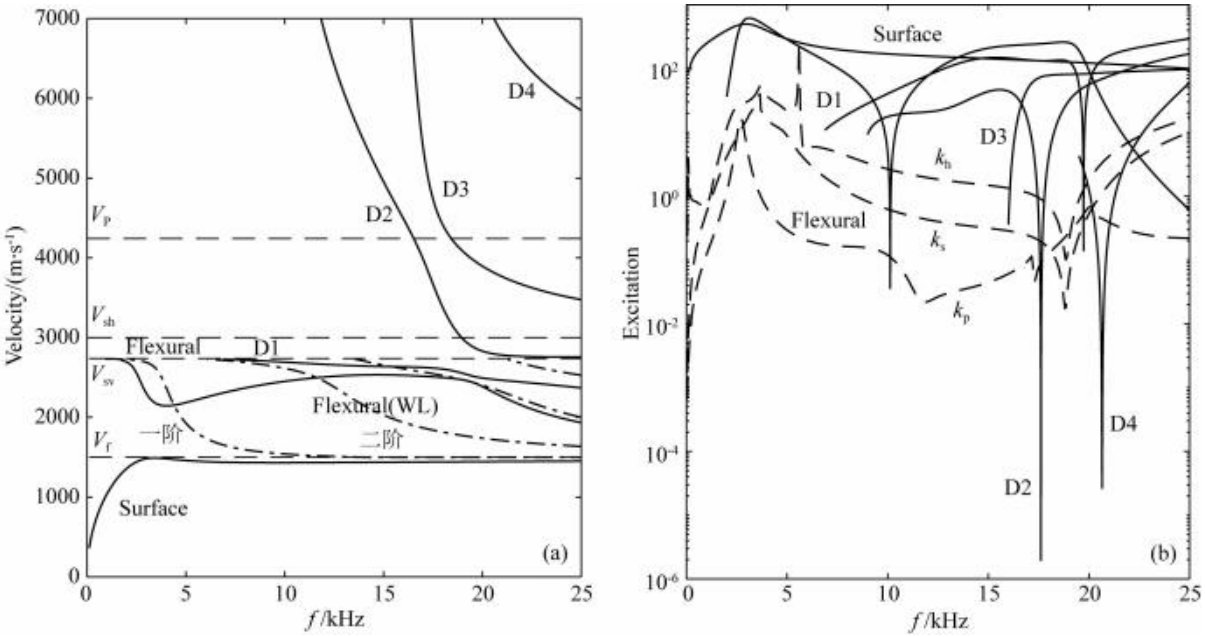


图 5 (a) VTI 地层偶极随钻声场模式波频散曲线;(b) 声场响应函数中的极点和支点对应的流体声压激发强度

Fig. 5 (a) LWD dipole wave velocity dispersion curves for a VTI formation; (b) Pressure excitation spectra for poles and branch points of the borehole acoustic response function

要成分;界面波幅度大速度慢,在其之后是偶极换能器激发的六级声场,值得指出的是分波计算时仅考虑了偶极声场,因此通过分波合成得到的全波声场中不包括其余的高阶声场(郑晓波,2012);钻铤模式波(D1-D4)以及支点 k_h 贡献的分波呈震荡状,但其前后部分叠加后相互抵消.各分波叠加得到合成全波(第 9 道黑实线)与实轴积分法得到的全波(红线)十分吻合.

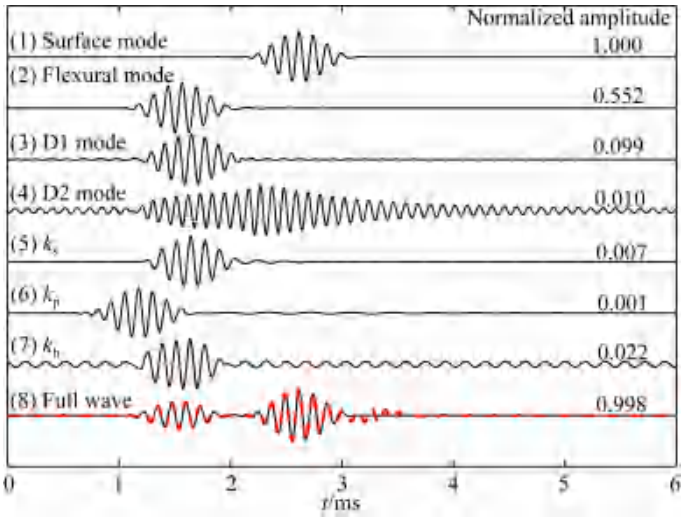


图 6　VTI 地层中偶极随钻声场的极点和支点对应的分波

Fig. 6　Component waves from poles and branch points of LWD dipole wavefield in a fast VTI formation

2.3　随钻四极声场中的分波特性

随钻横波测量采用四极声源(唐晓明和郑传汉,2004),且大多针对慢速地层的情况.图 7 给出了快速(图 7a、b)和慢速(图 7c、d)横向各向同性地层随钻四极声场中各模式波的频散曲线和分波的激发强度曲线,图 7a、c 中实线是随钻情况下的频散曲线,点划线是电缆情况下的频散曲线.快速地层中,测井频带范围内总共出现了四种模式波,分别是地层模式波(Q1、Q2)和钻铤模式波(C1、C2);地层模式波(Q1、Q2)的低频截止速度接近地层垂向横波速度.相对于电缆情况而言,钻铤使地层一阶模式波 Q1 的频散增强,不利于地层横波速度的测量,但二阶模式波 Q2 的频散变化却大为降低.由于受频散效应的影响较小,快速地层中采用二阶四极子模式波测量垂向地层横波速度较为有利,这与 Tang 等(2003)对快速各向同性地层四极子声波研究得出的结论一致.相比于快速地层,慢速地层中只有单一的地层模式波(Q1),其低频部分趋近于地层垂向横波速度,且频散程度(相对于快速地层)较弱.与快速地层类似,慢速地层中分波激发响应中支点的强度远小于极点的强度,所以测量中观察不到随钻四极子声场中的地层体波.

图 8a、b 分别给出了快速和慢速地层中的分波计算结果.快速地层中,全波列首波是由 Q2 四极子模式波与来自支点 k_s 和 k_h 的分波共同组成,其中 Q2 模式波占主要成分,这与 Tang 等(2003)认识一致.采用 Q2 模式而非 Q1 模式来提取沿井轴方向的横波速度,是因为 Q1 模式波的频散大,高频时其速度远小于地层垂向横波速度,这也是全波列中 Q2 模式波比 Q1 模式波到时超前的原因.虽然 Q1 模式波的激发强度大于 Q2 模式波,但两者无量级上的差异,因此利用 Q2 模式波来测量地层垂向横波速度是可行的.在随钻测井中,钻铤模式波可能严重干扰 Q2 模式波的波形,对此常通过在钻铤上周期性刻槽来削减钻铤模式波的干扰.除此之外,钻铤模式波频散特征与钻铤尺寸密切相关:当钻铤外径不变,内径减小时,频散曲线向高频偏移,反之则向低频偏移,因此在实际仪器设计中,也应选择合适的仪器结构来尽量避开钻铤模式波的干扰;慢速地层中,Q1 四极子模式波振幅最大,因此可利用该模式波来测量地层垂向横波速度.与单极和偶极的分析一样,将各分波叠加合成后的波形(黑线)与实轴积分计算结果(红色虚线)吻合.全波中的高频震荡是一阶钻铤模式波 C1 的干扰,测井时采用该钻铤模式波截止频率以下的频段便可消除这一干扰(唐晓明和郑传汉,2004).

2.4　VTI 地层随钻四极声波低频波速的讨论

虽然四极子声波适宜于随钻横波测量(唐晓明和郑传汉,2004),但对于 VTI 地层各向异性多种复杂变化情况对测量的影响加以讨论很有必要.Thomsen(1986)对实际地层岩石的 TI 各向异性数据做了大量调研,总结出了 56 组典型的 TI 岩石参数.He 和 Hu(2009)根据地层参数差异对这 56 组 TI 岩石进行分类,以式(21)的 Thomsen 参数及其组合来衡量,发现有接近 90%的岩石各向异性参数满足 $\delta \leqslant \varepsilon + c_{44}/2c_{33}$;考察这一普适条件对随钻四极子横波测量的影响,参照 Thomsen(1986)论文,选取其中 6 组典型 TI 地层岩石参数(见表 3 快地层 1～3、慢地层 1～3),依次是 Berea sandstone、Oil Shale、Green River shale、Aluminum-lucite composite、Pierre shale 以及 Gas sand-water sand.

计算结果如图 9 所示,实线为四极子模式波(Q1、Q2)的相速度,点划线为群速度频散曲线.图 9a 的快速地层中,4 条水平虚线自上而下依次代表 Berea sandstone、Oil Shale 以及 Green River shale

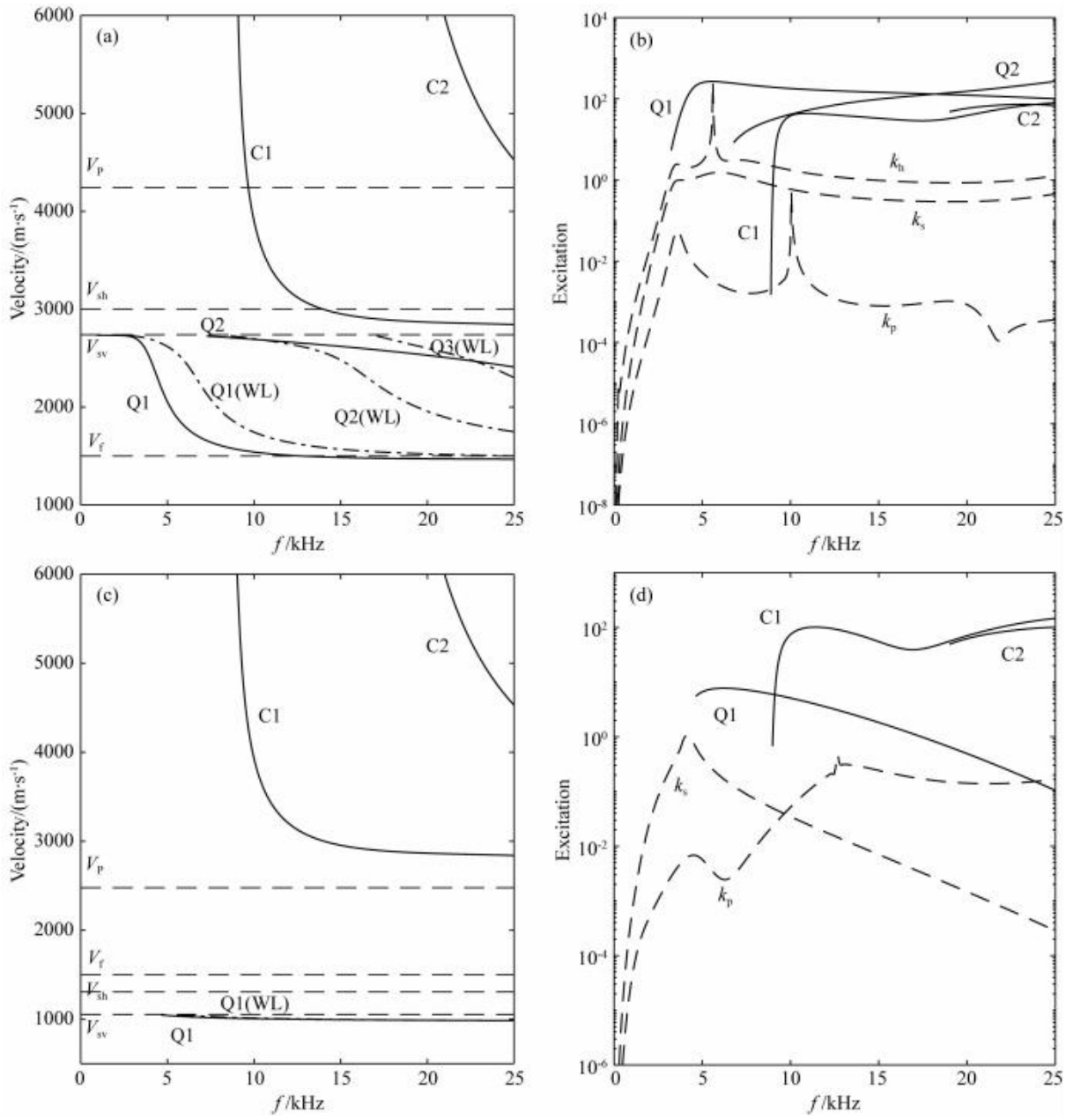


图 7 VTI 地层四极子随钻声场模式波频散曲线和声场响应函数中的极点和支点对应的流体声压激发强度

(a) 快速地层频散曲线;(b) 快速地层激发强度;(c) 慢速地层频散曲线;(d) 慢速地层激发强度.

Fig. 7 LWD quadrupole wave velocity dispersion curves in VTI formations and pressure excitation spectra for the poles and branch points of the borehole acoustic response function

(a) Fast formation dispersion curves; (b) Fast formation excitation; (c) Slow formation dispersion curves; (d) Slow formation excitation.

表 3 地层各向异性参数

Table 3 Anisotropic parameters of formations

	ρ /(kg·m^{-3})	纵波速度 /(m·s^{-1})	横波速度 /(m·s^{-1})	ε	δ	γ
快地层 1	2140	4206	2664	0.002	0.02	0.005
快地层 2	2370	4231	2539	0.2	0.1	0.145
快地层 3	2310	4167	2432	0.04	0.01	0.03
慢地层 1	1860	2868	1350	0.97	−0.09	1.3
慢地层 2	2255	2202	969	0.015	0.06	0.03
慢地层 3	2030	1409	780	0.022	0.018	0.004
快地层 4	2570	4449	2585	0.091	0.565	0.046
慢地层 4	2000	3162	1414	0.1	0.4	0

岩石的垂直向横波速度,图 9b 的慢速地层中,4 条水平虚线自上而下依次代表井内流体速度,Aluminum-lucite composite、Pierre shale 以及 Gas sand-water sand 岩石的垂直向横波速度;结果表明在满足条件 $\delta \lesssim \varepsilon + c_{44}/2c_{33}$ 的快速和慢速 TI 地层岩石中,地层四极子模式波的低频截止速度都接近于真实地层的垂向横波速度;并且,与图 7 类似,快速 VTI 地层的 Q1 四极子模式波为强频散模式,而 Q2 四极子模式波的频散相对较弱.

另外,He 和 Hu(2009)对 Thomsen 数据的统计也表明,约有 10%岩石的 TI 各向异性满足条件 $\delta > \varepsilon + c_{44}/2c_{33}$.针对这一类各向异性岩石计算随钻四

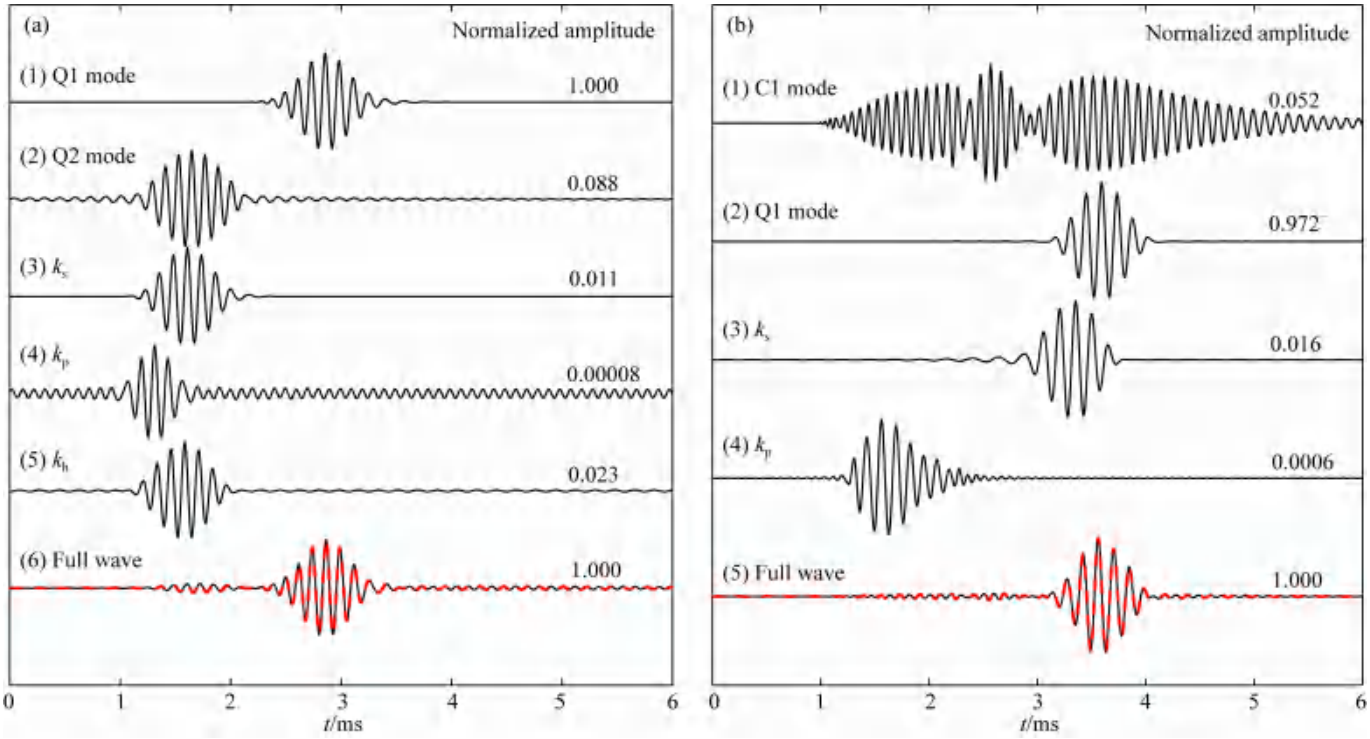


图 8　VTI 地层中四极随钻声场的极点和支点对应的分波

(a) 快速地层;(b) 慢速地层.

Fig. 8　Component waves from poles and branch points of LWD quadrupole wavefield in VTI formation

(a) Fast formation; (b) Slow formation.

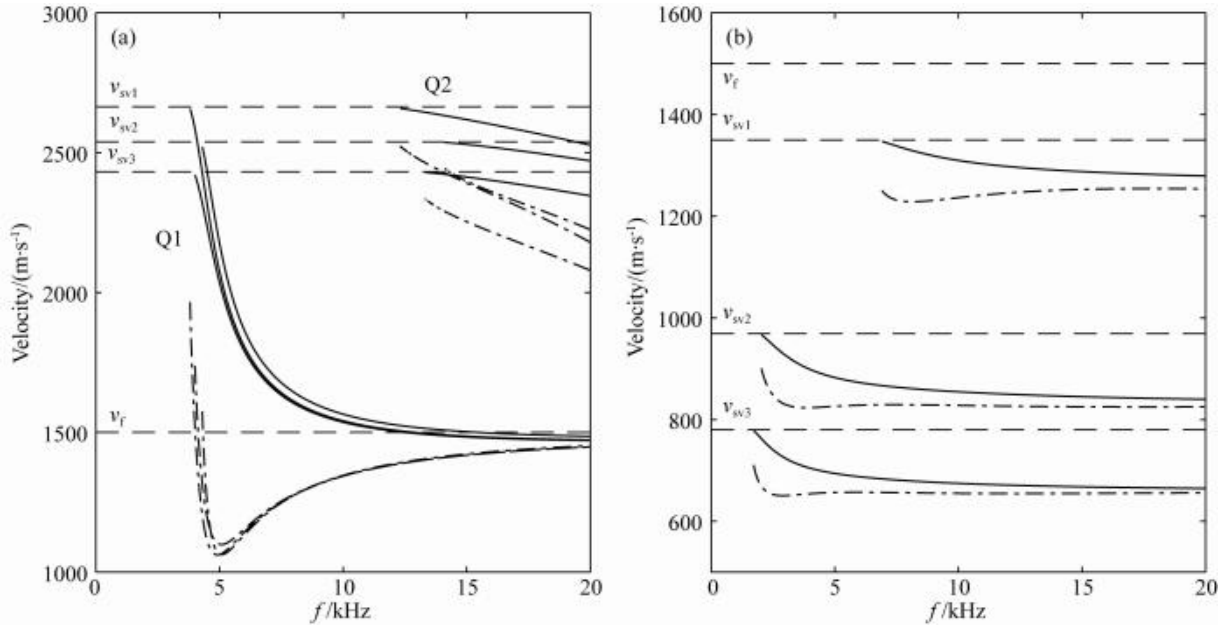


图 9　满足条件 $\delta \leqslant \varepsilon + c_{44}/2c_{33}$ 的 VTI 地层随钻四极子模式波频散曲线

(a) 快速地层;(b) 慢速地层.

Fig. 9　LWD quadrupole wave dispersion curves in VTI formations with $\delta \leqslant \varepsilon + c_{44}/2c_{33}$

(a) Fast formation; (b) Slow formation.

极子模式波的频散曲线,参数分别选自 Thomsen (1986)论文中典型的 Mesaverde laminated siltstone 和何晓(2010)论文,由表 3 快地层 4 和慢地层 4 给出.

图 10 分别给出了快速(图 10a)和慢速(图 10c) VTI 地层四极子模式波的相速度(实线)和群速度频散曲线(点划线),结果表明在满足 $\delta > \varepsilon + c_{44}/2c_{33}$ 的条件下,无论快速还是慢速 VTI 地层的四极子模式波截止频率处的波速均小于真实地层垂向横波速度,趋于实质支点 k_h 对应的速度 $v_h = \omega/k_h$(蓝色虚线),这与上述满足条件 $\delta \leqslant \varepsilon + c_{44}/2c_{33}$ 的各向异性地层很不相同. 图 10b、d 进一步给出了快速和慢速 VTI 地层的分波计算结果;图 10b 中自上而下分别是主频为 8 kHz 的 Q2 四极子模式波的分波,主频为 3.5 kHz 的 Q1 模式波分波,以及主频为 8 kHz

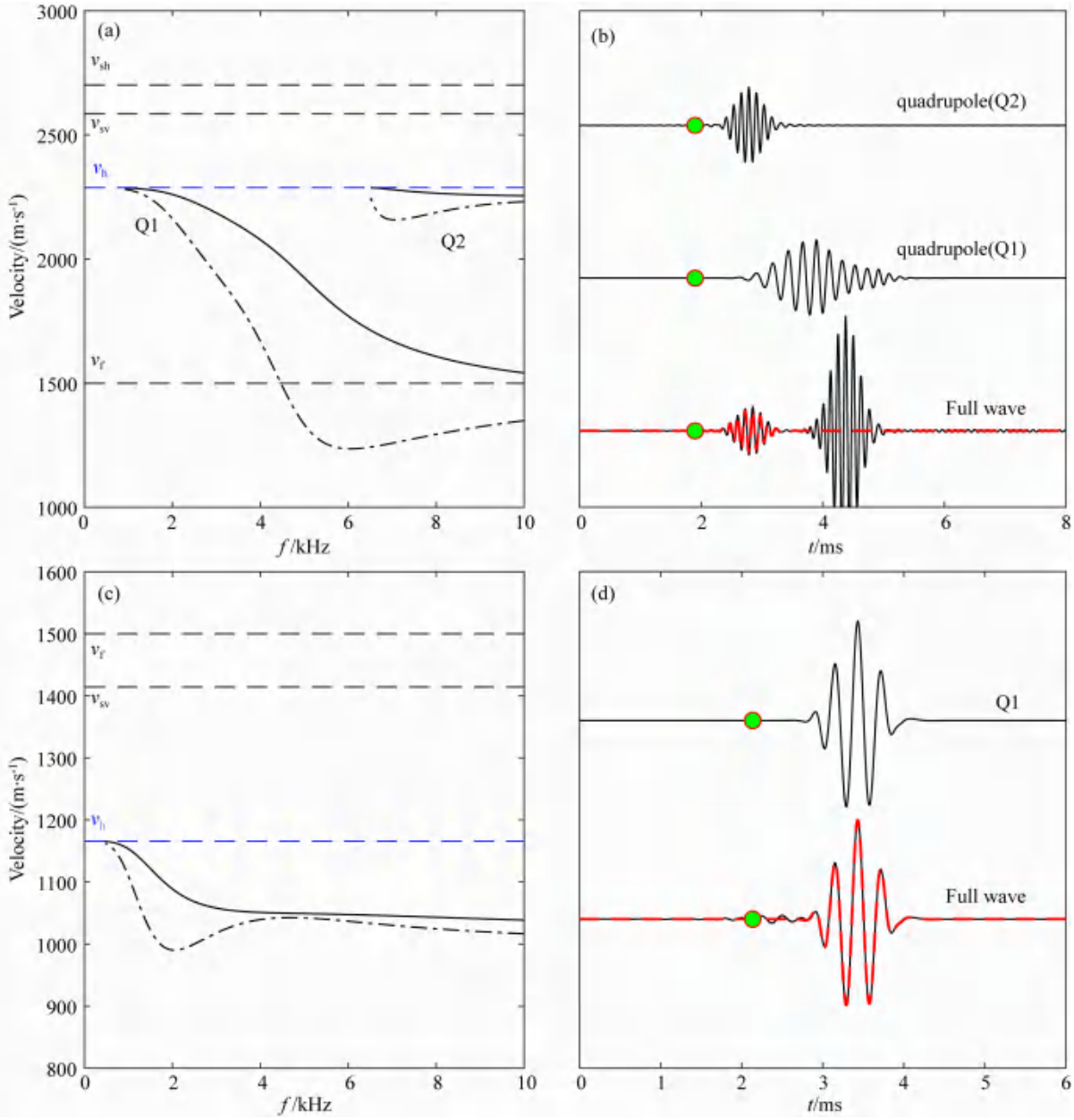


图 10 满足条件 $\delta>\varepsilon+c_{44}/2c_{33}$ 的 VTI 地层随钻四极子模式波频散曲线和分波分析

(a) 快速地层频散曲线;(b) 快速地层分波分析;(c) 慢速地层频散曲线;(d) 慢速地层分波分析.

Fig. 10 LWD quadrupole wave dispersion and component wave analysis in VTI formations with $\delta\leqslant\varepsilon+c_{44}/2c_{33}$

(a) Fast formation dispersion; (b) Fast formation complement wave; (c) Slow formation dispersion; (d) Slow formation complement wave.

的全波.作为对比,全波波形中画出了 Q2 模式波分波(红色虚线),说明此时首波仍是 Q2 四极子模式波;图中绿点代表地层垂向横波到时,可见快速地层中四极子模式波到时滞后于沿井孔传播的地层横波.图 10d 中主频为 3kHz 的地层四极子模式波 Q1 到时也同样出现滞后于地层横波的现象.值得指出的是,单极伪瑞利波和偶极弯曲波也有类似现象,但是在前文的算例中,V_h 与 V_{sv} 接近,所以这一现象不太明显.上述现象与 He 和 Hu(2009)对裸眼井的理论分析结果一致,其产生的原因是,在参数满足条件 $\delta>\varepsilon+c_{44}/2c_{33}$ 的 TI 地层中,实质支点 k_s 右侧将会出现新的实质支点 k_h,使四极子模式波的截止频率波速不是趋于地层垂向横波速度,而是趋于支点 k_h 对应的速度 v_h.测量该速度是有意义的,因为根据式(19),v_h 是地层各向异性参数的组合,可以用所测波速结合这些参数来求取地层垂向横波速度.

3 结论

本文通过对横向各向同性地层随钻声场的分波分析和计算,将声场全波分解成来自波数域中的奇异点(包括支点和极点)的分波的贡献,对比研究了单极、偶极和四极子声场模式波的传播特征,得出以下结论:

(1)与电缆测井结果相比,快速地层中钻铤的存在使得斯通利波和地层一阶四极子模式波(Q1)的

频散变化增加,不利于地层横波速度的测量;钻铤和地层的弯曲波频散特征和形态也发生了较大变化;伪瑞利波和地层二阶四极子模式波(Q2)的频散则大幅度减弱,有利于地层横波速度的测量.

(2)快速 VTI 地层随钻多极子声场的横波波群构成复杂,单极的横波波群由伪瑞利波与支点 k_s 和 k_h 贡献的分波共同组成,其中伪瑞利波占主要成分;偶极的横波波群由弯曲波和一阶钻铤模式波(D1)与支点 k_s 和 k_h 贡献的分波共同组成,其中弯曲波占主要成分;四极的横波波群由地层二阶四极子模式波(Q2)与支点 k_s 和 k_h 贡献的分波共同组成,其中地层二阶四极子模式波(Q2)占主要成分.慢速 VTI 地层中,横波波群由地层四极子模式波和支点 k_s 贡献的分波共同组成,其中地层四极子模式波占主要成分.因此,多极子声场中的伪瑞利波、弯曲波和四极子螺旋波可用于测量 VTI 地层的垂直向横波速度.

(3)在各向异性参数满足条件 $\delta>\varepsilon+c_{44}/2c_{33}$ 的 VTI 地层中,伪瑞利波、弯曲波以及四极子螺旋波的截止频率处的波速均小于垂直向地层横波速度,将这一波速与地层各向异性参数结合可以获得垂直向地层横波速度.

附录 A

井孔外 VTI 地层径向位移,径向、环向及轴向应力分量表达式为:

$$
\begin{aligned}
u_r^{\mathrm{VTI}} &= (1+\mathrm{i}ka')\left(\frac{n}{r_a}K_n(q_{\mathrm{p}}r_a)-q_{\mathrm{p}}K_{n+1}(q_{\mathrm{p}}r_a)\right)B_n^{\mathrm{VTI}}+\frac{n}{r_a}K_n(q_{\mathrm{sh}}r_a)D_n^{\mathrm{VTI}}\\
&\quad+(\mathrm{i}k+b')\left(\frac{n}{r_a}K_n(q_{\mathrm{sv}}r_a)-q_{\mathrm{sv}}K_{n+1}(q_{\mathrm{sv}}r_a)\right)F_n^{\mathrm{VTI}},\\
\sigma_{rr}^{\mathrm{VTI}} &= \left[\left(c_{11}q_{\mathrm{p}}^2-c_{13}k^2+(c_{11}-c_{13})\mathrm{i}ka'q_{\mathrm{p}}^2\right)K_n(q_{\mathrm{p}}r_a)+\frac{2c_{66}}{r_a}(1+\mathrm{i}ka')\left(\frac{n^2-n}{r_a}K_n(q_{\mathrm{p}}r_a)+q_{\mathrm{p}}K_{n+1}(q_{\mathrm{p}}r_a)\right)\right]B_n^{\mathrm{VTI}}\\
&\quad-2c_{66}\frac{n}{r_a}\left(\frac{1-n}{r_a}K_n(q_{\mathrm{sh}}r_a)+q_{\mathrm{sh}}K_{n+1}(q_{\mathrm{sh}}r_a)\right)D_n^{\mathrm{VTI}}+\left[\left((c_{11}q_{\mathrm{sv}}^2-c_{13}k^2)b'+(c_{11}-c_{13})\mathrm{i}kq_{\mathrm{sv}}^2\right)K_n(q_{\mathrm{sv}}r_a)\right.\\
&\quad\left.+2\frac{c_{66}}{r_a}(\mathrm{i}k+b')\left(\frac{n^2-n}{r_a}K_n(q_{\mathrm{sv}}r_a)+q_{\mathrm{sv}}K_{n+1}(q_{\mathrm{sv}}r_a)\right)\right]F_n^{\mathrm{VTI}},\\
\sigma_{r\theta}^{\mathrm{VTI}} &= 2c_{66}\frac{n}{r_a}(1+\mathrm{i}ka')\left(\frac{1-n}{r_a}K_n(q_{\mathrm{p}}r_a)+q_{\mathrm{p}}K_{n+1}(q_{\mathrm{p}}r_a)\right)B_n^{\mathrm{VTI}}\\
&\quad+\left[-c_{66}q_{\mathrm{sh}}^2\left(1+\frac{2n^2-2n}{q_{\mathrm{sh}}^2r_a^2}\right)K_n(q_{\mathrm{sh}}r_a)+\frac{2K_{n+1}(q_{\mathrm{sh}}r_a)}{r_aq_{\mathrm{sh}}}\right]D_n^{\mathrm{VTI}}\\
&\quad+2c_{66}\frac{n}{r_a}(\mathrm{i}k+b')\left(\frac{1-n}{r_a}K_n(q_{\mathrm{sv}}r_a)+q_{\mathrm{sv}}K_{n+1}(q_{\mathrm{sv}}r_a)\right)F_n^{\mathrm{VTI}},\\
\sigma_{rz}^{\mathrm{VTI}} &= c_{44}\left(2\mathrm{i}k-a'(k^2+q_{\mathrm{p}}^2)\right)\left(\frac{n}{r_a}K_n(q_{\mathrm{p}}r_a)-q_{\mathrm{p}}K_{n+1}(q_{\mathrm{p}}r_a)\right)B_n^{\mathrm{VTI}}+\mathrm{i}kn\frac{c_{44}K_n(q_{\mathrm{sh}}r_a)}{r_a}D_n^{\mathrm{VTI}}\\
&\quad+c_{44}(k^2+q_{\mathrm{sv}}^2-2\mathrm{i}kb')\left(\frac{-n}{r_a}K_n(q_{\mathrm{sv}}r_a)+q_{\mathrm{sv}}K_{n+1}(q_{\mathrm{sv}}r_a)\right)F_n^{\mathrm{VTI}}.
\end{aligned}
$$

附录 B

$\boldsymbol{H}$ 矩阵元素为(所有未列出的矩阵元素都为 0):

$$
\begin{aligned}
H_{11} &= -\left[\frac{n}{r_c}I_n(fr_c)+fI_{n+1}(fr_c)\right],\\
H_{12} &= \left[\frac{n}{r_c}I_n(p_{\mathrm{tool}}r_c)+p_{\mathrm{tool}}I_{n+1}(p_{\mathrm{tool}}r_c)\right],\\
H_{13} &= \frac{n}{r_c}K_n(p_{\mathrm{tool}}r_c)-p_{\mathrm{tool}}K_{n+1}(p_{\mathrm{tool}}r_c),\\
H_{14} &= \frac{n}{r_c}I_n(s_{\mathrm{tool}}r_c),\\
H_{15} &= \frac{n}{r_c}K_n(s_{\mathrm{tool}}r_c),\\
H_{16} &= \mathrm{i}k\left[\frac{n}{r_c}I_n(s_{\mathrm{tool}}r_c)+s_{\mathrm{tool}}I_{n+1}(s_{\mathrm{tool}}r_c)\right],\\
H_{17} &= \mathrm{i}k\left[\frac{n}{r_c}K_n(s_{\mathrm{tool}}r_c)-s_{\mathrm{tool}}K_{n+1}(s_{\mathrm{tool}}r_c)\right],\\
H_{21} &= \rho_{\mathrm{f}}\omega^2I_n(fr_c),\\
H_{22} &= \mu\left[\left(\frac{2n(n-1)}{r_c^2}+2k^2-k_{\mathrm{s}}^2\right)I_n(p_{\mathrm{tool}}r_c)-\left(\frac{2p_{\mathrm{tool}}}{r_c}I_{n+1}(p_{\mathrm{tool}}r_c)\right)\right],\\
H_{23} &= \mu\left[\left(\frac{2n(n-1)}{r_c^2}+2k^2-k_{\mathrm{s}}^2\right)K_n(p_{\mathrm{tool}}r_c)+\left(\frac{2p_{\mathrm{tool}}}{r_c}K_{n+1}(p_{\mathrm{tool}}r_c)\right)\right],
\end{aligned}
$$

$$H_{24} = 2\mu\left[\frac{n(n-1)}{r_c^2}I_n(s_{tool}r_c)+\frac{n}{r_c}s_{tool}I_{n+1}(s_{tool}r_c)\right],$$

$$H_{25} = 2\mu\left[\frac{n(n-1)}{r_c^2}K_n(s_{tool}r_c)-\frac{n}{r_c}s_{tool}K_{n+1}(s_{tool}r_c)\right],$$

$$H_{26} = 2\mu ik\left[\left(\frac{n(n-1)}{r_c^2}+s_{tool}^2\right)I_n(s_{tool}r_c)-\frac{s_{tool}}{r_c}I_{n+1}(s_{tool}r_c)\right],$$

$$H_{27} = 2\mu\, ik\left[\left(\frac{n(n-1)}{r_c^2}+s_{tool}^2\right)K_n(s_{tool}r_c)+\frac{s_{tool}}{r_c}K_{n+1}(s_{tool}r_c)\right],$$

$$H_{32} = 2ik\mu\left[\frac{n}{r_c}I_n(p_{tool}r_c)+p_{tool}I_{n+1}(p_{tool}r_c)\right],$$

$$H_{33} = 2ik\mu\left[\frac{n}{r_c}K_n(p_{tool}r_c)-p_{tool}K_{n+1}(p_{tool}r_c)\right],$$

$$H_{34} = ik\mu\left[\frac{n}{r_c}I_n(s_{tool}r_c)\right],$$

$$H_{35} = ik\mu\left[\frac{n}{r_c}K_n(s_{tool}r_c)\right],$$

$$H_{36} = \mu(k_s^2-2k^2)\left[\left(\frac{n}{r_c}I_n(s_{tool}r_c)+s_{tool}I_{n+1}(s_{tool}r_c)\right)\right],$$

$$H_{37} = \mu(k_s^2-2k^2)\left[\left(\frac{n}{r_c}K_n(s_{tool}r_c)-s_{tool}K_{n+1}(s_{tool}r_c)\right)\right],$$

$$H_{42} = 2\frac{n\mu}{r_c}\left[\frac{(1-n)}{r_c}I_n(p_{tool}r_c)-p_{tool}I_{n+1}(p_{tool}r_c)\right],$$

$$H_{43} = 2\frac{n\mu}{r_c}\left[\frac{(1-n)}{r_c}K_n(p_{tool}r_c)+p_{tool}K_{n+1}(p_{tool}r_c)\right],$$

$$H_{44} = \mu\left[\left(\frac{2n(1-n)}{r_c^2}-s_{tool}^2\right)I_n(s_{tool}r_c)+2\frac{s_{tool}}{r_c}I_{n+1}(s_{tool}r_c)\right],$$

$$H_{45} = \mu\left[\left(\frac{2n(1-n)}{r_c^2}-s_{tool}^2\right)K_n(s_{tool}r_c)-2\frac{s_{tool}}{r_c}K_{n+1}(s_{tool}r_c)\right],$$

$$H_{46} = 2ik\frac{n}{r_c}\left[\frac{(1-n)}{r_c}I_n(s_{tool}r_c)-s_{tool}I_{n+1}(s_{tool}r_c)\right],$$

$$H_{47} = 2ik\frac{n}{r_c}\left[\frac{(1-n)}{r_c}K_n(s_{tool}r_c)+s_{tool}K_{n+1}(s_{tool}r_c)\right],$$

$$H_{52} = \left[\frac{n}{r_b}I_n(p_{tool}r_b)+p_{tool}I_{n+1}(p_{tool}r_b)\right],$$

$$H_{53} = \left[\frac{n}{r_b}K_n(p_{tool}r_b)-p_{tool}K_{n+1}(p_{tool}r_b)\right],$$

$$H_{54} = \frac{n}{r_b}I_n(s_{tool}r_b),$$

$$H_{55} = \frac{n}{r_b}K_n(s_{tool}r_b),$$

$$H_{56} = ik\left[\frac{n}{r_b}I_n(s_{tool}r_b)+s_{tool}I_{n+1}(s_{tool}r_b)\right],$$

$$H_{57} = ik\left[\frac{n}{r_b}K_n(s_{tool}r_b)-s_{tool}K_{n+1}(s_{tool}r_b)\right],$$

$$H_{58} = -\left[\frac{n}{r_b}I_n(fr_b)+fI_{n+1}(fr_b)\right],$$

$$H_{59} = -\left[\frac{n}{r_b}K_n(fr_b)-fK_{n+1}(fr_b)\right],$$

$$H_{62} = \mu\left[\left(\frac{2n(n-1)}{r_b^2}+2k^2-k_s^2\right)I_n(p_{tool}r_b)-\left(\frac{2p_{tool}}{r_b}I_{n+1}(p_{tool}r_b)\right)\right],$$

$$H_{63} = \mu\left[\left(\frac{2n(n-1)}{r_b^2}+2k^2-k_s^2\right)K_n(p_{tool}r_b)+\left(\frac{2p_{tool}}{r_b}K_{n+1}(p_{tool}r_b)\right)\right],$$

$$H_{64} = 2\mu\left[\frac{n(n-1)}{r_b^2}I_n(s_{tool}r_b)+\frac{n}{r_b}s_{tool}I_{n+1}(s_{tool}r_b)\right],$$

$$H_{65} = 2\mu\left[\frac{n(n-1)}{r_b^2}K_n(s_{tool}r_b)-\frac{n}{r_b}s_{tool}K_{n+1}(s_{tool}r_b)\right],$$

$$H_{66} = 2\mu ik\left[\left(\frac{n(n-1)}{r_b^2}+s_{tool}^2\right)I_n(s_{tool}r_b)-\frac{s_{tool}}{r_b}I_{n+1}(s_{tool}r_b)\right],$$

$$H_{67} = 2\mu ik\left[\left(\frac{n(n-1)}{r_b^2}+s_{tool}^2\right)K_n(s_{tool}r_b)+\frac{s_{tool}}{r_b}K_{n+1}(s_{tool}r_b)\right],$$

$$H_{68} = \rho_f\omega^2 I_n(fr_b),$$

$$H_{69} = \rho_f\omega^2 K_n(fr_b),$$

$$H_{72} = 2ik\mu\left[\frac{n}{r_b}I_n(p_{tool}r_b)+p_{tool}I_{n+1}(p_{tool}r_b)\right],$$

$$H_{73} = 2ik\mu\left[\frac{n}{r_b}K_n(p_{tool}r_b)-p_{tool}K_{n+1}(p_{tool}r_b)\right],$$

$$H_{74} = ik\mu\left[\frac{n}{r_b}I_n(s_{tool}r_b)\right],$$

$$H_{75} = ik\mu\left[\frac{n}{r_b}K_n(s_{tool}r_b)\right],$$

$$H_{76} = \mu(k_s^2-2k^2)\left[\left(\frac{n}{r_b}I_n(s_{tool}r_b)+s_{tool}I_{n+1}(s_{tool}r_b)\right)\right],$$

$$H_{77} = \mu(k_s^2-2k^2)\left[\left(\frac{n}{r_b}K_n(s_{tool}r_b)-s_{tool}K_{n+1}(s_{tool}r_b)\right)\right],$$

$$H_{82} = 2\frac{n\mu}{r_b}\left[\frac{(1-n)}{r_b}I_n(p_{tool}r_b)-p_{tool}I_{n+1}(p_{tool}r_b)\right],$$

$$H_{83}=2\frac{n\mu}{r_b}\left[\frac{(1-n)}{r_b}K_n(p_{tool}r_b)+p_{tool}K_{n+1}(p_{tool}r_b)\right],$$

$$H_{84}=\mu\left[\left(\frac{2n(1-n)}{r_b^2}-s_{tool}^2\right)I_n(s_{tool}r_b)+\frac{2}{r_b}s_{tool}I_{n+1}(s_{tool}r_b)\right],$$

$$H_{85}=\mu\left[\left(\frac{2n(1-n)}{r_b^2}-s_{tool}^2\right)K_n(s_{tool}r_b)-\frac{2}{r_b}s_{tool}K_{n+1}(s_{tool}r_b)\right],$$

$$H_{86}=2ik\mu\frac{n}{r_b}\left[\frac{(1-n)}{r_b}I_n(s_{tool}r_b)-s_{tool}I_{n+1}(s_{tool}r_b)\right],$$

$$H_{87}=2ik\mu\frac{n}{r_b}\left[\frac{(1-n)}{r_b}K_n(s_{tool}r_b)+s_{tool}K_{n+1}(s_{tool}r_b)\right],$$

$$H_{98}=-\left[\frac{n}{r_a}I_n(fr_a)+fI_{n+1}(fr_a)\right],$$

$$H_{99}=-\left[\frac{n}{r_a}K_n(fr_a)-fK_{n+1}(fr_a)\right],$$

$$H_{9,10}=(1+ika')\left(\frac{n}{r_a}K_n(q_pr_a)-q_pK_{n+1}(q_pr_a)\right),$$

$$H_{9,11}=\frac{n}{r_a}K_n(q_{sh}r_a),$$

$$H_{9,12}=(ik+b')\left(\frac{n}{r_a}K_n(q_{sv}r_a)-q_{sv}K_{n+1}(q_{sv}r_a)\right),$$

$$H_{10,8}=\rho_f\omega^2I_n(fr_a),$$

$$H_{10,9}=\rho_f\omega^2K_n(fr_a),$$

$$H_{10,10}=(c_{11}q_p^2-c_{13}k^2+(c_{11}-c_{13})ika'q_p^2)K_n(q_pr_a)+\frac{2c_{66}}{r_a}(1+ika')\left(\frac{n^2-n}{r_a}K_n(q_pr_a)+q_pK_{n+1}(q_pr_a)\right),$$

$$H_{10,11}=-2c_{66}\frac{n}{r_a}\left(\frac{1-n}{r_a}K_n(q_{sh}r_a)+q_{sh}K_{n+1}(q_{sh}r_a)\right),$$

$$H_{10,12}=\left((c_{11}q_{sv}^2-c_{13}k^2)b'+(c_{11}-c_{13})ikq_{sv}^2\right)K_n(q_{sv}r_a)+2\frac{c_{66}}{r_a}(ik+b')\left(\frac{n^2-n}{r_a}K_n(q_{sv}r_a)+q_{sv}K_{n+1}(q_{sv}r_a)\right),$$

$$H_{11,10}=2c_{66}\frac{n}{r_a}(1+ika')\left(\frac{1-n}{r_a}K_n(q_pr_a)+q_pK_{n+1}(q_pr_a)\right),$$

$$H_{11,11}=-c_{66}q_{sh}^2\left(1+\frac{2n^2-2n}{q_{sh}^2r_a^2}\right)K_n(q_{sh}r_a)+\frac{2K_{n+1}(q_{sh}r_a)}{r_aq_{sh}},$$

$$H_{11,12}=2c_{66}\frac{n}{r_a}(ik+b')\left(\frac{1-n}{r_a}K_n(q_{sv}r_a)+q_{sv}K_{n+1}(q_{sv}r_a)\right),$$

$$H_{12,10}=c_{44}(2ik-a'(k^2+q_p^2))\left(\frac{n}{r_a}K_n(q_pr_a)-q_pK_{n+1}(q_pr_a)\right),$$

$$H_{12,11}=ikn\frac{c_{44}K_n(q_{sh}r_a)}{r_a},$$

$$H_{12,12}=c_{44}(k^2+q_{sv}^2-2ikb')\left(\frac{-n}{r_a}K_n(q_{sv}r_a)+q_{sv}K_{n+1}(q_{sv}r_a)\right),$$

式中,$\mu=\rho^{tool}(v_s^{tool})^2$ 为钻铤剪切模量;ρ^{tool} 为钻铤密度.

References

Cui Z W. 2004. Theoretical and numerical study of modified Biot's models, acoustoelectric well logging and acoustic logging while drilling excited by multipole acoustic sources [Ph. D. thesis] (in Chinese). Changchun: Jilin University.

He X. 2010. Simulations of acoustic logs in transversely isotropic formations and researches on permeability inversion [Ph. D. thesis](in Chinese). Harbin: Harbin Institute of Technology.

He X, Hu H S. 2009. Borehole flexural modes in transversely isotropic formations: Low-frequency asymptotic velocity. *Geophysics*, 74(4): E149-E158.

He X, Hu H S. 2010. Single-valued definition of the multivalued function for borehole acoustic waves in transversely isotropic formations. *Science China Physics, Mechanics and Astronomy*, 53(8): 1419-1426.

Hu H S, He X. 2009. The low-frequency asymptotic velocity of pseudo-Rayleigh, flexural, and screw waves in a transversely isotropic formation. *Chinese J. Geophys.* (in Chinese), 52(7): 1873-1880, doi: 10.3969/j.issn.0001-5733.2009.07.022.

Li X Q, Chen H, He X, et al. 2013. Analyses on mode waves of acoustic logging while drilling in transversely isotropic formations. *Chinese J. Geophys.* (in Chinese), 56(9): 3212-3222, doi: 10.6038/cjg20130933.

Lü Q D, Huang J P, Li Z C, et al. 2018. Efficient Gaussian beam method in time domain for anisotropic media. *Progress in Geophysics* (in Chinese), 33(6): 2428-2434, doi: 10.6038/pg2018BB0466.

Minear J, Birchak R, Robbins C, et al. 1995. Compressional slowness measurements while drilling. // SPWLA 36th Annual Logging Symposium. Paris, France: SPWLA.

Schmitt D P. 1988. Shear wave logging in elastic formations. *The Journal of the Acoustical Society of America*, 84(6): 2215-2229, doi: 10.1121/1.397015.

Song Y H, Chen H, Wang X M. 2020. Effect of pseudo-poles on the theoretical dispersion calculation of borehole mode waves in VTI formation. *Progress in Geophysics* (in Chinese), 35(2):

634-641, doi: 10.6038/pg2020CC0525.

Tang X M, Dubinsky V, Wang T, et al. 2003. Shear-velocity measurement in the logging-while-drilling environment: Modeling and field evaluations. *Petrophysics*, 44(2): 79-90.

Tang X M, Wang T, Patterson D. 2002. Multipole acoustic logging-while-drilling. //72nd Annual International Meeting. Salt Lake City, Utah: SEG, 364-367.

Thomsen L. 1986. Weak elastic anisotropy. *Geophysics*, 51(10): 1954-1966.

Wang R J, Qiao W X. 2015. Numerical study on quadrupole acoustic LWD in VTI formations. *Chinese J. Geophys.* (in Chinese), 58(8): 2862-2872, doi: 10.6038/cjg20150820.

Xu S. 2015. The theories and methods of inverting formation transverse isotropy using acoustic logging-while-drilling data [Master's thesis](in Chinese). Qingdao: China University of Petroleum (East China).

Zheng X B. 2012. The full-waveform simulation of acoustic logging while drilling [Master's thesis](in Chinese). Harbin: Harbin Institute of Technology.

Zheng X B. 2017. Theoretical simulations of monopole and dipole acoustic logging while drilling and investigations of propagation mechanism for individual waves [Ph. D. thesis](in Chinese). Harbin: Harbin Institute of Technology.

附中文参考文献

崔志文. 2004. 多孔介质声学模型与多极源声电效应测井和多极随钻声测井的理论与数值研究[博士论文]. 长春: 吉林大学.

胡恒山, 何晓. 2009. 横向各向同性地层井孔伪瑞利波、弯曲波、螺旋波的低频极限速度. 地球物理学报, 52(7): 1873-1880, doi: 10.3969/j.issn.0001-5733.2009.07.022.

何晓. 2010. 横观各向同性地层声波测井波场模拟与地层渗透率反演[博士论文]. 哈尔滨: 哈尔滨工业大学.

何晓, 胡恒山, 孙宝佃. 2010. 横向各向同性地层井孔中多值声场函数的单值化. 中国科学: 物理学 力学 天文学, 40(7): 850-857.

李希强, 陈浩, 何晓等. 2013. 横向各向同性地层中随钻声波测井模式波分析. 地球物理学报, 56(9): 3212-3222, doi: 10.6038/cjg20130933.

吕庆达, 黄建平, 李振春等. 2018. VTI 介质时间域高斯束偏移. 地球物理学进展, 33(6): 2428-2434, doi: 10.6038/pg2018BB0466.

宋云红, 陈浩, 王秀明. 2020. VTI 地层井孔模式波理论频散计算时伪极点的影响. 地球物理学进展, 35(2): 634-641, doi: 10.6038/pg2020CC0525.

唐晓明, 郑传汉. 2004. 定量测井声学. 赵晓敏译. 北京: 石油工业出版社.

王瑞甲, 乔文孝. 2015. VTI 地层随钻四极子声波测井数值研究. 地球物理学报, 58(8): 2862-2872, doi: 10.6038/cjg20150820.

许松. 2015. 随钻声波测井反演地层各向异性的理论与方法研究[硕士论文]. 青岛: 中国石油大学(华东).

郑晓波. 2012. 随钻声波测井的全波计算[硕士论文]. 哈尔滨: 哈尔滨工业大学.

郑晓波. 2017. 单极和偶极随钻声波测井理论模拟与分波传播特性研究[博士论文]. 哈尔滨: 哈尔滨工业大学.

(本文编辑 张正峰)

许松,苏远大,陈雪莲等. 2014. 含孔隙、裂隙地层随钻多极子声波测井理论. 地球物理学报,57(6):1999-2012,doi:10.6038/cjg20140630.

Xu S, Su Y D, Chen X L, et al. 2014. Numerical study on the characteristics of multipole acoustic logging while drilling in cracked porous medium. *Chinese J. Geophys.* (in Chinese),57(6):1999-2012,doi:10.6038/cjg20140630.

含孔隙、裂隙地层随钻多极子声波测井理论

许松,苏远大*,陈雪莲,唐晓明

中国石油大学(华东)地球科学与技术学院,青岛 266580

摘要 储层岩石中普遍存在孔隙与裂隙,对钻井中的测井声波产生重要影响.基于孔、裂隙介质弹性波理论,导出了随钻声波测井的井孔声场表达式.据此考察了地层裂隙密度与含气饱和度的变化时井孔内随钻多极子模式波(斯通利波、弯曲波和螺旋波)的速度、衰减与灵敏度以及地层纵、横波的响应特征.裂隙密度与含气饱和度对模式波的速度频散与衰减都有影响,且两参数的值越大,影响越大.具体来说,速度对裂隙密度更敏感,而衰减对含气饱和度更敏感.具有"艾里相"特征的随钻偶极和四极子波在地层含气时产生强烈衰减,可以作为判断地层含气的一个明显指示.理论模拟与实际测井数据分析结果符合较好.

关键词 随钻声波;裂隙密度;含气饱和度;频散;衰减;灵敏度;艾里相

doi:10.6038/cjg20140630 **中图分类号** P631 **收稿日期** 2013-12-09,2014-01-30 收修定稿

Numerical study on the characteristics of multipole acoustic logging while drilling in cracked porous medium

XU Song, SU Yuan-Da*, CHEN Xue-Lian, TANG Xiao-Ming

School of Geosciences, China University of Petroleum, Qingdao 266580, *China*

Abstract Cracks and pores universally exist in earth formation rocks, significantly affecting LWD acoustic waves. Using a cracked porous medium elastic wave theory, we derive LWD acoustic wave field for a fluid-filled borehole containing a drill collar and study the velocity dispersion, attenuation, and sensitivity of multipole wave modes (e.g. Stoneley, flexural and quadrupole waves) as a function of crack density and gas saturation. Increasing crack concentration and gas saturation can produce significant velocity change and attenuation. Relatively speaking, the velocity is more sensitive to crack density, while the attenuation is more sensitive to gas saturation. The dispersive LWD dipole and quadrupole waves characterized by a "Airy Phase" are strongly attenuated by gas saturation. This phenomenon can be used to detect the presence of gas in tight formations. The modeling and analysis results of this study are in agreement with results from field LWD data analyses.

Keywords Acoustic logging-while-drilling; Crack density; Gas saturation; Dispersion; Attenuation; Sensitivity; Airy phase

---

基金项目 国家自然科学基金(41174088,41204070),国家重点基础研究发展计划 973 项目(2014CB239006),中央高校基本科研业务费专项资金(14CX06076A)资助.

作者简介 许松,1990 年生,山东滨州人,在读研究生,主要从事随钻声波测井的方法和资料处理等方面的研究. E-mail: xusongupc@sina.com

***通讯作者** 苏远大,副教授,主要从事声波测井的方法和资料处理等方面研究. E-mail:syuanda@sina.com

1 引言

近年来,随钻声波测井技术发展迅速,渐有替代常规的电缆声波测井的趋势(唐晓明和郑传汉,2004).关于随钻声波测井在均质地层的传播规律,国内外已进行了大量工作(Tang et al., 2002; 崔志文, 2004; 苏远大等, 2006; 王华等, 2009).随钻声波测井在各向异性地层的模拟也取得了很大的进展(王瑞甲等, 2012; 李希强等, 2013).目前,随钻测井在非常规油气藏的勘探开发中应用也日益增大,已应用于页岩气的勘探开发(郝建飞等, 2012).

在非常规油气勘探中,地层中发育的裂隙或裂缝会极大地影响弹性波的传播,为此,唐晓明(2011)提出一个描述含孔隙、裂隙地层的弹性波统一理论.Tang 等(2012)进一步完善了该理论并将此应用于非常规的声波测井数据.陈雪莲和唐晓明(2012)将这一理论引入井孔声场中.模拟了不同裂隙参数下井孔中激发的模式波的频散曲线、衰减曲线、灵敏度及激发强度,并对多极子声源激发的全波特征进行了分析.Chen 等(2013)分析对比了孔裂隙地层电缆测井在井壁开孔与闭孔情况下的特征响应.

因此,研究随钻环境中的含孔隙、裂隙地层的声传播规律对非常规油气开发具有重要的意义.迄今为止,随钻环境下这方面的研究还未有报道.本文针对这一现状,模拟了随钻多极子波在低孔、低渗条件下裂隙发育地层的传播特征,并分析了声场在不同的孔隙流体下的响应.本文的工作为含孔隙、裂隙地层中的随钻声波测井数据解释和地层评价提供了理论依据.

2 随钻孔、裂隙介质井孔中的声场

随钻声波测井时,钻铤占据了井中流体相当大的部分.声源则模拟为贴钻铤壁的环状多极子声源,源在钻铤及其内外的流体中,以及井外的地层中激发出沿井轴方向传播的声场.图 1 给出了随钻声波测井模型的示意图.模型的界面有钻铤内流体与钻铤界面、钻铤与钻铤外流体界面、钻铤外流体界面与地层界面,三个界面据井眼中心轴距离分别为 r_a、r_b、R.

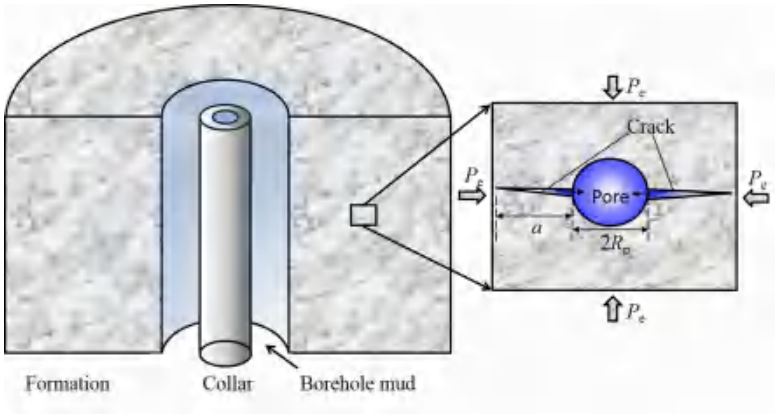


图 1 随钻声波测含孔隙、裂隙地层的物理模型

Fig. 1 A pore-crack model for acoustic LWD

2.1 钻铤内流体的声场

对于钻铤内的流体来讲,只有从外向内的入射波,而没有由内向外传播的波.采用柱坐标 (r,θ,z),则钻铤内流体声场的位移势 Φ' 为

$$\Phi'(k,\omega,r,\theta) = A'_n I_n(fr)\cos[n(\theta-\varphi)]e^{ikz}, \quad (1)$$

A'_n 为声场振幅系数,n 为多极子的阶数,φ 为多极子指向的参数方位角.由此得到钻铤内流体的径向位移 u'_f 以及应力 σ'_{rrf}:

$$u'_f(k,\omega,r,\theta) = A'_n\left[\frac{n}{r}I_n(fr) + fI_{n+1}(fr)\right]\cos[n(\theta-\varphi)]e^{ikz},$$

$$\sigma'_{rrf}(k,\omega,r,\theta) = -A'_n\rho_f\omega^2 I_n(fr)\cos[n(\theta-\varphi)]e^{ikz}, \quad (2)$$

式中 f 为流体径向波数,k 为轴向波数,I_n 为第一类 n 阶变形贝塞尔函数.

2.2 钻铤中的声场

钻铤中的纵波、SH 横波、SV 横波的位移势函数满足

$$\begin{cases}(\nabla^2+k_p^2)\Phi^{tool} = 0,\\ (\nabla^2+k_s^2)\chi^{tool} = 0,\\ (\nabla^2+k_s^2)\Gamma^{tool} = 0.\end{cases} \quad (3)$$

式中 Φ^{tool}、χ^{tool}、Γ^{tool} 分别为钻铤中纵波、SH 横波、SV 横波的位移势;$k_p = \omega/v_p^{tool}$ 纵波波数,v_p^{tool} 为钻铤纵波速度;$k_s = \omega/v_s^{tool}$ 横波波数,v_s^{tool} 为钻铤横波速度.

考虑从内向外的出射波和由外向内的入射波,(3)式的解形式为

$$\begin{cases}\Phi^{\text{tool}} = \\ [A_n^{\text{tool}} I_n(p_{\text{tool}} r) + B_n^{\text{tool}} K_n(p_{\text{tool}} r)]\cos[n(\theta-\varphi)]\mathrm{e}^{\mathrm{i}kz}, \\ \chi^{\text{tool}} = \\ [C_n^{\text{tool}} I_n(s_{\text{tool}} r) + D_n^{\text{tool}} K_n(s_{\text{tool}} r)]\sin[n(\theta-\varphi)]\mathrm{e}^{\mathrm{i}kz}, \\ \Gamma^{\text{tool}} = \\ [E_n^{\text{tool}} I_n(s_{\text{tool}} r) + F_n^{\text{tool}} K_n(s_{\text{tool}} r)]\cos[n(\theta-\varphi)]\mathrm{e}^{\mathrm{i}kz}. \end{cases} \tag{4}$$

式中 $p_{\text{tool}} = \sqrt{k^2 - (\omega/v_{\text{p}}^{\text{tool}})^2}$ 为钻铤纵波径向波数;$s_{\text{tool}} = \sqrt{k^2 - (\omega/v_{\text{s}}^{\text{tool}})^2}$ 为钻铤横波径向波数;I_n 和 K_n 分别为第一类和第二类 n 阶变形贝塞尔函数. $A_n^{\text{tool}}(B_n^{\text{tool}})$,$C_n^{\text{tool}}(D_n^{\text{tool}})$ 和 $E_n^{\text{tool}}(F_n^{\text{tool}})$ 分别是入射(出射)纵波,SH 和 SV 横波的振幅系数.

求得位移应力表达式如下:

$$\begin{cases} u^{\text{tool}} = \dfrac{\partial \Phi^{\text{tool}}}{\partial r} + \dfrac{1}{r}\dfrac{\partial \chi^{\text{tool}}}{\partial \theta} + \dfrac{\partial^2 \Gamma^{\text{tool}}}{\partial r \partial z}, \\ \sigma_{rr}^{\text{tool}} = \left[(\lambda^t + 2\mu^t)\dfrac{\partial^2 \Phi^{\text{tool}}}{\partial r^2} + \dfrac{\lambda^t}{r}\dfrac{\partial \Phi^{\text{tool}}}{\partial r} + \dfrac{\lambda^t}{r^2}\dfrac{\partial^2 \Phi^{\text{tool}}}{\partial \theta^2} + \lambda^t \dfrac{\partial^2 \Phi^{\text{tool}}}{\partial z^2}\right] + \dfrac{2\mu^t}{r}\left(\dfrac{\partial^2 \chi^{\text{tool}}}{\partial r \partial \theta} - \dfrac{1}{r}\dfrac{\partial \chi^{\text{tool}}}{\partial \theta}\right) \\ \qquad + \left[(\lambda^t + 2\mu^t)\dfrac{\partial^3 \Gamma^{\text{tool}}}{\partial r^2 \partial z} + \dfrac{\lambda^t}{r}\dfrac{\partial^2 \Gamma^{\text{tool}}}{\partial r \partial z} + \dfrac{\lambda^t}{r^2}\dfrac{\partial^3 \Gamma^{\text{tool}}}{\partial \theta^2 \partial z} + \lambda^t k_{\text{s}}^2 \dfrac{\partial \Gamma^{\text{tool}}}{\partial z} + \lambda^t \dfrac{\partial^3 \Gamma^{\text{tool}}}{\partial z^3}\right], \\ \sigma_{r\theta}^{\text{tool}} = \dfrac{2\mu^t}{r}\left[\left(\dfrac{\partial^2 \Phi^{\text{tool}}}{\partial r \partial \theta} - \dfrac{1}{r}\dfrac{\partial \Phi^{\text{tool}}}{\partial \theta}\right) + \left(\dfrac{1}{2r}\dfrac{\partial^2 \chi^{\text{tool}}}{\partial \theta^2} + \dfrac{\partial \chi^{\text{tool}}}{2\partial r} - \dfrac{r\partial^2 \chi^{\text{tool}}}{2\partial r^2}\right) + \left(\dfrac{\partial^3 \Gamma^{\text{tool}}}{\partial r \partial \theta \partial z} - \dfrac{1}{r}\dfrac{\partial^2 \Gamma^{\text{tool}}}{\partial \theta \partial z}\right)\right], \\ \sigma_{rz}^{\text{tool}} = \mu^t\left[2\dfrac{\partial^2 \Phi^{\text{tool}}}{\partial r \partial z} + \dfrac{1}{r}\dfrac{\partial^2 \chi^{\text{tool}}}{\partial \theta \partial z} + \left(k_{\text{s}}^2 \dfrac{\partial \Gamma^{\text{tool}}}{\partial r} + 2\dfrac{\partial^3 \Gamma^{\text{tool}}}{\partial z^2 \partial r}\right)\right]. \end{cases} \tag{5}$$

2.3　钻铤外流体的声场

对于钻铤外的流体来讲,既有从外向内的入射波,也有由内向外传播的波,钻铤外流体的位移势 Φ 为

$$\Phi(k,\omega,r,\theta) = [A_n I_n(fr) + B_n K_n(fr)]\cos[n(\theta-\varphi)]\mathrm{e}^{\mathrm{i}kz}, \tag{6}$$

由此得到,钻铤外流体的径向位移 u_{f} 以及应力 $\sigma_{rr\text{f}}$:

$$\begin{aligned} u_{\text{f}}(k,\omega,r,\theta) &= \left\{A_n\left[\frac{n}{r}I_n(fr) + fI_{n+1}(fr)\right] + B_n\left[\frac{n}{r}K_n(fr) - fK_{n+1}(fr)\right]\right\}\cos[n(\theta-\varphi)]\mathrm{e}^{\mathrm{i}kz}, \\ \sigma_{rr\text{f}}(k,\omega,r,\theta) &= -\rho_{\text{f}}\omega^2[A_n I_n(fr) + B_n K_n(fr)]\cos[n(\theta-\varphi)]\mathrm{e}^{\mathrm{i}kz}. \end{aligned} \tag{7}$$

2.4　含孔隙、裂隙地层的弹性波动理论及声场

含孔隙、裂隙地层的应力位移的本构关系由下式给出(Tang et al., 2012):

$$\sigma_{ij} = 2\mu e_{ij} + (\lambda e - \alpha p)\delta_{ij}, \tag{8}$$

其中 σ_{ij} 为介质平均应力;λ 为拉梅常数,且 $\lambda = K_{\text{d}} - 2\mu/3$,$\mu$ 为剪切模量,K_{d} 为介质干燥(或排水)条件下的体积模量;p 为孔隙流体压力,$p = -(\alpha\nabla\cdot\boldsymbol{u} + \nabla\cdot\boldsymbol{w})/[\beta + S(\omega)]$,$\boldsymbol{u}$ 是固体位移,$\boldsymbol{w}$ 是流体和固体的相对位移;e_{ij} 是应变张量,且 $e = \nabla\cdot u$;ω 是角频率;α 和 β 是由 $\alpha = 1 - K_{\text{d}}/K_{\text{s}}$ 和 $\beta = (\alpha - \phi)/K_{\text{s}} + \phi/K_{\text{f}}$ 分别给出的两个参数组合,其中 ϕ 为孔隙度,K_{s} 和 K_{f} 分别是介质基质和孔隙流体的体积模量. 函数 $S(\omega)$ 为描述裂隙和孔隙间的局部流动,即挤喷流效应. 具体表达式如下:

$$S(\omega) = \frac{\dfrac{8\varepsilon(1-\nu_0)(1+\xi)^3}{3\mu_0}\left(\dfrac{1/K_0 - 1/K_{\text{s}}}{1/K_{\text{d}} - 1/K_0}\right)M}{1 - \dfrac{2\mathrm{i}\omega\eta(1+2\xi)}{2K_{\text{f}}\xi\gamma^2}\left[1 + \dfrac{4(1-\nu_0)K_{\text{f}}(1+\xi)^3}{3\pi\mu_0\gamma(1+2\xi)}M\right]}, \tag{9}$$

其中 $M = 1 + \dfrac{4-5\nu_0}{2(7-5\nu_0)}\dfrac{\xi^3}{(1+\xi)^3} + \dfrac{9}{2(7-5\nu_0)}\dfrac{\xi^5}{(1+\xi)^5}$;$\xi$ 为孔隙与裂隙的体积比,表达式为 $\xi = [3\phi/(4\pi\varepsilon)]^{1/3}$;$\eta$ 为孔隙流体黏度,ε 是裂隙密度,γ 是裂隙纵横比,μ_0 和 ν_0 是没有挤喷流时背景介质的剪切模量和泊松比,这种情况下,μ 和 K_{d} 可由 Thomsen (1985)的 Biot 相恰理论计算得到.

孔、裂隙介质中存在三种模式波,分别是快、慢纵波和横波,现引入这三种波的位移势,表示如下:

$$\begin{aligned} \boldsymbol{u} &= \nabla\Phi_{\text{fast}} + \nabla\Phi_{\text{slow}} + \nabla\times(\chi\hat{\boldsymbol{z}}) + \nabla\times\nabla\times(\Gamma\hat{\boldsymbol{z}}), \\ \boldsymbol{w} &= b_{\text{fast}}\nabla\Phi_{\text{fast}} + b_{\text{slow}}\nabla\Phi_{\text{slow}} + b_{\text{s}}\left[\nabla\times(\chi\hat{\boldsymbol{z}}) + \nabla\times\nabla\times(\Gamma\hat{\boldsymbol{z}})\right], \end{aligned} \tag{10}$$

其中 Φ_{fast} 和 Φ_{slow} 分别表示快速和慢速纵波的位移势,χ 和 Γ 分别代表 SH 和 SV 横波势函数;$\hat{\boldsymbol{z}}$ 是沿井轴向的单位矢量.

对于井外的无限大孔、裂隙介质,由方程(8)到(10)可得到孔裂隙地层的应力和位移,其中 (k,ω) 域中的势函数表示如下(Chen et al., 2013):

$$\begin{Bmatrix}\Phi_{\text{fast}}\\ \Phi_{\text{slow}}\\ \chi\\ \Gamma\end{Bmatrix}=\begin{cases}A_n^{\text{fast}}K_n(q_{\text{fast}}r)\cos[n(\theta-\varphi)]\mathrm{e}^{\mathrm{i}kz}\\ A_n^{\text{slow}}K_n(q_{\text{slow}}r)\cos[n(\theta-\varphi)]\mathrm{e}^{\mathrm{i}kz}\\ C_nK_n(q_{\text{s}}r)\sin[n(\theta-\varphi)]\mathrm{e}^{\mathrm{i}kz}\\ D_nK_n(q_{\text{s}}r)\cos[n(\theta-\varphi)]\mathrm{e}^{\mathrm{i}kz}\end{cases}, \tag{11}$$

其中 q_{fast}、q_{slow}、q_{s} 分别为快纵波、慢纵波、横波径向波数,具体表达式如下:

$$\begin{aligned}q_{\text{fast}}&=\sqrt{k^2-k_{\text{fast}}^2},\\ q_{\text{slow}}&=\sqrt{k^2-k_{\text{slow}}^2},\\ q_{\text{s}}&=\sqrt{k^2-k_{\text{shear}}^2}.\end{aligned} \tag{12}$$

其中,k_{fast}、k_{slow}、k_{shear} 分别是快纵波、慢纵波、横波的波数,这些波的波数推导见 Chen 等(2013),波数的数学公式可见唐晓明等(2013),其中包含了描述孔隙、裂隙介质性质的渗透率 κ_0,孔隙弯曲度 τ,以及裂隙密度 ε 和纵横比 γ 等参数.

将方程(11)中的势函数表达为柱坐标下的形式,位移分量与孔隙压力和应力表示如下:

$$\begin{cases}u_r=\dfrac{\partial\Phi_{\text{fast}}}{\partial r}+\dfrac{\partial\Phi_{\text{slow}}}{\partial r}+\dfrac{1}{r}\dfrac{\partial\chi}{\partial\theta}+\dfrac{\partial^2\Gamma}{\partial r\partial z},\\ w_r=b_{\text{fast}}\dfrac{\partial\Phi_{\text{fast}}}{\partial r}+b_{\text{slow}}\dfrac{\partial\Phi_{\text{slow}}}{\partial r}+b_{\text{s}}\dfrac{1}{r}\dfrac{\partial\chi}{\partial\theta}+b_{\text{s}}\dfrac{\partial^2\Gamma}{\partial r\partial z},\\ p=k_{\text{fast}}^2\left\{(\alpha+b_{\text{fast}})/[\beta+S(\omega)]\right\}\Phi_{\text{fast}}+k_{\text{slow}}^2\left\{(\alpha+b_{\text{slow}})/[\beta+S(\omega)]\right\}\Phi_{\text{slow}},\\ \sigma_{rr}=2\mu\left[\dfrac{\partial^2\Phi_{\text{fast}}}{\partial r^2}+\dfrac{\partial^2\Phi_{\text{slow}}}{\partial r^2}-\dfrac{1}{r^2}\dfrac{\partial\chi}{\partial\theta}+\dfrac{1}{r}\dfrac{\partial^2\chi}{\partial r\partial\theta}+\dfrac{\partial^3\Gamma}{\partial r^2\partial z}\right]\\ \qquad-k_{\text{fast}}^2\Phi_{\text{fast}}\left[\lambda+\alpha\dfrac{\alpha+b_{\text{fast}}}{\beta+S(\omega)}\right]-k_{\text{slow}}^2\Phi_{\text{slow}}\left[\lambda+\alpha\dfrac{\alpha+b_{\text{slow}}}{\beta+S(\omega)}\right],\\ \sigma_{rz}=2\mu\left[\dfrac{\partial^2\Phi_{\text{fast}}}{\partial r\partial z}+\dfrac{\partial^2\Phi_{\text{slow}}}{\partial r\partial z}+\dfrac{\partial^3\Gamma}{\partial r\partial z^2}\right]+\mu\left[k_{\text{shear}}^2\dfrac{\partial\Gamma}{\partial r}+\dfrac{1}{r}\dfrac{\partial^2\chi}{\partial z\partial\theta}\right],\\ \sigma_{r\theta}=\dfrac{\mu}{r}\left(\dfrac{2\partial^2\Phi_{\text{fast}}}{\partial r\partial\theta}+\dfrac{2\partial^2\Phi_{\text{slow}}}{\partial r\partial\theta}-\dfrac{2\partial\Phi_{\text{fast}}}{r\partial\theta}-\dfrac{2\partial\Phi_{\text{slow}}}{r\partial\theta}\right)+\dfrac{\mu}{r}\left(\dfrac{1}{r}\dfrac{\partial^2\chi}{\partial\theta^2}+\dfrac{\partial\chi}{\partial r}-\dfrac{r\partial^2\chi}{\partial r^2}\right)+\dfrac{\mu}{r}\left(\dfrac{2\partial^3\Gamma}{\partial r\partial z\partial\theta}-\dfrac{2\partial^2\Gamma}{r\partial z\partial\theta}\right).\end{cases} \tag{13}$$

2.5 边界条件

以上理论给出了图 1 所示模型各部分的声场,由界面处的边界条件衔接.计算声场时,在钻铤表面放置一环状多极子压力声源,以实现声场的激发.

2.5.1 钻铤内流体与钻铤界面:

$$\begin{cases}u_{\text{f}}'\big|_{r=r_{\text{a}}}=u^{\text{tool}}\big|_{r=r_{\text{a}}},\\ \sigma_{rr\text{f}}'\big|_{r=r_{\text{a}}}=\sigma_{rr}^{\text{tool}}\big|_{r=r_{\text{a}}},\\ 0=\sigma_{rz}^{\text{tool}}\big|_{r=r_{\text{a}}},\\ 0=\sigma_{r\theta}^{\text{tool}}\big|_{r=r_{\text{a}}}.\end{cases} \tag{14}$$

2.5.2 钻铤与钻铤外流体界面

$$\begin{cases}u^{\text{tool}}\big|_{r=r_{\text{b}}}=u_{\text{f}}\big|_{r=r_{\text{b}}},\\ \sigma_{rr}^{\text{tool}}\big|_{r=r_{\text{b}}}=\sigma_{rr\text{f}}\big|_{r=r_{\text{b}}}+\sigma^{\text{s}},\\ \sigma_{rz}^{\text{tool}}\big|_{r=r_{\text{b}}}=0,\\ \sigma_{r\theta}^{\text{tool}}\big|_{r=r_{\text{b}}}=0.\end{cases} \tag{15}$$

其中,I 为环状声源,具体表达式为

$$\sigma^{\text{s}}=\begin{cases}p_0 & (n=0),\\ 2\sin(n\theta_0)p_0/(\pi n) & (n=1,n=2).\end{cases} \tag{16}$$

式(16)是力源的加载方式(崔志文, 2004),还可采用体积膨胀源的加载方式(唐晓明和郑传汉, 2004),将一环状多极子位移加于上述的位移边界条件,这里我们采用前一加载方式.

2.5.3 钻铤外流体与地层界面

考虑井壁为开放孔隙的情况,即井中流体与孔隙中流体可以自由交换,此时井中压力与地层孔隙中的流体压力相等.这时井壁处的边界条件如下:

$$\begin{cases}u_{r\text{f}}\big|_{r=R}=u_r\big|_{r=R}+w_r\big|_{r=R},\\ \sigma_{rr\text{f}}\big|_{r=R}=\sigma_{rr}\big|_{r=R},\\ p_{\text{f}}\big|_{r=R}=p\big|_{r=R},\\ 0=\sigma_{rz}\big|_{r=R},\\ 0=\sigma_{r\theta}\big|_{r=R}.\end{cases} \tag{17}$$

将(1)至(13)式中各部分声场的应力和位移用于(14)到(17)式的边界条件,得到以下矩阵方程:

$$\{H_{ij}\}_{13\times13}\cdot\{A'_n,A_n^{\text{tool}},B_n^{\text{tool}},C_n^{\text{tool}},D_n^{\text{tool}},E_n^{\text{tool}},F_n^{\text{tool}},A_n,B_n,A_n^{\text{fast}},A_n^{\text{slow}},C_n,D_n\}^{\mathrm{T}}$$
$$=\{0,0,0,0,0,\sigma^{\mathrm{s}},0,0,0,0,0,0,0\}^{\mathrm{T}},\tag{18}$$

矩阵 $\boldsymbol{H}$ 元素的表达式较冗繁,特地在附录中具体给出.

3　孔裂隙地层随钻多极子模式波频散和衰减特性

依照上述理论分析,我们对含孔隙、裂隙地层中的随钻多极子声波测井进行了数值模拟. 表 1 为模型的井内流体与钻铤的具体参数;地层为含孔隙、裂隙的无限大地层,本文模拟了不同的地层流体对声场的影响,表 2 列出了两组孔裂隙流体参数.

表 1　井内流体与钻铤参数

Table 1　Parameters of the fluid and the collar

	外半径/m	横波速度/(m·s^{-1})	纵波速度/(m·s^{-1})	密度/(m·s^{-1})
钻铤内流体	0.027	—	1500	1000
钻铤	0.090	3130	5860	7850
钻铤外流体	0.117	—	1500	1000

表 2　含孔隙、裂隙介质地层参数

Table 2　Parameters of formation which contains pores and cracks

	K_{s} /GPa	μ_{s} /GPa	ρ_{s} /(kg·m^{-3})	ϕ_{p}	ρ_{f} /(kg·m^{-3})	K_{f} /GPa	η/cp	κ_0 /mD	τ	ε	γ
地层含水	37.9	32.6	2650	0.10	1000	2.25	1	5	2.4	0～0.3	0.002
地层含气	37.9	32.6	2650	0.10	140	0.014	0.022	5	2.4	0～0.3	0.002

本文主要针对模式波的频散曲线与衰减曲线进行探讨,模式波的频散特性主要由频散方程(18)决定,令式(18)矩阵的行列式为零,得出该频散方程:

$$D(k,\omega)=\det H(k,\omega)=0,\tag{19}$$

通过求解方程(19)得到相应模式波波数在不同频率下的根,从而得到模式波的相速度与衰减:

$$v(\omega)=\frac{\omega}{\mathrm{Re}(k(\omega))},\tag{20}$$

$$Q^{-1}(\omega)=2\frac{\mathrm{Im}(k(\omega))}{\mathrm{Re}(k(\omega))}.\tag{21}$$

模式波的相速度与衰减对于某一模型参数 q 的灵敏度见下式(唐晓明和郑传汉, 2004),其实质就是归一化后的相速度或衰减对该参数的偏微分. 通过灵敏度分析可以探究不同频率条件下该参数对相速度或衰减的影响程度,有

$$\begin{aligned}\text{Sensitivity}\{v(\omega)\}&=\left(\frac{q}{v(\omega)}\right)\frac{\partial v(\omega)}{\partial q},\\ \text{Sensitivity}\{Q^{-1}(\omega)\}&=\left(\frac{q}{Q^{-1}(\omega)}\right)\frac{\partial Q^{-1}(\omega)}{\partial q}.\end{aligned}\tag{22}$$

3.1　随钻单极子斯通利波

图 2 是含水致密地层裂隙密度变化时,充液井孔中随钻单极子激发的钻铤外斯通利波的频散、衰减以及裂隙密度对相速度与衰减的灵敏度曲线. 具体参数见表 1 与表 2. 当裂隙密度从 0.00 增大到 0.25时,斯通利波相速度逐渐减小(图 2a),对应的衰减曲线逐渐增大(图 2b). 斯通利波相速度对裂隙密度的灵敏度曲线随频率增大而减小(图 2c),说明致密地层的裂隙发育可以对斯通利波产生可观的影响. 随着裂隙密度的增大,斯通利波的相速度与衰减对裂隙密度的灵敏度也会提高.

孔裂隙理论所预示的流体灵敏度在地层的油气识别中有着重要的作用. 为此,我们模拟了不同孔裂隙流体中含气饱和度下的变化规律. 流体为水、气混合而成,混合后流体密度、模量和黏度的表达式为(Brie et al., 1995)

$$\begin{aligned}\rho_{\mathrm{f}}&=(1-S_{\mathrm{g}})\rho_{\mathrm{w}}+S_{\mathrm{g}}\rho_{\mathrm{g}},\\ K_{\mathrm{f}}&=(K_{\mathrm{w}}-K_{\mathrm{g}})\cdot(1-S_{\mathrm{g}})^2+K_{\mathrm{g}},\\ \eta&=\eta_{\mathrm{w}}^{(1-S_{\mathrm{g}})}\cdot\eta_{\mathrm{g}}^{S_{\mathrm{g}}}.\end{aligned}\tag{23}$$

式中 S_{g} 为含气饱和度. 图 3 是致密地层裂隙密度一定时($\varepsilon=0.20$),不同的含气饱和度下充满液体井孔中随钻单极子激发的斯通利波的速度频散、衰减以及这两者对含气饱和度的灵敏度曲线. 当地层含气饱和度增加时,斯通利波相速度逐渐减小,尤其是对低频处频散曲线的影响(图 3a),含气饱和度对相速度的影响比裂隙密度对其影响要小(图 3a、图 2a),这一点通过灵敏度曲线也能很好地反映出来(图 2c、图 3c). 图 3b 表明衰减随含气饱和度提高逐渐增大. 图 3d 表明当含气饱和度增大时,对衰减的灵敏度也会急剧增大. 可见地层流体性质对斯通利波衰减的影响很大. 以上模拟表明,随钻单极斯通利波

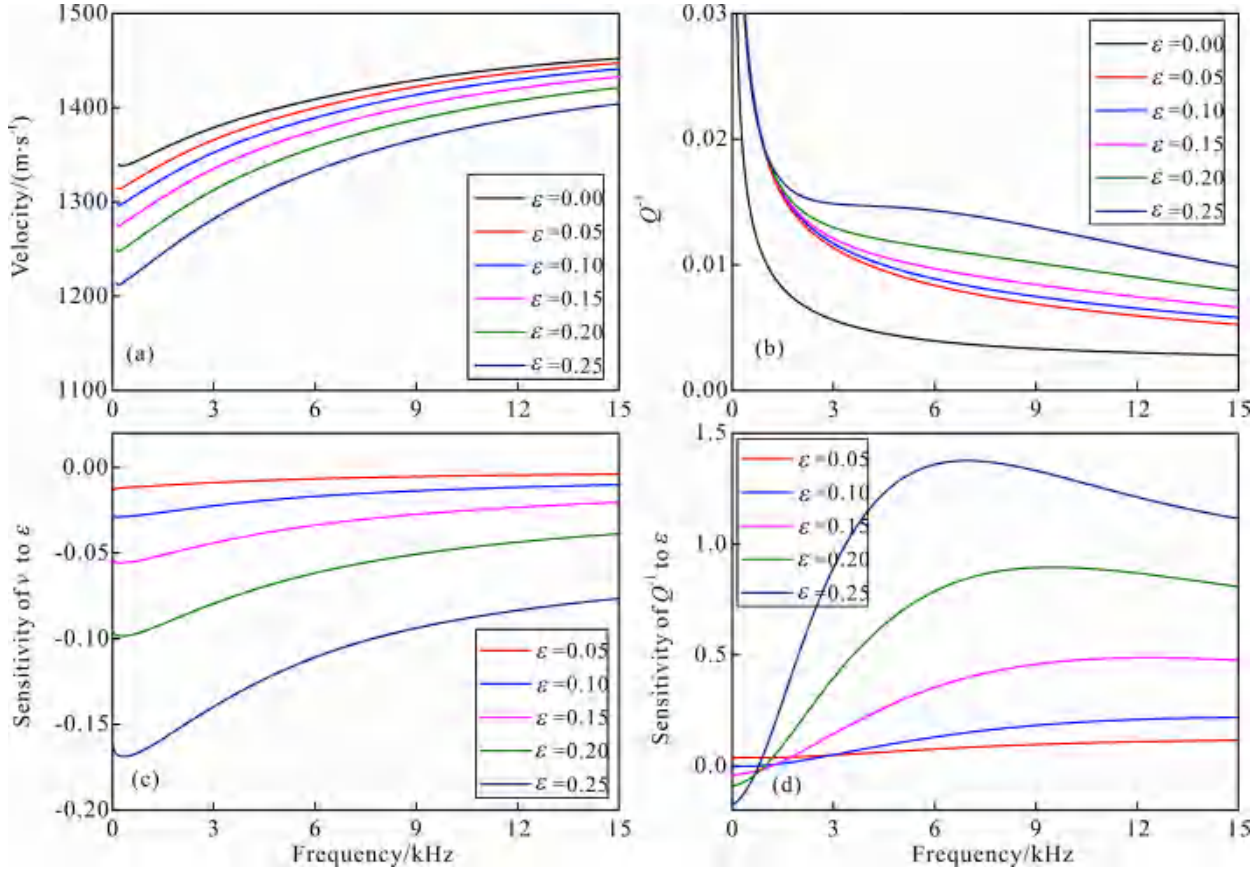


图 2 不同裂隙密度下的随钻单极子模拟

(a) 频散曲线；(b) 衰减曲线；(c)速度灵敏度曲线；(d) 衰减灵敏度曲线.

Fig. 2 Simulation of LWD monopole for different crack density values

(a) Phase velocity dispersion curves; (b) Attenuation curves; (c) Velocity sensitivity to ε; (d) Attenuation sensitivity to ε.

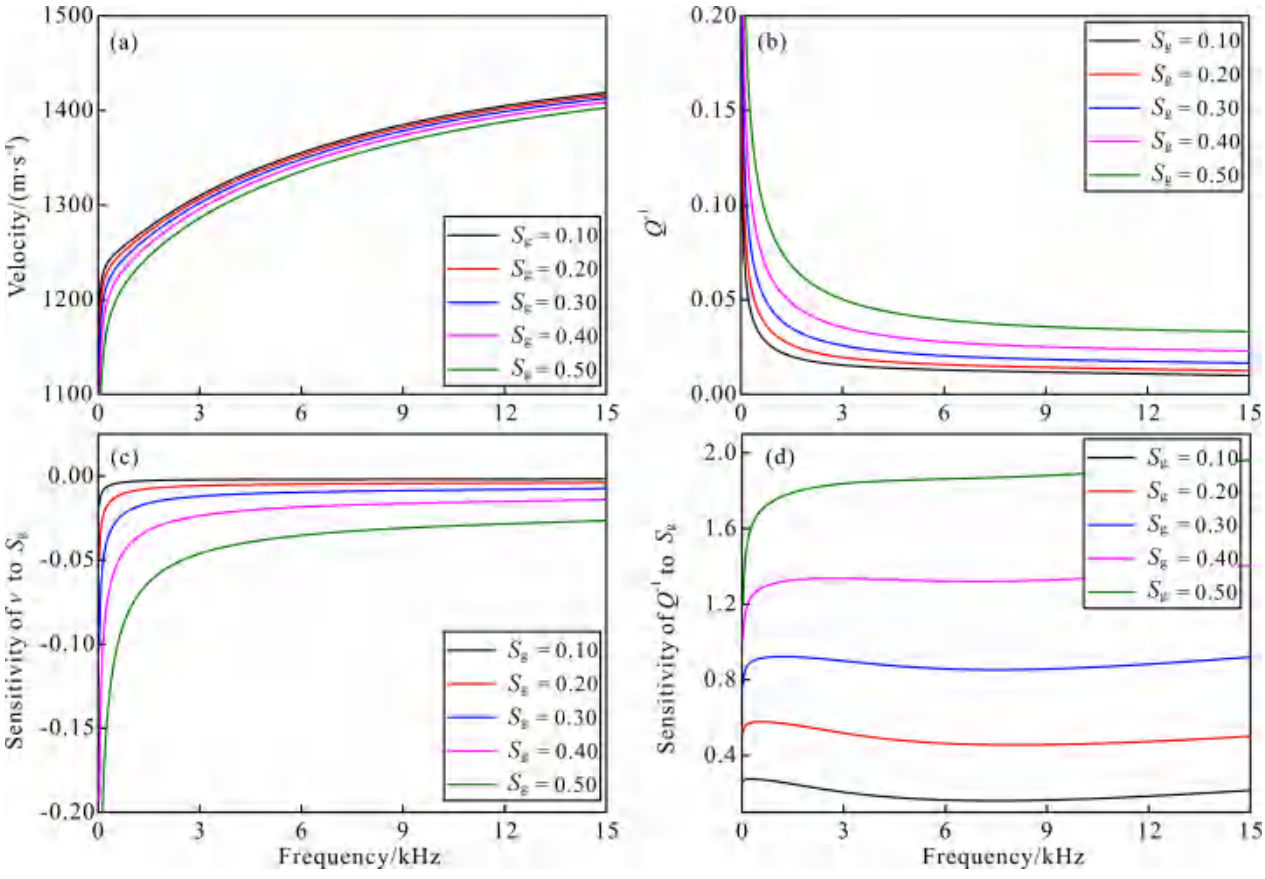


图 3 不同含气饱和度下的随钻单极子模拟

(a) 频散曲线；(b) 衰减曲线；(c) 速度灵敏度曲线；(d) 衰减灵敏度曲线.

Fig. 3 Simulation of LWD monopole for different gas saturations

(a) Phase velocity dispersion curves; (b) Attenuation curves; (c) Velocity sensitivity to S_g; (d) Attenuation sensitivity to S_g.

相速度对地层裂隙密度更加敏感,而波的衰减对地层流体性质更加敏感.这一现象可用于识别裂隙地层中的油气显示.

3.2　随钻偶极子模式波

式(18)中 $n=1$ 对应的是偶极激发的情况,同样,我们模拟了随钻偶极子的响应特征.图 4 是含水致密地层不同裂隙密度时随钻偶极子激发的弯曲波的频散、衰减以及灵敏度曲线.弯曲波相速度随裂隙密度的增加而减小(图 4a),与此相应的是衰减增加(图 4b).值得一提的是,低频处(3 kHz 左右)随钻偶极的群速度有一极小值,群速度的极小值在波列中产生,称为"艾里相"(Airy Phase)的波包,且在此频段内的衰减极大值形成一个明显的脊峰.随着频率的增大,受井眼中钻铤的影响,速度的频散特性与电缆偶极相比变化较大.偶极子弯曲波速度对裂隙密度的灵敏度在艾里相频段剧烈减小,随着频率增大受钻铤的影响有所提高(图 4c).在常规的测井频段内,速度对裂隙密度的灵敏度恰好落在极小值区域,从这个角度上也说明了随钻偶极测井的缺点,即测井频段内的强烈频散以及对地层裂隙的低灵敏度.图 5 表示不同的含气饱和度下充满液体井孔中偶极子弯曲波的特征响应.模拟表明,含气饱和度的增大会使得弯曲波速度减小,但变化不明显.衰减随着含气饱和度的增大而增加.

3.3　随钻四极子模式波

式(18)中 $n=2$ 对应的是四极激发的情况.鉴于四极子波已广泛应用于随钻横波测量(唐晓明和郑传汉, 2004),对此情况的模拟尤为重要.图 6 是含水致密地层不同裂隙密度时随钻四极子激发的螺旋波的频散、衰减、以及灵敏度曲线.裂隙密度的增大会使得四极子螺旋波相速度减小,而衰减增大.衰减曲线中的峰值区域对应着频散曲线的艾里相(图 6b)区域.随钻四极子波对不同裂隙密度和含气饱和度的变化特征与 Chen 等(2013)模拟的电缆偶极子变化规律很相似,说明了这类模式波(称为"低频相速度趋于横波波速"的横波型模式波)的一些共性.固定裂隙密度($\varepsilon=0.20$),含气饱和度增大会使得四极子螺旋波相速度减小,衰减增大(图 7a、b).通过对含气饱和度灵敏的模拟,表明地层流体对衰减的影响很大.

4　裂隙参数对随钻多极子波形的影响

随钻声波测井通常用单极子测量地层纵波和斯通利波,而用四极子测量横波信息(唐晓明和郑传汉, 2004).为了研究随钻多极子声波在孔、裂隙地层中的传播特征,本文数值模拟了随钻单极子和四极子的波形.数值模拟所用地层及仪器参数由表 1、2 中给出.

4.1　随钻单极子波形特征

随钻单极子数值模拟时,源距为 5 m.数值模拟采用高斯源加载于钻铤外壁,见文献(崔志文, 2004),主频为 9 kHz.图 8 给出了不同裂隙密度下随钻单极子全波波形对比.黑线表示地层流体完全含水,红线表示地层百分百含气.在全波列中,有钻铤拉伸波、P 波、S 波和 ST 波模式,由于横波和斯通利波能量主导,我们将钻铤波和地层纵波幅度放大 100 倍来加以显示.由于地层很致密,地层纵波与钻铤波由于速度相近,叠加在一起,为了区分两者,在理论模拟时加大了钻铤波的衰减($Q=5$),以此来模拟实际随钻声波仪器中隔声体的作用.为了方便对比,我们将裂隙密度为 0 和 0.25 影响下的波形起跳点连接起来.模拟表明,裂隙密度增大时,地层含气和含水情况下地层纵波、横波与斯通利波速度减小,幅度降低,钻铤波不受裂隙密度的影响.且斯通利波幅度减小,也就是说衰减会随裂隙密度增大而增大.红线与黑线对比可知,当地层流体性质发生变化,即地层含气时,流体的可压缩性变大,使得体积模量减小,孔、裂隙地层的纵波速度减小,在波形上表现为波至起跳点延迟,裂隙密度越大该现象越明显.流体性质的改变基本不影响横波速度,但对斯通利波产生巨大的衰减变化.以上模拟表明,地层含气时,纵横波速比会降低,斯通利波会严重衰减.相对比横波,地层纵波在地层含气时也会产生相当程度的衰减.可利用该特性判断地层是否含气.

4.2　随钻四极子波形特征

图 9 为孔裂隙地层随钻四极子声场模拟结果.源距为 3 m,声源主频 3 kHz.裂隙密度的增加会引起地层横波速度减小;对比地层含水和含气的模拟结果,黑线(水)与红线(气)起跳点一样,表明流体性质的变化不影响地层横波速度,这与随钻单极子模拟的结果吻合.值得注意的是,地层含气时,艾里相波的能量严重衰减,表明含气对具有艾里相的横波型导波衰减影响很大,图 7b 与图 7d 所对应的频域模拟结果也证明了这一点.这与 Chen 等(2013)模拟的电缆偶极子波的变化规律很相似,可以将此现象作为声波测井中此类模式波的一个共性来识别油气.

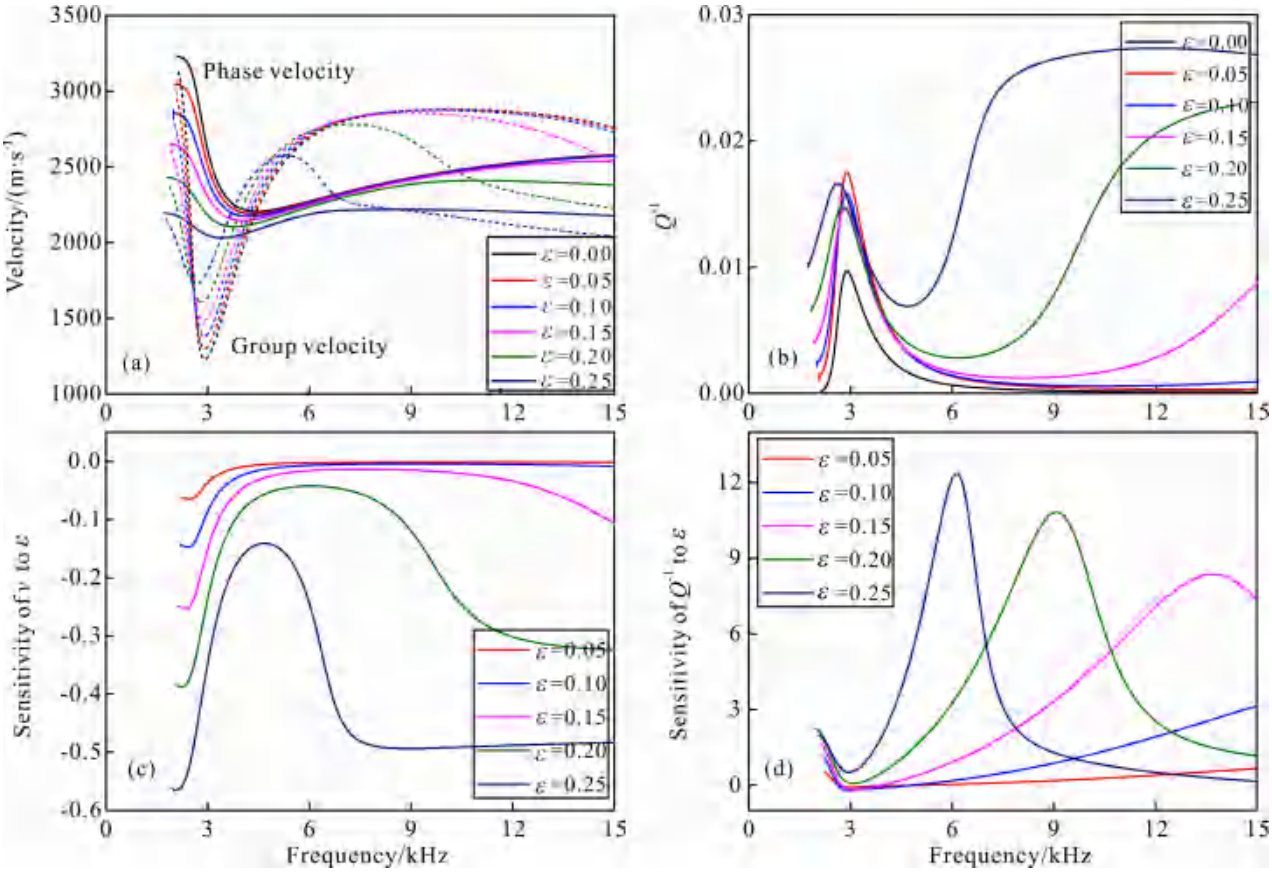


图 4 不同裂隙密度下的随钻偶极子模拟

(a) 频散曲线；(b) 衰减曲线；(c) 速度灵敏度曲线；(d) 衰减灵敏度曲线.

Fig. 4 Simulation of LWD dipole for different crack density values

(a) Phase velocity dispersion curves; (b) Attenuation curves; (c) Velocity sensitivity to ε; (d) Attenuation sensitivity to ε.

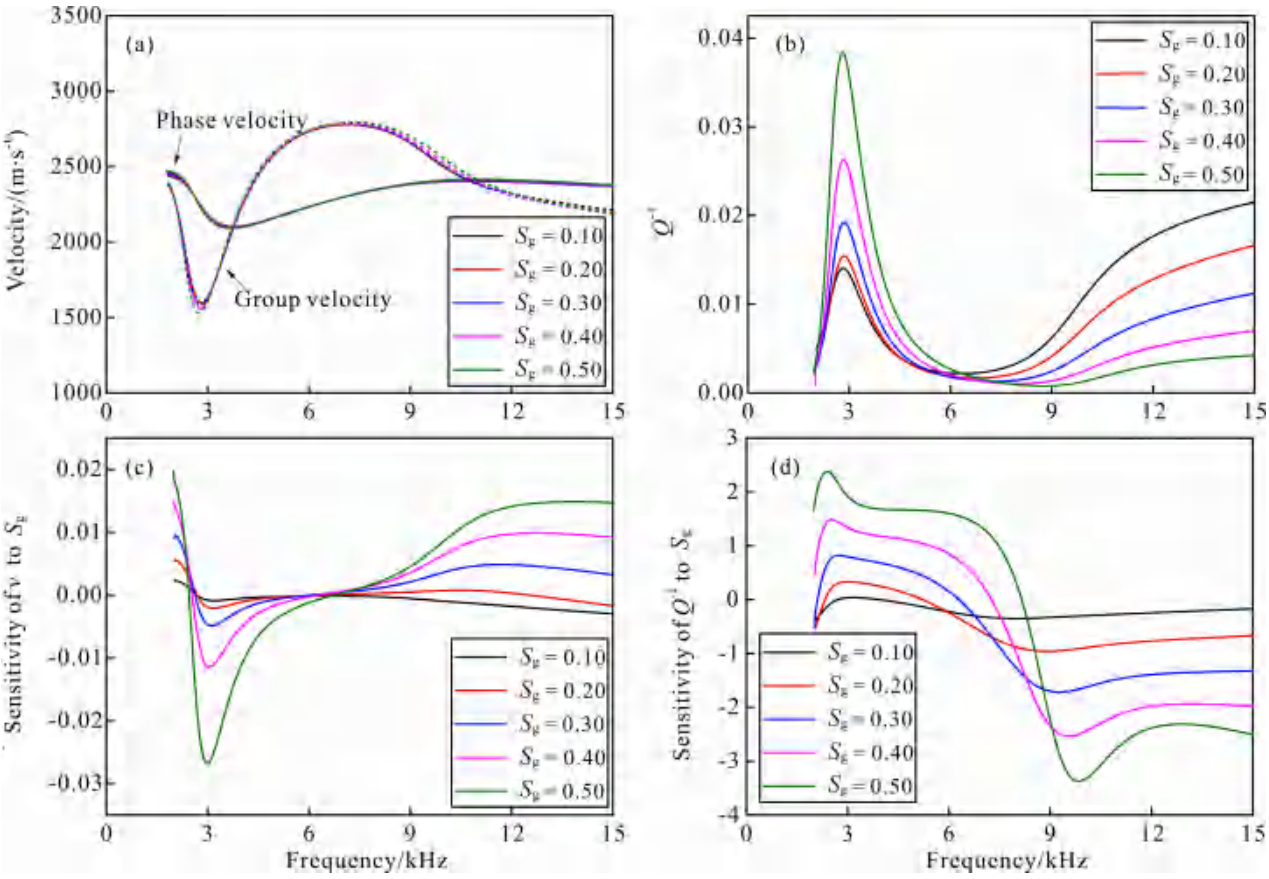


图 5 不同含气饱和度下的随钻偶极子模拟

(a) 频散曲线；(b) 衰减曲线；(c) 速度灵敏度曲线；(d) 衰减灵敏度曲线.

Fig. 5 Simulation of LWD dipole for different gas saturations

(a) Phase velocity dispersion curves; (b) Attenuation curves; (c) Velocity sensitivity to S_g; (d) Attenuation sensitivity to S_g.

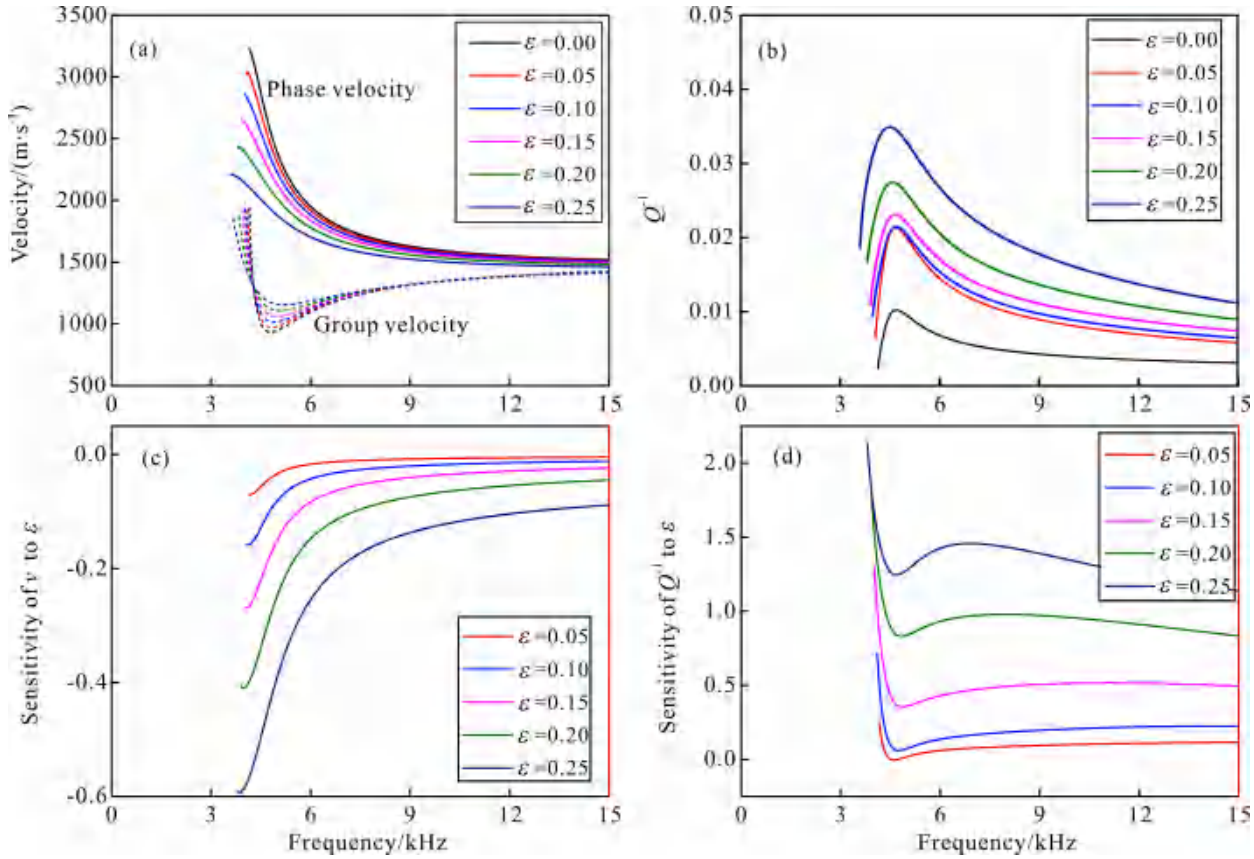


图 6　不同裂隙密度下的随钻四极子模拟

(a) 频散曲线；(b) 衰减曲线；(c) 速度灵敏度曲线；(d) 衰减灵敏度曲线.

Fig. 6　Simulation of LWD quadrupole for different crack density values

(a) Phase velocity dispersion curves; (b) Attenuation curves; (c) Velocity sensitivity to ε; (d) Attenuation sensitivity to ε.

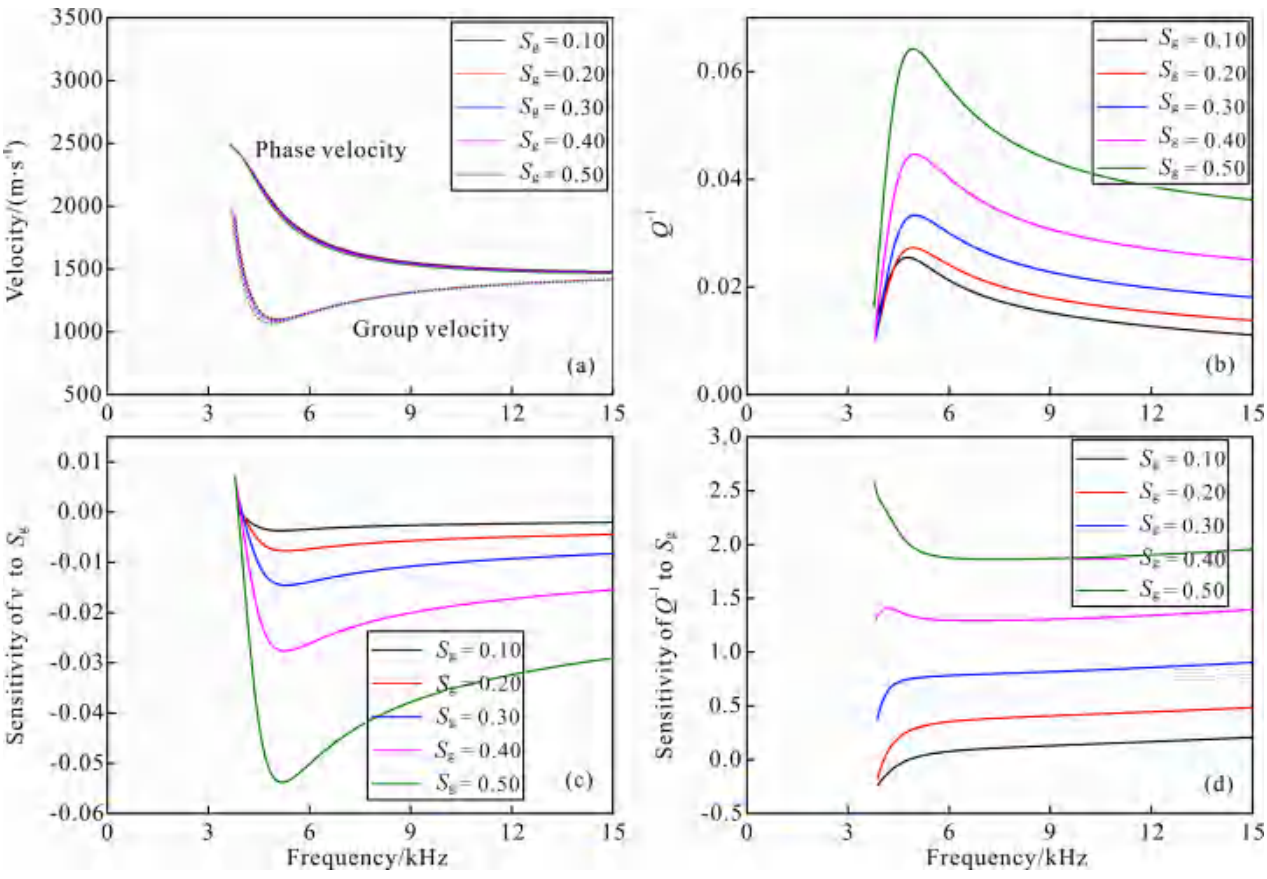


图 7　不同含气饱和度下的随钻四极子模拟

(a) 频散曲线；(b) 衰减曲线；(c) 速度灵敏度曲线；(d) 衰减灵敏度曲线.

Fig. 7　Simulation of LWD quadrupole for different gas saturation

(a) Phase velocity dispersion curves; (b) Attenuation curves; (c) Velocity sensitivity to S_g; (d) Attenuation sensitivity to S_g.

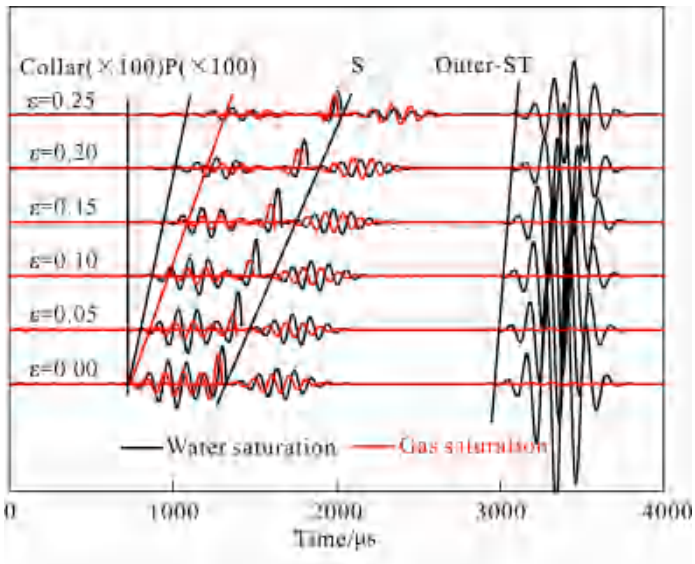


图 8 不同裂隙密度下随钻单极子波形模拟
地层含水(黑线),地层含气(红线).

Fig. 8 Simulation of LWD monopole waveform for different crack density values and saturation conditions for water (black) and gas (red)

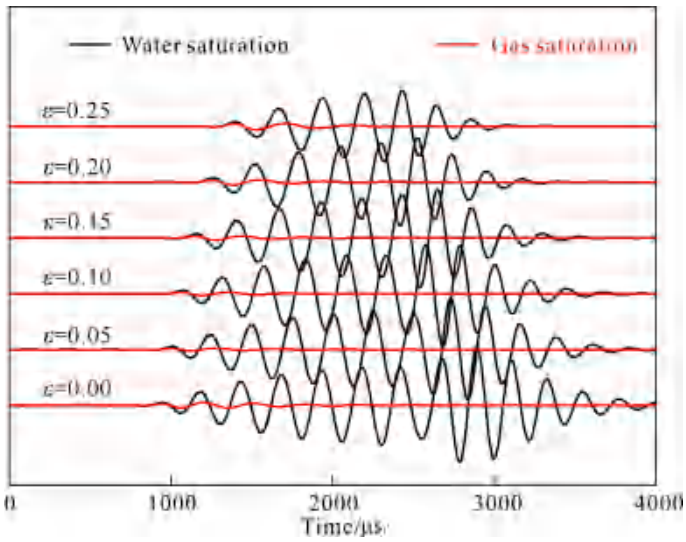


图 9 不同裂隙密度下随钻四极子波形模拟
地层含水(黑线),地层含气(红线).

Fig. 9 Simulation of LWD quadrupole waveform for different crack density values and saturation conditions for water (black) and gas (red)

5 现场实例

在声波测井的解释中,通常利用纵波慢度与纵横波速度比的交汇图来识别地层流体. 唐晓明(2011)对无限大地层含孔裂隙情况下的纵波慢度与纵横波速度比交汇图进行了详细的分析.

我们用一实测的随钻声波测井数据(仪器仅有单极采集模式)来验证本文的理论分析和模拟结果. 图 10 给出某快速地层的水平井的随钻声波数据. 由于施工顺利,采集到了高质量的单极子阵列波形数据. 图中第 1 道给出随钻单极子波形变密度显示. 第 2 道给出了处理后的波形时差相关分析图. 对单极子波形处理后得到地层的纵波(DTP)、横波(DTS)和斯通利波(DTST)时差曲线,在第 3 道画出.

图 11 中绿点数据表示为井段 3283～3309 m 的时差数据,该井段是岩性一致的含气段,岩石中具有发育很好的裂隙,且裂隙密度变化不大,该井段斯通利波有明显衰减,与前述理论模拟(图 2,3)类似;用第 3 道中的时差数据做交汇图分析(见图 11),该井段的数据为图中绿点. 含气饱和度不一导致该井段纵横波速比变化. 交汇图中橙点数据为 3321～3324 m 的数据,该井段岩石含气饱和度高;其时差的剧烈变化反映了井段中裂隙密度(或发育度)的变化.

作为一个例子,图 12 给出含气饱和度不同时实际随钻单极子波形. 我们从岩性一致的含气层段(3283～3309 m)找出三个点:a(3308.30 m)、b(3295.35 m)和 c(3286.51 m). 从交汇图可以看出,a、b、c 三点的含气饱和度依次增大(图 11). 在波形上体现的特征为纵波速度降低、幅度依次减小,而横波速度与幅度基本不变. 众所周知,页岩的孔隙度一般在 10%以下,按常规孔隙弹性波理论难以解释上述波形的变化特征. 图 12 的结果表明,当地层裂隙或裂缝发育程度高,含气饱和度变化时,在实际随钻波形中仍有明显的变化特征,与孔隙、裂隙介质弹性波理论相符. 这些波形特征可以应用在页岩气的勘探和开发.

6 结论

本文通过对孔裂隙介质中随钻声波的频散、衰减以及波形的数值计算,对比分析了裂隙密度与含气饱和度对斯通利波、弯曲波、螺旋波以及接收到地层纵横波的影响,得到以下结论:

(1)在单极子随钻测井中,孔隙、裂隙并存的致密地层中的斯通利波速度对裂隙非常敏感,衰减对含气饱和度更加敏感;

(2)随钻偶极子低频或随钻四极子群速度极小值处对应着波列的"艾里相",对应着衰减的峰值,在波形中显示为与艾里振相相关的能量大大落后于波的初至,含气影响导致振幅衰减很大,此现象可作为声波测井的一个标准来判断地层是否含气;

(3)地层中裂隙密度和含气饱和度的变化使测得的纵横波速产生可观的变化,可用于纵横波速比

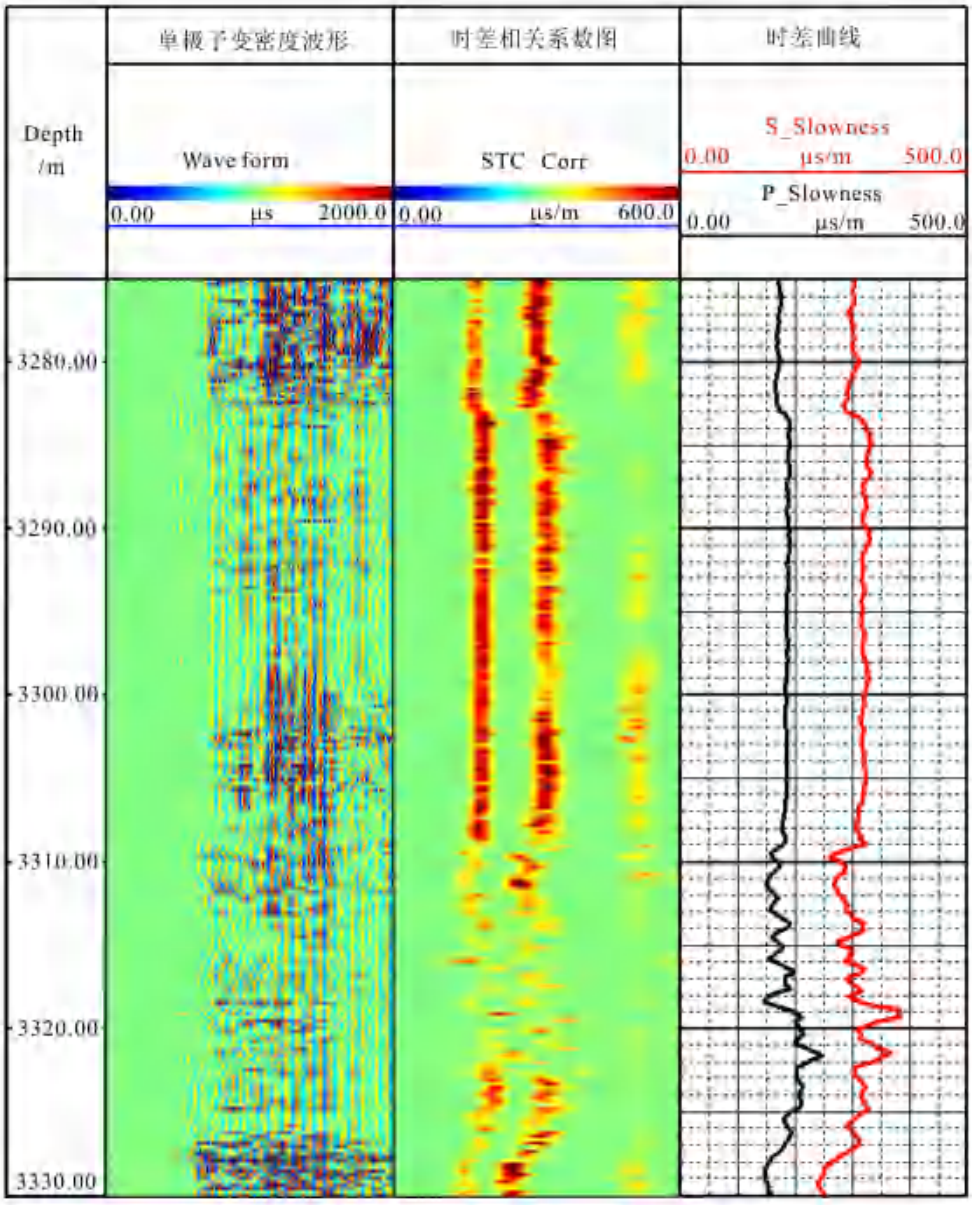


图 10　随钻孔裂隙地层现场实例

Fig. 10　Field LWD data example

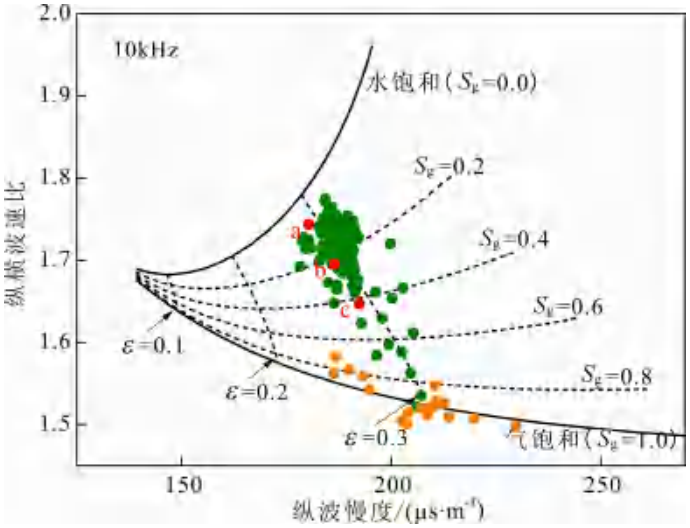


图 11　现场实例交汇图处理结果

Fig. 11　A crossplot of V_P/V_S ratio versus compressional 11 slowness using a field LWD data

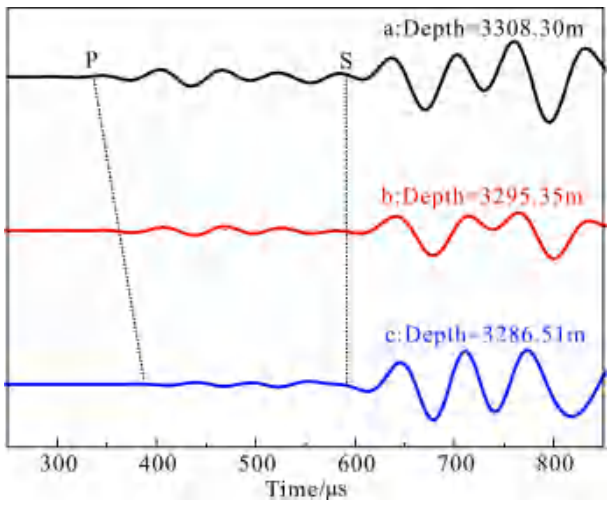


图 12　实际数据含气饱和度不同层段波形对比

Fig. 12　Comparison of LWD monopole waveform data for different saturation conditions

与纵波时差的交汇图分析,分析结果与理论预示一致.

致谢 感谢两位匿名审稿专家提出的宝贵意见和建设性建议,对本文的修改和提高很有助益.

附录

现给出(18)式矩阵 $\boldsymbol{H}=\begin{vmatrix} H_{1,1} & H_{1,2} & \cdots & H_{1,13} \\ H_{2,1} & H_{2,2} & \cdots & H_{2,13} \\ \vdots & \vdots & \ddots & \vdots \\ H_{13,1} & H_{13,2} & \cdots & H_{13,13} \end{vmatrix}$ 中的各个元素的表达式.为节省篇幅,我们采用以下符号来表示贝塞尔函数的组合:

$$\begin{cases} X_1(x)=\dfrac{n}{x}I_n(x)+I_{n+1}(x), \\ X_2(x)=\dfrac{n(n-1)}{x}I_n(x)-I_{n+1}(x), \\ X_3(x)=\dfrac{1-n}{x}I_n(x)-I_{n+1}(x), \\ X_4(x)=\left[1+\dfrac{2n(n-1)}{x^2}\right]I_n(x)-\dfrac{2}{x}I_{n+1}(x). \end{cases}$$

$$\begin{cases} Y_1(x)=\dfrac{n}{x}K_n(x)-K_{n+1}(x), \\ Y_2(x)=\dfrac{n(n-1)}{x}K_n(x)+K_{n+1}(x), \\ Y_3(x)=\dfrac{1-n}{x}K_n(x)+K_{n+1}(x), \\ Y_4(x)=\left[1+\dfrac{2n(n-1)}{x^2}\right]K_n(x)+\dfrac{2}{x}K_{n+1}(x). \end{cases}$$

矩阵 $\boldsymbol{H}$ 各元素的具体表达式如下:

$H_{1,1}=-fX_1(fr_a)$, $H_{1,2}=p_1X_1(p_1r_a)$,

$H_{1,3}=p_1Y_1(p_1r_a)$, $H_{1,4}=\dfrac{n}{r_a}I_n(s_1r_a)$,

$H_{1,5}=\dfrac{n}{r_a}K_n(s_1r_a)$, $H_{1,6}=\mathrm{i}ks_1X_1(s_1r_a)$,

$H_{1,7}=\mathrm{i}ks_1Y_1(s_1r_a)$, $H_{2,1}=\rho_f\omega^2I_n(fr_a)$,

$H_{2,2}=\mu^t[2k^2-(k_s^t)^2]I_n(p_1r_a)+\dfrac{2p_1\mu^t}{r_a}X_2(p_1r_a)$,

$H_{2,3}=\mu^t[2k^2-(k_s^t)^2]K_n(p_1r_a)+\dfrac{2p_1\mu^t}{r_a}Y_2(p_1r_a)$,

$H_{2,4}=-\dfrac{2\mu^tns_1}{r_a}X_3(s_1r_a)$, $H_{2,5}=-\dfrac{2\mu^tns_1}{r_a}Y_3(s_1r_a)$,

$H_{2,6}=2\mathrm{i}k\mu^ts_1\left[s_1I_n(s_1r_a)+\dfrac{1}{r_a}X_2(s_1r_a)\right]$,

$H_{2,7}=2\mathrm{i}k\mu^ts_1\left[s_1K_n(s_1r_a)+\dfrac{1}{r_a}Y_2(s_1r_a)\right]$,

$H_{3,2}=\dfrac{2p_1n\mu^t}{r_a}X_3(p_1r_a)$, $H_{3,3}=\dfrac{2p_1n\mu^t}{r_a}Y_3(p_1r_a)$,

$H_{3,4}=-s_1^2\mu^tX_4(s_1r_a)$, $H_{3,5}=-s_1^2\mu^tY_4(s_1r_a)$,

$H_{3,6}=\dfrac{2\mathrm{i}ks_1n\mu^t}{r_a}X_3(s_1r_a)$,

$H_{3,7}=\dfrac{2\mathrm{i}ks_1n\mu^t}{r_a}Y_3(s_1r_a)$,

$H_{4,2}=2\mathrm{i}kp_1\mu^tX_1(p_1r_a)$, $H_{4,3}=2\mathrm{i}kp_1\mu^tY_1(p_1r_a)$,

$H_{4,4}=\dfrac{\mathrm{i}kn\mu^t}{r_a}I_n(s_1r_a)$, $H_{4,5}=\dfrac{\mathrm{i}kn\mu^t}{r_a}K_n(s_1r_a)$,

$H_{4,6}=-(k^2+s_1^2)s_1\mu^tX_1(s_1r_a)$,

$H_{4,7}=-(k^2+s_1^2)s_1\mu^tY_1(s_1r_a)$,

$H_{5,2}=p_1X_1(p_1r_b)$, $H_{5,3}=p_1Y_1(p_1r_b)$,

$H_{5,4}=\dfrac{n}{r_b}I_n(s_1r_b)$, $H_{5,5}=\dfrac{n}{r_b}K_n(s_1r_b)$,

$H_{5,6}=\mathrm{i}ks_1X_1(s_1r_b)$, $H_{5,7}=\mathrm{i}ks_1Y_1(s_1r_b)$,

$H_{5,8}=-fX_1(fr_b)$, $H_{5,9}=-fY_1(fr_b)$,

$H_{6,2}=\mu^t[2k^2-(k_s^t)^2]I_n(p_1r_b)+\dfrac{2p_1\mu^t}{r_b}X_2(p_1r_b)$,

$H_{6,3}=\mu^t[2k^2-(k_s^t)^2]K_n(p_1r_b)+\dfrac{2p_1\mu^t}{r_b}Y_2(p_1r_b)$,

$H_{6,4}=-\dfrac{2\mu^tns_1}{r_b}X_3(s_1r_b)$, $H_{6,5}=-\dfrac{2\mu^tns_1}{r_b}Y_3(s_1r_b)$,

$H_{6,6}=2\mathrm{i}k\mu^ts_1\left[s_1I_n(s_1r_b)+\dfrac{1}{r_b}X_2(s_1r_b)\right]$,

$H_{6,7}=2\mathrm{i}k\mu^ts_1\left[s_1K_n(s_1r_b)+\dfrac{1}{r_b}Y_2(s_1r_b)\right]$,

$H_{6,8}=\rho_f\omega^2I_n(fr_b)$, $H_{6,9}=\rho_f\omega^2K_n(fr_b)$,

$H_{7,2}=\dfrac{2p_1n\mu^t}{r_b}X_3(p_1r_b)$, $H_{7,3}=\dfrac{2p_1n\mu^t}{r_b}Y_3(p_1r_b)$,

$H_{7,4}=-s_1^2\mu^tX_4(s_1r_b)$, $H_{7,5}=-s_1^2\mu^tY_4(s_1r_b)$,

$H_{7,6}=\dfrac{2\mathrm{i}ks_1n\mu^t}{r_b}X_3(s_1r_b)$, $H_{7,7}=\dfrac{2\mathrm{i}ks_1n\mu^t}{r_b}Y_3(s_1r_b)$,

$H_{8,2}=2\mathrm{i}kp_1\mu^tX_1(p_1r_b)$, $H_{8,3}=2\mathrm{i}kp_1\mu^tY_1(p_1r_b)$,

$H_{8,4}=\dfrac{\mathrm{i}kn\mu^t}{r_b}I_n(s_1r_b)$, $H_{8,5}=\dfrac{\mathrm{i}kn\mu^t}{r_b}K_n(s_1r_b)$,

$H_{8,6}=-(k^2+s_1^2)s_1\mu^tX_1(s_1r_b)$,

$H_{8,7}=-(k^2+s_1^2)s_1\mu^tY_1(s_1r_b)$,

$H_{9,8}=-fX_1(fR)$, $H_{9,9}=-fY_1(fR)$,

$H_{9,10}=(1+b_{\mathrm{fast}})q_{\mathrm{fast}}Y_1(q_{\mathrm{fast}}R)$,

$H_{9,11}=(1+b_{\mathrm{slow}})q_{\mathrm{slow}}Y_1(q_{\mathrm{slow}}R)$,

$H_{9,12}=(1+b_s)\dfrac{n}{R}K_n(q_sR)$,

$H_{9,13}=\mathrm{i}k(1+b_s)q_sY_1(q_sR)$,

$H_{10,8}=\rho_f\omega^2I_n(fR)$, $H_{10,9}=\rho_f\omega^2K_n(fR)$,

$H_{10,10}=\dfrac{2\mu q_{\mathrm{fast}}}{R}Y_2(q_{\mathrm{fast}}R)+\left[2\mu q_{\mathrm{fast}}^2-k_{\mathrm{fast}}^2(\lambda+\alpha\dfrac{\alpha+b_{\mathrm{fast}}}{\beta+S(\omega)})\right]K_n(q_{\mathrm{fast}}R)$,

$$H_{10,11}=\frac{2\mu q_{\text{slow}}}{R}Y_2(q_{\text{slow}}R)+\left[2\mu q_{\text{slow}}^2-k_{\text{slow}}^2(\lambda+\alpha\frac{\alpha+b_{\text{slow}}}{\beta+S(\omega)})\right]K_n(q_{\text{slow}}R),$$

$$H_{10,12}=\frac{2n\mu q_{\text{s}}}{R}\left[Y_1(q_{\text{s}}R)-\frac{K_n(q_{\text{s}}R)}{q_{\text{s}}R}\right],$$

$$H_{10,13}=\frac{2\text{i}k\mu q_{\text{s}}}{R}[Y_2(q_{\text{s}}R)+q_{\text{s}}RK_n(q_{\text{s}}R)],$$

$$H_{11,8}=\rho_{\text{f}}\omega^2 I_n(fR),\ H_{11,9}=\rho_{\text{f}}\omega^2 K_n(fR),$$

$$H_{11,10}=-k_{\text{fast}}^2\frac{\alpha+b_{\text{fast}}}{\beta+S(\omega)}K_n(q_{\text{fast}}R),$$

$$H_{11,11}=-k_{\text{slow}}^2\frac{\alpha+b_{\text{slow}}}{\beta+S(\omega)}K_n(q_{\text{slow}}R),$$

$$H_{12,10}=2\text{i}k\mu q_{\text{fast}}Y_1(q_{\text{fast}}R),$$

$$H_{12,11}=2\text{i}k\mu q_{\text{slow}}Y_1(q_{\text{slow}}R),$$

$$H_{12,12}=\text{i}k\mu\frac{n}{R}K_n(q_{\text{s}}R),$$

$$H_{12,13}=-\mu(k_{\text{shear}}^2-2k^2)q_{\text{s}}Y_1(q_{\text{s}}R),$$

$$H_{13,10}=-2\mu q_{\text{fast}}\frac{n}{R}Y_3(q_{\text{fast}}R),$$

$$H_{13,11}=-2\mu q_{\text{slow}}\frac{n}{R}Y_3(q_{\text{slow}}R),$$

$$H_{13,12}=\mu q_{\text{s}}^2Y_4(q_{\text{s}}R),$$

$$H_{13,13}=-2\text{i}k\mu\frac{n}{R}q_{\text{s}}Y_3(q_{\text{s}}R),$$

$H_{13\times13}$ 矩阵元素其他项为零;其中 k 波数;ω 角频率;n 声源极性;I 第一类贝塞尔函数;K 第二类贝塞尔函数;r_{a} 钻铤内径;r_{b} 钻铤外径;R 井眼外径;v_{f} 流体速度;v_{p}^t 钻铤纵波速度;v_{s}^t 钻铤横波速度;k_{f} 流体波数,$k_{\text{f}}=\omega/v_{\text{f}}$;$k_{\text{p}}^t$ 钻铤纵波波数,$k_{\text{p}}^t=\frac{\omega}{v_{\text{p}}^t}$;$k_{\text{s}}^t$ 钻铤纵波波数,$k_{\text{s}}^t=\frac{\omega}{v_{\text{s}}^t}$;$k_{\text{fast}}$ 孔裂隙地层快纵波波数;k_{slow} 孔裂隙地层慢纵波波数;k_{shear} 孔裂隙地层横波波数;f 流体径向波数,$f=\sqrt{k^2-k_{\text{f}}^2}$;$p_1$ 钻铤纵波径向波数,$p_1=\sqrt{k^2-(k_{\text{p}}^t)^2}$;$s_1$ 钻铤纵横径向波数,$s_1=\sqrt{k^2-(k_{\text{s}}^t)^2}$;$q_{\text{fast}}$ 孔裂隙地层快纵波径向波数,$q_{\text{fast}}=\sqrt{k^2-k_{\text{fast}}^2}$;$q_{\text{slow}}$ 孔裂隙地层慢纵波径向波数,$q_{\text{slow}}=\sqrt{k^2-k_{\text{slow}}^2}$;$q_{\text{s}}$ 孔裂隙地层横波径向波数,$q_{\text{s}}=\sqrt{k^2-k_{\text{shear}}^2}$;$\mu^t$ 钻铤剪切模量,$\mu^t=\rho_t\cdot(v_{\text{s}}^t)^2$;$\rho_t$ 钻铤密度;λ、μ 孔裂隙地层拉梅常数;$S(\omega)$ 挤喷流效应.

References

Brie A, Pampuri F, Marsala A F, et al. 1995. Shear sonic interpretation in gas-bearing sands. SPE Annual Technical Conference and Exhibition, 701-710.

Chen X L, Tang X M. 2012. Numerical study on the characteristics of acoustic logging response in the fluid-filled borehole embedded in crack-porous medium. *Chinese J. Geophysics*. (in Chinese), 55(6): 2139-2140.

Chen X L, Tang X M, Qian Y P. 2013. Simulation of multipole acoustic logging in cracked porous formations. *Geophysics*, 79(1): D1-D10.

Cui Z W. 2004. Theoretical and numerical study of modified Biot's models, acous to electric well logging and acoustic logging while drilling excited by multipole acoustic source[Ph. D. thesis](in Chinese). Changchun: Jilin University.

Hao Jian-fei, Zhou Can-can, Li Xia, et al. 2012. Summary of shale gas evaluation applying geophysical logging. *Progress in Geophysics*, 27(4): 1624-1632.

Li X Q, Chen H, He X, et al. 2013. Analyses on mode waves of acoustic logging while drilling in transversely isotropic formations. *Chinese J. Geophysics*. (in Chinese), 56(9): 3212-3222.

Su Y D, Sun J M, Fan Y R, et al. 2006. On numerical study of the LWD multipole source propagation characteristics in slow formation. *Well Logging Technology*, 30(3): 205-207.

Tang X M. 2011. A unified theory for elastic wave propagation through porous media containing cracks-An extension of Biot's poroelastic wave theory. *Sci China Earth Sci*, 41(6):784-795.

Tang X M, Chen X L, Xu X K. 2012. A cracked porous medium elastic wave theory and its application to interpreting acoustic data from tight formations. *Geophysics*, 77(6): D245-D252.

Tang X M, Qian Y P, Chen X L. 2013. Laboratory study of elastic wave theory for a cracked porous medium using ultrasonic velocity data of rock samples. *Chinese J. Geophysics*. (in Chinese), 56(12): 4226-4233

Tang X M, Wang T, Patterson D. 2002. Multipole acoustic logging-while-drilling. 72nd Annual International Meeting, SEG, Expanded Abstracts, 364-368.

Tang X M, Zheng C H. 2004. Quantitative Borehole Acoustic Methods (in Chinese). Beijing: Petroleum Industry Press: 20-39.

Thomsen L. 1985. Biot-consistent elastic moduli of porous rocks; low-frequency limit. *Geophysics*, 50(12): 2797-2807.

Wang R J, Qiao W X, Ju X D. 2012. Numerical study of formation anisotropy evaluation using cross dipole acoustic LWD. *Chinese J. Geophysics*. (in Chinese), 55(11): 3870-3882.

Wang H, Tao G, Wang B, et al. 2009. Wave field simulation and data acquisition scheme analysis for LWD acoustic tool. *Chinese J. Geophysics*. (in Chinese), 52(9): 2402-2409.

附中文参考文献

陈雪莲, 唐晓明. 2012. 孔、裂隙并存地层中的声波测井理论及多极子声场特征. 地球物理学报, 55(6): 2139-2140.

崔志文. 2004. 多孔介质声学模型与多极源声电效应测井和多极随钻声测井的理论与数值研究[博士论文]. 长春: 吉林大学.

郝建飞，周灿灿，李霞等. 2012. 页岩气地球物理测井评价综述. 地球物理学进展，27(4)：1624-1632.

李希强，陈浩，何晓等. 2013. 横向各向同性地层中随钻声波测井模式波分析. 地球物理学报，56(9)：3212-3222.

苏远大，孙建孟，范宜仁等. 2006. 基于软地层随钻多极子声源传播特性的数值研究. 测井技术，30(3)：205-207.

唐晓明. 2011. 含孔隙、裂隙介质弹性波动的统一理论-Biot 理论的推广. 中国科学 地球科学，41(6)：784-795.

唐晓明，钱玉萍，陈雪莲. 2013. 孔隙、裂隙介质弹性波理论的实验研究. 地球物理学报，56(12)：4226-4233，doi：10.6038/cjg20131225.

唐晓明，郑传汉. 2004. 定量测井声学. 赵晓敏译. 北京：石油工业出版社：20-39.

王瑞甲，乔文孝，鞠晓东. 2012. 利用随钻正交偶极子声波测井评价地层各向异性的数值研究. 地球物理学报，55(11)：3870-3882.

王华，陶果，王兵等. 2009. 多极子随钻声波测井波场模拟与采集模式分析. 地球物理学报，52(9)：2402-2409.

（本文编辑 胡素芳）

庄春喜，李杨虎，孔凡童等. 2019. 随钻斯通利波测井反演地层渗透率的理论、方法及应用. 地球物理学报，62(11)：4482-4492，doi：10.6038/cjg2019N0122.

Zhuang C X, Li Y H, Kong F T, et al. 2019. Formation permeability estimation using Stoneley waves from logging while drilling: theory, method, and application. *Chinese J. Geophys.* (in Chinese), 62(11): 4482-4492, doi: 10.6038/cjg2019N0122.

随钻斯通利波测井反演地层渗透率的理论、方法及应用

庄春喜[1,2]，李杨虎[1,2]，孔凡童[1,2]，陈鸣[3*]，张聪慧[4]，苏远大[1,2]，唐晓明[1,2]

1 中国石油大学(华东)地球科学与技术学院，山东青岛 266580

2 中国石油大学(华东)深层油气重点实验室，山东青岛 266580

3 中海石油(中国)有限公司湛江分公司，广东湛江 524057

4 中海油田股份有限公司油田技术事业部，北京 101149

摘要 针对孔隙渗透地层的随钻声波测井问题，用 Biot-Rosenbaum 孔隙弹性波测井理论推导了孔隙地层的随钻井孔声场表达式. 据此考察了随钻条件下井中斯通利波的波形、相速度频散、衰减以及相速度对渗透率的灵敏度，并与电缆测井中的情况进行了对比. 数值模拟结果表明，随钻条件下斯通利波对地层渗透率的灵敏度相对于电缆测井有明显增加，更有利于用来反演地层渗透率. 为快捷有效地处理现场测井数据和反演计算，采用简化 Biot-Rosenbaum 理论和钻铤的等效模型，对随钻斯通利波的频移和时滞进行联合反演. 结果表明，随钻斯通利波反演的渗透率与核磁渗透率和岩心覆压测试渗透率符合较好，并且与常规测井曲线所反映的储层性质具有较好的一致性，证明了利用随钻斯通利波评价地层渗透率的有效性.

关键词 渗透率；随钻斯通利波；简化 Biot-Rosenbaum 理论；等效仪器模型；频移和时滞

doi：10.6038/cjg2019N0122 **中图分类号** P631 **收稿日期** 2019-04-07，2019-08-12 收修定稿

Formation permeability estimation using Stoneley waves from logging while drilling: theory, method, and application

ZHUANG ChunXi[1,2], LI YangHu[1,2], KONG FanTong[1,2], CHEN Ming[3*], ZHANG CongHui[4], SU YuanDa[1,2], TANG XiaoMing[1,2]

1 *School of Geosciences, China University of petroleum, Shandong Qingdao* 266580, *China*

2 *Key Laboratory of Deep Oil and Gas, China University of Petroleum, Shandong Qingdao* 266580, *China*

3 *CNOOC (China) Limited Zhanjiang Branch Company, Guangdong Zhanjiang* 524057, *China*

4 *Well Tech of China Oilfield Services Limited, Beijing* 101149, *China*

Abstract Based on Biot-Rosenbaum theory for acoustic logging in a poroelastic formation, we investigate the Logging While Drilling (LWD) acoustic wavefield and calculate waveforms, phase-velocity dispersion, attenuation, and sensitivity to permeability for the LWD Stoneley waves. The results show that the sensitivity of the LWD Stoneley waves to formation permeability increases significantly compared with its counterpart in the wireline condition, which

基金项目 国家自然基金(41604109，41804124，41774138)、中国科学院战略性先导科技专项(XDA14020304，XDA14020302)和中央高校基本科研业务费专项资金(18CX02065A，27R1801025A)联合资助.

第一作者简介 庄春喜，男，1982 年生，讲师，主要从事声波测井数据处理方法研究. E-mail：zhuangchunxi@sina.com

*** 通讯作者** 陈鸣，男，1982 年生，高级工程师，主要从事海上测井方法及应用研究. E-mail：chenming4@cnooc.com.cn

favors the inversion of formation permeability using LWD Stoneley waves. To facilitate the inversion calculation in field data processing, we utilize the simplified Biot-Rosenbaum theory and the equivalent LWD tool model and formulate a joint inversion method using Stoneley wave frequency shift and travel-time delay data. The results reveal that the permeability calculated from the LWD Stoneley waves is in good agreement with both the permeability measured by NMR (Nuclear Magnetic Resonance) and the core permeability measured with overburden pressure. The result is also consistent with the reservoir properties from conventional logging curves. Results of this study demonstrate the validity of permeability estimation using LWD Stoneley waves.

Keywords Permeability; LWD Stoneley waves; Simplified Biot-Rosenbaum theory; Equivalent-tool model; Frequency shift and traveltime delay

0　引言

渗透率是表征储层特性的重要参数之一,目前普遍应用电缆测井作为储层渗透率计算的主要方法.然而,在深水和高温、高压井中,由于作业风险大、成本高,岩心实物资料无法普遍获取;深水井中由于必须使用高矿化度钻井液防水合物,核磁共振测井也无法适用;中子密度测井在进行渗透率计算时需要考虑放射源作业风险.针对以上问题,本文提出利用随钻声波测井数据评价地层渗透率的方法,在不增加现场测井作业成本的情况下,进一步挖潜声波波形数据信息.

在常用的声波测井模式中(单极子、偶极子和四极子),单极子源激发的斯通利波是一种以井内流体为载体的低频压力波,其对井中流体与地层孔隙流体之间的压力传递非常敏感,因而对地层渗透率的灵敏度最高.在传统的电缆声波测井中,斯通利波常被用来进行地层的渗透率评价.目前,国内外很多学者已经建立了一些理论模型用以模拟分析渗透率对声波在介质中传播的影响(Biot,1956a,b,1962;Rosenbaum,1974;Schmitt,1988).在理论模拟的基础上,Williams 等(1984)最早提出可根据斯通利波速度和振幅与地层渗透率的相关性评估渗透率.王克协和董庆德(1986)对渗透性地层油井中的声场进行了理论分析,指出斯通利波的振幅变化对孔隙度和渗透率均较为敏感.Tang 等(1991,1998)、Tang 和 Cheng(1993,1996)提出一种简化的 Biot-Rosenbaum 理论研究动态渗透率与斯通利波之间的关系,并利用斯通利波的频移和时滞来反演渗透率.张碧星等(1995)对双相介质井孔多极声波测井进行了理论分析和全波计算.伍先运等(1995)建立了利用斯通利波反演渗透率的图版,并开展了相应的应用研究.候春会等(1997)建立了一种利用斯通利波幅度衰减反演储层渗透率的线性化最小二乘反演模型.苏华和田洪(2002)、高坤等(2005)将 Tang 等提出的频移和时滞反演方法应用于实际测井解释.崔志文(2004)研究了随钻环境下可渗孔隙地层井孔中多极声场的传播特点和规律.崔志文等(2010)对利用斯通利波衰减反演渗透率的方法进行了改进.许孝凯等(2012)对斯通利波的影响因素进行研究,并分析了渗透率的反演结果.Tang 等(2010)研究发现,当地层存在渗透性时,随钻条件下井中斯通利波也会出现频移和时滞现象,并指出仪器偏心会严重影响斯通利波在井中的传播,可以通过在仪器两端安装扶正器降低偏心的影响.金武军等(2017)从孔隙结构出发,结合核磁测井资料,提取出孔隙结构参数,实现了页岩渗透率的精细评价.王宇竹等(2017)进一步总结了渗透率各向异性的获取方法.张丽华等(2018)对影响渗透率测量的实验条件进行分析,其结果为岩心渗透率的测量提供了实验依据.

电缆声波测井中,斯通利波在地层渗透率反演中的研究已经相对完善,但随钻情况下关于这方面的研究还相对较少.本文针对这一现状,模拟了随钻斯通利波在含孔隙渗透地层中的传播特征,并分析了其波形、频散、衰减和灵敏度在不同渗透率下的响应特性.在理论模拟的基础上,本文利用随钻斯通利波的频移和时滞特征进行地层渗透率反演,并通过考虑等效仪器的简化 Biot-Rosenbaum 随钻理论降低了模型的复杂度,大大提高了反演效率,为地层渗透率评价提供了行之有效的处理方法.

1　随钻孔隙地层井孔中的声场

图 1 给出了孔隙地层充液井孔中的随钻声波测

井模型示意图,分别为井孔示意图 1a 和横截面示意图 1b. 该模型由柱状径向分层介质组成,由内向外依次为钻铤内流体、钻铤、钻铤外流体和孔隙地层,各介质的外径分别为 r_a、r_b、R 和无穷大,并假设钻铤在井孔中完全居中.

1.1 含孔隙地层中的测井声波传播理论及声场

含孔隙地层的应力和位移的本构关系式为(Parra and Xu, 1994):

$$\sigma_{ij} = 2\mu e_{ij} + (\lambda e - \alpha p)\delta_{ij}, \tag{1}$$

本构方程中涉及的孔隙流体压力和动态达西定律分别为

$$p = -(\alpha \nabla \cdot \boldsymbol{u} + \nabla \cdot w)/\beta, \tag{2}$$

$$w = \phi(\boldsymbol{U} - \boldsymbol{u}) = \theta(\nabla p - \rho_{pf}\omega^2 \boldsymbol{u}), \tag{3}$$

其中:

$$\begin{cases} K_d = \lambda + 2\mu/3, \\ \lambda = (1-\phi)\lambda_s, \quad \rho = \rho_s(1-\phi) + \rho_{pf}\phi, \\ \mu = (1-\phi)\mu_s, \quad \beta = (\alpha-\phi)/K_s + \phi/K_{pf}, \\ \alpha = 1 - K_d/K_s, \quad \theta = \mathrm{i}\kappa(\omega)/\eta\omega. \end{cases} \tag{4}$$

式(1)—(4)中:σ_{ij} 为双相介质中的平均应力(或总体应力);e_{ij} 为应变张量,且 $e = \nabla \cdot \boldsymbol{u}$;$p$ 为孔隙流体压力,w 是流体和固体的相对位移;μ 为剪切模量,λ 为拉梅常数;$\boldsymbol{u}$ 和 $\boldsymbol{U}$ 分别是孔隙固体和流体的位移矢量;ρ_s 和 ρ_{pf} 分别是固体骨架和孔隙流体的密度;K_s、λ_s、μ_s 分别是孔隙固体骨架的体模量和两个拉梅常数,且 $\lambda_s = \rho_s v_p^2 - 2\mu_s$,$\mu_s = \rho_s v_s^2$,$v_p$ 和 v_s 分别为固体骨架的纵波和横波速度;K_d 为介质干燥(或排水)条件下的体积模量,K_{pf} 是孔隙流体的不可压缩模量(或体模量);ω 为角频率;ϕ 为孔隙度;η 为流体黏滞度;α 和 β 是两个参数组合. $\kappa(\omega)$ 采用 Johnson 等(1987)引进的动态渗透率,即:

$$\kappa(\omega) = \frac{\kappa_0}{\sqrt{1 - 4\mathrm{i}\tau^2\kappa_0^2\rho_{pf}\omega/(\eta\Lambda^2\phi^2)} - \mathrm{i}\tau\kappa_0\rho_{pf}\omega/(\eta\phi)}. \tag{5}$$

动态渗透率表征了孔隙内流体的流动性能. 其中 τ 是混浊度,代表孔隙中流动通道的形态;κ_0 是静态达西渗透率;$\Lambda = \sqrt{8\tau\kappa_0/\phi}$ 表示孔隙的尺寸大小(Johnson et al., 1987).

主要考虑井中单极子激发源的情况,对于孔隙井中声波传播的模拟问题,单极子源在孔隙地层中产生三种波,分别是快速纵波、慢速纵波和横波(SV 振型),三种波的位移势函数为

$$\begin{Bmatrix} \Phi_{fast} \\ \Phi_{slow} \\ \Psi \end{Bmatrix} = \begin{Bmatrix} B_{fast}K_0(q_{fast}r) \\ B_{slow}K_0(q_{slow}r) \\ D_sK_1(q_sr)q_s \end{Bmatrix} \mathrm{e}^{\mathrm{i}kz}, \tag{6}$$

其中,B_{fast}、B_{slow} 和 D_s 分别表示快、慢纵波和横波的振幅系数;q_{fast}、q_{slow} 和 q_s 分别为快、慢纵波和横波的径向波数,具体表达式为

$$\begin{cases} q_{fast} = \sqrt{k^2 - k_{fast}^2}, \\ q_{slow} = \sqrt{k^2 - k_{slow}^2}, \\ q_s = \sqrt{k^2 - k_{shear}^2}, \end{cases} \tag{7}$$

其中 k 是沿井轴方向的波数;k_{fast}、k_{slow}、k_{shear} 分别是快、慢纵波和横波的波数,其计算公式为

$$\begin{cases} k_{fast} = k_{p0}\sqrt{\dfrac{1 + b_{fast}\rho_{pf}/\rho}{1 - b_{fast}/b_0}}, \\ k_{slow} = k_{p0}\sqrt{\dfrac{1 + b_{slow}\rho_{pf}/\rho}{1 - b_{slow}/b_0}}, \\ k_{shear} = \sqrt{\dfrac{\omega^2}{\mu/(\rho + \rho_{pf}^2\omega^2\theta)}}, \end{cases} \tag{8}$$

式中:

$$\begin{cases} \begin{Bmatrix} b_{fast} \\ b_{slow} \end{Bmatrix} = \frac{1}{2}b_0\{c \mp \sqrt{c^2 - 4\alpha(1-c)/b_0}\}, \\ c = \dfrac{\alpha - b_s\rho/(\rho_{pf}b_0)}{\alpha + b_s}, \quad b_0 = -\dfrac{\beta(\lambda + 2\mu + \alpha^2/\beta)}{\alpha}, \\ k_{p0} = \dfrac{\omega}{\sqrt{(\lambda + 2\mu + \alpha^2/\beta)/\rho}}, \quad b_s = \rho_{pf}\theta\omega^2. \end{cases} \tag{9}$$

利用位移势函数可以将孔隙地层中的位移分量和应力分量表示为

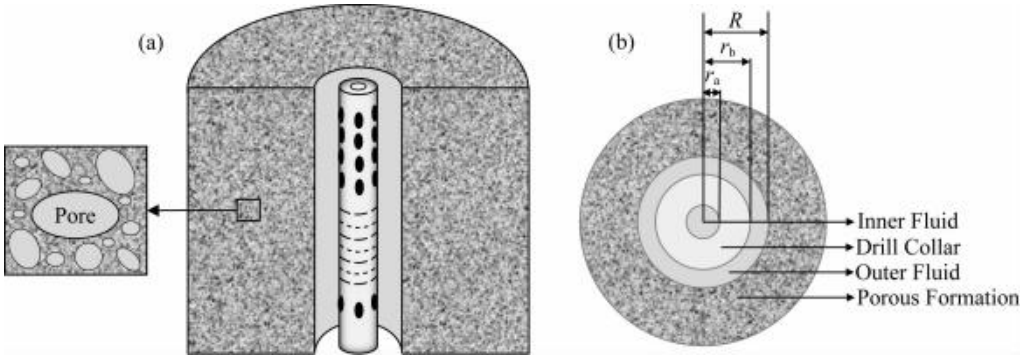


图 1 含孔隙地层随钻声波测量的物理模型示意图(a)及井孔截面示意图(b)

Fig. 1 Sketches of porous model for acoustic LWD (a) and cross section of borehole (b)

$$\begin{cases} u_{\mathrm{r}} = \dfrac{\partial \Phi_{\mathrm{fast}}}{\partial r} + \dfrac{\partial \Phi_{\mathrm{slow}}}{\partial r} - \dfrac{\partial \Psi}{\partial z}, \\ w_{\mathrm{r}} = b_{\mathrm{fast}} \dfrac{\partial \Phi_{\mathrm{fast}}}{\partial r} + b_{\mathrm{slow}} \dfrac{\partial \Phi_{\mathrm{slow}}}{\partial r} - b_{\mathrm{s}} \dfrac{\partial \Psi}{\partial z}, \\ \sigma_{\mathrm{rr}} = 2\mu\left[\dfrac{\partial^2 \Phi_{\mathrm{fast}}}{\partial r^2} + \dfrac{\partial^2 \Phi_{\mathrm{slow}}}{\partial r^2} - \dfrac{\partial^2 \Psi}{\partial r \partial z}\right] - k_{\mathrm{fast}}^2\left[\lambda + \dfrac{\alpha}{\beta}(\alpha + b_{\mathrm{fast}})\right]\Phi_{\mathrm{fast}} - k_{\mathrm{slow}}^2\left[\lambda + \dfrac{\alpha}{\beta}(\alpha + b_{\mathrm{slow}})\right]\Phi_{\mathrm{slow}}, \\ p = k_{\mathrm{fast}}^2[(\alpha + b_{\mathrm{fast}})/\beta]\Phi_{\mathrm{fast}} + k_{\mathrm{slow}}^2[(\alpha + b_{\mathrm{slow}})/\beta]\Phi_{\mathrm{slow}}, \\ \sigma_{\mathrm{rz}} = -k_{\mathrm{shear}}^2 \mu \Psi + 2\mu\left[\dfrac{\partial^2 \Phi_{\mathrm{fast}}}{\partial r \partial z} + \dfrac{\partial^2 \Phi_{\mathrm{slow}}}{\partial r \partial z} - \dfrac{\partial^2 \Psi}{\partial z^2}\right]. \end{cases} \tag{10}$$

1.2　边界条件

图 1 所示模型中各部分的声场由三个界面处的边界条件衔接,即钻铤内流体和钻铤内壁边界处,钻铤外壁和钻铤外流体边界处,钻铤外流体和地层边界处.计算声场时,本文采用体积膨胀源的加载方式(唐晓明和郑传汉,2004),将一环状多极子位移声源放置于钻铤表面,以实现声场的激发.

(1)钻铤内流体和钻铤界面($r=r_{\mathrm{a}}$),表达式为

$$\begin{cases} u_{\mathrm{f}}^{\mathrm{in}} = u_{\mathrm{tool}}, \\ \sigma_{\mathrm{rrf}}^{\mathrm{in}} = \sigma_{\mathrm{rr}}^{\mathrm{tool}}, \\ 0 = \sigma_{\mathrm{rz}}^{\mathrm{tool}}. \end{cases} \tag{11}$$

(2)钻铤和钻铤外流体界面($r=r_{\mathrm{b}}$),表达式为

$$\begin{cases} u_{\mathrm{tool}} = u_{\mathrm{f}}^{\mathrm{out}} + u_{\mathrm{f}}^{\mathrm{d}}, \\ \sigma_{\mathrm{rr}}^{\mathrm{tool}} = \sigma_{\mathrm{rrf}}^{\mathrm{out}}, \\ \sigma_{\mathrm{rz}}^{\mathrm{tool}} = 0. \end{cases} \tag{12}$$

其中,$u_{\mathrm{f}}^{\mathrm{d}}$ 为环状声源的位移,具体表达式为(唐晓明和郑传汉,2004):

$$u_{\mathrm{f}}^{\mathrm{d}} = -fK_1(fr_{\mathrm{b}})I_0(fr_{\mathrm{b}}). \tag{13}$$

1.3　钻铤外流体和地层界面($r=R$)

井壁处共有四个边条件,前三个分别是平均径向位移连续、平均正应力连续和剪切应力连续.其中,地层的位移由孔隙地层固体的位移 u_{fm} 和孔隙流体相对于固体的流动位移 w_{fm} 两部分组成.井壁处的最后一个边条件和压力传递有关,井壁处的压力传递受泥饼的影响,表达式为

$$p_{\mathrm{f}} - p_{\mathrm{fm}} = Tw_{\mathrm{fm}}, \tag{14}$$

其中,p_{f} 是井中流体压力;T 为阻抗因子,表征了泥饼的阻抗效应.当 $T=0$ 时,井中流体与地层孔隙中的流体相互连通,两者可以自由交换,此时为开放孔隙的情况;当 $T\to\infty$ 时,井中流体不能与地层孔隙中的流体交换,此时为封闭孔隙的情况.开放和封闭孔隙分别被用来模拟渗透性和非渗透性孔隙地层(Schmitt et al.,1988;Tang et al.,2010).随钻环境下,泥饼尚未形成,可以忽略泥饼的作用,此时井壁为开放孔隙的情况,井壁处对应的边界条件为

$$\begin{cases} u_{\mathrm{f}}^{\mathrm{out}} = u_{\mathrm{fm}} + w_{\mathrm{fm}}, \\ \sigma_{\mathrm{rrf}}^{\mathrm{out}} = \sigma_{\mathrm{rr}}^{\mathrm{fm}}, \\ 0 = \sigma_{\mathrm{rz}}^{\mathrm{fm}}, \\ p_{\mathrm{f}} = p_{\mathrm{fm}}. \end{cases} \tag{15}$$

将各部分声场的应力和位移代入边界条件,可得到矩阵方程为

$$\left\{H_{ij}\right\}_{10\times 10} \cdot \left\{O_j\right\}_{10\times 1} = \left\{b_i\right\}_{10\times 1}, \tag{16}$$

其中:

$$\left\{O_j\right\}_{10\times 1} = \left\{A^{in}, A^{\mathrm{tool}}, B^{\mathrm{tool}}, C^{\mathrm{tool}}, D^{\mathrm{tool}}, A^{out}, B^{out}, B_{\mathrm{fast}}, B_{\mathrm{slow}}, D_{\mathrm{s}}\right\}^{\mathrm{T}}, \tag{17}$$

$$\left\{b_i\right\}_{10\times 1} = \left\{0,0,0,u_{\mathrm{f}}^{\mathrm{d}},0,0,0,0,0,0\right\}^{\mathrm{T}}, \tag{18}$$

矩阵 $\boldsymbol{H}$ 中元素的表达式在附录给出.此时,随钻仪器外环上声波压力场的波形计算公式为(唐晓明和郑传汉,2004):

$$P(z,t) = \int_{-\infty}^{+\infty} \rho_{\mathrm{f}} \omega^2 S(\omega) \mathrm{e}^{-\mathrm{i}\omega t} \mathrm{d}\omega \int_{-\infty}^{+\infty} \left[A^{\mathrm{out}} I_0(fr_{\mathrm{b}}) + B^{\mathrm{out}} K_0(fr_{\mathrm{b}})\right] \mathrm{e}^{-\mathrm{i}kz} \mathrm{d}k, \tag{19}$$

其中,$S(\omega)$ 为源的频谱,其函数形式可以任意选取;本文中采用中心频率为 ω_0 的瑞克子波,$S(\omega) = (\omega/\omega_0)^2 \mathrm{e}^{-(\omega/\omega_0)^2}$.

2　含孔隙渗透地层中随钻斯通利波的频散和衰减特性

本文主要探讨斯通利波的频散、衰减以及灵敏度随渗透率的响应特征.其中频散特征主要和式(16)中矩阵 $\boldsymbol{H}$ 相关,令其行列式为零,得到随钻斯通利波的频散方程为

$$D(k,\omega) = \det \boldsymbol{H}(k,\omega) = 0. \tag{20}$$

通过求解该方程得到斯通利波波数在不同频率下的根,然后利用式(21)和(22)计算斯通利波的相速度频散及其衰减(品质因子 Q 的倒数),即:

$$v(\omega) = \frac{\omega}{\mathrm{Re}(k(\omega))}, \tag{21}$$

$$Q^{-1}(\omega) = 2\frac{\mathrm{Im}(k(\omega))}{\mathrm{Re}(k(\omega))}. \tag{22}$$

在井中导波传播的理论模拟中,波的传播特征受到众多参数的影响.灵敏度分析常被用来评估不同参数对波传播特性的影响程度.模型对某一参数 p 的灵敏度实际上就是归一化后的波的相速度对该参数的偏微分,计算公式为(唐晓明和郑传汉,2004):

$$\mathrm{Sens}\{v(\omega)\} = \left(\frac{p}{v(\omega)}\right)\frac{\partial v(\omega)}{\partial p}. \tag{23}$$

根据上述理论分析,下面对含孔隙渗透地层中随钻环境下斯通利波的传播特征进行数值模拟,井孔和孔隙地层的模拟参数分别见表 1 和表 2.图 2 展示了含水孔隙地层在不同渗透率下,充液井孔中随钻斯通利波的波形、频散及其衰减响应特征.图 2a 显示,当地层存在渗透性时,斯通利波的幅度和到时发生变化,并且渗透率越大,其幅度越小,到时越靠后.随着渗透率的增加,速度逐渐减小(图 2b).

表 1 随钻井孔流体与钻铤参数

Table 1 Parameters of fluids in LWD borehole and drill collar

	v_p /(m·s^{-1})	v_s /(m·s^{-1})	Density /(kg·m^{-3})	Radius/m
Inner Fluid	1500	—	1000	0.027
Drill Collar	5860	3130	7850	0.090
Outer Fluid	1500	—	1000	0.117

衰减曲线随着频率增加呈下降趋势,并随着渗透率增加而逐渐增大(图 2c).随着渗透率的增加,相同的渗透率变化量将会引起速度和衰减更大的变化,说明渗透率较大的含水地层会对斯通利波产生可观的影响.因此地层的渗透性越好,越有利于从斯通利波中评估地层渗透率.此外,从图 2b 和 2c 中可看出,频率越低,斯通利波速度和衰减随频率以及渗透率的变化越明显,指示采用低频段的斯通利波进行渗透率反演效果会更好.斯通利波速度和衰减随渗透率和频率的变化正是下文利用随钻斯通利波进行渗透率反演的理论依据.

表 2 含孔隙渗透地层参数

Table 2 Parameters of permeable formation containing pores

K_s/GPa	v_p/(m·s^{-1})	v_s/(m·s^{-1})	ρ_s/(kg·m^{-3})	ϕ/%	ρ_{Pf}/(kg·m^{-3})	K_{Pf}/GPa	η/(mPa·s)	κ_0/μm^2	τ
37.9	3800	2200	2650	25	1000	2.25	1	0.01,0.1,1	3.0

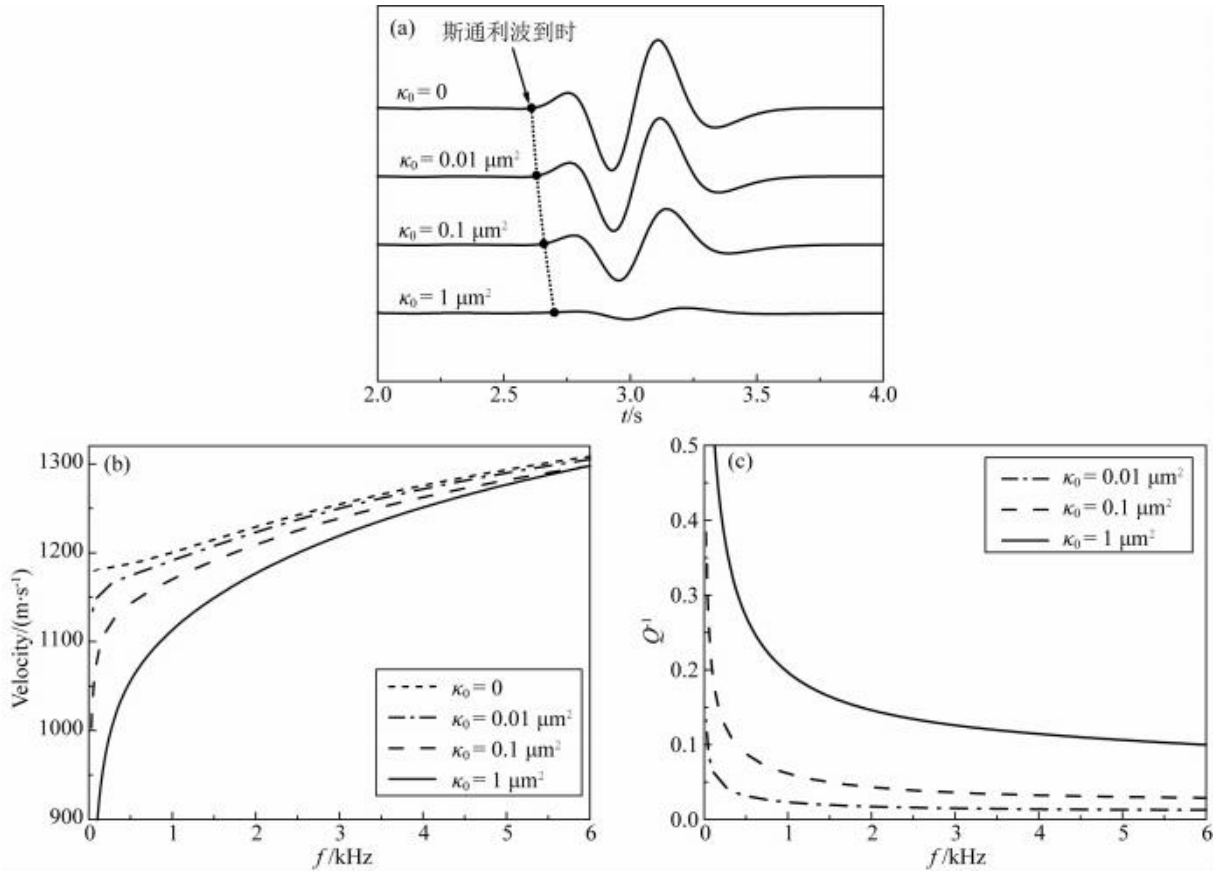


图 2 不同渗透率下的随钻斯通利波模拟

(a) 波形;(b) 频散曲线;(c) 衰减曲线.

Fig. 2 Simulation of LWD Stoneley waves for different permeability values

(a) Waveforms; (b) Phase velocity dispersion curves; (c) Attenuation curves.

为进一步研究电缆与随钻测量环境下,斯通利波受地层渗透率的影响情况,图 3 给出了含水地层渗透率一定时($\kappa_0=1\ \mu m^2$),充液井孔中随钻和电缆斯通利波的频散曲线以及相速度对渗透率的灵敏度曲线.为了对比,还给出了非渗透地层的频散曲线.当地层存在渗透性时,随钻和电缆斯通利波的相速度都会减小,但在随钻环境下斯通利波的变化量要比在电缆中更大(图 3a).图 3b 显示,在随钻中斯通利波的相速度对渗透率的灵敏度比在电缆中更高,特别是在低频段.图 3b 中还给出了频率为 0.5 kHz 时随钻和电缆情况下对应的灵敏度值,二者比值为 1.8,定量说明了随钻斯通利波相速度对渗透率的高灵敏度.数值模拟结果表明,利用随钻斯通利波反演地层渗透率比电缆斯通利波更具优势,其反演精度更高.

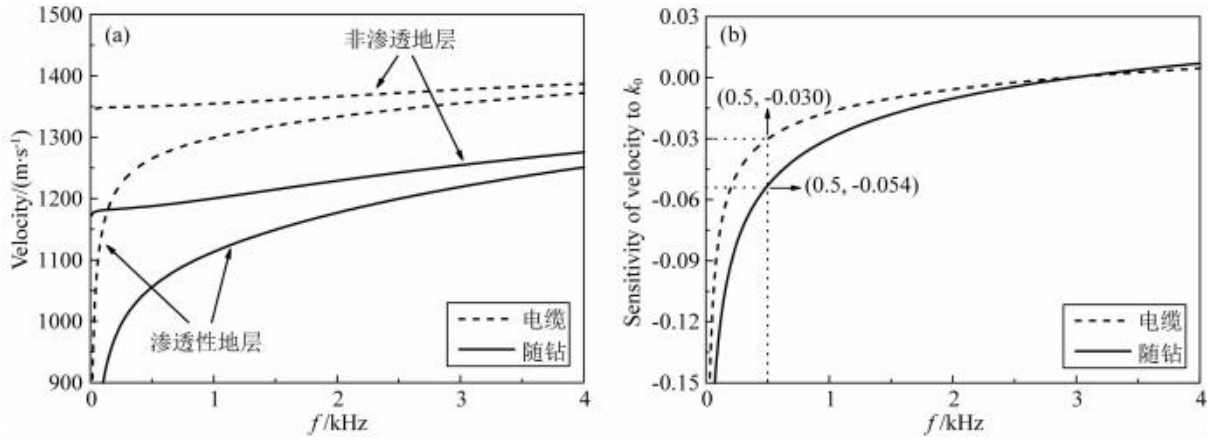


图 3　地层存在渗透性时的随钻和电缆斯通利波模拟对比

(a) 频散曲线;(b) 速度灵敏度曲线.

Fig. 3　Comparison of LWD and wireline Stoneley wave simulations for a permeable formation

(a) Phase velocity dispersion curves; (b) Velocity sensitivity to κ_0.

3　随钻斯通利波渗透率反演方法

3.1　考虑等效仪器的简化 Biot-Rosenbaum 随钻模型

利用频散方程(20)可以得到随钻斯通利波在孔隙地层的井孔中传播时的准确解,但由于完整的 Biot-Rosenbaum 理论中涉及到地层弹性参数和流体流动参数之间的耦合作用,反演过程中每一次循环迭代都需要同时计算弹性和流体的效应,使得计算比较繁琐,不适用于实际数据处理. Tang 等(1991)提出一种简化理论,通过将斯通利波与孔隙地层的相互作用分解为等效弹性孔隙地层问题和孔隙流体流动问题两部分,可以得到孔隙地层中斯通利波波数的简化计算公式为

$$k=\sqrt{k_e^2+\frac{2i\rho_{pf}\omega\kappa(\omega)R}{\eta(R^2-r_b^2)}\frac{\sqrt{-i\omega/D+k_e^2}}{1+BC^{(v_s/v_f)}}\frac{K_1(R\sqrt{-i\omega/D+k_e^2})}{K_0(R\sqrt{-i\omega/D+k_e^2})}},\tag{24}$$

其中,$BC=\sqrt{k_e^2-k_f^2}R\dfrac{I_1(f_eR)}{I_0(f_eR)}$ 为对软地层影响的校正;I_0 和 I_1 分别为第一类零阶和一阶变型贝塞尔函数,K_0 和 K_1 分别为第二类零阶和一阶变型贝塞尔函数;D 为动态孔隙流体的扩散率(唐晓明和郑传汉,2004);k_e 为等效弹性地层中对应于弹性仪器模型的斯通利波波数. Su 等(2011)采用等效仪器模型来考虑随钻测井仪器的影响,并验证了其在均匀地层中应用的可行性.仪器的效应由参数 E_{tool} 模拟,E_{tool} 定义为与仪器弹性和井孔流体有关的贝塞尔函数组合之比:

$$E_{tool}=\frac{(M_T/r_b)fI_1(fr_b)+\rho_f\omega^2I_0(fr_b)}{(M_T/r_b)fK_1(fr_b)-\rho_f\omega^2K_0(fr_b)},\tag{25}$$

其中,M_T 是等效仪器模量,该模量与弹性仪器的杨氏模量 E 和泊松比 ν 有关:$M_T\approx E/(1-\nu)$.

相比于完整的 Biot-Rosenbaum 理论,简化理论的优势在于利用一个简单的解析公式(24)代替了从频散方程(20)中求根的过程,并将随钻仪器的复杂结构等效为弹性仪器模型,从而大大加快理论计算的速度.在实际反演中,弹性波数只需要用测到的地层弹性参数计算一次,因而迭代过程中只需调整孔隙流体的流动参数并用公式(24)进行计算,反演效率将得到明显提高.

下面我们用数值模拟的方法验证在孔隙地层中使用考虑等效仪器的简化Biot-Rosenbaum随钻模

型的可行性.图 4 为随钻斯通利波在两种理论下的频散曲线.为了对比,图中同时给出了非渗透和渗透性地层中的结果.模拟结果显示,在非渗透地层中,采用简化随钻模型计算的结果与完整 Biot-Rosenbaum 理论计算的结果吻合较好;在渗透性地层中,两者的结果也基本一致.模拟结果的一致性表明考虑等效仪器的简化随钻模型不仅适用于非渗透地层,在渗透性地层中同样具有良好的应用效果.

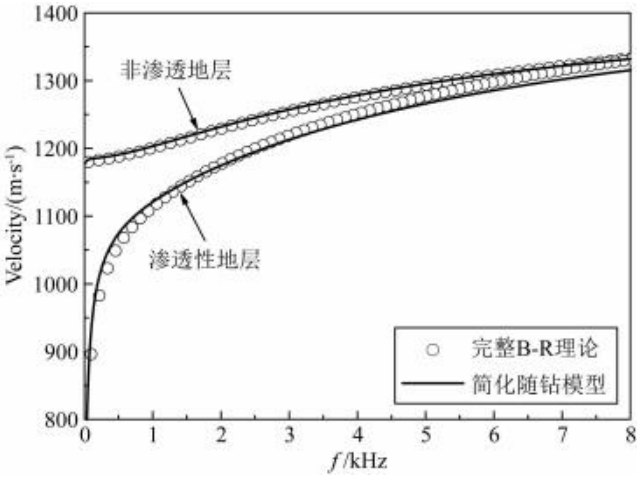


图 4 完整 Biot-Rosenbaum 理论和简化随钻模型模拟对比

Fig. 4 Comparison of complete Biot-Rosenbaum theory and simplified LWD model simulations

3.2 反演方法

利用频移和时滞联合反演地层渗透率,图 5 给出了相应的处理流程,其具体处理过程如下所述:

(1)利用波场分离(唐晓明和郑传汉,2004)技术处理测量得到的随钻单极子声波波形,得到直达斯通利波、上行反射斯通利波和下行反射斯通利波.

(2)上文提到的等效随钻仪器模型中,仪器半径可以通过仪器参数获得,但等效仪器模量无法获取.非渗透率地层中可以排除渗透率的影响,从而可以利用该层段测井得到的地层参数标定等效仪器模量(Lee et al.,2016),为后续简化理论提供准确参数.

(3)基于本文提到的简化理论,利用传播矩阵方法(Gelinsky and Tang, 1997)计算排除渗透率影响的理论直达斯通利波波形,该波形仅考虑地层弹性及井径的影响.

(4)根据 Tang 和 Cheng(1996)提出的计算方法,分别利用上述理论模拟及实测波形计算中心频率、走时和方差.两者之间的中心频率及走时之差确定了实测频移及时滞.

(5)除渗透率之外,井内流体和地层非弹性内耗散衰减也会影响斯通利波的衰减和走时,因此在反

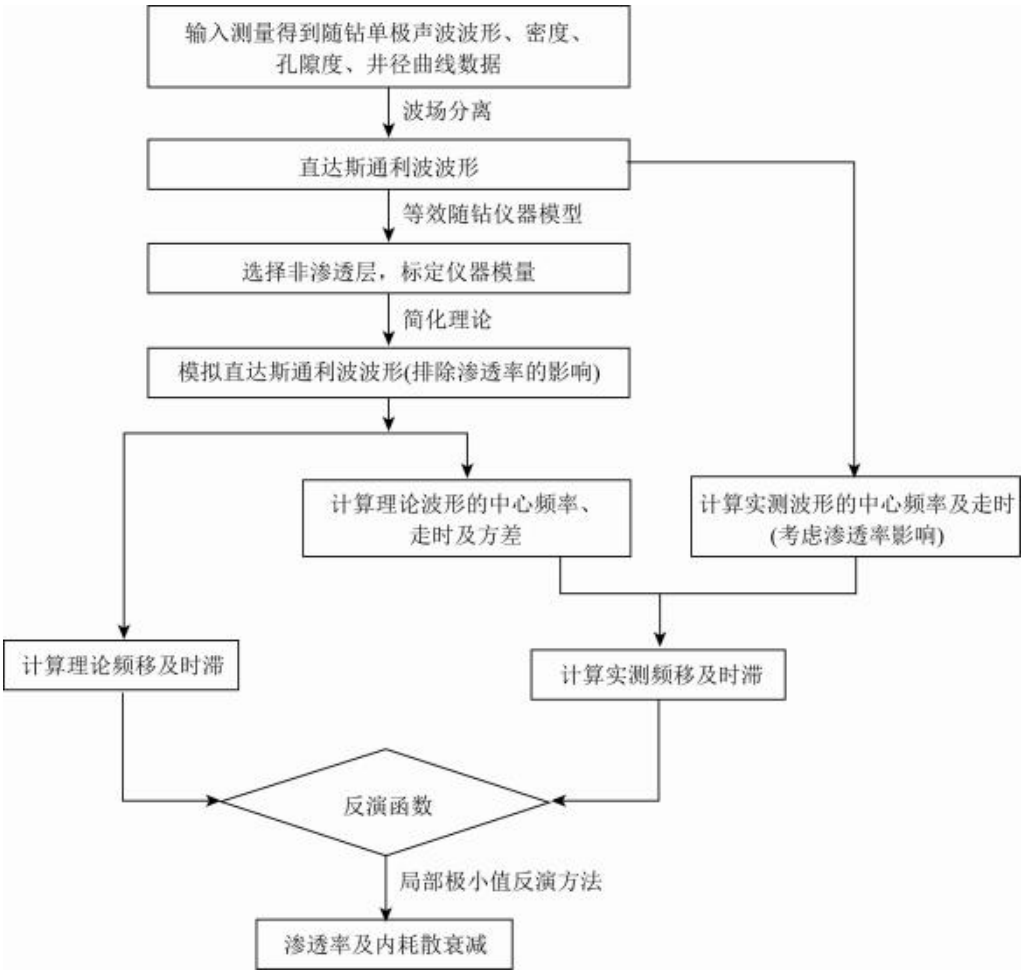


图 5 随钻斯通利波反演地层渗透率方法流程图

Fig. 5 Flow chart of inversion method for formation permeability with LWD Stoneley waves

演渗透率时需要同时反演内耗散衰减.对步骤 4 所述公式引入内耗散效应和渗透率影响(Tang and Cheng, 1996),并计算得到理论频移及时滞.

(6)利用上述理论及实测频移及时滞建立反演目标函数为

$$E(\kappa_0, Q^{-1}) = (\Delta f_c^{msd} - \Delta f_c^{theo})^2/\sigma_{syn}^2 + 2\pi\sigma_{syn}^2(\Delta T_c^{msd} - \Delta T_c^{theo})^2, \quad (26)$$

其中,Δf_c^{msd}、Δf_c^{theo} 分别为实测波形和理论模拟波形的频移;ΔT_c^{msd}、ΔT_c^{theo} 分别为实测波形和理论模拟波形的时间滞后;σ_{syn} 为理论斯通利波计算得到的方差,用来归一化频移及时滞对目标函数的影响.通过在合理的变化范围内同时调整地层渗透率 κ_0 和内耗散衰减 Q^{-1},利用共轭梯度法使上述目标函数达到极小值,从而反演出地层渗透率.

4　反演实例

利用随钻斯通利波对 L 井渗透率进行评价,其处理结果如图 6 所示.图中第 1 道给出了井径及自然伽马曲线,其中井径无明显变化,保证了声波测量数据的可靠性;自然伽马值较低的两个层段可划分为储层.从第 6 道岩性分析中可看出,两个层段的泥

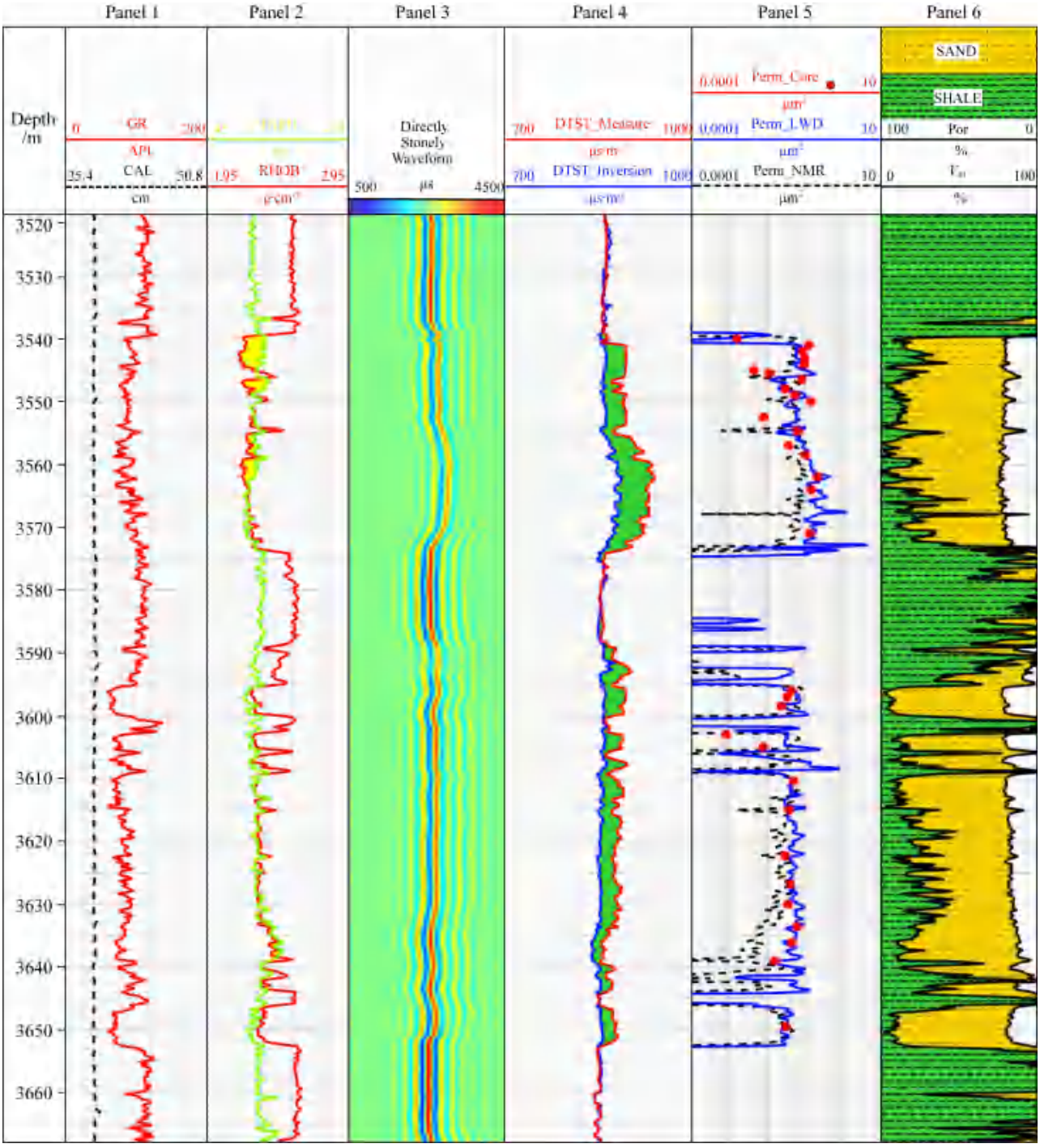


图 6　L 井随钻斯通利波反演渗透率结果图

Fig. 6　Results of permeability from inversion of LWD Stoneley waves for well L

质含量较低,孔隙度在 15%～25%,孔隙性较好.常规测井资料均显示具有良好的渗透性.第 3 道为波场分离后得到的直达斯通利波波形,第 4 道中分别为从实测波形和理论波形中提取出的斯通利波慢度曲线,存在明显相对时滞(即反演斯通利波慢度明显小于实测斯通利波慢度)层段可判断为渗透性地层.图中两个层段反演较测量得到的斯通利波时差出现相对时滞,指示地层存在渗透性,并且根据时滞的包络变化能够区分渗透率的相对大小.图中第 5 道不同渗透率处理结果的对比显示,随钻斯通利波反演的渗透率与核磁渗透率吻合较好,而且与核磁渗透率相比,随钻斯通利波反演渗透率与岩心覆压测试渗透率的匹配性更好.随钻斯通利波渗透率结果与伽马曲线及砂泥岩剖面对应一致性也较好,说明反演结果较为真实.良好的吻合性和一致性证明了利用随钻斯通利波反演地层渗透率的可行性和有效性.

5 结论

本文通过数值计算的方法,考察了地层渗透率对随钻斯通利波频散和衰减的影响,并与电缆测井情况下进行了对比,指出了利用随钻斯通利波反演地层渗透率的优势,分析了反演过程中采用的简化理论和反演方法,得到以下认识和结论:

(1)随钻斯通利波的相速度和衰减均受地层渗透率的影响,衰减比相速度受渗透率的影响更大.与电缆测井相比,随钻环境下斯通利波相速度对渗透率的灵敏度更高,说明随钻斯通利波更适用于反演地层渗透率.并且在随钻环境下,井壁处泥饼尚未形成,可以忽略泥饼的效应,其反演的渗透率结果更加接近真实的地层情况.

(2)渗透率越大,随钻斯通利波相速度和衰减的变化越大,因此地层的渗透性越好,其反演结果越准确.在低频区间,随钻斯通利波相速度和衰减随渗透率及频率的变化更加明显,指示渗透率反演时应选择低频段.

(3)数值模拟表明,考虑等效仪器的简化 Biot-Rosenbaum 随钻模型和完整理论的计算结果吻合较好,采用简化随钻模型可使反演效率得到明显提高.

(4)基于频移和时滞方法反演的随钻斯通利波渗透率与核磁和岩心覆压测试渗透率匹配较好,与常规测井资料反映的储层特性具有较好的一致性.并且理论分析和实例结果表明,中、高孔渗地层反演的渗透率精度较高,在低孔渗致密地层中反演精度有所降低.

附录 $\boldsymbol{H}$ 矩阵元素

式(16)中 $\boldsymbol{H}$ 矩阵各元素的具体表达式为(所有未列出的矩阵元素都为 0):

$$H_{1,1}=-fI_1(fr_a),\quad H_{1,2}=pI_1(pr_a),$$
$$H_{1,3}=-pK_1(pr_a),\quad H_{1,4}=\mathrm{i}ksI_1(sr_a),$$
$$H_{1,5}=-\mathrm{i}ksK_1(sr_a),\quad H_{2,1}=\rho_f\omega^2 I_0(fr_a),$$
$$H_{2,2}=\mu^t[2k^2-(k_s^t)^2]I_0(pr_a)-\frac{2p\mu^t}{r_a}I_1(pr_a),$$
$$H_{2,3}=\mu^t[2k^2-(k_s^t)^2]K_0(pr_a)+\frac{2p\mu^t}{r_a}K_1(pr_a),$$
$$H_{2,4}=2\mathrm{i}k\mu^t s\left[sI_0(sr_a)-\frac{1}{r_a}I_1(sr_a)\right],$$
$$H_{2,5}=2\mathrm{i}k\mu^t s\left[sK_0(sr_a)+\frac{1}{r_a}K_1(sr_a)\right],$$
$$H_{3,2}=2\mathrm{i}kp\mu^t I_1(pr_a),\ H_{3,3}=-2\mathrm{i}kp\mu^t K_1(pr_a),$$
$$H_{3,4}=-(k^2+s^2)s\mu^t I_1(sr_a),$$
$$H_{3,5}=(k^2+s^2)s\mu^t K_1(sr_a),$$
$$H_{4,2}=pI_1(pr_b),\quad H_{4,3}=-pK_1(pr_b),$$
$$H_{4,4}=\mathrm{i}ksI_1(sr_b),\quad H_{4,5}=-\mathrm{i}ksK_1(sr_b),$$
$$H_{4,6}=-fI_1(fr_b),\quad H_{4,7}=fK_1(fr_b),$$
$$H_{5,2}=\mu^t[2k^2-(k_s^t)^2]I_0(pr_b)-\frac{2p\mu^t}{r_b}I_1(pr_b),$$
$$H_{5,3}=\mu^t[2k^2-(k_s^t)^2]K_0(pr_b)+\frac{2p\mu^t}{r_b}K_1(pr_b),$$
$$H_{5,4}=2\mathrm{i}k\mu^t s\left[sI_0(sr_b)-\frac{1}{r_b}I_1(sr_b)\right],$$
$$H_{5,5}=2\mathrm{i}k\mu^t s\left[sK_0(sr_b)+\frac{1}{r_b}K_1(sr_b)\right],$$
$$H_{5,6}=\rho_f\omega^2 I_0(fr_b),\quad H_{5,7}=\rho_f\omega^2 K_0(fr_b),$$
$$H_{6,2}=2\mathrm{i}kp\mu^t I_1(pr_b),\ H_{6,3}=-2\mathrm{i}kp\mu^t K_1(pr_b),$$
$$H_{6,4}=-(k^2+s^2)s\mu^t I_1(sr_b),$$
$$H_{6,5}=(k^2+s^2)s\mu^t K_1(sr_b),$$
$$H_{7,6}=-fI_1(fR),\ H_{7,7}=fK_1(fR),$$
$$H_{7,8}=-q_{\mathrm{fast}}(1+b_{\mathrm{fast}})K_1(q_{\mathrm{fast}}R),$$
$$H_{7,9}=-q_{\mathrm{slow}}(1+b_{\mathrm{slow}})K_1(q_{\mathrm{slow}}R),$$
$$H_{7,10}=-\mathrm{i}kq_s(1+b_s)K_1(q_sR),$$
$$H_{8,6}=\rho_f\omega^2 I_0(fR),\ H_{8,7}=\rho_f\omega^2 K_0(fR),$$
$$H_{8,8}=2\mu[q_{\mathrm{fast}}^2K_0(q_{\mathrm{fast}}R)+q_{\mathrm{fast}}K_1(q_{\mathrm{fast}}R)/R]-k_{\mathrm{fast}}^2[\lambda+\alpha/\beta(\alpha+b_{\mathrm{fast}})]K_0(q_{\mathrm{fast}}R),$$
$$H_{8,9}=2\mu[q_{\mathrm{slow}}^2K_0(q_{\mathrm{slow}}R)+q_{\mathrm{slow}}K_1(q_{\mathrm{slow}}R)/R]-k_{\mathrm{slow}}^2[\lambda+\alpha/\beta(\alpha+b_{\mathrm{slow}})]K_0(q_{\mathrm{slow}}R),$$

$H_{8,10} = 2\mathrm{i}\mu k[q_s^2 K_0(q_s R) + q_s K_1(q_s R)/R]$,

$H_{9,8} = -2\mathrm{i}\mu k q_{\mathrm{fast}} K_1(q_{\mathrm{fast}} R)$,

$H_{9,9} = -2\mathrm{i}\mu k q_{\mathrm{slow}} K_1(q_{\mathrm{slow}} R)$,

$H_{9,10} = \mu(2k^2 - k_{\mathrm{shear}}^2) q_s K_1(q_s R)$,

$H_{10,6} = -\rho_f \omega^2 I_0(fR)$, $H_{10,7} = -\rho_f \omega^2 K_0(fR)$,

$H_{10,8} = k_{\mathrm{fast}}^2[(\alpha + b_{\mathrm{fast}})/\beta] K_0(q_{\mathrm{fast}} R)$,

$H_{10,9} = k_{\mathrm{slow}}^2[(\alpha + b_{\mathrm{slow}})/\beta] K_0(q_{\mathrm{slow}} R)$.

其中,I 为第一类贝塞尔函数;K 为第二类贝塞尔函数;v_f 为流体速度;v_p^t 为钻铤纵波速度;v_s^t 为钻铤横波速度;k_f 为流体波数,$k_f = \omega/v_f$;k_p^t 为钻铤纵波波数,$k_p^t = \omega/v_p^t$;k_s^t 为钻铤横波波数,$k_s^t = \omega/v_s^t$;f 为流体径向波数,$f = \sqrt{k^2 - k_f^2}$;p 为钻铤纵波径向波数,$p = \sqrt{k^2 - (k_p^t)^2}$;$s$ 为钻铤横波径向波数,$s = \sqrt{k^2 - (k_s^t)^2}$;$\mu^t$ 为钻铤剪切模量,$\mu^t = \rho_t \cdot (v_s^t)^2$;$\rho_t$ 为钻铤密度;其他符号定义与文中相同.

References

Biot M A. 1956a. Theory of propagation of elastic waves in a fluid-saturated porous solid. I: Low-frequency range. *The Journal of the Acoustical Society of America*, 28(2): 168-178.

Biot M A. 1956b. Theory of propagation of elastic waves in a fluid-saturated porous solid. II. Higher frequency range. *The Journal of the Acoustical Society of America*, 28(2): 179-191.

Biot M A. 1962. Mechanics of deformation and acoustic propagation in porous media. *Journal of Applied Physics*, 33(4): 1482-1498.

Cui Z W. 2004. Theoretical and numerical study of modified Biot's models, acoustoelectric well logging and acoustic logging while drilling excited by multipole acoustic sources[Ph. D. Thesis] (in Chinese). Changchun: Jilin University.

Cui Z W, Lü W G, Xie S L, et al. 2010. Improvement in inversion of permeability from attenuation of stoneley waves. *Journal of Jilin University* (*Earth Science Edition*) (in Chinese), 40(S1): 35-38.

Gao K, Tao G, Wang B. 2005. Algorithm for formation permeability from Stoneley wave logs and its field application. *Well Logging Technology* (in Chinese), 29(6): 507-510.

Gelinsky S, Tang X M. 1997. Fast forward modeling of Stoneley waves for irregular boreholes and heterogeneous formations. // 67th Ann. Internat Mtg., Soc. Expl. Geophys.. Expanded Abstracts, 317-320.

Hou C H, Wu X Y, Wang K X. 1997. Inversion of reservoir permeability from the attenuation of stoneley wave. *Well Logging Technology* (in Chinese), 21(3): 162-166.

Jin W J, Li J, Wu Q Z, et al. 2017. Study on well logging evaluation method of gas shale permeability. *Progress in Geophysics* (in Chinese), 32(1): 177-182, doi: 10.6038/pg20170124.

Johnson D L, Koplic J, Dashen R. 1987. Theory of dynamic permeability and tortuosity in fluid saturated porous media. *Journal of Fluid Mechanics*, 176: 379-402.

Lee S Q, Tang X M, Su Y D, et al. 2016. Model-based dispersive processing of borehole dipole wave data using an equivalent-tool theory. *Geophysics*, 81(1): D35-D43.

Parra J O, Xu P C. 1994. Dispersion and attenuation of acoustic guided waves in layered fluid-filled porous media. *The Journal of the Acoustical Society of America*, 95(1): 91-98.

Rosenbaum J H. 1974. Synthetic microseismograms: logging in porous formations. *Geophysics*, 39(1): 14-32.

Schmitt D P. 1988. Effects of radial layering when logging in saturated porous formations. *The Journal of the Acoustical Society of America*, 84(6): 2200-2214.

Schmitt D P, Bouchon M, Bonnet G. 1988. Full-wave synthetic acoustic logs in radially semiinfinite saturated porous media. *Geophysics*, 53(6): 807-823.

Su H, Tian H. 2002. Estimation of formation permeability using Stoneley wave. *Well Logging Technology* (in Chinese), 26(4): 298-301.

Su Y D, Tang X M, Hei C, et al. 2011. An equivalent-tool theory for acoustic logging and applications. *Applied Geophysics*, 8(1): 69-72.

Tang X M, Cheng C H. 1993. The effects of a logging tool on the Stoneley wave propagation in elastic and porous formations. *The Log Analysts*, 34: 46-56.

Tang X M, Cheng C H. 1996. Fast inversion of formation permeability from Stoneley wave logs using a simplified Biot-Rosenbaum model. *Geophysics*, 61(3): 639-645.

Tang X M, Cheng C H, Toksoz M N. 1991. Dynamic permeability and borehole Stoneley waves: A simplified Biot-Rosenbaum model. *The Journal of the Acoustical Society of America*, 90(3): 1632-1646.

Tang X M, Gelinsky S, Chunduru R K, et al. 1998-07-21. Method for estimating permeability of earth formations by processing Stoneley waves from an acoustic wellbore logging instrument: US, 5784333.

Tang X M, Patterson D, Wu L. 2010. Measurement of formation permeability using stoneley waves from an LWD acoustic tool. *Petrophysics*, 51(2): 66-74.

Tang X M, Zheng C H. 2004. Quantitative Borehole Acoustic Methods (in Chinese). Zhao X M Trans. Beijing: Petroleum Industry Press.

Wang K X, Dong Q D. 1986. Theoretical analysis and calculation of sound field in an oil well surrounded by a permeable formation. *Acta Petrolei Sinica* (in Chinese), 7(1): 59-69.

Wang Y Z, Pan B Z. 2017. Permeability anisotropy measurement and anisotropic evaluation method abstract. *Progress in Geophysics* (in Chinese), 32(6): 2552-2559, doi: 10.6038/pg20170636.

Williams D M, Zemanek J, Angona F A, et al. 1984. The long spaced acoustic logging tool. Spwla Annual Logging Symposium,

Paper T.

Wu X Y, Wang K X, Guo L, et al. 1995. Inversion of permeability from the full waveform acoustic logging data. *Acta Geophysica Sinica* (in Chinese), 38(S1): 224-231.

Xu X K, Chen X L, Fan Y R, et al. 2012. Influence factors of Stoneley wave and permeability inversion of formation. *Journal of China University of Petroleum* (in Chinese), 36(2): 97-104.

Zhang B X, Wang K X, Dong Q D. 1995. Theory of acoustic multipole logging and analysis of wave components and calculation of full waveforms for two-phase medium formation. *Acta Geophysica Sinica* (in Chinese), 38(S1): 178-192.

Zhang L H, Pan B Z, Shan G Y. 2018. Progress in experimental research on porosity and permeability of core samples. *Progress in Geophysics* (in Chinese), 33(2): 777-782, doi: 10.6038/pg2018AA0378.

附中文参考文献

崔志文. 2004. 多孔介质声学模型与多极源声电效应测井和多极随钻声测井的理论与数值研究[博士论文]. 长春: 吉林大学.

崔志文, 吕伟国, 谢树理等. 2010. 利用斯通利波衰减反演渗透率的方法改进. 吉林大学学报(地球科学版), 40(S1): 35-38.

高坤,陶果,王兵. 2005. 利用斯通利波计算地层渗透率的方法及应用. 测井技术, 29(6): 507-510.

侯春会, 伍先运, 王克协. 1997. 利用斯通利波衰减反演储层渗透率. 测井技术, 21(3): 162-166.

金武军, 李军, 武清钊等. 2017. 页岩气储层渗透率测井评价方法研究. 地球物理学进展, 32(1): 177-182, doi: 10.6038/pg20170124.

苏华, 田洪. 2002. 利用斯通利波估算地层渗透率. 测井技术, 26(4): 298-301.

唐晓明, 郑传汉. 2004. 定量测井声学. 赵晓敏译. 北京: 石油工业出版社.

王克协, 董庆德. 1986. 渗透性地层油井中声场的理论分析与计算. 石油学报, 7(1): 59-69.

王宇竹, 潘保芝. 2017. 渗透率各向异性测量和评价方法综述. 地球物理学进展, 32(6): 2552-2559, doi:10.6038/pg20170636.

伍先运, 王克协, 郭立等. 1995. 利用声全波测井资料求取储层渗透率的方法与应用研究. 地球物理学报, 38(S1): 224-231.

许孝凯, 陈雪莲, 范宜仁等. 2012. 斯通利波影响因素分析及渗透率反演. 中国石油大学学报(自然科学版), 36(2): 97-104.

张碧星, 王克协, 董庆德. 1995. 双相介质井孔多极源声测井理论及分波分析与全波计算. 地球物理学报, 38(S1): 178-192.

张丽华, 潘保芝, 单刚义. 2018. 岩心样品孔隙度渗透率实验研究进展. 地球物理学进展, 33(2): 777-782, doi:10.6038/pg2018AA0378.

(本文编辑 张正峰)

刘玉凯，唐晓明，苏远大. 2016. 随钻条件下井旁界面声电效应的辐射电磁波响应特征. 地球物理学报，59(5)：1898-1908，doi：10.6038/cjg20160532.

Liu Y K, Tang X M, Su Y D. 2016. Characteristics of radiating electromagnetic waves induced by the interface outside the borehole during seismoelectric logging while drilling. *Chinese J. Geophys.* (in Chinese), 59(5): 1898-1908, doi: 10.6038/cjg20160532.

随钻条件下井旁界面声电效应的辐射电磁波响应特征

刘玉凯，唐晓明，苏远大*

中国石油大学(华东)地球科学与技术学院，青岛 266580

摘要 孔隙地层中存在着动电耦合现象，弹性波作用在声阻抗或者电化学性质差异地层会产生辐射电磁波. 本文探讨了随钻条件下，利用孔隙地层中的动电耦合效应探测井旁地质体的可行性. 为此模拟了井外存在声阻抗差异和电化学差异界面时声波诱导的辐射电场响应特征. 求出柱坐标下介质中声场和电场函数表达式，由此计算并比较了均匀介质和弹性差异界面情况下井中接收到的电场. 发现随钻条件下，井外的弹性差异界面会产生以光速传播的辐射电磁波. 该电磁波反映了井外地质信息，并先于井中直达声波的伴随电磁场到达接收器，因而可以直接观测到. 此外，还发现界面辐射电磁波可以用来探测油、水等电化学性质差异大而弹性阻抗差异小的界面；声源频率以及界面两侧地层性质差异程度是辐射电磁波幅度的影响因素.

关键词 随钻测井；声电效应；辐射电磁波；地质导向

doi：10.6038/cjg20160532 **中图分类号** P631 **收稿日期** 2014-11-26，2016-03-13 收修定稿

Characteristics of radiating electromagnetic waves induced by the interface outside the borehole during seismoelectric logging while drilling

LIU Yu-Kai, TANG Xiao-Ming, SU Yuan-Da*

School of Geosciences, China University of Petroleum, Qingdao 266580, *China*

Abstract Porous formations often exhibit seismoelectric effects. When there is an interface in the medium, the discontinuity of the seismoelectric property gives rise to electromagnetic radiation. We study the feasibility of using the electrokinetic effect generated in porous formations to explore the geologic structure outside the borehole. In particular, we study the characteristics of the radiation of electromagnetic waves from an elastic impendence interface or an electrochemical interface outside the borehole with a seismoelectric logging tool. We first derive the solution for elastic and electric fields in the cylindrical coordinates. Then we calculate the electric fields in the borehole for a homogenous formation and for a formation with an elastic impendence interface. The results show that during the seismoelectric logging while drilling, the electromagnetic radiation can be induced at the interface outside the borehole and travels at speed of light. Because of the radiated electromagnetic waves arrive earlier than the seismoelectric signals

基金项目 国家自然科学基金(41474092)，中央高校基本科研业务费专项资金(15CX06016A)资助.

作者简介 刘玉凯，男，1988 年生，山东济南人，在读博士研究生，主要从事随钻声波以及声电测井的理论研究工作. E-mail：liuyukai.1008@163.com

* **通讯作者** 苏远大，男，副教授，主要从事声波测井的方法和资料处理等方面的研究. E-mail：syuanda@sina.com

traveling along the borehole, it can be used to detect the geologic structure outside the borehole. In addition, these radiated electromagnetic waves can be used to detect a low elastic impendence or high electrical impendence interface, such as an oil-water interface, which is usually difficult to recognize using the elastic wave reflection method only. We also show that the dominant frequency and contrast between two formations can influence the amplitude of the radiated electromagnetic waves.

Keywords　Acoustic logging-while-drilling; Seismoelectric effect; Radiating electromagnetic wave; Geosteering

1　引言

表面物理化学效应使孔隙地层存在着动电耦合现象,当弹性波在孔隙地层中传播时,引起流体相对于骨架的流动,产生电磁场(Morgan et al., 1989; Pride, 1994; Pride and Haartsen,1996).弹性波在均匀的孔隙介质中传播诱导的电磁场是一种局部场,它以弹性波速度传播,而当介质存在弹性或者电化学差异时,将会产生独立于弹性波传播的辐射电磁场(Thompson and Gist, 1993; Pride and Haartsen, 1996; Haartsen and Pride, 1997; Zhu et al., 1999).为认识井中声电转换波的产生和传播机理,胡恒山和王克协(1999, 2000)、胡恒山等(2003)最早进行了井孔中声电场的理论模拟,采用实轴积分法模拟出了点声源激发的井孔声场和电磁场的全波波形.在随钻动电测井方面,崔志文(2004)、Zhan 等(2006)、Guan 等(2013)、郑晓波等(2014)进行了理论模拟,讨论了随钻多极子动电测井测量地层纵、横波速度的可行性.为探测井外的地质构造,Zhu 和 Toksöz(2003)进行了井外孔隙地层有裂缝情况下的声电转换波实验,利用跨孔勘探方法接收到了两个井孔之间裂缝产生的以电磁波速度传播的辐射电磁波.王军(2012)进行了井中声电效应辐射电磁场特性的实验研究,提出界面的辐射电磁波可用于随钻地质导向.需要指出的是前人的理论模拟工作针对的均是井孔内的声电转换,而对于随钻条件下井旁界面的声诱导辐射电磁波响应特征未见详细理论分析.本文着眼于将声电转换效应用于井外地质界面的探边问题.测井中常采用声波远探测技术进行井外地质探边,分别用偶极横波(Tang and Patterson, 2009; 唐晓明和魏周拓,2012)和单极纵波(薛梅,2002;楚泽涵等,2005,乔文孝等,2004;车小花等,2004;何峰江,2005;陶果等,2008)探测远距离(二、三十米)和近距离(数米)内的地质体.在单极纵波探测中,一个常见的问题就是怎样把地层反射波从直达波的强干扰背景中提取出来.本文将从声电转换效应的角度来探讨这一问题.

本文的工作是基于孔隙地层中存在的动电耦合现象,利用简化的 Pride 动电耦合理论,数值模拟计算了随钻条件下井旁存在弹性差异界面时的辐射电磁波的响应特征,分析了其产生原因及传播特征;分析了声源频率、地层因素对辐射电场幅度的影响;针对传统的声波远探测中界面反射波易受井中直达波干扰这一问题,提出了一种利用界面声电效应的辐射电磁波进行随钻界面探测和地质导向的新型探测方法,并为该方法提供了理论依据.

2　基本理论和方法

2.1　计算模型

采用如图 1 所示的地层模型构造地层界面,包括钻铤内流体 I(黄色)、钻铤 C(紫色)、钻铤外流体 O(黄色),孔隙地层 1(蓝色)与孔隙地层 2(红色)五部分.模型界面包括钻铤内流体与钻铤界面、钻铤与钻铤外流体界面、钻铤外流体与孔隙地层 1 界面、孔

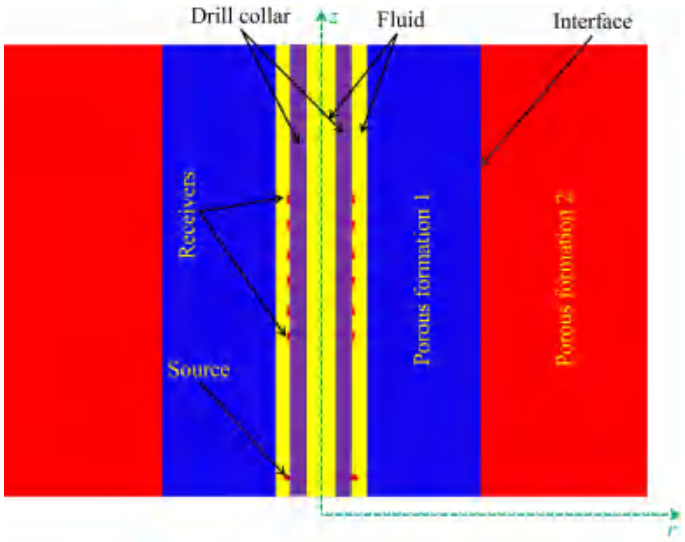


图 1　含地层界面的随钻物理模型

Fig. 1　Schematic model of LWD with formation interface

隙地层 1 与孔隙地层 2 界面,四个界面距离井眼中心轴的距离分别为 r_a,r_b,R,R_1.

2.2 Pride 方程组

为方便后文叙述,现将 Pride(1994)方程组进行简要介绍. Pride(1994)从基本的力学和电磁学原理出发,采用体积平均法,结合 Biot(1962)孔隙弹性波动方程和 Maxwell 电磁方程,导出了宏观声电耦合控制方程组,其中的动电耦合效应由如下两个方程控制:

$$\boldsymbol{J} = \sigma(\omega)\boldsymbol{E} + L(\omega)(-\nabla p + \omega^2\rho_f\boldsymbol{u}), \quad (1)$$

$$-\mathrm{i}\omega\boldsymbol{w} = L(\omega)\boldsymbol{E} + (-\nabla p + \omega^2\rho_f\boldsymbol{u})\kappa(\omega)/\eta, \quad (2)$$

方程中的 $\boldsymbol{J}$ 和 $\boldsymbol{E}$ 分别是电流密度与电场强度,$\sigma(\omega)$,$\kappa(\omega)$,$L(\omega)$ 分别为孔隙介质的电导率、动态渗透率和动电耦合系数,ω 为角频率,i 为虚数单位,ρ_f 为孔隙流体密度,η 为孔隙流体黏度,$\boldsymbol{u}$,p,$\boldsymbol{w}$ 分别是固相位移、孔隙流体压强、渗流位移. 式(1)表示压强梯度和固相位移加速度可以产生电流,式(2)表示电场反过来可以产生渗流. 当 $L(\omega)$ 取为 0 时,动、电解耦并分别退化为各自的 Biot 孔隙弹性波方程和 Maxwell 电磁方程.

由于声电转换中声场诱导的电磁场对声波的影响很小,胡恒山等(2003)忽略声-电测井时转换电场对声场的影响,提出了先计算声场再计算电场的解耦算法;更进一步,由于电磁波长远大于源距和井孔半径,计算时可以将电场看作似稳场. 上述两种假设大大提高了计算效率,本文亦采用该计算方法.

2.3 弹性场的求解

井内流体、钻铤的位移以及势函数在柱坐标中的通解可参考 Guan 等(2013),本文只考虑单极情况,其形式如下:

$$\begin{aligned}
&\varphi^{\mathrm{I}}(k,w,r,\theta) = A^{\mathrm{I}}I_0(\eta_f r)\mathrm{e}^{\mathrm{i}kz},\\
&\varphi^{\mathrm{C}}(k,w,r,\theta) = [A^{\mathrm{CP}}I_0(\eta_{cp}r) + B^{\mathrm{CP}}K_0(\eta_{cp}r)]\mathrm{e}^{\mathrm{i}kz},\\
&\xi^{\mathrm{C}}(k,w,r,\theta) = [A^{\mathrm{CSV}}I_0(\eta_{cs}r) + B^{\mathrm{CSV}}K_0(\eta_{cs}r)]\mathrm{e}^{\mathrm{i}kz},\\
&\varphi^{\mathrm{O}}(k,w,r,\theta) = [A^{\mathrm{O}}I_0(\eta_f r) + B^{\mathrm{O}}K_0(\eta_f r)]\mathrm{e}^{\mathrm{i}kz},\\
&\varphi^{\mathrm{pf1}}(k,w,r,\theta) = [A^{\mathrm{pf1}}K_0(\eta_{pf1}r) + B^{\mathrm{pf1}}I_0(\eta_{pf1}r)]\mathrm{e}^{\mathrm{i}kz},\\
&\varphi^{\mathrm{ps1}}(k,w,r,\theta) = [A^{\mathrm{ps1}}K_0(\eta_{ps1}r) + B^{\mathrm{ps1}}I_0(\eta_{ps1}r)]\mathrm{e}^{\mathrm{i}kz},\\
&\xi^{\mathrm{f1}}(k,w,r,\theta) = [A^{\mathrm{SV1}}K_0(\eta_{s1}r) + B^{\mathrm{SV1}}I_0(\eta_{s1}r)]\mathrm{e}^{\mathrm{i}kz},\\
&\varphi^{\mathrm{pf2}}(k,w,r,\theta) = A^{\mathrm{pf2}}K_0(\eta_{pf2}r)\mathrm{e}^{\mathrm{i}kz},\\
&\varphi^{\mathrm{ps2}}(k,w,r,\theta) = A^{\mathrm{ps2}}K_0(\eta_{ps2}r)\mathrm{e}^{\mathrm{i}kz},\\
&\xi^{\mathrm{f2}}(k,w,r,\theta) = A^{\mathrm{SV2}}K_0(\eta_{s2}r)\mathrm{e}^{\mathrm{i}kz}, \quad (3)
\end{aligned}$$

其中 $\varphi^N(N=\mathrm{I},\mathrm{C},\mathrm{O},\mathrm{pf1},\mathrm{ps1},\mathrm{pf2},\mathrm{ps2})$ 是图 1 分层区域中介质的纵波势函数,上标 I,C,O,1,2 含义如前所述,pf,ps 分别表示孔隙介质中的快、慢纵波. $\xi^N(N=\mathrm{C},\mathrm{f1},\mathrm{f2})$ 是相应介质的 SV 横波位移势函数. $\eta_l = \sqrt{k^2 - k_l^2}(l=\mathrm{f},\mathrm{cp},\mathrm{cs},\mathrm{pf1},\mathrm{ps1},\mathrm{s1},\mathrm{pf2},\mathrm{ps2},\mathrm{s2})$ 为各区域中的径向波数,k 为轴向波数,$k_l = \omega/v_l$ 为介质的总波数,v_l 为介质速度,I_n,K_n 分别为 n 阶第一类、第二类变形贝塞尔函数. 在计算泥浆纵波和钻铤纵波和横波的波数时,考虑耗散效应以及钻铤的隔声效果,设泥浆纵波以及钻铤纵波、横波的品质因子分别为 Q_f、Q_{cp} 和 Q_{cs},此时三者的总波数表示为 $k_m = \dfrac{\omega}{v_m}(1+Q_m)(m=\mathrm{f},\mathrm{cp},\mathrm{cs})$. 式(3)中的 16 个待定系数 $A^N(N=\mathrm{I},\mathrm{CP},\mathrm{CSV},\mathrm{O},\mathrm{pf1},\mathrm{ps1},\mathrm{SV1},\mathrm{pf2},\mathrm{ps2},\mathrm{SV2})$ 和 $B^N(N=\mathrm{CP},\mathrm{CSV},\mathrm{O},\mathrm{pf1},\mathrm{ps1},\mathrm{SV1})$ 由图 1 中模型界面上的 16 个力学(应力、位移)边界条件决定,可参考崔志文(2004).

将各个势函数带入到位移、应力的表达式(参见 Guan 等(2013))中,可以得到各个区域中相应的位移、应力,结合边界条件得到以下矩阵方程:

$$\begin{aligned}
&\{\boldsymbol{M}_{ij}\}_{16\times16}\cdot\{\boldsymbol{A}^{\mathrm{I}},\boldsymbol{A}^{\mathrm{CP}},\boldsymbol{B}^{\mathrm{CP}},\boldsymbol{A}^{\mathrm{CSV}},\boldsymbol{B}^{\mathrm{CSV}},\boldsymbol{A}^{\mathrm{O}},\boldsymbol{B}^{\mathrm{O}},\boldsymbol{A}^{\mathrm{pf1}},\boldsymbol{B}^{\mathrm{pf1}},\boldsymbol{A}^{\mathrm{ps1}},\boldsymbol{B}^{\mathrm{ps1}},\boldsymbol{A}^{\mathrm{SV1}},\boldsymbol{B}^{\mathrm{SV1}},\boldsymbol{A}^{\mathrm{pf2}},\boldsymbol{A}^{\mathrm{ps2}},\boldsymbol{A}^{\mathrm{SV2}}\}^{\mathrm{T}}\\
&\quad = \{0,0,0,0,u_s,0,0,0,0,0,0,0,0,0,0,0,0,0,0,0,0\}^{\mathrm{T}}, \quad (4)
\end{aligned}$$

其中位移源 u_s 的表达式及含义可参考唐晓明和郑传汉(2004).

求解出 16 个弹性场未知系数后,模型各区域弹性场的位移、应力等场量即可全部求得. 矩阵 M_{ij} 的表达式详见附录 A.

2.4 电场的求解

由于电磁波的波长远大于源距和井孔尺寸,因此可以将电磁场看做似稳场进行计算,地层、井中流体的电场 $\boldsymbol{E}$ 和电势 ϕ 满足 $\boldsymbol{E} = -\nabla\phi$. 地层中的电势有如下形式解:

$$\begin{aligned}
\phi^{\mathrm{F1}} &= [A^{\mathrm{E1}}I_0(kr) + B^{\mathrm{E1}}K_0(kr)]\mathrm{e}^{\mathrm{i}kz}\\
&\quad + \frac{L_1(\omega)}{\sigma_1(\omega)}\left[-p_1 + \omega^2\rho_{f1}(\varphi^{\mathrm{pf1}} + \varphi^{\mathrm{ps1}})\right], \quad (5)\\
\phi^{\mathrm{F2}} &= B^{\mathrm{E2}}K_0(kr)\mathrm{e}^{\mathrm{i}kz} + \frac{L_2(\omega)}{\sigma_2(\omega)}\left[-p_2 + \omega^2\rho_{f2}(\varphi^{\mathrm{pf2}} + \varphi^{\mathrm{ps2}})\right], \quad (6)
\end{aligned}$$

其中 p_1,p_2 分别为孔隙介质 1 与孔隙介质 2 中的孔隙声压,其表达式(高永新,2010)为

$$p_1 = -(C_1\nabla\cdot\boldsymbol{u}^{\mathrm{F1}} + M_1\nabla\cdot\boldsymbol{w}^{\mathrm{F1}}), \quad (7)$$

$$p_2 = -(C_2\nabla\cdot\boldsymbol{u}^{\mathrm{F2}} + M_2\nabla\cdot\boldsymbol{w}^{\mathrm{F2}}), \quad (8)$$

C_1、M_1、C_2、M_2 分别为孔隙介质 1,2 的弹性模量.

钻铤外流体的电场表达式(Guan et al., 2013)如下:

$$\phi^{O}=[A^{OE}I_0(kr)+B^{OE}K_0(kr)]e^{ikz}. \tag{9}$$

根据似稳场近似条件下电场与电势的关系 $\boldsymbol{E}=-\nabla\phi$,由式(5)、(6)和(9)可得孔隙地层 1、2 以及钻铤外流体的电场 $\boldsymbol{E}^{F1}$,$\boldsymbol{E}^{F2}$,$\boldsymbol{E}^{O}$. 将电场 $\boldsymbol{E}^{F1}$,$\boldsymbol{E}^{F2}$,$\boldsymbol{E}^{O}$ 代入式(1),结合弹性场的解 $\boldsymbol{u}$,即可得到相应介质中的电流密度 $\boldsymbol{J}^{F1}$,$\boldsymbol{J}^{F2}$,$\boldsymbol{J}^{O}$. 需要说明的是由于井中流体不存在动电耦合现象,由 $\boldsymbol{E}^{O}$ 求取钻铤外流体电流密度 $\boldsymbol{J}^{O}$ 时,只需考虑式(1)第一项即可.

下面给出钻铤外表面、井壁、孔隙介质 1 与 2 界面处的电磁场边界条件:

由于钻铤为良导体,钻铤外表面电场切向的 z 分量为 0,即

$$E_z^{O}|_{r=r_b}=0, \tag{10}$$

在井壁 $r=R$ 处,井内流体与孔隙介质 1 中的电势以及径向电流密度连续,即

$$\begin{aligned}\phi^{O}|_{r=R}&=\phi^{F1}|_{r=R},\\ J_r^{O}|_{r=R}&=J_r^{F1}|_{r=R}.\end{aligned} \tag{11}$$

在孔隙介质 1 与 2 界面 $r=R_1$ 处,孔隙介质 1 与 2 中的电势以及径向电流密度连续,即

$$\begin{aligned}\phi^{F1}|_{r=R_1}&=\phi^{F2}|_{r=R_1},\\ J_r^{F1}|_{r=R_1}&=J_r^{F2}|_{r=R_1}.\end{aligned} \tag{12}$$

根据以上 5 个边界条件得到如下矩阵方程:

$$\{\boldsymbol{N}_{ij}\}_{5\times5}\cdot\{\boldsymbol{A}^{OE},\boldsymbol{B}^{OE},\boldsymbol{A}^{E1},\boldsymbol{B}^{E1},\boldsymbol{B}^{E2}\}^{T}=\boldsymbol{b}, \tag{13}$$

矩阵 $\boldsymbol{N}_{ij}$ 与列向量 $\boldsymbol{b}$ 的表达式详见附录 B.

求解式(13)得到 A^{OE}、B^{OE}、A^{E1}、B^{E1}、B^{E2} 五个系数,进而可以求得各区域中的电场. 现给出钻铤外表面的径向电场表达式:

$$E_r^{O}=[-A^{OE}kI_1(kr_b)+B^{OE}kK_1(kr_b)]e^{ikz}. \tag{14}$$

3　数值计算结果及分析

依照上述的基本理论与方法,我们对随钻条件下,井外存在界面时的声电场进行了数值模拟. 表 1 是模拟时井内流体及钻铤的几何参数与物理参数. 表 2 是计算声电场所需的物理参数,其中井中流体的矿化度为 10^{-3} mol·L^{-1},黏滞系数为 10^{-3} Pa·s,流体相对介电常数为 80,其他各个参数详细的物理含义见高永新(2010). 由表 2 的物理参数可以计算相关的物理参数,如快慢纵波、横波、电磁波的慢度、等效介电常数、动态电导率、动态渗透率、渗流位移与固相位移幅度之比等. 计算动电耦合系数 $L(\omega)$ 时,取其低频极限(胡恒山和王克协,1999;郑晓波等,2014),表达式中其他变量的计算方法见 Pride (1994)、高永新(2010)、胡恒山和王克协(1999)等人的工作.

表 1　井内流体及钻铤参数

Table 1　Parameters of borehole fluid and collar

	纵波速度/(m·s^{-1})	横波速度/(m·s^{-1})	密度/(kg·m^{-3})	半径/m	品质因子
钻铤内流体	1500	—	1000	0.027	60
钻铤	5860	3130	7850	0.09	3
钻铤外流体	1500	—	1000	0.117	60

表 2　孔隙地层参数

Table 2　Porous formation parameters

参数	地层 1	地层 2
孔隙度 ϕ/(%)	0.3	0.3
渗透率 κ_0/m^2	10^{-12}	10^{-12}
弯曲度 α_∞	3	3
固相基质体积模量 K_s/GPa	35.7	90
岩石骨架体积模量 K_b/GPa	9.21	48
岩石骨架剪切模量 G/GPa	7.24	40
流体体积模量 K_f/GPa	2.25	2.25
固相密度 ρ_s/(kg·m^{-3})	2650	2650
流体密度 ρ_f/(kg·m^{-3})	1000	1000
流体黏滞系数 η/(Pa·s)	10^{-3}	10^{-3}
矿化度 C_0/(mol·L^{-1})	10^{-3}	10^{-3}
固相相对介电常数 ε_s	4	4
流体相对介电常数 ε_f	80	80

3.1　界面辐射电场响应特征

图 2 是存在界面(孔隙介质 1 与 2 分别取表 2 中的地层 1 与地层 2,计算结果为实线)与均匀介质(孔隙介质 1 与 2 均取地层 1,计算结果为虚线)条件下的阵列电场对比图. 接收器位于钻铤外表面,源距 12 m,间距 0.1524 m,井旁界面距井轴的距离 R_1 为 4 m,声源信号为主频 3 kHz 的 Ricker 子波. 本文模拟中源距选取的原则是:界面的辐射电磁波在井中声波伴随电磁场之前到达接收器. Meredith (1990)的工作指出井中单极声源可以向井外地层辐射出纵波和 SV 型横波. 这里我们关心的是这两种波在井外地层界面产生的电磁转换波.

从图 2 中可以看出,在考察的时间段内存在四个信号波包,波包 a-a,d-d 与界面存在与否无关. 从到时分析,波包 a-a 是声波从井内流体入射到井壁

产生的辐射电磁波,该辐射电磁波的传播速度为光速,因而该信号在各个接收器上无到时的差异.波包 d-d 是井中滑行纵波产生的伴随电场.与均匀介质相比,井外存在界面时产生了波包 b-b,c-c,它们同时到达各个接收器,没有到时差异.为分析波包 b-b,c-c 的变化规律及产生原因,现将界面逐渐由 3.50 m移动到 4.75 m,间隔 0.25 m,固定接收位置(源距 12 m 处),观察各个波包到时的变化规律,如图 3 所示.从图 3 中可以看出波包 a-a,d-d 与界面移动与否无关,而波包 b-b,c-c 到时随着界面的移动而变化,速度分别为地层 1 的纵波、横波速度.波包 b-b 是由于快纵波到达界面引起电流不平衡而产生的辐射电磁波,波包 c-c 是横波到达弹性差异界面后引起界面处电流的不平衡而产生的辐射电场.

波包 b-b,c-c 均是由于界面位置电流不平衡产生的辐射电磁波,可以反映井旁地质结构的位置,因而可以用来进行界面探边和随钻地质导向.更为重要的是,该电磁信号的回传时间可以忽略不计,因而其到时仅为源到界面的单程走时,因此源距较大的条件下可以在井中直达声波伴随电磁场之前到达接

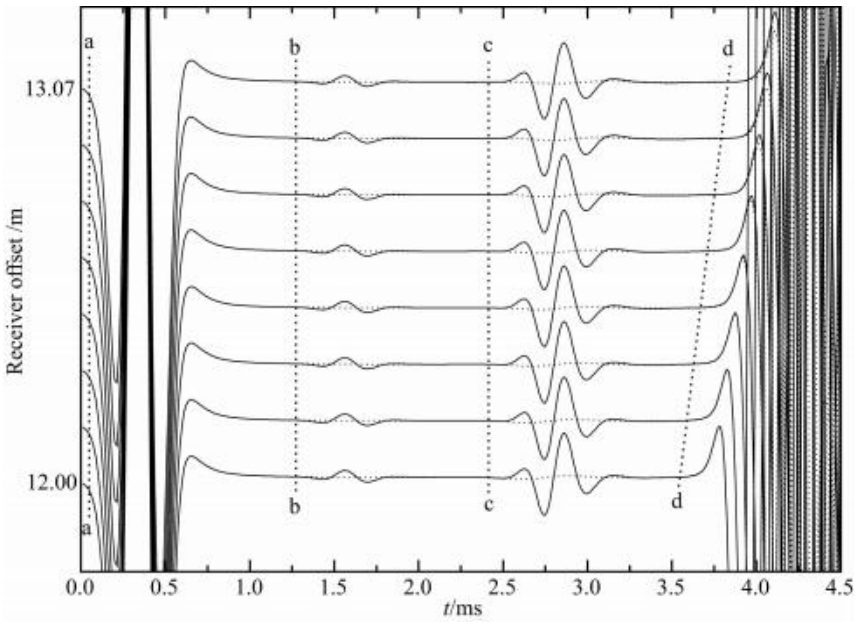


图 2 有(实线)、无(虚线)弹性差异界面时随钻电场阵列波形

Fig. 2 Synthetic electric field array waveforms of seismoelectric LWD with (solid lines) and without (dashed lines) elastic interface

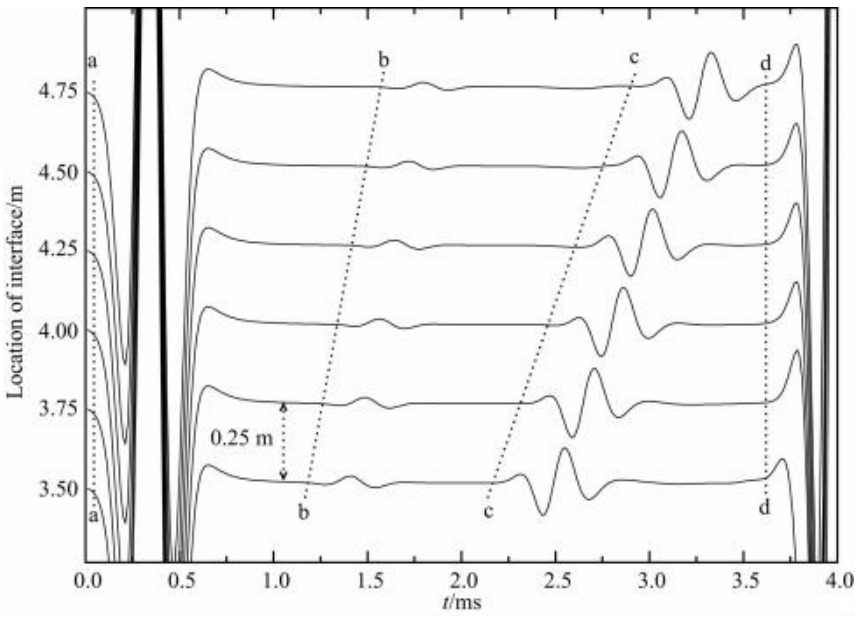


图 3 固定接收位置,界面位置不同时随钻电场波形

界面位置由距离井轴 3.75 m 移动到 4.75 m,间隔 0.25 m.

Fig. 3 Synthetic waveforms of seismoelectric LWD with different interface distances

Location of interface moves from 3.75 m to 4.75 m with spacing 0.25 m.

收器,从而可以避免常规弹性波远探测测井中反射波遭直达波干扰这一问题.但是,从图 2 可以看出波包 a-a 的幅度远大于波包 b-b,c-c,这种情况与常规远探测井中直达波幅度远大于反射波幅度类似,同样不利于反射信号的采集(魏周拓等,2013).然而,相对有利的情况是,波包 a-a 的到时只是声波从声源(在钻铤外表面)到达井壁的极短的传播时间,而声源的持续时间 t_0 是可控并且可知的,如果采用延迟记录的方式不记录该波包而只记录关心时段内的波形,则可以避免波包 b-b,c-c 远小于波包 a-a 这一问题.

3.2　界面辐射电磁波影响因素

声源在不同主频激励下辐射到地层内的能量不同,地层参数不同也会造成动电耦合系数的不同,为此我们讨论了声源主频以及地层界面两侧弹性阻抗差异与电化学差异的大小对辐射电磁波幅度的影响.

在考察声源主频对界面辐射电磁波的影响时,孔隙介质 1 与 2 分别取表 2 中的地层 1 与地层 2,界面距井轴的距离 R_1 为 3.5 m,源距 10 m.声源信号主频依次为 3～10 kHz 的 Ricker 子波,每隔 1 kHz 模拟一次.为清晰地显示计算结果我们把 2 ms 之前的信号放大了 10 倍,如图 4 所示.从图 4 中可以看出,在所计算的声源主频下纵、横波均可以在地层界面处诱导辐射电磁波 b-b 与 c-c,它们均在井中直达波之前到达接收器;此外,还可以看出辐射电磁波的幅度受声源主频控制,声源主频发生变化辐射电磁波的幅度也发生变化.因此,在利用声电效应进行井外地质结构探测时,需要考虑声源频率的影响.

在考察弹性性质差异时,孔隙度固定为 20%,通过改变岩石骨架的体积模量与剪切模量来构造弹性阻抗的差异,表 3 给出了岩石骨架体积模量与剪切模量.计算时孔隙介质 1 的体积模量与剪切模量取表 3 中的岩石 3 且保持不变,孔隙介质 2 的体积模量与剪切模量分别取表 3 中的岩石 1～5,其他物理参数见表 2 中地层 1,界面距井轴的距离 R_1 为 2.5 m.计算时声源信号为主频 8 kHz 的 Ricker 子波,提取源距 7 m 处钻铤外表面径向电场,为清晰地显示计算结果我们把 1 ms 之前的信号放大了 10 倍,如图 5 所示.从图 5 中可以看出,弹性波传播到岩石弹性模量存在差异界面时会在界面处产生辐射电磁波 b-b 与 c-c;随着孔隙介质 1 与孔隙介质 2 弹性模量之间的差异先减小再增大(与岩石 3 相比),辐射电磁波幅度 b-b,c-c 也有相同的变化规律(先减小再增大).因而利用声电效应进行井外地质结构探测时,界面两侧弹性阻抗差异会影响探测效果.

在考察电化学性质差异时,孔隙介质 1 矿化度固定为 1×10^{-3} mol·L^{-1}且保持不变,孔隙介质 2 的矿化度分别为 0.25×10^{-3},0.5×10^{-3},1×10^{-3},2×10^{-3},4×10^{-3} mol·L^{-1},所用的其他物理参数

表 3　岩石骨架的体积模量与剪切模量

Table 3　Skeleton bulk modulus and shear modulus of rock framework

岩石编号	1	2	3	4	5
骨架体积模量 K_b/GPa	30.62	22.63	14.39	8.09	4.35
骨架剪切模量 G/GPa	28.65	22.22	13.99	6.83	3.86

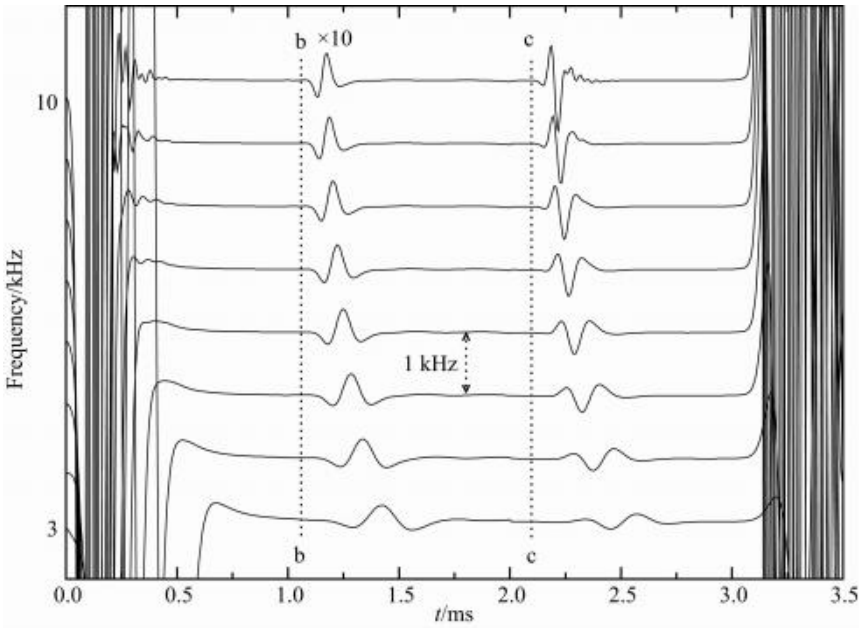


图 4　不同声源主频下的辐射电场

Fig. 4　Radiating electromagnetic waveforms with different dominant frequencies

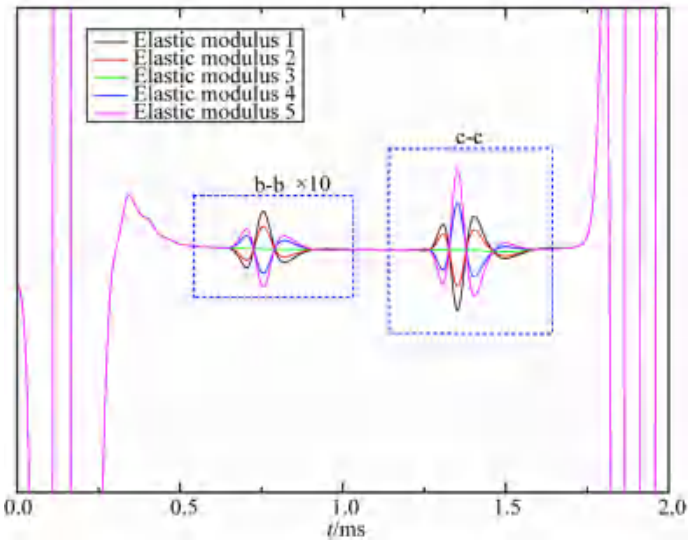


图 5 不同弹性差异下辐射电场波形

Fig. 5 Radiating electromagnetic waveforms with different elasticity

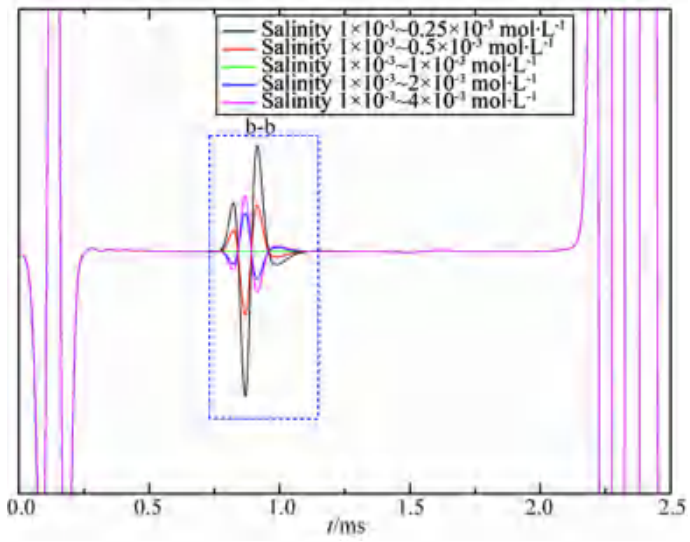


图 6 不同矿化度差异下辐射电场波形

Fig. 6 Radiating electromagnetic waveforms with different salinities

见表 2 中地层 1,界面距井轴的距离 R_1 为 2.5 m. 计算时声源信号为主频 8 kHz 的 Ricker 子波,提取源距 7 m 处钻铤外表面径向电场,计算结果如图 6 所示. 从图 6 中可以看出,弹性波传播到矿化度存在差异界面时会产生辐射电磁波 b-b,其幅度变化规律与存在弹性阻抗差异界面时相同. 因而利用声电效应进行井外地质结构探测时,界面两侧电化学性质会影响探测效果. 但是,与存在弹性差异界面不同的是,存在电化学性质差异界面时只有一个辐射电磁波信号 b-b,从到时分析,它是孔隙地层 1 中的纵波传播到电化学差异界面处产生的辐射电磁波,而横波到达化学性质不连续而弹性性质连续界面时不会转换成纵波,因此不会产生电流的不平衡.

声波反射波远探测针对弹性阻抗差异大的界面具有很好的效果,但对于油水等弹性阻抗差异小的界面则难以获取界面信息. 弹性波作用在电化学性质差异界面产生辐射电磁波这一现象可以用于探测弹性性质相同或者相近(如油、水界面)而电化学性质差异大的界面,这一性质比弹性波反射法探测界面具有优势.

4 结论

本文数值模拟了随钻条件下井旁界面声电效应的辐射电磁波响应特征以及影响因素,与前人关注井中声电转换不同,重点考察了井外界面产生的辐射电磁波,得到了如下的结论和认识:

(1) 随钻条件下,弹性波作用在井旁界面处会产生电流的不平衡从而诱导辐射电磁波,该电磁波以光速传播,在源距较大的条件下可以在井中直达声波伴随电磁场之前到达接收器,可以避免常规弹性波远探测测井中反射波受直达波干扰这一问题;

(2) 弹性波作用在电化学性质存在差异的界面将会产生辐射电磁波,该界面辐射电磁波可以用来探测油、水等电化学性质差异大而弹性阻抗差异小的界面;

(3) 声源频率以及界面两侧地层性质的差异程度是辐射电磁波幅度的影响因素.

致谢 感谢两位匿名审稿专家提出的宝贵意见和建设性建议,对本文的修改和提高有很大的帮助.

附录 A 声场矩阵

现给出公式(4)中矩阵 $\boldsymbol{M}_{16\times16}$ 中各个元素的表达式:

$$M_{1,1} = -\eta_f I_1(\eta_f r_a),\ M_{1,2} = I_1(\eta_{cp} r_a)\eta_{cp},$$

$$M_{1,3} = -K_1(\eta_{cp} r_a)\eta_{cp},\ M_{1,4} = \mathrm{i}kI_1(\eta_{cs} r_a)\eta_{cs},$$

$$M_{1,5} = -\mathrm{i}kK_1(\eta_{cs} r_a)\eta_{cs},$$

$$M_{2,1} = \rho_b\omega^2 I_0(\eta_f r_a),\ M_{2,2} = \frac{1}{r_a^2}\left(-2G_c I_1(\eta_{cp} r_a)\eta_{cp} r_a + 2I_0(\eta_{cp} r_a)\left(r_a^2\eta_{cp}^2 G_c - \frac{1}{2}r_a^2 k_{cp}^2\lambda_c\right)\right),$$

$$M_{2,3} = \frac{1}{r_a^2}\left(2G_c K_1(\eta_{cp} r_a)\eta_{cp} r_a + 2K_0(\eta_{cp} r_a)\left(r_a^2\eta_{cp}^2 G_c - \frac{1}{2}r_a^2 k_{cp}^2\lambda_c\right)\right),$$

$$M_{2,4} = \frac{1}{r_a^2}\left(2\mathrm{i}(-I_1(\eta_{cs} r_a)\eta_{cs} r_a + I_0(\eta_{cs} r_a)r_a^2\eta_{cs}^2)G_c k\right),\ M_{2,5} = \frac{1}{r_a^2}(2\mathrm{i}(K_1(\eta_{cs} r_a)\eta_{cs} r_a + K_0(\eta_{cs} r_a)r_a^2\eta_{cs}^2)G_c k),$$

$$M_{3,2}=2\mathrm{i}G_{\mathrm{c}}kI_1(\eta_{\mathrm{cp}}r_{\mathrm{a}})\eta_{\mathrm{cp}},\ M_{3,3}=-2\mathrm{i}G_{\mathrm{c}}kK_1(\eta_{\mathrm{cp}}r_{\mathrm{a}})\eta_{\mathrm{cp}},\ M_{3,4}=-G_{\mathrm{c}}(k^2+\eta_{\mathrm{cs}}^2)I_1(\eta_{\mathrm{cs}}r_{\mathrm{a}})\eta_{\mathrm{cs}},$$
$$M_{3,5}=G_{\mathrm{c}}(k^2+\eta_{\mathrm{cs}}^2)K_1(\eta_{\mathrm{cs}}r_{\mathrm{a}})\eta_{\mathrm{cs}},\ M_{4,2}=I_1(\eta_{\mathrm{cp}}r_{\mathrm{b}})\eta_{\mathrm{cp}},\ M_{4,3}=-K_1(\eta_{\mathrm{cp}}r_{\mathrm{b}})\eta_{\mathrm{cp}},\ M_{4,4}=\mathrm{i}kI_1(\eta_{\mathrm{cs}}r_{\mathrm{b}})\eta_{\mathrm{cs}},$$
$$M_{4,5}=-\mathrm{i}kK_1(\eta_{\mathrm{cs}}r_{\mathrm{b}}),\ M_{4,6}=-\eta_{\mathrm{f}}I_1(\eta_{\mathrm{f}}r_{\mathrm{b}}),\ M_{4,7}=\eta_{\mathrm{f}}K_1(\eta_{\mathrm{f}}r_{\mathrm{b}})r_{\mathrm{b}},$$
$$M_{5,2}=\frac{1}{r_{\mathrm{b}}^2}\Big(-2G_{\mathrm{c}}I_1(\eta_{\mathrm{cp}}r_{\mathrm{b}})\eta_{\mathrm{cp}}r_{\mathrm{b}}+2\Big(r_{\mathrm{b}}^2\eta_{\mathrm{cp}}^2G_{\mathrm{c}}-\frac{1}{2}r_{\mathrm{b}}^2k_{\mathrm{cp}}^2\lambda_{\mathrm{c}}\Big)I_0(\eta_{\mathrm{cp}}r_{\mathrm{b}})\Big),$$
$$M_{5,3}=\frac{1}{r_{\mathrm{b}}^2}\Big(2G_{\mathrm{c}}K_1(\eta_{\mathrm{cp}}r_{\mathrm{b}})\eta_{\mathrm{cp}}r_{\mathrm{b}}+2\Big(r_{\mathrm{b}}^2\eta_{\mathrm{cp}}^2G_{\mathrm{c}}-\frac{1}{2}r_{\mathrm{b}}^2k_{\mathrm{cp}}^2\lambda_{\mathrm{c}}\Big)K_0(\eta_{\mathrm{cp}}r_{\mathrm{b}})\Big),$$
$$M_{5,4}=\frac{1}{r_{\mathrm{b}}^2}(2\mathrm{i}(-I_1(\eta_{\mathrm{cs}}r_{\mathrm{b}})\eta_{\mathrm{cs}}r_{\mathrm{b}}+I_0(\eta_{\mathrm{cs}}r_{\mathrm{b}})r_{\mathrm{b}}^2\eta_{\mathrm{cs}}^2)G_{\mathrm{c}}k),$$
$$M_{5,5}=\frac{1}{r_{\mathrm{b}}^2}(2\mathrm{i}(K_1(\eta_{\mathrm{cs}}r_{\mathrm{b}})\eta_{\mathrm{cs}}r_{\mathrm{b}}+K_0(\eta_{\mathrm{cs}}r_{\mathrm{b}})r_{\mathrm{b}}^2\eta_{\mathrm{cs}}^2)G_{\mathrm{c}}k),\ M_{5,6}=\rho_{\mathrm{b}}\omega^2I_0(\eta_{\mathrm{f}}r_{\mathrm{b}}),\ M_{5,7}=\rho_{\mathrm{b}}\omega^2K_0(\eta_{\mathrm{f}}r_{\mathrm{b}}),$$
$$M_{6,2}=2\mathrm{i}G_{\mathrm{c}}kI_1(\eta_{\mathrm{cp}}r_{\mathrm{b}})\eta_{\mathrm{cp}},\ M_{6,3}=-2\mathrm{i}G_{\mathrm{c}}kK_1(\eta_{\mathrm{cp}}r_{\mathrm{b}})\eta_{\mathrm{cp}},$$
$$M_{6,4}=-G_{\mathrm{c}}(k^2+\eta_{\mathrm{cs}}^2)I_1(\eta_{\mathrm{cs}}r_{\mathrm{b}})\eta_{\mathrm{cs}},\ M_{6,5}=G_{\mathrm{c}}(k^2+\eta_{\mathrm{cs}}^2)K_1(\eta_{\mathrm{cs}}r_{\mathrm{b}})\eta_{\mathrm{cs}},$$
$$M_{7,6}=-\eta_{\mathrm{f}}I_1(\eta_{\mathrm{f}}R),\ M_{7,7}=\eta_{\mathrm{f}}K_1(\eta_{\mathrm{f}}R),\ M_{7,8}=-(a_{\mathrm{pf1}}+1)K_1(\eta_{\mathrm{pf1}}R)\eta_{\mathrm{pf1}},\ M_{7,9}=(a_{\mathrm{pf1}}+1)I_1(\eta_{\mathrm{pf1}}R)\eta_{\mathrm{pf1}},$$
$$M_{7,10}=-(a_{\mathrm{ps1}}+1)\eta_{\mathrm{ps1}}K_1(\eta_{\mathrm{ps1}}R),\ M_{7,11}=(a_{\mathrm{ps1}}+1)\eta_{\mathrm{ps1}}I_1(\eta_{\mathrm{ps1}}R),$$
$$M_{7,12}=-\mathrm{i}\eta_{\mathrm{s1}}(a_{\mathrm{s1}}+1)kK_1(\eta_{\mathrm{s1}}R),\ M_{7,13}=\mathrm{i}\eta_{\mathrm{s1}}(a_{\mathrm{s1}}+1)kI_1(\eta_{\mathrm{s1}}R),$$
$$M_{8,6}=\rho_{\mathrm{b}}\omega^2I_0(\eta_{\mathrm{f}}R),\ M_{8,7}=\rho_{\mathrm{b}}\omega^2K_0(\eta_{\mathrm{f}}R),\ M_{8,8}=-K_0(\eta_{\mathrm{pf1}}R)(k^2-\eta_{\mathrm{pf1}}^2)(M_1a_{\mathrm{pf1}}+C_1),$$
$$M_{8,9}=-I_0(\eta_{\mathrm{pf1}}R)(k^2-\eta_{\mathrm{pf1}}^2)(M_1a_{\mathrm{pf1}}+C_1),\ M_{8,10}=-K_0(\eta_{\mathrm{ps1}}R)(k^2-\eta_{\mathrm{ps1}}^2)(M_1a_{\mathrm{ps1}}+C_1),$$
$$M_{8,11}=-I_0(\eta_{\mathrm{ps1}}R)(k^2-\eta_{\mathrm{ps1}}^2)(M_1a_{\mathrm{ps1}}+C_1),\ M_{9,6}=\rho_{\mathrm{b}}\omega^2I_0(\eta_{\mathrm{f}}R),\ M_{9,7}=\rho_{\mathrm{b}}\omega^2K_0(\eta_{\mathrm{f}}R),$$
$$M_{9,8}=\frac{1}{R^2}\Big(2G_1K_1(\eta_{\mathrm{pf1}}R)\eta_{\mathrm{pf1}}R-K_0(\eta_{\mathrm{pf1}}R)\big((-2k^2G_1+(k^2-\eta_{\mathrm{pf1}}^2)(C_1a_{\mathrm{pf1}}+H_1))R^2\big)\Big),$$
$$M_{9,9}=\frac{1}{R^2}\Big(-2G_1I_1(\eta_{\mathrm{pf1}}R)\eta_{\mathrm{pf1}}R-I_0(\eta_{\mathrm{pf1}}R)\big((-2k^2G_1+(k^2-\eta_{\mathrm{pf1}}^2)(C_1a_{\mathrm{pf1}}+H_1))R^2\big)\Big),$$
$$M_{9,10}=\frac{1}{R^2}\Big(2G_1K_1(\eta_{\mathrm{ps1}}R)\eta_{\mathrm{ps1}}R-K_0(\eta_{\mathrm{ps1}}R)\big((-2k^2G_1+(k^2-\eta_{\mathrm{ps1}}^2)(C_1a_{\mathrm{ps1}}+H_1))R^2\big)\Big),$$
$$M_{9,11}=\frac{1}{R^2}\Big(-2G_1I_1(\eta_{\mathrm{ps1}}R)\eta_{\mathrm{ps1}}R-I_0(\eta_{\mathrm{ps1}}R)\big((-2k^2G_1+(k^2-\eta_{\mathrm{ps1}}^2)(C_1a_{\mathrm{ps1}}+H_1))R^2\big)\Big),$$
$$M_{9,12}=\frac{1}{R}\Big(2\mathrm{i}(\eta_{\mathrm{s1}}K_1(\eta_{\mathrm{s1}}R)+K_0(\eta_{\mathrm{s1}}R)\eta_{\mathrm{s1}}^2R)G_1k\Big),\ M_{9,13}=\frac{1}{R}\Big(2\mathrm{i}G_1(-\eta_{\mathrm{s1}}I_1(\eta_{\mathrm{s1}}R)+I_0(\eta_{\mathrm{s1}}R)\eta_{\mathrm{s1}}^2R)k\Big),$$
$$M_{10,8}=-2\mathrm{i}\eta_{\mathrm{pf1}}G_1kK_1(\eta_{\mathrm{pf1}}R),\ M_{10,9}=2\mathrm{i}\eta_{\mathrm{pf1}}G_1kI_1(\eta_{\mathrm{pf1}}R),\ M_{10,10}=-2\mathrm{i}\eta_{\mathrm{ps1}}G_1kK_1(\eta_{\mathrm{ps1}}R),$$
$$M_{10,11}=2\mathrm{i}\eta_{\mathrm{ps1}}G_1kI_1(\eta_{\mathrm{ps1}}R),\ M_{10,12}=G_1(\eta_{\mathrm{s1}}^2+k^2)\eta_{\mathrm{s1}}K_1(\eta_{\mathrm{s1}}R),$$
$$M_{10,13}=-G_1(\eta_{\mathrm{s1}}^2+k^2)\eta_{\mathrm{s1}}I_1(\eta_{\mathrm{s1}}R),\ M_{11,8}=-K_1(\eta_{\mathrm{pf1}}R_1)\eta_{\mathrm{pf1}},\ M_{11,9}=I_1(\eta_{\mathrm{pf1}}R_1)\eta_{\mathrm{pf1}},$$
$$M_{11,10}=-K_1(\eta_{\mathrm{ps1}}R_1)\eta_{\mathrm{ps1}},\ M_{11,11}=I_1(\eta_{\mathrm{ps1}}R_1)\eta_{\mathrm{ps1}},\ M_{11,12}=-\mathrm{i}k\eta_{\mathrm{s1}}K_1(\eta_{\mathrm{s1}}R_1),$$
$$M_{11,13}=\mathrm{i}k\eta_{\mathrm{s1}}I_1(\eta_{\mathrm{s1}}R_1),\ M_{11,14}=K_1(\eta_{\mathrm{pf2}}R_1)\eta_{\mathrm{pf2}},\ M_{11,15}=K_1(\eta_{\mathrm{ps2}}R_1)\eta_{\mathrm{ps2}},$$
$$M_{11,16}=\mathrm{i}k\eta_{\mathrm{s2}}K_1(\eta_{\mathrm{s2}}R_1),\ M_{12,8}=\mathrm{i}K_0(\eta_{\mathrm{pf1}}R_1)k,\ M_{12,9}=\mathrm{i}I_0(\eta_{\mathrm{pf1}}R_1)k,\ M_{12,10}=\mathrm{i}K_0(\eta_{\mathrm{ps1}}R_1)k,$$
$$M_{12,11}=\mathrm{i}I_0(\eta_{\mathrm{ps1}}R_1)k,\ M_{12,12}=-\eta_{\mathrm{s1}}^2K_0(\eta_{\mathrm{s1}}R_1),\ M_{12,13}=-\eta_{\mathrm{s1}}^2I_0(\eta_{\mathrm{s1}}R_1),$$
$$M_{12,14}=-\mathrm{i}K_0(\eta_{\mathrm{pf2}}R_1)k,\ M_{12,15}=-\mathrm{i}K_0(\eta_{\mathrm{ps2}}R_1)k,\ M_{12,16}=\eta_{\mathrm{s2}}^2K_0(\eta_{\mathrm{s2}}R_1),$$
$$M_{13,8}=-\eta_{\mathrm{pf1}}a_{\mathrm{pf1}}K_1(\eta_{\mathrm{pf1}}R_1),\ M_{13,9}=a_{\mathrm{pf1}}I_1(\eta_{\mathrm{pf1}}R_1)\eta_{\mathrm{pf1}},\ M_{13,10}=-\eta_{\mathrm{ps1}}a_{\mathrm{ps1}}K_1(\eta_{\mathrm{ps1}}R_1),$$
$$M_{13,11}=a_{\mathrm{ps1}}I_1(\eta_{\mathrm{ps1}}R_1)\eta_{\mathrm{ps1}},\ M_{13,12}=-\mathrm{i}a_{\mathrm{s1}}k\eta_{\mathrm{s1}}K_1(\eta_{\mathrm{s1}}R_1),\ M_{13,13}=\mathrm{i}a_{\mathrm{s1}}k\eta_{\mathrm{s1}}I_1(\eta_{\mathrm{s1}}R_1),$$
$$M_{13,14}=a_{\mathrm{pf2}}K_1(\eta_{\mathrm{pf2}}R_1)\eta_{\mathrm{pf2}},\ M_{13,15}=a_{\mathrm{ps2}}K_1(\eta_{\mathrm{ps2}}R_1)\eta_{\mathrm{ps2}},\ M_{13,16}=\mathrm{i}a_{\mathrm{s2}}k\eta_{\mathrm{s2}}K_1(\eta_{\mathrm{s2}}R_1),$$
$$M_{14,8}=\frac{1}{R_1^2}\Big(2G_1K_1(\eta_{\mathrm{pf1}}R_1)\eta_{\mathrm{pf1}}R_1-\big((-2k^2G_1+(k^2-\eta_{\mathrm{pf1}}^2)(C_1a_{\mathrm{pf1}}+H_1))R_1^2\big)K_0(\eta_{\mathrm{pf1}}R_1)\Big),$$
$$M_{14,9}=\frac{1}{R_1^2}\Big(-2G_1I_1(\eta_{\mathrm{pf1}}R_1)\eta_{\mathrm{pf1}}R_1-\big((-2k^2G_1+(k^2-\eta_{\mathrm{pf1}}^2)(C_1a_{\mathrm{pf1}}+H_1))R_1^2\big)I_0(\eta_{\mathrm{pf1}}R_1)\Big),$$
$$M_{14,10}=\frac{1}{R_1^2}\Big(2G_1K_1(\eta_{\mathrm{ps1}}R_1)\eta_{\mathrm{ps1}}R_1-\big((-2k^2G_1+(k^2-\eta_{\mathrm{ps1}}^2)(C_1a_{\mathrm{ps1}}+H_1))R_1^2\big)K_0(\eta_{\mathrm{ps1}}R_1)\Big),$$

$$M_{14,11}=\frac{1}{R_1^2}\left(-2G_1I_1(\eta_{ps1}R_1)\eta_{ps1}R_1-\left((-2k^2G_1+(k^2-\eta_{ps1}^2)(C_1a_{ps1}+H_1))R_1^2\right)I_0(\eta_{ps1}R_1)\right),$$

$$M_{14,12}=\frac{1}{R_1^2}\left(2\mathrm{i}G_1\left(\eta_{s1}K_1(\eta_{s1}R_1)R_1+K_0(\eta_{s1}R_1)\eta_{s1}^2R_1^2\right)k\right),$$

$$M_{14,13}=\frac{1}{R_1^2}\left(2\mathrm{i}G_1\left(-\eta_{s1}I_1(\eta_{s1}R_1)R_1+I_0(\eta_{s1}R_1)\eta_{s1}^2R_1^2\right)k\right),$$

$$M_{14,14}=\frac{1}{R_1^2}\left(-2G_2K_1(\eta_{pf2}R_1)\eta_{pf2}R_1+\left((-2k^2G_2+(k^2-\eta_{pf2}^2)(C_2a_{pf2}+H_2))R_1^2\right)K_0(\eta_{pf2}R_1)\right),$$

$$M_{14,15}=\frac{1}{R_1^2}\left(-2G_2K_1(\eta_{ps2}R_1)\eta_{ps2}R_1+\left((-2k^2G_2+(k^2-\eta_{ps2}^2)(C_2a_{ps2}+H_2))R_1^2\right)K_0(\eta_{ps2}R_1)\right),$$

$$M_{14,16}=-\frac{1}{R_1^2}\left(2\mathrm{i}\left(\eta_{s2}K_1(\eta_{s2}R_1)R_1+K_0(\eta_{s2}R_1)\eta_{s2}^2R_1^2\right)G_2k\right),$$

$M_{15,8}=-2\mathrm{i}\eta_{pf1}G_1kK_1(\eta_{pf1}R_1)$, $M_{15,9}=2\mathrm{i}G_1k\eta_{pf1}I_1(\eta_{pf1}R_1)$, $M_{15,10}=-2\mathrm{i}\eta_{ps1}G_1kK_1(\eta_{ps1}R_1)$,
$M_{15,11}=2\mathrm{i}G_1kI_1(\eta_{ps1}R_1)\eta_{ps1}$, $M_{15,12}=\eta_{s1}K_1(\eta_{s1}R_1)G_1(\eta_{s1}^2+k^2)$, $M_{15,13}=-G_1(\eta_{s1}^2+k^2)\eta_{s1}I_1(\eta_{s1}R_1)$,
$M_{15,14}=2\mathrm{i}\eta_{pf2}G_2kK_1(\eta_{pf2}R_1)$, $M_{15,15}=2\mathrm{i}\eta_{ps2}G_2kK_1(\eta_{ps2}R_1)$, $M_{15,16}=-\eta_{s2}K_1(\eta_{s2}R_1)G_2(\eta_{s2}^2+k^2)$,
$M_{16,8}=K_0(\eta_{pf1}R_1)(k^2-\eta_{pf1}^2)(M_1a_{pf1}+C_1)$, $M_{16,9}=I_0(\eta_{pf1}R_1)(k^2-\eta_{pf1}^2)(M_1a_{pf1}+C_1)$,
$M_{16,10}=K_0(\eta_{ps1}R_1)(k^2-\eta_{ps1}^2)(M_1a_{ps1}+C_1)$, $M_{16,11}=I_0(\eta_{ps1}R_1)(k^2-\eta_{ps1}^2)(M_1a_{ps1}+C_1)$,
$M_{16,14}=-K_0(\eta_{pf2}R_1)(k^2-\eta_{pf2}^2)(M_2a_{pf2}+C_2)$, $M_{16,15}=-K_0(\eta_{ps2}R_1)(k^2-\eta_{ps2}^2)(M_2a_{ps2}+C_2)$,

$\boldsymbol{M}_{16\times16}$ 矩阵元素其他项为零;其中 G_c、λ_c 为钻铤的拉梅常数,可由表 1 中钻铤的密度、纵波、横波计算得到;ρ_b 为井内流体密度,ρ_{f1}(ρ_{f2}) 为孔隙地层 1(2)流体密度,G_1(G_2) 为孔隙介质 1(2)骨架的剪切模量;a_{pf1}(a_{pf2})、a_{ps1}(a_{ps2})、a_{s1}(a_{s2}) 分别为弹性波在传播过程中快纵波、慢纵波和横波引起孔隙地层 1(2)中渗流位移与固相位移幅度之比(Pride and Haartsen,1996).

附录 B 电场矩阵

现给出公式(13)中矩阵 $N_{5\times5}$ 以及列向量 $\boldsymbol{b}$ 中各个元素的表达式:

$N_{1,1}=-\mathrm{i}I_0(kr_b)k$, $N_{1,2}=-\mathrm{i}K_0(kr_b)k$,
$N_{2,1}=-I_0(kR)k$, $N_{2,2}=-K_0(kR)$, $N_{2,3}=I_0(kR)$, $N_{2,4}=K_0(kR)$,
$N_{3,1}=\sigma_bI_1(kR)k$, $N_{3,2}=-\sigma_bK_1(kR)k$, $N_{3,3}=-\sigma_1I_1(kR)k$, $N_{3,4}=\sigma_1K_1(kR)k$,
$N_{4,3}=I_0(kR_1)$, $N_{4,4}=K_0(kR_1)$, $N_{4,5}=-K_0(kR_1)$,
$N_{5,3}=-\sigma_1I_1(kR_1)k$, $N_{5,4}=\sigma_1K_1(kR_1)k$, $N_{5,5}=-\sigma_2K_1(kR_1)k$,

$$b_2=-\frac{1}{\sigma_1}\left(\begin{bmatrix}B^{pf1}\left((-k^2+\eta_{pf1}^2)C_1+(-a_{pf1}k^2+a_{pf1}\eta_{pf1}^2)M_1+\omega^2\rho_{f1}\right)I_0(\eta_{pf1}R)\\+\left((-k^2+\eta_{ps1}^2)C_1+(-a_{ps1}k^2+a_{ps1}\eta_{ps1}^2)M_1+\omega^2\rho_{f1}\right)B^{ps1}I_0(\eta_{ps1}R)\\+\left((-k^2+\eta_{pf1}^2)C_1+(-a_{pf1}k^2+a_{pf1}\eta_{pf1}^2)M_1+\omega^2\rho_{f1}\right)A^{pf1}K_0(\eta_{pf1}R)\\+A^{ps1}\left((-k^2+\eta_{ps1}^2)C_1+(-a_{ps1}k^2+a_{ps1}\eta_{ps1}^2)M_1+\omega^2\rho_{f1}\right)K_0(\eta_{ps1}R)\end{bmatrix}L_1\right),$$

$$b_3=-\frac{1}{R}\left(L_1\rho_{f1}\omega^2\left(\mathrm{i}\eta_{s1}B^{SV1}I_1(\eta_{s1}R)Rk-\mathrm{i}\eta_{s1}A^{SV1}K_1(\eta_{s1}R)Rk\right)\right),$$

$$b_4=\frac{1}{\sigma_1\sigma_2}\begin{bmatrix}\left((M_1a_{pf1}+C_1)k^2-a_{pf1}\eta_{pf1}^2M_1-\omega^2\rho_{f1}-\eta_{pf1}^2C_1\right)\sigma_2L_1B^{pf1}I_0(\eta_{pf1}R_1)\\+\left((M_1a_{ps1}+C_1)k^2-a_{ps1}\eta_{ps1}^2M_1-\omega^2\rho_{f1}-\eta_{ps1}^2C_1\right)B^{ps1}\sigma_2L_1I_0(\eta_{ps1}R_1)\\+\left((M_1a_{pf1}+C_1)k^2-a_{pf1}\eta_{pf1}^2M_1-\omega^2\rho_{f1}-\eta_{pf1}^2C_1\right)\sigma_2L_1A^{pf1}K_0(\eta_{pf1}R_1)\\-L_2A^{pf2}\left((M_2a_{pf2}+C_2)k^2-\omega^2\rho_{f2}-\eta_{pf2}^2(M_2a_{pf2}+C_2)\right)\sigma_1K_0(\eta_{pf2}R_1)\\+\left((M_1a_{ps1}+C_1)k^2-a_{ps1}\eta_{ps1}^2M_1-\omega^2\rho_{f1}-\eta_{ps1}^2C_1\right)\sigma_2A^{ps1}L_1K_0(\eta_{ps1}R_1)\\-L_2\left((M_2a_{ps2}+C_2)k^2-\omega^2\rho_{f2}-\eta_{ps2}^2(M_2a_{ps2}+C_2)\right)A^{ps2}\sigma_1K_0(\eta_{ps2}R_1)\end{bmatrix},$$

$$b_5 = -\frac{1}{R_1}\Big(\omega^2\big(\mathrm{i}R_1 L_1 \rho_{f1}\eta_{s1} B^{SV1} I_1(\eta_{s1}R_1)k - \mathrm{i}R_1 L_1 \rho_{f1}\eta_{s1} A^{SV1} K_1(\eta_{s1}R_1)k + \mathrm{i}R_1 L_2 \rho_{f2}\eta_{s2} A^{SV2} K_1(\eta_{s2}R_1)k\big)\Big).$$

其中 σ_b 为井内流体的电导率;σ_1、σ_2 分别为孔隙地层 1 与 2 的电导率,是频率 ω 的函数,计算方法见高永新(2010)的工作.

References

Biot M A. 1962. Mechanics of deformation and acoustic propagation in porous media. *Journal of Applied Physics*, 33(4): 1482-1498.

Che X H, Qiao W X, Yan X Z. 2004. The effectivity of applying linear phased array transmitter in borehole acoustic reflection logging. *Well Logging Technology* (in Chinese), 28(2): 108-111.

Chu Z H, Xu L T, Yin Q W, et al. 2005. Progress of lab study on remote exploration acoustic reflection logging methods. *Well Logging Technology* (in Chinese), 29(2): 98-101.

Cui Z W. 2004. Theoretical and numerical study of modified Biot's models, acoustoelectric well logging and acoustic logging while drilling excited by multipole acoustic sources [Ph. D. thesis] (in Chinese). Changchun: Jilin University.

Gao Y X. 2010. Simulation of earthquake-induced electromagnetic wave field due to the electrokinetic effect [Ph. D. thesis] (in Chinese). Harbin: Harbin Institute of Technology.

Guan W, Hu H S, Zheng X B. 2013. Theoretical simulation of the multipole seismoelectric logging while drilling. *Geophysical Journal International*, 195(2): 1239-1250.

Haartsen M W, Pride S R. 1997. Electroseismic waves from point sources in layered media. *Journal of Geophysical Research: Solid Earth*, 102(B11): 24745-24769.

He F J. 2005. The study on the simulation of the borehole acoustic reflection imaging logging tool and it's waveform processing method [Ph. D. thesis] (in Chinese). Beijing: University of Petroleum (Beijing).

Hu H S, Wang K X. 1999. Coupled acoustic and electromagnetic waves around a borehole embedded in a porous formation: theory (1). *Well Logging Technology* (in Chinese), 23(6): 427-432.

Hu H S, Wang K X. 2000. Coupled acoustic and electromagnetic waves around a borehole embedded in a porous formation: numerical simulation of acoustically induced fields(Ⅱ). *Well Logging Technology* (in Chinese), 24(1): 3-13.

Hu H S, Liu J Q, Wang H B, et al. 2003. Simulation of acousto-electric well logging based on simplified pride equations. *Chinese J. Geophys.* (in Chinese), 46(2): 259-264.

Meredith J A. 1990. Numerical and analytical modelling of downhole seismic sources: the near and far field [Ph. D. thesis]. Cambridge: Massachusetts Institute of Technology.

Morgan F D, Williams E R, Madden T R. 1989. Streaming potential properties of westerly granite with applications. *Journal of Geophysical Research: Solid Earth*, 94(B9): 12449-12461.

Pride S. 1994. Governing equations for the coupled electromagnetics and acoustics of porous media. *Physical Review B*, 50(21): 15678-15696.

Pride S R, Haartsen M W. 1996. Electroseismic wave properties. *The Journal of the Acoustical Society of America*, 100(3): 1301-1315.

Qiao W X, Che X H, Li G, et al. 2004. The physical modeling of acoustic reflection image logging. *Geophysical Prospecting for Petroleum* (in Chinese), 43(3): 294-297.

Tang X M, Zheng C H. 2004. Quantitative Borehole Acoustic Methods (in Chinese). Zhao X M Trans. Beijing: Petroleum Industry Press, 31-35.

Tang X M, Patterson D J. 2009. Single-well S-wave imaging using multicomponent dipole acoustic-log data. *Geophysics*, 74(6): WCA211-WCA223.

Tang X M, Wei Z T. 2012. Single-well acoustic reflection imaging using far-field radiation characteristics of a borehole dipole source. *Chinese J. Geophys.* (in Chinese), 55(8): 2798-2807, doi: 10.6038/j.issn.0001-5733.2012.08.031.

Tao G, He F J, Wang B, et al. 2008. The study on 3D wave field simulation for acoustic reflection imaging logging in formation. *Science in China Series D: Earth Sciences* (in Chinese), 38(S1): 166-173.

Thompson A H, Gist G A. 1993. Geophysical applications of electrokinetic conversion. *The Leading Edge*, 12(12): 1169-1173.

Wang J. 2012. Experimental study on electrokinetic effects in porous rock samples and measurements of P and S wave velocities while drilling [Ph. D. thesis] (in Chinese). Harbin: Harbin Institute of Technology.

Wei Z T, Tang X M, Su Y D, et al. 2013. A new acoustic remote sensing method utilizing borehole low-frequency dipole shear wave. *Chinese J. Geophys.* (in Chinese), 56(8): 3572-3580, doi: 10.6038/cjg20131032.

Xue M. 2002. Study on remote exploration acoustic reflection well logging & it's acoustic sonde design [Ph. D. thesis] (in Chinese). Beijing: University of Petroleum (Beijing).

Zhan X, Chi Z H, Toksöz M N. 2006. Simulation of the converted electric field during multipole logging while drilling (LWD). // 76th SEG Annual International Meeting, New Orleans, Louisiana, USA, Expanded Abstracts, 25, 446-450.

Zheng X B, Hu H S, Guan W, et al. 2014. Theoretical simulation of the electric field induced by acoustic waves during the seismoelectric logging while drilling. *Chinese J. Geophys.* (in Chinese), 57(1): 320-330, doi: 10.6038/cjg20140128.

Zhu Z Y, Haartsen M W, Toksöz M N. 1999. Experimental studies of electrokinetic conversions in fluid-saturated borehole models. *Geophysics*, 64(5): 1349-1356.

Zhu Z Y, Toksöz M N. 2003. Crosshole seismoelectric measurements in borehole models with fractures. *Geophysics*, 68(5): 1519-1524.

附中文参考文献

车小花，乔文孝，阎相祯. 2004. 相控线阵声波辐射技术在反射声波测井中的应用探讨. 测井技术，28(2)：108-111.

楚泽涵，徐凌堂，尹庆文等. 2005. 远探测反射波声波测井方法实验研究进展. 测井技术，29(2)：98-101.

崔志文. 2004. 多孔介质声学模型与多极源声电效应测井和多极随钻声测井的理论与数值研究[博士论文]. 长春：吉林大学.

高永新. 2010. 地震电磁场——基于动电效应的波场模拟[博士论文]. 哈尔滨：哈尔滨工业大学.

何峰江. 2005. 声反射成像测井仪器仿真及波形处理技术研究[博士论文]. 北京：石油大学(北京).

胡恒山，王克协. 1999. 井孔周围轴对称声电耦合波：理论(Ⅰ). 测井技术，23(6)：427-432.

胡恒山，王克协. 2000. 井孔周围轴对称声电耦合波：声电效应测井数值模拟(Ⅱ). 测井技术，24(1)：3-13.

胡恒山，刘家琦，王洪滨等. 2003. 基于简化的 Pride 理论模拟声电效应测井响应. 地球物理学报，46(2)：259-264.

乔文孝，车小花，李刚等. 2004. 反射声波成像测井的物理模拟. 石油物探，43(3)：294-297.

唐晓明，郑传汉. 2004. 定量测井声学. 赵晓敏译. 北京：石油工业出版社，31-35.

唐晓明，魏周拓. 2012. 利用井中偶极声源远场辐射特性的远探测测井. 地球物理学报，55(8)：2798-2807，doi：10.6038/j.issn.0001-5733.2012.08.031.

陶果，何峰江，王兵等. 2008. 声反射成像测井在地层中的三维波场模拟方法研究. 中国科学 D 辑：地球科学，38(增刊 1)：166-173.

王军. 2012. 岩石动电效应实验及地层纵、横波速度的随钻测量[博士论文]. 哈尔滨：哈尔滨工业大学.

魏周拓，唐晓明，苏远大等. 2013. 利用井中低频偶极横波进行声波远探测的新方法. 地球物理学报，56(10)：3572-3580，doi：10.6038/cjg20131032.

薛梅. 2002. 远探测声波反射波测井方法研究和声系设计[博士论文]. 北京：石油大学(北京).

郑晓波，胡恒山，关威等. 2014. 随钻动电测井中声诱导电场的理论模拟. 地球物理学报，57(1)：320-330，doi：10.6038/cjg20140128.

(本文编辑 何燕)

02

专 题 / 02

远探测声波测井

理论、方法及应用

REMOTE DETECTION ACOUSTIC LOGGING

收录 15 篇论文

中国科学: 地球科学 2025 年 第 55 卷 第 7 期: 2210 ~ 2225
SCIENTIA SINICA Terrae earthcn.scichina.com
《中国科学》杂志社 SCIENCE CHINA PRESS
论 文

井中偶极横波远探测方位180°不确定性问题的求解: 理论、方法和实验

苏远大[1,2,3], 饶博[1,2], 庄春喜[1,2], 李盛清[1,2], 谭宝海[1,2], 唐晓明[1,2,3*]

1. 中国石油大学(华东)地球科学与技术学院, 青岛 266580
2. 深层油气全国重点实验室(中国石油大学(华东)), 青岛 266580
3. 崂山实验室海洋矿产资源评价与探测技术功能实验室, 青岛 266071
* 通讯作者, E-mail: tangxiam@aliyun.com

收稿日期: 2024-11-11; 收修改稿日期: 2025-04-19; 接受日期: 2025-05-14; 网络版发表日期: 2025-06-23
国家自然科学基金(U21B2064、42174145)、山东省自然科学基金(ZR2024YQ062)、崂山国家实验室科技创新项目(LSKJ202203407)和中石油重大科技项目(ZD2019-183-004)资助

摘要 近年发展起来的井中偶极横波远探测技术在深层油气勘探中成功应用, 能探测到井外几十米处的缝洞型油气构造. 该技术的进一步发展是要解决偶极声源(及接收器)对称性导致的反演结果方位相差180°是对称的, 测井界俗称的"方位180°不确定性问题", 如何唯一地确定方位, 是本文要讨论的问题, 这对深层油气的开发和施工(如侧钻)至关重要. 本文从弹性波与井孔和井外反射体的相互作用理论出发, 揭示了井中接收反射波的方位响应特征, 提出了井中多方位组合接收消除方位多解性的新型全方位偶极测量模式, 并在实验室方位模型井群中对该测量模式进行了实验验证. 理论和实验结果表明: 新型测量模式保持了传统四分量模式偶极波形振幅的方位变化, 并使其波形相位具备360°周期性变化特征, 即可利用波形相位的方位变化特征来有效消除偶极横波远探测的方位180°不确定性. 在此基础上, 研制了新型的全方位偶极横波远探测仪器样机, 并在塔里木油田一口水平开发井中开展了现场试验. 结果显示, 声波远探测成像清晰指示水平井穿过了约30米厚的断溶体, 井外探测范围达到65米, 通过对新模式数据的反射波幅度和相移进行分析, 获得了断溶体产状的准确信息. 本研究为井中深地声波方位远探测技术的发展和应用提供了理论和实验依据.

关键词 偶极横波远探测, 180°方位不确定性, 四分量数据组合, 波形相移

1 引言

声波远探测技术能够实现在井中对井外数十米甚至上百米范围内的地质体进行三维空间探测, 填补了地震勘探与常规测井之间的探测空白. 近年来, 该技术在井外地层裂缝和溶蚀孔洞等地质构造的探测和评价中被广泛应用, 成为了在深地、深水和非常规油气勘探开发中寻找油气甜点、发现隐蔽油气藏的利器(Tang和Patterson, 2009; Gong等, 2018; Bennett, 2019; Lee等, 2019; 许家旗和胡恒山, 2020; 唐晓明等, 2021; Zhao等, 2023, 2024).

声波远探测技术原理如下: 利用充液井中的声源

中文引用格式: 苏远大, 饶博, 庄春喜, 李盛清, 谭宝海, 唐晓明. 2025. 井中偶极横波远探测方位180°不确定性问题的求解: 理论、方法和实验. 中国科学: 地球科学, 55(7): 2210–2225, doi: 10.1360/SSTe-2024-0314
英文引用格式: Su Y, Rao B, Zhuang C, Li S, Tan B, Tang X. 2025. Solving the azimuthal 180°-ambiguity problem in borehole dipole shear wave reflection imaging: Theory, method and experiment. Science China Earth Sciences, 68(7): 2138–2153, https://doi.org/10.1007/s11430-024-1587-5

© 2025 《中国科学》杂志社 www.scichina.com
中国知网 https://www.cnki.net

向井外地层辐射弹性波，在井中接收井外地质体反射回来的声波，然后对接收信号进行偏移成像，从而实现对井外地质构造的探测．Tang(2004)提出的偶极横波远探测方法具有多种优势，例如裂缝探测方位灵敏度高、井外探测距离远、直达信号干扰少，在业界得到广泛应用．该方法通过对偶极四分量反射波数据进行环向的方位旋转变换，可以高效便捷地实现对地层反射体的周向扫描成像．随之而来的问题是，偶极声源(及接收器)的对称性导致反射成像结果方位存在180°对称性，即测井界俗称的“方位180°不确定性”．对于过井的地质构造，可以综合其他测井、地震或地质资料方法解决该问题(Tang, 2004; 杨海军等, 2014)，但对于井外远距离反射体的精准定位，目前还未见有切实有效的直接解决方法．随着该技术在现场应用的不断深入，反射体定位问题尤为突出，是缝洞型油藏定向侧钻和储层压裂开采的关键指导．因此，偶极横波远探测方位180°不确定性问题的求解成为了当前领域的研究热点．Zhang和Hu(2014)以弹性波动理论为基础，推导了井中接收远探测反射波声压和位移的相位响应特征，提出一种根据反射波相位对井外反射界面进行方位辨别的方法．Gong等(2015)提出在井中利用三分量位移传感器接收反射声场，借助垂直分量在增强实像的同时削弱伪像．Hirabayashi等(2017)将平面波入射-方位接收结果应用于偶极横波远探测，提出依据井中方位接收反射波的幅值差异来判断井外反射体方位；不同于平面波入射，声波远探测中入射波场是以球面波的形式向井孔传播，因此平面波假设的准确性受到限制．Xu等(2019)模拟了井旁存在反射界面时单极和偶极混合模式测量的反射波形，提出通过比较压力和位移与参考波形的极性关系可以唯一确定反射体的方位角．李超等(2020)提出同时利用单极和偶极远探测的方法进行反射体方位识别，但由于该方法需要单极和偶极同时探测到反射体，其方位识别能力受限于单极声源的探测深度．Li等(2021)和李杨虎(2023)基于虚源理论解析模拟了井中离轴接收的方位反射波形，并提出在井中放置方位偏心接收器来解决偶极声波远探测中反射体的定位问题．上述的研究工作大都为理论探讨，具有一定的前瞻性，但在目前的声波测井技术中不易实现，实际应用效果还需要进一步验证．

本文从弹性波与井孔的相互作用理论出发，理论分析了传统偶极测量模式存在方位180°对称的多解性，提出了井中多方位组合接收消除方位多解性的新型全方位偶极测量模式，并在实验室方位模型井群进行了实验验证．在测量井中放置多方位反射波接收声系，在相邻的一口副井中放置偶极发射声源向测量井定向辐射横波，以此等效模拟来自井外地质体的反射横波．这一实验思想的结果与实际地层中含反射体模型的结果等效．在数据处理上，提取反射体走向(即四分量数据最佳成像方向)两侧反射信号间的相移可有效消除偶极横波远探测方位180°不确定性．理论计算和实验测量的波形数据处理结果均表明新型偶极测量模式具有360°全方位灵敏度．在理论方法和实验验证的基础上，研制了新型的全方位偶极横波远探测仪器样机并在塔里木油田现场井中成功应用，获得了井旁构造的清晰成像及其准确产状，有效解决了偶极横波远探测方位180°不确定性问题．

2　方位偶极横波远探测理论与测量模式

2.1　井中方位偶极远探测理论

图1a给出了利用井中偶极声波测井仪对井外地质反射体进行探测的理论示意图．充液井中的偶极声源向井外地层辐射弹性波，经由井外地质体反射，最终被井中接收器所接收．在柱坐标系（r, φ, z）中，偶极声源上方间隔90°周向排布4个方位接收器(x_1, y_1, x_2, y_2)．接收横截面如图1b所示，图中标识符a表示井眼半径，e_r表示接收器的离轴距离．

井中发射的弹性波在辐射距离远大于波长的远场辐射条件下，图1a中偶极声源辐射到地层中的SH和SV横波位移势函数χ和Γ的远场渐近解为(Tang等, 2016)：

$$\begin{cases} \chi \sim \left[D_1(k_0,\omega)\sin(\varphi)\right]\dfrac{\mathrm{e}^{\mathrm{i}\omega R/\beta}}{R}S(\omega), \\ \Gamma \sim \left[F_1(k_0,\omega)\cos(\varphi)\right]\dfrac{\mathrm{e}^{\mathrm{i}\omega R/\beta}}{R}S(\omega), \end{cases} \tag{1}$$

式中，ω为圆频率；$k_0 = (\omega/\beta)\cos(\theta_t)$为辐射横波波数的最速下降解，$\beta$为井外地层的横波波速，$\theta_t$为波辐射方向与井轴正方向的夹角；$S$为声源频谱；$R$为井中声源到场点之间的辐射距离；$D_1$和$F_1$分别为SH和SV横波的远场振幅系数，由井壁处的边界条件求得(曹景记等, 2014)．

如图1a所示，在由虚源理论表征的偶极横波远探测模型中，辐射波与井外反射体作用后产生的反

中国知网　https://www.cnki.net

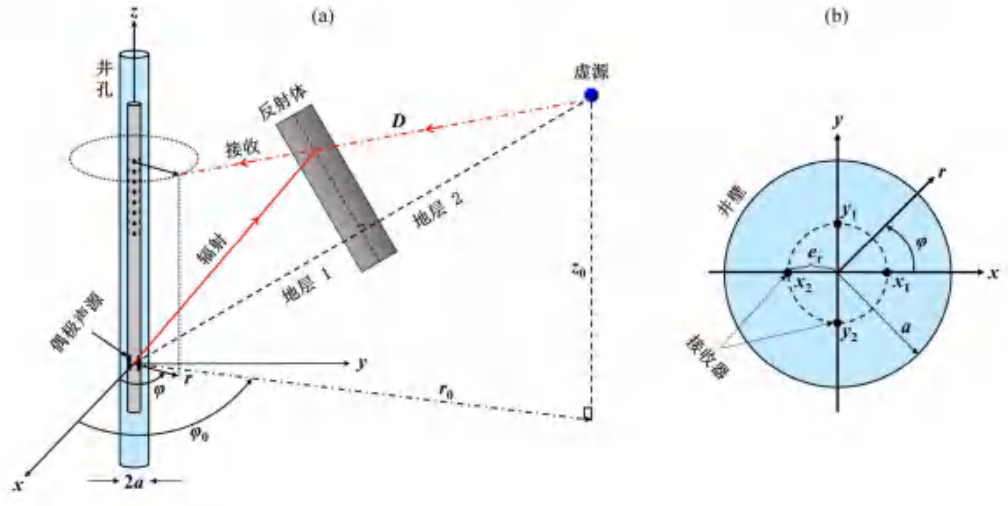


图 1　偶极横波远探测示意图(a)及井中方位接收截面图(b)

射波可以用虚源激发的入射波等效表征，其中虚源的位置与井中声源在反射体向外一侧的镜像重合. D为弹性波传播总距离，如图1a中红色点划线直线段所示. 在辐射距离远大于波长的远场条件下，入射SH和SV横波位移势χ^{i}和Γ^{i}在频率-波数域内可表示为:

$$\begin{cases} \chi^{\mathrm{i}}=S(\omega)\cdot RD_{\mathrm{SH}}(\omega)\cdot RF_{\mathrm{SH}}(\omega) \\ \quad \cdot\sum\limits_{n=0}^{\infty}\varepsilon_n I_n(sr)K_n(sr_0)\cos[n(\varphi-\varphi_0)], \\ \Gamma^{\mathrm{i}}=S(\omega)\cdot RD_{\mathrm{SV}}(\omega)\cdot RF_{\mathrm{SV}}(\omega) \\ \quad \cdot\sum\limits_{n=0}^{\infty}\varepsilon_n I_n(sr)K_n(sr_0)\cos[n(\varphi-\varphi_0)], \end{cases} \tag{2}$$

式中, 上标i表示入射波场; RD_{SH}和RD_{SV}分别为偶极SH横波和SV横波在井外地层中的辐射函数(即公式(1)中方括号内的项); RF_{SH}(RF_{SV})为声波在反射体处的反射系数，可通过Zoeppritz方程求得(Aki和Richards, 1980); n为方位序数; ε_n为纽曼因子，$n=0$时$\varepsilon_n=1$, $n>0$时$\varepsilon_n=2$; I_n和K_n分别为第一类和第二类n阶变型贝塞尔函数; r_0和φ_0分别为虚源的径向距离和环向方位; $s=(k^2-\omega^2/\beta^2)^{1/2}$为入射横波的径向波数，$k$为入射横波的轴向波数.

公式(2)表征的入射横波与井眼相互作用时，会引起井内外介质产生弹性波动. 基于亥姆霍兹分解理论, 透射到井内流体中的位移场$\mathbf{u}_{\mathrm{f}}$可以用透射纵波的位移势ϕ_{f}表示. 散射到井外地层中的位移场$\mathbf{u}_{\mathrm{s}}$可以用散射纵波位移势、SH横波位移势χ_{s}和SV横波位移势Γ_{s}联合表示. 为满足辐射条件，各位移势在频率-波数域内具有以下通解:

$$\begin{cases} \phi_{\mathrm{f}}=\sum\limits_{n=0}^{\infty}[A_n\cos(n\varphi)+A'_n\sin(n\varphi)]I_n(fr)K_n(sr_0), & (0<r<a) \\ \left.\begin{aligned} \phi_{\mathrm{s}}&=\sum\limits_{n=0}^{\infty}[B_n\cos(n\varphi)+B'_n\sin(n\varphi)]K_n(pr)K_n(sr_0) \\ \chi_{\mathrm{s}}&=\sum\limits_{n=0}^{\infty}[D_n\sin(n\varphi)-D'_n\cos(n\varphi)]K_n(sr)K_n(sr_0) \\ \Gamma_{\mathrm{s}}&=\sum\limits_{n=0}^{\infty}[F_n\cos(n\varphi)+F'_n\sin(n\varphi)]K_n(sr)K_n(sr_0) \end{aligned}\right\}, & (r\geqslant a) \end{cases} \tag{3}$$

中国知网　https://www.cnki.net

式中，$f=\left(k^2-\omega^2/\alpha_f^2\right)^{1/2}$为井内流体中纵波的径向波数，$\alpha_f$为流体纵波波速；$p=(k^2-\omega^2/\alpha^2)^{1/2}$为井外地层中纵波的径向波数，$\alpha$为地层纵波波速；$A_n(A'_n)\sim F_n(F'_n)$为各介质层待求解的振幅系数，可通过井壁处的边界条件求得:

$$\begin{cases} u_r^{\mathrm{i}}(a^+)+u_r^{\mathrm{s}}(a^+)=u_r^{\mathrm{f}}(a^-), \\ \sigma_{rr}^{\mathrm{i}}(a^+)+\sigma_{rr}^{\mathrm{s}}(a^+)=\sigma_{rr}^{\mathrm{f}}(a^-), \\ \sigma_{r\varphi}^{\mathrm{i}}(a^+)+\sigma_{r\varphi}^{\mathrm{s}}(a^+)=0, \\ \sigma_{rz}^{\mathrm{i}}(a^+)+\sigma_{rz}^{\mathrm{s}}(a^+)=0, \end{cases} \tag{4}$$

式中，上标s和f分别表示地层中的散射场和流体中的透射场；u_r和σ_{rr}表示场中径向位移和径向正应力，$\sigma_{r\varphi}$和σ_{rz}表示场中剪切应力.

将公式(2)和公式(3)代入位移势-位移关系中，结合胡克定律计算出入射横波、散射波和透射波的位移和应力，代入公式(4)中的边界条件可得到以下两个特征矩阵方程:

$$\mathbf{M}\begin{bmatrix}A_n\\B_n\\D_n\\F_n\end{bmatrix}=\begin{bmatrix}b_1\\b_2\\b_3\\b_4\end{bmatrix}\text{ 和 }\mathbf{M}\begin{bmatrix}A'_n\\B'_n\\D'_n\\F'_n\end{bmatrix}=\begin{bmatrix}b'_1\\b'_2\\b'_3\\b'_4\end{bmatrix}, \tag{5}$$

式中，$\mathbf{M}$为4×4的声场特征矩阵；等式右侧为虚源激发的入射横波向量，分别记为向量$\mathbf{b}$和$\mathbf{b}'$(对应元素表达式详见网络版附录A(http://earthcn.scichina.com)).

联立求解公式(5)可唯一确定井内外的声场，并将求解得到的井内流体位移势函数ϕ_{f}代入$p(r,\varphi)=\rho_{\mathrm{f}}\omega^2\phi_{\mathrm{f}}$关系式中，结合最速下降法(Tang等, 2014, 2016)可模拟计算井中方位接收的声压场:

$$p(r,\varphi)=S\cdot RD\cdot RF\cdot\frac{\mathrm{e}^{\mathrm{i}\omega D/\beta-\mathrm{i}\pi/4}}{D}\cdot\sum_{n=0}^{\infty}\rho_{\mathrm{f}}\omega^2[A_n\cos(n\varphi)+A'_n\sin(n\varphi)]I_n(f_0r), \tag{6}$$

式中，$D=\left[r_0^2+(z-z_0)^2\right]^{1/2}$，$z_0$为虚源的轴向距离；$\rho_{\mathrm{f}}$为井眼流体密度；$f_0=\left[\left(k_0^{\mathrm{i}}\right)^2-\omega^2/\alpha_f^2\right]^{1/2}$，$k_0^{\mathrm{i}}=(\omega/\beta)\cos(\pi-\theta_{\mathrm{i}})$为入射横波波数的梯度根，$\theta_{\mathrm{i}}$为入射波方向与井轴正方向的夹角. 公式(6)中关于反射体方位角的展开表达式详见网络版附录B.

公式(6)表明井内的环向波场为多极分量叠加的结果. 因此, 下文基于多极分解理论逐阶分析各成分波对井中方位接收响应的贡献以探究偶极180°不确定性问题的深层原因及解决方案. 基于上式可快速模拟分析各阶分量成分在井中接收的全波形中的占比. 以x向偶极源为例，采用图1中的计算模型和表1中的声学参数理论建模. 反射体为120°方位地层1和地层2之间倾角为60°的界面. 井中方位接收器的离轴距离为0.035m. 源距为1m. 虚源的径向距离为20m. 声源函数采用中心频率为3kHz的Ricker子波.

图2对比了井中0°方位接收的反射横波(SH波和SV波之和)的前四阶(即$n=0, 1, 2, 3$, 分别对应单极, 偶极, 四极和六极)分量波形. 结果按照偶极分量波幅最大值归一化, 相对波幅比在图右端给出. 对比发现, 井内接收波场以偶极分量为主，振幅贡献约为单极和四极成分的十倍. 其余高阶项快速收敛，振幅贡献可忽略不计. 因此，井内接收波场能量主要由前三阶分量控制. 因此，通过数据组合将没有方位特性的单极成分滤除，保留偶极和四极成分，将对识别井外反射体的方位具有重要意义.

2.2　井中接收偶极反射横波方位灵敏性分析

偶极声源的辐射特性以及接收器组合方式共同决定了井中接收的方位响应特征. 首先从井中偶极源在井外远场辐射SH横波(SV横波)的辐射函数$RD_{\mathrm{SH}}=D_1\cdot\sin(\varphi)$($RD_{\mathrm{SV}}=F_1\cdot\cos(\varphi)$)可看出满足$|RD(\varphi)|=|RD(\varphi+\pi)|$，即表明偶极源发射存在固有的180°对称性，具体的三维辐射特征由图3给出，从图中可看出SH横波和SV横波辐射图样均关于xoz和yoz平面对称. 这种声源辐射固有对称性是导致方位偶极远探测反演结果相差180°的原因之一. 接下来从接收模式入手进一步分析井中接收响应的方位灵敏性.

井中接收声压响应公式(6)中与接收器方位φ有关的因子$A_n\cos(n\varphi)+A'_n\sin(n\varphi)$的前三阶主项分量在四个正交方位上的贡献见表2. 当接收方位增加或减小$\pi/2$时，与原方位相比，接收波形中的单极成分相同，四极成分相位相反；当接收方位增加π时，接收波形中的单极和四极成分相同，偶极成分相位相反. 由此说明，对四个正交方位上接收的波形数据进行线性组合，可一定程度控制井中不同阶成分波的相对占比.

中国知网　https://www.cnki.net

表 1　井孔和井外地层的声学参数

介质	纵波速度 (m s^{-1})	横波速度 (m s^{-1})	密度 (kg m^{-3})	外径(m)
井眼流体	1500	—	1000	0.1
地层1	4000	2300	2500	—
地层2	4500	3000	2600	∞

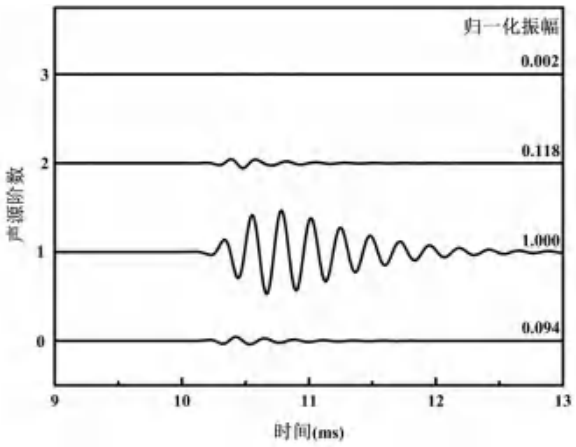


图 2　井中接收的反射横波的前四阶分量对比
各阶分量的归一化振幅比在图右端给出

传统偶极声波测井采用的数据组合方式是取方位相差180°的两个接收信号相减, 即$p_{\varphi}-p_{\varphi+\pi}$, 这种组合模式是为了获得纯的偶极成分. 声源指向φ时井中接收的同向分量xx_{1-3}为(下标数字代表表2中的序号):

$$xx_{1-3}=p_{\varphi}-p_{\varphi+\pi}=2[A_1\cos(\varphi)+A'_1\sin(\varphi)]. \quad (7)$$

上式说明传统偶极声波测井信号中消除了单极和四极成分, 只保留了偶极成分. 采用与图2相同的模型参数, 模拟对比反射体方位相差180°时井中接收的同向分量xx_{1-3}及其前三阶主项分量. 模型横截面如图4a所示, 反射体分别位于120°和300°方位, 声源和接收器均指向x轴方向. 根据公式(7)的计算结果如图4b所示, 对比发现, 反射体方位相差180°时, 井中接收的同向分量完全相同(单极和四极成分为零, 偶极成分相同), 存在方位判别180°不确定性, 这与附录B中公式(B-2)声场表达式的理论分析一致.

为了突破传统偶极接收模式的固有对称性, 采用3个方位线性组合接收新模式消除数据中的单极成分, 保留偶极成分, 增强四极成分. 声源指向φ时井中接收的同向分量$xx_{1-2+1-4}$为(下标数字代表表2中的序号):

$$\begin{aligned}xx_{1-2+1-4}&=p_{\varphi}-p_{\varphi+\pi/2}+p_{\varphi}-p_{\varphi-\pi/2}\\&=2[A_1\cos(\varphi)+A'_1\sin(\varphi)]\\&\quad+4[A_2\cos(2\varphi)+A'_2\sin(2\varphi)].\end{aligned} \quad (8)$$

对比公式(7)发现, 公式(8)中增加了具备方位特性的四极成分, 同时保留了偶极成分, 这对偶极远探测识别井外反射体的方位和走向具有重要意义. 按照如公式(8)所示新的接收模式, 图5给出了与图4相同计算参数的算例结果. 对比反射体方位相差180°的结果, 单极成分为零, 偶极成分相同, 四极成分振幅相同、相位相反, 致使叠加求和的波形信号同时存在振幅和相位差异, 为解决反射体方位180°不确定性问题提供了理论支撑基础.

2.3　方位偶极远探测模拟与测量模式对比

现有偶极横波远探测技术采用正交发射四分量接收数据(xx, xy, yx, yy)可以确定井外反射体的距离、倾角和走向(唐晓明和魏周拓, 2012; 唐晓明等, 2021). 井

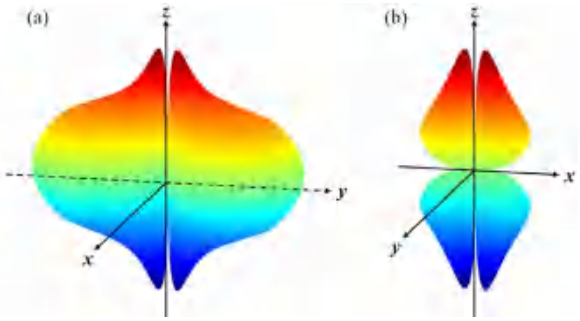


图 3　井中偶极声源激发SH横波(a)和SV横波(b)的三维辐射指向性图

中国知网　https://www.cnki.net

表 2　函数$A_n\cos(n\varphi)+A'_n\sin(n\varphi)$的前三阶主项分量在四个正交方位上的贡献对比

序号	方位	阶数		
		$n=0$	$n=1$	$n=2$
1	φ	A_0	$A_1\cos(\varphi)+A'_1\sin(\varphi)$	$A_2\cos(2\varphi)+A'_2\sin(2\varphi)$
2	$\varphi+\pi/2$	A_0	$-A_1\sin(\varphi)+A'_1\cos(\varphi)$	$-A_2\cos(2\varphi)-A'_2\sin(2\varphi)$
3	$\varphi+\pi$	A_0	$-A_1\cos(\varphi)-A'_1\sin(\varphi)$	$A_2\cos(2\varphi)+A'_2\sin(2\varphi)$
4	$\varphi-\pi/2$	A_0	$A_1\sin(\varphi)-A'_1\cos(\varphi)$	$-A_2\cos(2\varphi)-A'_2\sin(2\varphi)$

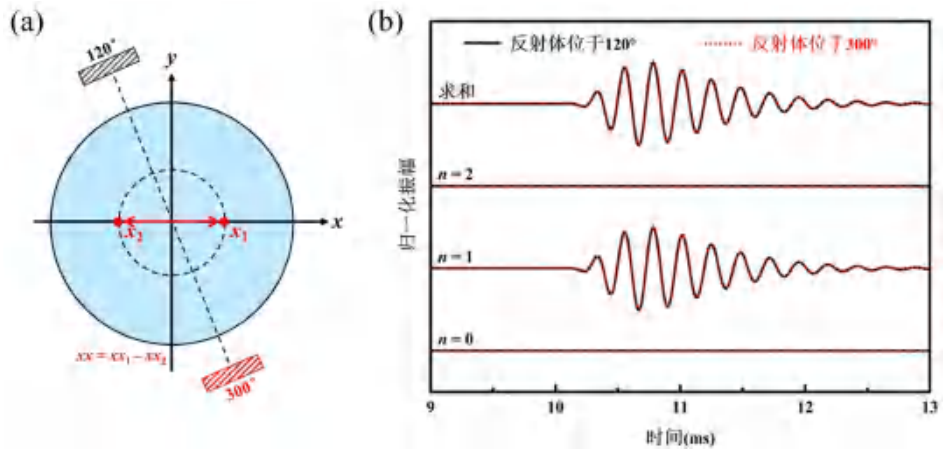


图 4　发射-接收系统示意图(a)及反射体方位相差180°时井中接收的同向分量xx_{1-3}及其前三阶主项分量对比(b)

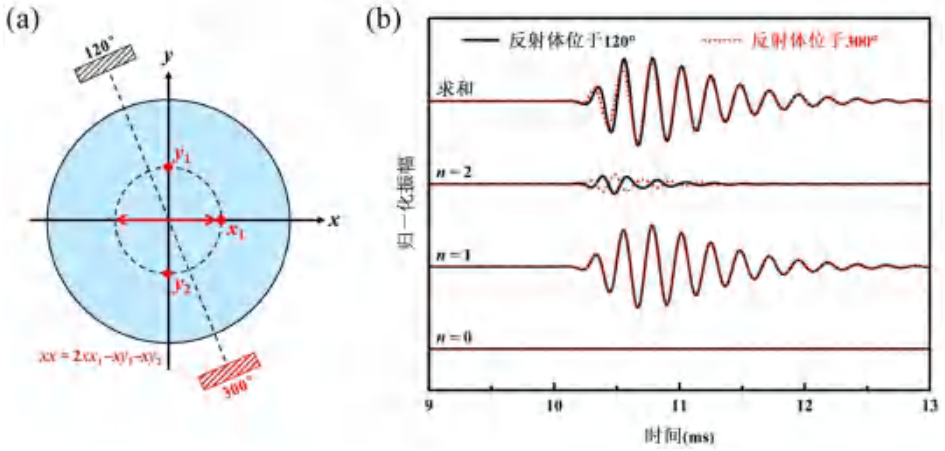


图 5　发射-接收系统示意图(a)反射体方位相差180°时井中接收的同向分量$xx_{1-2+1-4}$及其前三阶主项分量对比(b)

下仪器工作时, x和y向偶极源依次激发声波, 4个离轴放置的接收换能器记录4个正交方位的共8个分量信号, 即xx_1、xx_2、xy_1、xy_2以及yx_1、yx_2、yy_1、yy_2, 其中第一个字母代表声源指向, 第二个字母及数字代表接收器. 根据公式(6)给出的井中流体声压的解析表达式, 可以对四分量数据进行精确的模拟和分析. 模型参数

中国知网　https://www.cnki.net

与图2一致, 仅将反射体方位改为30°(从x轴方向顺时针计算, 走向为120°/300°).

2.3.1 传统四分量偶极测量模式

传统的四分量正交偶极测井仪器的数据接收组合模式如图6所示, 记录信号为相反方位接收数据之差.

利用公式(6)计算的传统四分量反射横波如图7a所示, 对该四分量数据做坐标旋转(李盛清等, 2020; 唐晓明等, 2021)得到反射波振幅随旋转角ϕ的变化曲线, 结果按照最大振幅归一化(波幅方位分布图), 如图7b所示, 其中Φ为沿仪器x轴方向顺时针计算的旋转角. 显示旋转角为120°和300°时, 曲线取得极大值, 此时对应反射体的走向. 在该方向的成像质量最佳, 这正是四

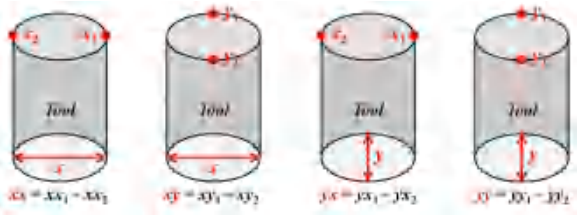


图 6 传统的四分量正交偶极测井仪器的数据接收组合模式示意图

分量偶极数据反演井外目标反射体方位的理论依据(方位与走向垂直), 但存在方位判别180°不确定性问题, 即此时井外反射体的方位可能为30°或210°. 图7c对比了最佳成像方位(300°, S0)及其两侧30°的反射信

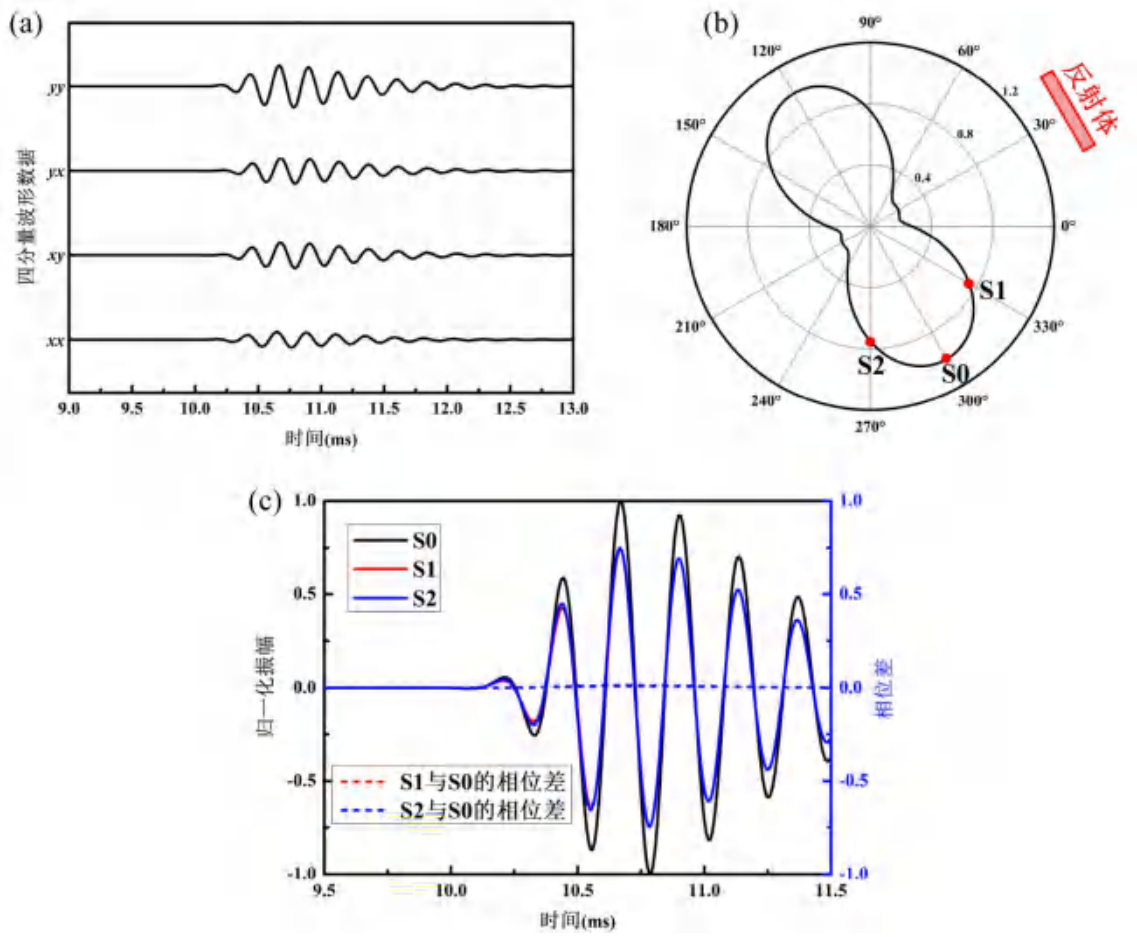


图 7 传统四分量偶极横波远探测测井响应

(a) 模拟的传统四分量偶极横波远探测数据; (b) 四分量数据旋转得到的波幅方位分布图; (c) 最佳成像方位及其两侧波形和相位差对比

中国知网 https://www.cnki.net

号(330°, S1和270°, S2), 结果均按照S0的最大振幅归一化. 其中, S0振幅最高, 两侧波形S1和S2的振幅相等, 与S0的相位差几乎为零, 如图中红色和蓝色虚线所示. 表明按传统的四分量数据接收组合模式仅能确定目标反射体的走向, 无法利用幅度和相位特征进一步区分反射体的方位.

2.3.2　新型全方位偶极测量模式

为解决偶极横波远探测方位180°不确定性问题, 参照公式(8)我们提出了井中多方位组合接收消除方位多解性的新型全方位偶极测量模式. 如图8所示, 每个接收分量均包含了相邻的3个正交方位的信息, 打破了传统的对称接收模式, 对识别井外反射体的方位具有重要意义.

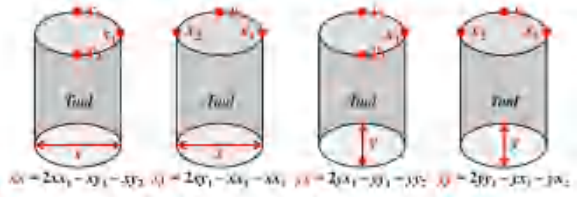


图 8　新型的全方位偶极横波远探测仪器的数据接收组合模式示意图

采用与图7相同的理论模型和计算参数, 模拟的新型四分量反射横波如图9a所示. 波幅方位分布图(图9b)仍然保留了传统四分量模式确定走向的优势, 准确

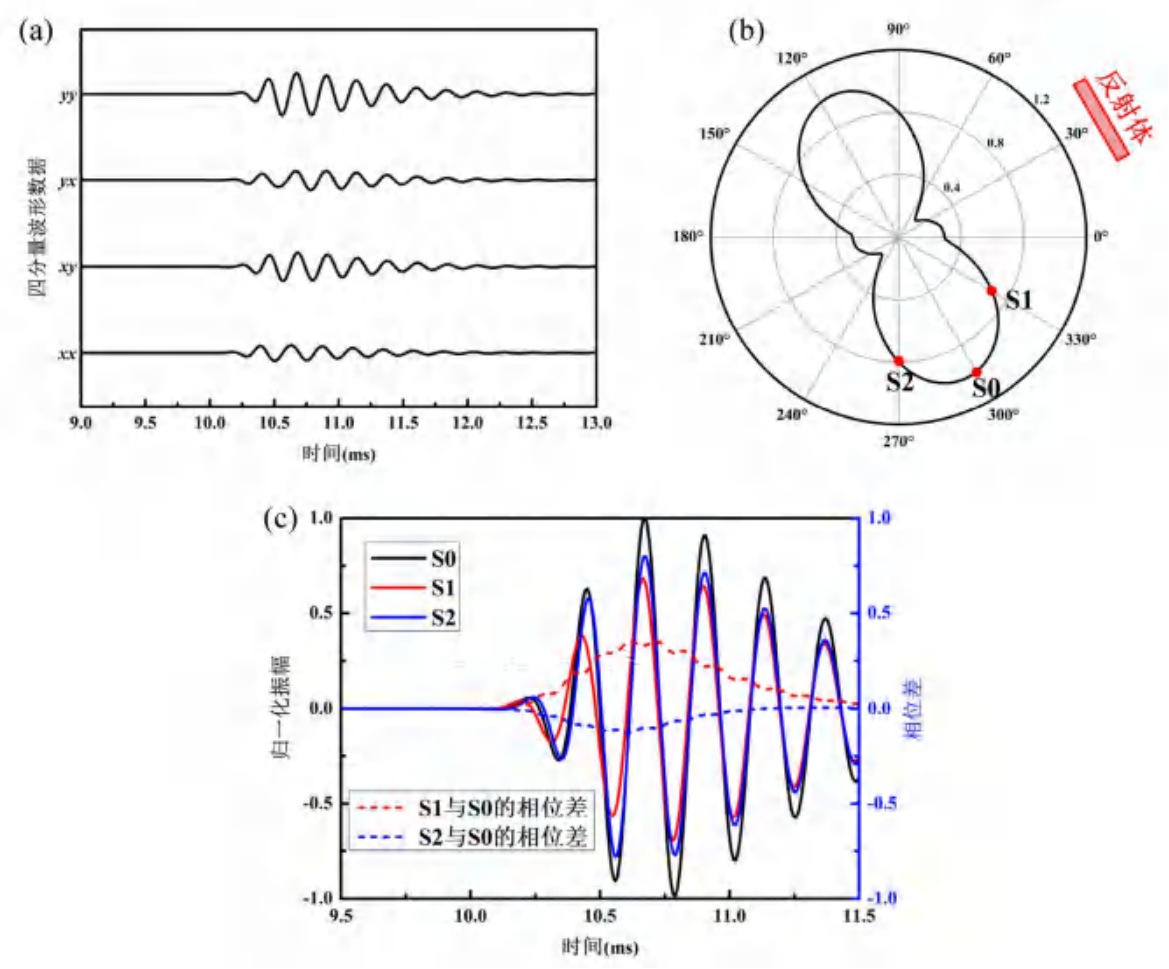


图 9　新型全方位偶极横波远探测测井响应

(a) 模拟的新型四分量偶极横波远探测数据; (b) 四分量数据旋转得到的波幅方位分布图; (c) 最佳成像方位及其两侧波形和相位差对比

中国知网　https://www.cnki.net

指示反射体的走向，但走向两侧波形S1和S2的振幅不等，且S1的相位超前于S0，相位差为正，如图9c中红色虚线所示；S2的相位滞后于S0，相位差为负，如图9c中蓝色虚线所示．此时，走向两侧信号S1和S2存在明显相移．值得指出的是，该相移的正负与井外反射体的方位密切相关，若反射体的方位相反，对应走向两侧信号间的相位差异号，这正是新型全方位测量模式消除偶极横波远探测方位180°不确定性的理论依据．

3　模型井中方位偶极横波远探测实验验证

以上理论计算结果表明提取反射体走向两侧反射信号间的相移可有效消除偶极横波远探测方位180°不确定性．下面依托实验室方位模型井群开展井中方位偶极横波远探测实验研究．

3.1　实验思想与理论验证

苏远大等(2024)论证了副井(发射井)中的单极辐射纵波和测量井外的界面反射纵波具有等效性．采用相同的方法考察偶极横波的适用性，实验设计思想示意图见图10a. 在副井中放置一偶极子声源先后正交激发纯SH横波和纯SV横波，在测量井中放置多方位离轴接收器环向360°扫描接收(环向接收间隔为10°)，以此来等效替代测量井外存在反射体的情况．两种模型的理论对比结果分别如图10b(SH横波)和图10c(SV横波)所示，图中黑色实线表示井外界面反射波，红色点线表示副井辐射波．波形均按照方位接收的SH横波振幅的最大值归一化. 两种模型的仿真结果几乎重合，说明在相邻井中激发的偶极声波可以等效替代测量井外反射体的反射波，为下一步在实验室模型井群中获取四分量偶极反射横波数据奠定了基础，同时也规避了在井旁构建反射体的难题．

3.2　实验方法与测量结果分析

在理论仿真的基础上，开展井中方位偶极反射横波数据采集实验．实验方法与模型井设计与苏远大等(2024)相同，仅将发射声源从单极源替换成偶极源即可．其中偶极发射换能器内部总成见图11a左上角的放大图，由长短两组共4对三叠片构成，中心频率为3kHz. 方位接收器由4片间隔90°的离轴接收换能器构成，能

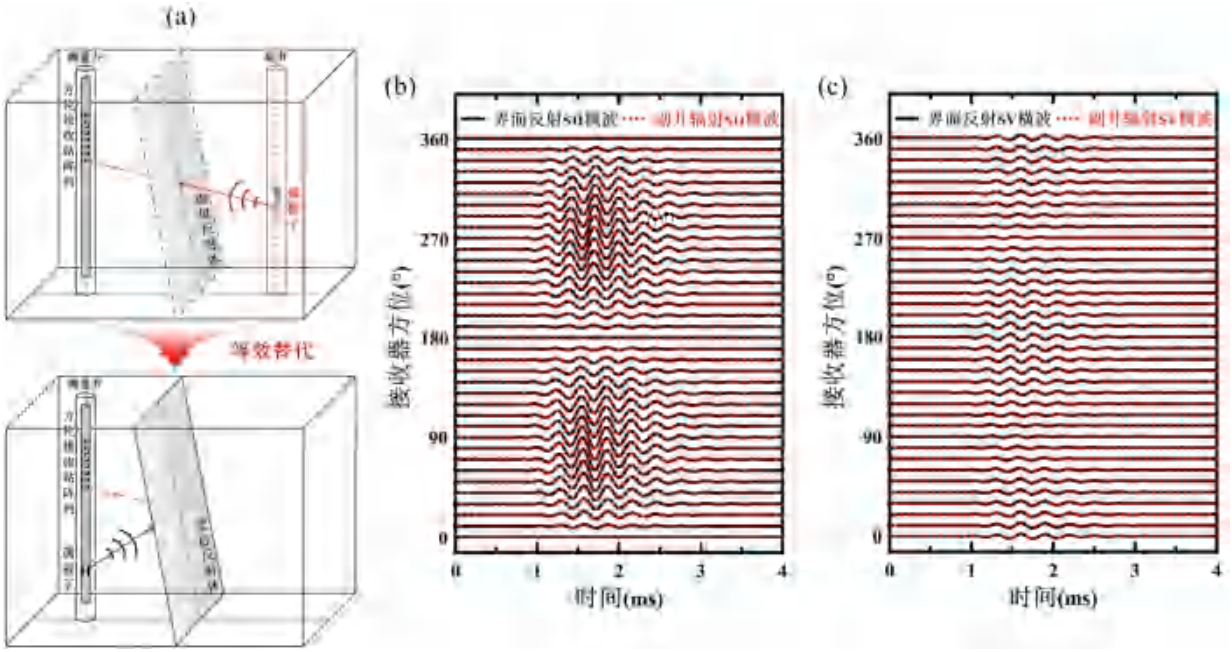


图 10　模拟界面反射波的等效实验思想示意图(a)及理论计算的测量井中方位接收的井外界面反射波形和副井辐射波形对比(b, c)

(b) 偶极SH横波; (c) 偶极SV横波. 波形振幅均按方位接收的SH横波振幅的最大值归一化

中国知网　https://www.cnki.net

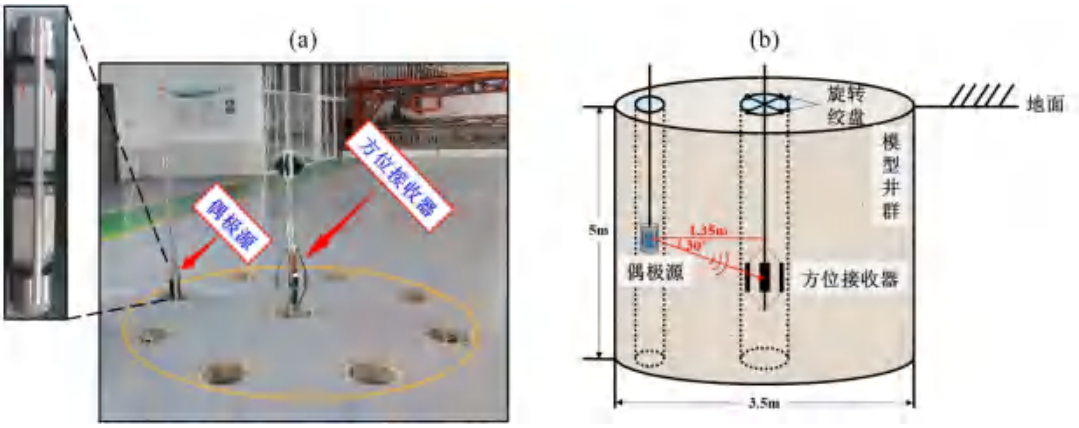


图 11　实验配置实物图(a)及发射-接收系统的相对位置示意图(b)

实现井下方位旋转测量. 实验井群均匀地层段深5m, 由中心的测量井及井外8口间隔45°的副井构成. 中心测量井直径25cm. 副井直径10cm, 距测量井1.35m. 井间地层的纵、横波速度和密度分别为3200m s^{-1}、2040m s^{-1}和2250kg m^{-3}. 实验过程中将偶极源和方位接收器分别下放至副井和测量井中, 下放深度错位, 保持声源在接收器上方0.78m处(声源辐射角度为水平向下30°, 如图11b所示). 在地面规律地旋转绞盘带动井下的方位接收器旋转以实现在测量井中环向360°方位接收, 旋转角度间隔为10°, 共接收37道波形.

3.2.1　测量信号的方位幅值响应特征

如图12a和图13a所示, 当副井中的偶极源指向与波的传播方向垂直(平行)时, 在测量井中方位接收的是来自副井中偶极源激发的纯SH横波(纯SV横波). 定义副井所在方位为180°(大地坐标系), 测量井中方位接收的纯SH横波和纯SV横波分别如图12b和图13b所示. 实验测量波形与图10中理论仿真波形的变化趋势一致, 具有明显的方位特征. 当接收器指向与声源指向平行(垂直)时, 接收到的SH横波振幅最大(最小), 且y轴两侧接收波形的极性发生了反转; 当接收器方位与副井方位相同时, 接收到的SV横波振幅最大, 且各方位接收波形的极性相同. 按方位接收的SH横波振幅最大值归一化所有波形, 并将各方位归一化后的SH横波和SV横波振幅绘制于极坐标系中(方位振幅曲线), 分别如图12c和图13c所示. 实验测量的方位振幅曲线(红色点线)与理论计算结果(黑色实线)的变化趋势一致, 充分验证了实验测量数据的可靠性.

3.2.2　最佳成像方位两侧信号的相移特征

基于上述实验测量结果, 定义图12a中与波传播方向垂直的声源指向为x向(激发纯SH横波), 则图12b中90°(270°)和180°(360°)方位接收波形分别为xx_1(xx_2)和xy_1(xy_2)分量; 类似地, 定义图13a中与波传播方向平行的声源指向为y向(激发纯SV横波), 则图13b中90°(270°)和180°(360°)方位接收波形分别为yx_1(yx_2)和yy_1(yy_2)分量. 在此基础上, 将上述8个分量按照图6和图8所示的数据组合方式分别组合形成传统和新型的四分量波形数据, 如图14a和图15a所示. 四分量数据坐标旋转后, 波幅方位分布图(图14b和图15b)均显示井外虚拟反射体的走向为90°/270°方向(大地坐标系), 与实验模型对应. 如图15c所示, 在新型数据组合模式下, 最佳成像方位(90°, S0)两侧30°的反射信号(120°, S1和60°, S2)存在明显的相移(S1超前于S2, 相位差为正), 而在传统数据组合模式下, S1和S2的相位差几乎为零(见图14c). 实验处理结果与图7和图9中的理论分析一致, 验证了新型全方位偶极测量模式的有效性.

4　新型全方位偶极横波远探测仪器与现场测试

在理论方法和实验验证的基础上, 研制了一支新型的全方位偶极横波远探测仪器样机, 在塔里木油田

中国知网　https://www.cnki.net

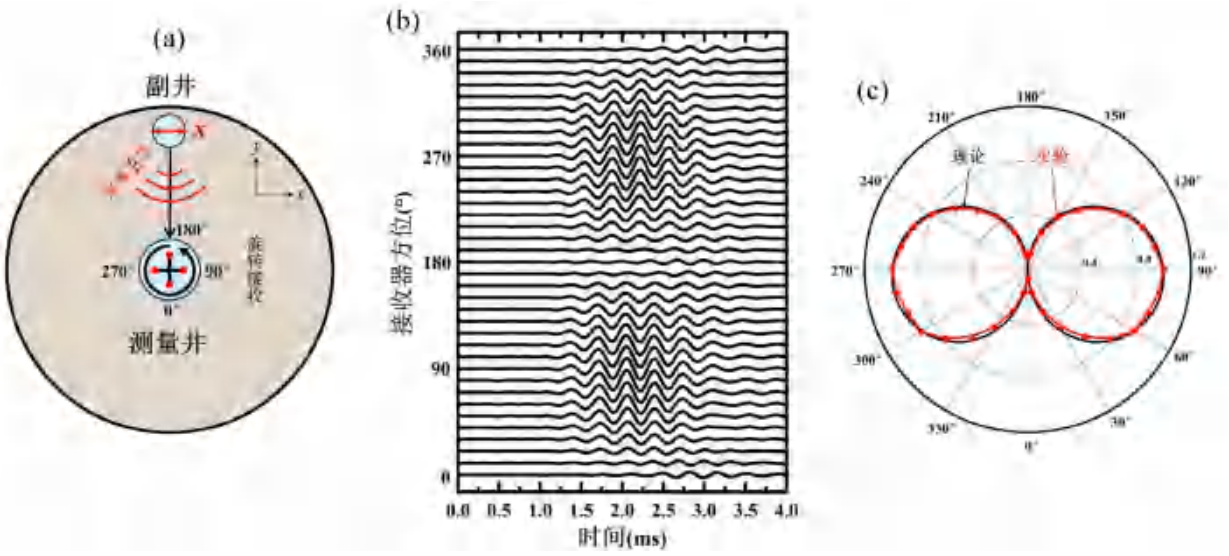


图 12　方位接收纯偶极SH横波实验示意图(a)及实测波形(b)和归一化的方位振幅曲线(c)

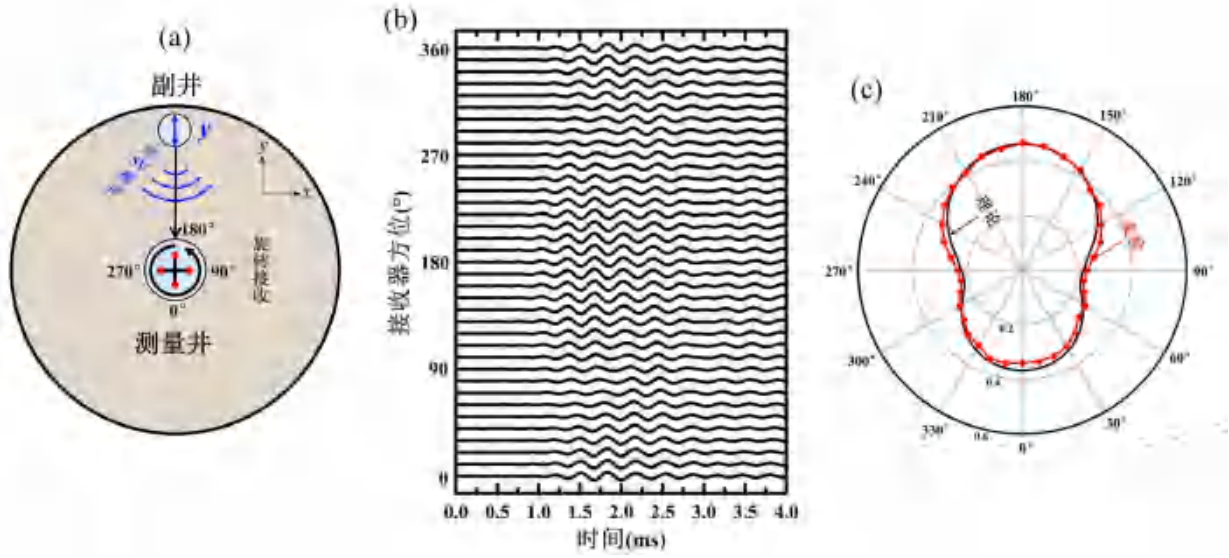


图 13　方位接收纯偶极SV横波实验示意图(a)及实测波形(b)和归一化的方位振幅曲线(c)

一口水平开发井中开展了现场试验，并取得了良好的应用效果.

4.1　新型全方位偶极横波远探测仪器结构

图16为新型全方位偶极横波远探测仪器样机及其结构图，仪器主体由发射电子短节、正交偶极发射声系、隔声体和接收电子短节四部分组成. 发射和接收电子短节分别控制信号的发射和采集；隔声体用以消除沿仪器壳体传播直达信号的干扰；接收部分由独立的4方位阵列接收条带组成，每个条带上包含8个间隔0.1524m的接收器，支持对井中4个方位上的阵列接收信号独立采集，满足基于新型全方位偶极测量模式的井中方位横波远探测方法的数据采集要求.

中国知网　https://www.cnki.net

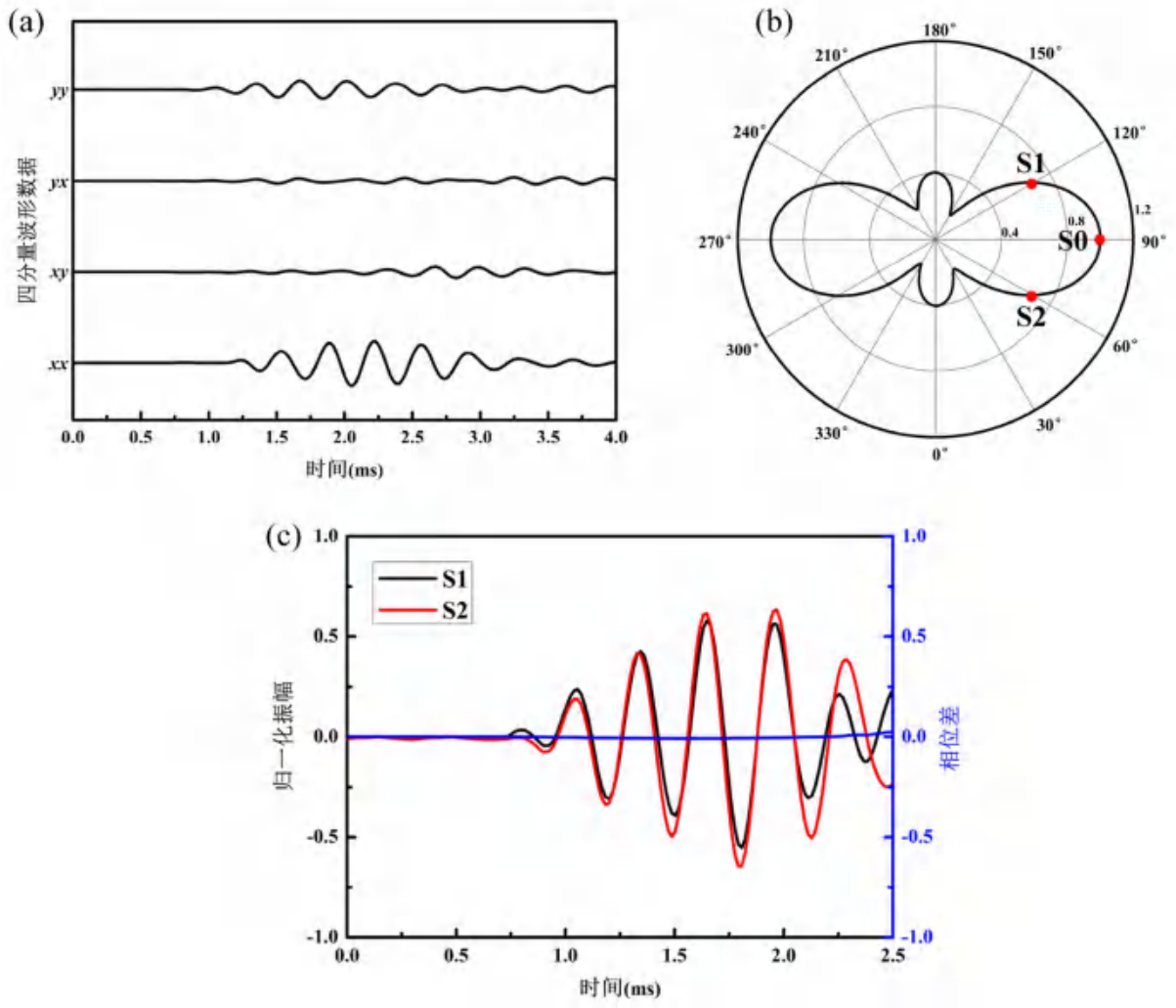


图 14　传统四分量偶极横波远探测测井响应

(a) 传统的四分量偶极横波远探测实验数据; (b) 四分量数据旋转得到的波幅方位分布图; (c) 最佳成像方位两侧波形和相位差对比

4.2　现场应用实例

图17给出了利用新型全方位偶极横波远探测仪器样机在塔里木油田一口打中断溶体的水平开发井中的成像实例，显示了X060~X187m井段的数据处理结果. 第1道中的自然伽马曲线(GR)显示该井段为碳酸盐岩地层; 井斜曲线(DEV)显示该井段为大斜度井, 井斜角约为80°; 仪器方位曲线(RB)显示在该井段中仪器几乎不旋转，仪器y轴相较于井眼高端约330°~360°. 第2道中的纵、横波时差曲线(DTP、DTS)显示该井段地层较硬, 纵波时差约为150μs m^{-1}, 横波时差约为300μs m^{-1} (仅在X100~X115m井段出现时差异常大现象). 第3道和第4道分别给出了顺时针相较于井眼高边30°/210°(成像最清晰)和120°/300°(成像最模糊)两个剖面的成像结果. 图中显示在该深度段内含有两个与井斜交的反射界面，向井外径向延伸约65m. X065~X100m井段对应反射体1, X130~X185m井段对应反射体2. 对比两个剖面的成像强度，反射体1和2在30°/210°方向成像最清晰，而在120°/300°方向成像模糊，因此可以判断这两个反射体的走向均为30°/210°方向. 单点的波幅方位分布图证实了这一结论(见第5道)，但由于四分量旋转固有的180°不确定性，这两个反射体的方位可能

中国知网　https://www.cnki.net

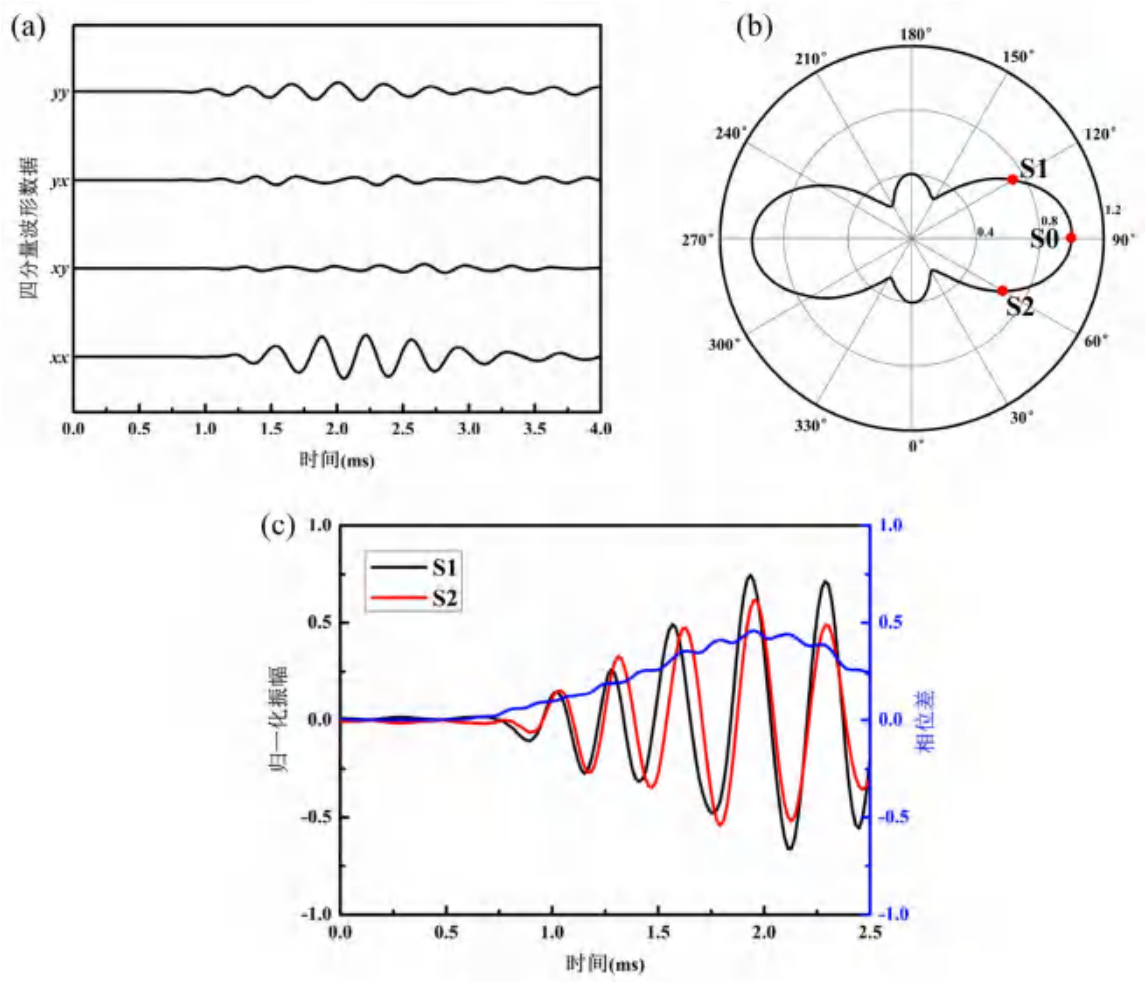


图 15　新型全方位偶极横波远探测测井响应

(a) 新型的四分量偶极横波远探测实验数据; (b) 四分量数据旋转得到的波幅方位分布图; (c) 最佳成像方位两侧波形和相位差对比

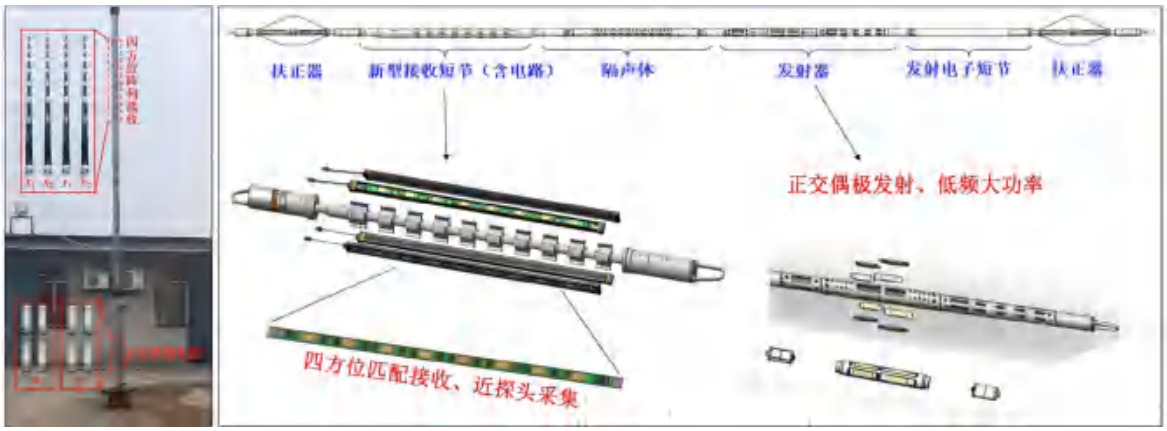


图 16　新型全方位偶极横波远探测仪器样机及其结构图

2222

中国知网　https://www.cnki.net

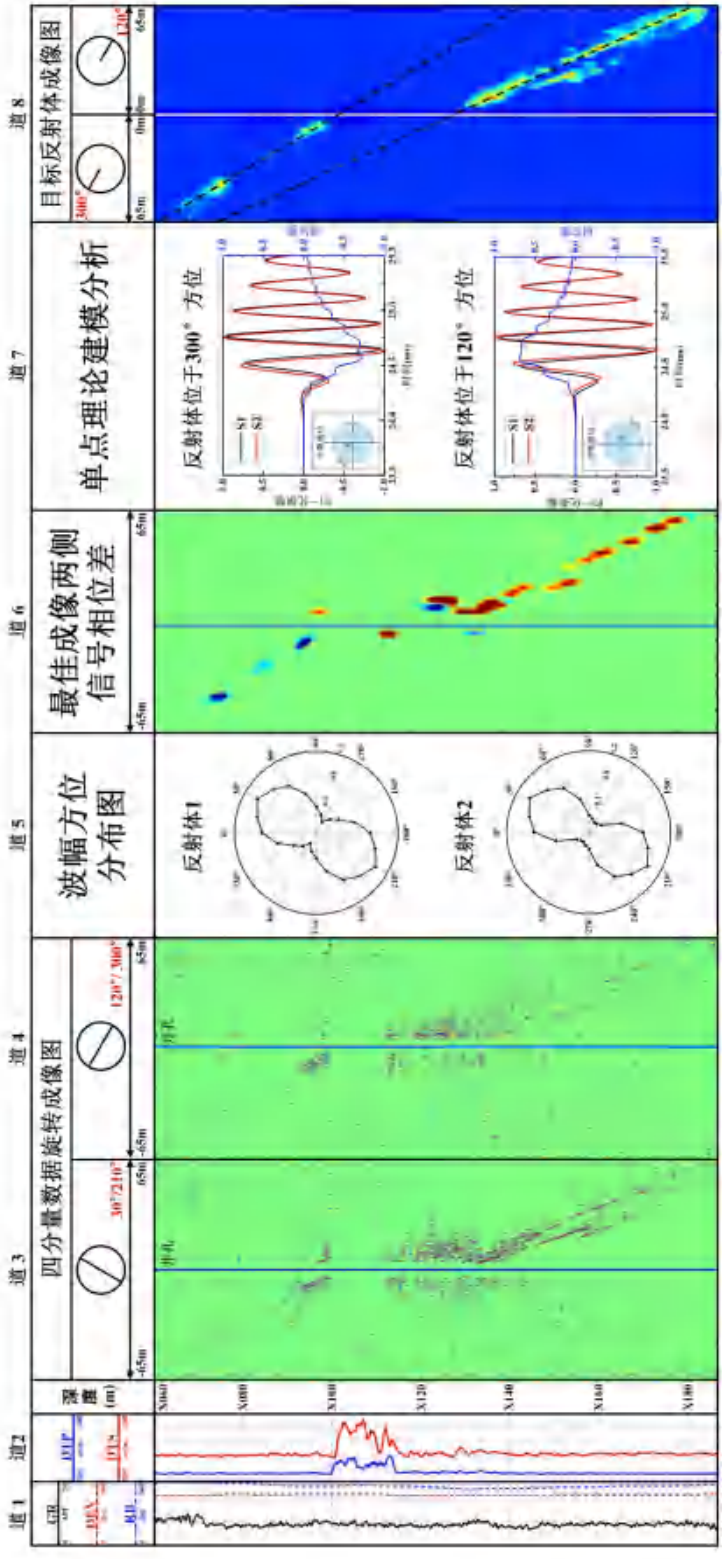


图 17　新型全方位偶极横波远探测成像实例

中国知网　https://www.cnki.net

为120°或300°.

在确定反射体走向的基础上, 下面通过提取走向两侧反射信号的相位差与理论结果对比进而消除方位多解性. 对比60°/240°剖面(S1)和0°/180°剖面(S2)成像数据的相位差, 结果在图中第6道给出, 其中红色(蓝色)表示该深度点处信号S1超前(滞后)于S2, 相位差为正(负). 显然, 在反射体1(反射体2)对应的深度段中信号S1滞后(超前)于S2, 说明两反射体的方位相反. 第7道进一步给出了X150m深度点(对应反射体2)处的理论建模结果, 对比了反射体分别位于120°方位和300°方位时的最佳成像方位两侧的波形及其相位差. 理论预测结果显示若反射体位于120°(300°)方位, 则信号S1超前(滞后)于S2, 相位差为正(负). 对应第6道中的实际相位差结果可判定反射体2的方位为120°, 则反射体1的方位为300°. 在对应方位下的重新偏移成像结果如图中第8道所示, 显示井眼轨迹穿过了约30米厚的断溶体, 探测到的两个反射体为该断溶体的上下边界. 结合井身方位(正东方向)和井斜角综合判断该断溶体走向为北东向, 倾向为东南向, 倾角约为60°. 由于断溶体内部介质疏松, 声衰减大, 如图第2道时差曲线在X100~X115m井段出现测量值异常大. 仪器在断溶体外无法同时测量到两个界面的反射信号, 进入断溶体内部由于衰减大导致来自界面的反射信号消失, 因此导致断溶体边界成像缺失. 成像解释结果与地质实际情况一致, 验证了方位反演结果的准确性.

5 结论

针对偶极横波远探测中的方位180°不确定性问题, 本文开展了井中方位偶极横波远探测理论模拟、实验验证和现场井应用. 基于弹性波与井孔和井外反射体的相互作用理论, 揭示了井中接收反射波的方位响应特征, 模拟分析了传统四分量偶极远探测模式的方位对称多解性. 在此基础上, 提出井中多方位组合接收消除方位多解性的新型全方位偶极测量模式, 指出通过提取并比较反射体走向两侧反射信号的相移可有效消除偶极横波远探测方位180°不确定性. 模型井实验结果证实了新测量模式和方法的有效性. 在新技术的现场应用中, 获得了井外断溶构造的清晰成像及其方位的正确信息, 为新技术的发展和应用提供了有力佐证.

致谢 感谢编委以及两位匿名审稿人提出的宝贵意见和建议, 这对文章的修改大有帮助. 感谢塔里木油田郭清滨、张承森、段文星在现场实验中的支持. 感谢中国石油大学(华东)李杨虎博士、古希浩博士和孔令文硕士在理论分析与实验上的帮助.

参考文献

曹景记, 唐晓明, 魏周拓. 2014. 偶极声源在裸眼井及套管井外的横波辐射特征. 地球物理学报, 57: 1683–1692

李杨虎. 2023. 方位远探测声波测井基础理论及应用研究. 博士学位论文. 青岛: 中国石油大学(华东)

李盛清, 苏远大, 唐晓明. 2020. 基于四分量偶极横波远探测的井周构造走向快速反演方法研究. 地球物理学报, 63: 2478–2487

李超, 张波, 许孝凯, 张晋言, 陈浩, 何晓, 王秀明. 2020. 多分量方 位远探测声波测井的理论与应用. 应用声学, 39: 292–299

苏远大, 饶博, 孔令文, 李盛清, 谭宝海, 庄春喜, 唐晓明. 2024. 井 中方位纵波远探测: 理论、实验与现场应用. 地球物理学报, 67: 630–640

唐晓明, 魏周拓. 2012. 利用井中偶极声源远场辐射特性的远探测 测井. 地球物理学报, 55: 2798–2807

唐晓明, 古希浩, 李杨虎, 苏远大. 2021. 井孔与弹性波的相互作用: 理论、方法和应用. 地球物理学报, 64: 4227–4238

许家旗, 胡恒山. 2020. 声波远探测中偏心声源的辐射以及接收波 场研究. 地球物理学报, 63: 3545–3561

杨海军, 肖承文, 祈新忠, 高楚桥. 2014. 塔里木盆地碳酸盐岩凝析 气藏测井评价新技术. 北京: 石油工业出版社

Aki K, Richards P. 1980. Quantitative Seismology: Theory and Methods. San Francisco: W. H. Freeman & Co

Bennett N N. 2019. 3D slowness time coherence for sonic imaging. Geophysics, 84: D179–D189

Gong H, Chen H, He X, Wang X M. 2015. Eliminating the azimuth ambiguity in single-well imaging using 3C sonic data. Geophysics, 80: A13–A17

Gong H, Chen H, He X, Su C, Wang X M, Wang B C, Yan X H. 2018. Modeling and inversions of acoustic reflection logging imaging using the combined monopole–dipole measurement mode. Appl Geophys, 15: 393–400

Hirabayashi N, Sakiyama N, Ikegami T. 2017. Characteristics of waveforms recorded by azimuthally spaced hydrophones of sonic logging tool for incident plane waves. Geophysics, 82: D353–D368

Lee S Q, Chen M, Gu X H, Su Y D, Tang X M. 2019. Application of four-component dipole shear reflection imaging to interpret the geological structure around a deviated well. Appl Geophys, 16: 291–301

Li Y H, Tang X M, Li H R, Lee S Q. 2021. Characterizing the borehole

中国知网 https://www.cnki.net

response for single-well shear-wave reflection imaging. Geophysics, 86: D15–D26

Su Y D, Tang X M, Hei C, Zhuang C X. 2011. An equivalent-tool theory for acoustic logging and applications. Appl Geophys, 8: 69–78

Tang X M, Cheng C H. 2004. Quantitative Borehole Acoustic Methods. Netherlands: Elsevier Science Publishing Inc

Tang X M. 2004. Imaging near-borehole structure using directional acoustic-wave measurement. Geophysics, 69: 1378–1386

Tang X M, Patterson D J. 2009. Single-well S-wave imaging using multicomponent dipole acoustic-log data. Geophysics, 74: WCA211–WCA223

Tang X M, Cao J J, Wei Z T. 2014. Shear-wave radiation, reception, and reciprocity of a borehole dipole source: With application to modeling of shear-wave reflection survey. Geophysics, 79: T43–T50

Tang X M, Cao J J, Li Z, Su Y D. 2016. Detecting a fluid-filled borehole using elastic waves from a remote borehole. J Acoust Soc Am, 140: EL211–EL217

Xu J Q, Hu H S, Wang Z. 2019. Asymptotic solution to a 3D dipole single-well imaging system with combined monopole and dipole receivers with an application in elimination of azimuth ambiguity. Geophysics, 84: D191–D207

Zhang Y D, Hu H S. 2014. A technique to eliminate the azimuth ambiguity in single-well imaging. Geophysics, 79: D409–D416

Zhao T, Che X H, Qiao W X, Cheng L. 2023. Borehole azimuthal acoustic imaging using 3D spatial scanning: Application in acoustic detection of nearby wells. Geophysics, 88: D131–D145

Zhao T, Che X H, Qiao W X. 2024. Azimuth estimation method for borehole acoustic reflection imaging using an acoustic vector array. IEEE Trans Geosci Remote Sens, 62: 1–10

(责任编委: 印兴耀)

中国知网 https://www.cnki.net

SCIENCE CHINA
Earth Sciences

•ARTICLE•

July 2025 Vol.68 No.7: 2138–2153
https://doi.org/10.1007/s11430-024-1587-5

Solving the azimuthal 180°-ambiguity problem in borehole dipole shear wave reflection imaging: Theory, method and experiment

Yuanda SU[1,2,3], Bo RAO[1,2], Chunxi ZHUANG[1,2], Shengqing LI[1,2], Baohai TAN[1,2] & Xiaoming TANG[1,2,3*]

[1] *School of Geosciences, China University of Petroleum (East China), Qingdao 266580, China*
[2] *National Key Laboratory of Deep Oil and Gas, China University of Petroleum (East China), Qingdao 266580, China*
[3] *Laboratory for Marine Mineral Resources, Laoshan Laboratory, Qingdao 266071, China*

Received November 11, 2024; revised April 19, 2025; accepted May 14, 2025; published online June 23, 2025

Abstract The recently developed borehole dipole shear wave (S-wave) reflection imaging technique has been successfully applied to deep hydrocarbon exploration, allowing for accurate detection of fracture-cavity reservoirs tens of meters away from the borehole. Further developments in this technology needs to resolve the azimuthal 180°-ambiguity caused by the symmetry of the dipole sources and receivers, known as the "180°-ambiguity problem" in the well logging community. This paper aims to determine the azimuth of reflectors outside a borehole uniquely, which is crucial for optimizing deep hydrocarbon exploration and critical field operations (such as directional drilling). Based on the theory of interaction between elastic waves and reflectors outside the borehole, this paper analyzes the azimuthal response characteristics of reflected waves received in the borehole. We propose a new full-azimuthal dipole measurement mode to eliminate the azimuthal ambiguity through a multi-azimuth data reception and combination method. The method has been validated in laboratory azimuthal model test wells. Theoretical and experimental results indicate that the new measurement method preserves the azimuthal amplitude variation characteristic of the conventional four-component (4C) measurement and possesses a 360° periodicity for the wave phase variation, which can be effectively used to resolve the azimuthal 180°-ambiguity of the dipole shear reflection imaging. Based on the new method, a new full-azimuthal dipole shear reflection imaging tool prototype has been developed and field tested in a horizontal development well in the Tarim oil field. The acoustic reflection imaging results clearly demonstrate that the horizontal well crosses an approximately 30 m thick fault-karst body, with the imaging range outside the borehole extending up to 65 m. By analyzing the amplitude and phase shift of the acoustic reflection data, allowing for delineating the fault-karst body in the formation. This research provides both theoretical and experimental foundations for the development and application of borehole azimuthal acoustic reflection imaging technology for deep hydrocarbon exploration.

Keywords Dipole shear reflection imaging, Azimuthal 180°-ambiguity, Four-component data combination, Waveform phase shift

Citation: Su Y, Rao B, Zhuang C, Li S, Tan B, Tang X. 2025. Solving the azimuthal 180°-ambiguity problem in borehole dipole shear wave reflection imaging: Theory, method and experiment. Science China Earth Sciences, 68(7): 2138–2153, https://doi.org/10.1007/s11430-024-1587-5

1. Introduction

Borehole acoustic reflection imaging is an important technology for detecting the three-dimensional structure in the range from several meters to even hundreds of meters outside the borehole, filling the gap between seismic exploration and conventional logging. In recent years, this technology has been widely used to detect and evaluate geological structures such as fractures and cavities outside the borehole. It is also a key method for identifying sweet spots and hidden reservoirs

* Corresponding author (email: tangxiam@aliyun.com)

© Science China Press 2025

in deep-ground, deep-water, and unconventional oil and gas exploration and development (Tang and Patterson, 2009; Gong et al., 2018; Bennett, 2019; Lee et al., 2019; Xu and Hu, 2020; Tang et al., 2021; Zhao et al., 2023, 2024).

The acoustic reflection imaging technology uses a borehole source to radiate elastic waves into the formations and receives the reflected waves from the geological structures in the same borehole. Processing the reflection signals using migration imaging delineates geological structures outside the borehole. The dipole acoustic reflection imaging method proposed by Tang (2004) is widely used in the industry owing to its advantages of azimuthal sensitivity for fracture detection and deep detection range. This method enables efficient and convenient azimuthal scanning imaging of reflectors outside the borehole by performing azimuthal rotational transformations on the 4C dipole reflection data. However, due to the symmetry of the dipole source (and receiver), the reflection imaging results have a 180°-ambiguity in the azimuth determination, commonly referred to as the "180° azimuthal uncertainty" in the well logging community. This problem can be solved by integrating conventional logging, seismic or geological data in cases where geological structures intersect the borehole (Tang, 2004; Yang et al., 2014), but no effective solution currently exists for structures located far from the borehole. As this technology has become more widely used in the field, the problem of resolving the reflector azimuth has become more prominent, particularly in directional sidetrack drilling in fracture-cavity reservoirs and fracturing production. Therefore, solving the azimuthal 180°-ambiguity problem in dipole acoustic reflection imaging has become a research hotspot in the logging community. Zhang and Hu (2014) derived the phase response characteristics of pressure and displacement of reflected waves received in the borehole, and proposed a method to determine the reflector azimuth using the phase of reflected waves. Gong et al. (2015) used a three-component displacement sensor in the borehole to enhance real-images while suppressing pseudo-images from the vertical component. Hirabayashi et al. (2017) applied the results of plane-wave incidence and azimuthal reception to dipole acoustic reflection imaging, proposing the idea of determining the reflector azimuth based on amplitude differences of azimuthally reflected waves. However, unlike plane-wave incidence, the incident wavefield in acoustic reflection imaging propagates as a spherical wave, which limits the accuracy of the plane-wave assumption. Xu et al. (2019) simulated reflected waveforms measured by monopole and dipole modes in the presence of a near-borehole reflector. They suggest comparing the polarity relationship of pressure and displacement with reference waveforms to determine the reflector azimuth. Li et al. (2020) proposed to use both monopole and dipole acoustic reflection imaging methods simultaneously for reflector positioning, but this method is limited by the detection range of the monopole source. Li et al. (2021) and Li (2023) analytically simulated azimuthal reflected waveforms in the borehole based on virtual source theory and proposed placing azimuthally eccentric receivers in the borehole to determine the reflector azimuth in dipole acoustic reflection imaging. Most of these studies are theoretical feasibility analyzes; their practical implementation in current acoustic logging remains challenging, and their effectiveness in field applications requires further validation.

Using the theory of elastic wave interaction with the borehole, this paper theoretically analyzes the azimuthal 180°-ambiguity in the conventional dipole measurement mode. A new full-azimuth dipole measurement mode, incorporating multi-azimuth data reception and combination to eliminate the azimuthal ambiguity, is proposed and experimentally validated in laboratory model test wells. A multi-azimuth receiving acoustic system is placed in the measurement hole, while a dipole source is placed in the other nearby borehole to radiate S waves into the measurement hole, which, using the virtual source analogy, simulates the reflected S waves from the interface outside the measurement hole. In data processing, extracting the phase shift between the reflected signals along the azimuths around the reflector strike (i.e., the best imaging azimuth for 4C data rotation) effectively eliminates the azimuthal 180°-ambiguity in dipole acoustic reflection imaging. Both theoretical calculations and experimental measurements show that the proposed new dipole measurement method possesses 360° azimuth sensitivity. Based on the validated method, a full-azimuth dipole acoustic reflection imaging tool prototype has been built and successfully applied in the Tarim oil field, with good structural imaging and azimuth detection results effectively solving the azimuthal 180°-ambiguity problem in dipole shear reflection imaging.

2. Theory and measurement mode of azimuthal dipole shear reflection imaging

2.1 Theory of azimuthal dipole acoustic reflection imaging

Figure 1a illustrates the theoretical schematic for detecting geological reflectors outside the borehole using a dipole acoustic logging tool. The dipole source within the fluid-filled borehole radiates elastic waves into the surrounding formation, which are reflected by the reflector and received by receivers inside the borehole. In the cylindrical coordinate system (r,φ,z), four azimuthal receivers (x_1,y_1,x_2,y_2) are placed along the borehole away from the dipole source. Figure 1b shows the cross section of the borehole receiving configuration, where symbol a denotes the borehole radius

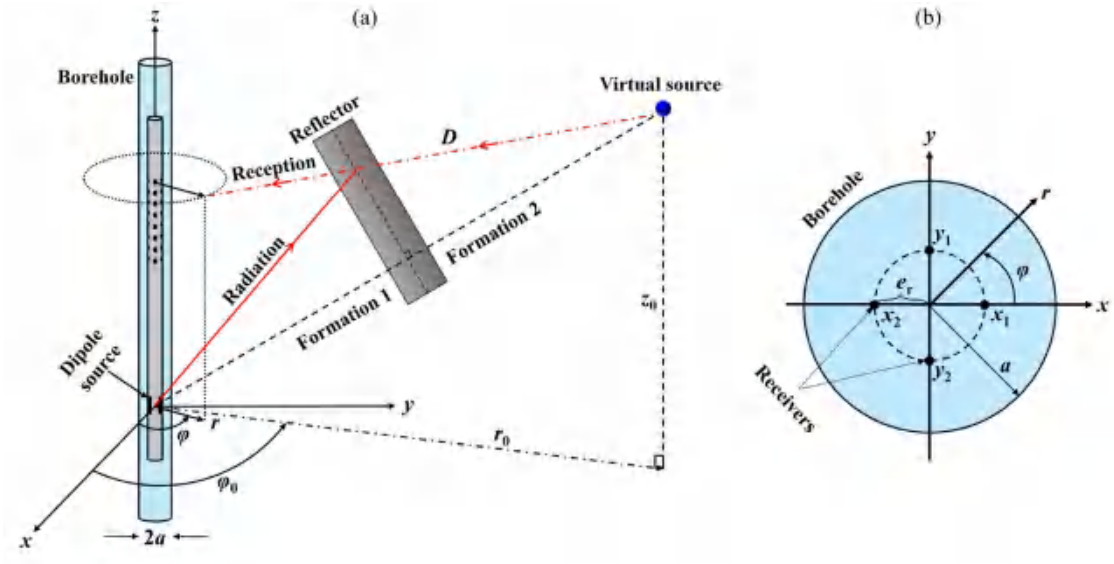


Figure 1 Schematic of single well dipole shear reflection imaging (a) and cross section of borehole receiving configuration using azimuthally spaced receivers (b).

and e_r indicates the off-axis distance of the receivers.

Under far-field radiation conditions where the radiation distance is several wavelengths away from the borehole, the far-field asymptotic solutions for the SH- and SV-wave displacement potential functions χ and Γ are given by (Tang et al., 2016):

$$\begin{cases} \chi \sim [D_1(k_0,\omega)\sin(\varphi)]\dfrac{e^{i\omega R/\beta}}{R}S(\omega), \\ \Gamma \sim [F_1(k_0,\omega)\cos(\varphi)]\dfrac{e^{i\omega R/\beta}}{R}S(\omega), \end{cases} \tag{1}$$

where ω is the angular frequency; $k_0 = (\omega/\beta)\cos(\theta_t)$ is the steepest descent solution for the wavenumber of the radiation S wave, with β and θ_t are formation S-wave velocity and wave radiation angle from the borehole axis, respectively; S is the source spectrum; R is the radiation distance of the source to the field point; D_1 and F_1 are the far-field wave amplitude coefficients for the SH and SV waves, respectively, which are determined by the boundary conditions at the borehole wall (Cao et al., 2014).

According to the virtual source analogy illustrated in Figure 1a, the reflected waves generated by the interaction between the radiated waves and the reflector outside the borehole can be represented equivalently as incident waves excited by the virtual source. The position of the virtual source coincides with the mirror image of the borehole source on the outward side of the reflector. The total elastic wave propagation distance D, denoted by the red dash-dotted line segment in Figure 1a, satisfies the far-field condition. The displacement potentials χ^i (SH wave) and Γ^i (SV wave) for the incident waves in the frequency-wavenumber domain are expressed as:

$$\begin{cases} \chi^i = S(\omega)\cdot RD_{SH}(\omega)\cdot RF_{SH}(\omega) \\ \quad \cdot \sum_{n=0}^{\infty}\varepsilon_n I_n(sr)K_n(sr_0)\cos[n(\varphi-\varphi_0)], \\ \Gamma^i = S(\omega)\cdot RD_{SV}(\omega)\cdot RF_{SV}(\omega) \\ \quad \cdot \sum_{n=0}^{\infty}\varepsilon_n I_n(sr)K_n(sr_0)\cos[n(\varphi-\varphi_0)], \end{cases} \tag{2}$$

where the superscript i denotes the incident wave in the formation; RD_{SH} and RD_{SV} are the borehole radiation functions for the dipole SH and SV waves (i.e., the terms in square brackets in eq. (1)); RF_{SH} (RF_{SV}) is the acoustic reflection coefficient at the reflector that can be calculated using the Zoeppritz equation (Aki and Richards, 1980); n denotes the azimuthal number; ε_n denotes the Neumann factor, with ε_n=1 for n=0 and ε_n=2 for n>0; I_n and K_n are, respectively, the first and second kind of the nth-order modified Bessel functions; r_0 and φ_0 are the radial distance and circumferential azimuth of the virtual source, respectively; $s=(k^2-\omega^2/\beta^2)^{1/2}$ is the radial wavenumber of the incident S wave, with k is axial wavenumber.

When the incident S wave characterized by eq. (2) interacts with the borehole, it will generate elastic wavefields in both the borehole and the formation. According to Helmholtz decomposition theory, the displacement in the borehole fluid $\mathbf{u}_f$ can be represented by the transmitted compressional wave (P-wave) potential ϕ_f, and the displacement $\mathbf{u}_s$ in the formation solid can be jointly represented by the scattered P-wave potential ϕ_s, SH-wave potential χ_s, and SV-wave potential Γ_s. To satisfy the far-field radiation condition, the general solution of these wave potentials, expressed in the frequency-wavenumber domain, can be written as:

$$\begin{cases} \phi_{\mathrm{f}} = \sum_{n=0}^{\infty}[A_n\cos(n\varphi) + A'_n\sin(n\varphi)]I_n(fr)K_n(sr_0), & (0 < r < a) \\ \left.\begin{aligned} \phi_{\mathrm{s}} &= \sum_{n=0}^{\infty}[B_n\cos(n\varphi) + B'_n\sin(n\varphi)]K_n(pr)K_n(sr_0) \\ \chi_{\mathrm{s}} &= \sum_{n=0}^{\infty}[D_n\sin(n\varphi) - D'_n\cos(n\varphi)]K_n(sr)K_n(sr_0) \\ \Gamma_{\mathrm{s}} &= \sum_{n=0}^{\infty}[F_n\cos(n\varphi) + F'_n\sin(n\varphi)]K_n(sr)K_n(sr_0) \end{aligned}\right\}, & (r \geqslant a) \end{cases} \tag{3}$$

where $f=(k^2-\omega^2/\alpha_{\mathrm{f}}^2)^{1/2}$ is the radial wavenumber for the borehole fluid, and α_{f} is the fluid velocity; $p=(k^2-\omega^2/\alpha^2)^{1/2}$ is the radial wavenumber of the formation P wave, and α is the formation P-wave velocity; $A_n(A'_n) \sim F_n(F'_n)$ are the wave amplitude coefficients that can be determined by the boundary conditions at the borehole wall:

$$\begin{cases} u_r^{\mathrm{i}}(a^+) + u_r^{\mathrm{s}}(a^+) = u_r^{\mathrm{f}}(a^-), \\ \sigma_{rr}^{\mathrm{i}}(a^+) + \sigma_{rr}^{\mathrm{s}}(a^+) = \sigma_{rr}^{\mathrm{f}}(a^-), \\ \sigma_{r\varphi}^{\mathrm{i}}(a^+) + \sigma_{r\varphi}^{\mathrm{s}}(a^+) = 0, \\ \sigma_{rz}^{\mathrm{i}}(a^+) + \sigma_{rz}^{\mathrm{s}}(a^+) = 0, \end{cases} \tag{4}$$

where the superscripts s and f denotes the scattered wave in the formation and transmitted wave in the borehole fluid, respectively; u_r and σ_{rr} denote the radial displacement and radial normal stress, while $\sigma_{r\varphi}$ and σ_{rz} represent the shear stress components.

Substituting eq. (2) and eq. (3) into the displacement potential-displacement relations and applying Hooke's law, the displacements and stresses of the incident S wave, scattered waves, and transmitted waves can be determined, which, combining with the boundary conditions in eq. (4), yield two eigenmatrix equations:

$$\mathbf{M}\begin{bmatrix} A_n \\ B_n \\ D_n \\ F_n \end{bmatrix} = \begin{bmatrix} b_1 \\ b_2 \\ b_3 \\ b_4 \end{bmatrix} \quad \text{and} \quad \mathbf{M}\begin{bmatrix} A'_n \\ B'_n \\ D'_n \\ F'_n \end{bmatrix} = \begin{bmatrix} b'_1 \\ b'_2 \\ b'_3 \\ b'_4 \end{bmatrix}, \tag{5}$$

where **M** is a 4×4 eigenmatrix. The right-hand side of the equation represents the incident S-wave vectors excited by the virtual source, denoted as vectors **b** and **b′**, respectively. Details of the elements are given in Appendix A (https://link.springer.com).

By solving eq. (5), the wavefields inside and outside the borehole can be fully determined. Furthermore, by substituting the solution of borehole fluid displacement potential ϕ_{f} into the relation $p(r,\varphi) = \rho_{\mathrm{f}}\omega^2\phi_{\mathrm{f}}$ and incorporating the steepest descent method (Tang et al., 2014, 2016), the fluid acoustic pressure wavefield inside the borehole can be calculated as follows:

$$p(r,\varphi)=S\cdot RD\cdot RF\cdot\frac{\mathrm{e}^{\mathrm{i}\omega D/\beta-\mathrm{i}\pi/4}}{D} \cdot\sum_{n=0}^{\infty}\rho_{\mathrm{f}}\omega^2[A_n\cos(n\varphi)+A'_n\sin(n\varphi)]I_n(f_0r), \tag{6}$$

where $D=[r_0^2+(z-z_0)^2]^{1/2}$, and z_0 is the axial distance of the virtual source; ρ_{f} is the borehole fluid density; $f_0=\left[(k_0^{\mathrm{i}})^2-\omega^2/\alpha_f^2\right]^{1/2}$, $k_0^{\mathrm{i}}=(\omega/\beta)\cos(\pi-\theta_{\mathrm{i}})$ is the steepest descent solution for the wavenumber of the incident S wave, and θ_{i} is the wave incident angle measured from the borehole axis. The expanded expression relating to the reflector azimuth angle in eq. (6) is detailed in Appendix B.

Eq. (6) demonstrates that the borehole wavefield from the acoustic reflection measurement is the superposition of multipole components. Therefore, a systematic analysis of the contribution of each component to the azimuthal response of the reflected wave is carried out using multipole decomposition theory, to elucidate the dipole 180°-ambiguity problem and derive a solution method. The analytical solution in eq. (6) allows us to efficiently simulate and analyze the contribution of the multipole component to the total reflected wave received in the borehole. Theoretical modeling is performed using the computational model in Figure 1 and the acoustic parameters in Table 1. In the modeling, we let the dipole source point in the *x*-direction, and set the reflector to be the interface between formations 1 and 2, with a dip angle of 60° and azimuth φ_0 = 120°. The source-to-receiver distance is 1 m, and the off-axis distance of the azimuthal receivers is 0.035 m. A 3 kHz Ricker wavelet is used to actuate the dipole source. The radial distance (r_0, see Figure 1a) of the virtual source on the other side of the reflector is assumed as 20 m.

Figure 2 compares the first four multipole components (i.e., n = 0, 1, 2 and 3, corresponding to monopole, dipole, quadrupole and hexapole, respectively) of the reflected S wave (the sum of SH and SV waves) received at 0° in the borehole. The results are normalized by the peak amplitude of the dipole component, and the relative amplitude ratios for each component are annotated on the right side of the figure. The comparative analysis shows that the borehole acoustic wavefield is dominated by dipole components with an am-

Table 1 Acoustic parameters of the borehole and formations

Medium	P-wave velocity (m s^{-1})	S-wave velocity (m s^{-1})	Density (kg m^{-3})	Outer diameter (m)
Borehole fluid	1500	—	1000	0.1
Formation 1	4000	2300	2500	—
Formation 2	4500	3000	2600	∞

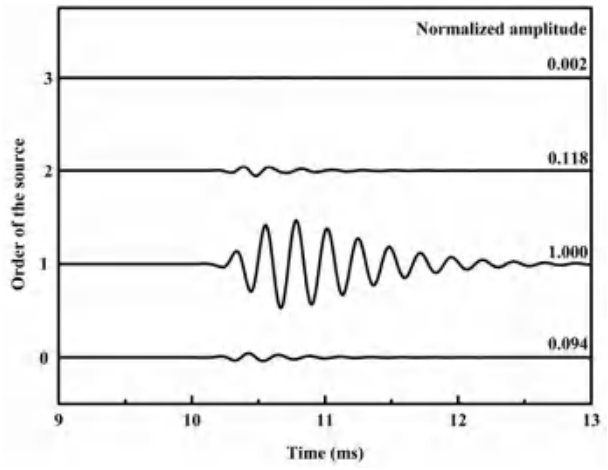


Figure 2 Comparison of the first four multipole components of reflected S wave received in the borehole, with normalized amplitude ratios for each component presented on the right side of the figure.

plitude contribution approximately one order of magnitude greater than the monopole and quadrupole components. Higher-order multipole terms converge rapidly and their contributions are negligible. Consequently, the borehole-received wavefield is predominantly controlled by the first three multipole components. Therefore, filtering out the azimuth-insensitive monopole components while preserving the dipole and quadrupole components through data combination provides an essential mechanism for identifying the azimuth of reflectors outside the borehole.

2.2 Analysis of azimuthal sensitivity of borehole-received dipole S wave

The azimuthal response characteristics of borehole-received wavefields are jointly determined by the radiation pattern of dipole sources and the data receiving configuration. The radiation function $RD_{SH} = D_1 \cdot \sin(\varphi)$ ($RD_{SV}=F_1 \cdot \cos(\varphi)$) for the dipole SH wave (SV wave) in the formation satisfies $|RD(\varphi)| = |RD(\varphi+\pi)|$, indicating that there is an inherent 180° symmetry for the dipole source, as can be seen from the three-dimensional radiation patterns shown in Figure 3. The SH- and SV-wave radiation patterns are symmetrical with respect to the *xoz* and *yoz* planes, which is the main cause of the 180°-ambiguity problem in azimuth determination for dipole S-wave imaging. The borehole-received azimuthal response is further analyzed below, starting with the data receiving configuration.

Table 2 lists the contributions of the monopole, dipole, and quadrupole components of the term $A_n\cos(n\varphi)+A'_n\sin(n\varphi)$ related to the receiver azimuth φ in eq. (6) for the four orthogonal receiving azimuths. It is found that when the receiver azimuth is altered by $\pm\pi/2$, the monopole component in the received waveforms is invariant while the quadrupole components exhibit a phase reversal; when the receiver azimuth is increased by π, the monopole and quadrupole components in the received waveforms remain identical, while the dipole components exhibit a phase reversal, suggesting that the contribution of each component can be adjusted by linearly combining the waveform data received in the four orthogonal azimuths.

Conventional dipole acquisition is done by subtracting the waveform data received in opposite azimuths, i.e., $p_\varphi - p_{\varphi+\pi}$, resulting in a pure dipole component. The inline data xx_{1-3} for the dipole source pointing in the φ direction is therefore expressed as (the subscripted numbers represent the serial numbers in Table 2):

$$xx_{1-3}=p_\varphi - p_{\varphi+\pi} = 2[A_1\cos(\varphi)+A'_1\sin(\varphi)]. \quad (7)$$

Eq. (7) demonstrates that the conventional dipole acoustic logging effectively eliminates monopole and quadrupole components, preserving pure dipole components in the processed waveforms. The same model parameters as in Figure 2 are used to simulate the borehole-received inline data xx_{1-3} and its first three multipole terms for the dipole acquisition configuration. The cross section of the model is shown in Figure 4a, with the reflectors at 120° and 300° azimuth, respectively, and the dipole source and receivers pointing in the *x*-axis direction. The calculation results based on eq. (7) are shown in Figure 4b. Comparative analysis reveals that the borehole-received inline data remain identical for the acquisition configuration (with monopole and quadrupole components vanishing while dipole components remain consistent), showing the root cause of the 180°-ambiguity in the dipole acquisition, which agrees with the theoretical prediction in eq. (B-2) from Appendix B.

To overcome the inherent symmetry constraints of conventional dipole acquisition, a new acquisition method is proposed. This method uses a linear combination of three azimuthal measurements to eliminate monopole contribution in the data, while preserving the dipole and enhancing quadrupole contributions. For this method, the inline data $xx_{1-2+1-4}$ for the dipole source pointing in the φ direction is

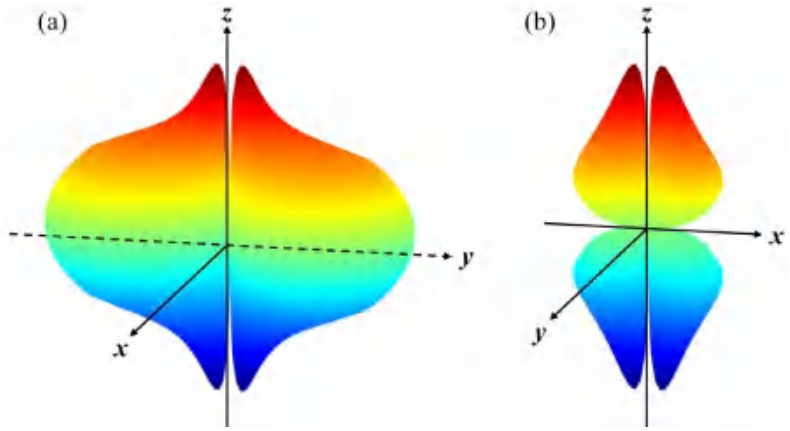


Figure 3 Three-dimensional radiation directivity patterns of SH wave (a) and SV wave (b) generated by a dipole source inside the borehole.

Table 2 Contributions of the monopole, dipole, and quadrupole components to $A_n\cos(n\varphi)+A'_n\sin(n\varphi)$ at the four orthogonal azimuths

Serial number	Azimuth	Order		
		n=0	n=1	n=2
1	φ	A_0	$A_1\cos(\varphi)+A'_1\sin(\varphi)$	$A_2\cos(2\varphi)+A'_2\sin(2\varphi)$
2	$\varphi+\pi/2$	A_0	$-A_1\sin(\varphi)+A'_1\cos(\varphi)$	$-A_2\cos(2\varphi)-A'_2\sin(2\varphi)$
3	$\varphi+\pi$	A_0	$-A_1\cos(\varphi)-A'_1\sin(\varphi)$	$A_2\cos(2\varphi)+A'_2\sin(2\varphi)$
4	$\varphi-\pi/2$	A_0	$A_1\sin(\varphi)-A'_1\cos(\varphi)$	$-A_2\cos(2\varphi)-A'_2\sin(2\varphi)$

expressed as (the subscripted numbers represent the serial numbers in Table 2):

$$\begin{aligned} xx_{1-2+1-4} &= p_{\varphi}-p_{\varphi+\pi/2}+p_{\varphi}-p_{\varphi-\pi/2} \\ &= 2[A_1\cos(\varphi)+A'_1\sin(\varphi)] \\ &\quad +4[A_2\cos(2\varphi)+A'_2\sin(2\varphi)]. \end{aligned} \tag{8}$$

By comparing eq. (7), it is observed that eq. (8) incorporates an azimuth-sensitive quadrupole component with the existing dipole component. For the new reception configuration of eq. (8), Figure 5 presents the simulation results with the same calculation parameters as in Figure 4. Comparing the results for opposite reflector azimuths, the monopole component vanishes, the dipole component is unchanged, and the quadrupole component exhibits identical amplitude but opposite phase, causing amplitude and phase changes in the combined waveforms. This phenomenon can be used to provide a theoretical foundation for solving the 180°-ambiguity problem for dipole S-wave imaging.

2.3 Azimuthal dipole acoustic reflection imaging simulation and data acquisition configuration comparison

Current dipole shear reflection imaging technology utilizes the 4C data (*xx*, *xy*, *yx*, *yy*) to determine the distance, dip angle and strike of reflectors outside the borehole (Tang and Wei, 2012; Tang et al., 2021). During operation of the downhole logging tool, the *x*- and *y*-oriented dipole sources are actuated sequentially and four off-axis receivers record a total of eight component signals for the four orthogonal azimuths, i.e., xx_1, xx_2, xy_1, xy_2, and yx_1, yx_2, yy_1, yy_2, where the first letter denotes the source orientation and the second letter with number indicates the receivers. Based on the analytical expression for the borehole fluid pressure given in eq. (6), the 4C data can be accurately modeled and analyzed. The modeling parameters are consistent with those in Figure 2, with only the reflector azimuth changed to 30° (the corresponding reflector strike is now 120°/300°, measured clockwise from the *x*-axis).

2.3.1 The conventional 4C dipole measurement configuration

The data acquisition configuration for the conventional 4C cross-dipole logging tool is shown in Figure 6, where the recorded signal is obtained by subtracting the received data from opposite azimuths.

The conventional 4C S-wave reflection data calculated using eq. (6) are shown in Figure 7a. By performing coordinate rotation (Li et al., 2020; Tang et al., 2021) on this data, the reflection amplitude versus rotation-angle ϕ variation pattern, is obtained, which, normalized by the maximum amplitude is illustrated in Figure 7b, where ϕ is measured clockwise from the tool *x*-axis direction. The pattern reaches

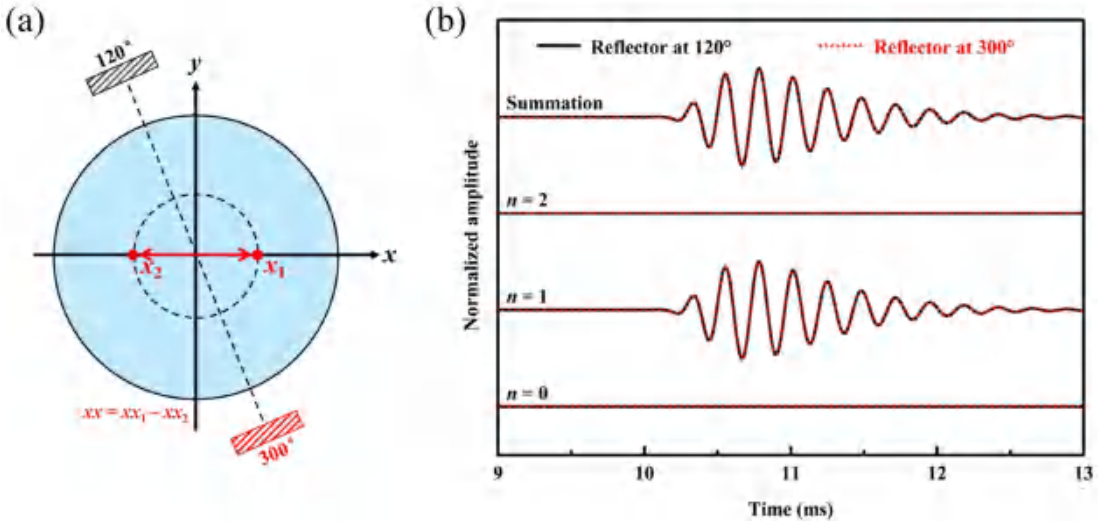


Figure 4 The schematic of the transmitter-receiver system (a) and comparison of borehole-received inline data xx_{1-3} and its first three multipole terms for the 120° (black) and 300° (red) reflector positions (b).

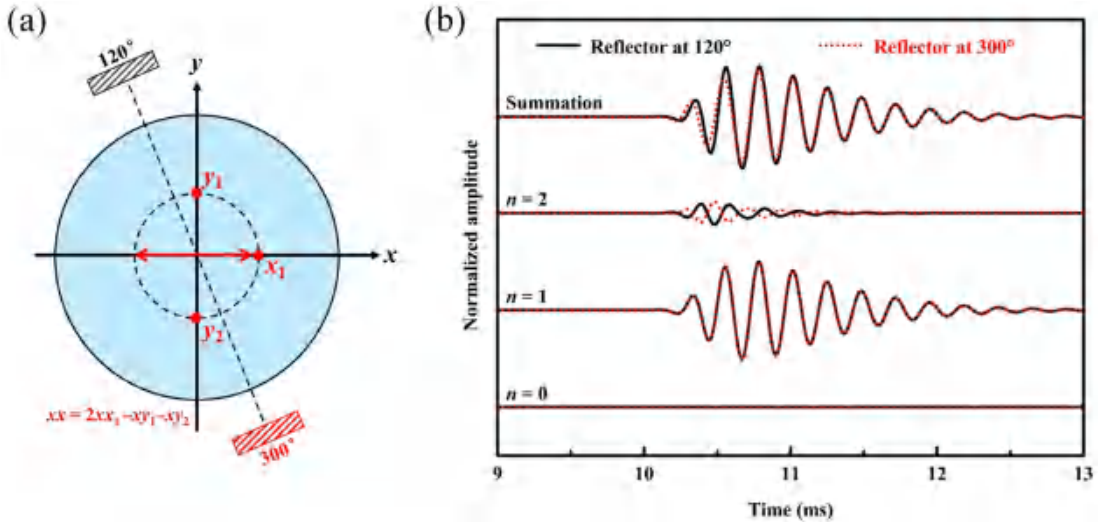


Figure 5 The schematic of the transmitter-receiver system (a) and comparison of borehole-received inline data $xx_{1-2+1-4}$ and its first three multipole terms for the 120° (black) and 300° (red) reflector positions (b).

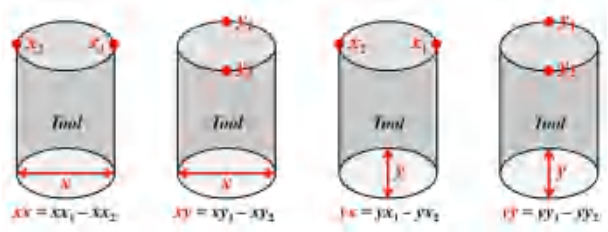


Figure 6 Schematic diagram of data acquisition configuration for the conventional 4C cross-dipole logging tool.

maximum amplitude at rotation angles of 120° and 300°, corresponding to the strike of the reflector. Optimal imaging quality occurs along these directions, which is the theoretical basis for determining the strike of the reflector from the 4C dipole data (note the reflector azimuth is perpendicular to the strike). However, there exists 180°-ambiguity in the azimuth determination, where the actual reflector azimuth could be either 30° or 210° in this case. Figure 7c compares reflected signals at the optimal imaging azimuth (300°, S0) with adjacent 30° offsets (330°, S1 and 270°, S2), all normalized by the maximum amplitude of S0. S0 exhibits the highest amplitude, while the waveforms of its adjacent signals S1 and S2 show equal amplitudes and near-zero phase differences relative to S0, as indicated by the red and blue dashed lines. This indicates that the conventional 4C data acquisition configuration can only determine the strike of the target reflectors, but neither the amplitude nor phase characteristics can further distinguish the reflector azimuth.

2.3.2 The new full-azimuth dipole measurement configuration

To address the azimuthal 180°-ambiguity problem in dipole

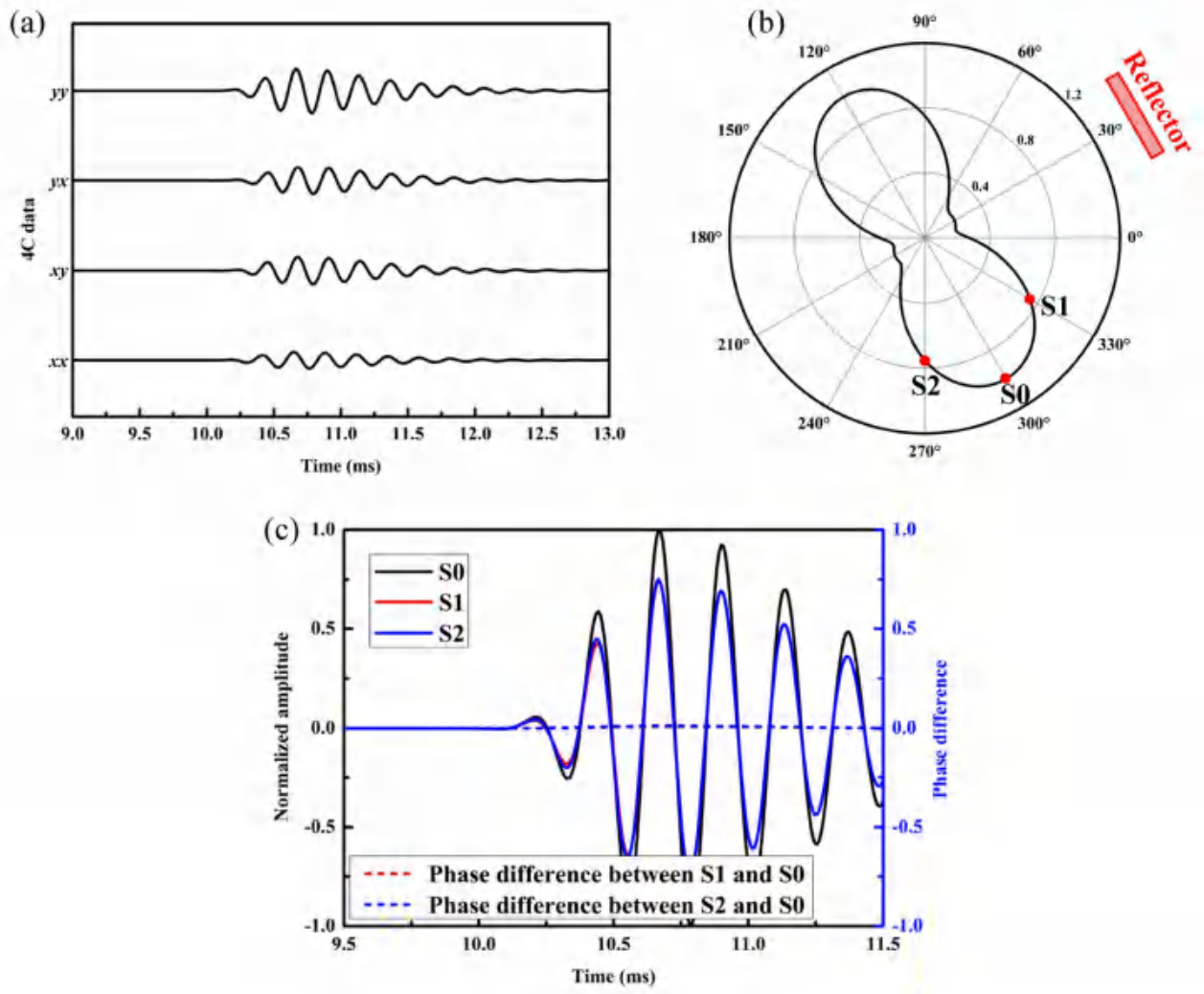


Figure 7 (a) Simulated 4C dipole S-wave reflection data for the conventional acquisition configuration; (b) the azimuthal amplitude variation pattern from the 4C data; (c) comparison of waveforms on both sides of the optimal imaging azimuth with the waveform at that azimuth and the phase difference between them.

S-wave imaging, we propose a new full-azimuth dipole acquisition method using a multi-azimuth data reception and combination configuration based on eq. (8). As shown in Figure 8, for the four reception azimuths, the data at each azimuth is combined with the data from the neighbouring two azimuths, breaking the symmetrical reception configuration of the conventional dipole data acquisition. This innovation provides a method for identifying the azimuth of reflectors outside the borehole.

Using the same theoretical model and computational parameters as those in Figure 7, the simulated 4C S-wave reflection data for the new acquisition configuration is shown in Figure 9a. The amplitude versus azimuth plot (Figure 9b) is similar to that of conventional dipole (Figure 7b), inheriting the strike determination capability of the conventional dipole. Worth noting is that the amplitudes of waveforms S1 and S2 on both sides of the strike are unequal, especially, S1 exhibits a phase lead relative to S0 with a positive phase difference, as indicated by the red dashed line in Figure 9c, while S2 shows a phase lag relative to S0 with a negative phase difference, as indicated by the blue dashed line in Figure 9c. Note, there is a significant phase shift between S1 and S2, and further, the polarity (positive/negative) of this phase shift correlates directly with the azimuth of the reflector outside the borehole. Specifically, an opposite reflector position induces a sign flip in the phase difference.

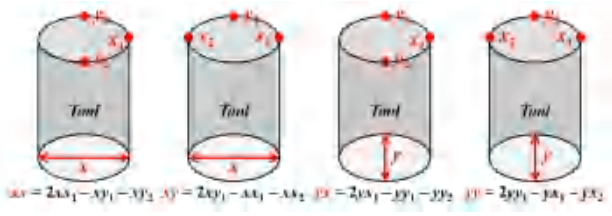


Figure 8 Schematic diagram of data acquisition configuration for the new full-azimuth dipole shear reflection imaging logging tool.

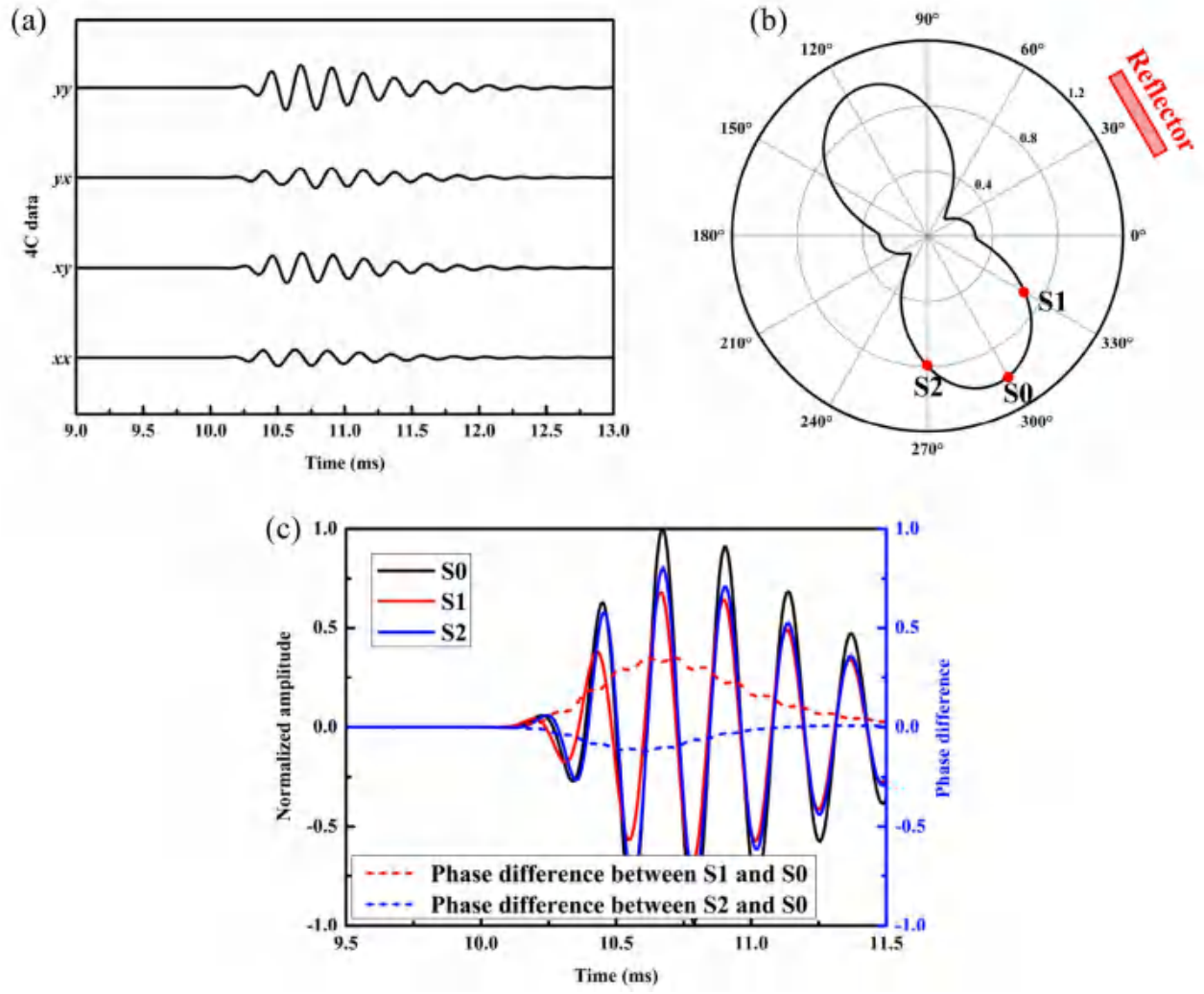


Figure 9 (a) Simulated 4C dipole S-wave reflection data for the new acquisition configuration; (b) the azimuthal amplitude variation pattern from the 4C data; (c) comparison of waveforms on both sides of the optimal imaging azimuth with the waveform at that azimuth and the phase difference between them.

This phenomenon provides the theoretical foundation for the new data acquisition method, which resolves the azimuthal 180°-ambiguity in dipole shear reflection imaging.

3. Experimental verification in model test wells

The above theoretical calculation results demonstrate that extracting the phase shift between reflected signals on both sides of the reflector strike can effectively resolve the azimuthal 180°-ambiguity in the dipole S-wave imaging. An experiment also carried out in the laboratory model test wells to validate the proposed data acquisition method and the associated theoretical modeling results.

3.1 Experimental ideas and theoretical validation

Su et al. (2024) demonstrated the monopole wavefield equivalence between the radiated P wave from a nearby borehole and the reflected P wave from the reflector outside the measurement hole. Using the same method, we investigate the applicability of the dipole S wave with the experimental design schematic illustrated in Figure 10a. A dipole source placed in a nearby borehole sequentially radiates SH and SV waves towards the measurement hole, where a rotating system with multi-azimuth off-axis receiver is used to record the waves. The measurement is done by rotating the system 360° at a 10° increment, in order to determine the wave incident (the simulated reflector) azimuth. Comparative results of two forward modeling approaches are presented in Figure 10b (SH wave) and Figure 10c (SV wave), where black solid lines denote the reflection modeling and red dotted lines represent the counterpart from the virtual source radiation analogy. All waveforms are normalized by the azimuthally received maximum SH-wave amplitude. Simulation results from both modeling show near-perfect agreement, demonstrating that the dipole waves excited in a nearby borehole can equivalently simulate the

reflected waves from a reflector outside the measurement borehole. This equivalence provides fundamental support for the acquisition of 4C dipole S-wave reflection data in the laboratory model test wells while saving the need of constructing physical reflectors outside the borehole.

3.2 Experimental methods and analysis of measurement results

Based on theoretical simulations, we conducted the downhole azimuthal dipole reflected S-wave data acquisition experiment using the same experimental method and model well configuration as Su et al. (2024). Note that dipole, instead of monopole, source was used. The internal assembly of the dipole source is shown in the magnified view at the top left of Figure 11a, consisting of four pairs (long and short groups) of trilaminar transducer with a center frequency of 3 kHz. The azimuthal receiver consists of four off-axis receiving transducers spaced at 90° to each other, enabling downhole azimuthal rotation measurement. The experimental test wells contain a 5 m thick homogeneous formation section with a central measurement well and eight surrounding sub-wells spaced at 45° around the central well. The central well has a diameter of 25 cm. Each sub-well

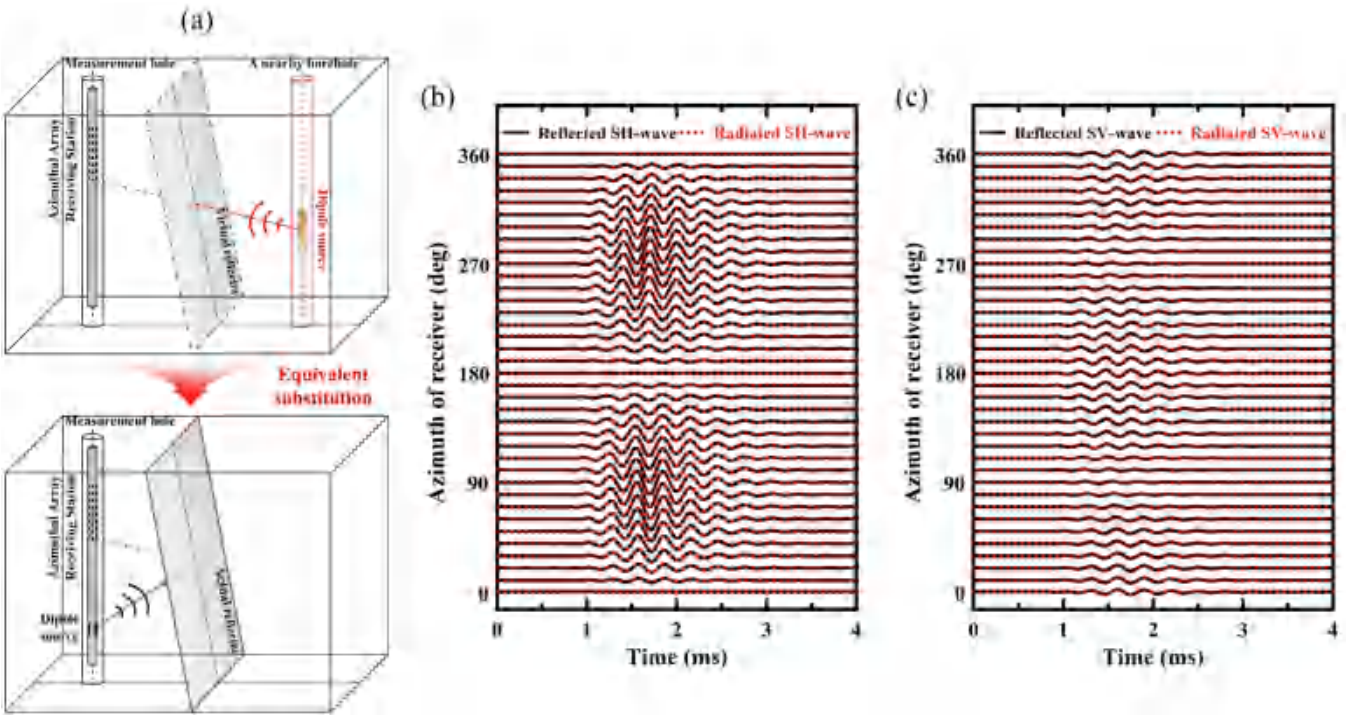


Figure 10 Schematic diagram illustrating the concept for simulating the reflected wave from the reflector outside the borehole using the virtual source radiation model to simulate the reflection model (a). The resulting SH wave (b) and SV wave (c) modeling from both models are identical.

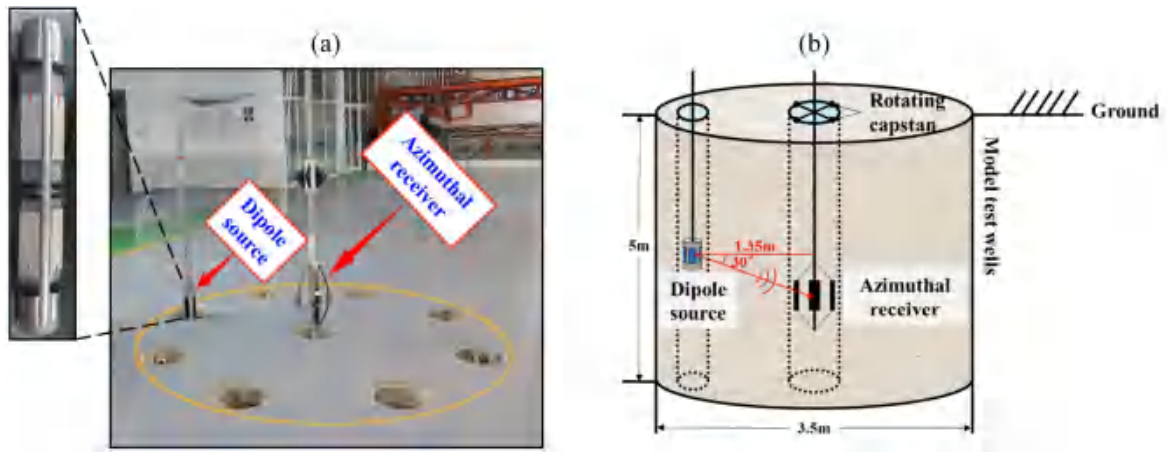


Figure 11 The physical diagram of experimental configuration (a) and the schematic of the relative position of the transmitter-receiver system (b).

(10 cm diameter) is positioned 1.35 m from the central well. The formation between the wells has a P-wave velocity of 3200 m s^{-1}, S-wave velocity of 2040 m s^{-1}, and density of 2250 kg m^{-3}, respectively. During the experiment, the dipole source and azimuthal receiver are lowered into a sub-well and the measurement well, respectively, with the source 0.78 m above the receiver (the source radiation angle is set to 30° downward from the horizontal, as shown in Figure 11b). By periodically turning the ground-level capstan, the azimuthal receiver in the measurement well is rotated 360° circumferentially with a 10° increment, acquiring 37 waveform channels.

3.2.1 *Azimuthal amplitude response of measured data*

As shown in Figures 12a and 13a, when the dipole source in the sub-well orients perpendicular (parallel) to the central well direction, the azimuthal receivers in the measurement well receive the pure SH wave (pure SV wave). Relative to the sub-well positioned at 180° azimuth in the geodetic coordinate system, the measured SH- and SV-wave waveforms in the measurement well are shown in Figures 12b and 13b, respectively. The experimental data agree well with the theoretical simulations in Figure 10, showing the typical dipole azimuthal variation characteristics. When the receiver orientation is parallel (perpendicular) to the source orienta-

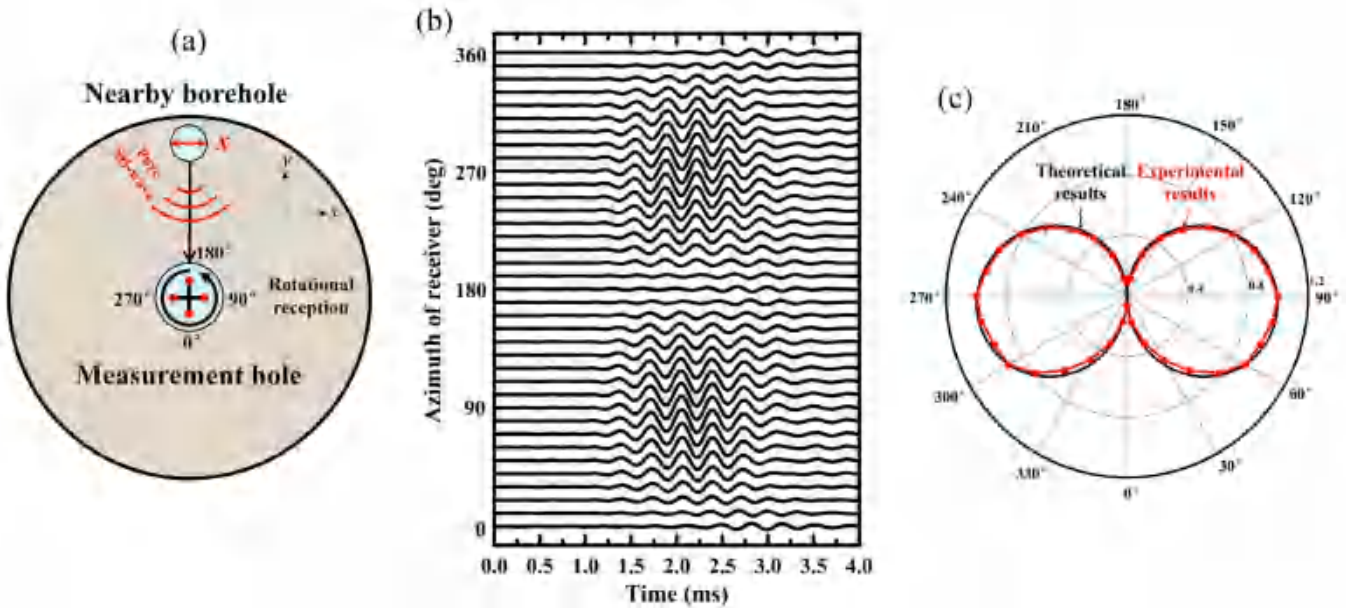


Figure 12 Schematic of azimuthal reception experiment for dipole SH wave (a), measured waveforms (b) and amplitude azimuthal variation pattern (c).

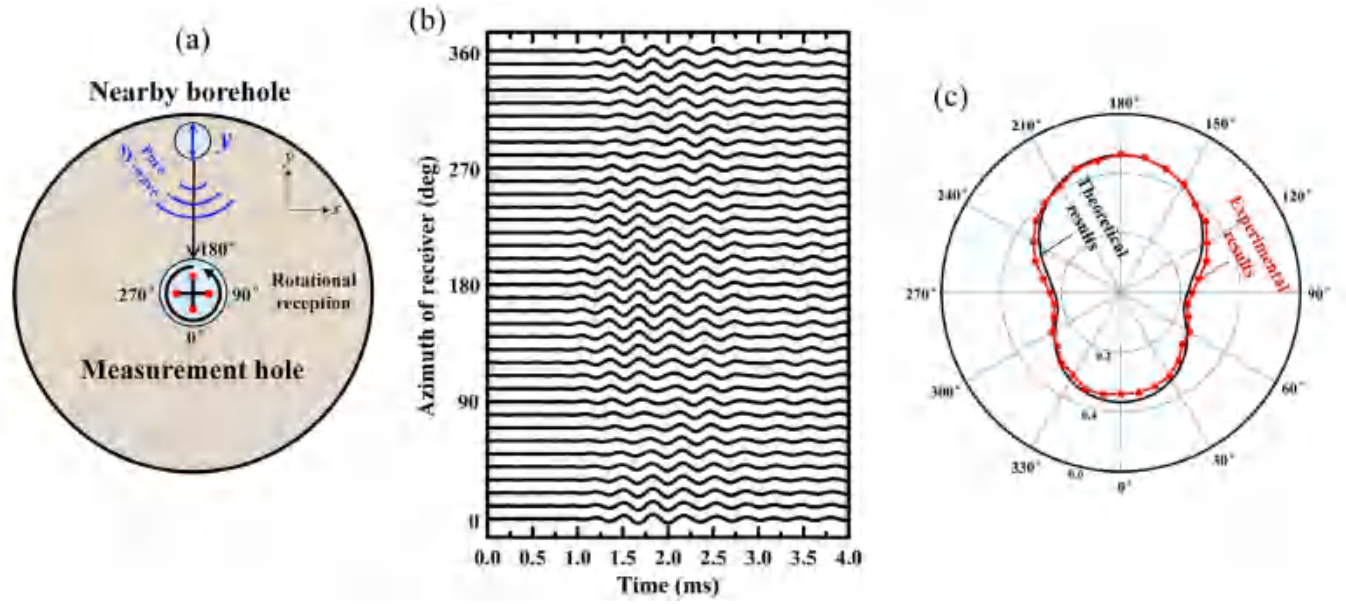


Figure 13 Schematic of azimuthal reception experiment for dipole SV wave (a), measured waveforms (b) and amplitude azimuthal variation pattern (c).

tion, the SH wave amplitude reaches its maximum (minimum), accompanied by polarity reversal on both sides of the y-axis. When the receiver azimuth coincides with the sub-well azimuth, the SV wave amplitude attains its maximum value with the same waveform polarity at all azimuths. All waveforms are normalized by the maximum amplitude of the azimuthally received SH waves, and the normalized SH- and SV-wave amplitude versus azimuth patterns are shown in Figures 12c and 13c, respectively. The experimental results (red dotted lines) exhibit trends consistent with theoretical results (black solid lines), confirming the reliability of the experimental measurement data.

3.2.2 Phase shift characteristics of signals on both sides of the optimal imaging azimuth

Based on the above experimental measurements, the source orientation perpendicular to the wave propagation direction in Figure 12a is defined as the x-direction (generating pure SH wave), where the waveforms received at 90° (270°) and 180° (360°) azimuths in Figure 12b correspond to the xx_1 (xx_2) and xy_1 (xy_2) components, respectively. Similarly, the source orientation parallel to the wave propagation direction in Figure 13a is defined as the y-direction (generating pure SV wave), with the waveforms acquired at 90° (270°) and 180° (360°) azimuths in Figure 13b corresponding to the yx_1 (yx_2) and yy_1 (yy_2) components, respectively. Based on this, the eight components are combined into the conventional and new 4C data using the respective data acquisition methods shown in Figures 6 and 8. The respective results are shown in Figures 14a and 15a. Coordinate-rotation analysis of the 4C data, i.e., the amplitude versus azimuth plots (Figures 14b and 15b), shows that the strike of the virtual reflector outside the measurement hole aligns with the 90°/270° azimuth in the geodetic coordinate system, consistent

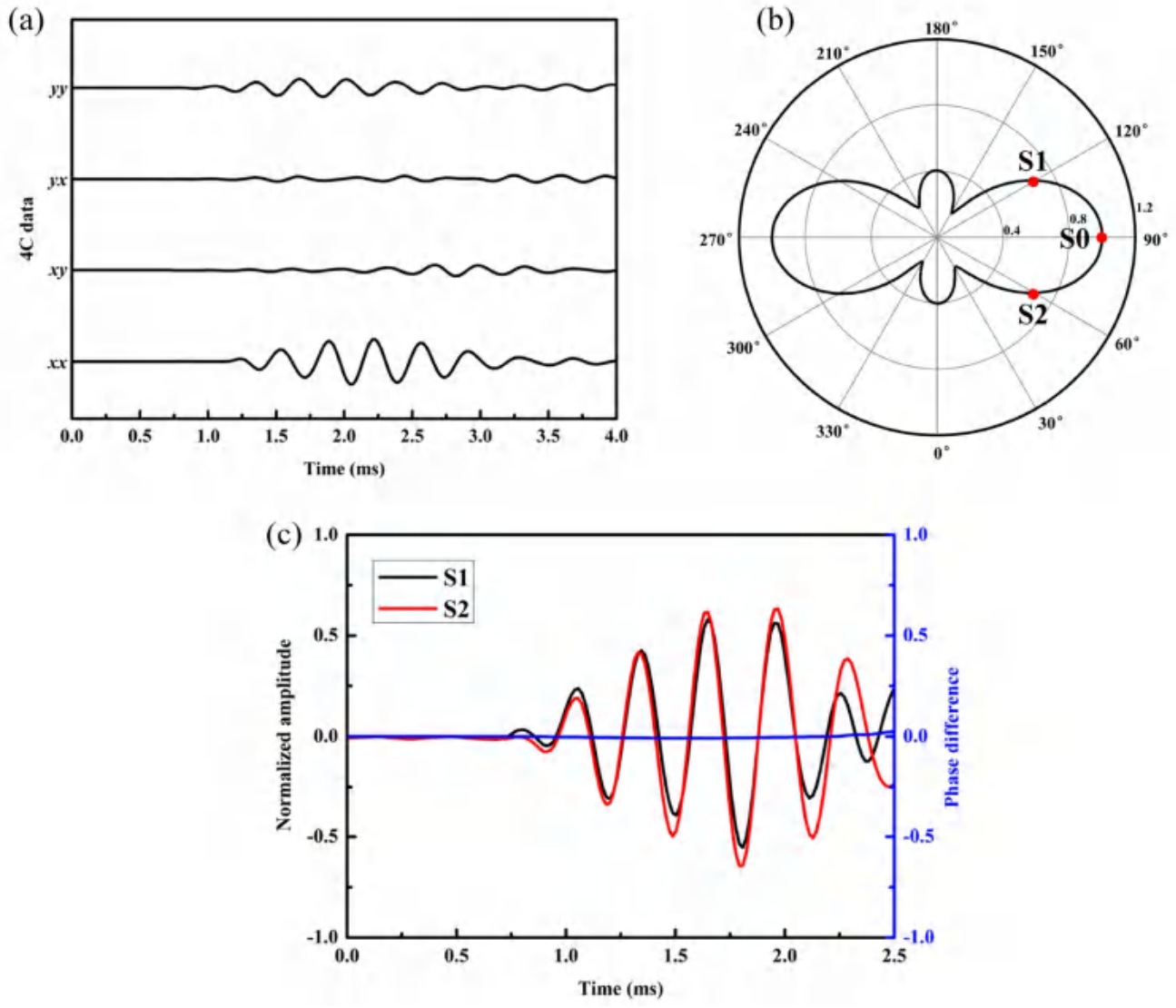


Figure 14 (a) Experimentally measured conventional 4C dipole S-wave reflection data; (b) The azimuthal amplitude variation pattern from the 4C data; (c) Comparison of waveforms at the opposite sides of the optimal imaging azimuth and their phase difference.

with the experimental model. As shown in Figure 15c, for the new data combination result, there is a significant phase shift (S1 leads S2 with a positive phase difference) between the reflection signals at 30° off the optimal imaging azimuth (90°, S0), specifically at 120° (S1) and 60° (S2). In contrast, the phase difference between S1 and S2 in the conventional acquisition is nearly zero (see Figure 14c). The experimental results agree well with the theoretical analysis presented in Figures 7 and 9, validating the new data acquisition method.

4. The new full-azimuth dipole shear reflection imaging tool and field test

Based on theoretical analysis and experimental verification, we developed a new full-azimuth dipole shear reflection imaging tool. Field tests conducted in a horizontal development well in the Tarim oil field demonstrated its effectiveness for field application.

4.1 The tool structure

Figure 16 shows the new full-azimuth dipole shear reflection imaging tool and structure, which consists of four main parts: A transmitting electronic cartridge, an orthogonal dipole transmitting acoustic system, an acoustic isolator, and a receiving electronic cartridge. The transmitting and receiving electronic cartridges control signal transmission and acquisition, respectively. The acoustic isolator is used to suppress the interference from direct signals propagating along the tool. The receiving part consists of four azimuthally placed array receiver strips, each containing eight receivers with a 0.1524 m spacing, enabling independent acquisition of array signals for the four azimuths. This design meets the new data

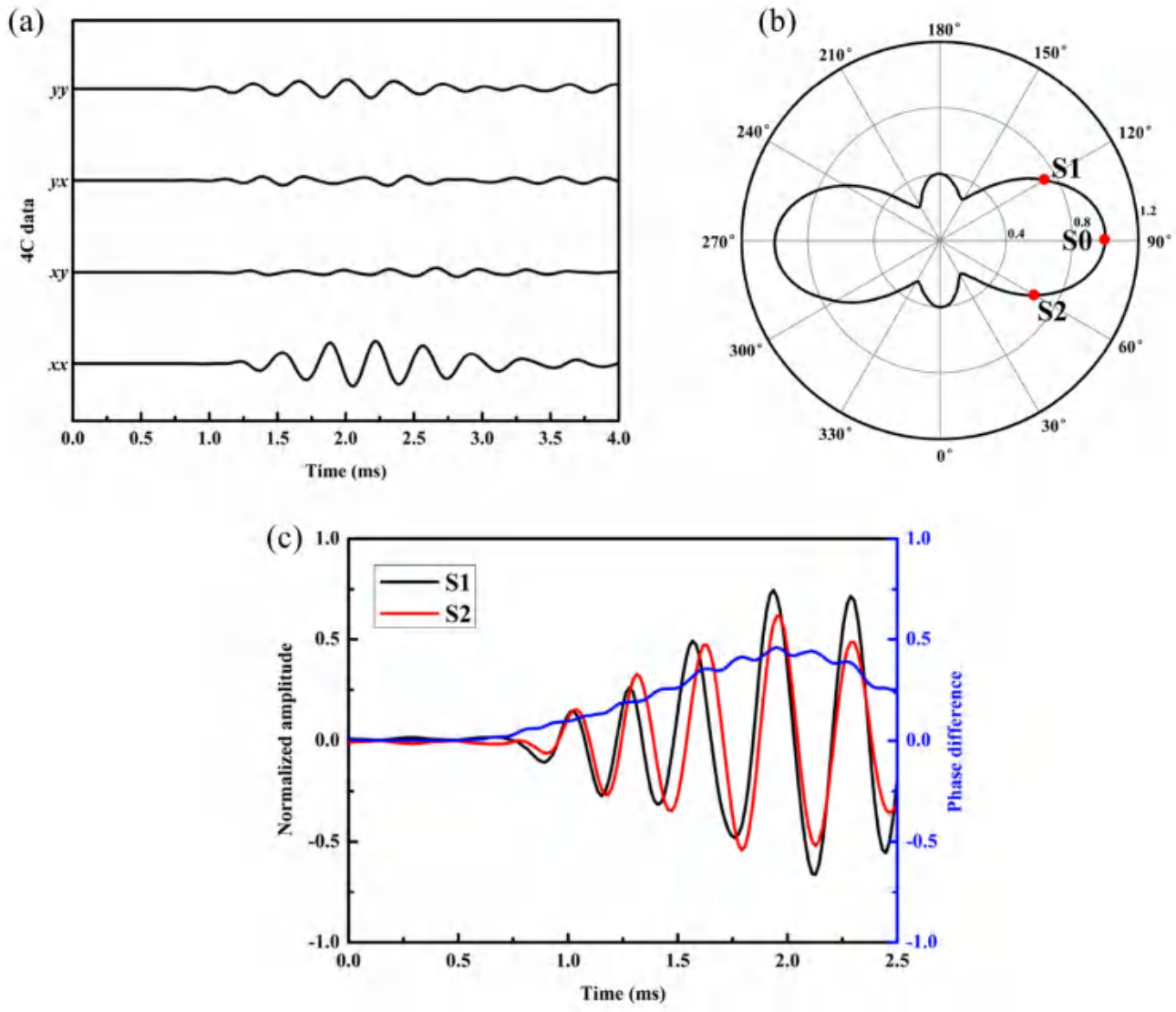


Figure 15 (a) Experimentally measured new 4C dipole S-wave reflection data; (b) The azimuthal amplitude variation pattern from the 4C data; (c) Comparison of waveforms at the opposite sides of the optimal imaging azimuth and their phase difference.

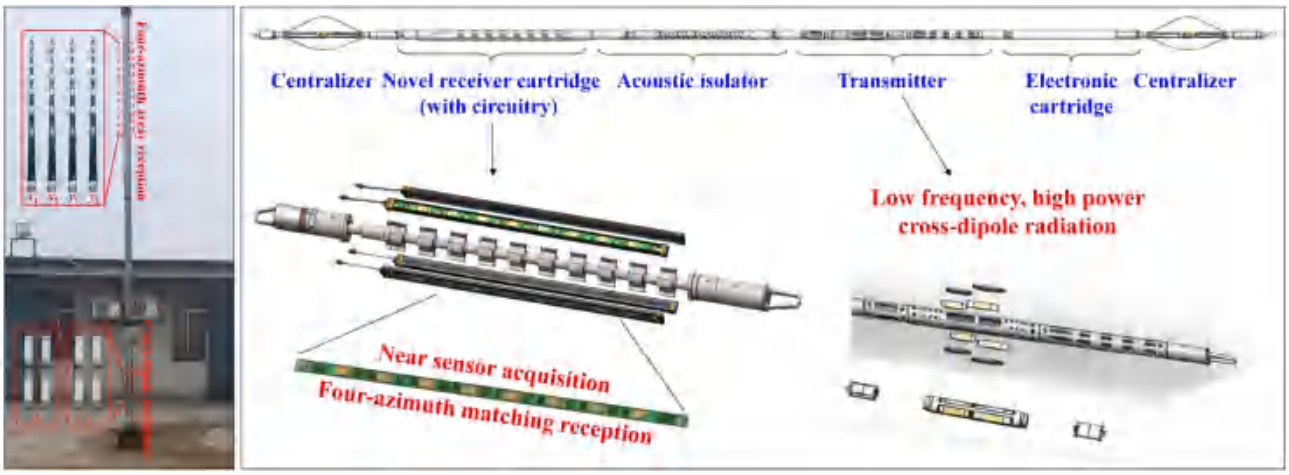


Figure 16 The new full-azimuth dipole shear reflection imaging tool and its structural diagram.

acquisition requirements for the azimuthal shear reflection imaging application.

4.2 Field application example

Figure 17 shows a field application example of the new tool in a horizontal development well in the Tarim oil field through a fault-karst structure showing the data processing results for the X060–X187 m well section. In panel 1, the gamma ray (GR) log curve indicates the carbonate lithology in this well section. The well deviation curve (DEV) shows that this interval is highly deviated, with a deviation angle of approximately 80°, and the tool azimuth curve (RB) shows that the logging tool azimuth is almost invariant throughout this interval, with the tool *y*-axis oriented between 330° and 360° relative to the high side of the borehole. The P- and S-wave slowness curves (DTP and DTS) in panel 2 indicate hard formations within this interval, with P-wave slowness values averaging 150 μs m^{-1} and S-wave slowness approximating 300 μs m^{-1}. Anomalously high slowness values occur in the X100–X115 m depth interval. Panels 3 and 4 present imaging profiles at 30°/210° (optimal imaging) and 120°/300° (blurrest imaging) azimuths (relative to the borehole high-side), respectively. The results reveal two reflectors intersecting the borehole at an angle within this depth interval, extending approximately 65 m radially outward from the borehole. The X065–X100 m and X130–X185 m intervals correspond to reflectors 1 and 2, respectively. Comparing the image intensity of the two profiles, reflectors 1 and 2 are best imaged in the 30°/210° azimuth, while the reflectors almost disappear in the 120°/300° azimuth, indicating that both reflectors strike along the 30°/210° direction. This interpretation is supported by the single-point amplitude versus azimuth plot (see panel 5). However, due to the inherent 180°-ambiguity in the 4C data rotation, the azimuths of these two reflectors could be either 120° or 300°.

To resolve the azimuth ambiguity, we extract the phase difference between the reflection signals on both sides of the strike and compare it with the theoretical results. The phase difference between the imaging data from the 60°/240° profile (S1) and the 0°/180° profile (S2) is compared, with the results displayed in panel 6 of the figure. Here, red (blue) indicates that signal S1 leads (lags) S2 at the corresponding depth, representing a positive (negative) phase difference. Notably, within the depth intervals corresponding to reflector 1 (reflector 2), signal S1 lags (leads) S2, demonstrating that the two reflectors have opposite azimuths. Panel 7 gives the theoretical modeling results at the X150 m (corresponding to reflector 2), comparing the waveforms and their phase differences on both sides of the optimal imaging azimuth for two reflector azimuths: 120° and 300°. Theoretical predictions demonstrate that S1 leads (lags) S2 with a positive (negative) phase difference when the reflector is positioned at 120° (300°) azimuth. Based on the actual phase difference results shown in panel 6, the azimuth of reflector 2 is at 120° azimuth, and that of reflector 1 is at 300°. The reflection image plot is shown in panel 8, which shows that the borehole trajectory has penetrated through a fault-karst body approximately 30 m thick, with two detected reflectors representing its upper and lower boundaries. Combined with the borehole azimuth (due east) and deviation angle, it is concluded that the fault-karst body strikes northeast and dips southeast, with a dip angle of approximately 60°. Due to the unconsolidated and highly attenuative material within the fault-karst body, as shown by the abnormally large measured values within the X100–X115 m interval (panel 2), the reflection signals within the interbed are weak and thus cannot image the internal structure of the fault body. The imaging interpretation is consistent with actual geological conditions, verifying the validity of the imaging and azimuth estimation results.

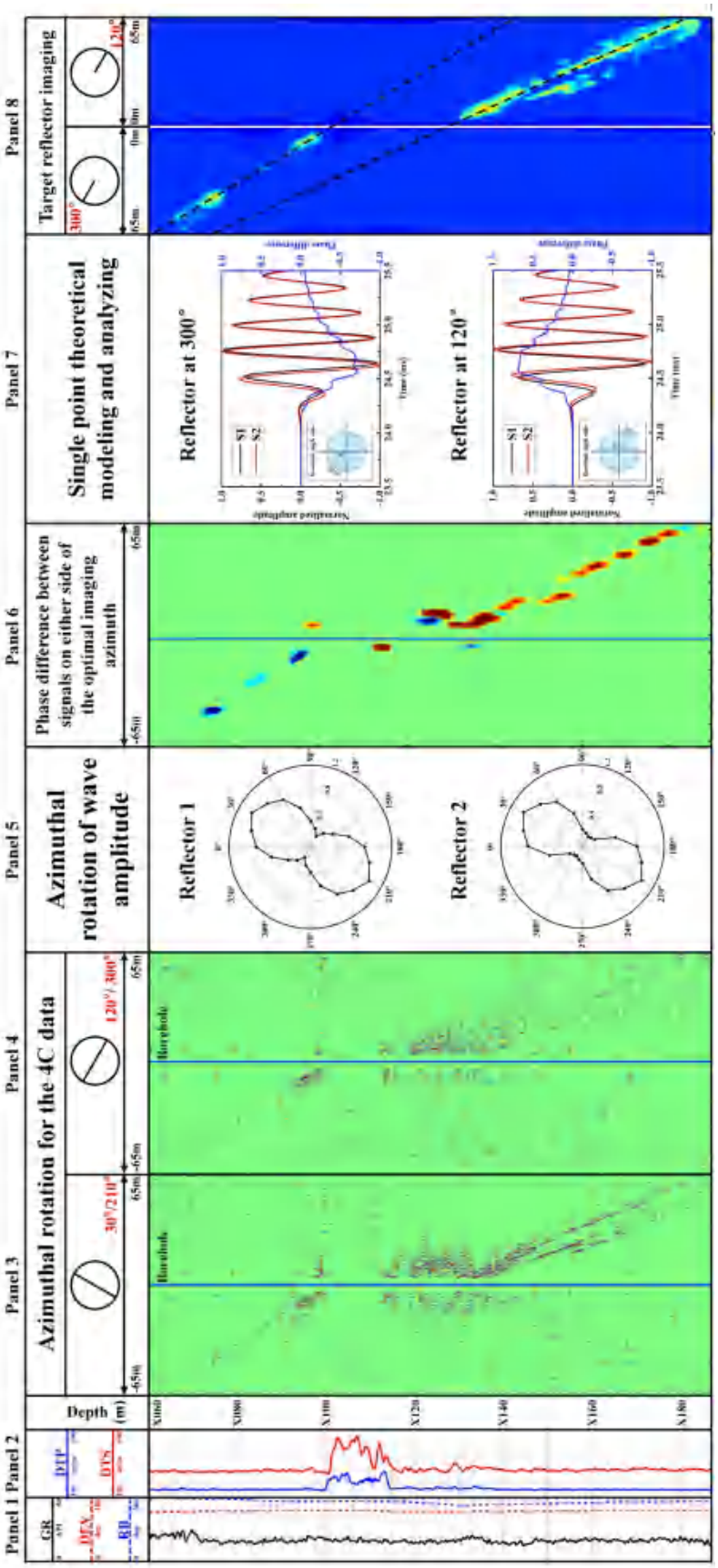


Figure 17 Field example of new full-azimuth dipole shear reflection imaging logging.

5. Conclusion

This study addresses the azimuthal 180°-ambiguity problem in dipole shear reflection imaging through a comprehensive theoretical modeling, experimental verification and field validation test of a new azimuthal dipole S-wave reflection imaging tool. By analyzing elastic wave interactions with a reflector outside the borehole, we systematically investigate the azimuthal response characteristic of the reflected S-wave in the borehole and demonstrate the inherent ambiguity in conventional 4C dipole measurement configurations. Based on this, we propose a new full-azimuth dipole acquisition method combining data from neighbouring azimuths, from which the phase difference between the reflected signals on both sides of the reflector strike can be used to solve the 180°-ambiguity problem in azimuth determination for dipole S-wave imaging. Experimental results from the model test wells confirmed the validity of the proposed method. Field applications successfully imaged a near-borehole fault-karst structure and determined its orientation, validating the developed technology.

Acknowledgements *The authors express sincere gratitude to the editorial board and the two anonymous reviewers for their valuable comments and suggestions, which significantly improved the manuscript. Appreciation is extended to Mr. Qingbin Guo, Mr. Chengsen Zhang, and Mr. Wenxing Duan from Tarim oil field for their field experiment support. Special thanks are given to Dr. Yanghu Li, Dr. Xihao Gu, and Mr. Lingwen Kong from China University of Petroleum (East China) for their contributions to theoretical analysis and experimental work. This work was supported jointly by the National Natural Science Foundation of China (Grant Nos. U21B2064 and 42174145), the Natural Science Foundation of Shandong Province (Grant No. ZR2024YQ062), the Laoshan National Laboratory Science and Technology Innovation Project (Grant No. LSKJ202203407), and the Major Scientific and Technological Projects of China National Petroleum Corporation (Grant No. ZD2019-183-004).*

References

Aki K, Richards P. 1980. Quantitative Seismology: Theory and Methods. San Francisco: W. H. Freeman & Co

Bennett N N. 2019. 3D slowness time coherence for sonic imaging. Geophysics, 84: D179–D189

Cao J J, Tang X M, Wei Z T. 2014. Radiation of an acoustic dipole source in open and cased borehole with application to single-well shear-wave imaging (in Chinese). Chin J Geophys, 57: 1683–1692

Gong H, Chen H, He X, Wang X M. 2015. Eliminating the azimuth ambiguity in single-well imaging using 3C sonic data. Geophysics, 80: A13–A17

Gong H, Chen H, He X, Su C, Wang X M, Wang B C, Yan X H. 2018. Modeling and inversions of acoustic reflection logging imaging using the combined monopole–dipole measurement mode. Appl Geophys, 15: 393–400

Hirabayashi N, Sakiyama N, Ikegami T. 2017. Characteristics of waveforms recorded by azimuthally spaced hydrophones of sonic logging tool for incident plane waves. Geophysics, 82: D353–D368

Lee S Q, Chen M, Gu X H, Su Y D, Tang X M. 2019. Application of four-component dipole shear reflection imaging to interpret the geological structure around a deviated well. Appl Geophys, 16: 291–301

Li S Q, Su Y D, Tang X M. 2020. Research on a fast inversion method for structural strike around a borehole based on four-component dipole shear wave reflection imaging (in Chinese). Chin J Geophys, 63: 2478–2487

Li C, Zhang B, Xu X K, Zhang J Y, Chen H, He X, Wang X M. 2020. Theory and application of multicomponent azimuthal remote exploration acoustic logging (in Chinese). J Appl Acoust, 39: 292–299

Li Y H, Tang X M, Li H R, Lee S Q. 2021. Characterizing the borehole response for single-well shear-wave reflection imaging. Geophysics, 86: D15–D26

Li Y H. 2023. Fundamental theory and application of borehole azimuthal acoustic reflection imaging logging (in Chinese). Doctoral Dissertation. Qingdao: China University of Petroleum (East China)

Su Y D, Tang X M, Hei C, Zhuang C X. 2011. An equivalent-tool theory for acoustic logging and applications. Appl Geophys, 8: 69–78

Su Y D, Rao B, Kong L W, Li S Q, Tan B H, Zhuang C X, Tang X M. 2024. Azimuthal reflected P-wave imaging: Theory, experiment and field application (in Chinese). Chin J Geophys, 67: 630–640

Tang X M, Cheng C H. 2004. Quantitative Borehole Acoustic Methods. Netherlands: Elsevier Science Publishing Inc

Tang X M. 2004. Imaging near-borehole structure using directional acoustic-wave measurement. Geophysics, 69: 1378–1386

Tang X M, Patterson D J. 2009. Single-well S-wave imaging using multicomponent dipole acoustic-log data. Geophysics, 74: WCA211–WCA223

Tang X M, Wei Z T. 2012. Single-well acoustic reflection imaging using far-field radiation characteristics of a borehole dipole source (in Chinese). Chin J Geophys, 55: 2798–2807

Tang X M, Cao J J, Wei Z T. 2014. Shear-wave radiation, reception, and reciprocity of a borehole dipole source: With application to modeling of shear-wave reflection survey. Geophysics, 79: T43–T50

Tang X M, Cao J J, Li Z, Su Y D. 2016. Detecting a fluid-filled borehole using elastic waves from a remote borehole. J Acoust Soc Am, 140: EL211–EL217

Tang X M, Gu X H, Li Y H, Su Y D. 2021. The interaction between borehole and elastic waves: theory, method and application (in Chinese). Chin J Geophys, 64: 4227–4238

Xu J Q, Hu H S, Wang Z. 2019. Asymptotic solution to a 3D dipole single-well imaging system with combined monopole and dipole receivers with an application in elimination of azimuth ambiguity. Geophysics, 84: D191–D207

Xu J Q, Hu H S. 2020. Study on the radiation and reception of the wave field in a single-well imaging system with an eccentric source (in Chinese). Chin J Geophys, 63: 3545–3561

Yang H J, Xiao C W, Qi X Z, Gao C Q. 2014. New Logging Evaluation Technology for Carbonate Condensate Gas Reservoirs in Tarim Basin (in Chinese). Beijing: Petroleum Industry Press

Zhang Y D, Hu H S. 2014. A technique to eliminate the azimuth ambiguity in single-well imaging. Geophysics, 79: D409–D416

Zhao T, Che X H, Qiao W X, Cheng L. 2023. Borehole azimuthal acoustic imaging using 3D spatial scanning: Application in acoustic detection of nearby wells. Geophysics, 88: D131–D145

Zhao T, Che X H, Qiao W X. 2024. Azimuth estimation method for borehole acoustic reflection imaging using an acoustic vector array. IEEE Trans Geosci Remote Sens, 62: 1–10

(Editorial handling: Xingyao YIN)

苏远大，饶博，孔令文等. 2024. 井中方位纵波远探测:理论、实验与现场应用. 地球物理学报,67(2):630-640,doi:10.6038/cjg2023R0249.

Su Y D, Rao B, Kong L W, et al. 2024. Azimuthal reflected P-wave imaging: theory, experiment and field application. *Chinese J. Geophys.* (in Chinese),67(2):630-640,doi:10.6038/cjg2023R0249.

井中方位纵波远探测:理论、实验与现场应用

苏远大[1,2,3]，饶博[1,2]，孔令文[1,4]，李盛清[1,2,3]*，谭宝海[1,2,3]，庄春喜[1,2,3]，唐晓明[1,2,3]

1 中国石油大学(华东)地球科学与技术学院，青岛 266580

2 深层油气全国重点实验室(中国石油大学(华东))，青岛 266580

3 崂山实验室海洋矿产资源评价与探测技术功能实验室，青岛 266071

4 中国石化石油勘探开发研究院无锡石油地质研究所，无锡 214126

摘要 能够测量井外数十米地质构造距离和方位的远探测声波测井正成为一种重要的地球物理应用技术.1:1 地层条件下井外含反射界面的远探测测量和分析为此技术提供了物理验证.本文首先利用虚源和柱面波展开理论推导了充液井孔中单极反射纵波方位接收声场的解析形式,通过模拟证明了单井的声波辐射和接收与双井之间的辐射和接收的等效性,在此基础上提出利用两口模型井来实现方位纵波远探测实验,即在测量井中放置多方位反射纵波接收声系,在另一口副井中放置单极子声源向测量井定向辐射纵波以等效来自井外地质体的反射波,依托实验室的模型井群进行井中方位纵波远探测实验研究.实验测量结果表明井中接收反射纵波的幅度和到时对井外反射体(定向辐射波)具有较好的方位灵敏度,可由此来实现井外地质异常体的精准定位.在理论与实验指导下自主设计研制了方位纵波远探测仪器样机并开展了现场井测试成功获得高信噪比的方位反射信号,充分验证了方位纵波远探测技术的准确性和有效性.

关键词 单极纵波远探测；平行双井模型；实验测量；测井仪器；方位接收响应

doi:10.6038/cjg2023R0249 **中图分类号** P631 **收稿日期** 2023-04-22，2023-08-24 **收修定稿**

Azimuthal reflected P-wave imaging: theory, experiment and field application

SU YuanDa[1,2,3], RAO Bo[1,2], KONG LingWen[1,4], LI ShengQing[1,2,3]*, TAN BaoHai[1,2,3], ZHUANG ChunXi[1,2,3], TANG XiaoMing[1,2,3]

1 *School of Geosciences, China University of Petroleum (East China), Qingdao* 266580, *China*

2 *National Key Laboratory of Deep Oil and Gas, China University of Petroleum (East China), Qingdao* 266580, *China*

3 *Laboratory for Marine Mineral Resources, Laoshan Laboratory, Qingdao* 266071, *China*

4 *Wuxi Research Institute of Petroleum Geology, Sinopec Petroleum Exploration and Production Research Institute, Wuxi* 214126, *China*

Abstract Azimuthal acoustic reflection imaging logging, which can measure the distance and azimuth of geological bodies within a range of tens of meters beside the borehole, is becoming an important technology for geophysical applications. Measurements and analysis for single-well

基金项目 国家自然科学基金(42074137,U21B2064,41821002,42174145),崂山国家实验室科技创新项目(LSKJ202203400),山东省自然科学基金(ZR201911120382),中国石油重大科技项目(ZD2019-183-004),中国石油大学(华东)研究生创新基金项目和中央高校基本科研业务费专项资金(23CX04016A)联合资助.

第一作者简介 苏远大,男,1978 年生,博士,教授,主要从事声波测井理论、方法及处理研究. E-mail:syuanda@sina.com

***通讯作者** 李盛清,男,1988 年生,博士,副教授,主要从事声波测井理论、方法及处理研究. E-mail:shidalishengqing@yeah.net

(C)1994-2024 China Academic Journal Electronic Publishing House. All rights reserved. http://www.cnki.net

acoustic reflection imaging in the model with 1∶1 reflection interface outside the borehole provide physical validation of this technique. In this paper, the analytical solution for the response wavefield of monopole P-wave in the fluid-filled borehole is deduced first by using the virtual source analogy combined with the cylindrical wave expansion method. The simulation proves that the radiation wave from the nearby borehole is equivalent to the reflected wave from the reflector outside the borehole. On this basis, the experimental idea of using two model wells to achieve the verification experiment of single-well azimuthal reflected P-wave imaging is proposed. That is, a multi-directional receiving acoustic system is placed in the measurement hole, and a monopole source is placed in the other nearby borehole to radiate P-waves to the measurement hole in order to equate the reflected P-waves from the interface outside the borehole. And the experiment about azimuthal reflected P-wave imaging logging was carried out relying on the laboratory model well group. The experimental measurement results show that the amplitude and arrival time of the azimuthal reflected P-wave are sensitive to the azimuth of the reflector outside the borehole (directional radiation wave), based on which the precise positioning of geological anomalies outside the borehole can be realized. Under the guidance of theoretical simulation and experiment, the prototype of azimuthal acoustic reflection imaging logging tool was designed and developed independently and field tests were conducted to successfully obtain azimuthal reflected P-wave with high signal-to-noise ratio, which fully verified the reliability and effectiveness of the azimuthal acoustic reflection imaging logging technology in measuring the azimuth of reflectors outside the borehole.

Keywords　Monopole P-wave reflection imaging; Parallel two-well model; Experimental measurement; Logging tool; Azimuthal reception response

0　引言

声波远探测成像测井技术是近年来不断发展且在缝洞型非均质储层中被广泛应用的井筒探测新技术，其在溶洞、裂缝等地质异常体的探测中获得了较好的应用成效，是非常规隐蔽性油气藏勘探开发的利器(Gong et al., 2018; Xu et al., 2019; Lee et al., 2019; Bennett, 2019; 董经利等, 2020).

声波远探测主要有单极纵波和偶极横波两大类成像测井方法(Hornby, 1989; 薛梅等, 2002; Tang and Patterson, 2009; 唐晓明等, 2012; Tang et al., 2016; 古希浩等, 2020; 刘汇鑫等, 2021). 其中单极纵波成像测井技术最早由 Hornby 提出，单极辐射高频纵波的波长较小，有利于小尺度地质散射体的探测，但声源均匀辐射不具备方位分辨能力；Tang(2004)提出的低频偶极反射横波测井技术方位灵敏度高，探测距离远，受直达波干扰小. 偶极四分量坐标旋转可以实现对井旁地质异常体全方位精细成像，确定其走向(Tang et al., 2014). 但偶极声源固有的对称辐射特性导致了反射体成像的 180° 方位模糊问题，不能进一步确定反射体倾向. 因此，精准识别井外反射体的方位成为了当前声波远探测领域的攻关重点. 为了唯一确定反射体的方位，Zhang 和 Hu(2014)提出检测接收波形中位移和声压分量的极性来精确定位反射体. Gong 等(2015)提出三维接收传感器可用于消除反射体方位的不确定性，继而又提出一种单偶极混合测量新方法联合常规测井资料来综合判断反射体方位(Gong et al., 2018). Li C 等(2021)提出利用偶极反射纵波来消除反射 SH 横波引起的方位模糊问题. 除此之外，还可以环向布置多方位接收器，利用方位接收信息来定位反射体(Haldorsen et al., 2006; Hirabayashi et al., 2017). 许家旗和胡恒山(2020)和 Li Y H 等(2021,2022)分别提出在井中放置偏心点源和方位偏心接收器的新型非对称测量模式来解决声波远探测中反射体的定位问题. 为了进一步论证声波远探测技术的方位识别能力，本建林(2020)开展了无井孔的水下方位实验研究. 但其实验模型未考虑井孔对弹性波调制的影响，且由于 1∶1 地层条件下井外含反射界面的固体介质模型构建困难，建造工程量巨大，一直未见有针对性的物理实验建模，因此仍需进一步开展井中方位远探测物理验证实验.

(C)1994-2024 China Academic Journal Electronic Publishing House. All rights reserved.　http://www.cnki.net

基于此,本文提出利用两口模型井来实现方位纵波远探测实验,即在测量井中放置多方位反射纵波接收声系,在另一口副井中放置单极子声源向测量井定向辐射纵波以等效井外地质体的反射波,规避了实际地层中构建反射体的难题. 从理论和实验方面验证了方位纵波远探测技术的准确性和有效性. 最后,给出自研样机在现场实测数据的成像实例. 本文的研究工作为方位纵波远探测技术的推广和运用提供了实验及理论支撑.

1 方位纵波远探测理论

1.1 井中方位远探测接收声场的解析解

图 1a 给出了在柱坐标系(r,ϕ,z)中由虚源理论表征的单极声波远探测示意图. 在点声源上方间隔 45°周向排布 8 个方位接收器. 接收横截面如图 1b 所示,图中标识符 a 表示井孔半径,e 表示接收器的偏心距离.

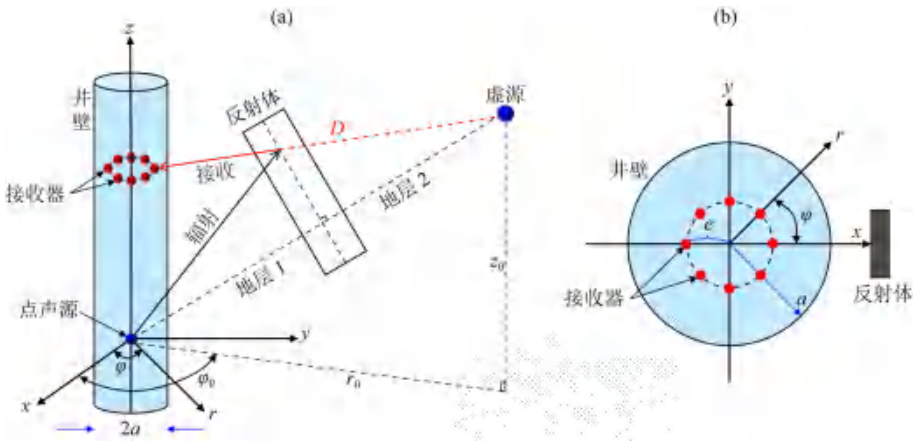


图 1 虚源理论表征的单极声波远探测示意图(a)及井中方位接收截面图(b)

Fig. 1 The schematic model of monopole single-well reflection imaging based on the virtual source theory (a) and the cross section of borehole receiving configuration using azimuthally spaced off-axis receivers (b)

井外存在反射体时,单极点源激发的辐射纵波被反射回井中,其接收表达式可写为(Tang et al., 2014):

$$Iwv(\omega) = S(\omega)\cdot RD_{\mathrm{P}}(\omega)\cdot RF_{\mathrm{P}}(\omega)\cdot\frac{\mathrm{e}^{\mathrm{i}\omega D/\alpha}}{D}, \quad (1)$$

式中,ω 为圆频率;S 为声源频谱;RD_{P} 为单极纵波在井外地层中的辐射函数(曹景记等,2016);RF_{P} 为纵波在反射体处的反射系数,可通过 Zoeppritz 方程求得(Aki and Richards, 1980);D 为纵波在地层中的传播总距离;α 为地层的纵波波速.

利用互易定理,考虑两次井孔的调制可以快速模拟多极子声波反射声场(Tang et al., 2014; 曹景记等, 2016; 许家旗和胡恒山, 2019),但这只限于分析井中发射-接收系统完全居中的情况,无法对井内接收声场的方位变化进行精细刻画. 因此,利用虚源法将反射体的反射等效成声源在反射体另一侧的镜像点的辐射,如图 1a 中红线所示. 公式(1)中的球面波传播因子可表示成无穷阶多极柱面波的叠加(Tang and Cheng, 2004; Li C et al., 2021):

$$\frac{\mathrm{e}^{\mathrm{i}\omega D/\alpha}}{D} = \frac{1}{\pi}\int_{-\infty}^{+\infty}\sum_{n=0}^{\infty}\varepsilon_n \mathrm{K}_n(pr_0)\mathrm{I}_n(pr)\cos[n(\varphi-\varphi_0)]$$
$$\times \mathrm{e}^{\mathrm{i}k(z-z_0)}\,\mathrm{d}k, \quad (2)$$

式中,(r_0,φ_0,z_0)为点虚源的位置;I_n 和 K_n 分别为第一类和第二类 n 阶变型贝塞尔函数,n 为方位序数;ε_n 为纽曼因子,$n=0$ 时 $\varepsilon_n=1$,$n>0$ 时 $\varepsilon_n=2$;$D=[r^2+r_0^2-2rr_0\cos(\varphi-\varphi_0)+(z-z_0)^2]^{1/2}$;$k$ 和 p 分别为入射纵波的轴向和径向波数,$p=(k^2-\omega^2/\alpha^2)^{1/2}$.

将公式(2)代入公式(1)中,可得到点虚源入射纵波的位移势表达式:

$$\phi^{\mathrm{i}} = S(\omega)\cdot RD_{\mathrm{P}}(\omega)\cdot RF_{\mathrm{P}}(\omega)\sum_{n=0}^{\infty}\varepsilon_n \mathrm{I}_n(pr)\mathrm{K}_n(pr_0)$$
$$\times\cos[n(\varphi-\varphi_0)], \quad (3)$$

式中,上标 i 表示入射波场.

当点虚源激发的入射纵波与井眼相互作用时,弹性波在井壁处会产生散射与透射效应. 基于亥姆霍兹分解理论,地层中的散射位移场 $\boldsymbol{u}_{\mathrm{s}}$ 可以由散射纵波位移势 ϕ_{s},SH 横波位移势 χ_{s} 以及 SV 横波位移势 Γ_{s} 联立表示. 井内流体中的透射位移场 $\boldsymbol{u}_{\mathrm{f}}$ 可以由透射纵波的位移势 ϕ_{f} 表示(Tang and Cheng, 2004). 其中各位移势在(ω,k)域内具有以下形式的通解:

(C)1994-2024 China Academic Journal Electronic Publishing House. All rights reserved. http://www.cnki.net

$$\begin{cases} \phi_{\mathrm{f}} = \sum_{n=0}^{\infty}[A_n\cos(n\varphi)+A'_n\sin(n\varphi)]\mathrm{I}_n(fr)\mathrm{K}_n(pr_0) & (0<r<a) \\ \phi_{\mathrm{s}} = \sum_{n=0}^{\infty}[B_n\cos(n\varphi)+B'_n\sin(n\varphi)]\mathrm{K}_n(pr)\mathrm{K}_n(pr_0) \\ \chi_{\mathrm{s}} = \sum_{n=0}^{\infty}[D_n\sin(n\varphi)-D'_n\cos(n\varphi)]\mathrm{K}_n(sr)\mathrm{K}_n(pr_0) & (r>a) \\ \Gamma_{\mathrm{s}} = \sum_{n=0}^{\infty}[F_n\cos(n\varphi)+F'_n\sin(n\varphi)]\mathrm{K}_n(sr)\mathrm{K}_n(pr_0) \end{cases}, \tag{4}$$

式中，$f=(k^2-\omega^2/\alpha_{\mathrm{f}}^2)^{1/2}$ 为井内流体中纵波的径向波数；α_{f} 为流体纵波波速；$s=(k^2-\omega^2/\beta^2)^{1/2}$ 为井外地层中横波的径向波数，β 为地层横波波速；$A_n(A'_n)\sim F_n(F'_n)$ 为各介质层待求解的振幅系数，求解步骤详见附录 A.

将求解得到的透射纵波位移势函数 ϕ_{f} 代入关系式 $p_{\mathrm{f}}=\rho_{\mathrm{f}}\omega^2\phi_{\mathrm{f}}$ 中，并结合最速下降法(Tang and Patterson，2009)可计算井中接收到的声压信号：

$$p_{\mathrm{f}}=\frac{\mathrm{e}^{\mathrm{i}\omega D/\alpha-\mathrm{i}\pi/4}}{D}\sum_{n=0}^{\infty}\rho_{\mathrm{f}}\omega^2[A_n\cos(n\varphi)+A'_n\sin(n\varphi)]\times\mathrm{I}_n(f_0r), \tag{5}$$

式中，ρ_{f} 为流体密度；$f_0=((k_0^{\mathrm{i}})^2-\omega^2/\alpha_{\mathrm{f}}^2)^{1/2}$ 为流体纵波的径向波数，$k_0^{\mathrm{i}}=(\omega/\alpha)\cos(\pi-\theta_i)$ 为入射纵波波数的梯度根，θ_i 为入射波的方向与井轴正方向的夹角；$D=[r_0^2+(z-z_0)^2]^{1/2}$，此处的 D 与公式(1)和公式(2)中等同，其中与径向距离 r 有关的项在满足远场辐射条件的情况下($r_0\gg\mathrm{r}$)被省略了；径向距离 r 和方位 φ 与图 1b 中对应，取 $r=e$ 并改变接收方位角 φ 即可模拟井中不同位置处的接收响应.

1.2　数值模拟结果与分析

采用如图 1 所示的方位纵波远探测模型，设置反射体为 0°方位上距离井轴 6 m 的倾角为 85°的裂缝面. 声系源距为 1 m. 接收器偏离井轴 0.09 m，即 $e=0.09$. 声源距模型底部高 1 m，采用主频为 10 kHz 的 Gauss 子波(带宽为 1.5 kHz). 计算所用的井孔及地层参数如表 1 所示.

表 1　模型的声学参数

Table 1　Acoustic parameters of the model

介质参数	纵波速度 /(m·s^{-1})	横波速度 /(m·s^{-1})	密度 /(kg·m^{-3})	外径 /m
流体	1500	—	1000	0.12
地层 1	3500	1800	2600	∞
地层 2	4500	3000	2500	∞

图 2a 给出了 8 方位接收纵波的计算结果，发现反射纵波的幅度和波至对井外反射体的方位敏感. 正对反射体接收时，波形的到时早，振幅高(如 0°方位接收波形所示). 相反，背对反射体接收时，波形的到时滞后，振幅减小(如 180°方位接收波形所示). 保持其余参数不变，只增加接收器个数(减小接收器环向间隔)加密计算，并通过阈值法提取各方位接收波形到时(波至)，如图 2b 所示. 发现反射波到时随接收器方位呈规律性变化. 越靠近反射体，接收波至越早(越远离反射体，接收波至越晚)，这与波的传播距离有关. 进一步根据到时曲线开时窗计算各方位窗内接收波形能量(时窗长固定为 300 μs)，将各方位窗内能量归一化后绘制于极坐标系中，如图 2c 所示. 井中接收波形的幅值响应具有明显的方位特征，接收纵波的方位幅值曲线整体向靠近反射体方向偏移，且波形振幅最大值所在的方位对应于反射体方位. 因此根据方位接收反射波的到时或振幅信息可以定位井外反射体.

2　模型井中方位纵波远探测实验验证

以上理论模拟表明，根据方位接收反射波的到时和振幅信息来定位井外反射体是可行的. 下面通过实际尺寸的物理实验来验证方位纵波远探测技术的准确性和有效性. 由于 1∶1 地层条件下井外含反射界面的固体介质实测模型构建难，因此设计了一种验证方位纵波远探测技术可行性的平行双井模型，在副井中定向辐射单极纵波来等效井外界面的反射波以实现测量井中方位纵波远探测的等效验证实验.

2.1　实验思想与理论验证

采用平行双井模型，如图 3 所示，在副井中放置一单极子膨胀声源向井外均匀辐射纵波，在测量井中偏心放置多方位接收器环向 360°接收波形，来等效替代井外存在反射体的情况. 首先从理论上验证上述实验思想的正确性. 副井中单极点源辐射的纵

(C)1994-2024 China Academic Journal Electronic Publishing House. All rights reserved.　http://www.cnki.net

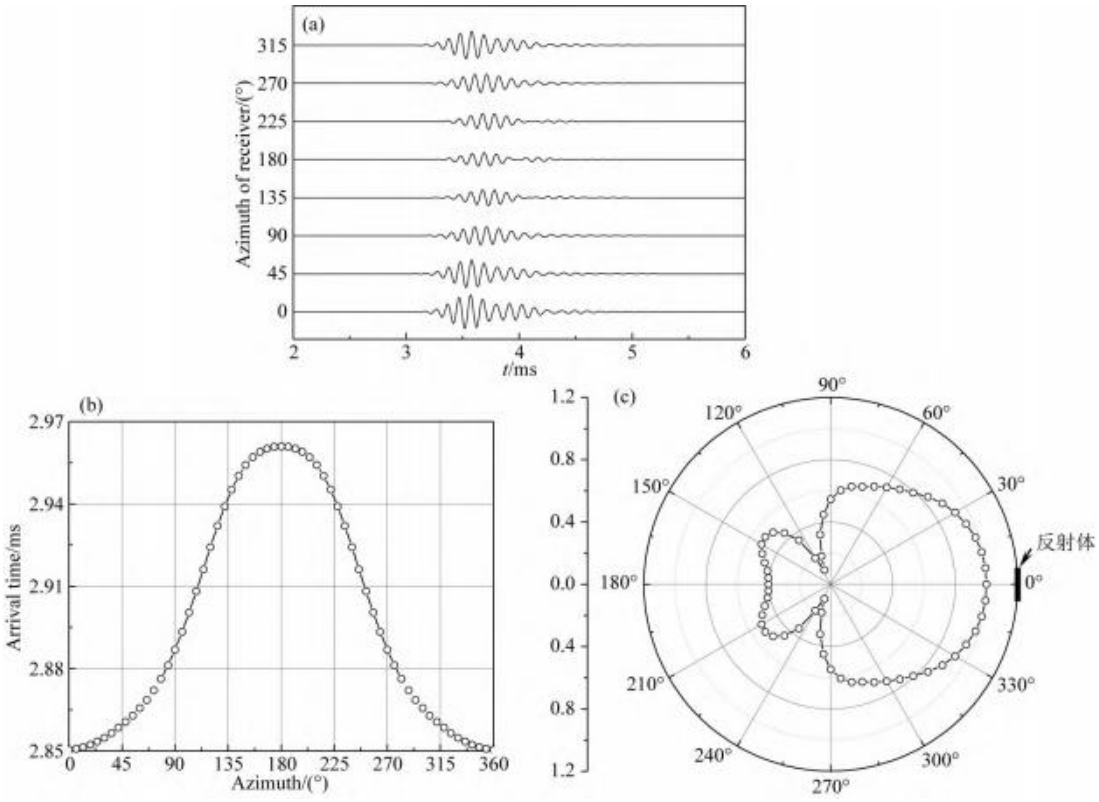


图 2 单极纵波入射引起的井内流体响应

(a) 方位接收波形；(b) 方位反射纵波到时；(c) 归一化的方位振幅.

Fig. 2 The borehole-fluid response for monopole P-wave incidence

(a) Azimuthal received waveform; (b) Arrival time of azimuthal reflected P-wave; (c) Normalized azimuthal amplitude.

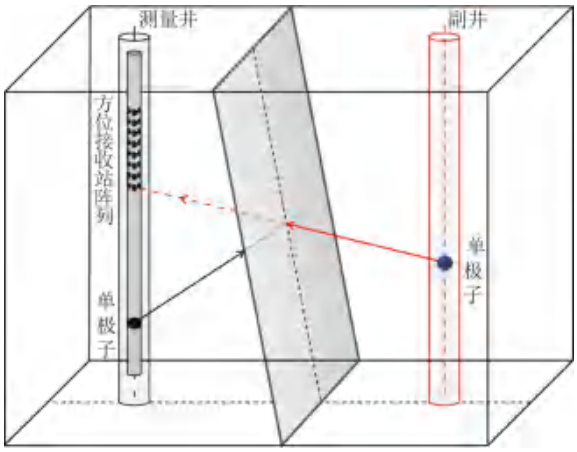


图 3 模拟界面反射波的实验思想示意图

Fig. 3 Schematic diagram of experimental ideas for simulating the reflected wave from the reflector outside the borehole

波以球面波的形式向测量井传播，在测量井井壁会产生散射与透射效应，与前节虚源入射的情况类似. 将单极声源置于副井中，通过求解测量井中的透射声场，即可实现井中方位接收波形的快速模拟.

设置两井眼尺寸相同，井间距 11.74 m，副井中声源位于单井发射源上方 0.027 m 处，其余参数与图 2 中一致. 计算结果如图 4a 中的红色点线所示，作为对比，图中也给出了利用虚源法计算的来自井外界面的方位反射波形(黑色实线). 各方位波形振幅均按照 0°方位接收纵波振幅的最大值归一化. 两种模型的波形计算结果几乎完全重合，从理论上验证了如图 3 所示的实验设计思想的正确性，证实了通过在相邻井中激发声波信号来等效替代井外反射体的反射信号是可行的，这样做的另一优势是可以避免单井发射和接收时井筒直达波的干扰，增强接收信号的信噪比. 图 4b 进一步对比了两种模型中 0°方位接收的波形，分别用红线和黑线表示，波形振幅按照副井中辐射纵波振幅的最大值归一化. 对比发现，两波形相位相同，但振幅差异明显，界面反射纵波的振幅约为副井中辐射纵波振幅的十分之一. 这是因为弹性波在界面处会发生反射、透射效应，并且反射系数一般小于透射系数.

2.2 实验方法与模型井设计

在理论仿真的基础上，下面采用平行双井模型进行物理实验研究. 图 5a 给出了实验室测量系统原理图. 将方位接收器 R 下放至测量井中，同时将单极子发射换能器 S 下放至旁边的副井中. 声源与功率放大器和信号发生器相连以驱动声波信号. 接收

(C)1994-2024 China Academic Journal Electronic Publishing House. All rights reserved. http://www.cnki.net

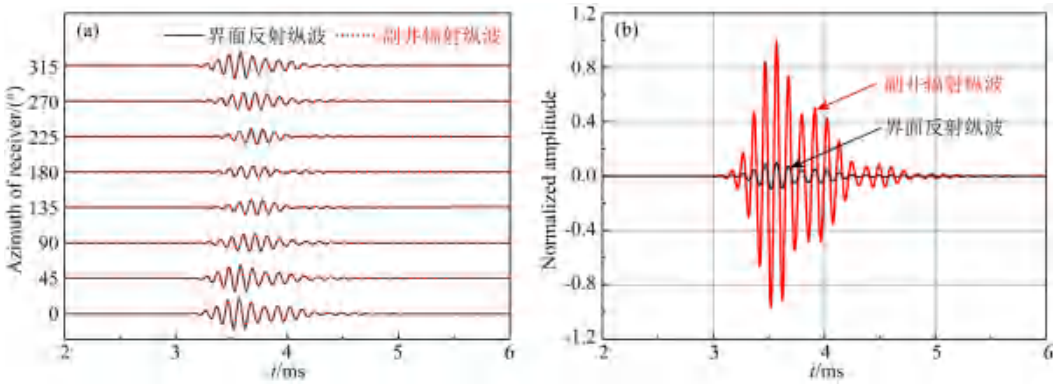


图 4　(a)测量井中方位接收的井外界面反射纵波和副井辐射纵波波形对比，波形振幅按 0°方位接收纵波振幅的最大值归一化；(b)0°方位接收波形对比，波形振幅按副井中辐射纵波振幅的最大值归一化

Fig. 4　(a) Comparison of the azimuthal receiving waveforms between the reflection P-wave from the reflector and the radiation P-wave from the nearby borehole. The amplitude of each curve is normalized by the maximum amplitude of the waveform received at 0°; (b) The comparison of the waveforms received at 0°. The amplitude of each curve is normalized by the maximum amplitude of the radiation P-wave from the nearby borehole

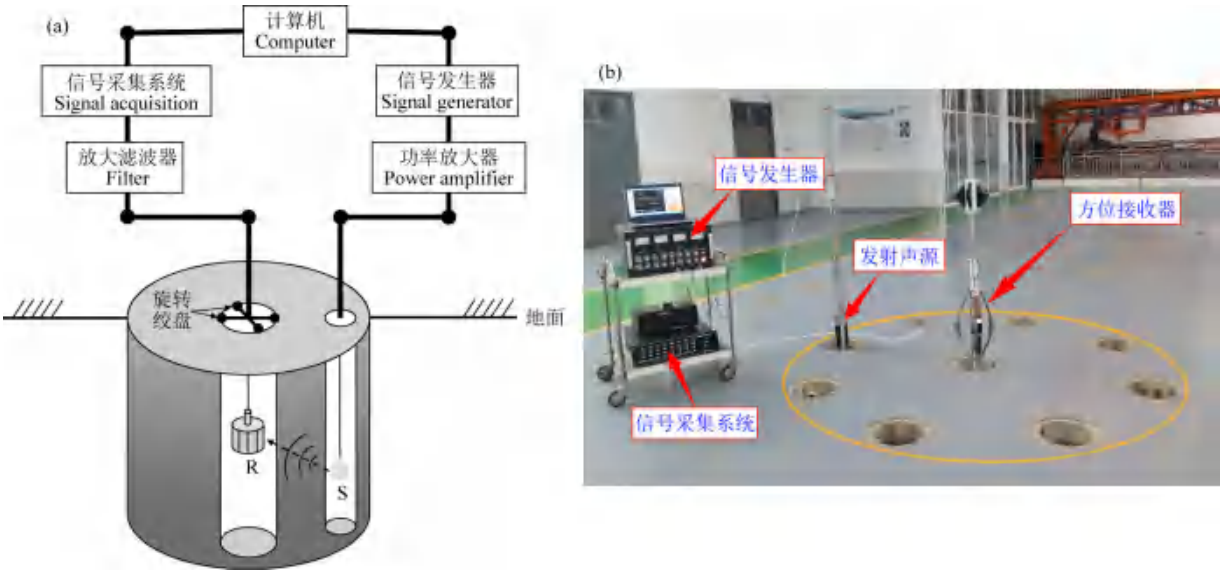


图 5　实验室测量系统原理图(a)及实验配置实物图(b)

Fig. 5　The schematic for the laboratory measurement system (a) and the physical diagram of experimental configuration (b)

器与放大滤波器和信号采集系统相连以接收声波信号. 信号的产生与数据的采集均由计算机控制. 固定井下发射声源，在地面规律旋转绞盘带动井下方位接收器旋转以实现在测量井中环向 360°方位接收，旋转间隔由人为控制. 在本次实验中固定旋转角为 10°，共记录 37 道波形. 声源函数采用三周期正弦脉冲信号，主频为 12 kHz；激励脉冲电压峰峰值为 400 V；波形记录采样点数为 1024，采样间隔为 2 μs.

图 5b 为配套的实验装置实物图，图中展示了在井口俯视拍摄的井群照片和配套的实验设备. 方位接收声系和单极子发射声系被分别悬挂在测量井和副井上方，其中方位接收器具备不接触井壁的居中/偏心测量和贴井壁测量两种工作模式，发射声源也可以居中或偏心工作(本次实验过程中，在发射声系下方安装了扶正装置，以降低声源偏心对远探测声波传播的影响). 地下的实验模型井群深 5 m，直径 3.5 m，由中心的测量井和井外分布八个方位的小副井眼构成. 其中测量井井眼直径为 25 cm，副井眼直径为 10 cm(井内均充注钻井液). 各副井眼环向间隔 45°排布，距离测量井中心 135 cm. 井间地层的声学参数见表 2.

2.3　实验测量结果分析

采用上述测量装置，使用电缆将发射声源下放至副井中 2.5 m 深度位置，将方位接收器下放至测量井中相同深度处，控制各瓣接收换能器偏离井轴 7 cm 接收. 定义 1 号接收极板的初始方位为 0°方

(C)1994-2024 China Academic Journal Electronic Publishing House. All rights reserved.　http://www.cnki.net

表 2 井间地层的声学参数

Table 2 Acoustic parameters of the formation between well group

纵波速度/(m·s^{-1})	横波速度/(m·s^{-1})	密度/(kg·m^{-3})
3200	2040	2250

位,声源方位角为 340°. 实验测量的全方位波形如图 6a 所示,图中红色点线为波至曲线,发现反射波的幅度和到时对井外反射体(定向辐射波)的方位敏感:正对声源接收时,波形的到时早,振幅高(如 300°～360°和 0°～20°方位接收波形所示). 相反,背对声源接收时,波形的到时滞后,振幅减小(如 60°～240°方位接收波形所示).

图 6b 给出了基于平行双井模型(图 3)理论计算的结果. 理论模型参数与实验室中模型井群相同(见表 2),声源和接收器位于相同深度,设置副井中单极子声源主频为 12 kHz,测量井中方位接收换能器偏心距为 7 cm. 理论计算波形的方位变化规律与实验测量结果相同. 图 6c、d 分别给出了进一步处理得到的反射波到时和能量随接收器方位变化的曲线. 图中红色点线为实测波形(对应图 6a)的处理结果,黑色实线为理论计算波形(对应图 6b)的处理结果. 实验与理论结果一致:正对声源接收,即 340°方位接收波形到时最早,振幅最高;背对声源接收,即 160°方位接收波形到时最晚,振幅小. 理论和实验的重复对比证实了方位纵波远探测技术的准确性和有效性.

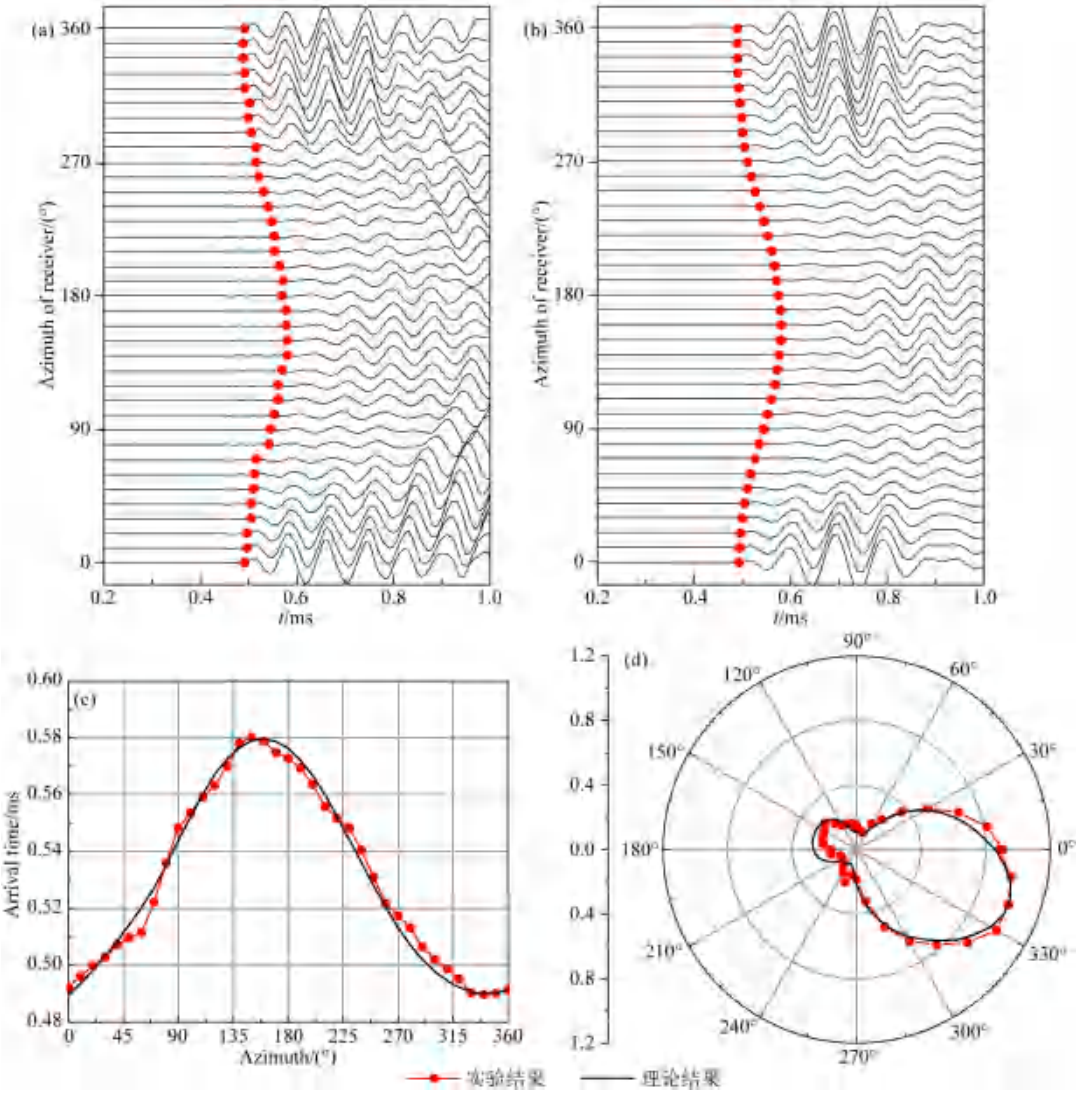


图 6 测量井中方位接收纵波响应

(a) 实验结果;(b) 理论结果;(c) 方位反射纵波到时;(d) 归一化的方位振幅.

Fig. 6 Azimuthal response of the received P-wave in the measurement borehole

(a) Experimental results; (b) Theoretical results; (c) Arrival time of azimuthal reflected P-wave; (d) Normalized azimuthal amplitude.

(C)1994-2024 China Academic Journal Electronic Publishing House. All rights reserved. http://www.cnki.net

3　方位纵波远探测声系设计与现场测试

在理论仿真和实验测量结果的指导下，团队自主研制了方位纵波远探测仪器样机，进行了现场井测试并取得了良好的应用效果.

3.1　方位远探测声波测井仪器

图 7 展示了方位纵波远探测仪器样机的实物照片. 仪器主要由单极子发射声源、隔声体和新型的接收短节（含阵列式方位接收器）组成. 其中发射电子短节和接收电子短节用于控制发射与接收信号的传输，隔声体用以消除在仪器中传播的直达信号.

阵列式方位接收器由 8 组间隔 0.1524 m 的接收站组成. 4 个独立工作的接收换能器组成一个接收站，负责采集来自不同方位的声波信号. 将位于同方位的 8 阵列接收换能器排布在同一接收条带上，并用波纹管密封以保证在超高温高压环境下换能器及电子器件稳定工作. 同时，将四条波纹管分别固定在仪器骨架的 4 个方位上，并在仪器外壳上对应的方位开孔（透声窗）来实现信号的高精度采集.



图 7　方位远探测声波测井仪器

Fig. 7　The logging tool for azimuthal acoustic reflection imaging

3.2　现场应用实例

图 8a 给出了方位纵波远探测仪器样机在某实验井中的实测结果. 测量过程中定义正东方位为 0° 方位，方位角沿逆时针方向增大. 图中第一道为岩性道，给出了井径（CAL）曲线和自然伽马（GR）曲线，显示了该测量井段井壁状况良好，岩性较纯. 第二道为深度道. 第三道给出了全方位接收波形的变密度图，图中颜色的深浅反应了波形振幅的强弱. 从图中可以看出，仪器记录的沿井传播的直达波到时早，幅度高，在远探测声波测井中常被视为干扰信号. 在强干扰噪声背景下，X415～X433 m 井段可以明显看到振幅较强的地层反射纵波信号（如图中红框标注处所示）.

在含反射体井段中提取单一深度点四方位接收条带记录的阵列波形绘制于图中第五道，从上至下分别显示了 0°，90°，180° 和 270° 方位接收的阵列波形. 为了避免高振幅直达波的干扰，图中仅显示了 8500 μs 后记录到的反射波波形. 对比发现，四个方位均记录到了高信噪比的反射纵波信号，但不同方位的反射波信号幅度存在明显差异，其中 90° 方位记录的波形振幅最高，其他方位接收的反射波幅度相对较弱. 进一步将相同源距处接收的四方位波形组合处理，来等效八方位环向扫描接收. 提取八方位波形的到时和窗内能量，分别如图 8b、c 所示. 图中显示 90° 方位（正北方位）接收到的反射纵波到时最早，振幅最高，可判定为该反射体的真实方位.

4　结论

针对声波远探测技术应用过程中，井外反射体方位定不准的难题，本文采用解析计算和物理实验相结合的方法研究了单极纵波远探测接收声场的方位响应，得出以下结论：

（1）利用虚源和柱面波展开理论推导了单极纵波远探测方位接收声场的渐进解，提供了一套方位纵波远探测声场快速计算方法.

（2）设计了一种验证方位声波远探测技术可行性的平行双井模型，从理论上预测了副井中定向辐射的弹性波与井外界面的反射波的等效性.

（3）物理实验测量和理论仿真的一致性证实了利用方位接收的反射波的到时和振幅信息定位井外反射体是可行的. 从理论和实验方面验证了方位纵波远探测技术的准确性和有效性.

（4）自主研制的方位纵波远探测仪器样机成功获得了高信噪比的地层反射纵波，且不同方位上反射信号的到时和幅度均存在明显差异，扫描接收处理后可以进一步确定井外反射体的方位. 本文工作为井外地质体的三维定位提供了依据.

(C)1994-2024 China Academic Journal Electronic Publishing House. All rights reserved.　http://www.cnki.net

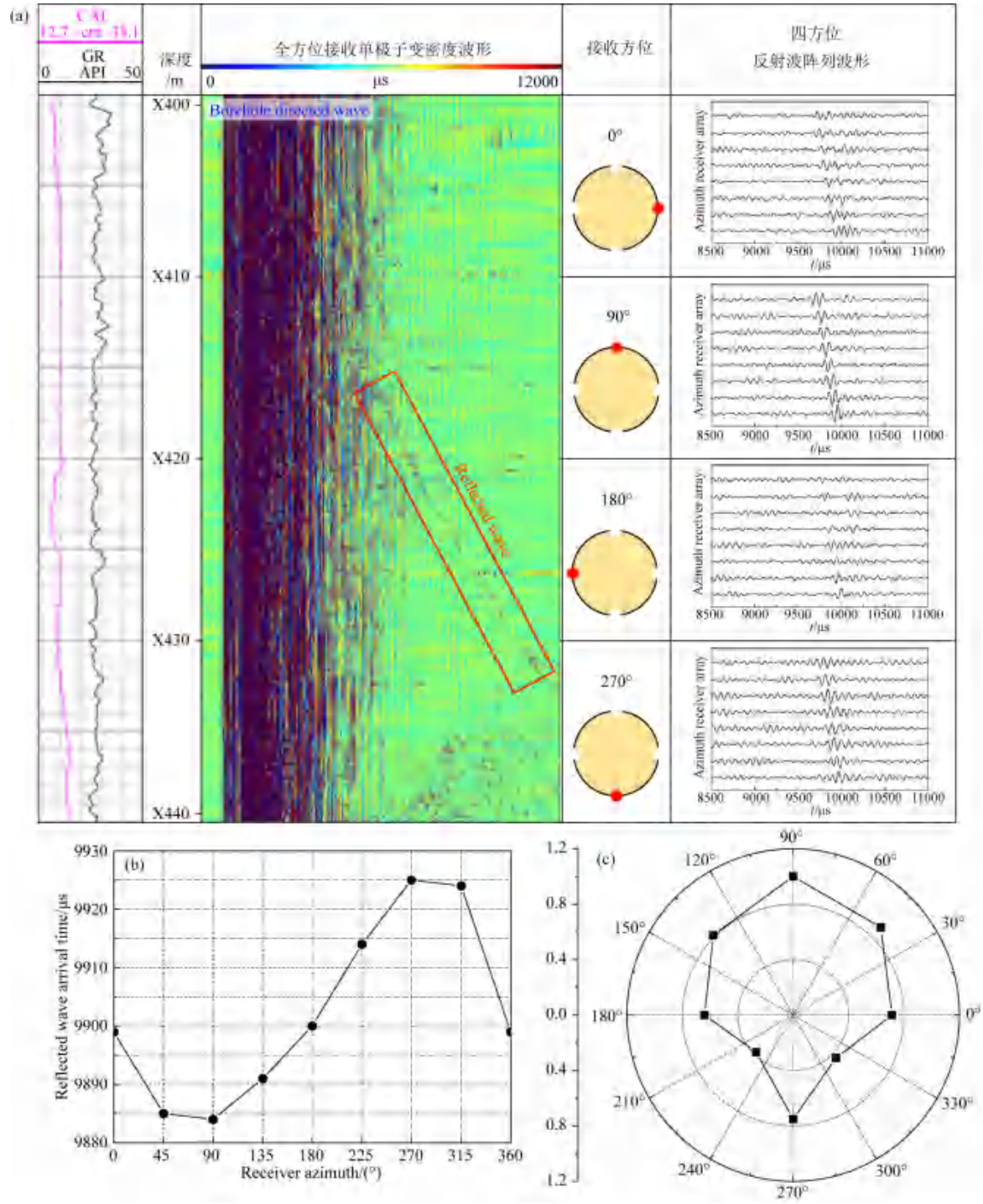


图 8 (a) 方位远探测声波测井现场实例；(b) 方位反射纵波到时；(c) 归一化的方位振幅

Fig. 8 (a) Field data of azimuthal acoustic reflection imaging; (b) Arrival time of azimuthal reflected P-wave; (c) Normalized azimuthal amplitude

附录 A 公式(4)中的振幅系数求解

点虚源激发的入射纵波与井眼相互作用，在井壁外侧(a^+)和内侧(a^-)的边界条件(径向位移和正应力连续，切应力为零)可写为

$$\begin{cases} u_r^{\mathrm{i}}(a^+)+u_r^{\mathrm{s}}(a^+)=u_r^{\mathrm{f}}(a^-), \\ \sigma_{rr}^{\mathrm{i}}(a^+)+\sigma_{rr}^{\mathrm{s}}(a^+)=\sigma_{rr}^{\mathrm{f}}(a^-), \\ \sigma_{r\varphi}^{\mathrm{i}}(a^+)+\sigma_{r\varphi}^{\mathrm{s}}(a^+)=0, \\ \sigma_{rz}^{\mathrm{i}}(a^+)+\sigma_{rz}^{\mathrm{s}}(a^+)=0. \end{cases} \tag{A1}$$

式中，上标 s 和 f 分别表示地层中的散射场和流体

(C)1994-2024 China Academic Journal Electronic Publishing House. All rights reserved. http://www.cnki.net

中的透射场. 由公式(3)和公式(4)计算出入射纵波、散射波和透射波的位移和应力，代入公式(A1)中可得到以下两个矩阵方程：

$$\boldsymbol{M}\begin{bmatrix}A_n\\B_n\\D_n\\F_n\end{bmatrix}=\begin{bmatrix}b_1\\b_2\\b_3\\b_4\end{bmatrix}\text{和}\boldsymbol{M}\begin{bmatrix}A'_n\\B'_n\\D'_n\\F'_n\end{bmatrix}=\begin{bmatrix}b'_1\\b'_2\\b'_3\\b'_4\end{bmatrix},\quad(A2)$$

式中，$\boldsymbol{M}$ 为 4×4 的声场特征矩阵；等式右侧为点虚源激发的入射纵波向量，分别记为向量 $\boldsymbol{b}$ 和 $\boldsymbol{b}'$.

矩阵 $\boldsymbol{M}$ 中各元素表达式如下：

$$\begin{aligned}
M_{11}&=-n\mathrm{I}_n(fa)/a-f\mathrm{I}_{n+1}(fa),\\
M_{12}&=n\mathrm{K}_n(pa)/a-p\mathrm{K}_{n+1}(pa),\\
M_{13}&=n\mathrm{K}_n(sa)/a,\\
M_{14}&=\mathrm{i}k[n\mathrm{K}_n(sa)/a-s\mathrm{K}_{n+1}(sa)],\\
M_{21}&=\rho_{\mathrm{f}}\omega^2\mathrm{I}_n(fa),\\
M_{22}&=2\rho\beta^2[(n^2-n)\mathrm{K}_n(pa)/a^2+p\mathrm{K}_{n+1}(pa)/a]\\
&\quad+\rho(2k^2\beta^2-\omega^2)\mathrm{K}_n(pa),\\
M_{23}&=2n\rho\beta^2[(n-1)\mathrm{K}_n(sa)/a^2-s\mathrm{K}_{n+1}(sa)/a],\\
M_{24}&=2\mathrm{i}k\rho\beta^2\{[(n^2-n)/a^2+s^2]\mathrm{K}_n(sa)\\
&\quad+s\mathrm{K}_{n+1}(sa)/a\},\\
M_{31}&=0,\\
M_{32}&=2n\rho\beta^2[(1-n)\mathrm{K}_n(pa)/a^2+p\mathrm{K}_{n+1}(pa)/a],\\
M_{33}&=-\rho\beta^2\{[2(n^2-n)/a^2+s^2]\mathrm{K}_n(sa)\\
&\quad+2s\mathrm{K}_{n+1}(sa)/a\},\\
M_{34}&=2\mathrm{i}kn\rho\beta^2[(1-n)\mathrm{K}_n(sa)/a^2+s\mathrm{K}_{n+1}(sa)/a],\\
M_{41}&=0,\\
M_{42}&=2\mathrm{i}k\rho\beta^2[n\mathrm{K}_n(pa)/a-p\mathrm{K}_{n+1}(pa)],\\
M_{43}&=\mathrm{i}kn\rho\beta^2\mathrm{K}_n(sa)/a,\\
M_{44}&=-(s^2+k^2)\rho\beta^2[n\mathrm{K}_n(sa)/a-s\mathrm{K}_{n+1}(sa)].
\end{aligned}\quad(A3)$$

向量 $\boldsymbol{b}$ 和 $\boldsymbol{b}'$ 中各元素表达式如下(省略公因子 $S(\omega)\cdot RD_{\mathrm{P}}(\omega)\cdot RF_{\mathrm{P}}(\omega)$)：

$$\begin{aligned}
b_1&=-\varepsilon_n[n\mathrm{I}_n(pa)/a+p\mathrm{I}_{n+1}(pa)]\cos(n\varphi_0),\\
b_2&=-\varepsilon_n\rho\{2\beta^2[(n^2-n)\mathrm{I}_n(pa)/a^2-p\mathrm{I}_{n+1}(pa)/a]\\
&\quad+(2k^2\beta^2-\omega^2)\mathrm{I}_n(pa)\}\cos(n\varphi_0),\\
b_3&=-2n\varepsilon_n\rho\beta^2[(1-n)\mathrm{I}_n(pa)/a^2-p\mathrm{I}_{n+1}(pa)/a]\\
&\quad\times\cos(n\varphi_0),\\
b_4&=-2\varepsilon_n\mathrm{i}k\rho\beta^2[n\mathrm{I}_n(pa)/a+p\mathrm{I}_{n+1}(pa)]\cos(n\varphi_0),\\
b'_1&=-\varepsilon_n[n\mathrm{I}_n(pa)/a+p\mathrm{I}_{n+1}(pa)]\sin(n\varphi_0),\\
b'_2&=-\varepsilon_n\rho\{2\beta^2[(n^2-n)\mathrm{I}_n(pa)/a^2-p\mathrm{I}_{n+1}(pa)/a]\\
&\quad+(2k^2\beta^2-\omega^2)\mathrm{I}_n(pa)\}\sin(n\varphi_0),\\
b'_3&=-2n\varepsilon_n\rho\beta^2[(1-n)\mathrm{I}_n(pa)/a^2-p\mathrm{I}_{n+1}(pa)/a]\\
&\quad\times\sin(n\varphi_0),\\
b'_4&=-2\varepsilon_n\mathrm{i}k\rho\beta^2[n\mathrm{I}_n(pa)/a+p\mathrm{I}_{n+1}(pa)]\sin(n\varphi_0),
\end{aligned}\quad(A4)$$

其中，ρ 为地层密度.

References

Aki K, Richards P G. 1980. Quantitative Seismology: Theory and Methods. San Francisco: W. H. Freeman & Co.

Ben J L. 2020. Inversion of borehole azimuthal acoustic reflection imaging logging data with beamforming [Ph. D. thesis] (in Chinese). Beijing: China University of Petroleum (Beijing).

Bennett NN. 2019. 3D slowness time coherence for sonic imaging. *Geophysics*, 84(5): D179-D189.

Cao J J, Tang X M, Su Y D, et al. 2016. Radiation efficiency of a multipole acoustic source in a fluid-filled borehole. *Chinese Journal of Geophysics* (in Chinese), 59(2): 757-766, doi: 10.6038/cjg20160233.

Dong J L, Xu X K, Zhang J Y, et al. 2020. Overview and development of acoustic far detection technology. *Progress in Geophysics* (in Chinese), 35(2): 566-572, doi: 10.6038/pg2020CC0180.

Gong H, Chen H, He X, et al. 2015. Eliminating the azimuth ambiguity in single-well imaging using 3C sonic data. *Geophysics*, 80(1): A13-A17.

Gong H, Chen H, He X, et al. 2018. An improved single-well imaging method based on the combined monopole-dipole measurement mode. *Applied Geophysics*, 15(3-4): 393-400.

Gu X H, Tang X M, Zhuang C X, et al. 2020. Simulation of dipole shear-wave reflection survey for multi-fracture system using liner slip interface theory. *Progress in Geophysics* (in Chinese), 35(3): 955-962, doi: 10.6038/pg2020DD0053.

Haldorsen J, Voskamp A, Thorsen R, et al. 2006. Borehole acoustic reflection survey for high resolution imaging. // SEG Expanded Abstracts. SEG, 314-318.

Hirabayashi N, Sakiyama N, Ikegami T. 2017. Characteristics of waveforms recorded by azimuthally spaced hydrophones of sonic logging tool for incident plane waves. *Geophysics*, 82(6): D353-D368.

Hornby B E. 1989. Imaging of near-borehole structure using full-waveform sonic data. *Geophysics*, 54(6): 747-757.

Lee S Q, Chen M, Gu X H, et al. 2019. Application of four-component dipole shear reflection imaging to interpret the geological structure around a deviated well. *Applied Geophysics*, 16(3): 291-301.

Li C, Chen H, He X, et al. 2021. Identifying reflector azimuth from borehole multicomponent cross-dipole acoustic measurement. *Geophysics*, 86(6): D201-D214.

(C)1994-2024 China Academic Journal Electronic Publishing House. All rights reserved. http://www.cnki.net

Li Y H, Tang X M, Li H R, et al. 2021. Characterizing the borehole response for single-well shear-wave reflection imaging. *Geophysics*, 86(1): D15-D26.

Li Y H, Tang X M, Su Y D. 2022. Borehole radiation and reception responses for azimuthal shear-wave reflection imaging with an off-centred dipole acoustic tool. *Journal of Geophysics and Engineering*, 19(5): 1180-1195.

Liu H X, Gu X H, Li H R, et al. 2021. Research of the dual dipole source of opposite polarity to suppress direct wave in single-well shear-wave imaging logging. *Progress in Geophysics* (in Chinese), 36(4): 1560-1565, doi: 10.6038/pg2021EE0301.

Tang X M. 2004. Imaging near-borehole structure using directional acoustic-wave measurement. *Geophysics*, 69(6): 1378-1386.

Tang X M, Cao J J, Li Z, et al. 2016. Detecting a fluid-filled borehole using elastic waves from a remote borehole. *The Journal of the Acoustical Society of America*, 140(2): EL211-EL217.

Tang X M, Cao J J, Wei Z T. 2014. Shear-wave radiation, reception, and reciprocity of a borehole dipole source: with application to modeling of shear-wave reflection survey. *Geophysics*, 79(2): T43-T50.

Tang X M, Cheng C H. 2004. Quantitative Borehole Acoustic Methods. Netherlands: Elsevier Science Publishing Inc.

Tang X M, Patterson D J. 2009. Single-well S-wave imaging using multicomponent dipole acoustic-log data. *Geophysics*, 74(6): WCA211-WCA223.

Tang X M, Wei Z T. 2012. Single-well acoustic reflection imaging using far-field radiation characteristics of a borehole dipole source. *Chinese Journal of Geophysics* (in Chinese), 55(8): 2798-2807, doi: 10.6038/j.issn.0001-5733.2012.08.031.

Xu J Q, Hu H S. 2019. Wave filed simulation of single-well imaging based on method of steepest descent and reciprocity. *Journal of Applied Acoustics* (in Chinese), 38(3): 293-300.

Xu J Q, Hu H S. 2020. Study on the radiation and reception of the wave field in a single-well imaging system with an eccentric source. *Chinese Journal of Geophysics* (in Chinese), 63(9): 3545-3561, doi: 10.6038/cjg2020N0015.

Xu J Q, Hu H S, Wang Z. 2019. Asymptotic solution to a 3D dipole single-well imaging system with combined monopole and dipole receivers with an application in elimination of azimuth ambiguity. *Geophysics*, 84(5): D191-D207.

Xue M. 2002. Study on remote exploration acoustic reflection well logging & its acoustic sonde design [Ph. D. thesis] (in Chinese). Beijing: University of Petroleum (Beijing).

Zhang Y D, Hu H S. 2014. A technique to eliminate the azimuth ambiguity in single-well imaging. *Geophysics*, 79(6): D409-D416.

附中文参考文献

本建林. 2020. **基于声波相控阵的方位反射声波测井反演方法研究**[**博士论文**]. **北京**: **中国石油大学**(**北京**).

曹景记, **唐晓明**, **苏远大等**. 2016. **充液井中多极声源的辐射效率**. **地球物理学报**, 59(2): 757-766, doi: 10.6038/cjg20160233.

董经利, **许孝凯**, **张晋言等**. 2020. **声波远探测技术概述及发展**. **地球物理学进展**, 35(2): 566-572, doi: 10.6038/pg2020CC0180.

古希浩, **唐晓明**, **庄春喜等**. 2020. **用滑移界面理论模拟多裂缝体系的偶极横波远探测声场**. **地球物理学进展**, 35(3): 955-962, doi: 10.6038/pg2020DD0053.

刘汇鑫, **古希浩**, **李焕然等**. 2021. **双偶极源反相激励压制井中直达波的横波远探测方法研究**. **地球物理学进展**, 36(4): 1560-1565, doi: 10.6038/pg2021EE0301.

唐晓明, **魏周拓**. 2012. **利用井中偶极声源远场辐射特性的远探测测井**. **地球物理学报**, 55(8): 2798-2807, doi: 10.6038/j.issn.0001-5733.2012.08.031.

许家旗, **胡恒山**. 2019. **基于鞍点法与互易性的远探测波场模拟**. **应用声学**, 38(3): 293-300.

许家旗, **胡恒山**. 2020. **声波远探测中偏心声源的辐射以及接收波场研究**. **地球物理学报**, 63(9): 3545-3561, doi: 10.6038/cjg2020N0015.

薛梅. 2002. **远探测声波反射波测井方法研究和声系设计**[**博士论文**]. **北京**: **石油大学**(**北京**).

(**本文编辑　张正峰**)

(C)1994-2024 China Academic Journal Electronic Publishing House. All rights reserved. http://www.cnki.net

魏周拓，唐晓明，苏远大等. 利用井中低频偶极横波进行声波远探测的新方法. 地球物理学报，2013，56(10)：3572-3580，doi：10.6038/cjg20131032.

Wei Z T, Tang X M, Su Y D, et al. A new acoustic remote sensing method utilizing borehole low-frequency dipole shear wave. *Chinese J. Geophys.* (in Chinese), 2013, 56(10):3572-3580, doi:10.6038/cjg20131032.

利用井中低频偶极横波进行声波远探测的新方法

魏周拓，唐晓明，苏远大，谭宝海

中国石油大学(华东)地球科学与技术学院，中海油田服务股份有限公司-中国石油大学(华东)声学测井联合实验室，青岛 266580

摘 要 为了突破目前声波远探测技术存在的局限性，提出了一种新的偶极横波远探测方法，即利用井中偶极子产生的井中弯曲波存在低频截止频率的现象，在声源截止频率以下激发偶极声波. 通过对比分析井中偶极声源分别在截止频率上、下激发时，井孔内外产生的辐射声场，明确了截止频率以下井中偶极声源的远场辐射特征和低频截止频率激发偶极横波的优势，结合数值模拟，进一步对其反射声场进行了分析. 结果表明，该方法可以避免艾里相的巨大振幅对数据量化产生的“饱和”效应，相比传统的远探测测井方式更具优势，常规源距即可满足专门的远探测测井仪器需求.

关键词 远探测测井，偶极声源，截止频率，横波辐射，反射声场

doi:10.6038/cjg20131032 **中图分类号** P631 **收稿日期** 2013-01-14，2013-09-22 **收修定稿**

A new acoustic remote sensing method utilizing borehole low-frequency dipole shear wave

WEI Zhou-Tuo, TANG Xiao-Ming, SU Yuan-Da, TAN Bao-Hai

COSL-UPC allied Borehole Acoustic Laboratory, School of Geosciences, China University of Petroleum (Huadong), Qingdao 266580, *China*

Abstract Acoustic remote sensing technology utilizes a borehole acoustic wave to radiate and receive elastic waves to and from a near-borehole geological structure or abnormity body. This paper aims to break through current limitations of single-well reflection imaging logging, proposes a new acoustic remote acoustic sensing method, i.e., the cut-off frequency phenomenon of the borehole flexural wave is used to emit acoustic wave of a borehole dipole source exciting below the cut-off frequency. Through the comparison and analysis of the radiation field inside and outside the borehole excited by a borehole dipole source above and below the cut-off frequency, we has pinpointed the far-field radiation characteristics and advantages of dipole shear wave below cut-off frequency excitation. Combined with numerical simulation, the paper analyzes further the reflected wave field above and below the cut-off frequency. These analysis results show that this method can avoid the" saturation" effect in the quantitative data because of the" airy phase" great amplitude, and it is more advantageous compared to the traditional measurement mode. Reflection wave amplitude is strong for near-offset and decreases when receiver offset increases and we do not need long offset tools for the imaging application.

基金项目 山东省自然科学基金项目(ZR2011DQ020)资助.

作者简介 魏周拓，男，1983 年生，博士，主要从事声波测井方法与应用研究工作. E-mail：zhout_wei@aliyun.com

(C)1994-2023 China Academic Journal Electronic Publishing House. All rights reserved. http://www.cnki.net

Keywords　Remote sensing logging, Dipole source, Cutoff frequency, Shear wave radiation, Reflection wave

1　引　言

声波远探测测井技术可以获知井旁地质构造的横向延伸范围和发育情况[1-4],它把常规测井"一孔之见"的测量范围提高到井周围数十米范围. 1998 年,Schlumberger 公司推出了单井反射波成像测井仪 BARS (Borehole Acoustic Reflection Survey)[5]. 国内,楚泽涵等[6]、乔文孝等[7]、陶果等[8]针对单极声源激励下的反射纵波,开展了大量的基础研究工作,但由于激发单极声源频率一般在 10 kHz 左右,较高频率的波衰减造成其探测范围有限,而且,由于单极声源辐射的无方向性,而无法确定井旁反射体的方位(走向). 为了改进不足,Tang [9]于 2004 年将偶极子声源引入到了单井声波远探测测井中,并提出了偶极横波远探测成像方法. 2009 年,Tang 等[10]利用四分量偶极数据对井旁裂缝和盐丘内部的精细构造进行了成像,取得了显著的应用效果. 2010 年,魏周拓[11]全面系统的结合对偶极辐射声场的数值模拟,加深了偶极远场辐射特征及反射声场的理解. 2012 年,唐晓明等[12]对偶极横波远探测测井技术所取得重要进展进行了全面总结,讨论了该技术发展潜力;随后,唐晓明等[13]利用数值模拟方法详述了该技术的基本原理,结合现场实例说明了偶极声波远探测的重要特征及其有效性. 由于偶极声源使用了相对较低的激发频率(约 3kHz),该方法解决了单极反射纵波存在的探测深度较浅及不能确定反射体空间位置的问题. 然而,在井中进行声波远探测测井,无论是对于单极反射纵波,还是对新近发展的偶极横波远探测,并没有考虑到远探测测井的实际需要,因此,该技术一个最大问题就是来自地层深部的反射信号相对于沿井传播的直达波来说是一个十分微弱的信号,其振幅只有井中传播声波(称为直达波)的几十到几百分之一,甚至几千分之一. 这种微弱信号往往被淹没在声波测井的数据噪声之中,难以测量和处理,这种测量的局限性极大地限制了现有远探测声波技术的广泛使用.

为了突破以上所述远探测声波方法的局限性,进一步提高远探测测井的有效性和测量范围,本文提出了一种新的远探测方法,即利用井中偶极子产生的井中弯曲波存在低频截止频率的现象,在声源截止频率以下激发偶极声波来达到增强反射波的目的. 首先,本文利用三维有限差分数值模拟方法对井中偶极声源在井孔内外产生的辐射声场进行了对比分析,从中明确了截止频率以下井中偶极声源的远场辐射特征和低频截止频率激发偶极横波的优势. 然后,分析了井中偶极声源激发的反射声场差异,最后给出本文的结论.

2　井中偶极声源的井孔内外声场对比分析

图 1 所示为井孔内外接收器阵列空间布置示意图,充液井孔半径为 0.1 m,圆弧阵列接收半径为 5.0 m,圆弧上每隔 10°放置一系列接收器,分别为 R_{90} 至 R_0 总计 10 个接收器,其中 R_0 接收器位于充液井孔内,其余 9 个接收器放置于井外地层中. 偶极声源位于空间 $x=1$ m, $y=3.5$ m 和 $z=1$ m 处,其偶极矩指向始终为 y 轴,采用 Kelly 子波作为声源的时间函数[14],其它相关地层参数见表 1. 本文在数值计算中设置了两种偶极激发频率,一种是常规偶极声波测井频率 3 kHz,另一种是低于弯曲波截止频率1 kHz,针对这两种激发频率,我们分别计算了

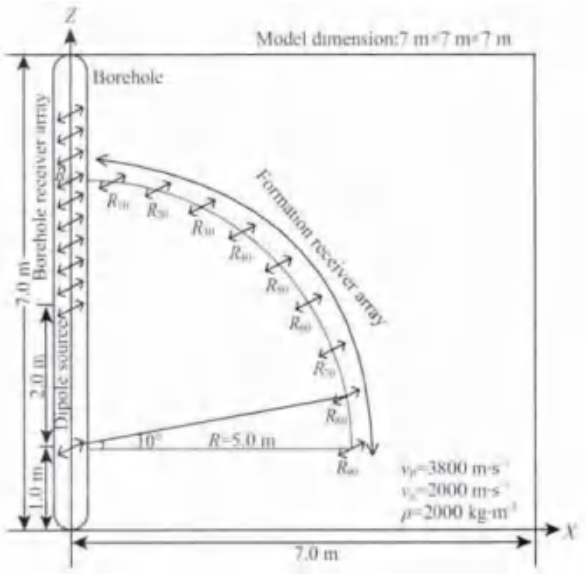


图 1　充液井孔中的偶极声源激发的沿井传播和向井外辐射声波的计算模型

Fig. 1　The simulation model used for a study of propagating along borehole and outside borehole radiation of a dipole source in a fluid-filled borehole

(C)1994-2023 China Academic Journal Electronic Publishing House. All rights reserved.　http://www.cnki.net

表 1 井孔流体和地层弹性参数

Table 1 Physical properties of medium and materials used in the numerical simulation

介质参数	v_P/(m·s^{-1})	v_S/(m·s^{-1})	ρ/(kg·m^{-3})
井孔流体	1500	—	1000
快速地层	3800	2000	2000

井内和井外与偶极矩平行的位移场,对于井外声场,这一位移方向的波动是 SH 型横波[10].

图 2 给出了常规偶极声波测井频率段(约 3 kHz)的井孔内外全波波形,第一个接收器(位于井中的 R_0)与其余接收器的波形(位于井外的 R_{10} 至 R_{90})对比,同时给出了对应的波形频谱. 从图 2a 中可以看出,位于井中的 R_0 接收器的波形振幅(虚线)与位于井外的其它接收器的波幅(实线)相比,前者超过后者一个量级以上,从图 2b 的频谱图,也说明了井中 R_0 接收器的波形幅度远大于辐射到井外的,这种情况对远探测测井时记录井外的反射声场是极为不利的,主要原因是当测井声波数据进行数字化采样时,需要将记录信号通过增益调节后,再送入模/数转换器进行量化. 量化时的最大信号振幅是由记录信号中的最大振幅所决定,即上述沿井中声波的最大振幅(图 2a 和图 2b 虚线所示). 而从井中偶极声源辐射出去的声波,经声阻抗不连续面反射回井中的信号,经过传播距离上的几何扩散和地层的非弹性吸收衰减后,将变得很小(与图2a中相对微弱的井外辐射声波信号相比,反射波幅度将更为微小). 显然,与井中的直达波振幅相比,反射波信号在量化采样时,只能在幅度很小的低位数上被数字化. 这样,在量化后的数字化波形数据中,反射波信号的振幅将非常的低,甚至会低于波形数据中的噪声信号的水平,从而会导致常规偶极测井的数据中很难观测到来自远处地层的反射信号.

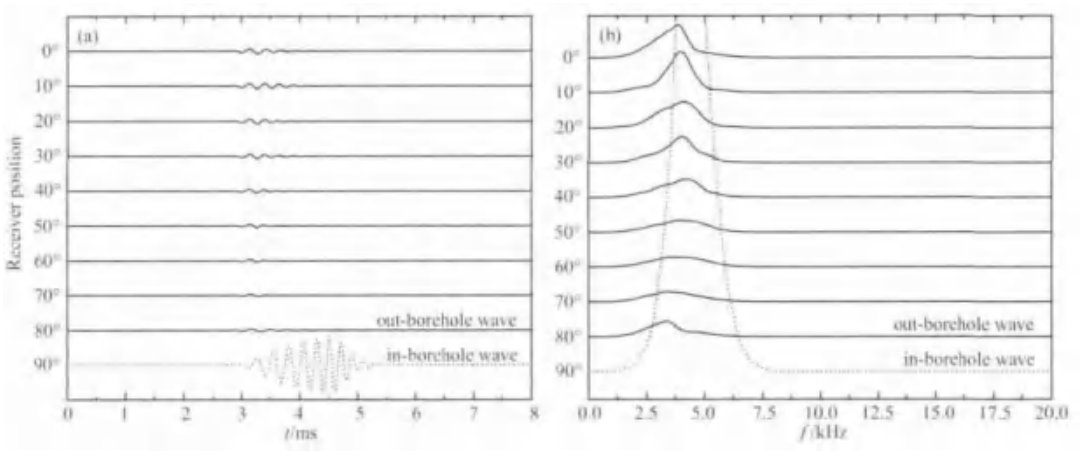


图 2 偶极声源频率为 3 kHz 时,井孔接收到的直达波和井外辐射的声波波形和幅度对比图

(a) 偶极声源频率为 3 kHz 时,井孔内外接收到的全波波形; (b) 偶极声源频率为 3 kHz 时,井孔内外接收到的全波波形频谱.

Fig. 2 Radiated wave amplitude relative to that of borehole wave (above cut-off frequency, dipole source frequency of 3 kHz)

(a) When dipole source frequency is 3 kHz, full waveform inside and outside borehole are shown; (b) When dipole source frequency is 3 kHz, frequency spectrum of full waveform inside and outside borehole are shown.

现分析常规偶极声波测井频率段下,井孔内外接收波形振幅差别的原因. 图 3 显示了井孔弯曲波相速度和群速度频散曲线和弯曲波的激发响应曲线,计算模型和参数分别如图 1 和表 1 所示. 可以看出,对应于相速度随频率剧烈下降的频率区间,群速度呈现出一极小值,在此极小值频率范围内激发和传播的导波称为艾里相,其具有能量传播速度低而激发振幅强的特征,在艾里相的频率范围内,弯曲波

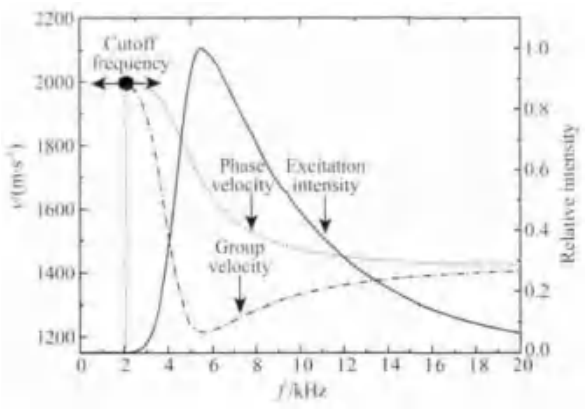


图 3 对应图 2 中的井孔弯曲波相速度、群速度频散曲线和弯曲波的激发响应强度曲线

Fig. 3 Borehole flexural wave phase velocity, the group velocity dispersion curve and flexural wave excitation response curve of the corresponding figure 2

(C)1994-2023 China Academic Journal Electronic Publishing House. All rights reserved. http://www.cnki.net

具有很强的频散效应[15],常规偶极声波测井频率恰好位于该范围内.此时,振幅激发强度曲线极大值对应于群速度的极小值,也就是说图 2a 中井孔波形(虚线)就是群速度曲线上极小值在波列中产生艾里相波包.按照上述模型和参数,本文计算了井中偶极声源激发频率为 3 kHz 时,井孔接收到的阵列波形及求取的频散曲线,如图 4 所示,可以看出,与艾里振相滞后相关的能量很明显大大落后于波的初至,呈现出强烈的频散特征(见图 4b),声源辐射的大部分能量都被集中在井孔附近,而向井外辐射的能量相对微弱.

通过以上分析可知,在艾里相附近,弯曲波的激发强度最大,在其两侧逐渐降低为零.当声源频率在艾里相附近时,地层横波和弯曲波都能被激发出来(图 4),全波列中出现了一个临界折射横波和一个高度频散的弯曲波.

为了避免艾里相的巨大振幅对数据量化时产生的饱和效应,以提高反射波信号在量化采样后的数字化数据中的相对振幅,一种有效的方法就是在井中弯曲波的截止频率以下测量地层反射波.根据图 3 的激发强度曲线可知,在低频范围内(<2 kHz)弯曲波的激发强度很小,几乎为零,此时弯曲波被截止,不能被有效激发,这个临界频率称为截止频率(cutoff frequency).当偶极声源频率低于弯曲波的截止频率时,无论是在井中,还是在井外地层中,接收到的波形只有一个占主导地位的地层横波波包[16],这一点可以在数学上加以证明[10].

按照同样的模型参数,我们计算了偶极激发频率为 1 kHz 的情况,此时,声源所产生的声波信号频率范围处在弯曲波的截止频率以下.图 5 显示了 1 kHz 偶极声源激发时,井孔内(虚线)和井外(实线)所接收到波形,与图 2 所示的 3 kHz 的情况完全不同,可以看出,井孔内、外接收到的声波幅度基本一致,从对应的频谱曲线也可以明显看出(见图 5b),十分接近其低频渐近式[10,13].图 6 给出了对应的井孔接收到的阵列波形以及求取的频散曲线,与图 4 相比,在截止频率以下,弯曲波无法被有效激发,井孔波形中只有一个占主导地位的沿井壁滑行的临界折射横波,频散曲线也证实了这个结论(见图 6b).

3　井中偶极声源的反射声场对比分析

为进一步说明井中直达的弯曲波在截止频率之上和之下对远探测声波测井波形数据的巨大差别,本文建立了如图 7 所示的井旁反射波计算模型[11],假设井旁反射体为一距井轴6.0 m的倾角为 85°的裂缝,裂缝平面的法线方向与偶极声源的偶极矩方向相互正交,此时偶极声源向井外辐射的 SH 横波经过裂缝后发生全反射,最后进入井孔被源距为 1.0～8.0 m的若干接收器接收,不考虑地层的非弹性衰减,这时反射波的振幅减少完全由传播路径上的几何扩散所致,模拟中采用的相关参数见表 1.需要指出的是,对于实际的偶极横波远探测测井过程,由于采用了四分量的偶极声源发射和数据采集技术,在任意偶极声源的偶极矩方向下,都可以通过对四个接收分量进行组合,得到所需要的对井旁反射

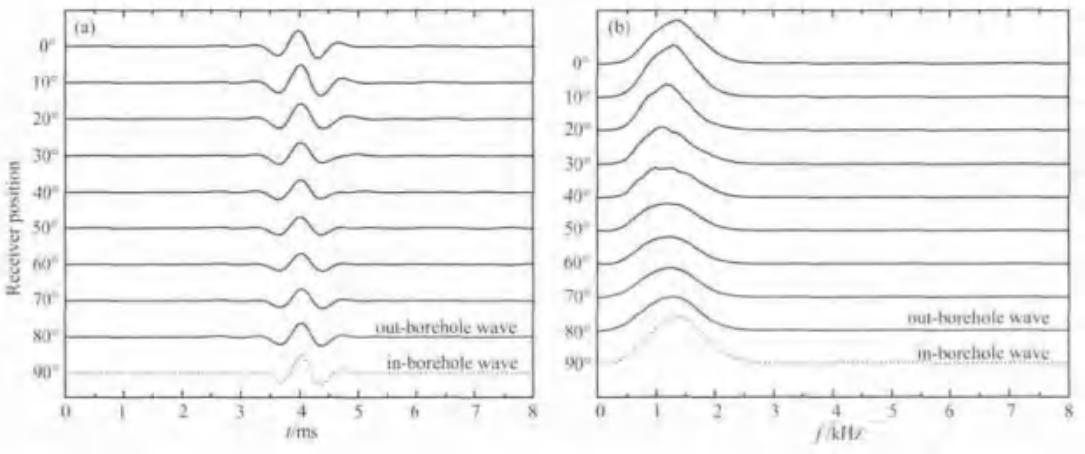


图 5　偶极声源频率为 1 kHz 时,井孔接收到的直达波和井外辐射的全波波形和幅度对比

(a) 偶极声源频率为 1 kHz 时,井孔内外接收到的全波波形;(b) 偶极声源频率为 1 kHz 时,井孔内外接收到的全波波形频谱.

Fig. 5　Radiated wave amplitude relative to that of borehole wave (above cut-off frequency, dipole source frequency of 1 kHz)

(a) When dipole source frequency is 1 kHz, full waveform inside and outside borehole are shown; (b) When dipole source frequency is 1 kHz, frequency spectrum of full waveform inside and outside borehole are shown.

(C)1994-2023 China Academic Journal Electronic Publishing House. All rights reserved.　http://www.cnki.net

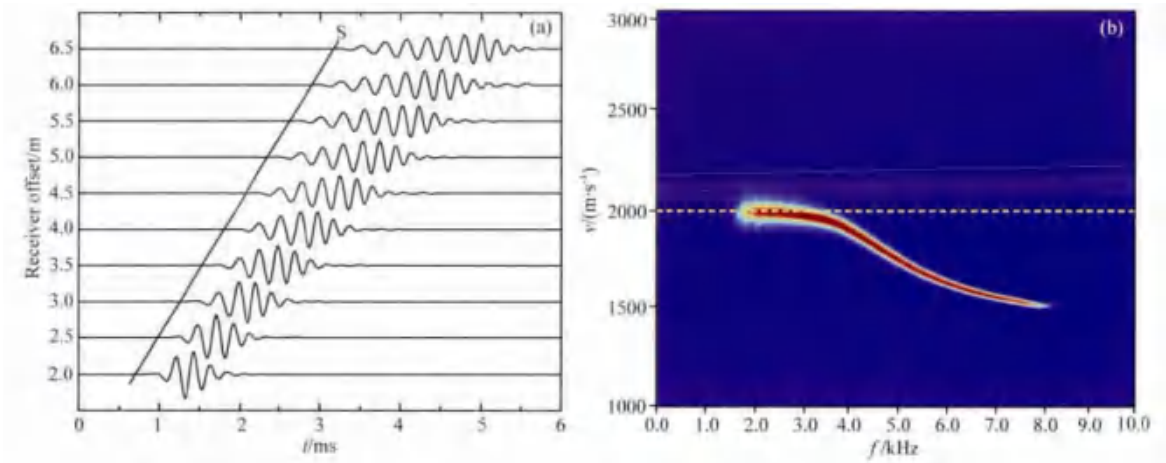


图 4 偶极声源频率为 3 kHz 时,充液井孔中接收到的阵列波形(a)和对应的频散曲线(b)

Fig. 4 When dipole source frequency is 3 kHz, array waveform and the corresponding dispersion curve in a fluid-filled borehole are shown

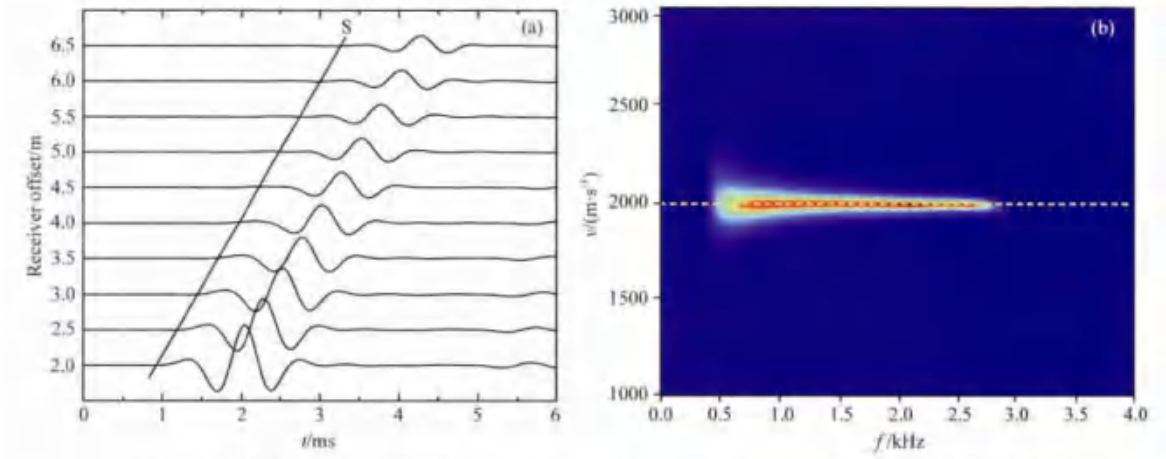


图 6 偶极声源频率为 1 kHz 时,充液井孔中接收到的阵列波形(a)和对应的频散曲线(b)

Fig. 6 When dipole source frequency is 1 kHz, array waveform and the corresponding dispersion curve in a fluid-filled borehole are shown

体探测最有利的 SH 反射横波(具体数据组合方式见文献[13]中公式(15—21)),然后就可以得到地质反射体的空间图像和方位,因此,本文对于偶极矩方向与裂缝平面的法线方向呈任意夹角的情况没有做进一步阐述. 现讨论井中偶极声源激发频率分别为 3 kHz 和 1 kHz 时,井中接收器阵列接收到的直达波和 SH 反射横波的波形.

图 8 给出了 1.0～8.0 m 源距范围内充液井孔内接收到的 SH 反射横波阵列波形,其中点线是计算的 SH 反射横波理论到时曲线,可以看出和数值模拟得到的反射波到时具有很好的一致性. 通过对比 3 kHz 和 1 kHz 两种激发频率下的井孔阵列波形,可以看出有两个方面的不同,其一,在截止频率以下 1 kHz 激发时,井外 SH 反射横波幅度相对于井中直达波大为增强,两者幅度具有可比性(相同的

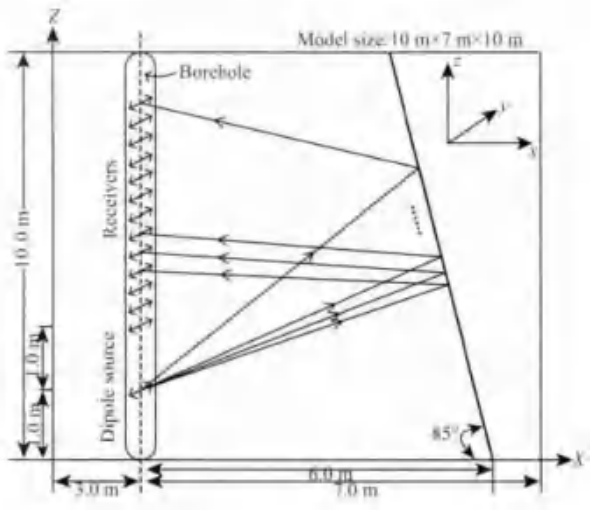


图 7 85°倾角的井旁声阻抗不连续面的反射声场计算模型

Fig. 7 The reflected wave field simulation model with a near-borehole acoustic impedance discontinuity of 85°dip

(C)1994-2023 China Academic Journal Electronic Publishing House. All rights reserved. http://www.cnki.net

量级),这种情况下对波形数据采样量化(波形中最大振幅作为归一化振幅)非常有利,反射波将被明确地记录下来;而在截止频率以上 3 kHz 激发时,波形量化时的最大振幅波形为井中弯曲波的艾里相,与这一振幅相比,来自井外的反射波的振幅十分微弱,而实际测量的反射波幅度往往更小,量化后的反射信号常常被淹没在量化噪声和其它数据噪声中,从而观测不到;其二,在远探测测井数据预处理中,为了减小井中直达波对于反射波提取的影响,通常会利用反褶积的方法对波形进行整形,减少振荡周期,便于成像处理. 相比而言,在截止频率以下激发,不论是井中直达波,还是来自井外的反射波,其波形持续周期都显著减少,这将大大有利于后续的反射波提取和偏移成像处理.

针对上述计算模型,我们将偶极声源的中心频率从 6 kHz 一直减小为 1 kHz,变化率为 0.5 kHz,总计 11 个声源频率,在每一种频率下,数值模拟得到对应井孔声场,然后从全波中波场分离出 SH 反射横波,利用开窗技术,计算源距范围内的反射横波幅度以及与井中弯曲波的相对大小,将计算得到的反射横波绝对幅值和相对大小显示在由源距和频率所构成的三维坐标系下,如图 9 所示. 从图 9a 可以看出,在常规偶极声波测井源距范围内,随着声源激发频率的增加,反射横波的绝对幅值在 2.5～4.0 kHz 范围内存在一个极值区域,该频率段正好对应常规偶极测井仪的激发频率,而这样的一个局部极值区域单纯从反射波强度来说对于远探测是有利的,但正如前面所述,这个极值区域所对应的井中直达波(弯曲波)的幅度在整个频率范围内也达到了最大值,这对于反射波形数据的量化采样又是非常不利的,往往会导致反射波信号被淹没在巨大的井中直达波中,难以观测和提取;而对于图 9b 来说,情况完全不同,在测井源距范围内,随着声源激发频率的降低,井中直达波与反射横波幅值的相对大小单调递减,在频率为 2 kHz 时基本不变,该分界位置恰恰是前面提到的截止频率. 在固定声源激发频率时,随着源距的增加,反射横波相对幅值逐渐减小,这和一般的认识是一致的,即随着源距的增加或者井旁反射体距井轴越远,反射波衰减越大,这就表明进行远探测测井并不需要长源距的声波测井仪,常规源

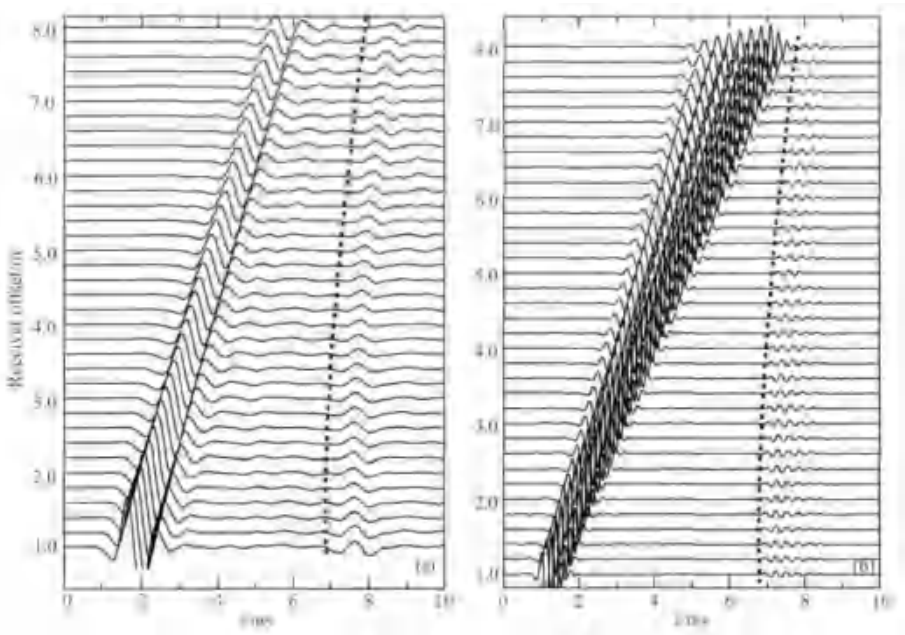


图 8　在井中弯曲波截止频率以上和以下,在充液井孔中接收到的全波阵列波形

(a) 在井中弯曲波截止频率以下(约 1 kHz)接收到的声波信号量化时,井外反射 SH 横波相对于井中直达波的有很大的振幅;(b) 在井中弯曲波截止频率以上(约 3 kHz)接收到的声波信号量化时,井外反射 SH 横波相对于井中直达波的有很小的振幅.

Fig. 8　Above and below cutoff frequency of the borehole flexural wave, received full-wave array waveform are shown in a fluid-filled borehole

(a) Below the cutoff frequency of borehole flexural wave (～1 kHz), the acoustic signal received is quantified, reflection SH shear wave amplitude outside borehole relative to the direct wave inside borehole is strong; (b) Below the cutoff frequency of borehole flexural wave (～3 kHz), the acoustic signal received is quantified, reflection SH shear wave amplitude outside borehole relative to the direct wave inside borehole is weak.

(C)1994-2023 China Academic Journal Electronic Publishing House. All rights reserved.　http://www.cnki.net

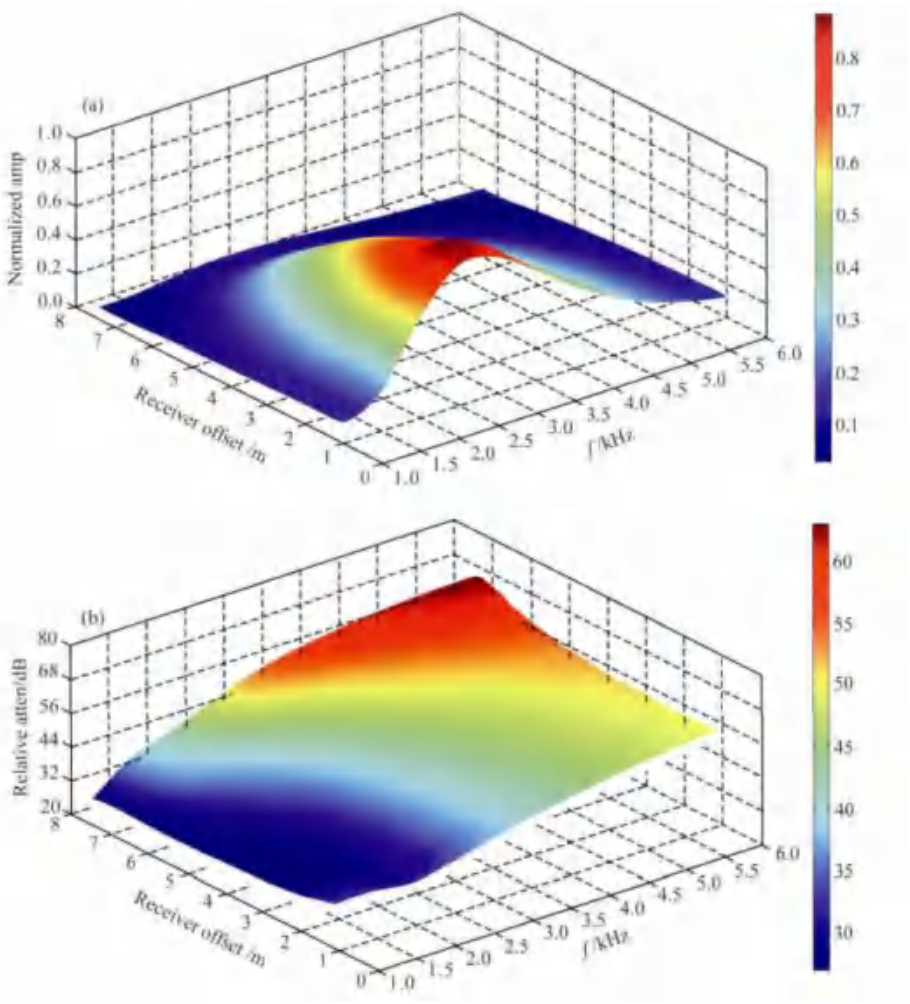


图 9 在井中弯曲波截止频率以上和以下时,SH 反射横波绝对幅度及相对井中直达波幅度与源距变化关系

(a) SH 反射横波绝对幅度与源距和声源频率的变化关系;(b) 弯曲波和 SH 反射横波幅度比与源距和声源频率的关系.

Fig. 9 The amplitude of SH reflection wave and with respect to the borehole direct wave and spacing and source frequency in a fluid-filled borehole

(a) The relationship between the amplitude of SH reflection wave and spacing and source frequency; (b) The relationship between amplitude ratio of flexural and SH reflection wave and spacing and source frequency.

距即可满足需求,以上的对比分析充分说明了在井中弯曲波截止频率以下进行偶极横波远探测测井的优越性.

总的来说,在井中弯曲波低频截止频率以下激发偶极横波的方法,对远探测反射声波十分有利.将低频声波信号在井中进行数字化采样时,虽然量化中的最大信号幅度仍由井中的声场控制,但量化后的反射波相对于井中直达波的振幅,较之图 2 的情况将有量级上的提高.正如上述分析结果表明,这种情况由两个因素决定,第一,偶极声源在井中激发和向井外辐射的声场具有相同量级的振幅(如图 5 所示);第二,由于偶极声源在低频激发,从辐射到反射,最后进入井孔被接收器接收所经历的衰减较高频声波(截止频率上的)要小很多.综合这两个因素,数字量化后的低频反射波相对于直达波的振幅将大大增强,从而有利于远探测声波测井.

4 讨 论

现有的偶极横波远探测数据是常规偶极或交叉偶极测井仪器采集的,其并没有考虑远探测测井的需要.结合上述分析可知,要提高远探测测井的有效性和测量范围,就必须在发射功率、接收灵敏度、数据量化精度以及工作频率范围等方面按远探测测井的需求对现有仪器做进一步优化和改进,其中偶极工作频率的选择至关重要,频率选择过低,低频发射换能器以及测井仪器的工程实现将遇到极大挑战,无法达到测井高分辨率和探测深度的折中;而频率

(C)1994-2023 China Academic Journal Electronic Publishing House. All rights reserved. http://www.cnki.net

选择过高,将不能有效压制井中直达波信号,无法改善直达波和反射波分离的效果,因此,就必须综合考虑以上两点,既要保证对井旁反射体的高分辨率识别能力,又要达到有效压制井中直达波和增强地层反射信号的目的.

具体来说,当一远探测测井仪放置于半径为 r 的充液井孔中,地层横波速度为 β,井中弯曲波的截止频率可以通过下式估算[17]:

$$f_c = \gamma \cdot \frac{\beta}{r}$$

其中,γ 为一比例系数,随地层横波速度由低至高的变化,其取值范围为 $0.11 < \gamma < 0.14$.

对于专门的远探测测井仪器,不仅需要具有低频偶极远探测的数据采集功能,同时兼具常规偶极或交叉偶极测井仪器功能.首先,需要确定地层横波速度,根据不同地层的横波波速范围,估算出不同地层下井孔中偶极子波的截止频率范围,进而确定偶极子声源的工作频率范围.按照这样的思路,具体可以通过如下过程实现测量目的,在一个较宽的频段内(包括弯曲波截止频率在内),进行偶极声源的发射和数据采集.之后,分别针对井中的直达波和井外的反射波进行两次数据采集.第一次采集,设置一个宽带滤波器,其带宽与所选的宽带声源频段相当.这时采集到的波形数据,主要是沿井中传播的直达波(或者弯曲波).因此,这种波形数据即为常规的偶极声波测井数据,可直接用于地层横波速度的确定.根据地层横波速度,结合上述弯曲波截止频率估算公式,确定该地层下的弯曲波截止频率,进行第二次数据采集,将上述采集到的数据送入滤波器带宽仅限于确定的弯曲波截止频率以下的频段.通过这样的滤波器就会将截止频率上的弯曲波成分滤掉,从而使得截止频率以下辐射出井外的波动与井中直达的波形振幅相当,得到所需的幅度与井中直达波幅度相当的反射横波.最后,对远探测测井仪采集的包含地层反射波信号的数据进行分析处理,可以进一步得到反映井旁反射体的信息,从而达到大幅提高井旁反射体成像效果的目的.

5　结论和认识

通过对比弯曲波截止频率以上和以下两种激发频率时井中偶极声源的远场辐射和反射声场,本文得到以下结论和认识:

(1) 常规偶极测井仪工作频率通常处在艾里相附近,此时弯曲波的激发强度最大,全波列中出现了一个临界折射横波(波至部分)和一个高度频散的弯曲波,声源辐射的大部分能量都被集中在井孔附近,而向井外辐射的能量相对微弱;

(2) 在井中弯曲波低频截止频率以下工作,弯曲波被截止,不能被有效激发,无论是沿井壁传播的滑行横波,还是辐射到井外地层中的 SH 横波,都是纯粹的剪切横波,两者具有相同量级的振幅,这种特性对于远探测测井非常有利,相比传统的方式更具优势;

(3) 在井中弯曲波的低频截止频率以下激发偶极横波的远探测方法,既可以避免艾里相的巨大振幅对数据量化产生的饱和效应,明确地记录反射波,还可以使得井中直达波和接收到的反射波波形持续周期显著减少,将大大有利于后续的反射波提取和偏移成像处理效果;

(4) 对于专门的远探测测井仪必须采用低频偶极横波换能器,提高测量灵敏度和接收精度,根据地层横波波速范围,估算出不同地层井孔中偶极子波的截止频率范围.仪器的源距采用常规源距即可满足需求.

参考文献(References)

[1] Hornby B E. Imaging of near-borehole structure using full-waveform sonic data. *Geophysics*, 1989, 54(6): 747-757.

[2] Esmersoy C, Chang C, Kane M R, et al. Sonic Imaging: A tool for high resolution reservoir description. 67th Annual International Meeting, SEG, Extended Abstracts, 1997: 250.

[3] Yamamoto H, Watanabe S, Mikada H, et al. Fracture imaging using borehole acoustic reflection survey, Proceedings of the 4th SEGJ International Symposium, Tokyo, 1998: 375-382.

[4] Tang X M, Zheng Y, Patterson D. Processing array acoustic-logging data to image near-borehole geologic structures. *Geophysics*, 2007, 72(2): E87-E97.

[5] Schlumberger G. Geoframe BARS user guide. Version 1. 0. Kanagawa: Schlumberger K K, 1998: 1-6.

[6] 楚泽涵, 徐凌堂, 尹庆文等. 远探测反射波声波测井方法实验研究进展. 测井技术, 2005, 29(2): 98-101.
Chu Z H, Xu L T, Yin Q W, et al. Progress of lab study on remote exploration acoustic reflection logging methods. *Well Logging Technology* (in Chinese), 2005, 29(2): 98-101.

[7] 乔文孝, 车小花, 李刚等. 反射声波成像测井的物理模拟. 石油物探, 2004, 43(3): 294-297.
Qiao W X, Che X H, Li G, et al. The physical modeling of acoustic reflection image logging. *Geophysical Prospecting for Petroleum* (in Chinese), 2004, 43(3): 294-297.

[8] 陶果, 何峰江, 王兵等. 声反射成像测井在地层中的三维波

(C)1994-2023 China Academic Journal Electronic Publishing House. All rights reserved.　http://www.cnki.net

场模拟方法研究. 中国科学 D 辑(地球科学), 2008, 38(s1): 166-173.
Tao G, He F J, Wang B, et al. The study on 3D wave field simulation for acoustic reflection imaging logging in formation. *Science in China*, *Series D* (*Earth Sciences*) (in Chinese), 2008, 51(2): 186-194.

[9] Tang X M. Imaging near borehole structure using directional acoustic wave measurement. *Geophysics*, 2004, 69(6): 1378-1386.

[10] Tang X M, Patterson D. Single-well S-wave imaging using multicomponent dipole acoustic log data. *Geophysics*, 2009, 74(6): 211-223.

[11] 魏周拓. 反射声波测井数值与物理模拟研究[博士论文]. 青岛: 中国石油大学(华东), 2010.
Wei Z T. Research on single-well acoustic imaging logging by using numerical modeling and experimental measurement [Ph. D. thesis] (in Chinese). Qingdao: China University of Petroleum (East China), 2010.

[12] 唐晓明, 魏周拓. 声波测井技术的重要进展—偶极横波远探测测井. 应用声学, 2012, 31(1): 10-17.
Tang X M, Wei Z T. Significant progress of acoustic logging technology: remote acoustic reflection imaging of a dipole acoustic system. *Applied Acoustics* (in Chinese), 2012, 31(1): 10-17.

[13] 唐晓明, 魏周拓. 利用井中偶极声源远场辐射特性的远探测测井. 地球物理学报, 2012, 55(8): 2798-2807.
Tang X M, Wei Z T. Single-well acoustic reflection imaging using far-field radiation characteristics of a borehole dipole source. *Chinese J. Geophys.* (in Chinese), 2012, 55(8): 2798-2807.

[14] Kelly K R, Ward R W, Treitel S, et al. Synthetic seismogram, a finite difference approach. *Geophysics*, 1976, 41(1): 2-27.

[15] 唐晓明, 郑传汉. 定量测井声学. 北京: 石油工业出版社, 2004: 29-30.
Tang X M, Zheng C H. Quantitative Borehole Acoustic Methods (in Chinese). Beijing: Petroleum Industry Press, 2004: 29-30.

[16] 王克协, 马俊, 刘继生等. 对声波测井中软地层也存在滑行横波的诠释. 测井技术, 1998, 22(1): 19-23.
Wang K X, Ma J, Liu J S, et al. Interpretation on being gliding shear wave in soft formation for acoustic logging. *Well Logging Technology* (in Chinese), 1998, 22(1): 19-23.

[17] Winbow G A. A theoretical study of acoustic S-wave and P-wave velocity logging with conventional and dipole sources in soft formations. *Geophysics*, 53(10): 1334-1342.

(本文编辑 汪海英)

(C)1994-2023 China Academic Journal Electronic Publishing House. All rights reserved. http://www.cnki.net

GEOPHYSICS, VOL. 91, NO. 1 (JANUARY-FEBRUARY 2026); P. D49–D60, 12 FIGS., 1 TABLE.
10.1190/GEO-2025-0152

SH wavefield simulation of dipole acoustic reflection survey for multi-fracture system

Shengyuan Chen[1,2], Yuanda Su[1,2,3], Xihao Gu[1,2,4], Shengqing Li[1,2,3], and Xiaoming Tang[1,2,3]

ABSTRACT

Numerical simulation of borehole acoustic reflection imaging of far-borehole fractures requires consideration of the borehole size and the fine structure of the fractures. The 3D discretization for fine structure modeling results in a huge number of grid nodes and extremely long computational time, which severely limits the efficiency of forward modeling of far-borehole reflection wave fields in fractured reservoirs. To address this problem, an analytical method was proposed for quickly calculating snapshots of acoustic reflection imaging wave fields on both sides of a fracture using the far-field asymptotic solution of dipole radiation shear wave displacement. This method combines the angular spectrum method with the slip interface theory. The waveforms obtained are consistent with those obtained by 3D finite-difference time-domain elastic wave simulations. For the same fracture model, the computational efficiency of the analytical method is two orders of magnitude faster than that of the finite-difference numerical method. Using this method, the effect of shear stiffness changes on the real-time propagation of dipole SH wave fields in a double-fracture system was analyzed. These findings can be used to characterize and interpret multi-fracture systems in single-well reflection imaging using field data. The results show that shear stiffness changes caused by near-fracture filling materials are a prerequisite for the effective identification of far-fractures in multi-fracture systems. The analysis results provide a theoretical basis for time domain simulation and imaging analysis of dipole acoustic reflection imaging wave fields in multi-fracture systems.

INTRODUCTION

With the increasing demand for oil and gas exploration and production, characterizing fractures in reservoirs became an important task because they provide conduits for oil and gas migration and storage spaces for oil and gas (Hornby et al., 1989; Gale et al., 2007; Ostojic et al., 2012; Zhao et al., 2021; Wang et al., 2025). For elastic waves incident on fractures, shear waves are particularly sensitive to shear stiffness discontinuities in fractures and can image fractures more effectively than compressional waves (Hirabayashi et al., 2010). The dipole acoustic reflection imaging technology developed in recent years can detect fractures within tens of meters around the borehole (Tang and Patterson, 2009; Bolshakov et al., 2011; Tang, 2016; Li et al., 2024), which greatly improves the accuracy and efficiency of fracture identification, providing important information for reservoir characterization and production development strategies (Gong et al., 2015; Xu et al., 2019; Li et al., 2021; Tang et al., 2022).

The effective identification of far-borehole fractures using single-well imaging technology needs forward modeling of the fracture wave field response characteristics. Wang et al. (2019) use the 3D finite-difference (FD) time-domain method

Manuscript received by the Editor 21 March 2025; revised manuscript received 15 July 2025; published ahead of production 2 November 2025; published online 2 March 2026.
[1]China University of Petroleum East China, State Key Laboratory of Deep Oil and Gas, Qingdao, Shandong, China. E-mail: chensy981031@163.com; syuanda@sina.com (corresponding author); guxih@sina.com; shidalishengqing@yeah.net; tangxiam@aliyun.com.
[2]China University of Petroleum East China, School of Geosciences, Qingdao, Shandong, China.
[3]Laoshan Laboratory, Qingdao, Shandong, China.
[4]Chengdu University of Technology, College of Geophysics, Chengdu, Sichuan, China.
© 2025 Society of Exploration Geophysicists. All rights reserved.

Downloaded from pubs.geoscienceworld.org/seg/geophysics/article-pdf/91/1/D49/7452165/geo-2025-0152.pdf by Univ of Petroleum (Beijing) - Library user on 08 October 2026

to study the effects of fracture dip angle, width, and radial and extension depth on the reflected shear wave amplitude and analyze the sensitivity of the fracture parameters. Deng (2019) and Tang et al. (2023) numerically simulate the wave field characteristics of fractures filled with different media and show that the solid and fluid in the fracture can be distinguished by the differences in the reflected wave amplitude. For numerical modeling of small thickness fractures, fine grid nodes are required to accurately characterize their spatial structure, resulting in oversampling of the computational domain and a significant reduction in computational efficiency (Coates and Schoenberg, 1995; Lee et al., 2000; Li, 2019). In contrast, the analytical method has the advantages of fast calculation and time consumption reduction. Zhang et al. (2016) use the acoustic impedance difference between the geological body and the background medium, in connection with the generalized Radon transform to rapidly image single fractures and fracture zones outside the borehole, which, combined with field dipole shear wave reflection survey data, allows for developing a set of theoretical interpretation maps. When the fracture thickness is much smaller than the wavelength of elastic waves in the formation, Schoenberg (1980) propose the linear slip interface theory, in which the stress is continuous across the fracture interface, whereas displacement is discontinuous, to describe the wave propagation around the fracture. The theory has been validated by laboratory and field tests and is widely used in geophysics to simulate the effects of fractures, faults, and thin layers on elastic waves (Pyrak-Nolte et al., 1990; Peterson et al., 1993; Chen et al., 2012; Xu et al., 2021). Gu et al. (2020) apply the slip interface theory to characterize the shear wave reflection of fractures and their fillings and efficiently simulated the dipole reflection SH waves received in the borehole under a multi-fracture system, providing an important foundation for identifying and interpreting fractures in dipole shear wave reflection survey data. However, there is currently no analytical method that can visualize the propagation process of the reflected and transmitted wave fields in the vicinity of the fracture. Such visualization would be extremely helpful for studying the reflection characteristics associated with fractures and their fillings.

In the far-field scenario, the elastic waves from a borehole dipole source propagate in the form of spherical waves (Tang et al., 2014), and the fracture can be modeled as a slip interface. Using the angular spectrum method, one can decompose the incident spherical wave into a superposition of cylindrical waves. Using the known reflection and transmission coefficients (Aki and Richards, 1980), the spherical wave fields on both sides of the fracture can be synthesized (Atalar, 1978; Brekhovskikh and Lysanov, 1991; Zhang, 2021). This study proposes an analytical method for quickly calculating snapshots of acoustic reflection wave fields on both sides of a fracture. This study focuses on the modeling of SH waves that dominate the far-borehole wavefield radiated from a dipole source (Wei and Tang, 2012). The validity and accuracy of the analytical results are first verified by comparing with the 3D FD time-domain simulation results. Subsequently, a geometric model of a double-fracture system is established to simulate the propagation of dipole SH waves in near- and far-borehole fractures, and the influence of near-fracture fillings on the SH waves received in the borehole is analyzed. Finally, the simulation results are used to identify and interpret multi-fracture systems from field dipole shear wave reflection survey data.

THEORY AND METHOD

Figure 1 illustrates the configuration of the borehole acoustic reflection imaging and the cylindrical coordinate system $r\phi z$ used for the analysis. A dipole source pointing parallel to the x-axis is positioned within a fluid-filled borehole of radius a. Considering only the SH shear waves, the elastic waves generated from the source can be classified into three distinct categories:

1) Flexural waves propagating along the borehole and SH waves radiating into the formation outside the borehole.
2) Reflection and transmission of SH waves at fracture 1.
3) Reflected SH waves are received in the borehole.

Under the condition that the radiation distance is greater than wavelength, the far-field asymptotic solution of the radiation SH wave displacement u_ϕ is given by Tang et al. (2014)

$$u_\phi = \frac{\mathrm{RD}\cdot S(\omega)}{\rho_1 v_{s1}^2}\cdot\frac{e^{\mathrm{i}\omega R/v_{s1}}}{4\pi R}, \tag{1}$$

$$\mathrm{RD}(\omega,\theta,\phi) = \mathrm{i}\rho_1 v_{s1}\omega D_1(\omega,k_0)sin\theta cos\phi, \tag{2}$$

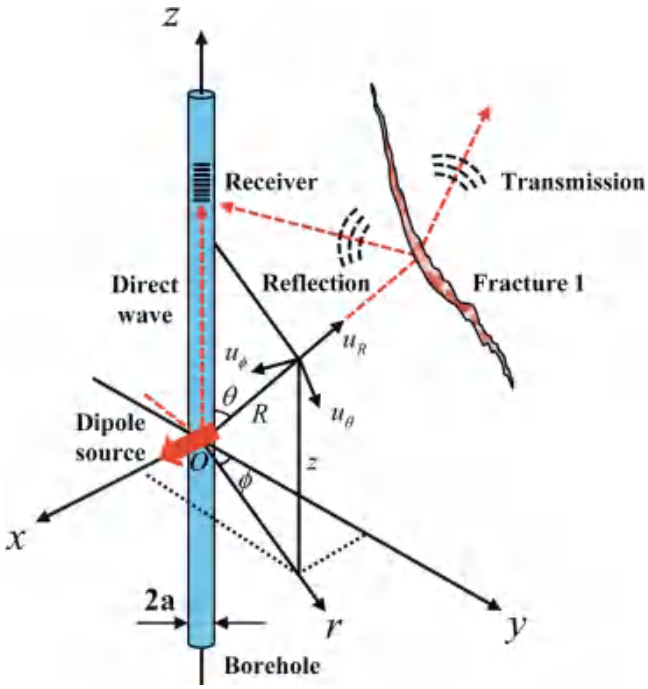


Figure 1. In the cylindrical coordinate system, a dipole source not only excites direct wave propagation along the borehole, but also radiates waves toward the fracture reflector to generate reflection and transmission.

Downloaded from pubs.geoscienceworld.org/seg/geophysics/article-pdf/91/1/D49/7452165/geo-2025-0152.pdf by Univ of Petroleum (Beijing) - Library user on 08 October 2026

where RD is the far-field radiation function for the SH wave; ω and $S(\omega)$ are the angular frequency and the source spectrum, respectively; R is the radiation distance between the field point and the source; ρ_1 and v_{s1} are the density and shear wave velocity of the formation 1, respectively; θ is the angle of the radiation direction of the field point and the positive direction from the z-axis; ϕ is the azimuthal angle of the radiation direction measured from the yOz plane; $k_0 = \omega\cos\theta/v_{s1}$ is the steepest descent solution for the wavenumber of the incident shear wave; and the amplitude coefficients $D_1(\omega, k_0)$ are obtained from the fluid-solid boundary conditions at the borehole wall (Tang and Cheng, 2004).

Figure 2 shows multiple parallel fractures in the rOz plane. Each fracture has an azimuth of ϕ and an inclination of θ_0. The distance from the mth fracture to the source is $|Od_m|$. ρ_m and v_{sm} are the density and shear wave velocity of formation m, respectively. An $x'O'y'$ coordinate system is defined on fracture 1, where the vector $O'O$ (positive z'-axis) is perpendicular to the fracture surface, the positive x'-axis is parallel and identically oriented to e_ϕ, and the y'-axis orientation follows the right-hand rule ($e_{x'} \times e_{y'} = e_{z'}$). $r' = \sqrt{x_r^2 + y_r^2}$ and $\phi_r = arctan(x_r/y_r)$ are the radial distance and azimuthal angle in the cylindrical coordinate system $r_r\phi_r z_r$, respectively. The coordinate transformation between the field points (x_r, y_r, z_r) and (x, y, z) can be expressed as

$$\begin{bmatrix} x_r \\ y_r \\ z_r \\ 1 \end{bmatrix} = \begin{bmatrix} \cos\phi & -\sin\phi & 0 & 0 \\ -\cos\theta_0\sin\phi & -\cos\theta_0\cos\phi & \sin\theta_0 & 0 \\ -\sin\theta_0\sin\phi & -\sin\theta_0\cos\phi & -\cos\theta_0 & |Od_1| \\ 0 & 0 & 0 & 1 \end{bmatrix} \begin{bmatrix} x \\ y \\ z \\ 1 \end{bmatrix}. \tag{3}$$

Considering the $r_r O_r z_r$ plane coplanar with rOz (Figure 2), the spherical wave propagation factor in equation 1 can be expanded as the superposition of a cylindrical wave $J_0(k_{r_r} r_r) e^{ik_{z1,}|z_r - |Od_1||}$ with the direction $\theta_{1i} = arccos(k_{z1,}/k_1)$. The expansion of a spherical wave into cylindrical waves is described more fully in Appendix A. Hence, the far-field incident SH spherical wave can be represented by summing

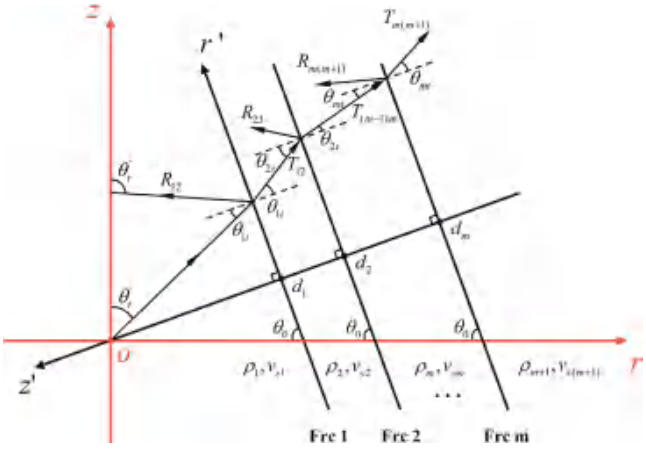


Figure 2. The SH wave fields on both sides of the multiple parallel fractures in the $r_r O_r z_r$ coordinate system are converted to the rOz coordinate system.

(angle-weighted) cylindrical waves of all radiation (specified by RD) directions:

$$u_i = \frac{S(\omega)}{\rho_1 v_{s1}^2} \cdot \frac{1}{2} \int_0^\infty \mathrm{RD}(\omega, \theta_t', \phi) P_0'(k_{r_r}) J_0(k_{r_r} r_r) e^{ik_{z1,}|z_r - |Od_1||} k_{r_r} dk_{r_r}, \tag{4}$$

where $k_1 = \omega/v_{s1}$ is the shear wavenumber of the formation 1, and $k_{r_r}^2 + k_{z1,}^2 = k_1^2$; when $k_{r_r}^2 > k_1^2$, $k_{z1,}$ becomes a purely imaginary number, resulting in evanescent waves. These waves can be suppressed by applying band-limited processing to the propagation factor $e^{ik_{z1,}|z_r - |Od_1||}$ in the wavenumber domain using a low-pass filter with a cutoff wavenumber of k_1 (Matsushima and Shimobaba, 2009). This numerical processing procedure is similar to the real axis integration method, which avoids singularities by introducing complex frequencies to move the integration path into the complex plane (Tsang and Rader, 1979; Kurkjian and Chang, 1986). θ_t' is the radiation angle in the $r_r O_r z_r$ plane, where $\theta_t' = \theta_0 - \theta_{1i}$ when $\phi_r = 0°$ and $\theta_t' = \theta_0 + \theta_{1i}$ for $\phi_r = 180°$; $J_0(*)$ is the zero-order Bessel function of first kind; and the weighted coefficient $P_0'(k_{r_r})$ is the angular spectrum of incident SH spherical wave.

Equation 4 allows the incident SH wave field on any plane, z_r, to be expressed in terms of the angular spectrum, obtained from calculations on the plane $z_r = 0$. At fracture 1 surface ($z_r = 0$), the angular spectra of reflected and transmitted SH spherical waves are as follows:

$$\begin{cases} P_{1r}'(k_{r'}) = P_0'(k_{r'}) R_{12}(k_{r'}) e^{ik_{z1'}|Od_1|} \\ P_{1t}'(k_{r'}) = P_0'(k_{r'}) T_{12}(k_{r'}) e^{ik_{z1'}|Od_1|} \end{cases}, \tag{5}$$

where $R_{12}(k_{r'})$ and $T_{12}(k_{r'})$ are the reflection and transmission coefficient of incident SH plane wave to fracture 1, respectively.

Multiplying the spectrums $P_{1r}'(k_{r'})$ and $P_{1t}'(k_{r'})$ in equation 5 by $e^{ik_{z1'}z'}$ and $e^{-ik_{z2'}z'}$, respectively, can obtain the angular spectra of the reflected wave ($z' > 0$) and transmitted wave ($z' < 0$) on both sides of fracture 1. Then the reflected and transmitted SH spherical waves generated on both sides of fracture 1 can be expressed as

$$u_{1r} = \frac{i \cdot S(\omega)}{4\pi\rho_1 v_{s1}^2} \int_0^\infty \frac{\mathrm{RD}(\omega, \theta_t', \phi) R_{12}(k_{r_r}) J_0(k_{r_r} r_r) e^{ik_{z1'}(z' + |Od_1|)}}{k_{z1'}} k_{r_r} dk_{r_r}, \quad (z' > 0) \tag{6}$$

$$u_{1t} = \frac{i \cdot S(\omega)}{4\pi\rho_1 v_{s1}^2} \int_0^\infty \frac{\mathrm{RD}(\omega, \theta_t', \phi) T_{12}(k_{r'}) J_0(k_{r'} r') e^{i(k_{z1'}|Od_1| - k_{z2'}z')}}{k_{z1'}} k_{r'} dk_{r'}, \quad (z' < 0) \tag{7}$$

Downloaded from pubs.geoscienceworld.org/seg/geophysics/article-pdf/91/1/D49/7452165/geo-2025-0152.pdf by Univ of Petroleum (Beijing) - Library user on 08 October 2026

where $k_2 = \omega/v_{s2}$ is the wavenumber of wavefield in formation 2, with $k_{r'}^2 + k_{z2'}^2 = k_2^2$. For simplicity, the term $\mathrm{i} \cdot S(\omega)/4\pi\rho_1 v_{s1}^2$ is omitted in the following wave spectra calculation formulation.

Generalizing equations 6 and 7, the reflected and transmitted wave fields generated by the transmitted SH wave from the $(m-1)$th fracture on both sides of the mth fracture can be expressed as

$$u_{mr} = \int_0^\infty \frac{\mathrm{RD}(\omega,\theta_t',\phi)T^* R_{m(m+1)}(k_{r'})J_0(k_{r'}r')e^{\mathrm{i}(k_{z1'}|Od_1| + k_{zm'}(z'+|d_1d_m|))}}{k_{z1'}} k_{r'}dk_{r'}cc, (z' > -|d_1d_m|) \tag{8}$$

$$u_{mt} = \int_0^\infty \frac{\mathrm{RD}(\omega,\theta_t',\phi)T^* T_{m(m+1)}(k_{r'})J_0(k_{r'}r')e^{\mathrm{i}(k_{z1'}|Od_1| - k_{z(m+1)'}(z'+|d_1d_m|))}}{k_{z1'}} k_{r'}dk_{r'} \quad (z' < -|d_1d_m|) \tag{9}$$

where $R_{m(m+1)}(k_{r'})$ and $T_{m(m+1)}(k_{r'})$ are the reflection and transmission coefficients of incident SH plane wave to the mth fracture; $k_m = \omega/v_{sm}$ is the wavenumber of wavefield in formation m, with $k_{r'}^2 + k_{zm'}^2 = k_m^2$; and $T^* = \prod_{j=1}^{m-1} T_{j(j+1)}(k_{r'})e^{\mathrm{i}k_{z(j+1)'}|d_jd_{j+1}|}$.

For an incident SH plane wave with polarization parallel to the mth fracture, its reflection and transmission at the fracture can be effectively described by the slip interface theory (Schoenberg, 1980):

$$\begin{cases} R_{m(m+1)}(\omega,\theta_{mi},\eta_{\mathrm{Tm}}) = \dfrac{(Z_m - Z_{m+1})\eta_{\mathrm{Tm}} - \mathrm{i}\omega Z_m Z_{m+1}cos\theta_{mi}}{(Z_m + Z_{m+1})\eta_{\mathrm{Tm}} - \mathrm{i}\omega Z_m Z_{m+1}cos\theta_{mi}} \\ T_{m(m+1)}(\omega,\theta_{mi},\eta_{\mathrm{Tm}}) = \dfrac{2Z_m\eta_{\mathrm{Tm}}}{(Z_m + Z_{m+1})\eta_{\mathrm{Tm}} - \mathrm{i}\omega Z_m Z_{m+1}cos\theta_{mi}} \end{cases} \tag{10}$$

where $Z_m = \rho_m v_{sm}$ is shear wave impedance in formation m. The incident angle $\theta_{mi} = arccos(k_{zm'}/k_m)$ and transmitted angle θ_{mt} are related through Snell's law. $\eta_{\mathrm{Tm}} = \mu_{\mathrm{Tm}}/h_m$ is the shear stiffness of the mth fracture, which is determined by the fracture thickness h_m and the shear modulus μ_{Tm} of the filling material. Note that the subscripts $m(m+1)$ of the coefficients denote waves propagating from formation m to formation $(m+1)$.

The reflected SH waves travel back to the borehole via multiple fractures and are received by an array of receivers in the well. The received wave signal RWV, represented in the frequency domain, can be expressed as

$$\mathrm{RWV}(\omega) = \sum_{m=1}^{M} RW_m(\omega) \tag{11}$$

where M denotes the number of fractures, the reflected wave from the mth fracture can be written as

$$\mathrm{RW}_m(\omega) = \int_0^\infty \frac{\mathrm{RC}(\omega,\theta_r',\phi)\mathrm{RD}(\omega,\theta_t',\phi)R^* R_{m(m+1)}(k_{r'})J_0(k_{r'}r')e^{\mathrm{i}k_{z1'}(|Od_1| + z')}}{k_{z1'}} k_{r'}dk_{r'} \tag{12}$$

where $R^* = 1$ when m is 1. $R^* = \prod_{j=1}^{m-1} T_{j(j+1)}(k_{r'})T_{(j+1)j}(k_{r'})e^{2\mathrm{i}k_{z(j+1)'}|d_jd_{j+1}|}$ for other cases. RC is the borehole reception function for the SH wave (Tang et al., 2014), and $\theta_r' = \theta_t' + 2\theta_{1i}$ is the reception angle in the $r,O,z,$ plane.

For the SH wave field in rOz plane, the wave spectra (e.g., equations 8 and 9) on both sides of the mth fracture in the $r,O,z,$ plane are Fourier-transformed into time domain to get the waveforms. Repeat the above calculation for each field point $(r,,z,)$ and convert the results to the field point (r,z) in the rOz coordinate system using transform relation $\begin{pmatrix} r \\ z \end{pmatrix} = \begin{pmatrix} -cos\theta_0 & -sin\theta_0 \\ sin\theta_0 & -cos\theta_0 \end{pmatrix} \begin{pmatrix} r, \\ z, -|Od_1| \end{pmatrix}$, the SH wave field snapshots at time t and the received wave in the borehole can be obtained.

THEORETICAL MODELING RESULTS

Numerical validation

Equations 6 and 7 give a fast analytical method for simulating the reflected and transmitted SH wavefields on both sides of a single fracture. To verify this method, a far-borehole fracture model is calculated using the 3D FD method. The analytical results are compared with the FD counterparts. The FD computational model is shown in Figure 3a, where the model size (x,y,z) is 4.5 × 9 × 9 m, the center of the borehole is located at (0,0) in the xOy plane, and the borehole diameter is 0.2 m. A dipole source (red arrow) located at the origin points to the x-axis, and the source uses a Ricker wavelet with a center frequency of 3 kHz. The distance between the fracture and the source is 6 m, and the fracture inclination and shear stiffness are set to 90° and 50 GPa/m, respectively. Figure 3b shows the measurement point configuration on both sides of the fracture in the yOz plane. The receiving lines from A to H and A′ to H′ are parallel to the fracture surface, and the coordinates of A, H, A′, and H′ are (4.5, 2), (4.5, 5.5), (7.5, 2), and (7.5, 5.5), respectively. The distance between the two lines is 3.0 m. The grid size and time step for the FD calculation are 0.005 m and 0.5 μs, respectively. A complex frequency-shifted perfectly matched layer (CFS-PML) with a thickness of 40 grid nodes is used to absorb boundary reflections (Wang et al., 2013).

Figure 4a and 4b shows snapshots of the incident SH wave field at 2.7 ms in the yOz plane calculated by the analytical method and the FD method, respectively. The far-field SH wave emitted by the dipole source is a spherical wave. Due to the effects of borehole modulation, the dominant radiation for the SH wave is in the horizontal direction, a characteristic conducive to identifying high-angle fractures outside the well.

Downloaded from pubs.geoscienceworld.org/seg/geophysics/article-pdf/91/1/D49/7452165/geo-2025-0152.pdf by Univ of Petroleum (Beijing) - Library user on 08 October 2026

The numerical and analytical waveform snapshots are in quite good agreement, validating the theoretical approach outlined in equation 4. Figure 5a and 5b shows snapshots of Figure 4 for the time instant of 4.7 ms. At this time, the incident SH wave generates reflected and transmitted SH waves, which propagate as spherical waves on both sides of the fracture. Again, the snapshots from both methods agree very well, thereby verifying the validity and accuracy of the analytical method.

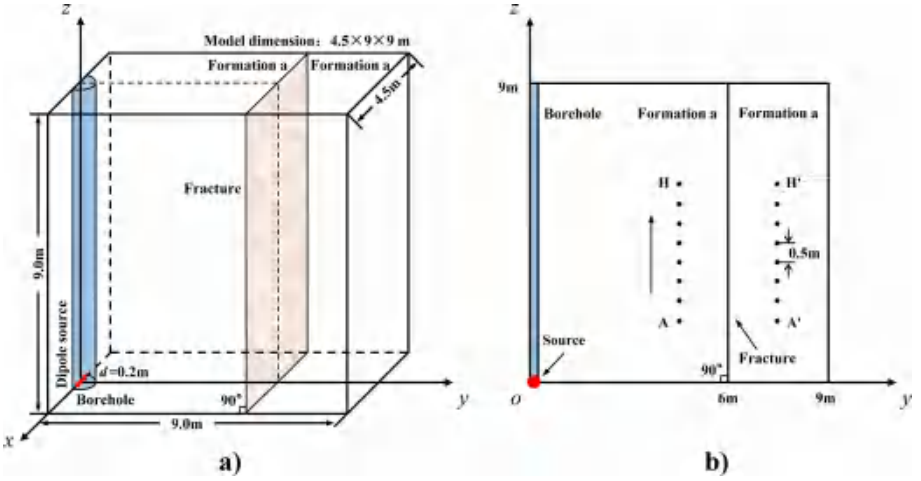


Figure 3. The 3D computation model with a far-borehole fracture (a) and measurement point configuration in the *yOz* plane (b).

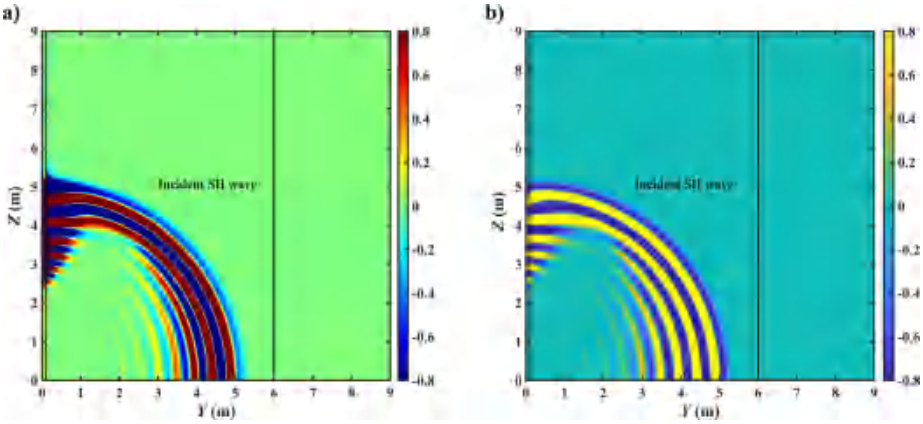


Figure 4. Snapshots of the incident SH wave field simulated by the analytical solution (a) and the 3D FD method (b) in the *yOz* plane at time 2.7 ms.

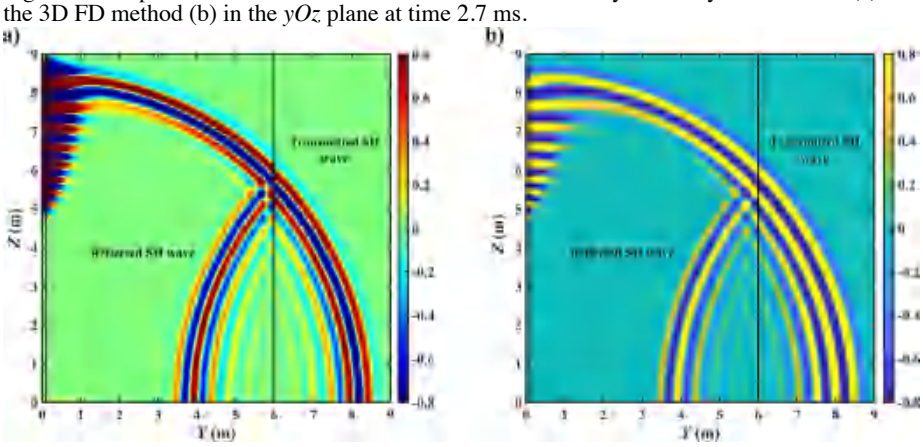


Figure 5. Comparison of the reflected and transmitted SH wavefield snapshots calculated using the analytical solution (a) and the 3D FD method (b) in the *yOz* plane at time 4.7 ms.

Figure 6 shows the comparison between the analytical (solid black lines) and the FD (dashed red lines) of the SH waveforms along the receiving line on both sides of the fracture in the *yOz* plane. Figure 6a shows the incident SH wave and the reflected SH waves at the points A to H on the left side of the fracture. The incident SH wave arrives first, followed by the reflected SH wave from the fracture. As the receiving points change from A, B to H, the incident angle θ (travel distance R) gradually decreases (increases), causing the amplitude reduction in the calculated waveforms (Tang et al., 2014). Along with the amplitude decrease of the incident wave, the reflection coefficient also decreases monotonically (Gu et al., 2020), resulting in a gradual decrease in the amplitude of the reflected SH wave. Figure 6b shows the transmitted SH wave (waveform amplitude doubled) received by the receiving points A′ to H′ on the right side of the fracture. The amplitude of the transmitted SH waves decreases monotonically from the receiving point A′ to H′. This is because as the receiving distance increases, the rate at which the amplitude of the incident SH wave decreases is faster than the rate at which the transmission coefficient increases.

We further computed the normalized root mean square error (NRMSE) between the analytical and FD results for the incident, reflected, and transmitted waveforms (Figure 7). All values are below 10%, indicating a high level of agreement (Dettori et al., 2011). These additions confirm the analytical method's accuracy and the FD method's numerical adequacy. With a 3 kHz Ricker wavelet and v_{s1} = 1800 m/s, the dominant wavelength is λ = 0.6 m, and our grid size Δy = 0.005 m gives approximately 120 points per wavelength. This ensures minimal numerical dispersion and negligible dissipation at the fracture interface.

Downloaded from pubs.geoscienceworld.org/seg/geophysics/article-pdf/91/1/D49/7452165/geo-2025-0152.pdf by Univ of Petroleum (Beijing) - Library user on 08 October 2026

However, the computational efficiency of the two methods differs significantly. For the above 3D model with 900 × 1800 × 1800 mesh points, the FD calculation required 35.6 h on a 64-core workstation, whereas the proposed analytical solution only takes 16.5 min, which is two orders of magnitude improvement on the computational efficiency.

SH wavefield in a double fracture system

To investigate the effect of the shear stiffness due to different fracture filling materials on the propagation characteristics, the analytical method is used to calculate the SH wave field in the double fracture system. Change the single fracture in Figure 3 to two parallel fractures. The distances from the source to fracture 1 and fracture 2 are 5 and 7 m, respectively. The shear stiffness η_{T1} of fracture 1 is assigned to various values at 1, 20, 60 and 50,000 GPa/m, respectively, and the shear stiffness η_{T2} of fracture 2 is fixed at 1 GPa/m. The fracture inclination is 80°. Other simulation conditions are unchanged to the model shown in Figure 3.

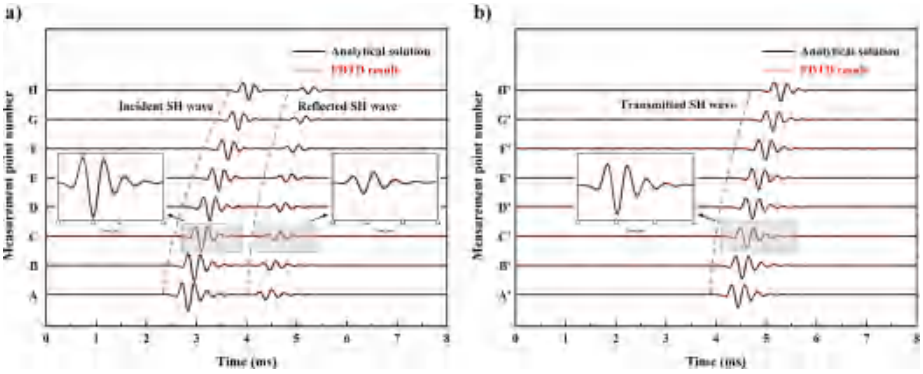


Figure 6. Comparison of SH waveforms calculated using the analytical solution (solid black lines) and the 3D FD method (red dashed lines) in the *yOz* plane. (a) Incident and reflected SH waveforms on the left side of the fracture, and (b) transmitted SH waveforms on the right side of the fracture (wave amplitude doubled).

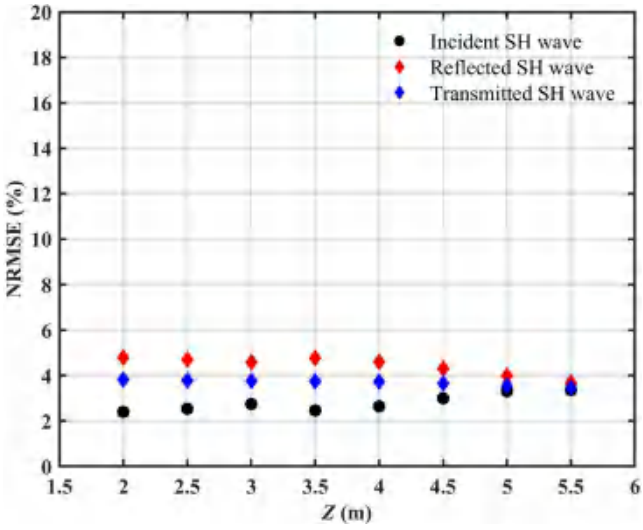


Figure 7. NRMSE comparison of the incident (black circles), reflected (red diamonds), and transmitted (blue diamonds) SH waves derived from analytical solutions and 3D FD method.

Figure 8 shows the snapshots of the SH wave field corresponding to different shear stiffness η_{T1} values in the double-fracture system. The snapshot time range is 3.5–6.5 ms, with an increment of 1 ms. When the shear stiffness η_{T1} is 1 GPa/m, the incident SH wave is almost completely reflected at fracture 1, and only a small part of the energy penetrates fracture 1 to be reflected at fracture 2. The reflected waves from fractures 1 and 2 are denoted as SH1 and SH2, respectively. For the intermediate stiffness values of 20 and 60 GPa/m, the energy penetrating through fracture 1 increases relative to the η_{T1} = 1 GPa/m case, the transmitted SH wave from fracture 1 is reflected at fracture 2, and subsequently reflected back and forth between the two fractures. When the shear stiffness η_{T1} reaches 50,000 GPa/m, the incident SH wave completely penetrates through fracture 1 and generates a reflected SH wave (SH2) at fracture 2. This indicates that for the double fracture system, the shear stiffness of the near-fracture determines whether reflection waves from the far-fracture can be recorded in the borehole.

We further analyze the borehole reception of the dipole acoustic reflection wave field for the double fracture system in Figure 8. Figure 9 shows the SH waveforms received in the borehole for the different shear stiffness η_{T1} values, where the source-receiver distance is 3 m. As the shear stiffness η_{T1} increases, the amplitude of the reflected SH wave (SH1) from fracture 1 gradually decreases, whereas that of the reflected SH wave (SH2) from fracture 2 gradually increases. This is consistent with analyzing the snapshots shown in Figure 8. Note that multiple reflected waves propagating between fractures undergo energy attenuation, resulting in substantially reduced amplitudes. Therefore, this paper only considers one reflection of the SH wave on the fracture in the received waveform.

When the shear stiffness η_{T2} is 1 GPa/m, the transmitted SH wave from fracture 1 is almost completely reflected at fracture 2. Therefore, the amplitude of the reflected SH wave (SH2) from fracture 2 mainly depends on the shear stiffness of fracture 1. Figure 10 shows the SH2 amplitude calculated using equation 12 at different shear stiffness η_{T1} values. When stiffness values approach zero (e.g., 1 GPa/m), fracture 1 models an open or fluid-filled fracture, such as water- or gas-filled fracture. The incident SH wave is completely reflected at fracture 1, causing the reflected SH wave (SH2) to almost disappear from the received waveform, and fracture 2 signal is nearly masked by fracture 1. As stiffness values increase (e.g., 20 or 60 GPa/m), fracture 1 represents soft-filled or partially mineralized fracture, with filling materials such as unconsolidated clay minerals or viscous hydrocarbons. As the SH2 amplitude increases, the fracture 2 signal gradually intensifies. Fully closed fractures and high-modulus minerals would yield even higher

Downloaded from pubs.geoscienceworld.org/seg/geophysics/article-pdf/91/1/D49/7452165/geo-2025-0152.pdf by Univ of Petroleum (Beijing) - Library user on 08 October 2026

stiffness values (e.g., 50,000 GPa/m). In this case, fracture 1 models a mechanically tight fracture, potentially filled with harder mineral phases (e.g., cemented calcite or quartz) and small apertures. The incident SH wave almost completely penetrates fracture 1, and fracture 2 signal can be effectively detected. Therefore, the shear stiffness change caused by the near-fracture filling material is a prerequisite for effectively detecting the far-fracture in the double-fracture system.

FIELD DATA EXAMPLES

We use the above modeling results to help interpret field dipole acoustic reflection imaging for a formation containing a multi-fracture system, as shown in panel 5 of Figure 11, where the imaging result shows single and multiple reflectors. Panel 1 of this figure is the model of a multiple fracture system for the interpretation. The background of the model is formation *b* of Table 1, the radial and vertical extent being 27 and 12 m, respectively. The vertical depth is segmented

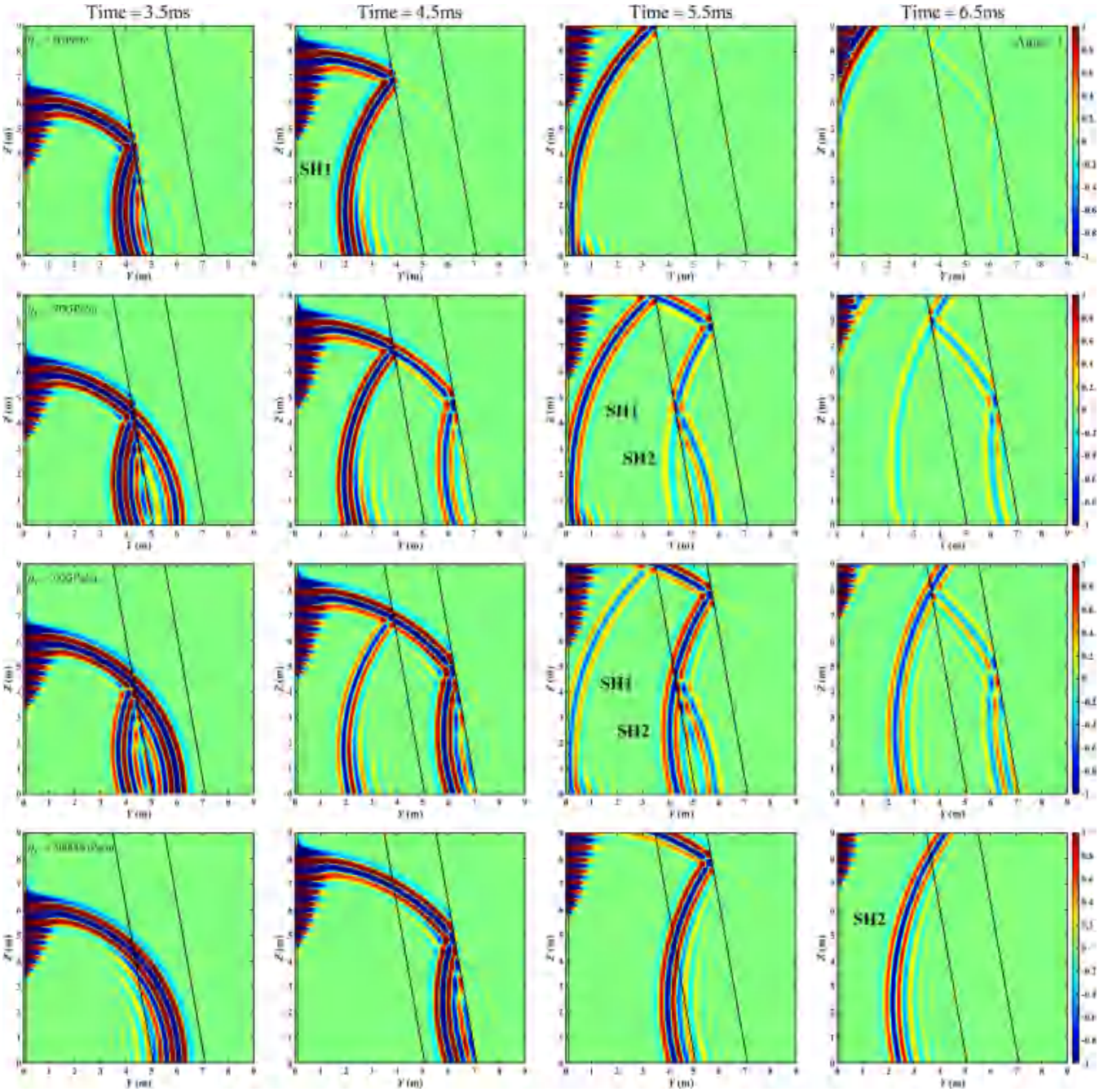


Figure 8. SH wavefield snapshots corresponding to different shear stiffness η_{T1} values in a double fracture system. Note that when the shear stiffness η_{T1} is 1 GPa/m, the SH-wave amplitude is magnified three times at time 6.5 ms to visualize the very weak signal.

Downloaded from pubs.geoscienceworld.org/seg/geophysics/article-pdf/91/1/D49/7452165/geo-2025-0152.pdf by Univ of Petroleum (Beijing) - Library user on 08 October 2026

into three parts according to the vertical extent of the three parallel fractures. Fracture 3 penetrates the entire model, whereas fractures 1 and 2 are confined in the depth segment from 5.1 to 8.8 m. The radial distance to the starting point of fractures 1, 2, and 3 is 13.44, 15.35, and 19.54 m,

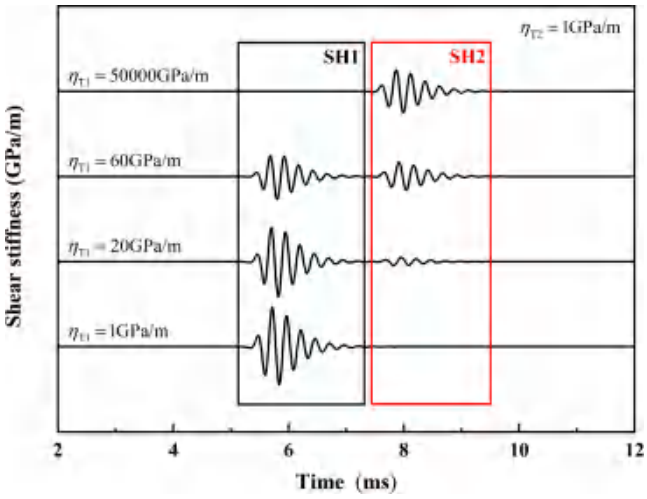


Figure 9. SH reflection wave received in the borehole at different shear stiffness η_{T1} values in the double fracture system.

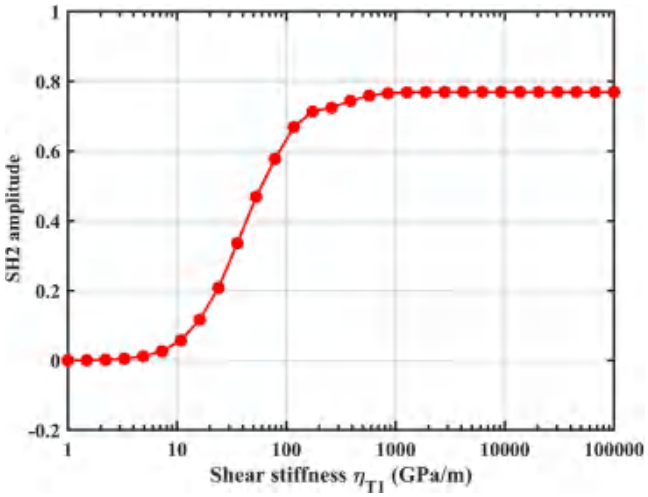


Figure 10. SH2 amplitude at different shear stiffness η_{T1} values in the double fracture system. Note that the shear stiffness η_{T2} = 1 GPa/m.

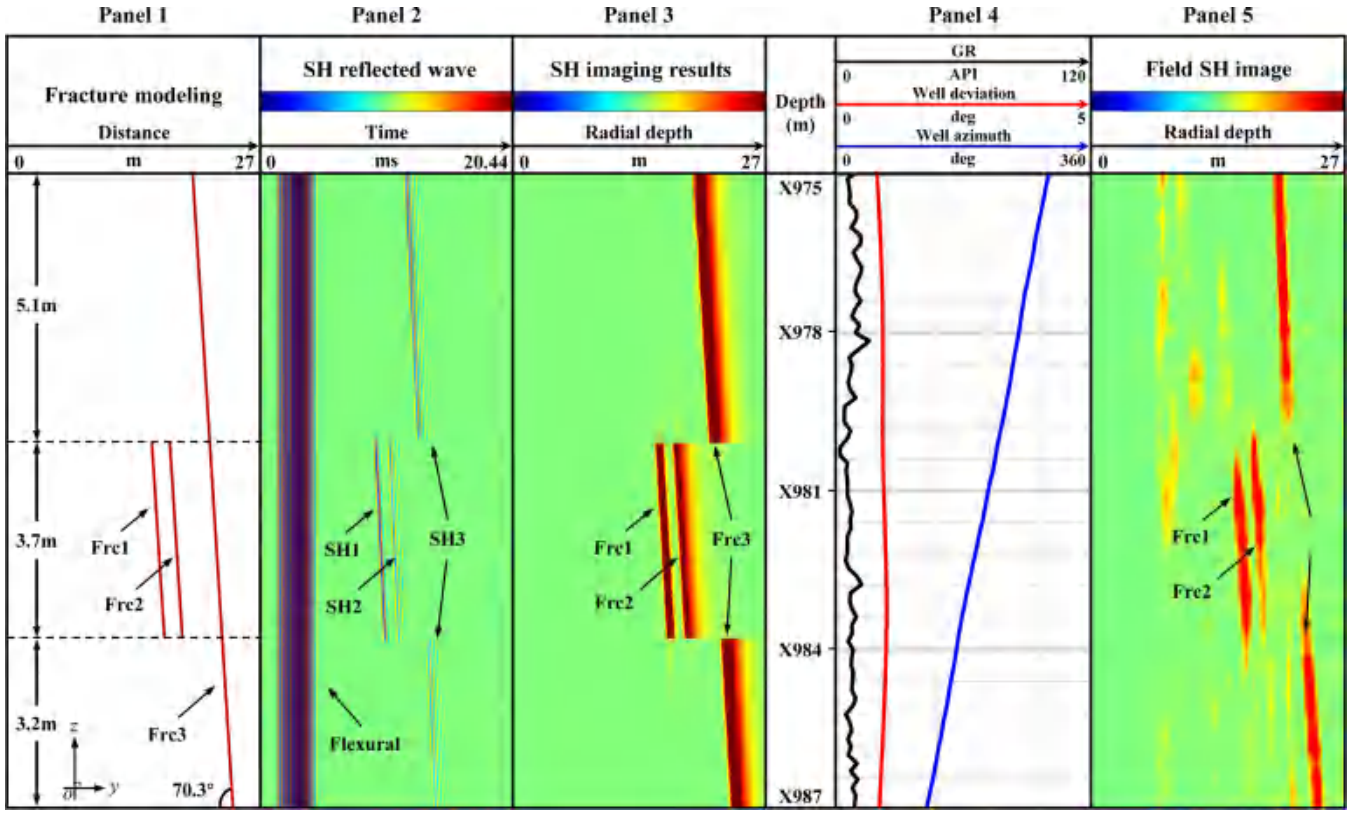


Figure 11. Complex three parallel fracture system: panel 1 is the fracture modeling; panels 2 and 3 are the SH reflected wave and SH imaging results, respectively; panel 4 displays the gamma ray, deviation, and azimuth curves related to the formation lithology and well trajectory; panel 5 is a field example, where parallel fractures are observed in the EW direction.

Downloaded from pubs.geoscienceworld.org/seg/geophysics/article-pdf/91/1/D49/7452165/geo-2025-0152.pdf by Univ of Petroleum (Beijing) - Library user on 08 October 2026

respectively. The shear stiffness values of the fractures are 100, 20, and 60 GPa/m, respectively. All fractures have an inclination angle of 70.3°.

Panel 2 shows the variable density display of the waveform data calculated for the model of panel 1 for the actual logging configuration (a 1 m source-receiver spacing tool with a 0.1524 m logging increment). The first arrival of the data is the large amplitude borehole flexural wave, followed by the reflected waves from the fracture system. It is worth noting that, in segment 2, the amplitude of the reflected SH wave (SH3) from fracture 3 in segment 2 is very weak, because, after reflection by fractures 1 and 2, the transmitted wave incident on fracture 3 is already very weak. Panel 3 shows the results of migrating the data of panel 2. Fracture 3 is imaged only at depth segments 1 and 3; its presence in depth segment 2 is obscured by fractures 1 and 2; the modeling result is used to interpret the field data imaging result in panel 5.

We process field data using procedures that include reflection signal extraction, reflector azimuth determination, migration, imaging, and image enhancement (Bolshakov et al., 2011; Tang, 2016) to image far-borehole structures. The image result of panel 5 for a vertical borehole is from a fractured carbonate formation interval of X975 to X987 m (see gamma ray (GR), deviation, and azimuth curves in panel 4). A high-angle fracture (fracture 3) with an inclination of approximately 70° is visible at about 21 m from the borehole, which abruptly terminates between the depth intervals X980 and X983 m. Additionally, there are two parallel fractures (fractures 1 and 2) at 17 m from the borehole in the same depth segment. Our modeling results (panels 2 and 3) show that these fractures may be charged with hydrocarbons, such that their relatively low shear stiffness reduces wave penetration onto fracture 3 and makes it "hidden" behind the images of fractures 1 and 2. The interpretation is confirmed by the field test, which indicates that fracture 3 in depth segment 2 is obscured and cannot be detected.

The example of Figure 12 further demonstrates the application to multi-fracture imaging and interpretation for a fracture carbonate formation. Panel 1 shows the GR curve for the depth interval X690 to X760 m, the low GR value indicating the typical carbonate lithology. Panels 2–5 show the azimuthal dipole SH reflection imaging results for four azimuths from NS to N135°E at 45° increment, in the radial depth range of 30 m (for the processing procedure of imaging results from 4 C cross-dipole data, see Tang and Patterson, 2009). At the depth interval X738 to X760 m, there are two high-angle single fractures about 11 m away from the borehole. These fractures are best imaged in the EW direction, indicating that they strike along the EW direction. At the depth interval X723 to X750 m, there is a double fracture system about 10 m away from the borehole, striking approximately at N135°E direction. It can be seen that the incident SH wave generates a strong reflection at the far-fracture after penetrating the near-fracture. Simulation results indicate that the near-fracture is filled with hard minerals, whereas the far-fracture may be hydrocarbon charged. Between X694 and X715 m, there is a multi-fracture system about 11 m away from the borehole, and at least four parallel vertical fractures can be seen on the NS image. The modeling-based interpretation is that these fractures contain multiple hard mineral closures in their extension direction. Their moderate shear stiffness allows wave propagation across the fracture system, the resulting reflection data allowing each individual fracture to be clearly imaged. This well explains the phenomenon of multi-fracture systems in dipole reflection wave imaging.

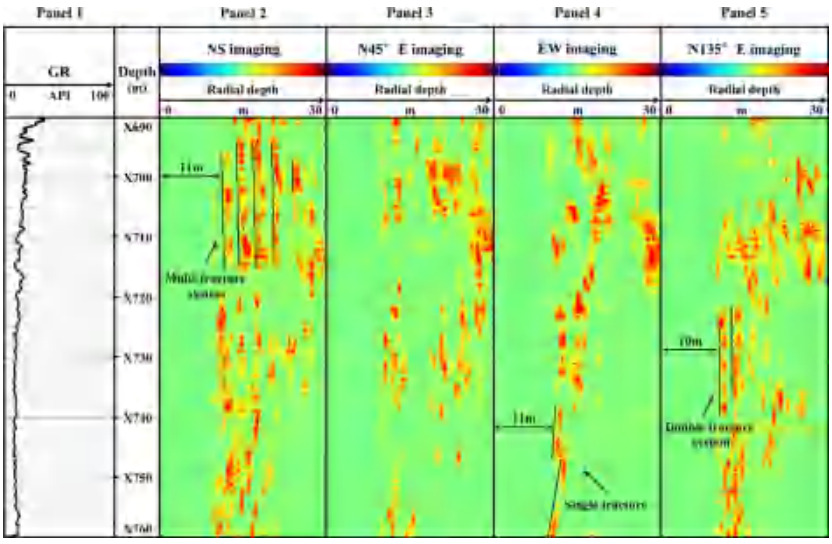


Figure 12. Fracture imaging example of dipole SH reflected wave for four azimuths in carbonate formation, with a 45° increment from NS (panel 2) to N135°E (panel 5). The GR data are shown in panel 1.

Table 1. Model parameters for calculation.

Medium	P-wave velocity (m/s)	S-wave velocity (m/s)	Density (kg/m^3)	Radius (m)
Fluid	1500	—	1000	0.1
Formation a	3000	1800	2000	—
Formation b	4500	3330	2600	—

DISCUSSION

In this study, we developed an analytical method to simulate SH wavefields for multi-fractures embedded in an isotropic formation. Although the current work focuses on parallel fracture systems, the method can be extended to

Downloaded from pubs.geoscienceworld.org/seg/geophysics/article-pdf/91/1/D49/7452165/geo-2025-0152.pdf by Univ of Petroleum (Beijing) - Library user on 08 October 2026

more complex nonparallel geometries by treating each fracture individually using superposition principles (Gu et al., 2020). Furthermore, borehole acoustic measurements are often conducted in anisotropic formations. The influence of anisotropy on wavefield characteristics plays a critical role in borehole acoustic reflection imaging. Understanding these anisotropic effects remains an important area for future research. In far-field conditions, a dipole source radiates elastic energy into anisotropic media in the form of spherical waves (Gu et al., 2023). The analytical framework presented in this study can be further adapted to investigate SH wave propagation and reflection characteristics in anisotropic formations. Such extensions will provide important insights into how anisotropic stiffness affects the amplitude and angular response of reflected shear waves, thereby enhancing the interpretability of acoustic imaging results in complex geological settings.

CONCLUSION

Using the far-field SH wave solution of a borehole dipole source, this study combines the angular spectrum method and the slip interface theory to accurately simulate the spatial and temporal wavefield characteristics in the formation with a multi-fracture system. The accuracy and validity of the analytical method results are verified by comparison with the 3D FD simulation results. Compared with the 3D FD method, our method improves the computational efficiency by two orders of magnitude. Because of the improved efficiency, our method can be effectively used to help interpret dipole acoustic reflection imaging results in fractured formations, relating the relative intensity of multi-fractures to the fracture filling material property. Field application examples have validated the effectiveness and results of the application.

ACKNOWLEDGMENTS

The authors thank Z. Zhendong, N. Hirabayashi, L. Yang, L. Zhen, W. Wenhao, and the anonymous reviewers for their comments and suggestions that helped to improve the manuscript. This work was supported by Shandong Provincial Natural Science Foundation (Grant No. ZR2024YQ062), Natural Science Foundation of China (U21B2064, 42174145, 42574150, 42074137), State Key Laboratory of Deep Oil and Gas (SKLDOG2024-ZYTS-04), Laoshan National Laboratory Science and Technology Innovation Project (No. LSKJ202203407), the Fundamental Research Funds for the Central Universities (No. 25CX02007A, No. 24CX02006A).

DATA AND MATERIALS AVAILABILITY

Data associated with this research are confidential and cannot be released.

APPENDIX A. EXPANSION OF A SPHERICAL WAVE INTO CYLINDRICAL WAVES

In the cylindrical coordinate system $r_,, \phi_,, z_,$, the spherical wave emitted by a point source located at the origin is Green's function:

$$P_i = \frac{exp(ik_1 R_,)}{4\pi R_,} \tag{A-1}$$

where $R_, = \sqrt{r_,^2 + z_,^2}$ is the radiation distance between field point $(r_,, \phi_,, z_,)$ and the origin.

The spherical wave propagation factor in equation A-1 is expanded by the angular spectrum as follows:

$$\frac{exp(ik_1 R_,)}{R_,} = \int_0^{2\pi}\int_0^{\infty} P_i'(k_{r_,}, \alpha_,) e^{ik_{r_,} r_, cos(\phi_, - \alpha_,) + ik_{z1,}|z_,|} k_{r_,} dk_{r_,} d\alpha_, \tag{A-2}$$

where α' is angle between the $k_{r_,}$ and $k_{y_,}$, the weighting coefficient $P_i'(k_{r_,}, \alpha_,)$ is the angular spectrum. Note that the absolute value of $z_,$ due to $e^{ik_{z1,}z_,}$ stands for the wave propagating in the $+z_,$ direction $(z_, > 0)$ and $e^{-ik_{z1,}z_,}$ stands for the wave propagating in the $-z_,$ direction $(z_, < 0)$.

In the $z_, = 0$ plane, where $R_, = r_,$, applying the two-dimensional inverse Fourier transform to equation A-2 yields (Brekhovskikh and Lysanov, 1991)

$$P_i'(k_{r_,}, \alpha_,) = \frac{1}{(2\pi)^2}\int_0^{2\pi} d\phi_, \int_0^{\infty} e^{ir_,[k_1 - k_{r_,} cos(\alpha_, - \phi_,)]} dr_, = \frac{i}{2\pi k_{z1,}} \tag{A-3}$$

On the right side of equation A-2, $P_i'(k_{r_,}, \alpha_,)$ and $e^{ik_{r_,} r_, cos(\phi_, - \alpha_,)}$ are periodic functions of $\alpha`$ and $\phi`$ with a period of 2π, can be expanded in Fourier series as follows (Zhang, 2021):

$$P_i'(k_{r_,}, \alpha_,) = \sum_{m_, = -\infty}^{\infty} i^{-m_,} P'_{m_,}(k_{r_,}) e^{-im_, \alpha_,} \tag{A-4}$$

$$e^{ik_{r_,} r_, cos(\phi_, - \alpha_,)} = \sum_{m_, = -\infty}^{\infty} i^{m_,} J_{m_,}(k_{r_,} r_,) e^{-im_,(\phi_, - \alpha_,)} \tag{A-5}$$

where $J_{m_,}(k_{r_,} r_,)$ is first kind Bessel function of order $m_,$. The Fourier coefficients of equation A-4 are given by

$$P'_{m'}(k_{r'}) = \frac{i^{m'}}{2\pi}\int_0^{2\pi} P_i'(k_{r'}, \alpha') e^{im'\alpha'} d\alpha' \tag{A-6}$$

Combining equations A-4 to A-6, equation A-2 can be written as follows:

Downloaded from pubs.geoscienceworld.org/seg/geophysics/article-pdf/91/1/D49/7452165/geo-2025-0152.pdf by Univ of Petroleum (Beijing) - Library user on 08 October 2026

$$\frac{exp(ik_1R')}{R'} = 2\pi \sum_{m'=-\infty}^{\infty} \int_0^{+\infty} P'_{m'}(k_{r'})J_{m'}(k_{r'}r') e^{i(k_{z1'}|z'| - m'\phi')}k_{r'}dk_{r'} \quad \text{(A-7)}$$

Equation A-7 represents the incident spherical wave field as a superposition of cylindrical waves $J_{m,}(k_{r,}r_{,})e^{i(k_{z1,}|z_{,}| - m,\phi_{,})}$. Considering the axisymmetric of the wave field, only the term with $m_{,} = 0$ is non-zero and independent of $\phi_{,}$, then equations A-4 and A-7 can be expressed as, respectively,

$$P'_i(k_{r'}, \alpha') = P'_0(k_{r'}) = \frac{i}{2\pi k_{z1'}} \quad \text{(A-8)}$$

$$\frac{exp(ik_1R')}{R'} = 2\pi \int_0^{+\infty} P'_0(k_{r'})J_0(k_{r'}r')e^{ik_{z1'}|z'|}k_{r'}dk_{r'} \quad \text{(A-9)}$$

Substituting equation A-9 into equation A-1, according to translation invariance, the incident spherical wave excited by the point source at the point $(0, 0, |Od_1|)$ is expressed as a superposition of cylindrical waves:

$$\frac{e^{i\omega R''/v_{s1}}}{4\pi R''} = \frac{1}{2}\int_0^{\infty} P'_0(k_{r'})J_0(k_{r'}r')e^{ik_{z1'}|z' - |Od_1||}k_{r'}dk_{r'} \quad \text{(A-10)}$$

where $R_{,} = \sqrt{r_{,}^2 + (z_{,} - |Od_1|)^2}$ is the radiation distance between field point $(r_{,}, \phi_{,}, z_{,})$ and the source at the point $(0, 0, |Od_1|)$.

REFERENCES

Aki, K., and P. Richards, 1980, Quantitative Seismology: Theory and Methods: W: H. Freeman & Co.

Atalar, A., 1978, An angular-spectrum approach to contrast in reflection acoustic microscopy: Journal of Applied Physics, **49**, no. 10, 5130–5139, doi: 10.1063/1.324460.

Bolshakov, A. O., D. J. Patterson, and C. Lan, 2011, October 30, Deep Fracture Imaging Around the Wellbore Using Dipole Acoustic Logging: SPE Annual Technical Conference and Exhibition, Denver, Colorado, USAVol.**146769**. doi: 10.2118/146769-MS.

Brekhovskikh, L. M., and Y. P. Lysanov, 1991, Fundamentals of ocean acoustics: Springer-Verlag, doi: 10.1007/978-3-662-07328-5.

Chen, T. R., M. Fehler, X. D. Fang, X. F. Shang, and D. Burns, 2012, SH wave scattering from 2-D fractures using boundary element method with linear slip boundary condition: Geophysical Journal International, **188**, no. 1, 371–380, doi: 10.1111/j.1365-246X.2011.05269.x.

Coates, R. T., and M. Schoenberg, 1995, Finite-difference modeling of faults and fractures: Geophysics, **60**, 1514–1526, doi: 10.1190/1.1443884.

Deng, C. X., 2019, Research on three-dimensional numerical modeling and imaging method of single-well acoustic reflection imaging logging: Ph. D. dissertation, China University of Geosciences.

Dettori, M., C. Cesaraccio, A. Motroni, D. Spano, and P. Duce, 2011, Using CERES-Wheat to simulate durum wheat production and phenology in Southern Sardinia, Italy: Field Crops Research, **120**, no. 1, 179–188, doi: 10.1016/j.fcr.2010.09.008.

Gale, J. F. W., R. M. Reed, and J. Holder, 2007, Natural fractures in the Barnett Shale and their importance for hydraulic fracture treatments: AAPG Bulletin, **91**, no. 4, 603–622, doi: 10.1306/11010606061.

Gong, H., H. Chen, X. He, and X. Wang, 2015, Eliminating the azimuth ambiguity in single-well imaging using 3C sonic data: Geophysics, **80**, no. 1, A13–A17, doi: 10.1190/geo2014-0337.1.

Gu, X. H., X. M. Tang, Y. D. Su, and S. Q. Li, 2023, Elastic wave radiation and reception of a borehole dipole source in a vertically transverse isotropic formation: Geophysics, **88**, no. 2, D177–D191, doi: 10.1190/geo2022-0174.1.

Gu, X. H., X. M. Tang, C. X. Zhuang, C. Jiang, and S. Q. Li, 2020, Simulation of dipole shear-wave reflection survey for multi-fracture system using liner slip interface theory: Progress in Geophysics, **35**, no. 3, 955–962, doi: 10.6038/pg2020DD0053.

Hirabayashi, N., K. Torii, H. Yamamoto, J. Haldorsen, and A. Voskamp, 2010, Fracture detection using borehole acoustic reflection survey data: 80th Annual International Meeting, SEG, Expanded Abstracts, 523–527. doi: 10.1190/1.3513836.

Hornby, B. E., D. L. Johnson, K. W. Winkler, and R. A. Plumb, 1989, Fracture evaluation using reflected Stoneley-wave arrivals: Geophysics, **54**, 1274–1288, doi: 10.1190/1.1442587.

Kurkjian, A. L., and S. K. Chang, 1986, Acoustic multipole sources in fluid-filled boreholes: Geophysics, **51**, 148–163, doi: 10.1190/1.1442028.

Lee, S. H., C. L. Jensen, and M. F. Lough, 2000, Efficient finite-difference model for flow in a reservoir with multiple length-scale fractures: SPE Journal, **5**, no. 3, 268–275, doi: 10.2118/65095-PA.

Li, Z., 2019, Basic theory and applied research of borehole acoustic remote sensing technology: Ph. D. dissertation, China University of Petroleum (East China).

Li, N., P. Liu, H. L. Wu, Y. S. Li, W. H. Zhang, K. W. Wang, F. Zhou, and H. Wang, 2024, Development and prospect of acoustic reflection imaging logging technology: Petroleum Exploration and Development, **51**, no. 4, 1–12, doi: 10.11698/PED.20240314.

Li, D., W. X. Qiao, X. H. Che, X. D. Ju, S. B. Yang, J. Q. Lu, and B. Y. Men, 2021, Eliminating the azimuth ambiguity in reflected S-wave imaging logging based on the azimuthal receiver mode: Journal of Petroleum Science and Engineering, **199**, 108295, doi: 10.1016/j.petrol.2020.108295.

Matsushima, K., and T. Shimobaba, 2009, Band-limited angular spectrum method for numerical simulation of free-space propagation in far and near fields: Optics Express, **17**, no. 22, 19662–19673, doi: 10.1364/OE.17.019662.

Ostojic, J., R. Rezaee, and H. Bahrami, 2012, Production performance of hydraulic fractures in tight gas sands, a numerical simulation approach: Journal of Petroleum Science and Engineering, **88–89**, 75–81, doi: 10.1016/j.petrol.2011.11.002.

Peterson, J. E., D. Hopkins, and L. Myer, 1993, Application of seismic displacement discontinuity theory to Hanford data: 63rd Ann Internat Mtg, SEG, Expanded Abstracts, no. 12, 1006–1009, doi: 10.1190/1.1822280.

Pyrak-Nolte, L. J., L. R. Myer, and N. G. W. Cook, 1990, Transmission of seismic waves across single natural fractures: Journal of Geophysical Research, **95**, no. B6, 8617–8638, doi: 10.1029/JB095iB06p08617.

Schoenberg, M., 1980, Elastic wave behavior across linear slip interfaces: The Journal of the Acoustical Society of America, **68**, no. 5, 1516–1521, doi: 10.1121/1.385077.

Tang, X. M., 2016, Reflection imaging away from borehole: A paradigm shift: 86th Annual International Meeting, SEG, Expanded Abstracts, 4873–4877. doi: 10.1190/segam2016-13771414.1.

Tang, X. M., J. Cao, and Z. Wei, 2014, Shear-wave radiation, reception, and reciprocity of a borehole dipole source: With application to modeling of shear-wave reflection survey: Geophysics, **79**, no. 2, T43–T50, doi: 10.1190/geo2013-0096.1.

Tang, X. M., and C. H. Cheng, 2004, Quantitative borehole acoustic methods: Elsevier Science Publishing Inc.

Tang, X. M., and D. J. Patterson, 2009, Single-well S-wave imaging using multicomponent dipole acoustic-log data: Geophysics, **74**, no. 6, WCA211–WCA223, doi: 10.1190/1.3227150.

Tang, W. H., M. J. Tan, H. L. Cao, and Q. Z. Wu, 2023, Numerical simulation and characteristic analysis of remote detection acoustic reflection imaging logging of near-borehole fracture and vuggy reservoirs: IEEE Transactions on Geoscience and Remote Sensing, **62**, 1–12, doi: 10.1109/TGRS.2023.3338856.

Tang, X. M., P. C. Wang, S. Q. Li, L. Xiong, and H. L. Zhang, 2022, Fracture characterization combining borehole acoustic reflection imaging and geomechanical analyses: Petrophysics, **63**, no. 6, 650–657, doi: 10.30632/PJV63N6-2022a5.

Tsang, L., and D. Rader, 1979, Numerical evaluation of the transient acoustic waveform due to a point source in a fluid-filled borehole: Geophysics, **44**, . , 1706–1720, doi: 10.1190/1.1440932.

Wang, H., N. Li, C. Z. Wang, H. L. Wu, P. Liu, Y. S. Li, Y. M. Liu, and Y. Yuan, 2019, Influence of rock fractures on the amplitude of dipole-source reflected shear wave: Applied Geophysics, **16**, no. 1, 1–13, doi: 10.1007/s11770-019-0757-2.

Downloaded from pubs.geoscienceworld.org/seg/geophysics/article-pdf/91/1/D49/7452165/geo-2025-0152.pdf by Univ of Petroleum (Beijing) - Library user on 08 October 2026

Wang, W. H., S. Q. Li, C. X. Zhuang, Y. D. Su, and X. M. Tang, 2025, Dynamic seismic S-wave anisotropy in vertically fractured rocks: Modeling and field application: Geophysics, **90**, no. 5, A31–A35, doi: 10.1190/geo2024-0908.1.

Wang, H., G. Tao, X. F. Shang, X. D. Fang, and D. R. Burns, 2013, Stability of finite difference numerical simulations of acoustic logging-while-drilling with different perfectly matched layer schemes: Applied Geophysics, **10**, no. 4, 384–396, doi: 10.1007/s11770-013-0400-6.

Wei, Z. T., and X. M. Tang, 2012, Numerical simulation of radiation, reflection, and reception of elastic waves from a borehole dipole source: Geophysics, **77**, no. 6, D253–D261, doi: 10.1190/geo2012-0061.1.

Xu, J. Q., H. S. Hu, and Z. Wang, 2019, Asymptotic solution to a 3D dipole single-well imaging system with combined monopole and dipole receivers with an application in elimination of azimuth ambiguity: Geophysics, **84**, no. 5, D191–D207, doi: 10.1190/geo2018-0658.1.

Xu, J. Q., Q. H. Liu, H. S. Hu, and Y. Zhong, 2021, Simulation of borehole acoustic wavefields in fractured media by combining the spectral-element method and linear-slip model: Geophysics, **86**, no. 5, D177–D192, doi: 10.1190/geo2020-0840.1.

Zhang, H. L., 2021. Computational Acoustics: Science Press.

Zhang, C. H., X. M. Tang, M. Chen, X. F. Sun, and X. Qi, 2016, Application of forward modeling to fracture and vug characterization using borehole reflection imaging: SEG Global Meeting Abstracts, 69–72. doi: 10.1190/RP2016-019.

Zhao, H., W. Li, H. Pu, and K. Yang, 2021, Formation applicability analysis of stimulated reservoir volume fracturing and case analysis: Petroleum, **7**, no. 2, 160–167, doi: 10.1016/j.petlm.2020.04.002.

Biographies and photographs of the authors are not available.

Downloaded from pubs.geoscienceworld.org/seg/geophysics/article-pdf/91/1/D49/7452165/geo-2025-0152.pdf by Univ of Petroleum (Beijing) - Library user on 08 October 2026

GEOPHYSICS, VOL. 88, NO. 5 (SEPTEMBER-OCTOBER 2023); P. D325–D337, 11 FIGS., 1 TABLE.
10.1190/GEO2022-0756.1

Effects of collar eccentricity on azimuthal response characteristics for acoustic reflection measurement while drilling

Bo Rao[1], Yuanda Su[2], Shengqing Li[1], and Xiaoming Tang[2]

ABSTRACT

Acoustic reflection imaging has been successfully applied in postdrilling wireline logging, and the technique is potentially more valuable in acoustic logging while drilling (ALWD), particularly in geosteering while drilling. Because of the common occurrence of tool eccentering in drilling, the impact of drill collar eccentricity on the acoustic wavefield inside and outside the borehole must be considered. Therefore, we analyze the effect of an eccentric drill collar on acoustic reflection imaging while drilling using analytical solutions in a dual-cylindrical coordinate system. The virtual source analogy and the translational addition theorem for cylindrical Bessel functions are used to calculate the response of the fluid-filled borehole with an eccentric collar to the incident wavefield from a formation reflector. The analysis results are validated with those from 3D finite-difference simulations. We also have studied the azimuthal variation of the received wavefield and compared the results with their centralized counterparts, for which the effects of collar eccentricity, frequency of the source, and formation elastic property are analyzed. The results indicate that the asymmetric feature of the wavefield due to the eccentric collar allows for determining the azimuth of the reflector, providing a solution to the azimuth ambiguity problem of borehole acoustic reflection imaging. Our results, besides developing an effective method for eccentric collar ALWD modeling, can be used to provide a theoretical foundation for ALWD tool development and data interpretation.

INTRODUCTION

With the exploration and development of deepwater, deep, and unconventional oil and gas resources, there is an increasing need for logging-while-drilling (LWD) measurements in highly deviated wells and horizontal wells. In addition to measuring reservoir parameters, LWD technology can be used for real-time geosteering to effectively delineate the reservoir and the formation interface and detect formation boundaries near the drill bit (Christian et al., 2010).

In recent years, postdrilling wireline (WL) multipole (monopole and dipole) acoustic reflection imaging technology has been rapidly developing. Hornby (1989) is the first to use the monopole reflected P-wave data to image the formation interface outside the well, which stimulated numerous studies on monopole P-wave reflection imaging (Esmersoy et al., 1998; Xue, 2002; Che and Qiao, 2004; Hirabayashi et al., 2010; Ben et al., 2020). In addition, an azimuthal receiver system was proposed for P-wave reflection to increase azimuth sensitivity for the monopole source (Li et al., 2018; Bennett, 2019). Following the monopole P-wave technology, Tang (2004) is the first to develop the theory and method of S-wave reflection imaging using the low-frequency dipole source, enabling azimuthal sensitivity and enhancing penetration depth for the imaging application. With many years of development and practice, dipole S-wave reflection imaging is now a maturing technology in field applications (Tang and Patterson, 2009, Tang and Wei, 2012, Tang et al., 2014, 2016; Lee et al., 2019; Xu et al., 2019). Nevertheless, it should be noted that a drawback of dipole S-wave imaging is the 180° ambiguity. That is, the dipole S-wave imaging can determine the striking, but not the dipping, azimuth of a reflector. To solve the 180° ambiguity problem of the dipole S-wave imaging, recent developments have focused on analyzing the azimuthal response of the dipole tool (Gong et al., 2015, 2018; Li et al., 2021a). Furthermore, Xu and Hu (2020) and Li et al. (2021b) propose a new measurement method by using an eccentric point source and azimuthal

Manuscript received by the Editor 24 December 2022; revised manuscript received 18 April 2023; published ahead of production 26 June 2023; published online 23 August 2023.
[1]China University of Petroleum (East China), School of Geosciences, Qingdao 266580, China. E-mail: 1004062422@qq.com; shidalishengqing@yeah.net.
[2]China University of Petroleum (East China), School of Geosciences, Qingdao 266580, China and Lao Shan National Laboratory, Qingdao 266580, China. E-mail: syuanda@sina.com; tangxiam@aliyun.com (corresponding author).
© 2023 Society of Exploration Geophysicists. All rights reserved.

Downloaded from http://pubs.geoscienceworld.org/geophysics/article-pdf/doi/10.1190/geo2022-0756.1/5943043/geo-2022-0756.1.pdf
by China Univ Petroleum (East China) Library Serials Dept user
on 03 September 2023

eccentric receivers inside the borehole. The method is only applicable for WL configuration because it does not consider the effect of the tool on the wavefield. Tang et al. (2007) present the first LWD acoustic reflection imaging example, which demonstrates the feasibility of using this technology for geosteering. This work stimulated significant research interest. Chen and Wei (2012) and Wang et al. (2015a, 2015b, 2018) simulate the monopole P-wave reflection wavefield for the LWD configuration using the finite-difference method. Yang et al. (2019) simulate the use of the linear-phased array acoustic transmitters in LWD for enhancing the reflected P-wave amplitude. Tan et al. (2016), Cao et al. (2016), and Wei et al. (2019) study the use of dipole sources for acoustic LWD (ALWD) reflection imaging, emphasizing its application in geosteering.

However, the aforementioned theoretical studies for ALWD reflection imaging are limited to centralized drill collar cases. In drilling operations, the drill collar eccentering is a common occurrence and its effect on the ALWD measurement must be considered, especially in highly deviated and horizontal wells. The ALWD wavefield with an eccentered collar is usually modeled using numerical and analytical methods. Zheng et al. (2004) calculate the effect of tool eccentricity on the ALWD guided-wave modes using a finite-element method and demonstrate the decrease of the Stoneley-wave velocity and the splitting of dipole and quadrupole wave modes due to collar eccentricity. Huang et al. (2004) carry out a similar study using a finite-difference method, which, besides obtaining similar results, shows that the collar-eccentricity-induced mode splitting and interference degrade the signal quality. Wang et al. (2013) use a frequency-domain finite-element method to calculate the wavefield of a multipole ALWD tool in a horizontal or highly deviated well and propose a method of dipole ALWD to determine the tool eccentricity. Pardo et al. (2013) compare the acoustic responses of eccentric monopole tools for WL and LWD cases. Wei et al. (2018) use the finite-difference method to study the wavefield of a point source on the eccentric collar and show the azimuthal effect of the wavefield due to tool eccentricity. Based on the analytical solution of Haugland (2004a, 2004b) for an eccentric solid mandrel in a borehole, Ji et al. (2021) derive an analytical solution for the ALWD model using the dual-cylindrical coordinate system and simulate the azimuthal variation of the wavefield with varying tool eccentricity.

All of these theoretical studies on the eccentric collar ALWD model address the wave propagation along the borehole. This study focuses on the ALWD wavefield to and from a reflector in formation. Specifically, we establish the ALWD model for reflection imaging with an eccentric collar to study the radiation characteristics of the multipole source and analyze the azimuthal response of the reflection wavefield. The accuracy of our modeling results will be validated by those obtained using the 3D finite-difference method.

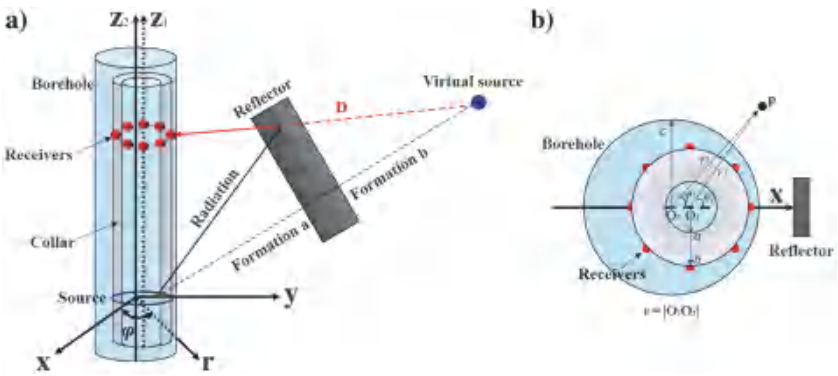


Figure 1. (a) Schematic ALWD model with the eccentric collar and (b) the cross section of the borehole receiving configuration using azimuthally spaced receivers.

THEORY AND METHOD

Figure 1 shows a theoretical ALWD model with an eccentered drill collar. Looking outward from the collar axis, the four layers represent the inner fluid, drill collar, outer borehole fluid, and formation, respectively. The steel collar is homogeneous and isotropic. The dual-cylindrical coordinate system with coordinates $(r_1; \varphi_1; z_1)$ and $(r_2; \varphi_2; z_2)$ is used for the analysis, as shown in Figure 1a, with the radii r_1 and r_2 originating from the center of the collar and borehole, respectively. The collar and borehole are assumed parallel to each other such that z_1 and z_2 can be represented by one common variable z. An eight-receiver array is circumferentially placed at the outer surface of the collar with a 45° azimuthal increment (Figure 1b). The labels a, b, and c represent the internal and external radii of the collar and the radius of the borehole, respectively. Here, O_1 and O_2 denote the origin of the collar and borehole, respectively; $e = |O_1O_2|; (0 \le e \le c - b)$; is the collar offset. For convenience, Ji et al. (2021) define a normalized eccentricity coefficient $Ecc = e/(c - b)$, such that $Ecc = 0\%$ (centered collar) and $Ecc = 100\%$ (collar touching borehole) define the range of collar eccentricity.

For the theoretical analysis using the dual coordinates, the wavefield in the borehole containing the collar and inner and outer fluids is represented in the first coordinate centered around O_1, and the wavefield in the formation is represented in the second coordinate centered around O_2. Therefore, the radiation and reflection of the elastic waves in formation can be conveniently described in the borehole coordinates, for which the incident wave from the formation reflector is given by Tang et al. (2014, 2016) as follows:

$$Iwv(\omega) = S(\omega) \cdot RD(\omega) \cdot RF(\omega) \cdot \frac{e^{i\omega D/v}}{D}; \qquad (1)$$

where ω is the angular frequency; v is the elastic wave velocity; D is the total traveled distance of the wave propagating in the formation (the solid path in Figure 1a); S is the source spectrum; RF is the reflection coefficient at the reflector that can be calculated using the Zoeppritz equation (Aki and Richards, 1980); and RD is the borehole radiation function, which, for the eccentric collar case, is described in detail in Appendix A.

For a centralized multipole source and receiver system, equation 1, in connection with the elastic reciprocity theory, can be used to efficiently calculate the reflection wavefield in the borehole (Tang et al., 2014; Cao et al., 2016; Xu et al., 2019). However, for the eccentric source-receiver system, additional efforts are needed for modeling the wavefield variation in and around the borehole. Li et al. (2021b) use the "virtual source" analysis to synthesize the wavefield using cylindrical wave expansion, where the virtual source is located at the mirror image of the borehole source with respect to the reflector plane

Downloaded from http://pubs.geoscienceworld.org/geophysics/article-pdf/doi/10.1190/geo2022-0756.1/5943043/geo-2022-0756.1.pdf
by China Univ Petroleum (East China) Library Serials Dept user
on 03 September 2023

(Figure 1a). In this analysis, the spherical propagation factor in equation 1 is expanded into the sum of multipole cylindrical waves (Tang and Cheng, 2004), as follows:

$$\frac{e^{i\omega D=v}}{D} = \frac{1}{\pi}\int_{-\infty}^{+\infty}\sum_{m=-\infty}^{\infty} K_m(\eta_v^F r_2')I_m(\eta_v^F r_2) \times \cos[m(\varphi_2-\varphi_2')]e^{ik(z-z')}dk; \quad (2)$$

where $(r_2';\varphi_2';z')$ and $(r_2;\varphi_2;z)$ are the locations of the virtual source and field point, respectively; I_m and K_m are the first and second kind of mth-order modified Bessel functions, respectively; m denotes the azimuthal number in the borehole coordinates; $D=[r_2^2+r_2'^2-2r_2r_2'\cos(\varphi_2-\varphi_2')+(z-z')^2]^{1=2}$; and k and η_v^F are the axial and radial wavenumber of the incident wave, respectively. For P-wave incidence, $\eta_v^F=\eta_p^F=(k^2-\omega^2=\alpha^2)^{1=2}$, and for S-wave incidence, $\eta_v^F=\eta_s^F=(k^2-\omega^2=\beta^2)^{1=2}$, where α and β are the formation P- and S-wave velocities, respectively.

Substituting equation 2 into equation 1, the displacement potential functions for the incident P, SH, and SV waves are given as

$$\begin{cases}\phi^i=S(\omega)\cdot RD_P(\omega)\cdot RF_P(\omega)\sum_{m=-\infty}^{\infty}I_m(\eta_p^F r_2)K_m(\eta_p^F r_2')\cos[m(\varphi_2-\varphi_2')]\\ \chi^i=S(\omega)\cdot RD_{SH}(\omega)\cdot RF_{SH}(\omega)\sum_{m=-\infty}^{\infty}I_m(\eta_s^F r_2)K_m(\eta_s^F r_2')\cos[m(\varphi_2-\varphi_2')]\\ \Gamma^i=S(\omega)\cdot RD_{SV}(\omega)\cdot RF_{SV}(\omega)\sum_{m=-\infty}^{\infty}I_m(\eta_s^F r_2)K_m(\eta_s^F r_2')\cos[m(\varphi_2-\varphi_2')]\end{cases}; \quad (3)$$

where superscript i denotes the incident waves and subscripts P, SH, and SV indicate that the RD and RF functions should be calculated for the P, SH, and SV waves, respectively.

We consider the interaction of the borehole with the incident wave. Based on the Helmholtz decomposition theory, the displacement u_s in the formation solid can be represented by a P-wave potential ϕ_s and two S-wave potentials χ_s and Γ_s as follows:

$$u_s = \nabla\phi_s + \nabla\times(\chi_s\hat{z}) + \nabla\times\nabla\times(\Gamma_s\hat{z}); \quad (4)$$

where $\hat{z}$ is the unit vector along the z-axis and $\phi_s;\chi_s$, and Γ_s denote the potentials of the collar or formation P, SH, and SV waves, respectively. In the following, these functions are expressed as $\phi^{tool};\chi^{tool};\Gamma^{tool}$ and $\phi^F;\chi^F;\Gamma^F$, respectively.

The particle displacement in the borehole fluid u_f can be represented by the fluid acoustic wave ϕ_f as given by

$$u_f = \nabla\phi_f: \quad (5)$$

In the following, wave potentials for the inner and outer fluid are expressed as ϕ^{in} and ϕ^{out}, respectively. With the wavefield expansion exemplified in equation 2, the general solution for the potentials of equations 4 and 5 in the ω-k domain can be derived as follows.

In the collar coordinates, the P-wave potential in the inner fluid and the P- and S-wave potentials in the collar are given by, respectively,

$$\phi^{in} = \sum_{n=-\infty}^{\infty}[A_n^{in}\cos(n\varphi_1) + A_n^{in\prime}\sin(n\varphi_1)]I_n(\eta_f r_1)K_n(\eta_v^F r_2'); \quad (6)$$

$$\begin{cases}\phi^{tool}=\sum_{n=-\infty}^{\infty}\{[A_n^{tool}\cos(n\varphi_1)+A_n^{tool'}\sin(n\varphi_1)]I_n(\eta_p^{tool}r_1)\\ \quad +[B_n^{tool}\cos(n\varphi_1)+B_n^{tool'}\sin(n\varphi_1)]K_n(\eta_p^{tool}r_1)\}K_n(\eta_v^F r_2')\\ \chi^{tool}=\sum_{n=-\infty}^{\infty}\{[C_n^{tool}\sin(n\varphi_1)-C_n^{tool'}\cos(n\varphi_1)]I_n(\eta_s^{tool}r_1)\\ \quad +[D_n^{tool}\sin(n\varphi_1)-D_n^{tool'}\cos(n\varphi_1)]K_n(\eta_s^{tool}r_1)\}K_n(\eta_v^F r_2')\\ \Gamma^{tool}=\sum_{n=-\infty}^{\infty}\{[E_n^{tool}\cos(n\varphi_1)+E_n^{tool'}\sin(n\varphi_1)]I_n(\eta_s^{tool}r_1)\\ \quad +[F_n^{tool}\cos(n\varphi_1)+F_n^{tool'}\sin(n\varphi_1)]K_n(\eta_s^{tool}r_1)\}K_n(\eta_v^F r_2')\end{cases}; \quad (7)$$

Similarly, the P-wave potential in the outer fluid is given by

$$\phi^{out}=\sum_{n=-\infty}^{\infty}\{[A_n^{out}\cos(n\varphi_1)+A_n^{out'}\sin(n\varphi_1)]I_n(\eta_f r_1) +[B_n^{out}\cos(n\varphi_1)+B_n^{out'}\sin(n\varphi_1)]K_n(\eta_f r_1)\}K_n(\eta_v^F r_2'); \quad (8)$$

where n denotes the azimuthal number in the collar coordinates; $\eta_f=(k^2-\omega^2=\alpha_f^2)^{1=2}$ is the radial wavenumber for the borehole fluid; α_f is the fluid acoustic velocity; $\eta_p^{tool}=(k^2-\omega^2=\alpha_{tool}^2)^{1=2}$ and $\eta_s^{tool}=(k^2-\omega^2=\beta_{tool}^2)^{1=2}$ are the radial wavenumbers for the collar P and S waves, respectively; and α_{tool} and β_{tool} are the collar P- and S-wave velocities, respectively.

In equations 7 and 8, the terms associated with Bessel function I (K) describe the wave propagation toward (away from) the collar center.

In the borehole coordinates, the displacement potentials for the scattered waves in the formation are given by

$$\begin{cases}\phi^F=\sum_{m=-\infty}^{\infty}[B_m^F\cos(m\varphi_2)+B_m^{F'}\sin(m\varphi_2)]K_m(\eta_p^F r_2)K_m(\eta_v^F r_2')\\ \chi^F=\sum_{m=-\infty}^{\infty}[D_m^F\sin(m\varphi_2)-D_m^{F'}\cos(m\varphi_2)]K_m(\eta_s^F r_2)K_m(\eta_v^F r_2'):\\ \Gamma^F=\sum_{m=-\infty}^{\infty}[F_m^F\cos(m\varphi_2)+F_m^{F'}\sin(m\varphi_2)]K_m(\eta_s^F r_2)K_m(\eta_v^F r_2')\end{cases} \quad (9)$$

The wave amplitude coefficients in equations 6–9 (i.e., from A_n^{in} to $F_m^{F'}$) are determined by the fluid-solid boundary conditions at the collar (inner and outer) interfaces and the borehole wall, which require the continuity of the displacement and stress in the normal direction, and vanishing of the shear stresses in the tangential direction, of the interfaces. For the dual-coordinate system, the boundary conditions at the collar inner and outer interfaces are specified in the collar coordinates, and those at the borehole wall are specified in the borehole coordinates, as follows:

At the inner collar interface ($r_1=a$):

$$\begin{cases}u_r^{in}(a^-)=u_r^{tool}(a^+)\\ \sigma_{rr}^{in}(a^-)=\sigma_{rr}^{tool}(a^+)\\ 0=\sigma_{rz}^{tool}(a^+)\\ 0=\sigma_{r\varphi}^{tool}(a^+)\end{cases}; \quad (10)$$

at the outer collar interface ($r_1=b$):

$$\begin{cases}u_r^{tool}(b^-)=u_r^{out}(b^+)\\ \sigma_{rr}^{tool}(b^-)=\sigma_{rr}^{out}(b^+)\\ \sigma_{rz}^{tool}(b^-)=0\\ \sigma_{r\varphi}^{tool}(b^-)=0\end{cases}; \quad (11)$$

Downloaded from http://pubs.geoscienceworld.org/geophysics/article-pdf/doi/10.1190/geo2022-0756.1/5943043/geo-2022-0756.1.pdf
by China Univ Petroleum (East China) Library Serials Dept user
on 03 September 2023

at the borehole-formation interface ($r_2 = c$):

$$\begin{cases} u_r^{out}(c^-) = u_r^F(c^+) + u_r^i(c^+) \\ \sigma_{rr}^{out}(c^-) = \sigma_{rr}^F(c^+) + \sigma_{rr}^i(c^+) \\ 0 = \sigma_{rz}^F(c^+) + \sigma_{rz}^i(c^+) \\ 0 = \sigma_{r\varphi}^F(c^+) + \sigma_{r\varphi}^i(c^+) \end{cases}; \tag{12}$$

where superscripts in, tool, out, and F denote the wavefield in the inner fluid, eccentric collar, outer fluid, and formation, respectively.

We now transform the wavefield solution of the dual-coordinate system into the one-coordinate system solution using equation 8 as an example. The transformation uses the classic form of the translational addition theorem for cylindrical Bessel functions (Ji et al., 2021) as follows:

$$\begin{cases} I_n(\eta_f r_1)\begin{Bmatrix}\cos(n\varphi_1)\\ \sin(n\varphi_1)\end{Bmatrix} = \sum_{m=-\infty}^{\infty}(-1)^{n-m} I_{n-m}(\eta_f e) I_m(\eta_f r_2)\begin{Bmatrix}\cos(m\varphi_2)\\ \sin(m\varphi_2)\end{Bmatrix} \\ K_n(\eta_f r_1)\begin{Bmatrix}\cos(n\varphi_1)\\ \sin(n\varphi_1)\end{Bmatrix} = \sum_{m=-\infty}^{\infty} I_{n-m}(\eta_f e) K_m(\eta_f r_2)\begin{Bmatrix}\cos(m\varphi_2)\\ \sin(m\varphi_2)\end{Bmatrix} \end{cases}; \tag{13}$$

Substituting equation 13 into equation 8, the potential function of the borehole fluid is now expressed by the borehole coordinate variables:

$$\phi^{out} = \sum_{m=-\infty}^{\infty} \begin{matrix} \{[A_m^{out}\cos(m\varphi_2) + A_m^{out'}\sin(m\varphi_2)] I_m(\eta_f r_2) \\ + [B_m^{out}\cos(m\varphi_2) + B_m^{out'}\sin(m\varphi_2)] K_m(\eta_f r_2)\} K_m(\eta_f^F r_2') \end{matrix}; \tag{14}$$

$$\begin{cases} A_m^{out} = \sum_{n=-\infty}^{\infty}(-1)^{n-m} A_n^{out} I_{n-m}(\eta_f e);\ A_m^{out'} = \sum_{n=-\infty}^{\infty}(-1)^{n-m} A_n^{out'} I_{n-m}(\eta_f e) \\ B_m^{out} = \sum_{n=-\infty}^{\infty} B_n^{out} I_{n-m}(\eta_f e);\ B_m^{out'} = \sum_{n=-\infty}^{\infty} B_n^{out'} I_{n-m}(\eta_f e) \end{cases}; \tag{15}$$

With the transformation, the boundary conditions at the borehole wall (equation 12) can be solved precisely in the borehole coordinates system. The displacement and stresses of the incident, scattered, and transmitted waves are first calculated using equations 4 and 5 and Hooke's law, and then substituted into the preceding boundary conditions (equations 10–12), which, after truncating the series summation of the displacement and stresses at a sufficiently larger number N, i.e., $n; m = 0; \pm 1; \cdots; \pm N$, yields two matrix equations for determining the unknown amplitude coefficients in equations 6–9:

$$\begin{cases} M_{(24N+12)\cdot(24N+12)} X_{(24N+12)\cdot 1} = Q_{(24N+12)\cdot 1} \\ M_{(24N+12)\cdot(24N+12)} X'_{(24N+12)\cdot 1} = Q'_{(24N+12)\cdot 1} \end{cases}; \tag{16}$$

where M is a $(24N + 12) \times (24N + 12)$ square matrix, X and X′ are the $(24N + 12) \times 1$ vectors of the amplitude coefficients (see Appendix A), and Q and Q′ are the $(24N + 12) \times 1$ vectors related to the incident wave (their expressions are given in Appendix B). Through numerical experiments and by comparison with finite-difference modeling, we determined that $N = 5$ is adequate to ensure the accuracy and efficiency of the calculation.

By solving equation 16 to find the amplitude coefficients for equations 6–9, the wavefields inside and outside the borehole can be fully determined. In particular, the incident-wave-induced fluid pressure in the outer fluid annulus is calculated in the collar coordinates system using $p = \rho_f \omega^2 \phi^{out}$ as follows:

$$p(r_1;\varphi_1;z;\omega) = \frac{\rho_f \omega^2}{\pi}\int_{-\infty}^{+\infty}\sum_{n=-N}^{N} \begin{matrix} \{[A_n^{out}\cos(n\varphi_1) + A_n^{out'}\sin(n\varphi_1)] I_n(\eta_f r_1) \\ + [B_n^{out}\cos(n\varphi_1) + B_n^{out'}\sin(n\varphi_1)] K_n(\eta_f r_1)\} K_n(\eta_v^F r_2') e^{ik(z-z')} dk \end{matrix}; \tag{17}$$

where ρ_f is the fluid density.

For reflection imaging away from the borehole, the virtual source distance r_2' is many wavelengths away from the borehole, such that $|\eta_v^F r_2'| \gg 1$. This allows us to accurately calculate the wavenumber integration of equation 17 using the steepest descent method (Tang and Patterson, 2009) as follows:

$$p(r_1;\varphi_1;z;\omega) = \frac{e^{i\omega D/v - i\pi/4}}{D} \sum_{n=-N}^{N} \rho_f \omega^2 \begin{Bmatrix} [A_n^{out}\cos(n\varphi_1) + A_n^{out'}\sin(n\varphi_1)] I_n(f_0 r_1) \\ + [B_n^{out}\cos(n\varphi_1) + B_n^{out'}\sin(n\varphi_1)] K_n(f_0 r_1) \end{Bmatrix}; \tag{18}$$

where $f_0 = ((k_0^i)^2 - \omega^2/\alpha_f^2)^{1/2}$ is the radial wavenumbers for the borehole fluid, $k_0^i = (\omega/v)\cos(\pi - \theta_i)$ is the steepest descent solution for the wavenumber of the incident wave, θ_i is the wave incident angle measured from the z-axis, and $D = [r_2'^2 + (z - z')^2]^{1/2}$.

Taking the Fourier transform of equation 18, we can calculate the pressure waveform at the receiver locations as

$$p(r_1;\varphi_1;z;t) = \frac{1}{2\pi}\int_{-\infty}^{+\infty} p(r_1;\varphi_1;z;\omega) e^{-i\omega t} d\omega; \tag{19}$$

where r_1 and φ_1 are the cylindrical coordinates of the azimuthal receivers shown in Figure 1b. Using equation 19, the fluid pressure response at different azimuths on the eccentric collar ($r_1 = b$) can be calculated accurately.

THEORETICAL MODELING RESULTS

Result validation

To validate the result of the preceding modeling approach, the ALWD reflection model with an eccentric collar (see Figure 1) is calculated using our analytical solution (equations 18 and 19) and the 3D finite-difference method, respectively. For the model shown in Figure 1, the reflector is the dipping interface between formations a and b, with a dip angle of 85° and azimuth $\varphi_2' = 0°$, i.e., dipping (striking) along the x- (y)-axis; the reflector-to-borehole source distance is 6 m. The azimuthally spaced (with a 45° increment) receivers at the collar outer surface are located 1 m above the source, the eccentricity of the collar being 12 mm toward 0°. The source is located at 1 m from the bottom of the model. An 8 kHz (3 kHz) Gaussian wavelet with a bandwidth of 1.5 kHz is used to actuate the monopole (dipole) source. We let the dipole source point to the y-direction. Because this is the striking direction of the reflector, a pure SH wave will be reflected back to

Downloaded from http://pubs.geoscienceworld.org/geophysics/article-pdf/doi/10.1190/geo2022-0756.1/5943043/geo-2022-0756.1.pdf
by China Univ Petroleum (East China) Library Serials Dept user
on 03 September 2023

the borehole. The borehole and formation parameters are provided in Table 1. The finite-difference waveform modeling uses the technique described by Wei and Tang (2012). The modeling uses a grid size of 3 mm and an iteration time step of 0.28 μs.

Figure 2 compares the borehole fluid pressure response from the analytical solution (the black curves) and the 3D finite-difference method (the red curves or markers) using the fast formation parameters in Table 1. The monopole P-reflection waveform is shown in Figure 2a, and the dipole SH-reflection waveform is shown in Figure 2c. Because the finite-difference method models the wave propagation inside and outside of the borehole, the interference of large-amplitude borehole propagation waves appears in the early portion of the modeled full-wave data. In comparison, the analytical solution calculates only the wave propagation outside the borehole. For a better comparison of the reflection events, Figure 2a and 2c shows only the later portion of the wave data. The analytical and numerical results agree very well, verifying the validity and accuracy of our analytical solution.

Table 1. Acoustic parameters of the model.

Medium	P-wave velocity ($m \cdot s^{-1}$)	S-wave velocity ($m \cdot s^{-1}$)	Density ($kg \cdot m^{-3}$)	Radius (m)
Fluid in collar	1500	—	1000	0.027
Metallic collar	5860	3130	7850	0.09
Fluid out of collar	1500	—	1000	0.12
Formation a	3500	1800	2600	—
Formation b	4500	3000	2500	Infinity
Slow formation	2800	1200	2150	—

To further explore the azimuthal sensitivity of the modeled data, each waveform in Figure 2a and 2c is normalized by respective maximum amplitude and displayed using a polar plot in Figure 2b and 2d for the monopole and dipole data, respectively. Using the efficiency of the analytical modeling, the analytical results can be calculated at a small azimuthal increment, giving the continuous polar plot in Figure 2b and 2d (the black curve) to compare with their numerical counterparts (the red markers). For the P-wave (Figure 2b) and SH-wave (Figure 2d) cases with quite different azimuthal variation patterns, the analytical and numerical results agree quite well for the specified receiver azimuths (see Figure 1b).

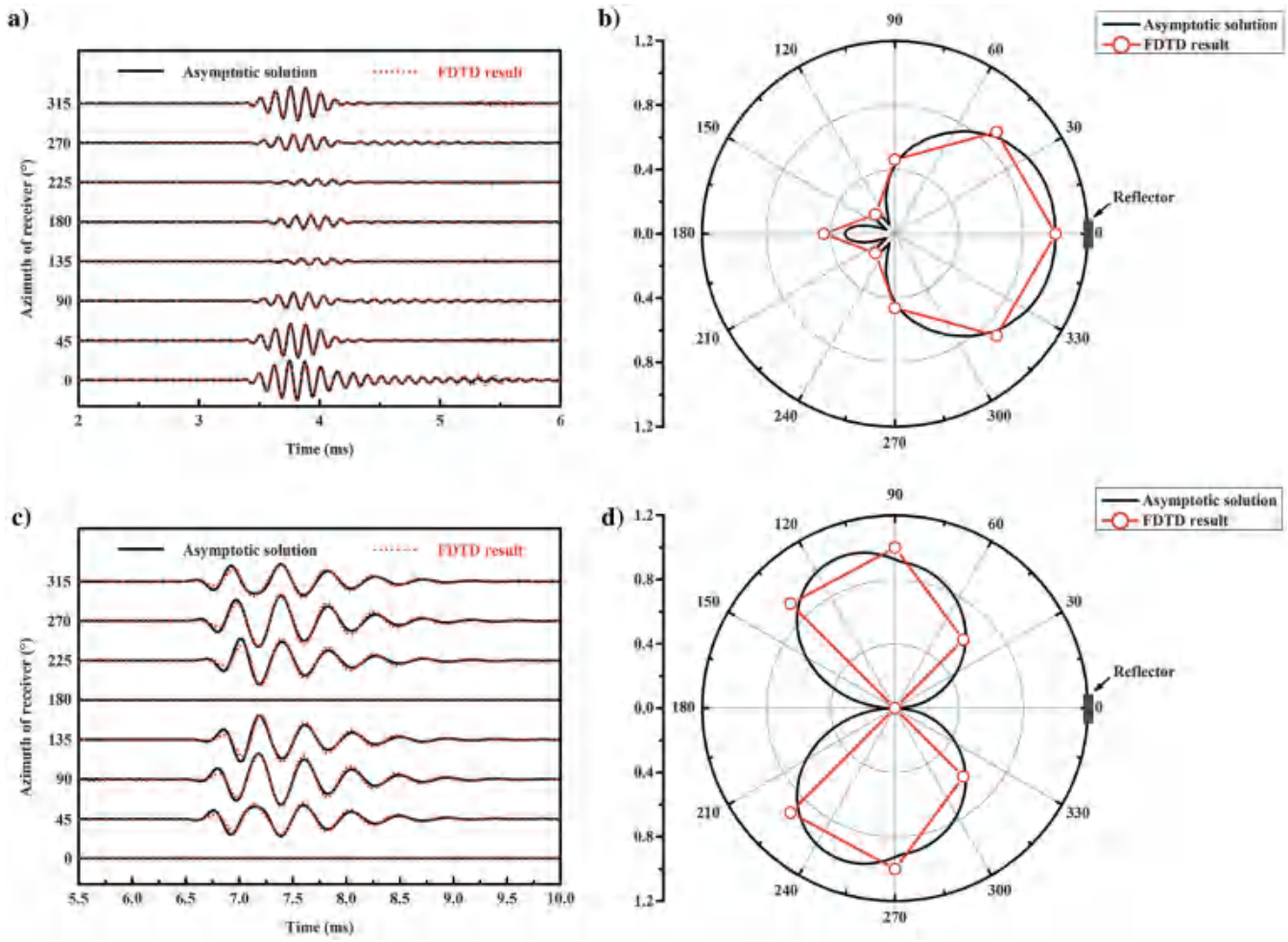


Figure 2. Comparison of the borehole-fluid pressure response calculated using the analytical solution and the 3D finite-difference method for the (a and b) monopole P-wave and (c and d) dipole SH-wave reflection modeling.

Downloaded from http://pubs.geoscienceworld.org/geophysics/article-pdf/doi/10.1190/geo2022-0756.1/5943043/geo-2022-0756.1.pdf
by China Univ Petroleum (East China) Library Serials Dept user
on 03 September 2023

It is worthwhile to mention that the computational efficiency of the two methods differs greatly. To model the effects of collar eccentricity accurately, small grid sizes must be used in the 3D finite-difference modeling. Using the results of Figure 2 as an example, the finite-difference method will take several days to complete the simulation. In contrast, our analytical method takes only a few minutes to obtain the result. Therefore, compared with the commonly used 3D numerical modeling, our analytical solution is much more advantageous for the ALWD reflection modeling with an eccentric tool system.

After validating our analytical solution, we use it to analyze the effect of collar eccentricity on the azimuthal response characteristics for monopole P-wave and dipole SH-wave reflection cases. The analysis will reveal the substantial influence of the drill collar and its eccentricity on the ALWD reflection measurement.

Comparison of LWD and WL

We first investigate the effects of the centralized drill collar as a reference for subsequent eccentered cases. The same model in Figure 1 and the fast formation parameters of Table 1 are used. Figure 3a and 3c (3b and 3d) shows, respectively, the azimuthal reflection waveforms (amplitude variation pattern [also called the reception pattern]) of the monopole P-wave and dipole SH-wave reflection modeling. The corresponding WL scenario without the tool is also modeled, with the red and black curves denoting the ALWD and WL results, respectively. In the WL case, the azimuthal P wave received at the borehole axis is identical in amplitude and phase (Figure 3a) and the variation pattern of the P-wave amplitude is a circle (Figure 3b), showing no sensitivity to the reflection azimuth. In comparison, the ALWD pattern is directed toward the reflector, attaining the maximum amplitude and earliest arrival along the reflector azimuth.

For the dipole modeling in Figure 3c and 3d, the radial displacement is calculated by differentiating fluid pressure along the receiving direction for WL (for ALWD, the pressure difference of two receivers at the opposite sides of the collar is taken). The WL amplitude variation for the SH-wave incidence shows symmetric patterns at 90° and 270°, showing the typical 180° ambiguity of dipole measurement (Tang and Patterson, 2009). In contrast, the ALWD pattern shows strong azimuthal asymmetry. Relative to the symmetric pattern of the WL case, the ALWD pattern is shifted away from the reflector, making it possible to assess the azimuth of the reflector.

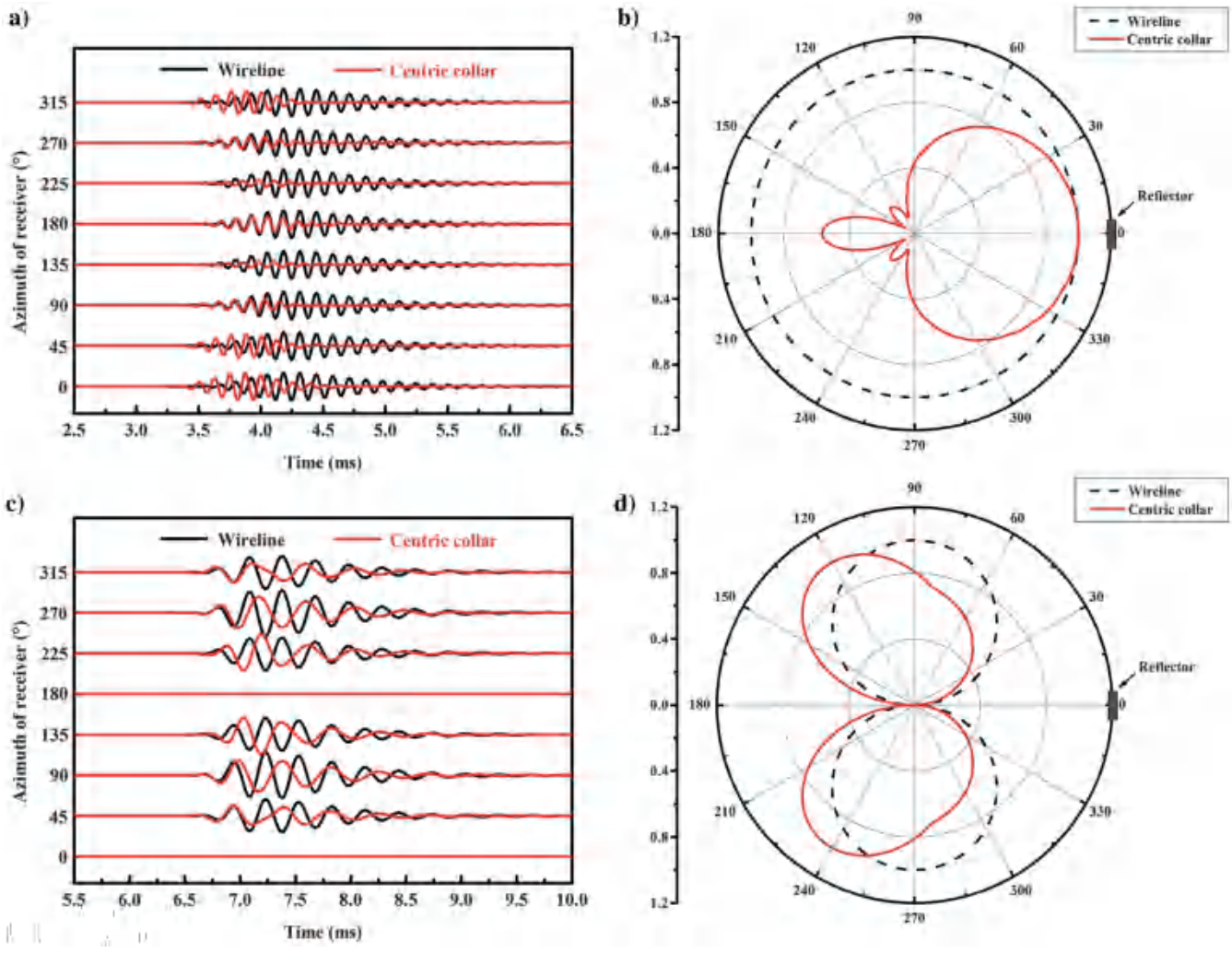


Figure 3. Comparison of the azimuthal variation of the WL and LWD waveforms and reception patterns for (a and b) the monopole P wave and (c and d) dipole SH wave.

Downloaded from http://pubs.geoscienceworld.org/geophysics/article-pdf/doi/10.1190/geo2022-0756.1/5943043/geo-2022-0756.1.pdf
by China Univ Petroleum (East China) Library Serials Dept user
on 03 September 2023

Influence of an eccentric collar on acoustic wavefields

In the ALWD measurement, the drill collar is often eccentric, particularly in horizontal or highly deviated wells. Relative to the azimuth of the geologic reflector in formation, Figure 4 classifies three cases of collar eccentering: eccentering toward (Figure 4a) or away from (Figure 4c) the reflector and eccentering along the direction parallel with the reflector strike (Figure 4b).

Figure 5 shows the monopole P-wave and dipole SH-wave reception patterns (markers) for the three eccentering scenarios. For comparison, their centered counterparts (the solid curves) are also plotted. The results of Figure 5 are calculated using the same borehole-collar model and formation parameters as those of Figure 3. The reflector is located at 0°. The eccentricity of the collar is 27 mm (Ecc = 90%) toward 0°, 90°, and 180°.

The P-wave reception patterns in Figure 5a show that the collar eccentricity significantly affects the azimuthal variation of the wave amplitude. Relative to the centered case, eccentering toward (away from) the reflector makes the front (back) side of the collar more sensitive (insensitive) to the reflector azimuth, whereas eccentering away from the reflector decreases this front versus back sensitivity difference. Eccentering 90° from the reflector azimuth significantly increases the receiving sensitivity in the eccentering direction, such that the maximum sensitivity is no longer toward the reflector azimuth.

The dipole SH-wave reception patterns shown in Figure 5b are also sensitive to the collar eccentricity. Relative to the centered case, eccentering toward (away from) the reflector reduces (enhances) the asymmetry between the upper and lower patterns, and eccentering 90° from the reflector azimuth significantly increases the receiving sensitivity in the eccentering direction, with the maximum sensitivity leaning toward the reflector.

For the three eccentering directions of Figure 4, Figure 6 shows the monopole P-wave (Figure 6a–6c) and dipole SH-wave (Figure 6d–6f) reception patterns for different eccentricity values from 0% to 90%. The patterns of the intermediate eccentricity values depict their evolution from the centered to severely eccentered positions in each direction. Worth mentioning is the monopole P-wave pattern for the case of eccentering away from the reflector. The receiving sensitivity at the back side of the collar increases with increasing eccentricity and exceeds that of the front side at an intermediate eccentricity value.

For the three eccentering directions of Figure 4, Figure 7 shows the monopole P-wave (Figure 7a–7c) and dipole SH-wave (Figure 7d–7f) reception patterns for different frequencies (6, 8, and 10 kHz for monopole and 1, 3, and 5 kHz for dipole). The eccentering offset is 27 mm and the corresponding Ecc value is 90%. These patterns show the azimuthal variation of receiving sensitivity with frequency in each eccentering direction. The general trend is that the (monopole and dipole) patterns are more (less) variable with increasing (decreasing) frequency.

Considering the ALWD reflection measurement in different formations, Figure 8 compares the monopole P-wave and dipole SH-wave reception patterns for the same collar-borehole model with a fast and a slow formation (see the formation parameters in Table 1). In the theoretical modeling, the eccentricity of the collar is 27 mm (Ecc = 90%), and the center frequency of the source is 8 kHz for the monopole and 3 kHz for the dipole. The fast formation results have already been shown in Figures 6 and 7 and are replotted here for comparison. As shown in Figure 8, the fast- and slow-formation monopole (Figure 8a–8c) and dipole (Figure 8d–8f) patterns for the three eccentering directions show some differences. The maximum difference is shown in Figure 8c and 8f where the collar is eccentered away from the reflector. This difference may need to be considered when interpreting the ALWD reflection measurement in different types of formations.

The preceding modeling examples show that the reception pattern for the ALWD reflection measurement is influenced by many factors such as the borehole and collar dimension and property, the eccentricity of the collar, the frequency of the source, and the formation property, with the collar eccentricity being the most influential factor.

ALWD reflection waveform modeling

As an important application of the preceding theory and modeling method, we use them to model the ALWD reflection measurement. The reflector model is shown in Figure 9c, which consists of a 100 m depth section with two oppositely dipping interfaces intersecting the borehole at 40 m (the upper reflector) and 60 m (the lower reflector) at an angle of 30°, respectively. The formation surrounding the borehole is the fast formation in Table 1. For description convenience, the up-dip and down-dip sides of the upper

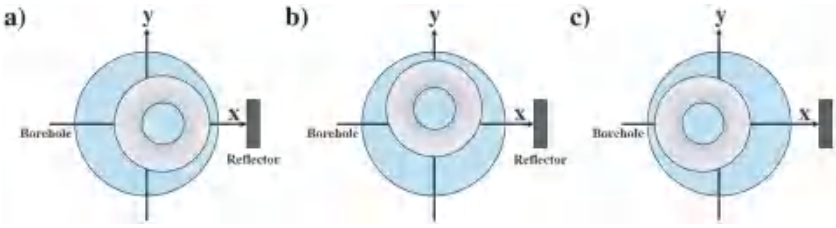


Figure 4. Scenarios of drill collar eccentering with respect to the reflector: (a) toward the reflector, (b) along the direction parallel to the reflector strike, and (c) away from the reflector.

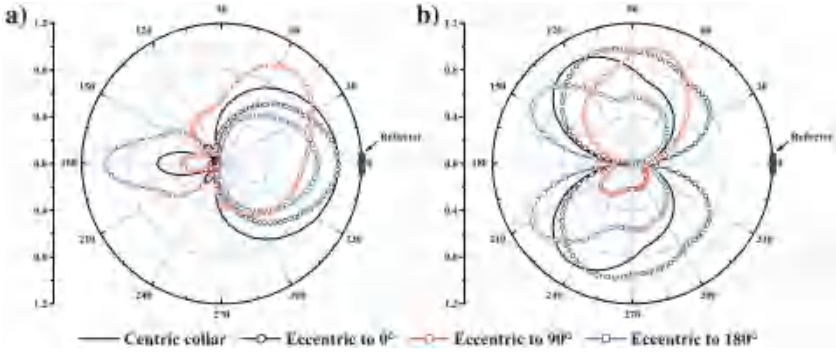


Figure 5. The ALWD pattern for different tool eccentric directions: (a) monopole P wave and (b) dipole SH wave. For comparison, the centered result (the solid curve) is also plotted. The amplitude of each curve is normalized by the maximum value of the curve.

Downloaded from http://pubs.geoscienceworld.org/geophysics/article-pdf/doi/10.1190/geo2022-0756.1/5943043/geo-2022-0756.1.pdf
by China Univ Petroleum (East China) Library Serials Dept user
on 03 September 2023

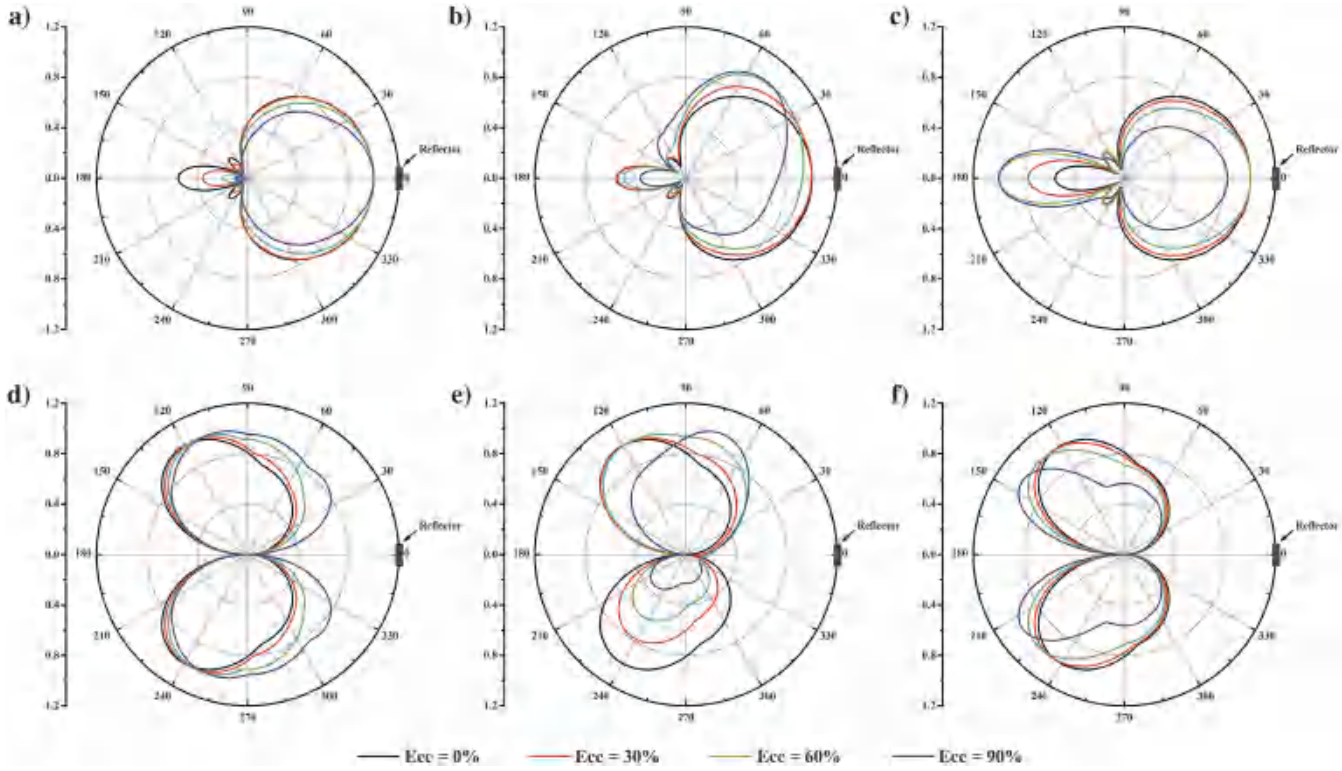


Figure 6. The ALWD reception pattern variation with tool eccentricity for the three eccentering directions of Figure 4: (a–c) monopole P wave and (d–f) dipole SH wave. (a, c, d, and f) The eccentering direction is toward (away from) the reflector. (b and e) The eccentering direction is parallel to the strike of the reflector. The amplitude of each curve is normalized by the maximum value of the curve.

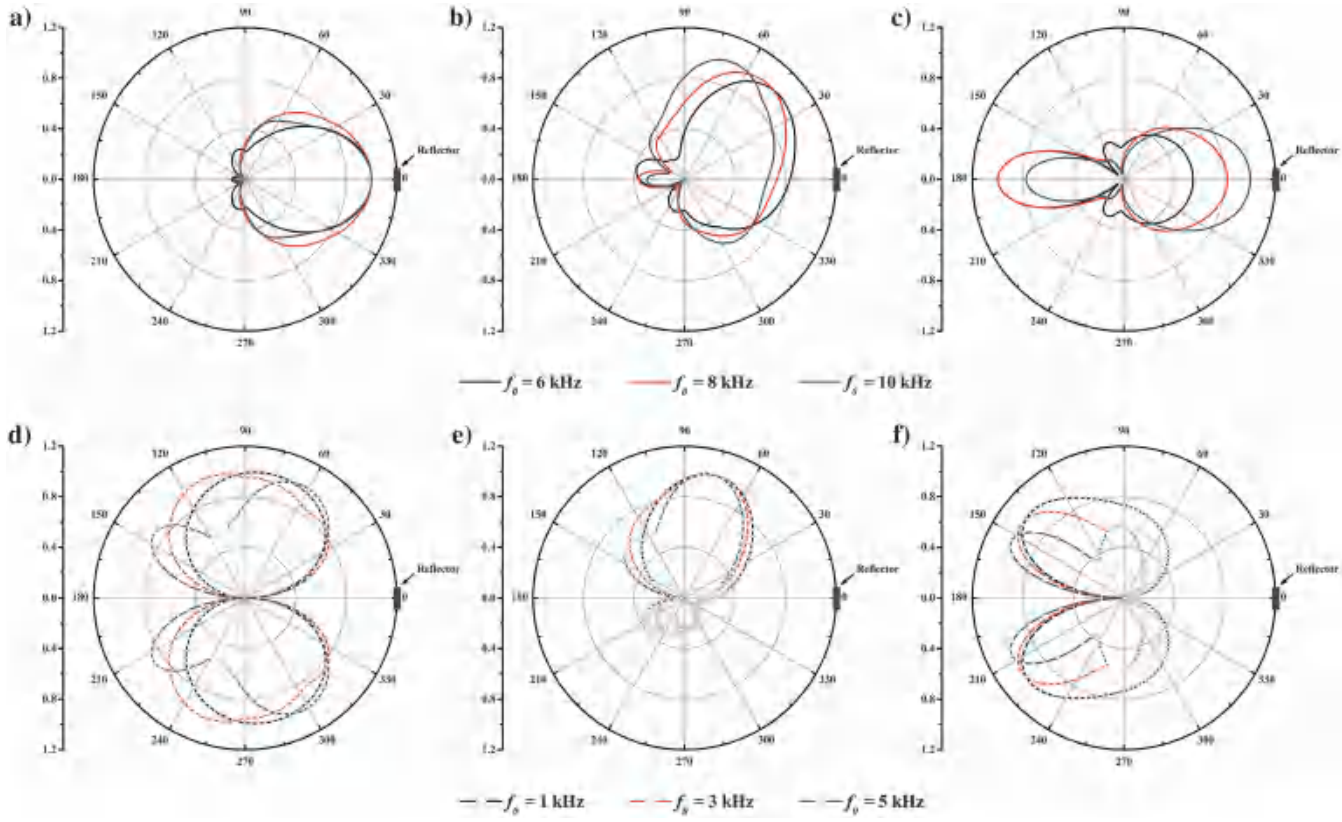


Figure 7. The ALWD reception patterns for different source frequencies: (a–c) monopole P wave and (d–f) dipole SH wave. (a, c, d, and f) The eccentering direction is toward (away from) the reflector. (b and e) The eccentering direction is parallel to the strike of the reflector. The amplitude of each curve is normalized by the maximum value of the curve.

Downloaded from http://pubs.geoscienceworld.org/geophysics/article-pdf/doi/10.1190/geo2022-0756.1/5943043/geo-2022-0756.1.pdf
by China Univ Petroleum (East China) Library Serials Dept user
on 03 September 2023

(lower) reflector are denoted by j and k (l and m), respectively. The borehole and collar parameters are the same as used previously. Two collar positions will be modeled: centered and eccentered (offset by 27 mm along the x-axis) for the 8 kHz monopole and 3 kHz dipole (pointing to the y-axis) sources, respectively. The modeling results are shown in Figure 9a and 9b (monopole) and Figure 9d and 9e (dipole).

The left (right) panels show the P-wave (SH-wave) reflection waves (displayed as a variable-density image) of the centered

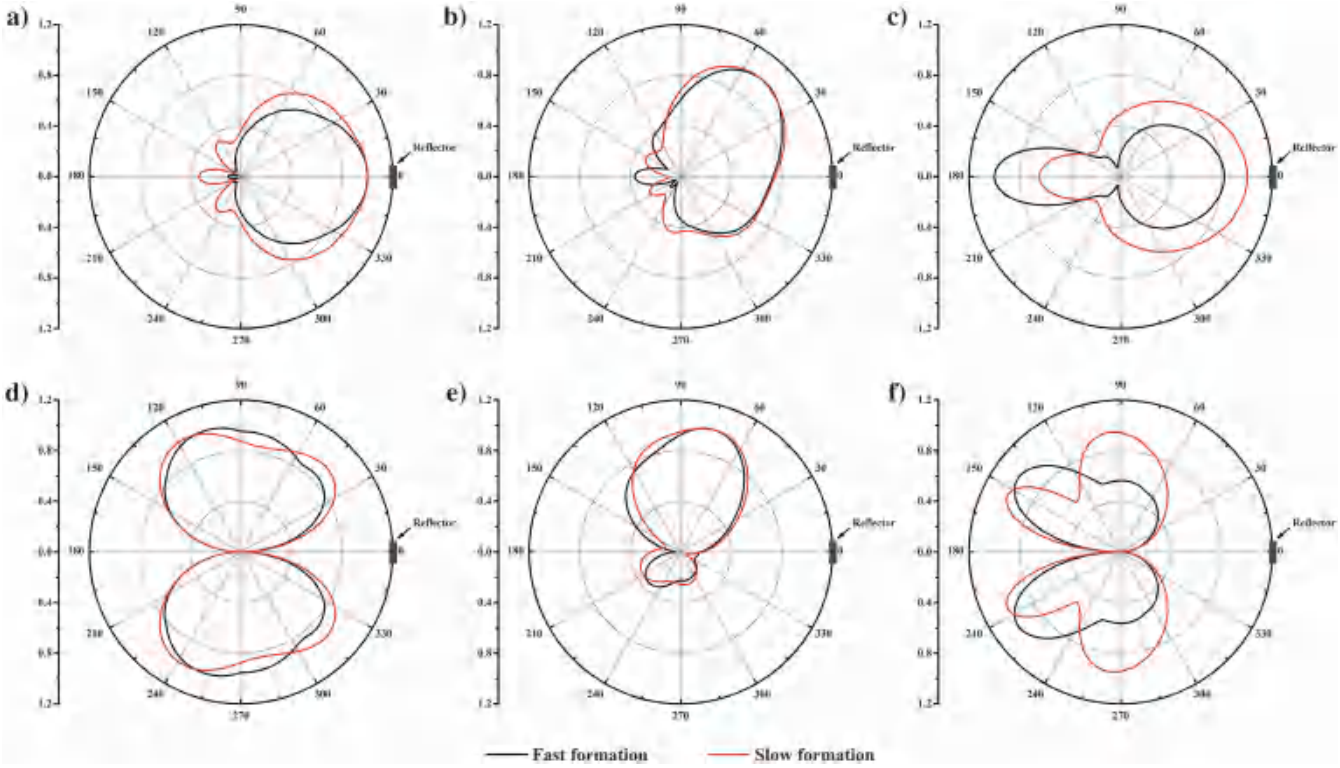


Figure 8. The ALWD reception patterns in the fast and slow formations: (a–c) monopole P wave and (d–f) dipole SH wave. (a, c, d, and f) The eccentering direction is toward (away from) the reflector. (b and e) The eccentering direction is parallel to the strike of the reflector. The amplitude of each curve is normalized by the maximum value of the curve.

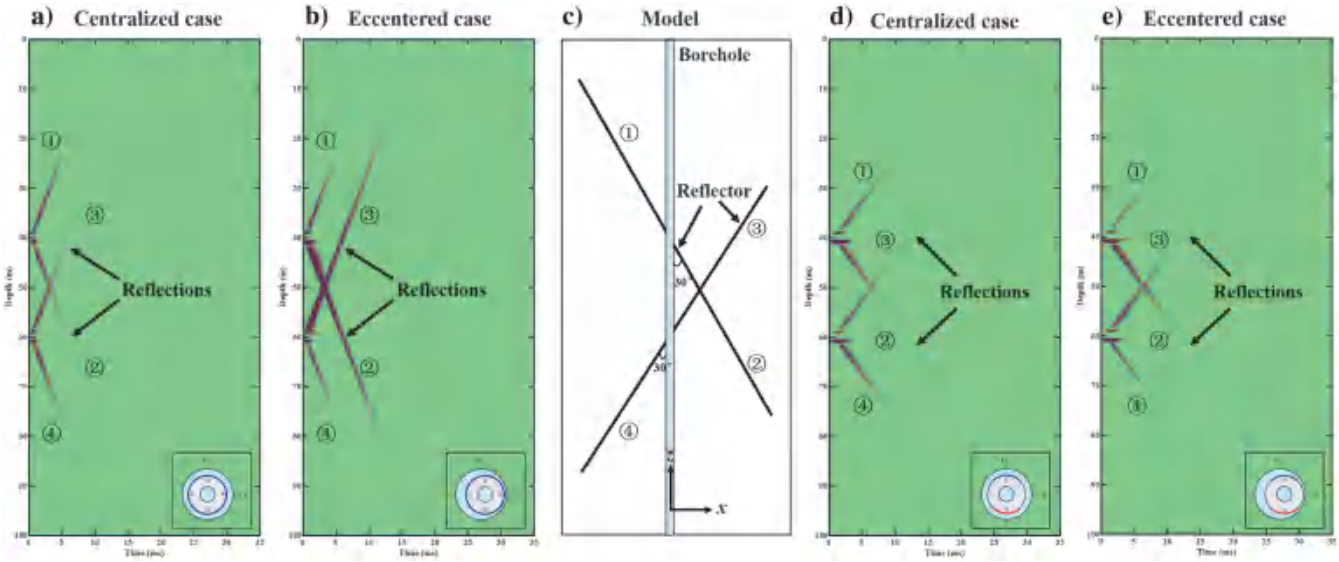


Figure 9. (c) Multipole reflector model for modeling the (a and b) monopole and (d and e) dipole ALWD reflection measurement with and without collar eccentering. The asymmetric reflection pattern due to tool eccentricity can be used to solve the 180° ambiguity of the reflector azimuth.

Downloaded from http://pubs.geoscienceworld.org/geophysics/article-pdf/doi/10.1190/geo2022-0756.1/5943043/geo-2022-0756.1.pdf
by China Univ Petroleum (East China) Library Serials Dept user
on 03 September 2023

and eccentered cases. For monopole reception, the waves are the average pressure of the receivers at 0°, 90°, 180°, and 270°. For dipole reception, the waves are the pressure difference of the receivers at 90° and 270°. For the centered case, the upgoing reflections j and l from the up-dip reflectors are almost symmetric with respect to their downgoing counterparts k and m, unable to resolve which side the reflection is from. The situation is quite different for the eccentered case. Because of the eccentricity effect, the downgoing k (upgoing l) P- or SH-wave reflection of the upper (lower) reflector is significantly stronger compared with its upgoing j (downgoing m) counterpart. According to our previous modeling results (see Figure 5), this indicates that the downgoing k (upgoing l) reflection is from the down-dip k (up-dip l) part of the upper (lower) reflector, which is on the right side of the borehole. This modeling example shows that a potential benefit of tool eccentering is to use the resulting asymmetric amplitude variation to help resolve the reflector azimuth.

CONCLUSION

This study analyzes the ALWD reflection measurement with a multipole acoustic source on an eccentric drill collar. The problem is formulated by treating the wave reflection as the wave incidence from a virtual source in the borehole and collar coordinates system. The far-field solution of the problem is obtained by using the translational Bessel addition theorem to solve the dual-coordinate system and using the steepest descent method to facilitate the wavenumber integration. The validity and accuracy of our analytical solution have been verified by comparison with 3D finite-difference modeling results. Our analysis and modeling results show that among many factors that influence the ALWD reflection measurement, such as borehole and collar dimension and property, source frequency, and the formation property, the degree and direction of collar eccentricity are the most influential factors affecting the azimuthal reception of the reflected waves. Our results also show that the asymmetric reflection and reception pattern due to tool eccentricity can be used to solve the 180° reflector azimuth ambiguity.

ACKNOWLEDGMENTS

The authors thank the reviewers for their comments and suggestions that helped to improve the manuscript. This work was supported by the National Natural Science Foundation of China (grant nos. U21B2064, 42074137, 41821002, and 42174145), the Natural Science Foundation of Shandong Province (grant no. ZR201911120382), the Laoshan National Laboratory Science and Technology Innovation Project (grant no. LSKJ202203400), and the Innovation fund project for a graduate student at China University of Petroleum (East China) supported by the Fundamental Research Funds for the Central Universities (23CX04016A).

DATA AND MATERIALS AVAILABILITY

Data associated with this research are available and can be obtained by contacting the corresponding author.

APPENDIX A

THE FAR-FIELD RADIATION PATTERNS IN ALWD WITH AN ECCENTRIC COLLAR

By analogy with equation 16 for the wave incidence problem, a similar system of linear equations can be derived for wave radiation from the acoustic source on the LWD tool as follows:

$$\mathbf{M}_{(24N+12)\cdot(24N+12)}\mathbf{X}_{(24N+12)\cdot 1} = \mathbf{P}_{(24N+12)\cdot 1}; \tag{A-1}$$

where $\mathbf{M}$ is a $(24N + 12) \times (24N + 12)$ square matrix and N is set to five for calculating the far-field radiation with sufficient accuracy. Here, $\mathbf{X}$ and $\mathbf{P}$ are the $(24N + 12) \times 1$ vectors given by

$$\mathbf{X}_{(24N+12)\times 1} = \begin{bmatrix} A^{tool}_{-N}; A^{tool}_{-N+1}; \cdots; A^{tool}_{N-1}; A^{tool}_{N}; B^{tool}_{-N}; B^{tool}_{-N+1}; \cdots; B^{tool}_{N-1}; B^{tool}_{N}; \\ C^{tool}_{-N}; C^{tool}_{-N+1}; \cdots; C^{tool}_{N-1}; C^{tool}_{N}; D^{tool}_{-N}; D^{tool}_{-N+1}; \cdots; D^{tool}_{N-1}; D^{tool}_{N}; \\ E^{tool}_{-N}; E^{tool}_{-N+1}; \cdots; E^{tool}_{N-1}; E^{tool}_{N}; F^{tool}_{-N}; F^{tool}_{-N+1}; \cdots; F^{tool}_{N-1}; F^{tool}_{N}; \\ A^{in}_{-N}; A^{in}_{-N+1}; \cdots; A^{in}_{N-1}; A^{in}_{N}; A^{out}_{-N}; A^{out}_{-N+1}; \cdots; A^{out}_{N-1}; A^{out}_{N}; \\ B^{out}_{-N}; B^{out}_{-N+1}; \cdots; B^{out}_{N-1}; B^{out}_{N}; B^{F}_{-N}; B^{F}_{-N+1}; \cdots; B^{F}_{N-1}; B^{F}_{N}; \\ D^{F}_{-N}; D^{F}_{-N+1}; \cdots; D^{F}_{N-1}; D^{F}_{N}; F^{F}_{-N}; F^{F}_{-N+1}; \cdots; F^{F}_{N-1}; F^{F}_{N} \end{bmatrix}^{T}; \tag{A-2}$$

$$\mathbf{P}_{(24N+12)\times 1} = (0; \cdots; 0; \sigma^{s}; 0; \cdots; 0)^{T}: \tag{A-3}$$

In equation A-3, the source strength σ^s is the (11 N + 6)th element of the column vector for monopole; the value of σ^s is set to 10^5 Pa (Cui, 2004). For the dipole case, σ^s is the (11 N + 7)th element of the column vector (omitting the contribution of higher order terms).

Solving equation A-1 to determine the amplitude coefficients outside the borehole, the wavefield away from the borehole is fully determined. For far-field conditions, $\eta^F_p r_2 \gg 1; \eta^F_s r_2 \gg 1$, the steepest descent solution for the potential functions can be derived as follows:

$$\begin{cases} \phi^{F'} = -\frac{e^{i\omega R=\alpha - i\pi=4}}{4\pi R}\sum_{m=-\infty}^{\infty} B^F_m(k_{p0};\omega)\cos(m\varphi_2) \\ \chi^{F'} = -\frac{e^{i\omega R=\beta - i\pi=4}}{4\pi R}\sum_{m=-\infty}^{\infty} D^F_m(k_{s0};\omega)\sin(m\varphi_2) \\ \Gamma^{F'} = -\frac{e^{i\omega R=\beta - i\pi=4}}{4\pi R}\sum_{m=-\infty}^{\infty} F^F_m(k_{s0};\omega)\cos(m\varphi_2) \end{cases}; \tag{A-4}$$

where $R = (r_2^2 + z^2)^{1=2}$ is the radiation distance of the borehole axis to the field point; $k_{p0} = \omega \cos \theta_t = \alpha$ and $k_{s0} = \omega \cos \theta_t = \beta$ are the steepest descent solutions for the wavenumber of formation P and S waves, respectively; and θ_t is the wave radiation angle from the z-axis.

From the potential functions of equation A-4, the far-field displacement spectrum for the radiation P, SH, and SV waves can be derived as follows:

$$\begin{cases} u_P = \left[i\rho\alpha\omega\sum_{m=-\infty}^{\infty} B^F_m(k_{p0};\omega)\cos(m\varphi_2)\right]\frac{e^{i\omega R=\alpha - i\pi=4}}{4\pi\rho\alpha^2 R} \\ u_{SH} = \left[-i\rho\beta\omega\sin\theta_t\sum_{m=-\infty}^{\infty} D^F_m(k_{s0};\omega)\sin(m\varphi_2)\right]\frac{e^{i\omega R=\beta - i\pi=4}}{4\pi\rho\beta^2 R}; \\ u_{SV} = \left[\rho\omega^2\sin\theta_t\sum_{m=-\infty}^{\infty} F^F_m(k_{s0};\omega)\cos(m\varphi_2)\right]\frac{e^{i\omega R=\beta - i\pi=4}}{4\pi\rho\beta^2 R} \end{cases} \tag{A-5}$$

where ρ is the formation density.

Downloaded from http://pubs.geoscienceworld.org/geophysics/article-pdf/doi/10.1190/geo2022-0756.1/5943043/geo-2022-0756.1.pdf
by China Univ Petroleum (East China) Library Serials Dept user
on 03 September 2023

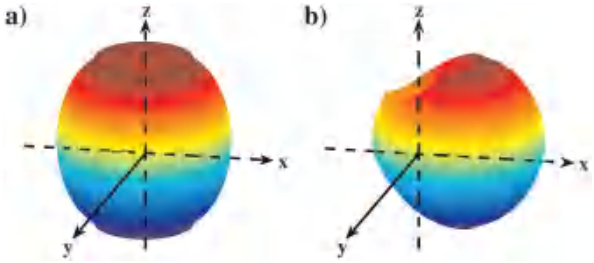


Figure A-1. The 3D radiation pattern of the monopole P wave at 8 kHz for (a) centralized case and (b) eccentered case (eccentric toward the x-axis).

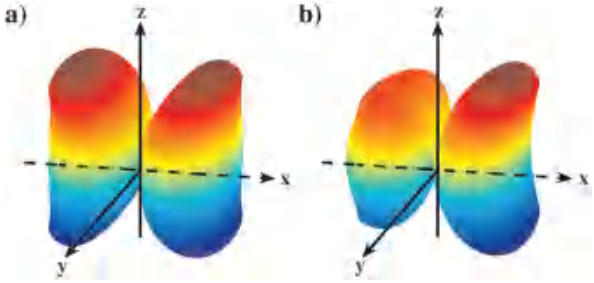


Figure A-2. The 3D radiation pattern of the dipole SH wave at 3 kHz for (a) centralized case and (b) eccentered case (eccentric toward the x-axis).

The dimensionless expressions in square brackets of equation A-5 define the far-field radiation directivity of P, SH, and SV waves, respectively, as follows:

$$\begin{cases} RD_P(\omega;\theta;\varphi_2) = \sum_{m=-\infty}^{\infty} B_m^F(k_{p0};\omega)\cos(m\varphi_2) \\ RD_{SH}(\omega;\theta;\varphi_2) = \sum_{m=-\infty}^{\infty} D_m^F(k_{s0};\omega)\sin(m\varphi_2) \\ RD_{SV}(\omega;\theta;\varphi_2) = \sum_{m=-\infty}^{\infty} F_m^F(k_{s0};\omega)\cos(m\varphi_2) \end{cases} \tag{A-6}$$

Using a 3D color diagram, Figures A-1 and A-2 compare the ALWD P-wave (S-wave) radiation pattern for an 8 kHz monopole source (a 3 kHz dipole source, pointing to the y-axis) of an eccentered tool with its centered counterpart. For both cases, the eccentricity of the tool enhances the energy of radiation toward the eccentering direction, which is beneficial for detecting a reflector in that direction.

APPENDIX B

EXPRESSIONS OF THE ELEMENTS OF VECTORS Q AND Q′ IN EQUATION 16

Note that vectors Q and Q′ in equation 16 are different for the different types of incident waves, as given in the following:

For the incident P wave (omitting the common factor $S(\omega)\cdot RD_P(\omega)\cdot RF_P(\omega)$):

$$\begin{pmatrix} q_{16N+9} \\ \vdots \\ q_{18N+9} \end{pmatrix} = -\left[\frac{mI_m(\eta_p^F c)}{c} + \eta_p^F I_{m+1}(\eta_p^F c)\right]\cos(m\varphi_2');$$

$$\begin{pmatrix} q_{18N+10} \\ \vdots \\ q_{20N+10} \end{pmatrix} = -\left(\left\{2\mu^F\left[k^2 + \frac{m^2-m}{c^2}\right] - \rho\omega^2\right\} I_m(\eta_p^F c) - \frac{2\mu^F \eta_p^F I_{m+1}(\eta_p^F c)}{c}\right)\cos(m\varphi_2');$$

$$\begin{pmatrix} q_{20N+11} \\ \vdots \\ q_{22N+11} \end{pmatrix} = -2ik\mu^F\left[\frac{mI_m(\eta_p^F c)}{c} + \eta_p^F I_{m+1}(\eta_p^F c)\right]\cos(m\varphi_2');$$

$$\begin{pmatrix} q_{22N+12} \\ \vdots \\ q_{24N+12} \end{pmatrix} = -2\mu^F\left[\frac{(m-m^2)I_m(\eta_p^F c)}{c^2} - \frac{m\eta_p^F I_{m+1}(\eta_p^F c)}{c}\right] \times\cos(m\varphi_2');$$

$$\begin{pmatrix} q'_{16N+9} \\ \vdots \\ q'_{18N+9} \end{pmatrix} = -\left[\frac{mI_m(\eta_p^F c)}{c} + \eta_p^F I_{m+1}(\eta_p^F c)\right]\sin(m\varphi_2');$$

$$\begin{pmatrix} q'_{18N+10} \\ \vdots \\ q'_{20N+10} \end{pmatrix} = -\left(\left\{2\mu^F\left[k^2 + \frac{m^2-m}{c^2}\right] - \rho\omega^2\right\} I_m(\eta_p^F c) - \frac{2\mu^F \eta_p^F I_{m+1}(\eta_p^F c)}{c}\right)\sin(m\varphi_2');$$

$$\begin{pmatrix} q'_{20N+11} \\ \vdots \\ q'_{22N+11} \end{pmatrix} = -2ik\mu^F\left[\frac{mI_m(\eta_p^F c)}{c} + \eta_p^F I_{m+1}(\eta_p^F c)\right]\sin(m\varphi_2');$$

$$\begin{pmatrix} q'_{22N+12} \\ \vdots \\ q'_{24N+12} \end{pmatrix} = -2\mu^F\left[\frac{(m-m^2)I_m(\eta_p^F c)}{c^2} - \frac{m\eta_p^F I_{m+1}(\eta_p^F c)}{c}\right] \times\sin(m\varphi_2'): \tag{B-1}$$

For the incident SH wave (omitting the common factor $S(\omega)\cdot RD_{SH}(\omega)\cdot RF_{SH}(\omega)$):

$$\begin{pmatrix} q_{16N+9} \\ \vdots \\ q_{18N+9} \end{pmatrix} = \frac{-mI_m(\eta_s^F c)}{c}\sin(m\varphi_2');$$

$$\begin{pmatrix} q_{18N+10} \\ \vdots \\ q_{20N+10} \end{pmatrix} = -2m\mu^F\left(\frac{(m-1)I_m(\eta_s^F c)}{c^2} + \frac{\eta_s^F I_{m+1}(\eta_s^F c)}{c}\right) \times\sin(m\varphi_2');$$

Downloaded from http://pubs.geoscienceworld.org/geophysics/article-pdf/doi/10.1190/geo2022-0756.1/5943043/geo-2022-0756.1.pdf
by China Univ Petroleum (East China) Library Serials Dept user
on 03 September 2023

$$\begin{pmatrix} q_{20N+11} \\ \vdots \\ q_{22N+11} \end{pmatrix} = \frac{-ikm\mu^F I_m(\eta_s^F c)}{c} \sin(m\varphi_2');$$

$$\begin{pmatrix} q_{22N+12} \\ \vdots \\ q_{24N+12} \end{pmatrix} = \mu^F \left\{ \left[\frac{2(m^2-m)}{c^2} + (\eta_s^F)^2 \right] I_m(\eta_s^F c) - \frac{2\eta_s^F I_{m+1}(\eta_s^F c)}{c} \right\} \sin(m\varphi_2');$$

$$\begin{pmatrix} q'_{16N+9} \\ \vdots \\ q'_{18N+9} \end{pmatrix} = \frac{m I_m(\eta_s^F c)}{c} \cos(m\varphi_2');$$

$$\begin{pmatrix} q'_{18N+10} \\ \vdots \\ q'_{20N+10} \end{pmatrix} = 2m\mu^F \left[\frac{(m-1) I_m(\eta_s^F c)}{c^2} + \frac{\eta_s^F I_{m+1}(\eta_s^F c)}{c} \right] \times \cos(m\varphi_2'); \begin{pmatrix} q'_{20N+11} \\ \vdots \\ q'_{22N+11} \end{pmatrix} = \frac{ikm\mu^F I_m(\eta_s^F c)}{c} \cos(m\varphi_2');$$

$$\begin{pmatrix} q'_{22N+12} \\ \vdots \\ q'_{24N+12} \end{pmatrix} = -\mu^F \left\{ \left[\frac{2(m^2-m)}{c^2} + (\eta_s^F)^2 \right] I_m(\eta_s^F c) - \frac{2\eta_s^F I_{m+1}(\eta_s^F c)}{c} \right\} \cos(m\varphi_2'): \tag{B-2}$$

For the incident SV wave (omitting the common factor $S(\omega) \cdot RD_{SV}(\omega) \cdot RF_{SV}(\omega)$):

$$\begin{pmatrix} q_{16N+9} \\ \vdots \\ q_{18N+9} \end{pmatrix} = -ik \left[\frac{m I_m(\eta_s^F c)}{c} + \eta_s^F I_{m+1}(\eta_s^F c) \right] \cos(m\varphi_2');$$

$$\begin{pmatrix} q_{18N+10} \\ \vdots \\ q_{20N+10} \end{pmatrix} = -2ik\mu^F \left\{ \left[\frac{m^2-m}{c^2} + (\eta_s^F)^2 \right] I_m(\eta_s^F c) - \frac{\eta_s^F I_{m+1}(\eta_s^F c)}{c} \right\} \cos(m\varphi_2');$$

$$\begin{pmatrix} q_{20N+11} \\ \vdots \\ q_{22N+11} \end{pmatrix} = \mu^F [(\eta_s^F)^2 + k^2] \left[\frac{m I_m(\eta_s^F c)}{c} + \eta_s^F I_{m+1}(\eta_s^F c) \right] \times \cos(m\varphi_2');$$

$$\begin{pmatrix} q_{22N+12} \\ \vdots \\ q_{24N+12} \end{pmatrix} = -2ikm\mu^F \left[\frac{(1-m) I_m(\eta_s^F c)}{c^2} - \frac{\eta_s^F I_{m+1}(\eta_s^F c)}{c} \right] \times \cos(m\varphi_2');$$

$$\begin{pmatrix} q'_{16N+9} \\ \vdots \\ q'_{18N+9} \end{pmatrix} = -ik \left[\frac{m I_m(\eta_s^F c)}{c} + \eta_s^F I_{m+1}(\eta_s^F c) \right] \sin(m\varphi_2');$$

$$\begin{pmatrix} q'_{18N+10} \\ \vdots \\ q'_{20N+10} \end{pmatrix} = -2ik\mu^F \left\{ \left[\frac{m^2-m}{c^2} + (\eta_s^F)^2 \right] I_m(\eta_s^F c) - \frac{\eta_s^F I_{m+1}(\eta_s^F c)}{c} \right\} \sin(m\varphi_2');$$

$$\begin{pmatrix} q'_{20N+11} \\ \vdots \\ q'_{22N+11} \end{pmatrix} = \mu^F [(\eta_s^F)^2 + k^2] \left[\frac{m I_m(\eta_s^F c)}{c} + \eta_s^F I_{m+1}(\eta_s^F c) \right] \times \sin(m\varphi_2');$$

$$\begin{pmatrix} q'_{22N+12} \\ \vdots \\ q'_{24N+12} \end{pmatrix} = -2ikm\mu^F \left[\frac{(1-m) I_m(\eta_s^F c)}{c^2} - \frac{\eta_s^F I_{m+1}(\eta_s^F c)}{c} \right] \times \sin(m\varphi_2'); \tag{B-3}$$

where Q and Q′ are the $(24N + 12) \times 1$ vectors (only the nonzero elements have been listed previously); $\mu^F = \rho\beta^2$ is the shear modulus of the formation; φ_2' is the azimuth of the reflector; and $m = (-N; -N+1; \ldots; N-1; N)$ is the vector of circumferential periodic numbers in the borehole coordinates system.

REFERENCES

Aki, K., and P. Richards, 1980, Quantitative seismology: Theory and methods: Freeman and Co.

Ben, J. L., W. X. Qiao, X. H. Che, X. D. Ju, J. Q. Lu, and B. Y. Men, 2020, Experimental simulation of obtaining the reflector azimuth using azimuthal acoustic reflection tool in the underwater environment: Journal of Petroleum Science and Engineering, 195, 107649, doi: 10.1016/j.petrol.2020.107649.

Bennett, N. N., 2019, 3D slowness time coherence for sonic imaging: Geophysics, 84, no. 5, D179–D189, doi: 10.1190/geo2018-0077.1.

Cao, J. J., X. M. Tang, Y. D. Su, Z. T. Wei, and C. X. Zhuang, 2016, Radiation characteristics of the single-well imaging field in while-drilling logging using an acoustic dipole source (in Chinese): Chinese Journal of Geophysics, 59, 3503–3513, doi: 10.6038/cjg20160932.

Che, X. H., and W. X. Qiao, 2004, Acoustic field in formation generated by linear phased array transmitters in fluid-filled boreholes (in Chinese): Chinese Journal of Geophysics, 47, 830–836, doi: 10.1002/cjg2.3556.

Chen, X. L., and Z. T. Wei, 2012, Numerical simulation of monopole acoustic reflection imaging logging in the logging-while-drilling condition (in Chinese): Acta Petrolei Sinica, 33, 835–840, doi: 10.7623/syxb201205013.

Christian, F., H. Andreas, and G. Matthias, 2010, High resolution electrical imaging while drilling: Presented at the 51st Annual Logging Symposium, SPWLA.

Cui, Z. W., 2004, Theoretical and numerical study of modified Biot's models, acoustoelectric well logging and acoustic logging while drilling excited by multipole acoustic sources: Ph.D. dissertation, Jilin University.

Downloaded from http://pubs.geoscienceworld.org/geophysics/article-pdf/doi/10.1190/geo2022-0756.1/5943043/geo-2022-0756.1.pdf
by China Univ Petroleum (East China) Library Serials Dept user
on 03 September 2023

Esmersoy, C., C. Chang, M. Kane, R. Coates, B. Tichelaar, and E. Quint, 1998, Acoustic imaging of reservoir structure from a horizontal well: The Leading Edge, 17, 940–946, doi: 10.1190/1.1438075.
Gong, H., H. Chen, X. He, C. Su, X. M. Wang, B. C. Wang, and X. H. Yan, 2018, Modeling and inversions of acoustic reflection logging imaging using the combined monopole-dipole measurement mode: Applied Geophysics, 15, 393–400, doi: 10.1007/s11770-018-0700-y.
Gong, H., H. Chen, X. He, and X. M. Wang, 2015, Eliminating the azimuth ambiguity in single-well imaging using 3C sonic data: Geophysics, 80, no. 1, A13–A17, doi: 10.1190/geo2014-0337.1.
Haugland, S. M., 2004a, Mandrel eccentricity effects on acoustic borehole-guided waves: 74th Annual International Meeting, SEG, Expanded Abstracts, 282–285, doi: 10.1190/1.1851265.
Haugland, S. M., 2004b, Analytical solution for an eccentric mandrel in a fluid-filled borehole: The acoustic case: 74th Annual International Meeting, SEG, Expanded Abstracts, 330–333, doi: 10.1190/1.1842392.
Hirabayashi, N., K. Torii, H. Yamamoto, J. Haldorsen, and A. Voskamp, 2010, Fracture detection using borehole acoustic reflection survey data: 80th Annual International Meeting, SEG, Expanded Abstracts, 523–527, doi: 10.1190/1.3513836.
Hornby, B. E., 1989, Imaging of near-borehole structure using full-waveform sonic data: Geophysics, 54, 747–757, doi: 10.1190/1.1442702.
Huang, X., Y. Zheng, and M. N. Toksöz, 2004, Effects of tool eccentricity on acoustic logging while drilling (LWD) measurements: 74th Annual International Meeting, SEG, Expanded Abstracts, 290–293, doi: 10.1190/1.1851266.
Ji, Y. J., X. He, H. Chen, X. M. Wang, and H. L. Zhang, 2021, Acoustic fields for monopole logging while drilling with an eccentric collar: Geophysics, 86, no. 2, D43–D63, doi: 10.1190/geo2019-0744.1.
Lee, S. Q., M. Chen, X. H. Gu, Y. D. Su, and X. M. Tang, 2019, Application of four-component dipole shear reflection imaging to interpret the geological structure around a deviated well: Applied Geophysics, 16, 291–301, doi: 10.1007/s11770-019-0778-x.
Li, C., H. Chen, X. He, and X. M. Wang, 2021a, Identifying reflector azimuth from borehole multicomponent cross-dipole acoustic measurement: Geophysics, 86, no. 6, D201–D214, doi: 10.1190/geo2020-0460.1.
Li, G. Y., X. Y. Chai, X. D. Ju, W. X. Qiao, C. G. Ji, M. M. Han, and W. D. Li, 2018, Azimuth remote exploration acoustic reflection imaging logging tool: Well Logging Technology, 42, 221–226.
Li, Y. H., X. M. Tang, H. R. Li, and S. Q. Lee, 2021b, Characterizing the borehole response for single-well shear-wave reflection imaging: Geophysics, 86, no. 1, D15–D26, doi: 10.1190/geo2020-0212.1.
Pardo, D., P. J. Matuszyk, I. Muga, C. Torres-Verdín, A. Mora, and V. M. Calo, 2013, Influence of borehole-eccentered tools in wireline and LWD sonic logging measurements: Geophysical Prospecting, 61, 268–283, doi: 10.1111/1365-2478.12022.
Tan, B. H., X. M. Tang, Z. T. Wei, J. J. Cao, and Y. D. Su, 2016, Dominant frequency band and reflected wave field of LWD dipole shear wave remote detection (in Chinese): Acta Petrolei Sinica, 37, 1152–1158, doi: 10.7623/syxb201609009.
Tang, X. M., 2004, Imaging near-borehole structure using directional acoustic-wave measurement: Geophysics, 69, 1378–1386, doi: 10.1190/1.1836812.
Tang, X. M., J. J. Cao, Z. Li, and Y. D. Su, 2016, Detecting a fluid-filled borehole using elastic waves from a remote borehole: Journal of the Acoustical Society of America, 140, EL211–EL217, doi: 10.1121/1.4960143.
Tang, X. M., J. J. Cao, and Z. T. Wei, 2014, Shear-wave radiation, reception, and reciprocity of a borehole dipole source: With application to modeling of shear-wave reflection survey: Geophysics, 79, no. 2, T43–T50, doi: 10.1190/geo2013-0096.1.
Tang, X. M., and C. H. Cheng, 2004, Quantitative borehole acoustic methods: Elsevier Science Publishing Inc.
Tang, X. M., and D. J. Patterson, 2009, Single-well S-wave imaging using multicomponent dipole acoustic-log data: Geophysics, 74, no. 6, WCA211–WCA223, doi: 10.1190/1.3227150.
Tang, X. M., and Z. T. Wei, 2012, Single-well acoustic reflection imaging using far-field radiation characteristics of a borehole dipole source (in Chinese): Chinese Journal of Geophysics, 55, 65–75, doi: 10.1002/cjg2.1701.
Tang, X. M., Y. Zheng, and D. Patterson, 2007, Processing array acoustic logging data to image near-borehole geologic structures: Geophysics, 72, no. 2, E87–E97, doi: 10.1190/1.2435083.
Wang, B., Z. Kuo, T. Guo, L. He, and X. L. Zhang, 2018, Acoustic reflection well logging modeling using the frequency-domain finite-element method with a hybrid PML: Applied Geophysics, 15, 35–45, doi: 10.1007/s11770-018-0666-9.
Wang, H., G. Tao, and M. C. Fehler, 2015b, Investigation of the high-frequency wavefield of an off center monopole acoustic logging-while-drilling tool: Geophysics, 80, no. 4, D329–D341, doi: 10.1190/geo2014-0426.1.
Wang, H., G. Tao, and X. F. Shang, 2015a, A method to determine the strike of interface outside of borehole by monopole borehole acoustic reflections: Journal of Petroleum Science and Engineering, 133, 304–312, doi: 10.1016/j.petrol.2015.05.025.
Wang, H., G. Tao, and K. Zhang, 2013, Wavefield simulation and analysis with the finite-element method for acoustic logging while drilling in horizontal and deviated wells: Geophysics, 78, no. 6, D525–D543, doi: 10.1190/geo2012-0542.1.
Wei, J. Q., X. He, H. Chen, and X. M. Wang, 2018, Wavefield characteristics of unipole sonic LWD with eccentric tools: 88th Annual International Meeting, SEG, Expanded Abstracts, 734–738, doi: 10.1190/segam2018-2996720.1.
Wei, Z. T., and X. M. Tang, 2012, Numerical simulation of radiation, reflection, and reception of elastic waves from a borehole dipole source: Geophysics, 77, no. 6, D253–D261, doi: 10.1190/geo2012-0061.1.
Wei, Z. T., X. M. Tang, and J. J. Cao, 2019, Acoustic radiation and reflection of a logging-while-drilling dipole source: Geophysical Journal International, 219, 108–128, doi: 10.1093/gji/ggz193.
Xu, J. Q., and H. S. Hu, 2020, Study on the radiation and reception of the wave field in a single-well imaging system with an eccentric source (in Chinese): Chinese Journal of Geophysics, 63, 3545–3561, doi: 10.6038/cjg2020N0015.
Xu, J. Q., H. S. Hu, and Z. Wang, 2019, Asymptotic solution to a 3D dipole single-well imaging system with combined monopole and dipole receivers with an application in elimination of azimuth ambiguity: Geophysics, 84, no. 5, D191–D207, doi: 10.1190/geo2018-0658.1.
Xue, M., 2002, Study on remote exploration acoustic reflection well logging and its acoustic sonde design: Ph.D. dissertation, China University of Petroleum (Beijing).
Yang, S. B., W. X. Qiao, and X. H. Che, 2019, Numerical simulation of acoustic fields in formation generated by linear phased array acoustic transmitters during logging while drilling: Journal of Petroleum Science and Engineering, 182, 106184, doi: 10.1016/j.petrol.2019.106184.
Zheng, Y., X. Huang, and M. N. Toksöz, 2004, A finite element analysis of the effects of tool eccentricity on wave dispersion properties in borehole acoustic logging while drilling: 74th Annual International Meeting, SEG, Expanded Abstracts, 294–297, doi: 10.1190/1.1839721.

Biographies and photographs of the authors are not available.

Downloaded from http://pubs.geoscienceworld.org/geophysics/article-pdf/doi/10.1190/geo2022-0756.1/5943043/geo-2022-0756.1.pdf
by China Univ Petroleum (East China) Library Serials Dept user
on 03 September 2023

OXFORD

Journal of Geophysics and Engineering

Journal of Geophysics and Engineering (2022) **19**, 1180–1195 https://doi.org/10.1093/jge/gxac077

Borehole radiation and reception responses for azimuthal shear-wave reflection imaging with an off-centred dipole acoustic tool

Yanghu Li [1], **Xiaoming Tang** [1,2,3,*] **and Yuanda Su** [1,2,3]

[1] School of Geosciences, China University of Petroleum (East China), Qingdao 266580, China
[2] Key Laboratory of Deep Oil and Gas, China University of Petroleum (East China), Qingdao 266580, China
[3] Qingdao National Laboratory for Marine Science and Technology, Qingdao 266580, China

*Corresponding author: Xiaoming Tang. E-mail: tangxiam@aliyun.com

Received 12 July 2022, revised 0 00
Accepted for publication 8 September 2022

Abstract

Radiation and reception responses of a dipole acoustic logging tool placed eccentrically in borehole fluid are an interesting and important topic in acoustic reflection imaging. Herein, we present a thorough research study on these responses. We treat the wave incidence from the reflector as the radiation from a virtual source and use the cylindrical-wave expansion method to solve both the wave radiation and reception problems for the off-centred tool, which, by using the steepest-descent method, yields asymptotic solutions for modelling the radiation and reception wavefield characteristics. The modelling results from the analytical solution and the 3D finite-difference method were in good agreement. Specifically, we analysed the radiation directivity of an eccentric dipole source in a fluid-filled borehole. The results revealed that the radiation pattern was asymmetric with respect to the borehole, and the asymmetry was determined by the eccentric distance, source frequency and formation properties. In particular, for the typical 3 kHz dipole logging frequency, the radiation was stronger in the off-centred direction than in the opposite direction. The asymmetry of the eccentric radiation resulted in a significant amplitude difference relative to its centred counterpart, which provided a potential method for addressing the 180° azimuth ambiguity of the dipole source. We used a theoretical waveform modelling example to demonstrate this advantage. Therefore, the results of this study provide a theoretical foundation for the development and application of dipole shear-wave imaging technology.

Keywords: borehole dipole reflection imaging, far-field radiation patterns, azimuthal reception response, tool eccentricity, azimuth ambiguity

1. Introduction

In recent years, dipole shear-wave imaging has made significant progress detecting geological structures outside the well, such as fractures, faults, and dissolution caves (Tang & Patterson 2009; Bradley *et al.* 2011; Tang *et al.* 2014; Patterson *et al.* 2016; Lee *et al.* 2019; Wang *et al.* 2020). It has also been used to delineate an existing open or cased borehole from a nearby well (Tang *et al.* 2016; Gu *et al.* 2021). The use of a dipole source for acoustic reflection imaging was first proposed by Tang (2004). Dipole shear imaging technology has deep penetration, sensitive orientation and fracture identification compared to a traditional monopole source (Hornby 1989; Meredith 1990). Recent developments have focused on analysing the azimuthal

© The Author(s) 2022. Published by Oxford University Press on behalf of the SINOPEC Geophysical Research Institute Co., Ltd. This is an Open Access article distributed under the terms of the Creative Commons Attribution License (https://creativecommons.org/licenses/by/4.0/), which permits unrestricted reuse, distribution, and reproduction in any medium, provided the original work is properly cited.

Downloaded from academic.oup.com/jge/article/19/5/1180/6762354 by China University of Petroleum - Beijing user on 08 October 2026

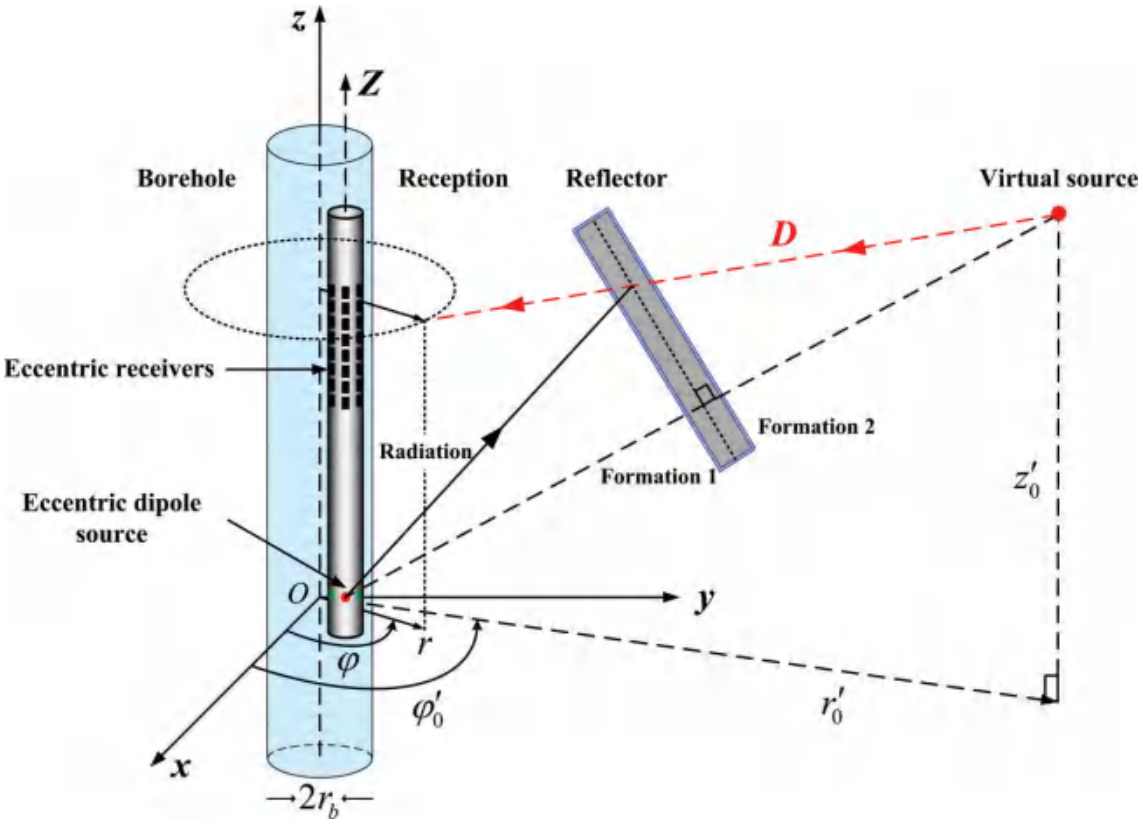


Figure 1. Model of shear-wave reflection imaging with an off-centred acoustic dipole tool, for which the virtual-source analogy is used to analyse the wave incidence to borehole.

response of the dipole tool to resolve the 180° ambiguity (Gong *et al.* 2015, 2018; Bennett 2019; Xu *et al.* 2019; Ben *et al.* 2020; Li *et al.* 2020; Hirabayashi 2021; Li *et al.* 2021a; Li *et al.* 2021b), and on the effects of casing and cement to facilitate imaging through the casing (Tang *et al.* 2020; Gu *et al.* 2021).

An important and challenging problem is the effect of tool off-centring on imaging applications, as is commonly encountered in downhole logging, especially in high-angle and/or horizontal wells. For acoustic modelling with an off-centred dipole tool, existing studies have investigated the wavefield inside a borehole for acoustic logging applications (Leslie & Randall 1990; Schmitt 1993; Byun & Toksöz 2006; Pardo *et al.* 2013; Kayama *et al.* 2021). However, we have not yet seen such analyses and results in the literature for the wavefield outside the borehole relevant to reflection imaging applications.

Therefore, the goal of this study was to extend previous analyses to determine the response characteristics of radiation and reception for the borehole-eccentred tool configuration. In detail, we first derived the far-field displacement asymptotic solution and radiation directivity of an eccentric dipole source. Then, combining the imaginary-source, cylindrical-wave expansion and steepest-descent methods, an efficient algorithm to model the reception responses of the azimuthally placed receivers was derived for the eccentric dipole tool case. The accuracy of our approach was validated using a 3D finite-difference method. Using these solutions, the effects of the off-centred distance, frequency and formation properties on the far-field radiation pattern of an eccentric dipole source in borehole fluid were analysed. Finally, we demonstrated an essential application of eccentric dipole reflection measurement in eliminating azimuth ambiguity through a theoretical synthetic example.

2. Theoretical analysis

2.1. Radiation from an off-centred dipole source inside the borehole

A borehole model with an off-centred tool for analysing azimuthal shear-wave reflection imaging is shown in figure 1. To obtain the analytical wavefield solution for this case, two coordinate systems (X, Y, Z) and (x, y, z) were used, with the origin of the first (second) system located at the tool (borehole) centre. The tool was immersed in the borehole fluid and was parallel to the borehole. In logging-while-drilling (LWD) measurements (Wang *et al.* 2015a, 2015b, 2017; Ji *et al.* 2021a, 2021b; Fu & Gou 2022), the effect of the drill collar should be considered because it occupies most of the borehole. However, in wireline

Downloaded from academic.oup.com/jge/article/19/5/1180/6762354 by China University of Petroleum - Beijing user on 08 October 2026

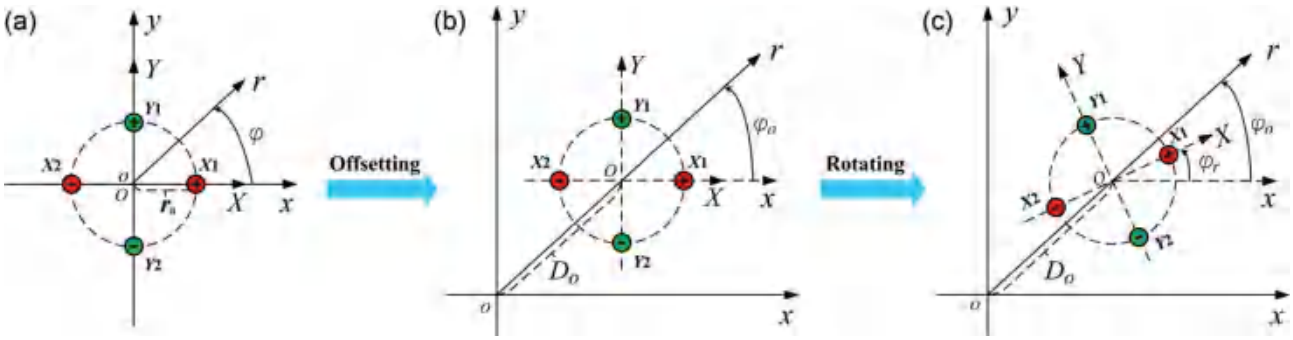


Figure 2. Construction of an eccentric cross-dipole-source system from the centred position (a) to the off-centre position (c) by offsetting (b) and rotating (c) the system.

logging measurements, the tool size was significantly smaller than in the LWD case. In practice, the logging tool has notches in the transmitting and receiving parts, where the steel shell is very thin and is connected by soft materials such as rubber. This results in a significantly reduced effect of the tool body on field wireline measurements. Therefore, this study mainly considered the effects of the sources and receivers in the tool-eccentricity scenario, and the effect of the tool body was not considered.

The model in figure 1 depicts three wave processes: eccentric-source radiation, wave reflection and borehole reception of the reflected wave. We first analyse the source radiation along the X- and Y-directions, where the X (Y) source consists of two eccentric point sources, $X1$ ($Y1$) and $X2$ ($Y2$), of the same amplitude but opposite polarity, as shown in figure 2a. For the borehole cylindrical coordinates (r, φ, z), the off-centring of the source system is derived in two steps. First, the centred system (figure 2a) is offset along the direction φ_o by a distance D_o (figure 2b). Then, it was rotated by the angle φ_r (figure 2c), which allowed us to simulate an arbitrary eccentric case of a dipole source. For the centred cross-dipole source (figure 2a), the coordinates of the four point sources were $X1(r_0, 0, 0)$, $Y1(r_0, \pi/2, 0)$, $X2(r_0, \pi, 0)$ and $Y2(r_0, 3\pi/2, 0)$, respectively. The symbol r_0 is the dipole-source radius. After offsetting and rotating, the four point sources in figure 2c were located at $X1(r_{X1}, \varphi_{X1}, 0)$, $Y1(r_{Y1}, \varphi_{Y1}, 0)$, $X2(r_{X2}, \varphi_{X2}, 0)$ and $Y2(r_{Y2}, \varphi_{Y2}, 0)$, respectively. The method for determining the coordinates of the eccentric-source locations in figure 2c is given in Appendix A.

For the eccentric point source $X1(r_{X1}, \varphi_{X1}, 0)$ in figure 2c, the displacement potential in the borehole fluid can be written as (Tang & Cheng 2004)

$$\phi_f^d = -\frac{e^{ik_f R}}{4\pi R}, \tag{1}$$

where $R = \sqrt{r^2 + r_{X1}^2 - 2rr_{X1}\cos(\varphi - \varphi_{X1}) + z^2}$ denotes the distance between the field point and the source; (r, φ, z) is the field point location in the borehole cylindrical coordinate system; $k_f = \omega/\alpha_f$ stands for the borehole-fluid wavenumber, α_f is the borehole-fluid velocity and ω denotes the circular frequency. The spherical-wave propagation factor $e^{ik_f R}/R$ can be expanded in the form of the multipole superposition of cylindrical waves (Tang & Cheng 2004)

$$\phi_f^d = -\frac{1}{4\pi^2}\int_{-\infty}^{+\infty}\sum_{m=0}^{+\infty}\varepsilon_m \cos\left[m(\varphi - \varphi_{X1})\right]\begin{Bmatrix} I_m(fr_{X1})K_m(fr), & (r > r_{X1}) \\ I_m(fr)K_m(fr_{X1}), & (r < r_{X1}) \end{Bmatrix} e^{ikz}dk, \tag{2}$$

where k stands for the axial wavenumber of both the fluid and formation; $f = \sqrt{k^2 - k_f^2}$ stands for the radial borehole-fluid wavenumber; I_m (K_m) represents the modified Bessel function of the first (second) kind with order m and ε_m represents Neumann's factor, which is defined as 1 for $m = 0$ and 2 for $m \neq 0$. The waves interacting with the borehole induce the reflected wavefield in the fluid inside and radiated wavefield in the formation outside the borehole. Using the Helmholtz theorem, the particle displacements $\mathbf{u}_f$ and $\mathbf{u}_s$ in the borehole fluid and elastic formation, respectively, are defined as

$$\begin{cases} \mathbf{u}_f = \nabla\left(\phi_f^d + \phi_f^r\right) \\ \mathbf{u}_s = \nabla\phi + \nabla\times(\chi\vec{\mathbf{z}}) + \nabla\times\nabla\times(\Gamma\vec{\mathbf{z}}) \end{cases}, \tag{3}$$

Downloaded from academic.oup.com/jge/article/19/5/1180/6762354 by China University of Petroleum - Beijing user on 08 October 2026

where $\vec{\mathbf{z}}$ is the unit vector along the z-axis; ϕ_f^d and ϕ_f^r represent the direct and reflected potentials in the borehole fluid and ϕ, χ and Γ represent the radiated P-, SH- and SV-wave potentials in the formation, respectively. To match the functional forms in equation (2), the general solutions of these displacement potentials in equation (3) are expressed as

$$\begin{cases} \phi_f^r = \sum_{m=0}^{+\infty} A_m I_m(fr) I_m(fr_{X1}) \cos\left[m(\varphi - \varphi_{X1})\right] \quad (0 < r < r_b) \\ \left.\begin{aligned} \phi &= \sum_{m=0}^{+\infty} B_m K_m(pr) I_m(fr_{X1}) \cos\left[m(\varphi - \varphi_{X1})\right] \\ \chi &= \sum_{m=0}^{+\infty} D_m K_m(sr) I_m(fr_{X1}) \sin\left[m(\varphi - \varphi_{X1})\right] \\ \Gamma &= \sum_{m=0}^{+\infty} F_m K_m(sr) I_m(fr_{X1}) \cos\left[m(\varphi - \varphi_{X1})\right] \end{aligned}\right\} \quad (r > r_b) \end{cases}, \tag{4}$$

where r_b is the radius of the borehole; $p = \sqrt{k^2 - (\omega/\alpha)^2}$ is the radial wavenumber of the formation P-wave where α is the velocity of the formation P-wave; $s = \sqrt{k^2 - (\omega/\beta)^2}$ is the radial wavenumber of the formation S-wave where β is the velocity of the formation S-wave. For different orders m, the wave amplitude coefficients $A_m \sim F_m$ are obtained by applying the boundary conditions at the wall of the well ($r = r_b$), where the radial displacement and radial stress are continuous, and the azimuthal and axial stresses vanish, as follows

$$\begin{cases} u_r(r_b^+) - u_{rf}^r(r_b^-) = u_{rf}^d(r_b^-) \\ \sigma_{rr}(r_b^+) - \sigma_{rrf}^r(r_b^-) = \sigma_{rrf}^d(r_b^-) \\ \sigma_{r\varphi}(r_b^+) = 0 \\ \sigma_{rz}(r_b^+) = 0 \end{cases}. \tag{5}$$

The displacements in the borehole fluid and formation were determined using equations (2)–(4). Substituting the formation displacements into the strain-displacement relation to calculate the strains, the strains, in turn, are used to calculate the stresses using Hook's law. To obtain the unknown amplitude coefficients in equation (4), substituting these displacements and stresses into equation (5) yields the following matrix equation

$$\mathbf{M} \times \left[A_m, B_m, D_m, F_m\right]^T = \mathbf{b}, \tag{6}$$

where $\mathbf{M}$ is a 4×4 matrix and $\mathbf{b}$ is a 4×1 vector, whose expressions are given in Appendix B. Solving the coefficients from equation (6), the radiated waves can be obtained with discrete wavenumber integration (Tang & Cheng 2004). For the reflection imaging survey, the conditions of $|pr| \gg 1$ and $|sr| \gg 1$ are satisfied when the wavelength is less than the radiation distance, which allows us to determine the far-field solutions of the radiated waves by replacing this wavenumber integration with the steepest-descent solution (Aki & Richards 1980), as follows

$$\begin{cases} \phi = -\dfrac{e^{i\omega R/\alpha - i\pi/4}}{4\pi R} \sum_{m=0}^{+\infty} B_m(\omega, k_{p0}) I_m(f_{p0} r_{X1}) \cos\left[m(\varphi - \varphi_{X1})\right], \\ \chi = -\dfrac{e^{i\omega R/\beta - i\pi/4}}{4\pi R} \sum_{m=0}^{+\infty} D_m(\omega, k_{s0}) I_m(f_{s0} r_{X1}) \sin\left[m(\varphi - \varphi_{X1})\right], \\ \Gamma = -\dfrac{e^{i\omega R/\beta - i\pi/4}}{4\pi R} \sum_{m=0}^{+\infty} F_m(\omega, k_{s0}) I_m(f_{s0} r_{X1}) \cos\left[m(\varphi - \varphi_{X1})\right], \end{cases} \tag{7}$$

where $k_{p0} = (\omega/\alpha) \cdot \cos\theta_t$ and $k_{s0} = (\omega/\beta) \cdot \cos\theta_t$ denote, respectively, the steepest-descent solutions of the formation P- and S-wave wavenumbers; θ_t indicates the angle between the direction of the radiated wave and the z-axis; $f_{p0} = \sqrt{k_{p0}^2 - (\omega/\alpha_f)^2}$ and $f_{s0} = \sqrt{k_{s0}^2 - (\omega/\alpha_f)^2}$ correspond, respectively, to the fluid radial wavenumbers calculated using k_{p0}

Downloaded from academic.oup.com/jge/article/19/5/1180/6762354 by China University of Petroleum - Beijing user on 08 October 2026

and k_{s0}; $R=\sqrt{r^2+z^2}$, note that the terms related to r_{X1} are omitted under the condition of $r_{X1} \ll r$. Substituting equation (7) into equation (3) and ignoring $O(1/R^2)$ results in the radiated far-field displacements of the P-, SH- and SV-waves, as follows

$$\begin{cases} u_P = \left\{ (-i\rho\alpha\omega) \sum_{m=0}^{+\infty} B_m(\omega, k_{p0}) I_m(f_{p0} r_{X1}) \cos\left[m(\varphi-\varphi_{X1})\right] \right\} \dfrac{e^{i\omega R/\alpha - i\pi/4}}{4\pi\rho\alpha^2 R} \\ u_{SH} = \left\{ (i\rho\beta\omega \sin\theta_t) \sum_{m=0}^{+\infty} D_m(\omega, k_{s0}) I_m(f_{s0} r_{X1}) \sin\left[m(\varphi-\varphi_{X1})\right] \right\} \dfrac{e^{i\omega R/\beta - i\pi/4}}{4\pi\rho\beta^2 R} \\ u_{SV} = \left\{ (\rho\omega^2 \sin\theta_t) \sum_{m=0}^{+\infty} F_m(\omega, k_{s0}) I_m(f_{s0} r_{X1}) \cos\left[m(\varphi-\varphi_{X1})\right] \right\} \dfrac{e^{i\omega R/\beta - i\pi/4}}{4\pi\rho\beta^2 R} \end{cases}, \tag{8}$$

where ρ denotes the formation density. The bracketed parts of equation (8) give the far-field radiation directivities of the P-, SH- and SV-waves, respectively, as follows

$$\begin{cases} \mathfrak{R}_P(\omega; \theta_t, \varphi) = (-i\rho\alpha\omega) \sum_{m=0}^{+\infty} B_m(\omega, k_{p0}) I_m(f_{p0} r_{X1}) \cos\left[m(\varphi-\varphi_{X1})\right], \\ \mathfrak{R}_{SH}(\omega; \theta_t, \varphi) = (i\rho\beta\omega \sin\theta_t) \sum_{m=0}^{+\infty} D_m(\omega, k_{s0}) I_m(f_{s0} r_{X1}) \sin\left[m(\varphi-\varphi_{X1})\right], \\ \mathfrak{R}_{SV}(\omega; \theta_t, \varphi) = (\rho\omega^2 \sin\theta_t) \sum_{m=0}^{+\infty} F_m(\omega, k_{s0}) I_m(f_{s0} r_{X1}) \cos\left[m(\varphi-\varphi_{X1})\right]. \end{cases} \tag{9}$$

By repeating the derivation to obtain the solution for the other three eccentric point sources in figure 2c and combining the $(X1, X2)$ and $(Y1, Y2)$ pairs to form a cross-dipole source, the far-field wave solutions of the source system are determined. The P-, SH- and SV-wave potentials are

$$\begin{cases} \phi^{X,Y} = -\dfrac{e^{i\omega R/\alpha - i\pi/4}}{4\pi R} \sum_{m=0}^{+\infty} B_m(\omega, k_{p0}) \begin{bmatrix} I_m(f_{p0} r_{X1,Y1}) \cos m(\varphi-\varphi_{X1,Y1}) \\ -I_m(f_{p0} r_{X2,Y2}) \cos m(\varphi-\varphi_{X2,Y2}) \end{bmatrix} \\ \chi^{X,Y} = -\dfrac{e^{i\omega R/\beta - i\pi/4}}{4\pi R} \sum_{m=0}^{+\infty} D_m(\omega, k_{s0}) \begin{bmatrix} I_m(f_{s0} r_{X1,Y1}) \sin m(\varphi-\varphi_{X1,Y1}) \\ -I_m(f_{s0} r_{X2,Y2}) \sin m(\varphi-\varphi_{X2,Y2}) \end{bmatrix} \\ \Gamma^{X,Y} = -\dfrac{e^{i\omega R/\beta - i\pi/4}}{4\pi R} \sum_{m=0}^{+\infty} F_m(\omega, k_{s0}) \begin{bmatrix} I_m(f_{s0} r_{X1,Y1}) \cos m(\varphi-\varphi_{X1,Y1}) \\ -I_m(f_{s0} r_{X2,Y2}) \cos m(\varphi-\varphi_{X2,Y2}) \end{bmatrix} \end{cases}, \tag{10}$$

and their respective far-field radiation directivities are

$$\begin{cases} \mathfrak{R}_P^{X,Y}(\omega; \theta_t, \varphi) = (-i\rho\alpha\omega) \sum_{m=0}^{+\infty} B_m(\omega, k_{p0}) \begin{bmatrix} I_m(f_{p0} r_{X1,Y1}) \cos m(\varphi-\varphi_{X1,Y1}) \\ -I_m(f_{p0} r_{X2,Y2}) \cos m(\varphi-\varphi_{X2,Y2}) \end{bmatrix} \\ \mathfrak{R}_{SH}^{X,Y}(\omega; \theta_t, \varphi) = (i\rho\beta\omega \sin\theta_t) \sum_{m=0}^{+\infty} D_m(\omega, k_{s0}) \begin{bmatrix} I_m(f_{s0} r_{X1,Y1}) \sin m(\varphi-\varphi_{X1,Y1}) \\ -I_m(f_{s0} r_{X2,Y2}) \sin m(\varphi-\varphi_{X2,Y2}) \end{bmatrix} \\ \mathfrak{R}_{SV}^{X,Y}(\omega; \theta_t, \varphi) = (\rho\omega^2 \sin\theta_t) \sum_{m=0}^{+\infty} F_m(\omega, k_{s0}) \begin{bmatrix} I_m(f_{s0} r_{X1,Y1}) \cos m(\varphi-\varphi_{X1,Y1}) \\ -I_m(f_{s0} r_{X2,Y2}) \cos m(\varphi-\varphi_{X2,Y2}) \end{bmatrix} \end{cases}, \tag{11}$$

where the superscript X (Y) denotes the excitation of the X (Y) dipole source of the system, and correspondingly, the radius and azimuth parameters of the point source pair, as denoted by subscripts $X1$ and $X2$ ($Y1$ and $Y2$), should be used. The radiation patterns of the radiated waves can be calculated by evaluating the amplitude of the expressions in equation (11) relative to θ_t in the vertical plane.

Downloaded from academic.oup.com/jge/article/19/5/1180/6762354 by China University of Petroleum - Beijing user on 08 October 2026

2.2. *Reception response of the borehole to the incident elastic waves*

After reflection in the formation, the spherical wave for the (centred or off-centred) borehole source was returned to the borehole. The incident wave can be expressed as a coupling of multiple functions as follows

$$Iwave = S \cdot RD \cdot RF \cdot \frac{e^{i\omega D/v}}{D}, \tag{12}$$

where v denotes the velocity of the formation P- or S-wave; S stands for the source spectrum; RD stands for the borehole radiation function, which is obtained by removing the spherical-wave propagation factor $e^{i\omega R/v}/R$ from equation (10); RF stands for the reflection coefficient at the reflector, which can be calculated using the Zoeppritz equation; RD and RF are determined by the type of reflected wave being considered, P, SV or SH, and D indicates the distance the wave travels in the formation. By treating the reflected wave from the reflector as a spherical wave generated by a 'virtual source' whose location coincides with the mirror image of the eccentric source relative to the reflector (as shown in figure 1), we can express the spherical-wave factor $e^{i\omega D/v}/D$ of equation (12) in a similar way to equation (2) (Li *et al.* 2021b)

$$\frac{e^{i\omega D/v}}{D} = \frac{1}{\pi}\int_{-\infty}^{+\infty}\sum_{m=0}^{+\infty}\varepsilon_m I_m(k_v r)K_m(k_v r_0')\cos\left[m(\varphi-\varphi_0')\right]e^{ik(z-z_0')}dk, \tag{13}$$

where $k_v = \sqrt{k^2-(\omega/v)^2}$ stands for the radial wavenumber of the incident P-, SV- or SH-wave and (r_0', φ_0', z_0') denotes the virtual-source location in the borehole cylindrical coordinates and $D = \sqrt{r^2 + r_0'^2 - 2rr_0'\cos(\varphi-\varphi_0') + (z-z_0')^2}$. The incident waves on the borehole cause wave responses in the borehole fluid and formation, and the potentials of these waves given in equation (4) become

$$\begin{cases} \phi_f = \sum_{m=0}^{+\infty}\left[A_m\cos(m\varphi) + A_m'\sin(m\varphi)\right] I_m(fr)K_m(k_v r_0') & (0<r<r_b) \\ \left.\begin{aligned} \phi &= \sum_{m=0}^{+\infty}\left[B_m\cos(m\varphi) + B_m'\sin(m\varphi)\right] K_m(pr)K_m(k_v r_0') \\ \chi &= \sum_{m=0}^{+\infty}\left[D_m\sin(m\varphi) - D_m'\cos(m\varphi)\right] K_m(sr)K_m(k_v r_0') \\ \Gamma &= \sum_{m=0}^{+\infty}\left[F_m\cos(m\varphi) + F_m'\sin(m\varphi)\right] K_m(sr)K_m(k_v r_0') \end{aligned}\right\} & (r>r_b) \end{cases} \tag{14}$$

Correspondingly, equation (5), which describes the boundary conditions, needs to be changed to determine the amplitude coefficients in equation (14)

$$\begin{cases} u_r^i(r_b^+) + u_r^s(r_b^+) = u_r^f(r_b^-) \\ \sigma_{rr}^i(r_b^+) + \sigma_{rr}^s(r_b^+) = \sigma_{rr}^f(r_b^-) \\ \sigma_{r\varphi}^i(r_b^+) + \sigma_{r\varphi}^s(r_b^+) = 0 \\ \sigma_{rz}^i(r_b^+) + \sigma_{rz}^s(r_b^+) = 0 \end{cases} \tag{15}$$

where superscripts i and s refer to the incident and scattered waves in the elastic formation, respectively, and f refers to the transmitted wave in the borehole fluid. Substituting equation (13) into equation (12) yields the displacement potential

Downloaded from academic.oup.com/jge/article/19/5/1180/6762354 by China University of Petroleum - Beijing user on 08 October 2026

functions of the incident waves

$$\begin{cases} \phi^i = S(\omega)\cdot RD_P^{X,Y}(\omega)\cdot RF_P(\omega)\sum\limits_{m=0}^{+\infty}\varepsilon_m I_m(pr)K_m(pr_0')\cos\left[m(\varphi-\varphi_0')\right], \\ \chi^i = S(\omega)\cdot RD_{SH}^{X,Y}(\omega)\cdot RF_{SH}(\omega)\sum\limits_{m=0}^{+\infty}\varepsilon_m I_m(sr)K_m(sr_0')\cos\left[m(\varphi-\varphi_0')\right], \\ \Gamma^i = S(\omega)\cdot RD_{SV}^{X,Y}(\omega)\cdot RF_{SV}(\omega)\sum\limits_{m=0}^{+\infty}\varepsilon_m I_m(sr)K_m(sr_0')\cos\left[m(\varphi-\varphi_0')\right], \end{cases} \tag{16}$$

where the subscripts *P*, *SH* and *SV* represent the type of incident wave.

The displacements and stresses of wave motions in and out of the borehole are calculated from equations (3), (14) and (16). After substitution into the boundary conditions of equation (15), this results in two matrix equations

$$\mathbf{M}\times[A_m, B_m, D_m, F_m]^T = \mathbf{c} \quad \text{and} \quad \mathbf{M}\times[A_m', B_m', D_m', F_m']^T = \mathbf{c}', \tag{17}$$

where the matrix **M** is the same as equation (6) (see Appendix B), and **c** and **c**′ are 4×1 vectors representing the contribution of the incident wave from the virtual source (see Appendix C for a detailed description). After determining wavefields in and out of the borehole with equation (17), incident-wave-induced fluid pressure and radial and azimuthal displacements inside the borehole could be obtained based on the formulae $p = \rho_f\omega^2\phi_f$, $u_r^f = \partial\phi_f/\partial r$, and $u_\varphi^f = (1/r)\partial\phi_f/\partial\varphi$

$$\begin{cases} p = \dfrac{\rho_f\omega^2}{\pi}\displaystyle\int_{-\infty}^{+\infty}\sum_{m=0}^{+\infty}[A_m\cos(m\varphi)+A_m'\sin(m\varphi)]I_m(fr)K_m(k_v r_0')e^{ik(z-z_0')}dk, \\ u_r^f = \dfrac{1}{\pi}\displaystyle\int_{-\infty}^{+\infty}\sum_{m=0}^{+\infty}[A_m\cos(m\varphi)+A_m'\sin(m\varphi)]\left[fI_{m+1}(fr)+\dfrac{m}{r}I_m(fr)\right]K_m(k_v r_0')e^{ik(z-z_0')}dk, \\ u_\varphi^f = \dfrac{1}{\pi}\displaystyle\int_{-\infty}^{+\infty}\sum_{m=0}^{+\infty}[-A_m\sin(m\varphi)+A_m'\cos(m\varphi)]\dfrac{m}{r}I_m(fr)K_m(k_v r_0')e^{ik(z-z_0')}dk, \end{cases} \tag{18}$$

where ρ_f denotes fluid density. The radial distance of the virtual source is usually greater than the wavelength, $|k_v r_0'| \gg 1$, and the wavenumber integration can be replaced with the steep-descent method

$$\begin{Bmatrix} p \\ u_r^f \\ u_\varphi^f \end{Bmatrix} = \frac{e^{i\omega D/v - i\pi/4}}{D}\sum_{m=0}^{+\infty}\begin{Bmatrix} \rho_f\omega^2[A_m\cos(m\varphi)+A_m'\sin(m\varphi)]I_m(f_0 r) \\ [A_m\cos(m\varphi)+A_m'\sin(m\varphi)]\left[f_0 I_{m+1}(f_0 r)+\dfrac{m}{r}I_m(f_0 r)\right] \\ [-A_m\sin(m\varphi)+A_m'\cos(m\varphi)]\dfrac{m}{r}I_m(f_0 r) \end{Bmatrix}, \tag{19}$$

Where $f_0 = \sqrt{k_0^2 - (\omega/\alpha_f)^2}$, $k_0 = (\omega/v)\cdot\cos\theta_i$ represents the steep-descent solution of the incident-wave wavenumber, θ_i indicates the angle between the direction of the incident wave and the negative *z*-axis; $D = \sqrt{r_0'^2 + (z-z_0')^2}$. Note that the terms related to *r* are omitted under the condition of $r \ll r_0'$. Equation (19) calculates the fluid response in the borehole coordinate system. For the wavefield measured by the tool, the results from equation (19) need to be converted to the tool coordinate system. Because pressure is a scalar, the results are the same in the two coordinate system cases, so only displacements need to be converted. The off-centring of the receiver is the same as that of the source (see figure 2). Figure 3 illustrates the projection method to obtain the fluid radial displacement in the tool coordinate system. Thus, the fluid pressure and radial displacement measured by the tool are calculated using

$$\begin{Bmatrix} \tilde{p} \\ \tilde{u}_r^f \end{Bmatrix} = \left\{ \begin{matrix} p \\ u_r^f\cos(\varphi_{R0}+\varphi_r-\varphi_{Re}) + u_\varphi^f\sin(\varphi_{R0}+\varphi_r-\varphi_{Re}) \end{matrix} \right| \begin{matrix} r = r_{Re} \\ \varphi = \varphi_{Re} \end{matrix}, \tag{20}$$

where $R_0(r_{R0}, \varphi_{R0}, z_{R0})$ and $R_e(r_{Re}, \varphi_{Re}, z_{R0})$ are the receiver locations in the centred and off-centred tool cases, respectively.

Downloaded from academic.oup.com/jge/article/19/5/1180/6762354 by China University of Petroleum - Beijing user on 08 October 2026

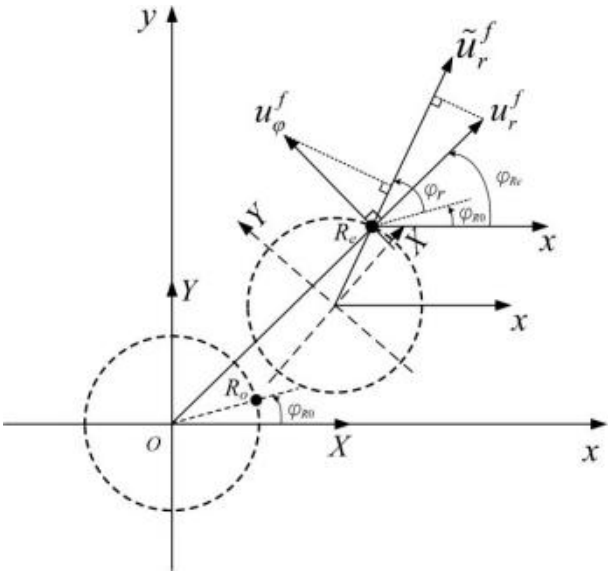


Figure 3. The projection method to obtain the radial displacement in the tool coordinate system.

Table 1. Borehole and formation parameters for simulation

	P-velocities (m s^{-1})	S-velocities (m s^{-1})	Densities (kg m^{-3})	Radii (m)
Borehole fluid	1500	–	1000	0.1
Fast formation	4000	2300	2500	–
Slow formation	2074	869	2250	–
Formation 2	4500	3000	2600	Infinity

3. Result validation

Having obtained the analytical solution to model the received reflection data from a reflector in formation, we now verify the analytical solution result of equation (20) using the 3D finite-difference numerical method (Wei & Tang 2012). The borehole model in figure 1 and the parameters in Table 1 were used in the simulation, where the interface between formations 1 (fast formation used) and 2 was considered the reflector. The dip angle and azimuth of the reflector are 45° and 0°, respectively. The radial distance (r_0', as shown in figure 1) of the virtual source was assumed to be 10 m. Receivers were placed 0.035 m from the tool centre and circumferentially separated by 45° angles. The tool was offset along the x-axis by 0.05 m. The vertical distance between the planes where the source and receivers were located is 1 m. We selected the Ricker wavelet with a frequency of 3 kHz to actuate the X-dipole source, assuming the radius (r_0, as shown in figure 2a) of the dipole source is 0.035 m. Set the grid size and the iteration time step to 0.005 m and 0.6 μs for the finite-difference simulation, respectively. Figure 4 shows the borehole-fluid radial displacement (figure 4a) and pressure (figure 4b) calculated from the asymptotic analytical solution (solid curves) and numerical method (dashed curves), respectively. For the dipole-source orientation and reflector strike, P- and SV-waves will be simultaneously excited, which results in a finite-difference simulation containing the P- and SV-waves reflections, and the P-SV and SV-P converted wave reflections. In contrast, equation (20) is only used to model an individual reflected wave. For clarity, figure 4 only compares the SV-wave reflection results. Despite the interferences, the SV-wave results were in good agreement between the two methods for both radial displacement and pressure, demonstrating the accuracy and validity of the analytical solution. Note that the 3D finite-difference method requires several tens of hours for the simulation, whereas the analytical solution of equation (20) requires only a few seconds to generate accurate results. Thus, our approach provides an efficient algorithm for simulating borehole eccentric dipole reflection surveys.

4. Far-field radiation characteristics of an eccentric dipole source

These theoretical results allow us to calculate the far-field radiation patterns of an off-centred dipole acoustic tool and investigate its dependence on the eccentric offset and source frequency as well as on the formation properties. For simplicity, we present modelling examples for the $\varphi_r = \varphi_o$ case. Without loss of generality, the cross-dipole source shown in figure 2

Downloaded from academic.oup.com/jge/article/19/5/1180/6762354 by China University of Petroleum - Beijing user on 08 October 2026

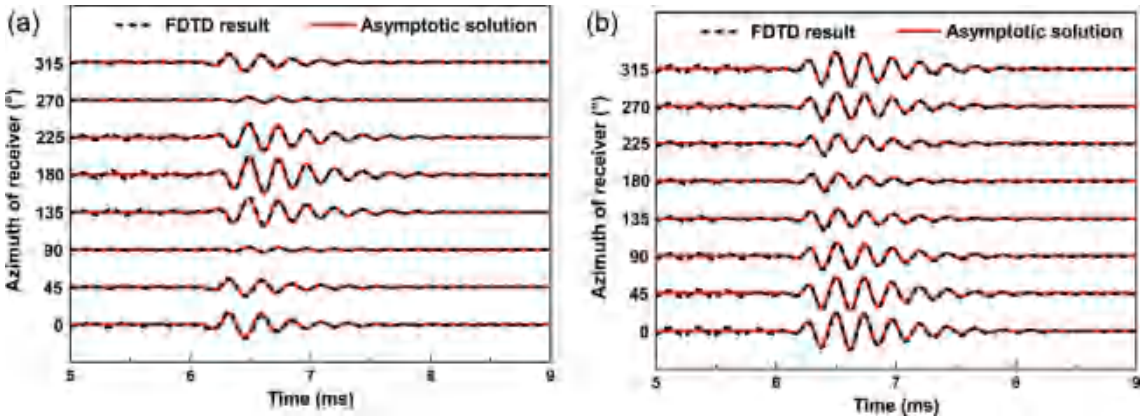


Figure 4. Comparisons of the borehole-fluid (a), radial displacement and (b) pressure responses calculated using the 3D finite-difference numerical method (dashed curves) and asymptotic analytical solution (solid curves) for SV-wave incidence. The dipole acoustic tool is offset along the *x*-axis by 0.05 m.

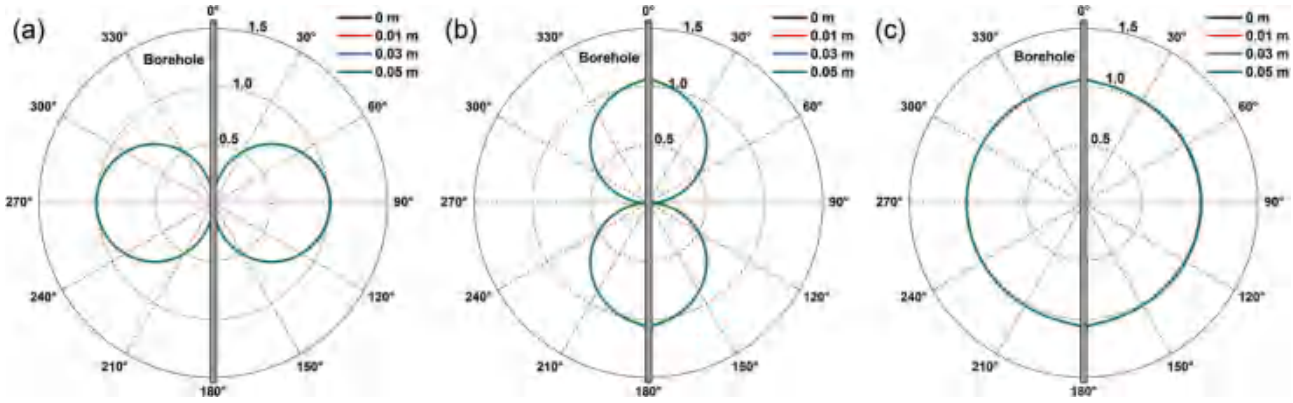


Figure 5. P (a), SV (b) and SH (c) radiation patterns of a borehole cross-dipole source in a fast formation for different eccentricity offsets at 0.5 kHz frequency.

was eccentrically placed along the *x*-axis (i.e. $\varphi_r = \varphi_o = 0^o$). The *X*-dipole source was excited to model the P- and SV-wave radiations in the $\varphi = 0^o$ (or 180°) plane and the *Y*-dipole source was excited to model the SH-wave radiation in the same plane.

4.1. Dependence on eccentric offset

Figure 5 compares the radiation patterns of an eccentric cross-dipole source for four eccentricity offset values of 0, 0.01, 0.03 and 0.05 m at 0.5 kHz frequency in the fast formation scenario. The types of radiated waves were P- (figures 5a and 6a), SV- (figures 5b and 6b) and SH- (figures 5c and 6c) waves. The circumferential label represents the radiation angle θ_t, and the radial label marks the amplitude of the radiation directivities. Figure 5 shows that, for the low-frequency value of 0.5 kHz, the patterns are hardly affected by tool eccentricity and closely resemble those from a centred dipole source, indicating that the influence of eccentricity on the radiated wavefield can be ignored at low frequencies. For a frequency value of 3 kHz (figure 6), the results show that the directivity patterns of an eccentric dipole source are asymmetric relative to the borehole axis, as compared to their centred counterparts. With increasing eccentric offsets from 0 to 0.05 m, the P- and SH-wave patterns enlarge (shrink) toward (away from) the eccentric direction. In comparison, the eccentricity had only a small effect on the SV-wave patterns. It is worth noting that compared to P- and SV-waves, the SH-wave had better radiation performance and coverage, which means that the SH-wave dominated the radiated wavefield of the eccentric dipole source and was the optimal type of wave used for dipole imaging in the fast formation of the eccentric tool condition.

The radiation analysis for the same model in the slow formation case (see Table 1) is shown in figures 7 and 8. For the low-frequency value of 0.5 kHz (figure 7), the P- and SH-wave radiation patterns were hardly affected by eccentricity, whereas the SV-wave radiation pattern changed, and there were four evident mutation regions when the dipole source was eccentric.

Downloaded from academic.oup.com/jge/article/19/5/1180/6762354 by China University of Petroleum - Beijing user on 08 October 2026

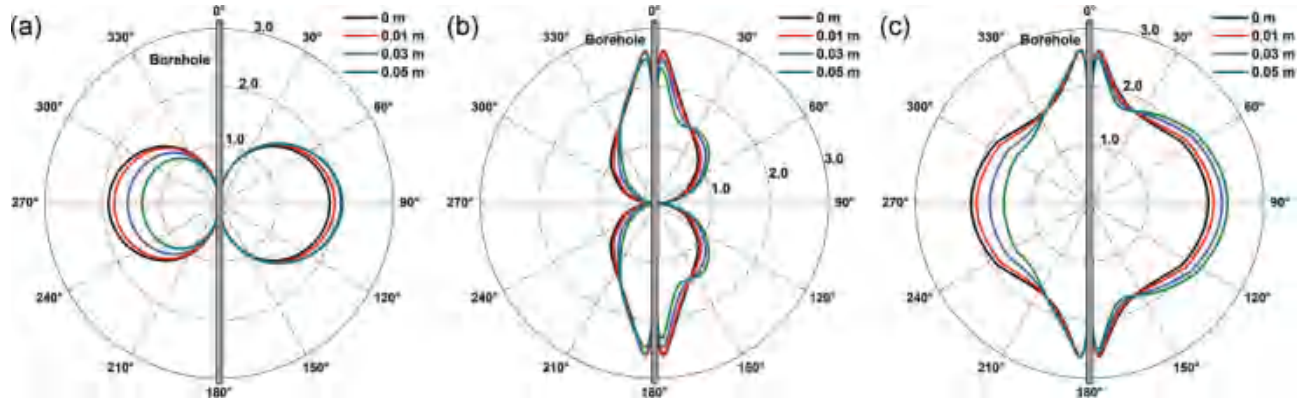


Figure 6. P (a), SV (b) and SH (c) radiation patterns of a borehole cross-dipole source in a fast formation for different eccentricity offsets at 3 kHz frequency.

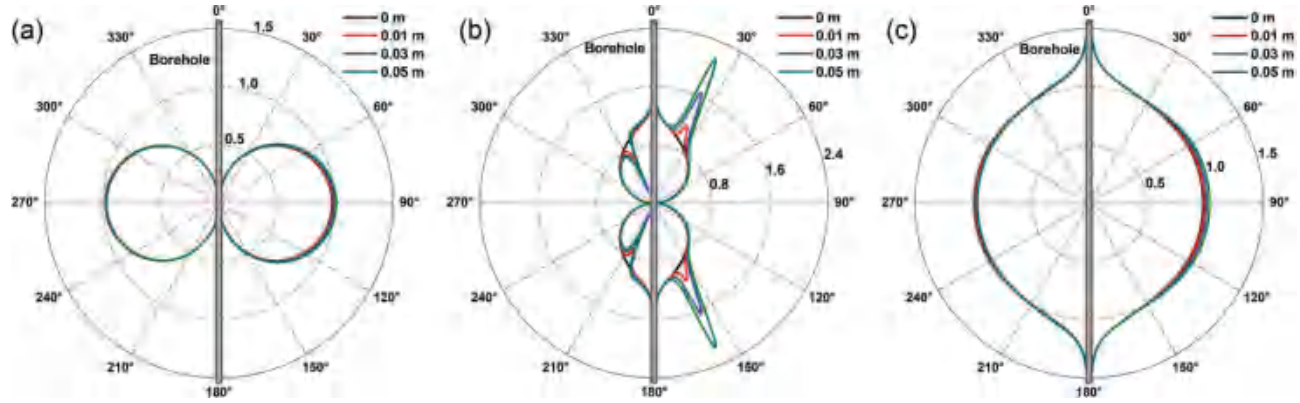


Figure 7. P (a), SV (b) and SH (c) radiation patterns of a borehole cross-dipole source in a slow formation for different eccentricity offsets at 0.5 kHz frequency.

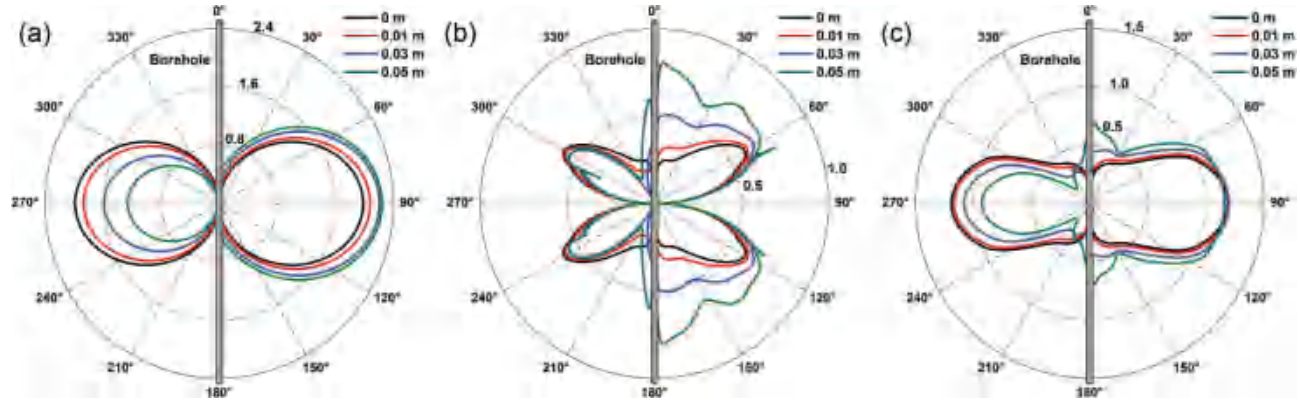


Figure 8. P (a), SV (b) and SH (c) radiation patterns of a borehole cross-dipole source in a slow formation for different eccentricity offsets at 3 kHz frequency.

With increasing eccentric offsets, the SV-wave directivity factor increased sharply near 24° and 156°, whereas it decreased sharply near 204° and 336°. For the frequency value of 3 kHz, the asymmetry of the patterns is enhanced relative to the fast formation case in figure 6, especially for the P- and SV-wave, as depicted in figure 8. Figure 8 shows that the amplitude of the radiated P-wave is stronger than that of the radiated SV- and SH-waves, indicating that the P-wave can also be used for eccentric dipole reflection imaging in slow formation. More importantly, for the typical 3 kHz dipole logging frequency, the radiation performances of P-, SV- and SH-waves are better in the off-centring direction than in the opposite direction in the fast and slow formation scenarios. An important implication of eccentric-source modelling is that the asymmetry of the source radiation can help resolve the 180° azimuth uncertainty of dipole shear reflection imaging (Li *et al.* 2021b).

Downloaded from academic.oup.com/jge/article/19/5/1180/6762354 by China University of Petroleum - Beijing user on 08 October 2026

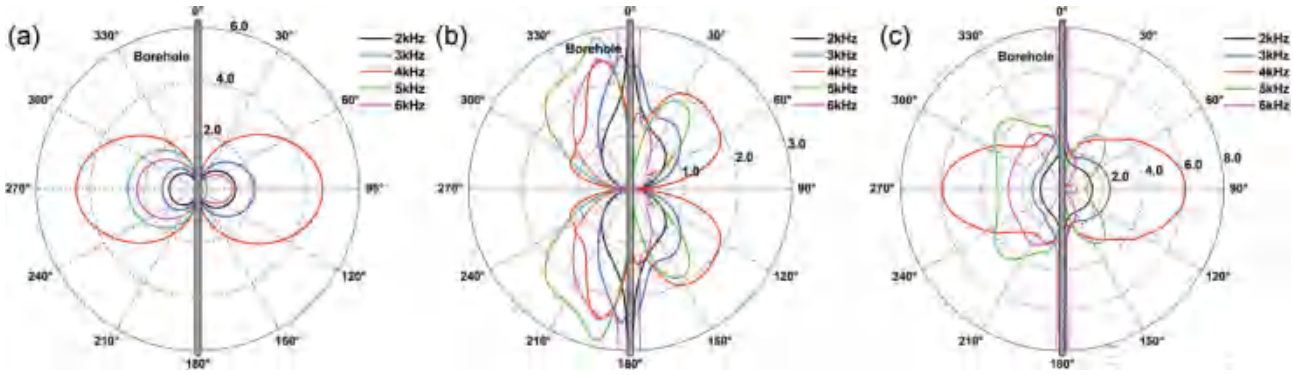


Figure 9. P (a), SV (b) and SH (c) radiation patterns of a borehole cross-dipole source in a fast formation for different frequencies on 0.05 m eccentric offset.

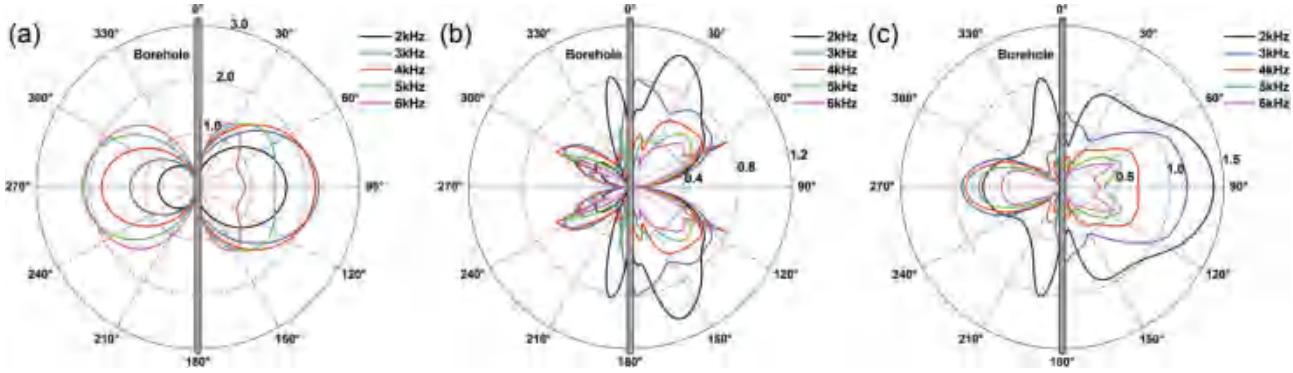


Figure 10. P (a), SV (b) and SH (c) radiation patterns of a borehole cross-dipole source in a slow formation for different frequencies on 0.05 m eccentric offset.

4.2. Dependence on frequency

Figures 9 and 10 compare the radiation patterns of an eccentric cross-dipole source for the five frequencies of 2, 3, 4, 5 and 6 kHz in the fast and slow formation scenarios, respectively. The eccentric offset of the dipole-source system was 0.05 m. In general, radiation patterns exhibit complex frequency-dependent characteristics. In the fast formation case (figure 9), as the frequency increased from 2 to 6 kHz, the P-, SV- and SH-wave radiation factors increased gradually to a maximum and then decreased. When the frequency was 2 or 3 kHz, radiation performance was better in the off-centring direction than the opposite direction, whereas the trend was reversed when the frequency increased to 5 or 6 kHz. For the slow formation case shown in figure 10, with increasing frequency, the P-wave radiation factor increased gradually to a maximum and then decreased, whereas the SV- and SH-wave radiation factors gradually decreased. Comparing the radiation patterns at different frequencies shows that the optimal excitation frequency for an eccentric cross-dipole source is ~4 kHz in the fast and 2 kHz in the slow formation case. This is almost consistent with the results from their centred counterpart, suggesting the influence of tool eccentricity on the optimal excitation frequency is small. A detailed comparison of the radiation patterns with eccentric offset and frequency showed that the formation elasticity substantially influences the radiation pattern.

5. Application to eliminate the azimuth ambiguity

As a significant application of the theoretical solution of equation (20), it can be used to calculate the reflection data generated and recorded by an off-centred dipole tool for any reflector location in the formation. Figure 11 (left panel) shows a 100 m model containing two reflectors with opposite dipping directions at 0° (relative to the borehole x-axis). The cross-dipole acoustic tool was offset along the x-axis by 0.05 m. We calculated the SH-wave reflection data of the receiver array by actuating the Y-dipole source with a 3 kHz Ricker wavelet. The dipole receivers were placed 0.035 m from the tool centre. The dipole source was at a distance of 3 m below the array receivers, and the data-sample depth and time were 0.1524 m and 36 μs, respectively. The formation properties in Table 1 were used, and the slow formation was used as formation 1 in figure 1. The pressure difference between the two receivers on opposite sides of the tool was calculated to simulate dipole acquisition.

Downloaded from academic.oup.com/jge/article/19/5/1180/6762354 by China University of Petroleum - Beijing user on 08 October 2026

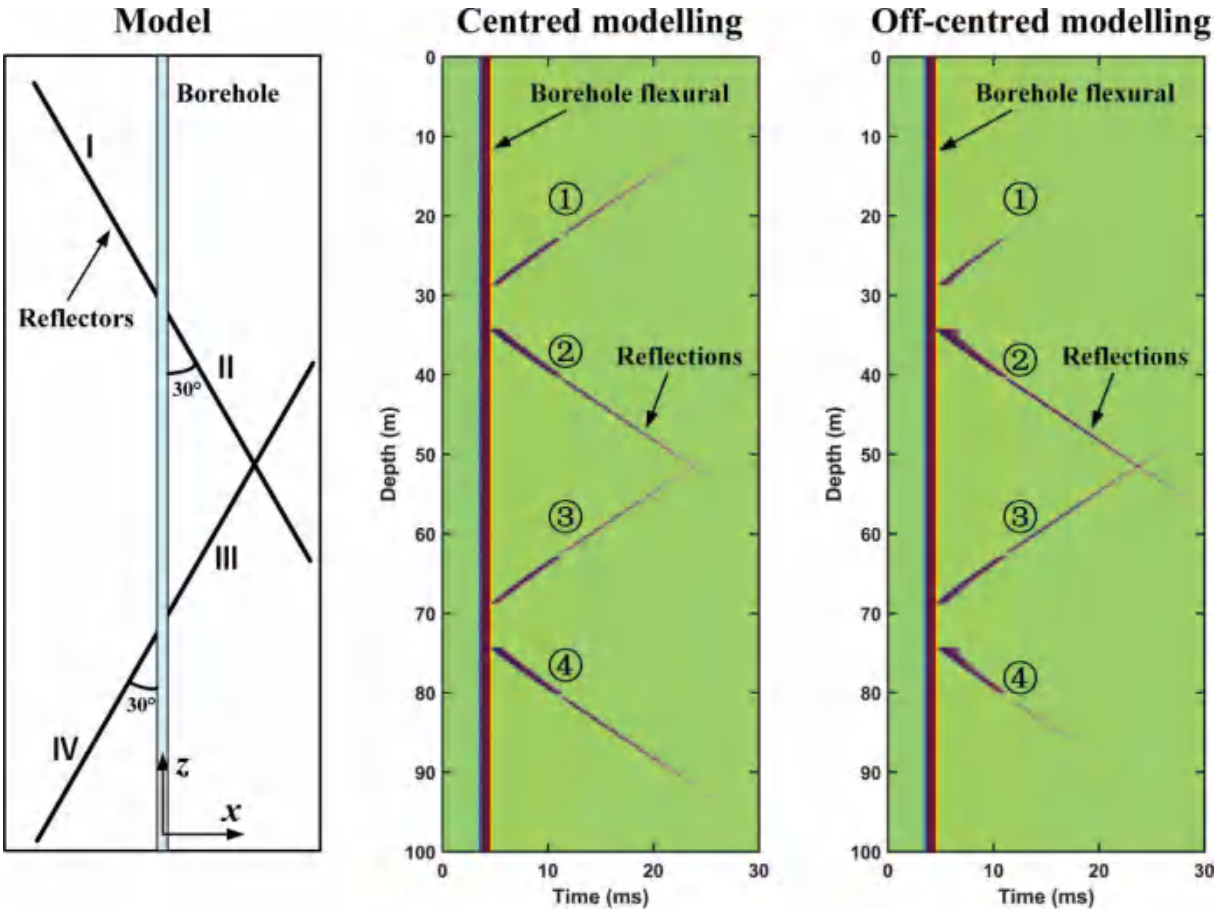


Figure 11. A model of two reflectors (lines in the left panel) for SH-wave reflection modelling. Note the apparent amplitude difference between the reflection signals measured using centred (middle panel) and off-centred (right panel) dipole tools.

Figure 11 compares the simulated first-receiver data for the centred (middle panel) and off-centred (right panel) scenarios. The data contain the flexural wave along the borehole and the reflected waves from the reflectors. The modelled data are displayed as a variable density diagram, and the intensity of the colour represents the wave amplitude strength. As can be seen from the middle and right panels, the amplitude of the borehole flexural waves is larger than that of the reflected waves from the reflectors. For convenience, the two cross-well reflectors in the left panel were divided into sections I, II, III and IV. The corresponding wave data are labelled ①, ②, ③ and ④. For the centred tool (middle panel), the reflection data from both sides of the borehole are similar owing to the 180° azimuth ambiguity of the dipole tool. In contrast, for the eccentric tool, the reflection data (② and ③) from reflectors (II and IV) on the eccentric side show higher amplitudes relative to their centred tool counterparts, whereas the reverse is valid for the reflection data (① and ④) from reflectors (I and IV) on the opposite side of the off-centre direction. The wave phenomena are consistent with the radiation analysis results shown in figure 8c, which have the potential to resolve the 180° uncertainty.

6. Conclusion

This paper presents a theoretical analysis of wave radiation and signal acquisition for a dipole acoustic reflection survey using an off-centred tool. We provide a fast and accurate algorithm to simulate borehole responses for the azimuthally placed off-axis receivers of an eccentric dipole tool. Compared with a centred tool, a prominent feature of an eccentric dipole source is the asymmetry of the source radiation. Thus, reflection data from the eccentric side of the borehole tended to show higher amplitude than the data from the opposite side. This provides a potential application for resolving 180° azimuth ambiguity in dipole shear-wave imaging. Our results also show that the asymmetry effect depends strongly on the degree of eccentricity, source frequency and formation elasticity. These factors should also be considered when using the effect to help resolve reflector azimuth ambiguity.

Downloaded from academic.oup.com/jge/article/19/5/1180/6762354 by China University of Petroleum - Beijing user on 08 October 2026

Acknowledgements

This work was supported by the National Natural Science Foundation of China (grant nos. 42074137 and 41821002), the Natural Science Foundation of Shandong Province (grant no. ZR201911120382), the National Key Research and Development Program of China (grant no. 2019YFC0605504) and the Major Scientific and Technological Projects of China National Petroleum Corporation (grant no. ZD2019-183-004).

Appendix A. Determining the coordinates of the source and receiver locations for an off-centred dipole acoustic tool

Consider an off-centre point source in the borehole fluid, as shown in figure 2. Assuming the original coordinates are $(r_0, \varphi_0, 0)$, after offsetting along the direction of φ_o by the distance D_o and rotating by the angle φ_r, the point source is located at $(r_e, \varphi_e, 0)$

$$\begin{cases} r_e = \sqrt{x_e^2 + y_e^2}, \\ \varphi_e = a\tan\left(\dfrac{y_e}{x_e}\right), \end{cases} \tag{A-1}$$

where $(x_e, y_e, 0)$ denotes the location of the eccentric point source in Cartesian coordinates and is given by

$$\begin{cases} x_e = r_0\cos(\varphi_0 + \varphi_r) + D_o\cos\varphi_o \\ y_e = r_0\sin(\varphi_0 + \varphi_r) + D_o\sin\varphi_o \end{cases} \tag{A-2}$$

According to equations (A-1) and (A-2), the coordinates of the four eccentric point sources shown in figure 2c are given by

$$\begin{cases} r_{X1} = \sqrt{r_0^2 + D_o^2 + 2r_0D_o\cos(\varphi_o - \varphi_r)}, & \varphi_{X1} = a\tan\left(\dfrac{r_0\sin\varphi_r + D_o\sin\varphi_o}{r_0\cos\varphi_r + D_o\cos\varphi_o}\right) \\ r_{Y1} = \sqrt{r_0^2 + D_o^2 + 2r_0D_o\sin(\varphi_o - \varphi_r)}, & \varphi_{Y1} = a\tan\left(\dfrac{r_0\cos\varphi_r + D_o\sin\varphi_o}{-r_0\sin\varphi_r + D_o\cos\varphi_o}\right) \\ r_{X2} = \sqrt{r_0^2 + D_o^2 - 2r_0D_o\cos(\varphi_o - \varphi_r)}, & \varphi_{X2} = a\tan\left(\dfrac{r_0\sin\varphi_r - D_o\sin\varphi_o}{r_0\cos\varphi_r - D_o\cos\varphi_o}\right) \\ r_{Y2} = \sqrt{r_0^2 + D_o^2 - 2r_0D_o\sin(\varphi_o - \varphi_r)}, & \varphi_{Y2} = a\tan\left(\dfrac{-r_0\cos\varphi_r + D_o\sin\varphi_o}{r_0\sin\varphi_r + D_o\cos\varphi_o}\right) \end{cases} \tag{A-3}$$

Note that the eccentric angles calculated using equations (A-1) and (A-3) are periodic functions with a period of π, which means that the function values need to be selected according to the actual location of the eccentric point source. For example, π (2π) should be added to φ_e for the $x_e < 0$ ($x_e > 0$) case. The coordinate solution method for the receiver location is similar to that for the source location.

Appendix B. Details of matrix equation (6) for borehole radiation

In equation (6), the expressions of the matrix **M** and the vector **b** are given next

$$\begin{aligned} M_{11} &= -fI_{m+1}(fr_b) - mI_m(fr_b)/r_b, \\ M_{12} &= -pK_{m+1}(pr_b) + mK_m(pr_b)/r_b, \\ M_{13} &= mK_m(sr_b)/r_b, \\ M_{14} &= -ik\left[sK_{m+1}(sr_b) - mK_m(sr_b)/r_b\right], \\ M_{21} &= \rho_f\omega^2 I_m(fr_b), \\ M_{22} &= 2\rho\beta^2\left[pK_{m+1}(pr_b)/r_b + m(m-1)K_m(pr_b)/r_b^2\right] + \rho(2k^2\beta^2 - \omega^2)K_m(pr_b), \\ M_{23} &= -2m\rho\beta^2\left[sK_{m+1}(sr_b)/r_b - (m-1)K_m(sr_b)/r_b^2\right], \end{aligned}$$

Downloaded from academic.oup.com/jge/article/19/5/1180/6762354 by China University of Petroleum - Beijing user on 08 October 2026

$$
\begin{aligned}
M_{24} &= 2ik\rho\beta^2\left\{sK_{m+1}(sr_b)/r_b + \left[m(m-1)/r_b^2 + s^2\right]K_m(sr_b)\right\},\\
M_{31} &= 0,\\
M_{32} &= 2m\rho\beta^2\left[pK_{m+1}(pr_b)/r_b - (m-1)K_m(pr_b)/r_b^2\right],\\
M_{33} &= -\rho\beta^2\left\{2sK_{m+1}(sr_b)/r_b + \left[2m(m-1)/r_b^2 + s^2\right]K_m(sr_b)\right\},\\
M_{34} &= 2ikm\rho\beta^2\left[sK_{m+1}(sr_b)/r_b - (m-1)K_m(sr_b)/r_b^2\right],\\
M_{41} &= 0,\\
M_{42} &= -2ik\rho\beta^2\left[pK_{m+1}(pr_b) - mK_m(pr_b)/r_b\right],\\
M_{43} &= ikm\rho\beta^2K_m(sr_b)/r_b.\\
M_{44} &= (s^2+k^2)\rho\beta^2\left[sK_{m+1}(sr_b) - mK_m(sr_b)/r_b\right],\\
b_1 &= -\varepsilon_m\left[fK_{m+1}(fr_b) - mK_m(fr_b)/r_b\right],\\
b_2 &= -\varepsilon_m\rho_f\omega^2K_m(fr_b),\\
b_3 &= 0, b_4 = 0,
\end{aligned}
$$

where r_b is the borehole radius; ω is the circular frequency; k stands for the axial wavenumber; $f = \sqrt{k^2 - (\omega/\alpha_f)^2}$ stands for the radial wavenumber of the borehole fluid, α_f is the fluid velocity; $p = \sqrt{k^2 - (\omega/\alpha)^2}$ and $s = \sqrt{k^2 - (\omega/\beta)^2}$ stand for the radial wavenumbers of the formation P- and S-waves, α and β are the formation P- and S-wave velocities, respectively; I_m (K_m) represents the modified Bessel functions of the first (second) kind with order m; the symbol ε_m represents Neumann's factor, which is defined as 1 for $m = 0$ and 2 for $m \neq 0$ and the symbol r_0 denotes the dipole-source radius. Note that when calculating the radiation pattern using equations (9) and (11), the vector **b** needs to be divided by $(2\rho_f\omega^2 r_0)$ to unify dimensions.

Appendix C. Details of matrix equation (17) for borehole reception

In matrix equation (17), the left-hand-side matrix **M** is the same as equation (6) (see Appendix B), whereas the right-hand side vectors **c** and **c′** are different, which depends on the type of the incident wave, as given next.

For the P incident wave (with the common factor $[S(\omega)\cdot RD_P^{X,Y}(\omega)\cdot RF_P(\omega)]$),

$$
\begin{aligned}
c_1 &= -\varepsilon_m\left[pI_{m+1}(pr_b) + mI_m(pr_b)/r_b\right]\cos(m\varphi_0'),\\
c_2 &= \varepsilon_m\rho\left\{\begin{array}{c}2\beta^2\left[pI_{m+1}(pr_b)/r_b - m(m-1)I_m(pr_b)/r_b^2\right]\\ -(2k^2\beta^2-\omega^2)I_m(pr_b)\end{array}\right\}\cos(m\varphi_0'),\\
c_3 &= 2m\varepsilon_m\rho\beta^2\left[pI_{m+1}(pr_b)/r_b + (m-1)I_m(pr_b)/r_b^2\right]\cos(m\varphi_0'),\\
c_4 &= -2\varepsilon_m ik\rho\beta^2\left[pI_{m+1}(pr_b) + mI_m(pr_b)/r_b\right]\cos(m\varphi_0'),\\
c_1' &= -\varepsilon_m\left[pI_{m+1}(pr_b) + mI_m(pr_b)/r_b\right]\sin(m\varphi_0'),\\
c_2' &= \varepsilon_m\rho\left\{\begin{array}{c}2\beta^2\left[pI_{m+1}(pr_b)/r_b - m(m-1)I_m(pr_b)/r_b^2\right]\\ -(2k^2\beta^2-\omega^2)I_m(pr_b)\end{array}\right\}\sin(m\varphi_0'),\\
c_3' &= 2m\varepsilon_m\rho\beta^2\left[pI_{m+1}(pr_b)/r_b + (m-1)I_m(pr_b)/r_b^2\right]\sin(m\varphi_0'),\\
c_4' &= -2\varepsilon_m ik\rho\beta^2\left[pI_{m+1}(pr_b) + mI_m(pr_b)/r_b\right]\sin(m\varphi_0').
\end{aligned}
\tag{C-1}
$$

Downloaded from academic.oup.com/jge/article/19/5/1180/6762354 by China University of Petroleum - Beijing user on 08 October 2026

For the SH incident wave (with the common factor $[S(\omega)\cdot RD_{SH}^{X,Y}(\omega)\cdot RF_{SH}(\omega)]$),

$$\begin{aligned}
c_1 &= -m\varepsilon_m I_m(sr_b)\sin(m\varphi'_0)/r_b,\\
c_2 &= -2m\varepsilon_m\rho\beta^2\left[sI_{m+1}(sr_b)/r_b+(m-1)I_m(sr_b)/r_b^2\right]\sin(m\varphi'_0),\\
c_3 &= -\varepsilon_m\rho\beta^2\left\{2sI_{m+1}(sr_b)/r_b-\left[2m(m-1)/r_b^2+s^2\right]I_m(sr_b)\right\}\sin(m\varphi'_0),\\
c_4 &= -ikm\varepsilon_m\rho\beta^2 I_m(sr_b)\sin(m\varphi'_0)/r_b,\\
c'_1 &= m\varepsilon_m I_m(sr_b)\cos(m\varphi'_0)/r_b,\\
c'_2 &= 2m\varepsilon_m\rho\beta^2\left[sI_{m+1}(sr_b)/r_b+(m-1)I_m(sr_b)/r_b^2\right]\cos(m\varphi'_0),\\
c'_3 &= \varepsilon_m\rho\beta^2\left\{2sI_{m+1}(sr_b)/r_b-\left[2m(m-1)/r_b^2+s^2\right]I_m(sr_b)\right\}\cos(m\varphi'_0),\\
c'_4 &= ikm\varepsilon_m\rho\beta^2 I_m(sr_b)\cos(m\varphi'_0)/r_b.
\end{aligned}\tag{C-2}$$

For the SV incident wave (with the common factor $[S(\omega)\cdot RD_{SV}^{X,Y}(\omega)\cdot RF_{SV}(\omega)]$),

$$\begin{aligned}
c_1 &= -ik\varepsilon_m\left[sI_{m+1}(sr_b)+mI_m(sr_b)/r_b\right]\cos(m\varphi'_0),\\
c_2 &= 2ik\varepsilon_m\rho\beta^2\left\{sI_{m+1}(sr_b)/r_b-\left[m(m-1)/r_b^2+s^2\right]I_m(sr_b)\right\}\cos(m\varphi'_0),\\
c_3 &= 2ikm\varepsilon_m\rho\beta^2\left[sI_{m+1}(sr_b)/r_b+(m-1)I_m(sr_b)/r_b^2\right]\cos(m\varphi'_0),\\
c_4 &= \varepsilon_m(s^2+k^2)\rho\beta^2\left[sI_{m+1}(sr_b)+mI_m(sr_b)/r_b\right]\cos(m\varphi'_0),\\
c'_1 &= -ik\varepsilon_m\left[sI_{m+1}(sr_b)+mI_m(sr_b)/r_b\right]\sin(m\varphi'_0),\\
c'_2 &= 2ik\varepsilon_m\rho\beta^2\left\{sI_{m+1}(sr_b)/r_b-\left[m(m-1)/r_b^2+s^2\right]I_m(sr_b)\right\}\sin(m\varphi'_0),\\
c'_3 &= 2ikm\varepsilon_m\rho\beta^2\left[sI_{m+1}(sr_b)/r_b+(m-1)I_m(sr_b)/r_b^2\right]\sin(m\varphi'_0),\\
c'_4 &= \varepsilon_m(s^2+k^2)\rho\beta^2\left[sI_{m+1}(sr_b)+mI_m(sr_b)/r_b\right]\sin(m\varphi'_0),
\end{aligned}\tag{C-3}$$

where S stands for the source spectrum; RD stands for the radiation function; RF stands for the reflection coefficient; the superscript X (Y) denotes the excitation of the X (Y) dipole source of the system; the subscripts P, SH and SV represent the types of incident waves, P-, SH- or SV-wave; φ'_0 is the virtual-source azimuth and other symbols are defined in Appendix B.

Conflict of interest statement. None declared.

References

Aki, K. & Richards, P., 1980. *Quantitative Seismology: Theory and Methods*, University Science Books.

Ben, J.L., Qiao, W.X., Che, X.H., Ju, X.D. & Liu, J.Q., 2020. Experimental simulation of obtaining the reflector azimuth using azimuthal acoustic reflection tool in the underwater environment, *Journal of Petroleum Science and Engineering*, **195**, 107649.

Bennett, N.N., 2019. 3D slowness time coherence for sonic imaging, *Geophysics*, **84**, D179–D189.

Bradley, T., Patterson, D. & Tang, X.M., 2011. Applying a through-casing acoustic imaging technique to identify gas migration paths in a salt body, *First Break*, **29**, 75–84.

Byun, J. & Toksöz, M.N., 2006. Effects of an off-centered tool on dipole and quadrupole logging, *Geophysics*, **71**, F91–F100.

Fu, X. & Gou, Y., 2022. An analysis for unipole acoustic logging while drilling wavefelds with varying eccentered collar positions, *Journal of Geophysics and Engineering*, **19**, 475–493.

Gong, H., Chen, H., He, X., Chang, S., Wang, X.M., Wang, B.C. & Yan, X.H., 2018. Modeling and inversions of acoustic reflection logging imaging using the combined monopole-dipole measurement mode, *Applied Geophysics*, **15**: 393–400.

Gong, H., Chen, H., He, X. & Wang, X.M., 2015. Eliminating the azimuth ambiguity in single-well imaging using 3C sonic data, *Geophysics*, **80**, A13–A17.

Gu, X.H., Tang, X.M. & Su, Y.D., 2021. Delineating a cased borehole in unconsolidated formations using dipole acoustic data from a nearby well, *Geophysics*, **86**, D139–D147.

Hirabayashi, N., 2021. Beamform processing for sonic imaging using monopole and dipole sources, *Geophysics*, **86**, D1–D14.

Hornby, B.E., 1989. Imaging of near-borehole structure using full-waveform sonic data, *Geophysics*, **54**, 747–757.

Ji, Y.J., He, X., Chen, H. & Wang, X.M., 2021a. The effects of tool eccentricity on individual P and S waves in monopole acoustic LWD, *Journal of Geophysics and Engineering*, **18**, 74–84.

Downloaded from academic.oup.com/jge/article/19/5/1180/6762354 by China University of Petroleum - Beijing user on 08 October 2026

Ji, Y.J., He, X., Chen, H., Wang, X.M. & Zhang, H.L., 2021b. Acoustic fields for monopole logging while drilling with an eccentric collar, *Geophysics*, **86**, D43–D63.

Kayama, K., Mikada, H., Takekawa, J. & Xu, S.B., 2021. Influence of eccentered/tilted sonic logging tool on dispersive wave, *First International Meeting for Applied Geoscience & Energy*, pp. 367–371.

Lee, S.Q., Tang, X.M. & Su, Y.D., 2019. Shear wave imaging to determine near-borehole faults for ocean drilling exploration, *Geophysical Journal International*, **217**, 288–293.

Leslie, H.D. & Randall, C.J., 1990. Eccentric dipole sources in fluid-filled boreholes: numerical and experimental results, *The Journal of the Acoustical Society of America*, **87**, 2405–2421.

Li, C., Chen, H., He, X. & Wang, X.M., 2021a. Identifying reflector azimuth from borehole multicomponent cross-dipole acoustic measurement, *Geophysics*, **86**, D201–D214.

Li, D., Qiao, W.X., Che, X.H., Ju, X.D., Yang, S.B., Lu, J.Q. & Men, B.Y., 2020. Eliminating the azimuth ambiguity in reflected S-wave imaging logging based on the azimuthal receiver mode, *Journal of Petroleum Science and Engineering*, **199**, 108295.

Li, Y.H., Tang, X.M., Li, H.R. & Lee, S.Q., 2021b. Characterizing the borehole response for single-well shear-wave reflection imaging, *Geophysics*, **86**, D15–D26.

Meredith, J.A., 1990. *Numerical and analytical modelling of downhole seismic sources: the near and far field*, *PhD. thesis*, Massachusetts Institute of Technology.

Pardo, D., Matuszyk, P.J., Torres-Verdín, C., Mora, A., Muga, I. & Calo, V.M., 2013. Influence of borehole-eccentred tools on wireline and logging-while-drilling sonic logging measurements, *Geophysical Prospecting*, **61**, 268–283.

Patterson, D.J., Middleton, D., Bourgeois, C., Quinn, T., Duncan, A., Sabaa, K., Priest, J. & Cazeneuve, E., 2016. New acoustic acquisition and processing method assist in delineating structure in an exploration play in the Gulf of Mexico, in *SPWLA 57th Annual Logging Symposium*, paper no. SPWLA-2016-NNNN.

Schmitt, D.P., 1993. Dipole logging in cased boreholes, *The Journal of the Acoustical Society of America*, **93**, 640–657.

Tang, X.M., 2004. Imaging near-borehole structure using directional acoustic-wave measurement, *Geophysics*, **69**, 1378–1386.

Tang, X.M., Cao, J.J., Li, Z. & Su, Y.D., 2016. Detecting a fluid-filled borehole using elastic waves from a remote borehole, *The Journal of the Acoustical Society of America*, **140**, EL211–EL217.

Tang, X.M., Cao, J.J. & Wei, Z.T., 2014. Shear-wave radiation, reception, and reciprocity of a borehole dipole source: with application to modeling of shear-wave reflection survey, *Geophysics*, **79**, T43–T50.

Tang, X.M. & Cheng, C.H., 2004. *Quantitative Borehole Acoustic Methods*, Elsevier Science Publishing.

Tang, X.M., Gu, X.H. & Lee, S.Q., 2020. Borehole acoustic reflection imaging through casing: theory and application, in *82nd EAGE Conference & Exhibition*, pp. 1–5.

Tang, X.M. & Patterson, D.J., 2009. Single-well S-wave imaging using multicomponent dipole acoustic-log data, *Geophysics*, **74**, WCA211–WCA223.

Wang, H., Fehler, M.C. & Miller, D., 2017. Reliability of velocity measurements made by monopole acoustic logging-while-drilling tools in fast formations, *Geophysics*, **82**, D225–D233.

Wang, H., Li, N., Wang, C.Z., Wu, H.L., Liu, P., Li, Y.S. & Liu, Y.M., 2020. Responses of dipole-source reflected shear waves in acoustically slow formations, *Journal of Geophysics and Engineering*, **17**, 1–17.

Wang, H., Tao, G. & Fehler, M.C., 2015a. Investigation of the high-frequency wavefield of an off-center monopole acoustic logging-while-drilling tool, *Geophysics*, **80**, D329–D341.

Wang, H, Tao, G. & Shang, X.F., 2015b. A method to determine the strike of interface outside of borehole by monopole borehole acoustic reflections, *Journal of Petroleum Science and Engineering*, **133**, 304–312.

Wei, Z.T. & Tang, X.M., 2012. Numerical simulation of radiation, reflection, and reception of elastic waves from a borehole dipole source, *Geophysics*, **77**, D253–D261.

Xu, J.Q., Hu, H.S. & Wang, Z., 2019. Asymptotic solution to a 3D dipole single-well imaging system with combined monopole and dipole receivers with an application in elimination of azimuth ambiguity, *Geophysics*, **84**, D191–D207.

Downloaded from academic.oup.com/jge/article/19/5/1180/6762354 by China University of Petroleum - Beijing user on 08 October 2026

Detecting a fluid-filled borehole using elastic waves from a remote borehole

Xiaoming Tang,[a] Jingji Cao, Zhen Li, and Yuanda Su
School of Geosciences, China University of Petroleum (East China), Qingdao, China
tangxiam@aliyun.com, caojingji19891116@163.com, lizhen9099@hotmail.com, syuanda@sina.com

Abstract: The interaction of a fluid-filled borehole with incident elastic waves is an important topic for downhole acoustic measurements. By analyzing the wave phenomena of this problem, one can simulate the detection of a borehole target using a source-receiver system in a remote borehole. The analysis result shows that the wave signals from the target borehole are of sufficient amplitude even though the borehole size is small compared to wavelength. Consequently, the target borehole can be detected when the two boreholes are far away from each other. The result can be utilized to provide a method for testing downhole acoustic imaging tools.

© 2016 Acoustical Society of America
[OAG]
Date Received: May 19, 2016 Date Accepted: July 13, 2016

1. Introduction

The response of a fluid-filled borehole to passing elastic waves has long been an important topic in the borehole geophysics community, because many downhole seismic/acoustic wave measurements, e.g., vertical seismic profiling (Toksöz et al., 1992), cross-well seismic (De Hoop et al., 1994), and single-well acoustic imaging (Tang and Patterson, 2009; Tang et al., 2014), etc., are made in the borehole. White (1953) developed a borehole-coupling theory to study the elastic response of the borehole in the low-frequency limit. Schoenberg (1986) and Peng (1994) extended the theory into frequency domain to model the wave phenomena at higher frequencies. The wave phenomena include the radiation of an acoustic source away from the borehole, the reception of elastic waves inside the borehole, and the scattering of the waves by the borehole. The radiation and reception problems have been studied in detail. For example, Meredith (1990) modeled the radiation of a (axisymmetric) monopole source. Tang et al. (2014) studied the radiation of a (anti-symmetric) dipole source and the reception of elastic waves using a dipole receiver in borehole. In comparison, the problem of borehole scattering has been overlooked in borehole geophysics for lack of application. In this study, we analyze the scattered waves and provide a useful application for these waves using single-well acoustic imaging.

Single-well dipole shear-wave imaging has recently emerged as an important borehole geophysical application (Tang and Patterson, 2009; Tang et al., 2014). This application uses an acoustic dipole source-receiver system to radiate and receive elastic waves to and from a remote reflector in the formation surrounding the well. To validate the application, and to test whether the borehole acoustic system is capable of imaging a designated reflector target in the formation, it is desirable to build a testing facility. Two parallel boreholes with some distance apart may be used for such a facility. However, it is usually difficult to understand that the target borehole, with its size much smaller than wavelength, can generate wave scattering of sufficient amplitude. For this purpose, we analyze wave scattering from a fluid-filled borehole and study the detection of the scattered waves from a remote borehole. Because the dipole source generates primarily the SH-wave (Tang et al., 2014), we will focus on using the SH-wave for the borehole detection problem.

2. Theoretical analysis

Figure 1 illustrates the configuration for the borehole detection problem. Two parallel boreholes are located in an infinite elastic formation, separated at distance r_0. In the

[a]Author to whom correspondence should be addressed.

08 October 2026 03:49:50

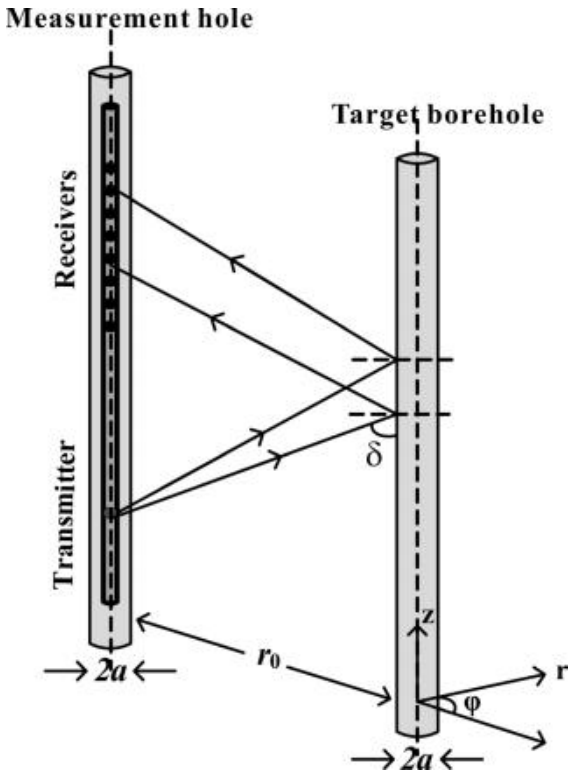


Fig. 1. Configuration for detecting a target borehole using elastic waves from a remote borehole.

08 October 2026 03:49:50

measurement hole, a transmitter source radiates elastic waves into the formation. After reflected or scattered by the nearby borehole, designated as the target borehole, the waves are received by a receiver (or an array of receivers) in the measurement borehole. The spectrum of the wave that is radiated from the measurement hole and incident on the target hole is given by (Tang et al., 2014)

$$\mathrm{Iwv}(x) = S(x)RD(x)\frac{e^{ixR/v}}{R}, \tag{1}$$

where S is the source spectrum, RD is the borehole radiation function, and v is wave velocity. Both S and RD can vary with angular frequency x. The wave propagates in the formation as a spherical wave, with a geometric spreading factor 1/R, where R is propagation distance.

Consider the interaction of the incident elastic wave with the fluid-filled target borehole, as shown in Fig. 1. Using cylindrical coordinate (r, u, z) for the target borehole, the particle displacements in the fluid u_f and formation solid u_s are given by their respective potential functions

$$\begin{cases} u_f = \nabla /_f \\ u_s = \nabla / + \nabla \times (C\hat{z}) + \nabla \times \nabla \times (v\hat{z}), \end{cases} \tag{2}$$

where $\hat{z}$ is unit vector along z-axis. For the target borehole, we expand the spherical incident wave as the summation of cylindrical waves (Tang and Cheng, 2004)

$$\frac{e^{ixR/v}}{R} = \frac{1}{p}\int_{-\infty}^{+\infty}\sum_{n=0}^{+\infty} e_n K_n(k_v r_0) I_n(k_v r)\cos[n(u-u_0)]e^{ik(z-z_0)}dk, \tag{3}$$

where (r_0, u_0, z_0) is the source location; $R = \sqrt{r^2 + r_0^2 - 2rr_0\cos(u-u_0) + (z-z_0)^2}$; $e_n = 1$ for $n = 0$ and 2 for $n \geq 1$; k is axial wavenumber. Note in the argument of the first and second kind of modified Bessel functions I_n and K_n, $k_v = \sqrt{k^2 - x^2/v^2}$ is the radial wavenumber for the incident wave. Corresponding to the functional forms of Eq. (3), the general solution for the potentials of Eq. (2) in the $x - k$ domain can be written as (Tang and Cheng, 2004)

$$\left\{\begin{array}{ll} /_f = \sum_{n=0}^{\infty}[A_n\cos(nu)+A'_n\sin(nu)]I_n(k_f r)K_n(k_v r_0)e^{ik(z-z_0)} & (0<r<a)\\ / = \sum_{n=0}^{\infty}[B_n\cos(nu)+B'_n\sin(nu)]K_n(k_p r)K_n(k_v r_0)e^{ik(z-z_0)} & \\ v = \sum_{n=0}^{\infty}[C_n\cos(nu)+C'_n\sin(nu)]K_n(k_s r)K_n(k_v r_0)e^{ik(z-z_0)} & (r>a)\\ C = \sum_{n=0}^{\infty}[D_n\sin(nu)-D'_n\cos(nu)]K_n(k_s r)K_n(k_v r_0)e^{ik(z-z_0)} & \end{array}\right. \quad (4)$$

where a is borehole radius; $k_f = \sqrt{k^2 - x^2/a_f^2}$, $k_p = \sqrt{k^2 - x^2/a^2}$, and $k_s = \sqrt{k^2 - x^2/b^2}$ are the radial wavenumber for borehole fluid, formation compressional, and formation shear waves, respectively; a, b, and a_f are formation P and S velocity, and fluid velocity, respectively. The wave amplitude coefficients A_n, B_n, C_n, D_n, and A'_n, B'_n, C'_n, D'_n are determined by the following boundary conditions at the borehole wall:

$$\left\{\begin{array}{ll} u_r^s(a^+)+u_r^i(a^+)=u_r^f(a^-) & \text{(Continuity of radial displacement)}\\ r_{rr}^s(a^+)+r_{rr}^i(a^+)=r_{rr}^f(a^-) & \text{(Continuity of radial stress)}\\ r_{ru}^s(a^+)+r_{ru}^i(a^+)=0 & \text{(Vanishing of azimuthal shear stress)}\\ r_{rz}^s(a^+)+r_{rz}^i(a^+)=0 & \text{(Vanishing of axial shear stress).}\end{array}\right. \quad (5)$$

The fluid and formation displacements are calculated using Eq. (2) and Eq. (4). The formation displacement is used to calculate strain, which, when used in Hook's law, yields the normal and shear stresses. Substitution of the displacements and stresses into the above boundary conditions leads to two matrix equations to determine the unknown amplitude coefficients:

$$M\times[A_n\ B_n\ C_n\ D_n]^T = b \quad \text{and} \quad M\times[A'_n\ B'_n\ C'_n\ D'_n]^T = b', \quad (6)$$

where M is a 4×4 matrix and b and b′ are 1×4 vectors; the expressions for M, b, and b′ are given in Schoenberg (1986) and Peng (1994). In fact, b and b′ are calculated from the incident wave and are evaluated at the borehole wall. For an SH incident wave, the displacement potential, in terms of Eq. (1) and Eq. (3), is given by

$$C^i = S(x)RD(x)\sum_{n=0}^{\infty}e_n I_n(k_s r)K_n(k_s r_0)[\cos(nu)\cos(nu_0)+\sin(nu)\sin(nu_0)]e^{ik(z-z_0)}, \quad (7)$$

where the superscript i denotes incident wave. In the above expression, we have replaced v with b for the shear-wave incidence. The azimuthal displacements inside the target borehole can be calculated using

$$u_u^f = \sum_{n=0}^{\infty}\frac{n}{r}\left[-A_n\sin(nu)+A'_n\cos(nu)\right]I_n(k_f r)K_n(k_s r_0)e^{ik(z-z_0)}. \quad (8)$$

With the given incident wave, Eqs. (6) are solved to find the amplitude coefficients. By substituting them into Eq. (4) and then using Eq. (2), the elastic wavefield solutions inside and outside the target borehole are completely specified. For example, the scattered SH-wave displacement from the target borehole is calculated using

$$u_u^s(k;x;r,u,z) = \sum_{n=0}^{\infty}[-D_n\sin(nu)+D'_n\cos(nu)][nK_n(k_s r)/r - k_s K_{n+1}(k_s r)]K_n(k_s r_0)e^{ik(z-z_0)}. \quad (9)$$

For a wave incident angle d measured from borehole axis (see Fig. 1), the axial wavenumber becomes $k = (x/b)\cos d$, one can calculate the transmission coefficient across the target borehole interface using

$$T_{SH}(x;r_f,u,d) = ||u_u^f(r_f)||/||u^i(r_f)|| \quad (0\le r_f<a). \quad (10)$$

For a receiver at the borehole center ($r_f = 0$), Eq. (10) defines the receiving directivity of the fluid-filled borehole to the incident wave, and is therefore designated as borehole

08 October 2026 03:49:50

reception pattern (Peng, 1994). More interestingly, for a borehole dipole source, Tang et al. (2014) show that the SH or SV shear wave radiation directivity or pattern away from the borehole is equal to the reception pattern of the same borehole to the SH or SV shear-wave incidence. By this equivalence, we can calculate the source radiation directivity in Eq. (1) and Eq. (7) using

$$\mathrm{RD} = \mathrm{T_{SH}}(\mathrm{x};\mathrm{u},\mathrm{d}). \tag{11}$$

The central part of this study is to analyze the wave signal in the measurement borehole that is generated by the scattered wave from the target borehole. This analysis allows us to find out whether the signal is of sufficient amplitude for the detection of the target borehole. For the SH-wave displacement u_u^s in Eq. (9), we perform a wavenumber-k integration to obtain the scattered wave spectrum at distance r away from the target borehole

$$u_u^s(\mathrm{x};\mathrm{r},\mathrm{u},\mathrm{z}) = \frac{1}{\mathrm{p}}\int_{-\infty}^{+\infty} u_u^s(\mathrm{k};\mathrm{x};\mathrm{r},\mathrm{u},\mathrm{z})\mathrm{e}^{\mathrm{ik}(\mathrm{z}-\mathrm{z}_0)}\mathrm{dk}. \tag{12}$$

If the receiver is in the far-field of the scattering borehole, the steepest-descent method (Aki and Richards, 1980) can be used to find the far-field asymptotic solution for the scattered SH-wave displacement u_u^s, as

$$u_u^s(\mathrm{x};\mathrm{r},\mathrm{u},\mathrm{z}) = \sum_{\mathrm{n}=0}^{\infty}\sqrt{\frac{\mathrm{p}\,\mathrm{x}\sin^3\mathrm{d}}{2\mathrm{b}\mathrm{r}\mathrm{r}_0(\mathrm{r}+\mathrm{r}_0)}}\left[\mathrm{D_n}(\mathrm{x},\mathrm{k}_0)\sin(\mathrm{nu}) - \mathrm{D_n'}(\mathrm{x},\mathrm{k}_0)\cos(\mathrm{nu})\right] \times \mathrm{e}^{\mathrm{i}(\mathrm{R}'+\mathrm{r}_0\sin\mathrm{d})\mathrm{x}/\mathrm{b}-(\mathrm{pi})/4}, \tag{13}$$

where $\mathrm{k}_0 = (\mathrm{x}/\mathrm{b})\cos\mathrm{d}$ and $\mathrm{R}' = \sqrt{\mathrm{r}^2 + (\mathrm{z}-\mathrm{z}_0)^2}$.

Now for a dipole source at $\mathrm{z}_0 = 0$ and $\mathrm{u}_0 = \mathrm{p}$, we place the dipole receiver in the source borehole along the borehole axis (see Fig. 1) and, for the SH-wave problem, orient the source and receiver alignment perpendicular to the sagittal plane containing the two boreholes. At the receiver location, the same wave incidence and scattering process occurs, for which the above analysis result can be readily applied. Multiplying Eq. (13) with the receiver borehole response function gives the received wave signal inside the borehole

$$\mathrm{RWV}(\mathrm{x}) = \mathrm{T_{SH}}(\mathrm{x};\mathrm{p},\mathrm{d})u_u^s(\mathrm{x};\mathrm{r}_0,\mathrm{p},\mathrm{z}), \tag{14}$$

where u_u^s is now evaluated at the measurement borehole ($\mathrm{r} = \mathrm{r}_0, \mathrm{u} = \mathrm{p}$) for a receiver at distance z from the source.

3. Result validation and discussion

By specifying the source function $\mathrm{S}(\mathrm{x})$ in Eq. (7) (a Kelly wavelet of 4 kHz center frequency is used), we can calculate the received wave signal in the measurement borehole. For the configuration of Fig. 1 and model parameters of Table 1, the measurement to target borehole distance is 10 m. The measurement system consists of a dipole source and receiver array with source-to-receiver distance of 1.6 m and receiver-spacing of 0.2 m. For validation, we also use finite-difference modeling (Wei and Tang, 2012) to calculate the received wave signals for the same configuration of Fig. 1.

Figure 2(a) shows the SH-wave radiation (also the reception) pattern of a 4 kHz dipole source for the fast and slow formations in Table 1, calculated using Eq. (10). The patterns are shown as a function of the incident angle d, where the angular labels are for the radiation (incident) angle d and radial labels are for radiation (reception) amplitude (dimensionless). The results show that the fast-formation radiation (dots) is much stronger than the slow-formation radiation (solid curve). Figures 2(b) and 2(c) show the calculated waveforms for a receiver array ranging from 1.6 to 4.8 m along the borehole for the fast (b) and slow (c) formation models, respectively. The asymptotic solution [Eq. (14)] result is the dotted line and the finite difference result is the solid curve. The two sets of waveforms from very different modeling approaches

Table 1. Model calculation parameters.

	vp/(m s^{-1})	vs/(m s^{-1})	q/(kg m^{-3})	Radius/(m)
Borehole fluid	1500	—	1000	0.1
Fast formation	3800	2100	2300	
Slow formation	2700	1300	2000	

08 October 2026 03:49:50

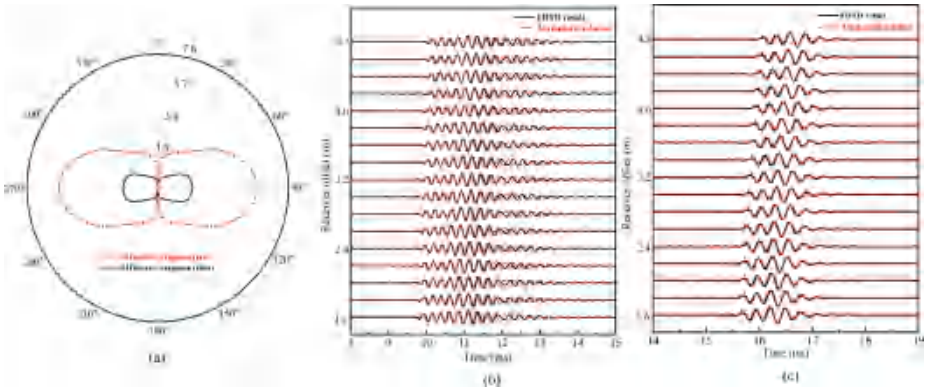


Fig. 2. (Color online) (a) SH-wave radiation (reception) pattern for a borehole dipole source (receiver) in fast (dots) and slow (solid curve) formations. The wave frequency is 4 kHz. Array SH-waves calculated for the configuration of Fig. 1 for (b) fast and (c) slow formations. For validation, the results from the asymptotic solution (dots) and the finite-difference modeling (solid curve) are compared.

agree quite well. The agreement validates the solution result of this study. The result also shows that the target borehole signal received in the measurement hole are strongly modulated by both boreholes and by the surrounding formation, as is shown in the radiation/reception patterns of Fig. 2(a). The modulation effect is also evident in the waveform modeling result; for the same source, the fast formation signals (b) are more ringing than their slow formation counterpart (c). This suggests that the borehole modulation effect must be considered for the downhole imaging application.

The above modeling and analysis result is both interesting and important. It shows that, despite the small radius of the target borehole compared to wavelength, the scattered waves from the target can be detected in the measurement borehole far away from the target. More important, if the signal is of sufficient amplitude, we can use the configuration in Fig. 1 to test the design and performance of the acoustic measurement system. For this purpose, the borehole scattering is compared with the reflection from another known reflector of infinite extent, e.g., a geological interface or bed boundary.

Let us replace the target borehole of Fig. 1 with a planar reflector parallel with the measurement borehole. For this situation, the SH-wave signal that is radiated by a borehole source, reflected from the reflector, and received in the same borehole, can be generally written as (Tang et al., 2014)

$$\mathrm{Rwv}(x) = \mathrm{S}(x)\mathrm{RD}(x)\mathrm{RF}(x)\mathrm{T}(x)\frac{e^{ixL/b}}{L}, \tag{15}$$

where the borehole radiation and reception functions $\mathrm{RD}(x)$ and $\mathrm{T}(x)$ can both be calculated using Eq. (10); $L = 2\sqrt{r^2 + z^2}$ is the total distance traveled to and from the reflector; RF is the reflection coefficient that can be calculated using Zoeppritzs equation (Aki and Richards, 1980). For modeling the geological interface between two formations, the fast and slow formation parameters in Table 1 are used and the wave is incident from the fast formation.

Figure 3 compares the scattered waves (solid curve) from the target borehole using Eq. (14) with the reflected waves (dots) from the planar reflector using Eq. (15). The calculation parameters are given in Table 1. The waves are received by the same receiver array in the borehole (see Fig. 1). The reflection waves have higher amplitude compared to the scattered waves. Despite the difference, the two sets of waves are about the same order of amplitude. Because shear-wave imaging of bedding boundaries is a proven technology (Tang and Patterson, 2009), the comparison shows that the technology is also capable of imaging a remote borehole.

It should be noted that the scattered wave amplitude from the target borehole, as given in Eq. (13) and Eq. (14), is strongly dependent on frequency and the measurement-to-target borehole offset r_0. The offset dependence, according to Eq. (13), is $r_0^{-1.5}$. Although the wave decays faster with offset compared to the planar reflector case [which has an offset dependence of r_0^{-1}, as from Eq. (15)], the impact on the wave amplitude is not extraordinary. (For example, changing the offset from 10 to 20 m only reduces the amplitude by a factor of 0.35, which, in the planar reflector case, is 0.5.) The frequency-dependence, on the other hand, can change the wave amplitude substantially. For example, if Fig. 3 was calculated for a 1 kHz source, the

08 October 2026 03:49:50

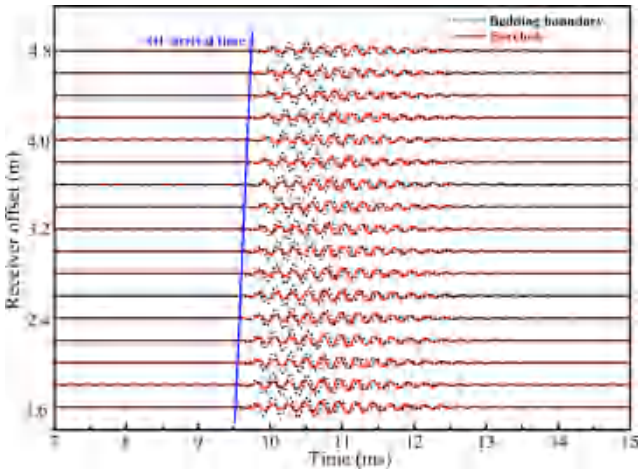


Fig. 3. (Color online) Comparison of SH-wave signals in the measurement borehole that are scattered from the target borehole (solid curve) and from the planar reflector (dots).

wave amplitude of the target borehole would be an order of magnitude smaller than that of the planar reflector. This shows that, as the wavelength is substantially large compared to borehole size, the back scattered wave from the target borehole will become small. Nevertheless, for the nominal borehole size and frequency used in dipole shear imaging, the result of Fig. 3 shows the back scattered wave is measurable.

A field shear-wave imaging experiment has been conducted for the configuration in Fig. 1 using a dipole logging tool. Figure 4 (panel 1) shows the gamma ray and borehole caliper of the measurement borehole with a volcanic tuff formation. The target borehole of similar size is located 10 m away. The measurement frequency is 3.5 kHz. Panel 2 shows the imaging result. In the depth interval below 130 m, the borehole condition is quite good (see the borehole caliper curve), and a reflector image is clearly identified. This reflector is vertical (which means it is parallel with the measurement borehole) and is about 10 m away from the measurement hole, coinciding with the target borehole position. The experiment result confirms our theoretical prediction result.

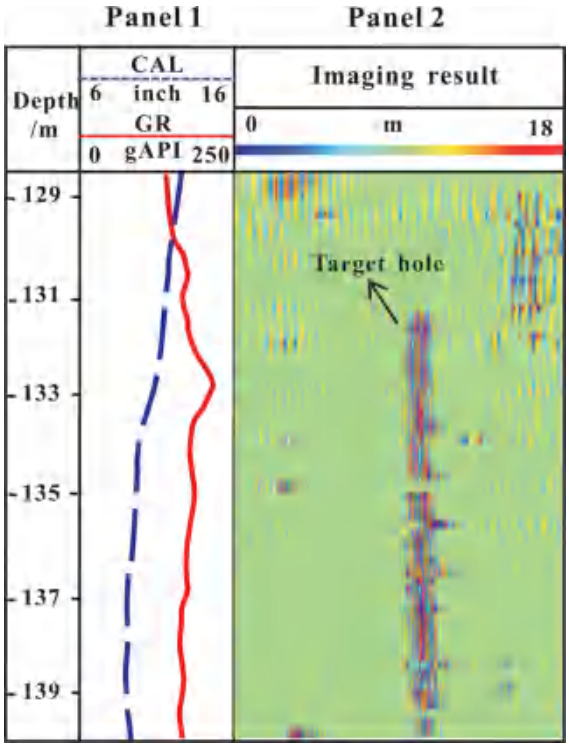


Fig. 4. (Color online) Imaging result of a field measurement data where the measurement and target boreholes are 10 m apart from each other.

08 October 2026 03:49:50

4. Conclusions

By analyzing the interaction of a fluid-filled borehole with passing elastic waves, the effects of the borehole on the wave radiation, reception, and wave scattering relating to the downhole acoustic measurement can all be understood and modeled. We have demonstrated that, although the borehole size is small compared to wavelength in the borehole scattering problem, the scattered wave amplitude is comparable to the reflection wave amplitude from a geological boundary of infinite extent. The result can be used to provide a theoretical foundation for imaging a target borehole using downhole acoustic measurement.

Acknowledgments

The authors thank the associate editor and reviewers for their constructive comments and suggestions that helped improve the manuscript. This work is supported by the China Fundamental Research and Development Program under Grant No. 2014CB239006 and the Fundamental Research Funds for the Central Universities (15CX06003A).

References and links

Aki, K., and Richards, P. (1980). Quantitative Seismology: Theory and Methods (W. H. Freeman and Co, New York).

De Hoop, A. T., De Hon, B. P., and Kurkjian, A. L. (1994). "Calculation of transient tube-wave signals in cross-borehole acoustics," J. Acoust. Soc. Am. 95(4), 1773–1789.

Meredith, J. A. (1990). "Numerical and analytical modeling of downhole seismic sources: The near and far field," Ph.D. thesis, Massachusetts Institute of Technology, Cambridge, MA.

Peng, C. B. (1994). "Borehole effects on downhole seismic measurements," Ph.D. thesis, Massachusetts Institute of Technology, Cambridge, MA.

Schoenberg, M. (1986). "Fluid and solid motion in the neighborhood of a fluid-filled borehole due to the passage of a low-frequency elastic plane wave," Geophysics 51, 1191–1205.

Tang, X. M., Cao, J. J., and Wei, Z. T. (2014). "Shear-wave radiation, reception, and reciprocity of a borehole dipole source: With application to modeling of shear-wave reflection survey," Geophysics 79(2), T43–T50.

Tang, X. M., and Cheng, C. H. (2004). Quantitative Borehole Acoustic Methods (Elsevier Science Publishing, Amsterdam, the Netherlands), Chap. 2.

Tang, X. M., and Patterson, D. J. (2009). "Single-well S-wave imaging using multicomponent dipole acoustic-log data," Geophysics 74(6), WCA211–WCA223.

Toksöz, M. N., Cheng, C. H., and Cicerone, R. D. (1992). "Fracture detection and characterization from hydrophone vertical seismic profiling data," in Fauh Mechanics and Transport Properties of Rocks (Academic Press, New York), pp. 389–414.

Wei, Z. T., and Tang, X. M. (2012). "Numerical simulation of radiation, reflection, and reception of elastic waves from a borehole dipole source," Geophysics. 77(6), D253–D261.

White, J. E. (1953). "Signals in a borehole due to plane waves in the solid," J. Acoust. Soc. Am. 25, 906–915.

08 October 2026 03:49:50

唐晓明，古希浩，李杨虎等. 2021. 井孔与弹性波的相互作用:理论、方法和应用. 地球物理学报,64(12):4227-4238,doi:10.6038/cjg2021O0396.

Tang X M, Gu X H, Li Y H, et al. 2021. The interaction between borehole and elastic waves: theory, method and application. *Chinese J. Geophys.* (in Chinese),64(12):4227-4238,doi:10.6038/cjg2021O0396.

井孔与弹性波的相互作用:理论、方法和应用

唐晓明[1,2,3]，古希浩[1,2]，李杨虎[1,2]，苏远大[1,2,3]*

1 中国石油大学(华东)地球科学与技术学院，青岛 266580

2 青岛海洋科学与技术国家实验室海洋矿产资源评价与探测技术功能实验室，青岛 266071

3 中国石油大学(华东)深层油气重点实验室，青岛 266580

摘要 本文概述了井孔与弹性波相互作用这一经典理论问题的求解方法以及近期的一些重要进展和应用.特别是,用球面波的柱面波展开式同时求解井孔的弹性波辐射和入射(及散射)问题，避免了后一问题常用的平面波入射假设，由此可正确描述远探测波场球面传播的物理实质.介绍了将远场渐近方法和互易性原理用于求解这一问题的快捷有效的分析方法.将这一方法用于井中的声波远探测技术,可以准确模拟和分析井中的声源辐射,波在地层中的反射,以及井对入射弹性波的散射和透射等复杂波动现象.对于指向性声源(如偶极声源),还可以模拟其接收声场的方位特征,进而通过四分量测量确定反射体的走向.分析结果不仅为远探测技术奠定了扎实的理论基础，而且在实际应用中取得了良好的效果.

关键词 井孔辐射和接收；井孔散射；声波远探测

doi:10.6038/cjg2021O0396 **中图分类号** P631 **收稿日期** 2020-10-14，2020-12-12 收修定稿

The interaction between borehole and elastic waves: theory, method and application

TANG XiaoMing[1,2,3], GU XiHao[1,2], LI YangHu[1,2], SU YuanDa[1,2,3]*

1 *School of Geosciences, China University of Petroleum, Qingdao* 266580, *China*

2 *Laboratory for Marine Mineral Resources, Qingdao National Laboratory for Marine Science and Technology, Qingdao* 266071, *China*

3 *Key Laboratory of Deep Oil and Gas, China University of Petroleum, Qingdao* 266580, *China*

Abstract This paper elaborates the theory and method for solving the classic problem of the elastic-wave interaction with a borehole, emphasizing the recent important developments and applications. The use of the cylindrical-wave expansion method to solve both the borehole wave radiation and reception (and scattering) problems avoids the plane-wave incidence approximation commonly used in the latter problem, allowing for correctly modeling the spherical-wave propagation characteristics of the wavefield. By employing the far field asymptotic solution and the reciprocity of borehole radiation and reception, a fast and effective analysis method is obtained. Applying the analysis method to single-well acoustic imaging, one can accurately model and analyze the complex wave phenomena in the borehole wave radiation, scattering/reflection, and reception process. This

基金项目 国家自然科学基金(41821002、42074137),中石油重大科技项目(ZD2019-183-004),山东省自然科学基金(ZR201911120382)联合资助.

第一作者简介 唐晓明,男,1955 年生,教授,1982 年获北京大学地球物理学学士学位;1984 年获国家地震局地球物理研究所地球物理学硕士学位;1986 年起在美国麻省理工学院地球资源实验室从事声波测井研究工作,1990 年获麻省理工学院理学博士学位.多年来一直致力于地球物理(特别是声波)测井、岩石物理学、地震波传播及测量等方面的研究和技术开发工作.

E-mail: tangxiam@aliyun.com

***通讯作者** 苏远大,男,1978 年生,教授,博士,主要从事声波测井理论、方法及处理研究. E-mail: syuanda@sina.com

(C)1994-2022 China Academic Journal Electronic Publishing House. All rights reserved. http://www.cnki.net

method can also be used to simulate the azimuthal characteristics of the wavefield from a directional acoustic source (such as borehole dipole source), enabling the determination of the reflector azimuth using the four-component measurement. The analysis results not only laid a solid theoretical foundation for the single-well imaging technology, but also achieved good results in practical applications.

Keywords Borehole radiation and reception; Borehole scattering; Borehole acoustic reflection survey

0 引言

地壳岩石中钻井与弹性波的相互作用是一个经久不衰的科学问题,从早期各种井中的地震勘探测量(如垂直地震反射剖面、井间地震等),声波测井,到近期发展起来的声波远探测技术,都与该问题密切相连.地震测量主要关心井孔对入射的低频弹性波场的调制和响应(参见 White,1953;Schoenberg,1986;Peng et al.,1993),而声波远探测则要考虑中高频段的井中声源对井外地层的辐射波在地层中的反射,以及在井中对反射声波接收的全过程(唐晓明和魏周拓,2012; Tang et al.,2014; Xu et al.,2019).对于偶极横波远探测技术,还必须考虑声源发射和接收的方位效应.除了波的辐射和接收,另一个重要的问题是井对弹性波的反射和散射,这个问题由于远探测技术在邻井探测(苏远大等,2014; Tang et al.,2016)和井丛防碰中的应用变得重要起来.

综上所述,我们将井中的辐射和接收以及井对波的散射统一归结为井孔与弹性波的相互作用问题,并结合远探测技术的应用对此进行理论分析、求解.远探测波场的特点是波的井外辐射及对井的入射都具有球面波的传播特征,而很多早期,甚至包括近期(如 Hirabayashi et al.,2017)对井孔的弹性波入射分析大都采用平面波入射的假设.许家旗和胡恒山(2019)结合虚源法和互易定理求解井孔的球面波入射问题,将辐射到地层界面、反射回井孔的入射波等效为来自虚源的球面波,在此基础上利用虚源与井中声源的互易关系得到该球面波在井中的激发响应.本文采用将入射球面波展开为柱面波的方法(Tang and Cheng,2004),可以像求解井孔的辐射问题那样,方便地得到对井孔入射问题的解.

远探测波场的分析结果为近期发展起来的声波远探测技术奠定了理论基础并获得了良好的应用效果.鉴于该课题的重要性和挑战性,许多学者在各个方面做了大量工作.这些工作和结果在相关的文献中都已有介绍;本文的重点在于介绍和讨论在实际应用中被证明是行之有效的理论分析和结果,这些应用包括运用井孔散射理论的邻井探测和具有方位特征的偶极声波远探测.

1 井中声源辐射的理论分析

图 1 给出了利用井中声波测井仪对井旁地质反射体进行探测的示意图,仪器上的声源向井外辐射弹性波,经反射后入射到井中,被仪器上的探测器接收.采用柱坐标系,井中流体中位于坐标(r_0,φ_0,z_0)处的点声源向场点(r,φ,z)辐射的球面波可写成柱面波展开的形式(Tang and Cheng,2004):

$$\begin{aligned}\frac{\mathrm{e}^{\mathrm{i}\omega R/v}}{R}=&\frac{1}{\pi}\int_{-\infty}^{+\infty}\sum_{n=0}^{+\infty}\varepsilon_n \mathrm{I}_n(k_v r_<)\mathrm{K}_n(k_v r_>)[\cos(n\varphi)\cos(n\varphi_0)\\&+\sin(n\varphi)\sin(n\varphi_0)]\mathrm{e}^{\mathrm{i}k(z-z_0)}\,\mathrm{d}k,\\ r_<=&\min(r,r_0)\\ r_>=&\max(r,r_0),\end{aligned}\qquad \varepsilon_n=\begin{cases}1 & n=0\\ 2 & n>0\end{cases}\tag{1}$$

其中$R=\sqrt{r^2+r_0^2-2rr_0\cos(\varphi-\varphi_0)+(z-z_0)^2}$,$\mathrm{I}_n$ 和 K_n 分别是 n 阶第一类和第二类变型贝塞尔函数,k 和 $k_v=\sqrt{k^2-\omega^2/v^2}$ 分别为轴向和径向波数,v 为波速.K_n 中的径向距离取 r 和 r_0 的较大值是为了满足远处声幅有限的辐射条件.将(1)式乘以声源的频谱函数 $S(\omega)$可以模拟声源在给定频段中的激发.

将(1)式的声源置于井中,将在井内流体和井外弹性地层中激发出弹性波动,井内外的位移场可分别表示为

$$\begin{cases}\boldsymbol{u}_\mathrm{f}=\nabla\phi_\mathrm{f},\\ \boldsymbol{u}_\mathrm{s}=\nabla\phi+\nabla\times(\chi\hat{\boldsymbol{z}})+\nabla\times\nabla\times(\Gamma\hat{\boldsymbol{z}}),\end{cases}\tag{2}$$

其中 ϕ_f 和 ϕ 分别是流体和地层中纵(P)波的位移势,χ 和 Γ 分别是地层中 SH 和 SV 横波的位移势,$\hat{\boldsymbol{z}}$ 为 z 轴方向的单位向量.频率-波数域中各个位移势函数的通解一般表达为

(C)1994-2022 China Academic Journal Electronic Publishing House. All rights reserved. http://www.cnki.net

$$\begin{cases} \phi_{\mathrm{f}} = \sum\limits_{n=0}^{\infty}[A_n\cos(n\varphi)+A'_n\sin(n\varphi)]\mathrm{I}_n(fr_0)\mathrm{I}_n(fr), & (0<r<a) \\ \phi = \sum\limits_{n=0}^{\infty}[B_n\cos(n\varphi)+B'_n\sin(n\varphi)]\mathrm{I}_n(fr_0)\mathrm{K}_n(pr), \\ \chi = \sum\limits_{n=0}^{\infty}[C_n\sin(n\varphi)-C'_n\cos(n\varphi)]\mathrm{I}_n(fr_0)\mathrm{K}_n(sr), \\ \Gamma = \sum\limits_{n=0}^{\infty}[D_n\cos(n\varphi)+D'_n\sin(n\varphi)]\mathrm{I}_n(fr_0)\mathrm{K}_n(sr), \end{cases} \quad (r>a) \tag{3}$$

式中 a 为井径，$f=\sqrt{k^2-\omega^2/\alpha_{\mathrm{f}}^2}$，$p=\sqrt{k^2-\omega^2/\alpha^2}$，$s=\sqrt{k^2-\omega^2/\beta^2}$ 分别是流体纵波和地层纵波和横波的径向波数，ω 为圆频率，α_{f}、α、β 分别是流体纵波和地层纵波和横波的波速. (3)式中波动的振幅系数 A_n、A'_n、B_n、B'_n、C_n、C'_n、D_n、D'_n 由井壁边界条件确定. (4)式中井壁内侧(a^-)和外侧(a^+)的固-液界面的边界条件依次为:径向位移和应力连续,环向和轴向的剪切应力为零.

$$\begin{cases} u_r(a^+)-u_r^{\mathrm{f}}(a^-)=u_r^{\mathrm{d}}(a^-), \\ \sigma_{rr}(a^+)-\sigma_{rr}^{\mathrm{f}}(a^-)=\sigma_{rr}^{\mathrm{d}}(a^-), \\ \sigma_{r\varphi}(a^+)=0, \\ \sigma_{rz}(a^+)=0, \end{cases} \tag{4}$$

式中的上标 d 和 f 分别表示声源辐射的直达声场和井壁在流体中产生的反射声场. 由(1)、(2)和(3)式计算出直达波和井壁在流体和地层中的位移和应力,代入(4)式得到两个矩阵方程:

$$\begin{aligned} \boldsymbol{M}\times[A_n \quad B_n \quad C_n \quad D_n]^{\mathrm{T}} &= \boldsymbol{b}, \\ \boldsymbol{M}\times[A'_n \quad B'_n \quad C'_n \quad D'_n]^{\mathrm{T}} &= \boldsymbol{b}', \end{aligned} \tag{5}$$

式中的 $\boldsymbol{M}$ 为一 4×4 矩阵；$\boldsymbol{b}$ 和 $\boldsymbol{b}'$ 为 4×1 向量,它们的表达式由附录 A 给出. (3)式中的波幅系数确定后,声源在井内流体和井外地层中激发的波场就完全确定. 举例来说,由(3)式得到地层辐射的 SH 位移势的频谱函数为

$$\chi = \frac{1}{\pi}\int_{-\infty}^{+\infty}\sum_{n=0}^{+\infty}[C_n\sin(n\varphi)-C'_n\cos(n\varphi)]\mathrm{I}_n(fr_0) \times \mathrm{K}_n(sr)\mathrm{e}^{\mathrm{i}k(z-z_0)}\,\mathrm{d}k. \tag{6}$$

与远探测有关的波场辐射范围,一般都在远大于波长的距离之外,满足 $|sr|\gg 1$ 的条件,由此可对(6)式中的波数积分采用最速下降方法求解(郭敦仁,1978;Tang and Patterson, 2009),得到

$$\chi = \frac{\mathrm{e}^{\mathrm{i}\omega R/\beta-\mathrm{i}\pi/4}}{R}\sum_{n=0}^{+\infty}[C_n\sin(n\varphi)-C'_n\cos(n\varphi)]\mathrm{I}_n(f_0r_0), \tag{7}$$

式中 $R=\sqrt{r^2+(z-z_0)^2}$，$f_0=\sqrt{k_0^2-\omega^2/\alpha_{\mathrm{f}}^2}$；$k_0=(\omega/\beta)\cos\theta$ 为波数的最速下降解，θ 为波辐射方向与 z 轴的夹角(参见图 1). 由(7)式可见,远场辐射波场由两项的乘积组成,一项是典型的球面波传播因子 $\mathrm{e}^{\mathrm{i}\omega R/\beta}/R$ (注意式中的 R 与(1)式中等同,只是井中声源的偏心距在 $r_0\ll r$ 的条件下被略去了),另一项与声源的辐射有关(由式(5)解出的系数 C_n 和 C'_n 确定).

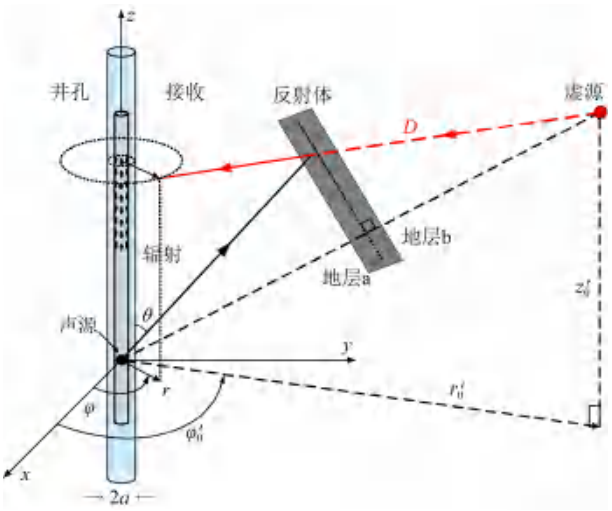


图 1　井外地层反射体声波远探测示意图

Fig. 1　A schematic model of a borehole with a reflector in the formation

将(1)式中的点声源加以组合,可以构造出各种形态的声源,最为典型的是测井常用的多极子声源. 例如,将(1)式中的点源居中放置(取 $r_0=0$)，这时(3)式的级数求和中只有 $n=0$ 项的贡献,即辐射是轴对称的,不产生 SH 波,这时该式地层的位移势函数中 $\chi=0$,而 ϕ 和 Γ 分别对应于居中单极声源辐射的 P 波和 SV 波. 这个问题在 Meredith(1990)和唐晓明和魏周拓(2012)论文中讨论过.

对于偶极声源,可以把(1)式所示的两个点源放在(r_0,φ_0,z_0)和(r_0,$\varphi_0+\pi$,z_0)的位置上;二者的激发声源函数 $S(\omega)$ 大小相等,符号相反,在两源足够靠近($r_0\to 0$)的条件下形成偶极辐射,这时(3)式的级数求和中只有 $n=1$ 项的贡献,在类似于(7)式的远场渐近条件下,可以得到 φ、χ 和 Γ 的表达式,分

(C)1994-2022 China Academic Journal Electronic Publishing House. All rights reserved.　http://www.cnki.net

别求出 P、SH 和 SV 波的远场解及其辐射指向性.偶极辐射的问题也有多人讨论过(Tang et al.,2014;Xu et al.,2019).类似地,把四个正负相间的点源相对于井心对称放置,可组成四极声源,不复赘述.

对于分布式的声源结构,可将(1)式的点声源沿结构的表面积分,点源的激发强度由其在结构表面的分布函数决定,由此可得任意声源在井外的辐射波场.一个很好的例子是随钻声波仪器上的环状声源(唐晓明和郑传汉,2004;Xu et al.,2018),将(1)式按强度分布为 $\cos(n\varphi_0)$ 的圆环积分,可得到环状多极子声源及其激发的波场.

2 井对入射弹性波的响应

以上的讨论给出了井中声源在井外地层产生的辐射波场的理论分析和求解方法.采用相同的理论和方法,也可以分析井对弹性波入射的响应,这种响应包括了两个重要方面:一是在井内流体中对入射波场进行接收,二是井对入射波场的反射或散射.

井中声源辐射的球面波(参考(7)式)被地层中的反射体反射后,在反射体尺寸大于波长的条件下,反射波也以球面波的形式传播(Aki and Richards,1980),其形式如下:

$$\frac{\mathrm{RF}}{D}\mathrm{e}^{\mathrm{i}\omega D/v}, \tag{8}$$

其中 v 为(P 或 S)波速;RF 为(平面波入射)反射系数(对 P、SH 和 SV 波,各自的反射系数可以由 Zoeppritz 方程计算(Aki and Richards,1980)).但这时的传播距离 D 不是一条直线,而是从声源到反射点,再从反射点到接收点的折线.为了将(8)式与(1)式联系起来,我们将反射波视为图 1 所示的虚源产生的球面波,虚源的位置 (r_0', φ_0', z_0') 与井中声源在反射面向外一侧的镜像重合.这样一来 D 就是从虚源出发的一条直线,而球面波 $\mathrm{e}^{\mathrm{i}\omega D/v}/D$ 就可以由(1)式来表示.注意这时 D 与(1)式中的 R 虽然形式相同,$D=\sqrt{r^2+r_0'^2-2rr_0'\cos(\varphi-\varphi_0')+(z-z_0')^2}$,但此时 r_0' 表示距井很远的虚源的径向距离,而不是井中点源的偏心距.相应地,为满足辐射条件,(1)式中与 r_0 有关的贝塞尔函数 I_n 和 K_n 对调,如 $\mathrm{I}_n(k_v r_0)\to\mathrm{K}_n(k_v r_0')$,表达井内、外波场的(3)式变为

$$\begin{cases}\phi_{\mathrm{f}}=\sum\limits_{n=0}^{\infty}[A_n\cos(n\varphi)+A_n'\sin(n\varphi)]\mathrm{K}_n(k_v r_0')\mathrm{I}_n(fr), & (0<r<a)\\ \left.\begin{aligned}\phi&=\sum\limits_{n=0}^{\infty}[B_n\cos(n\varphi)+B_n'\sin(n\varphi)]\mathrm{K}_n(k_v r_0')\mathrm{K}_n(pr),\\ \chi&=\sum\limits_{n=0}^{\infty}[C_n\sin(n\varphi)-C_n'\cos(n\varphi)]\mathrm{K}_n(k_v r_0')\mathrm{K}_n(sr),\\ \Gamma&=\sum\limits_{n=0}^{\infty}[D_n\cos(n\varphi)+D_n'\sin(n\varphi)]\mathrm{K}_n(k_v r_0')\mathrm{K}_n(sr),\end{aligned}\right\} & (r>a)\end{cases} \tag{9}$$

(1)式对(8)式的应用将界面反射波转化为来自虚源的球面入射波;而上述贝塞尔函数的调整使得(9)式的波场通解可以用来求解球面波对井孔的入射问题,避免了对此问题常用的平面波入射假设(例如 White,1953;Schoenberg,1986;Peng et al.,1993;Hirabayashi et al.,2017).确定(9)式中波幅系数的边界条件方程(4)也要做相应的改变,即把井中声源在井壁处产生的反射和向外辐射变为井外虚源在井壁处产生的散射和透射.

$$\begin{aligned}u_r^{\mathrm{i}}(a^+)+u_r^{\mathrm{s}}(a^+)&=u_r^{\mathrm{f}}(a^-),\\ \sigma_{rr}^{\mathrm{i}}(a^+)+\sigma_{rr}^{\mathrm{s}}(a^+)&=\sigma_{rr}^{\mathrm{f}}(a^-),\\ \sigma_{r\varphi}^{\mathrm{i}}(a^+)+\sigma_{r\varphi}^{\mathrm{s}}(a^+)&=0,\\ \sigma_{rz}^{\mathrm{i}}(a^+)+\sigma_{rz}^{\mathrm{s}}(a^+)&=0,\end{aligned} \tag{10}$$

式中的上标 i,s 和 f 分别表示(虚源)入射、散射和井中流体的透射波场.(10)式中的入射波即为井中声源辐射到地层,遇到反射体后的反射波,其形式与(8)式类似.以(7)式中的 SH 波势函数 χ 为例,将式中的辐射距离 R 用(8)式中的传播距离 D 置换,再运用(1)式,就得到其入射波的表达式.根据这一推导,可以得到入射 P、SH 和 SV 波势函数的一般形式

$$\begin{cases}\phi^{\mathrm{i}}=\dfrac{S(\omega)\cdot\mathrm{RD_P}(\omega)\cdot\mathrm{RF_P}(\omega)}{4\pi\rho\alpha^2}\sum\limits_{n=0}^{\infty}\varepsilon_n\mathrm{I}_n(pr)\mathrm{K}_n(pr_0')[\cos(n\varphi)\cos(n\varphi_0')+\sin(n\varphi)\sin(n\varphi_0')],\\ \chi^{\mathrm{i}}=\dfrac{S(\omega)\cdot\mathrm{RD_{SH}}(\omega)\cdot\mathrm{RF_{SH}}(\omega)}{4\pi\rho\beta^2}\sum\limits_{n=0}^{\infty}\varepsilon_n\mathrm{I}_n(sr)\mathrm{K}_n(sr_0')[\cos(n\varphi)\cos(n\varphi_0')+\sin(n\varphi)\sin(n\varphi_0')],\\ \Gamma^{\mathrm{i}}=\dfrac{S(\omega)\cdot\mathrm{RD_{SV}}(\omega)\cdot\mathrm{RF_{SV}}(\omega)}{4\pi\rho\beta^2}\sum\limits_{n=0}^{\infty}\varepsilon_n\mathrm{I}_n(sr)\mathrm{K}_n(sr_0')[\cos(n\varphi)\cos(n\varphi_0')+\sin(n\varphi)\sin(n\varphi_0')],\end{cases} \tag{11}$$

(C)1994-2022 China Academic Journal Electronic Publishing House. All rights reserved. http://www.cnki.net

式中的下标 P、SH、SV 分别表示 P、SH、SV 波,RD 为井中声源的辐射函数(其幅值即为随角度(θ,φ)的变化的辐射指向因子),由求解(5)式中的波幅系数得到;ρ 为地层密度; RF 为反射体的反射系数(参见(8)式).

与从(2)、(3)和(4)式推导出(5)式的过程类似,可从(2)、(9)、(10)和(11)式推导出与(5)式形式相同的矩阵方程组.矩阵 $\boldsymbol{M}$ 与(5)式的相同(在附录 A 中给出).但是,代表声源激发贡献的向量 $\boldsymbol{b}$ 和 $\boldsymbol{b}'$ 与井中流体激发时很不相同,因为它们代表着来自虚源的 P、SH、SV 波的贡献,可根据(2)式和(11)式计算得到,具体形式由附录 B 给出.

向量 $\boldsymbol{b}$ 和 $\boldsymbol{b}'$ 确定之后,便可从(5)式中求解出(9)式中的波幅系数,从而得到井中的透射和井外的散射波场.散射波位移势的谱函数可写为

$$\begin{pmatrix}\phi^{\mathrm{s}}\\ \chi^{\mathrm{s}}\\ \Gamma^{\mathrm{s}}\end{pmatrix}=\frac{1}{\pi}\int_{-\infty}^{+\infty}\sum_{n=0}^{+\infty}\begin{pmatrix}[B_n\cos(n\varphi)+B'_n\sin(n\varphi)]\mathrm{K}_n(pr)\\ [C_n\sin(n\varphi)-C'_n\cos(n\varphi)]\mathrm{K}_n(sr)\\ [D_n\cos(n\varphi)+D'_n\sin(n\varphi)]\mathrm{K}_n(sr)\end{pmatrix}\mathrm{K}_n(k_v r'_0)\mathrm{e}^{\mathrm{i}k(z-z'_0)}\,\mathrm{d}k. \tag{12}$$

注意式中的 k_v 及各个波幅系数取决于入射波的类型(P、SH 或 SV).同理,可求出井中流体透射波的势函数 ϕ_{f},从而进一步求出井中的流体声压 $P=\rho_{\mathrm{f}}\omega^2\phi_{\mathrm{f}}$ 和径向位移 $u_r^{\mathrm{f}}=\partial\phi_{\mathrm{f}}/\partial r$,

$$\begin{cases}P=\dfrac{\rho_{\mathrm{f}}\omega^2}{\pi}\displaystyle\int_{-\infty}^{+\infty}\sum_{n=0}^{\infty}[A_n\cos(n\varphi)+A'_n\sin(n\varphi)]\mathrm{I}_n(fr)\mathrm{K}_n(k_v r'_0)\mathrm{e}^{\mathrm{i}k(z-z_0)}\,\mathrm{d}k,\\ u_r^{\mathrm{f}}=\dfrac{1}{\pi}\displaystyle\int_{-\infty}^{+\infty}\sum_{n=0}^{\infty}[A_n\cos(n\varphi)+A'_n\sin(n\varphi)]\left[\frac{n}{r}\mathrm{I}_n(fr)+f\mathrm{I}_{n+1}(fr)\right]\mathrm{K}_n(k_v r'_0)\mathrm{e}^{\mathrm{i}k(z-z_0)}\,\mathrm{d}k,\end{cases} \tag{13}$$

其中 ρ_{f} 为流体密度.与(6)式中的辐射分析一样,(12)和(13)式中的波数积分可用最速下降法准确求解.两式贝塞尔函数 $\mathrm{K}_n(k_v r'_0)$ 中的虚源的径向距离远大于波长,满足 $|k_v r'_0|\gg 1$ 的条件.以(13)式中的流体径向位移为例,其最速下降解为

$$u_r^{\mathrm{f}}=\frac{\mathrm{e}^{\mathrm{i}\omega R/\beta-\mathrm{i}\pi/4}}{D}\sum_{n=0}^{\infty}[A_n\cos(n\varphi)+A'_n\sin(n\varphi)]\times\left[\frac{n}{r}\mathrm{I}_n(f_0 r)+f_0\mathrm{I}_{n+1}(f_0 r)\right], \tag{14}$$

其中 $D=\sqrt{r'^2_0+(z-z'_0)^2}$; f_0 和 k_0 的意义与(7)式中相同;D 与(8)式中等同,只是井中场点的偏心距在 $r\ll r'_0$ 的条件下被略去了,类似于(1)式和(7)式中的 R.

3　理论的应用

3.1　基于井孔散射分析的邻井探测和应用实例

井孔对弹性波的散射问题在地震测量中一直不受重视,原因是缺少应用需求.随着井中远探测技术的发展和需要,其重要性日益突出,主要的应用是邻井探测:对两个相邻的钻井,把其中一个作为目标井,另一个作为探井放置测量仪器,用测得的声波数据对目标井成像.邻井探测的一个重要应用是验证偶极横波远探测技术.在中国石油大学(华东)钻了两口相距 10 m 的井(地层岩性为火山凝灰岩),SH 横波的探测结果获得了目标井的良好成像.相关的理论分析和结果可参见 Tang 等(2016).邻井探测的一个新近的重要应用是井丛的防碰问题.在海上油田密集的井丛中钻井,井之间的防碰问题对油田的安全生产至关重要.密集的井丛一般位于浅海松软的地层中,对此采用偶极声源产生的低频纵波,而不是横波,会获得较好的应用效果.

邻井探测的理论分析如图 2 所示,包括了波与目标井和探测井的两次入射/散射过程.波从探井出发,经目标井散射后回到探井,波在探井井壁处被再次散射,其透射部分被井中仪器接收后进行成像处理.

参见前面对偶极声源辐射的描述及远场渐近解,得到其辐射到目标井的纵波位移势函数为

$$\phi^{\mathrm{i}}=\frac{S(\omega)\mathrm{RD}_{\mathrm{P}}(\omega;\theta,\varphi)}{4\pi\rho\alpha^2}\cdot\frac{\mathrm{e}^{\mathrm{i}\omega R/\alpha}}{R}, \tag{15}$$

式中 R 为探井至目标井的传播距离,θ 为波的出射角,RD_{P} 是偶极声源的纵波辐射因子.

被目标井散射回探井的纵波位移势由(12)式中的 ϕ^{s} 函数给出.但需要注意的是,对于此时的井孔散射问题,柱坐标系的原点移到了目标井,r'_0 在这里表示二井的间距,如图 2 所示.由 $u_r^{\mathrm{s}}=\partial\varphi^{\mathrm{s}}/\partial r$ 给出散射纵波的径向位移为

$$u_r^{\mathrm{s}}=\frac{1}{\pi}\int_{-\infty}^{+\infty}\sum_{n=0}^{\infty}[B_n\cos(n\varphi)+B'_n\sin(n\varphi)][n\mathrm{K}_n(pr)/r-p\mathrm{K}_{n+1}(pr)]\mathrm{K}_n(k_v r'_0)\mathrm{e}^{\mathrm{i}k(z-z_0)}\,\mathrm{d}k, \tag{16}$$

式中的波幅系数 B_n 和 B'_n 需在(15)式中的纵波对目标井入射的条件下求解(5)式得到.在井间距离 r'_0 远大于波长及(入射方向)波长在井轴方向投影的条件下($|k_v r'_0|\gg 1$, $|pr|\gg 1$)得到(16)式在探井周围的最

(C)1994-2022 China Academic Journal Electronic Publishing House. All rights reserved.　http://www.cnki.net

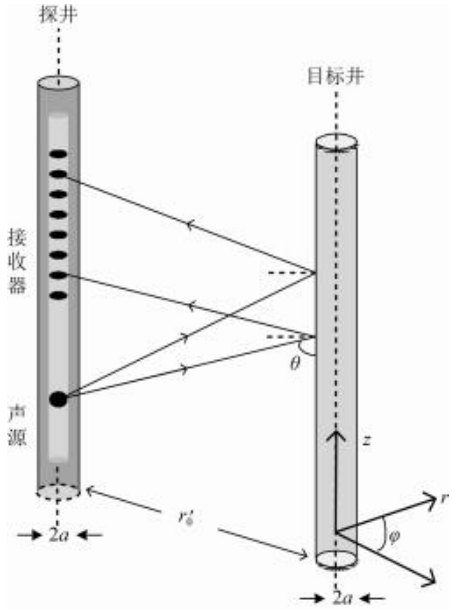


图 2 邻井探测的理论分析模型

Fig. 2 Analysis model for delineating a target borehole using elastic waves from a nearby well

速下降解为:

$$u_r^s(\omega;r,\varphi,z)=\sqrt{\frac{\pi\omega\sin^3\theta}{2\alpha(r+r_0')rr_0'}}\sum_{n=0}^{\infty}[B_n\cos(n\varphi)+B_n'\sin(n\varphi)]\mathrm{e}^{\mathrm{i}\omega(R'+r_0'\sin\theta)/\alpha-\pi\mathrm{i}/4},\quad(17)$$

其中 $R'=\sqrt{r^2+(z-z_0')^2}$,这时系数 B_n 和 B_n' 中的波数 k 的取值为最速下降波数 $k_0=(\omega/\alpha)\cos\theta$. 对上述散射波的远场渐近解稍加讨论有助于理解邻井探测的物理基础,以解释为什么能远距离探测井径小于波长的目标井. 在(17)式中取 $r\sim r_0'$,可以看出散射波的几何扩散因子为 $r^{-1.5}$,即在球面波扩散因子 $1/r$ 上乘上了柱面波扩散因子 $1/\sqrt{r}$,这反映了探井辐射的球面波经目标井散射后以柱面波形式回到探井的传播过程. 正是这种柱腔散射的特征,使得较远距离的目标井在井径小于波长的情况下仍能被探测到.

在探井中接收(17)式的散射波,从原理上可以再次求解(5)式的矩阵方程得到井中流体的透射波,也可以用大家熟知的源与接收之间的互易性来简化这个问题. 对于(17)式的入射纵波位移,其在井中接收到的流体位移可表示为

$$u_r^f=u_r^s\cdot\mathrm{RC}(\omega),\quad(18)$$

式中 RC 称为井的接收响应函数(Peng et al.,1993). 在源和接收器都位于井轴的条件下,运用弹性波的互易原理,可以证明(Tang et al.,2014;Xu et al.,2019)

$$\mathrm{RC}(\omega)=\mathrm{RD}(\omega),\quad(19)$$

即井的声源辐射函数与井对同一声源产生的波场的接收响应函数是等同的. 这样一来,远探测模拟分析中波从井中的出射和入射只需使用同一个 RD 函数,大大提高了计算效率.

我们用一个计算实例来验证以上分析的正确性. 表 1 给出了流体和地层(软地层)的声学参数,井径为 0.2 m,探测井与目标井的距离为 5 m. 井中放置偶极声源和 8 个接收器,其至源的井轴距离为 3 到 4.05 m,声源的激发函数是中心频率为 3 kHz 的 Kelly 子波. 为了模拟探井中声源激发后来自目标井的纵波信号,分别采用了解析方法((15)到(18)式)和有限差分数值方法,差分法采用的空间网格和时间步长分别是 4.5 mm 和 0.42 μs. 图 3 给出了解析法(实线)和差分法(虚线)的比较,二者的结果几乎完全一致,但计算效率差别巨大,差分法需耗时十几小时,而解析法仅需数十秒便得到图中的结果.

表 1 模型参数

Table 1 Model parameters

	$v_P/(\mathrm{m\cdot s^{-1}})$	$v_S/(\mathrm{m\cdot s^{-1}})$	$\rho/(\mathrm{kg\cdot m^{-3}})$
流体	1500	—	1000
软地层	1724	450	2000
硬地层 a	3500	1800	2600
硬地层 b	4500	3000	2500

为了说明邻井探测的重要应用,图 4 给出了浅海井丛防碰的一个应用实例. 第一道给出了 30～60 m 井段地层的自然伽马(GR)和纵波慢度(DTP)的测井曲线. 对于这种浅海超软慢速地层,纵波较横波易于激发且所需记录时间较短,适宜于采用上述的纵波邻井探测的分析方法. 第二道给出了偶极测井的全波波形的变密度图,声源的中心频率为3 kHz.

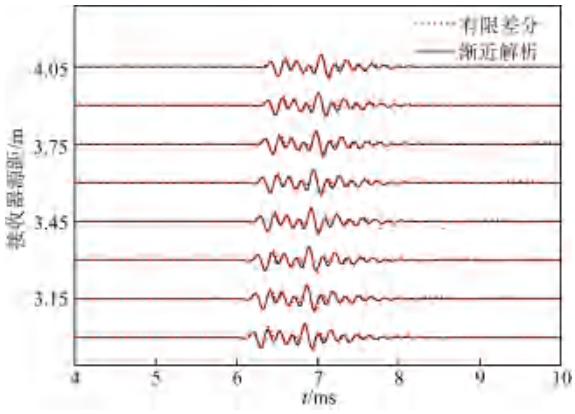


图 3 分别利用有限差分方法和渐近解析方法计算的邻井散射纵波的结果对比

Fig. 3 Comparison of compressional waves scattered from a nearby well. Solid and dashed curves are calculated using analytical and finite difference modeling, respectively

(C)1994-2022 China Academic Journal Electronic Publishing House. All rights reserved. http://www.cnki.net

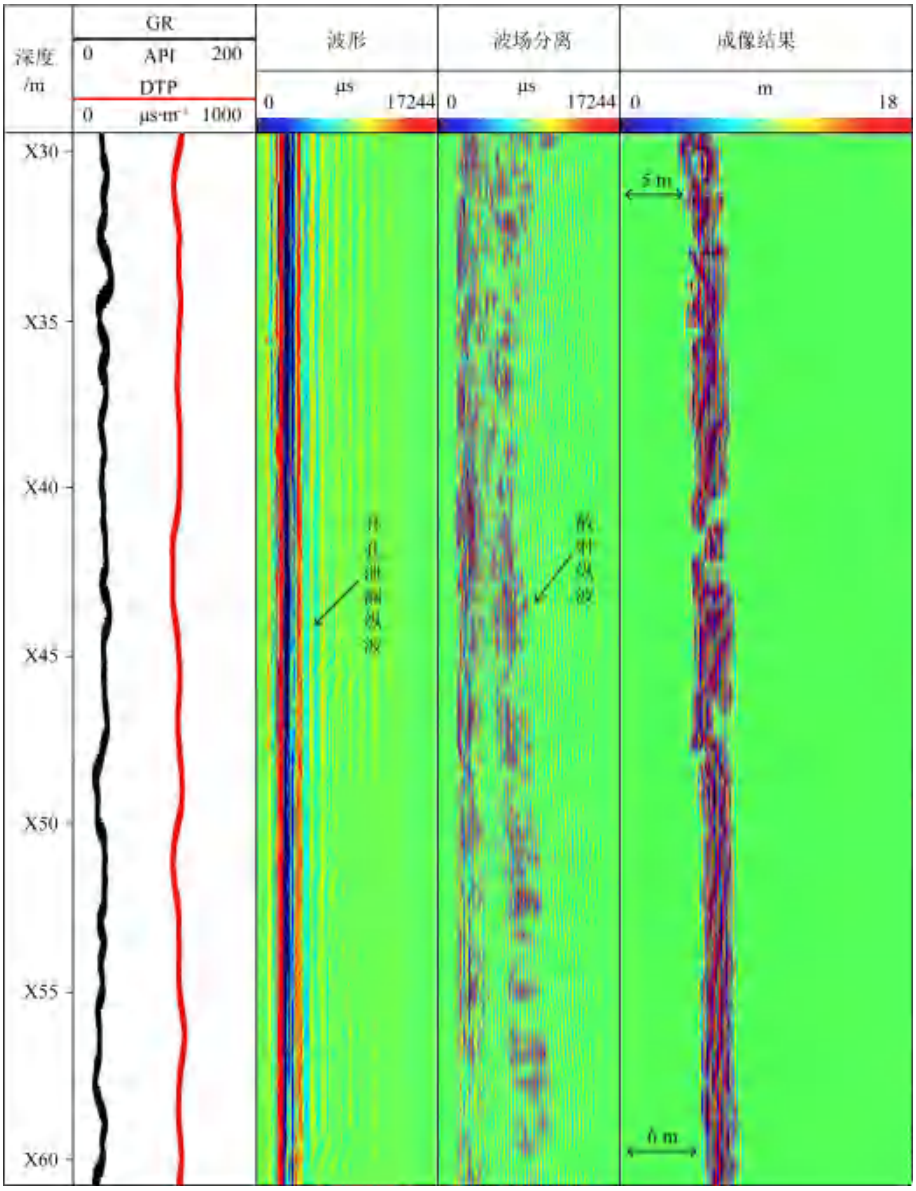


图 4　偶极纵波邻井探测在浅海井丛防碰中的应用实例

Fig. 4　Field example of nearby borehole target delineation in a shallow-marine densely drilled area using dipole P-wave data

图中高波幅的振相为沿井筒传播的直达纵波(对软地层称之为泄漏式纵波). 对全波信号进行分波处理后提取的邻井散射波的变密度图见第三道，处理后的直达波相对于原始数据被大幅压制，较弱的邻井散射波得以显示. 将其用第一道中的纵波慢度偏移成像后，给出了井旁的一个高角度反射体，如第四道中的近竖直条带所示，距井仅 5～6 m. 经地表井位分布图验证后，证实这是井旁的一个高角度邻井. 对于间距仅数米的邻井，钻井继续下钻需要不断检测两井之间的距离，防止碰撞发生.

3.2　四分量偶极横波远探测数据的模拟分析和成像实例

偶极横波远探测采用四分量数据(xx，xy，yx，yy)可以确定反射体距井的位置和走向(唐晓明和魏周拓，2012). 根据(14)式给出的井中流体位移，可以对四分量数据进行精确的模拟和分析. 实际四分量正交偶极仪器的数据接收的组合如图 5 所示，x(或 y)向换能器偏心放置. 将位于$+x$ 和$-x$(或$+y$ 和$-y$)轴两个换能器的声压相减，便得到 x(或 y)向的接收位移. 例如，取(13)式中的声压径向导数 $\partial P/\partial r$，再除以 $\rho_f\omega^2$，便得到(14)式中的径向位移. 在 r 很小($r\to 0$)的条件下，级数求和中只有 $A_1\cos\varphi+A_1'\sin\varphi$ 这一项，对应于仪器居中时的偶极响应. 可见，对称偏心换能器的数据组合，是居中测量流体位移的一个很好的近似. 在居中接收的条件下，可以采用前述的源和接收的互易性(如(19)式)来模拟四分

(C)1994-2022 China Academic Journal Electronic Publishing House. All rights reserved.　http://www.cnki.net

量数据.以交叉分量为例,这样模拟的数据满足 $xy=yx$,因为根据该互易性原理,y-向接收的由 x-向偶极源发射的数据必须等于 x-向接收的由 y-向偶极源发射的数据.

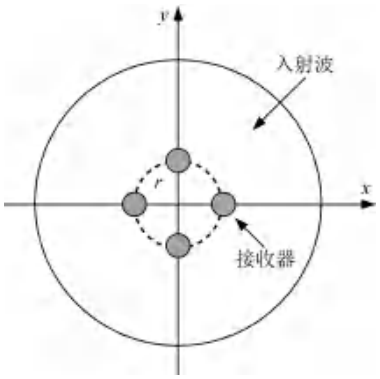


图 5 井中 x 和 y 轴指向的接收器接收入射波场的示意图

Fig. 5 Sensor configuration in x and y coordinates for receiving incident waves

但是,如果接收的位移不居中,例如在偏心距为 r 的 $+x$ 和 $+y$ 轴上接收 yx 和 xy 位移,这样的数据就不满足互易性,即 $xy \neq yx$.由此产生的一个重要问题是:实际测量中仪器偏心对四分量偶极数据的采集和处理会有多大的影响?我们用(14)式来模拟分析这种情况.采用图 1 中的模型,反射体为表 1 硬地层 a 和 b 之间的界面,倾角为 60°,走向为 150°(从 x 轴方向顺时针计算).井中仪器与图 3 相同,x 和 y 换能器的偏心距 $r=0.04$ m.声源到反射体一侧的虚源径向距离为 30 m,源的中心频率为 3 kHz,由此模型计算得到的反射横波数据如图 6a 所示.其中下、中、上图分别显示了计算得到的 SV、SH 和 SH+SV(即模拟数据)的四分量(xx,xy,yx,yy)波形图.显然 xy 与

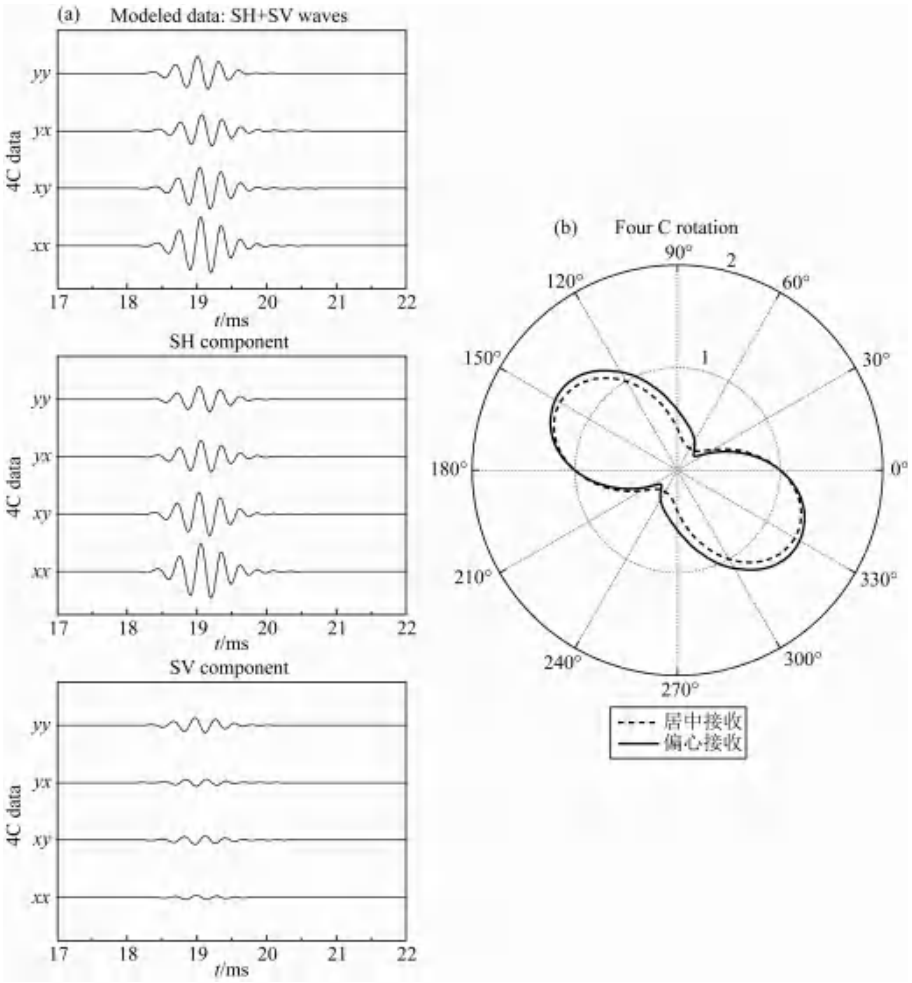


图 6 (a) 图 1 模型计算的偏心接收的四分量偶极横波远探测数据(上图),其中的 SH 和 SV 波的贡献由中、下图分别给出;(b) 四分量数据旋转得到的波幅方位分布图(实线,居中接收结果由图中虚线给出),其峰值对应着反射体走向

Fig. 6 (a) Simulation of four-component dipole shear-wave data (xx, xy, yx, yy) acquisition for the eccentric reception (upper figure) for the model in Fig. 1. The middle (lower) figure shows the SH (SV) component of the modeled data. (b) The azimuthal rotation of wave amplitude (solid line, dotted line is the centered reception result) for the 4C data, with the peak amplitude corresponding to reflector strike

(C)1994-2022 China Academic Journal Electronic Publishing House. All rights reserved. http://www.cnki.net

yx 的幅度出现了差别($xy>yx$)，说明 x 和 y 接收器不在同一位置上时，上述的互易性就不严格成立. 从模拟结果还可以看到，SV 分量比 SH 分量的幅度小很多，说明偏心接收的数据 SH＋SV 中仍以 SH 的贡献为主.

将图 6a 上图中的四分量数据，按实际偶极数据处理那样，做四分量旋转，组成一个新的 XX 分量(Li et al.，2019；李盛清等，2020)

$$XX = xx\cos^2\varphi - \sin\varphi\cos\varphi(xy + yx) + yy\sin^2\varphi, \tag{20}$$

其中 φ 为 x 轴方向顺时针计算的旋转角. 图 6b 的极坐标图给出幅值 $|XX(\varphi)|$ 随旋转角 φ 的变化曲线，曲线的极大值(极小值)正好对应反射体的走向(倾向)，这正是四分量偶极数据求取反射体方位的理论依据(这是因为换能器居中时 $xy=yx$，四分量数据组成的对称矩阵存在最大和最小两个特征方向，如图中的虚线图形所示). 图中换能器居中(虚线)与偏心(实线)的结果对比还表明：测井时接收换能器的偏心并不太影响反射体方位的确定. 但是，按(20)式得到的反射体(走向)的方位存在 180°不确定性，因为图 6b 图形的峰值大小相等、方向相反(即差 180°). 这时，考虑偏心和居中接收的差别(如图 6b 所示)有助于解决 180°不确定性，值得进一步研究(许家旗和胡恒山，2020).

四分量偶极横波远探测技术在油气勘探和生产中已经取得了良好的应用效果. 我们用一个远探测方位成像的可重复性实例来说明这种方法的方位特征和可靠性. 在西北某油田六千多米的深井井段做了四分量偶极横波的重复测井. 图 7 给出了 40 m 井段内两次测量数据的成像处理结果. 如第一道所示，用 Run 1 和 Run 2 表示的两次测量过程中仪器都在井中旋转，且仪器的方位(即 x 或 y 极板的指向)很不相同. 将两套四分量数据分别用(20)式做旋转变换，再用图 6b 所示的方式求取反射体的走向，得出的结果十分一致，都在北北西/南南东(NNW/SSE)方向，如图 7 右边的方位玫瑰图所示. 沿此方位所做的两套数据在井旁 20 m 范围内的远探测成像分别在第二道和第三道给出. 两图中数米到数十米尺度的反射体成像都十分一致(个别除外). 特别是图中箭头所指的高角度反射体，被解释为 NNW/SSE 走向的裂缝/断层. 该裂缝在六千多米深处的地层压力下还能清晰成像，说明其被高压油气充注呈开启状态，是油气运移的重要通道. 对远探测技术来说，在仪器声源发射和接收任意指向的条件下，对地层反射的小振幅信号(相对于井筒直达波而言)成像的可重复性说明了技术的可靠性和结果的准确性.

4　结语和展望

随着井孔弹性波测量技术的发展和需求，井孔

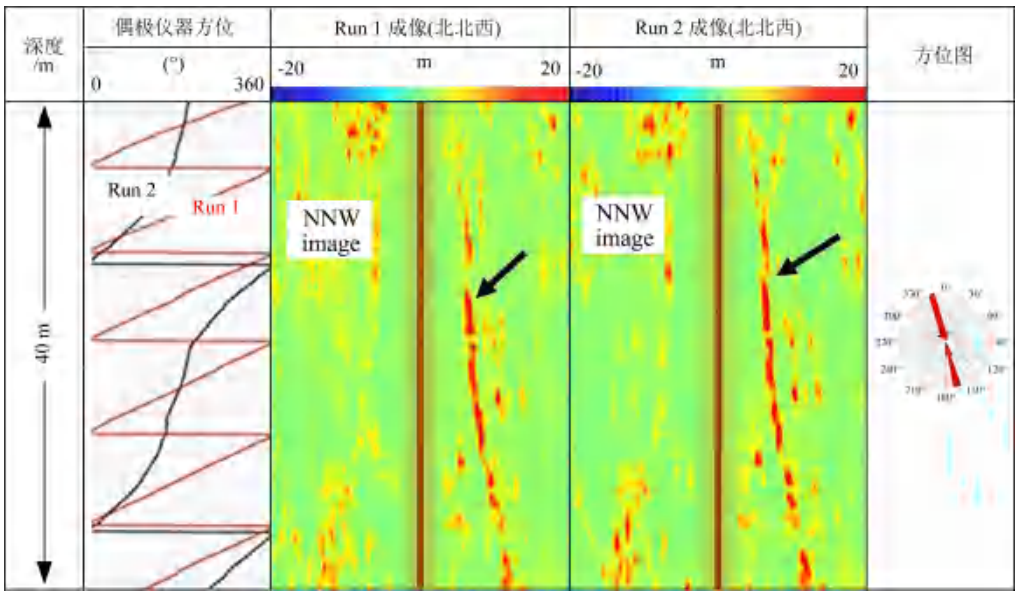


图 7　四分量偶极横波远探测方位成像重复性验证实例. 尽管是在两次测量(Run 1 和 Run 2)完全不同的仪器方位(第一道)条件下，但是反射体走向的识别结果(第四道)在成像图(第二道和第三道)中具有相当好的可重复性

Fig. 7　Repeatability test of four-component dipole shear-wave reflection imaging. Despite the very different tool rotation (Panel 1) for two logging passes (Run 1 and Run 2), repeatable imaging results (Panels 2 and 3) are obtained along the reflector strike (Panel 4)

(C)1994-2022 China Academic Journal Electronic Publishing House. All rights reserved.　http://www.cnki.net

与弹性波相互作用这一经典问题变得日益重要起来,这种相互作用主要包括井中声源向外的辐射以及波从井外反射体向井的入射、散射和透射.将井孔波场的柱面波展开和波数积分通解与波的远场渐近解及井孔辐射和接收的互易性相结合,得到了求解这一问题的快速有效方法.根据这一方法,可以准确模拟该问题中各种有关的波动现象并分析其波场特征,这些分析结果为近期发展起来的声波远探测技术奠定了理论基础并获得了良好的应用效果.具体而言,对偶极声源的辐射特性及其远探测波场的方位特征进行四分量数据采集能够对井外反射体准确成像并确定其走向;超软慢速地层钻井中纵波的辐射和接收响应特征分析促进了邻井探测技术在浅海井丛防碰工程中的应用.远探测技术的进展和应用也带来了更多的需求和亟待解决的问题.例如,该技术在深部油气藏中探测到许多断溶构造,油气开发需要确定断溶体的方位,为此必须克服偶极探测方位的180°不确定性.这是一个挑战性的课题,不仅需要更深入的理论探讨和分析,还需要在实际应用中验证分析结果的有效性.

致谢 谨此祝贺陈颙先生从事地球物理教学科研工作60周年.

附录 A

矩阵方程(5)式的完整形式如下:

$$\begin{bmatrix} M_{11} & M_{12} & M_{13} & M_{14} \\ M_{21} & M_{22} & M_{23} & M_{24} \\ M_{31} & M_{32} & M_{33} & M_{34} \\ M_{41} & M_{42} & M_{43} & M_{44} \end{bmatrix} \begin{bmatrix} A_n \\ B_n \\ C_n \\ D_n \end{bmatrix} = \begin{bmatrix} b_1 \\ b_2 \\ b_3 \\ b_4 \end{bmatrix}, \quad \text{(A1)}$$

和

$$\begin{bmatrix} M_{11} & M_{12} & M_{13} & M_{14} \\ M_{21} & M_{22} & M_{23} & M_{24} \\ M_{31} & M_{32} & M_{33} & M_{34} \\ M_{41} & M_{42} & M_{43} & M_{44} \end{bmatrix} \begin{bmatrix} A'_n \\ B'_n \\ C'_n \\ D'_n \end{bmatrix} = \begin{bmatrix} b'_1 \\ b'_2 \\ b'_3 \\ b'_4 \end{bmatrix}. \quad \text{(A2)}$$

矩阵 $\boldsymbol{M}$ 中各元素的具体表达式如下:

$$\begin{aligned}
M_{11} &= -n\mathrm{I}_n(fa)/a - f\mathrm{I}_{n+1}(fa),\\
M_{12} &= n\mathrm{K}_n(pa)/a - p\mathrm{K}_{n+1}(pa),\\
M_{13} &= n\mathrm{K}_n(sa)/a,\\
M_{14} &= \mathrm{i}k[n\mathrm{K}_n(sa)/a - s\mathrm{K}_{n+1}(sa)],\\
M_{21} &= \rho_{\mathrm{f}}\omega^2\mathrm{I}_n(fa),\\
M_{22} &= 2\rho\beta^2[(n^2-n)\mathrm{K}_n(pa)/a^2 + p\mathrm{K}_{n+1}(pa)/a]\\
&\quad + \rho(2k^2\beta^2-\omega^2)\mathrm{K}_n(pa),\\
M_{23} &= 2n\rho\beta^2\left[(n-1)\mathrm{K}_n(sa)/a^2 - s\mathrm{K}_{n+1}(sa)/a\right],\\
M_{24} &= 2\mathrm{i}k\rho\beta^2\left\{\left[(n^2-n)/a^2+s^2\right]\mathrm{K}_n(sa)\right.\\
&\quad \left. + s\mathrm{K}_{n+1}(sa)/a\right\},\\
M_{31} &= 0,\\
M_{32} &= 2n\rho\beta^2\left[(1-n)\mathrm{K}_n(pa)/a^2 + p\mathrm{K}_{n+1}(pa)/a\right],\\
M_{33} &= -\rho\beta^2\left\{\left[2(n^2-n)/a^2+s^2\right]\mathrm{K}_n(sa)\right.\\
&\quad \left. + 2s\mathrm{K}_{n+1}(sa)/a\right\},\\
M_{34} &= 2\mathrm{i}kn\rho\beta^2\left[(1-n)\mathrm{K}_n(sa)/a^2 + s\mathrm{K}_{n+1}(sa)/a\right],\\
M_{41} &= 0,\\
M_{42} &= 2\mathrm{i}k\rho\beta^2\left[n\mathrm{K}_n(pa)/a - p\mathrm{K}_{n+1}(pa)\right],\\
M_{43} &= \mathrm{i}kn\rho\beta^2\mathrm{K}_n(sa)/a,\\
M_{44} &= -(s^2+k^2)\rho\beta^2\left[n\mathrm{K}_n(sa)/a - s\mathrm{K}_{n+1}(sa)\right].
\end{aligned} \quad \text{(A3)}$$

声源位于井内流体中时,向量 $\boldsymbol{b}$ 和 $\boldsymbol{b}'$ 中各元素的具体表达式如下:

$$\begin{aligned}
b_1 &= \varepsilon_n\left[n\mathrm{K}_n(fa)/a - f\mathrm{K}_{n+1}(fa)\right]\cos(n\varphi_0),\\
b_2 &= -\varepsilon_n\rho_{\mathrm{f}}\omega^2\mathrm{K}_n(fa)\cos(n\varphi_0),\\
b_3 &= 0,\ b_4 = 0,\\
b'_1 &= \varepsilon_n\left[n\mathrm{K}_n(fa)/a - f\mathrm{K}_{n+1}(fa)\right]\sin(n\varphi_0),\\
b'_2 &= -\varepsilon_n\rho_{\mathrm{f}}\omega^2\mathrm{K}_n(fa)\sin(n\varphi_0),\\
b'_3 &= 0,\ b'_4 = 0.
\end{aligned} \quad \text{(A4)}$$

其中,a 为井径;I 和 K 分别为第一类和第二类变型贝塞尔函数;k 为轴向波数;α_{f},α 和 β 分别为流体纵波、地层纵波和横波速度;f 为流体径向波数,$f=\sqrt{k^2-\omega^2/\alpha_{\mathrm{f}}^2}$;$p$ 为地层纵波径向波数,$p=\sqrt{k^2-\omega^2/\alpha^2}$;$s$ 为地层横波径向波数,$s=\sqrt{k^2-\omega^2/\beta^2}$;$\rho$ 和 ρ_{f} 分别为地层和流体密度;φ_0 为井中点声源的方位;$n=0$ 时,$\varepsilon_n=1$,$n\geqslant 1$ 时,$\varepsilon_n=2$.

附录 B

对于位于井外的虚源,入射波类型不同,其向量 $\boldsymbol{b}$ 和 $\boldsymbol{b}'$ 中的元素也不一样.

当P波入射时,向量 $\boldsymbol{b}$ 和 $\boldsymbol{b}'$ 中各元素的具体表达式如下$\left(\text{省略公共因子 } \frac{\mathrm{S}(\omega)\cdot\mathrm{RD_P}(\omega)\cdot\mathrm{RF_P}(\omega)}{4\pi\rho\alpha^2}\right)$:

$$\begin{aligned}
b_1 &= -\varepsilon_n\left[n\mathrm{I}_n(pa)/a + p\mathrm{I}_{n+1}(pa)\right]\cos(n\varphi'_0),\\
b_2 &= -\varepsilon_n\rho\left\{2\beta^2\left[(n^2-n)\mathrm{I}_n(pa)/a^2 - p\mathrm{I}_{n+1}(pa)/a\right]\right.\\
&\quad \left. + (2k^2\beta^2-\omega^2)\mathrm{I}_n(pa)\right\}\cos(n\varphi'_0),\\
b_3 &= -2n\varepsilon_n\rho\beta^2\left[(1-n)\mathrm{I}_n(pa)/a^2 - p\mathrm{I}_{n+1}(pa)/a\right]
\end{aligned}$$

(C)1994-2022 China Academic Journal Electronic Publishing House. All rights reserved. http://www.cnki.net

$$\times\cos(n\varphi_0'),$$

$$b_4=-2\varepsilon_n \mathrm{i}k\rho\beta^2\left[n\mathrm{I}_n(pa)/a+p\mathrm{I}_{n+1}(pa)\right]\cos(n\varphi_0'),$$

$$b_1'=-\varepsilon_n\left[n\mathrm{I}_n(pa)/a+p\mathrm{I}_{n+1}(pa)\right]\sin(n\varphi_0'),$$

$$b_2'=-\varepsilon_n\rho\left\{2\beta^2\left[(n^2-n)\mathrm{I}_n(pa)/a^2-p\mathrm{I}_{n+1}(pa)/a\right]+(2k^2\beta^2-\omega^2)\mathrm{I}_n(pa)\right\}\sin(n\varphi_0'),$$

$$b_3'=-2n\varepsilon_n\rho\beta^2\left[(1-n)\mathrm{I}_n(pa)/a^2-p\mathrm{I}_{n+1}(pa)/a\right]\times\sin(n\varphi_0'),$$

$$b_4'=-2\varepsilon_n \mathrm{i}k\rho\beta^2\left[n\mathrm{I}_n(pa)/a+p\mathrm{I}_{n+1}(pa)\right]\sin(n\varphi_0'). \quad (B1)$$

当 SH 横波入射时,向量 $\boldsymbol{b}$ 和 $\boldsymbol{b}'$ 中各元素的具体表达式如下(省略公共因子 $\frac{S(\omega)\cdot RD_{SH}(\omega)\cdot RF_{SH}(\omega)}{4\pi\rho\beta^2}$):

$$b_1=-n\varepsilon_n\mathrm{I}_n(sa)\sin(n\varphi_0')/a,$$

$$b_2=-2n\varepsilon_n\rho\beta^2\left[(n-1)\mathrm{I}_n(sa)/a^2+s\mathrm{I}_{n+1}(sa)/a\right]\times\sin(n\varphi_0'),$$

$$b_3=\varepsilon_n\rho\beta^2\left\{\left[2(n^2-n)/a^2+s^2\right]\mathrm{I}_n(sa)-2s\mathrm{I}_{n+1}(sa)/a\right\}\times\sin(n\varphi_0'),$$

$$b_4=-\mathrm{i}kn\varepsilon_n\rho\beta^2\mathrm{I}_n(sa)\sin(n\varphi_0')/a,$$

$$b_1'=n\varepsilon_n\mathrm{I}_n(sa)\cos(n\varphi_0')/a,$$

$$b_2'=2n\varepsilon_n\rho\beta^2\left[(n-1)\mathrm{I}_n(sa)/a^2+s\mathrm{I}_{n+1}(sa)/a\right]\times\cos(n\varphi_0'),$$

$$b_3'=-\varepsilon_n\rho\beta^2\left\{\left[2(n^2-n)/a^2+s^2\right]\mathrm{I}_n(sa)-2s\mathrm{I}_{n+1}(sa)/a\right\}\times\cos(n\varphi_0'),$$

$$b_4'=\mathrm{i}kn\varepsilon_n\rho\beta^2\mathrm{I}_n(sa)\cos(n\varphi_0')/a. \quad (B2)$$

当 SV 横波入射时,向量 $\boldsymbol{b}$ 和 $\boldsymbol{b}'$ 中各元素的具体表达式如下(省略公共因子 $\frac{S(\omega)\cdot RD_{SV}(\omega)\cdot RF_{SV}(\omega)}{4\pi\rho\beta^2}$):

$$b_1=-\mathrm{i}k\varepsilon_n\left[n\mathrm{I}_n(sa)/a+s\mathrm{I}_{n+1}(sa)\right]\cos(n\varphi_0'),$$

$$b_2=-2\mathrm{i}k\varepsilon_n\rho\beta^2\left\{\left[(n^2-n)/a^2+s^2\right]\mathrm{I}_n(sa)-s\mathrm{I}_{n+1}(sa)/a\right\}\times\cos(n\varphi_0'),$$

$$b_3=-2\mathrm{i}kn\varepsilon_n\rho\beta^2\left[(1-n)\mathrm{I}_n(sa)/a^2-s\mathrm{I}_{n+1}(sa)/a\right]\cos(n\varphi_0'),$$

$$b_4=\varepsilon_n(s^2+k^2)\rho\beta^2\left[n\mathrm{I}_n(sa)/a+s\mathrm{I}_{n+1}(sa)\right]\times\cos(n\varphi_0'),$$

$$b_1'=-\mathrm{i}k\varepsilon_n\left[n\mathrm{I}_n(sa)/a+s\mathrm{I}_{n+1}(sa)\right]\sin(n\varphi_0'),$$

$$b_2'=-2\mathrm{i}k\varepsilon_n\rho\beta^2\left\{\left[(n^2-n)/a^2+s^2\right]\mathrm{I}_n(sa)-s\mathrm{I}_{n+1}(sa)/a\right\}\sin(n\varphi_0'),$$

$$b_3'=-2\mathrm{i}kn\varepsilon_n\rho\beta^2\left[(1-n)\mathrm{I}_n(sa)/a^2-s\mathrm{I}_{n+1}(sa)/a\right]\times\sin(n\varphi_0'),$$

$$b_4'=\varepsilon_n(s^2+k^2)\rho\beta^2\left[n\mathrm{I}_n(sa)/a+s\mathrm{I}_{n+1}(sa)\right]\times\sin(n\varphi_0'). \quad (B3)$$

其中,S 为声源函数;RD 为辐射函数;RF 为反射系数;φ_0' 为虚源的方位;其他符号定义与附录 A 相同,在此不复赘述.

References

Aki K, Richards P G. 1980. Quantitative Seismology: Theory and Methods. San Francisco: W. H. Freeman & Co.

Guo D R. 1978. Methods of Mathematical Physics (in Chinese). Beijing: People's Education Press.

Hirabayashi N, Sakiyama N, Ikegami T. 2017. Characteristics of waveforms recorded by azimuthally spaced hydrophones of sonic logging tool for incident plane waves. *Geophysics*, 82(6): D353-D368.

Li S Q, Chen M, Gu X H, et al. 2019. Application of four-component dipole shear reflection imaging to interpret the geological structure around a deviated well. *Applied Geophysics*, 16(3): 291-301.

Li S Q, Su Y D, Tang X M. 2020. Research on a fast inversion method for structural strike around a borehole based on four-component dipole shear wave reflection imaging. *Chinese Journal of Geophysics* (in Chinese), 63(6): 2478-2487, doi: 10.6038/cjg2020N0322.

Meredith J A. 1990. Numerical and analytical modelling of downhole seismic sources: the near and far field [Ph. D. thesis]. Cambridge, MA: Massachusetts Institute of Technology.

Peng C B, Cheng C H, Toksöz M N. 1993. Borehole effects on downhole seismic measurements. *Geophysical Prospecting*, 41(7): 883-912.

Schoenberg M. 1986. Fluid and solid motion in the neighborhood of a fluid-filled borehole due to the passage of a low-frequency elastic plane wave. *Geophysics*, 51(6): 1191-1205.

Su Y D, Wei Z T, Tang X M. 2014. A validation method of dipole shear-wave remote reflection imaging from adjacent borehole reflection. *Journal of Applied Acoustics* (in Chinese), 33(1): 29-34.

Tang X M, Cheng A. 2004. Quantitative Borehole Acoustic Methods. Netherlands: Elsevier Science Publishing Inc.

Tang X M, Patterson D J. 2009. Single-well S-wave imaging using multicomponent dipole acoustic-log data. *Geophysics*, 74(6): WCA211-WCA223.

Tang X M, Wei Z T. 2012. Single-well acoustic reflection imaging using far-field radiation characteristics of a borehole dipole source. *Chinese Journal of Geophysics* (in Chinese), 55(8): 2798-2807, doi: 10.6038/j.issn.0001-5733.2012.08.031.

Tang X M, Cao J J, Wei Z T. 2014. Shear-wave radiation, reception, and reciprocity of a borehole dipole source: with application to modeling of shear-wave reflection survey. *Geophysics*, 79(2): T43-T50.

(C)1994-2022 China Academic Journal Electronic Publishing House. All rights reserved. http://www.cnki.net

Tang X M, Cao J J, Li Z, et al. 2016. Detecting a fluid-filled borehole using elastic waves from a remote borehole. *Journal of the Acoustical Society of America*, 140(2): EL211, doi: 10.1121/1.4960143.

Tang X M, Zheng C H. 2004. Quantitative Borehole Acoustic Methods (in Chinese). Beijing: Petroleum Industry Press.

White J E. 1953. Signals in a borehole due to plane waves in the solid. *Journal of the Acoustical Society of America*, 25(5): 906-915.

Xu J Q, Hu H S. 2019. Wave filed simulation of single-well imaging based on method of steepest descent and reciprocity. *Journal of Applied Acoustics* (in Chinese), 38(3): 293-300.

Xu J Q, Hu H S, Wang Z. 2019. Asymptotic solution to a 3D dipole single-well imaging system with combined monopole and dipole receivers with an application in elimination of azimuth ambiguity. *Geophysics*, 84(5): D191-D207.

Xu J Q, Hu H S. 2020. Study on the radiation and reception of the wave field in a single-well imaging system with an eccentric source. *Chinese Journal of Geophysics* (in Chinese), 63(9): 3545-3561, doi: 10.6038/cjg2020N0015.

Xu S, Zhuang C X, Su Y D, et al. 2018. Acoustic source characterization for a logging while drilling tool: Theoretical and experimental modeling. *Journal of the Acoustical Society of America*, 144(3): EL178, doi: 10.1121/1.5053105.

附中文参考文献

郭敦仁. 1978. 数学物理方法. 北京: 人民教育出版社.

李盛清, 苏远大, 唐晓明. 2020. 基于四分量偶极横波远探测的井周构造走向快速反演方法研究. 地球物理学报, 63(6): 2478-2487, doi: 10.6038/cjg2020N0322.

苏远大, 魏周拓, 唐晓明. 2014. 基于邻井反射的偶极横波远探测验证方法. 应用声学, 33(1): 29-34.

唐晓明, 郑传汉. 2004. 定量测井声学. 赵晓敏译. 北京: 石油工业出版社.

唐晓明, 魏周拓. 2012. 利用井中偶极声源远场辐射特性的远探测测井. 地球物理学报, 55(8): 2798-2807, doi: 10.6038/j.issn.0001-5733.2012.08.031.

许家旗, 胡恒山. 2019. 基于鞍点法与互易性的远探测波场模拟. 应用声学, 38(3): 293-300.

许家旗, 胡恒山. 2020. 声波远探测中偏心声源的辐射以及接收波场研究. 地球物理学报, 63(9): 3545-3561, doi: 10.6038/cjg2020N0015.

(本文编辑 何燕)

(C)1994-2022 China Academic Journal Electronic Publishing House. All rights reserved. http://www.cnki.net

陈声远, 苏远大, 段文星等. 2025. 基于角谱法的偶极 SH 横波远探测声场模拟方法. 地球物理学报, 68(6): 2404-2415, doi: 10.6038/cjg2024S0048.
Chen S Y, Su Y D, Duan W X, et al. 2025. Simulation method of the SH wavefield for dipole acoustic reflection imaging based on the angular spectrum method. *Chinese J. Geophys.* (in Chinese), 68(6): 2404-2415, doi: 10.6038/cjg2024S0048.

基于角谱法的偶极 SH 横波远探测声场模拟方法

陈声远[1,2], 苏远大[1,2,3*], 段文星[4], 李盛清[1,2,3], 唐晓明[1,2,3]

1 中国石油大学 (华东) 深层油气全国重点实验室, 青岛 266580
2 中国石油大学 (华东) 地球科学与技术学院, 青岛 266580
3 崂山国家实验室, 青岛 266071
4 中国石油天然气股份有限公司塔里木油田公司, 库尔勒 841000

摘要 偶极子横波作为远探测测井在近年来得到了快速发展, 井中偶极子声源在地层中的辐射、反射和透射声场的可视化有助于更加直观地研究远探测声场特征. 本文基于偶极横波远探测技术的基本原理和方法, 提出了一种利用角谱法快速计算远探测声场的解析方法, 其计算结果与三维时域有限差分计算结果对比验证了该方法的正确性. 利用解析方法计算了井旁多层平行地层界面下 SH 横波的远探测声场快照, 并对解析模拟和现场实测的裸眼井 SH 横波远探测测井数据进行偏移成像. 多尺度模型计算结果表明: 即便是对常规小尺度模型的 SH 横波的远探测声场模拟, 在相同精度的条件下, 解析方法的计算效率与有限差分数值方法相比提高了两个量级, 在大尺度模型的模拟上, 本文方法较数值方法更具优势. 本文的结果为模拟井外远探测声场特征提供了一种快速有效方法.

关键词 声波远探测; 偶极 SH 横波; 角谱法; 反射和透射; 声场快照
中图分类号 P631 **收稿日期** 2024-01-18, 2024-07-12 收修定稿
DOI: 10.6038/cjg2024S0048 **CSTR:** 32084.14.cjg2024S0048

Simulation method of the SH wavefield for dipole acoustic reflection imaging based on the angular spectrum method

CHEN ShengYuan[1,2], SU YuanDa[1,2,3*], DUAN WenXing[4], LI ShengQing[1,2,3], TANG XiaoMing[1,2,3]

1 *State Key Laboratory of Deep Oil and Gas, China University of Petroleum (East China), Qingdao* 266580, *China*
2 *School of Geosciences, China University of Petroleum (East China), Qingdao* 266580, *China*
3 *Laoshan National Laboratory, Qingdao* 266071, *China*
4 *Tarim Oilfield Company, PetroChina, Korla* 841000, *China*

Abstract In recent years, the dipole shear wave in acoustic reflection logging has developed rapidly. The visualization of the radiation, reflection, and transmission wavefield of the dipole source in the formation is conducive to a more direct study of the wavefield characteristics of acoustic reflection imaging. To this end, based on the basic principle and method of dipole shear wave reflection imaging technology, an analytical method using the angle spectrum method is presented to rapidly calculate the wavefield of acoustic reflection imaging. The 3D finite difference time domain (3D FDTD) calculation results verify the correctness of the proposed method's calculation results. The SH wavefield snapshot of a three-layer parallel formation interface

基金项目 国家自然科学基金 (U21B2064, 42174145, 42074137), 山东省自然科学基金 (ZR2024YQ062), 深层油气全国重点实验室课题 (SKLDOG2024-ZYTS-04) 和崂山国家实验室科技创新项目 (No.LSKJ202203407) 联合资助.

第一作者简介 陈声远, 男, 1998 年生, 博士研究生, 主要从事声波测井理论方法研究. E-mail: chensy981031@163.com
*** 通讯作者** 苏远大, 男, 1978 年生, 博士, 教授, 主要从事声波测井理论、方法及处理研究. E-mail: syuanda@sina.com

中国知网 https://www.cnki.net

near the wellbore is calculated by the analytical method, and the SH full-wave logging data of the open hole between the analytical simulation and the field measurements are processed by migration imaging. The multi-scale model calculation results show that the computational efficiency of the analytical method is two orders of magnitude higher than that of the finite difference numerical method, even for the simulation of the conventional small-scale model. In the simulation of the large-scale model, the proposed method has more advantages than the numerical method. The results of this paper provide a fast and effective method for simulating the wavefield characteristics of acoustic reflection imaging outside the well.

Keywords Single-well reflection imaging; Dipole SH waves; Angular spectrum method; Reflection and transmission; Wavefield snapshot

0　引言

近年来, 偶极横波远探测测井技术在地球物理勘探领域中得到了快速发展. 该技术利用井中低频偶极子声源向井外辐射具有方位指向性的横波, 并接收经井外地质体反射回井中的横波, 可以对井旁数十米内的油气构造进行有效识别 (Tang and Patterson, 2009; Bolshakov et al., 2011; Patterson et al., 2013; Tang, 2016). 该技术在非常规油气的勘探开发中发挥着至关重要的作用 (李宁等, 2024; 刘航等, 2023; 董经利等, 2020), 有效提高了勘探效率和准确性, 为油气勘探开发带来了新的可能性和机遇.

在井旁存在大尺度地层构造或地质体的情况下, 偶极横波远探测声场的特征及其模拟比较复杂, 此时远探测声场的快速计算方法尤为重要. 国内外许多学者在这方面做了大量工作. Tang 等 (2014) 通过最速下降法得到了偶极声源在地层中辐射横波位移的远场渐近解, 指出波长相对于辐射距离非常小的情况下渐近解计算的结果是准确的. 在此基础上, 曹景记等 (2016a) 利用偶极声源辐射波位移的远场渐近解计算地层中辐射波的能流密度和能流, 指出偶极声源在低频段具有最佳的辐射效率. 对于井中接收反射声场, Tang 等 (2014) 利用互易性原理快速模拟了井旁存在地层界面情况下井中接收到的反射声场. 曹景记等 (2016b) 将上述快速模拟方法应用到随钻偶极横波远探测中, 对过井多反射界面进行了快速成像. 许家旗和胡恒山 (2019) 将来自井外地层界面的反射波场等效为一虚源点处辐射的集中力源, 利用井中偶极声源辐射和集中力源之间的互易性, 也可以精确有效地模拟远探测声场. Li 等 (2021) 和李杨虎等 (2022) 将井中接收反射声场等效为一虚源点处激发出的辐射声场, 求解得到井中方位接收波场的解析渐近解, 实现了对方位接收声场的快速模拟. 但是利用解析方法对偶极声源在井外地层界面处产生的反射和透射远探测声场传播过程的可视化模拟尚未有报道, 而这种模拟对直观地研究声场特征很有助益. 井中偶极声源以球面波的形式向井外倾斜的地层界面辐射声场, 需要三维的模拟计算方法, 通常采用有限差分进行数值模拟 (唐晓明和魏周拓, 2012a; Wei et al., 2015; Gong et al., 2015; 邓呈祥, 2019), 然而, 利用数值方法模拟远探测声场快照, 尤其是当井旁反射体距离井轴数十米时, 模型网格体系巨大, 模拟时间超长, 极大地限制了数值方法的有效性, 因此亟需一种在井外存在大尺度倾斜地层界面时的远探测声场快照的可视化快速模拟方法.

声场计算中常用的角谱法将上述球面波入射问题展开成平面波或柱面波叠加的形式, 再利用平面波的反射和透射, 计算界面两侧的反射和透射球面波场 (Atalar, 1978; Brekhovskikh and Lysanov, 1991; 张海澜, 2021). 本文基于角谱法提出了一种快速计算远探测声场的解析方法, 由于偶极横波远探测声场中主要利用反射 SH 横波进行反射体成像 (唐晓明和魏周拓, 2012b; Tang et al., 2014), 本文主要讨论 SH 横波在井外的辐射、反射和透射声场情况, 分别利用解析方法和三维时域有限差分进行 SH 横波远探测声场快照和波形的模拟对比, 验证了解析方法的正确性和高效性; 针对有限差分方法难于模拟的大尺度模型, 利用解析方法模拟了井旁大尺度单一界面和多层平行界面情况下的 SH 横波远探测声场; 最后对比分析了解析模拟和现场实测的多层平行界面下的裸眼井 SH 横波远探测波形和成像结果. 本文方法为偶极 SH 横波远探测声场快照的可视化快速模拟提供了一种行之有效的方法.

中国知网　https://www.cnki.net

1 基本理论和方法

在图 1 所示的柱坐标系下，指向x轴正方向的偶极声源位于半径为a的充液井孔中；r和z分别为辐射场点的径向和轴向距离，R为声源到场点的辐射距离；θ为声源到场点辐射方向与z轴正方向之间的夹角，ϕ为辐射方向在xoy平面内投影与y轴的夹角；u_R为 P 波产生的位移，u_θ和u_ϕ分别为 SV 横波和 SH 横波产生的位移；在yoz平面内，当井外存在一走向与声源指向平行的倾斜地层界面时，偶极声源在井内外的声场主要分为三部分：一是沿着井轴传播的弯曲波和向井外辐射的纯 SH 横波；二是入射 SH 横波在井旁地层界面处的反射和透射声场；最终井中接收到来自地层界面处的反射 SH 横波声场.

1.1 偶极声源在井孔内外的辐射声场

在常规偶极声波测井频率范围 (1 ~ 6 kHz) 内，偶极声源在井中产生轴向 (z轴) 传播的弯曲波，同时向井外地层辐射于yoz平面偏振的 SH 横波，此时井内流体和井外辐射 SH 横波的位移可以表示为

$$\begin{cases} u_f = \dfrac{\sin\phi}{4\pi}\displaystyle\int_{-\infty}^{+\infty}\int_{-\infty}^{+\infty}[\varepsilon_1(\mathrm{K}_1(fr)/r - f\mathrm{K}_2(fr)) + A_1'(\mathrm{I}_1(fr)/r + f\mathrm{I}_2(fr))]S(\omega)\mathrm{e}^{\mathrm{i}kz-\mathrm{i}\omega t}\mathrm{d}k\mathrm{d}\omega \\ u_\phi = \dfrac{\cos\phi}{4\pi}\displaystyle\int_{-\infty}^{+\infty}\int_{-\infty}^{+\infty}[-D_1(\mathrm{K}_1(sr)/r - s\mathrm{K}_2(sr)) + \mathrm{i}kF_1\mathrm{K}_1(sr)/r]S(\omega)\mathrm{e}^{\mathrm{i}kz-\mathrm{i}\omega t}\mathrm{d}k\mathrm{d}\omega \end{cases}, \tag{1}$$

式中ω为圆频率；u_f为井内流体位移；u_ϕ为井外地层中 SH 横波的位移；k和$f=\sqrt{k^2-(\omega/v_{\mathrm{f}})^2}$分别为井内流体的轴向与径向波数；$s=\sqrt{k^2-(\omega/v_{\mathrm{s1}})^2}$为地层横波径向波数；$v_{\mathrm{f}}$和$v_{\mathrm{s1}}$分别是井内流体速度和地层横波速度；$A_1'$、$D_1$和$F_1$为振幅系数. $\mathrm{I}_n(*)$和$\mathrm{K}_n(*)$分别为第一类和第二类n阶变型贝塞尔函数，$\varepsilon_1=2$；$S(\omega)$为声源的频谱函数；式 (1) 的推导过程见附录 A.

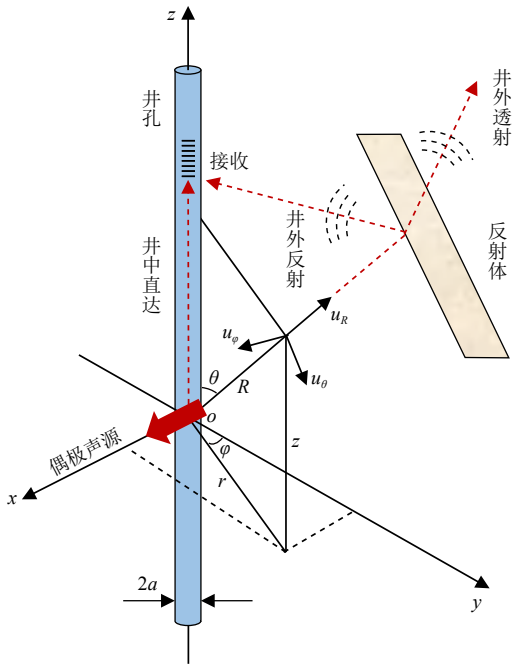


图 1 柱坐标系下偶极声源在激发沿井传播的波动的同时向井外地层辐射声波产生反射和透射

Fig. 1 In the cylindrical coordinate system, a dipole source not only excites wave propagation along the borehole, but also radiates waves into the formation outside the borehole to create reflection and transmission

通过求解井壁处($r=a$)固/液边界条件所满足的方程组 (式 (A4))，得到不同径向距离r下井内流体和井外地层中纵波、SH 横波和 SV 横波对应的振幅系数A_1'、D_1和F_1，分别用快速傅里叶变换计算对频率ω和波数k的二重积分 (唐晓明和郑传汉，2004)，可以得到偶极声源在井内外的辐射声场.

在远场 (辐射距离大于波长) 情况下，SH 横波位移频谱的渐近解由 Tang 等 (2014) 给出：

$$u_\phi \sim \frac{RD\cdot S(\omega)}{\rho_1 v_{\mathrm{s1}}^2}\cdot\frac{\mathrm{e}^{\mathrm{i}\omega R/v_{\mathrm{s1}}}}{4\pi R}, \tag{2}$$

$$RD(\omega,\theta) = \mathrm{i}\rho_1 v_{\mathrm{s1}}\omega D_1(\omega,k_0)\sin\theta\cos\phi, \tag{3}$$

式中RD为偶极 SH 横波的辐射指向性因子；ρ_1为地层的密度；$k_0=\omega\cos\theta/v_{\mathrm{s1}}$为地层横波波数的最速下降解.

从式 (2) 可以看出，远场情况下，偶极 SH 横波向地层以球面波的形式辐射，在θ方向上的幅度变化取决于辐射因子RD.

1.2 偶极辐射声场在地层界面处的反射和透射

我们首先考虑入射 SH 球面波在单个水平地层界面上的反射和透射声场，如图 2 所示，在$y'o'z'$坐标系下，界面$z'=0$两侧地层的密度和横波速度分别为ρ_1, v_{s1}和ρ_2, v_{s2}，对位于$r'=(0,z_0)$的偶极声源 (声源指向为x'正方向)，将式 (2) 中的球面波传播因子通过角谱法展开成不同方向 (波矢k_1) 的柱面波乘以相应的加权系数$P_i'(k_{y'},k_{z'})$在平面$k_{y'}k_{z'}$上的叠加的形式有 (张海澜，2021)：

中国知网 https://www.cnki.net

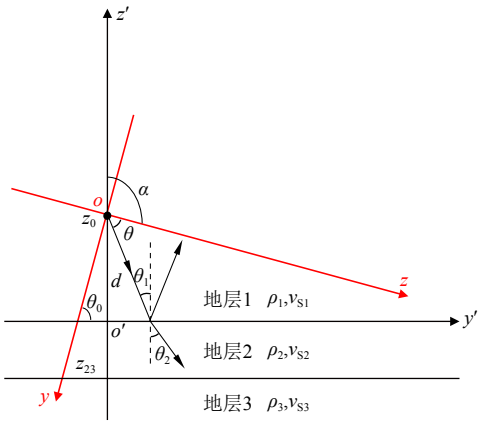


图 2　平界面上的球面波和坐标系旋转

Fig. 2　Spherical wave incident on a horizontal stratigraphic interface and coordinate system rotation

$$P_i=\frac{S(\omega)}{\rho_1 v_{s1}^2}\cdot\frac{1}{2}\int_0^{\infty}RD(\omega,\theta)P_i'(k_{y'})\mathrm{J}_0(k_{y'}y')\mathrm{e}^{\mathrm{i}k_{z1'}|z'-z_0|}k_{y'}\mathrm{d}k_{y'},\tag{4}$$

$$P_i'(k_{y'})=\frac{\mathrm{i}}{2\pi k_{z1'}},\tag{5}$$

式中$k_1=\omega/v_{s1}$为声场在地层 1 中的波数, $k_{y'}^2+k_{z1'}^2=k_1^2$; 加权系数$P_i'(k_{y'})$为入射 SH 球面波的角谱; $\mathrm{J}_0(*)$为 0 阶第一类贝塞尔函数.

式 (4) 表示入射 SH 球面波在远场情况下可以通过对不同方向 (波矢k_1) 加权后的柱面波在幅度上乘以对应θ方向上的辐射指向性因子RD叠加得到, 在界面$z'=0$处, 反射 SH 球面波和透射 SH 球面波的角谱分别为

$$\begin{cases}P_r'(k_{y'})=P_i'(k_{y'})R_{12}\left(k_{y'}\right)\\ P_t'(k_{y'})=P_i'(k_{y'})T_{12}\left(k_{y'}\right)\end{cases},\tag{6}$$

$$R_{12}(k_{y'})=\frac{\rho_1 v_{s1}\cos\theta_1-\rho_2 v_{s2}\cos\theta_2}{\rho_1 v_{s1}\cos\theta_1+\rho_2 v_{s2}\cos\theta_2}=\frac{\rho_1 v_{s1}^2 k_{z1'}-\rho_2 v_{s2}^2 k_{z2'}}{\rho_1 v_{s1}^2 k_{z1'}+\rho_2 v_{s2}^2 k_{z2'}},\tag{7}$$

$$T_{12}(k_{y'})=\frac{2\rho_1 v_{s1}\cos\theta_1}{\rho_1 v_{s1}\cos\theta_1+\rho_2 v_{s2}\cos\theta_2}=\frac{2\rho_1 v_{s1}^2 k_{z1'}}{\rho_1 v_{s1}^2 k_{z1'}+\rho_2 v_{s2}^2 k_{z2'}},\tag{8}$$

其中, $R_{12}\left(k_{y'}\right)$和$T_{12}\left(k_{y'}\right)$分别为入射 SH 平面波的反射系数和透射系数 (Aki and Richards, 1980; Pujol, 2003); k_2为声场在地层 2 中的波数, $k_{y'}^2+k_{z2'}^2=k_2^2=(\omega/v_{s2})^2$; θ_1和θ_2分别是 SH 平面波的入射角和透射角.

结合式 (4)—(6), 界面$z'=0$两侧产生的反射 SH 球面波P_r和透射 SH 球面波P_t分别为:

$$P_r=\frac{\mathrm{i}\cdot S(\omega)}{4\pi\rho_1 v_{s1}^2}\int_0^{\infty}\frac{RD(\omega,\theta)R_{12}(k_{y'})\mathrm{J}_0(k_{y'}y')\mathrm{e}^{\mathrm{i}k_{z1'}(z'+z_0)}}{k_{z1'}}\times k_{y'}\mathrm{d}k_{y'},\tag{9}$$

$$P_t=\frac{\mathrm{i}\cdot S(\omega)}{4\pi\rho_1 v_{s1}^2}\int_0^{\infty}\frac{RD(\omega,\theta)T_{12}(k_{y'})\mathrm{J}_0(k_{y'}y')\mathrm{e}^{\mathrm{i}(k_{z1'}z_0-k_{z2'}z')}}{k_{z1'}}\times k_{y'}\mathrm{d}k_{y'}.\tag{10}$$

上述为入射 SH 球面波在单个水平界面$z'=0$处的反射和透射声场, 对于入射 SH 球面波在多层平行地层介质中的传播, 如在$z'=z_{23}$处另有一水平地层界面 (z_{ij}表示地层 i 和地层 j 之间的界面位置), 界面$z'=z_{23}$两侧地层的密度和声速分别为ρ_2, v_{s2}和ρ_3, v_{s3}, 同样根据角谱法可以得到透射 SH 球面波P_t在界面$z'=z_{23}$上的入射声场为:

$$P_{ti}=\frac{\mathrm{i}\cdot S(\omega)}{4\pi\rho_1 v_{s1}^2}\int_0^{\infty}\frac{RD(\omega,\theta)T_{12}(k_{y'})\mathrm{J}_0(k_{y'}y')\mathrm{e}^{\mathrm{i}(k_{z1'}z_0-k_{z2'}z_{23})}}{k_{z1'}}k_{y'}\mathrm{d}k_{y'},\tag{11}$$

透射 SH 球面波P_t在界面$z'=z_{23}$两侧产生的反射声场和透射声场分别为:

$$P_{tr}=\frac{\mathrm{i}\cdot S(\omega)}{4\pi\rho_1 v_{s1}^2}\int_0^{\infty}\frac{RD(\omega,\theta)T_{12}(k_{y'})R_{23}(k_{y'})\mathrm{J}_0(k_{y'}y')\mathrm{e}^{\mathrm{i}(k_{z1'}z_0-k_{z2'}z_{23}+k_{z2'}(z'-z_{23}))}}{k_{z1'}}k_{y'}\mathrm{d}k_{y'},\tag{12}$$

$$P_{tt}=\frac{\mathrm{i}\cdot S(\omega)}{4\pi\rho_1 v_{s1}^2}\int_0^{\infty}\frac{RD(\omega,\theta)T_{12}(k_{y'})T_{23}(k_{y'})\mathrm{J}_0(k_{y'}y')\mathrm{e}^{\mathrm{i}(k_{z1'}z_0-k_{z2'}z_{23}-k_{z3'}(z'-z_{23}))}}{k_{z1'}}k_{y'}\mathrm{d}k_{y'},\tag{13}$$

式中$R_{23}\left(k_{y'}\right)$和$T_{23}\left(k_{y'}\right)$分别为入射 SH 平面波在界面$z'=z_{23}$上的反射系数和透射系数 (与式 (7) 和式 (8) 类似, 不再赘述), k_3为声场在地层 3 中的波数; $k_{y'}^2+k_{z3'}^2=k_3^2=(\omega/v_{s3})^2$, 对于后续波在界面上的反射和透射情况类似.

当 SH 球面波入射至井旁单个或多个平行倾斜地层界面时, d为声源至倾斜地层界面的距离, θ_0为地层界面的倾角; 通过上述方法得到$y'o'z'$坐标系下

中国知网　https://www.cnki.net

位于$r'=(0,d)$处的偶极声源在界面$z'=0$两侧产生的反射和透射 SH 球面波，通过坐标系平移和旋转，如图 2 所示，将坐标系$y'o'z'$沿z'正方向平移距离d，再顺时针旋转角度α，得到新坐标系yoz；式 (14) 给出了新坐标系中的点(y,z)坐标在原坐标系下的表示，利用新旧坐标系的关系可以得到入射 SH 球面波在倾斜地层界面两侧产生的反射和透射声场. 式 (14) 为

$$\begin{pmatrix} y \\ z \end{pmatrix}=\begin{pmatrix} \cos\alpha & -\sin\alpha \\ \sin\alpha & \cos\alpha \end{pmatrix}\begin{pmatrix} y' \\ z'-d \end{pmatrix}. \tag{14}$$

通过角谱法得到式 (4) 中的波场频谱在界面$z'=0$两侧产生的反射和透射波场频谱 (例如式 (9) 和式 (10))，再用快速傅里叶变换计算时域波形，对坐标系$y'o'z'$中的每个场点(y',z')重复以上计算并转换到yoz坐标系的场点(y,z)中，便得到给定时刻t下的波场快照.

2 数值计算结果及分析

2.1 有限差分对比验证

根据以上井中偶极声源辐射声场的远场渐近解，着重研究了入射 SH 横波声场在地层界面两侧产生的反射和透射 SH 横波声场. 为了验证该方法的可靠性和正确性，将计算得到的声场快照以及波形和三维时域有限差分得到的结果进行对比验证，模拟过程中所用的模型如图 3a 所示：模型在三个坐标轴上的大小为 7 m × 7 m × 7 m，井孔半径为 0.1 m 且中心位于 (0,0)，指向为x轴正方向的偶极声源 (红色箭头) 位于原点，声源信号是中心频率为 3 kHz 的雷克子波，声源到地层界面的距离为 5 m，地层界面倾角为80°，井内流体和地层界面两侧的参数见表 1，若无其他说明，计算均采用表 1 的参数. 图 3b 给出了yoz平面内地层界面两侧接收点分布情况，位于地层 1 的接收点 A 至 H 所在直线与地层界面平行，接收点 A 到地层界面的距离为 2 m，两接收点间距为 0.5 m，接收点A′至H′位于地层 2 中，分布情况类似. 有限差分模拟时迭代空间步长为 0.005 m，迭代时间步长为 0.5 μs，设置 40 个网格厚度的复频移完美匹配层 (CFS-PML) 来吸收边界反射 (Wang et al., 2013).

表 1 模型计算参数

Table 1 Parameters used for modeling

介质参数	纵波速度/(m·s^{-1})	横波速度/(m·s^{-1})	密度/(kg·m^{-3})
井内流体	1500	–	1000
地层1	3000	1800	2000
地层2	4500	2650	2400
地层3	4000	2400	2200
地层4	3300	1200	1850

式 (4) 表示了入射 SH 球面波可以通过角谱法展开成柱面波叠加的形式，因此我们首先分析 SH 平面波在倾斜地层界面上的反射和透射情况. 根据式 (7) 和式 (8)，图 4a 给出了不同入射角度下 SH 平面波在界面两侧的反射系数 (黑色实线) 和透射系数 (红色虚线)，平面波由地层 1 入射至地层 2 中，SH 平面波在低入射角度时反射系数较小且随角度

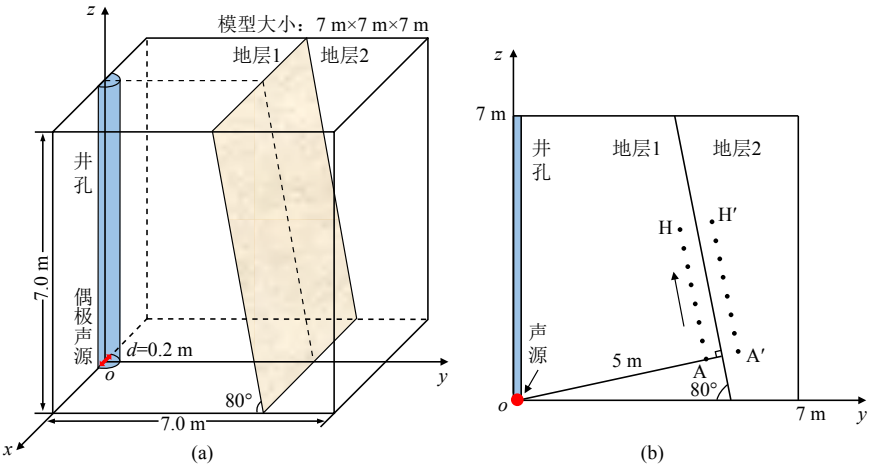


图 3 井旁反射界面计算模型

(a) 偶极声源和单个反射面；(b) yoz 平面内地层界面以及接收点分布情况.

Fig. 3 Calculation model with a near-borehole geological interface

(a)Dipole source with a reflector; (b) Layer interface and receiver distribution in the yoz plane.

中国知网 https://www.cnki.net

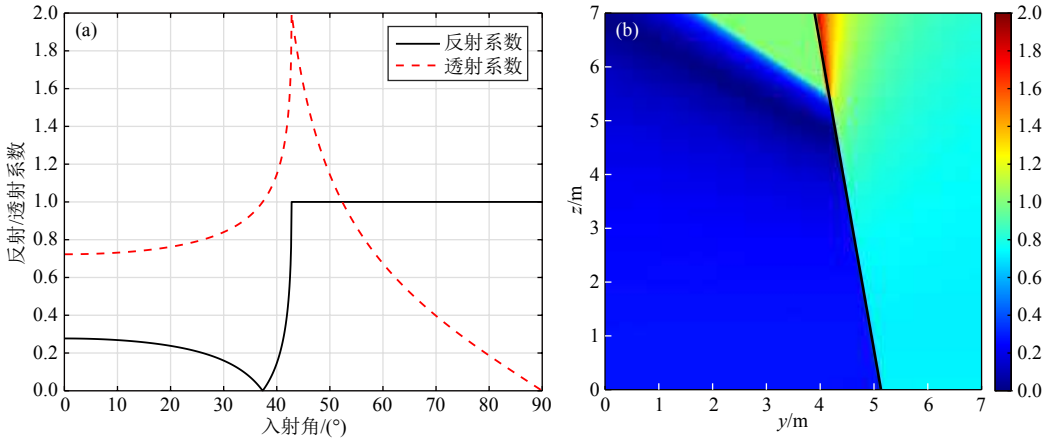


图 4　SH 平面波反射和透射系数

(a) 不同入射角度情况下对应的反射与透射系数; (b) 反射透射系数在界面两侧的分布情况.

Fig. 4　Reflection and transmission coefficients of SH plane waves

(a) Coefficients under different incidence angles; (b) Coefficients distribution near the interface.

增加单调递减, 透射系数单调递增; 当入射角度大于临界入射角时, 反射系数迅速增大至全反射, 透射系数单调递减至零. 根据反射系数随着入射角度的变化规律可知, 在临界入射角附近, 反射 SH 横波在幅度上会存在"突变". 按照图 3b 所示的模型, 在 *yoz* 坐标系中, 对于地层 1 中 θ 方向辐射的 SH 平面波 (见图 2), 通过虚源法和斯奈尔定律可以计算入射角 θ_1 和透射角 θ_2, 再根据式 (7) 和式 (8) 可以得到该 SH 平面波在界面两侧路径上的反射和透射系数. 图 4b 给出了 *yoz* 平面内 SH 平面波反射和透射系数在地层界面两侧的分布情况, 可以看出在界面两侧大部分区域 (入射角小于临界入射角) 反射和透射系数基本不变; 在入射角大于临界入射角区域, SH 平面波达到全反射且透射系数单调递增.

图 5 给出了 *yoz* 平面内 2.5 ms 时刻入射 SH 横波在地层界面附近的声场快照对比情况, 其中图 5a 为有限差分模拟结果, 图 5b 为解析解模拟结果. 可以看出, 偶极声源在地层中辐射的 SH 横波的波前呈一球面波的形态, 受井筒的调制作用, 不同方向辐射的波幅和相位有较大差异. 对于这种波场特征, 解析解和有限差分的模拟结果基本一致. 图 6 给出了 *yoz* 平面内 4.3ms 时刻声场快照对比情况, 此时入射 SH 球面波在地层界面两侧产生了反射和透射波, 二者均以球面波的形态向界面两侧传播. 图 6a 为有限差分模拟结果, 图 6b 为解析解模拟结果, 二者的波场特征基本一致, 且界面两侧的反射和透射 SH 球面波幅度变化与图 4 中讨论的 SH 平面波反射和透射系数分布情况一致.

图 7 给出了 *yoz* 平面内地层界面两侧接收点处 SH 横波声场解析解 (黑色实线) 与有限差分 (红色点线) 的结果对比. 图 7a 为地层界面左侧接收点 A 至 H 接收到的入射 SH 横波和反射 SH 横波声场, 最先到达的为入射 SH 横波, 其次是来自地层界面的反射 SH 横波, 从接收点 A, B, 至 H, 辐射角 θ 依次减小, 辐射强度降低, 入射 SH 横波幅度单调递减, 按图 1 的模型计算, A 到 H 的接收点位于图 4a 所示的低入射角度区域, 因此, 由 A 至 H 反射系数单调递减, 加上入射 SH 横波幅度也单调递减, 使得反射 SH 横波幅度单调递减. 图 7b 为地层界面右侧接收点 A′至 H′接收到的透射 SH 横波声场, 透射 SH 横波幅度从接收点 A′至 H′单调递减, 这是波幅强度随接收距离减少的速率比透射系数增加速率大的缘故. 解析方法与有限差分计算的波形在幅度和相位上几乎完全重合, 再次验证了入射 SH 球面波通过角谱法计算倾斜地层界面两侧的反射和透射 SH 横波声场的正确性. 值得指出的是, 对于上述模型声场的模拟, 三维时域有限差分模拟时长通常为数十小时, 相比之下, 解析方法用时仅需数十分钟, 计算效率提高了两个量级.

2.2　远距离井旁单层界面下的 SH 横波声场

从实际远探测成像处理结果可以看出, 偶极横波远探测技术能够在井旁数十米的范围内有效识别多个高倾角反射体. 对于这种井外大尺度模型的声场模拟, 三维时域有限差分需要设置庞大的网格体系, 消耗大量的计算资源, 并且模型中弹性波的传播距离达到数个波长, 其数值频散现象更加明显,

中国知网　https://www.cnki.net

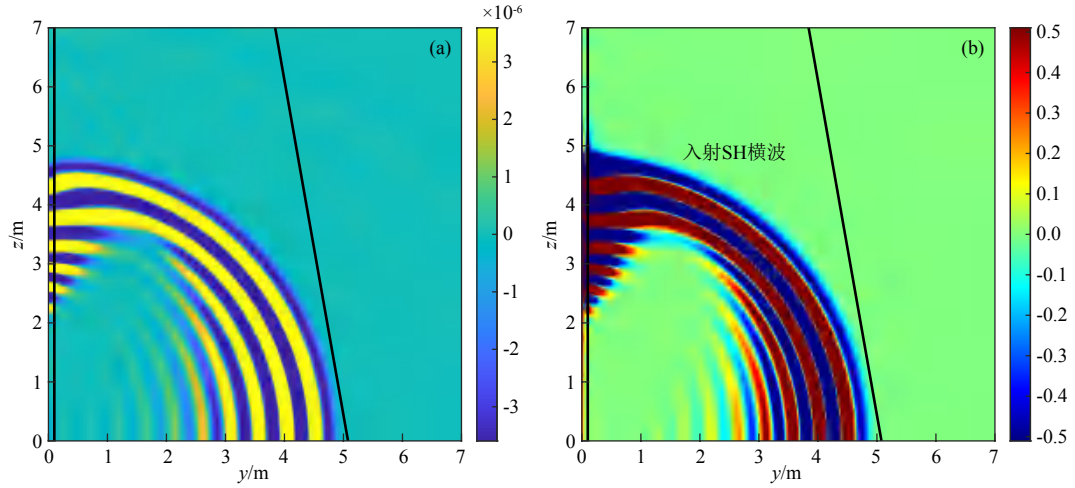


图 5 *yoz* 平面内 2.5ms 时刻入射 SH 横波声场快照对比

(a) 有限差分；(b) 解析解.

Fig. 5 Comparison of the incident SH wavefield snapshot in the *yoz* plane at 2.5 ms

(a) 3D finite-difference method; (b) Analytical solution.

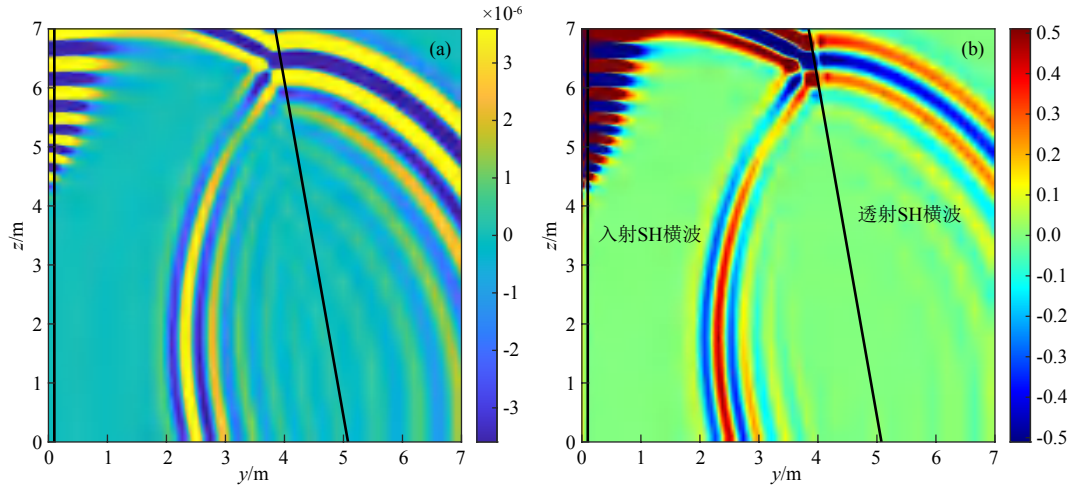


图 6 *yoz* 平面内 4.3ms 时刻反射和透射 SH 横波声场快照对比

(a) 有限差分；(b) 解析解.

Fig. 6 Comparison of reflected and transmitted SH wavefield snapshots in the *yoz* plane at 4.3 ms

(a) 3D finite-difference method; (b) Analytical solution.

不适合大尺度模型的声场模拟 (李振, 2019). 为克服有限差分方法的局限性，我们利用上述解析方法进行了大尺度远探测模型的声场模拟，在图 3b 所示的计算模型基础上，模型大小变为 y=50 m 和 z=25 m，声源至地层界面的距离变为 30 m，其余参数保持不变. 图 8 给出了不同时刻下大尺度井旁单一地层界面的 SH 横波声场快照，图 8a—l 的时间分别是 5～27 ms，快照时间间隔为 2 ms，可以看出，由于界面距离很远，15 ms 时偶极辐射 SH 横波才传播至界面附近，在传播过程中辐射 SH 横波在水平方向上的辐射强度最大，随着传播距离的增加，辐射 SH 横波由于衰减使得波形幅度和持续周期不断减小. 17 ms 时辐射 SH 横波传播至界面处，19 ms 时在界面两侧分别产生反射和透射 SH 横波，21～27 ms 时反射和透射 SH 横波幅度在传播过程中不断减弱. 对于这种大尺度模型，其反射界面通常距离井孔很远，模拟远探测声场所需要的记录时间更长，产生的数据量更大，相比于利用有限差分等数值方法模拟，解析方法对于模拟井旁反射界面距离远、波形持续时间长的大尺度远探测声场更具有优势性.

2.3 井旁多界面 SH 横波声场

对于裂缝性发育地层，往往能够从远探测成像

中国知网 https://www.cnki.net

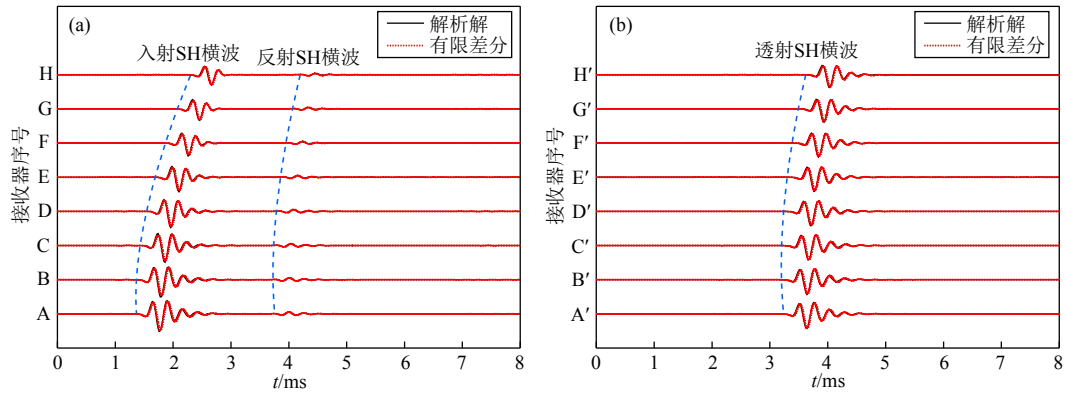


图 7　*yoz* 平面内地层界面两侧接收点处 SH 横波声场解析解与有限差分结果对比

(a) 界面左侧入射 SH 横波与反射 SH 横波; (b) 界面右侧透射 SH 横波.

Fig. 7　Comparison of SH waveforms analytical solutions and finite-difference results at receiving points on both sides of the inner stratigraphic interface of the *yoz* plane

(a) Incident and reflected SH waveforms on the left side of the interface; (b) Transmitted SH waveforms on the right side of the interface.

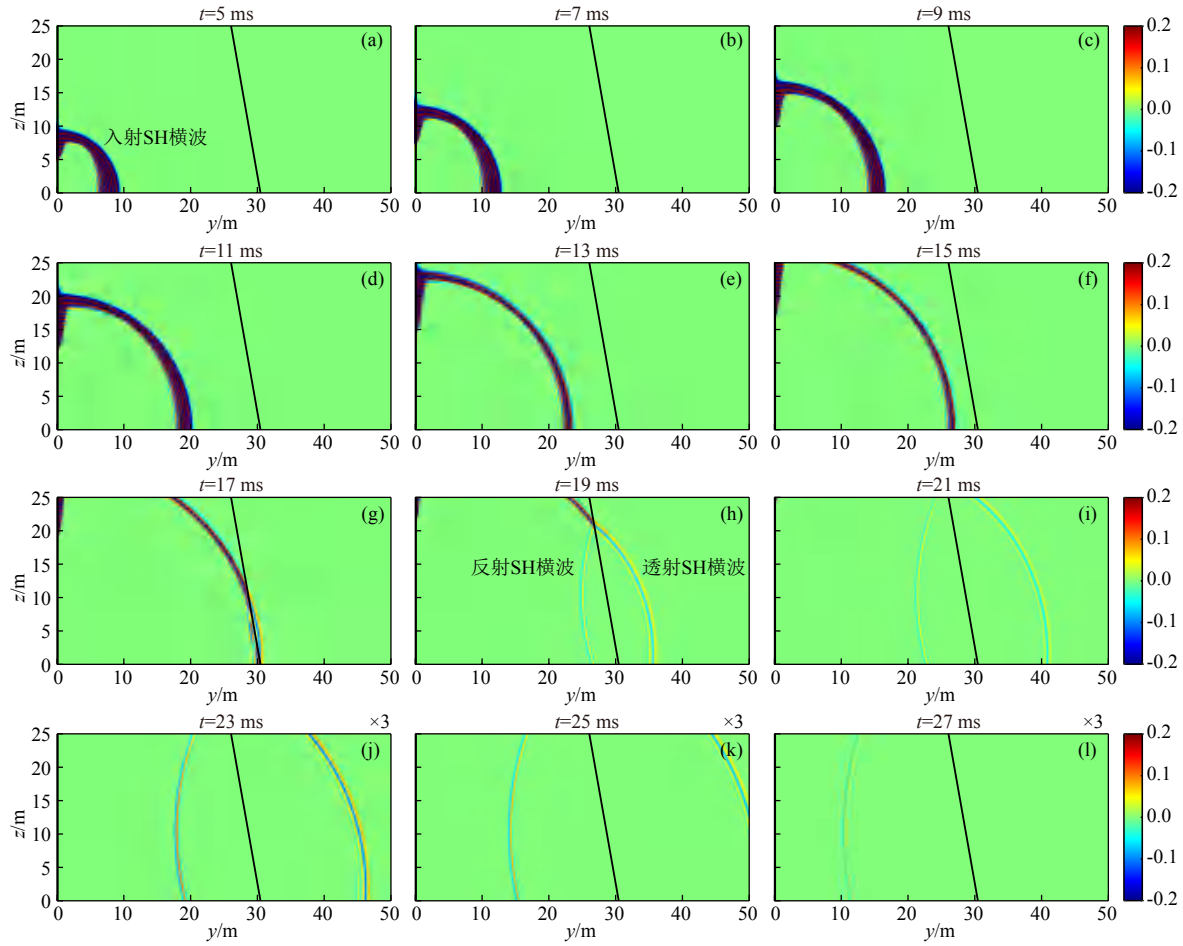


图 8　不同时刻下的大尺度井旁单层界面 SH 横波声场快照

(a)—(l) 的时间分别是 5~27ms, 时间间隔 2 ms.

Fig. 8　SH wavefield snapshots were taken at the single-layer interface near the well under different time conditions in the large-scale model

The time of snapshots (a)—(l) is from 5 ms to 27 ms, and the time interval is 2 ms.

中国知网　https://www.cnki.net

结果中清晰的看到井旁存在多条平行裂缝 (古希浩等, 2020). 为了更加直观地研究井中偶极声源辐射声场在多层平行介质中的传播特征, 我们利用解析方法进行井旁多层平行地层界面模型的 SH 横波声场模拟. 图 9 所示的模型大小为 y=20 m、z=25 m, 模拟时偶极声源采用中心频率为 3 kHz 的雷克子波, 声源 (红点) 位于(0,0)点, 声源指向为 x 轴正方向, 声源距离地层界面 1 的距离为 10 m, 地层界面倾角都为 80°, 地层界面间距为 3 m.

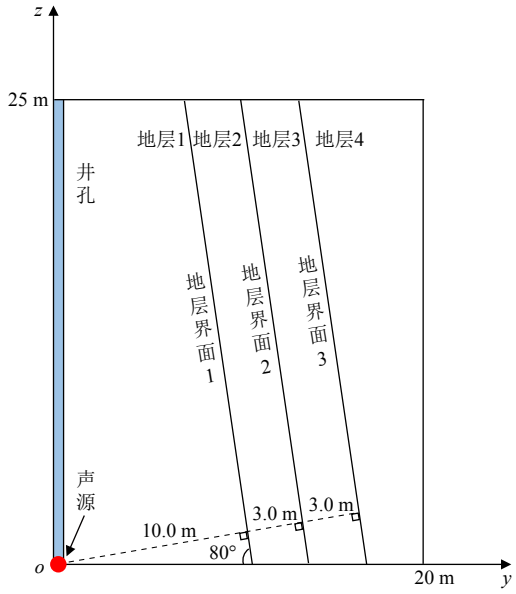


图 9 yoz 平面内井旁三层平行地层界面模型示意图
Fig. 9 Schematic of a three-layer parallel formation interface near the wellbore in the yoz plane

图 10 给出了井旁存在三层平行地层界面情况下 8 个不同时刻的 SH 横波声场快照, 它们的时间分别是 4.5 ~ 15 ms, 快照时间间隔为 1.5 ms; 图 10a 显示入射 SH 球面波以地层 1 中的横波速度向井外辐射, 其在水平方向辐射强度最大, 波形持续周期最长; 图 10b 显示此时入射 SH 球面波在地层界面 1 的两侧反射和透射; 图 10c 为 7.5 ms 时刻下 SH 横波的声场快照, 此时来自地层界面 1 处的透射 SH 横波在地层界面 2 两侧产生相应的反射和透射 SH 球面波, 之后在图 10d 中来自地层界面 2 处的反射 SH 横波在地层界面 1 处又产生相应的反射和透射, 在地层 1 中有两组振幅较强的反射 SH 横波 (SH1 和 SH2), 它们分别来自地层界面 1 和地层界面 2 处的反射; 图 10e 为 10.5 ms 时刻下 SH 横波的声场快照, 此时来自地层界面 3 处的反射 SH 横波在地层界面 2 两侧产生反射和透射 SH 波; 图 10f—h 显示地层 2 和地层 3 中的后续反射和透射 SH 球面波在三层平行地层界面间不断产生新的反射和透射波, 波的幅度逐渐减弱, 同时在地层 1 中存在来自地层界面 3 处的反射 SH 横波 (SH3). 从井旁三层平行地层界面模型下的 SH 横波声场快照中可以看出, 当声源指向与地层界面走向平行时, 偶极声源辐射的纯 SH 横波在各个地层界面处都产生了反射 SH 横波, 由于入射 SH 横波在反射界面上不产生转换波, 存在三组振幅较强的反射 SH 横波向井中入射, 对其偏移成像后可以对井旁多层界面进行识别.

图 11 为井旁三层平行地层界面模型下解析模拟和现场实测的 SH 横波远探测波形和成像结果对比. 在图 9 所示的计算模型基础上, 图 11 第一道给出了远探测测井数据模拟时的井旁三层平行地层界面模型, 深度区间为 100 m, 深度点 0 m 位于地层界面 1 和井轴交点下方 20 m, 其余参数保持不变. 第二道是第一个接收器在井段深度上接收到的 SH 横波远探测模拟波形对应的变密度图. 其中图的颜色越深表示波形幅度越大, 可以看出, 最先接收到的是井筒弯曲波, 其波幅明显要比来自多层平行地层界面的反射 SH 横波的幅度大; 之后依次是来自地层界面 1 至地层界面 3 处的反射 SH 横波, 反射波的幅度随着其在地层 1 中传播时间的增加而减小. 第三道是对 SH 横波远探测模拟波形进行成像处理 (Tang, 2004) 的结果, 可以清晰的看到井旁存在三层平行的地层反射界面, 并且地层反射界面与模型中界面的位置基本吻合. 第四道为现场实测远探测数据的深度道, 井段深度为 X470 ~ X570 m. 第五道为现场实测 SH 反射波波形对应的变密度图, 可以看到来自不同地层界面的多组反射 SH 横波依次到达, 这些反射波的到时在井段深度上的连线几乎平行, 且波幅的变化与解析模拟的波形一致. 第六道为实测 SH 反射波波形的偏移成像结果, 可以看到井外 30 m 范围内存在多个高倾角且相互平行的反射体. 当入射 SH 横波在地层中传播遇到不同波阻抗的反射界面时, 其产生的反射波在不同地层间传播, 最终被井中接收器所接收, 界面两侧地层的波阻抗差异反映了反射界面成像的强弱, 这解释了远探测成像中的多反射体现象.

3 结论与认识

本文将角谱法用于偶极横波远探测声场的模拟计算. 以 SH 横波为例, 在其远场渐近解的基础

中国知网 https://www.cnki.net

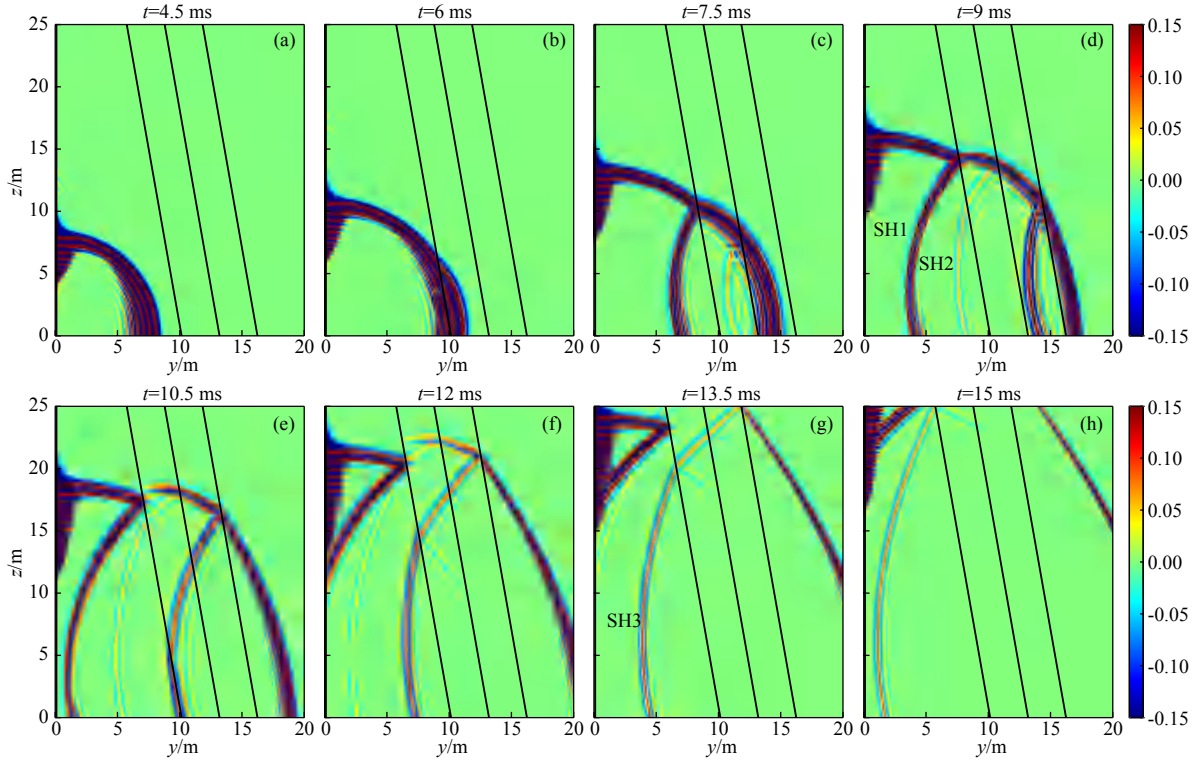


图 10　不同时刻下的井旁多层平行地层界面 SH 横波声场快照

(a)—(h) 的时间分别是 4.5 ms, 6 ms, 7.5 ms, 9 ms, 10.5 ms, 12 ms, 13.5 ms, 15 ms.

Fig. 10　SH wavefield snapshots at different times of a three-layer parallel formation interface near the wellbore

The times of the snapshots (a)—(h) are 4.5 ms, 6 ms, 7.5 ms, 9 ms, 10.5 ms, 12 ms, 13.5 ms, 15 ms, respectively.

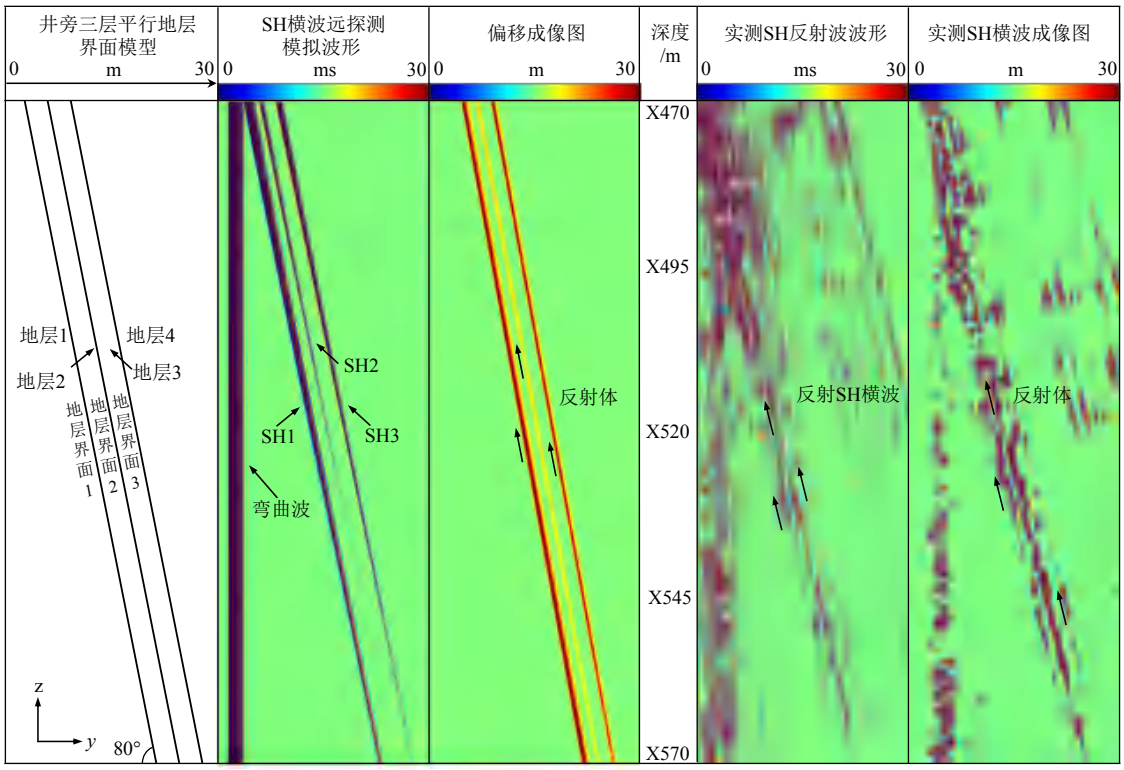


图 11　井旁三层平行地层界面模型下解析模拟和现场实测的 SH 横波远探测波形和成像结果对比

Fig. 11　Comparison of SH full-wave and imaging results between analytical simulation and field measurements under the three-layer parallel formation interface model near the wellbore

中国知网　https://www.cnki.net

上,利用角谱法可以方便地描述波在地层界面两侧的反射和透射,得到了一种快速计算远探测声场快照的解析方法,并利用有限差分方法验证了该解析方法的正确性和高效性,得到的主要结论和认识如下:

(1) 偶极声源辐射的 SH 横波在远场情况下以球面波的形式向外传播,将远场渐近解中的球面波传播因子用角谱法展开成柱面波叠加的形式,在此基础上计算入射波在界面两侧的反射和透射,得到偶极远探测声场.

(2) 相同模型下通过解析方法和三维时域有限差分方法模拟得到的 SH 横波声场快照和波形在相位和幅度变化上基本一致,但解析方法与有限差分相比,计算效率可提高两个量级.

(3) 利用解析方法计算了井旁三层平行地层界面模型下的反射和透射 SH 横波声场,解析模拟和现场实测 SH 横波远探测数据偏移成像后均存在多个反射体,很好地解释了远探测成像中的多反射体现象.

附录 A

柱坐标系下偶极子声源在井内外的位移势函数可以表示为 (唐晓明和郑传汉, 2004):

$$\begin{cases} \Phi_{\mathrm{f}} = \dfrac{\sin\phi}{4\pi}\displaystyle\int_{-\infty}^{+\infty}\int_{-\infty}^{+\infty}[\varepsilon_1 \mathrm{K}_1(fr) + A_1'(\omega,k)\mathrm{I}_1(fr)]S(\omega)\mathrm{e}^{\mathrm{i}kz-\mathrm{i}\omega t}\mathrm{d}k\mathrm{d}\omega \\ \Phi = \dfrac{\sin\phi}{4\pi}\displaystyle\int_{-\infty}^{+\infty}\int_{-\infty}^{+\infty}B_1(\omega,k)\mathrm{K}_1(pr)S(\omega)\mathrm{e}^{\mathrm{i}kz-\mathrm{i}\omega t}\mathrm{d}k\mathrm{d}\omega \\ \chi = \dfrac{\cos\phi}{4\pi}\displaystyle\int_{-\infty}^{+\infty}\int_{-\infty}^{+\infty}D_1(\omega,k)\mathrm{K}_1(sr)S(\omega)\mathrm{e}^{\mathrm{i}kz-\mathrm{i}\omega t}\mathrm{d}k\mathrm{d}\omega \\ \Gamma = \dfrac{\sin\phi}{4\pi}\displaystyle\int_{-\infty}^{+\infty}\int_{-\infty}^{+\infty}F_1(\omega,k)\mathrm{K}_1(sr)S(\omega)\mathrm{e}^{\mathrm{i}kz-\mathrm{i}\omega t}\mathrm{d}k\mathrm{d}\omega \end{cases}, \tag{A1}$$

其中, Φ_{f}是井内流体位移势函数, k和 f分别为流体中纵波的轴向和径向波数, Φ、χ和Γ分别为地层中纵波、SH 横波和 SV 横波的位移势函数, p和s分别为地层纵波和横波的径向波数.

将流体位移势函数Φ_{f}代入关系式$u_{\mathrm{f}} = \dfrac{\partial \Phi_{\mathrm{f}}}{\partial r}$便可得到偶极子声源在井内的径向位移:

$$u_{\mathrm{f}} = \frac{\sin\phi}{4\pi}\int_{-\infty}^{+\infty}\int_{-\infty}^{+\infty}[\varepsilon_1(\mathrm{K}_1(fr)/r - f\mathrm{K}_2(fr)) + A_1'(\mathrm{I}_1(fr)/r + f\mathrm{I}_2(fr))]S(\omega)\mathrm{e}^{\mathrm{i}kz-\mathrm{i}\omega t}\mathrm{d}k\mathrm{d}\omega. \tag{A2}$$

同样将 SH 横波的位移势函数χ和 SV 横波的位移势函数Γ代入势函数-位移关系式 (唐晓明和郑传汉, 2004) 中便可得到偶极声源在井外地层中的 SH 横波位移:

$$u_{\phi} = \frac{\sin\phi}{4\pi}\int_{-\infty}^{+\infty}\int_{-\infty}^{+\infty}[-D(\mathrm{K}_1(sr)/r - s\mathrm{K}_2(sr)) + \mathrm{i}kF\mathrm{K}_1(sr)/r]S(\omega)\mathrm{e}^{\mathrm{i}kz-\mathrm{i}\omega t}\mathrm{d}k\mathrm{d}\omega. \tag{A3}$$

式 (A2)、式 (A3) 中的振幅系数A_1'、D_1和F_1可以通过以下矩阵确定 (矩阵元素及具体推导过程见唐晓明和郑传汉, 2004):

$$\begin{bmatrix} \boldsymbol{M}_{11} & \boldsymbol{M}_{12} & \boldsymbol{M}_{13} & \boldsymbol{M}_{14} \\ \boldsymbol{M}_{21} & \boldsymbol{M}_{22} & \boldsymbol{M}_{23} & \boldsymbol{M}_{24} \\ \boldsymbol{M}_{31} & \boldsymbol{M}_{32} & \boldsymbol{M}_{33} & \boldsymbol{M}_{34} \\ \boldsymbol{M}_{41} & \boldsymbol{M}_{42} & \boldsymbol{M}_{43} & \boldsymbol{M}_{44} \end{bmatrix}\begin{bmatrix} \boldsymbol{A_1'} \\ \boldsymbol{B_1} \\ \boldsymbol{D_1} \\ \boldsymbol{F_1} \end{bmatrix} = \begin{bmatrix} u_{\mathrm{f}}^d \\ \sigma_{\mathrm{rrf}}^d \\ 0 \\ 0 \end{bmatrix}, \tag{A4}$$

其中, u_{f}^d和σ_{rrf}^d分别为偶极子声源在井壁 ($r=a$) 处的径向位移及应力, 如式 (A5) 所示:

$$\begin{cases} u_{\mathrm{f}}^d = \varepsilon_1[\mathrm{K}_1(fa)/a - f\mathrm{K}_2(fa)] \\ \sigma_{\mathrm{rrf}}^d = -\varepsilon_1\rho_{\mathrm{f}}\omega^2\mathrm{K}_1(fa) \end{cases}, \tag{A5}$$

注意式 (A4) 左侧的$\boldsymbol{M}$矩阵元素已约去共同因子 $(fr_0/2)\cos(\phi-\pi/2)\exp(\mathrm{i}kz)$, ρ_{f}为井内流体密度.

References

Aki K, Richards P G. 1980. Quantitative Seismology: Theory and Methods. San Francisco: W. H. Freeman & Co.

Atalar A. 1978. An angular-spectrum approach to contrast in reflection acoustic microscopy. *Journal of Applied Physics*, 49(10): 5130-5139.

Bolshakov A, Patterson D, Lan C. 2011. Deep fracture imaging around the wellbore using dipole acoustic logging. //SPE Annual Technical Conference and Exhibition. Denver: SPE, SPE-146769-MS, doi: 10.2118/146769-MS.

Brekhovskikh L M, Lysanov Y P. 1991. Fundamentals of Ocean Acoustics. 2nd ed. Berlin: Springer-Verlag.

Cao J J, Tang X M, Su Y D, et al. 2016a. Radiation efficiency of a multipole acoustic source in a fluid-filled borehole. *Chinese Journal of Geophysics*

中国知网 https://www.cnki.net

(in Chinese), 59(2): 757-766, doi: 10.6038/cjg20160233.

Cao J J, Tang X M, Su Y D, et al. 2016b. Radiation characteristics of the single-well imaging field in while-drilling logging using an acoustic dipole source. *Chinese Journal of Geophysics* (in Chinese), 59(9): 3503-3513, doi: 10.6038/cjg20160932.

Deng C X. 2019. Research on three-dimensional numerical modeling and imaging method of single-well acoustic reflection imaging logging [Ph. D. thesis](in Chinese). Wuhan: China University of Geosciences.

Dong J L, Xu X K, Zhang J Y, et al. 2020. Overview and development of acoustic far detection technology. *Progress in Geophysics* (in Chinese), 35(2): 566-572, doi: 10.6038/pg2020CC0180.

Gong H, Chen H, He X, et al. 2015. Numerical simulation of the 3C single well imaging technique. //2015 Symposium on Piezoelectricity, Acoustic Waves, and Device Applications (SPAWDA). Jinan: IEEE, 63-66.

Gu X H, Tang X M, Zhuang C X, et al. 2020. Simulation of dipole shear-wave reflection survey for multi-fracture system using liner slip interface theory. *Progress in Geophysics* (in Chinese), 35(3): 955-962, doi: 10.6038/pg2020DD0053.

Li N, Liu P, Wu H L, et al. 2024. Development and prospect of acoustic reflection imaging logging processing and interpretation method. *Petroleum Exploration and Development* (in Chinese), 51(4): 731-742.

Li Y H, Tang X M, Li H R, et al. 2021. Characterizing the borehole response for single-well shear-wave reflection imaging. *Geophysics*, 86(1): D15-D26.

Li Y H, Tang X M, Su Y D. 2022. Azimuthal response of the received wavefield in open and cased boreholes for dipole shear-wave reflection imaging. *Chinese Journal of Geophysics* (in Chinese), 65(10): 4122-4140, doi: 10.6038/cjg2022P0378.

Li Z. 2019. Basic theory and applied research of borehole acoustic remote sensing technology [Ph. D. thesis](in Chinese). Qingdao: China University of Petroleum (East China).

Liu H, Wu Y Y, He H J, et al. 2023. Application of new processing technology of array acoustic logging in carbonate reservoir evaluation. *Progress in Geophysics* (in Chinese), 38(1): 220-228, doi: 10.6038/pg2023FF0220.

Patterson D, Mekic N, Bolshakov A, et al. 2013. Unconventional reservoir fracture evaluation utilizing deep shear-wave imaging. //International Petroleum Technology Conference. Beijing: IPTC, IPTC-16958-MS, doi: 10.2523/IPTC-16958-MS.

Pujol J. 2003. Elastic Wave Propagation and Generation in Seismology. Cambridge: Cambridge University Press.

Tang X M. 2004. Imaging near-borehole structure using directional acoustic-wave measurement. *Geophysics*, 69(6): 1378-1386.

Tang X M, Patterson D J. 2009. Single-well S-wave imaging using multicomponent dipole acoustic-log data. *Geophysics*, 74(6): WCA211-WCA223.

Tang X M, Wei Z T. 2012a. Single-well acoustic reflection imaging using far-field radiation characteristics of a borehole dipole source. *Chinese Journal of Geophysics* (in Chinese), 55(8): 2798-2807, doi: 10.6038/j.issn.0001-5733.2012.08.031.

Tang X M, Wei Z T. 2012b. Significant progress of acoustic logging technology: remote acoustic reflection imaging of a dipole acoustic system. *Applied Acoustics* (in Chinese), 31(1): 10-17.

Tang X M, Cao J J, Wei Z T. 2014. Shear-wave radiation, reception, and reciprocity of a borehole dipole source: with application to modeling of shear-wave reflection survey. *Geophysics*, 79(2): T43-T50.

Tang X M. 2016. Reflection imaging away from borehole: a paradigm shift. //SEG Technical Program Expanded Abstracts. Tulsa: SEG, 4873-4877.

Wang H, Tao G, Shang X F, et al. 2013. Stability of finite difference numerical simulations of acoustic logging-while-drilling with different perfectly matched layer schemes. *Applied Geophysics*, 10(4): 384-396.

Wei Z T, Wang H, Tang X M, et al. 2015. Directional P-wave remote acoustic imaging in an acoustically slow formation. *The Open Petroleum Engineering Journal*, 8(1): 333-343.

Xu J Q, Hu H S. 2019. Wave filed simulation of single-well imaging based on method of steepest descent and reciprocity. *Journal of Applied Acoustics* (in Chinese), 38(3): 293-300.

Zhang H L. 2021. Computational Acoustics (in Chinese). Beijing: Science Press.

附中文参考文献

曹景记, 唐晓明, 苏远大等. 2016a. 充液井中多极声源的辐射效率. 地球物理学报, 59(2): 757-766, doi: 10.6038/cjg20160233.

曹景记, 唐晓明, 苏远大等. 2016b. 随钻偶极远探测声场的辐射特性. 地球物理学报, 59(9): 3503-3513, doi: 10.6038/cjg20160932.

邓呈祥. 2019. 井中声波远探测三维数值模拟及成像方法研究 [博士论文]. 武汉: 中国地质大学.

董经利, 许孝凯, 张晋言等. 2020. 声波远探测技术概述及发展. 地球物理学进展, 35(2): 566-572, doi: 10.6038/pg2020CC0180.

古希浩, 唐晓明, 庄春喜等. 2020. 用滑移界面理论模拟多裂缝体系的偶极横波远探测声场. 地球物理学进展, 35(3): 955-962, doi: 10.6038/pg2020DD0053.

李宁, 刘鹏, 武宏亮等. 2024. 远探测声波测井处理解释方法发展与展望. 石油勘探与开发, 51(4): 731-742.

李杨虎, 唐晓明, 苏远大. 2022. 偶极横波远探测在裸眼井及套管井中接收波场的方位响应特征. 地球物理学报, 65(10): 4122-4140, doi: 10.6038/cjg2022P0378.

李振. 2019. 远探测声波测井基础理论和应用研究 [博士论文]. 青岛: 中国石油大学 (华东).

刘航, 吴煜宇, 贺洪举等. 2023. 阵列声波测井处理新技术在碳酸盐岩储层评价方面的应用. 地球物理学进展, 38(1): 220-228, doi: 10.6038/pg2023FF0220.

唐晓明, 郑传汉. 2004. 定量测井声学. 赵晓敏译. 北京: 石油工业出版社.

唐晓明, 魏周拓. 2012a. 利用井中偶极声源远场辐射特性的远探测测井. 地球物理学报, 55(8): 2798-2807, doi: 10.6038/j.issn.0001-5733.2012.08.031.

唐晓明, 魏周拓. 2012b. 声波测井技术的重要进展——偶极横波远探测测井. 应用声学, 31(1): 10-17.

许家旗, 胡恒山. 2019. 基于鞍点法与互易性的远探测波场模拟. 应用声学, 38(3): 293-300.

张海澜. 2021. 计算声学. 北京: 科学出版社.

（本文编辑　张正峰）

中国知网　https://www.cnki.net

李杨虎，唐晓明，苏远大. 2022. 偶极横波远探测在裸眼井及套管井中接收波场的方位响应特征. 地球物理学报，65(10)：4122-4140，doi：10.6038/cjg2022P0378.

Li Y H, Tang X M, Su Y D. 2022. Azimuthal response of the received wavefield in open and cased boreholes for dipole shear-wave reflection imaging. *Chinese J. Geophys.* (in Chinese), 65(10): 4122-4140, doi: 10.6038/cjg2022P0378.

偶极横波远探测在裸眼井及套管井中接收波场的方位响应特征

李杨虎[1,2]，唐晓明[1,2,3*]，苏远大[1,2,3]

1 中国石油大学(华东)地球科学与技术学院，青岛 266580

2 中国石油大学(华东)深层油气重点实验室，青岛 266580

3 青岛海洋科学与技术国家实验室海洋矿产资源评价与探测技术功能实验室，青岛 266071

摘要 偶极横波远探测技术的快速发展及其在裸眼和套管井中应用的需求增加使得研究井中远探测波场的方位特征和接收响应具有重要意义.将远探测声场看作是声源在反射体一侧的镜像点的辐射声场并对其做柱面波展开，得到了充液裸眼和套管井中偶极横波方位远探测接收声场的渐近解.据此对声场在井内流体中产生的径向位移和声压进行了模拟分析，深入研究了接收器偏心距、声源频率和地层类型对井中方位接收波场的影响，并对裸眼和套管井中的响应特征进行了对比，预示了快速和慢速地层条件下声场方位响应中的 180°相位反转现象.渐近解析解与三维有限差分数值解的结果对比证实了这一现象，同时也验证了解析解的正确性和普适性.结果表明：接收器偏心距、声源频率和地层类型是井中接收声场方位响应特征的主要影响因素；SH 横波入射引起的井内流体的径向位移和声压方位响应特征基本一致，而 SV 横波入射时二者特征却有较大差异；因此，接收信号中的 SV 分量有助于识别反射体方位；相对于裸眼井，套管井中接收声场的方位灵敏度更高，更有利于识别井外反射体的方位.本文的分析结果为偶极横波方位远探测技术的进一步发展和应用提供了理论支持.

关键词 偶极横波远探测；井孔声场；方位接收响应；套管井

doi：10.6038/cjg2022P0378 **中图分类号** P631 **收稿日期** 2021-06-03，2022-05-19 **收修定稿**

Azimuthal response of the received wavefield in open and cased boreholes for dipole shear-wave reflection imaging

LI YangHu[1,2], TANG XiaoMing[1,2,3*], SU YuanDa[1,2,3]

1 *School of Geosciences, China University of Petroleum, Qingdao* 266580, *China*

2 *Key Laboratory of Deep Oil and Gas, China University of Petroleum, Qingdao* 266580, *China*

3 *Laboratory for Marine Mineral Resources, Qingdao National Laboratory for Marine Science and Technology, Qingdao* 266071, *China*

Abstract With the rapid development of dipole shear-wave reflection imaging technology and the increasing demand for its application in open- and cased-boreholes, there is a strong need for studying the azimuthal response characteristics of the borehole to the incident elastic wavefield of

基金项目 国家自然科学基金(42074137，41821002)，山东省自然科学基金(ZR201911120382)和中国石油大学(华东)研究生创新工程项目(YCX2020007)联合资助.

第一作者简介 李杨虎，男，1993 年生，博士研究生，主要从事声波测井理论、方法与应用等方面的研究. E-mail：lyanghu@outlook.com

***通讯作者** 唐晓明，男，1955 年生，教授，多年来一直致力于地球物理(特别是声波)测井、岩石物理学、地震波传播及测量等方面的研究和技术开发工作. E-mail：tangxiam@aliyun.com

(C)1994-2022 China Academic Journal Electronic Publishing House. All rights reserved. http://www.cnki.net

a borehole dipole source. By treating the wave incidence as the radiation from the mirror point of the borehole source with respect to the reflector, the wavefield can be expanded as the series summation of cylindrical waves, leading to an asymptotic solution for the response wavefield in the fluid-filled (open or cased) borehole. Using the solution, the borehole acoustic radial displacement and pressure are calculated, and the effects of frequency, receiver eccentricity, and the formation elastic property on the borehole wavefield are analyzed. The response characteristics for open- and cased-borehole conditions are also compared, which show a marketed 180° phase reversal between the fast and slow formation conditions. The results of the asymptotic solution, including the phase reversal phenomenon, are confirmed by the 3D finite-difference modeling results, verifying the validity and universality of the analytical solution. The results show that the receiver eccentricity, source frequency, and formation type are the key factors controlling the azimuth response characteristics of the borehole acoustic wavefield. For SH-wave incidence, the radial fluid displacement and pressure have the same azimuthal response characteristics. But the characteristics are markedly different for SV-wave incidence, indicating that the SV component in the received wavefield can help determining the orientation of the reflector. Relative to the open-hole condition, the wavefield in the cased borehole has higher azimuthal response sensitivity and is more favorable for the reflector azimuth determination. The analysis results of this study provide theoretical support for the development and application of the dipole shear-wave reflection imaging technology.

Keywords　Dipole shear-wave reflection imaging; Borehole acoustic wavefield; Azimuthal reception response; Cased borehole

0　引言

近年来,偶极横波远探测成像测井技术取得长足发展,其在裂缝、断层、溶蚀孔洞等地质构造的探测中取得了良好的应用效果. Tang(2004)于 2004 年首次提出了偶极横波远探测成像方法,该方法通过充液井中的偶极声源向地层辐射横波,并在井中接收经反射体反射回来的横波进行井周成像. 与常规的单极纵波法相比(Hornby, 1989; 薛梅, 2002; 乔文孝等, 2004; 陶果等, 2008),偶极横波法具有以下优势:一、偶极声源具有方位灵敏度,采用多分量发射和接收可以确定反射体的走向;二、偶极声源的工作频率为 3 kHz 左右的低频,因而其径向探测深度更深. 此后,国内外学者针对偶极横波远探测技术开展了大量的研究工作,其现已成为非常规油气勘探中寻找油气甜点的利器(Tang and Patterson, 2009; 唐晓明和魏周拓, 2012; 苏远大等, 2014; Tang et al., 2014, 2016; Hirabayashi et al., 2017; 宫昊等, 2018; Bennett, 2019; Lee et al., 2019; Xu et al., 2019; 董经利等, 2020; 古希浩等, 2020; 刘汇鑫等, 2021).

研究井孔对声场的调制作用对偶极横波远探测具有重要意义,包括井内偶极声源在地层中的辐射特性以及井孔对入射波的方位接收响应. 对于偶极声源在井外的辐射声场,国内学者已经做了充分研究. Tang 等(2014)给出了偶极声源在井外无限大地层中辐射横波的位移远场渐近解及其辐射指向性表达式. 在此基础上,曹景记等(2014)和唐晓明等(2019)研究了偶极声源在裸眼和套管井外的横波辐射特征,并证实了在套管井中进行偶极横波远探测的可行性. 井孔对入射波的接收响应可分为平面波和球面波入射两种情况,对于平面波入射引起的井内声场的方位响应,人们已经进行了深入研究,见 White(1953)、Schoenberg(1986)、Peng 等(1993)以及 Hirabayashi 等(2017)发表的研究成果. 然而,声波远探测中入射波场是以球面波的形式向井孔传播,对于球面波入射引起的井内声场的方位响应尚未做深入研究. 虽然前人能够对偶极横波远探测的接收声场进行快速模拟(Tang et al., 2014; 许家旗和胡恒山, 2019),但这些研究中都使用了互易定理来求解井孔的球面波入射响应,该方法主要用于分析井中声源和接收器位置同轴线的情况,不能对实际测井时仪器接收到的方位波场进行有效模拟. 针

(C)1994-2022 China Academic Journal Electronic Publishing House. All rights reserved.　http://www.cnki.net

对此,Li 等(2021)在虚源法的基础上,结合柱面波展开法(Tang and Cheng,2004),求解得到了充液裸眼井中偶极横波方位远探测接收声场的解析解,为方位声波远探测的模拟奠定了理论基础.

目前,利用偶极横波远探测进行井周成像或反射体方位识别的相关方法主要是根据井中接收波形的幅度变化特征(Tang and Patterson, 2009; Hirabayashi et al., 2017; 李盛清等, 2020; 许家旗和胡恒山, 2020; Li et al., 2021),但充液井中远探测波场的方位接收响应还缺乏详尽的理论分析.因此,对偶极横波远探测声场在井内流体中产生的径向位移和声压的方位响应特征进行深入研究具有重要意义.另一方面,基于全球各地油田中套管井的大量存在以及被证实的过套管偶极横波远探测的可行性(唐晓明等, 2019),本文将裸眼井中远探测声场的方位解析解延展到套管井中,研究了不同胶结情况套管井中接收波场的方位响应特征,并与裸眼井情况进行了对比分析.最后,利用三维有限差分法证实了声场幅值方位响应中的 180°反转现象.本文的研究对偶极横波远探测测井时裸眼和套管井中接收声场的方位响应特性有了更为全面的认识,为偶极横波方位远探测的技术发展、仪器研制以及现场解释提供了理论支持.

1 充液井中偶极横波方位远探测接收声场的解析解

图 1a 给出了当井外存在反射体时,充液裸眼或套管井中偶极声波远探测模拟所用的坐标系.在测井仪器的偶极声源上方环向布置了多组偏心距为 e 的接收器,其接收横截面如图 1b 中模型所示.按照不同的声源—接收器组合方式,可模拟不同的测量工作模式,如正交偶极发射—正交偶极接收模式,正交偶极发射—多方位接收模式,本文采用多方位接收模式对井中接收波场的方位响应进行研究.偶极声波远探测包含三个过程,即充液井孔内偶极声源在井外的辐射、井外地质体的反射以及充液井孔对反射波的接收调制.在辐射距离远大于波长的远场辐射条件下,图 1a 中偶极声源辐射到地层中的 SH 和 SV 横波位移势函数 χ 和 Γ 的远场渐近解为(唐晓明和魏周拓, 2012):

$$\begin{cases} \chi \sim [D_1(\omega,k_0^t)\sin\varphi]\dfrac{e^{i\omega R/\beta}}{R}S(\omega) \\ \Gamma \sim [F_1(\omega,k_0^t)\cos\varphi]\dfrac{e^{i\omega R/\beta}}{R}S(\omega) \end{cases}, \tag{1}$$

其中,$k_0^t = (\omega/\beta)\cos\theta_t$ 为辐射横波波数的最速下降解,ω 为圆频率,β 为地层横波速度,θ_t 为波辐射方向与 z 轴正向的夹角;S 为声源函数谱;R 是井中声源到场点之间的辐射距离;D_1 和 F_1 分别为 SH 和 SV 横波的远场振幅系数,由井壁处的边界条件求得(曹景记等, 2014).

当辐射横波与地层中的反射体作用后,可将反射回井孔的入射横波波场表示为(Tang et al., 2014, 2016):

$$Iwv(\omega) = S(\omega)\cdot RD(\omega)\cdot RF(\omega)\cdot\frac{e^{i\omega D/\beta}}{D}, \tag{2}$$

式中,RD 为声源在井外远处的辐射函数,由式(1)的中括号里的部分组成;RF 为声波在反射体处的反射系数,可由佐普利兹方程求得(Aki and Richards,

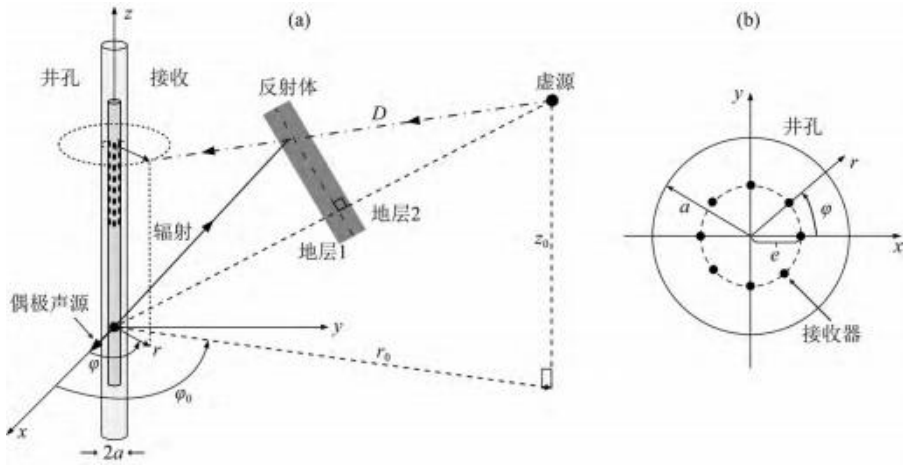


图 1 基于虚源法的偶极声波远探测示意图(a)及方位接收井孔截面示意图(b)

Fig. 1 The schematic model of dipole single-well reflection imaging based on the virtual source analogy (a) and the cross section of borehole receiving configuration using azimuthally spaced off-axis receivers (b)

(C)1994-2022 China Academic Journal Electronic Publishing House. All rights reserved. http://www.cnki.net

1980);S、RD、RF 都是关于圆频率 ω 的函数;D 为声波在地层中总的传播距离,其传播路径为一条折线. Li 等(2021)通过将远探测声场看作是声源在反射体向外一侧的镜像点的辐射声场,此时声波的传播路径 D 转化为一条直线,如图 1a 中所示,从而式(2)中的球面波传播因子可以展开为多极子柱面波叠加的形式(唐晓明和郑传汉, 2004):

$$\frac{\mathrm{e}^{\mathrm{i}\omega D/\beta}}{D}=\frac{1}{\pi}\int_{-\infty}^{+\infty}\sum_{n=0}^{\infty}\varepsilon_n K_n(sr_0)I_n(sr)\cos[n(\varphi-\varphi_0)]\times\mathrm{e}^{\mathrm{i}k(z-z_0)}\,\mathrm{d}k,\tag{3}$$

式中,(r_0,φ_0,z_0)和(r,φ,z)分别为虚源和场点的位置;k 和 s 分别为入射横波的轴向和径向波数,$s=(k^2-\omega^2/\beta^2)^{1/2}$;$I_n$ 和 K_n 分别表示第一类和第二类 n 阶变型贝塞尔函数;n 为多极子的阶数;ε_n 为纽曼因子,$n=0$ 时 $\varepsilon_n=1$,$n>0$ 时 $\varepsilon_n=2$;$D=[r^2+r_0^2-2rr_0\cos(\varphi-\varphi_0)+(z-z_0)^2]^{1/2}$.

将式(3)代入式(2),对于图 1a 中所示的偶极声源指向,入射 SH 和 SV 横波的位移势函数表达式为:

$$\begin{pmatrix}\chi^i\\ \Gamma^i\end{pmatrix}=S(\omega)\begin{pmatrix}RD_{\mathrm{SH}}\cdot RF_{\mathrm{SH}}\\ RD_{\mathrm{SV}}\cdot RF_{\mathrm{SV}}\end{pmatrix}\sum_{n=0}^{\infty}\varepsilon_n I_n(sr)K_n(sr_0)\times\cos[n(\varphi-\varphi_0)],\tag{4}$$

其中,上标 i 表示入射波场;下标 SH 和 SV 表示计算声源的辐射函数 RD 和反射系数 RF 时应分别对应 SH 和 SV 横波.

考虑径向包含多层的井眼模型,假设井壁与地层之间共有 $N-1$ 圆柱层,其中第 m 层为固体层,第 j 层为液体层. 当入射横波与井眼相互作用时,根据赫姆霍兹方程,在柱坐标系 (r,φ,z) 下井内流体中的位移场 $\boldsymbol{u}_f$、第 j 层流体中的位移场 $\boldsymbol{u}_{f(j)}$ 和第 m 层固体中散射波的位移场 $\boldsymbol{u}_{s(m)}$ 分别为:

$$\begin{cases}\boldsymbol{u}_f=\nabla\phi_f,\\ \boldsymbol{u}_{f(j)}=\nabla\phi_{f(j)},\\ \boldsymbol{u}_{s(m)}=\nabla\phi_m+\nabla\times(\chi_m\hat{\boldsymbol{z}})+\nabla\times\nabla\times(\Gamma_m\hat{\boldsymbol{z}}),\end{cases}\tag{5}$$

其中,$\hat{\boldsymbol{z}}$ 是沿 z 轴方向的单位矢量;ϕ_f 和 $\phi_{f(j)}$ 分别为井内和第 j 层流体中纵波的位移势函数;ϕ_m、χ_m 和 Γ_m 分别为第 m 层固体中散射 P 波、SH 和 SV 横波的位移势函数. 类比于式(4)中入射波的函数形式,式(5)中各位移场在频率-波数域内具有以下形式的通解(唐晓明和郑传汉, 2004):

$$\begin{cases}\phi_f=\sum_{n=0}^{\infty}[A_n^f\cos(n\varphi)+A^{f\prime}_n\sin(n\varphi)]I_n(fr)K_n(sr_0),\\ \phi_{f(j)}=\sum_{n=0}^{\infty}\{[A_n^{f(j)}\cos(n\varphi)+A_n^{f'(j)}\sin(n\varphi)]I_n(f^{(j)}r)+[B_n^{f(j)}\cos(n\varphi)+B_n^{f'(j)}\sin(n\varphi)]K_n(f^{(j)}r)\}K_n(sr_0),\\ \phi_m=\sum_{n=0}^{\infty}\{[A_n^{(m)}\cos(n\varphi)+A_n^{(m)'}\sin(n\varphi)]I_n(p^{(m)}r)+[B_n^{(m)}\cos(n\varphi)+B_n^{(m)'}\sin(n\varphi)]K_n(p^{(m)}r)\}K_n(sr_0),\\ \chi_m=\sum_{n=0}^{\infty}\{[C_n^{(m)}\sin(n\varphi)-C_n^{(m)'}\cos(n\varphi)]I_n(s^{(m)}r)+[D_n^{(m)}\sin(n\varphi)-D_n^{(m)'}\cos(n\varphi)]K_n(s^{(m)}r)\}K_n(sr_0),\\ \Gamma_m=\sum_{n=0}^{\infty}\{[E_n^{(m)}\cos(n\varphi)+E_n^{(m)'}\sin(n\varphi)]I_n(s^{(m)}r)+[F_n^{(m)}\cos(n\varphi)+F_n^{(m)'}\sin(n\varphi)]K_n(s^{(m)}r)\}K_n(sr_0),\end{cases}\tag{6}$$

其中,$f=(k^2-\omega^2/\alpha_f^2)^{1/2}$ 和 $f^{(j)}=(k^2-\omega^2/\alpha_{f(j)}^2)^{1/2}$ 分别为井内和第 j 层流体的纵波径向波数;α_f 和 $\alpha_{f(j)}$ 分别为井内和第 j 层流体的纵波速度;$p^{(m)}=(k^2-\omega^2/\alpha_m^2)^{1/2}$ 和 $s^{(m)}=(k^2-\omega^2/\beta_m^2)^{1/2}$ 分别为第 m 层固体中纵波和横波的径向波数;α_m 和 β_m 分别为第 m 层固体的纵波和横波速度;振幅系数 $A_n^f\sim F_n^{(m)'}$ 由井壁处的边界条件求得,对于最外面的无限大地层,其辐射条件决定了系数 $A_n^{(m)}=A_n^{(m)'}=C_n^{(m)}=C_n^{(m)'}=E_n^{(m)}=E_n^{(m)'}=0$.

在裸眼井情况下,式(5)中的模型由井内流体和地层两部分组成,此时井壁处的边界条件为:径向位移和正应力连续,环向和轴向的剪切应力为零,表达式为:

$$\begin{cases}u_r^i(a^+)+u_r^s(a^+)=u_r^f(a^-),\\ \sigma_{rr}^i(a^+)+\sigma_{rr}^s(a^+)=\sigma_{rr}^f(a^-),\\ \sigma_{r\varphi}^i(a^+)+\sigma_{r\varphi}^s(a^+)=0,\\ \sigma_{rz}^i(a^+)+\sigma_{rz}^s(a^+)=0,\end{cases}\tag{7}$$

式中,a 为井孔半径;上标 s 和 f 分别表示地层中的散射波场和流体中的透射波场.

由式(4)、(5)、(6)计算出入射波、散射波和透射波的位移和应力,代入式(7)的边界条件得到两个矩阵方程:

(C)1994-2022 China Academic Journal Electronic Publishing House. All rights reserved.　http://www.cnki.net

$$\begin{bmatrix} M_{11} & M_{12} & M_{13} & M_{14} \\ M_{21} & M_{22} & M_{23} & M_{24} \\ M_{31} & M_{32} & M_{33} & M_{34} \\ M_{41} & M_{42} & M_{43} & M_{44} \end{bmatrix} \begin{bmatrix} A_n^f \\ B_n \\ D_n \\ F_n \end{bmatrix} = \begin{bmatrix} b_1 \\ b_2 \\ b_3 \\ b_4 \end{bmatrix} \text{和}$$

$$\begin{bmatrix} M_{11} & M_{12} & M_{13} & M_{14} \\ M_{21} & M_{22} & M_{23} & M_{24} \\ M_{31} & M_{32} & M_{33} & M_{34} \\ M_{41} & M_{42} & M_{43} & M_{44} \end{bmatrix} \begin{bmatrix} A^{f\prime}{}_n \\ B_n' \\ D_n' \\ F_n' \end{bmatrix} = \begin{bmatrix} b_1' \\ b_2' \\ b_3' \\ b_4' \end{bmatrix}, \quad (8)$$

为了便于描述,将式(8)中方程左侧与井中透射波和地层中散射波有关的矩阵记为矩阵 $\boldsymbol{M}$,右侧与地层中入射波有关的向量分别记为向量 $\boldsymbol{b}$ 和 $\boldsymbol{b}'$. 矩阵 $\boldsymbol{M}$,向量 $\boldsymbol{b}$ 和 $\boldsymbol{b}'$ 中的元素表达式详见附录 A.

套管井主要考虑胶结良好和自由套管两种情况. 对于胶结良好的套管井,套管-水泥环-地层之间的声场可由汤姆森-哈斯克传播矩阵 $\boldsymbol{T}$ 进行连接(唐晓明和郑传汉,2004). 将井壁处的位移-应力矢量和地层中的位移-应力矢量连接后的矩阵乘积记为 $\boldsymbol{G}=\left[\prod_{m=1}^{N-1}\boldsymbol{T}(m,R_{\text{in}})\cdot\boldsymbol{T}^{-1}(m,R_{\text{out}})\right]\boldsymbol{T}(N,R_{\text{fm}})$,其中 $\boldsymbol{T}(m,R_{\text{in}})$ 和 $\boldsymbol{T}(m,R_{\text{out}})$ 分别为第 m 固体层在该层内半径 R_{in} 和外半径 R_{out} 下对应的矩阵,$\boldsymbol{T}(N,R_{\text{fm}})$ 为地层中的矩阵,$\boldsymbol{T}^{-1}$ 表示矩阵 $\boldsymbol{T}$ 的逆矩阵. 矩阵 $\boldsymbol{G}$ 将多个界面简化为一个流-固界面,按照裸眼井中 $\boldsymbol{M}$ 矩阵的推导,得到两个矩阵方程:

$$\begin{bmatrix} N_{11} & G_{12} & G_{14} & G_{16} \\ N_{21} & G_{42} & G_{44} & G_{46} \\ N_{31} & G_{52} & G_{54} & G_{56} \\ N_{41} & G_{62} & G_{64} & G_{66} \end{bmatrix} \begin{bmatrix} A_n^f \\ B_n \\ D_n \\ F_n \end{bmatrix} = \begin{bmatrix} c_1 \\ c_2 \\ c_3 \\ c_4 \end{bmatrix} \text{和}$$

$$\begin{bmatrix} N_{11} & G_{12} & G_{14} & G_{16} \\ N_{21} & G_{42} & G_{44} & G_{46} \\ N_{31} & G_{52} & G_{54} & G_{56} \\ N_{41} & G_{62} & G_{64} & G_{66} \end{bmatrix} \begin{bmatrix} A_n^{f'} \\ B_n' \\ D_n' \\ F_n' \end{bmatrix} = \begin{bmatrix} c_1' \\ c_2' \\ c_3' \\ c_4' \end{bmatrix}, \quad (9)$$

其中,矩阵元素 $N_{11}\sim N_{41}$ 及向量 $\boldsymbol{c}$ 和 $\boldsymbol{c}'$ 可由方程(8)中与之相对应的部分将井孔半径置换为套管内径后得到;$\boldsymbol{G}$ 矩阵为 6×6 阶复数矩阵,计算 $\boldsymbol{G}$ 矩阵所用到的 $\boldsymbol{T}$ 矩阵的元素表达式详见附录 B.

在套管和地层之间添加一流体层来模拟自由套管的情况,此时由井中流体-套管-流体环-地层组成的模型中所包含的 3 个界面均为流-固界面. 与固-固界面不同,对流-固界面的每一个边界条件都要单独进行处理,通过连接边界条件,最后整合得到矩阵方程:

$$\begin{cases} \boldsymbol{H}\times\left[A_n^f \quad A_n^1 \quad B_n^1 \quad C_n^1 \quad D_n^1 \quad E_n^1 \quad F_n^1 \quad A_n^2 \quad B_n^2 \quad B_n^3 \quad D_n^3 \quad F_n^3\right]^{\mathrm{T}} = \boldsymbol{d}, \\ \boldsymbol{H}\times\left[A_n^{f'} \quad A_n^{1'} \quad B_n^{1'} \quad C_n^{1'} \quad D_n^{1'} \quad E_n^{1'} \quad F_n^{1'} \quad A_n^{2'} \quad B_n^{2'} \quad B_n^{3'} \quad D_n^{3'} \quad F_n^{3'}\right]^{\mathrm{T}} = \boldsymbol{d}', \end{cases} \quad (10)$$

式中,$\boldsymbol{H}$ 为 12×12 矩阵,$\boldsymbol{d}$ 和 $\boldsymbol{d}'$ 为 12×1 向量;系数向量中的上标 1、2 和 3 表示该振幅系数分别对应套管、流体环和地层介质. 矩阵 $\boldsymbol{H}$,向量 $\boldsymbol{d}$ 和 $\boldsymbol{d}'$ 中的元素表达式详见附录 C.

求解矩阵方程(8)、(9)和(10)可分别得到裸眼井、胶结良好套管井和自由套管井中声场所对应的振幅系数 A_n^f 和 $A_n^{f'}$,将其代入式(6)中便可确定入射横波引起的井内声场. 进一步,根据关系式 $p=\rho_f\omega^2\phi_f$ 和 $u_r^f=\partial\phi_f/\partial r$ 可分别计算井内流体的声压和径向位移场,表达式为:

$$\begin{cases} p = \dfrac{\rho_f\omega^2}{\pi}\displaystyle\int_{-\infty}^{+\infty}\sum_{n=0}^{\infty}\left[A_n^f\cos(n\varphi)+A_n^{f'}\sin(n\varphi)\right]I_n(fr)K_n(sr_0)\mathrm{e}^{\mathrm{i}k(z-z_0)}\,\mathrm{d}k, \\ u_r^f = \dfrac{1}{\pi}\displaystyle\int_{-\infty}^{+\infty}\sum_{n=0}^{\infty}\left[A_n^f\cos(n\varphi)+A_n^{f'}\sin(n\varphi)\right]\left[\dfrac{n}{r}I_n(fr)+fI_{n+1}(fr)\right]K_n(sr_0)\mathrm{e}^{\mathrm{i}k(z-z_0)}\,\mathrm{d}k, \end{cases} \quad (11)$$

其中,ρ_f 为流体密度. 对于远场辐射,虚源的径向距离 r_0 远大于弹性波的波长,满足 $|sr_0|\gg1$ 的条件,由此可对式(11)中的波数积分运用最速下降方法求解(Tang and Patterson, 2009; Li et al., 2021),整理得到:

$$\begin{Bmatrix} p \\ u_r^f \end{Bmatrix} = \frac{\mathrm{e}^{\mathrm{i}\omega D/\beta-\mathrm{i}\pi/4}}{D}\sum_{n=0}^{\infty}\begin{cases} \rho_f\omega^2\left[A_n^f\cos(n\varphi)+A_n^{f'}\sin(n\varphi)\right]I_n(f_0r) \\ \left[A_n^f\cos(n\varphi)+A_n^{f'}\sin(n\varphi)\right]\left[\dfrac{n}{r}I_n(f_0r)+f_0I_{n+1}(f_0r)\right], \end{cases} \quad (12)$$

式中,$f_0=((k_0^i)^2-\omega^2/\alpha_f^2)^{1/2}$ 为流体纵波的径向波数,$k_0=(\omega/\beta)\cos(\pi-\theta_i)$ 为入射横波波数的最速下降解,θ_i 为波入射方向与 z 轴正向的夹角;$D=[r_0^2+(z-z_0)^2]^{1/2}$,此处的 D 与式(2)和式(3)中等

(C)1994-2022 China Academic Journal Electronic Publishing House. All rights reserved. http://www.cnki.net

同,只是与井内场点的径向距离 r 有关的项在 $r \ll r_0$ 的条件下被略去了. 式(12)中的第一项为波在井外(辐射和入射)的球面波传播因子,其后的级数是以柱面波叠加表示的井内声场的径向和环向分布,级数中的振幅系数包含了井对波(辐射和入射)的调制作用. 此外,式中的径向距离 r 和方位 φ 与图 1b 中相对应,通过改变这两个参数,便可以模拟图 1b 中接收器位于井内不同位置时记录到的流体响应. 在特殊条件下,当式(12)中的 $r=0$(即接收器的偏心距为 0)时,可得到井轴处的声压和径向位移场(具体求解过程见附录 D):

$$\left.\begin{matrix} p\,|_{r=0} \\ u_r^f\,|_{r=0} \end{matrix}\right\} = \frac{\mathrm{e}^{\mathrm{i}\omega D/\beta - \mathrm{i}\pi/4}}{D} \begin{cases} \rho_f \omega^2 A_0^f \\ \dfrac{f_0}{2}(A_1^f \cos\varphi + A_1^f \sin\varphi) \end{cases}, \quad (13)$$

式(13)指出,井轴上接收到的流体声压只有单极项($n=0$)贡献,而径向位移只有偶极项($n=1$)贡献.

综上所述,利用式(12)和式(13)便可计算偶极横波远探测声场在裸眼和套管井情况下所引起的井内流体的径向位移和声压的方位响应.

2　算法对比验证及分析

我们首先利用三维有限差分法验证上述解析解的正确性,采用胶结良好的套管井模型. 计算所用的井孔及地层参数如表 1 所示,其中反射体设为地层 1 和地层 2 之间倾角为 45°的界面,位于 0°方位,虚源的径向距离为 10 m. 声源上方 1 m 处共有 8 个接收器间隔 45°环向布置,接收器的偏心距离均为 0.035 m. 声源采用中心频率为 3 kHz 的 Ricker 子波,差分模拟时的空间网格和迭代时间步长分别为 0.005 m 和 0.48 μs.

表 1　模型计算参数

Table 1　Model parameters for calculation

介质参数	纵波速度 /(m·s^{-1})	横波速度 /(m·s^{-1})	密度 /(kg·m^{-3})	外径/m
井内流体	1500	—	1000	0.070
套管	5930	3250	7500	0.080
水泥	2823	1729	1920	0.104
地层 1	4000	2300	2500	∞
地层 2	4500	3000	2600	∞
慢速地层	2074	869	2250	∞

通过将偶极声源指向 $y(x)$ 来模拟 SH(SV)横波入射,图 2 和图 3 给出了对比结果. 其中,虚线为有限差分计算的结果,实线为解析解计算的结果. 由于有限差分法模拟的是井内和井外的全波波场,而解析解式(12)只模拟了井外的反射波部分,因此图 2 和图 3 中只显示了反射横波的到时区间. 当声源指向 y 向时,产生纯 SH 入射波. 从图 2 中可以看出,无论是井内流体的径向位移(图 2a)还是声压(图 2b),采用解析解得到的渐近结果与有限差分模拟的数值结果几乎完全重合,这说明解析解是准确可靠的. 图 2 中也显示出了井中接收波形的方位特征:当接收器指向与反射体走向平行(即 90°和 270°)时,接收到的径向位移和声压的幅度最大;而当接收器指向垂直于反射面(即 0°和 180°)时,接收不到径向位移和声压;此外,x 轴上下两侧接收到的径向位移和声压的极性均反生反转. 上述分析表明,SH 横波入射引起的井内流体的径向位移和声压响

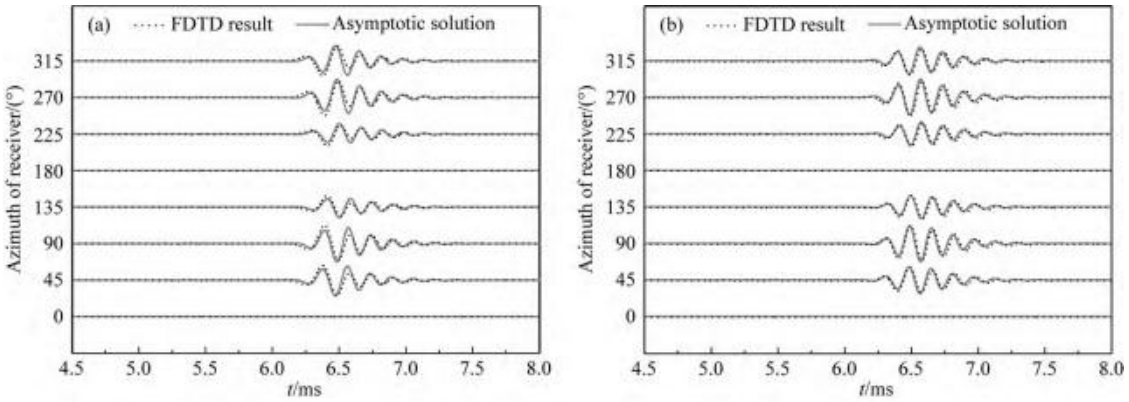


图 2　SH 横波入射引起的井内流体响应的渐近解(实线)和三维有限差分(虚线)的计算结果对比

(a) 径向位移;(b) 声压.

Fig. 2　Comparison of the borehole-fluid response calculated using the analytical solution (solid curves) and the 3D finite-difference method (dashed curves) for SH-wave incidence

(a) Radial displacement; (b) Pressure.

(C)1994-2022 China Academic Journal Electronic Publishing House. All rights reserved.　http://www.cnki.net

应对井外反射体方位的灵敏度高,且两者特征具有较好的一致性,说明在进行远探测时采用反射波中的SH分量更具优势;但该分析也表明了其存在的180°方位不确定性.

当声源指向x向时,利用解析解式(12)计算的是纯SV横波入射,但实际上声源在产生SV横波的同时还会产生P波入射,因此有限差分结果中还包含一些小振幅的P-SV和SV-P转换波(如图3中4.5～5.5 ms所示).尽管如此,图中显示两种方法计算的SV横波反射结果吻合较好.与图2中SH横波的入射结果相比,SV横波入射引起的井内流体的径向位移和声压的方位特征存在较大差异.对于径向位移而言(图3a),当接收器靠近反射体时接收到的幅度最大,当接收器指向平行于反射面(即90°和270°)时接收到的幅度最小但不为零;y轴左右两侧接收到的位移的极性反生反转.而声压(图3b)则表现出较强的方位性,靠近反射体的接收器接收到的声压幅度最大,并且不同方位接收的声压极性相同.结果表明,在进行远探测时,考虑反射波中的SV分量有助于识别井外反射体的方位.

在套管井复杂模型下所表现出的良好的吻合性,验证了解析解的正确性和普适性.然而,两种方法的计算效率相差很大,为了更准确地模拟接收器的偏心效应以及套管的影响,在三维有限差分建模中必须使用毫米级的网格尺寸,这需要花费数10 h才能完成模拟.相比之下,式(12)的解析解只需要数秒便可以得到准确的结果,为偶极横波方位远探测提供了一种快速高效的模拟方法.

为了进一步详细考察图2和图3中所示波形的方位响应特征,我们增加了接收器的个数并缩小其环向布置间隔.考虑到偶极横波反射成像中存在的180°方位不确定性问题,图4和图5的极坐标图分别给出了SH和SV横波入射时两个相反反射体方位($\varphi_0=0°,180°$)的计算结果(图中实线),其他参数与图2中相同,结果按不同方位接收波形的最大幅值进行归一化处理.如极坐标图中所示,其结果在0°～180°和180°～360°之间具有对称性,因此直角坐标系中只显示了0°～180°的结果.为了对比,同时模拟了当接收器居中时(即位于井轴上)接收的结果,如图中虚线所示.从图4中可以看出,对于SH横波入射,接收器居中时接收到的流体径向位移的方位幅值响应关于90°和270°对称,并且接收不到声压;而当接收器偏心时,接收到的径向位移和声压的幅度最大值所在方位均由90°和270°向靠近反射体一侧偏移.对于SV横波入射(图5),接收器居中时接收到的流体径向位移和声压的方位幅值响应均关于90°和270°对称,并且声压为一常数值;而接收器偏心时接收到的径向位移的幅度最小值所在方位由90°和270°向靠近反射体一侧偏移,并且靠近反射体的接收器将接收到最大幅值的径向位移和声压.接收器居中时声场响应具有的对称现象可从式(13)中得到,这种对称性正是我们所熟知的180°不确定性.相比之下,接收器偏心接收数据所展示出的非对称性对井外反射体的方位更加敏感,其方位灵敏度有助于解决180°不确定问题.

接下来我们将重点分析不同接收器偏心距、声源频率和地层类型下裸眼及套管井中接收波场的方位响应特征.

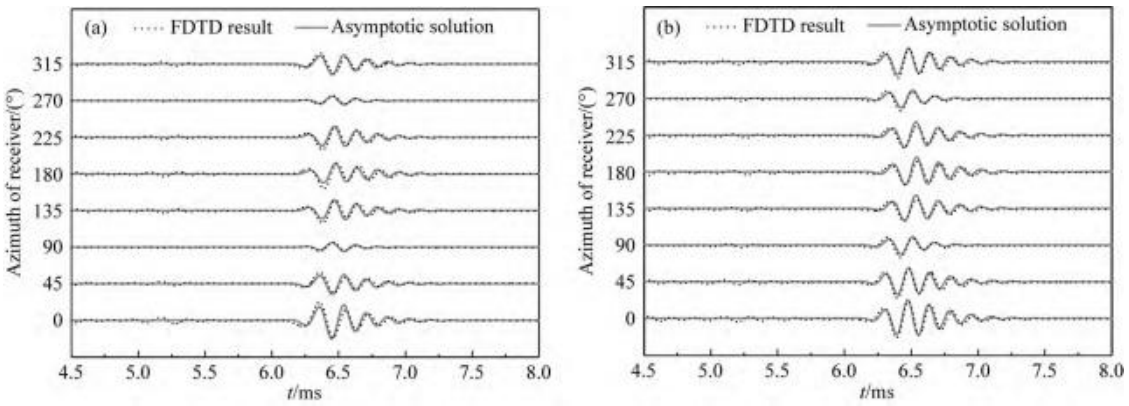


图3 SV横波入射引起的井内流体响应的渐近解(实线)和三维有限差分(虚线)的计算结果对比

(a)径向位移;(b)声压.

Fig. 3 Comparison of the borehole-fluid response calculated using the analytical solution (solid curves) and the 3D finite-difference method (dashed curves) for SV-wave incidence

(a) Radial displacement; (b) Pressure.

(C)1994-2022 China Academic Journal Electronic Publishing House. All rights reserved. http://www.cnki.net

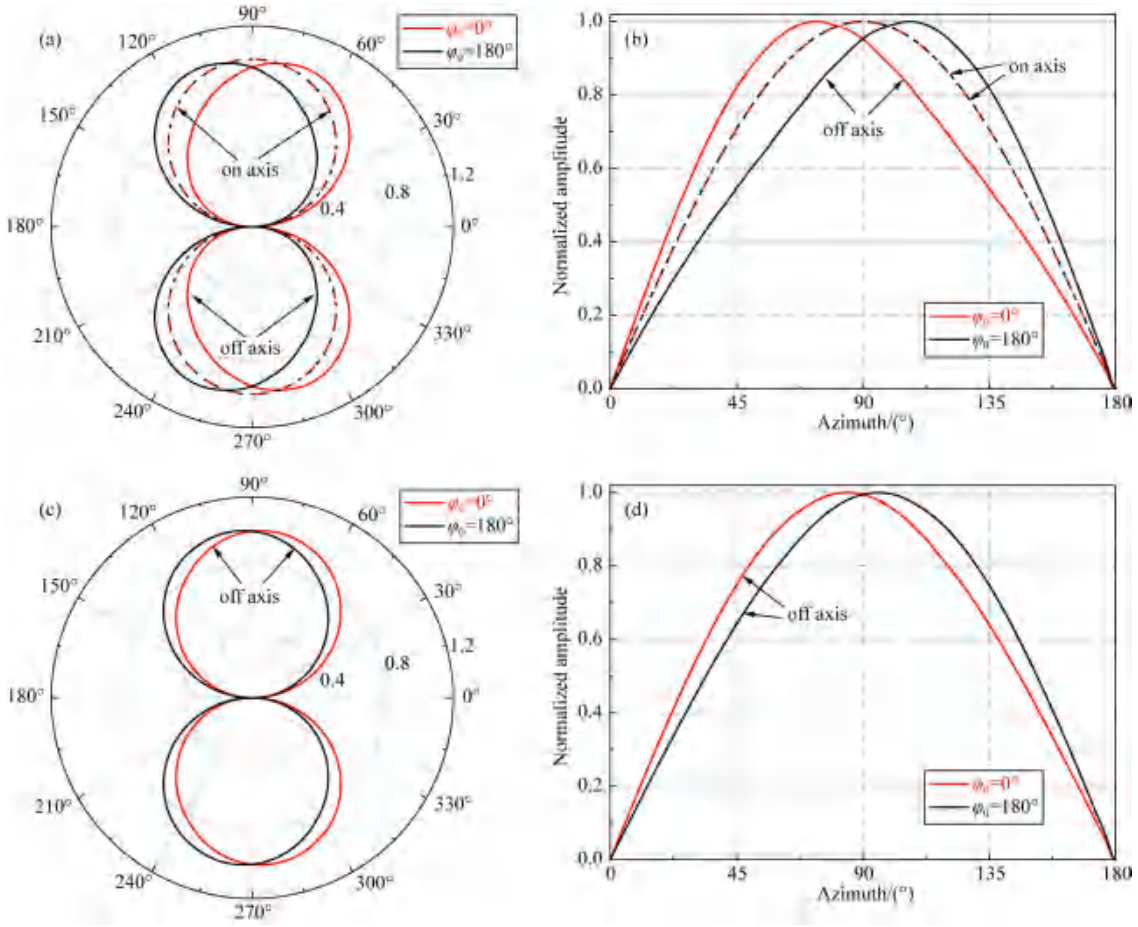


图 4　对于两个相反方位的反射体,SH 横波入射引起的井内波场的方位响应

(a)、(b) 径向位移; (c)、(d) 声压.

Fig. 4　The azimuthal response of waveforms inside borehole for SH-wave incidence for the 0° (red) and 180° (black) reflector positions. For comparison, the on-axis result (dashed curves) is also plotted (a) and (b) Radial displacement; (c) and (d) Pressure.

3　裸眼和套管井中接收波场方位响应的影响因素研究

3.1　接收器偏心距对井中接收波场的影响

图 6 和图 7 分别给出了裸眼井、自由套管和套管胶结良好情况下,SH 和 SV 横波入射时,不同偏心距接收器接收到的井内流体径向位移和声压的方位幅值响应曲线. 计算所用声源的中心频率为 3000 Hz,源距为 3 m,反射体倾角为 60°,位于 0°方位,虚源的径向距离为 30 m,井孔和地层参数见表 1(采用地层 1). 对于 0.001 m 的微小偏心距,三种情况下 SH 和 SV 横波入射引起的井内流体的径向位移响应相对于 90°方位几乎对称,与图 4 和图 5 中接收器居中接收的结果相似,此时径向位移的测量结果主要以偶极成分为主,这也说明较小的偏心距对测量结果的影响可以忽略. 随着偏心距离从 0.001 m 增加到 0.05 m,当 SH 横波入射时,裸眼井和自由套管情况下井中接收径向位移和声压的振幅最大值所在方位均逐渐偏离反射体位置,而胶结良好套管井中呈现出偏离方位相反的现象;当 SV 横波入射时,三种情况下井中接收径向位移的振幅最小值所在方位均逐渐靠近反射体位置,并且其振幅最小值随着偏心距的增加而逐渐增大. 此外,SV 横波入射时井内声压的振幅最大值所在方位不受接收器偏心距的影响,但受井类型的影响,在裸眼井和胶结良好套管井中,靠近反射体一侧的接收器接收到的声压幅值最大,而在自由套管中则是远离反射体一侧的接收器将接收到最大幅值的声压. 值得注意的是,虽然加套管之后井中方位接收响应的变化规律不尽相同,但与裸眼井情况相比,自由套管和套管胶结良好时井中接收波场的方位响应受接收器偏心距的影响更大,说明套管井中的波场响应对井外反射体方位的灵敏度更高.

(C)1994-2022 China Academic Journal Electronic Publishing House. All rights reserved.　http://www.cnki.net

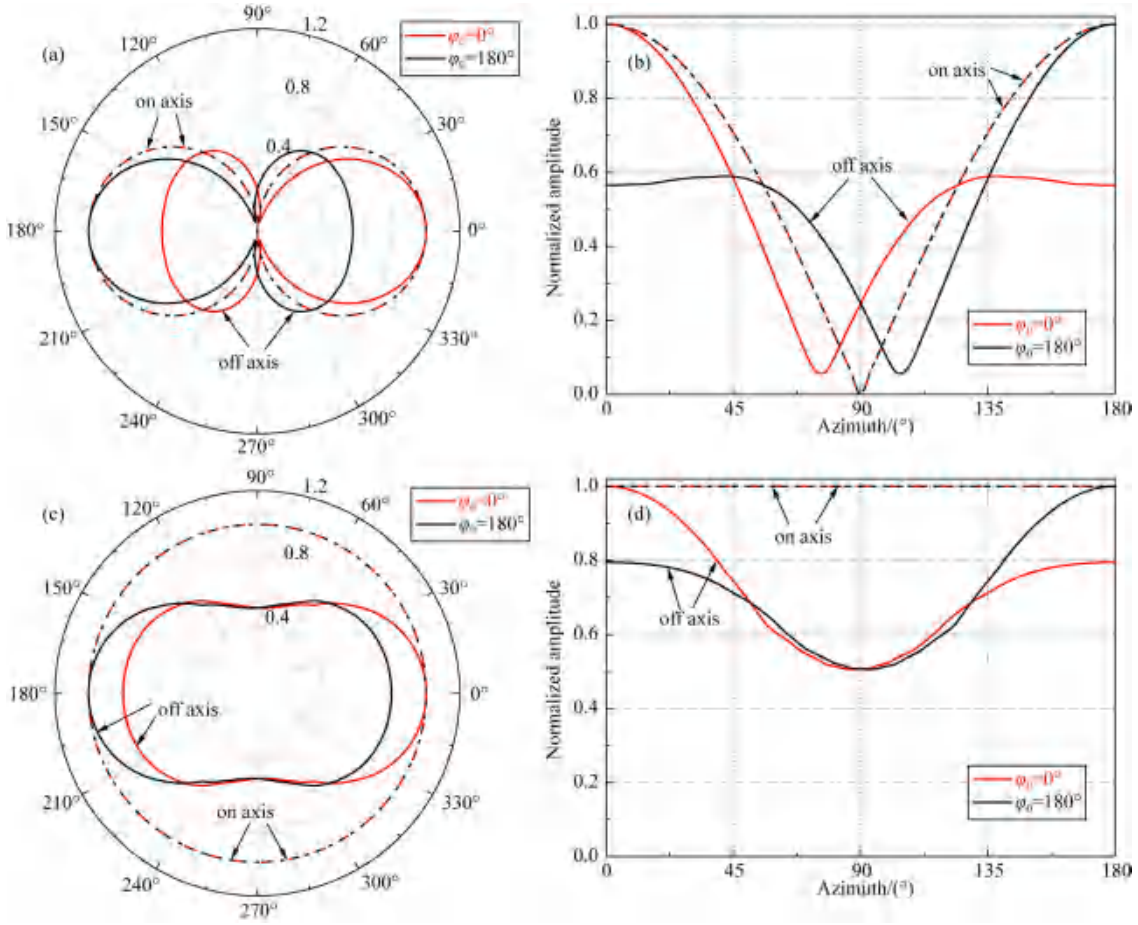


图 5 对于两个相反方位的反射体,SV 横波入射引起的井内波场的方位响应

(a)、(b) 径向位移; (c)、(d) 声压.

Fig. 5 The azimuthal response of waveforms inside borehole for SV-wave incidence for the 0° (red) and 180° (black) reflector positions. For comparison, the on-axis result (dashed curves) is also plotted

(a) and (b) Radial displacement; (c) and (d) Pressure.

3.2 声源频率对井中接收波场的影响

图 8 和图 9 是声源频率变化时,SH 和 SV 横波入射到裸眼井、自由套管和胶结良好套管井中引起的井内流体的径向位移和声压的方位幅值响应曲线. 计算时接收器的偏心距离为 0.035 m,其他参数与图 6 中相同. 从图中可看出,对于 100 Hz 的低频情况,SH 和 SV 横波入射引起的井内流体的径向位移响应相对于 90°方位几乎对称. 这是因为频率非常低时,声波波长远大于井径,使井孔的调制作用明显减弱,说明低频时可忽略接收器的偏心效应. 随着频率从 100 Hz 增加到 5000 Hz,当 SH 横波入射时,自由套管和胶结良好情况下井中接收径向位移和声压的振幅最大值所在方位均先靠近后偏离反射体位置,但在裸眼井情况下则表现出先靠近后偏离再靠近反射体位置的现象. 当 SV 横波入射时,随着频率增加,三种情况下井中接收径向位移和声压的方位响应较为复杂,其幅度最大值所在方位发生了 180°反转. 并且某些频率下,声压最大值所在方位既不位于靠近反射体一侧,也不位于远离反射体一侧(比如裸眼井在 500 Hz 和 1000 Hz 时,以及胶结良好套管井在 500 Hz、1000 Hz 和 2000 Hz 时). 上述结果表明,虽然声源频率能够显著改变井内接收波场的方位响应特征,但方位响应随频率呈复杂变化.

3.3 地层类型对井中接收波场的影响

除了接收器偏心距和声源频率外,地层类型也会影响井中接收波场的方位响应. 图 10 和图 11 对比了快速和慢速地层条件下,SH 和 SV 横波入射到裸眼井、自由套管和胶结良好套管井中引起的井内流体的径向位移和声压的方位幅值响应. 计算时接收器的偏心距为 0.035 m,声源主频为 3000 Hz,其他参数与图 6 中相同. 从图 10 中可以看出,当 SH 横波入射时,裸眼井和自由套管井中流体径向位移和声压的振幅最大值所在方位在快速地层条件下均由 90°向远离反射体一侧偏移,而在慢速地层中均

(C)1994-2022 China Academic Journal Electronic Publishing House. All rights reserved. http://www.cnki.net

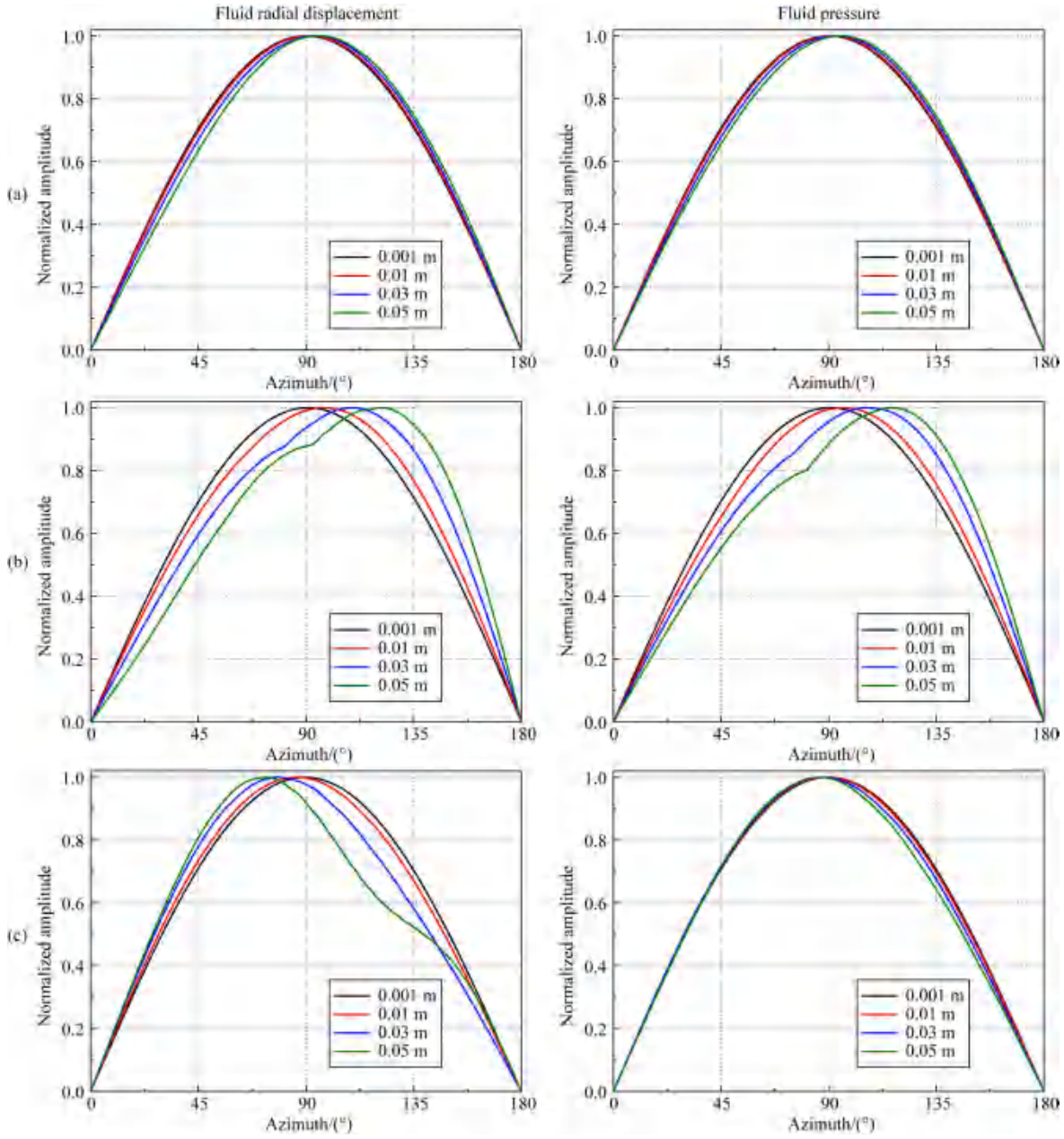


图 6　快速地层条件下，SH 横波入射时，不同偏心距接收器接收到的井内波场的方位响应

(a) 裸眼井；(b) 自由套管；(c) 胶结良好.

Fig. 6　The azimuthal response of waveforms inside borehole received by receivers with different eccentric distances for SH-wave incidence in the fast formation

(a) Open hole; (b) Cased hole with free pipe; (c) Cased hole with good bonding.

向靠近反射体一侧偏移，呈现出相反的现象；在快速和慢速地层条件下，胶结良好时的结果均由 90°向靠近反射体一侧偏移. 当 SV 横波入射时(图 11)，无论在快速还是慢速地层中，三种情况下井中流体径向位移的振幅最小值所在方位的变化趋势相同，均由 90°向靠近反射体一侧偏移，并且靠近反射体的接收器将接收到最大幅值的径向位移；相对于快速地层，在慢速地层中三种情况下的声压方位响应均反生 180°反转. 上述分析表明，当根据井内接收波场的幅值信息对井外反射体进行方位识别时，需要考虑地层性质的影响.

4　井中声场方位幅值响应反转现象的正确性验证

上一节研究了偶极横波远探测在裸眼和套管

(C)1994-2022 China Academic Journal Electronic Publishing House. All rights reserved.　http://www.cnki.net

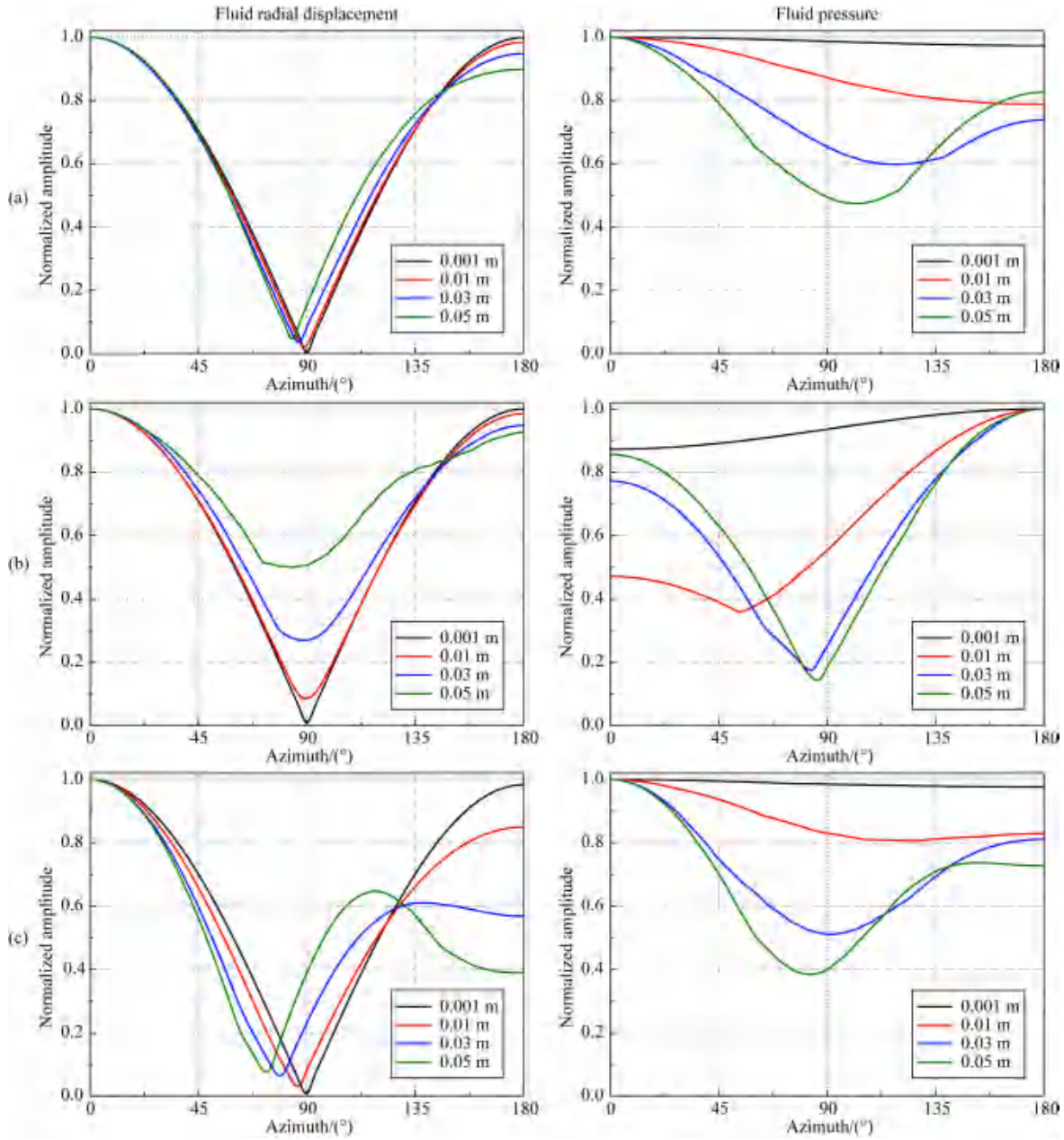


图 7 快速地层条件下,SV 横波入射时,不同偏心距接收器接收到的井内波场的方位响应

(a) 裸眼井;(b) 自由套管;(c) 胶结良好.

Fig. 7 The azimuthal response of waveforms inside borehole received by receivers with different eccentric distances for SV-wave incidence in the fast formation

(a) Open hole; (b) Cased hole with free pipe; (c) Cased hole with good bonding.

井中接收波场的方位响应特征,我们注意到对于不同的模型参数,井中接收波场的方位幅值特征存在较大差异,在某些情况下甚至会出现相反的现象,过去文献中鲜有类似报道. 为了证实这一现象,以 SV 横波入射到裸眼井中为例,进一步通过三维有限差分法模拟不同频率下井中接收波场的方位响应特征. 差分模拟时声源上方共有 32 个接收器等间隔环向布置,其他参数与图 3 中相同. 考虑声源频率为 1500 Hz 和 4000 Hz 两种情况,三维有限差分的计算结果分别如图 12 中圆圈和三角形标记所示,其中图 12a、b 分别为流体径向位移和声压的方位响应. 为了对比,图中同时给出了利用式(12)得到的解析结果(实线和虚线). 从图中可以看出,无论频率为 1500 Hz 还是 4000 Hz 时,两种方法计算得到的流体径向位移和声压的方位响应结果均吻合较好. 此外,在不同频率下,两种方法均显示出了相反的结果:当频率为 1500 Hz 时,靠近(远离)反射体一侧的接收器接收到的径向

(C)1994-2022 China Academic Journal Electronic Publishing House. All rights reserved. http://www.cnki.net

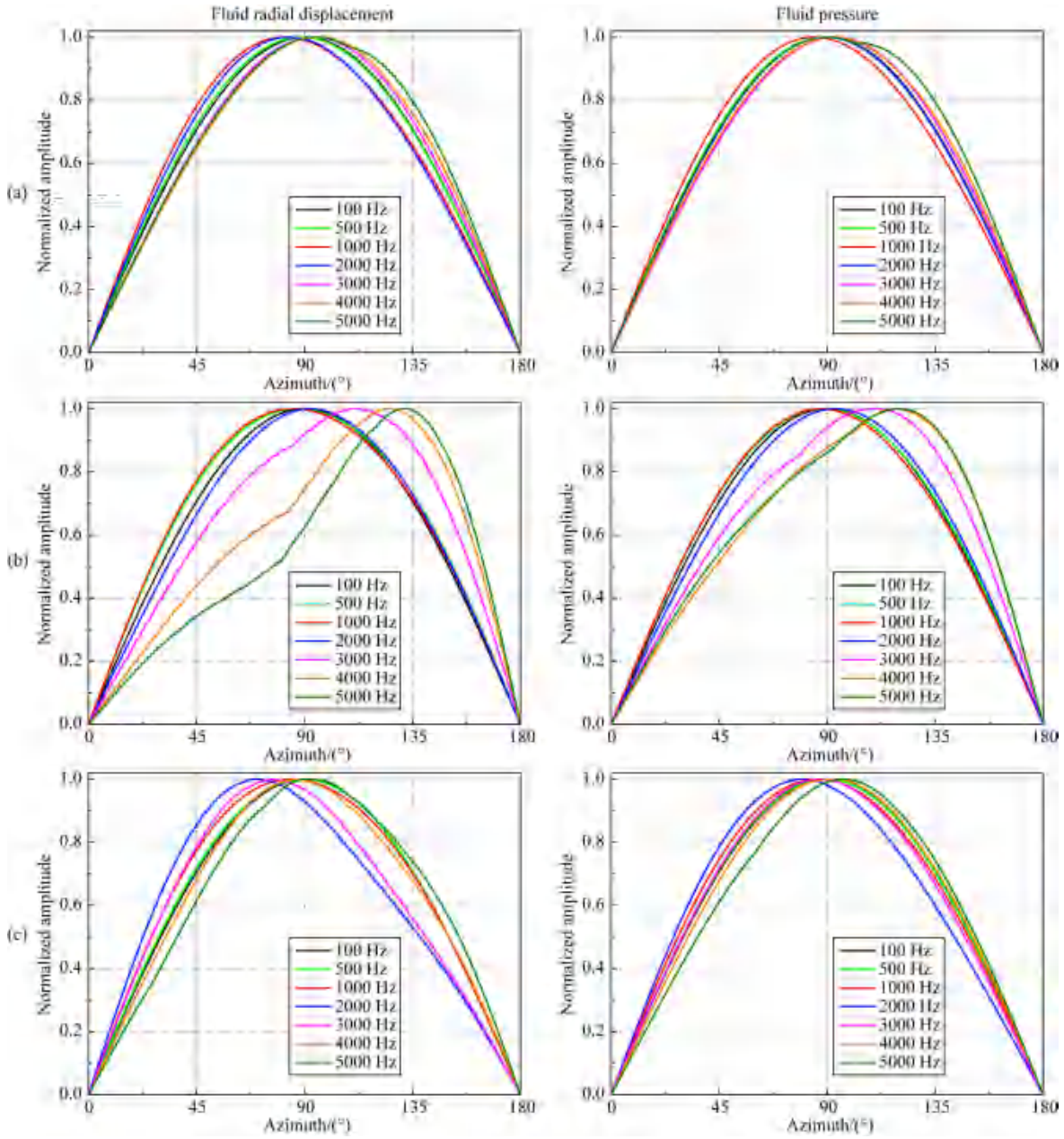


图 8　快速地层条件下,声源频率不同时,SH 横波入射引起的井内波场的方位响应

(a) 裸眼井;(b) 自由套管;(c) 胶结良好.

Fig. 8　The azimuthal response of waveforms inside borehole at different frequencies for SH-wave incidence in the fast formation

(a) Open hole; (b) Cased hole with free pipe; (c) Cased hole with good bonding.

位移(声压)幅值最大;而当频率为 4000 Hz 时,则是远离(靠近)反射体一侧的接收器将接收到最大幅值的径向位移(声压). 三维有限差分计算结果证实了方位幅值响应存在 180°反转现象,指示利用井中接收波场幅值特征进行井外反射体方位识别时需要考虑接收器偏心距、声源频率和地层性质等因素的影响,这对于仪器研制和现场解释具有重要的指导意义.

5　结论

本文采用解析法和三维有限差分法对偶极横波远探测在裸眼和套管井中接收波场的方位响应特征进行了研究,得到以下认识和结论:

(1)结合虚源和球面波的柱面波展开,采用最速下降法得到了充液裸眼和套管井中偶极横波方位远

(C)1994-2022 China Academic Journal Electronic Publishing House. All rights reserved.　http://www.cnki.net

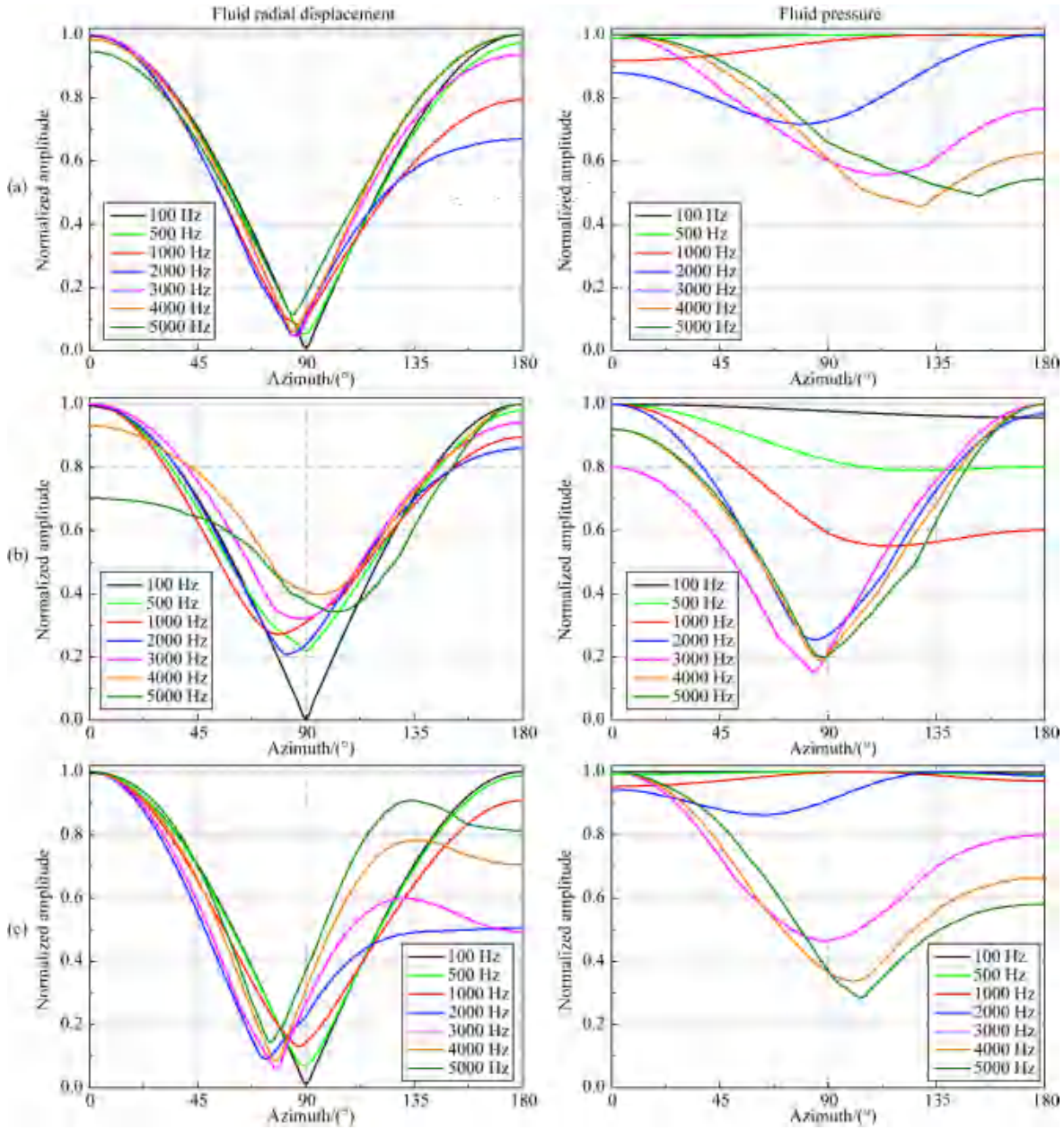


图 9 快速地层条件下,声源频率不同时,SV 横波入射引起的井内波场的方位响应

(a) 裸眼井;(b) 自由套管;(c) 胶结良好.

Fig. 9 The azimuthal response of waveforms inside borehole at different frequencies for SV-wave incidence in the fast formation

(a) Open hole; (b) Cased hole with free pipe; (c) Cased hole with good bonding.

探测接收波场的渐近解析解. 通过解析法和三维有限差分法对套管井中方位接收波场的模拟对比,验证了渐近解的正确性和普适性.

(2)SH 横波入射引起的井内流体的径向位移和声压的方位响应特征具有较好的一致性,而 SV 横波入射时二者特征却存在较大差异. 值得注意的是,SV 横波入射时,井内波场的方位幅值响应对井外反射体位置具有唯一性,即在常用偶极测井频率下,靠近或远离反射体的接收器接收到的波形幅值最大. 这表明在进行声波远探测成像解释时,考虑井内接收信号中的 SV 分量有助于识别井外反射体的方位,但需要注意接收换能器记录的信号类型(径向位移/声压)的不同响应.

(3)偶极横波远探测井内接收波场的方位响应特征受井眼环境、接收器偏心距、声源频率和地层性质等多个因素的影响,在不同参数下方位幅值响应甚至会出现反转现象,渐近解析解和三维有限差分数值解的结果对比证实了这一现象,实际数据解释

(C)1994-2022 China Academic Journal Electronic Publishing House. All rights reserved. http://www.cnki.net

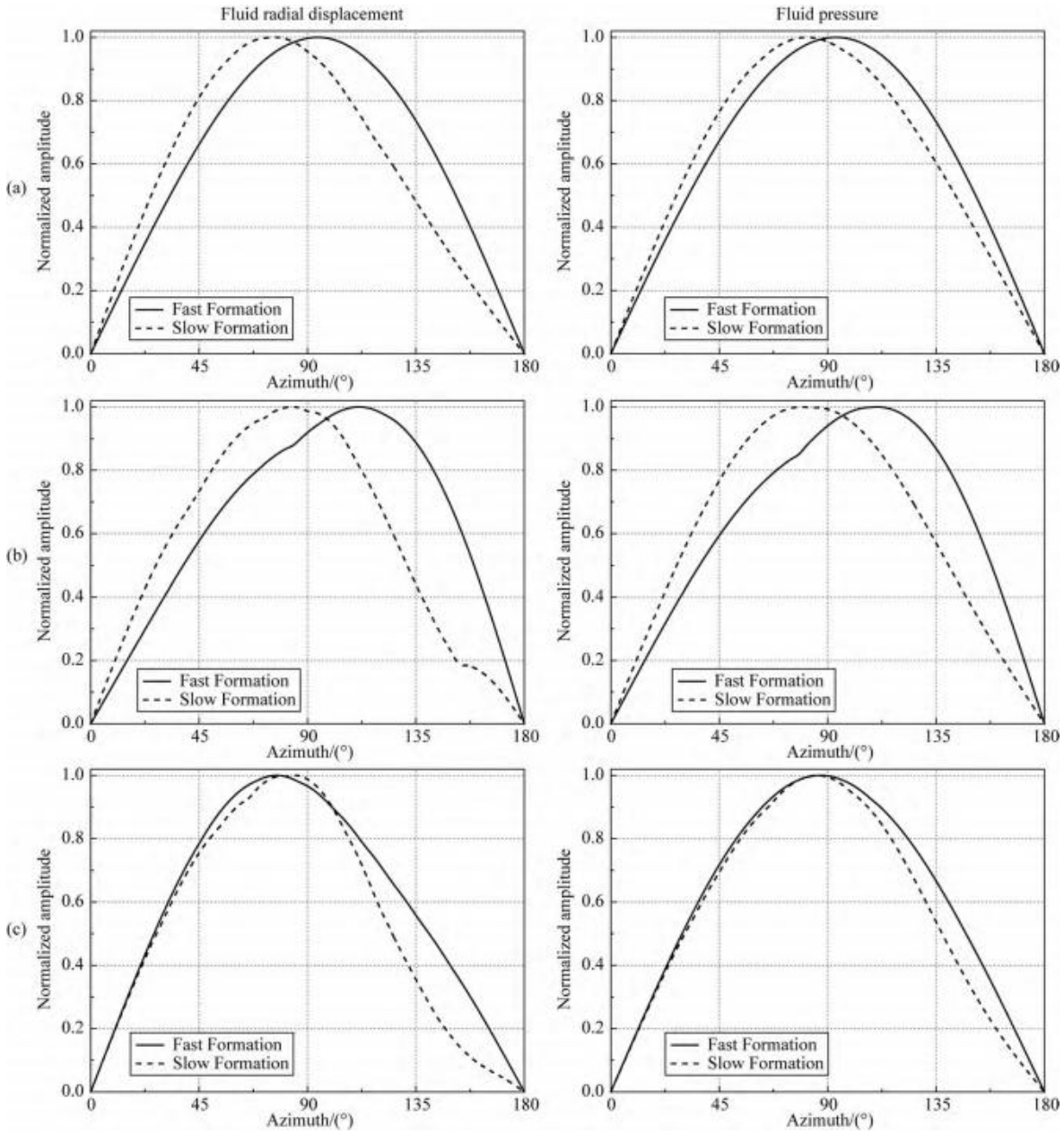


图 10　快速和慢速地层条件下,SH 横波入射引起的井内波场的方位响应

(a) 裸眼井;(b) 自由套管;(c) 胶结良好.

Fig. 10　The azimuthal response of waveforms inside borehole for SH-wave incidence in the fast and slow formations

(a) Open hole; (b) Cased hole with free pipe; (c) Cased hole with good bonding.

时需要考虑这些因素的影响.此外,在影响井内声场方位响应的众多因素当中,最重要的主控因素是接收器偏心距.正是由于偏心接收才有文中不同于偶极 180°对称性的变化现象(即图 4—图 12 所示结果),其物理实质是声场在偏离井心位置上的复杂三维变化;而居中时三维变化就降到了二维,复杂性减少但(180°)对称现象出现.

(4)相对于裸眼井,套管井中接收波场的方位响应对井外反射体位置的灵敏度更高,受接收器偏心距、声源频率和地层性质的影响也更大,说明在套管井中进行偶极横波方位远探测更有利于井外反射体的方位识别.

(5)现有的偶极横波测井仪将仪器两侧的接收换能器记录的信号之差作为测量信号,此时无论换能器记录的是流体径向位移还是声压,相减后的测量信号中都主要包含偶极成分,可以得到反射体的走向信息;接收器的偏心效应包含了反射体的倾向信息,有助于解决偶极横波远探测方位的 180°不确定性问题.

(C)1994-2022 China Academic Journal Electronic Publishing House. All rights reserved.　http://www.cnki.net

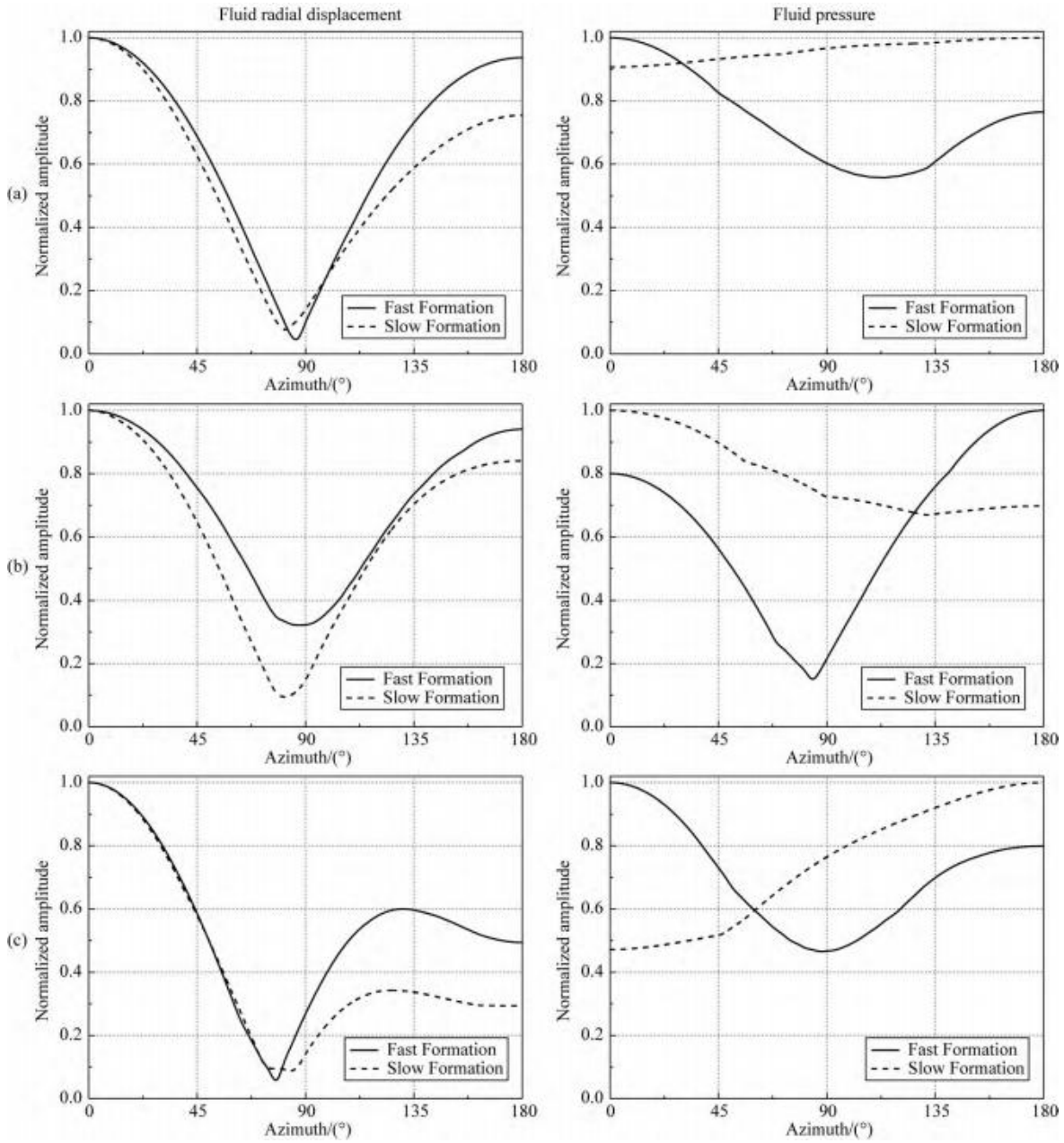


图 11 快速和慢速地层条件下,SV 横波入射引起的井内波场的方位响应

(a) **裸眼井**;(b) **自由套管**;(c) **胶结良好**.

Fig. 11 The azimuthal response of waveforms inside borehole for SV-wave incidence in the fast and slow formations

(a) Open hole; (b) Cased hole with free pipe; (c) Cased hole with good bonding.

附录 A 裸眼井情况下矩阵方程中的元素表达式

矩阵 M 中各元素的具体表达式为:

$$M_{11} = -nI_n(fa)/a - fI_{n+1}(fa),$$

$$M_{12} = nK_n(pa)/a - pK_{n+1}(pa),$$

$$M_{13} = nK_n(sa)/a,$$

$$M_{14} = \mathrm{i}k[nK_n(sa)/a - sK_{n+1}(sa)],$$

$$M_{21} = \rho_f\omega^2 I_n(fa),$$

$$M_{22} = 2\rho\beta^2[(n^2-n)K_n(pa)/a^2 + pK_{n+1}(pa)/a] + \rho(2k^2\beta^2-\omega^2)K_n(pa),$$

$$M_{23} = 2n\rho\beta^2[(n-1)K_n(sa)/a^2 - sK_{n+1}(sa)/a],$$

$$M_{24} = 2\mathrm{i}k\rho\beta^2\{[(n^2-n)/a^2 + s^2]K_n(sa) + sK_{n+1}(sa)/a\},$$

$$M_{31} = 0,$$

$$M_{32} = 2n\rho\beta^2[(1-n)K_n(pa)/a^2 + pK_{n+1}(pa)/a],$$

$$M_{33} = -\rho\beta^2\{[2(n^2-n)/a^2 + s^2]K_n(sa) + 2sK_{n+1}(sa)/a\},$$

$$M_{34} = 2\mathrm{i}kn\rho\beta^2[(1-n)K_n(sa)/a^2 + sK_{n+1}(sa)/a],$$

(C)1994-2022 China Academic Journal Electronic Publishing House. All rights reserved. http://www.cnki.net

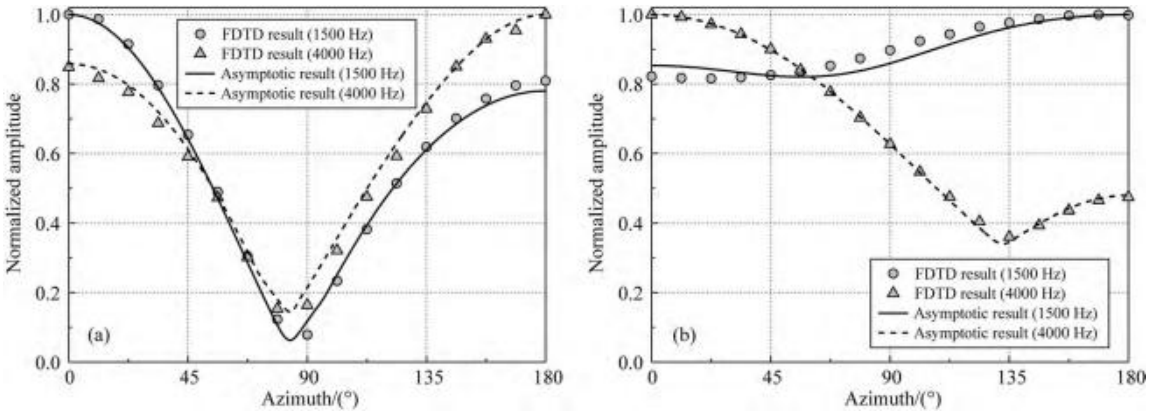


图 12　快速地层条件下,声源频率为 1500 Hz 和 4000 Hz 时,SV 横波入射引起的井中接收波场的方位响应

(a) 径向位移;(b) 声压.为了对比,同时给出了渐近解(曲线)和三维有限差分(标记)的计算结果.

Fig. 12　The azimuthal response of waveforms inside borehole at frequencies 1500 Hz and 4000 Hz for SV-wave incidence in the fast formation

(a) Radial displacement; (b) Pressure. The curves and circles are calculated using analytical (curves) and 3D finite-difference (markers) modeling, respectively.

$$
\begin{aligned}
M_{41} &= 0,\\
M_{42} &= 2\mathrm{i}k\rho\beta^2[nK_n(pa)/a - pK_{n+1}(pa)],\\
M_{43} &= \mathrm{i}kn\rho\beta^2 K_n(sa)/a.\\
M_{44} &= -(s^2+k^2)\rho\beta^2[nK_n(sa)/a - sK_{n+1}(sa)].
\end{aligned}
\tag{A1}
$$

向量 b 和 b' 中的元素由于入射波的类型不同而有所区别.当 SH 横波入射时,向量 b 和 b' 中各元素的具体表达式为(省略公共因子 $S(\omega)\cdot RD_{\mathrm{SH}}(\omega)\cdot RF_{\mathrm{SH}}(\omega)$):

$$
\begin{aligned}
b_1 &= -n\varepsilon_n I_n(sa)\sin(n\varphi_0)/a,\\
b_2 &= -2n\varepsilon_n\rho\beta^2[(n-1)I_n(sa)/a^2 + sI_{n+1}(sa)/a]\sin(n\varphi_0),\\
b_3 &= \varepsilon_n\rho\beta^2\{[2(n^2-n)/a^2+s^2]I_n(sa) - 2sI_{n+1}(sa)/a\}\sin(n\varphi_0),\\
b_4 &= -\mathrm{i}kn\varepsilon_n\rho\beta^2 I_n(sa)\sin(n\varphi_0)/a,\\
b'_1 &= n\varepsilon_n I_n(sa)\cos(n\varphi_0)/a,\\
b'_2 &= 2n\varepsilon_n\rho\beta^2[(n-1)I_n(sa)/a^2 + sI_{n+1}(sa)/a]\times\cos(n\varphi_0),\\
b'_3 &= -\varepsilon_n\rho\beta^2\{[2(n^2-n)/a^2+s^2]I_n(sa) - 2sI_{n+1}(sa)/a\}\cos(n\varphi_0),\\
b'_4 &= \mathrm{i}kn\varepsilon_n\rho\beta^2 I_n(sa)\cos(n\varphi_0)/a.
\end{aligned}
\tag{A2}
$$

当 SV 横波入射时,向量 b 和 b' 中各元素的具体表达式为(省略公共因子 $S(\omega)\cdot RD_{\mathrm{SV}}(\omega)\cdot RF_{\mathrm{SV}}(\omega)$):

$$
\begin{aligned}
b_1 &= -\mathrm{i}k\varepsilon_n[nI_n(sa)/a + sI_{n+1}(sa)]\cos(n\varphi_0),\\
b_2 &= -2\mathrm{i}k\varepsilon_n\rho\beta^2\{[(n^2-n)/a^2+s^2]I_n(sa) - sI_{n+1}(sa)/a\}\cos(n\varphi_0),\\
b_3 &= -2\mathrm{i}kn\varepsilon_n\rho\beta^2[(1-n)I_n(sa)/a^2 - sI_{n+1}(sa)/a]\times\cos(n\varphi_0),\\
b_4 &= \varepsilon_n(s^2+k^2)\rho\beta^2[nI_n(sa)/a + sI_{n+1}(sa)]\cos(n\varphi_0),\\
b'_1 &= -\mathrm{i}k\varepsilon_n[nI_n(sa)/a + sI_{n+1}(sa)]\sin(n\varphi_0),\\
b'_2 &= -2\mathrm{i}k\varepsilon_n\rho\beta^2\{[(n^2-n)/a^2+s^2]I_n(sa) - sI_{n+1}(sa)/a\}\sin(n\varphi_0),\\
b'_3 &= -2\mathrm{i}kn\varepsilon_n\rho\beta^2[(1-n)I_n(sa)/a^2 - sI_{n+1}(sa)/a]\sin(n\varphi_0),\\
b'_4 &= \varepsilon_n(s^2+k^2)\rho\beta^2[nI_n(sa)/a + sI_{n+1}(sa)]\sin(n\varphi_0),
\end{aligned}
\tag{A3}
$$

其中,a 为井孔半径;I_n 和 K_n 分别为第一类和第二类 n 阶变型贝塞尔函数;k 为轴向波数,f、p 和 s 分别为流体纵波、地层纵波和横波的径向波数,且 $f=(k^2-\omega^2/\alpha_f^2)^{1/2}$、$p=(k^2-\omega^2/\alpha^2)^{1/2}$、$s=(k^2-\omega^2/\beta^2)^{1/2}$;$\rho_f$ 和 ρ 分别为流体和地层密度;α_f、α 和 β 分别为流体纵波、地层纵波和横波速度;ω 为圆频率;φ_0 为反射体方位;ε_n 是纽曼因子,$n=0$ 时 $\varepsilon_n=1$,$n>0$ 时 $\varepsilon_n=2$;S 为声源函数谱;RD 为辐射函数,RF 为反射系数,下标 SH/SV 代表按照 SH/SV 横波进行计算;需要注意对于裸眼井和套管井,RD 有所不同(曹景记等, 2014).实际计算时将上述中的所有 k 都替换为最速下降解 k_0(下同).

附录 B　套管井(胶结良好)情况下 T 矩阵的元素表达式

T 矩阵的元素表达式为:

$$
\begin{aligned}
T_{11} &= nI_n(pR)/R + pI_{n+1}(pR),\\
T_{12} &= nK_n(pR)/R - pK_{n+1}(pR),\\
T_{13} &= nI_n(sR)/R,\\
T_{14} &= nK_n(sR)/R,
\end{aligned}
$$

(C)1994-2022 China Academic Journal Electronic Publishing House. All rights reserved.　http://www.cnki.net

$$
\begin{aligned}
T_{15} &= \mathrm{i}k[nI_n(sR)/R + sI_{n+1}(sR)],\\
T_{16} &= \mathrm{i}k[nK_n(sR)/R - sK_{n+1}(sR)],\\
T_{21} &= -nI_n(pR)/R,\\
T_{22} &= -nK_n(pR)/R,\\
T_{23} &= -nI_n(sR)/R - sI_{n+1}(sR),\\
T_{24} &= -nK_n(sR)/R + sK_{n+1}(sR),\\
T_{25} &= -\mathrm{i}knI_n(sR)/R,\\
T_{26} &= -\mathrm{i}knK_n(sR)/R,\\
T_{31} &= \mathrm{i}kI_n(pR),\\
T_{32} &= \mathrm{i}kK_n(pR),\\
T_{33} &= 0,\\
T_{34} &= 0,\\
T_{35} &= -s^2 I_n(sR),\\
T_{36} &= -s^2 K_n(sR),\\
T_{41} &= 2\rho\beta^2[(n^2-n)I_n(pR)/R^2 - pI_{n+1}(pR)/R]\\
&\quad + \rho(2k^2\beta^2-\omega^2)I_n(pR),\\
T_{42} &= 2\rho\beta^2[(n^2-n)K_n(pR)/R^2 + pK_{n+1}(pR)/R]\\
&\quad + \rho(2k^2\beta^2-\omega^2)K_n(pR),\\
T_{43} &= 2n\rho\beta^2[(n-1)I_n(sR)/R^2 + sI_{n+1}(sR)/R],\\
T_{44} &= 2n\rho\beta^2[(n-1)K_n(sR)/R^2 - sK_{n+1}(sR)/R],\\
T_{45} &= 2\mathrm{i}k\rho\beta^2\{[(n^2-n)/R^2 + s^2]I_n(sR)\\
&\quad - sI_{n+1}(sR)/R\},\\
T_{46} &= 2\mathrm{i}k\rho\beta^2\{[(n^2-n)/R^2 + s^2]K_n(sR)\\
&\quad + sK_{n+1}(sR)/R\},\\
T_{51} &= 2n\rho\beta^2[(1-n)I_n(pR)/R^2 - pI_{n+1}(pR)/R],\\
T_{52} &= 2n\rho\beta^2[(1-n)K_n(pR)/R^2 + pK_{n+1}(pR)/R],\\
T_{53} &= -\rho\beta^2\{[2(n^2-n)/R^2 + s^2]I_n(sR)\\
&\quad - 2sI_{n+1}(sR)/R\},\\
T_{54} &= -\rho\beta^2\{[2(n^2-n)/R^2 + s^2]K_n(sR)\\
&\quad + 2sK_{n+1}(sR)/R\},\\
T_{55} &= 2\mathrm{i}kn\rho\beta^2[(1-n)I_n(sR)/R^2 - sI_{n+1}(sR)/R],\\
T_{56} &= 2\mathrm{i}kn\rho\beta^2[(1-n)K_n(sR)/R^2 + sK_{n+1}(sR)/R],\\
T_{61} &= 2\mathrm{i}k\rho\beta^2[nI_n(pR)/R + pI_{n+1}(pR)],\\
T_{62} &= 2\mathrm{i}k\rho\beta^2[nK_n(pR)/R - pK_{n+1}(pR)],\\
T_{63} &= \mathrm{i}kn\rho\beta^2 I_n(sR)/R,\\
T_{64} &= \mathrm{i}kn\rho\beta^2 K_n(sR)/R,\\
T_{65} &= -(s^2+k^2)\rho\beta^2[nI_n(sR)/R + sI_{n+1}(sR)],\\
T_{66} &= -(s^2+k^2)\rho\beta^2[nK_n(sR)/R - sK_{n+1}(sR)]. \qquad \text{(B1)}
\end{aligned}
$$

附录 C 套管井(自由套管)情况下矩阵方程中的元素表达式

矩阵 $\boldsymbol{H}$ 中各元素的具体表达式为(未列出的元素取值为 0):

$$
\begin{aligned}
H_{11} &= -nI_n(fr_1)/r_1 - fI_{n+1}(fr_1),\\
H_{12} &= T^{r_1}_{11},\ H_{13} = T^{r_1}_{12},\ H_{14} = T^{r_1}_{13},\ H_{15} = T^{r_1}_{14},\\
H_{16} &= T^{r_1}_{15},\ H_{17} = T^{r_1}_{16},\\
H_{21} &= \rho_f\omega^2 I_n(fr_1),\ H_{22} = T^{r_1}_{41},\ H_{23} = T^{r_1}_{42},\\
H_{24} &= T^{r_1}_{43},\ H_{25} = T^{r_1}_{44},\ H_{26} = T^{r_1}_{45},\ H_{27} = T^{r_1}_{46},\\
H_{32} &= T^{r_1}_{51},\ H_{33} = T^{r_1}_{52},\ H_{34} = T^{r_1}_{53},\ H_{35} = T^{r_1}_{54},\\
H_{36} &= T^{r_1}_{55},\ H_{37} = T^{r_1}_{56},\\
H_{42} &= T^{r_1}_{61},\ H_{43} = T^{r_1}_{62},\ H_{44} = T^{r_1}_{63},\ H_{45} = T^{r_1}_{64},\\
H_{46} &= T^{r_1}_{65},\ H_{47} = T^{r_1}_{66},\\
H_{52} &= T^{r_2}_{11},\ H_{53} = T^{r_2}_{12},\ H_{54} = T^{r_2}_{13},\ H_{55} = T^{r_2}_{14},\\
H_{56} &= T^{r_2}_{15},\ H_{57} = T^{r_2}_{16},\\
H_{58} &= -nI_n(fr_2)/r_2 - fI_{n+1}(fr_2),\\
H_{59} &= -nK_n(fr_2)/r_2 + fK_{n+1}(fr_2),\\
H_{62} &= T^{r_2}_{41},\ H_{63} = T^{r_2}_{42},\ H_{64} = T^{r_2}_{43},\ H_{65} = T^{r_2}_{44},\\
H_{66} &= T^{r_2}_{45},\ H_{67} = T^{r_2}_{46},\ H_{68} = \rho_f\omega^2 I_n(fr_2),\\
H_{69} &= \rho_f\omega^2 K_n(fr_2),\\
H_{72} &= T^{r_2}_{51},\ H_{73} = T^{r_2}_{52},\ H_{74} = T^{r_2}_{53},\ H_{75} = T^{r_2}_{54},\\
H_{76} &= T^{r_2}_{55},\ H_{77} = T^{r_2}_{56},\\
H_{82} &= T^{r_2}_{61},\ H_{83} = T^{r_2}_{62},\ H_{84} = T^{r_2}_{63},\ H_{85} = T^{r_2}_{64},\\
H_{86} &= T^{r_2}_{65},\ H_{87} = T^{r_2}_{66},\\
H_{98} &= -nI_n(fa)/a - fI_{n+1}(fa),\\
H_{99} &= -nK_n(fa)/a + fK_{n+1}(fa),\\
H_{9,10} &= T^{a}_{12},\ H_{9,11} = T^{a}_{14},\ H_{9,12} = T^{a}_{16},\\
H_{10,8} &= \rho_f\omega^2 I_n(fa),\ H_{10,9} = \rho_f\omega^2 K_n(fa),\\
H_{10,10} &= T^{a}_{42},\ H_{10,11} = T^{a}_{44},\ H_{10,12} = T^{a}_{46},\\
H_{11,10} &= T^{a}_{52},\ H_{11,11} = T^{a}_{54},\ H_{11,12} = T^{a}_{56},\\
H_{12,10} &= T^{a}_{62},\ H_{12,11} = T^{a}_{64},\ H_{12,12} = T^{a}_{66}, \qquad \text{(C1)}
\end{aligned}
$$

其中,r_1 和 r_2 分别为套管的内半径和外半径;T 的右上标表示计算时半径 R 的取值.

根据入射波类型的不同(即 SH 或 SV 横波入射),向量 $\boldsymbol{d}$ 和 $\boldsymbol{d}'$ 中的元素也有所区别,其各元素的具体表达式为(未列出的元素取值为 0):

$$
\begin{aligned}
d_9 &= b_1,\ d_{10} = b_2,\ d_{11} = b_3,\ d_{12} = b_4,\\
d'_9 &= b'_1,\ d'_{10} = b'_2,\ d'_{11} = b'_3,\ d'_{12} = b'_4. \qquad \text{(C2)}
\end{aligned}
$$

附录 D 井轴处的声压和径向位移

首先求解井轴处的声压,第一类变型贝塞尔函数具有如下性质:

$$
I_n(0) = \begin{cases} 1, & n = 0 \\ 0, & n \neq 0 \end{cases}, \qquad \text{(D1)}
$$

其中,n 为阶数. 接收器位于井轴时,式(12)中的 $r=0$,由式(D1)可知,此时声压的多极响应中只有 $n=0$

(C)1994-2022 China Academic Journal Electronic Publishing House. All rights reserved. http://www.cnki.net

这一项有值,其余全为 0,表达式为:

$$p\,|_{r=0} = \frac{e^{i\omega D'/\beta - i\pi/4}}{D'}\rho_f\omega^2 A_0^f. \quad (D2)$$

进一步,联系附录 A 中向量 b 的表达式可知:对于 SH 横波入射,$A_0^f = 0$,因此井轴上接收不到声压;而对于 SV 横波入射,$A_0^f \neq 0$,井轴上接收的声压不为 0.

求解井轴处的径向位移时,需要用到第一类变型贝塞尔函数的递推公式:

$$I_n(x) = \frac{x}{2n}[I_{n-1}(x) - I_{n+1}(x)], \quad (D3)$$

其中,x 为变量. 将式(D3)代入式(12)的径向位移表达式中可得:

$$u_r^f = \frac{e^{i\omega D'/\beta - i\pi/4}}{2D'} f_0 \sum_{n=0}^{\infty}[A_n^f \cos(n\varphi) + A_n^{f'} \sin(n\varphi)] \times [I_{n-1}(f_0 r) + I_{n+1}(f_0 r)]. \quad (D4)$$

$n=0$ 时,式(D4)中将出现负数阶贝塞尔函数,可根据整阶贝塞尔函数的奇偶性进行计算,公式为:

$$I_{-n}(x) = I_n(x). \quad (D5)$$

令式(D4)中的 $r=0$,将式(D1)和(D5)代入式(D4)中,得到井轴处的径向位移为:

$$u_r^f\,|_{r=0} = \frac{e^{i\omega D'/\beta - i\pi/4}}{2D'} f_0 (A_1^f \cos\varphi + A_1^{f'} \sin\varphi), \quad (D6)$$

式(D6)表明,井轴处的径向位移只有偶极项($n=1$)贡献.

References

Aki K, Richards P G. 1980. Quantitative Seismology: Theory and Methods. San Francisco: W. H. Freeman.

Bennett N N. 2019. 3D slowness time coherence for sonic imaging. *Geophysics*, 84(5): D179-D189.

Cao J J, Tang X M, Wei Z T. 2014. Radiation of an acoustic dipole source in open and cased borehole with application to single-well shear-wave imaging. *Chinese Journal of Geophysics* (in Chinese), 57(5): 1683-1692, doi: 10.6038/cjg20140531.

Dong J L, Xu X K, Zhang J Y, et al. 2020. Overview and development of acoustic far detection technology. *Progress in Geophysics* (in Chinese), 35(2): 566-572, doi: 10.6038/pg2020CC0180.

Gong H, Chen H, He X, et al. 2018. Modeling and inversions of acoustic reflection logging imaging using the combined monopole-dipole measurement mode. *Applied Geophysics*, 15(3-4): 393-400.

Gu X H, Tang X M, Zhuang C X, et al. 2020. Simulation of dipole shear-wave reflection survey for multi-fracture system using liner slip interface theory. *Progress in Geophysics* (in Chinese), 35(3): 955-962, doi: 10.6038/pg2020DD0053.

Hirabayashi N, Sakiyama N, Ikegami T. 2017. Characteristics of waveforms recorded by azimuthally spaced hydrophones of sonic logging tool for incident plane waves. *Geophysics*, 82(6): D353-D368.

Hornby B E. 1989. Imaging of near-borehole structure using full-waveform sonic data. *Geophysics*, 54(6): 747-757.

Lee S Q, Chen M, Gu X H, et al. 2019. Application of four-component dipole shear reflection imaging to interpret the geological structure around a deviated well. *Applied Geophysics*, 16(3): 291-301.

Li S Q, Su Y D, Tang X M. 2020. Research on a fast inversion method for structural strike around a borehole based on four-component dipole shear wave reflection imaging. *Chinese Journal of Geophysics* (in Chinese), 63(6): 2478-2487.

Li Y H, Tang X M, Li H R, et al. 2021. Characterizing the borehole response for single-well shear-wave reflection imaging. *Geophysics*, 86(1): D15-D26.

Liu H X, Gu X H, Li H R, et al. 2021. Research of the dual dipole source of opposite polarity to suppress direct wave in single-well shear-wave imaging logging. *Progress in Geophysics* (in Chinese), 36(4): 1560-1565, doi: 10.6038/pg2021EE0301.

Peng C B, Cheng C H, Toksöz M N. 1993. Borehole effects on downhole seismic measurements. *Geophysical Prospecting*, 41(7): 883-912.

Qiao W X, Che X H, Li G, et al. 2004. The physical modeling of acoustic reflection image logging. *Geophysical Prospecting for Petroleum* (in Chinese), 43(3): 294-297.

Schoenberg M. 1986. Fluid and solid motion in the neighborhood of a fluid-filled borehole due to the passage of a low-frequency elastic plane wave. *Geophysics*, 51(6): 1191-1205.

Su Y D, Wei Z T, Tang X M. 2014. A validation method of dipole shear-wave remote reflection imaging from adjacent borehole reflection. *Journal of Applied Acoustics* (in Chinese), 33(1): 29-34.

Tang X M. 2004. Imaging near-borehole structure using directional acoustic-wave measurement. *Geophysics*, 69(6): 1378-1386.

Tang X M, Cao J J, Li Z, et al. 2016. Detecting a fluid-filled borehole using elastic waves from a remote borehole. *The Journal of the Acoustical Society of America*, 140(2): EL211-EL217.

Tang X M, Cao J J, Wei Z T. 2014. Shear-wave radiation, reception, and reciprocity of a borehole dipole source: with application to modeling of shear-wave reflection survey. *Geophysics*, 79(2): T43-T50.

Tang X M, Cheng C H A. 2004. Quantitative Borehole Acoustic Methods. Amsterdam: Elsevier.

Tang X M, Gu X H, Su Y D. 2019. Theoretical analysis and field data application of through-casing dipole shear-wave imaging. *Journal of China University of Petroleum (Edition of Natural Science)* (in Chinese), 43(5): 65-72.

Tang X M, Patterson D J. 2009. Single-well S-wave imaging using multicomponent dipole acoustic-log data. *Geophysics*, 74(6): WCA211-WCA223.

Tang X M, Wei Z T. 2012. Single-well acoustic reflection imaging using far-field radiation characteristics of a borehole dipole source. *Chinese Journal of Geophysics* (in Chinese), 55(8): 2798-2807, doi: 10.6038/j.issn.0001-5733.2012.08.031.

Tao G, He F J, Wang B, et al. 2008. Study on 3D simulation of wave

(C)1994-2022 China Academic Journal Electronic Publishing House. All rights reserved. http://www.cnki.net

fields in acoustic reflection image logging. *Science in China Series D*: *Earth Sciences*, 51(2): 186-194.

White J E. 1953. Signals in a borehole due to plane waves in the solid. *The Journal of the Acoustical Society of America*, 25(5): 906-915.

Xu J Q, Hu H S. 2019. Wave filed simulation of single-well imaging based on method of steepest descent and reciprocity. *Journal of Applied Acoustics* (in Chinese), 38(3): 293-300.

Xu J Q, Hu H S. 2020. Study on the radiation and reception of the wave field in a single-well imaging system with an eccentric source. *Chinese Journal of Geophysics* (in Chinese), 63(9): 3545-3561, doi: 10.6038/cjg2020N0015.

Xu J Q, Hu H S, Wang Z. 2019. Asymptotic solution to a 3D dipole single-well imaging system with combined monopole and dipole receivers with an application in elimination of azimuth ambiguity. *Geophysics*, 84(5): D191-D207.

Xue M. 2002. Study on remote exploration acoustic reflection well logging & its acoustic sonde design[Ph. D. thesis](in Chinese). Beijing: University of Petroleum.

附中文参考文献

曹景记, 唐晓明, 魏周拓. 2014. **偶极声源在裸眼井及套管井外的横波辐射特征**. **地球物理学报**, 57(5): 1683-1692, doi: 10.6038/cjg20140531.

董经利, 许孝凯, 张晋言等. 2020. **声波远探测技术概述及发展**. **地球物理学进展**, 35(2): 566-572, doi: 10.6038/pg2020CC0180.

宫昊, 陈浩, 何晓等. 2018. **基于单偶极混合测量模式的反射波测井方法研究(英文)**. **应用地球物理**, 15(3-4): 393-400.

古希浩, 唐晓明, 庄春喜等. 2020. **用滑移界面理论模拟多裂缝体系的偶极横波远探测声场**. **地球物理学进展**, 35(3): 955-962, doi: 10.6038/pg2020DD0053.

李盛清, 苏远大, 唐晓明. 2020. **基于四分量偶极横波远探测的井周构造走向快速反演方法研究**. **地球物理学报**, 63(6): 2478-2487, doi: 10.6038/cjg2020N0322.

刘汇鑫, 古希浩, 李焕然等. 2021. **双偶极源反相激励压制井中直达波的横波远探测方法研究**. **地球物理学进展**, 36(4): 1560-1565, doi: 10.6038/pg2021EE0301.

乔文孝, 车小花, 李刚等. 2004. **反射声波成像测井的物理模拟**. **石油物探**, 43(3): 294-297.

苏远大, 魏周拓, 唐晓明. 2014. **基于邻井反射的偶极横波远探测验证方法**. **应用声学**, 33(1): 29-34.

唐晓明, 古希浩, 苏远大. 2019. **过套管偶极横波远探测理论与应用**. **中国石油大学学报(自然科学版)**, 43(5): 65-72.

唐晓明, 魏周拓. 2012. **利用井中偶极声源远场辐射特性的远探测测井**. **地球物理学报**, 55(8): 2798-2807, doi: 10.6038/j.issn.0001-5733.2012.08.031.

唐晓明, 郑传汉. 2004. **定量测井声学**. **赵晓敏译**. **北京: 石油工业出版社**.

陶果, 何峰江, 王兵等. 2008. **声反射成像测井在地层中的三维波场模拟方法研究**. **中国科学 D 辑: 地球科学**, 38(SI): 166-173.

许家旗, 胡恒山. 2019. **基于鞍点法与互易性的远探测波场模拟**. **应用声学**, 38(3): 293-300.

许家旗, 胡恒山. 2020. **声波远探测中偏心声源的辐射以及接收波场研究**. **地球物理学报**, 63(9): 3545-3561, doi: 10.6038/cjg2020N0015.

薛梅. 2002. **远探测声波反射波测井方法研究和声系设计[博士论文]**. **北京: 石油大学**.

(本文编辑 张正峰)

(C)1994-2022 China Academic Journal Electronic Publishing House. All rights reserved. http://www.cnki.net

GEOPHYSICS, VOL. 86, NO. 5 (SEPTEMBER-OCTOBER 2021); P. D139–D147, 7 FIGS., 1 TABLE.
10.1190/GEO2020-0570.1

Delineating a cased borehole in unconsolidated formations using dipole acoustic data from a nearby well

Xi-Hao Gu[1], Xiao-Ming Tang[2], and Yuan-Da Su[2]

ABSTRACT

A potential application for single-well acoustic imaging is the detection of an existing cased borehole in the vicinity of the well being drilled, which is important for drilling toward (when drilling a relief well) or away from (collision prevention) the existing borehole. To fulfill this application in the unconsolidated formation of shallow sediments, we have developed a detection method using low-frequency P-waves from dipole acoustic logging. For this application, we perform theoretical analyses on elastic wave scattering from the cased borehole and derive the analytical expressions for the scattered wavefield for the incidence of P- and S-waves from a borehole dipole source. The analytical solution, in conjunction with the elastic reciprocity theorem, provides a fast algorithm for modeling the whole process of wave radiation, scattering, and reception for the borehole acoustic detection problem. The analytical results agree well with those from 3D finite-difference simulations. The results indicate that P-waves, instead of S-waves as commonly used for dipole acoustic imaging, are particularly advantageous for the borehole detection in the unconsolidated formation. Field data examples are used to demonstrate the application in a shallow marine environment, where dipole-P-wave data in the measurement well successfully delineate a nearby cased borehole, validating our analysis results and application.

INTRODUCTION

Single-well acoustic imaging has been used for decades in borehole geophysical exploration to characterize geologic structures outside the borehole (Hornby, 1989; Tang and Patterson, 2009; Gong et al., 2015). This technology can effectively detect reflectors tens of meters away from boreholes (Hirabayashi and Leaney, 2019; Li et al., 2020). Besides imaging geologic structures, acoustic imaging also has applications in locating an existing borehole close to the measurement borehole. This is important for safe drilling in densely drilled areas, especially in very soft formations frequently encountered in poorly consolidated sediments (Hornby and Pasternark, 2000; Wang and Tao, 2011) in shallow-water marine environments.

The wave phenomena involved in the borehole detection problem consist of the radiation of a borehole acoustic source from the measurement hole, the wave scattering from the target borehole, and the reception of the scattered wave in the measurement hole. In the past few decades, the borehole geophysics community has studied borehole-related wave-propagation problems. Meredith (1990) analyzes the radiation patterns for a volume point (monopole) source in a fluid-filled borehole based on the far-field asymptotic solution. Due to the fact that many acoustic measurements are made in cased boreholes, the effects of the casing and cement were also analyzed. Gibson (1994) investigates the monopole source radiation in a concentrically layered borehole model using the propagator matrix technique in conjunction with a far-field asymptotic (i.e., the stationary phase) solution. Peng (1994) develops the borehole coupling theory to study the interaction of an incident elastic wave with the cased borehole. For the single-well acoustic imaging application, the azimuthal sensitivity of the directional source (e.g., the borehole dipole source) has been used (Tang and Patterson, 2009). Tang et al. (2014) analyze the dipole S-wave imaging problem and show that the existing reciprocity between the reception, which is defined as the borehole response to the incident waves, and the radiation could be used to facilitate the analysis.

Existing theoretical modeling and analyses of single-well imaging primarily focus on planar reflectors (Tang, 2004; Wei and Tang, 2012; Li et al., 2017; Wei et al., 2019; Xu et al., 2019). The application of these imaging techniques to the problem of borehole

Manuscript received by the Editor 5 August 2020; revised manuscript received 11 May 2021; published ahead of production 17 June 2021; published online 18 August 2021.
[1]China University of Petroleum (East China), School of Geosciences, Qingdao 266580, China. E-mail: guxih@sina.com.
[2]China University of Petroleum (East China), School of Geosciences, Qingdao 266580, China; Key Laboratory of Deep Oil and Gas, China University of Petroleum (East China), Qingdao 266580, China; and Qingdao National Laboratory for Marine Science and Technology, Qingdao 266580, China. E-mail: tangxiam@aliyun.com (corresponding author); syuanda@sina.com.
© 2021 Society of Exploration Geophysicists. All rights reserved.

Downloaded from pubs.geoscienceworld.org/seg/geophysics/article-pdf/86/5/D139/5436635/geo-2020-0570.1.pdf by Univ of Petroleum (Beijing) - Library user on 08 October 2026

detection was investigated only recently. For example, Tang et al. (2016) analyze the detection of a borehole target in a fast formation using dipole-generated SH-waves. However, for detecting a borehole in a very slow formation environment, this application needs to be revisited for two reasons: First, in a very slow formation whose P-wave slowness is close to the borehole fluid slowness, the P-wave, instead of the S-wave, is effectively excited by a (monopole or dipole) source (Tang, 2004; Hornby et al., 2018) and should be used for the imaging application; second, most boreholes in shallow soft formations are cased and the effects of casing and cement should be included in the wavefield analysis. The main objective of this study is to develop a theoretical analysis for detecting a cased borehole using dipole acoustic (P-wave) data acquired in a nearby well in the very slow formation environment.

In this work, we first develop the theoretical formulation for analyzing the interaction between the cased borehole and the incident elastic wave from another borehole. Then, together with the steepest-descent method and the reciprocity theorem, we develop an asymptotic solution to analyze the scattered P-waves in the measurement well. For validation, we compare the analytical solution result with that from a 3D finite-difference modeling. The analysis results are used to demonstrate the advantages of P-waves over S-waves for the borehole detection in the slow formation. The azimuthal sensitivity of the P-wave method is also analyzed. Finally, we present field data examples to validate our analysis and demonstrate the effective application.

THEORETICAL ANALYSIS

The schematic of the borehole detection model is illustrated in Figure 1. A dipole acoustic tool is placed in a newly drilled (uncased) borehole called the measurement hole, which, for simplicity, is assumed to be parallel with the nearby cased borehole called the target hole (for the following analysis of wave scattering from the target hole, the parallel assumption can be relaxed and the two wells need only be coplanar to each other). The two boreholes are separated by a distance r_0. The dipole transmitter of the tool radiates an elastic wave into the formation (modeled as a very slow formation). After incidence on the target hole, the wave is scattered back to the measurement hole and is received by an array of receivers in the borehole fluid. The incident elastic wave, as radiated from the measurement hole, is a spherical wave. The wave spectrum can be generally written as (Tang and Patterson, 2009; Tang et al., 2016)

$$\mathrm{Iwv}(\omega) = \mathrm{S}(\omega)\frac{\mathrm{RD}(\omega;\theta;\varphi)}{4\pi\rho\mathrm{V}^2}\left[\frac{\mathrm{e}^{\mathrm{i}\omega\mathrm{R}/\mathrm{V}}}{\mathrm{R}}\right]; \tag{1}$$

where the expression in the brackets is typical of the spherical wave with a geometric spreading factor $1/\mathrm{R}$, where R is the propagation distance, ρ is the formation density, and V is the wave velocity of the formation, which, depending on the type of incident wave, can be the P- or S-wave velocity and S and RD are the spectrum and radiation function of the acoustic source in the measurement hole, respectively, both varying as a function of the angular frequency ω. In fact, RD, a dimensionless quantity, is also called the far-field radiation directivity because it governs the wave amplitude variation with the azimuthal and incidence angles, φ and δ, respectively. Meredith (1990) derives the expressions of RD for P- and SV-waves from a monopole source. Tang et al. (2014) obtain the far-field SH- and SV-wave radiation functions ($\mathrm{RD_{SH}}$ and $\mathrm{RD_{SV}}$) for a borehole dipole source. The general method for deriving the far-field solution is the steepest-descent method (Aki and Richards, 1980). For the P-wave far-field radiation ($\mathrm{RD_P}$), which is of particular interest for this study, Xu et al. (2019) derive for the dipole source using the same method

$$\mathrm{RD_P}(\omega;\varphi) = \mathrm{i}\rho\alpha\omega\mathrm{B}(\omega;\mathrm{k_{p0}})\cos\varphi; \tag{2}$$

where α is the formation P-wave velocity and B is the radiated P-wave amplitude coefficient for a dipole source in the fluid-filled borehole, which is derived from the fluid-solid boundary condition at the borehole wall (Tang and Cheng, 2004) and solved for the far-field condition with the steepest-descent P wavenumber $\mathrm{k_{p0}} = (\omega/\alpha)\cos\delta$.

The wave incidence on the cased borehole induces wave motion in the fluid inside the casing and in the layered casing-cement structure surrounding the borehole. According to the Helmholtz theorem, the particle displacements in the fluid $\mathrm{u_f}$ and scattered wave in the mth layer of the structure $\mathrm{u_s}$ can be expressed in terms of their respective potential functions as

$$\begin{cases} \mathrm{u_f} = \nabla\varphi_\mathrm{f}; \\ \mathrm{u_m^s} = \nabla\varphi_\mathrm{m} + \nabla\times(\chi_\mathrm{m}\hat{\mathrm{z}}) + \nabla\times\nabla\times(\Gamma_\mathrm{m}\hat{\mathrm{z}}); \end{cases} \tag{3}$$

where φ_f denotes the P-wave potential in the borehole fluid; φ_m, χ_m, and Γ_m are the P-, SH-, and SV-wave potentials in the layer m, respectively; and $\hat{\mathrm{z}}$ is a unit vector along the z-axis.

For the cylindrical geometry of the target borehole, it is convenient to express the spherical incident wave of equation 1 as a series summation of cylindrical waves using the Sommerfeld integral and Bessel addition theorem (Tang et al., 2016):

$$\frac{\mathrm{e}^{\mathrm{i}\omega\mathrm{R}/\mathrm{V}}}{\mathrm{R}} = \frac{1}{\pi}\int_{-\infty}^{+\infty}\sum_{\mathrm{n}=0}^{+\infty}\varepsilon_\mathrm{n}\mathrm{K_n}(\mathrm{k_v r_0})\mathrm{I_n}(\mathrm{k_v r}) \times\cos[\mathrm{n}(\varphi-\varphi_0)]\mathrm{e}^{\mathrm{ik}(z-z_0)}\mathrm{d}k; \tag{4}$$

where ε_n is 1 for $\mathrm{n}=0$ and 2 for $\mathrm{n}>0$, $\mathrm{I_n}$ and $\mathrm{K_n}$ are the nth-order modified Bessel functions of the first and second kind, respectively, $(\mathrm{r_0}, \varphi_0, \mathrm{z_0})$ are the cylindrical coordinates of the borehole source, k is the axial wavenumber, and $\mathrm{k_v} = \sqrt{\mathrm{k}^2-\omega^2/\mathrm{V}^2}$ is the radial wavenumber.

For the functional forms of the incident wave in equation 4, the wavenumber-frequency domain solution for the displacement potentials of equation 3 can be generally written as (Tang and Cheng, 2004)

$$\begin{cases} \varphi_\mathrm{f} = \sum_{n=0}^{\infty}[\mathrm{A_n^f}\cos(\mathrm{n}\varphi)+\mathrm{A_n^{\prime f}}\sin(\mathrm{n}\varphi)]\mathrm{I_n}(\mathrm{k_f r})\mathrm{K_n}(\mathrm{k_v r_0})\mathrm{e}^{\mathrm{ik}(z-z_0)}; & (0<\mathrm{r}<\mathrm{r_1}) \\ \varphi_\mathrm{m} = \sum_{n=0}^{\infty}\{[\mathrm{A_n^{(m)}}\cos(\mathrm{n}\varphi)+\mathrm{A_n^{\prime(m)}}\sin(\mathrm{n}\varphi)]\mathrm{I_n}(\mathrm{k_p^{(m)} r}) \\ \quad +[\mathrm{B_n^{(m)}}\cos(\mathrm{n}\varphi)+\mathrm{B_n^{\prime(m)}}\sin(\mathrm{n}\varphi)]\mathrm{K_n}(\mathrm{k_p^{(m)} r})\}\mathrm{K_n}(\mathrm{k_v r_0})\mathrm{e}^{\mathrm{ik}(z-z_0)}; \\ \chi_\mathrm{m} = \sum_{n=0}^{\infty}\{[\mathrm{C_n^{(m)}}\sin(\mathrm{n}\varphi)-\mathrm{C_n^{\prime(m)}}\cos(\mathrm{n}\varphi)]\mathrm{I_n}(\mathrm{k_s^{(m)} r}) \\ \quad +[\mathrm{D_n^{(m)}}\sin(\mathrm{n}\varphi)-\mathrm{D_n^{\prime(m)}}\cos(\mathrm{n}\varphi)]\mathrm{K_n}(\mathrm{k_s^{(m)} r})\}\mathrm{K_n}(\mathrm{k_v r_0})\mathrm{e}^{\mathrm{ik}(z-z_0)}; \\ \Gamma_\mathrm{m} = \sum_{n=0}^{\infty}\{[\mathrm{E_n^{(m)}}\cos(\mathrm{n}\varphi)+\mathrm{E_n^{\prime(m)}}\sin(\mathrm{n}\varphi)]\mathrm{I_n}(\mathrm{k_s^{(m)} r}) \\ \quad +[\mathrm{F_n^{(m)}}\cos(\mathrm{n}\varphi)+\mathrm{F_n^{\prime(m)}}\sin(\mathrm{n}\varphi)]\mathrm{K_n}(\mathrm{k_s^{(m)} r})\}\mathrm{K_n}(\mathrm{k_v r_0})\mathrm{e}^{\mathrm{ik}(z-z_0)}; & (\mathrm{r}>\mathrm{r_1}) \end{cases} \tag{5}$$

where $\mathrm{r_1}$ is the inner radius of the casing, $\mathrm{k_f} = \sqrt{\mathrm{k}^2-\omega^2/\alpha_\mathrm{f}^2}$, $\mathrm{k_p^{(m)}} = \sqrt{\mathrm{k}^2-\omega^2/\alpha_\mathrm{m}^2}$, and $\mathrm{k_s^{(m)}} = \sqrt{\mathrm{k}^2-\omega^2/\beta_\mathrm{m}^2}$, and α_m, β_m, and α_f are the P- and S-wave velocities of the mth layer and the acoustic

Downloaded from pubs.geoscienceworld.org/seg/geophysics/article-pdf/86/5/D139/5436635/geo-2020-0570.1.pdf by Univ of Petroleum (Beijing) - Library user on 08 October 2026

wave velocity of the borehole fluid, respectively. The first- and second-kind modified Bessel functions I_n and K_n are needed to model the incoming and outgoing cylindrical waves in the elastic layer, with the $A_n^{(m)}$, $C_n^{(m)}$, $E_n^{(m)}$ and $B_n^{(m)}$, $D_n^{(m)}$, $F_n^{(m)}$ (and $A'^{(m)}_n$ :::, etc.) representing the amplitude coefficients of these waves. The coefficients are determined by the boundary condition at each interface in the cased-borehole model (Tubman et al., 1984). In the outermost formation layer, the coefficients $A_n^{(3)}$, $C_n^{(3)}$, and $E_n^{(3)}$ (and $A'^{(3)}_n$ :::, etc.) are set to zero to satisfy the radiation condition at infinity. For the fluid inside the casing, only the I_n function with the coefficients A_n^f and A'^f_n is needed to model the transmitted wave through the layered structure. The wave amplitude coefficients are determined by the boundary condition at the fluid-casing interface ($r = r_1$), which consists of the continuity of radial displacement and radial stress

$$\begin{cases} u_r^s(r_1^+) + u_r^i(r_1^+) = u_r^f(r_1^-); \\ \sigma_{rr}^s(r_1^+) + \sigma_{rr}^i(r_1^+) = \sigma_{rr}^f(r_1^-); \end{cases} \tag{6}$$

and the vanishing of azimuthal and axial shear stress

$$\begin{cases} \sigma_{r\varphi}^s(r_1^+) + \sigma_{r\varphi}^i(r_1^+) = 0; \\ \sigma_{rz}^s(r_1^+) + \sigma_{rz}^i(r_1^+) = 0; \end{cases} \tag{7}$$

where superscripts i, s, and f denote the incident, scattered, and transmitted (to fluid) waves, respectively.

Assuming a well-bonded boundary condition for the layered structure of the cased borehole, the propagator matrix technique is used to model wave propagation through the casing-cement layers (Tubman et al., 1984). The product of the propagator matrices of all layers results in a 6×6 matrix G (see Appendix A), which connects the wavefield in the formation ($r > r_3$) to the wavefield inside the casing ($r < r_1$), will be explained. The displacement components of equations 6 and 7 are calculated using equations 3 and 5, which are used to calculate strain and the stresses needed in the boundary conditions, resulting in two matrix equations to determine the unknown coefficients:

$$\begin{bmatrix} M_{11} & G_{12} & G_{14} & G_{16} \\ M_{21} & G_{42} & G_{44} & G_{46} \\ M_{31} & G_{52} & G_{54} & G_{56} \\ M_{41} & G_{62} & G_{64} & G_{66} \end{bmatrix} \begin{bmatrix} A_n^f \\ B_n^{(3)} \\ D_n^{(3)} \\ F_n^{(3)} \end{bmatrix} = \begin{bmatrix} d_1 \\ d_2 \\ d_3 \\ d_4 \end{bmatrix} \quad \text{and}$$

$$\begin{bmatrix} M_{11} & G_{12} & G_{14} & G_{16} \\ M_{21} & G_{42} & G_{44} & G_{46} \\ M_{31} & G_{52} & G_{54} & G_{56} \\ M_{41} & G_{62} & G_{64} & G_{66} \end{bmatrix} \begin{bmatrix} A_n'^f \\ B_n'^{(3)} \\ D_n'^{(3)} \\ F_n'^{(3)} \end{bmatrix} = \begin{bmatrix} d_1' \\ d_2' \\ d_3' \\ d_4' \end{bmatrix}; \tag{8}$$

where M is 4×4 matrix that relates the wavefield in fluid to the wavefield of the infinite formation in the absence of the casing and cement (see Peng, 1994; Tang and Cheng, 2004). In the presence of the casing and cement, the G matrix is involved, as shown in equation 8, and the elements of M that relate to the formation are now replaced by their corresponding elements in G (these elements are related to the Bessel function K_n for outgoing waves; see Appendix A); only the elements of M relating to fluid are retained (these elements are also given in Appendix A). On the right side of equation 8, d and d′ are the 4×1 vectors whose elements are calculated from the incident wave and evaluated at the inner casing interface ($r = r_1$). Again, the G matrix is used to calculate the incident wavefield at $r = r_1$. The incident wave of equation 1, depending on its radiation function and propagation velocity, needs to be calculated individually, as follows.

For P-wave incidence:

$$\begin{pmatrix} d_1 \\ d_2 \\ d_3 \\ d_4 \end{pmatrix} = -\frac{\varepsilon_n S(\omega) R D_P}{4\pi\rho\alpha^2} \begin{pmatrix} G_{11} \\ G_{41} \\ G_{51} \\ G_{61} \end{pmatrix} \cos(n\varphi_0);$$

$$\begin{pmatrix} d_1' \\ d_2' \\ d_3' \\ d_4' \end{pmatrix} = -\frac{\varepsilon_n S(\omega) R D_P}{4\pi\rho\alpha^2} \begin{pmatrix} G_{11} \\ G_{41} \\ G_{51} \\ G_{61} \end{pmatrix} \sin(n\varphi_0): \tag{9}$$

For SH-wave incidence:

$$\begin{pmatrix} d_1 \\ d_2 \\ d_3 \\ d_4 \end{pmatrix} = \frac{\varepsilon_n S(\omega) R D_{SH}}{4\pi\rho\beta^2} \begin{pmatrix} G_{13} \\ G_{43} \\ G_{53} \\ G_{63} \end{pmatrix} \sin(n\varphi_0);$$

$$\begin{pmatrix} d_1' \\ d_2' \\ d_3' \\ d_4' \end{pmatrix} = -\frac{\varepsilon_n S(\omega) R D_{SH}}{4\pi\rho\beta^2} \begin{pmatrix} G_{13} \\ G_{43} \\ G_{53} \\ G_{63} \end{pmatrix} \cos(n\varphi_0): \tag{10}$$

For SV-wave incidence:

$$\begin{pmatrix} d_1 \\ d_2 \\ d_3 \\ d_4 \end{pmatrix} = -\frac{\varepsilon_n S(\omega) R D_{SV}}{4\pi\rho\beta^2} \begin{pmatrix} G_{15} \\ G_{45} \\ G_{55} \\ G_{65} \end{pmatrix} \cos(n\varphi_0);$$

$$\begin{pmatrix} d_1' \\ d_2' \\ d_3' \\ d_4' \end{pmatrix} = -\frac{\varepsilon_n S(\omega) R D_{SV}}{4\pi\rho\beta^2} \begin{pmatrix} G_{15} \\ G_{45} \\ G_{55} \\ G_{65} \end{pmatrix} \sin(n\varphi_0): \tag{11}$$

The case of SH-wave incidence onto an open hole has been analyzed by Tang et al. (2016). In this case, the related elements of G in equation 10 should be replaced by their corresponding M matrix elements. The present study focuses on the P-wave incidence from a borehole dipole source onto a cased borehole in a very slow formation. For the P-wave incidence, the $\omega - k$ domain expression of the displacement potential Φ^i, according to equations 1 and 4, can be written as

Downloaded from pubs.geoscienceworld.org/seg/geophysics/article-pdf/86/5/D139/5436635/geo-2020-0570.1.pdf by Univ of Petroleum (Beijing) - Library user on 08 October 2026

$$\Phi^{i} = \frac{S(\omega)\cdot RD_P(\omega)}{4\pi^2\rho\alpha^2}\int_{-\infty}^{+\infty}\sum_{n=0}^{\infty}\varepsilon_n K_n(k_p r_0) I_n(k_p r) \times [\cos(n\varphi)\cos(n\varphi_0)+\sin(n\varphi)\sin(n\varphi_0)]e^{ik(z-z_0)}dk; \quad (12)$$

where RD_P is the P-wave radiation function from a borehole dipole source (see equation 2) and wave velocity V should now be replaced by α for the P-wave incidence. Solving equation 8 to determine the coefficients of equation 5 for the P-wave incidence, the radial displacement spectrum of the scattered wave from the target borehole can be written as

$$u_r^s(\omega; r; \varphi; z) = \frac{1}{\pi}\int_{-\infty}^{+\infty}\sum_{n=0}^{\infty}[B_n^{(3)}\cos(n\varphi)+B_n'^{(3)}\sin(n\varphi)] \times [nK_n(k_p r)/r - k_p K_{n+1}(k_p r)]K_n(k_p r_0)e^{ik(z-z_0)}dk: \quad (13)$$

This scattered wavefield will be measured by the receiver array in the measurement hole. For this case, the radial distance $(r \sim r_0)$ from the target borehole is large compared to the wavelength such that $|k_p r| \gg 1$ and $|k_p r_0| \gg 1$, and the steepest-descent method (Aki and Richards, 1980; Tang and Patterson, 2009) can be readily applied to equation 13 to replace the wavenumber integration with the steepest-descent solution:

$$u_r^s(\omega; r; \varphi; z) = \sqrt{\frac{\pi\omega\sin^3\delta}{2\alpha(r+r_0)rr_0}}\sum_{n=0}^{\infty}[B_n^{(3)}(\omega; k_{p0})\cos(n\varphi) + B_n'^{(3)}(\omega; k_{p0})\sin(n\varphi)]e^{i\omega(R'+r_0\sin\delta)/\alpha-\pi i/4}; \quad (14)$$

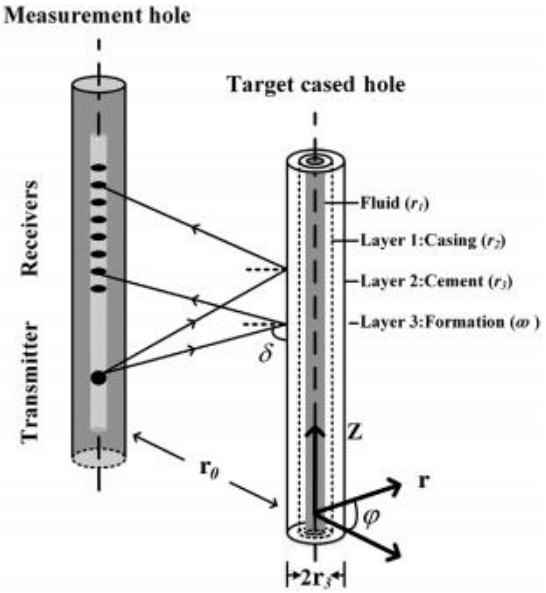


Figure 1. The configuration and coordinate system for delineating a target cased borehole using elastic waves from a nearby well.

where $k_{p0} = (\omega/\alpha)\cos\delta$ and $R' = \sqrt{r^2 + (z-z_0)^2}$. The P-wave asymptotic solution of equation 14 is similar to its SH-wave counterpart obtained by Tang et al. (2016), except that the amplitude coefficients and wavenumber are now those of the P-wave, and the coefficients contain the effects of casing and cement. It is worthwhile to discuss an important characteristic for the scattered wave of equation 14. For r values close to r_0, one notices that the wave's geometric spreading factor is $r^{-1.5}$, which is the product of the spreading factor of the spherical wave, $1/r$, and that of the cylindrical wave, $1/\sqrt{r}$. The combined wave spreading factor correctly reflects the physical wave propagation process as the combination of spherical wave radiation to the target hole and cylindrical wave scattering back to the measurement hole. This characteristic of cylindrical cavity scattering is the physical basis of remotely detecting a target borehole even though its diameter is small compared to the wavelength.

In principle, the reception of the scattered wave in the measurement hole can be calculated by solving equation 8 for the open-hole condition with the wave in equation 14 as the incident wave. Here, we use the source-receiver reciprocity theorem to simplify the problem. Receiving the incident wave inside borehole fluid is governed by a borehole reception function (Peng et al., 1993)

$$RWV(\omega) = RC_P(\omega)\cdot u_r^s(\omega; r; \varphi; z); \quad (15)$$

where RWV denotes the received wave signal inside the borehole. For the S- and P-wave incidence scenarios, Tang et al. (2014) and Wang et al. (2015) show, by applying the source-receiver reciprocity, that the reception function $RC(\omega)$ is equivalent to the borehole radiation function $RD(\omega)$. Thus, the P-wave reception function in equation 15 is given by

$$RC_P(\omega) = RD_P(\omega); \quad (16)$$

where $RD_P(\omega)$ is the borehole radiation function for the dipole source, as given in equation 2.

THEORETICAL MODELING AND VALIDATION

Equations 14 and 15 provide a fast analytical method to calculate the acoustic signal from a nearby cased well for the dipole acoustic logging in the measurement hole. For the model of two parallel boreholes and the coordinates system of Figure 1, the source is at $z_0 = 0$ and the source and receivers are colocated at the measurement borehole axis ($r = r_0 = 5$ m, $\varphi = \varphi_0 = 180°$), with the source-to-receiver spacing varying from 3.0 to 4.05 m. The elastic parameters of the two boreholes and the formation are provided in Table 1. For the same model of Figure 1, a 3D finite-difference numerical waveform modeling method (Li et al., 2018) was also used to calculate the received wave signal (radial displacement along $\varphi = 180°$) in the measurement hole. The finite-difference modeling used the 3D Cartesian grid to discretize the model. The grid size is 0.004 m, and the time iteration step is 0.4 μs. The analytical and numerical modeling use the same source function $S(\omega)$, which is a 3 kHz center frequency Kelly wavelet.

Figure 2 compares the calculated fluid displacement signals at the borehole center from the analytical (the solid curve) and numerical (the dots) modeling. The 3D finite-difference modeling calculates wave propagations along and outside the borehole, whereas the analytical method calculates only the propagation outside the borehole.

Downloaded from pubs.geoscienceworld.org/seg/geophysics/article-pdf/86/5/D139/5436635/geo-2020-0570.1.pdf by Univ of Petroleum (Beijing) - Library user on 08 October 2026

For this reason, the two results are compared in the time window of 5–10 ms for the scattered wave signal from the target borehole. The analytical and numerical waveforms agree very well with regard to their arrival time, amplitude, and phase across the receiver array, considering the complicated wave-borehole interactions in the radiation, scattering, and reception processes of the respective modeling calculations. However, the computational efficiency of the two methods differs by orders of magnitude. The analytical solution takes only a few tens of seconds to get the result of Figure 2, whereas the 3D finite-difference modeling needs many tens of hours of calculation. Therefore, our analytical solution provides a fast algorithm for forward modeling the elastic-wave interaction between two boreholes.

Furthermore, we discuss the advantage of P-waves over S-waves for the target borehole detection in very slow formations. For fast formations where the S-wave velocity is greater than the acoustic velocity of the borehole fluid, it has been shown that the dipole-generated S-waves, instead of P-waves, are better suited for imaging a formation reflector (Tang et al., 2014) and a target borehole (Tang et al. 2016). In contrast, in a slow formation, especially a very slow formation with high P-to-S velocity ratios, the reverse is true, as will be demonstrated using the following modeling examples.

Figure 3a and 3b compares the calculated 3 kHz P-wave and SH- and SV-wave radiation/reception directivity patterns, respectively (i.e., the amplitude of the RD_P, RD_{SH}, and RD_{SV} functions in equations 9–11) for the measurement borehole and the formation parameters of Table 1. The patterns are shown in the vertical plane as a function of the incident angle δ in a polar plot, where the polar angle indicates the value of δ and the radius indicates the radiation/reception amplitude (dimensionless). The result shows that the amplitude of the RD_P directivity (black in Figure 3a) is much larger than those of the RD_{SH} (red in Figure 3b) and RD_{SV} (black in Figure 3b) directivities. Of particular interest is the angle range at approximately $\delta = 90°/270°$. For the measurement configuration of Figure 1, this is the range where wave radiation and incidence occur. At $\delta = 90°/270°$, RD_{SV} is null, whereas RD_P and RD_{SH} are in their respective high value range, with the magnitude of the RD_P curve (Figure 3a) being approximately 20 times larger than that of the RD_{SH} curve (the red curve in Figure 3b). Consider that the wave signal generated and measured in the same borehole will be modulated by the radiation and reception processes. Using the equivalence of the borehole radiation and reception, and considering the propagation of P- and S-waves in the formation ($1/\rho V^2$ in equation 1), one can estimate that the P-wave amplitude is approximately 30 times larger than the SH-wave amplitude. To verify this estimation, the modeling is repeated for the SH-wave incidence (equation 10) of the same model to calculate the received fluid displacement normal to the wave incidence plane. The result is compared to that of the P-wave scenario in the 5–28 ms time range, as shown in Figure 4. In this figure, the 10–20 ms interval is skipped because the very slow SH-wave arrives at approximately 22 ms. The SH-wave amplitude is multiplied by a factor of 30 to visualize this very weak event, which confirms our estimation based on the radiation/reception amplitude comparison. In addition, the SH-wave has much lower frequency content compared to the P-wave. The wave phenomena shown in Figure 4 are very similar to those observed in dipole logging along the borehole with a very slow formation, where the data consist of the (higher frequency and

Table 1. Model calculation parameters.

	P-wave velocity (m/s) $V_P(m \cdot s^{-1})$	S-wave velocity (m/s) $V_S(m \cdot s^{-1})$	Density (kg/m^3) ρ $(kg \cdot m^{-3})$	Radius (m)
Measurement borehole fluid	1500	—	1000	0.200
Target borehole fluid	1500	—	1000	0.164
Casing	6098	3354	7500	0.172
Cement	2823	1729	1920	0.220
Slow formation	1724	450	2000	—

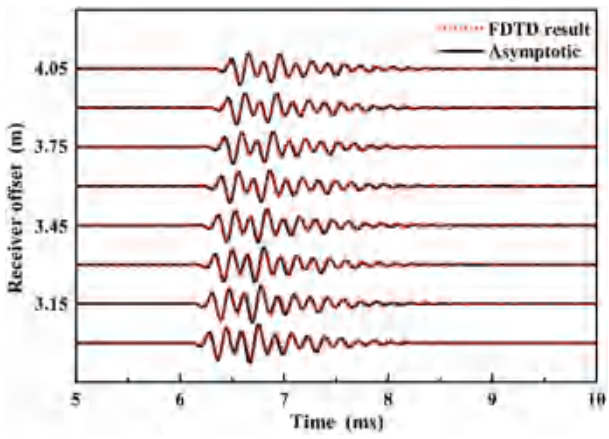


Figure 2. Comparison of received P-waves calculated using the analytical solution (the solid curve) and numerical modeling from a 3D finite-difference method (the dots) for a 3 kHz dipole source.

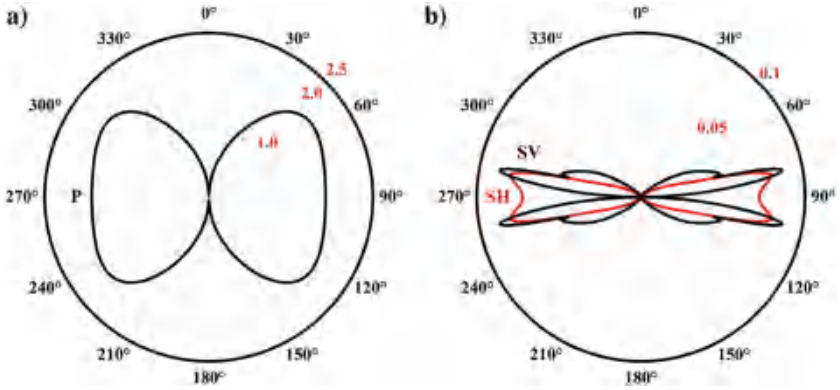


Figure 3. (a) The P-wave and (b) SH- and SV-wave radiation/reception directivity patterns in a very slow formation for a 3 kHz dipole source. Note the dominance of the P-wave directivity compared with the S-wave directivities. Radial labels mark the directivity amplitude (dimensionless).

Downloaded from pubs.geoscienceworld.org/seg/geophysics/article-pdf/86/5/D139/5436635/geo-2020-0570.1.pdf by Univ of Petroleum (Beijing) - Library user on 08 October 2026

amplitude) P-waves and (much lower frequency and amplitude) S-waves (Hornby and Pasternark, 2000). Therefore, one can conclude that it is more effective and advantageous to use P-waves than S-waves for detecting a target borehole with a very slow formation.

Finally, we discuss the azimuthal variation of the scattered wave in conjunction with the 4C dipole acoustic data (xx, xy, yx, yy) for determining the nearby well azimuth. The model of Figure 1 (and Table 1) is still used, but now the target hole angle is set to $\varphi = 30°$. By firing the dipole source, along the x ($\varphi_0 = 0°$) and y ($\varphi_0 = 90°$) directions, and calculating the x- and y-displacement at the receiver location using equations 14 and 15 for each firing, the 4C scattered wave data (xx, xy, yx, yy) from the target hole are obtained. Then, the 4C dipole rotation formula (Tang and Patterson, 2009) is used to rotate the data to an arbitrary angle φ to form a new XX-component data, as follows:

$$XX(\varphi) = xx\cos^2\varphi - \sin\varphi\cos\varphi(xy + yx) + yy\sin^2\varphi: \quad (17)$$

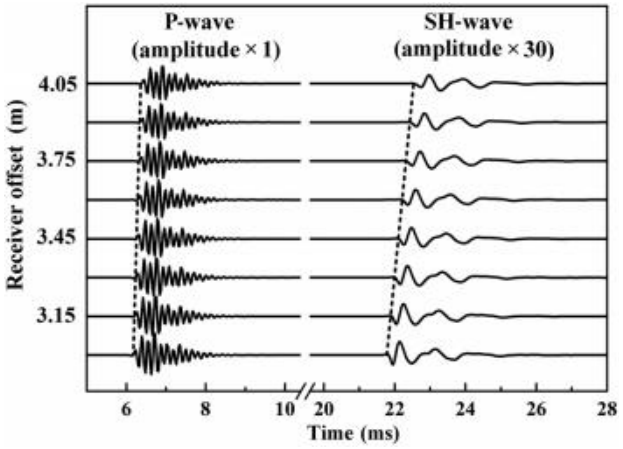


Figure 4. Comparison of the P- (early arrival) and SH- (later arrival) waves scattered from the target borehole. The amplitude of SH-wave is increased by a factor of 30 to visualize the very weak signal.

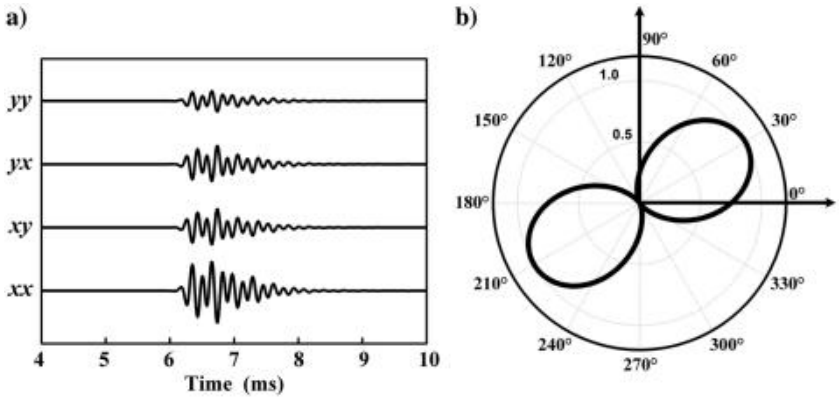


Figure 5. (a) The 4C data (xx, xy, yx, yy) modeling for a target-hole at the 30° azimuth. (b) Polar plot of the 4C-data-rotated wave shows that the wave attains the maximum (minimum) amplitude along (perpendicular to) the target-hole azimuth. Radial labels mark the rotated wave amplitude, which is normalized by its maximum value in the range.

Figure 5a shows the 4C P-wave data for a source-to-receiver spacing of 3 m in the measurement hole. The 4C-rotated wave amplitude $|XX(\varphi)|$ is shown as a polar plot in the ($0 < \varphi < 360°$) range, the amplitude being normalized by its maximum value in the range. The polar plot exhibits the typical dipole variation pattern, showing two peak values at $\varphi = 30°$ and $\varphi = 210°$, respectively. The first peak is at the orientation of the target hole. The latter peak is the result of the 180° ambiguity of the dipole data (Li et al., 2021). This modeling example shows that the target-hole azimuth, with a 180° ambiguity, can be determined using the 4C dipole logging data.

FIELD DATA EXAMPLES

We use field data examples to demonstrate the application of the preceding theoretical results for delineating a cased borehole in the unconsolidated formation of a shallow marine environment. Panel 1 of Figure 6 shows the gamma ray (GR) and P-wave slowness delta time of the P-wave (DTP) log curves for the 160–190 m interval of the measurement well. A 4C dipole acoustic data set (xx, xy, yx, yy) was acquired for this well, and the x-dipole orientation (AZ, relative to north) is also shown. Panel 2 shows the variable density (VD) display of the xx-component data of this interval (only the first receiver of an array of eight is displayed). The center frequency of the dipole source is approximately 3 kHz, and the data recording time length is 17,244 μs. For this very slow formation, the early portion of the data shows mainly the high-amplitude P-waves traveling along the borehole, from which the DTP curve of panel 1 was derived.

The 4C data (xx, xy, yx, yy) are first processed using a wave separation technique (e.g., f-k filtering of Hornby, 1989) to suppress the large-amplitude borehole arrivals in the data. Afterward, the data are rotated using equation 17 to find the azimuth that maximizes (minimizes) the rotated wave amplitude. Note that, in the data rotation, the tool azimuth curve AZ of panel 1 is added to the rotation angle φ such that the resulting azimuth is referenced to the north. With these processing steps, the wave signal from the nearby (cased) borehole can be obtained. Panel 3 (panel 4) shows the VD display of the maximum (minimum) signal, as indicated by an arrow and traced by a dashed curve (a theoretical arrival time curve to be explained). For this example, the maximum and minimum azimuths are in the north–south and east–west directions, respectively. The existence and absence of the signal in the north–south and east–west azimuths agree with the theoretical modeling result of Figure 5b, which shows that the maximum and minimum azimuths are 90° apart.

The wave event of panel 3 is migrated using the DTP data of panel 1 to image the nearby borehole. The migration uses data from all receivers of the array tool and, to obtain the image for one depth, the data of all relevant depths are summed (Tang et al., 2007). Image enhancement techniques (Tang, 2016) can also be used to improve the quality of the imaging result. This gives the image of a well-defined, steeply dipping reflector in the vicinity of the borehole (see panel 6), with the distance of the reflector ranging from 6.0 to 7.8 m in this 30 m depth interval. The well location maps of the drilling area confirmed that this event is a cased well near the

Downloaded from pubs.geoscienceworld.org/seg/geophysics/article-pdf/86/5/D139/5436635/geo-2020-0570.1.pdf by Univ of Petroleum (Beijing) - Library user on 08 October 2026

logging well. Then, we performed a forward modeling to simulate the dipole acoustic data of panel 2. The P-wave slowness data and a P-to-S velocity ratio of 3.5 were used to generate the S-wave slowness data. The distance between the measurement and target hole is taken from the imaging result of panel 6. The borehole and casing parameters are taken from Table 1. Panel 5 shows the 3 kHz synthetic full-wave xx-dipole data (in the VD display) to compare with the field data of panels 2 and 3. In the modeling, the borehole dipole wave propagation was calculated using the method of Tang and Cheng (2004) and the wave propagation from the target hole was calculated using the method from this study. For the noise-free synthetic data, the strong and weak wave events that are separate in arrival time can all be visualized. They are, as labeled by the arrows in the panel, the borehole P- and S-waves and the scattered P-wave from the nearby well. The modeled borehole S-wave is very weak, which explains why it is not seen in the measured data. The modeled scattered P-wave in panel 4 and its measured counterpart in panel 3 have approximately the same arrival time (the dashed curve in panel 3, as overlain with the measured data, is the theoretical arrival time for the scattered P-wave), confirming that the wave event in panel 3 is the scattered wave from the nearby well. This field data example indicates that the P-wave data from 4C dipole acoustic logging can indeed be used to delineate the nearby (cased) well in unconsolidated soft formations.

To further demonstrate the validity and effectiveness of the preceding analysis and processing methods, an example of nearby borehole delineation in a longer depth range (80 m) is shown in Figure 7. Panel 1 shows the GR and P-wave slowness (DTP) log curves for the 110–190 m interval of the measurement well. A 4C dipole acoustic data set (xx, xy, yx, yy) was acquired for this well. Panel 2 shows the VD display of the xx-component data of this interval (only the first receiver of an array of eight is displayed). Using the preceding data processing and rotation finds the maximum signal at the east–northeast azimuth, which is the azimuth of the nearby well. Note that the minimum signal at the south–southeast azimuth is not shown for brevity. Panel 3 shows the signal event, as indicated by an arrow and traced by a dashed (traveltime) curve. The wave event is migrated using the DTP data of panel 1 to give the nearby borehole image in panel 5. The distance of the reflector increases from 4.8 m at the top to 15.1 m at the bottom of this 80 m depth interval. Using the reflector distance information and performing the same synthetic modeling as done for panel 5 of Figure 6, the synthetic counterpart of panel 2 data is obtained, as shown in panel 4. The arrival time for the scattered P-wave of panel 4 is plotted in panel 3 (the dashed curve) with the field data, which tracks well with the scattered P-wave event in the data. The wave event is quite visible in the upper interval and becomes very weak in the lower interval as the distance between the wells increases. Despite the weakened signal, the nearby well can still be clearly imaged (panel 5), showing that the technique is capable of imaging a far-away target well even though its diameter is small compared to the wavelength.

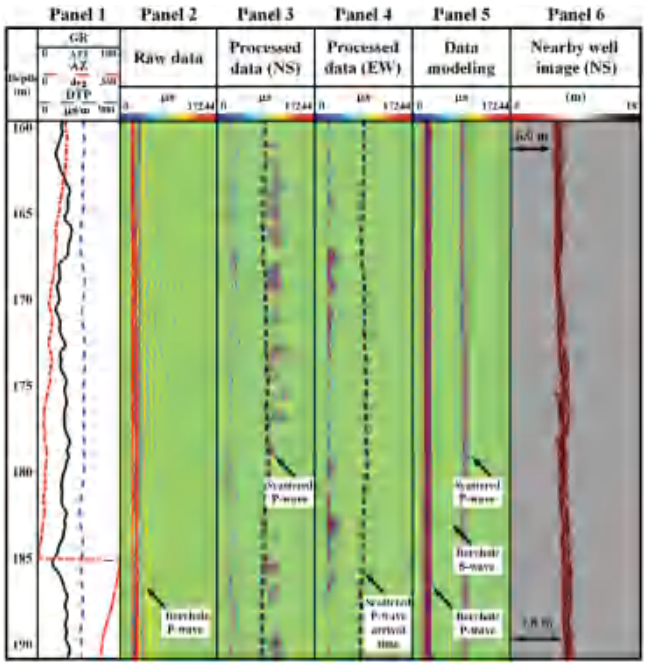


Figure 6. Field example of using 4C dipole acoustic data (the xx-component shown in panel 2) to delineate a nearby borehole target (the image in panel 6) for an unconsolidated formation (the GR and DTP data given in panel 1). The maximum P-wave signal scattered from the target hole is shown in panel 3 and confirmed by the modeling result in panel 5. The maximum (minimum) signal in panel 3 (panel 4) is obtained by using the azimuth curve (AZ in panel 1) in the 4C data rotation.

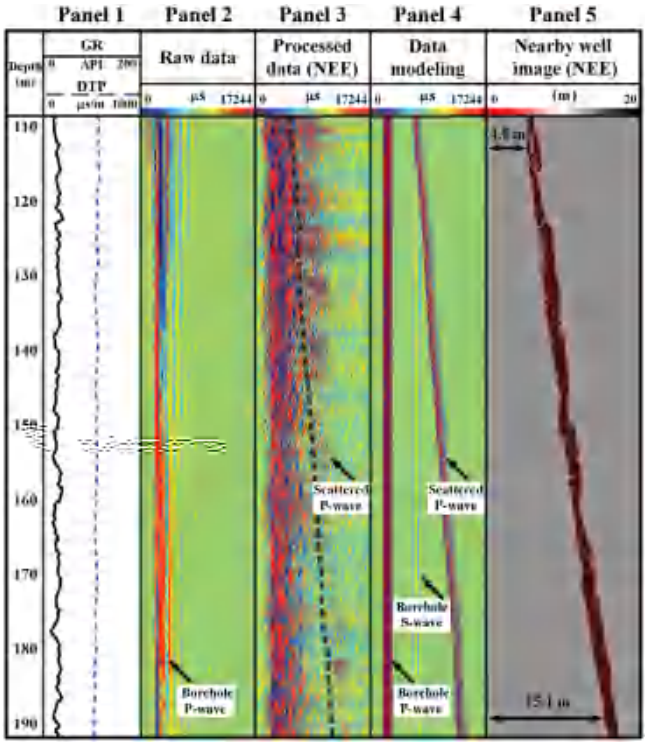


Figure 7. Field example of using dipole wave data (panel 2) to delineate a nearby borehole target (the image in panel 5) for an 80 m interval in an unconsolidated formation (the GR and DTP data given in panel 1). The P-wave signal scattered from the target hole is shown in panel 3 and is confirmed by the modeling result in panel 4.

Downloaded from pubs.geoscienceworld.org/seg/geophysics/article-pdf/86/5/D139/5436635/geo-2020-0570.1.pdf by Univ of Petroleum (Beijing) - Library user on 08 October 2026

CONCLUSION

By analyzing the interaction of the elastic wave propagation with a cased borehole in the very slow formation environment, the effects of wave radiation, reception, and borehole scattering on the dipole acoustic measurement in the nearby borehole can be well understood and correctly modeled. The combination of the steepest-descent solution and reciprocity provides a fast modeling method. The accuracy of the modeling result was verified by comparing it with the 3D finite-difference modeling result. The results show that the dipole-generated P-wave, because of its dominance over the S-wave, is advantageous to use for imaging a near-well borehole target in the very slow formation situation. A novelty of this study is the derivation and validation of the P-wave analysis for the borehole detection problem. The result can be used to provide a method for delineating a nearby borehole target using dipole acoustic logging in shallow unconsolidated sediments.

ACKNOWLEDGMENTS

The authors thank the reviewers for their comments and suggestions that helped to improve the paper. This work was supported by the National Natural Science Foundation of China (grant nos. 41821002 and 42074137), the Natural Science Foundation of Shandong Province (grant no. ZR201911120382), and the Fundamental Research Funds for the Central Universities (YCX2020007).

DATA AND MATERIALS AVAILABILITY

Data associated with this research are confidential and cannot be released.

APPENDIX A

MATRIX ELEMENTS OF EQUATION 8

For the well-bonded cased borehole with N layers (steel, cement, and formation) surrounding the innermost fluid layer, the Thomson-Haskell type propagator matrix T can be used to relate the displacements and stresses across all the layers (Tang and Cheng, 2004). For layer m with an outer radius of R_{out} and an inner radius of R_{in}, the propagator matrix of the layer g_m is given by

$$g_m = T(m; r_{in})T^{-1}(m; r_{out}): \tag{A-1}$$

The matrix G of all layers is defined by

$$G = \left[\left(\prod_{m=1}^{N-1} g_m\right) T(N; r_{fm})\right]; \tag{A-2}$$

where matrix $T(N; r_{fm})$ is related to the outermost formation with an inner radius r_{fm}. The elements of the 6 × 6 matrix T are given as

$$\begin{cases} T_{11} = 1/RI_1(pR) + pI_2(pR) \\ T_{12} = 1/RK_1(pR) - pK_2(pR) \\ T_{13} = 1/RI_1(sR) \\ T_{14} = 1/RK_1(sR) \\ T_{15} = ik(1/RI_1(sR) + sI_2(sR)) \\ T_{16} = ik(1/RK_1(sR) - sK_2(sR)) \end{cases} \quad \begin{cases} T_{21} = -1/RI_1(pR) \\ T_{22} = -1/RK_1(pR) \\ T_{23} = -1/RI_1(sR) - sI_2(sR) \\ T_{24} = -1/RK_1(sR) + sK_2(sR) \\ T_{25} = -ik/RI_1(sR) \\ T_{26} = -ik/RK_1(sR) \end{cases}$$

$$\begin{cases} T_{31} = ikI_1(pR) \\ T_{32} = ikK_1(pR) \\ T_{33} = 0 \\ T_{34} = 0 \\ T_{35} = -s^2I_1(sR) \\ T_{36} = -s^2K_1(sR) \end{cases} \quad \begin{cases} T_{41} = \rho(2k^2\beta^2 - \omega^2)I_1(pR) - 2p\rho\beta^2/RI_2(pR) \\ T_{42} = \rho(2k^2\beta^2 - \omega^2)K_1(pR) + 2p\rho\beta^2/RK_2(pR) \\ T_{43} = 2s\rho\beta^2/RI_2(sR) \\ T_{44} = -2s\rho\beta^2/RK_2(sR) \\ T_{45} = \rho 2ik\beta^2(s^2I_1(sR) - s/RI_2(sR)) \\ T_{46} = \rho 2ik\beta^2(s^2K_1(sR) + s/RK_2(sR)) \end{cases}$$

$$\begin{cases} T_{51} = -2p\rho\beta^2/RI_2(pR) \\ T_{52} = 2p\rho\beta^2/RK_2(pR) \\ T_{53} = -\rho\beta^2(s^2I_1(sR) - 2s/RI_2(sR)) \\ T_{54} = -\rho\beta^2(s^2K_1(sR) + 2s/RK_2(sR)) \\ T_{55} = -2ik\rho\beta^2 s/RI_2(sR) \\ T_{56} = 2ik\rho\beta^2 s/RK_2(sR) \end{cases}$$

$$\begin{cases} T_{61} = 2\rho\beta^2(ikI_1(pR)/R + ikpI_2(pR)) \\ T_{62} = 2\rho\beta^2(ikK_1(pR)/R - ikpK_2(pR)) \\ T_{63} = ik\rho\beta^2/RI_1(sR) \\ T_{64} = ik\rho\beta^2/RK_1(sR) \\ T_{65} = (k^2 + s^2)\rho\beta^2(-sI_2(sR) - I_1(sR)/R) \\ T_{66} = (k^2 + s^2)\rho\beta^2(sK_2(sR) - K_1(sR)/R): \end{cases} \tag{A-3}$$

The elements of the 4 × 4 matrix M used in equation 8 are given as

$$\begin{cases} M_{11} = -1/RI_1(fR) - fI_2(fR) \\ M_{21} = \rho_f\omega^2 I_1(fR) \\ M_{31} = 0 \\ M_{41} = 0: \end{cases} \tag{A-4}$$

In these expressions, R is the inner radius of the given layer, ρ is the layer density, and ρ_f is the fluid density; α, β, and α_f are the P- and S-wave and fluid acoustic velocity, respectively; k is the axial wavenumber; and $p = \sqrt{k^2 - \omega^2/\alpha^2}$, $s = \sqrt{k^2 - \omega^2/\beta^2}$, and $f = \sqrt{k^2 - \omega^2/\alpha_f^2}$ are, respectively, the P- and S-wave and fluid acoustic radial wavenumbers.

REFERENCES

Aki, K., and P. Richards, 1980, Quantitative seismology: Theory and methods, 2nd ed.: University Science Books.

Gibson, R. L., 1994, Radiation from seismic sources in cased and cemented boreholes: Geophysics, 59, 518–533, doi: 10.1190/1.1443613.

Gong, H., H. Chen, X. He, and X. Wang, 2015, Eliminating the azimuth ambiguity in single-well imaging using 3C sonic data: Geophysics, 80, no. 1, A13–A17, doi: 10.1190/geo2014-0337.1.

Hirabayashi, N., and W. S. Leaney, 2019, Wavefield separation for borehole acoustic reflection survey using parametric decomposition and waveform inversion: Geophysics, 84, no. 4, D151–D159, doi: 10.1190/geo2018-0330.1.

Downloaded from pubs.geoscienceworld.org/seg/geophysics/article-pdf/86/5/D139/5436635/geo-2020-0570.1.pdf by Univ of Petroleum (Beijing) - Library user on 08 October 2026

Hornby, B. E., 1989, Imaging of near-borehole structure using full-waveform sonic data: Geophysics, 54, 747–757, doi: 10.1190/1.1442702.
Hornby, B. E., and E. Pasternark, 2000, Analysis of full-waveform sonic data acquired in unconsolidated gas sands: Petrophysics, 41, 363–374.
Hornby, B. E., P. Peterman, C. Hager, A. Draucker, and A. Bolshakov, 2018, Reflection sonic imaging of complex near-borehole structure in slow formations: 88th Annual International Meeting, SEG, Expanded Abstracts, 684–688, doi: 10.1190/segam2018-2996849.1.
Li, D., X. Tian, H. Hu, X. M. Tang, X. Fang, and Y. Zheng, 2020, Gaussian beam imaging of fractures near the wellbore using sonic logging tools after removing dispersive borehole waves: Geophysics, 85, no. 4, D133–D143, doi: 10.1190/geo2019-0104.1.
Li, J. X., K. A. Innanen, G. Tao, K. Zhang, and L. Line, 2017, Wavefield simulation of 3D borehole dipole radiation: Geophysics, 82, no. 3, D155–D169, doi: 10.1190/geo2016-0145.1.
Li, Y. H., X. M. Tang, H. R. Li, and S. Q. Lee, 2021, Characterizing the borehole response for single-well shear-wave reflection imaging: Geophysics, 86, no. 1, D15–D26, doi: 10.1190/geo2020-0212.1.
Li, Z., Y. D. Su, X. M. Tang, H. R. Li, and Q. H. Liu, 2018, A hybrid method to simulate elastic wave scattering of three-dimensional objects: The Journal of the Acoustical Society of America, 144, EL268–EL274, doi: 10.1121/1.5059332.
Meredith, J., 1990, Numerical and analytical modeling of downhole seismic sources: The near and far field: Ph.D. thesis, Massachusetts Institute of Technology.
Peng, C., 1994, Borehole effects on downhole seismic measurements: Ph.D. dissertation, Massachusetts Institute of Technology.
Peng, C., C. H. Cheng, and M. N. Toksöz, 1993, Borehole effects on downhole seismic measurements: Geophysical Prospecting, 41, 883–912, doi: 10.1111/j.1365-2478.1993.tb00889.x.
Tang, X. M., 2004, Imaging near-borehole structure using directional acoustic-wave measurement: Geophysics, 69, 1378–1386, doi: 10.1190/1.1836812.
Tang, X. M., 2016, Reflection imaging away from borehole: A paradigm shift: 86th Annual International Meeting, SEG, Expanded Abstracts, 4873–4877, doi: 10.1190/segam2016-13771414.1.
Tang, X. M., J. J. Cao, Z. Li, and Y. D. Su, 2016, Detecting a fluid-filled borehole using elastic waves from a remote borehole: The Journal of the Acoustical Society of America, 140, EL211–EL217, doi: 10.1121/1.4960143.
Tang, X. M., J. J. Cao, and Z. T. Wei, 2014, Shear-wave radiation, reception, and reciprocity of a borehole dipole source: With application to modeling of shear-wave reflection survey: Geophysics, 79, no. 2, T43–T50, doi: 10.1190/geo2013-0096.1.
Tang, X. M., and C. H. Cheng, 2004, Quantitative borehole acoustic methods: Elsevier Science Publishing Inc.
Tang, X. M., and D. Patterson, 2009, Single-well S-wave imaging using multicomponent dipole acoustic-log data: Geophysics, 74, no. 6, WCA211–WCA223, doi: 10.1190/1.3227150.
Tang, X. M., Y. Zheng, and D. Patterson, 2007, Processing array acoustic-logging data to image near-borehole geologic structures: Geophysics, 72, no. 2, E87–E97, doi: 10.1190/1.2435083.
Tubman, K. M., C. H. Cheng, and M. N. Toksöz, 1984, Synthetic full waveform acoustic logs in cased boreholes: Geophysics, 49, 1051–1059, doi: 10.1190/1.1441720.
Wang, H., and G. Tao, 2011, Wavefield simulation and data-acquisition-scheme analysis for LWD acoustic tools in very slow formations: Geophysics, 76, no. 3, E59–E68, doi: 10.1190/1.3552929.
Wang, Z., H. S. Hu, and Y. F. Yang, 2015, Reciprocity relations for the elastodynamic fields generated by multipole sources in a fluid-solid configuration: Geophysical Journal International, 203, 883–892, doi: 10.1093/gji/ggv308.
Wei, Z. T., and X. M. Tang, 2012, Numerical simulation of radiation, reflection, and reception of elastic waves from a borehole dipole source: Geophysics, 77, no. 6, D253–D261, doi: 10.1190/geo2012-0061.1.
Wei, Z. T., X. M. Tang, and J. J. Cao, 2019, Acoustic radiation and reflection of a logging-while-drilling dipole source: Geophysical Journal International, 219, 108–128, doi: 10.1093/gji/ggz193.
Xu, J., H. Hu, and Z. Wang, 2019, Asymptotic solution to a 3D dipole single-well imaging system with combined monopole and dipole receivers with an application in elimination of azimuth ambiguity: Geophysics, 84, no. 5, D191–D207, doi: 10.1190/geo2018-0658.1.

Biographies and photographs of the authors are not available.

Downloaded from pubs.geoscienceworld.org/seg/geophysics/article-pdf/86/5/D139/5436635/geo-2020-0570.1.pdf by Univ of Petroleum (Beijing) - Library user on 08 October 2026

GEOPHYSICS, VOL. 90, NO. 2 (MARCH-APRIL 2025); P. A15–A19, 4 FIGS.
10.1190/GEO2024-0621.1

Acoustic ranging of multiple nearby wells using dipole acoustic logging

Xi-Hao Gu[1], Xiao-Ming Tang[2], Yuan-Da Su[2], and Sheng-Qing Li[2]

ABSTRACT

The increasing use of cluster wells in recent oil and gas drilling has raised concerns about well collisions. Although the successful application of single-well acoustic reflection imaging for nearby well detection has made it a potential ranging technique for collision prevention, further analyses are needed to demonstrate its utility for detecting multiple target wells around the measurement well. We develop a multiple-well acoustic ranging method that uses 4C dipole logging data to azimuthally scan multiple nearby wells and determine their distances and directions. To this aim, we develop a fast analytical method to model elastic wave radiation from the measurement well and wave scattering from multiple nearby wells and analyze the sensitivity and effectiveness of the 4C dipole tool in the generation of the transmitted wave and detection of the scattered waves. By means of 4C rotation and migration, the scattered wave data, as measured by the tool, are used to image the targeted wells and determine their distance and azimuth relative to the measurement well. Field data application is presented to demonstrate the effectiveness of this multiple-well acoustic ranging technique.

INTRODUCTION

Single-well reflection imaging has recently been successfully applied to the acoustic ranging of a nearby well (Jervis et al., 2018; Tang et al., 2021). This application analyzes the acoustic signals scattered from the nearby well to determine its azimuth and distance (Haldorsen et al., 2010; Hirabayashi and Leaney, 2019), making this technique a potential tool for relief well drilling (Gu et al., 2021). With the increasing use of cluster wells in oilfields, constructing multiple wells in a limited space raised the need for collision prevention (Yan et al., 2022), for which the acoustic ranging technique has been proposed (Ben et al., 2020). In such an application environment, the trajectories of the measurement well and target wells vary with depth, and the acoustic signals scattered from the target wells could be potentially masked by the strong direct borehole waves and logging tool rotation effects (Fehler and Pearson, 1984; Ji et al., 2021), making it a challenging task to determine the azimuth and location of the target wells (Wang et al., 2015). Therefore, theoretical analyses and data processing methods need to be developed to demonstrate acoustic imaging feasibility with multiple target wells.

A commonly used method for locating nearby wells is magnetic ranging, which requires the presence of a casing target well (Yan et al., 2022). In comparison, acoustic methods do not have such limitations as they rely solely on the impedance contrast between the formation and the target well (Xu et al., 2024). Acoustic ranging methods can be classified as monopole and dipole methods based on the borehole acoustic source used (Esmersoy et al., 1998; Zhao et al., 2023). Using the elastic spectral element method, Jervis et al. (2018) model the response of an acoustic logging instrument with three monopole acoustic sources to identify the location of a target vertical borehole from a nearby high-angle well. Tang et al. (2016) analyze the use of dipole-generated SH waves for detecting the target well in a fast formation. The type of elastic wave data used for acoustic ranging also varies with the elastic parameters of the formation. Although dipole S waves are commonly used for fracture characterization in hard rock formations (Li et al., 2021), Gu et al. (2021) demonstrate that in shallow unconsolidated formations, the dipole P wave, instead of the S wave, is more effective in detecting a nearby well. Note that previous studies focus on the acoustic ranging of a single nearby well, whereas the present study focuses on the acoustic ranging of multiple nearby wells.

In this study, we present a multiwell ranging method using 4C dipole logging data (xx, xy, yx, yy). We develop a fast algorithm

Manuscript received by the Editor 5 September 2024; ; published ahead of production 25 November 2024; published online 18 February 2025.
[1]China University of Petroleum, East China, School of Geosciences, Qingdao, China and State Key Laboratory of Deep Oil and Gas, China University of Petroleum, East China, Qingdao, China. E-mail: guxih@sina.com.
[2]China University of Petroleum, East China, School of Geosciences, Qingdao, China; State Key Laboratory of Deep Oil and Gas, China University of Petroleum, East China, Qingdao, China; and Laoshan Laboratory, Qingdao, China. E-mail: tangxiam@aliyun.com (corresponding author); syuanda@sina.com; shidalishengqing@yeah.net.
© 2025 Society of Exploration Geophysicists. All rights reserved.

Downloaded from pubs.geoscienceworld.org/seg/geophysics/article-pdf/90/2/A15/7117776/geo-2024-0621.1.pdf by Univ of Petroleum (Beijing) - Library user on 08 October 2026

for calculating the elastic wave scattering from multiple wells and analyze the azimuthal sensitivity of the scattered 4C dipole P-wave data in the slow formation environment. By combining the rotation of the 4C scattered wave data with a migration method, we can image the nearby wells and determine their locations. Applying the proposed method to field data processing, we demonstrate that this acoustic multiwell ranging technique, under normal logging conditions, can accurately determine the distance and azimuth of multiple nearby wells.

THEORY AND METHOD

The configuration of the acoustic ranging of multiple wells is shown in Figure 1a. A dipole source orienting in the x-axis is placed in a newly drilled borehole (called the measurement well) and radiates the elastic waves into the formation. The elastic waves are scattered by two nearby wells (called the target wells) back to the borehole and then received by an array of receivers that are azimuthally spaced in the measurement well. The received wave signal RWV, represented in the frequency domain, can be expressed as

$$\mathrm{RWV}(\omega;\varphi_0)=\sum_{i=1}^{m}\mathrm{RW}_i(\omega;\varphi_0;\varphi_i); \tag{1}$$

where m denotes the number of nearby wells, the wavefield scattered from the ith nearby well (RW_i) can be written as (Gu et al., 2021)

$$\mathrm{RW}_i(\omega;\varphi_0;\varphi_i)=\frac{S(\omega)}{4\pi V_P^2}\cdot \mathrm{RD}(\omega;\varphi_0;\varphi_i)\cdot u_r^s(\omega;\varphi)\cdot \mathrm{RC}(\omega;\varphi_0;\varphi_i); \tag{2}$$

where S denotes the acoustic source spectrum, and V_P is the formation P-wave velocity. The scattered wave spectrum contains the radiation pattern of the dipole source RD, the scattered wave displacement u_r^s, and the borehole reception pattern RC, where φ_0 denotes the angle between the x-axis and the source/receiver orientation, and φ_i denotes the angle between the x-axis and the ith target well (see Figure 1a). The solution of the scattered wave displacement from an individual target well is given by (Gu et al., 2021)

$$u_r^s(\omega;\varphi)=\sqrt{\frac{-i\pi\omega\sin^3\delta}{2V_P(r+r_0)rr_0}}\sum_{n=0}^{\infty}[B_n^s\cos(n\varphi)+B_n'^s\sin(n\varphi)]e^{i\omega(R'+r_0\sin\delta)/V_P}; \tag{3}$$

where δ is the incidence angle (see Figure 1a) and r_0 and R' denote the distance between the measurement well and the target well and the propagation distance of the scattered wave, respectively. The amplitude coefficients B_n^s and $B_n^{s'}$ of the scattered P waves are determined by the boundary conditions at the target well wall, assuming that the casing-well cylindrical layered structure is well bonded. This model can be simplified to the case of an open hole by setting the parameters of each cylindrical layered structure to those of the formation. Here, we have assumed that the formation is uniform and there are no geologic layers present within the region of concern.

Equation 1 presents a fast analytical method for calculating acoustic signals from multiple nearby cased wells around the measurement well where the dipole acoustic tool is located. For example, using the model shown in Figure 1a, the source and receivers are placed along the measurement borehole axis, with the source-to-receiver spacing ranging from 3.0 to 4.05 m. The two target wells are situated at distinct azimuths and distances ($r_{0A}=3$ m, $r_{0B}=4$ m, $\varphi_0=0°$, $\varphi_A=30°$, and $\varphi_B=0°$ where the subscripts A and B denote the target wells A and B in Figure 1a, respectively). The elastic properties of the cased boreholes and the formation are the same as those described by Gu et al. (2021). Figure 1b shows the fluid displacement signals at the borehole center computed using the analytical (the dots) and 3D finite-difference (Hei and Xiao, 2019) numerical (the solid line) modeling. The signals are displayed over a 4–8 ms time window wherein the scattered waves from the two target wells can be seen. The analytical and numerical results agree very well, but the computation speed of the analytical method is three orders of magnitude faster than that of the numerical method. Thus, our analytical solution provides a fast and effective tool for modeling multiple well acoustic ranging using dipole acoustic logging.

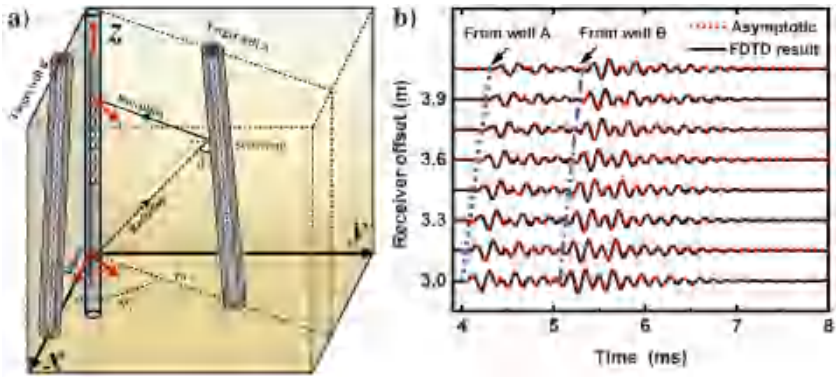


Figure 1. (a) The schematic model of the acoustic ranging of multiple wells using dipole acoustic logging. (b) Acoustic signals that are scattered from the two nearby wells and received in the measurement well as calculated for the model of (a) using the analytical (the dots) and the 3D finite-difference (the solid line) methods.

4C SCANNING OF NEARBY WELLS

We use the rotation property of the 4C dipole waves (Tang, 2004) to formulate an azimuthal scanning method and use it to determine the azimuth of multiple nearby wells. We use the model shown in Figure 1a to demonstrate this method. For this demonstration, the azimuthal angle and distance to target wells A and B are specified as $r_{0A}=7$ m, $r_{0B}=4$ m, $\varphi_A=60°$, and $\varphi_B=10°$, respectively. By firing the source in the x ($\varphi_0=0°$) and y ($\varphi_0=90°$)-directions, respectively, and computing the x- and y-displacement at the receiver location using equations 1 and 3 for each firing, we obtain the 4C scattered wave data (xx, xy, yx, yy) from the target wells. Figure 2a shows the 4C P-wave data for a receiver located at a 3 m distance above the source. The scattered waves from well B arrive earlier than those from well A, and the amplitude of the two wave sets varies according to the azimuth of the target wells relative to the source. The 4C dipole rotation (Tang, 2004) is then applied to rotate the data to an arbitrary angle ϕ, generating a new XX-component wave data:

Downloaded from pubs.geoscienceworld.org/seg/geophysics/article-pdf/90/2/A15/7117776/geo-2024-0621.1.pdf by Univ of Petroleum (Beijing) - Library user on 08 October 2026

$$XX(\phi) = \int_W [xx\cos^2(\phi) - \sin(\phi)\cos(\phi)(xy + yx) + yy\sin^2(\phi)]dt: \quad (4)$$

By varying the angle ϕ in the range of 0°–360°, the XX wave scans around the borehole and detects the nearby target wells in the full azimuth range. Different from single-well ranging, in the 4C dipole rotation of multiwell ranging, a window W is placed on the scattered wave (or its migrated image) data to distinguish the signals from different wells (for the application of equation 4, we assume that the target wells locate at different distances from the measurement well such that their reflected waves do not overlap with each other). For example, for the target wells A and B of model Figure 1a, two windows, each about three wavelengths long, are used, as shown in Figure 2a. The two windowed data sets shown in Figure 2a are used in equation 4 to give the amplitude azimuth patterns in Figure 2b, wherein the wave amplitudes are normalized relative to their maximum values. The polar plots from the two windowed signals show two characteristic symmetric dipole patterns: one peaks at $\phi = 60°$ and $\phi = 240°$ for well A, and the other peaks at $\phi = 10°$ and $\phi = 190°$ for well B. The first peak corresponds to the azimuth of the target well, whereas the second peak arises from the 180° azimuth ambiguity due to the dipole symmetry. This modeling example demonstrates that the target well's azimuth, albeit with a 180° ambiguity, can be determined from the 4C dipole logging

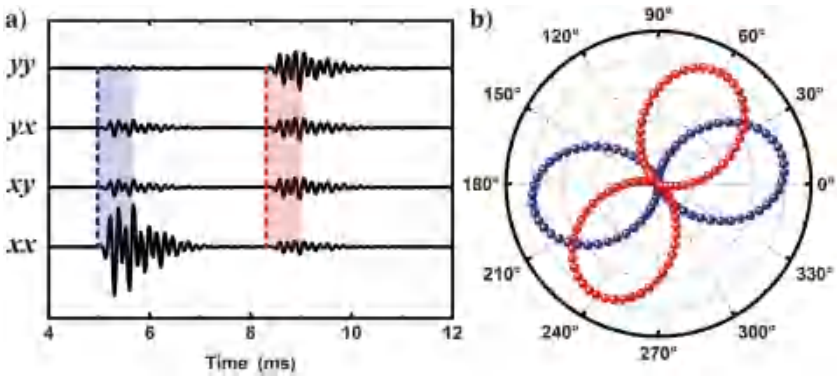


Figure 2. (a) Simulated 4C data (xx, xy, yx, yy) for two target wells positioned at the azimuths of 10° and 60°, respectively. (b) A polar diagram displaying the windowed amplitudes of the 4C rotated waves from wells A and B. The amplitudes are individually normalized to their respective maximum values within the range.

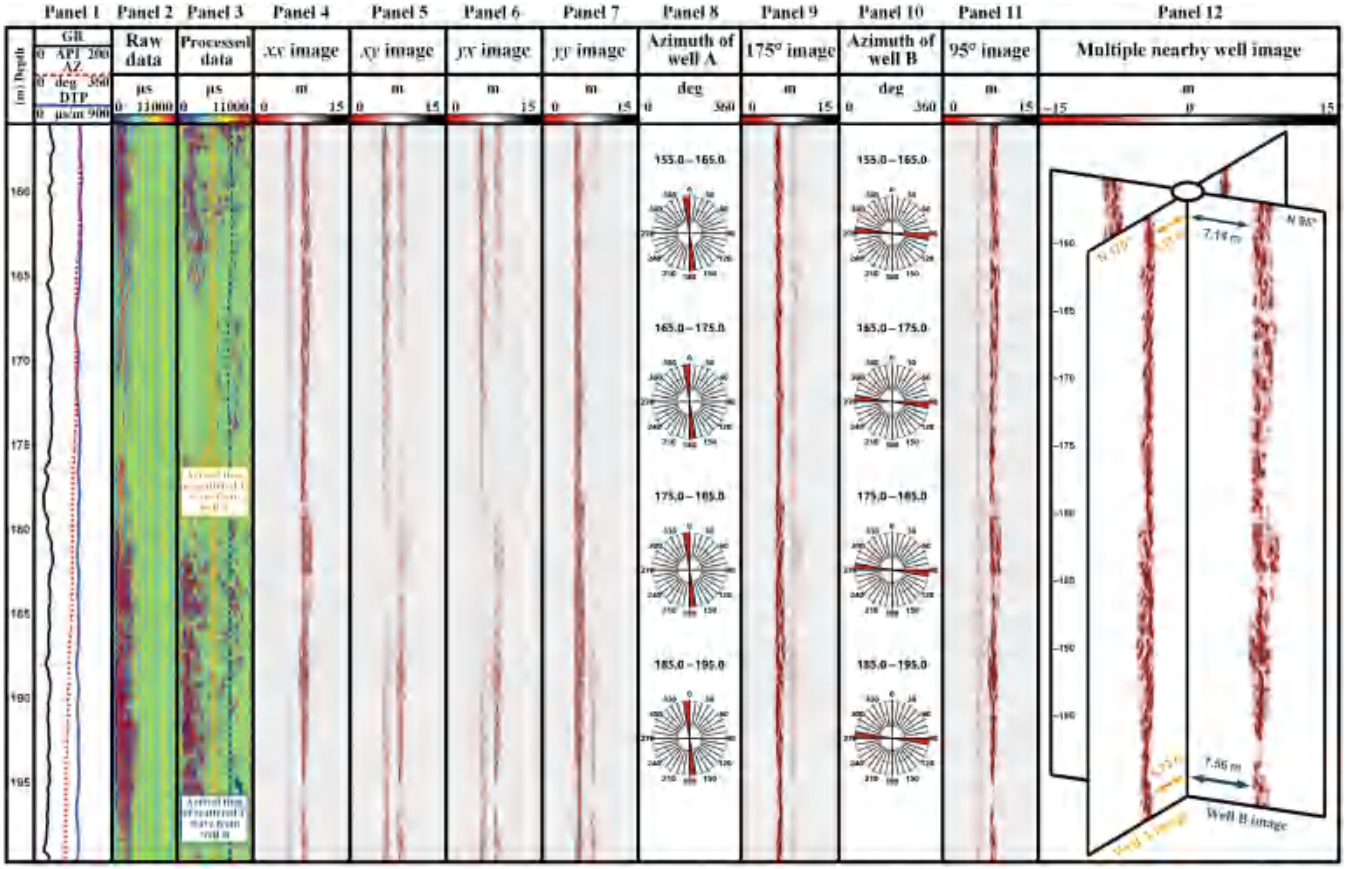


Figure 3. The field example of the 4C dipole acoustic ranging of multiple wells. Panel 1 displays the AZ, GR, and DTP curves. For illustration, panels 2 and 3 show the xx-component data and their processing result, respectively. Panels 4–7 show the migration images of the 4C data, where the data of the two imaged events are, respectively, windowed to determine the azimuth of panel 8 (10) and the image of panel 9 (11) for well A (B). Panel 12 is a 3D overview of the two imaged wells.

Downloaded from pubs.geoscienceworld.org/seg/geophysics/article-pdf/90/2/A15/7117776/geo-2024-0621.1.pdf by Univ of Petroleum (Beijing) - Library user on 08 October 2026

data. In field application, the 180° ambiguity can be resolved by the surface location map of the drilled wells.

APPLICATION

We demonstrate the application of the multiple-well dipole acoustic ranging technique using field data examples. The example in Figure 3 shows a 155–200 m section logged with a 4C dipole array acoustic tool. Panel 1 displays the gamma ray (GR), P-wave slowness (DTP), and tool azimuth (AZ, measured from the y-dipole relative to the north) log curves. The xx-component data (panel 2) are used for illustration. The data are first processed to suppress the large-amplitude borehole arrivals (e.g., Hornby, 2023). The result in panel 3 shows two events, as delineated by the two arrival-time curves (calculated from the imaged well location and the DTP curve). The events are better identified from their migration images (the images of all components, xx, xy, yx, and yy, are shown in panels 4–7, respectively), which are obtained using the data of all the receivers in the array and all relevant depths (Gu et al., 2021). The imaging result identifies two cased wells, called A and B, located at distances of approximately 5.5 and 7.4 m, respectively. For the 4C images, a 1 m length window is placed on each event, and the windowed data are, respectively, input into equation 4 to determine the azimuth of the two wells (for the actual determination procedure, see Li et al., 2020). Panel 8 (10) shows the azimuth rose diagram of well A (B), indicating that well A (B) is along the N175°/N355° (N95°/N275°) azimuth. The migration images for the two well azimuths (panels 9 and 11) confirm the 4C rotation results, showing that the well image attains its strongest intensity at its determined azimuth. Panel 12 provides a 3D overview of the two imaged wells. Across the depth interval, their distance varies from 5.23 to 5.72 m (well A) and 7.14 to 7.56 m (well B). The surface well location map of the area confirms the imaging results and shows that, of the two possible azimuth solutions, the correct azimuth of well A (B) is 175° (95°), thus resolving the 180° ambiguity of the dipole imaging result.

To further demonstrate the effectiveness of the technique, Figure 4 shows the processing and analysis results for a deeper section (460–505 m) of the well. The same as in Figure 3, panel 1 shows the GR, DTP, and AZ log curves of the section. Using the same analysis procedure shown in Figure 3, we obtain two well azimuths at N175°/N355° (panel 2) and N105°/N285° (panel 4), respectively. Their corresponding imaging results are shown in panels 3 and 5, respectively. The first solution coincides with that of well A in Figure 3. However, the second solution exhibits significant azimuth and distance changes compared with its counterpart of well B in Figure 3. As observed from the 3D overview of the image results (panel 6), the well B distance in this deeper section varies between 7.25 and 12.58 m, and its azimuth is rotated approximately 10° relative to the shallower section shown in Figure 3. This example shows that under normal field conditions, the multiple-well ranging technique can effectively determine the two nearby wells with varying trajectories.

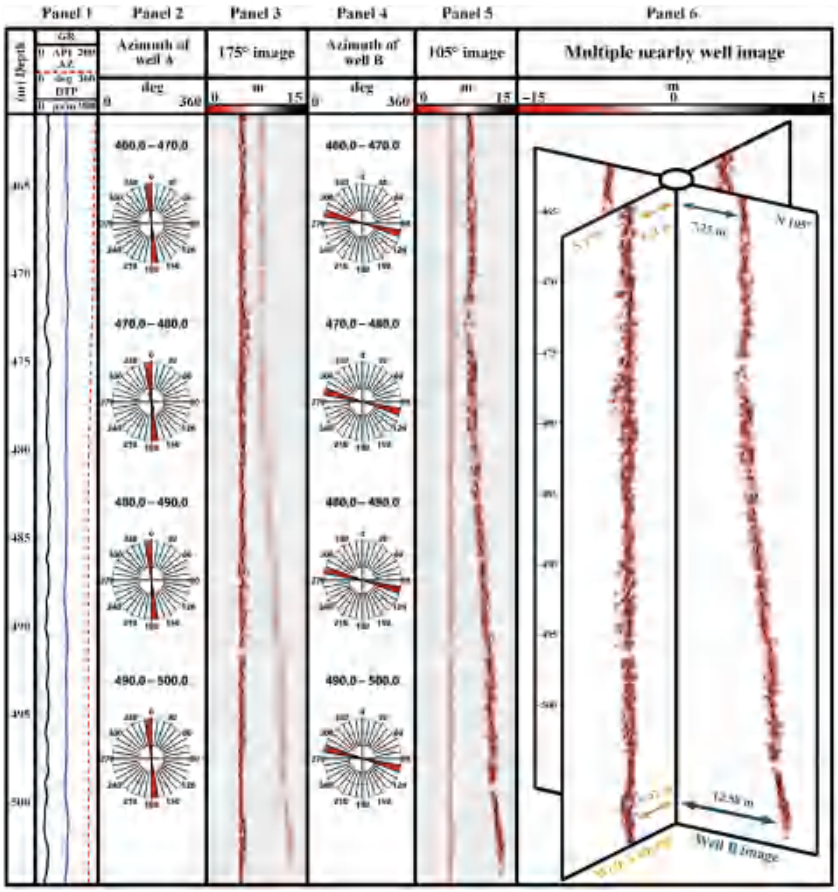


Figure 4. The 4C dipole acoustic ranging result for a deeper section shown in Figure 3. Panel 1 displays the GR, DTP, and AZ curves of the depth section. Compared with Figure 3, the well A trajectory (panels 2 and 3) is almost unchanged, but the well B trajectory (panels 4 and 5) changes significantly in azimuth and inclination. Panel 6 is a 3D overview of the two imaged wells.

CONCLUSION

A multiple-well ranging method using 4C dipole logging data is developed to delineate multiple nearby wells surrounding the logged well. Along with the application, a fast modeling algorithm is provided for simulating elastic wave scattering and reception from multiple wells. Combining the rotation and migration/imaging of the 4C scattered wave data, we can determine the location and azimuth of the nearby well targets when the wells are well separated from each other such that their scattered wave does not overlap at the receiver and can be easily separated. In a shallow, soft formation environment, the dipole P wave, instead of the S wave, should be used for the application. The method has been validated in a field application where two wells with varying trajectories are successfully delineated.

ACKNOWLEDGMENTS

This work was supported by the National Natural Science Foundation of China (grant nos. U21B2064 and 42174145), the Natural Science Foundation of Shandong Province (grant no. ZR2024YQ062), and the State Key Laboratory of Deep Oil and Gas (grant no. SKLDOG2024-ZYTS-04). The authors thank K. Innanen, S. de

Downloaded from pubs.geoscienceworld.org/seg/geophysics/article-pdf/90/2/A15/7117776/geo-2024-0621.1.pdf by Univ of Petroleum (Beijing) - Library user on 08 October 2026

Ridder, and A. Guitton for their helpful comments on the manuscript. Five anonymous reviewers are also acknowledged for their comments and suggestions that significantly improved the manuscript.

DATA AND MATERIALS AVAILABILITY

Data associated with this research are available and can be obtained by contacting the corresponding author.

REFERENCES

Ben, J., W. Qiao, X. Che, X. Ju, J. Lu, and B. Men, 2020, Field validation of imaging an adjacent borehole using scattered P-waves: Petroleum Science, 17, 1272–1280, doi: 10.1007/s12182-020-00475-5.

Esmersoy, C., C. Chang, M. Kane, R. Coates, B. Tichelaar, and E. Quint, 1998, Acoustic imaging of reservoir structure from a horizontal well: The Leading Edge, 17, 940–946, doi: 10.1190/1.1438075.

Fehler, M., and C. Pearson, 1984, Cross-hole seismic surveys: Applications for studying subsurface fracture systems at a hot dry rock geothermal site: Geophysics, 49, 37–45, doi: 10.1190/1.1441559.

Gu, X. H., X. M. Tang, and Y. D. Su, 2021, Delineating a cased borehole in unconsolidated formations using dipole acoustic data from a nearby well: Geophysics, 86, no. 5, D139–D147, doi: 10.1190/geo2020-0570.1.

Haldorsen, J. B. U., F. Zhu, N. Hirabayashi, W. H. Borland, H. Karniawan, H. Yamamoto, K. Al-Ghammari, and R. T. Coates, 2010, Borehole acoustic reflection survey (BARS) using full waveform sonic data: First Break, 28, 33–38, doi: 10.3997/1365-2397.28.7.40645.

Hei, C., and Z. Xiao, 2019, Borehole elastic wave anisotropic scattering and application to hydraulic fracturing: Journal of Petroleum Science and Engineering, 183, 106405, doi: 10.1016/j.petrol.2019.106405.

Hirabayashi, N., and W. S. Leaney, 2019, Wavefield separation for borehole acoustic reflection survey using parametric decomposition and waveform inversion: Geophysics, 84, no. 4, D151–D159, doi: 10.1190/geo2018-0330.1.

Hornby, B., 2023, The road to achieving business value with reflection sonic imaging: 64th Annual Logging Symposium, SPWLA, Extended Abstracts, doi: 10.30632/SPWLA-2023-0063.

Jervis, M., T. Tonellot, A. Bakulin, and I. A. Ghamdi, 2018, High-resolution acoustic imaging from a borehole to detect a nearby well: The Leading Edge, 37, 812–817, doi: 10.1190/tle37110812.1.

Ji, Y., X. He, H. Chen, X. Wang, and H. Zhang, 2021, Acoustic fields for monopole logging while drilling with an eccentric collar: Geophysics, 86, no. 2, D43–D63, doi: 10.1190/geo2019-0744.1.

Li, C., H. Chen, X. He, and X. Wang, 2021, Identifying reflector azimuth from borehole multicomponent cross-dipole acoustic measurement: Geophysics, 86, no. 6, D201–D214, doi: 10.1190/geo2020-0460.1.

Li, S. Q., Y. D. Su, and X. M. Tang, 2020, Research on a fast inversion method for structural strike around a borehole based on four-component dipole shear wave reflection imaging: Chinese Journal of Geophysics, 63, 2478–2487, doi: 10.6038/cjg2020N0322.

Tang, X. M., 2004, Imaging near-borehole structure using directional acoustic-wave measurement: Geophysics, 69, 1378–1386, doi: 10.1190/1.1836812.

Tang, X. M., J. J. Cao, Z. Li, and Y. D. Su, 2016, Detecting a fluid-filled borehole using elastic waves from a remote borehole: The Journal of the Acoustical Society of America, 140, EL211–EL217, doi: 10.1121/1.4960143.

Tang, X. M., X. H. Gu, Y. H. Li, and Y. D. Su, 2021, The interaction between borehole and elastic waves: Theory, method and application: Chinese Journal of Geophysics, 64, 4227–4238, doi: 10.6038/cjg2021O0396.

Wang, H., G. Tao, and X. F. Shang, 2015, A method to determine the strike of interface outside of borehole by monopole borehole acoustic reflections: Journal of Petroleum Science and Engineering, 133, 304–312, doi: 10.1016/j.petrol.2015.05.025.

Xu, J., H. Hu, and B. Han, 2024, A fast algorithm for simulation and analysis of wavefields in acoustic single-well imaging of logging-while-drilling considering arbitrary types of sources: Geophysics, 89, no. 2, D99–D112, doi: 10.1190/geo2023-0177.1.

Yan, X., H. Liang, X. Dou, M. Qing, and X. Cao, 2022, An active magnetic ranging method for drilling cluster wells based on casing current excitation: Journal of Petroleum Science and Engineering, 208, 109784, doi: 10.1016/j.petrol.2021.109784.

Zhao, T., X. Che, W. Qiao, and L. Cheng, 2023, Borehole azimuthal acoustic imaging using 3D spatial scanning: Application in acoustic detection of nearby wells: Geophysics, 88, no. 2, D131–D145, doi: 10.1190/geo2022-0083.1.

Biographies and photographs of the authors are not available.

Downloaded from pubs.geoscienceworld.org/seg/geophysics/article-pdf/90/2/A15/7117776/geo-2024-0621.1.pdf by Univ of Petroleum (Beijing) - Library user on 08 October 2026

Geophysical Journal International

Geophys. J. Int. (2019) **217,** 288–293
Advance Access publication 2019 January 15
GJI Marine geosciences and applied geophysics

doi: 10.1093/gji/ggz023

EXPRESS LETTER

Shear wave imaging to determine near-borehole faults for ocean drilling exploration

Sheng-Qing Lee,[1,2] Xiao-Ming Tang[1,3] and Yuan-da Su[1]

[1]*School of Geosciences, China University of Petroleum, East China, Qingdao 266580, China. E-mail: tangxiam@aliyun.com*
[2]*Shandong Provincial Key Laboratory of Depositional Mineralization & Sedimentary Mineral, Shandong University of Science and Technology, Qingdao 266590, China*
[3]*Laboratory for Marine Mineral Resources, Qingdao National Laboratory for Marine Science and Technology, Qingdao 266237, China*

Accepted 2019 January 13. Received 2018 December 22; in original form 2018 June 29

SUMMARY

The Deep Sea Drilling Project (DSDP) or Ocean Drilling Program (ODP), and the recent International Discovery Program (IODP) usually acquire borehole geophysical data for planetary exploration. A recently developed shear wave imaging technique was applied to the acoustic waveform log data of the IODP U1473A hole to image a fault system about 40 m away from the borehole. The shear wave imaging not only allowed us to delineate the fault structure in the vicinity of the borehole, but also to determine the orientation of the fault system, providing much needed information for the interpretation of the tectonic situation of the well site. Theory and method for the imaging application are elaborated and data processing results are presented along with the supporting borehole geophysical data. Its successful application to the IODP U1473A hole suggests that the shear wave imaging technique can be applied to the previously recorded and future ODP/IOPD borehole acoustic data, promising the extraction of valuable geophysical and geological information.

Key words: Donwhole methods; Fracture, faults and high stain deformation zones; Indian Ocean; Ocean drilling; Image processing.

1 INTRODUCTION

The international Earth science community has been conducting ocean drilling and research for planetary exploration for decades (Dick *et al.* 1991; Dick *et al.* 2017). The U1473A hole of the International Ocean Discovery Program (IODP) was completed during Expedition 360 in early 2016. The hole was drilled on the summit of the Atlantis Bank, the east flank of the Atlantis II transform of the Southwest Indian Ocean Ridge (Dick *et al.* 2017). The entire 789.7 m drilled depth below seafloor primarily consists of gabbroic rocks cut by dikes and faults. Much effort has been spent to determine the fault systems in the gabbro massif, which is a prerequisite for understanding the interplay of magmatic and tectonic process (Dick *et al.* 1991, 2017; Muller *et al.* 2000; MacLeod *et al.* 2017). Through extensive coring, seven distinct fault systems were identified in the upper 469 meters below seafloor (mbsf). In the lower section below 500 m, however, distinct faults were not as easily identifiable from the cores as in the upper section, although a fault system is suspected around 570 m (Dick *et al.* 2017). Although the cores are valuable for providing direct information of the rock along the borehole, the information is limited to a small lateral distance from the borehole. For example, it is usually difficult to determine whether a planar discontinuity on the core sample is associated with a fracture or fault without knowing how this feature extends away from the borehole.

Borehole geophysical data are used to determine *in situ* physical properties of rocks and geological information of the formation (Goldberg 1997). A key component is the data acquired from borehole acoustic logging using a multipole array acoustic tool (e.g. Schlumberger DSI tool). A modern multipole acoustic tool consists of a monopole and a four-component (4C) cross-dipole acoustic system. In ODP/IODP projects, monopole logging is traditionally used to measure seismic velocities around the wellbore, and the cross-dipole logging is used to analyse shear wave anisotropy of formation rocks (Zakharova & Goldberg 2015). In this study, we apply a recently developed borehole geophysical imaging technique, called shear wave reflection imaging, to the cross-dipole data acquired by ODP/IODP, focusing on the suspected, ambiguous fault system around and below 570 m depth.

2 THEORY AND METHOD

Shear wave reflection imaging technique is a recent advance in wireline acoustic logging that has been used for fracture detection in hydrocarbon exploration (Tang 2004; Tang & Patterson 2009).

© The Author(s) 2019. Published by Oxford University Press on behalf of The Royal Astronomical Society.

Downloaded from academic.oup.com/gji/article/217/1/288/5289575 by China University of Petroleum - Beijing user on 08 October 2026

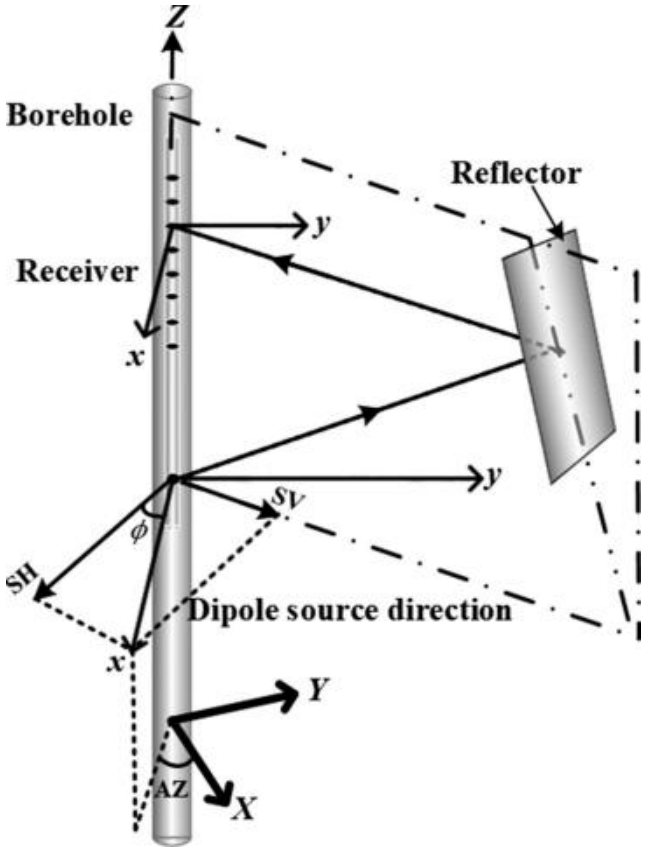


Figure 1. Shear wave imaging using a four-component cross-dipole tool in a borehole. The *x*-dipole source is projected along the wave incident plane to generate *SV* waves towards the reflector and normal to that plane to generate *SH* waves. At the receiver location, the reflected *SV* and *SH* waves are projected onto the *x*- and *y*-dipole receivers where they are recorded. AZ is the angle between the *X*-axis of the new coordinates and the *x*-axis of the tool-frame coordinates.

A the dipole acoustic source–receiver system is used in a borehole to radiate and receive shear waves to and from remote geologic reflectors in the formation, thus potentially allowing for imaging geological features, such as fractures, faults, bed boundaries, etc. (Tang 2004; Tang & Patterson 2009; Bolshakov *et al.* 2011; Tang *et al.* 2014; Tang 2016, 2017). Compared to the reflected *P*-wave imaging with a monopole (Hornby 1989), the particular advantage for the dipole-shear imaging is that, by combing the 4C data of the cross-dipole system, the strike azimuth of the geological reflector can be determined.

Fig. 1 illustrates the concept of dipole-shear wave imaging of a planar reflector in the vicinity of the borehole. A Cartesian coordinates (*x*, *y*, *z*) system is chosen such that the borehole is along the *z*-axis. The dipole source, a directed vector source, is located at the origin (0, 0, 0), pointing in the *x*-direction and radiating shear waves to the reflector. The wave incident plane contains the borehole and the reflector normal, forming an angle ϕ with the *y*-axis. At low-frequencies where wavelength is large compared to borehole diameter, the dipole is equivalent to a point force source in an infinite elastic medium (Ben Menahem & Kostek 1991) whose radiation characteristics are well known (Aki & Richard 1980).

With respect to the reflector orientation, the vector dipole source can be decomposed into two components, labelled *SH* and *SV* (Fig. 1). The component parallel to the strike direction of the reflector corresponds to a horizontally polarized shear wave (*SH* wave), while the component contained in the (vertical) incident plane corresponds to a shear wave whose polarization is in the vertical plane (*SV* wave). The reflected *SH* and *SV* shear waves are recorded by the *x*- and *y*-dipole receivers of the cross-dipole system, which are oriented along the *x*- and *y*-axes (Fig. 1). Due to the vector nature of the dipole recording, the oriented dipole receiver measures the projection of the wave vector (*SH* and *SV*) onto the receiver direction. As a result, the recorded particle velocity or displacement data of the *x*- and *y*-receivers are expressed as

$$\begin{aligned} xx &= SH\cos^2\phi + SV\sin^2\phi \quad \text{and} \\ xy &= -(SH - SV)\cos\phi\sin\phi. \end{aligned} \tag{1}$$

The double letters are used to denote the cross-dipole data, with the first (second) letter referring to the source (receiver) orientation. The symbol *SH* (*SV*) in eq. (1) now denotes the received shear wave reflection data when the source–receiver orientation is parallel to (perpendicular to) the reflector strike direction. Similarly, for a dipole source oriented along the *y*-axis, the recorded data are

$$\begin{aligned} yx &= -(SH - SV)\cos\phi\sin\phi \quad \text{and} \\ yy &= SH\sin^2\phi + SV\cos^2\phi. \end{aligned} \tag{2}$$

From the 4C data *xx*, *xy*, *yx* and *yy*, the pure *SH*- and *SV*-wave data can be obtained for any tool orientation angle ϕ by

$$\begin{aligned} SH &= xx\cos^2\phi - (xy + yx)\cos\phi\sin\phi + yy\sin^2\phi \quad \text{and} \\ SV &= xx\sin^2\phi + (xy + yx)\cos\phi\sin\phi + yy\cos^2\phi. \end{aligned} \tag{3}$$

For the borehole dipole source–receiver system, the SH-component is much larger than the SV-component, especially for a high-angle (nearly vertical) reflector (see Tang & Patterson 2009; Tang *et al.* 2014). This property can be easily understood using the analogy of the single force source radiation (Aki & Richards 1980). When the force is parallel to (perpendicular to) the reflector plane, the radiated *SH* (*SV*) wave is strongest (weakest). This property will later be used to interpret and determine the strike azimuth of a fracture/fault system. Eq. (3) shows that the 4C data form a 2×2 symmetric matrix that can be used to generate a new 4C data for any given azimuthal direction using the coordinate transformation or matrix rotation

$$\begin{pmatrix} XX & XY \\ YX & YY \end{pmatrix} = \begin{pmatrix} \cos AZ & \sin AZ \\ -\sin AZ & \cos AZ \end{pmatrix} \begin{pmatrix} xx & xy \\ yx & yy \end{pmatrix} \times \begin{pmatrix} \cos AZ & -\sin AZ \\ \sin AZ & \cos AZ \end{pmatrix}. \tag{4}$$

where *AZ* is the angle between the *X*-axis of the new coordinates and the *x*-axis of the tool-frame coordinates. Thus, by varying the azimuth *AZ* to diagonalize the rotated matrix, such that

$$\begin{pmatrix} XX & XY \\ YX & YY \end{pmatrix} \xrightarrow{AZ} \begin{pmatrix} SH & 0 \\ 0 & SV \end{pmatrix}, \tag{5}$$

the true reflector strike azimuth *AZ* can be determined.

3 DATA ANALYSIS AND INTERPRETATION

We analyse borehole geophysical data recorded in the U1473A well for a 100 m depth section below 565 m (Fig. 2). The average *Vp* and *Vs* values for the depth interval, obtained from downhole monopole waveform by an array acoustic data processing method (Kimball & Marzetta 1984), are 6.9 and 3.82 km s^{-1}, respectively, giving a *Vp/Vs* ratio of 1.81, consistent with the laboratory-measured value for shallow oceanic gabbroic rock (Hyndman 1979). The *Vs* curve

Downloaded from academic.oup.com/gji/article/217/1/288/5289575 by China University of Petroleum - Beijing user on 08 October 2026

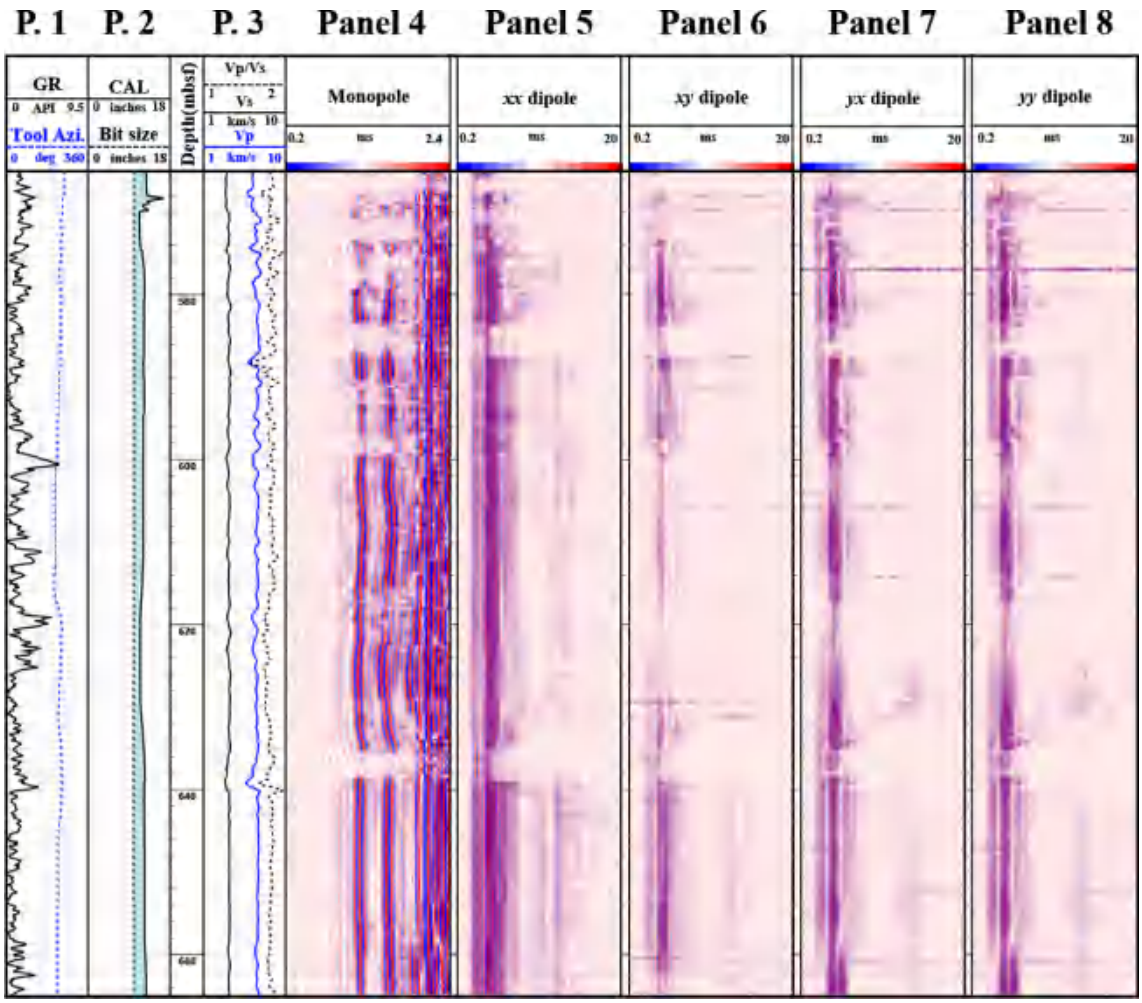


Figure 2. Relevant borehole geophysical data for the processing interval of the IODP Hole U1473A. Panels 1 and 2 show, respectively, the gamma-ray, tool azimuth and borehole caliper log curves (shading between caliper and bit size indicates borehole changes). Panel 3 shows the compressional (*Vp*) and shear (*Vs*) velocity profiles and their ratio (*Vp/Vs*), obtained from processing the monopole waveform data in panel 4. The 4C cross-dipole data *xx*, *xy*, *yx* and *yy* are respectively displayed in panels 5–8 using the VDL (variable density log) display. Only data from the first receiver of an eight receiver array are shown.

is particularly important for the shear wave imaging application, because it is used to migrate the reflected shear wave data to the reflector position. The central frequency of the dipole data is around 3–4 kHz and the waveform recording length is about 20 ms. Taking this as the two-way shear wave traveltime to and from a remote (vertical) reflector, the maximum radial distance of a reflector detectable by the data is estimated to be about 38 m for the average formation shear wave velocity of 3.82 km s^{-1}.

The tool azimuth curve (panel 1) must also be included in the imaging processing. This azimuth measures the orientation of the *x*-axis of the tool frame relative to North. Using the tool azimuth as a reference, the 4C data are rotated to a given azimuth *AZ*. Using this *AZ* in eq. (4), the *XX* component of the rotated data matrix is migrated to image geological reflectors on both sides of the borehole. The imaging can be done for a number of azimuths. According to eq. (5), a reflector is best imaged when the given azimuth coincides with the strike direction of the reflector, where the *XX* corresponds to the *SH*-wave image. Likewise, when the azimuth is normal to the reflector strike, where the *XX* corresponds to the SV-wave image, the reflector image becomes weak and may vanish.

Imaging result for four consecutive azimuths, NS, NE, EW and SE, reveals dipping features on both sides of the borehole. A high-angle (∼60° dip) reflector is clearly identified, which crosses the borehole at about 639 m (Fig. 3). Interestingly, the reflector (indicated by an arrow or line) is seen on the NE, EW and SE (best on the EW, see dashed line) images, but almost vanishes on the NS image, as predicted by eqs (4) and (5). When the dipole source–receiver system is rotated to be oriented along (perpendicular to) the reflector strike direction, a pure *SH* (*SV*) image will be produced. Because the recorded shear wave reflection is strongest for *SH* and weakest for *SV* (the latter will almost vanish for a high angle reflector), one can deduce that the reflector on the lower sector strikes along EW direction (Fig. 3).

Compared to the section below 639 m, the images of the depth interval are more complex. Several steeply dipping (60°–70° dip) features can be identified in the vicinity of the borehole around 580–620 m. These features are dominantly seen on the NE, EW and SE images. The largest number of features can be seen on the SE image. Although fewer features are seen on the NS image, a strong, high-angle feature around 610 m can be identified on the image (also on the SE image), which appears to be connected to the vertical features on the core images to be discussed. The variation

Downloaded from academic.oup.com/gji/article/217/1/288/5289575 by China University of Petroleum - Beijing user on 08 October 2026

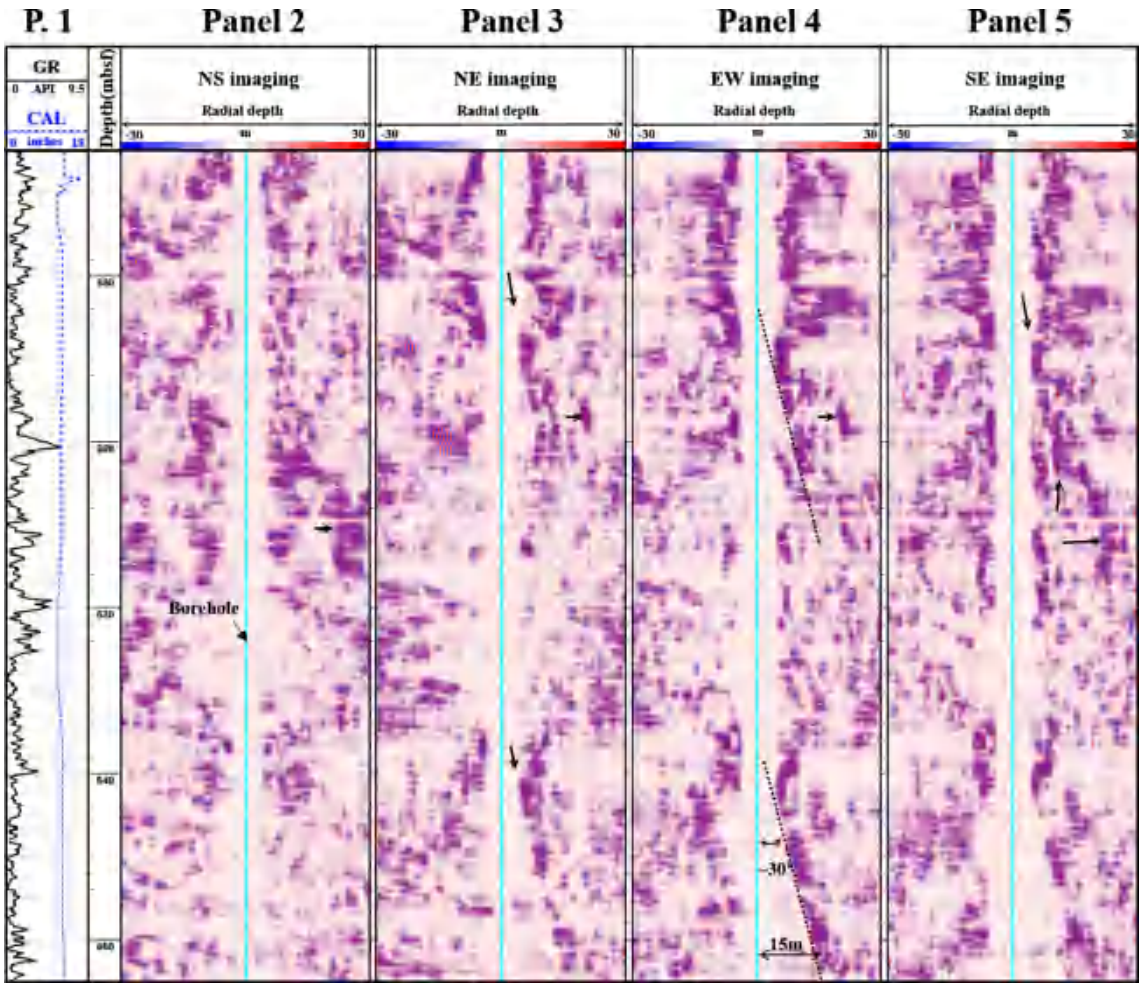


Figure 3. Shear wave imaging result for the NS, NE, EW and SE azimuths (panels 2–5). In the lower part, a dipping feature is best seen in the EW image (dashed line in panel 4) but vanishes in the NS image. The upper part shows dipping (and near-vertical) features on all images (some are indicated by a line or arrows), but more features are seen on the EW and SE azimuths.

of reflector features with azimuth suggests that most reflectors on the upper section of Fig. 3 have a dominant EW strike direction, while some of them may have different strike directions.

The imaging results can be verified and interpreted using the core and borehole-wall image data for the depths of interest (Fig. 4). A major feature on the borehole wall image (outlined by red lines) strikes approximately in EW direction with a $\sim 60^{\circ}$ dip angle. Core description in the Hole U1473A report (MacLeod *et al.* 2017) interprets the feature as clay-filled fractures. The configuration of the fracture agrees well with our shear wave imaging result on Fig. 3, which suggests that the fracture extends away from borehole at least 15 m without changing its orientation. Core images for 568, 581 and 582 m depths show features of various dip angles and azimuthal orientations. However, they are dominated by high-angle and even vertical (see panel 4) features, in agreement with the shear wave images that show near-vertical features, especially on SE and NS images (Fig. 3). Overall, the strike azimuths of the core image features are towards the EW and SE directions. The core data provide an explanation for the complexity in the azimuthal images of Fig. 3. A rose diagram of the strike azimuth distribution for the borehole-wall features for the depth interval chosen for the shear wave imaging (Fig. 3), as prepared from results of a borehole-wall electric resistivity imaging tool (called FMS tool, see MacLeod *et al.* 2017), shows that the borehole-wall geological features have a dominant EW strike, in agreement with the shear wave imaging result (Fig. 3).

Based on the shear wave imaging result and the core and FMS image data, one can conclude that the imaged features in the depth interval correspond to a steeply dipping fault system, which extends below 570 m depth and strikes dominantly in EW direction. Comparing to the NS trend of the Atlantis II Transform, the EW striking fault system might have resulted from the bending of the Atlantis Bank in the detachment faulting process of the oceanic ridge (Dick *et al.* 2017).

4 CONCLUSIONS

The vast amount of ODP/IODP borehole geophysical data contain valuable information for planetary exploration. One particular example is the waveform data acquired by a multipole acoustic logging tool. With the data analysis and processing technique advanced in this paper, the data can be utilized to image geological reflectors several tens of metres away from borehole. Particularly advantageous is the ability of the technique to determine the strike azimuth of the reflector using the azimuthal sensitivity of the dipole shear waves. The shear wave imaging technique was applied to the IODP U1473A Hole data to investigate a fault system in the deep part

Downloaded from academic.oup.com/gji/article/217/1/288/5289575 by China University of Petroleum - Beijing user on 08 October 2026

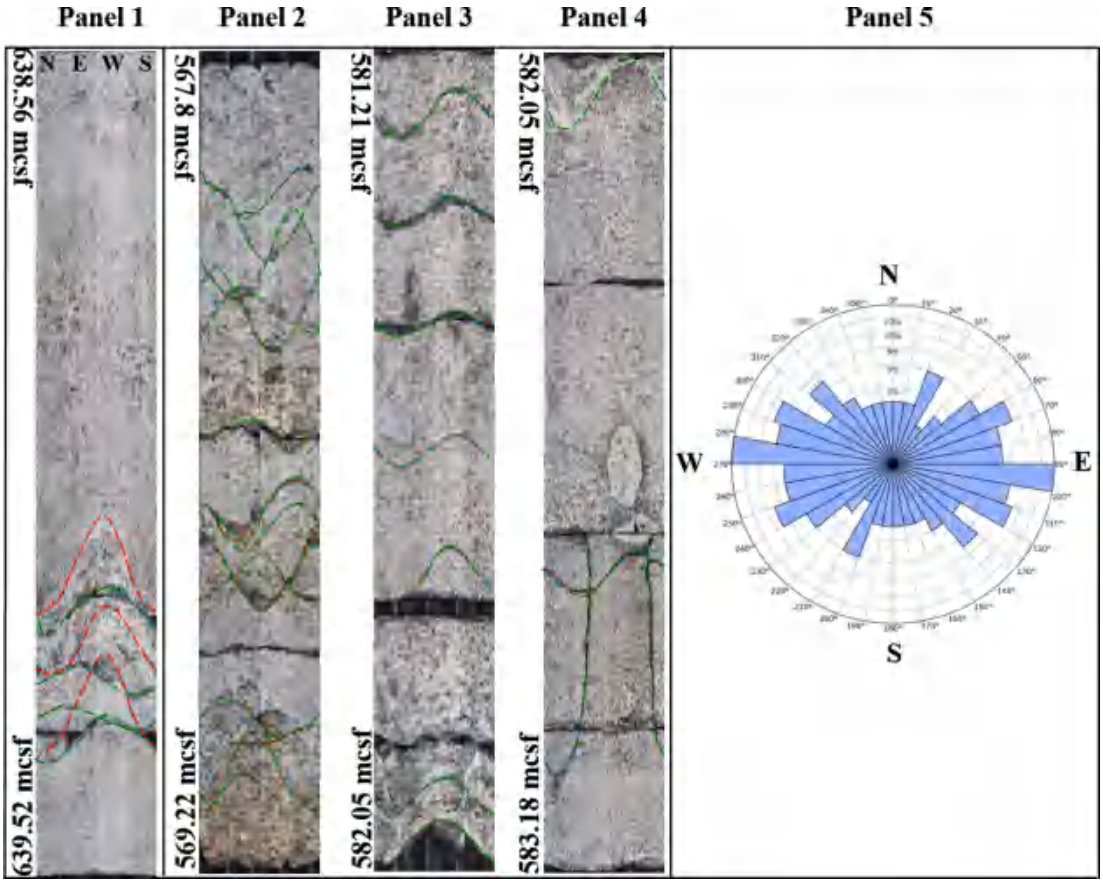


Figure 4. The whole-round core images of the relevant depths. The approximately EW striking dipping features of panel 1 correlate to the imaged feature in the lower part of Fig. 3. Panels 2–4 show features of various azimuths and dips (a vertical feature is seen in panel 4), corresponding to the complex image features in the upper part of Fig. 3. Panel 5 shows the azimuth distribution of the borehole-wall features for the depth interval of Fig. 3, which were measured by a borehole-wall resistivity imaging tool. The symbol 'mcsf' stands for meter of core depth below seafloor.

of the borehole that could not unambiguously be derived from previous core and wireline data. The successful application suggests that shear wave imaging can be applied to the existing and future ODP/IODP data, extending the scope of the borehole measurements to a scale of tens of metres.

ACKNOWLEDGEMENTS

The authors thank all related researchers and staffs in International Discovery Program (IODP) Expedition 360 for acquiring and providing the data of this study. This research work is supported by the China Natural Science Foundation (grant nos. 41804124 and 41474101),the Fundamental Research and Development Program (grant no. 2014CB239006),the Postdoctoral Science Foundation (grant no. 2018M632745) and Open Fund of Shandong Provincial Key Laboratory of Depositional Mineralization & Sedimentary Minerals, Shandong University of Science and Technology (grant no. DMSM2018045). Thanks also go to Professor J. Renner, whose comments and suggestions have helped to significantly improve the manuscript.

REFERENCES

Aki, K. & Richards, P.G., 1980. *Quantitative Seismology,* W.H. Freeman.

Ben Menahem, A. & Kostek, S., 1991. The equivalent force system of a monopole source in a fluid-filled open borehole, *Geophysics,* **56,** 1477–1481.

Bolshakov, A.O., Patterson, D.J. & Lan, C., 2011, Deep fracture imaging around the wellbore using dipole acoustic logging, *Paper Presented at SPE Annual Technical Conference and Exhibition,* Denver, CO.

Downloaded from academic.oup.com/gji/article/217/1/288/5289575 by China University of Petroleum - Beijing user on 08 October 2026

Dick, H.J.B. *et al*. 1991. Tectonic evolution of the Atlantis II Fracture Zone, in *Proceedings of the Ocean Drilling Program, Scientific Results*, **118,** pp. 359–398, eds. Von Herzen, R.P., Robinson, P.T. *et al*. Ocean Drilling Program, College Station, TX.

Dick, H.J.B., MacLeod, C.J., Blum, P., Abe, N., Blackman, D.K., Bowles, J.A., Cheadle, M.J. & Viegas, L.G.F., 2017. Expedition 360 summary, in *Southwest Indian Ridge Lower Crust and Moho, Proceedings of the International Ocean Discovery Program*, **360,** eds. MacLeod, C.J., Dick, H.J.B. & Blum, P., the Expedition 360 Scientists, International Ocean Discovery Program, College Station, TX.

Goldberg, D., 1997. The role of downhole measurements in marine geology and geophysics, *Rev. Geophys.,* **35,** 315–342.

Hyndman, R.D., 1979. Poisson's ratio in the oceanic crust – a review, *Tectonophysics,* **59,** 321–333.

Kimball, C.V. & Marzetta, T.L., 1984. Semblance processing of borehole acoustic array data, *Geophysics,* **49,** 274–281.

MacLeod, C.J., Dick, H.J.B., Blum, P., Abe, N., Blackman, D.K., Bowles, J.A. & Viegas, L.G.F., 2017. Site U1473, in *Southwest Indian Ridge Lower Crust and Moho, Proceedings of the International Ocean Discovery Program*, **360,** eds. MacLeod, C.J., Dick, H.J.B. & Blum, P., the Expedition 360 Scientists, International Ocean Discovery Program, College Station, TX.

Muller, M.R., Minshull, T.A. & White, R.S., 2000. Crustal structure of the Southwest Indian Ridge at the Atlantis II Fracture Zone, *J. geophys. Res.,* **105,** 25 809–25 828.

Tang, X.M., 2004. Imaging near-borehole structure using directional acoustic-wave measurement, *Geophysics,* **69,** 1378–1386.

Tang, X.M., 2016. Reflection imaging away from borehole: a paradigm shift, *Paper Presented at SEG International Exposition and Annual Meeting*, Dallas, TX.

Tang, X.M., 2017. Advances in borehole acoustic reflection imaging, *Proceedings of Meetings on Acoustics*, **32,** 32001, doi:10.1121/2.0000705.

Tang, X.M. & Patterson, D., 2009. Single-well S-wave imaging using multicomponent dipole acoustic-log data, *Geophysics,* **74,** A211–A223.

Tang, X.M., Cao, J.J. & Wei, Z.T., 2014. Shear-wave radiation, reception, and reciprocity of a borehole dipole source: with application to modeling of shear-wave reflection survey, *Geophysics,* **79,** T43–T50.

Zakharova, N.V. & Goldberg, D.S., 2015. Data report: analysis of shear wave anisotropy in upper oceanic crust, ODP/IODP Hole 1256D, in *Proceedings of the Integrated Ocean Drilling Program,* **335,** eds Teagle, D.A.H., Ildefonse, B. & Blum, P., the Expedition 335 Scientists, Integrated Ocean Drilling Program Management International, Inc., Tokyo.

Downloaded from academic.oup.com/gji/article/217/1/288/5289575 by China University of Petroleum - Beijing user on 08 October 2026

APPLIED GEOPHYSICS, Vol. 16, No. 3 (September 2019), P. 291—301, 9 Figures.
DOI:10.1007/s11770-019-0778-x

Application of four-component dipole shear reflection imaging to interpret the geological structure around a deviated well*

Lee Sheng-Qing[1, 2], Chen Ming[3], Gu Xi-Hao[1,2], Su Yuan-Da[1, 2, 4], and Tang Xiao-Ming♦[1, 2, 4]

Abstract: Acoustic reflection imaging in deep water wells is a new application scope for offshore hydrocarbon exploration. Two-dimensional (2D) geological structure images can be obtained away from a one-dimensional (1D) borehole using single-well acoustic reflection imaging. Based on the directivity of dipole source and four-component dipole data, one can achieve the azimuth detection and the three-dimensional (3D) structural information around the wellbore can be obtained. We first perform matrix rotation on the field four-component data. Then, a series of processing steps are applied to the rotated dipole data to obtain the reflector image. According to the above dipole shear-wave imaging principle, we used four-component cross-dipole logging data from a deviated well in the South China Sea to image geological structures within 50 m of a deviated well, which can delineate the structural configuration and determine its orientation. The configuration of near-borehole bedding boundaries and fault structures from shear-wave imaging results agrees with those from the Inline and Xline seismic profiles of the study area. In addition, the configuration and orientation of the fault structure images are consistent with regional stress maps and the results of the borehole stress anisotropy analysis. Furthermore, the dip azimuth of the bedding boundary images was determined using borehole wall resistivity data. Results of this study indicate that integrating borehole acoustic reflection with seismic imaging not only fills the gap between the two measurement scales but also accurately delineates geological structures in the borehole vicinity.

Keywords: four-component cross-dipole logging, single-well shear-wave imaging, seismic-well tie, geological structure imaging, fault imaging

Introduction

The South China Sea is near the junctions of tectonic plates and a major deep-water oil and gas exploration and development area in the world (Jia et al., 2016). Seismic imaging of the South China Sea has revealed numerous large-scale faults (Zhou et al., 2018; Zhang et

Manuscript received by the Editor June 7, 2019; revised manuscript received September 1, 2019.
*This work was supported by the National Natural Science Foundation of China (Nos. 41804124, 41774138, 41804121, 41604109), China Academy of Sciences Strategic Leading Science and Technology Project (Grant Nos. XDA14020304, XDA14020302), Shandong Provincial Natural Science Foundation, China (No. ZR2019BD039), Shandong Province Post-doctoral Innovation Project (No. 201901011) and China Postdoctoral Science Foundation (Grant Nos. 2019T120615, 2018M632745).
1. School of Geosciences, China University of Petroleum, Qingdao 266580, China.
2. Key Laboratory of Deep Oil and Gas, China University of petroleum, Qingdao 266580.
3. Zhanjiang Branch of CNOOC Ltd., Zhanjiang 524057, China.
4. China Laboratory for Marine Mineral Resources, Qingdao National Laboratory for Marine Science and Technology, Qingdao 266071, China.
♦Corresponding author: Tang Xiao-Ming (Email: tangxiam@aliyun.com).
©2019 Chinese Geophysical Society. All rights reserved.

al., 2019). The development of fractures and their tectonic movement play a significant role in controlling hydrocarbon migration (Jiang et al., 2015). For well drilling operations, small-scale faults also cause well leakage problems and need to be determined (Chen et al., 2017). Single-well acoustic reflection imaging can offer an effective tool to determine the near-borehole fault system and compensate for the deficiencies of seismic imaging resolution.

Single-well reflection imaging uses a seismic source in a fluid-filled borehole to radiate elastic waves into a formation, which are reflected by the geological reflectors around the borehole. These reflected signals are then used to image the geological reflectors in formation (Hornby, 1989; Tang, 2004). Single-well reflection imaging can be classified as reflected P-wave imaging using a monopole source and reflected S-wave imaging with a dipole source. Hornby (1989) first proposed a monopole-exciting and monopole-receiving imaging system. The monopole source center frequency is approximately 10 kHz, and the system primarily uses reflected P-waves for imaging. This method has a short detection distance away from the borehole, and the acoustic measurements in borehole are interfered by various borehole wave modes, such as compressional, pseudo-Rayleigh, and Stoneley waves (in soft formations the borehole waves contain only compressional and Stoneley waves). The latest development in single-well reflection imaging is the use of reflected shear waves for structural imaging around the borehole, i.e., the dipole reflected-shear wave imaging (Tang, 2004; Tang and Patterson, 2009; Tang et al., 2014). Compared to the traditional monopole reflected-compressional wave method (Hornby, 1989), the dipole shear wave imaging has the following advantages: 1) the azimuth of the reflector can be determined by the directional characteristics of the dipole source-receiver system; 2) owing to the low frequency (0.5-6 kHz) nature of the dipole source, the dipole-shear wave has less attenuation (compared to the 10 kHz compressional waves) can thus achieve a greater detection distance; 3) because shear-wave propagation depends on the shear modulus, thus the shear wave has a high detection sensitivity for fractures characterized as a shear modulus discontinuity; and 4) the borehole measurement is dominantly interfered by borehole flexural waves, which can be easily suppressed compared to the monopole waves. Over many years of research/development and field application, the single-well shear-wave reflection imaging has been proven to be an effective technology for delineating geological structures around boreholes. This technology plays a crucial role in the comprehensive interpretation of subtle oil and gas reservoirs, such as geothermal reservoirs, scientific ocean drilling, as well as reservoir stimulation (Bradley et al., 2017; Hornby et al., 2018; Amer et al., 2019; Lee et al., 2019).

Single-well acoustic reflection imaging is currently used mostly in onshore oil and gas fields, and its application in offshore oil and gas fields has been rarely studied. Utilizing the sensitivity of the dipole shear waves for fracture/fault imaging and the capability for azimuth detection, this study uses the cross-dipole four-component (4C) data from a deviated deep-water well in South China Sea to image the bedding boundary and fault structures ~50 m away from the borehole. The imaging results agree with seismic profiles and regional crustal stress information. With the positive results, this study shows a new application prospect of integrating borehole acoustic reflection imaging and seismic imaging for geological structure interpretation.

Principle and methods of dipole shear wave imaging

A cross-dipole acoustic logging tool consists of the following: 1) a receiver sub-section comprising multiple (8–13) azimuth receivers with 0.1524 m spacing and 2) a transmitter sub-section containing one monopole and two orthogonally-oriented dipole transmitters. The instrument transmits and receives signals in two orthogonal directions can thus collect four-component dipole data (*xx*, *xy*, *yx*, and *yy*). For each component (such as *xy*), the first letter indicates the source direction (*x*-direction) and the second letter indicates the receiver direction (*y*-direction). The shear velocity profile required for the reflection imaging can be obtained using the monopole and dipole array waveforms via slowness-time-coherence processing (the STC method, Kimball and Marzetta, 1984). Azimuth imaging of the reflected shear wave can be performed using 4C dipole data and the shear wave velocity profile.

Figure 1 shows a diagram of dipole shear wave reflection imaging of a planar reflector near a borehole. A Cartesian coordinate system (*x*, *y*, *z*) is chosen such that the borehole is along the *z*-axis. The dipole source, a directed vector source, is located at the origin (0, 0, 0) and points in the *x*-direction; it radiates shear waves to the reflector. At low frequencies, for which the wavelength is large relative to borehole diameter, the dipole is equivalent to a point force source in an infinite elastic medium.

Under low-frequency conditions, the far-field radiation field of the dipole source is identical to the single force source of the infinite medium (Ben-Menahem and Kostek, 1991), the radiation characteristics of which have been documented in literature (Aki and Richards, 1980; Tang and Patterson, 2009). The radiated shear waves can be decomposed into two orthogonal components (labeled *SH* and *SV*) using vector projection as shown in Figure 1. These components are reflected back into the borehole and received by receivers in the *x* and *y* directions, respectively.

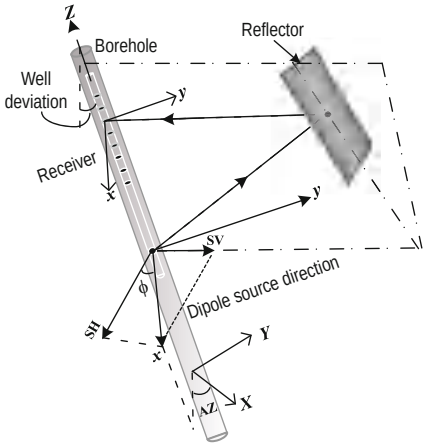


Fig. 1 Schematic of dipole shear wave reflection imaging in deviated well.

The S_H- and S_V-wave data can be obtained from the 4C data (*xx*, *xy*, *yx*, and *yy*) for any given tool orientation angle ϕ using the following equations (Tang and Patterson, 2009) as

$$\begin{aligned} SH &= xx\cos^2\phi - (xy + yx)\cos\phi\sin\phi + yy\sin^2\phi \\ SV &= xx\sin^2\phi + (xy + yx)\cos\phi\sin\phi + yy\cos^2\phi \end{aligned}. \quad (1)$$

According to the radiation analysis results of dipole shear waves (Tang and Patterson, 2009; Tang et al., 2014), the S_H-wave has better radiation coverage and stronger radiation energy than the S_V-wave for reflectors with different dip angles. Besides, there is no wave conversion for S_H-wave at the reflector boundary (the shear modulus discontinuity). Particularly, when the reflector is nearly parallel to the borehole, the reflected S_V-wave has negligible energy and the reflected shear waves are dominated by S_H-wave. The analogy of the single force source radiation may be used to explain the S_H- and S_V-wave radiation characteristics of a dipole source: when the force is parallel to the reflector plane, the radiated S_H-wave is the strongest, when the force is perpendicular to the reflector plane, the radiated S_V-wave is the weakest. Therefore, the S_H-wave has good azimuth directivity and high sensitivity to reflectors around a borehole, which is the most important theoretical basis for dipole shear wave reflection imaging. However, as shown in equation (1), a 180° azimuth ambiguity exists for strike determination, because the S_H- and S_V-wave from this equation are identical for ϕ and $\phi+\pi$. Thus, dipole shear wave imaging does not determine reflector dip and it can only determine reflector strike (Tang and Patterson, 2009).

The cross-dipole tool will rotate during borehole logging owing to changes in cable torque and friction between the instrument centralizer and the borehole wall. As the tool rotates, the dipole source azimuth ϕ with respect to a reflector varies accordingly, which affects the recorded reflection wave amplitude. Because of the tool rotation, the reflector azimuth's angle estimated from the 4C data is only relative to the tool-frame coordinate system (see Figure 1) and thus has no geological significance. To eliminate the tool rotation effect on the reflected waves and ensure the continuity of reflector imaging along the borehole, the recorded 4C cross-dipole tool data is transformed from the tool-frame coordinate system to a fixed coordinate system. By this transformation, the 4C dipole data is projected parallel to (perpendicular to) the reflector strike direction and, after reflection, is re-projected back to the receiver in borehole. Using the coordinate transformation or matrix rotation, one can form a new 2 × 2 symmetric matrix (Tang, 2004) for any given fixed coordinate system as

$$\begin{pmatrix} XX & XY \\ YX & YY \end{pmatrix} = \begin{pmatrix} \cos\alpha & \sin\alpha \\ -\sin\alpha & \cos\alpha \end{pmatrix} \begin{pmatrix} xx & xy \\ yx & yy \end{pmatrix} \begin{pmatrix} \cos\alpha & -\sin\alpha \\ \sin\alpha & \cos\alpha \end{pmatrix}, \quad (2)$$

where α is the angle between the *X*-axis of the fixed coordinate system and the reflector's strike direction. *XX*, *XY*, *YX*, and *YY* are the new 4C data in the new coordinate system. The angle between the *X*-axis of this coordinate system and the *x*-axis of the tool-frame coordinate system is the tool-frame azimuth (*AZ*) recorded during logging, as given by (Tang and Patterson, 2009)

$$\alpha = AZ + \phi. \quad (3)$$

As a common practice with the vertical well cross-dipole shear wave anisotropy processing (Tang and Patterson, 2005) using a geodesic system, the *X*-axis of the fixed coordinate system is generally chosen to point to the Earth's magnetic north. For deviated or horizontal wells, however, if the magnetic north pole

is still used, the borehole trajectory will affect reflector strike determination. Thus, for the case of high-angle or horizontal wells, the high side of borehole (referred to as HS) is chosen as the *X*-axis direction. The schemes and conditions for reference coordinates selection in deviated/horizontal wells can be found in the works of De and Schmitt (2005) and Tang and Patterson (2005).

The 2 × 2 matrix formed by the four-component data (*XX*, *XY*, *YX*, *YY*) in equation (2) can be diagonalized by varying the azimuth to yield the S_H- and S_V-reflection waves from the data, as follows (Lee et al., 2019)

$$\begin{pmatrix} XX & XY \\ YX & YY \end{pmatrix} \xrightarrow{\alpha} \begin{pmatrix} SH & 0 \\ 0 & SV \end{pmatrix}. \quad (4)$$

By this operation, the angle α and the true reflector strike azimuth, as from equation (3), can be determined.

Compared with seismic exploration, the acoustic signals reflected from a formation reflector have low amplitude and weak coherence due to the strong interference from the waves propagating along the borehole. It is usually difficult to visually identify the reflected wave from the recorded waveform data. After waveform rotation using equation (2), the data are processed using borehole wave suppression, up- and down-going wave separation, and reflected wave enhancement and migration to obtain images of geological reflectors around the borehole. The specific processing steps are as follows.

Step 1: borehole wave suppression. Based on the reflection signal's frequency characteristics, band-pass filtering is applied to the rotated waveform data to remove low- and high-frequency noise. The borehole waves, in the common-offset gather along borehole, has a constant travel time and has a low wavenumber; hence, one can use an *f-k* filter to suppress high-amplitude borehole waves (Hornby, 1989).

Step 2: wave separation. Based on the time-moveout differences between the reflected and direct borehole waves in the receiver array, a combined transmitter-receiver array strategy is used to separate up- and down-going reflection waves, respectively (Tang et al., 2007; Hirabayashi et al., 2008). The remaining borehole waves can be further suppressed using median filtering (Hirabayashi et al., 2008).

Step 3: migration. Using seismic migration methods, the reflected signals are migrated to image formation reflectors. Commonly used methods in acoustic logging include generalized Radon transform migration (Hornby, 1989), Kirchhoff migration (Esmersoy et al., 1998), modified *f-k* domain migration (Zheng et al., 2005), and equivalent offset migration (Chabot et al., 2001).

The above processing steps can be applied to the data rotated to any given azimuth. By varying the azimuth to scan around the borehole, one can obtain 3D structural images in the vicinity of the borehole.

Analysis and interpretation of single-well imaging for a deviated well

We applied the methods from the previous section to a deviated well at the junction zone of the South China Sea ocean-continent tectonic plate. The South China Sea lies at the intersection of the Eurasian, Indo-Australian, Philippine, and Pacific Ocean plates. Figure 2 shows a topographic map of the study area in the northern part of the South China Sea. There are three oceanic and continental plates in the region: the Sunda Plate, the Yangtze Plate, and the Tibet-Burma Plate. The deviated well is near the plate boundary and on the side of the Sunda Plate, which belongs to the deep-water area of the Hainan Southeast Basin in the northern part of the South China Sea (red solid circle). Water depth in this area is more than 500 m. The rose diagram indicates that the wellbore is drilling toward the NNW direction, i.e., from the Sunda Plate toward the plate boundary. The Hainan Southeast Basin has experienced three periods of tectonic evolution: the Paleogene rifting period, the Early-Miocene thermal subsidence period, and the Neotectonic period existing since the Late Miocene. Previous studies have shown that many groups of faults developed in the northern part of the South China Sea, mainly normal faults of NE-WE direction and strike-slip normal faults of NW direction (Zhang et al., 2007; Zhang, 2019).

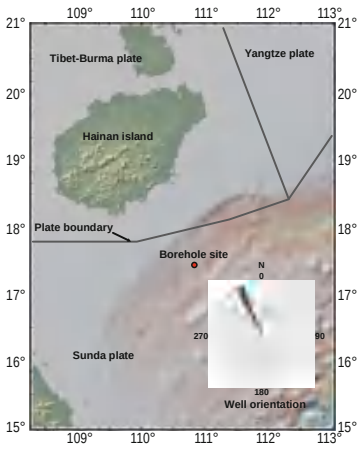


Fig. 2 Study area terrain, plate tectonics, and borehole location and orientation.

An interval of about 70 m for the well shown in Figure 2 is chosen for a detailed analysis and interpretation. This interval belongs to the Paleogene-Oligocene sedimentation. The basic data required for the analysis are displayed in Figure 3. The first track presents the natural gamma (GR), well deviation (*DEV*), well orientation (*DAZ*), and tool azimuth relative to the high side of the wellbore (*AZ*). The well's deviation is ~32°, the orientation of the borehole trajectory is ~331°, and the HS orientation of the tool is ~231°. The last track is the sandstone/shale porosity percentage profile obtained from the shale content curve (*Vsh*) and porosity curve (*POR*), showing the intersection of a shale zone on the top of the interval. It can be seen that the upper interval is a shale formation and the lower interval is dominated by sandstone rocks. Tracks three to seven show the first receiver waveform data from the monopole and the 4C dipole (*xx*, *xy*, *yx*, *yy*) logging measurements. Slowness processing from the monopole waveform using the STC method (Kimball and Marzetta, 1984) provides the compressional and shear wave slowness in the third track of Figure 3. The compressional- and shear-wave slowness and their velocity ratio (*Vp/Vs*) for the upper shale formation are 277 μs/m, 488 μs/m, and 1.75, respectively. The compressional- and shear-wave slowness and velocity ratio (*Vp/Vs*) of the sandstone formation are 178 μs/m, 341 μs/m, and 1.9, respectively. The shear-wave velocity is more important for single-well shear wave reflection imaging, which is used to migrate the reflected shear wave and determine the reflector's distance from the wellbore. To get a greater imaging distance and longer reflected signal recording, the exciting frequency of the dipole source is reduced to 2 kHz and recording time length increases to 40 ms (Hao et al., 2014). Taking recording time as the two-way travel time and using the average shear wave slowness for the sandstone formation, the maximum imaging distance for this interval is estimated about 58 m.

In the *yy* component data at the depth of X850 m, the arrival of the reflected wave trailing the borehole flexural wave can be observed, as indicated by the arrow in Figure 3. The reflected wave comes from the upper shale boundary and extends to the lower part of the wellbore. When the tool is far away from the boundary, the reflected signal's amplitude weakens and becomes invisible from the data. Notably, the reflected wave exists only in the *yy* component, whereas the other components have no reflected waves. This phenomenon shows the azimuthal sensitivity of the dipole source. Dipole radiation theory states that the strongest reflected S_H-wave can be recorded when the source orientation is parallel to the reflector strike. The direction of the tool *x*-axis is given by the tool azimuth curve (the *AZ* curve in Figure 2). Thus, the *y*-axis in the orthogonal direction is about 141°, which coincides with the strike of the shale formation relative to the high side of the wellbore. Relative to the high side of this deviated well, the shale formation is calculated by using the following formula (De and Schmitt, 2005; Tang and Patterson, 2005)

$$\tan(\theta_1 - DAZ)\cos(DEV) = \tan(\theta_2 + AZ), \quad (5)$$

where θ_1 is the angle relative to Earth's magnetic north, *DAZ* is the orientation angle of the well trajectory, and *DEV* is the well deviation. θ_2 is the angle relative to borehole high side, and *AZ* is the tool azimuth measured from the high side, which is the *AZ* curve in Figure 2. Estimated using equation (5), the shale formation's strike relative to North is approximately in the SSE-WNN direction. This strike direction is approximately along the borehole trajectory, as will be confirmed by the imaging results to be presented. The observed reflected wave event, as described above, indicates that the borehole trajectory

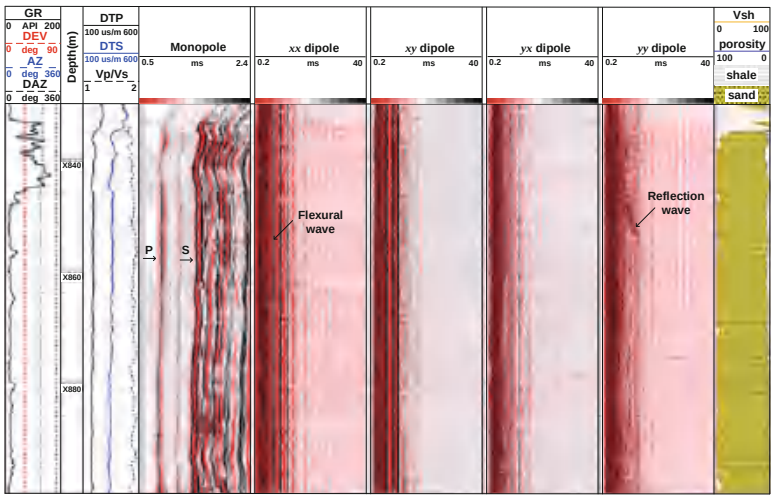


Fig. 3 Logging data of a deviated well.

has a certain angle of intersection with the shale formation. The above analysis shows that, using the theory of borehole dipole radiation and well configuration, one can quickly analyze the geometric information of the geological structure around the wellbore from the observed reflection wave event.

Using the tool azimuth *AZ*, the 4C data can be rotated to any azimuth angle α from the high side of the well. The rotated array waveform can be obtained using equation (2) and the geological structures around the wellbore can be imaged using the data processing steps described previously. By varying the azimuth angle α, one can obtain a sequence of reflector images around the borehole. Equation (3) shows that the recorded wave amplitude is the largest and the reflection image is clearest when the rotated *XX* component becomes an S_H-wave. Then, the azimuth is the reflector strike. Conversely, when the *XX* component direction is perpendicular to the reflector strike, the *XX* component becomes an S_V-wave and the recorded wave is the weakest or even disappears.

As shown in Figure 3, reflected waves from a reflector around the borehole have a low-amplitude signal with a low signal-to-noise ratio compared to the borehole flexural wave. Thus, the rotated data requires a combination of signal processing and migration methods to obtain geological imaging. Such signal processing methods include the *f-k* filtering (Hornby, 1989) and wave separation (Tang et al., 2007). The *f-k* filtering method is used for common offset data gather: it can remove borehole waves and separate up- and down-going reflection waves. In the *f-k* domain, the reflection events from a reflector that is parallel, or makes a small angle, with the borehole are in the low-wavenumber region, whereas the events from a reflector that intersects the borehole with a large angle are in the high wavenumber region. Therefore, different filtering parameters can be applied to extract the desired reflection events for imaging. Wave separation divides the total reflected signal into up- and down-going waves. Then, using the pre-stacked *f-k* migration method, one can obtain an image of the up-dip and down-dip side of an intersecting reflector. (Tang et al., 2007).

By using the *f-k* filtering method to extract the intersecting shale formation, the boundary of the shale formation is imaged. Figure 4 shows the images for 10°, 50°, 100°, and 140°, the four azimuths are measured from the high side of the borehole. The first track shows the GR curve and the other four tracks show the images. As shown from the imaging results, starting from the intersecting depth zone, the shale reflector (marked with high GR values) makes an angle of ~41° with the borehole and extends downward to about 50 m away from the borehole. The layered structure of the shale formation can be seen from the two imaged sedimentary interfaces (marked as RF1 and RF2) that are parallel to each other. Comparing imaging results of the four azimuths, the shale boundary is visible at 100°, 140°, and 10°, but is weakest at 50°. According to the dipole source directivity characteristics shown in equations (2) and (4), when the data rotation azimuth is parallel to the reflector strike, the pure S_H-wave is obtained and the corresponding reflection image becomes the strongest; when the data rotation azimuth is perpendicular to the reflector strike, the pure S_V-wave is obtained and the corresponding reflection image becomes the weakest. At other azimuths, the recorded shear wave data is a combination of S_H- and S_V-wave. Although the magnitude of S_V-wave amplitude is generally much smaller than the S_H-wave amplitude, the S_V-wave can have measurable amplitude for an angled reflector (Tang et al., 2014). This explains why the image of the 50° azimuth in Figure 3 is at the *SV*-wave azimuth but is still visible. The above theoretical analysis shows that the shale formation strike is at the 140° azimuth relative to the high side of the wellbore, which is consistent with the previous analysis result with Figure 3.

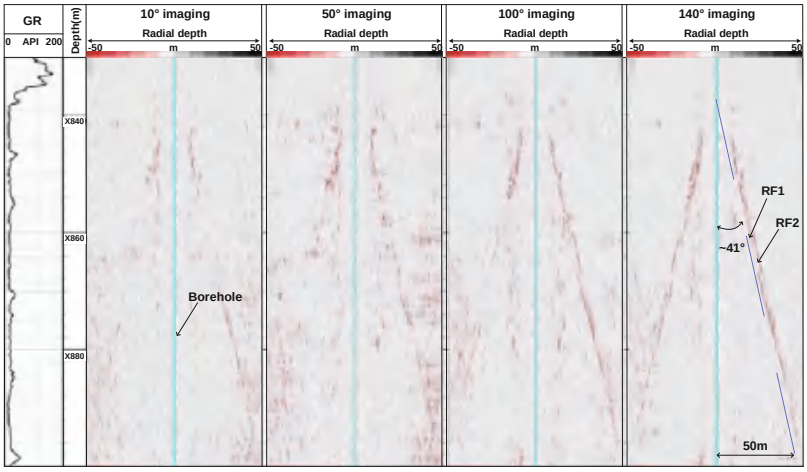


Fig. 4 Azimuth imaging of the shale formation boundary with the deviated well.

By applying low-pass *f-k* filtering in the wavenumber domain, one can obtain S_H-wave imaging for reflectors that are approximately parallel to the borehole. Figure 5 shows imaging results for 30°, 70°, 120°, and 160°, the four azimuths are measured from the high side of the borehole. The reflectors are located at two different distances from the borehole in the sandstone formation interval (identified as NRF and FRF). The near reflector is about 10–17 m away from the wellbore and the far reflector is about 14–20 m away from the borehole. The near reflector extends approximately 50 m along the wellbore axis. Notably, the near reflector can be imaged at 70°, 120°, and 160°; however, the image is the best at 120° (dotted line in Figure 5) and disappears at 30°. In contrast, far reflectors can be imaged at 30°, 70°, and 160°, but the image is the best at 30° (dotted line in Figure 5) and disappears at 120°. Based on the S_H-wave radiation characteristics mentioned previously, it can be inferred that the near reflector strike is at 120° from high side of the borehole, whereas the strike of the near reflector is at 30°. These two reflectors are orthogonal to each other and exhibit the conjugated geological pattern. They are associated with the fault system of the region described below.

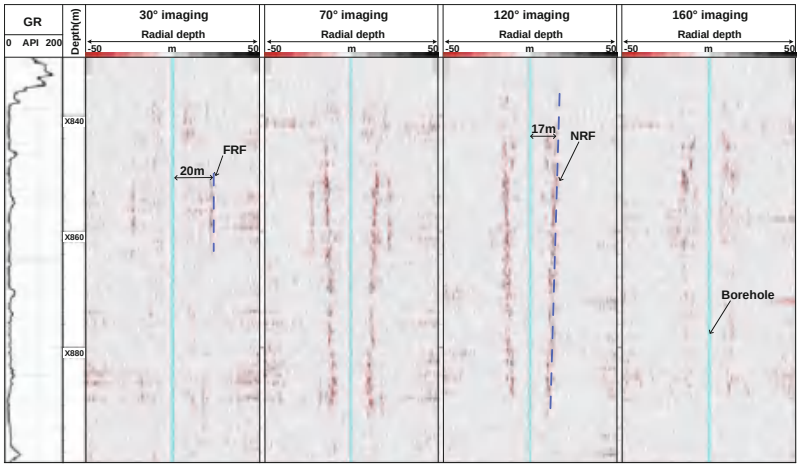


Fig. 5 Azimuth image of orthogonal reflectors parallel to the well.

With the help of the Inline and crossline (Xline) seismic profiles of the study area in Figure 6, one can further explain the results of shear wave reflection imaging from the deviated well. The line direction is indicated by the arrow within the circle in the figure. Additionally, a vertical well has also been drilled in the study area. The Xline profile direction is coplanar with both the vertical and deviated wells, with a profile orientation of 151/331° (approximately an ESS-WNN direction). The Inline profile is orthogonal to Xline and passes through the vertical well with an orientation of 61/241° (approximately NEE-SWW). The studied interval of the deviated well in this work is shown in Figure 6a for the lower portion of the well. The entire deviated well is on the upper plate of a normal fault. Five normal faults are identified from the seismic profile (Xline) passing through the wellbore (as indicated by the arrow in the figure, fault colors are dark green, light green, cyan, lilac, and red) with a NEE-SWW strike direction. The fault strikes are consistent with that of the near reflector in Figure 5. Two normal faults (red and blue lines) are identified from the orthogonal seismic section (Inline) with ESS-WNN strike direction. The fault strikes are consistent with the far reflector in Figure 5. More interestingly, the seismic profiles indicate that there are multiple normal fault systems with conjugate characteristics in this region. The presence of structural complexity indicates complex plate tectonic movements,

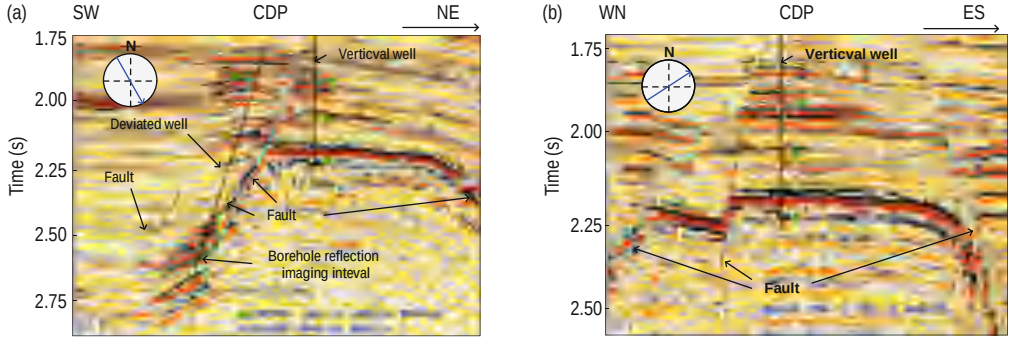


Fig. 6 Xline (a) and Inline (b) seismic profiles of the study area.

resulting from the mutual movement and tectonic evolution of the three major plates in this region. The complex fault morphology is consistent with the results of previous studies of this region (Zhang, 2019). According the fractal theory for fracture development and distribution, large faults are often accompanied by secondary faults: the primary and secondary faults and their distribution at different scales form fault zones (Okubo and Aki, 1987; Bonnet et al., 2001). The major faults on the seismic profile are far from the wellbore and cannot be identified from the borehole shear wave reflection imaging. However, their accompanying secondary, smaller faults and the extension of the fault system in the vicinity of the well can be observed from the borehole reflection imaging. Therefore, one can conclude that the near reflector imaged in Figure 5 is a secondary fault associated with the large fault system from the Xline profile, whereas the far reflector imaged herein is a secondary fault associated with the large fault system from the Inline profile.

As shown in equation (1), there is a 180° azimuth ambiguity in dipole shear wave reflection imaging. Thus, the imaging results of Figure 4 cannot determine whether the shale formation is above (17° angle of intersection with the horizontal plane) or below (81° angle of intersection with the horizontal) the wellbore. This must be further investigated by combining imaging results with other geophysical information. The formation sedimentary structure of the seismic profile in Figure 6 shows that the stratigraphic sediments are relatively flat. Figure 7a is a stratigraphic dip angle histogram from borehole wall resistivity imaging analysis, with a dominant occurring frequency mainly at a small dip angle. This shows that the shale formation in Figure 4 is above the borehole and has a 17° angle (instead of the 81° angle) to the horizontal plane. Resistivity imaging (Figure 7b) shows that the shale formation dip direction is to the SW, which is consistent with the nearly ES strike direction obtained from single-well imaging (in Figure 4, the strike direction is perpendicular to the dip direction).

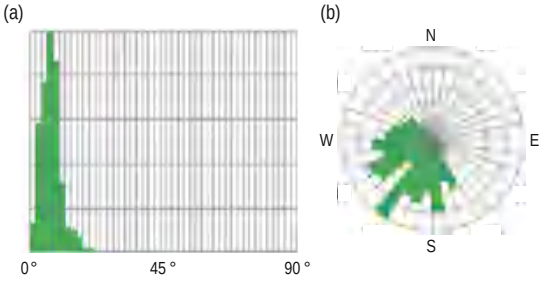


Fig. 7 Stratigraphic dip angle histograms and dip direction of borehole-wall electrical imaging (FMI).

By integrating the borehole logging and seismic data analysis results with the dipole shear-wave imaging, the geometric parameters of the three reflectors were obtained as follows: the wellbore's deviation is 32° and its dip direction is 331°. The shale formation strike is 140°, and its dip angle is 17° (the minimum angle to the horizontal plane). Its dip azimuth is ~230°, and the shale formation intersects with the wellbore and extends up to 50 m away from the wellbore. The strike of the near fault (NRF) is 120°, and NRF is 10–17 m away from the wellbore. The strike of the far fault (FRF) is 30°, and FRF is 14–20 m away from the wellbore. NRF and FRF are both parallel to the wellbore, with a minimum angle of 57° from the horizontal plane. Based on these parameters, Figure 8 shows the spatial geometrical relations between the borehole and reflectors. Figure 8a is the cross-plane over the wellbore, and Figure 8b is the three-dimensional shape of the reflector around the wellbore. Because of the ambiguity 180° azimuth

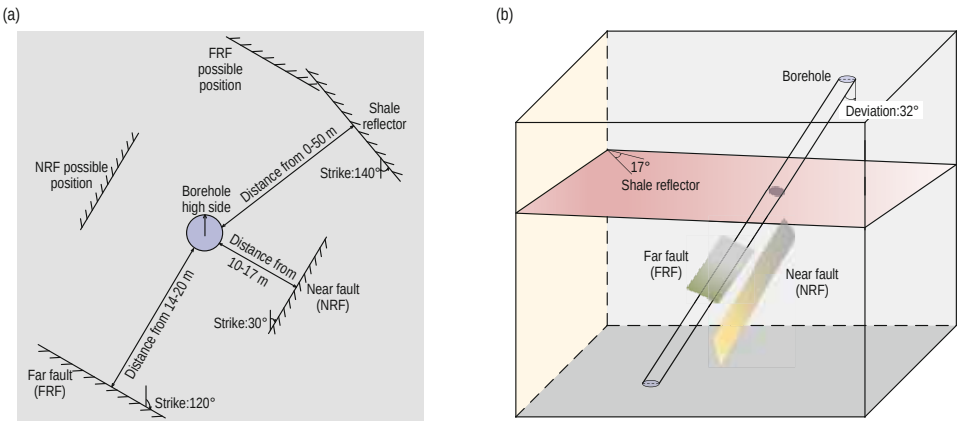


Fig. 8 Schematic of the spatial geometric relationship between the wellbore and reflectors under cross and vertical sections.

ambiguity, shear wave reflection imaging can only determine the strike of the reflector, but not its dip azimuth. Thus, for NRF and FRF in Figure 8a, two possible positions exist (reflection interface is indicated by a dotted line). For simplicity, the 3D diagram in Figure 8b only shows one possible location. Combined with the world stress map of this area and logging stress analysis, we can further analyze this wellbore's structure information.

The complexity of the single-well imaging results is closely related to ancient and present tectonic stresses in this area. Crustal stress is an important cause of formation structure, and stress information can be used to analyze fault activity. Based on data from focal mechanisms, borehole breakouts, drilling-induced fractures, hydraulic fracturing, and overcoring, Heidbach et al. (2018) and Hu et al. (2017) provided world stress maps that can determine crustal stress directions and fault types. Figure 9a shows crustal stresses in this area, and the black dotted line in Figure 9a shows the movement direction of the Sunda Plate relative to the African Plate. In the study area, the Sunda Plate moves to the east and the Yangtze Plate moves to the west (Figure 9a dotted arrow). Under the background plate movement, the crustal stress direction in this area can be divided into two categories: NNW-SSE and E-W directions, wherein the NNW-SSE direction is dominant. The major tectonic fault systems in the area are therefore characterized by normal and strike-slip patterns.

Regional stress imbalances will cause a concentration of stress and shear-wave anisotropy around the wellbore. This anisotropy can be determined using 4C cross-dipole shear-wave logging and analysis (Tang and Cheng, 2004). Both laboratory experiments (Rai and Hanson, 1988) and field logging results (Tang and Cheng, 2004) show that shale formations exhibit negligible stress-induced anisotropy, while sandstones are sensitive to the stress-induced effect. Thus, anisotropy in sandstone can reflect the effects of present crustal stress. However, because of the transversely isotropy (TI) properties of the shale formation, shales in a deviated well often exhibit apparent TI-anisotropy that can be measured along the borehole trajectory. The TI-anisotropy is described by the Thomsen parameters ε, δ, and γ (Thomsen, 1986) and seismic wave propagation in a TI rock is strongly influenced by the relative value of ε and δ (Tang and Patterson, 2005). As shown in the first rose diagram of Figure 9b, the shale anisotropy orientation of the deviated well has an approximate NNE-SSW orientation relative to the high side of the wellbore, which is perpendicular to the wellbore trajectory. Combined with the borehole-wall resistivity image result shown in Figure 7b, the dip direction of the shale formation is approximately the SSW direction (strike direction and dip angle are shown in Figures 4 and 7). The shear-wave anisotropy of the shale formation in the deviated well is influenced by formation dip direction, whereas the direction of the shear-wave reflection imaging is influenced by formation strike. Thus, the two orientations are orthogonal to each other. Because the well deviation is less than 45° and the shear-wave anisotropy azimuth is perpendicular to the well trajectory, the Thomson anisotropy parameters of the shale formation belong to the $\varepsilon>\delta$ category (Tang and Patterson, 2005).

The shear wave anisotropy orientation in the sandstone formation is approximately NNW-SSE (Figure 9b) and the well deviation is 32°. For the moderately deviated well, the cross-dipole measured shear-wave anisotropy from the sandstone formation mainly reflect the horizontal stress effect. This anisotropy azimuth is consistent with the world regional stress direction shown in Figure 9a. This deviated well, similar to most other wells in the area, is mainly affected by the southward

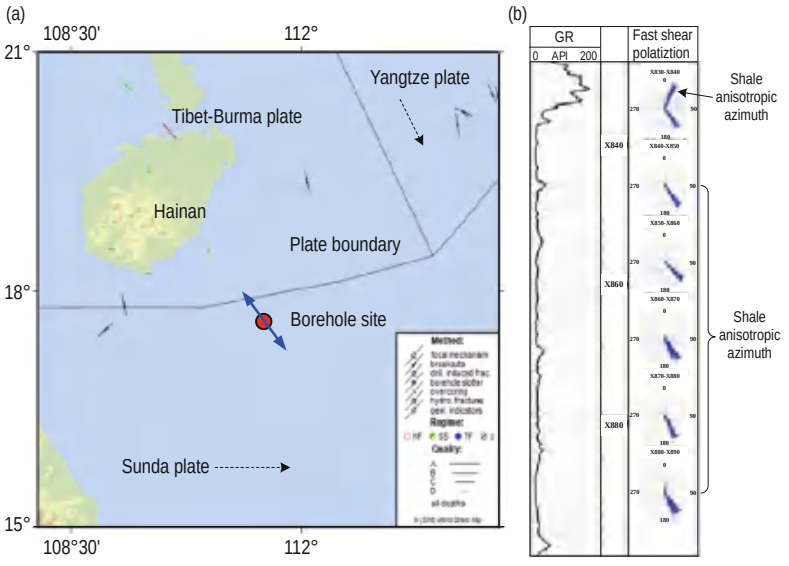


Fig. 9 World stress map and orientation of cross-dipole shear wave anisotropy.

movement of the Yangtze Plate, which causes the current horizontal stress to orient along the NNW-SSE direction (blue arrow in Figure 9a). The current stress direction is parallel to the strike of NRF around the wellbore (Figure 5) and is normal to the strike of FRF around the wellbore (Figure 5). Under the current stress regime, NRF and the normal faults in Figure 6a will laterally slip and become slip-positive faults, which is consistent with the regional tectonic analysis of Zhang et al. (2007) and Zhang et al. (2019). These types of faults may become tectonically active under the horizontal stress and provide pathways for hydrocarbon migration, whereas FRF around the wellbore may be a secondary fault from ancient stress action. Because the FRF activity is less than that of NRF, FRF has a certain sealing effect on hydrocarbon migration. Therefore, based on geo-stress information, one can assess the tectonic activity characteristics of the faults identified from shear-wave imaging and their effect on hydrocarbon migration.

Conclusions

Using 4C cross-dipole logging data, one can perform azimuthal imaging for the geological structure several tens of meters away from borehole. In this study, the bedding boundary of the shale formation and the conjugate fault system around the wellbore were successfully imaged using dipole shear wave imaging. With the help of the seismic profile of this area, it was further concluded that the imaged near borehole faults are secondary faults associated with regional tectonic faults. The spatial morphology and occurrence of these geological structures can be depicted through the seismic-well tie. By combining the regional stress map and dipole shear wave anisotropy analysis, these faults can be identified as slip-normal faults associated with the regional tectonic stresses and the anisotropy of the shale formation can be categorized as $\varepsilon > \delta$ type. The results of this study show that combining single-well shear-wave reflection imaging with seismic imaging can not only fill the gap between these two measurement scales, but also improve imaging interpretation accuracy and reliability.

References

Amer, A., Sajer, A., Al-Adwani, T., Salem, H., and Abu-Taleb, R., 2019, The application of downhole seismic imaging in identifying natural fracture systems: An integrated approach utilizing core and borehole image data: SPE Middle East Oil and Gas Show and Conference, SPE-194903-MS, Manama, Bahrain.

Aki, K., and Richards, P. G., 1980, Quantitative seismology: Theory and methods: W. H. Freeman and Company, CA, America.

Ben-Menahem, A., and Kostek, S., 1991, The equivalent force system of a monopole source in a fluid-filled open borehole: Geophysics, **56**(9), 1477–1481.

Bonnet, E., Bour, O., Odling, N. E., Davy, P., Main I., Cowie, P., and Berkowitz B., 2001, Scaling of fracture systems in geological media: Reviews of Geophysics, **39**(3), 347–383.

Bradley, T., Patterson, D., and Koscheev, G., 2017, Modern advances in acoustic reflection imaging: 58th SPWLA Annual Logging Symposium, Oklahoma, USA.

Chabot, L., Henley, D. C., Brown, R. J., and Bancroft, J. C., 2001, Single-well imaging using the full waveform of an acoustic sonic: 71th SEG Annual International Meeting, Expanded Abstracts, 420–423.

Chen, M., Yang, H., Wang, X., Sun, B., and Wang, S., 2017, Application of acoustic reflection imaging technology to complicated block reservoirs: Fault-Block Oil and Gas Field (in Chinese), **3**(24), 351–354.

De, G. S., and Schmitt, D. P., 2005, Issues with shear-wave azimuthal anisotropy in highly deviated wells: Offshore Technology Conference, OTC 17647, Houston, Texas.

Esmersoy, C., Chang, C., Kane, M., Coates, R., Tichelar, B., and Quint, E., 1998, Acoustic imaging of reservoir structure from a horizontal well: The Leading Edge, **17**(7), 940–946.

Hao, Z., Sun, X., Liu, X, Chen, H., and Zhang, G., 2014, The application research of dipole acoustic reflection imaging technology: Progress in Geophysics, **29**(5), 2172–2177.

Heidbach, O., Rajabi, M., and Cui, X., 2018, The World Stress Map database release 2016: Crustal stress pattern across scales: Tectonophysics, **744**, 484–498.

Hirabayashi, N., Leaney, W. S., and Haldorsen, J. B. U., 2008, Wavefield separation for borehole acoustic reflection surveys using parametric inversion: 78th SEG Annual International Meeting, Expanded Abstracts , 344–348.

Hornby, B. E., 1989, Imaging of near-borehole structure using full-waveform sonic data: Geophysics, **54**(6), 747–757.

Hornby, B., Peterman, P., Hager, C., Draucker, A., and Bolshakov, A., 2018, Reflection sonic imaging of complex near-borehole structure in slow formations:

88th SEG Annual International Meeting, Expanded Abstracts, 684–688.

Hu, X., Zang, A., Heidbach, O., Cui, X., Xie, F., and Chen, J., 2017, Crustal stress pattern in China and its adjacent areas: Journal of Asian Earth Sciences, **149**, 20–28.

Jia, C., Jiang, F., and Pang, X., 2016, Research status and development directions of hydrocarbon resources in China: Petroleum Science Bulletin (in Chinese), **1**(1), 2–23.

Jiang, H., Pang, X., Shi, H., Liu, L., Bai, J., and Zou, S., 2015, Effects of fault activities on hydrocarbon migration and accumulation in the Zhu I Depression, Pearl River Mouth Basin, South China Sea: Australian Journal of Earth Sciences, **62**(6), 775–788.

Kimball, C. V., and Marzetta, T. L., 1984, Semblance processing of borehole acoustic array data: Geophysics, **49**(3), 274–281.

Lee, S. Q., Tang, X. M., and Su, Y. D., 2019, Shear wave imaging to determine near-borehole faults for ocean drilling exploration: Geophysical Journal International, **217**(1), 288–293.

Okubo, P. G., and Aki, K., 1987, Fractal geometry in the San Andreas Fault System: Journal of Geophysical Research: Solid Earth, **92**(B1), 345–355.

Rai, C. S., and Hanson, K. E., 1988, Shear-wave velocity anisotropy in sedimentary rocks: A laboratory study: Geophysics, **53**(6), 800–806.

Tang, X. M., 2004, Imaging near-borehole structure using directional acoustic-wave measurement: Geophysics, **69**(6), 1378–1386.

Tang, X. M., Cao, J., and Wei, Z., 2014, Shear-wave radiation, reception, and reciprocity of a borehole dipole source: With application to modeling of shear-wave reflection survey: Geophysics, 79(2), T43̃T50.

Tang, X. M., and Cheng, C. H., 2004, Quantitative borehole acoustic methods: Elsevier Science Publishing Inc, America.

Tang, X. M., and Patterson, D., 2005, Characterizing seismic anisotropy using cross-dipole measurement in deviated wells: 75th SEG Annual International Meeting, Expanded Abstracts, 372–375.

Tang, X. M., and Patterson, D. J., 2009, Single-well S-wave imaging using multicomponent dipole acoustic-log data: Geophysics, **74**(6), WCA211–WCA223.

Tang, X. M., Zheng, Y., and Patterson, D., 2007, Processing array acoustic-logging data to image near-borehole geologic structures: Geophysics, **72**(2), E87–E97.

Thomsen, L., 1986, Weak elastic anisotropy: Geophysics, **51**(10), 1954–1966.

Zhang, G., Mi, L., Wu, S., Tao, W., He, S., and Lu, J., 2007, Deepwater area: The new prospecting targets of northern continental margin of South China Sea: Acta Petrolei Sinica (in Chinese), **2**(28), 15–21.

Zhang, Y., Qi, J., and Wu, J., 2019, Cenozoic faults systems and its geodynamics of the continental margin basins in the Northern of South China Sea: Journal of China University of Geosciences (in Chinese), **2**(44), 603–625.

Zhou, Z., Mei, L., Liu, J., Zheng, J., Chen, L., and Hao, S., 2018, Continentward-dipping detachment fault system and asymmetric rift structure of the Baiyun Sag, northern South China Sea: Tectonophysics, **726**(15), 121–136.

Zheng, Y. B., and Tang, X. M., 2005, Imaging near-borehole structure using acoustic logging data with pre-stack F-K migration: 75th SEG Annual International Meeting, Expanded Abstracts, 360–363.

Lee Sheng-Qing received his Ph.D. degree from China



Petroleum University (East China) in 2017. He is currently a postdoctoral fellow at China Petroleum University (East China), and he is mainly engaged in the study of borehole acoustic theory, methodology and field data interpretation, and gas hydrate logging.

Email: shidalishengqing@yeah.net.

♦Corresponding author: Tang Xiao-Ming is a professor with the China Petroleum University (East China). He received a B.S. degree from Beijing University in 1982 and a Sc.D. degree from MIT in 1990. His major research interests are in geophysical (sonic) well logging, seismic wave propagation, and rock physics.

李盛清，苏远大，唐晓明. 2020. 基于四分量偶极横波远探测的井周构造走向快速反演方法研究. 地球物理学报，63(6)：2478-2487，doi：10.6038/cjg2020N0322.

Li S Q, Su Y D, Tang X M. 2020. Research on a fast inversion method for structural strike around a borehole based on four-component dipole shear wave reflection imaging. *Chinese J. Geophys.* (in Chinese), 63(6): 2478-2487, doi: 10.6038/cjg2020N0322.

基于四分量偶极横波远探测的井周构造走向快速反演方法研究

李盛清[1,2,3]，苏远大[1,2,3*]，唐晓明[1,2,3]

1 中国石油大学(华东)地球科学与技术学院，青岛 266580

2 中国石油大学(华东)深层油气重点实验室，青岛 266580

3 青岛海洋科学与技术国家实验室海洋矿产资源评价与探测技术功能实验室，青岛 266071

摘要 偶极声源的辐射特性及仪器的四分量正交采集系统使得偶极横波远探测可在一维井筒中对井外构造进行方位探测. 基于反射横波幅度随声源偏振方向呈余弦平方变化这一特征，本文提出一种利用函数拟合快速反演井周构造走向的方法. 根据这一规律，该方法仅用 4 个方位剖面数据即可准确反演井周构造走向，同时得到井周构造的离井距离和倾角. 数值模拟和物理实验模拟均验证了幅度随方位的变化以及反演方法的可行性. 根据这一方法做的现场实例也进一步证明了该方法的适用性. 本文工作为利用四分量偶极数据进行井周构造的反射横波成像提供了实用而有效的处理方法.

关键词 正交偶极四分量；横波远探测；方位探测；反射体走向

doi：10.6038/cjg2020N0322 **中图分类号** P631 **收稿日期** 2019-08-02，2020-03-26 **收修定稿**

Research on a fast inversion method for structural strike around a borehole based on four-component dipole shear wave reflection imaging

LI ShengQing[1,2,3], SU YuanDa[1,2,3*], TANG XiaoMing[1,2,3]

1 *School of Geosciences, China University of petroleum, Qingdao* 266580, *China*

2 *Key Laboratory of Deep Oil and Gas, China University of petroleum, Qingdao* 266580, *China*

3 *China Laboratory for Marine Mineral Resources, Qingdao National Laboratory for Marine Science and Technology, Qingdao* 266071, *China*

Abstract The directional radiation characteristics of the dipole source and four component acquisition of the tool allow dipole shear wave reflection imaging to determine the orientation of geological structures from the 1D borehole. Based on the amplitude variation of the reflected shear waves with the source, we propose an efficient method for determining the strike of geological structures around the borehole. This method uses the reflection images of only four azimuths to determine the strike of structure, the distance from the borehole and dip of structure can be obtained by this method with only four azimuth profile data, The azimuthal variation characteristics of the reflection waves and the validity of the processing method are verified by

基金项目 国家自然科学基金(41804124, 41821002)，国家重点研发计划(2019YFC0605504)，山东省自然基金(ZR2019BD039)，山东省博士后创新项目(201901011)，中国博士后科学基金(2019T120615，2018M632745)，中石油重大科技项目(ZD2019-183-004)和中国科学院战略性先导科技专项(XDA14020304，XDA14020302)联合资助.

第一作者简介 李盛清，男，1988 年生，博士后，主要从事声波测井理论、方法及处理研究. E-mail：shidalishengqing@yeah.net

***通讯作者** 苏远大，男，1978 年生，博士，教授，主要从事声波测井理论、方法及处理研究. E-mail：suyuanda@upc.edu.cn

(C)1994-2023 China Academic Journal Electronic Publishing House. All rights reserved. http://www.cnki.net

both the theoretical modeling and laboratory experiment results. Examples of field data processing further confirm the application validity of the method. This paper provides a practical and effective processing method for determining the geological structures around the borehole using four-component dipole shear wave reflection imaging.

Keywords Cross-dipole four component; Single-well shear-wave imaging; Azimuth detection; Reflector strike

0　引言

声波远探测技术是将声源与接收器布置在同一井中,通过向井外地层辐射弹性波并接收来自井外远处地质体的反射信号,实现井外地质构造成像,在隐蔽油气储层、地热储层和大洋科学钻探的综合评价以及储层改造设计中发挥重要作用(Amer et al.,2019; Bradley et al.,2017;Hornby et al.,2018;Tang,2016;Lee et al.,2019).在探测尺度和分辨率上,该技术填补了常规测井和地震勘探之间的空白(郝仲田等,2014;吴晓光等,2016).该技术可以利用仪器辐射到地层的纵波和横波进行成像.最早是使用单极辐射的纵波进行成像(Hornby,1989).单极纵波远探测的不足是:其声源振动没有方向性并且接收换能器只测量来自反射体的声压信号(Tang and Cheng,2004),对反射体方位不敏感.最新的进展是使用偶极辐射的横波进行三维成像(Tang and Cheng,2004).相比于传统的单极纵波方法,偶极横波远探测最大的优势是利用偶极横波的方位灵敏性对反射体进行方位/走向探测.四分量偶极数据使得对井外反射体的连续成像成为可能.四分量偶极横波远探测实现方位探测的原因是仪器使用指向发射和接收的正交测量系统,换能器测量来自反射体的速度信号以及横波有偏振特性(唐晓明和魏周拓,2012).

反射体方位探测遇到的主要挑战是反射波信噪比低.与地震勘探相比,来自井外远处的反射波信号具有幅度低、相干性弱、被井筒直达波强烈干扰等特点.同时,井下高温高压的测井环境还会产生随机噪声.此外,仪器偏心、井径变化及地层岩性突变等情况,还会存在沿着井壁上下传播的干扰反射波(如井壁反射波).这些不利因素的存在使得准确的方位探测变得困难.Tang 和 Cheng(2004)、Tang 和 Patterson(2009)分别提出利用 SH 横波与 SV 横波能量比和交叉分量能量最小化来反演反射体方位,但这些方法由于反射波信噪比低以及虚假反射波的干扰在业界未得到广泛应用.根据偶极辐射特性(曹景记等,2014,2016),Lee 等(2019)提出对四分量数据进行旋转,通过对比不同方位的成像信号强弱来识别反射体走向,该方法的精度依赖于旋转角度的疏密程度,同时精度的增加以成像处理时间成指数增长为代价.考虑经济性和实用性,该方法在实际应用中只能实现反射体走向的定性判断.

本文首先数值模拟分析偶极反射横波幅度随声源指向的变化规律,并在此基础上提出利用余弦平方函数拟合反射波幅度,建立反射体方位快速反演方法.利用数值模拟和物理实验分析了反射横波的方位特性和反演有效性.通过现场数据处理和对比分析,说明本文方法不仅可以得到反射体离井距离和倾角,还能快速精确地反演反射体走向.本文工作为四分量偶极横波远探测技术提供了实用而有效的处理方法.

1　原理和方法

1.1　反射横波幅度随声源指向变化规律

图 1 为充液井孔三维有限差分法(Wei and Tang,2012)计算模型图.在直角坐标 xyz 系统中,

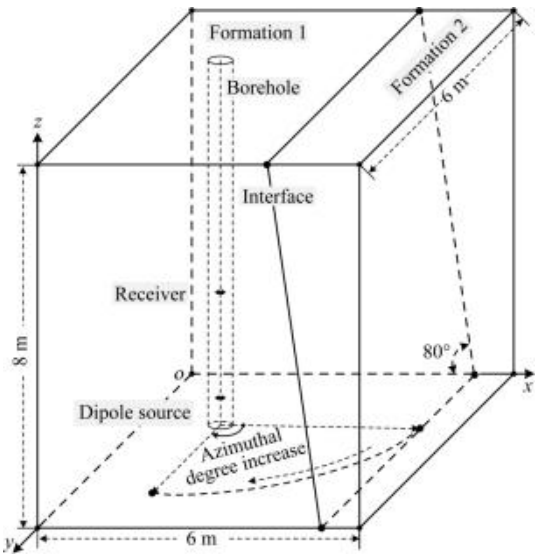


图 1　三维有限差分计算模型

Fig. 1　Calculation model of three-dimensional finite difference

(C)1994-2023 China Academic Journal Electronic Publishing House. All rights reserved.　http://www.cnki.net

模型大小为 6 m×6 m×8 m,充液井孔半径 0.1 m,偶极声源位于(1,1,0.3)处,差分网格大小为 0.01 m,时间步长 1.65 μs.声源主频为 3 kHz.地层 1 的纵波速度为 3000 m·s^{-1},横波速度 1800 m·s^{-1},密度为 2000 kg·m^{-3};地层 2 的纵波速度为 4500 m·s^{-1},横波速度为 2650 m·s^{-1},密度为 2400 kg·m^{-3}.井内流体速度为 1500 m·s^{-1},密度为 1000 kg·m^{-3}.井旁地质界面始终垂直于 xoz 面,距离井轴 4 m.偶极声源振动指向按照图中箭头所示方向进行移动,从垂直反射面到平行反射面旋转.声源指向垂直于(平行于)反射界面设定为 0°(90°)方位.反射界面与 x 轴夹角为 80°.偶极源到接收器距离为 2.2 m.

图 2 展示 xx 分量在不同偶极指向情况下对应的反射横波波形,为方便分析,图中仅显示了反射横波部分.从图中可看出,偶极指向为 90°时(0°时),反射横波幅度最大(小).为进一步分析接收的反射横波幅度随偶极指向的变化规律,对图 2 中不同方位的反射横波幅度进行归一化,如图 3 实心黑色线所示.随着偶极偏振方向与 x 轴夹角增大,即偶极指向从垂直到平行于反射体走向,接收的反射横波幅度逐渐增加.当声源偏振方向平行反射体走向,此时反射横波幅度达到最大值.井周环向方位扫描时,可根据该变化特征,判断接收反射横波幅度最大的方位为反射体走向.

反射横波幅度变化特征可以使用偶极辐射理论解释(Tang and Patterson,2009).偶极声源的辐射特性主要包括过井孔平面内对不同倾角反射体的覆盖探测特性和垂直井孔平面对反射体的方位灵敏探测特性.图 4 为过井孔平面内偶极辐射指向性图,指示偶极对不同倾角反射体的辐射能量.偶极辐射指向性受频率大小、井孔尺寸以及地层参数影响,详细计算方法及不同参数的指向性分析见文献 Tang 等(2014)和曹景记等(2014,2016).从图中可看出 SH 波较 SV 波对井外不同倾角的反射体具有更好的辐射覆盖特性和更强的辐射能量.特别是井外反射体与井近乎平行时(图 4 中 90°倾角位置),SH 波能量最强,而 SV 波可以忽略不计,即 SH≫SV(或 SV≈0).除此之外,SH 波在反射界面(剪切间断面)不发生波形转换.因此 SH 波主导反射横波随声源偏振方向的变化规律,其主要影响垂直井孔平面内对反射体的方位探测特性.SH 波对井外反射界面具有较好的方位指向性和较高的探测灵敏度,是偶极反射横波进行方位远探测的重要理论基础.

在垂直井孔平面内,声源发声方向平行于反射界面走向时接收到反射 SH 波,如图 3 的 90°方位;垂直于反射界面接收到反射 SV 波,如图 3 的 0°方位.对比反射波幅度,SH 波幅度明显大于 SV 波.介于两者之间的任何角度发声,接收的反射横波为 SH 和 SV 波组合.当界面与井轴不平行时(如图 4,与井孔夹角为 80°),在 0°方位依然能接收到微弱反射 SV 波.这是图 3 中方位角小于 20°时,反射横波幅度并未减小为零的原因.在不考虑 SV 波影响情况下,反射波幅度随方位的变化特征可使用余弦平方函数进行拟合,如图 3 红色星线所示.由于反射横波主要成分为 SH 波,余弦平方函数能较好的拟合反射波随方位的变化特征(SH 波与拟合函数关系见后文).值得注意的是,余弦平方函数相移 90°时拟合误差最小,该角度正是反射体走向.下文将从实际数据处理角度,建立方位反演方法.

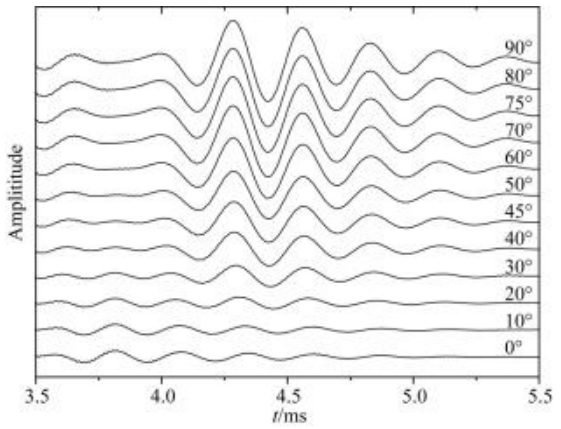


图 2 不同偶极指向时充液井孔中接收到的反射横波波形

Fig. 2 Reflected shear wave waveforms received in a fluid-filled borehole with different dipole exciting directions

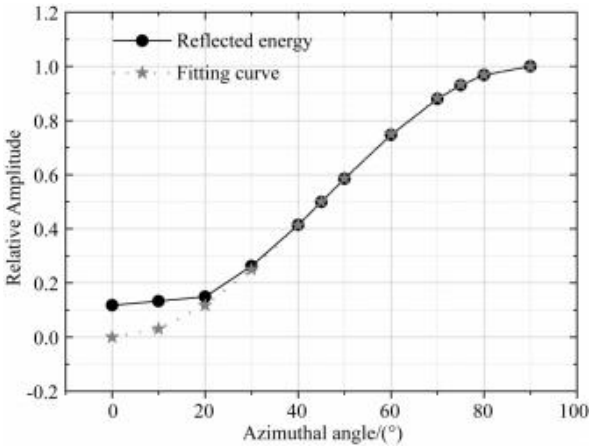


图 3 数值模拟不同偶极指向时反射横波能量变化及拟合曲线

Fig. 3 Numerical simulation result of amplitude variation of the reflected shear waves with the source and the fitting curve

(C)1994-2023 China Academic Journal Electronic Publishing House. All rights reserved. http://www.cnki.net

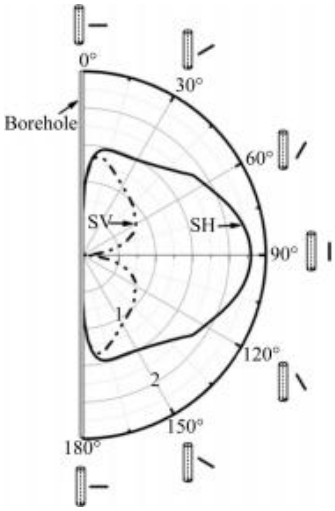


图 4　不同倾角反射体在过井孔平面内偶极辐射指向性图

Fig. 4　Radiation pattern of dipole source at reflectors with different dip angles

1.2　四分量数据的反射体方位反演方法

图 5 为偶极反射横波成像测井示意图. 仪器坐标系采用笛卡尔坐标系(x,y,z). 偶极声源位于原点$(0,0,0)$,沿 x 轴指向并对井外反射体辐射横波. x 轴指向与反射体走向的夹角为 ϕ. 在低频条件下,偶极声源的远场辐射声场与无限大介质的单力源相同(Ben-Menahem and Kostek,1991),因此可以采用矢量投影将其分解到两个正交的方向上,即位于图 5 中垂直于反射界面和平行于反射界面的两个方向. 激发出在这两个平面内偏振的 SV 和 SH 波,反射回井中后分别被仪器 x 和 y 方向的接收器接收. 声源振动发声并在同向和交叉方向采集波形可以得到四分量偶极数据$(xx、xy、yx、yy)$:

$$\begin{pmatrix} xx & xy \\ yx & yy \end{pmatrix} = \begin{pmatrix} \cos\phi & \sin\phi \\ -\sin\phi & \cos\phi \end{pmatrix} \begin{pmatrix} \mathrm{SH} & 0 \\ 0 & \mathrm{SV} \end{pmatrix} \begin{pmatrix} \cos\phi & -\sin\phi \\ \sin\phi & \cos\phi \end{pmatrix}. \tag{1}$$

根据前文所述偶极接收器接收的反射横波以 SH 波为主,特别是当反射体与井近乎平行时更是如此. 此时式(1) 简化为

$$\begin{cases} xx = \mathrm{SH}\cos^2\phi, \\ yy = \mathrm{SH}\sin^2\phi, \end{cases} \mathrm{SV} \approx 0, \tag{2}$$

从式(2)可以看出,反射横波随方位角呈余弦平方变化,这与上文拟合结果吻合. 偶极方位指向性和该公式的形式是本文建立反射体方位反演方法的重要基础.

正交偶极测井过程中,仪器会由于电缆扭矩的变化及仪器扶正器与井壁摩擦而发生旋转. 为了消除仪器旋转对反射波测量的影响,保证反射体沿着

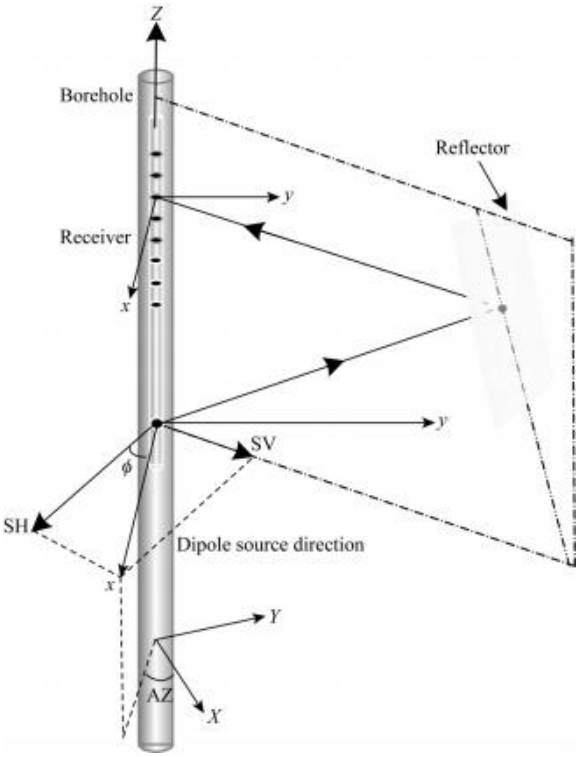


图 5　四分量偶极反射横波测井示意图

Fig. 5　Schematic diagram of shear wave logging by a four-component cross-dipole tool

井轴成像的连续性,需要将正交偶极测量的原始数据从仪器坐标系变换到固定坐标系下. 由仪器声源向反射体走向(或法向)投影,经反射再投影于接收器指向所采集的四分量数据可以组成 2×2 对称矩阵(Tang and Cheng,2004),将此矩阵通过坐标变换或旋转得到任意固定坐标系下的四分量数据:

$$\begin{pmatrix} XX & XY \\ YX & YY \end{pmatrix} = \begin{pmatrix} \cos\alpha & \sin\alpha \\ -\sin\alpha & \cos\alpha \end{pmatrix} \begin{pmatrix} xx & xy \\ yx & yy \end{pmatrix} \begin{pmatrix} \cos\alpha & -\sin\alpha \\ \sin\alpha & \cos\alpha \end{pmatrix}, \tag{3}$$

式中 α 为固定坐标系 X 轴(一般为磁北极)与反射体走向的夹角. $XX、XY、YX、YY$ 为新坐标下四分量数据. 对相对于某一特定方位记录的仪器方位角 AZ,式中 α 可通过仪器与固定坐标之间的方位表示:

$$\alpha = AZ + \phi, \tag{4}$$

式中 AZ 为 X 轴与仪器坐标 x 轴之间角度. 对(3)式中由四分量数据(XX,XY,YX,YY)组成的 2×2 矩阵可以进一步进行坐标旋转,通过调整方位角 α 使对称矩阵对角化,即:

$$\begin{pmatrix} XX & XY \\ YX & YY \end{pmatrix} \xrightarrow{\alpha} \begin{pmatrix} \mathrm{SH} & 0 \\ 0 & \mathrm{SV} \end{pmatrix}, \tag{5}$$

此时的方位角便为确定反射体走向.

根据式(5),当反射体走向与偶极 x 指向一致

(C)1994-2023 China Academic Journal Electronic Publishing House. All rights reserved.　http://www.cnki.net

时,交叉分量数据消失.由此 Tang 和 Cheng(2004)提出利用交叉分量能量最小化来反演反射体走向的方法.该方法需要不断旋转四分量数据,类似于偶极横波各向异性处理(Esmersoyet al.,1995).由于需要大量最优化计算,该方法对实际的微弱反射信号进行快速定量分析存在困难.

四分量数据确定反射体方位的方法比较复杂,但在忽略 SV 波的条件下,反射体方位可以用"xx 和 yy 主分量"做快捷分析(Tangand Patterson,2009).该方法通过对比反射信号在两个分量上的相对强弱,来确定反射体的方位,特别适合与井平行反射体(如图 4 中 90°位置).当反射横波只存在 xx 分量(yy 分量)时,反射体就在 x(y) 声源指向方向;若是两个分量都有反射横波能量,则反射体方位介于两个分量之间的方位.这种通过对比两分量上成像信号的相对强弱变化的方法只适用于定性分析反射体走向和实际资料的初步解释.

目前,基于四分量数据识别反射体方位的实用方法是:利用式(5)将 α 从 0°到 180°(由式(3)知,α 与 $\alpha+\pi$ 结果相同)等间隔(如每 45°)旋转数据,对不同方位数据采用相同的成像处理参数,实现井周环向方位扫描,称为"偶极方位扫描成像".反射体方位识别是在"方位扫描成像图"中对比不同方位的成像强弱,幅度最强方位即为反射体的走向.该方法依赖于肉眼观测,同时其精度取决于方位扫描的角度间隔.角度间隔越小,井周方位剖分越密,则反射体方位识别越准确,然而减小角度间隔意味着需要增加成像处理时间.角度间隔每减小一半(如由 90°减为 45°),井周方位扫描则加密一倍,而所需的方位剖面数增加两倍(由 2 个方位增加为 4 个剖面),最终成像处理时间在原来基础上增加两倍.远探测成像处理主要是借鉴地震方法(Tang and Cheng, 2004),声波沿着井轴测量长度达几百米甚至上千米,产生大量 3 维数据(测井深度维-波形时间维-阵列接收器维),方位剖面数量的增加将极大占用数据处理机时,也增加资料解释的时间.采用以下的方法,可以快速有效地求取反射体的方位.

根据偶极辐射特性(见图 4)和式(2)可知,井中接收的反射波幅度以 SH 波为主.当忽略 SV 波时,反射横波幅度随方位角呈余弦平方的变化规律.根据井中不同方位反射横波幅度与余弦平方的相似性,将反射波幅度与余弦平方进行最小二乘拟合,可快速反演反射体方位.反射体方位反演的目标函数表示为

$$\begin{cases} f(\alpha) = \sum\limits_{i=1}^{M}\left[\cos^2(\alpha_i-\alpha) - \mathrm{Norm}[\mathrm{AMP}(\alpha_i)]\right]^2, \\ \alpha_0 = \min[f(\alpha)], \end{cases} \tag{6}$$

式中 M 表示 0°～180°之间多方位扫描成像的剖面个数,如角度间隔为 90°,则 $M=2$;角度间隔为 45°,则 $M=4$.α_i 表示旋转波形的第 i 个方位角.AMP 表示反射波幅度峰峰值.Norm 表示对反射波幅度归一化.$f(\alpha)$为拟合的目标函数.min 表示对目标函数进行最小二乘拟合求解.α_0 表示反射体方位,当反射成像剖面的方位与该方位重合时,拟合函数与归一化的反射波幅度数据在该方位均趋于 1,此时目标函数,即二者之间的拟合误差为最小.式(6)为单参数最小值问题,可用单参数的最优化方法快速得到反射体方位角.

拟合过程是对余弦平方函数进行相移,并比较其与实际反射波数据的相似性.实际成像数据和余弦数据在数值上存在量级差异,为避免在反演过程中出现"大数吃小数"现象,需对各个方位的反射波幅度进行归一化处理,使实际数据和余弦平方函数统一到同一参考尺度,反演的精度和灵敏性因此得到提高,最优化时收敛速度加快.

一般而言,四个点可确定曲线形态,所以即使周向方位扫描仅有 4 个剖面,式(6)的方法也能较精确的反演反射体的真实方位.本文将进一步以实际数据展示这种条件下上述方位反演的稳定性.由于井下环境复杂,仪器偏心、井径变化和岩性变化界面等会产生井壁直达反射波,同时测井环境还受随机噪声影响,这些虚假信号甚至与来自地层深部的弱反射信号幅度相当,影响井外有效信息的判别.但这些虚假信号不具有随方位变化规律,在方位成像剖面中幅度没有较大变化,此时式(6)的拟合误差变大.这样通过拟合误差可以识别真实反射体和虚假反射.

下面,我们使用物理实验说明反演方法的可行性.在物理实验方面,柳俊杰(2015)和吕宗扬(2017)使用缩尺模型井研究了声源指向对反射横波幅度影响,进一步验证了反射横波幅度与声源指向的变化规律.模型井材料为 POM(聚甲醛树脂),该材料纵波速度 2300 m·s^{-1},横波速度 990 m·s^{-1}.模型井外径 30 cm,高 30 cm,井眼直径 1.4 cm.实验所用激励信号的主频为 40 kHz.模型井置于水槽中,反射界面为固-液界面,界面与井眼夹角为 75°.声源从 0°(声源指向反射界面)、22.5°、45°、67.5°和 90°(声

(C)1994-2023 China Academic Journal Electronic Publishing House. All rights reserved. http://www.cnki.net

源平行反射界面)依次旋转测量.从实验波形中提取反射横波并进行归一化,如图 6 所示.可以看出,声源指向从垂直于反射界面到平行于反射界面变化时,反射横波幅度逐渐增加,这与数值模拟结果一致.采用本文的反演方法,余弦平方曲线在相移 91°后拟合误差最小.在考虑实验误差情况下,该结果可满足反演要求.数值模拟结果和物理实验模拟表明:利用余弦平方相移方法可以满足反射体走向的精确反演.

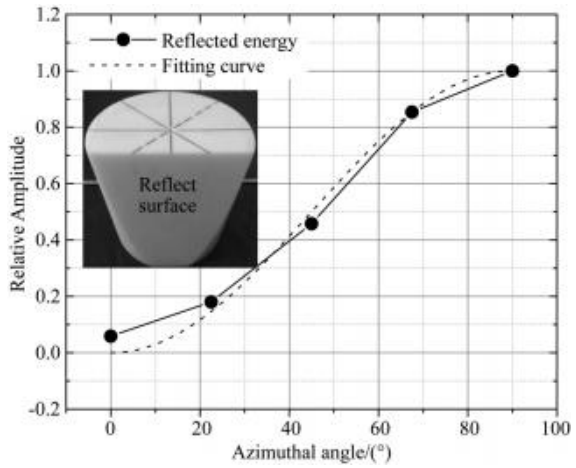


图 6　物理实验模拟不同偶极指向时反射横波能量变化及拟合曲线

Fig. 6　Experimental result of amplitude variation of the reflected shear waves with the source and the fitting curve

2　现场资料处理实例

为验证本文反演方法的实用性和可靠性,下面采用四分量数据进行偶极横波方位远探测的现场实例分析.图 7 所示测井井段长度为 80 m,地层为泥页岩沉积.第一道给出自然伽马(GR)和地层横波时差(DTS).地层横波时差为 500～600 $\mu s \cdot m^{-1}$.时差曲线将用于反射横波偏移成像,以确定反射体离井距离.第二道为仪器相对于北极的方位,可以看出仪器在井中测量时不断旋转.波形道给出四个分量偶极波形数据 (xx,xy,yx,yy),可以看到在直达弯曲波之后的反射波.值得注意的是该反射波随着仪器的旋转,在 xx 和 yy 分量交替出现.这是由于偶极声源的偏振具有指向性,对反射体有方位识别能力.当声源偏振方向平行于反射界面走向,此时能接收到最强的反射波.随着仪器旋转,反射波在四分量波形中交替出现,是偶极方位探测性的重要标识.

目前常用方位扫描成像的方法来估算反射体方位.即使用正交偶极四分量数据对井周 0°～180°范围内每隔 10°进行方位扫描,得到 18 个方位成像剖面.图 8 为两个正交方位(30°和 120°)的三维成像图(为了节省篇幅起见,其他方位的成像图未给出).反射体能量在 120°方位较强,而在 30°方位最弱,可以定性估计反射体方位在 120°左右,这就是偶极横波远探测确定方位的方法.但这种估算方法的准确度依赖于对井周方位扫描的疏密程度,同时受解释人员视觉感官影响,属于定性方位识别方法.

取图 8 中深度为 X295 m 处(图中蓝色截面)18 个方位反射波能量进行方位剖面显示,如图 9.可以看出,该深度点上反射体在 100°～140°之间幅度最强,离井孔距离约为 7 m.下面我们通过本文提出的方法定量反演反射体的方位并说明其实用性.

首先分析井周方位扫描剖面数量不等时,方位反演的稳定性.井周扫描角度间隔不同,得到的成像剖面数量也不同.图 10a 至图 10d 扫描角度间隔分别为 10°、30°、40°和 50°,则在 0°～180°范围内每个测井深度点分别有 18、6、4 和 4 个成像值.图中给出了现场数据反射波能量、拟合误差最小时的余弦平方曲线及反演的方位.可以看出,余弦平方曲线很好地拟合现场数据,同时反演的方位都为 121.1°.图 10a 至图 10d 用于拟合的实际数据逐渐减少,但方位反演结果较稳定,说明该反演方法抗噪性较强.

图 10a 至图 10c 的现场成像值中有一个方位为 120°,与反演的最终方位比较接近这种情况不同,图 10d 中离反射体准确方位较近的成像剖面是 100°和 150°方向,最大值在 100°方位,如果使用目前常用的方位估算方法,则该反射体方位将被估算为 100°方位,这与反射体实际方位有较大误差.虽然从图中拟合后的曲线形态上也难直接看出反射体的具体方位,但余弦平方曲线是在相移 121.1°后拟合误差最小.根据反射横波能量与余弦平方的相似性,反射横波在该方位达到最大值,即此时为 SH 波,该方位为反射体的方位(走向).这说明只要在 0°～180°方位内,井周扫描 4 个方位,不管扫描的方位是否接近反射体真实方位,该方法都可准确地反演反射体真实方位.本文反演方法的优势是,将目前反射体方位估算精度严重依赖于井周方位扫描数量的方法,变为只需 4 个方位就能确定反射体方位,在减少处理时间的同时,还能保证方位反演精度.

下面,我们将本文方法应用于整个井段的现场数据,并进行反射体空间形态探测.图 11 的第一道和第二道分别为30°和120°方位成像结果,其中30°

(C)1994-2023 China Academic Journal Electronic Publishing House. All rights reserved.　http://www.cnki.net

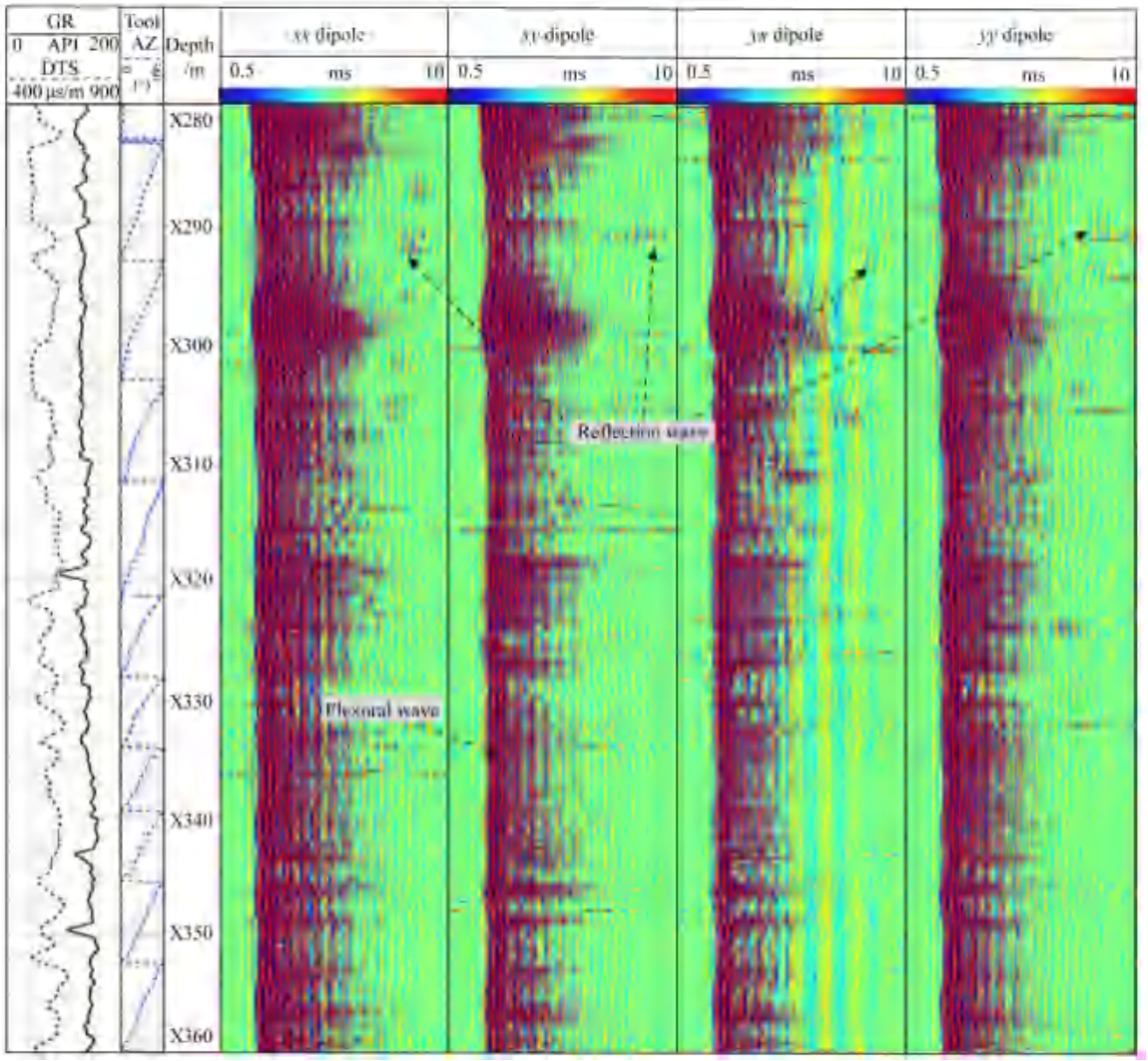


图 7 常规测井曲线及四分量正交偶极横波数据

Fig. 7 Conventional logging curves and four-component orthogonal dipole waveforms

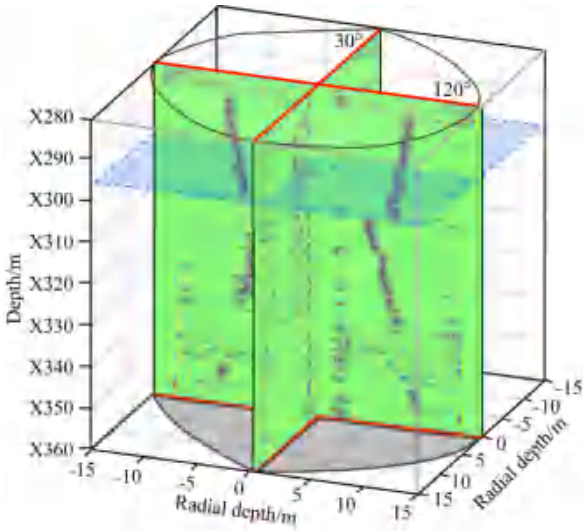


图 8 正交方位横波远探测三维成像图

Fig. 8 Shear wave imaging with orthogonal azimuth

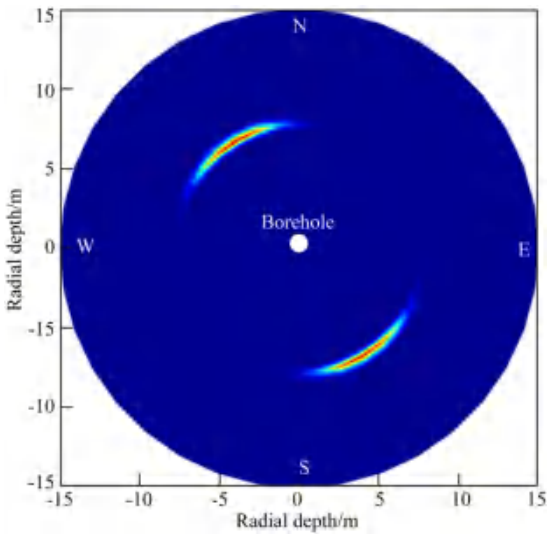


图 9 深度为 X295m 处方位成像结果

Fig. 9 Azimuth imaging result at depth X295 meter

(C)1994-2023 China Academic Journal Electronic Publishing House. All rights reserved. http://www.cnki.net

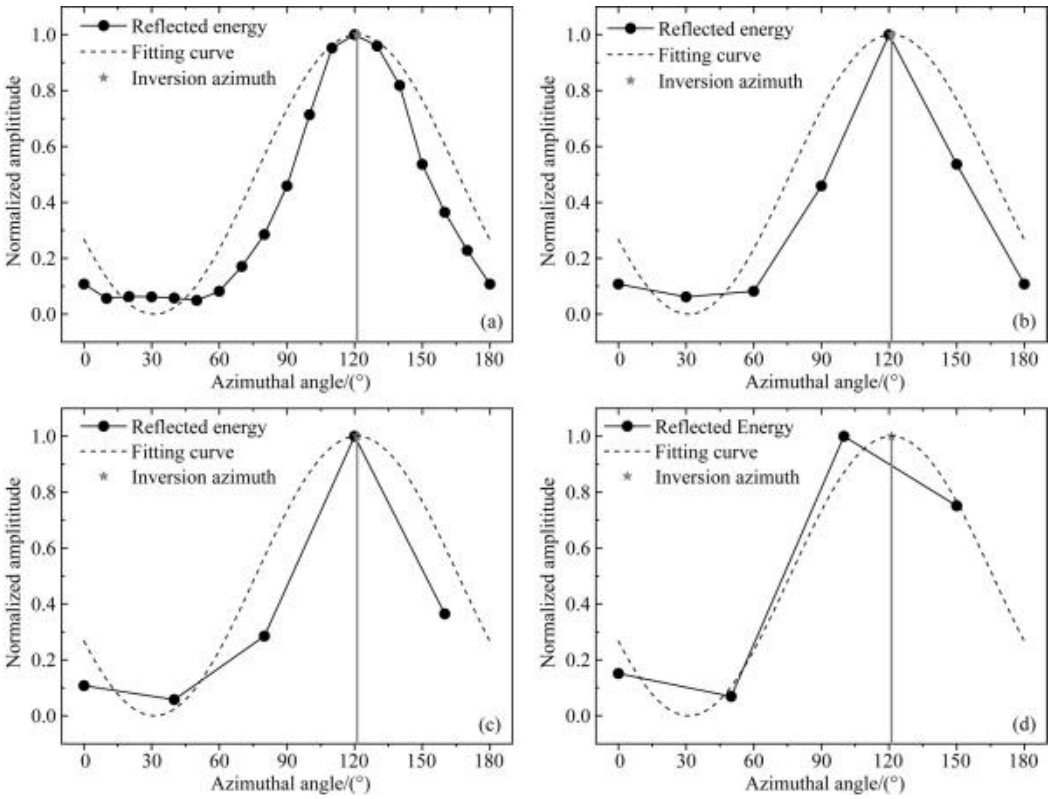


图 10　不同扫描间隔下反射体方位反演结果一致性分析

Fig. 10　The consistency analysis of azimuthal inversion of reflector with different scanning intervals

主要为噪声信号,而与其正交的 120°方位上反射波幅度较强,该方位以 SH 波成像为主. 对井外的强反射像体进行追踪,得到反射体的离井距离,如图中第二道的蓝色虚线,其形态与反射波最大振幅一致,可以从该曲线中确定反射体与井眼的空间距离. 第三道彩色图为各个深度和方位上反射波能量剖面. 反射波能量最大处所对应的方位为该深度点反射体方位,这与正交偶极各向异性处理的显示方式类似(Patterson and Tang, 2001). 对不同深度点追踪最大值即得到反射体方位(走向)曲线. 第五道为反射体方位的玫瑰图,每个玫瑰图统计的井段长度为 18 m. 从图中可以看出,反射体方位为 120±20°,为 EEN-WWS 向. 第五道为反射体倾角的玫瑰图,从图中可以看出处理井段为高倾角反射体,基本与井平行. 第六道为拟合误差,用于质量监控分析. 在处理的井段内存在三种情况,在第六道中分别用不同颜色标出. 在绿色井段内拟合误差小,从第二道可以看出清晰的反射体成像,同时第三道中对应的反射波能量较强,此时识别的反射体方位、离井距离和倾角等参数比较可信;与之相比,在蓝色井段内,拟合误差较大,虽然该井段也给出了反射体方位、离井距离和倾角等参数,但此时这些参数可信度较低,同时第二道和第三道也证实反射波能量较弱;在底部的红色井段是人机交互后,解释为无反射体井段,该井段内不进行反射体识别,第三道至第六到的曲线被赋无效值(一般为-999.25 或-32767),曲线绘图时将不显示. 实际数据处理中,拟合误差高的蓝色井段在确认无反射体后,也可通过人机交互标记为红色,本文为阐述质量监控方法,对该井段未做交互处理. 第七道给出两个深度点处理结果. 从不同方位的成像图中看出,深度 X296 m 和 X340 m 处反射体离井距离分别为 7.6 m 和 7 m,且成像图中深度 X296 m 的反射波幅度更强. 在深度 X296 m 处,反射波幅度随方位变化特征明显,与余弦平方拟合效果好. 在深度 X340 m 处,反射波幅度随方位变化幅度小,此时与余弦平方拟合效果差. 这样通过本文方法,使用四分量正交偶极数据得到反射体方位、离近距离和倾角等空间几何属性.

3　结论

偶极的指向性发射和接收以及 SH 横波辐射特性,可以确定反射体的走向. 根据偶极辐射特性,本文提出一种采用余弦平方快速确定反射体走向的反演方法. 数值模拟结果和实验室物理模拟均表明偶

(C)1994-2023 China Academic Journal Electronic Publishing House. All rights reserved.　http://www.cnki.net

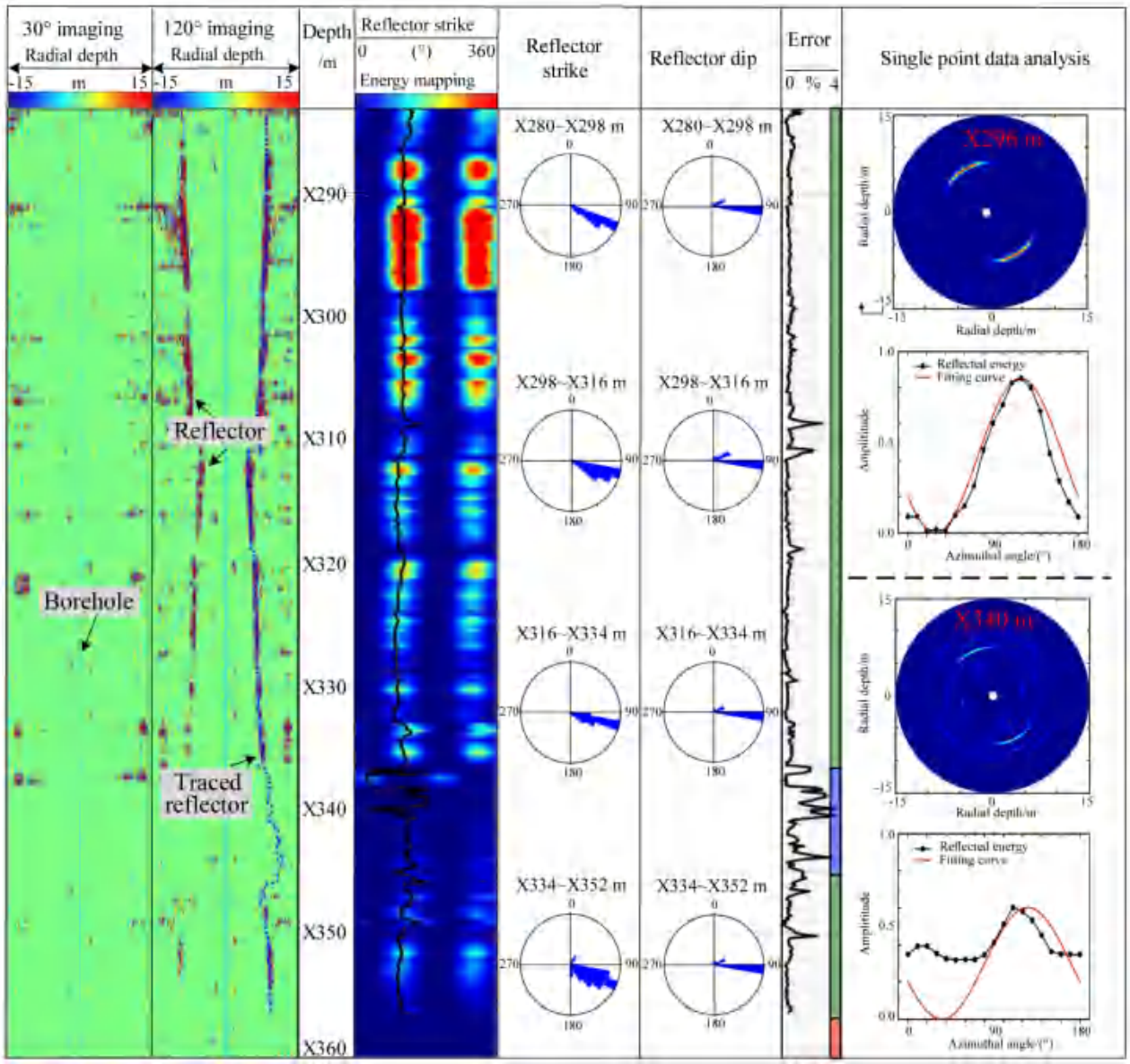


图 11 反射体空间形态探测的现场实例

Fig. 11 Field example of detecting spatial form of reflector

极声源对井旁反射体具有较高的方位灵敏度,同时本文方法能准确反演反射体走向.现场实例表明使用四分量偶极横波数据可以在最少为 4 个剖面的情况下,准确反演反射体方位,在此基础上确定反射体离井距离和倾角.本文方法在提高解释精度同时还减少处理解释时间.本文工作为四分量偶极横波声波远探测提供了实用而有效的处理方法.本文方法的高效性,也为声波远探测在随钻地质导向的应用奠定了基础.

References

Amer A, SajerA, Al-Adwani T. 2019. The application of downhole seismic imaging in identifying natural fracture systems: an integrated approach utilizing core and borehole image data. // 89thAnn. Internat Mtg., Soc. Expi. Geophys.. Expanded Abstracts.

Ben-MenahemA, Kostek S. 1991. The equivalent force system of a monopole source in a fluid-filled open borehole. *Geophysics*, 56(9): 1477-1481.

Bradley T, PattersonD, Koscheev G. 2017. Modern advances in acoustic reflection imaging. // 87thAnn. Internat Mtg., Soc. Expi. Geophys.. Expanded Abstracts.

Cao J J, Tang X M, Su Y D, et al. 2016. Radiation efficiency of a multipole acoustic source in a fluid-filled borehole. *Chinese Journal of Geophysics* (in Chinese), 59(2): 757-766, doi: 10.6038/cjg20160233.

Cao J J, Tang X M, Wei Z T. 2014. Radiation of an acoustic dipole source in open and cased borehole with application to single-

(C)1994-2023 China Academic Journal Electronic Publishing House. All rights reserved. http://www.cnki.net

well shear-wave imaging. *Chinese Journal of Geophysics* (in Chinese), 57(5): 1683-1692, doi: 10.6038/cjg20140531.

Esmersoy C, KaneM, Boyd A. 1995. Fracture and stress evaluation using dipole-shear anisotropy logs. //65thAnn. Internat Mtg., Soc. Expi. Geophys.. Expanded Abstracts.

Hao Z T, Sun X F, Liu X E, et al. 2014. The application research of dipole acoustic reflection imaging technology. *Progress in Geophysics* (in Chinese). 29(5): 2172-2177. doi: 10.6038/pg20140527.

Hornby B, Peterman P, Hager C, et al. 2018. Reflection sonic imaging of complex near-borehole structure in slow formations. //88thAnn. Internat Mtg., Soc. Expi. Geophys.. Expanded Abstracts, 684-688.

Hornby B E. 1989. Imaging of near-borehole structure using full-waveform sonic data. *Geophysics*, 54(6): 747-757.

Lee S Q, TangX M, Su Y D. 2019. Shear wave imaging to determine near-borehole faults for ocean drilling exploration. *Geophysical Journal International*, 217(1): 288-293.

Liu J J. 2015. The physical simulation of borehole acoustic reflection imaging with dipole source [Master's thesis] (in Chinese). Beijing: China University of Petroleum (Beijing).

Lü Z Y. 2017. Influences of polarization direction of acoustic source on imaging logging of reflected shear waves [Master's thesis] (in Chinese). Beijing: China University of Petroleum (Beijing).

Patterson D, Tang X M. 2001. Shear wave anisotropy measurement using cross-dipole acoustic logging: an overview. *Petrophysics*, 42(2): 107-117.

Tang X M. 2016. Reflection imaging away from borehole: A paradigm shift. //86thAnn. Internat Mtg., Soc. Expi. Geophys.. Expanded Abstracts, 4873-4877.

Tang X M, Cao J J, Wei Z T. 2014. Shear-wave radiation, reception, and reciprocity of a borehole dipole source: with application to modeling of shear-wave reflection survey. *Geophysics*, 79(2): T43-T50.

Tang X M, Cheng C H. 2004. Quantitative Borehole Acoustic Methods. San Diego: Elsevier Science Publishing Inc.

Tang X M, Patterson D. 2009. Single-well S-wave imaging using multicomponent dipole acoustic-log data. *Geophysics*, 74(6): WCA211-WCA223.

Tang X M, Wei Z T. 2012. Single-well acoustic reflection imaging using far-field radiation characteristics of a borehole dipole source. *Chinese Journal of Geophysics* (in Chinese), 55(8): 2798-2807, doi: 10.6038/j.issn.0001-5733.2012.08.031.

Wei Z T, Tang X M. 2012. Numerical simulation of radiation, reflection, and reception of elastic waves from a borehole dipole source. *Geophysics*, 77(6): D253-D261.

Wu X G, Ji F L, Li D C. 2016. Application status and research progress of dipole acoustic well logging. *Progress in Geophysics* (in Chinese). 31(1): 380-389. doi: 10.6038/pg20160144.

附中文参考文献

曹景记, 唐晓明, 苏远大等. 2016. **充液井中多极声源的辐射效率. 地球物理学报**, 59(2): 757-766, doi: 10.6038/cjg20160233.

曹景记, 唐晓明, 魏周拓. 2014. **偶极声源在裸眼井及套管井外的横波辐射特征. 地球物理学报**, 57(5): 1683-1692, doi: 10.6038/cjg20140531.

郝仲田, 孙小芳, 刘西恩等. 2014. **偶极横波远探测测井技术应用研究. 地球物理学进展**, 29(5): 2172-2177. doi: 10.6038/pg20140527.

柳俊杰. 2015. **反射横波声波测井的物理模拟研究[硕士论文]. 北京: 中国石油大学 (北京)**.

吕宗扬. 2017. **声源偏振方向对反射横波成像测井的影响[硕士论文]. 北京: 中国石油大学 (北京)**.

唐晓明, 魏周拓. 2012. **利用井中偶极声源远场辐射特性的远探测测井. 地球物理学报**, 55(8): 2798-2807, doi: 10.6038/j.issn.0001-5733.2012.08.031.

吴晓光, 季凤玲, 李德才. 2016. **偶极声波测井技术应用现状及研究进展. 地球物理学进展**, 31(1): 380-389. doi: 10.6038/pg20160144.

(本文编辑　张正峰)

(C)1994-2023 China Academic Journal Electronic Publishing House. All rights reserved.　http://www.cnki.net

03

专 题 / 03

过套管声波测井

理论、方法及应用

THROUGH-CASING ACOUSTIC LOGGING

赵岳, 苏远大, 饶博等. 2026. 过套管声波测井的双源反激参数优化实验研究. 地球物理学报, 69(9): 4321-4334, doi: 10.6038/cjg2026T0741.

Zhao Y, Su Y D, Rao B, et al. 2026. Experimental studies on parameter optimization of dual source transmitters excitation in through casing acoustic logging. *Chinese J. Geophys.* (in Chinese), 69(9): 4321-4334, doi: 10.6038/cjg2026T0741.

过套管声波测井的双源反激参数优化实验研究

赵岳[1,2], 苏远大[1,2,3*], 饶博[1,2], 郭尚静[1,4], 周建文[5], 李盛清[1,2,3], 唐晓明[1,2,3]

1 中国石油大学 (华东) 地球科学与技术学院, 山东青岛 266580
2 深层油气全国重点实验室 (中国石油大学 (华东)), 山东青岛 266580
3 崂山实验室海洋矿产资源评价与探测技术功能实验室, 山东青岛 266071
4 中海油田服务股份有限公司油田技术研究院, 北京 101149
5 杭州丰禾石油科技有限公司, 杭州 311100

摘要 过套管声波测井在剩余油气开采、注采井监测、油气饱和度评价以及套管完整性评估等方面具有重要作用. 然而在固井水泥胶结质量较差时, 声波信号主要为沿着套管传播的套管波, 对地层时差提取形成挑战. 为解决这一难题, 提出了过套管双源反激声波测井技术, 该技术采用固定的双源激励参数 (即双源间的延迟时间和激励幅度比) 来压制套管波. 当套管波频散效应较为显著时, 传统的双源激励参数难以获得最优压制效果, 亟需优化双源激励参数以获得高信噪比地层信号. 本文首先基于分波理论计算了不同激励参数下的套管井声场响应, 通过对比归一化后的套管波振幅, 确定了压制套管波的最优激励参数. 在此基础上, 设计声系结构并在模型井中开展物理实验. 通过改变双源间的延迟时间和激励幅度比来测量套管波振幅. 结果表明, 虽然传统的双源激励参数能够有效压制套管波, 但采用最优双源激励参数可明显提升压制效果, 由此得到的地层纵波时差与裸眼井结果一致. 在理论和实验指导下设计研制了新型过套管双源反激声波测井仪器样机, 该仪器集成了双源激励参数优化功能, 实测结果显示双源数据信噪比显著提升, 地层纵波时差相关性明显增强, 表明了双源激励参数优化的必要性和有效性.

关键词 过套管声波测井; 双源反激; 套管波压制; 分波; 地层速度

中图分类号 P631 **收稿日期** 2025-12-11, 2026-03-09 收修定稿

DOI: 10.6038/cjg2026T0741 **CSTR:** 32084.14.cjg2026T0741

Experimental studies on parameter optimization of dual source transmitters excitation in through casing acoustic logging

ZHAO Yue[1,2], SU YuanDa[1,2,3*], RAO Bo[1,2], GUO ShangJing[1,4], ZHOU JianWen[5], LI ShengQing[1,2,3], TANG XiaoMing[1,2,3]

1 *School of Geosciences, China University of Petroleum (East China), Qingdao Shandong* 266580, *China*
2 *National Key Laboratory of Deep Oil and Gas, China University of Petroleum (East China), Qingdao Shandong* 266580, *China*
3 *Laboratory for Marine Mineral Resources, Laoshan Laboratory, Qingdao Shandong* 266071, *China*
4 *Well Tech R & D, China Oilfield Services Limited, Beijing* 101149, *China*
5 *Hangzhou Fenghe Petroleum Technology Co., Ltd., Hangzhou* 311100, *China*

Abstract Through casing acoustic logging plays an important role in residual oil and gas recovery, injection and production well monitoring, oil and gas saturation evaluation, and casing integrity assessment. However,

基金项目 国家自然科学基金 (42574180, 42574150) 和山东省自然科学基金 (ZR2024YQ062) 联合资助.

第一作者简介 赵岳, 男, 2000 年生, 博士研究生, 主要从事声波测井理论方法研究. E-mail: 873353289@qq.com

*** 通讯作者** 苏远大, 男, 1978 年生, 博士, 教授, 主要从事声波测井理论、方法及处理研究. E-mail: syuanda@sina.com

when the cement bonding quality is poor, the acoustic signal is mainly the casing wave propagating along the casing, which poses a challenge to the extraction of formation slowness. To address this problem, the through casing acoustic logging technology using the dual source transmitters has been proposed. This technology uses fixed dual source excitation parameters (delay time and excitation amplitude ratio between the dual source) to suppress casing waves. When the casing wave dispersion effect is significant, it is difficult to achieve the optimal suppression effect with traditional dual source excitation parameters. It is urgent to optimize the dual source excitation parameters to obtain formation signals with a high signal-to-noise ratio. This paper first calculates the acoustic field response of a cased well with different dual source excitation parameters based on the wave separation theory. By comparing the normalized casing wave amplitude, the optimal excitation parameters for suppressing the casing wave were determined. Based on this, an acoustic system was designed and physical experiments were conducted in a model well. By changing the delay time and excitation amplitude ratio between the dual source, the casing wave amplitude results show that although the traditional dual source excitation parameters can effectively suppress the casing wave, the optimal dual source excitation parameters can significantly improve the suppression effect. The resulting formation compressional wave slowness is consistent with the open hole well result. Guided by theory and experiments, a new through casing acoustic logging tool using the dual source transmitters was designed and developed. This tool integrates a self-optimization function for dual-source excitation parameters. The signal-to-noise ratio of dual source data was significantly improved, and the correlation between formation compressional wave slowness was significantly enhanced, demonstrating the necessity and effectiveness of optimizing dual source excitation parameters.

Keywords Through casing acoustic logging; Dual source transmitters; Casing wave suppression; Component wave; Formation acoustic velocity

0 引言

随着对石油和天然气需求的不断增长，老油气田的二次勘探开发中的过套管测井，特别是声波测井，成为重要的关键技术 (原宏壮等, 2005). 由于套管和水泥环的存在，沿着管柱传播的套管波严重影响地层信号的测量 (Tubman et al., 1984), 尤其在固井质量较差时，常规阵列波形处理方法 (Kimball and Marzetta, 1984) 难以提取到准确的地层时差 (Tubman et al., 1986; Tang and Pattserson, 2005; Wang and Fehler, 2018).

为透过套管获取到地层信息，国内外学者提出了一系列处理算法用于压制套管波，突出地层波 (Valero et al., 2003; 唐晓明等, 2015; 许松等, 2017; Kong et al., 2020). 然而，由于测井仪器的自动增益主要受制于幅度更强的套管波，地层信号只能在较低位数范围内数字化，对信噪比极低的地层波，上述处理算法失效. 针对这种情况，张博等 (2015) 提出一种过套管双源反激声波测井方法，采用极性相反的双源声系结构从数据源头上压制套管波，增强地层波，并在小尺寸胶结质量差的模型井中成功测量到准确的地层纵波时差. 张博等 (2016) 提出将双源反激技术应用于随钻声波测井中，通过实验验证了双源反激方法在 5–16 kHz 频段内可显著压制钻铤波 (其传播机制与套管波类似). 丁浩然等 (2016) 针对孔隙地层的随钻声电测井，利用双发射声源延迟激励方法，实现了对钻铤模式波在声场与电场响应中的有效压制. 王军等 (2019, 2021) 通过实验系统地研究了钻铤波的传播机制与压制方法，表明通过合理优化声源配置并结合信号处理方法能够有效削弱钻铤波干扰. Tang 等 (2019) 给出了过套管双源反激声波测井的现场应用实例，从实测双源数据中提取到的地层纵波时差与套前裸眼井中测量结果吻合良好. 刘汇鑫等 (2021) 提出采用双偶极源反相激励的声波远探测测井方法，可大幅压制井筒直达波信号，提高井外反射波信号的信噪比. Xu (2023) 研究了双源激励在套管井不同胶结情况下的远场辐射指向性，结果表明，采用双源激励能够显著增强地层信号. 庄春喜等 (2026) 设计了双源反激过套管声波测井仪，现场应用验证了双源反激技术能够有效压制套管波，提高地层波信噪比. 但前人研究尚未考虑套管波的频散效应对双源激励参数 (即双源间的延

迟时间和激励幅度比) 的影响, 这种影响在胶结质量较差时十分明显, 采用传统的双源激励参数的压制效果较差, 亟需进一步优化以提高地层信号的信噪比.

针对以上问题, 本文基于过套管双源反激声波测井的基本原理 (唐晓明等, 2016), 采用分波方法 (郑晓波, 2017; 饶博等, 2022; Ji et al., 2025) 计算了不同双源激励参数下的套管井声场响应, 对比双源激励时的套管波振幅, 确定了最优的双源激励参数. 在此基础上, 设计双源声系结构在模型井中开展物理实验. 改变延迟时间和激励幅度比来观测套管波振幅, 所得的最优双源激励参数与理论计算结果一致. 相较于传统双源激励方式 (套管波振幅为单源激励时的 0.19 倍), 采用优化后的双源激励参数可将套管波振幅进一步降低至单源激励时的 0.08 倍, 压制效果显著增强. 最后, 给出新型过套管双源反激声波测井仪器样机的现场实测数据处理实例. 结果表明, 在固井胶结质量较差的井段, 最优双源激励参数采集到的地层波信噪比显著提升, 纵波时差相关性明显增强, 充分验证了双源激励参数优化的必要性和有效性. 本文所做的理论和实验改进了已有的过套管双源反激声波测井技术, 为该技术的推广和应用提供了有力的实验和现场支撑.

1　过套管双源反激声波测井理论

1.1　基本原理

图 1a 给出了过套管双源反激声波测井示意图. 过套管双源反激声波测井仪居中放置于充液套管井中, 外层依次是流体环、水泥和井外地层. 仪器的声系结构由轴向上的两个极性相反的发射声源 (远单源T_f和近单源T_n, 间距为D) 和八个阵列排布的接收器构成. 图 1b 给出了双源激励时的时域波形示意图. 测井时, 远单源T_f首先以激励幅度C_f激发, 经过延迟时间τ后, 极性与远单源T_f相反的近单源T_n以激励幅度C_n激发, 通过调节延迟时间τ以及声源激励幅度C_f和C_n, 使得两个声源激发的套管波在到达接收器阵列时相互抵消.

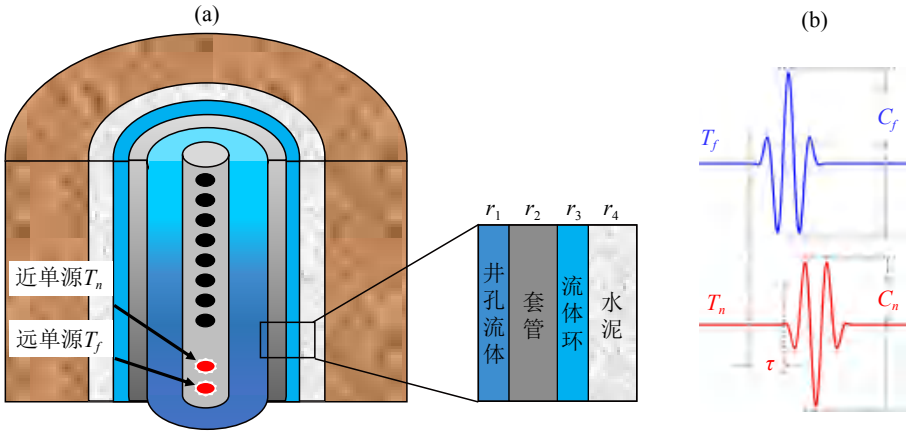


图 1　(a) 过套管双源反激声波测井示意图; (b) 双源激励时域波形示意图

Fig. 1　(a) Schematic diagram for the through casing acoustic logging tool using the dual source transmitters; (b) Schematic diagram of dual source excitation time domain waveform

在井轴上距离远声源 z 处的双源激励的声压表达式为 (张博, 2016):

$$p_{\mathrm{Dual}}(z,t)=\frac{1}{(2\pi)^2}\int_{-\infty}^{+\infty}\int_{-\infty}^{+\infty}\rho_{\mathrm{f}}\omega^2A'(k,\omega)\xi(k,\omega)S(\omega)\cdot\mathrm{e}^{\mathrm{i}kz}\mathrm{e}^{-\mathrm{i}\omega t}\mathrm{d}k\mathrm{d}\omega, \tag{1}$$

式中, ρ_{f}为流体密度, ω为圆频率; z 为轴向距离; $\tau=D/v_{\mathrm{casing}}$, v_{casing}为套管波的传播速度; $\xi(k,\omega)=[1-\gamma\exp(\mathrm{i}\omega\tau-\mathrm{i}kD)]$, $\gamma=C_n/C_f$为双源激励幅度比; $S(\omega)$为声源函数; $A'(k,\omega)$为井孔流体中的响应函数, 由套管井模型下的井孔边界条件确定, 该理论模型的具体求解过程见附录 A.

套管井声场的构成十分复杂, 难以从全波波形中区分出套管波与地层波. 本文采用分波计算的方法分析延迟时间和双源激励幅度比对套管波影响. 根据柯西积分定理, 将波数域中的沿实轴积分的路径转化为实质支点的割线积分与极点的留数贡献之和. 值得注意的是, 在选择积分路径时, 仅需对井外地层中纵、横波的径向波数做单值化处理即可 (胡恒山等, 1999).

参考江灿 (2020) 等文献, 极点留数对应模式波对声场的贡献, 双源激励的模式波声压表达式为:

$$P_{\text{poleDual}}(z,t)=\frac{1}{2\pi}\int_{-\infty}^{+\infty}\mathrm{i}\rho_{\mathrm{f}}\omega^{2}\xi_{k_{\text{pole}}}\frac{\det(D_1(k,\omega))}{\partial[\det(D(k,\omega))]/\partial k}\cdot S(\omega)\mathrm{e}^{\mathrm{i}kz}|_{k=k_{\text{pole}}}\mathrm{e}^{-\mathrm{i}\omega t}\mathrm{d}\omega, \tag{2}$$

式中，$\xi_{k_{\text{pole}}}(k,\omega)=[1-\gamma\exp(\mathrm{i}\omega\tau-\mathrm{i}k_{\text{pole}}D)]$，$k_{\text{pole}}$为模式波一阶极点；$D(k,\omega)$和$D_1(k,\omega)$的具体表达式见附录 A. 将全波的实轴积分路径转化为复波数域中的圆弧与绕过地层纵、横波支点的积分路径. 根据约当定理，只有竖直围道的路径对积分有贡献，分别对应沿井壁传播的地层纵、横波的贡献：

$$\begin{aligned}P_{\text{p-cutDual}}(z,t)&=\frac{1}{(2\pi)^2}\int_{-\infty}^{+\infty}\int_{k_{\mathrm{p}}}^{k_{\mathrm{p}}+\mathrm{i}\infty}\rho_{\mathrm{f}}\omega^{2}[A'_{\mathrm{R}}(k,\omega)-A'_{\mathrm{L}}(k,\omega)]\xi_{k_{\mathrm{p}}}(k_{\mathrm{p}},\omega)S(\omega)\mathrm{e}^{\mathrm{i}kz-\mathrm{i}\omega t}\mathrm{d}k\mathrm{d}\omega\\ P_{\text{s-cutDual}}(z,t)&=\frac{1}{(2\pi)^2}\int_{-\infty}^{+\infty}\int_{k_{\mathrm{s}}}^{k_{\mathrm{s}}+\mathrm{i}\infty}\rho_{\mathrm{f}}\omega^{2}[A'_{\mathrm{R}}(k,\omega)-A'_{\mathrm{L}}(k,\omega)]\xi_{k_{\mathrm{s}}}(k_{\mathrm{s}},\omega)S(\omega)\mathrm{e}^{\mathrm{i}kz-\mathrm{i}\omega t}\mathrm{d}k\mathrm{d}\omega\end{aligned}, \tag{3}$$

式中，A'_{R}和A'_{L}分别表示沿割线右侧和左侧积分路径求得的井孔流体中的响应函数；

$$\xi_{k_{\mathrm{p}}}(k,\omega)=[1-\gamma\exp(\mathrm{i}\omega\tau-\mathrm{i}k_{\mathrm{p}}D)],$$

$$\xi_{k_{\mathrm{s}}}(k,\omega)=[1-\gamma\exp(\mathrm{i}\omega\tau-\mathrm{i}k_{\mathrm{s}}D)],$$

k_{p}和k_{s}分别对应地层的纵波支点和横波支点.

1.2 数值模拟结果与分析

基于上述过套管双源反激声波测井的基本原理，以自由套管井模型为例，理论模拟了单源激励、不同双源参数激励时的声场响应. 计算所用声源为高斯声源，接收器与远单源的距离为 3.65 m，接收器间距为 0.15 m，远单源与近单源的距离为 0.15 m. 模型声学参数详见表 1.

表 1 模型井的声学参数

Table 1 Acoustic parameters of the model well

	纵波速度 /(m·s^{-1})	横波速度 /(m·s^{-1})	密度 /(kg·m^{-3})	内径 /m	外径 /m
井孔流体	1500	–	1000	–	0.08
套管	5959	3229	7800	0.08	0.09
流体环	1500	–	1000	0.09	0.125
地层	3000	1200	2300	0.125	–

图 2a 给出了自由套管情况下的套管波频散曲线及激发强度曲线 (实线为频散曲线，点划线为激发强度曲线). 结果表明，在测井频段内 (0 ~ 20 kHz) 存在三阶模式套管波 (即 C1、C2 和 C3)，其相速度和激发强度均随频率变化明显，因此双源延迟时间τ和激励幅度比γ的确定需考虑套管波的频散效应. 利用式 (2)、(3) 可计算出各个极点和支点对应套管井声场 (模拟所用声源主频为 8 kHz，延迟时间为 27 μs，激励幅度比为 1.0)，如图 2b 所示，黑线 (红线) 为单源 (双源) 激励时的各模式波波形，绿线为单源和双源激励时的全波波形，紫线为单源和双源激励时的各模式波的叠加波形，图的右侧给出了各模式波的幅度放大倍数. 计算结果表明，全波中的首波是由 C1、C2 和 C3 组成的套管模式波波群；地层纵波波群包括泄漏纵波 (Lp1、Lp2、Lp3) 以及支点 kp 的贡献，其中泄漏纵波 Lp2、支点 kp 占主要成分，泄漏纵波 Lp1、Lp3 对井中接收波形贡献微弱，基本可以忽略；斯通利波-地层横波波群包括内斯通利波、外斯通利波和支点 ks 的贡献，内斯通利波与外斯通利波组成的波包在全波波形中幅度最大，到时最晚. 最后两道分别给出了单源激励和双源激励时，实轴积分计算的全波波形 (绿线) 和各模式波的叠加波形 (紫线)，二者无论在相位还是幅度上都十分吻合，验证了过套管双源反激声场分波计算的正确性. 对比单源与双源激励时的分波波幅发现，单源激励时套管波波群幅度大，明显掩盖了地层纵波，而采用双源激励后，套管波波群幅度显著减小，地层纵波波群成分突出.

图 3 给出了不同双源激励参数的套管波分波波形及归一化套管波振幅 (即双源与单源激励时的套管波振幅比η). 改变延迟时间 ($23\ \mu\text{s}\leqslant\tau\leqslant 33\ \mu\text{s}$) 和激励幅度比 ($0.6\leqslant\gamma\leqslant 1.2$) 计算单源和双源激励的套管波分波波形. 计算结果分别如图 3a 和图 3b 所示 (声源激发频率为 10 kHz). 图中右侧给出了归一化套管波振幅曲线. 对比单源情况，双源激励的套管波幅度明显减弱，且减弱程度受控于双源延迟时间和激励幅度比.

图 3c 给出了在声源主频为 10 kHz 时不同双源激励参数情况下的归一化套管波振幅 (其中颜色映射数值对应归一化套管波振幅)，显示压制套管波最优的双源延迟时间为 27μs，激励幅度比为 0.97. 此时的压制效果明显优于传统延迟时间 25 μs 和激励幅度比 1.0 的情况 (张博，2016). 基于图 3c 的计算结果，利用式 (1) 理论模拟了传统双源激励参数和最优双源激励参数的全波阵列波形，结果如图 3d 所示. 相较于传统双源参数激励结果，归一化套管波振

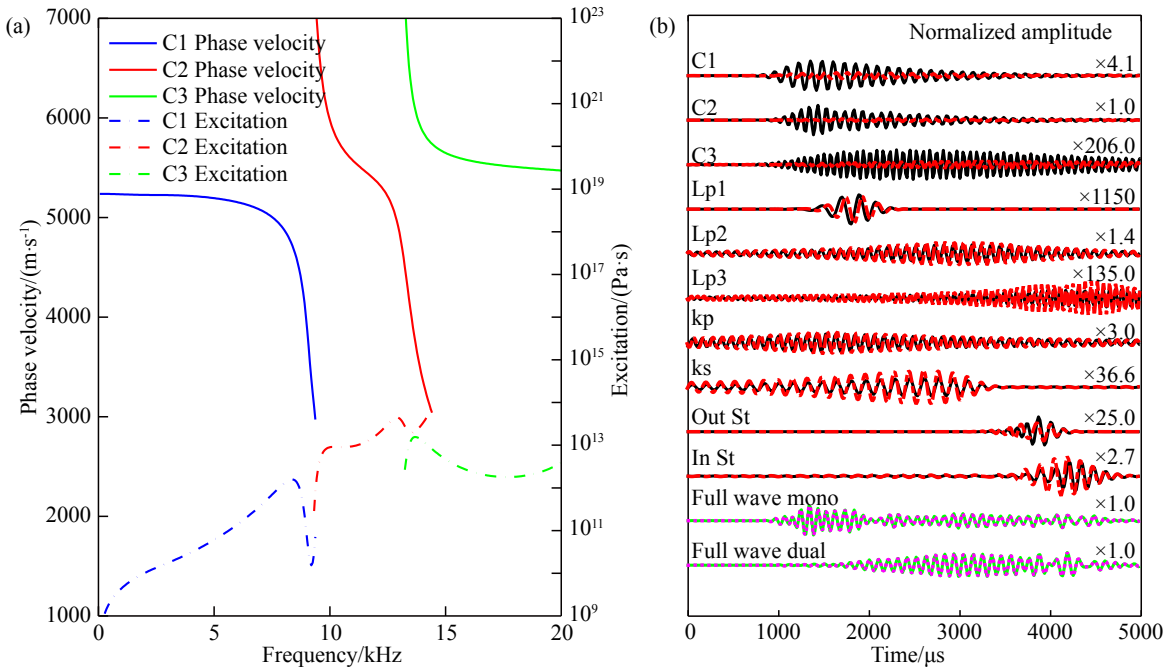


图 2　(a) 自由套管情况下的套管波频散曲线和激发强度曲线; (b) 单源激励与双源激励时分波波形与全波波形对比

Fig. 2　(a) Dispersion curves and excitation spectrum curves of casing wave propagated in the free casing borehole; (b) Comparison of component wave and full wave waveforms for mono source and dual source excitation

幅从 0.21 削弱至 0.09, 从理论上验证了优化双源激励参数的必要性和有效性.

2　模型井中双源反激参数优化实验验证

上述模拟结果从理论上验证了针对套管波频散效应优化双源激励参数的正确性与必要性. 下面依托模型井开展物理验证实验.

图 4a 给出了实验测量原理图. 实验声系由 2 个管状单极发射换能器和 7 个管状接收换能器构成, 2 个单极换能器的距离为 0.15 m, 阵列接收换能器间距为 0.15 m. 最短源距为 1.2 m, 最长源距为 2.1 m. 图 4b 给出了实验测量系统的实物照片. 发射换能器与阵列接收换能器均通过电路与信号发射及采集装置连接, 并由计算机下发指令, 控制激励信号的产生与数据采集. 实验所用的双源发射电路可分别调控远单源和近单源的激励电压幅度及延迟时间, 延迟时间参数在 0 ~ 50 μs 可控, 激励电压幅度可调, 最大幅度可达 120 V.

实验在一口裸眼模型井中展开, 如图 4c 所示, 通过在裸眼井孔中插入一根套管来模拟自由套管的情况, 其中裸眼井孔直径为 25 cm、套管外径为 18 cm, 套管及地层的声学参数与表 1 一致. 图 4d 给出了实物配置图. 实验过程中, 将声系结构居中下放至充液套管井中. 采用三周期正弦波电压信号激励换能器, 换能器实际辐射的激励波形与数值模拟所用高斯源特征类似. 数据采样点数为 512, 采样时间间隔为 12 μs. 远、近声源为两个独立的信号发生和采集通道, 计算机同时记录和存储远声源和双源激发时的阵列波形数据.

采用上述实验装置, 改变延迟时间 (23 μs ⩽ τ ⩽ 33 μs) 和激励幅度比 (0.6 ⩽ γ ⩽ 1.2) 测量双源激励时的阵列波形, 并与单源激励的结果作对比. 图 5a (图 5b) 对比了声源主频为 10 kHz 时, 激励幅度比为 1.0 (延迟时间为 28 μs) 时不同延迟时间 (激励幅度比) 单源 (黑线) 和双源 (红线) 情况首个接收器记录的波形, 图中右侧给出了归一化套管波振幅曲线. 实验结果表明, 传统的双源激励参数, 即延迟时间 τ = 25 μs、双源激励幅度比 γ = 1.0, 并非最优的参数组合.

进一步分析不同声源主频情况下双源激励时的归一化套管波振幅随延迟时间和激励幅度比的变化. 计算结果分别如图 5c 和图 5d 所示. 图中颜色映射数值对应归一化套管波振幅, 黑线指示了在不同声源主频情况下最优的延迟时间和激励幅度比. 对比发现, 二者均随声源主频变化, 这与前文套管波速度和激发强度频散现象对应. 图 5e 给出了不同双源激励参数情况下的归一化套管波振幅, 当延迟时间 τ = 27 μs、双源激励幅度比 γ = 0.97时压制效果最佳, 这与图 3 中的理论计算结果一致.

在上述实验结果的指导下, 设定延迟时间为

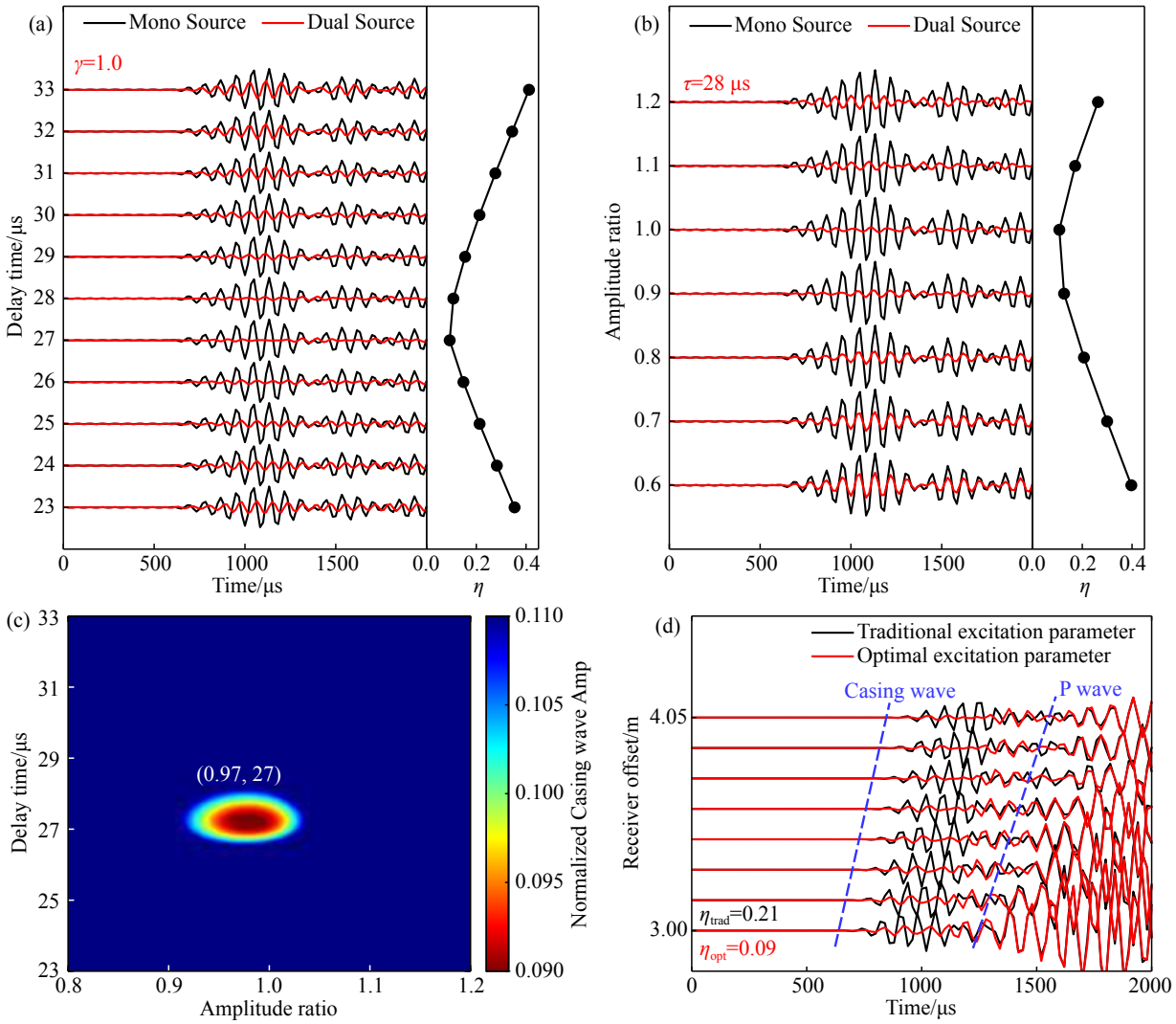


图 3 (a) 不同延迟时间的套管波波形 ($\gamma = 1.0$) 及归一化套管波振幅曲线; (b) 不同激励幅度比的套管波波形 ($\tau = 28$ μs) 及归一化套管波振幅曲线; (c) 不同延迟时间和激励幅度比的归一化套管波振幅 ($f = 10$ kHz); (d) 传统双源参数激励和最优双源参数激励的阵列波形对比

Fig. 3 (a) Casing waveforms with different delay times ($\gamma = 1.0$) and normalized casing wave amplitude curve; (b) Casing waveforms with different excitation amplitude ratios ($\tau = 28$ μs) and normalized casing wave amplitude curve; (c) Normalized casing wave amplitude with different delay times and excitation amplitude ratios ($f = 10$ kHz); (d) Comparison of array waveforms between traditional dual source parameter excitation and optimal dual source parameter excitation

27 μs、双源激励幅度比为 0.97 重采数据. 作为对比, 也给出了单源激励和传统双源参数激励的结果, 如图 6a 所示, 地层纵波几乎被强振幅的套管波完全掩盖, STC 处理结果只显示了套管波的相关性 (见图 6b, 其中颜色映射代表 STC 处理得到的相关系数). 传统双源激励时的结果见图 6c 和图 6d, 最优双源激励时的结果见图 6e 和图 6f. 对比可见, 相较于单源激励时的波形, 套管波的振幅明显减小 (归一化套管波振幅从 1.0 削弱至 0.19), 地层纵波信号得以突显. 同时, 相较于传统双源参数激励时的波形, 残余套管波幅度被有效压制 (归一化套管波振幅从 0.19 进一步削弱至 0.08), STC 图中套管波的相关性大幅降低, 地层纵波相关性增强. 作为对比, 图 6g 和图 6h 进一步给出了裸眼井中 (即将套管拔出) 单源激励的结果. 对比双源情况, 处理得到的地层纵波时差值完全相同, 充分验证了优化双源参数的必要性和有效性.

3 过套管双源反激声波测井仪器设计与现场应用

在理论模拟和物理实验结果的指导下, 设计研制了新型过套管双源反激声波测井仪器样机, 进行了现场井测试并取得了高信噪比的地层波数据.

3.1 过套管双源反激声波测井仪器

图 7a 展示了新型过套管双源反激声波测井仪器样机的实物照片, 该仪器主要由发射短节、隔声体和接收短节组成. 发射短节由 2 个间距为 0.15 m 的单极源构成, 其中远单极源与第一个接收器的距离为 3.65 m. 隔声短节采用柔性隔声体替代传统刻

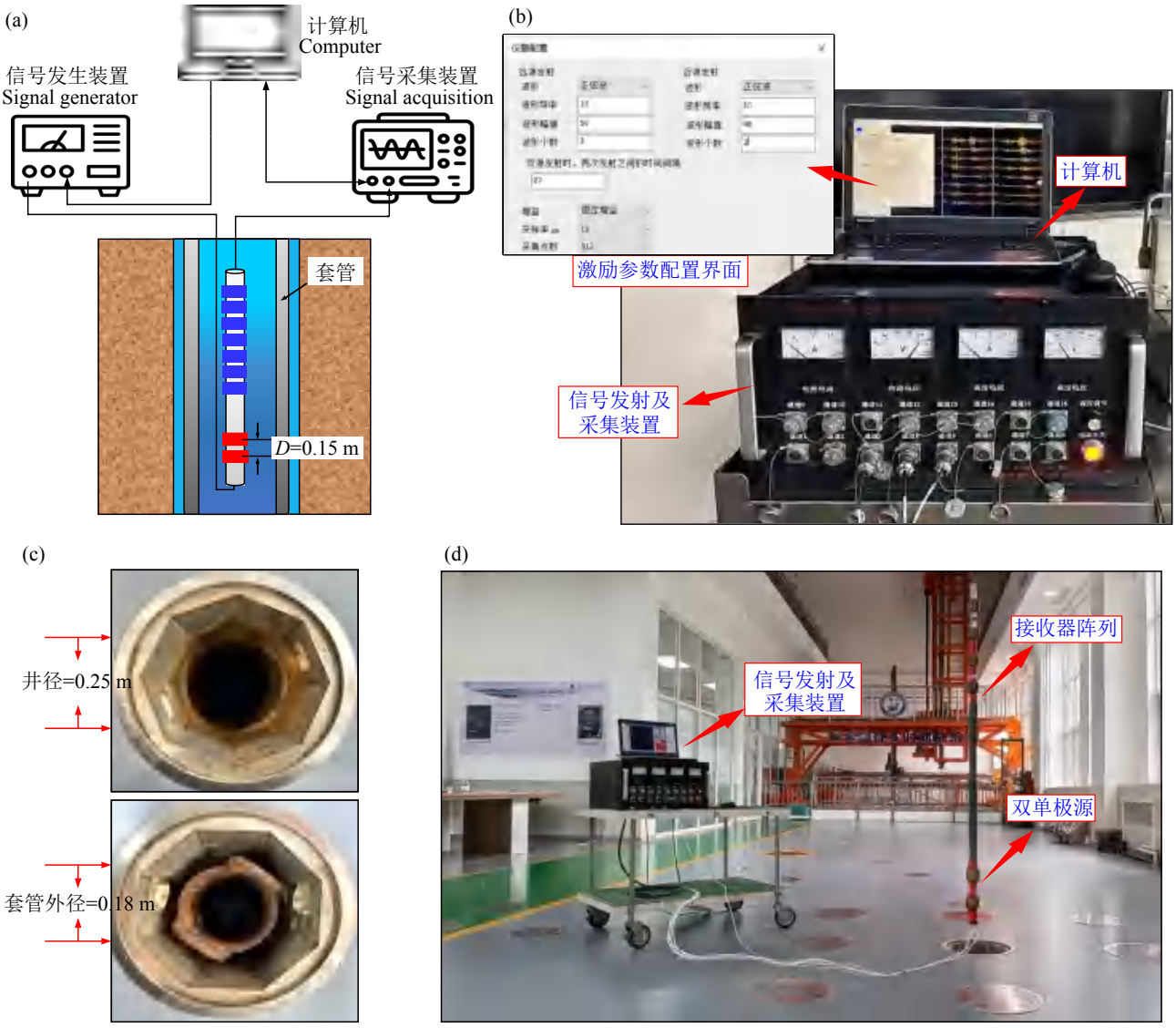


图 4　(a) 模型井实验测量系统原理图; (b) 实验测量系统; (c) 模型井截面图; (d) 实物配置图

Fig. 4　(a) Schematic diagram of model well experimental measurement system; (b) Experimental measurement system; (c) Diagram of model well cross section; (d) The physical diagram of experimental configuration

槽隔声体, 能有效衰减仪器直达波. 接收短节由 8 个间距为 0.15 m 的接收换能器组成, 采用传统皮囊与硅油透声结构, 设计宽透声窗以提高接收信号能量, 提高信噪比.

图 7b 给出了双源激励参数井下自动优化流程图. 在实际测井作业中, 由于套管尺寸差异导致套管波的频散特性存在差异, 故在实际测井前, 确定声源激发主频后, 先将仪器下放至自由套管段, 调节双源激励参数进行多次数据采集, 利用井下 DSP 芯片自动反演得到最优双源激励参数组合, 该流程将最优参数组合反馈给双源激励电路, 并应用于整个井段的测量, 可最大程度压制套管波, 提高地层波信噪比.

3.2　现场应用实例

图 8 给出了仪器样机在某一套管井中的现场应用实例. 将仪器下放至 X120 m (对应自由套管段),339 调测得到该井最优的双源激励参数 (其中声源主频为 8 kHz, 延迟时间调测区间为 23 ~ 33 μs, 步长为 0.5 μs, 激励幅度调测比区间为 0.8 ~ 1.2, 步长为 0.05), 并采用该激励参数全井段测井, 测量的波形变密度图和 STC 处理结果在图中第五道和第六道显示. 作为对比, 也给出了单源激励和传统双源参数激励时的结果, 分别在第一、二道和第三、四道中显示. 对比可见, 在 X320 ~ X420 m 套管胶结质量良好井段, 套管波几乎消失, 三组数据均能测到高信噪比、强相关的地层纵波信号. 而在 X220 ~ X320 m 套管胶结质量中等井段, 套管波振幅显著增强, 地层纵波的信噪比和相关性减弱. 其中单源激励和传统双源参数激励时, 地层纵波明显被强振幅套管波干扰. 这一现象在 X120 ~ X220 m 自由套管段更加明显. 相较于单源激励, 传统双源参数激励时的套管波首波被有效压制, 但后续波的压制效果仍不理想. 而在最优双源参数激励时, 套管波压制效果明显提升, 地层纵波的信噪比显著提高, 可提取到连续的

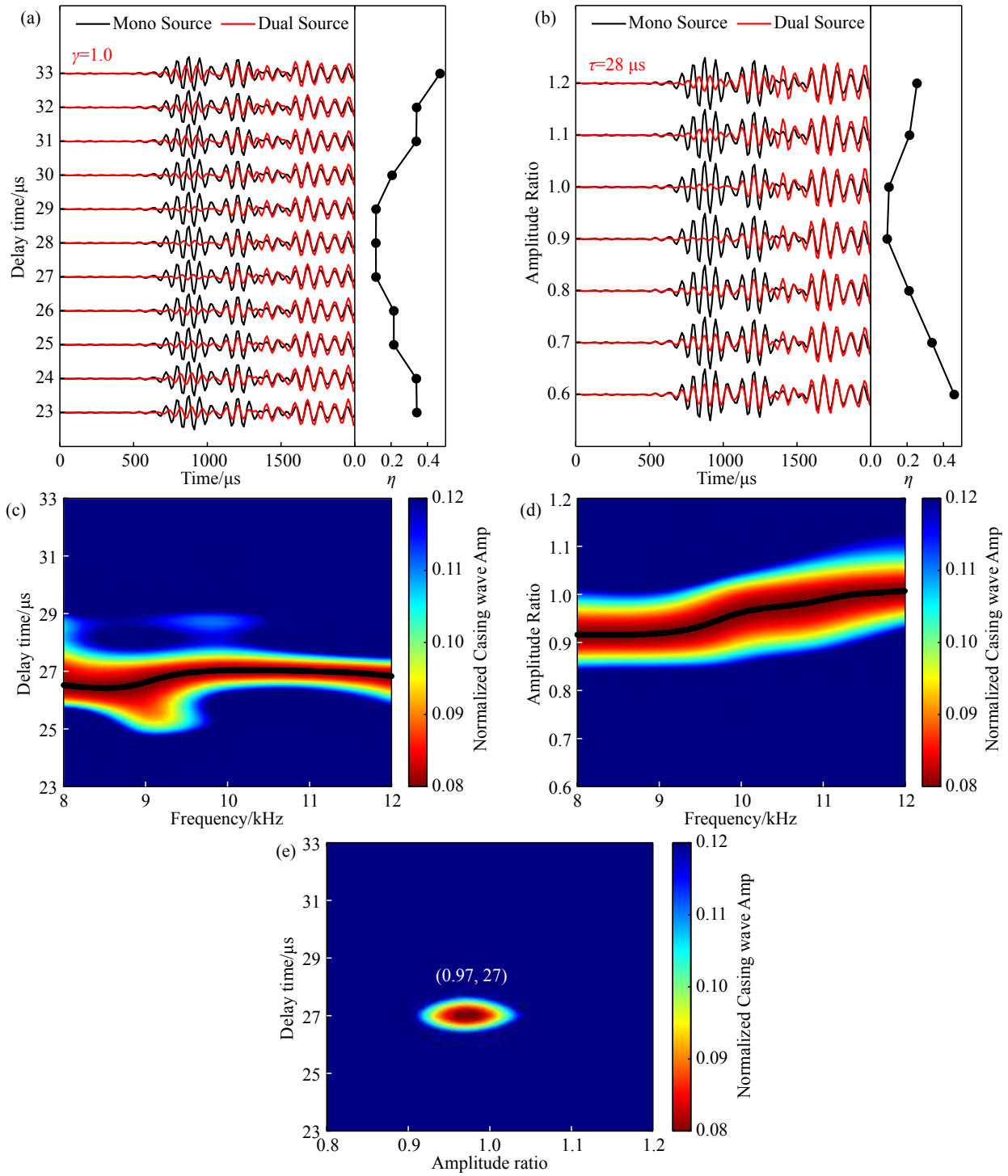


图 5 自由套管模型井中不同双源参数对套管波的压制效果

(a) 不同延迟时间的实验波形 (γ = 1.0) 及归一化套管波振幅曲线; (b) 不同激励幅度比的实验波形 (τ = 28 μs) 及归一化套管波振幅曲线; (c) 不同延迟时间和声源激发频率的归一化套管波振幅 (γ = 1.0); (d) 不同激励幅度比和声源激发频率的归一化套管波振幅 (τ = 28 μs); (e) 不同延迟时间和激励幅度的归一化套管波振幅 (f = 10 kHz).

Fig. 5 Effect of different dual source parameters on casing wave suppression in the free casing model well

(a) Casing waveforms with different delay times (γ = 1.0) and normalized casing wave amplitude curve; (b) Casing waveforms with different excitation amplitude ratios (τ = 28 μs) and normalized casing wave amplitude curve; (c) Normalized casing wave amplitude with different delay times and source excitation frequencies (γ = 1.0); (d) Normalized casing wave amplitude with different excitation amplitude ratios and source excitation frequencies (τ = 28 μs); (e) Normalized casing wave amplitude with different delay times and excitation amplitude ratios (f = 10 kHz).

全井段地层纵波时差曲线, 在第七道中用红线表示. 作为对比, 也给出了单源激励时的时差提取结果 (黑线). 采用最优双源参数激励时, 在自由套管段 (X120 ~ X220 m) 获得了高质量的地层纵波时差, 在套管胶结质量中等或者良好井段 (X220 ~ X420 m), 红线和黑线高度重叠. 第八道给出了 STC 图中纵波的相关系数 (黑线为传统双源激励参数, 红线为最优双源激励参数), 最优双源激励参数的纵波相关系数大幅提高, 充分说明了本文研究的双源激励参数优化方法的有效性和结果的准确性.

340

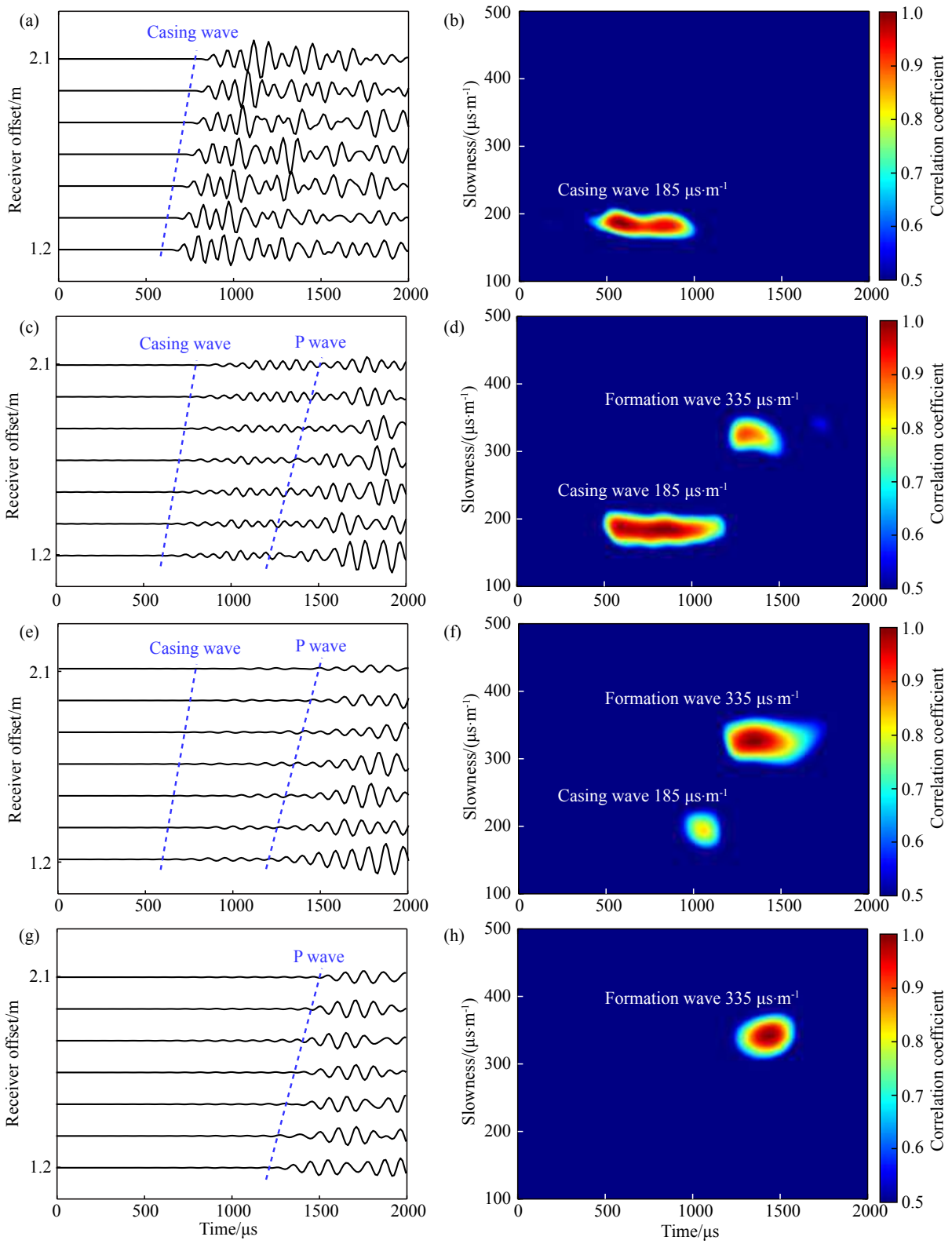


图 6　模型井实验波形和处理结果

(a) 单源激励的测量波形；(b) 图 (a) 中波形的时间-慢度相关图；(c) 传统双源参数激励的测量波形；(d) 图 (c) 中波形的时间-慢度相关图；(e) 最优双源参数激励的测量波形；(f) 图 (e) 中波形的时间-慢度相关图；(g) 裸眼井测量波形；(h) 图 (g) 中波形的时间-慢度相关图.

Fig. 6　Model well experimental waveforms and processing results.

(a) Measurement waveform of mono source excitation; (b) STC analysis result for the Fig.(a); (c) Measurement waveform of traditional dual source parameters excitation; (d) STC analysis result for the Fig.(c); (e) Measurement waveform of optimal dual source parameters excitation; (f) STC analysis result for the Fig.(e); (g) Mono source waveform from an openhole; (h) STC analysis result for the Fig.(g).

4　结论

针对过套管双源反激声波测井技术中双源激励参数 (即双源间的延迟时间和激励幅度比) 的优化问题，本文从理论计算、物理实验和现场应用三个方面论证了双源激励参数优化的必要性及其应用于过套管双源反激声波测井技术的有效性，得到以下成果和结论：

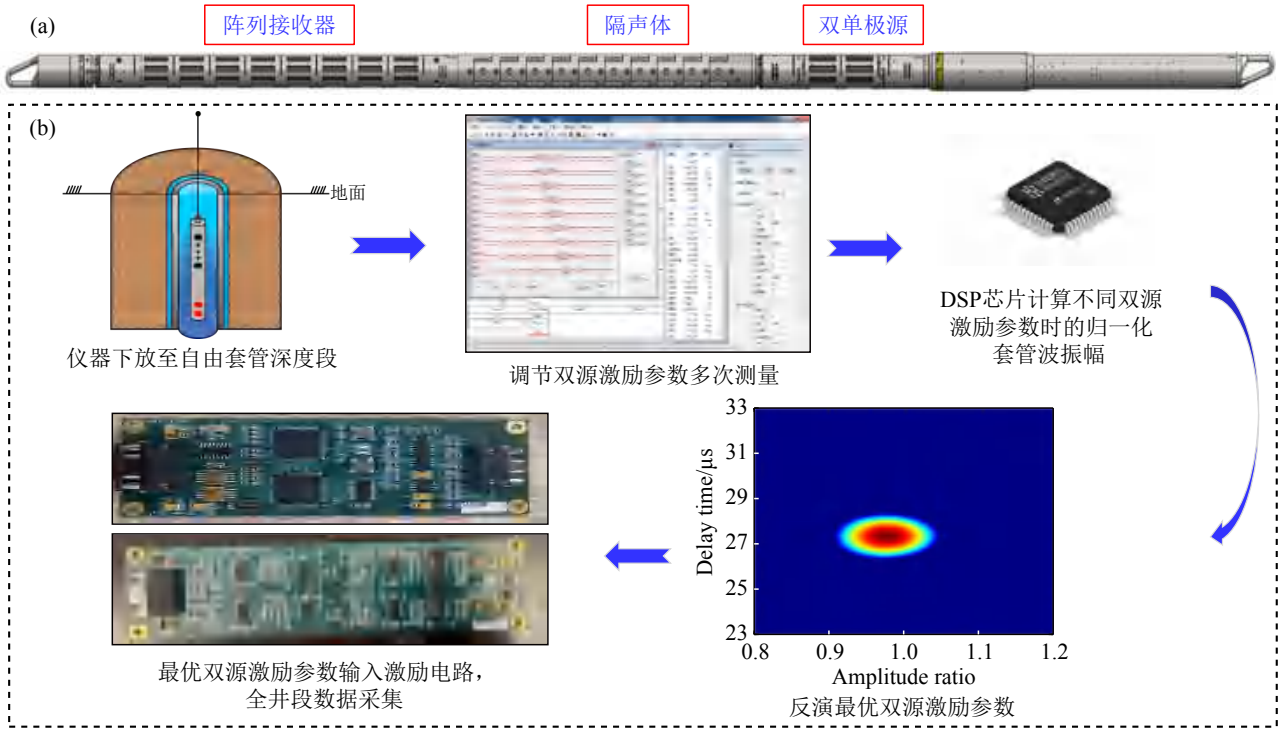


图 7 (a) 过套管双源反激声波测井仪器样机; (b) 双源激励参数井下自动优化流程图

Fig. 7 (a) The through casing acoustic logging tool using the dual source transmitters; (b) Flow chart of downhole automatic optimization of dual source excitation parameters

(1) 采用分波理论计算了不同双源激励参数 (延迟时间和激励幅度比) 下的套管波波形, 通过对比双源激励时的归一化套管波幅度, 确定了最优的双源激励参数, 实现了套管波的最大程度压制.

(2) 设计了双源激励的声系结构并在模型井中开展了物理实验, 通过改变延迟时间和激励幅度比的多次测量对比, 归一化套管波幅度确定的最优激励参数与理论计算结果一致; 相较于传统双源参数激励, 最优参数激励的套管波压制效果更佳, 由此提取的地层纵波时差与裸眼井测量一致, 进一步提升了过套管双源反激声波测井技术的有效性.

(3) 按优化流程设计的新型过套管双源反激声波测井仪器样机成功获得高信噪比的地层波数据, 其信噪比相较于传统双源仪器数据大为提高, 阵列数据中地层纵波的时差相关性明显增强, 验证了激励参数优化的必要性和有效性. 现场测井和数据处理结果对比表明, 新仪器在固井质量较差井段获得了现有仪器难以测量的地层时差, 而在固井质量较好井段, 所得时差与常规测量一致, 为过套管双源反激声波测井技术提供了佐证.

附录 A 公式 (1) 中的振幅系数求解

自由套管模型下的套管、地层及内外层流体的位移势函数表达式为 (唐晓明和郑传汉, 2004):

$$\begin{cases}\Phi^{\mathrm{in}}(k,\omega,r,z)=A_n'I_n(fr)\mathrm{e}^{\mathrm{i}kz}\\ \Phi^{\mathrm{ca}}(k,\omega,r,z)=[A_n^{\mathrm{ca}}I_n(p_{\mathrm{ca}}r)+B_n^{\mathrm{ca}}K_n(p_{\mathrm{ca}}r)]\mathrm{e}^{\mathrm{i}kz}\\ \chi^{\mathrm{ca}}(k,\omega,r,z)=[C_n^{\mathrm{ca}}I_n(s_{\mathrm{ca}}r)+D_n^{\mathrm{ca}}K_n(s_{\mathrm{ca}}r)]\mathrm{e}^{\mathrm{i}kz}\\ \Gamma^{\mathrm{ca}}(k,\omega,r,z)=[E_n^{\mathrm{ca}}I_n(s_{\mathrm{ca}}r)+F_n^{\mathrm{ca}}K_n(s_{\mathrm{ca}}r)]\mathrm{e}^{\mathrm{i}kz}\\ \Phi^{*}(k,\omega,r,z)=[A_n^{*}I_n(fr)+B_n^{*}K_n(fr)]\mathrm{e}^{\mathrm{i}kz}\\ \Phi^{\mathrm{for}}(k,\omega,r,z)=B_n^{\mathrm{for}}K_n(p_{\mathrm{for}}r)\mathrm{e}^{\mathrm{i}kz}\\ \chi^{\mathrm{for}}(k,\omega,r,z)=D_n^{\mathrm{for}}K_n(s_{\mathrm{for}}r)\mathrm{e}^{\mathrm{i}kz}\\ \Gamma^{\mathrm{for}}(k,\omega,r,z)=F_n^{\mathrm{for}}K_n(s_{\mathrm{for}}r)\mathrm{e}^{\mathrm{i}kz}\end{cases}, \quad (A1)$$

式中, n 为环向方位序数, n=0 时为单极源; r 为径向距离; ′、ca、*和 for 分别表示井内流体、套管、流体环和地层; $A_n^{\mathrm{ca}}(B_n^{\mathrm{ca}})$、$C_n^{\mathrm{ca}}(D_n^{\mathrm{ca}})$、$E_n^{\mathrm{ca}}(F_n^{\mathrm{ca}})$为套管的入射波 (出射波) 振幅系数; B_n^{for}、D_n^{for}、F_n^{for}为地层的出射波振幅系数; A_n^{*}、B_n^{*}为流体环中纵波的振幅系数; $f=\sqrt{k^2-(\omega/\alpha_{\mathrm{f}})^2}$为流体的纵波径向波数, α_{f}为流体的纵波速度; $p_{\mathrm{ca}}=\sqrt{k^2-(\omega/\alpha_{\mathrm{ca}})^2}$、$s_{\mathrm{ca}}=\sqrt{k^2-(\omega/\beta_{\mathrm{ca}})^2}$分别为套管的纵波径向波数和横波径向波数, α_{ca}和β_{ca}分别为套管的纵波速度和横波速度; $p_{\mathrm{for}}=\sqrt{k^2-(\omega/\alpha_{\mathrm{for}})^2}$、$s_{\mathrm{for}}=\sqrt{k^2-(\omega/\beta_{\mathrm{for}})^2}$分别为地层的纵波径向波数和横波径向波数, α_{for}和β_{for}分别为地层的纵波速度和横波速度. I_n和K_n分别表示第一类和第二类 n 阶变型贝塞尔函数, 分别描述从外向内传

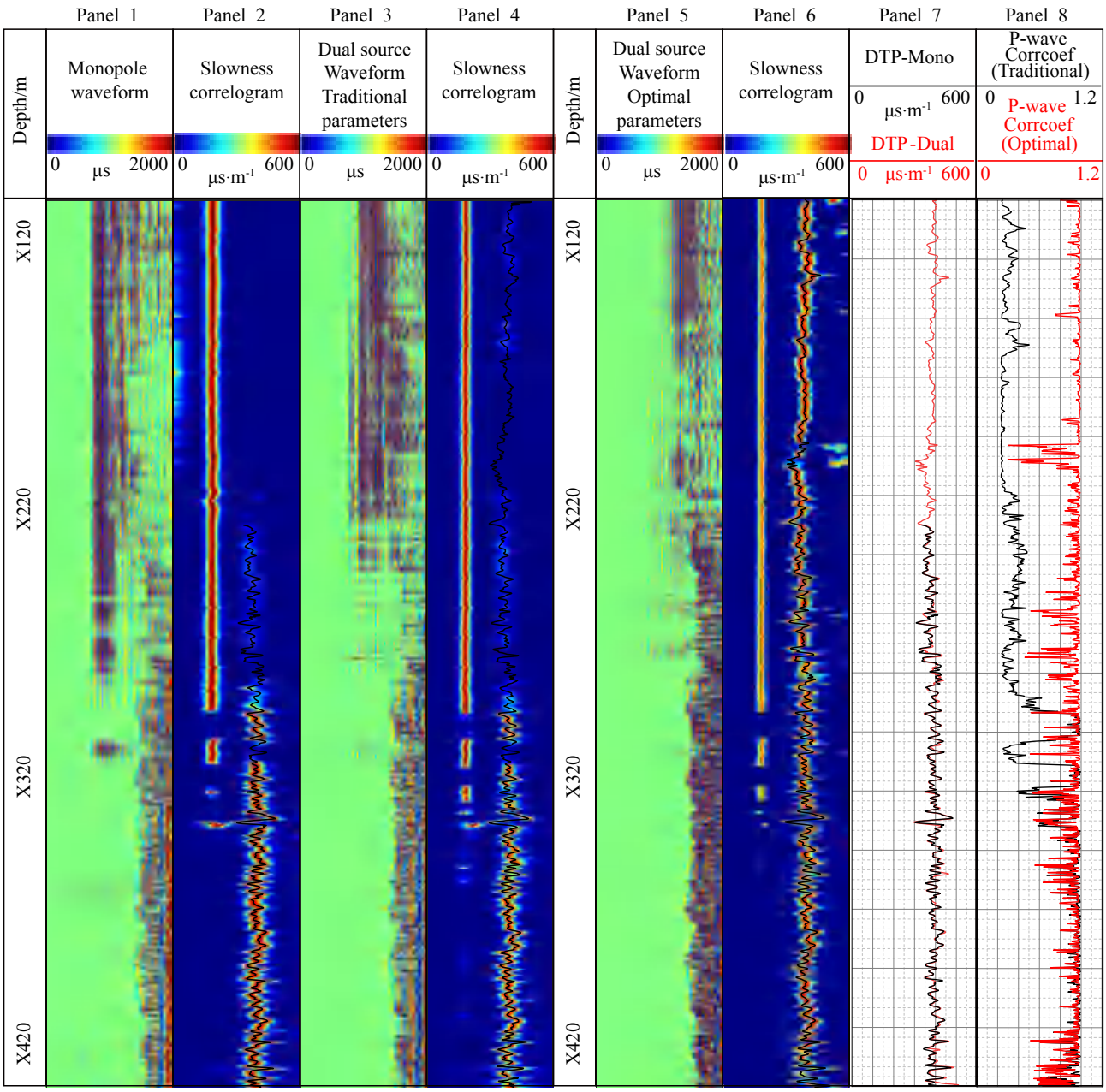


图 8　过套管双源反激声波测井仪器现场应用实例

Fig. 8　Field data of through casing acoustic logging tool using the dual source transmitters

播的声波和从内向外传播的声波.

固液界面的边界条件为径向位移和径向正应力连续，切向应力为零，自由套管模型下的各层边界条件可写为：

$$\begin{cases} \boldsymbol{u}_{\mathrm{f}}'|_{r=r_1}=\boldsymbol{u}^{\mathrm{ca}}|_{r=r_1} \\ \boldsymbol{\sigma}_{\mathrm{rrf}}'|_{r=r_1}=\boldsymbol{\sigma}_{rr}^{\mathrm{ca}}|_{r=r_1} \\ 0=\boldsymbol{\sigma}_{r\theta}^{\mathrm{ca}}|_{r=r_1} \\ 0=\boldsymbol{\sigma}_{rz}^{\mathrm{ca}}|_{r=r_1} \end{cases},\quad \begin{cases} \boldsymbol{u}^{\mathrm{ca}}|_{r=r_2}=\boldsymbol{u}_{\mathrm{f}}^{*}|_{r=r_2} \\ \boldsymbol{\sigma}_{rr}^{\mathrm{ca}}|_{r=r_2}=\boldsymbol{\sigma}_{\mathrm{rrf}}^{*}|_{r=r_2} \\ \boldsymbol{\sigma}_{r\theta}^{\mathrm{ca}}|_{r=r_2}=0 \\ \boldsymbol{\sigma}_{rz}^{\mathrm{ca}}|_{r=r_2}=0 \end{cases},\quad \begin{cases} \boldsymbol{u}_{\mathrm{f}}^{*}|_{r=a}=\boldsymbol{u}^{\mathrm{for}}|_{r=a} \\ \boldsymbol{\sigma}_{\mathrm{rrf}}^{*}|_{r=a}=\boldsymbol{\sigma}_{rr}^{\mathrm{for}}|_{r=a} \\ 0=\boldsymbol{\sigma}_{r\theta}^{\mathrm{for}}|_{r=a} \\ 0=\boldsymbol{\sigma}_{rz}^{\mathrm{for}}|_{r=a} \end{cases}, \tag{A2}$$

式中，r_1和r_2分别为套管的内径和外径，a 为井径. 将散射波和透射波的位移和应力，代入式 (A2) 中即可得到矩阵方程：

$$\{\boldsymbol{H}_{ij}\}_{12\times12}\cdot\left\{A_n',A_n^{\mathrm{ca}},B_n^{\mathrm{ca}},C_n^{\mathrm{ca}},D_n^{\mathrm{ca}},E_n^{\mathrm{ca}},F_n^{\mathrm{ca}},A_n^{*},B_n^{*},B_n^{\mathrm{for}},D_n^{\mathrm{for}},F_n^{\mathrm{for}}\right\}^{\mathrm{T}}=\left\{\boldsymbol{u}_{\mathrm{f}}^{d},\boldsymbol{\sigma}_{\mathrm{rrf}}^{d},0,0,0,0,0,0,0,0,0,0\right\}^{\mathrm{T}}, \tag{A3}$$

式 (A3) 中各定解元素具体表达式为 (未列出的元素取值为 0)：

$$H_{11}=-nI_n(fr_1)/r_1-fI_{n+1}(fr_1),$$

$$H_{12}=nI_n(p_{\mathrm{ca}}r_1)/r_1+p_{\mathrm{ca}}I_{n+1}(p_{\mathrm{ca}}r_1),$$

$$H_{13}=nK_n(p_{ca}r_1)/r_1-p_{ca}K_{n+1}(p_{ca}r_1),$$

$$H_{14}=nI_n(s_{ca}r_1)/r_1,$$

$$H_{15}=nK_n(s_{ca}r_1)/r_1,$$

$$H_{16}=\mathrm{i}k[nI_n(s_{ca}r_1)/r_1+s_{ca}I_{n+1}(s_{ca}r_1)],$$

$$H_{17}=\mathrm{i}k[nK_n(s_{ca}r_1)/r_1-s_{ca}K_{n+1}(s_{ca}r_1)],$$

$$H_{21}=\rho_f\omega^2 I_n(fr_1),$$

$$\begin{aligned}H_{22}=&2\rho_{ca}\beta_{ca}^2\left[\left(n^2-n\right)I_n(p_{ca}r_1)/r_1^2-p_{ca}I_{n+1}(p_{ca}r_1)/r_1\right]\\&+\rho_{ca}\left(2k^2\beta_{ca}^2-\omega^2\right)I_n(p_{ca}r_1)\end{aligned}$$

$$\begin{aligned}H_{23}=&2\rho_{ca}\beta_{ca}^2\left[\left(n^2-n\right)K_n(p_{ca}r_1)/r_1^2+p_{ca}K_{n+1}(p_{ca}r_1)/r_1\right]\\&+\rho_{ca}\left(2k^2\beta_{ca}^2-\omega^2\right)K_n(p_{ca}r_1)\end{aligned}$$

$$H_{24}=2n\rho_{ca}\beta_{ca}^2\left[(n-1)I_n(s_{ca}r_1)/r_1^2+s_{ca}I_{n+1}(s_{ca}r_1)/r_1\right],$$

$$H_{25}=2n\rho_{ca}\beta_{ca}^2\left[(n-1)K_n(s_{ca}r_1)/r_1^2-s_{ca}K_{n+1}(s_{ca}r_1)/r_1\right],$$

$$\begin{aligned}H_{26}=&2\mathrm{i}k\rho_{ca}\beta_{ca}^2\left\{\left[\left(n^2-n\right)/r_1^2+s_{ca}^2\right]I_n(s_{ca}r_1)\right.\\&\left.-s_{ca}I_{n+1}(s_{ca}r_1)/r_1\right\},\end{aligned}$$

$$\begin{aligned}H_{27}=&2\mathrm{i}k\rho_{ca}\beta_{ca}^2\left\{\left[\left(n^2-n\right)/r_1^2+s_{ca}^2\right]K_n(s_{ca}r_1)\right.\\&\left.+s_{ca}K_{n+1}(s_{ca}r_1)/r_1\right\},\end{aligned}$$

$$H_{32}=2n\rho_{ca}\beta_{ca}^2\left[(1-n)I_n(p_{ca}r_1)/r_1^2-p_{ca}I_{n+1}(p_{ca}r_1)/r_1\right],$$

$$H_{33}=2n\rho_{ca}\beta_{ca}^2\left[(1-n)K_n(p_{ca}r_1)/r_1^2+p_{ca}K_{n+1}(p_{ca}r_1)/r_1\right],$$

$$\begin{aligned}H_{34}=&-\rho_{ca}\beta_{ca}^2\left\{\left[2\left(n^2-n\right)/r_1^2+s_{ca}^2\right]I_n(s_{ca}r_1)\right.\\&\left.-2s_{ca}I_{n+1}(s_{ca}r_1)/r_1\right\},\end{aligned}$$

$$\begin{aligned}H_{35}=&-\rho_{ca}\beta_{ca}^2\left\{\left[2\left(n^2-n\right)/r_1^2+s_{ca}^2\right]K_n(s_{ca}r_1)\right.\\&\left.+2s_{ca}K_{n+1}(s_{ca}r_1)/r_1\right\},\end{aligned}$$

$$H_{36}=2\mathrm{i}kn\rho_{ca}\beta_{ca}^2\left[(1-n)I_n(s_{ca}r_1)/r_1^2-s_{ca}I_{n+1}(s_{ca}r_1)/r_1\right],$$

$$H_{37}=2\mathrm{i}kn\rho_{ca}\beta_{ca}^2\left[(1-n)K_n(s_{ca}r_1)/r_1^2+s_{ca}K_{n+1}(s_{ca}r_1)/r_1\right],$$

$$H_{42}=2\mathrm{i}k\rho_{ca}\beta_{ca}^2[nI_n(p_{ca}r_1)/r_1+p_{ca}I_{n+1}(p_{ca}r_1)],$$

$$H_{43}=2\mathrm{i}k\rho_{ca}\beta_{ca}^2[nK_n(p_{ca}r_1)/r_1-p_{ca}K_{n+1}(p_{ca}r_1)],$$

$$H_{44}=\mathrm{i}kn\rho_{ca}\beta_{ca}^2I_n(s_{ca}r_1)/r_1,$$

$$H_{45}=\mathrm{i}kn\rho_{ca}\beta_{ca}^2K_n(s_{ca}r_1)/r_1,$$

$$H_{46}=-\left(s_{ca}^2+k^2\right)\rho_{ca}\beta_{ca}^2[nI_n(s_{ca}r_1)/r_1+s_{ca}I_{n+1}(s_{ca}r_1)],$$

$$H_{47}=-\left(s_{ca}^2+k^2\right)\rho_{ca}\beta_{ca}^2[nK_n(s_{ca}r_1)/r_1-s_{ca}K_{n+1}(s_{ca}r_1)],$$

$$H_{52}=nI_n(p_{ca}r_2)/r_2+p_{ca}I_{n+1}(p_{ca}r_2),$$

$$H_{53}=nK_n(p_{ca}r_2)/r_2-p_{ca}K_{n+1}(p_{ca}r_2),$$

$$H_{54}=nI_n(s_{ca}r_2)/r_2,$$

$$H_{55}=nK_n(s_{ca}r_2)/r_2,$$

$$H_{56}=\mathrm{i}k[nI_n(s_{ca}r_2)/r_2+s_{ca}I_{n+1}(s_{ca}r_2)],$$

$$H_{57}=\mathrm{i}k[nK_n(s_{ca}r_2)/r_2-s_{ca}K_{n+1}(s_{ca}r_2)],$$

$$H_{58}=-nI_n(fr_2)/r_2-fI_{n+1}(fr_2),$$

$$H_{59}=-nK_n(fr_2)/r_2+fK_{n+1}(fr_2),$$

$$\begin{aligned}H_{62}=&2\rho_{ca}\beta_{ca}^2\left[\left(n^2-n\right)I_n(p_{ca}r_2)/r_2^2-p_{ca}I_{n+1}(p_{ca}r_2)/r_2\right]\\&+\rho_{ca}\left(2k^2\beta_{ca}^2-\omega^2\right)I_n(p_{ca}r_2),\end{aligned}$$

$$\begin{aligned}H_{63}=&2\rho_{ca}\beta_{ca}^2\left[\left(n^2-n\right)K_n(p_{ca}r_2)/r_2^2+p_{ca}K_{n+1}(p_{ca}r_2)/r_2\right]\\&+\rho_{ca}\left(2k^2\beta_{ca}^2-\omega^2\right)K_n(p_{ca}r_2),\end{aligned}$$

$$H_{64}=2n\rho_{ca}\beta_{ca}^2\left[(n-1)I_n(s_{ca}r_2)/r_2^2+s_{ca}I_{n+1}(s_{ca}r_2)/r_2\right],$$

$$H_{65}=2n\rho_{ca}\beta_{ca}^2\left[(n-1)K_n(s_{ca}r_2)/r_2^2-s_{ca}K_{n+1}(s_{ca}r_2)/r_2\right],$$

$$H_{66}=2\mathrm{i}k\rho_{ca}\beta_{ca}^2\left\{\left[\left(n^2-n\right)/r_2^2+s_{ca}^2\right]I_n(s_{ca}r_2)-s_{ca}I_{n+1}(s_{ca}r_2)/r_2\right\},$$

$$H_{67}=2\mathrm{i}k\rho_{ca}\beta_{ca}^2\left\{\left[\left(n^2-n\right)/r_2^2+s_{ca}^2\right]K_n(s_{ca}r_2)+s_{ca}K_{n+1}(s_{ca}r_2)/r_2\right\},$$

$$H_{68}=\rho_f\omega^2 I_n(fr_2),$$

$$H_{69}=\rho_f\omega^2 K_n(fr_2),$$

$$H_{72}=2n\rho_{ca}\beta_{ca}^2\left[(1-n)I_n(p_{ca}r_2)/r_2^2-p_{ca}I_{n+1}(p_{ca}r_2)/r_2\right],$$

$$H_{73}=2n\rho_{ca}\beta_{ca}^2\left[(1-n)K_n(p_{ca}r_2)/r_2^2+p_{ca}K_{n+1}(p_{ca}r_2)/r_2\right],$$

$$H_{74}=-\rho_{ca}\beta_{ca}^2\left\{\left[2\left(n^2-n\right)/r_2^2+s_{ca}^2\right]I_n(s_{ca}r_2)-2s_{ca}I_{n+1}(s_{ca}r_2)/r_2\right\},$$

$$H_{75}=-\rho_{ca}\beta_{ca}^2\left\{\left[2\left(n^2-n\right)/r_2^2+s_{ca}^2\right]K_n(s_{ca}r_2)+2s_{ca}K_{n+1}(s_{ca}r_2)/r_2\right\},$$

$$H_{76}=2\mathrm{i}kn\rho_{ca}\beta_{ca}^2\left[(1-n)I_n(s_{ca}r_2)/r_2^2-s_{ca}I_{n+1}(s_{ca}r_2)/r_2\right],$$

$$H_{77}=2\mathrm{i}kn\rho_{ca}\beta_{ca}^2\left[(1-n)K_n(s_{ca}r_2)/r_2^2+s_{ca}K_{n+1}(s_{ca}r_2)/r_2\right],$$

$$H_{82}=2\mathrm{i}k\rho_{ca}\beta_{ca}^2[nI_n(p_{ca}r_2)/r_2+p_{ca}I_{n+1}(p_{ca}r_2)],$$

$$H_{83}=2\mathrm{i}k\rho_{ca}\beta_{ca}^2[nK_n(p_{ca}r_2)/r_2-p_{ca}K_{n+1}(p_{ca}r_2)],$$

$$H_{84}=\mathrm{i}kn\rho_{ca}\beta_{ca}^2I_n(s_{ca}r_2)/r_2,$$

$$H_{85}=\mathrm{i}kn\rho_{\mathrm{ca}}\beta_{\mathrm{ca}}^2K_n(s_{\mathrm{ca}}r_2)/r_2,$$

$$H_{86}=-\left(s_{\mathrm{ca}}^2+k^2\right)\rho_{\mathrm{ca}}\beta_{\mathrm{ca}}^2[nI_n(s_{\mathrm{ca}}r_2)/r_2+s_{\mathrm{ca}}I_{n+1}(s_{\mathrm{ca}}r_2)],$$

$$H_{87}=-\left(s_{\mathrm{ca}}^2+k^2\right)\rho_{\mathrm{ca}}\beta_{\mathrm{ca}}^2[nK_n(s_{\mathrm{ca}}r_2)/r_2-s_{\mathrm{ca}}K_{n+1}(s_{\mathrm{ca}}r_2)],$$

$$H_{98}=-nI_n(fa)/a-fI_{n+1}(fa),$$

$$H_{99}=-nK_n(fa)/a+fK_{n+1}(fa),$$

$$H_{9,10}=nK_n(p_{\mathrm{for}}a)/a-p_{\mathrm{for}}K_{n+1}(p_{\mathrm{for}}a),$$

$$H_{9,11}=nK_n(s_{\mathrm{for}}a)/a,$$

$$H_{9,12}=\mathrm{i}k[nK_n(s_{\mathrm{for}}a)/a-s_{\mathrm{for}}K_{n+1}(s_{\mathrm{for}}a)],$$

$$H_{10,8}=\rho_{\mathrm{f}}\omega^2I_n(fa),$$

$$H_{10,9}=\rho_{\mathrm{f}}\omega^2K_n(fa),$$

$$H_{10,10}=2\rho_{\mathrm{for}}\beta_{\mathrm{for}}^2\left[\left(n^2-n\right)K_n(p_{\mathrm{for}}a)/a^2+p_{\mathrm{for}}K_{n+1}(p_{\mathrm{for}}a)/a\right]+\rho_{\mathrm{for}}\left(2k^2\beta_{\mathrm{for}}^2-\omega^2\right)K_n(p_{\mathrm{for}}a)$$

$$H_{10,11}=2n\rho_{\mathrm{for}}\beta_{\mathrm{for}}^2\left[(n-1)K_n(s_{\mathrm{for}}a)/a^2-s_{\mathrm{for}}K_{n+1}(s_{\mathrm{for}}a)/a\right],$$

$$H_{10,12}=2\mathrm{i}k\rho_{\mathrm{for}}\beta_{\mathrm{for}}^2\left\{\left[\left(n^2-n\right)/a^2+s_{\mathrm{for}}^2\right]K_n(s_{\mathrm{for}}a)+s_{\mathrm{for}}K_{n+1}(s_{\mathrm{for}}a)/a\right\},$$

$$H_{11,10}=2n\rho_{\mathrm{for}}\beta_{\mathrm{for}}^2\left[(1-n)K_n(p_{\mathrm{for}}a)/a^2+p_{\mathrm{for}}K_{n+1}(p_{\mathrm{for}}a)/a\right],$$

$$H_{11,11}=-\rho_{\mathrm{for}}\beta_{\mathrm{for}}^2\left\{\left[2\left(n^2-n\right)/a^2+s_{\mathrm{for}}^2\right]K_n(s_{\mathrm{for}}a)+2s_{\mathrm{for}}K_{n+1}(s_{\mathrm{for}}a)/a\right\},$$

$$H_{11,12}=2\mathrm{i}kn\rho_{\mathrm{for}}\beta_{\mathrm{for}}^2\left[(1-n)K_n(s_{\mathrm{for}}a)/a^2+s_{\mathrm{for}}K_{n+1}(s_{\mathrm{for}}a)/a\right],$$

$$H_{12,10}=2\mathrm{i}k\rho_{\mathrm{for}}\beta_{\mathrm{for}}^2[nK_n(p_{\mathrm{for}}a)/a-p_{\mathrm{for}}K_{n+1}(p_{\mathrm{for}}a)],$$

$$H_{12,11}=\mathrm{i}kn\rho_{\mathrm{for}}\beta_{\mathrm{for}}^2K_n(s_{\mathrm{for}}a)/a,$$

$$H_{12,12}=-\left(s_{\mathrm{for}}^2+k^2\right)\rho_{\mathrm{for}}\beta_{\mathrm{for}}^2[nK_n(s_{\mathrm{for}}a)/a-s_{\mathrm{for}}K_{n+1}(s_{\mathrm{for}}a)]$$

$$u_{\mathrm{f}}^d=\varepsilon_n\left[\frac{n}{a}K_n(fr_1)-fK_{n+1}(fr_1)\right],$$

$$\sigma_{\mathrm{rrf}}^d=\varepsilon_n\rho_{\mathrm{f}}\omega^2K_n(fr_1),\qquad(\mathrm{A4})$$

式中, ρ_{ca}和ρ_{for}分别为套管密度和地层密度; ε_n为纽曼因子, n=0 时$\varepsilon_n=1$, n>0 时$\varepsilon_n=2$.

式 (2) 中的$D(k,\omega)$为矩阵$\boldsymbol{H}$的行列式, $D_1(k,\omega)$为式 (A4) 中的边界条件替换$\boldsymbol{D}$中的第一列所得.

References

Ding H R, Cui Z W, Lü W G, et al. 2016. Theoretical simulation of the seismoelectric logging while drilling technique using the dual source. *Chinese Journal of Geophysics* (in Chinese), 59(9): 3524-3532, doi: 10.6038/cjg20160934.

Hu H S, Ma J, Wang K X. 1999. The choice of Riemann sheets in the calculation of the borehole acoustic waves. *Acta Scientiarum Naturalium Universitatis Jilinensis* (in Chinese), (4): 66-70.

Ji Y J, Huang J, Wang H, et al. 2025. Full-wave decomposition and mode wave analysis of through-tubing monopole acoustic logging. *IEEE Transactions on Geoscience and Remote Sensing*, 63: 5900910, doi: 10.1109/TGRS.2024.3515195.

Jiang C. 2020. Acoustic-wave theory and method for casing bond evaluation using slip boundary modeling[Ph. D. thesis] (in Chinese). Qingdao: China University of Petroleum (East China).

Kimball C V, Marzetta T L. 1984. Semblance processing of borehole acoustic array data. *Geophysics*, 49(3): 274-281.

Kong F T, Jiang C, Su Y D, et al. 2020. A multiple filtering and correlation array signal processing technique for cased-hole acoustic logging and applications. *Interpretation*, 8(3): SL1-SL8, doi: 10.1190/int-2019-0116.1.

Liu H X, Gu X H, Li H R, et al. 2021. Research of the dual dipole source of opposite polarity to suppress direct wave in single-well shear-wave imaging logging. *Progress in Geophysics* (in Chinese), 36(4): 1560-1565, doi: 10.6038/pg2021EE0301.

Rao B, Tang X M, Su Y D. 2022. Theoretical calculation and mechanism analysis for component waves of acoustic logging while drilling in transversely isotropic formations. *Chinese Journal of Geophysics* (in Chinese), 65(8): 3198-3212, doi: 10.6038/cjg2022O0423.

Tang X M, Zheng C H. 2004. Quantitative Borehole Acoustic Methods. Netherlands: Elsevier Science Publishing Inc.

Tang X M, Patterson D. 2005. Analyzing and processing acoustic logging data for poorly-bonded cased boreholes. //SPWLA 46th Annual Logging Symposium. New Orleans, Louisiana: Society of Petrophysicists and Well-log Analysis.

Tang X M, Qi X, Zhang B, et al. 2015. An interference-based array signal processing technique for cased-hole acoustic logging and applications. *Chinese Journal of Geophysics* (in Chinese), 58(4): 1447-1457, doi: 10.6038/cjg20150430.

Tang X M, Su Y D, Zhang B. 2016. An advancement in through casing acoustic logging technology. *Well Logging Technology* (in Chinese), 40(4): 387-391, doi: 10.16489/j.issn.1004-1338.2016.04.001.

Tang X M, Su Y D, Zhang B. 2019. A through-casing acoustic logging tool using dual-source transmitters. *Petrophysics*, 60(5): 631-639.

Tubman K M, Cheng C H, Toksöz M N. 1984. Synthetic full waveform acoustic logs in cased boreholes. *Geophysics*, 49(7): 1051-1059.

Tubman K M, Cheng C H, Cole S P, et al. 1986. Synthetic full-waveform acoustic logs in cased boreholes, II—Poorly bonded casing. *Geophysics*, 51(4): 902-913.

Valero H P, Skelton O, Almeida C M. 2003. Processing of monopole sonic waveforms through cased hole. //SEG Technical Program Expanded Abstracts 2003. Dallas, Texas: SEG, 285-288.

Wang H, Fehler M. 2018. The wavefield of acoustic logging in a cased-hole with a single casing–Part I: a monopole tool. *Geophysical Journal International*, 212(1): 612-626.

Wang J, Li H Y, Guan W, et al. 2019. Experimental studies on the mechanism of monopole acoustic collar wave. *Chinese Journal of Geophysics* (in Chinese), 62(4): 1541-1553, doi: 10.6038/cjg2019M0042.

Wang J, Nie C Y, Hou X J, et al. 2021. Experimental studies on the mechanism of monopole acoustic collar wave 2. *Chinese Journal of Geophysics* (in Chinese), 64(5): 1797-1810, doi: 10.6038/cjg2021O0189.

Xu S, Su Y D, Tang X M. 2017. A super-mixing-virtual interferometric array signal processing technique and its applications to cased-hole acoustic logging. *Chinese Journal of Geophysics* (in Chinese), 60(7): 2904-2912, doi: 10.6038/cjg20170734.

Xu S. 2023. Acoustic-wave radiations of mono- and dual-sources in poorly bonded cased boreholes: Modeling and field applications. *IEEE Transactions on Geoscience and Remote Sensing*, 61: 5904610, doi: 10.1109/TGRS.2023.3249250.

Yuan H Z, Lu D W, Zhang X Y, et al. 2005. An overview of recent advances in well logging technology. *Progress in Geophysics* (in Chinese), 20(3): 786-795.

Zhang B. 2016. Acoustic logging in cased boreholes and in the while drilling environment [Ph. D. thesis] (in Chinese). Qingdao: China University of Petroleum (East China).

Zhang B, Su Y D, Tang X M, et al. 2015. A cased-hole acoustic logging technique using the dual source of opposite polarity. *Acta Acustica* (in Chinese), 40(6): 863-870.

Zhang B, Tang X M, Su Y D, et al. 2016. An acoustic logging while drilling technique using the dual source of opposite polarity. *Chinese Journal of Geophysics* (in Chinese), 59(3): 1151-1160, doi: 10.6038/cjg20160335.

Zheng X B. 2017. Theoretical simulations of monopole and dipole acoustic logging while drilling and investigations of propagation mechanism for individual waves [Ph. D. thesis] (in Chinese). Harbin: Harbin Institute of Technology.

Zhuang C X, Su Y D, Zhang K, et al. 2026. Design of dual-source through casing acoustic logging tool and application examples. *Progress in Geophysics* (in Chinese), 41(3): 1430-1438, doi: 10.6038/pg2026JJ0008.

附中文参考文献

丁浩然, 崔志文, 吕伟国等. 2016. 双声源激发随钻测井声电耦合波理论模拟. 地球物理学报, 59(9): 3524-3532, doi: 10.6038/cjg20160934.

胡恒山, 马俊, 王克协. 1999. 井孔声场计算中的黎曼叶选择. 吉林大学自然科学学报, (4): 66-70.

江灿. 2020. 滑移界面理论表征的固井声波测井评价方法研究 [博士论文]. 青岛: 中国石油大学 (华东).

刘汇鑫, 古希浩, 李焕然等. 2021. 双偶极源反相激励压制井中直达波的横波远探测方法研究. 地球物理学进展, 36(4): 1560-1565, doi: 10.6038/pg2021EE0301.

饶博, 唐晓明, 苏远大. 2022. 横向各向同性地层随钻多极子测井声场的分波分析与特性研究. 地球物理学报, 65(8): 3198-3212, doi: 10.6038/cjg2022O0423.

唐晓明, 郑传汉. 2004. 定量测井声学. 赵晓敏译. 北京: 石油工业出版社.

唐晓明, 祁晓, 张博等. 2015. 基于波干涉原理的套管井阵列声波处理方法及其应用. 地球物理学报, 58(4): 1447-1457, doi: 10.6038/cjg20150430.

唐晓明, 苏远大, 张博. 2016. 过套管声波测井技术新进展. 测井技术, 40(4): 387-391, doi: 10.16489/j.issn.1004-1338.2016.04.001.

王军, 李红一, 关威等. 2019. 单极源钻铤波传播机制的实验研究. 地球物理学报, 62(4): 1541-1553, doi: 10.6038/cjg2019M0042.

王军, 聂成洋, 侯许佳等. 2021. 单极源钻铤波传播机制的实验研究 2. 地球物理学报, 64(5): 1797-1810, doi: 10.6038/cjg2021O0189.

许松, 苏远大, 唐晓明. 2017. 基于超级混合虚折射干涉法的阵列声波处理方法及其在套管井中的应用. 地球物理学报, 60(7): 2904-2912, doi: 10.6038/cjg20170734.

原宏壮, 陆大卫, 张辛耘等. 2005. 测井技术新进展综述. 地球物理学进展, 20(3): 786-795.

张博, 苏远大, 唐晓明等. 2015. 一种过套管双源反激声波测井方法. 声学学报, 40(6): 863-870.

张博. 2016. 过套管和随钻条件下的声波测井研究 [博士论文]. 青岛: 中国石油大学 (华东).

张博, 唐晓明, 苏远大等. 2016. 一种利用双源反激的随钻声波测井方法. 地球物理学报, 59(3): 1151-1160, doi: 10.6038/cjg20160335.

郑晓波. 2017. 单极和偶极随钻声波测井理论模拟与分波传播特性研究 [博士论文]. 哈尔滨: 哈尔滨工业大学.

庄春喜, 苏远大, 张凯等. 2026. 双源反激过套管测井仪设计与应用实例. 地球物理学进展, 41(3): 1430-1438, doi: 10.6038/pg2026JJ0008.

（本文编辑　张正峰）

PETROPHYSICS, VOL. 60, NO. 5 (OCTOBER 2019); PAGES 631–639; 7 FIGURES. DOI: PJV60N5-2019a7

A Through-Casing Acoustic Logging Tool Using Dual-Source Transmitters[1]

Xiaoming Tang[2], Yuanda Su[2], and Bo Zhuang[3]

ABSTRACT

A new acoustic tool has been developed to measure formation acoustic properties through casing. This measurement is important for oil and gas production in mature fields, and for wells that are cased without logging due to borehole stability issues. Conventional acoustic logging through casing in poorly bonded boreholes has been a difficult task due to the presence of overwhelming casing waves that mask the formation acoustic signal. To overcome this difficulty, we developed an acoustic tool using dual-source transmitters and the processing technique for the data acquired by the tool. This paper elaborates the operating principle of the new dual-source technology and demonstrates its application to casedhole acoustic logging. By using the dual-source design, the overwhelming casing waves from the poorly bonded casing are largely suppressed. On the basis of the casing-wave suppression and the condition that the formation is acoustically slower than casing, the formation acoustic-wave amplitude is significantly enhanced in the dual-source data-acquisition process. Subsequent processing of the data reliably obtains the acoustic velocity of the formation. The new tool has been tested in many cased wells with proven performance for various cement-bond conditions. The success of this technology makes casedhole acoustic logging an effective operation that can be routinely used to obtain reliable formation information through casing for slow to moderately fast formations.

INTRODUCTION

Through-casing logging is an indispensable technology for exploration and production in brownfields, considering the huge number of cased wells around the world. The logging community has made breakthroughs in through-casing nuclear and resistivity measurements, but acoustic logging through casing remains a challenging issue for the industry. The issue is caused by the strong interference of casing waves in the casedhole logging data, especially when the casing and formation are poorly bonded (Tubman et al., 1986; Tang and Cheng, 2004; Tang and Patterson, 2005).

Signal-processing techniques have been developed to suppress the casing waves and extract formation acoustic properties from the casedhole data (e.g., Valero et al. 2003, Tang and Patterson, 2005; Tang et al., 2014a). However, a condition for the signal processing is that the data should maintain certain signal/noise ratio for extracting the desired information from the data. This condition may not be satisfied in the presence of overwhelming casing waves of a poorly bonded borehole because, in the data digitization during logging, the gain for the digitizer is primarily controlled by the large-amplitude casing waves, rendering the small formation signal poorly digitized and the signal information inextricable. From the above root-cause problem analysis, one can see that the solution to the problem resides in suppressing the casing-wave amplitude before the data digitization. The dual-transmitter acquisition technique is developed to achieve this goal.

OPERATION PRINCIPLE

Figure 1 illustrates the dual-transmitter casedhole acoustic logging model and its operating principle. The acoustic tool with dual transmitters is centered in the cased-borehole model. A fluid annulus between casing and cement (or between cement and formation) is used to symbolize the poor bonding condition. The tool consists of a receiver array of N receivers R_1, R_2, …,R_N and two transmitters, named the near transmitter, T_n, and far transmitter, T_f, respectively. The

Manuscript received by the Editor July 23, 2019; revised manuscript received September 5, 2019; manuscript accepted September 13, 2019.
[1]Originally presented at the SPWLA 60th Annual Logging Symposium, The Woodlands, Texas, USA, June 17–19, 2019, Paper TTTT.
[2]China University of Petroleum, School of Geosciences, No. 66, West Changjiang Road, Huangdao District, Qindao, China, 266580; tangxiam@aliyun.com; syuanda@sina.com
[3]Shuoren Times Technology, Suite 304, Rainbow Plaza, 11 Information Rd, Haidian District, Beijing China, 100085; zhangbo_upc@163.com
Corresponding author: X. Tang (tangxiam@aliyun.com)

Downloaded from onepetro.org/petrophysics/article-pdf/60/05/631/2203169/spwla-2019-v60n5a7.pdf by China University of Petroleum Beijing user on 08 October 2026

distance between them is *D*.

During logging, T_f is fired first with an excitation amplitude C_f. After a time-delay τ, T_n is fired with an excitation amplitude C_n. The polarity of the T_n firing signal is opposite to that of the T_f firing. By electronically adjusting the values of C_f, C_n, and τ through instrumentation, the two casing waves sequentially excited by the two transmitters cancel each other as they propagate toward the receiver array position. The operation principle of the dual-transmitter acquisition method can be mathematically described in the following.

At the receiver distance *z* from the near transmitter, the acoustic pressure signal from the far and near transmitters is respectively given by (Tang and Cheng, 2004).

$$p_f(z,t) = \frac{C_f}{2\pi}\int_{-\infty}^{\infty} S(\omega)d\omega \int_{-\infty}^{\infty} G(k,\omega)e^{i[k(z+D)-\omega t]}dk, \quad (1)$$

and

$$p_n(z,t) = -\frac{C_n}{2\pi}\int_{-\infty}^{\infty} S(\omega)d\omega \int_{-\infty}^{\infty} G(k,\omega)e^{i[kz-\omega(t+\tau)]}dk, \quad (2)$$

where $G(k,\omega)$ is the ω-k (frequency-wavenumber) response function, or Green's function, of the system including tool and the casedhole model; $S(\omega)$ is the frequency spectrum of source excitation signal (assume the two transmitters use the same source signal). By superposition of the two signals of Eqs. 1 and 2, the total pressure signal at the receiver position is given by

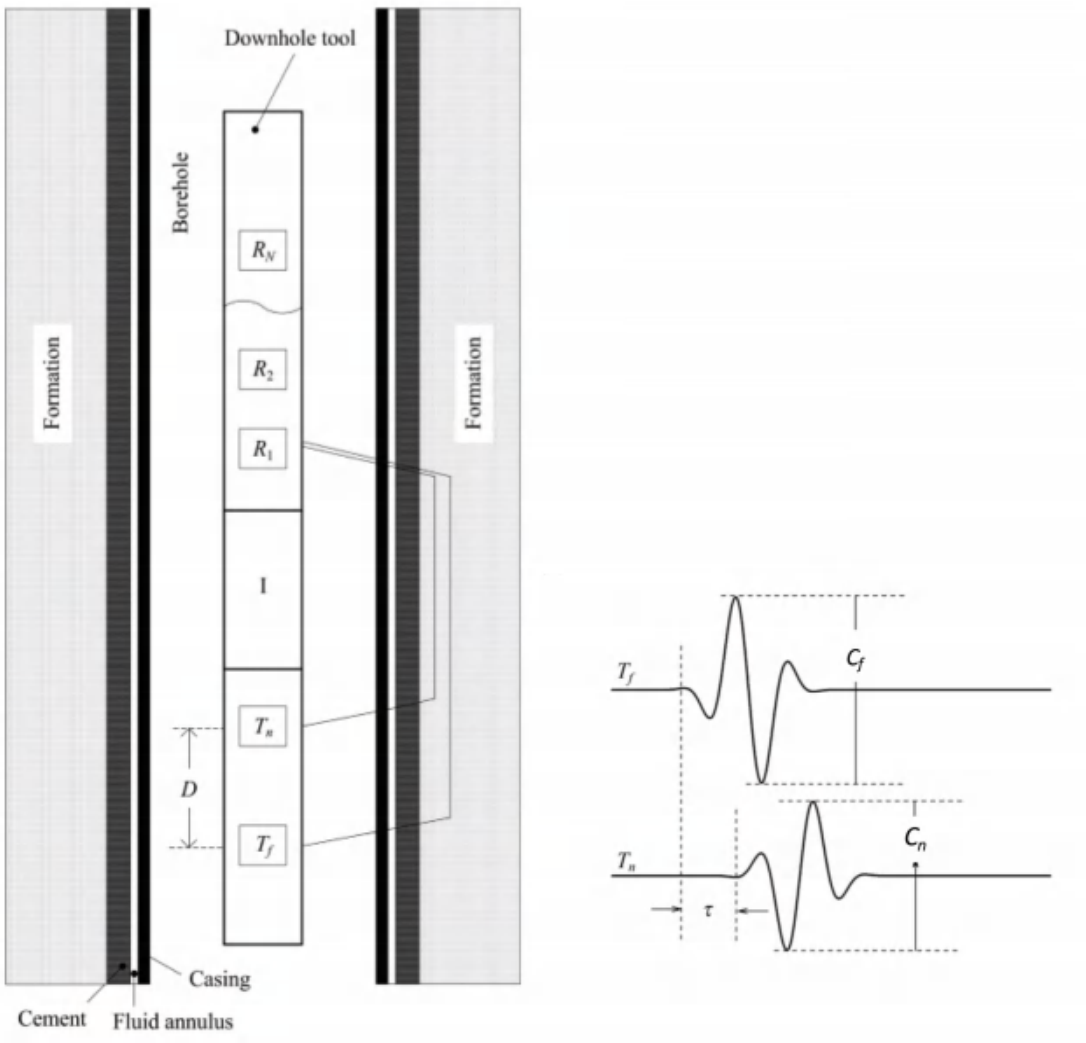


Fig. 1—(a) Schematic diagram for the dual-source through-casing acoustic tool consisting of the near (T_n) and far (T_f) transmitters. (b) Source excitation scheme for the transmitters.

Downloaded from onepetro.org/petrophysics/article-pdf/60/05/631/2203169/spwla-2019-v60n5a7.pdf by China University of Petroleum Beijing user on 08 October 2026

$$p(z,t)=\frac{C_f}{2\pi}\int_{-\infty}^{\infty}S(\omega)d\omega\int_{-\infty}^{\infty}\left(1-\frac{C_n}{C_f}e^{i(kD-\omega\tau)}\right)G(k,\omega)e^{i(kz-\omega t)}dk, \quad (3)$$

Adjust the delay time τ such that it equals the propagation time of the casing wave between the two transmitters

$$\tau=\frac{D}{v_t}, \quad (4)$$

where v_t is the casing-wave velocity. We also adjust the excitation amplitude ratio C_n/C_f to equal 1. By these adjustments, the terms in the bracket of Eq. 3 become a narrow stop-band (or notch) filter function in the ω-k domain,

$$f(\omega,k)=1-\exp\left[\frac{i\omega D}{v_t}\left(\frac{kv_t}{\omega}-1\right)\right]. \quad (5)$$

By this stop-band filtering, the casing-wave component with a wavenumber $k = \omega/v_t$, as contained in the response function $G(k,\omega)$ for a poorly bonded casing, will be suppressed. The formation acoustic signal, assuming its propagation velocity is slower than v_t, will be preserved and even enhanced for slow formations. Zhang et al. (2015) give a detailed discussion of the filter function and performed numerical modeling using Eqs. 3 through 5. The result shows that, for a poorly bonded cased borehole, the dual-transmitter acquisition method can eliminate the casing wave and obtain the desired formation acoustic-wave signal.

To demonstrate the effectiveness of the casing-wave suppression scheme, a numerical experiment using finite-difference waveform simulation was carried out. The model consists of a standard 7-in. casing placed in water. Wave propagation along the casing was simulated for the single-source and dual-source excitation conditions. Figure 2 shows the snapshot 650 μs after the source firing for the single- (a) and dual-source (b) conditions, respectively. For both conditions, an 8-kHz Ricker wavelet was used for actuating the source at the borehole axis. In the dual-source firing, the spacing between the near and far sources is 0.1524 m. The snapshot from the single source shows the strong, fast-traveling casing wave along the casing. In contrast, the snapshot for the dual source shows that the casing wave is drastically attenuated across the near-source position and gradually disappears away from the source. The numerical modeling shows that the dual-source casing-wave suppression scheme works very well for the ideal theoretical model condition.

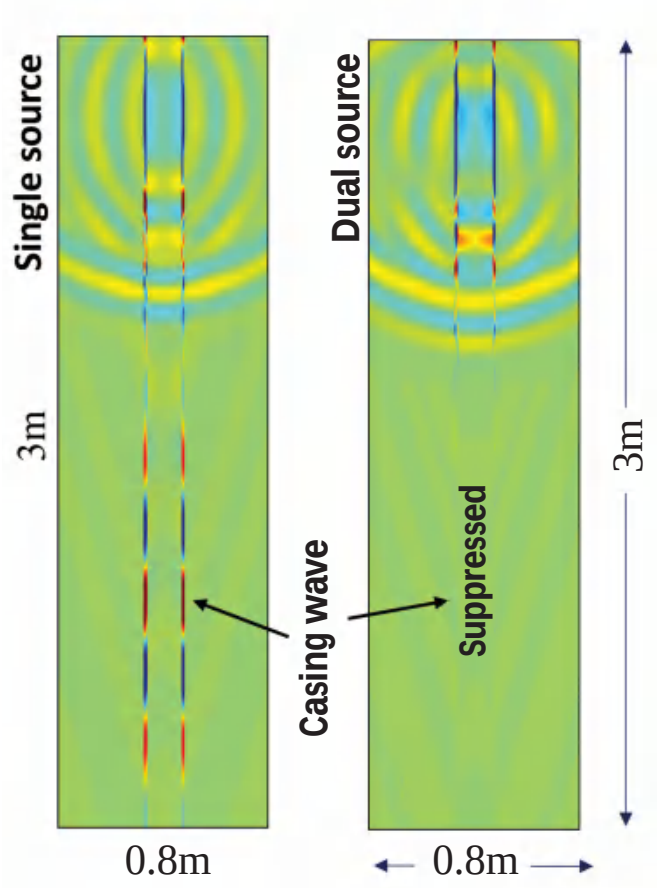


Fig. 2—Wavefield snapshots from numerical modeling of the single-source (left) and dual-source (right) excitation conditions. At 650 μs after source actuation, strong casing waves are generated for the single-source condition. The casing waves away from the source are suppressed in the dual-source condition.

EXPERIMENT AND ENGINEERING

Application of the above theoretical principle to downhole logging faces many challenges from tool engineering and varying logging conditions. For example, it is usually difficult to generate identical signals from the near and far transmitters in order to cancel the casing waves, because in engineering practice there is always some mismatch between the two transmitters. Even for perfectly matched transmitters, the varying downhole condition around the transmitter, such as tool eccentering and mud/casing property changes, etc., can modify the output signal. Besides, the casing-wave velocity v_t may not be a constant

Downloaded from onepetro.org/petrophysics/article-pdf/60/05/631/2203169/spwla-2019-v60n5a7.pdf by China University of Petroleum Beijing user on 08 October 2026

due to wave dispersion, casing damage or erosion, and bonding condition variation, etc. These factors will all affect the actual performance of the dual-transmitter logging tool. To test the applicability of the theory to the actual measurement condition, a laboratory experiment was carried out on a scaled borehole model.

Figure 3 illustrates the laboratory model and the measurement system. The model has a 1:10 scale ratio relative to the actual field logging condition, with a 2-cm diameter borehole in a formation made of standard G grade cement. The compressional and shear velocities and density of the cement are 3,728 m/s, 2,196 m/s, and 2,200 kg/m^3, respectively. A 2-mm thick steel tubing with 18-mm OD is placed in the water-filled borehole. Because of the 0.5-mm gap between the tubing and cement, the casing-cement coupling of the model is a free-pipe condtion. Piezoelectric cylindrical transducers with a working frequency of 120 kHz were chosen as the transmitters; the ID, OD, and height of the transducers are 6, 8, and 5 mm, respectively. The spacing between the far and the near transmitters is 0.016 m. The model was measured for the single- and dual-transmitter excitation conditions. The computer-controlled two-channel transmit circuits were used to excite the transmitters. A virtual oscilloscope HS4 was used to monitor and to record the experimental waveforms. The transmit circuits generate a square-wave pulse as the synchronous signal. In the experiment, the transmitters were fixed, and a hydrophone receiver was moved along the borehole to record the waveform data. The data were successively recorded at an increment of 0.01 m, from which an array of waveform data was obtained to simulate the acoustic waveform logging of an array acoustic tool.

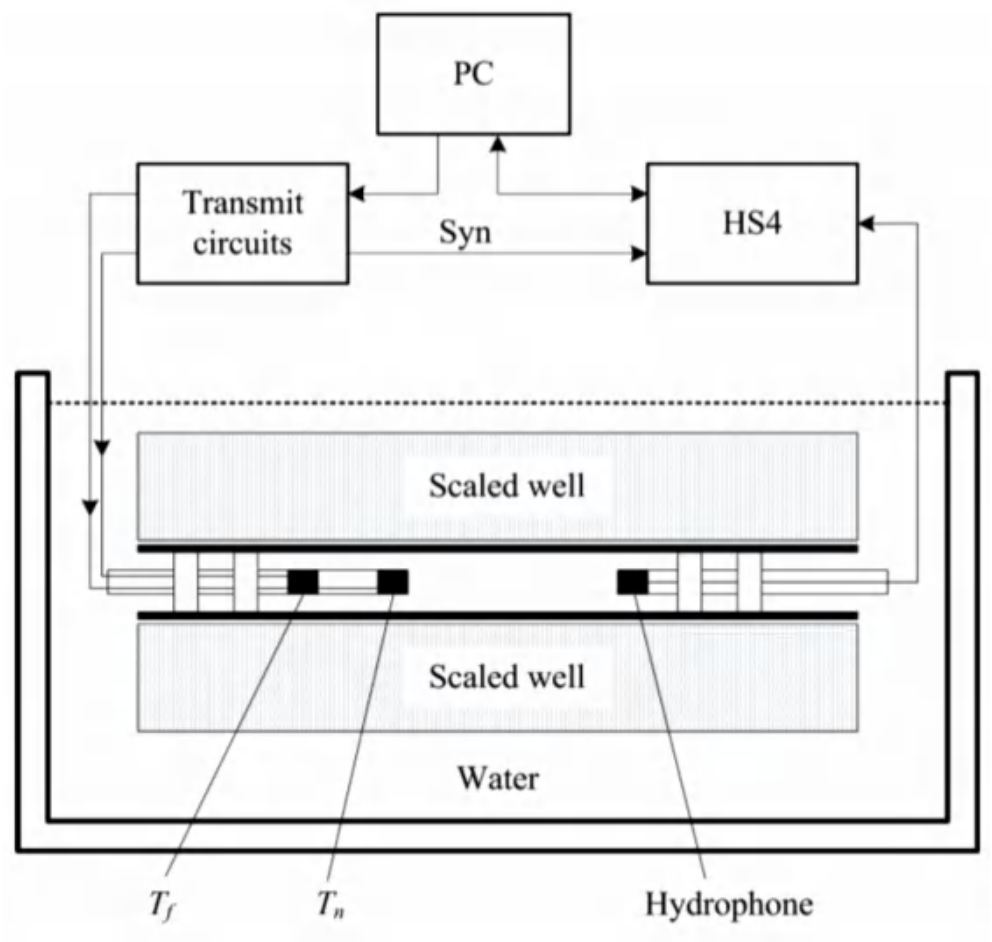


Fig. 3—Experiment setup for the dual-source measurement in a poorly-bonded casedhole model.

Downloaded from onepetro.org/petrophysics/article-pdf/60/05/631/2203169/spwla-2019-v60n5a7.pdf by China University of Petroleum Beijing user on 08 October 2026

Figure 4a shows the array waveform data for the single-transmitter (T_f) firing, with the source-receiver spacing of 0.15 m and receiver increment of 0.01 m. The received signal is primarily the casing wave, whose arrival time across array is marked by a dashed line labeled by *T*. Figure 4b shows the data from the dual-transmitter acquisition, where the near-transmitter, T_n, is at 0.016 m from the far-transmitter, T_f. Compared to its counterpart in Fig. 4a, the casing wave (labeled by *T*) is largely suppressed and the formation compressional wave (labeled by *P*), which cannot be seen in Fig. 4a, is now clearly identified. For verification, the data in Fig. 4b are overlain with the openhole data (measured using T_f) in Fig. 4c. The two sets of wave data, after proper normalization with their respective amplitude, show quite good agreement, especially in the P-wave portion where the two waves show similar moveout across the array. Applying the slowness time coherence (STC) processing to both data gives the formation P-wave velocity value of about 3,700 m/s, in close agreement of the model value of 3,728 m/s. The comparison in Fig. 4c demonstrates that, by suppressing casing wave amplitude using the dual-transmitter method, the acoustic signal from the formation can be measured through the poorly bonded casing.

It is worthwhile to mention that, due to the deviations from the ideal theoretical condition, as mentioned above, the casing wave in the actual dual-transmitter measurement may not be completely canceled. In the above laboratory experiment, about 90% of the casing-wave amplitude in Fig. 4a is canceled in Fig. 4b. This means that casing waves will still exist in the data of a dual-transmitter tool. Nevertheless, compared to the conventional single-source acquisition, the situation is much improved in the dual-source acquisition. By suppressing the casing-wave amplitude using the dual-source acquisition, the formation acoustic signal can now get adequate sampling in the A/D digitization processing and the signal/noise ratio of the recorded data is significantly enhanced. The remaining casing-wave signal in the data can further be suppressed using signal-processing methods (e.g., Valero et al., 2003; Tang et al., 2014a).

The above theoretical development, numerical modeling, and laboratory experiment results prove the feasibility of the dual-transmitter logging technology and lay the foundation for the tool engineering and development. A prototype tool has been built based on the configuration in Fig. 1 (Tang et al., 2014b). Key in this technology is the engineering of the dual-source excitation electronics for the source transmitters T_n and T_f. A low-voltage source signal is magnified and used to produce two high-voltage signals for T_n and T_f, respectively. The signal amplitude, frequency, polarity, and delay time are electronically adjusted according to the conditions leading to Eq. 5. Apart from the dual-transmitter design and the excitation electronics, the rest of the tool is the same as that of a conventional array acoustic tool. Figure 5 shows a photograph of the transmitter section of the dual-transmitter tool prototype.

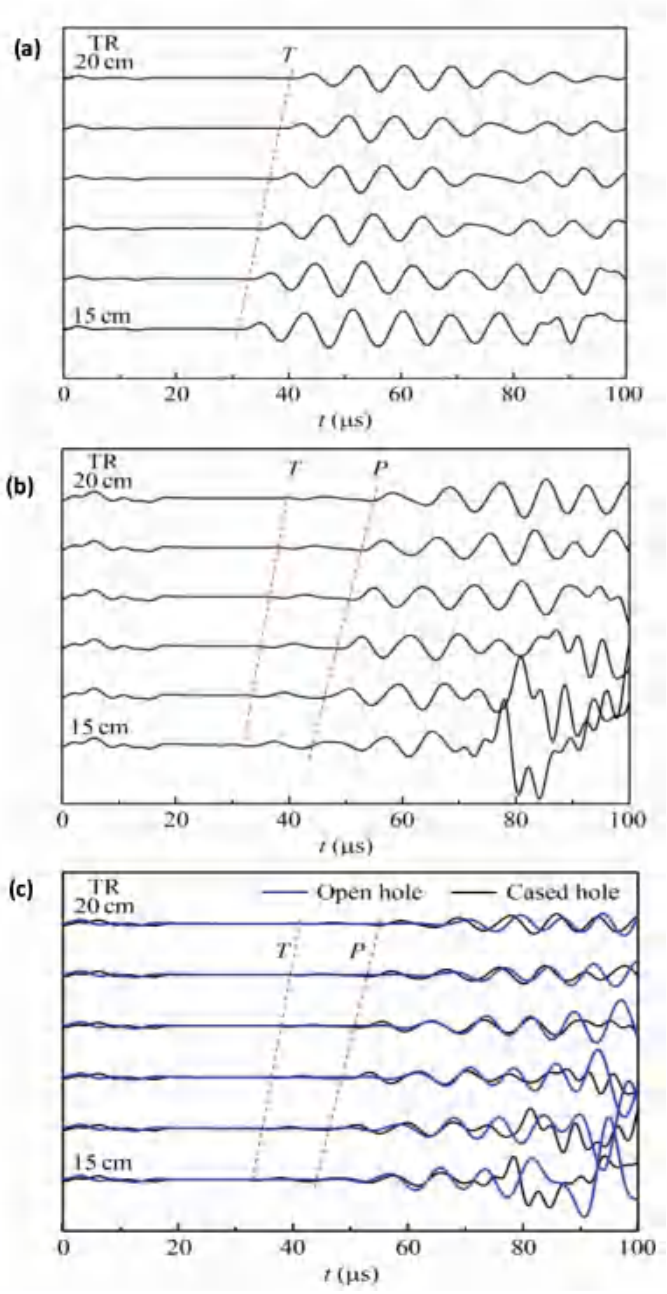


Fig. 4—Experiment measurement results. (a) Casing waves (labeled as *T*) from the single source; (b) Formation compressional waves (labeled as *P*) from the dual source; and (c) comparison of wave data from openhole and casedhole (dual-source) measurements.

Downloaded from onepetro.org/petrophysics/article-pdf/60/05/631/2203169/spwla-2019-v60n5a7.pdf by China University of Petroleum Beijing user on 08 October 2026

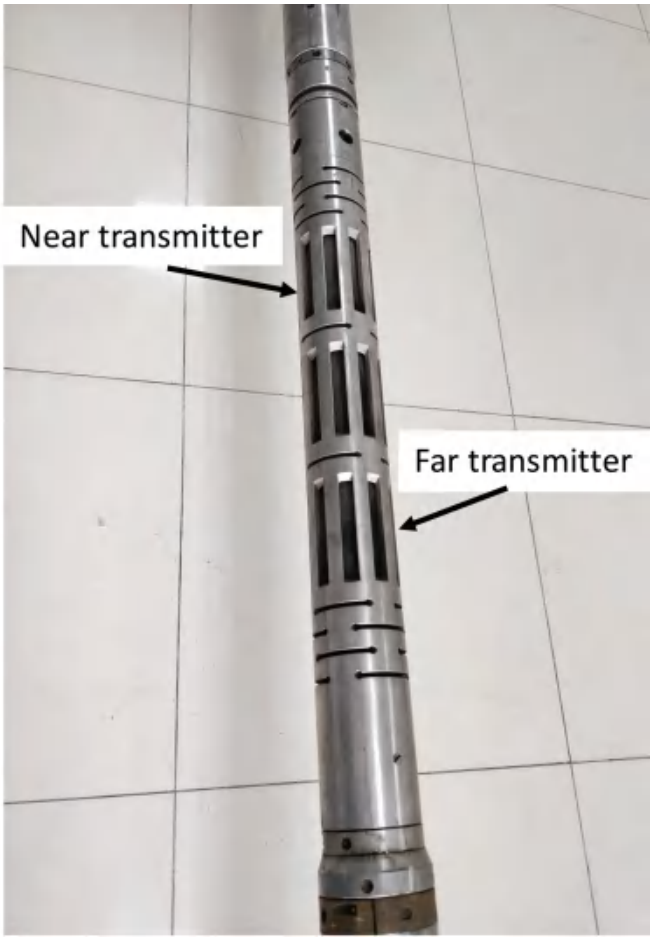


Fig. 5—The transmitter section of the through-casing acoustic logging tool prototype.

DOWNHOLE TEST AND RESULTS

The prototype tool was tested first in a designated cased well. The well is 40 years old in a depleted oil field and is known to have poor cement-bond conditions. Openhole sonic logging was done in the lower part of the well and the result is available for comparison with the result of the new measurement. The poor bonding condition of the cased well and the available openhole data provide a direct test for the through-casing acoustic technology.

A 300-m depth section across a depleted reservoir was logged. For comparison with the dual-transmitter result, the single-transmitter data were also acquired using the far transmitter during logging. Figure 6a shows the data (left panel) and the processing result (right panel). The variable density log (VDL) display of the first receiver waveform data clearly shows the strong and almost invariant casing-wave arrival in the first 1,200 μs time section. The formation signal (i.e., the P-wave arrival) is overwhelmed by the casing wave and cannot be visually detected in the time section. Consequently, the STC correlogram (right panel) from the array data processing shows a strong coherence strip with an almost constant slowness value of 190 μs/m corresponding to the casing-wave slowness, together with some low-coherence events corresponding to the slowness values of the formation P-wave signal that is buried in the casing waves.

Using the single-transmitter data as a reference, Fig. 6b shows the dual-transmitter data (left panel) and the processing result (right panel). The casing wave in the single-transmitter data (Fig. 6a) is now largely suppressed. Although there are still some residual casing waves on the VDL display background, the formation P-wave arrival can now be clearly identified and its variation with the depth can be traced. (Note the reflection wave at the casing joint can also be identified for every 10-m depth interval.) The waveform comparison demonstrates that, by suppressing the casing waves with the dual-transmitter acquisition method, the signal/noise ratio of the formation acoustic signal is significantly enhanced.

The dual-source data processing result is shown in the STC correlogram of the right panel of Fig. 6b. The STC processing steps are demonstrated in Fig. 6c using the data for the depth of 1,451m (indicated by an arrow in the panel). The left plot is the STC function displayed over the 2D (slowness and time) domain for the single-source data, which shows the strong casing and weak formation P-wave events. The middle figure is the same STC plot for the dual-source data, in which the coherence of the formation P-wave is significantly enhanced over its single-source counterpart. Note the casing event in this plot is still quite strong because the residual casing wave in Fig. 6b is still quite coherent. Using a signal-processing method (e.g., Valero et al., 2003; Tang et al., 2014a) to further suppress the weakened casing signal, the resulting STC on the right shows the formation-wave event only. Projection of the 2D STC function of the left and right plots on to the slowness axis (Tang and Cheng, 2004) gives the correlogram of Figs. 6a and b, respectively.

The correlogram in Fig. 6b shows a continuous event of high-coherence value across the depth section. Picking this event obtains the formation P-wave slowness profile. The transit time computed from the slowness profile tracks well with the formation acoustic wave (left panel). The slowness profile, when overlain with the correlogram in Figure 6a, tracks the weak formation P-wave event of the single-transmitter data quite well. This shows that the dual-transmitter logging tool successfully obtains the formation

Downloaded from onepetro.org/petrophysics/article-pdf/60/05/631/2203169/spwla-2019-v60n5a7.pdf by China University of Petroleum Beijing user on 08 October 2026

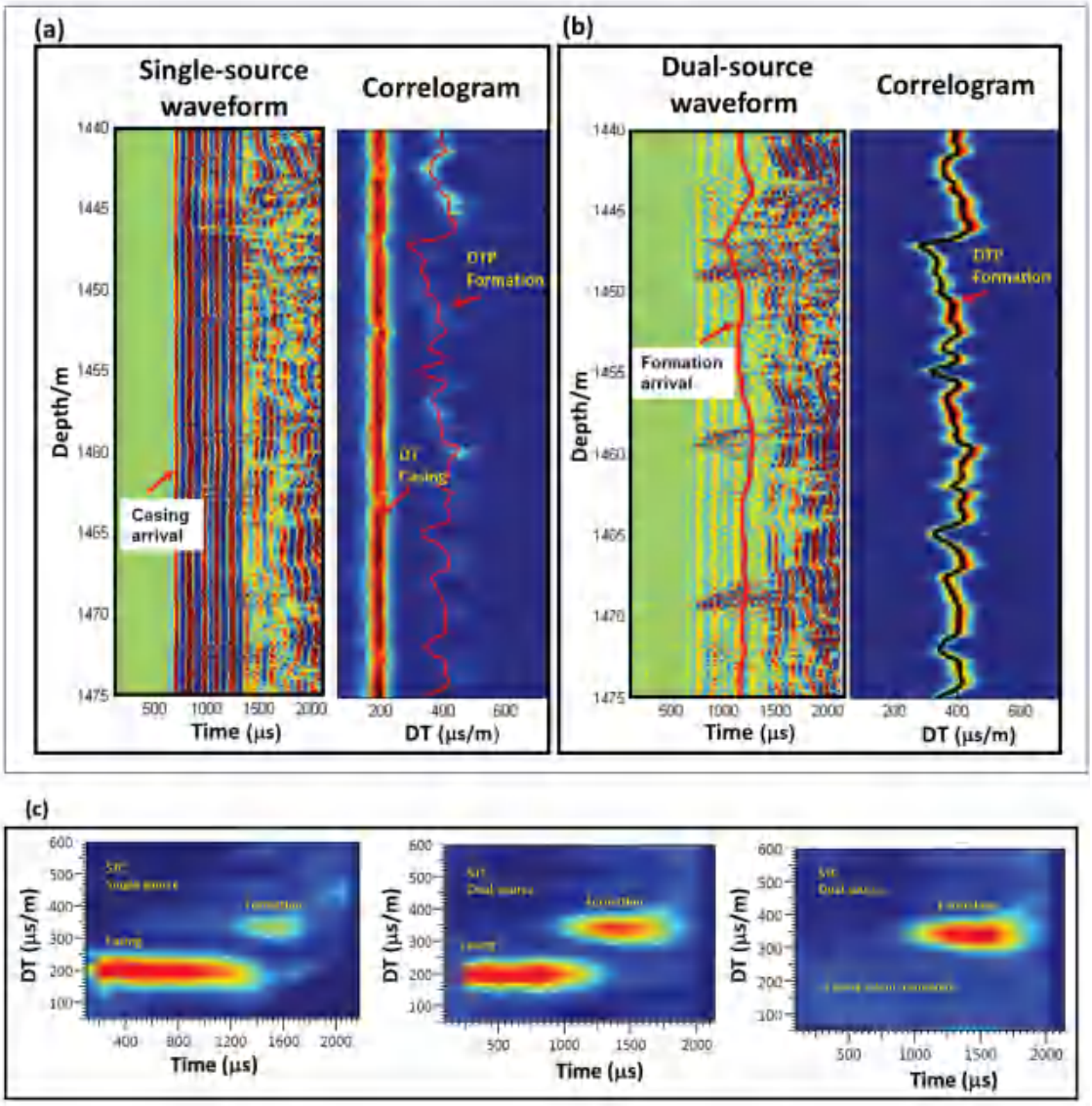


Fig. 6—Downhole test of the through-casing acoustic logging tool. (a) Single-source logging result, where the casing wave dominates both the waveform data (left panel) and the STC correlogram (right panel). (b) Dual-source logging results, where the formation acoustic wave is clearly identified (left panel) and its STC correlogram (right panel) is significantly improved over its single-source counterpart in (a). (c) Demonstration of the processing steps involved in (a) and (b).

slowness profile through this poorly bonded cased well, whereas the conventional logging has difficulty measuring the profile.

Figure 7 compares the through-casing slowness profile from the dual-transmitter tool with the openhole profile measured 40 years ago. Tracks 2 and 3 show the waveform data VDL and the STC correlogram from the data, respectively. Similar to its counterpart in Fig. 6, the waveform data consist primarily of the formation P-wave together with the first-arriving casing wave, whose amplitude is largely suppressed by the dual-transmitter acquisition. A transit time computed from the slowness profile marks the arrival of the formation acoustic wave and tracks the wave signal quite well. Track 1 shows the openhole (red) and through-casing (black) formation P-wave slowness profiles. In general, there is good agreement between the two measurement results. The minor difference at some intervals may be caused by various factors, such as production-induced reservoir property changes, errors in the respective measurements, etc. (Note the openhole data were measured with a two-receiver tool and the slowness profiles were smoothed with a five-point averaging filter.) Overall, this comparison provides a direct verification of the through-casing acoustic technology.

Downloaded from onepetro.org/petrophysics/article-pdf/60/05/631/2203169/spwla-2019-v60n5a7.pdf by China University of Petroleum Beijing user on 08 October 2026

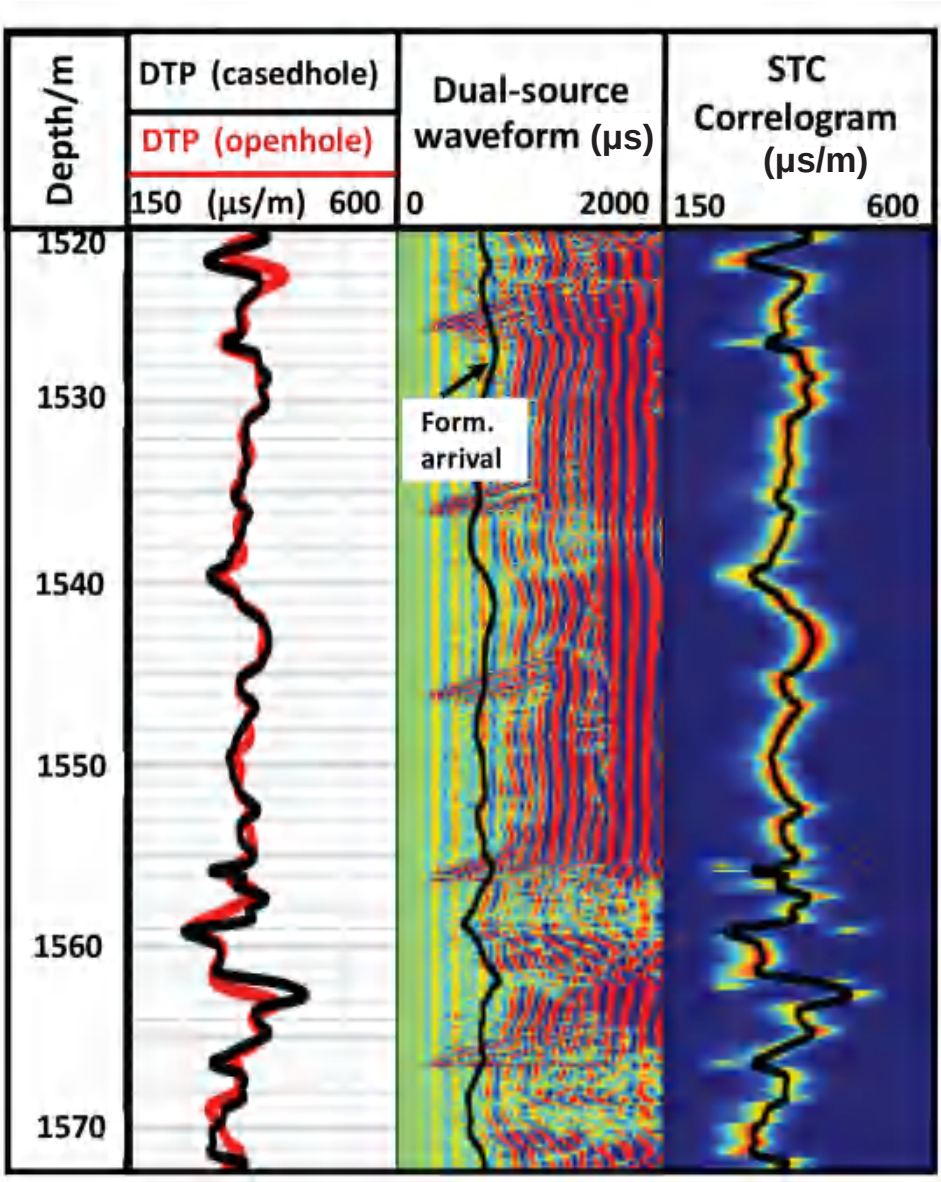


Fig. 7—Comparison of through-casing (DTP, black) and openhole (DTP, red) slowness profiles (Track 1), where the casedhole result is obtained from the dual-source logging data (Track 2) and the processed STC correlogram (Track 3).

DISCUSSION AND CONCLUSIONS

We have developed a through-casing acoustic logging tool using the dual-transmitter excitation and data acquisition method. The theoretical foundation for this development has been validated by numerical modeling and laboratory experiment results. The performance of the tool has also been verified by the results of many downhole measurements. However, one should be reminded that the performance of the tool in very fast formations approaches a theoretical limit, which is caused by the stop-band function in Eq. 5. That is, when the formation acoustic velocity is close to the casing-wave velocity, the formation acoustic signal will be affected by the dual-source scheme. Nevertheless, the application scope for this new technology is quite broad since most reservoir rocks are acoustically slower than the steel casing. Aside from this limitation, the technology can be applied to cased boreholes with slow to moderately fast formations to obtain reliable through-casing acoustic data for various applications.

Downloaded from onepetro.org/petrophysics/article-pdf/60/05/631/2203169/spwla-2019-v60n5a7.pdf by China University of Petroleum Beijing user on 08 October 2026

ACKNOWLEDGEMENTS

The authors thank the editor for the invitation for publishing this paper in *Petrophysics*. Thanks also go to the anonymous reviewers whose comments and suggestions helped improve the manuscript.

NOMENCLATURE

C_f = far-transmitter excitation amplitude
C_n = near-transmitter excitation amplitude
D = distance between near and far transmitters
f = stop-band filter function for the dual-source transmitters
G = Green's function of the tool-casing-formation system
k = wavenumber (1/m)
N = number of receivers in array
p = total acoustic pressure from far and near transmitters
p_f = acoustic pressure from far transmitter
p_n = acoustic pressure from near transmitter
R_1 = first receiver in array
R_N = last receiver in array
S = source excitation signal
t = recording time from far transmitter actuation (μs)
T_f = far transmitter
T_n = near transmitter
v_t = casing-wave velocity (m/s)
z = recording distance from near transmitter (m)
τ = delay time between far and near transmitter actuation times (μs)
ω = angular frequency (kHz)

REFERENCES

Tang, X.M., and Cheng, C.H., 2004, *Quantitative Borehole Acoustic Methods*, Handboook of Geoophysicsal Exploraito: Seismic Exploration, 24, Pergamon Press, Elsevier. ISBN: 978-0080440514.

Tang, X.M., and Patterson, D., 2005, Analyzing and Processing Acoustic Logging Data For Poorly Bonded Cased Boreholes, Paper OO, *Transactions, SPWLA 46th Annual Logging Symposium*, New Orleans, Louisiana, USA, 26–29 June.

Tang, X., Qi, X., and Su, Y., 2014a, Method for Extracting Earth Formation Acoustic Property Through Cased Borehole Using the Interference of Casing and Formation Acoustic Waves, Chinese Patent Bureau Patent ZL201410372976.1, granted July 31, 2014.

Tang, X., Zhang, B., Su, Y., and Tan, B**.,** 2014b, Method and Apparatus for Through-Casing Acoustic Logging Using Dual Transmitter Sources, Chinese Patent Bureau Patent ZL20141066882.9, granted November 20, 2014.

Tubman, K.M., Cheng, C.H., Cole, S.P., and Toksöz, M.N.,1986, Synthetic Full-Waveform Acoustic Logs in Cased Boreholes, II—Poorly Bonded Casing: *Geophysics*, **51**(4), 902–913, DOI: 10.1190/1.1442148.

Valero, H., Skelton, O., and Almeida, C.M., 2003, Processing of Monopole Sonic Waveforms Through Cased Hole, *SEG Technical Program Expanded Abstracts*, 285–288. DOI: 10.1190/1.1817899.

Zhang, B., Su, Y., Tang, X.M., Qi, X., and Tan, B.H., 2015, A Cased-Hole Acoustic Logging Technique Using the Dual Source of Opposite Polarity, *Chinese Journal of Acoustics*, **40**, DOI: 10.158049/j.cnki.0217-9776.2015.003.005.

ABOUT THE AUTHORS

Xiaoming Tang is professor of Geoscience at China University of Petroleum, Qingdao, China. He received a Doctor of Science degree from MIT in 1990 and worked for the petroleum industry for more than 20 years. He has broad interests in oil and gas exploration, including seismic-wave theory, borehole geophysics, petrophysics, and rock mechanics.

Yuanda Su is a professor of China University of Petroleum, Qingdao, China. He received his PhD in geological engineering from the university in 2014. His main interest is in well-logging technology development, acoustic processing, and well-log interpretation.

Bo Zhang is a senior engineer of the Beijing Shuoren Times Technology corporation. He received his PhD in geological engineering from China University of Petroleum in 2016. He has many years of experience in well-logging tool electronics design and engineering.

Downloaded from onepetro.org/petrophysics/article-pdf/60/05/631/2203169/spwla-2019-v60n5a7.pdf by China University of Petroleum Beijing user on 08 October 2026

第 40 卷第 6 期　　声　学　学　报　　Vol. 40, No. 6
2015 年 11 月　　ACTA　ACUSTICA　　Nov., 2015

一种过套管双源反激声波测井方法*

张　博[1,2]　苏远大[1†]　唐晓明[1]　祁　晓[1]　谭宝海[1]

(1　中国石油大学 (华东) 地球科学与技术学院　青岛　266580)

(2　中国电波传播研究所　新乡　453003)

2014 年 7 月 9 日收到

2014 年 9 月 23 日定稿

摘要　套管井胶结差时，地层声速的测量是一个很重要的测井难题。为解决这一难题，提出了一种过套管双源反激声波测井方法，从数据采集上压制套管波，增强地层波的信噪比。模拟计算了这种情况下双源反激的测井声波波形，并在实验室制作了 1:10 的套管模型井，进行了物理模拟实验。计算结果表明利用该方法可以有效压制套管波，并能清晰地识别出地层纵波。对实测波形的分析表明，实验条件下采用双源反激方法套管波幅度能够被压制到单源激励时的 0.12 倍，有效提高了地层波的信噪比，并能有效提取地层波的速度。理论和物理模拟结果验证了该方法的可行性，为其工程应用奠定了基础。

PACS 数：43.58

A cased-hole acoustic logging technique using the dual source of opposite polarity

ZHANG Bo[1,2]　SU Yuanda[1]　TANG Xiaoming[1]　QI Xiao[1]　TAN Baohai[1]

(1　*College of Geosciences, China University of Petroleum*　Qingdao　266580)

(*China Research Institute of Radiowave Propagation*　Xinxiang　453003)

Received Jul. 9, 2014

Revised Sept. 29, 2014

Abstract　It is usually difficult to measure acoustic velocity through casing, especially when the casing is poorly bonded with formation. An acoustic logging technique using the dual source of opposite polarity is proposed to enhance the Signal to Noise Ratio of the formation signal while reducing casing wave in the data acquisition process. In what follows, theoretical modeling is used to caculate the wavefroms of cased wells. Then a scaled experiment was conducted in the 1:10 scaled experimental well using the technique in the poorly bonded condition. The results show that this technique can effectively suppress casing wave and enhance formation wave, even in the poorly bonded condition. By analyzing the measured wavefroms, the casing wave amplitude is reduced to 12% and the compressional wave velocity can be easily obtained from the measurement technique. Both the theoretical modeling and experiment results demonstrate the feasibility of the proposed technique. This study establishes the theoretical and experimental foundation for cased-hole dual source of opposite polarity acoustic logging tool development.

引言

近年来，由于对老油田剩余油气开发，或者裸眼井测井的缺失，需要在套管井中进行声波测井。由于钢套管和水泥的存在，声波的传播受到很大的影响，尤其是，在套管与地层胶结不好的情况下，测井声波的能量的相当一部分以套管波的形式传播，而辐射到地层的能量大为减弱。同时，由于很强套管波的影响，地层波的信号往往被套管波淹没，难以识别[1−8]。为了解决胶结不好的套管井声波测井问题，人们在此领域开展了不少研究工作[9−17]。陈雪莲等人以增强地层波幅度为出发点将相控线阵声源引入到套管井声波测量仪器的设计中[9−11]。对此所做的数值模拟结果表明在套管与水泥或水泥与地层界面存在微环时，通过选择相邻阵元间合适的激励延迟时间，可有效地增强地层滑行纵横波的幅度，同时还可较好地抑制套管波的能量。陈雪莲等人开展了套管井

*　国家自然科学基金 (41474092, 41204070) 资助

†　通讯作者：苏远大，　Email: syuanda@sina.com

缩小模型的声波测井物理模拟研究，实验验证了数值模拟结果的正确性[11]。Pampuri 等、唐晓明等、陈雪莲等对套管井偶极子测井也进行了理论研究。结果表明，在自由套管情况下，选择适当的中心频率，波列中可清晰地看到地层纵波，表明横向偏振的声源比纵向振动的声源有更好的穿透套管的能力[12,5,13]。Pampuri 等利用这一现象来解决套管井胶结质量差时纵波时差的测量问题[12]。此外，在过套管声波测井数据的处理方面，前人也开展了大量的研究工作，Hsu 等、Tang 等提出了最大似然函数法、F-K 滤波法等数据处理方法[14−17]。

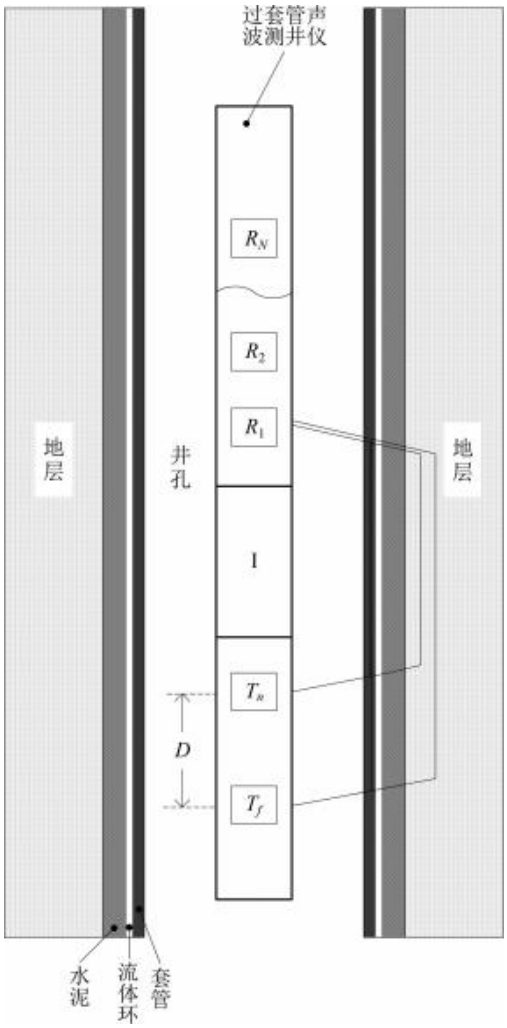
对套管井条件下的井孔声场理论模拟表明，即使是在自由套管的情况下，井中接收到的声波信号中也含有地层波的成分[3]。然而，在对这种声波信号进行量化采集时，模数转换器在量化过程中的信号的增益往往由波幅较大的套管波所控制，使得波幅较低的地层波在模数转换中在低位数字上被量化。这样采集的地层声波信号的信噪比较低，很难准确提取到地层的声速。如果能对套管波的波幅进行压制，那么在声波信号的采集过程中地层波信号就能得到相对增强，从而有可能从地层波信噪比较高的声波数据中获得地层声速。

本文提出了一种过套管双源反激声波测井方法，从数据采集着手对套管波进行压制，从而提高地层波的信噪比。这样，即使在胶结不好的情况下也能获取地层纵波速度，和传统单源激励声波测井方法相结合可以提高套管井地层评价声波测井的适用范围。

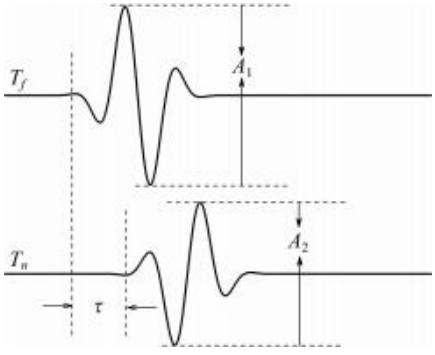
在下文中，我们先叙述该方法的工作原理，再从理论模拟上对该方法进行论证，然后通过实验室测量对该方法进行实际验证。

1 基本原理

如图 1(a) 所示的套管井模型，从内向外依次是井眼流体、套管、流体环 (用来模拟套管和水泥胶结不好的情况) 、水泥和地层。基于双源反激方法的过套管声波测井仪有间距为 D 的两个发射，分别是远发射 T_f 和近发射 T_n 。I 为隔声体，其作用是延迟和衰减沿仪器传播的仪器波。测井时，T_f 首先激发，发射幅度为 A_1, T_n 延时一段时间 τ 之后激发，发射极性与 T_f 相反，发射幅度为 A_2, 发射时序见图 1(b) 。在双源发射的同时，对 N 个接收器上的信号进行采集并记录。通过选择合适的参数 A_1, A_2 及 τ, 使得在接收器的位置上 T_f 和 T_n 所激发的二套管波同时到达，但极性相反、幅度相同。这样，接收波形中的套管波相互叠加后被抵消，即套管波得到压制。而对于接收波形中 T_f 和 T_n 产生的地层信号，只要地层波和套管波速度存在差异，其到达接收器的时间就不一致，相互叠加后仍能保留。相对于套管波，地层波就得到了增强。通常，套管井的套管波的波速是已知的，或者是可测的。因此，只要固定发射间距并选取固定的延迟时间进行上述双源激发，即可实现压制套管波的目的。



(a) 过套管声波测井仪及套管井模型示意图



(b) 双源反激激励时序图

图 1 过套管双源反激声波测井工作原理示意图

双源反激激励方式在对套管波压制或抵消的同时, 对地层波也会产生影响。这与声源的主频、地层声速、套管声速及测量声系参数 (如远近发射间距) 、远近发射匹配程度等都有关系。这种影响到底有多大？对这个问题的分析将在下节的理论模拟中给出, 现将分析结果叙述在此，根据理论分析得到的式 (8), 计算了频率为 12 kHz 、双源间距为 0.15 m 时双源反激激励下地层波的相对幅度曲线, 如图 2 所示。横坐标表示地层波的速度，纵坐标为相对于单源激励时地层波的幅度。从图中可以看出, 地层波的相对幅度在 0∼2 之间的范围变化，当地层波的速度为 5400 m/s, 即和套管波速度一致时, 地层波也被完全抵消掉。随着地层波速度和套管波速度差异的增大，地层波相对幅度大体呈增大趋势。

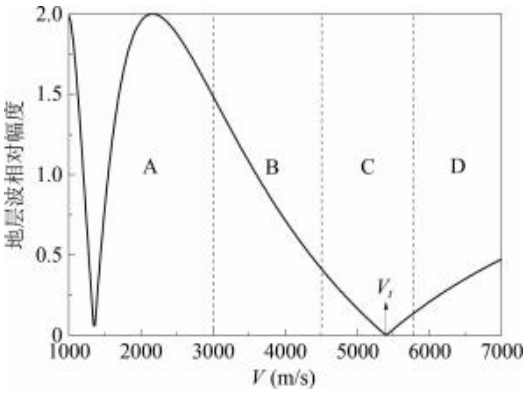


图 2　双源反激激励对地层波幅度的影响

图 2 中 3 条虚线大体将图分成 4 个区间 A, B, C, D。A 区地层波速度最低，由于地层波速度和套管波速度差异很大, 在到时上比较容易分开, 这在实际测井中通常不存在问题。B 区地层波速度与套管波速度比较接近，在测量波列中地层波通常淹没在套管波中, 但由于地层波和套管波存在速度差异, 用双源反激的方法有望将地层信号提取出来。C 区的地层波速度接近于套管波速度，难以用双源反激方法解决, 所以不在本文讨论之列。D 区地层波速度快于套管波速度, 因此地层波成为首波, 所以在测量中也不存在问题。

在 A 区和 B 区内用双源反激的方法来压制套管波, 使得 B 区速度较高的一端的地层波有所削弱 (见图 2), 但其与套管波的相对幅度得到增强，甚至占主导地位。这样, 通过增大声源的发射功率来增加信号强度, 并针对信号到达的时段进行数据采集, 就能得到信噪比较高的地层声波信号。

2　双源反激方法理论模拟

过套管声波测井的理论模拟可用图 1(a) 所示的层状地层模型来描述 [1−7,9−10,18]。从井轴向外依次是：井眼流体、套管、流体环、水泥，最外层是无限大的地层。声源和接收器位于井轴上。对声源 T_f, 距源 z 处井轴上的声压表达式为 [5]:

$$p_f(z,t)=\frac{1}{2\pi}\int_{-\infty}^{+\infty}\int_{-\infty}^{+\infty}s_f(\omega)A(k,\omega)\exp(\mathrm{i}kz-\mathrm{i}\omega t)\mathrm{d}k\mathrm{d}\omega, \tag{1}$$

其中 $s_f(\omega)$ 为 T_f 声源频谱， $A(k,\omega)$ 为图 1(a) 所示模型在井中流体的响应函数，由井孔各边界条件确定 [5]。

同理，对距 T_f 声源 D 处的声源 T_n, 同一接收点上的流体声压为：

$$p_n(z,t)=\frac{1}{2\pi}\int_{-\infty}^{+\infty}\int_{-\infty}^{+\infty}s_n(\omega)A(k,\omega)\exp[\mathrm{i}k(z-D)-\mathrm{i}\omega t]\mathrm{d}k\mathrm{d}\omega, \tag{2}$$

其中 $s_n(\omega)$ 为 T_n 声源频谱。将式 (1) 和式 (2) 叠加得到该双源系统激发时的声压：

$$p(z,t)=p_f(z,t)+p_n(z,t)=\frac{1}{2\pi}\int_{-\infty}^{+\infty}\int_{-\infty}^{+\infty}[s_f(\omega)+s_n(\omega)\exp(\mathrm{i}kD)]A(k,\omega)\exp(\mathrm{i}kz-\mathrm{i}\omega t)\mathrm{d}k\mathrm{d}\omega. \tag{3}$$

对声源 T_f, 我们令：

$$s_f(\omega)=c_1s(\omega), \tag{4}$$

其中 c_1 为 T_f 波谱的振幅系数。

对声源 T_n, 除采用同样的频谱 $s(\omega)$ 外，还在时间上对源信号延迟 τ, 这样， T_n 的声源函数可表示为：

$$s_n(\omega)=-c_2s(\omega)\exp(\mathrm{i}\omega\tau), \tag{5}$$

其中 c_2 为 T_n 波谱的振幅系数。上式中的负号 “−” 表示 T_n 相对于 T_f 是极性相反的反向激励。将式 (4) 和式 (5) 代入式 (3), 得到双源反向激励的井中声压信号为：

$$p(z,t)=\frac{1}{2\pi}\int_{-\infty}^{+\infty}\int_{-\infty}^{+\infty}\left[1-\frac{c_2}{c_1}\exp(\mathrm{i}kD-\mathrm{i}\omega\tau)\right]c_1s(\omega)A(k,\omega)\exp(\mathrm{i}kz-\mathrm{i}\omega t)\mathrm{d}k\mathrm{d}\omega. \tag{6}$$

调节延迟时间 τ, 使之等于套管波在距离 D 上传播时间：

$$\tau=\frac{D}{v_t}, \tag{7}$$

其中， v_t 为套管波速度。再调节 T_n 相对于 T_f 的幅度比 c_2/c_1, 使之接近于 1。这样做相当于在频率−波数域 $(\omega-k)$ 内嵌入了一个带阻滤波函数：

$$f(k,\omega)=1-\exp\left[\frac{\mathrm{i}\omega D}{v_t}\left(\frac{kv_t}{\omega}-1\right)\right]. \qquad (8)$$

采用上述带阻滤波函数，当响应函数 $A(k,\omega)$ 中含有 $k=\omega/v_t$ 的波数成分的波 (如胶结不好时激发出的套管波) 时，这种波将被压制甚至抵消。我们用一理论模拟的例子来说明这种双源反向激励的效果。D 取 0.15 m, v_t 取 5400 m/s, 从式 (7) 得到 τ 为 27.8 μs。接收阵列距 T_f 的距离为 1.5 m, 接收间距为 0.15 m。模拟的模型参数见表 1。声源函数采用中心频率为 12 kHz 的雷克子波 [5]。

用图 1(a) 的模型计算式 (6) 中的响应函数 $A(k,\omega)$, 再用实轴积分方法 [5] 计算式 (6), 得到的接收阵列波形如图 3 所示。为了对比，将常规单源激励的波形图画在同一个图中。图中蓝色的波形为采用传统单源发射时接收到的阵列波形图，接收波形中首先到达的是套管波 (波至由标示为 T 的虚线给出), 由于其幅度大且持续时间较长，地层纵波完全淹没在套管波中无法识别。图中黑色的波形为采用双源反激发射时接收到的阵列波形图, 由于双源反激的带阻滤波作用 (见式 (8)), 套管波的幅度被大大压制，能够清晰地观测到幅度较小的地层纵波波列 (波至为标示为 P 的虚线给出)。

图 4 为上述理论阵列波形的慢度时间相关 (STC) 处理结果。STC 慢度时间相关法利用波形相干叠加方法得到以时间和慢度 (慢度即速度的倒数) 为变量的二维相关函数。图中的横坐标代表波形中某个振型在第一接收器上的到达时间，纵坐标代表慢

表 1 过套管声波测井的理论模拟模型参数

参数	纵波速度 (m/s)	横波速度 (m/s)	密度 (kg/m^3)	外径 (m)
井眼流体	1500	0	1000	0.14
套管	6098	3354	7500	0.16
流体环	1500	0	1000	0.17
水泥层	2823	1729	1920	0.2
地层	4000	2300	2500	∞

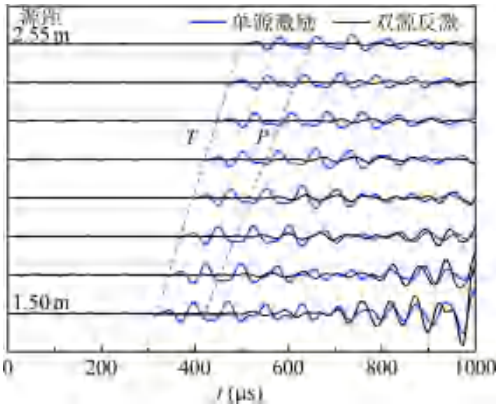
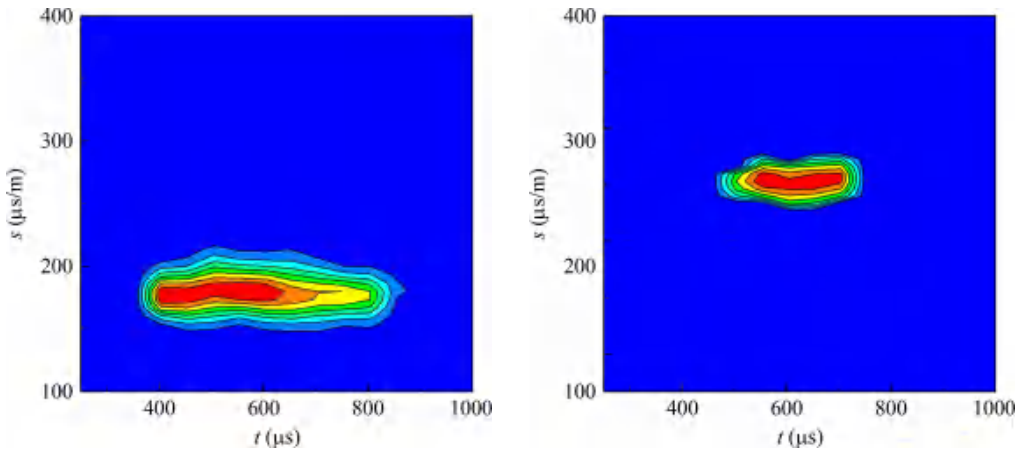


图 3 套管胶结差时传统单源 (蓝色) 与双源反激 (黑色) 的理论阵列波形对比



(a) 单源激励 (b) 双源反向激励

图 4 套管胶结差时传统单源激励与双源反激激励理论阵列波形 STC 图

度, 相关函数的峰值对应该振型的到时及慢度[1,19]。单源激励时由于套管波占主导地位, STC 相关图中在 100~400 μs/m 范围内只有一个峰与套管波相对应。波幅较小的地层纵波的相关性被套管波完全屏蔽, 不能体现出来。采用双源反向激励时, 套管波被压制(在理论模拟中, 两个源的幅度和时间延迟可以精确控制, 可以基本消除套管波), 在 STC 相关图中能够清晰地看到与地层波对应的峰, 其慢度为 250 μs/m, 与模型参数相符。这个理论模拟的例子验证了用双源反激方法来压制套管波的思想。下面我们用物理实验来考察该方法在工程实现中的可行性。

3 物理模拟实验

3.1 实验装置

为了验证双源反激理论模拟结果的正确性和该方法在实际测量中的可行性, 在实验室制作了模型井并设计了实验双源激励电路, 在此基础上进行了物理模拟研究。为了使实验室的物理模拟与现场实际工作的情况相似, 实验室模型井的尺寸及声波换能器的尺寸和频率之间的比例关系与实际的声波测井情况下各参数之间满足相似性原理[11,20]。模型井井眼大小与现场井眼的比例关系是 1:10, 因此发射的工作频率应是现场工作频率的 10 倍, 为此选取了中心频率为 120 kHz 的压电陶瓷管状换能器做发射换能器, 发射的内径、外径和高度分别是 6 mm, 8 mm, 5 mm 。远发射和近发射间距为 0.016 m 。模型井中的套管采用长度为 1 m, 内、外直径分别为 18 mm 和 20 mm 的无缝不锈钢管, 在套管和水泥环之间是 0.3 mm 厚的塑料层, 用来模拟 I 界面胶结差的情况。水泥环由固井水泥制作, 厚度为 4 mm 。超声测定水泥环样品的纵横波速度分别为 3062 m/s 和 1734 m/s 。模型井的地层用一定配比的混凝土浇注而成, 超声测定地层样品的纵横波速度分别为 3731 m/s 和 2174 m/s (即纵横波慢度分别为 268 μs/m 和 460 μs/m), 密度为 2140 kg/m^3。为了便于实验对比, 同时设计了相同尺寸的裸眼井模型井, 裸眼井模型井只有地层, 无水泥环及套管和塑料。

实验装置如图 5 所示。将模型井浸没在水池中, 发射器和接收器通过缠绕胶带进行居中, 由 PC 控制自制的双路发射电路进行激励, 同时用 HS4 虚拟示波器观测并记录实验波形。采样间隔设置为 0.1μs。发射电路产生一个方波脉冲作为示波器的同步信号。实验中发射器位置固定, 用水听器沿井轴进行移动接收, 每移动 0.01 m 记录一次波形, 通过多次推移来实现阵列波形的记录。

实验采用的双源反激发射电路能够对输出激励高压的幅度、延迟时间进行控制。延时参数在 0~100 μs 可控, 最小步长为 0.1 μs; 幅度连续可调, 最大幅度可达 120 V。两路发射电路发射幅度及延迟时间等参数最终由 PC 终端控制设定。图 6 为测量到的两路发射高压的波形图。

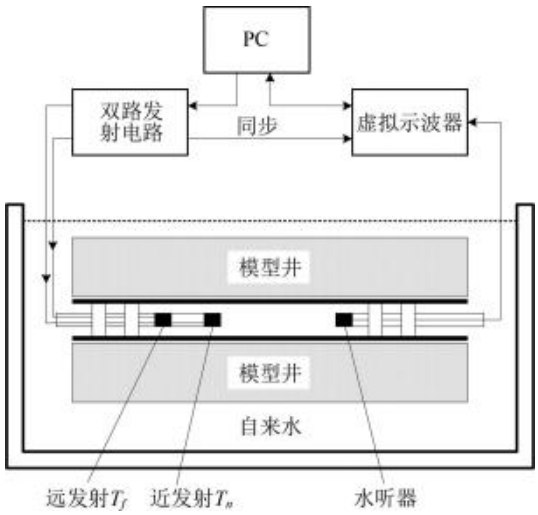


图 5　实验装置示意图

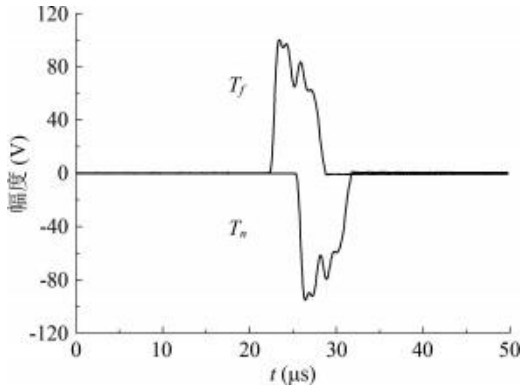


图 6　实验发射电路输出双源反激的高压波形图

3.2 实验结果及分析

实验时首先通过调节近发射激励高压的幅度, 使得只有近发射激励时和只有远发射激励时接收到的套管波幅度比接近 1。图 7 为远发射到接收之间的距离固定为 0.20 m 时, 不同延时下接收到的波形图, 虚线 T 对应套管波的到时, 虚线 P 对应地层纵波的到时。从图中可以看出随着延时时间的变化, 套管波幅度也跟着改变, 当延时时间为 3 μs 时, 套管波的幅度最小, 此时套管波幅度大约为只有远发射时的 0.12 倍。地层纵波的到时变得清晰。以下实验中近发射延迟时间均设置为 3 μs 。虽然双源反激的理论模拟 (见图 3), 可以比较彻底地消除接收波列中的套管波, 但实际测量中, 远、近声源很难做到完全一致, 再加上其他因素如波的衰减和频散以及发射换能器及

其工作载荷的差异等, 难以将套管波完全抵消。尽管如此, 实验测量中的套管波得到有效的压制, 使得地层波相对增强, 提高了其测量的信噪比和灵敏度。这在实际的井下测量中是至关重要的。

图 8 为裸眼井单源激励与双源反激激励时接收到的阵列波形对比, 从图中可以看出在实验条件下, 单源激励与双源反激激励时地层波的幅度差别不大, 这与图 2 中双源反激激励时地层波的相对幅度基本一致 (图 2 中双源间距 0.15 m, 声源主频 12 kHz; 实验中双源间距 0.016 m, 声源主频 120 kHz, 基本满足相似性原理) 。图 7 和图 8 的例子说明, 在上述实验条件下采用双源反激激励时地层波幅度变化不大, 而套管波可以被压制到原来的 0.12 倍, 地层波信噪比得到有效提高。

图 9(a) 、图 9(c) 、图 9(e) 为实验中记录到的套管井模型中源距为 0.15~0.20 m 范围内的阵列波形图。图 9(a) 为只有远发射 (单源激励) 时接收到的阵列波形图, 在 100 μs 的时段之内是套管波 (到时线 T 标示), 其幅度很高以至于看不到地层波。图 9(c) 是套管井采用双源反激激励时记录到的阵列波形图, 图中到时线 T 、P 分别对应套管波和地层纵波的到时。从图中可以看出, 尽管套管波没有被完全压制, 但其波幅大幅度降低, 在地层纵波到时线附近能看到地层纵波的到达。图 9(e) 将裸眼井双源反激激励时接收到波形和套管井双源反激激励时接收到的波形显示在同一张图中。从图中可以看出, 套管井双源反激激励时地层纵波和和裸眼井双源反激激励时地层纵波到时有较好的一致性, 说明了前者的波形中地层波的成分占据了相当大的部分。

位于上述实验记录到的波形图右侧的图 9(b) 、图 9(d) 、图 9(f) 为相应阵列波形的 STC 慢度时间相关图。图 9(f) 是裸眼井双源反激激励时接收阵列波形的 STC 图, 从图中可以看出地层纵波慢度约为 270 μs/m, 与地层样品超声测量结果一致。图 9(b) 是套管井单源激励时接收阵列波形的 STC 图, 在 100~400 μs/m 范围内, 只有一个很强的峰对应于套管波, 其慢度大约为 187 μs/m。图 9(d) 是套管井双源反向激励时接收阵列波形的 STC 图, 图中能够看到一个与地层纵波对应的峰, 其慢度大约为 270 μs/m。由于在实验条件下, 套管波未被完全压制及其很强的相干性, 所以仍有一个较强的对应于套管波的峰。但是, 从双源反激激励时接收到的阵列波形中已经能够清晰地识别和提取地层纵波, 为进一步处理和获取地层波速度提供了有效的测量数据。

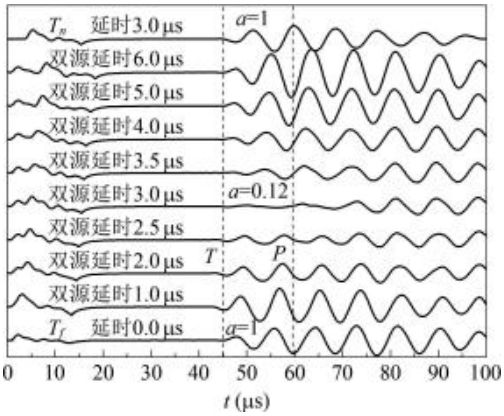


图 7 套管井不同延时下接收到的波形 (源距 0.20 m)

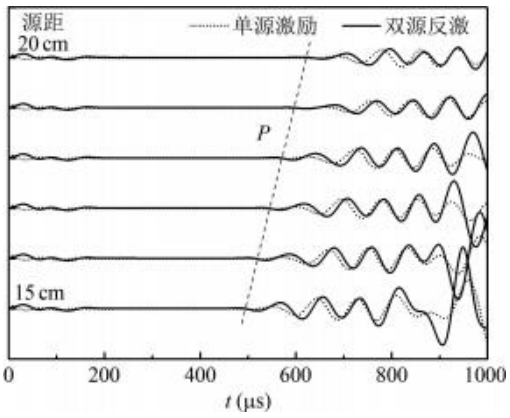
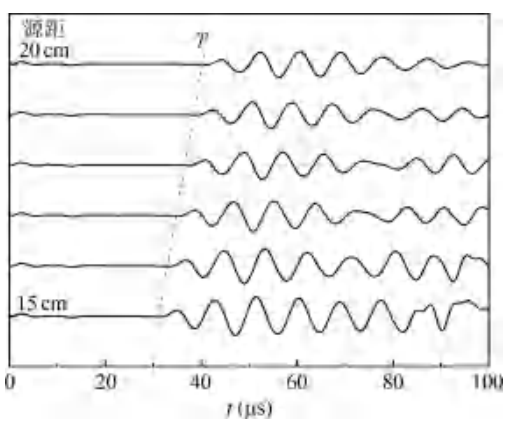
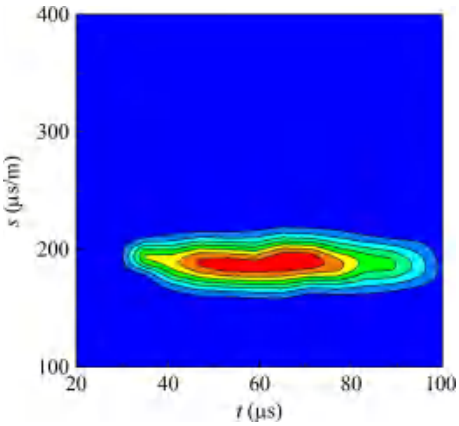


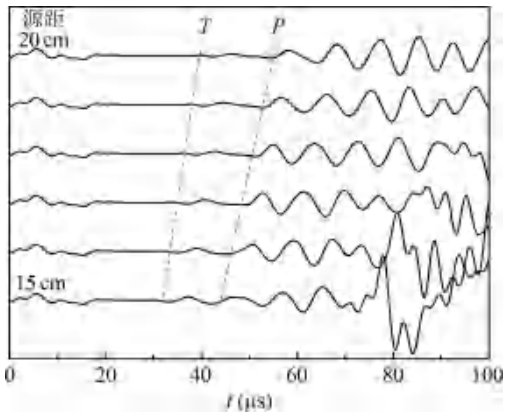
图 8 裸眼井单源激励时波形 (虚线) 和双源反激激励时波形 (实线) 对比



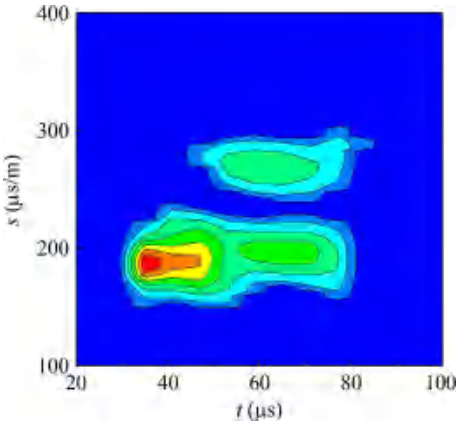
(a) 套管井单源激励时接收到的波形



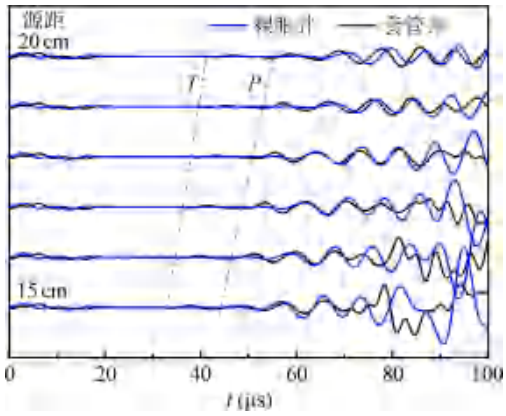
(b) 套管井单源激励接收波形 STC 图



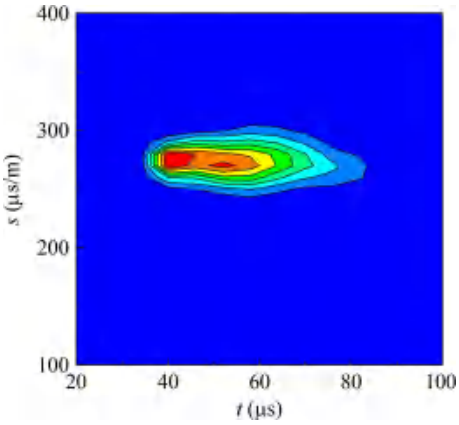
(c) 套管井双源反激激励时接收到的波形



(d) 套管井双源反激激励时接收波形 STC 图



(e) 套管井和裸眼井波形对比



(f) 裸眼井接收波形 STC 图

图 9　实验波形图及 STC 处理结果

4　结论及认识

(1) 理论计算和实际测量表明胶结不好情况下的套管井测井声波中存在很强的套管波, 严重地影响对地层声速的测量。

(2) 对此情况的理论模拟表明采用双源反激方法能够消除套管波，提高地层波的信噪比。

(3) 实验室 1:10 比例缩小的物理模拟实验表明, 在胶结质量差的实验模型井中, 采用上述双源反激方法，套管波幅度能够被有效地压制 (实验中套管波幅减小为单源激励时的 0.12 倍), 从而从实测波形数据中能够很容易地提取地层波慢度。物理模拟实验验证了该方法的正确性和有效性。

(4) 双源反激方法也可以看作是相控线阵方法的一个特例, 但本文方法以压制套管波为出发点来增强地层波的信噪比。文献 9 — 文献 11 中相控线阵方法研究思路是以增强地层波为出发点, 这种方法在工程

应用时的一个问题是地层波的速度往往是未知的。而对于双源反激方法，套管波的速度通常是已知的或者是容易获取的，因此可以有针对性的压制套管波，最佳延时不受地层速度变化的影响。此外，该方法在仪器设计上只需增加一个发射，在工程应用上简单易行。

(5) 双源反激方法在套管井地层评价中有很好的潜在应用价值. 目前只是在实验模型井中进行了初步验证, 尚需进一步设计工程样机在实际测井中评估该方法的测量效果。

参 考 文 献

1 Chang S K, Everhart A H. A study of sonic logging in a cased borehole. *Journal of Petroleum Technology*, 1983; **35**: 1745—1750

2 Tubman K H, Cheng C H, Toksoz M N. Synthetic full waveform acoustic logs in cased hole. *Geophysics*, 1984; **49**(7): 1051—1059

3 Tubman K M, Cheng C H, Nafi Toksöz M. Wave propagation in boreholes with unbonded casing. SEG Technical Program Expanded Abstracts, 1984: 15—17

4 Tubman K H, Cheng C H, Cole S P, Toksoz M N. Synthetic full waveform acoustic logs in cased hole, Poorly bonded casing. *Geophysics*, 1986; **51**(4): 902—913

5 唐晓明，郑传汉. 定量测井声学. 赵晓敏译 (第一版) . 北京: 石油工业出版社， 2004: 20—39

6 张海澜，王秀明，张碧星. 井孔中的声场和波 (第一版) . 北京: 科学出版社， 2004: 61—72

7 李整林，杜光升，王耀俊. 套管井体胶结状态对井孔中声传播的影响. 声学学报， 2001; **26**(1): 6—12

8 Valero H P, Skelton O, Cao H. A practical sonic slowness evaluation behind casing. SEG Technical Program Expanded Abstracts, 2001: 329—332

9 陈雪莲，乔文孝. 套管井中相控线阵声源激发的声场研究. 声学学报， 2007; **32**(4): 328—332

10 陈雪莲，许孝凯. 相控线阵技术在套管井声波测井地层信息测量中的应用. 石油学报， 2008; **29**(5): 777—781

11 陈雪莲，董兴蒙，谭宝海，李刚. 套管井中相控线阵声源激发声场的实验室物理模拟研究. 声学学报， 2013; **38**(4): 433—439

12 Pampuri F, Borghi M, Deias S, Giorgioni M, Brambillla F, Tang X M, Patterson D. Compressional slowness determination behind poorly-cemented casing (case history). OMC 2003, 6th Offshore Mediterranean Conference and Exhibition, Ravenna, Italy, March 26-28

13 陈雪莲，陈晓晓，王瑞甲，苏远大. 偶极子声源在套管井中的应用研究. 测井技术， 2007; **31**(3): 245—248

14 Hsu K, Baggeroer A B. Application of the maximum-likelihood method (MLM) for sonic velocity logging. *Geophysics*, 1986; **51**(3): 780—787

15 Valero H, Skelton O, Almeida C M. Processing of monopole sonic waveforms through cased hole. SEG Technical Program Expanded Abstracts, 2003: 285—288

16 Tang Xiaoming, Patterson D. Analyzing and processing acoustic logging data for poorly bonded cased boreholes. SPWLA 46th Annual Logging Symposium, New Orleans, Louisiana, United States, June 26-29, 2005

17 Kitazawa M, Valero H P. Processing of pseudo-Rayleigh waves in cased hole. Proceedings of the 10th SEGJ International Symposium, Kyoto, Japan, November 20-22, 2011: 1—4

18 陈德华，王秀明，张海澜，王东，魏涛，刘力平. 水泥密度和套管尺寸对油井套管波的影响. 声学学报， 2008; **33**(1): 15—20

19 Kimball C V, Marzetta T L. Semblance processing of borehole acoustic array data. *Geophysics*, 1984; **49**(3): 274—281

20 乔文孝，陈雪莲，杜光升，房军，李刚. 相控声波测井的模拟实验研究. 声学学报， 2003; **28**(2): 116—122

Check for updates

A multiple filtering and correlation array signal processing technique for cased-hole acoustic logging and applications

Fan-Tong Kong[1], Can Jiang[1], Yuan-Da Su[1], and Xiao-Ming Tang[1]

Abstract

In cased-hole acoustic logging, estimating the formation velocity is often problematic when the casing is poorly bonded with the formation. The overwhelmingly large casing waves dominate the measured waveforms and overlap with the low-coherence, weak formation arrival, contributing to the failure of conventional semblance processing method. To tackle this problem, we have developed a filtered frequency semblance array waveform signal processing technique. The multiple filter technique is first used to filter the measured waveforms. We then apply the nth root stacking method to the filtered signals. Consequently, the coherence of the formation signal on the obtained 3D semblance correlogram is significantly enhanced and clearly separated with the casing waves. We have applied the method to process synthetic and field cased-hole acoustic waveform data. Our results indicate that the new method significantly enhances the coherence of the desired formation signal and simultaneously estimates the formation of the P- and S-wave velocity.

Introduction

Acoustic logging is often applied to estimate formation acoustic properties for the geologic and geophysical applications in open holes. However, in the offshore fields in which the difficult well conditions are usually encountered, the acoustic measurements have to be made after the casing is set. The presence of the steel casing limits the energy radiating into the formation and reduces the signal-to-noise ratio of the formation waves, as compared to the open-hole situation. The significant signal propagating along the casing, commonly known as casing waves, contaminates the formation signal if the casing is poorly bonded with the formation. Especially in the free-pipe situation in which the casing is entirely detached with cement (Tubman et al., 1986; Wang and Fehler, 2018a, 2018b), the formation signal is almost indiscernible in the presence of overwhelmingly casing waves. The slowness-time-coherence (STC) method (Kimball and Marzetta, 1984), most frequently used to process the open-hole acoustic waveform data, may fail to detect the low-coherence event corresponding to the formation arrival for the determination of formation velocity because of the large casing waves' interference (Tang and Cheng, 2004).

Various research has been done to extract formation acoustic velocity from cased-hole acoustic logging data in poorly bonded/free-pipe conditions. Hsu and Baggeroer (1986) incorporate time windowing and slowness steering to the maximum likelihood method, being able to estimate the signal strength of the interfering wave components propagating at similar speeds. But the formation signal may not be resolved if its amplitude is much lower than the other wave components. By projecting the semblance map onto the time axis, the waveform subtraction method (Valero et al., 2003) defines the duration of casing waves and then removes them in the time domain. Afterward, the semblance processing is applied to the filtered waveform, enhancing the coherence of the formation signal. However, the formation signal will simultaneously be removed when the formation signal and casing waves overlap in the time domain. Bose et al. (2009) modify the semblance method to suppress the unwanted signal whose energy is below a given threshold value. The method may yet damage the desirable formation signal when its energy is lower than the threshold value. A time- and frequency-semblance method (Mukhopadhyay et al., 2013), using the coherence-phase information of the measured signal, could extract the dispersion curve of weak formation signals in the presence of mode interference. It can be seen that the low signal-to-noise ratio and interference with the overwhelming casing waves of the formation signal makes the cased-hole acoustic data processing a difficult task.

In the paper, we present a filtered frequency semblance (FFS) signal processing technique to enhance the coherence and signal-to-noise ratio of the formation signal. The multiple filter technique, which consists of a set of Gaussian filters, is first applied to the acoustic

[1]China University of Petroleum, Qingdao, China. E-mail: kft_upc@hotmail.com; jiangcan_upc@sina.com; syuanda@sina.com; tangxiam@aliyun.com.

Manuscript received by the Editor 27 June 2019; revised manuscript received 24 August 2019; published ahead of production 18 December 2019; published online 23 March 2020. This paper appears in Interpretation, Vol. 8, No. 3 (August 2020); p. SL1–SL8, 6 FIGS., 1 TABLE.
http://dx.doi.org/10.1190/INT-2019-0116.1. © 2020 Society of Exploration Geophysicists and American Association of Petroleum Geologists. All rights reserved.

Downloaded 07/11/21 to 120.224.221.2. Redistribution subject to SEG license or copyright; see Terms of Use at http://library.seg.org/page/policies/terms
DOI:10.1190/INT-2019-0116.1

Downloaded 07/11/21 to 120.224.221.2. Redistribution subject to SEG license or copyright; see Terms of Use at http://library.seg.org/page/policies/terms
DOI:10.1190/INT-2019-0116.1

logging data in the frequency range of interest. Afterward, we use the nth root stacking method to the filtered waveforms, obtaining a correlation function of time, frequency, and slowness. The technique significantly enhances the coherence of the formation signal, enabling the formation velocity to be determined from the peak of the function. We have examined the performance of the method through the synthetic casing-hole logging waveform data in a free-pipe borehole. More importantly, the new technique has been applied to field acoustic data sets, and the processing results demonstrate the effectiveness and robustness of the new method.

Propagation characteristics analysis of cased-hole acoustic logging

Using numerical modeling method, we first demonstrate the complicated acoustic wave phenomena in a free-pipe cased borehole. Figure 1 illustrates a cross section of the free-pipe model. A fluid annulus is inserted between the casing and cement. The cement is surrounded by an infinite formation. The parameters are shown in Table 1. The source and array receivers are located in the center axis of the borehole. Using the discrete-wavenumber integration method (Tang and Cheng, 2004), we can simulate the synthetic array acoustic waveform for the model in Figure 1.

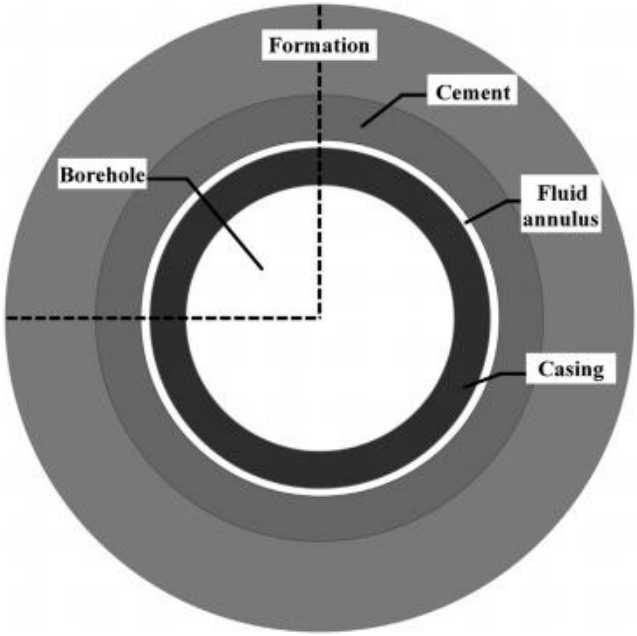


Figure 1. Cross section of the free-pipe cased-hole model.

Table 1. Parameters of the free-pipe cased-hole model.

Medium	P-velocity (m/s)	S-velocity (m/s)	Density (kg/m^3)	Radius (m)
Borehole fluid	1500	—	1000	0.075
Casing	5800	3000	7800	0.085
Fluid annulus	1500	—	1000	0.086
Cement	3000	1800	2000	0.109
Slow formation	3000	1200	2500	∞
Fast formation	4200	2400	2500	∞

Figure 2 shows the synthetic waveform for a slow formation (Table 1) and the corresponding processing results. The array receivers consist of eight receivers, and the source-to-first-receiver offset and receiver spacing are 3 and 0.1524 m, respectively. The center frequency of the source is 6 kHz. The first arrival in Figure 2a is the casing waves, followed by the formation P-wave, which is too weak to be distinguished. The largest amplitude arrival in the later portion of the waveform corresponds to the Stoneley wave. A band-pass filter between 3 and 14 kHz is first applied to the synthetic raw waveform. Then the STC method, usually used to identify the slowness of the coherent wave propagating along the array, is applied to the filtered waveform and the corresponding STC correlogram is displayed in Figure 2b. Two peaks can be seen. The left lower peak with slowness of 187 μs/m represents the casing arrival. Although the coherence of the upper right peak, corresponding to the formation P-wave, is much weaker than the lower peak, from which the formation P-slowness can also be determined as 332 μs/m. Because of the great difference of the casing waves and formation P-wave slowness, the formation signal can be measured even in a free-pipe situation and the STC method can determine the true formation slowness. However, when measuring in a fast formation, the ringing casing waves will completely obscure the formation P-wave, resulting in the failure of the conventional STC method (it can be seen from the example discussed below). Then, we will detail and illustrate the FFS method, which can tackle this problem.

The FFS method

The first part of the processing method consists of filtering acoustic waveform through the multiple filter technique (Dziewonski et al., 1969). A constant relative bandwidth Gaussian filter bank is constructed to transform the array acoustic data to a series of waveforms, whose center frequency is associated with the center frequency of Gaussian filters. The filter function with the center angular frequency ω_i is given by

$$G(\omega;\omega_i) = e^{-\eta\left(\frac{\omega-\omega_i}{\omega_i}\right)^2} \quad (1)$$

with the parameter η given by the relative bandwidth parameter Q:

$$Q = \frac{\omega_i}{\Delta\omega} = \frac{\omega_i}{\omega_h - \omega_l} = \frac{1}{2\sqrt{\frac{|\ln 0.7079|}{\eta}}}; \quad (2)$$

where $\Delta\omega$ is the filter bandwidth and ω_l and ω_h are the low- and high-frequency limits, respectively, corresponding to the −3 dB points of the Gaussian function.

Downloaded 07/11/21 to 120.224.221.2. Redistribution subject to SEG license or copyright; see Terms of Use at http://library.seg.org/page/policies/terms
DOI:10.1190/INT-2019-0116.1

The parameter η, controlling the shape of filter, is constant to a given Q. With the constant relative bandwidth Q, the bandwidth of the Gaussian filter increases with the increase of the center frequency, which is in a similar manner of wavelet transform, leading to the optimal frequency-time resolution (Li, 1997). The higher Q-value results in the narrower bandwidth of the Gauss filter (which can be seen from Figures 3a and 4c). Therefore, the higher value of Q is better when the formation velocity becomes faster.

The filtering is operated in the frequency domain by the fast Fourier transform (Cooley and Tukey, 1965), which is usually several times faster than the corresponding convolution in the time domain. For the array wave spectral data $X_n(\omega)$; $(n = 1; 2; \cdots; M)$, where M is the number of array receivers, the band-pass filter bank is applied to the data, yielding a set of waveforms with center frequency ω_i:

$$X_n(t;\omega_i) = \int_{-\infty}^{+\infty} X_n(\omega)G(\omega;\omega_i)e^{j\omega t}d\omega: \quad (3)$$

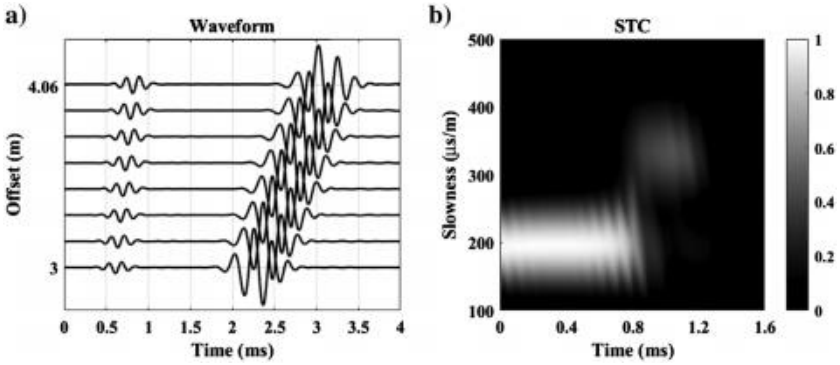


Figure 2. Modeling result and analysis of the free-pipe cased-hole model. (a) Synthetic acoustic array waveform data and (b) STC map.

The waveform data from the above filtering are used in the nth root correlation calculation. The nth root stacking method (McFadden et al., 1986) takes the nth root of the waveform. Consequently, the amplitude of the peak and trough in the waveform is preserved relative to the rest. After coherence stacking, the peak of the correlation function becomes sharper, contributing to the improvement of the slowness resolution (Smith et al., 1991). The correlation function of the nth root stack is

$$\rho(s;T;\omega_i) = \frac{\int_T^{T+T_w}\left|\sum_{n=1}^{M}|X_n[t+s(n-1)d;\omega_i]|^{\frac{1}{N}}\mathrm{sgn}\{X_n[t+s(n-1)d;\omega_i]\}\right|^N dt}{\int_T^{T+T_w}\left|\sum_{n=1}^{M}|X_n[t+s(n-1)d;\omega_i]|^{\frac{1}{N}}\right|^N dt}; \quad (4)$$

where sgn is the sign function and d denotes the receiver spacing. The 3D correlogram $\rho(s;T;\omega_i)$ is a function of arrival time T, slowness s, and center frequency ω_i of the Gaussian filter. The term N represents the power exponent, commonly set as an even number. The resolution of the function is improved from the filtering and the use of the nth root correlation.

By finding the peak value of the 3D correlogram in the time window T_w of interest and projecting the values to the frequency-slowness domain, a 2D slowness-frequency coherence (SFC) map is obtained:

$$\rho(s;\omega_i) = \mathrm{Max}_{T_w}[\rho(s;T;\omega_i)]: \quad (5)$$

In the 2D coherence map, the coherence of the desired formation signal is significantly enhanced. Stacking the peak coherence value of frequency-slowness map for the filter frequency range, we obtain a correlation function of slowness, from which the formation P-wave slowness is determined by a peak finding routine:

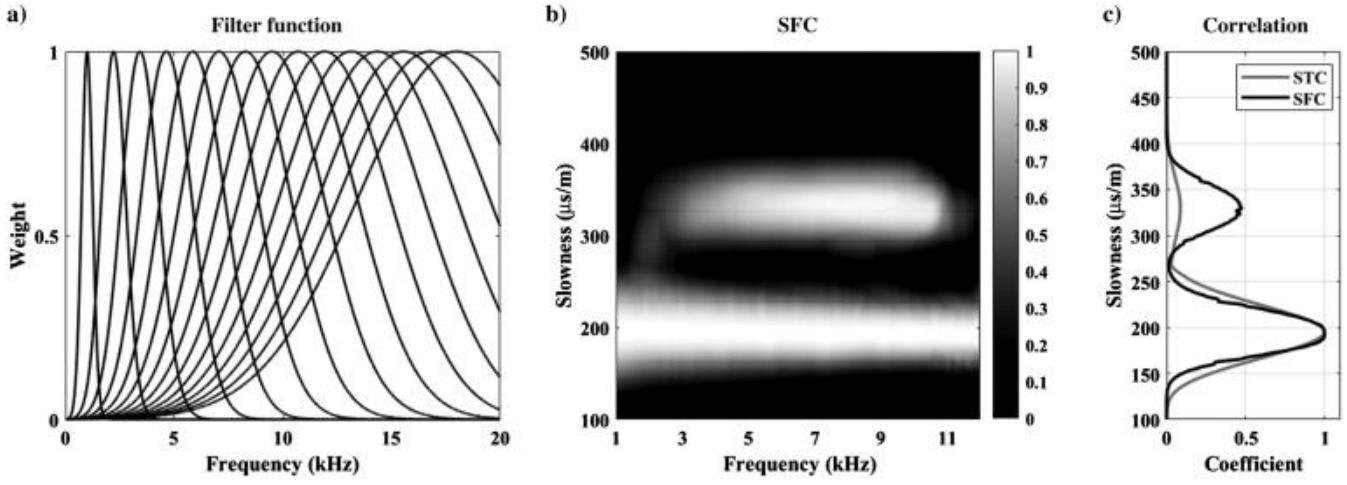


Figure 3. Testing of the FFS method using synthetic data. (a) Filter functions of the Gaussian filter bank with the relative bandwidth of 2.5. (b) SFC map calculated by the new method. (c) Correlation function derived from the STC map (the gray line) and the SFC map (the black line).

$$\rho(s) = \sum_{\omega} \rho(s; \omega_i): \quad (6)$$

Enhancing the coherence of the formation signal, the FFS method can accurately extract the formation slowness under strong casing wave interference.

Application to synthetic data

We use the above synthetic cased-hole acoustic data (Figure 2a) to demonstrate the validity of the FFS method. We first construct a Gaussian filter bank with constant relative bandwidth Q of 2.5, displayed in Figure 3a. The bandwidth of the filters decreases monotonically with the decrease of center frequency, yielding high frequency domain resolution of filters toward low frequencies (Rao and Toksöz, 2005). Applying the Gaussian filters to the array spectrum data and then processing the result using the nth root stacking, whose power exponent N is set to four, we obtain a 3D correlogram. By finding the peak of the 3D correlogram in the time window of 100–2000 μs, we get the SFC map in the frequency range of 3–14 kHz (Figure 3b). It is noticeable that this frequency range is the same as the filter band of the band-pass filter before the STC method. There are two distinct coherence events, corresponding to the casing and formation P-wave, respectively. Stacking the SFC map along the frequency axis, we obtain the correlation function (the black line) of slowness, as shown in Figure 3c. By finding the peak value, the P-slowness is determined as 334 μs/m, being identical to the modeling parameters. More importantly, the correlation function (the gray line) calculated by stacking the STC map of Figure 2b along the time axis is also plotted for comparison. The peaks of two correlation functions correspond to the same slowness, intuitively demonstrating the validity of the FFS method.

However, the strong ringing casing waves can significantly obstruct the formation P-wave in a fast formation, increasing the difficulty of formation slowness determination. To further verify the effectiveness of the new method, we model the synthetic waveform for a fast formation (Table 1) whose P-wave slowness is close to the casing waves. The other parameters are the same as Figure 2a.

Figure 4a shows the synthetic cased-hole acoustic waveform data calculated with the 8 kHz center-frequency source. The dominant wave event is the large amplitude casing waves in the early arrival. The formation P-wave trailing the casing wave is almost invisible because of the overwhelming casing waves. A standard STC and a band-pass filter between 14 and 19 kHz are applied to the array waveform data. The STC correlogram of Figure 4b shows a mixed coherence peak due to the interference of the casing and formation P-wave, from which the true formation P-wave slowness cannot be determined.

Following the same procedure as in Figure 3, we process the waveform data in Figure 4a and the relative bandwidth ($Q = 11$) of the Gaussian filter bank is displayed in Figure 4c. Figure 4d shows the SFC map in the frequency range of 14–19 kHz. We find a high-valued, well-defined

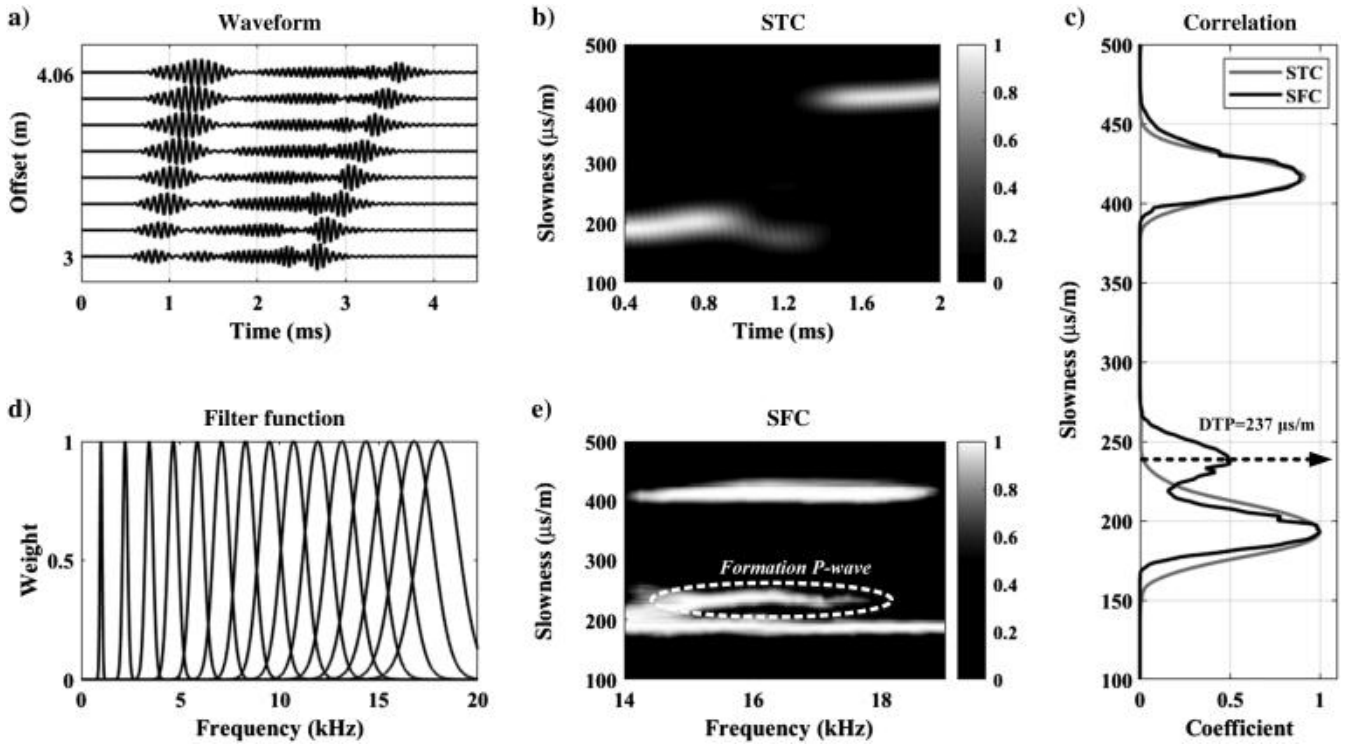


Figure 4. Processing results of the synthetic data in the fast formation. (a) Synthetic free-pipe acoustic data in fast formation. (b) STC plot from a semblance analysis of the data in (a). (c) Filter bank with relative bandwidth of 11. (d) SFC plot from the new method. (e) Correlation function derived from STC plot (the gray line) and SFC plot (the black line).

Downloaded 07/11/21 to 120.224.221.2. Redistribution subject to SEG license or copyright; see Terms of Use at http://library.seg.org/page/policies/terms
DOI:10.1190/INT-2019-0116.1

Downloaded 07/11/21 to 120.224.221.2. Redistribution subject to SEG license or copyright; see Terms of Use at http://library.seg.org/page/policies/terms
DOI:10.1190/INT-2019-0116.1

peak coherence event in the slowness range from 200 to 250 μs/m, corresponding to the formation P-wave. Compared to the STC result, the coherence of the desired formation P-wave is significantly enhanced and separated from that of the casing signal. The peaks of the casing waves and formation P-wave are mixed between 14 and 14.5 kHz because of the mode interference in the time domain. By stacking the SFC map along the frequency axis, we get the derived correlation value (the black line in Figure 4e). Unlike the STC coherence curve (the gray line), the SFC result has three distinct peaks and the corresponding slowness values are 192, 237, and 412 μs/m, respectively. The effect of mode interference in the SFC map is decreased by stacking and does not affect the extraction of formation slownesses. The lower and upper peaks, corresponding to the casing waves and formation S-wave, respectively, are consistent with the result calculated from the STC map. The middle peaks between the casing waves and formation S-wave are the formation P-wave, which cannot be determined by the conventional STC method.

The above processing results of synthetic cased-hole acoustic data demonstrate that the novel method can obviously enhance the coherence of the desired formation signal and simultaneously estimate the formation P- and S-slowness even in the free-pipe fast formation conditions.

Application to field data

In this section, we apply the FFS method to two field data sets to demonstrate its robustness and advantages in the background of the large-amplitude casing waves: one from a slow formation cased hole and another from a very fast formation.

Slow formation example

Figure 5 displays the processing results for slow-formation cased-hole acoustic data using the above-described FFS method. Panel 1 shows the variable density display of the cased-hole acoustic waveform data (only the data from first receiver are displayed). In the depth interval

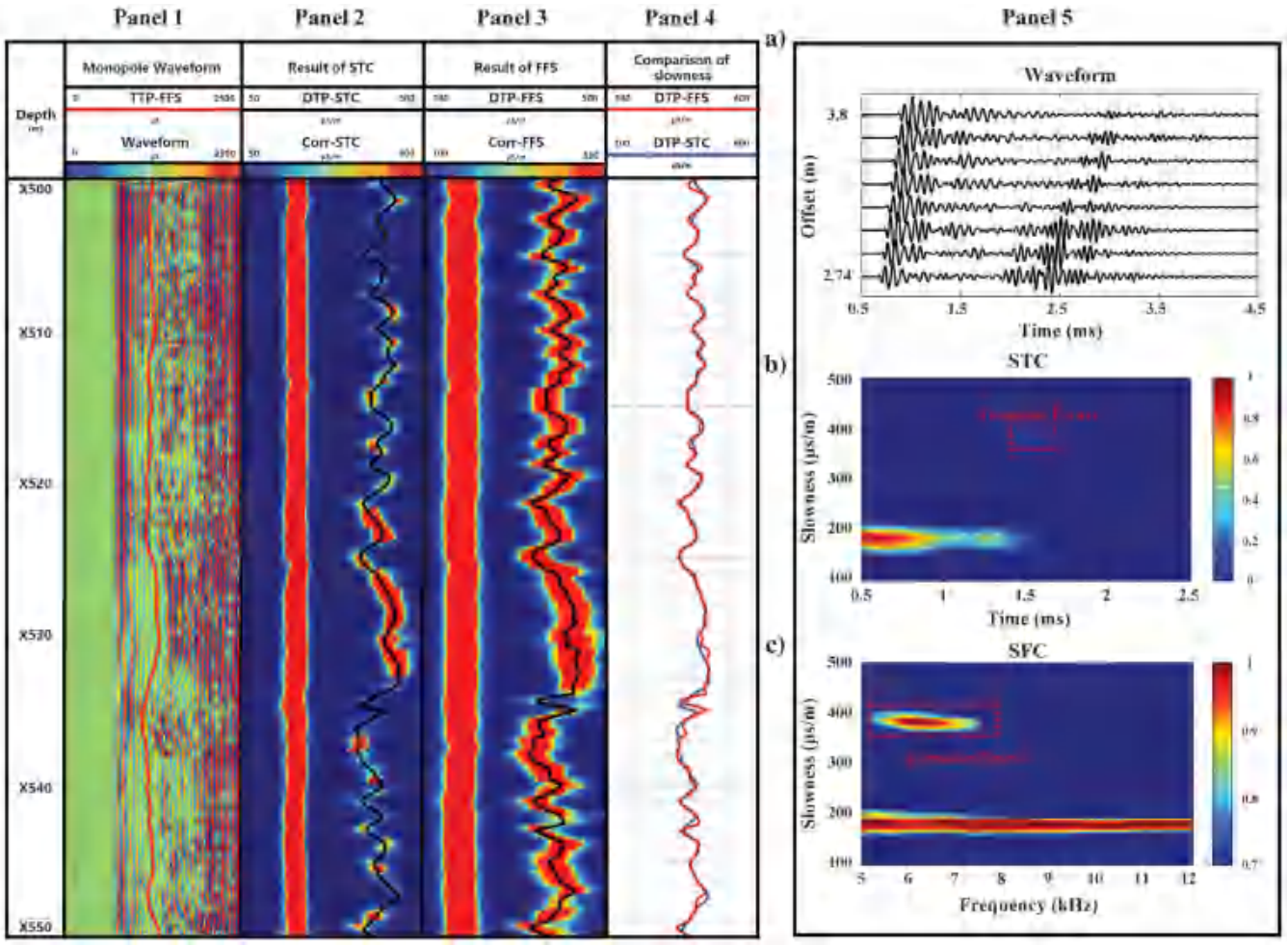


Figure 5. Processing results from an acoustic data set logged in a cased borehole with the slow formation. Panel 1 shows the waveform data and panels 2 and 3 show the STC and FFS result from the data, respectively. Panel 4 shows that the slowness from the STC (blue) method is identical with the FFS (red) method, providing the validity of the new method. Panel 5 shows processing results of (a) the measured acoustic data of the depth point of X506.2 m using (b) the STC and (c) FFS method.

between X521 and X533 m, there is a clear formation P-wave arrival, which can be easily identified, indicating the good bonding conditions (Tubman et al., 1984). The STC correlogram, as shown in panel 2, shows a traceable coherence event depicting the formation P-wave slowness variability across this section. In the other depth section, however, especially in the X500–X512 m, the large-amplitude and long-duration casing waves significantly contaminate the formation P-wave event and the corresponding coherence values are low and discontinuous, signifying the poor bonding or even possibly free-pipe situation (Tubman et al., 1986). Panel 3 gives the processing result by the new method. Obviously, the formation P-wave coherence in poorly bonded sections is remarkably improved. The extracted P-wave slowness by the FFS method (the red curve) and the STC method (the blue curve) is displayed in panel 4. The good agreement demonstrates the validity of the processing result. Moreover, the traveltime curve (the red line) in panel 1 calculated from the FFS processing P-slowness tracks the formation P-wave well.

To explain in detail the advantages of the new method, the processing results at the depth point of X506.2 m are shown in panel 5. The measured waveform in panel 5a shows a large-amplitude casing wave in the early part. The following formation P-wave is too weak to be distinguished. The coherence peak event corresponding to the formation P-wave, whose peak value is less than 0.1, is almost invisible in the STC map, as shown in panel 5b. We cannot determine the formation P-slowness through the conversional STC method. Applying the new method to the measured waveform, the derived SFC map is shown in panel 5c. The coherence value of the formation P-wave increases to 0.9, and the formation P-slowness is easily extracted as 383 μs/m.

The slow formation example, in which the formation P-wave is clearly separated from the casing arrival, provides an intuitionistic validation for the new technique. The following example of very fast formation shows that the formation slowness can be efficiently extracted even when the casing waves severely contaminate the formation P-wave.

Very fast formation example

The second example shown in Figure 6 corresponds to a cased borehole in the very fast formation. Panel 1

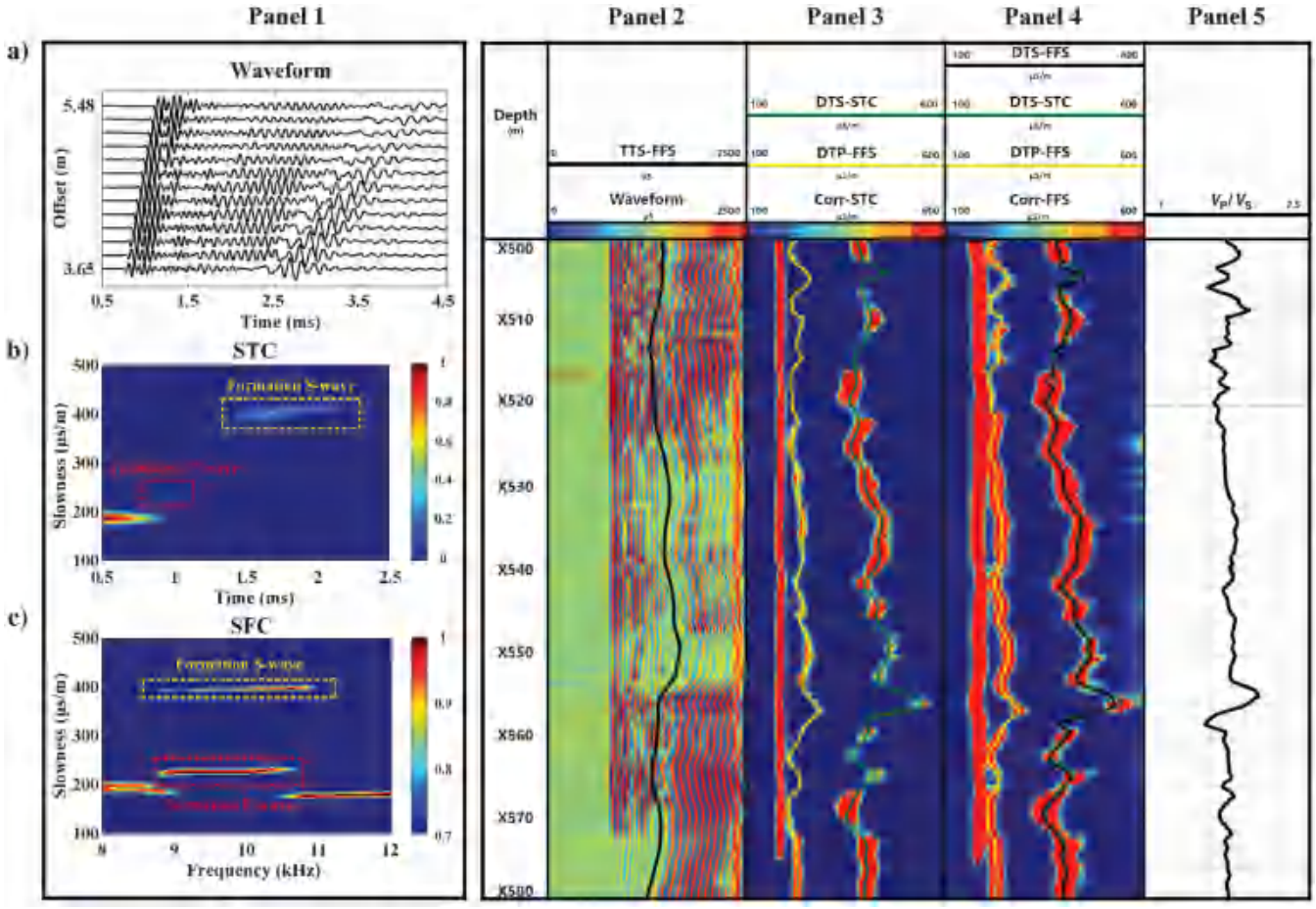


Figure 6. Processing results from an acoustic data set logged in a cased borehole with the very fast formation. Panel 1 shows processing (a) the measured acoustic data of the depth point of X510.8 m using (b) the STC and (c) FFS methods. Panel 2 shows the cased-hole waveform data. Panels 3 and 4 show the STC and FFS processing result from the data, respectively. Panel 5 shows the ratio of P- and S-velocity calculated using the corresponding slowness in panel 4.

Downloaded 07/11/21 to 120.224.221.2. Redistribution subject to SEG license or copyright; see Terms of Use at http://library.seg.org/page/policies/terms
DOI:10.1190/INT-2019-0116.1

shows the acoustic data and processing results in a representative depth of X510.8 m in the free-pipe condition. The measured cased-hole acoustic array waveform is dominated by the ringing casing waves, and the formation arrival event can hardly be detected, as shown in panel 1a. Using the STC method, the semblance correlogram is plotted in panel 1b. The coherence of the formation P-wave is discernible, and its peak value is less than 0.1, making it almost impossible to pick the slowness. Panel 1c shows the FFS processing correlogram. The coherence value of the desirable formation P-wave is significantly enhanced to reach a value of approximately 0.9. The coherence of the formation S-wave is also enhanced, and the picked S-slowness is consistent to the value obtained from the STC correlogram, which is identical to the above modeling example (Figure 4). To further verify that the obtained strong coherence is associated with the formation P-wave, the processing results of the entire depth interval are shown in other panels.

Panel 2 shows the variable density display of acoustic waveform data, in which the formation S-wave arrival can be traced but the P-wave arrival is not distinguishable from the strong casing waves. The depth interval between X576 and X580 m has good bonding because the measured waveform data show a clear formation P-wave event without casing-wave interference. The conventional STC processing result is illustrated in panel 3. Most of the interval, except for the X576–580 m section, shows that it is difficult to pick the true formation P-slowness, although picking the formation S-wave slowness (the green line) is relatively easier. Panel 4 shows the correlogram and picked slowness from the new method (the S-slowness [the green line] from panel 3 is also plotted for comparison). The new method simultaneously enhances the coherence of the P- and S-wave correlogram, enabling the slowness to be picked from them. Furthermore, the picked S-slowness (the black line) agrees with the STC result quite well, and the corresponding S-wave traveltime curve (the black line) well tracks the measured waveform in panel 2. Moreover, the P-slowness (the yellow line) is consistent with the weak coherence of the formation P-wave event and is well correlated with the S-slowness, as shown in panel 3, validating the processing results. The ratio of FFS processing P- and S-slowness is shown in panel 5, the value of which is in a range from 1.5 to 2.1 and the mean value is 1.75, being identical to the values of the well-bonded section (X578–X579 m). The above-described examples have verified the effectiveness of the FFS method in the application of field cased-hole acoustic data.

Conclusion

The formation signal usually has a weak amplitude and low coherence, due to the significant interference with the overwhelmingly large casing waves if the casing is poorly bonded or even detached with cement, leading to the great challenge for estimating the accurate formation velocity. A filter frequency semblance method based on multiple filters and correlation is present in the paper, providing an effective technique for cased-hole acoustic logging data processing. Using the multiple filter technique, the waveforms of the casing waves and formation signal are separated in the time and frequency domains. The following nth root method calculates the coherence map across the filtered array waveform, from which the formation velocity could be accurately determined. The new technique significantly enhances the coherence of the desired formation signal and improves the measurability of the formation acoustic velocity through the casing. The synthetic and field data processing examples show the validity and effectiveness of the new methods. Even in the fast formation, in which the slowness of the formation P-wave is close to that of the casing waves, the method can also detect the true formation P-slowness in the presence of serious mode interference and low signal-to-noise ratio.

Acknowledgments

This work is supported by the Strategic Priority Research Program of the Chinese Academy of Sciences (grant nos. XDA14020302 and XDA14020304) and the Fundamental Research Funds for the Central Universities (grant nos. 18CX06021A and 17CX06035).

Data and materials availability

Data associated with this research are confidential and cannot be released.

References

Bose, S., H. P. Valero, and A. Dumont, 2009, Semblance criterion modification to incorporate signal energy threshold: 79th Annual International Meeting, SEG, Expanded Abstracts, 376–380, doi: 10.1190/1.3255652.

Cooley, J. W., and J. W. Tukey, 1965, An algorithm for the machine calculation of complex Fourier series: Mathematics of Computation, 19, 297–301, doi: 10.2307/2003354.

Dziewonski, A., S. Bloch, and M. Landisman, 1969, A technique for the analysis of transient seismic signals: Bulletin of the Seismological Society of America, 59, 427–444.

Hsu, K., and A. B. Baggeroer, 1986, Application of the maximum-likelihood method (MLM) for sonic velocity logging: Geophysics, 51, 780–787, doi: 10.1190/1.1442130.

Kimball, C. V., and T. L. Marzetta, 1984, Semblance processing of borehole acoustic array data: Geophysics, 49, 274–281, doi: 10.1190/1.1441659.

Li, X. P., 1997, Decomposition of vibroseis data by the multiple filter technique: Geophysics, 62, 980–991, doi: 10.1190/1.1444204.

McFadden, P. L., B. J. Drummond, and S. Kravis, 1986, The n-th root stack: Theory, application, and examples: Geophysics, 51, 1879–1892, doi: 10.1190/1.1442045.

Mukhopadhyay, P., A. Cheng, and P. Tracadas, 2013, The differential-phase based time- and frequency-semblance algorithm for array-acoustic processing and its application to formation-slowness measurement: SPWLA.

Downloaded 07/11/21 to 120.224.221.2. Redistribution subject to SEG license or copyright; see Terms of Use at http://library.seg.org/page/policies/terms
DOI:10.1190/INT-2019-0116.1

Rao, R., and M. N. Toksöz, 2005, Dispersive wave analysis — Method and applications: Annual Report, 2005–04, Earth Resources Laboratory Industry Consortia.
Smith, M. L., C. H. Sondergeld, and J. O. Norris, 1991, The Amoco array sonic logger: SPWLA.
Tang, X. M., and C. H. Cheng, 2004, Quantitative borehole acoustic methods: Elsevier Science Publishing Company.
Tang, X. M., and D. J. Patterson, 2005, Analyzing and processing acoustic logging data for poorly-bonded cased boreholes: SPWLA.
Tubman, K. M., C. H. Cheng, and M. N. Toksöz, 1984, Synthetic full waveform acoustic logs in cased boreholes: Geophysics, 49, 1051–1059, doi: 10.1190/1.1441720.
Tubman, K. M., C. H. Cheng, and M. N. Toksöz, 1986, Synthetic full waveform acoustic logs in cased boreholes — 2: Poorly bonded casing: Geophysics, 51, 902–913, doi: 10.1190/1.1442148.
Valero, H. P., O. Skelton, and C. M. Almeida, 2003, Processing of monopole sonic waveforms through cased hole: 73rd Annual International Meeting, SEG, Expanded Abstracts, 285–288, doi: 10.1190/1.1817899.
Wang, H., and M. Fehler, 2018a, The wavefield of acoustic logging in a cased-hole with a single casing — Part 1: A monopole tool: Geophysical Journal International, 212, 612–626, doi: 10.1093/gji/ggx437.
Wang, H., and M. Fehler, 2018b, The wavefield of acoustic logging in a cased-hole with a single casing — Part 2: A dipole tool: Geophysical Journal International, 212, 1412–1428, doi: 10.1093/gji/ggx475.

Biographies and photographs of the authors are not available.

Downloaded 07/11/21 to 120.224.221.2. Redistribution subject to SEG license or copyright; see Terms of Use at http://library.seg.org/page/policies/terms
DOI:10.1190/INT-2019-0116.1

唐晓明,祁晓,张博等. 2015. 基于波干涉原理的套管井阵列声波处理方法及其应用. 地球物理学报,58(4):1447-1457,doi:10.6038/cjg20150430.

Tang X M, Qi X, Zhang B, et al. 2015. An interference-based array signal processing technique for cased-hole acoustic logging and applications. *Chinese J. Geophys.* (in Chinese),58(4):1447-1457,doi:10.6038/cjg20150430.

基于波干涉原理的套管井阵列声波处理方法及其应用

唐晓明, 祁晓, 张博, 李盛清, 苏远大

中国石油大学(华东)地球科学与技术学院, COSL-UPC 声学测井联合实验室, 青岛 266580

摘要 在套管井测井中,沿着钢管产生的拉伸波(即管波)在声波数据中产生很强的干扰,使得地层声速的提取十分困难. 基于管波与地层声波的干涉原理,本文提出了一种声波处理方法. 管波的传播特征是已知的,且管波和地层波都由同一声源激发,因此,可以用管波来改造测井声波数据. 对改造后数据采用希尔伯特变换作进一步处理,得到与地层信息相关的解析信号,从该信号中即可提取出地层声速. 通过对理论模拟数据的处理和现场测井数据的应用,验证了新方法的正确性和有效性.

关键词 套管井测井; 管波; 波干涉; 希尔伯特变换

doi:10.6038/cjg20150430 **中图分类号** P631 **收稿日期** 2014-08-20,2014-12-18 **收修定稿**

An interference-based array signal processing technique for cased-hole acoustic logging and applications

TANG Xiao-Ming, QI Xiao, ZHANG Bo, LI Sheng-Qing, SU Yuan-Da

COSL-UPC Allied Borehole Acoustic Laboratory, School of Geosciences & Technology, China University of Petroleum, Qingdao 266580, *China*

Abstract In cased boreholes, acoustic logging waveforms are often contaminated by casing waves, making it difficult to extract formation acoustic velocity from the acoustic data, especially when the casing is poorly bonded with formation. Various methods have been tested to solve the problem with only limited success, due to the weak signal amplitude and poor coherence compared to the dominant casing waves. The new technique of this paper utilizes the modulation of wave power spectrum caused by the interference of casing and formation waves. The advantage of the technique is its ability to suppress the coherence of the casing wave and significantly enhance the coherence of the formation wave, allowing for determining the formation acoustic velocity from the latter wave signal. For an acoustic logging instrument composed of an array of equally spaced receivers, the waveform data containing casing and formation waves are windowed and transformed into frequency domain to obtain the power spectrum for each receiver in array. The average power spectrum of the array is calculated and subtracted from the power spectrum of each receiver, yielding a residue power spectrum. The residue spectrum and its Hilbert transform form the real and imaginary parts of an analytical signal, which, after transformation into time domain, results in a new waveform array data whose phase moveout across array is entirely

基金项目 国家重点基础研究发展计划(2014CB239006)资助.

作者简介 唐晓明,1955 年生,男,教授,多年来一直致力于地球物理(特别是声波)测井、岩石物理学、地震波传播及测量等方面的研究和技术开发工作. E-mail:tangxiam@aliyun.com

?1994-2015 China Academic Journal Electronic Publishing House. All rights reserved. http://www.cnki.net

controlled by the velocity of the formation wave. Processing the new array data using an array velocity analysis method, e. g., the slowness-time-coherence (STC) method, yields the formation slowness behind the steel casing.

The new technique was tested on synthetic waveform data calculated for a poorly bonded casing. The synthetic data processing example shows that the technique effectively cancels the coherence of the casing signal and significantly enhances the coherence of the desired formation signal. The technique has also been applied to processing field acoustic logging data acquired in cased boreholes. In depth intervals with poor bonding conditions, the STC result of the new technique shows that the casing wave coherence almost disappears and the formation wave coherence is significantly enhanced. Further, the validity of the velocity curve is verified by comparing it with its counterpart from the raw data. The much improved result in the poorly bonded section indicates the ability of the new technique to extract and enhance weak formation signals in the presence of strong casing wave interference.

Keywords Cased-hole logging; Casing wave; Wave interference; Hilbert transform

1 引言

在石油测井中,套管井测井占有相当比例(吴奇等, 2011).为了对已有油田挖潜改造,需要在套管井中进行声波测井(陶宏根等, 2004).在这种情况下,沿着钢管传播的波(声学上称为拉伸波,以下统称为管波)有时会严重地影响对地层声波信号的测量,这在套管与地层胶结不好时尤为如此(李整林等, 2001;张宏兵等, 2009).为了在上述情况下获得地层信息,测井界已尝试了多种方法(Block 等, 1991;朱云生, 1994; Tang and Patterson, 2005;陈雪莲等,2015).现代声波测井仪器采用阵列接收方式.阵列数据的处理常用波形相关法(又称为时间慢度相关法 STC,见 Kimball and Marzetta, 1984),该方法根据波在阵列中的相干性对数据进行时间和慢度扫描,以确定不同声波信号(如纵波、横波和斯通利波等)的慢度和到时.但是,在地层声波信号受管波干扰的情况下,波形相关法很难将二者区分开来. Hsu 和 Baggeroer (1986)等曾尝试使用最大似然法来增强地层信号的分辨率,但增强的效果取决于地层波信号与管波信号的相对幅度,因此,该方法不能提取弱信噪比、低相关性的地层信号.为了提取地层信号,必须提高其相对于管波信号的信噪比. Valero 等(2003)提出了另一种方法,通过隔离先于地层波到达的管波信号,并且从原波形中将其扣除,使地层信号在阵列波形中的相关性得到增强,再通过波形相关法处理把地层信息提取出来,然而,当地层信号与管波信号在时间上重叠时,该方法就得不到好的处理结果. Bose 等(2009)提出了能量阈值法,该方法是对波形相关法的一种改进,根据管波与地层波的波形能量设置阈值,低于该值的波形相关性为零,高于该值的波形相关性则采用波形相关法求得,最终得到能量大于能量阈值的波形的慢度,但当管波能量比地层波能量强时,也无法得到地层信息.通过对以上一些套管井声波处理方法的描述,我们看出,应该着重于地层波与管波信号在时间上重叠及二者之间的干涉来从测井数据中提取地层信息.

本文提出了一种新的处理方法——波形干涉法,来解决上述问题.该方法是基于管波与地层波的干涉原理,干涉结果使波形数据的功率谱在阵列中产生有规律的调制,将此调制分量用希尔伯特(Hilbert)变换(陆光华等,2005)得到一种解析信号,信号的相位由地层波速控制,通过阵列波形相关法处理该信号,就可以获得地层波速.我们用理论数据验证了该方法的正确性,将此方法应用于套管井测井数据处理,可以在套管胶结很差的情况下有效地提取地层波速.本文对阵列信号的特殊处理提出了一种新的理论和方法,为套管井中的声波测井提供了一项有效的处理技术.

2 自由套管中测井声波的传播特征

套管与地层耦合不好的情况叫做自由套管情况(Tubman et al., 1986),这时井内声波特征主要由套管及流体控制.我们用测井声波的数值模拟来说明这种情况下波的传播特征.如图 1 的模型所示,模

?1994-2015 China Academic Journal Electronic Publishing House. All rights reserved. http://www.cnki.net

型中井眼内充满流体，井外套管及套管外面的水泥环用井和无限大地层介质之间的同心圆柱层来模拟；其中，在套管和水泥环之间含有一个流体薄层来模拟自由套管情况，模型参数见表 1. 模拟例子中假设点源和接收阵列都位于井中心轴处的流体中. 声波波形理论模拟的方法和步骤参见唐晓明和郑传汉(2004). 我们模拟了自由套管井在慢速地层中的声波测井波形，计算中所用声源的中心频率为 6 kHz. 数值模拟的波形及波形处理结果如图 2 所示.

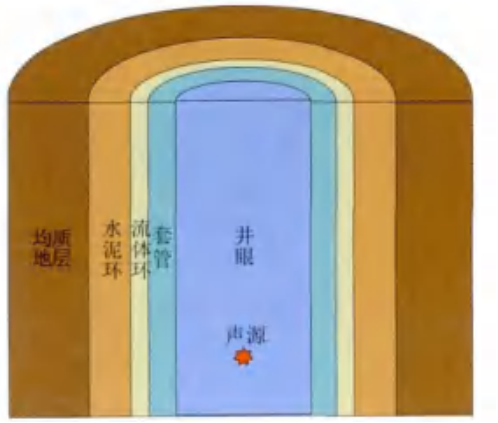


图 1　自由套管井模型

Fig. 1　Free-pipe acoustic model used for synthetic waveform modeling

表 1　模型计算参数

Table 1　Model calculation parameters

介质参数	纵波速度 ($m \cdot s^{-1}$)	横波速度 ($m \cdot s^{-1}$)	密度 ($kg \cdot m^{-3}$)	半径 (m)
井眼流体	1500	—	1000	0.075
套管	5800	3000	7800	0.085
流体环	1500	—	1000	0.086
水泥环	3000	1800	2000	0.109
慢速地层	3000	1200	2500	∞
快速地层	4200	2400	2500	∞

图 2a 为在慢速地层中自由套管井声波测井的数值模拟波形，在波形中可以清晰地看到首先到达的管波和跟随其后的地层纵波. 采用波形相关法对该波形进行处理得到时间-慢度相关图. 如图 2b 所示，由下而上，相关图中的第一个极值对应的慢度值为 185 μs/m，对应于管波的慢度；第二个极值对应的慢度值为 334 μs/m，为模型中地层纵波的慢度；第三个极值是套管中的 Stoneley 波(唐晓明和郑传汉，2004).

以上模拟结果表明，即便是在地层与套管解耦的自由套管情况下，测井声波中也包含有来自地层的声波信号. 对慢速地层模型，地层波与管波因速度差别较大可以加以识别(这将为以下提出的理论和方法提供直观的例证)，但在快速地层中，地层波与管波混叠在一起很难识别(可参见稍后图 4 的例子). 为此，我们提出一种波形干涉法来提取地层的声波信号.

3　波形干涉法的基本理论及方法验证

3.1　基本理论

设测井仪器的接收阵列由 N 个间距为 d 的接收器组成. 在所关心的时间范围内，波形数据主要由管波和地层纵波组成. 管波在阵列中传播的慢度(即速度的倒数) s_T 及其在第一个接收器上的到达时间 t_0^T 是已知的(从图 2b 的相关图中的第一个极值可得：$s_T = 185\ \mu s/m$，$t_0^T = s_T \cdot L$，其中 L 为源到第一

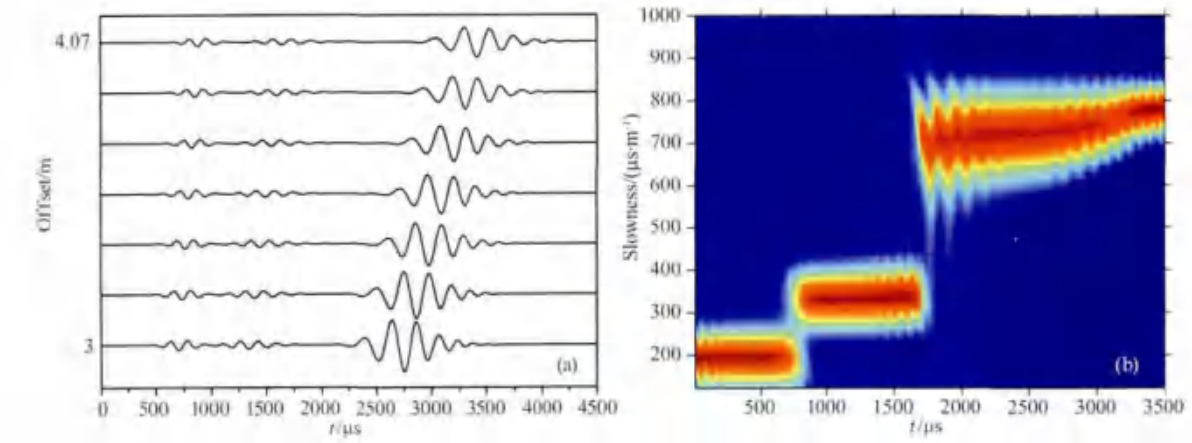


图 2　(a) 在慢速地层中，自由套管井声波测井的理论模拟波形；(b) 图(a)中波形的时间-慢度相关图

Fig. 2　(a) Calculated synthetic array waveform in a slow formation with a free-pipe condition; (b) STC analysis result for the data.

?1994-2015 China Academic Journal Electronic Publishing House. All rights reserved.　http://www.cnki.net

接收器的距离). 对管波和地层纵波组成的双波波形,第 n 个接收器上的波形数据 $D_n(t)$ 可以表示为

$$D_n(t) = W_n^{\mathrm{T}}[t - t_0^{\mathrm{T}} - s_{\mathrm{T}}(n-1)d] + W_n^{\mathrm{f}}[t - t_0^{\mathrm{f}} - s_{\mathrm{f}}(n-1)d]. \quad (1)$$

对(1)式做傅里叶变换,其在频域内的表达式如下:

$$D_n(\omega) = \| W_n^{\mathrm{T}}(\omega) \| \mathrm{e}^{-\mathrm{i}\omega[t_0^{\mathrm{T}} + s_{\mathrm{T}}(n-1)d]} + \| W_n^{\mathrm{f}}(\omega) \| \mathrm{e}^{-\mathrm{i}\omega[t_0^{\mathrm{f}} + s_{\mathrm{f}}(n-1)d]}, \quad (2)$$

其中,t_0^{f} 是地层纵波波至到时,s_{f} 是地层纵波的慢度,ω 是圆频率,$W_n^{\mathrm{T}}(\omega)$ 和 $W_n^{\mathrm{f}}(\omega)$ 分别为接收器 n 上记录的管波和地层纵波的波谱. 由于管波和地层纵波都由同一声源激发,因此可假设二者的波谱在感兴趣的频率范围内具有相似性,可以用常数 r 来表示地层纵波与管波的波谱比值.

令 $\| W_n^{\mathrm{T}}(\omega) \| = \| W(\omega) \|$,则有

$$\| W_n^{\mathrm{f}}(\omega) \| = r \cdot \| W(\omega) \|, \quad (3)$$

将(3)式代入到(2)式中,计算波形的功率谱,其表达式如下:

$$P_n(\omega) = \| W(\omega) \|^2 \{1 + r^2 + 2r \cdot \cos[\omega(\delta t_0 + \delta s(n-1)d)]\}, \quad (4)$$

式中 $\delta t_0 = t_0^{\mathrm{f}} - t_0^{\mathrm{T}}$,$\delta s = s_{\mathrm{f}} - s_{\mathrm{T}}$. 将(4)式移项得到

$$(1 + r^2) \| W(\omega) \|^2 = P_n(\omega) - 2r \| W(\omega) \|^2 \cos[\omega(\delta t_0 + \delta s(n-1)d)]. \quad (5)$$

将上式对 n 个接收器求平均,注意到余弦函数的相位在各接收器互不相同,叠加后相互抵消,作为近似,可以令该项的平均值为零,从而得到平均功率谱:

$$\bar{P}(\omega) = \frac{1}{N}\sum_{n=1}^{N} P_n(\omega) = (1 + r^2) \| W(\omega) \|^2, \quad (6)$$

从接收器 n 的功率谱中减去平均功率谱可得到下式:

$$R_n(\omega) = P_n(\omega) - \bar{P}(\omega) = 2rW(\omega)^2 \cos(\omega[\delta t_0 + \delta s(n-1)d]). \quad (7)$$

由(7)式可以看出,第 n 个接收器上波形的功率谱与平均功率谱之差 $R_n(\omega)$ 是信号加载谱(即源功率谱 $\| W(\omega) \|^2$)与管波和地层纵波干涉后的相位调制谱 $\cos[\omega(\delta t_0 + \delta s(n-1)d)]$ 两者的乘积. 该调制谱包含了管波与地层波相互干涉的信息,这种干涉对差谱 $R_n(\omega)$ 所组成的数据阵列产生有规律的调制. 事实上,(4)式中的阵列功率谱 $P_n(\omega)$ 中也含有该相位调制谱. 采用 $P_n(\omega) - \bar{P}(\omega)$ 得到的差谱 $R_n(\omega)$,而不是 $P_n(\omega)$ 本身进行处理是为了使这种调制作用更加突出(可参见稍后的图 3b). 无论计算差谱时(6)式中的近似是否严格成立,这种处理方法总是有效的,其正确性在以下的理论和实际数据处理中得到了进一步的验证. 下面我们对差谱 $R_n(\omega)$ 中的调制信号作进一步处理,将地层声速信息提取出来.

对(7)式做希尔伯特变换,假设管波和地层纵波都没有频散,即 δs 与频率无关,变换后得到 $I_n(\omega)$:

$$I_n(\omega) = \mathrm{Hilbert}\{R_n(\omega)\} = 2r \| W(\omega) \|^2 \sin(\omega[\delta t_0 + \delta s(n-1)d]), \quad (8)$$

其中,$\mathrm{Hilbert}\{\cdot\}$ 表示对括弧 $\{\cdot\}$ 中的函数取希尔伯特变换. 将(7)式与(8)式合并组成一个复数解析信号谱:

$$A_n(\omega) = R_n(\omega) + \mathrm{i} \cdot I_n(\omega) = 2r \| W(\omega) \|^2 \mathrm{e}^{\mathrm{i}\omega[\delta t_0 + \delta s(n-1)d]}. \quad (9)$$

利用已知的管波波至到时 t_0^{T} 及其慢度 s_{T} 代入,再用平均振幅谱(即 $\| \bar{P}(\omega) \|^{1/2}$)归一化,得到

$$A_n^{\mathrm{f}}(\omega) = \frac{A_n(\omega)}{\sqrt{\| P(\omega) \|}} \mathrm{e}^{\mathrm{i}\omega[t_0^{\mathrm{T}} + s_{\mathrm{T}}(n-1)d]} = \frac{2r}{\sqrt{1 + r^2}} W(\omega) \mathrm{e}^{\mathrm{i}\omega[t_0^{\mathrm{f}} + s_{\mathrm{f}}(n-1)d]}. \quad (10)$$

由(10)式可以看出,得到的波谱 $A_n^{\mathrm{f}}(\omega)$ 的相位中只含有与地层波有关的信息,将该波谱用傅里叶逆变换到时域,得到如下时域信号:

$$A_n^{\mathrm{f}}(t) = F^{-1}\{A_n^{\mathrm{f}}(\omega)\} = H[t - t_0^{\mathrm{f}} - s_{\mathrm{f}}(n-1)d], \quad (11)$$

其中 $H(t)$ 为(10)式中振幅谱的逆变换. 上述时域信号的相位,即在阵列接收器上的相移完全由地层纵波的慢度 s_{f} 所控制,对此信号用阵列波形相关法处理便可以提取出地层纵波慢度 s_{f}.

利用复数解析信号谱 $A_n(\omega)$ 和平均功率谱 $\bar{P}(\omega)$,可以得到地层纵波与管波的波幅比值 r,如下式:

$$\frac{\| A_n(\omega) \|}{\bar{P}(\omega)} = R = \frac{2r}{1 + r^2}. \quad (12)$$

对阵列数据,R 应取上式波谱比在频域和阵列中的平均值. 利用(12)式得到的 r 值,我们可以评估波形干涉法的适用性. 若 r 值太小,说明地层信号很弱,提取的时差值可能不可靠;反之,若 r 值远大于 1,说明地层信号较强,套管与地层耦合良好,不需要用该方法处理.

3.2 方法验证

我们用图 2 中自由套管的测井声波模拟数据来说明以上方法的处理步骤. 对图 2a 中的波形在 0~2 ms 的时段内取窗,所得阵列波形(图 3a)只含有管

?1994-2015 China Academic Journal Electronic Publishing House. All rights reserved. http://www.cnki.net

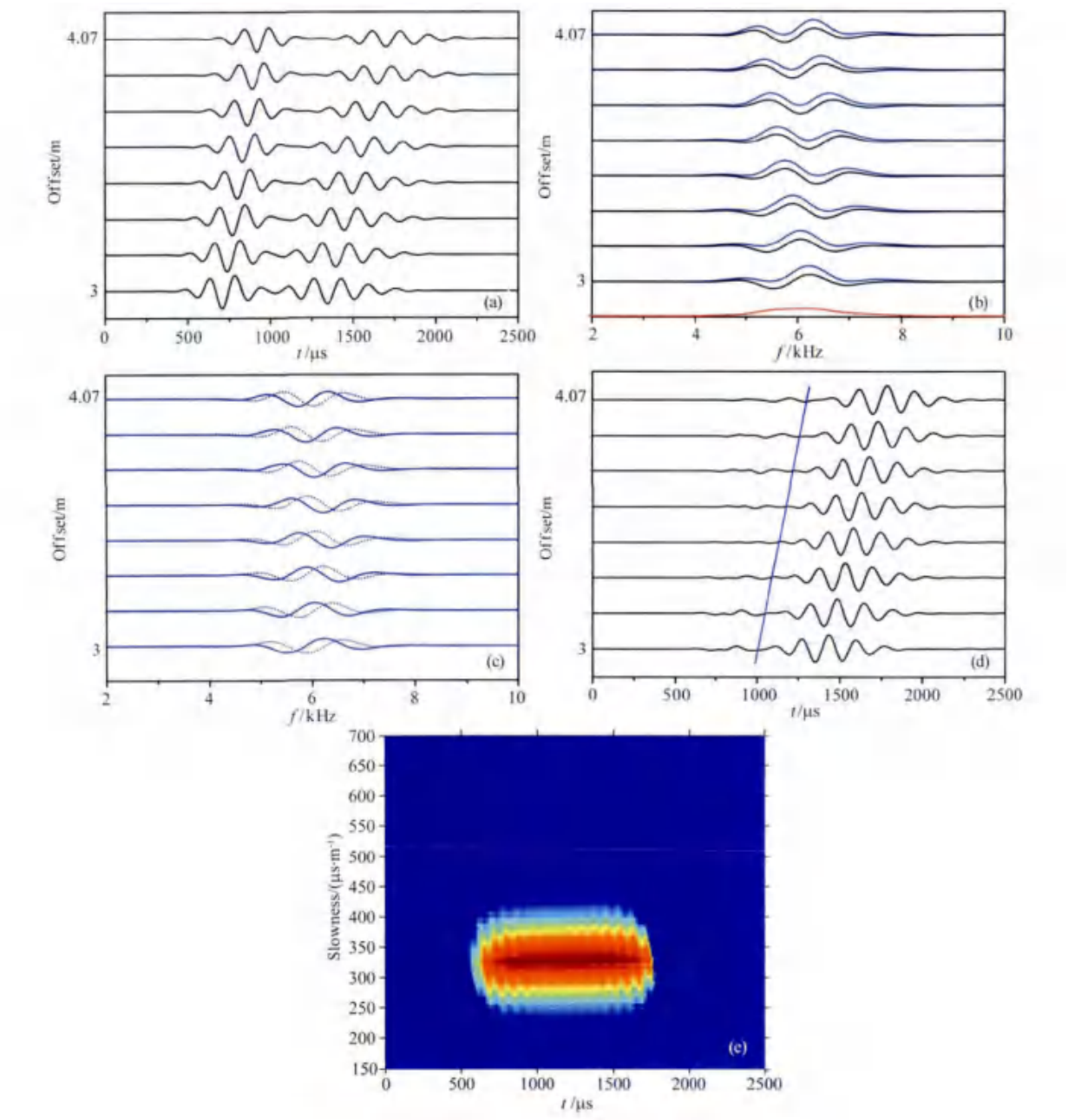


图 3　(a) **图 2a 中波形数据在** 0～2 ms **时段内取窗后的波形**;(b) **图**(a)**中波形的功率谱**(**蓝色曲线**)、**平均功率谱**(**红色曲线**)**和差谱**(**黑色曲线**);(c) **对差谱进行** Hilbert **变换后所得频谱** $A_n(\omega)$ **的实部**(**实线**)**和虚部**(**虚线**);(d) **采用波形干涉方法处理图**(a)**中波形后的新阵列波形**;(e) **图**(d)**中波形的时间-慢度相关图**

Fig. 3　(a) Windowed array waveform containing only pipe and formation P-waves; (b) Power spectrum (blue curve), average power spectrum (bottom red curve), and the difference spectrum (black curve) for the data in (a); (c) The real (solid line) and imaginary (dotted line) part of the complex analytical signal $A_n(\omega)$; (d) Extracted formation signal; (e) STC analysis result for the data in (d)

波和地层波,即为(1)**式中的** $D_n(t)$. **将图** 3a **的波形数据做傅里叶变换得到的阵列功率谱** $P_n(\omega)$, **如图** 3b **中的蓝色曲线所示. 图** 3b **中的红色曲线为** $P_n(\omega)$ **求和得到的平均功率谱** $\bar{P}(\omega)$. **二者之差是图** 3b **中黑色曲线所表示的差谱** $R_n(\omega)$. **管波和地层波的干涉在功率谱** $P_n(\omega)$ **和差谱** $R_n(\omega)$ **中产生调制现象,这种调制在阵列中呈有规律的变化. 图** 3c **中显示了差谱** $R_n(\omega)$ (**实线**)**和其希尔伯特变换结果** $I_n(\omega)$ (**虚线**),**将二者组成复数解析信号,再经**(10)**和**(11)**式的运算后得到图** 3d **中的波形. 与图** 3a **原始波形中的地层波相比较,图** 3d **中的波即为地层纵波. 虽然地层波之前还有残余的管波(这种残**

?1994-2015 China Academic Journal Electronic Publishing House. All rights reserved.　http://www.cnki.net

差主要是由(6)式中的近似产生的,只有在接收器数目 N 很大时(6)式才严格成立),但残余的管波完全没有相关性. 图 3e 为图 3d 波形数据的时间-慢度相关图,图中只存在对应于地层纵波的极值,相关值为 0.9 左右,且其慢度值与模型中慢速地层的纵波慢度相等. 利用(12)式计算得到的地层与管波的波幅比值 r 为 0.55,这与图 3a 中二者波形幅度的相对大小吻合.

在上述例子中,利用慢速地层中管波与地层波的分离,我们可以直观地验证波形干涉法所提取的地层纵波信息的正确性. 下面我们证明,当管波与地层波重叠时,该方法仍能正确提取地层信息.

为了进一步验证波形干涉方法在自由套管井声波测井中的应用效果,本文模拟了在快速地层(参见表 1)中自由套管井的声波测井波形,计算所用声源中心频率为 12 kHz 时,数值模拟的波形及波形处理结果如图 4 所示.

图 4a 为在快速地层自由套管井中声波测井的数值模拟结果,波形的初至部分主要是管波的贡献,地层纵波被淹没其中. 采用波形相关法对波形进行分析得到时间-慢度相关图,如图 4b 所示. 由下而上,相关图中第一个极大值对应的是套管波的慢度值 185 μs/m. 由于地层纵波与振幅很强的管波混叠在一起,图中很难看到地层纵波信息. 采用波形干涉方法处理上述波形,图 4c 为处理后的波形,图 4d 为该波形的时间-慢度相关图. 图 4c 中管波被有效地压制,使得原本较弱的地层纵波变得较明显,相应地,图 4d 中地层纵波的相关性大大增强,相关值在 0.9 左右,且其慢度值为 240 μs/m,与模型中的地层纵波慢度一致. 利用(12)式计算得到的地层与管波的波幅比值 r 为 0.26,说明地层信号较弱,并且与管波相混难以识别. 上述理论模拟数据处理结果表明该方法能够有效地压制管波,消除管波的相关性,显著地增强地层波的相关性,在理论上证明了波形干涉法在胶结不好的套管井中提取地层信息的有效性.

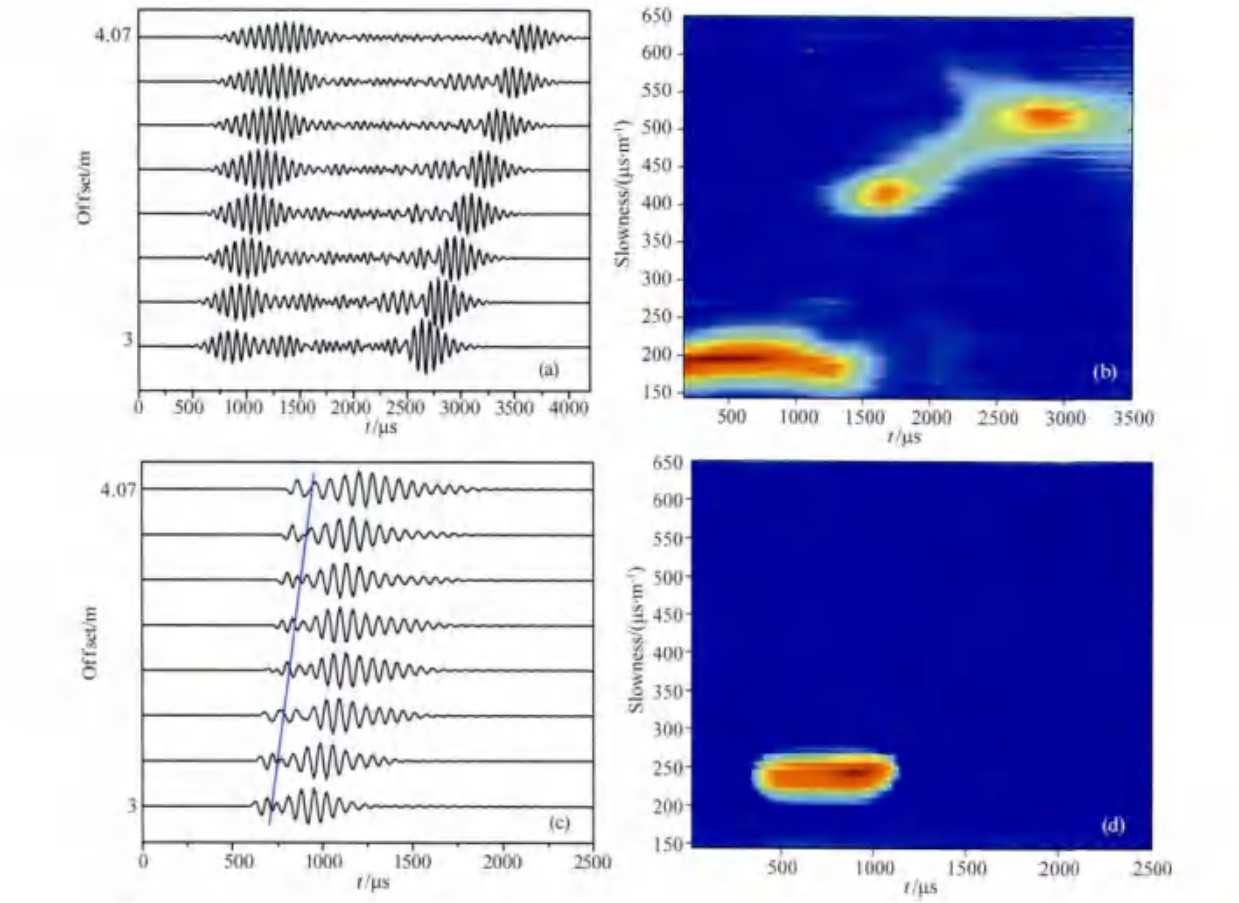


图 4 (a)在快速地层中,自由套管井声波测井的理论模拟波形;(b) 图(a)中波形的时间-慢度相关图;(c) 采用波形干涉方法处理图(a)中波形后的新阵列波形;(d) 图(c)中波形的时间-慢度相关图

Fig. 4 (a) Calculated synthetic array waveform in a fast formation with a free-pipe condition; (b) STC analysis result for the data in (a); (c) Extracted formation signal from the data; (d) STC analysis result for the extracted data

?1994-2015 China Academic Journal Electronic Publishing House. All rights reserved. http://www.cnki.net

4　现场资料处理实例

4.1　实例 I

为初步验证波形干涉方法在现场套管井测井中的应用效果,本文给出了某一中速地层的套管井现场数据处理实例. 首先给出了该数据中套管胶结不好的某一深度上的阵列波形、原始数据对应的时间-慢度相关图及波形干涉方法的处理结果,如图 5 所示.

图 5a 为原始阵列波形,图 5b 是该波形数据的时间-慢度相关图,由下而上,相关图中第一个极大值对应的是管波的慢度值 185 μs/m. 第二个相关性较差的极值对应的慢度值约为 315 μs/m,为地层纵波慢度,其余的两个波依次为地层横波和斯通利波. 采用波形干涉方法处理该波形,图 5c 为处理后的波形,图 5d 为该波形的时间-慢度相关图. 图 5c 中地层纵波幅度大大增强,管波虽有残余,但其在图 5d 中的相关值几乎为 0,地层纵波的相关值在 0.9 左右,且其慢度值与图 5b 中的地层纵波慢度一致. 地层波与管波的波幅比值为 0.3. 上述处理结果表明在管波干涉情况下,该方法能够有效地提取地层纵波.

将上述现场套管井测井资料采用波形干涉方法进行处理,套管井中的声波测井数据和处理结果如图6所示. 图中第一道为套管井中声波测井数据的变密度图,在深度区间 2048～2053 m 和 2065～2072 m 内,可以看到清晰的地层纵波波至,并且管波幅度很低,由此可知,这两个深度段处的固井质量良好. 在其他深度段,尤其是在 2053～2063 m 的深度段内,管波幅度特别强,地层纵波幅度相对较低,固井质量差. 在第二道的联合相关图中,胶结差井段地层纵波的相关性很低,而固井质量好的井段相关性很好,可以直接提取地层纵波慢度. 采用新方法处理该井段数据,显著地改善了胶结差井段地层纵波的相关性. 第三道为处理后波形数据的联合相关图以及提取的声波时差曲线,在该联合相关图中,管波的相关性被有效地消除,地层纵波的相关性显著增

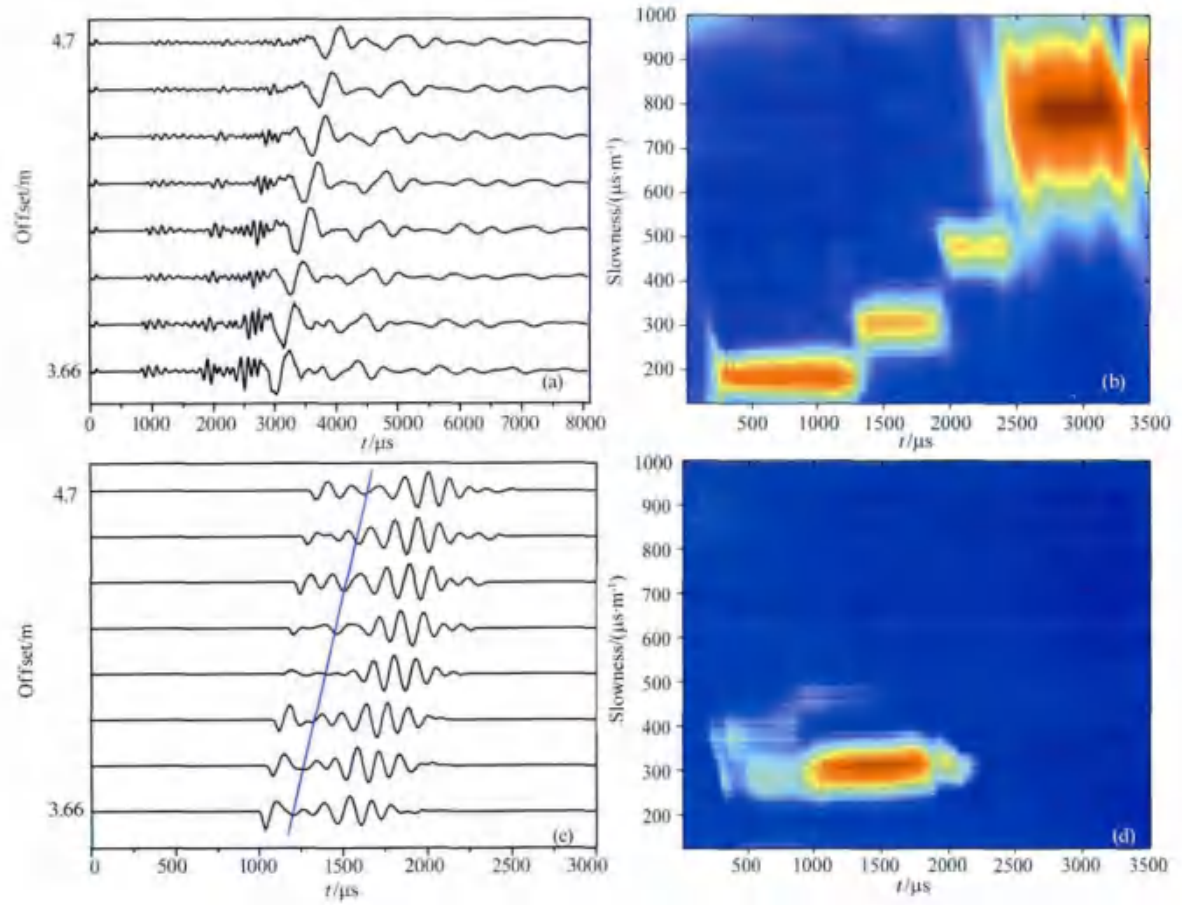


图 5　(a) 套管胶结不好的某一深度上的原始阵列波形;(b) 图(a)中波形的时间-慢度相关图;(c) 采用波形干涉方法处理图(a)中波形后的新阵列波形;(d) 图(c)中波形的时间-慢度相关图

Fig. 5　(a) Array data from a poorly-bonded cased-hole; (b) STC analysis result for the data; (c) Extracted formation signal from the data; (d) STC analysis result for the data in (c)

?1994-2015 China Academic Journal Electronic Publishing House. All rights reserved.　http://www.cnki.net

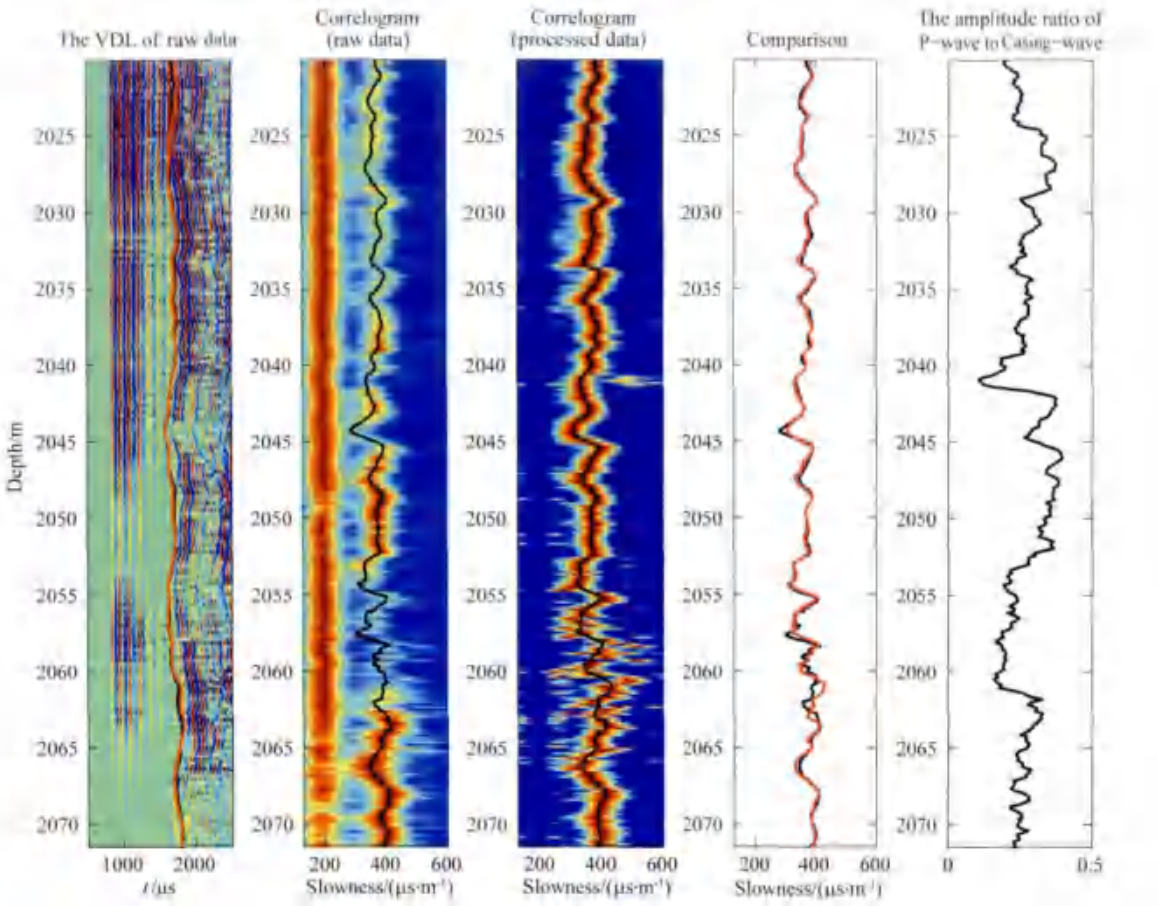


图 6 某一中速地层的套管井测井数据处理结果图. 从左到右:第一道为原始波形数据;第二道为原始数据联合相关图;第三道为采用波形干涉法得到的地层纵波的联合相关图;第四道为采用现有方法(黑线)和新方法(红线)所得地层纵波时差的对比;第五道为地层纵波与管波的波幅比值

Fig. 6 Processing results from an acoustic data set logged in a cased borehole with various cement bond conditions. From left to right: Panel 1 shows the waveform data; panel 2 is the STC result from the data; panel 3 is the STC result using the new technique; panel 4 shows the comparison of the slowness from the existing (black) and new (red) techniques; panel 5 shows the formation P- to casing wave amplitude ratio

强. 在第四道中,将第二道和第三道中的地层纵波时差曲线(其中黑色曲线和红色曲线分别为第二道和第三道中的声波时差曲线)进行对比,两条曲线吻合的很好,验证了处理结果的正确性. 利用时差曲线得到的地层纵波波至曲线与第一道中波形变密度图中的地层纵波波至吻合得很好,并且,在第五道中,地层纵波与管波的波幅比值的变化情况与第一道中的这两种波波幅的相对变化情况具有很好的一致性,比值在 0.25 左右变化,说明处理方法的适用性和处理结果的正确性. 这一现场数据处理例子中,当管波与地层波有较大分离时,可以直观地验证该方法提取地层波的有效性. 下面的例子说明,当管波与地层波重叠时,也可以有效提取地层波信息.

4.2 实例Ⅱ

为进一步验证波形干涉方法在胶结不好的快速地层套管井中的应用效果,本文给出了一现场资料处理实例,井段为 3990～4027 m. 首先给出了胶结不好的 3991.2 m 深度处的实测波形、对应的时间-慢度相关图及波形干涉方法的处理结果,如图 7 所示.

图 7a 为原始阵列波形,阵列中管波波幅很强,相关性很好,而地层纵波与管波混叠在一起,难以识别,相关性很差,如图 7b 的时间-慢度相关图所示,图中管波的相关值在 0.8 以上,而地层纵波的相关值低于 0.4. 采用波形干涉方法进行处理,图 7c 为处理后的波形,其中纵波幅度和相关性都明显增强,地层波与管波的波幅比值为 0.31,其相关值在 0.9 左右,如图 7d 所示,管波被有效地压制,相关性基本消失. 为了证明该相关数据提取的确实为地层纵波,我们对整个井段的处理结果进行对比和分析.

将上述整个套管井井段的测井资料采用波形干

?1994-2015 China Academic Journal Electronic Publishing House. All rights reserved. http://www.cnki.net

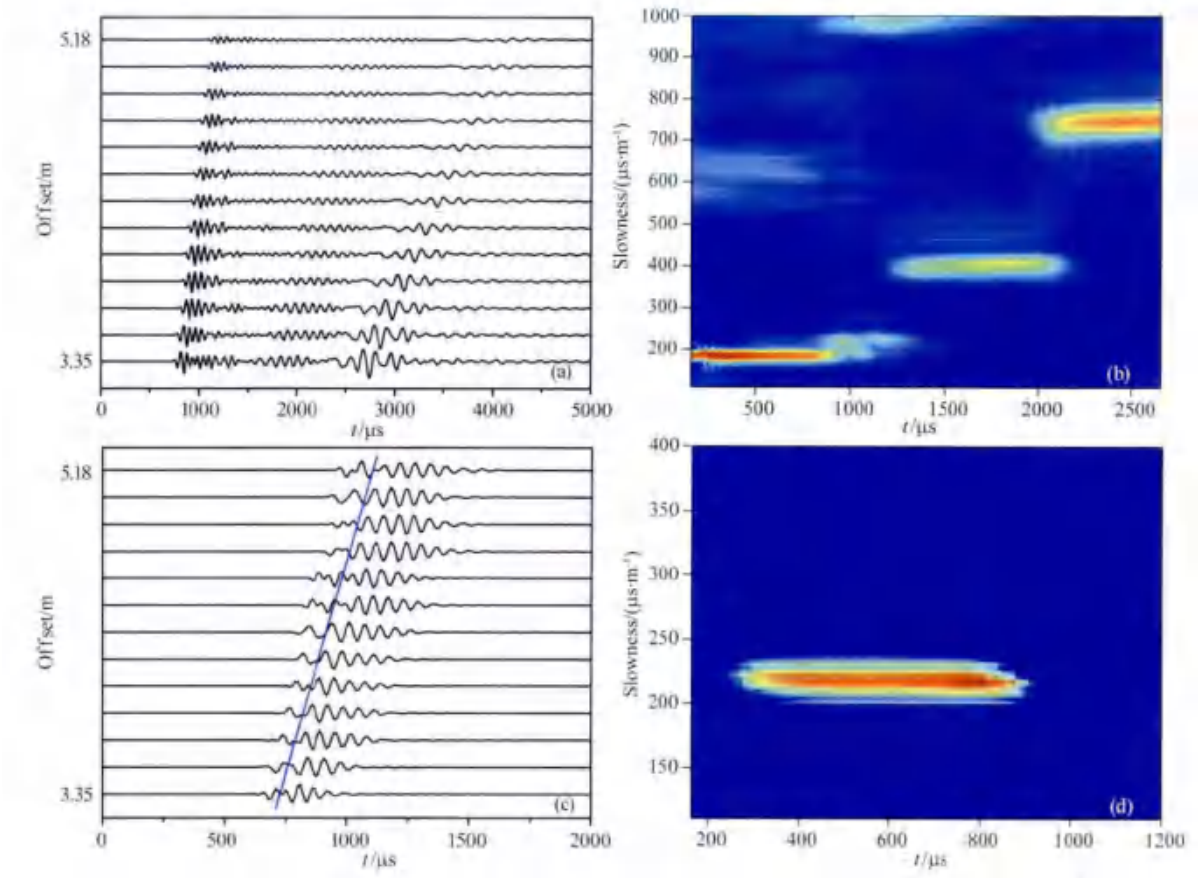


图 7　(a) 3991.2 m 深度处的实测波形;(b) 图(a)中波形的时间-慢度相关图;(c) 采用波形干涉方法处理图(a)中波形后的新阵列波形;(d) 图(c)中波形的时间-慢度相关图

Fig. 7　Array data from a poorly-bonded cased-hole; (b) STC analysis result for the data; (c) Extracted formation signal from the data; (d) STC analysis result for the data in (c)

涉方法进行处理,测井声波数据和处理结果如图 8 所示. 图中第一道为套管井中声波测井数据的变密度图,在整个井段内,可以看到清晰的地层横波波至. 在深度区间 4026～4027 m 的井段内,几乎没有管波信息,可以看到幅度很小但清晰的地层纵波,说明该井段固井质量良好. 在剩余井段固井质量差,管波幅度很强,由于是地层较快,地层纵波和管波混叠在一起,且地层纵波幅度低. 第二道为原始波形数据的联合相关图及提取的地层横波时差曲线,图中地层纵波的相关性很差,且在多处与管波的相关极值靠得很近,难以提取. 相比之下,地层横波的相关性很好,可以用来验证地层纵波的信息. 采用新方法处理该井段数据,显著地改善了地层纵波的相关性. 第三道为处理后波形数据的联合相关图以及提取的地层纵波时差曲线,在该图中管波的相关性被有效地消除,地层纵波的相关性显著增强. 为了验证所得地层纵波慢度的正确性,将其与从第二道中提取的地层横波慢度相比较,可见二者存在很好的相关性,反映着地层的变化,由提取的纵波慢度与横波慢度计算得到纵横波速比,如图第四道中所示,纵横波速比值在 1.5 和 2 的范围内,均值为 1.75,与固井质量良好井段(即4026～4027 m井段)的值相符. 将利用第三道中地层纵波时差曲线得到的地层纵波波至曲线(红色曲线)和第二道中地层横波时差曲线得到的地层横波波至曲线(黑色曲线)进行对比,可见两者相关性很好,如第一道中所示,后者与横波波至吻合得很好,并且,在第五道中,地层纵波与管波的波幅比值的变化情况与第一道中的这两种波波幅的相对变化情况具有很好的一致性,比值在 0.3 左右变化,说明处理方法的适用性和地层纵波处理结果的正确性. 上述套管井中现场数据的处理结果证明了波形干涉法对实际测井数据应用的有效性.

5　结论

对于套管井声波测井及数据处理,理论数值模

?1994-2015 China Academic Journal Electronic Publishing House. All rights reserved.　http://www.cnki.net

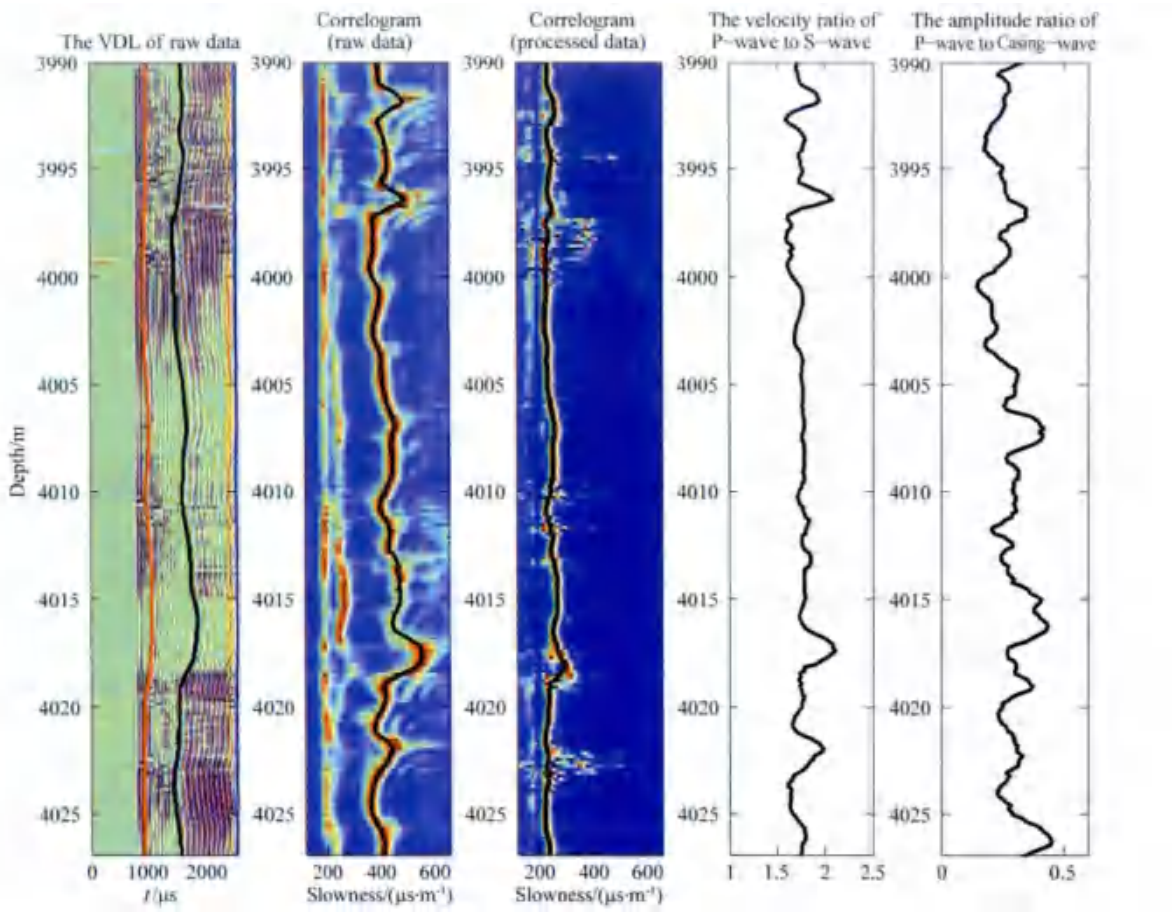


图 8 某一快速地层的套管井测井数据处理结果图. 从左到右:第一道为原始波形数据;第二道为原始数据联合相关图;第三道为采用波形干涉法得到的地层纵波的联合相关图;第四道为地层纵、横波波速比值;第五道为地层纵波与管波的波幅比值

Fig. 8 Processing results from an acoustic data set logged in a cased borehole with poor bond condition. From left to right: Panel 1 shows the raw waveform data; panel 2 is the STC result from the data; panel 3 is the STC result for the formation P-wave extracted using the new technique; panel 4 shows the V_p/V_s ratio from the processing; panel 5 shows the formation P- to casing wave amplitude ratio

拟和现场数据处理表明在套管胶结差的情况下,管波信号会干扰地层声波信号,并且会降低地层信号的相关性. 对于这种情况,我们提出了一种新的声波处理方法——波形干涉法. 该方法利用管波与地层波的干涉对阵列波形数据的功率谱产生的调制作用来提取地层信息. 通过处理数值模拟的波形,验证了该方法的正确性和适用性;通过处理现场数据充分验证了该方法的应用效果和有效性. 运用这一方法,可以有效地压制管波,显著地增强地层信号的信噪比及其相关性,提高地层信息探测的有效性,为套管井声波数据处理提供了一种有效的工具.

References

Bose S, Valero H P, Dumont A. 2009. Semblance criterion modification to incorporate signal energy threshold. SEG Houston 2009 International Exposition and Annual Meeting, 376-380.

Block L V, Cheng C H, Duckworth G L. 1991. Velocity analysis of multi-receiver full waveform acoustic logging data in open and cased holes. *The Log Analyst*, 32: 188-200.

ChenX L, Tang X M, Zhang C H, et al. 2015. Finite-difference numerical and analysis on nonaxisymmetrical acoustic fields in cased boreholes. *Chinese J. Geophyc.* (in Chinese), 58(1): 318-326, doi: 10.6038/cjg20150129.

Hsu K, Baggeroer A B. 1986. Application of the maximum-likelihood method (MLM) for sonic velocity logging. *Geophysics*, 51(3): 780-787.

Kimball C V, Marzetta T L. 1984. Semblance processing of borehole acoustic array data. *Geophysics*, 49(3): 274-281.

Li Z L, Du G S, Wang Y J. 2001. The effects of bonding conditions on the propagation of acoustic wave along a cased borehole. *Journal of Acoustics* (in Chinese), 26(1): 6-12, doi: 10.

?1994-2015 China Academic Journal Electronic Publishing House. All rights reserved. http://www.cnki.net

15949/j. cnki. 0371-0025. 2001. 01. 002.

Tao H G, Zhang H B, Hou C H, Zhang Y J. 2004. Developing cementing quality control technology to meet the requirement of oilfield exploration. *Well Logging Technology* (in Chinese), 28(S02):9-12.

Tang X M, Patterson D J. 2005. Analyzing and processing acoustic logging data for poorly bonded boreholes. 46th Annual Logging Symposium, Society of Petrophysics and Well-log Analysis. Paper OO.

Tubman K M, Cheng C H, Toksoz M N. 1986. Synthetic full waveform acoustic logs in cased boreholes. Ⅱ: Poorly bonded casing. *Geophysics*, 51(4): 902-913.

Valero H P, Skelton O, Almeida C M. 2003. Processing of monopole sonic waveforms through cased hole. 73th Ann. Internat. Mtg., Soc. Expl. Geophys., 285-288.

Wu Q, Li G X, Liu J P, et al. 2011. Progresses, needs and prospects of casedhole logging technologies in Petro China. *Well Logging Technology* (in Chinese), 35(6):497-501.

Zhang H B, Qin Z G, Shang Z P, et al. 2009. Amplitude features of formation wave in acoustic full waveform of casing wells. *Progress in Geophysics* (in Chinese), 24(3): 1006-1012, doi: 10. 3969/j. issn. 1004-2903. 2009. 03. 026.

Zhu Y S. 1994. Application of full waveform acoustic log information to detect poor bond condition at the second interface behind casing. *Chinese J. Geophys.* (in Chinese), 37(1):586-596.

附中文参考文献

陈雪莲,唐晓明,张聪慧等. 2015. **套管井贴壁声源激发的非轴对称声场的有限差分模拟及结果分析**. **地球物理学报**, 58(1):318-326, doi:10. 6038/cjg20150129.

李整林, 杜光升, 王耀俊. 2001. **套管井体胶结状态对井孔中声传播的影响**. **声学学报**, 26(1):6-12, doi:10. 15949/j. cnki. 0371-0025. 2001. 01. 002.

陆光华, 张林让, 谢智波. 2005. **数字信号处理**. **西安: 西安电子科技大学出版社**.

唐晓明, 郑传汉. 2004. **定量测井声学**. **北京: 石油工业出版社**.

陶宏根,张宏兵,侯春会,张彦君. 2004. **发展固井质量检测技术满足油田勘探开发需求**. **测井技术**, 28(S02):9-12.

吴奇,李国欣,刘军平等. 2011. **中国石油套管井测井技术的进展、需求与展望**. **测井技术**, 35(6):497-501.

张宏兵, 秦正贵, 尚作萍等. 2009. **套管井声波全波列中地层波的幅度特性**. **地球物理学进展**, 24(3): 1006-1012, doi:10. 3969/j. issn. 1004-2903. 2009. 03. 026.

朱云生. 1994. **应用声测井全波信息探测第二界面窜槽**. **地球物理学报**, 37(1):586-596.

(本文编辑　胡素芳)

?1994-2015 China Academic Journal Electronic Publishing House. All rights reserved.　http://www.cnki.net

许松，苏远大，唐晓明. 2017. 基于超级混合虚折射干涉法的阵列声波处理方法及其在套管井中的应用. 地球物理学报，60(7)：2904-2912，doi：10.6038/cjg20170734.

Xu S, Su Y D, Tang X M. 2017. A super-mixing-virtual interferometric array signal processing technique and its applications to cased-hole acoustic logging. *Chinese J. Geophys.* (in Chinese), 60(7): 2904-2912, doi: 10.6038/cjg20170734.

基于超级混合虚折射干涉法的阵列声波处理方法及其在套管井中的应用

许松，苏远大，唐晓明*

中国石油大学(华东)地球科学与技术学院，COSL-UPC 声学测井联合实验室，山东青岛 266580

摘要 在声学测井勘探时，复杂多变的测井条件(如胶结不好的套管井和随钻测井等)下的强直达干扰信号会导致地层信号的信噪比降低，使得地层有用信号的提取十分困难. 本文在超级虚折射法的基础上，利用声源与接收器的互易原理，对原始波场信号进行互相关和褶积重建，并对所有可能的位形产生的信号进行叠加，将该叠加波场与超级虚折射波场进行叠加，重构出超级混合虚折射波场，使不同接收器上的折射波信噪比在超级虚折射的基础上进一步得到提高，显著提高了有用信号的信噪比，同时解决了超级虚折射近场能量不足的问题. 套管井测井的理论模拟及实际处理表明，该方法可以很好地压制套管波信号、提高地层信号的信噪比.

关键词 超级虚折射；阵列声波；套管波；互易原理

doi：10.6038/cjg20170734 **中图分类号** P631 **收稿日期** 2016-12-12，2017-03-16 收修定稿

A super-mixing-virtual interferometric array signal processing technique and its applications to cased-hole acoustic logging

XU Song, SU Yuan-Da, TANG Xiao-Ming*

COSL-UPC Allied Borehole Acoustic Laboratory, School of Geosciences & Technology, China University of Petroleum, Shandong Qingdao 266580, *China*

Abstract During acoustic logging using an array acoustic tool, the signal-to-noise (S/N) ratio of formation signals are often contaminated by the background noise and by the interference of the strong unwanted direct signals (e. g., casing waves in cased hole logging and collar waves in logging while drilling conditions), making it different to extract the formation acoustic signal from the data. In this paper, we present a super-mixing-virtual (SMV) interferometry based on the super-virtual (SV) interferometric method. Based on the principle of reciprocity, we reconstruct a new wavefield, which is called the super-reverse-virtual (SRV), by processing the raw wavefield using cross-correlation and deconvolution over all receivers positioned at stationary-phase points. We finally reconstruct the super-mixing-virtual (SMV) by averaging the SRV and SV results over all receiver positions in the array. The S/N ratio of formation signals can be significantly enhanced. At

基金项目 国家重点基础研究发展计划 973 项目(2014CB239006)，国家自然科学基金(41474101，41474092)，中央高校基本科研业务费专项资金(16CX06040A)资助.

第一作者简介 许松，男，1990 年生，博士生，主要从事声波测井方法、资料处理及岩石物理等方面的研究工作. E-mail：xusongupc@sina.com

* **通讯作者** 唐晓明，男，1955 年生，教授，致力于地球物理(特别是声波)测井、岩石物理学、地震波传播及测量等方面的研究和技术开发工作. E-mail：tangxiam@aliyun.com

the same time, it can significantly improve the near-field performance of the existing SV method. The new technique was tested on synthetic waveform data and the cased hole acoustic logging data. The results show that the new technique effectively suppresses the coherence of the casing waves and significantly enhances the S/N ratio and the coherence of the formation acoustic signal.

Keywords　Super-virtual interferometry; Array acoustic wave; Casing wave; Reciprocity principle

1　引言

随着油气勘探与开发重心转向非常规资源领域,所面临的地下情况也变得为更为复杂(贾承造等,2012;邹才能等,2013).针对于此,学者进行了相关的理论研究(Tang et al., 2012; Chen et al., 2013;邹才能等,2014;许松等,2014).对于声波测井而言,由于地层介质的复杂性,常常使得声波测量信号的信噪比(SNR)较差;此外,在特殊的测量环境下,如胶结不好的套管井、隔声效果不好的随钻声波测井及软地层偶极测井产生的泄露模式波等,这些情况下都会在接收器中产生比较强的干扰信号,妨碍对地层有用信号的提取.以套管井为例,当与地层胶结不好时,会产生相干性很强的套管波信号,对此测井数据做常规的阵列波形相关(STC)处理(Kimball and Marzetta, 1984)很难将地层波与套管波很好地区分开来(唐晓明和郑传汉, 2004).为获取套管井中的地层信息,测井界发展了一些数据采集和处理方法,目的都是压制套管信号、提高地层波的信噪比(Hsu and Baggeroer, 1986; Block et al., 1991; Valero et al., 2003; Tang and Patterson, 2005; Bose et al., 2009; 唐晓明等, 2015).值得一提的是,唐晓明等(2016)提出一种过套管双源反激声波测井方法,从数据采集的源头上压制套管波,使得地层波获得较高的采样精度,从而提高信噪比.

虚折射干涉法是通过对波形进行相关叠加来增强地层折射波信息的方法,起初主要应用于地震数据的处理上(Claerbout, 1968; Schuster, 2001; Draganov et al., 2006; Dong et al., 2006).为了解决虚折射干涉法远偏移距折射波能量不足的问题,Mallinson 等(2011)在褶积型互易定理(Schuster, 2010)的基础上,提出了超级虚折射干涉法(Bharadwaj et al., 2011; Hanafy et al., 2011; Alshuail et al.,2012),可以进一步确定原始波场的激发位置和时间,但该方法不能有效恢复出近偏移距处的折射波场.乔宝平等(2014)提出一种逆序折射干涉法,通过虚折射波场和原始折射波场的互相关,并对所有位于固定相位点上的检波点进行叠加,重构出逆虚折射波场,用于解决近偏移距处的折射波场问题.

本文在前人工作的基础上提出一种超级混合虚折射干涉的阵列声波处理方法,可用于套管井测井数据的声速提取和后期处理.利用声源和接收器的互易关系(Wapenaar and Fokkema,2006),对超级虚折射干涉公式进行修正,对原始波场信号进行互相关和褶积重建,并对所有可能的位形产生的信号进行叠加,将叠加波场与超级虚折射波场进行叠加,重构出超级混合虚折射波场.以套管井声波测井为例,用理论数据验证了该方法的正确性,实际测井数据的处理结果表明,该方法可以有效改善套管井胶结不好情况下地层波的信噪比,并准确提取地层声速.本文工作为阵列声波测井提出了一种新的数据处理理论,为套管井的声波处理和地层评价提供了有效的处理方法.

2　超级逆虚折射干涉法的基本理论

利用 Wapenaar 逆辐射条件和远场近似(Wapenaar and Fokkema, 2006; Wapenaar et al., 2010),可得虚折射干涉法的表达式

$$\mathrm{Im}[G(R_b\,|\,R_a)^{\mathrm{virt.}}]=k\int_{S_C}G(R_a\,|\,S)^{*}\,G(R_b\,|\,S)\,\mathrm{d}S_C,\tag{1}$$

其中,$G(R_b\,|\,R_a)^{\mathrm{virt.}}$ 为重构的虚折射波场;Im 为重构波场的虚部,$G(R_a\,|\,S)$、$G(R_b\,|\,S)$ 分别为声源 S 激发在接收器 R_a、R_b 记录的复信号谱;* 代表取信号谱的复共轭;k 为波数,S_C 代表声源所在位置.对于式(1)所示的虚折射干涉的解释为:将源 S 在 R_a 和 R_b 处接收的信号做互相关(图 1a),得到的信号等效于一位于 R_a 处的虚拟源 V 在 R_b 处产生的信号;将所有的声源位形叠加(即沿声源轨迹 S_c 积分),便得到在 R_a 点激发,R_b 点接收到的虚折射场 $G(R_b\,|\,R_a)^{\mathrm{virt}}$.(图 1b).

对于声波测井而言,仪器是采用单源激发、阵列接收的滑动测量方式.假设声波仪器上的接收阵列有 n 个接收器.若取 R_a、R_b 为相邻的两个接收器,

那么,通过一系列互相关和叠加,可以将重构波场的信噪比提高 $\sqrt{n-1}$ 倍;若取 R_a、R_b 为最大间距上的两个接收器,则重构波场的信噪比与原始信号相同,但第一个接收器不能进行该项处理.此外,构建虚折射干涉场所做的互相关处理会引起小波缺失,降低时间分辨率并引起虚假的人为信号.针对这些问题,学者进行了相关的研究(Vasconcelos and Snieder, 2008; Nakata et al. 2011; 乔宝平,2014).

虚折射干涉法存在的问题是,无法根据虚震源确定虚折射波场的原始激发位置和时间,同时,由于可利用的声源位置有限,不能很大程度上提高折射波的信噪比和信息拾取的精度.为了解决这些问题,采用褶积型互易定理,对公式(1)的虚折射波场进行褶积处理,该方法称之为超级虚折射干涉法(Mallinson et al.,2011; Schuster, 2010)

$$G(R_b \mid S)^{\text{Super}} = 2ik\int_{R_C} G(R_b \mid R_a)^{\text{virt.}}\, G(R_a \mid S)\,\mathrm{d}R_C, \tag{2}$$

其中,$i=\sqrt{-1}$,$G(R_b \mid S)^{\text{Super}}$ 为重构的超级虚折射波场;R_C 代表除 R_b 以外的接收器所在位置.

对于超级虚折射干涉的解释是:将 R_a 和 R_b 间的虚折射波场 $G(R_b \mid R_a)^{\text{virt.}}$ 与源 S 在 R_a 处产生的信号 $G(R_a \mid S)$ 做褶积得到源 S 在 R_b 处的信号(图2a),再将 R_a 所有的可能的位形所产生的信号叠加(即式(2)中沿 R_a 的位形 R_c 的积分,图2b),便得到源 S 在 R_b 处的超级虚折射波场 $G(R_b \mid S)^{\text{Super}}$,这样做的结果是将虚折射波场信号重建回到原始声源处.

下面来分析一下实际测井过程中超级虚折射波场及其重建的效果,对声波仪器上等间距排列的 n 个接收器,测井时声源移动的间隔为接收器的间距.首先考虑第二个接收器,该接收位置与声源之间只能有一个虚拟声源.由前述的虚折射波场分析可知,随着仪器按接收器间隔上下移动,该虚拟声源可以将接收信号的信噪比提高 $\sqrt{n-1}$ 倍;进一步采用超级虚折射,利用第一个接收器信号与该虚拟声源进行褶积,可以得到第二个接收器的超级虚折射波

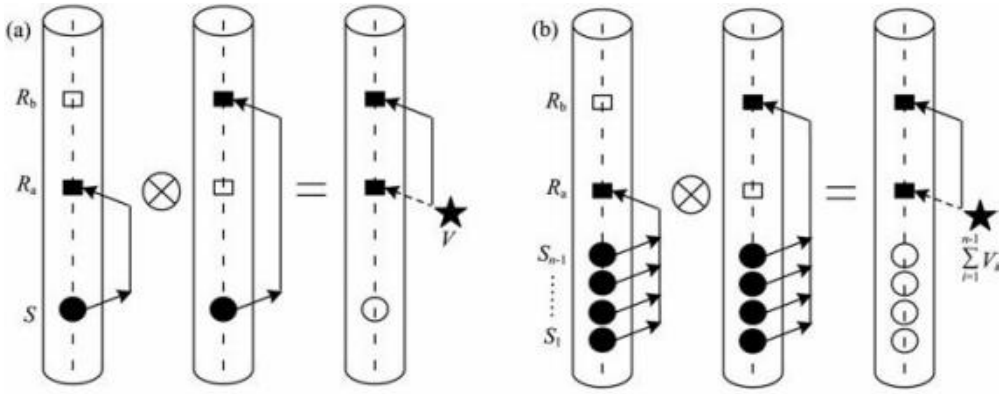


图 1 虚折射波场构建示意图

(a) 信号互相关处理; (b) 声源信号叠加.

Fig. 1 Schematic ray diagrams for virtual sonic wavefield

(a) Correlation-type datuming; (b) Sum the waveforms over all sources.

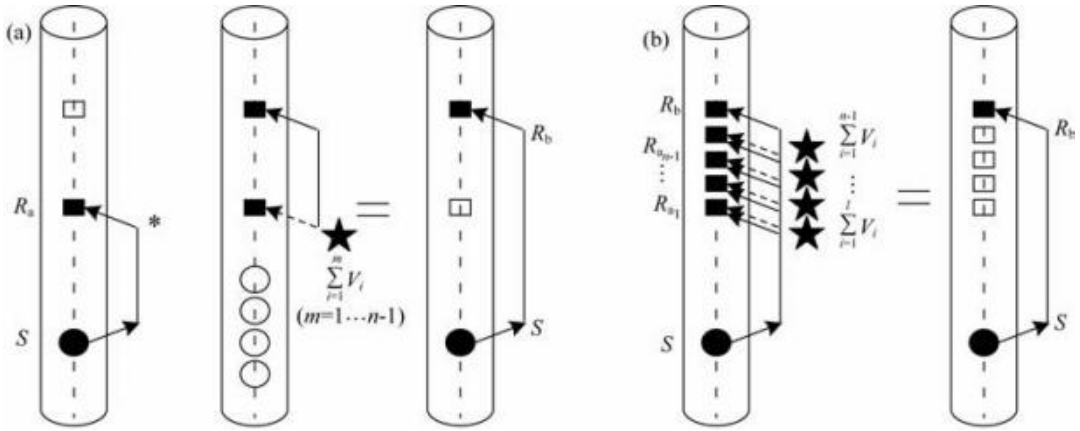


图 2 超级虚折射波场构建示意图

(a) 褶积重建; (b) 接收信号叠加.

Fig. 2 Schematic ray diagrams for super-virtual wavefield

(a) Convolution-type de-datuming; (b) Sum the data over virtual positions.

形,这样处理的结果的信噪比与原始信号相比提高了$\sqrt{n-1}$倍;接下来依次考虑第三到第 n 个接收器,如图 2b 所示,声源 S 与 R_b 之间可以有 $n-1$ 个虚拟声源,且叠加倍数依次从 1 变化到 $n-1$;对每一个虚拟声源对 R_b 进行超级虚折射处理,则最终结果的叠加倍数为全部虚源倍数之和,即 $n(n-1)/2$,则该接收位置波形的信噪比提高 $\sqrt{n(n-1)/2}$ 倍.

上述方法主要适用于远场的声波信号,即声源与接收器之间距离越远效果越好,而距离越近时效果越差.具体原因是:随着源与接收之间的距离不断减小,位于两者之间的虚震源数会不断减少,从而造成超级虚折射波场信噪比的改善程度随着距离的减小而降低的现象.

为了解决超级虚折射在近场接收时的缺陷,乔宝平(2014)提出一种逆虚折射干涉法:通过两次互相关,对虚折射干涉表达式(1)进行修正,最后实现逆虚折射干涉处理.为了保持原公式在处理过程中的形式不变,利用声源和接收器的互易关系(Wapenaar and Fokkema,2006)来对超级虚折射干涉法进行修正,可以达到同样的目的,将其称之为超级逆虚折射干涉法,其数学表达式如下:

$$\mathrm{Im}[G(R_a\,|\,R_b)^{\mathrm{virt.\_Rev}}]=k\int_{S_C}G(R_b\,|\,S)^{*}\,G(R_a\,|\,S)\,\mathrm{d}S_C,\tag{3}$$

$$G(R_a\,|\,S)^{\mathrm{Super\_Rev}}=2ik\int_{R_C}G(R_a\,|\,R_b)^{\mathrm{virt.\_Rev}}G(R_b\,|\,S)\,\mathrm{d}R_C.\tag{4}$$

对于超级逆虚折射干涉的原理阐述如下:S 点处的源在接收点 R_a 产生的超级逆虚折射波场 $G(R_a\,|\,S)^{\mathrm{Super\_Rev}}$,可以通过将位于 R_b 处的源在 R_a 处产生的波场 $G(R_a\,|\,R_b)^{\mathrm{virt.\_Rev}}$ 与 S 点的源在 R_b 处的接收信号褶积得到.图 3a、3b 为超级逆虚折射波场构建的第一步,该过程与图 1 所示的超级虚折射第一步中的虚折射波场构建为互易的两个过程(注意式(3)与式(1)相比,R_a 和 R_b 做了对调).图 3b,3d 展示的是式(4)所做的褶积处理,即为超级逆虚折射波场的构建的第二步.与图 2 对比可见,超级逆虚折射波场的构建过程是由远到近,与超级虚折射场由近到远的构造过程正好相反.由于采用了互易原理,处理过程中超级逆虚折射与超级虚折射处理的形式一致,都是先相关后褶积的处理流程.

通过将超级逆虚折射波场和超级虚折射波场进行叠加,得到超级混合虚折射波场的表达式如下:

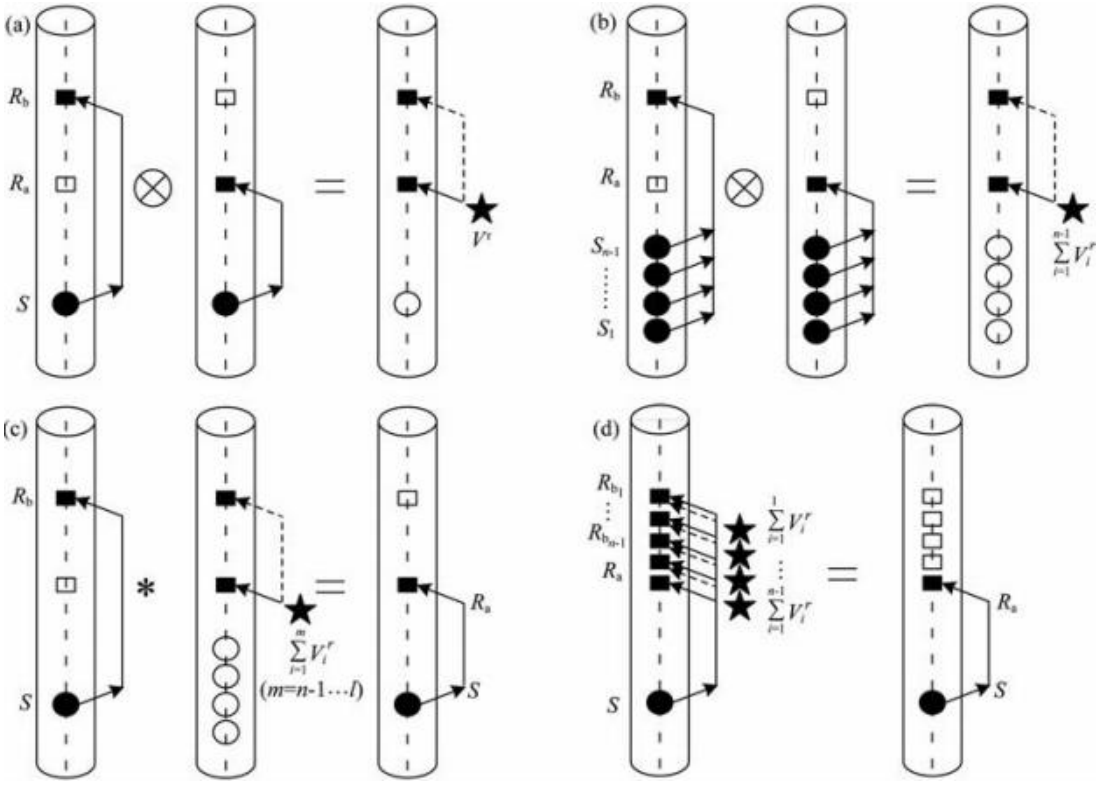


图 3　超级逆虚折射波场构建示意图

(a) 信号互相关;(b) 信号叠加;(c) 褶积重建;(d) 接收信号叠加.

Fig. 3　Schematic ray diagrams for super-reverse-virtual wavefield

(a) Correlation-type datuming; (b) Sum the waveforms over all sources; (c) Convolution-type de-datuming; (d) Sum the data over virtual positions.

$$G(R_a \mid S)^{\text{Super\_Mix}} = G(R_a \mid S)^{\text{Super}} + G(R_a \mid S)^{\text{Super\_Rev}}, \quad (5)$$

其中,上标 Sup_Mix 代表重构的波场为超级混合虚折射波场.值得一提的是,由于超级逆虚折射和超级虚折射是互补的.将二波场相加,结果是不同接收器上的波场信噪比在超级虚折射的基础上进一步提高,且更为均衡,从而解决了超级虚折射干涉处理时近场信噪比较低的问题.

3 方法验证

将上述方法用于套管井阵列声波的数据处理,以期能够压制数据中的套管波,提升地层声波的信噪比.首先采用一自由套管(Tubman et al., 1986)模型的理论计算波形来验证该方法.该模型如图 4 所示,其中套管与水泥环之间的薄流体层用来模拟套管与地层之间耦合不好的情况.这种环状分层模型的测井声场的具体模拟方法详见唐晓明和郑传汉(2004).模拟计算结果如图 5 所示,模型中声源和接收器都位于井轴,源距为 4.0 m,接收间距为 0.1524 m,声源主频 6 kHz,表 1 给出了模型中不同介质的尺寸及声学参数,其中的地层为一慢速地层.图 5 的阵列波形可以清晰地看到三个振型,首先到达的为套管波,其次是地层纵波,最后到达的是斯通利波.

表 1 模型计算参数

Table 1 Model calculation parameters

介质参数	纵波速度 ($m \cdot s^{-1}$)	横波速度 ($m \cdot s^{-1}$)	密度 ($kg \cdot m^{-3}$)	半径(m)
井眼流体	1500	—	1000	0.0750
套管	5800	3000	7800	0.0850
流体环	1500	—	1000	0.0855
水泥环	3000	1800	2000	0.1000
地层参数	2750	1200	2500	∞

对图 5 的阵列波形用干涉法进行处理的过程和结果如图 6 所示.图 6a 为原始波形时间取窗去掉其中的斯通利波,保留套管波和地层波;对取窗后的数据采用传统的超级虚折射法进行处理,所得结果如图 6b 中绿线所示;该处理时过程中采用相关法来压制子波旁瓣(Nakata et al.,2011).作为对比,图中也给出了未作处理的原始波形(图 6b 中虚线).为了方便对比,图 6b 中不同接收器的波形按各自的幅值做了归一化处理.可以看出,由于该方法适用于远场的处理,阵列中距源较远的接收器上套管波的压制

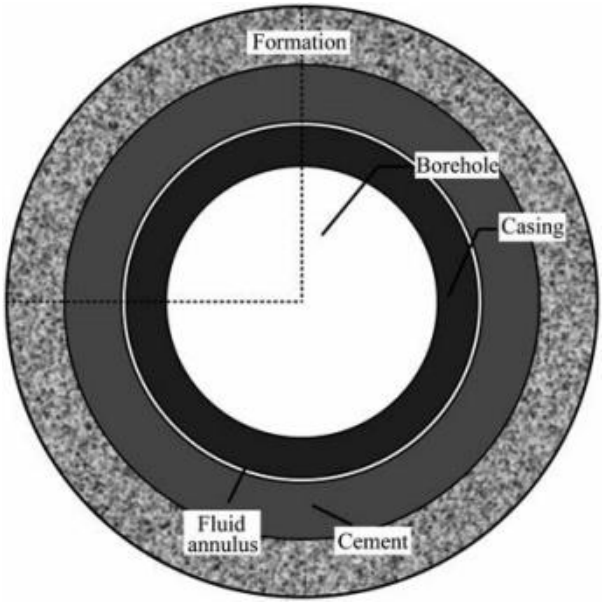


图 4 自由套管模型示意图

Fig. 4 Free-pipe acoustic model used for synthetic waveform modeling

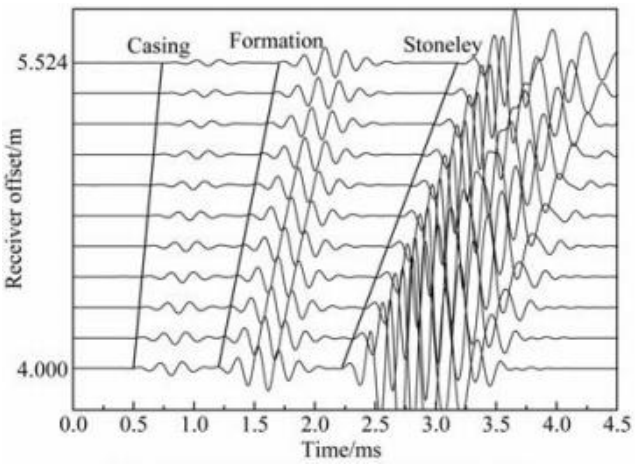


图 5 套管胶结不好的阵列波形模拟结果

Fig. 5 Calculated acoustic array waveform result with a poorly-bonded cased-hole

效果明显;靠近声源的接收器上效果明显变差,而第一道波形无法进行处理,这与之前的理论分析是一致的.

若对取窗后的数据用超级逆虚折射干涉处理,所得结果如图 6c 中蓝色波形所示(其中的原始波形用虚线绘出).同样地,为了方便对此,对各接收器的波形做了归一化处理.图 6c 所示的逆虚折射法的结果与图 6b 的虚折射结果正好相反:越靠近声源,套管波的压制效果越好.将图 6b 和图 6c(归一化前)的处理结果相互叠加就得到图 6d 所示的最终处理结果,相对于图 6b 和图 6c 的结果,套管波在所有的接收器上都得到很好的压制,且压制效果较为均衡.对实际测井数据,这种压制会有效地提升地层声波的信噪比,获得可靠的地层声速信息.

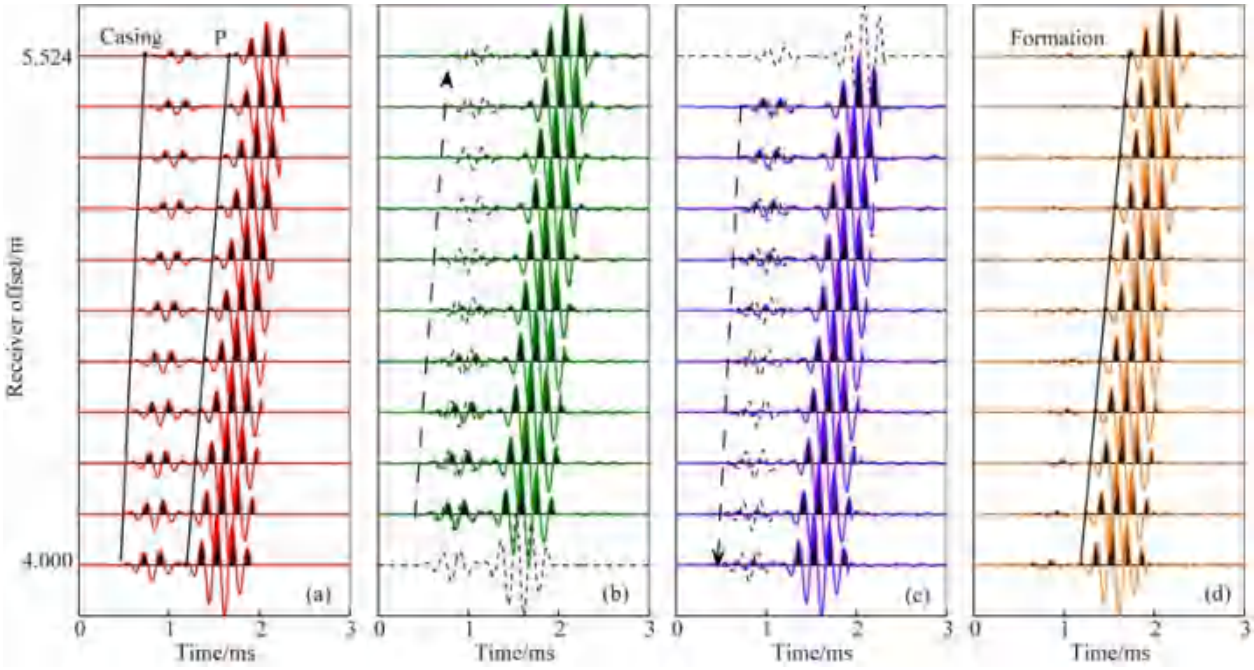


图 6　套管胶结不好的单点波形处理结果

Fig. 6　Processing of acoustic array waveform result with a poorly-bonded cased-hole

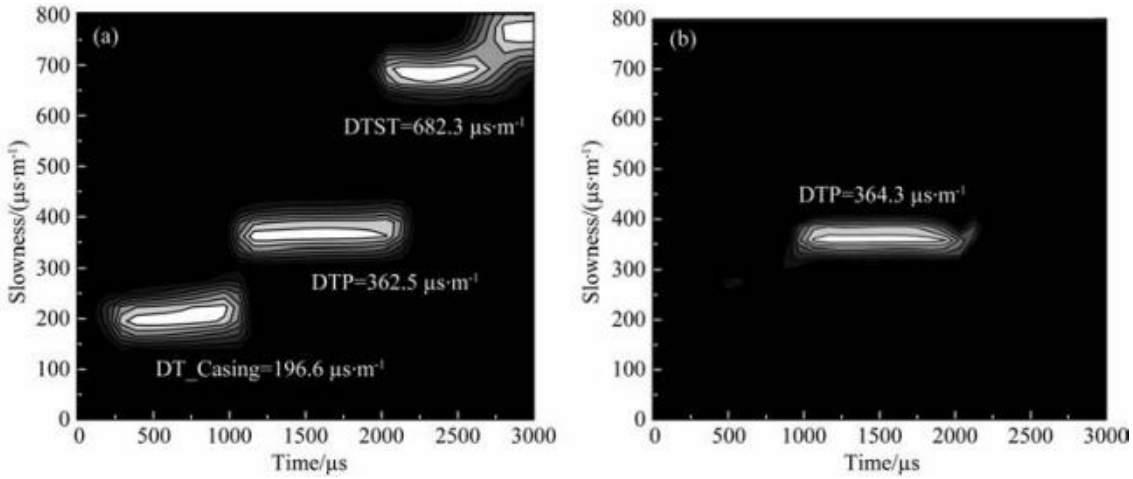


图 7　波形处理前后的时间-慢度相关对比

Fig. 7　STC analysis results for the raw and processed waveform

为了检验上述处理对地层声速提取的效果,对处理前后的阵列波形用时间慢度相干法(STC)进行处理,得到其时间-慢度相关图(图 7). 其中,图 7a 为原始波形处理的时间-慢度相关图,由下而上,相关图中的极致对应的慢度为 196.6 $\mu s \cdot m^{-1}$、362.5 $\mu s \cdot m^{-1}$、682.3 $\mu s \cdot m^{-1}$,分别对应套管波、地层纵波、斯通利波;相干图上,套管波的相干性很强,相关系数接近 1. 图 7b 为上述方法处理后波形的时间-慢度相干图,从结果中可以看出,套管信号的相干性被大大压制,及至消失,而相干图上显示的是地层纵波信号,由其提取的慢度正是表 1 模型的地层纵波慢度. 对理论模拟数据的处理结果表明,本文的方法可以应用于套管井的测井数据处理,以压制套管胶结不好的情况下产生的套管波,提升地层声波的信噪比和地层声速提取的精度.

4　实例应用

进一步验证本文方法对实际套管井声波数据处理的应用效果. 套管与地层胶结不好时产生的套管波会严重影响地层声波信号的提取,这种现象在快速地层(速度与套管波速度接近)尤为严重,因此,采用一快速地层的套管井现场数据来验证本文方法.

图 8 是对该数据的处理结果,其中第一道为该套管井中声波测井数据的变密度图,在整个井段内,数据的前部分(1200 μs 以内)几乎全是相关性很强、呈直线条状的套管波,表明该井段的套管胶结质量不好(Tubman et al., 1986);在 X511. 5-X516. 5m 井段,套管与水泥环胶结有所改善,套管波幅度相对减小,且在套管波后面可以看到幅度较小的地层波

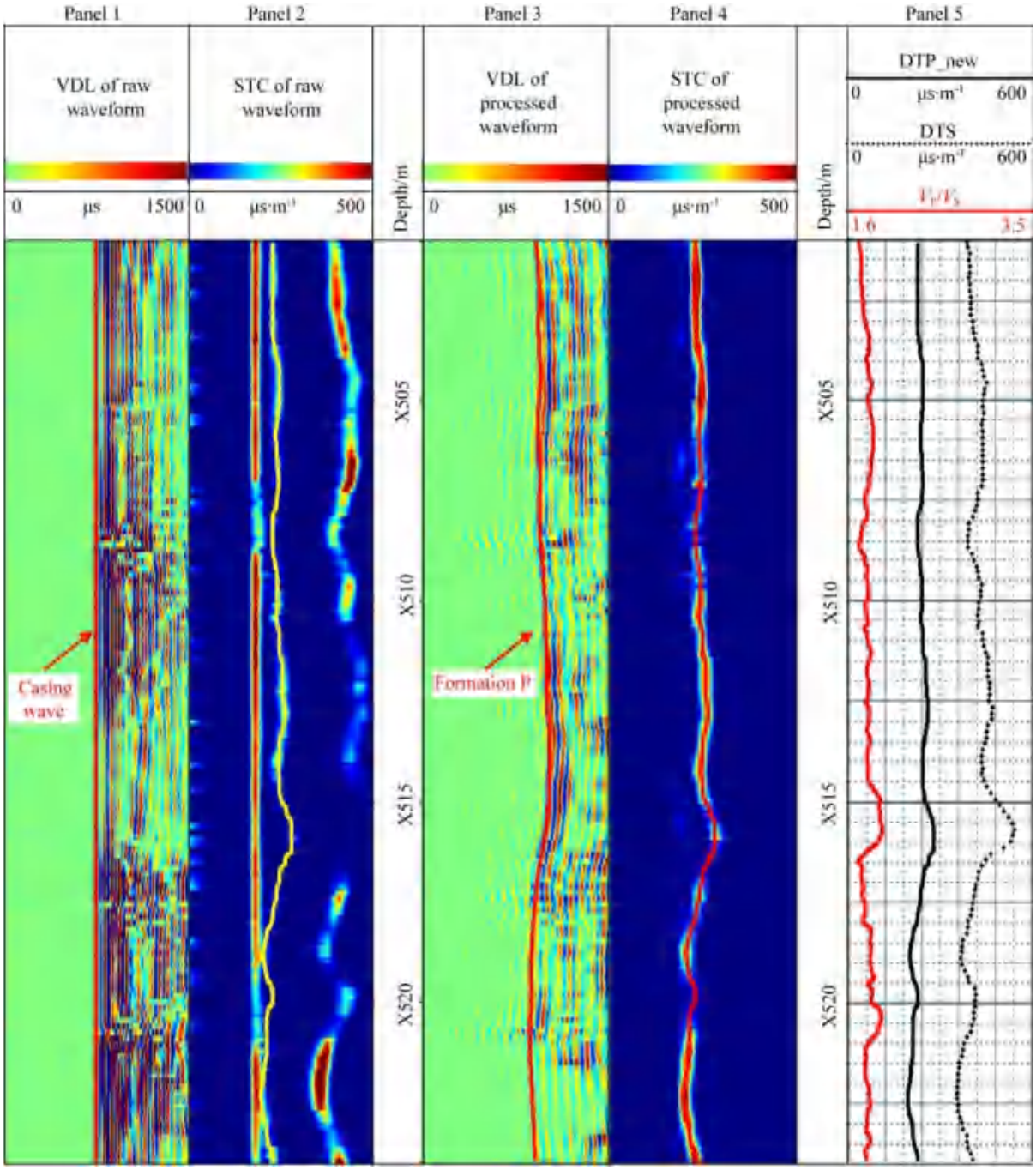


图 8 某一快速地层套管井测井数据及处理结果

Fig. 8 Processing results from a fast-formation data set logged in a cased borehole with bad cement bond conditions

信号,剩余井段尤其是在 X506.5m-X511.5,X516.5m 以下,数据前部皆为幅度很强的套管波,由于地层速度较快,套管波与地层波叠在一起,在原始波形中几乎看不到地层信号,这种条件下的地层声速提取较为困难.对原始波形数据用时间-慢度相关(STC)方法进行慢度提取,得到其慢度信息(见图中第二道).从相干图中可以看到深度自上而下相干性很强的一直条带,对应的慢度约为 186.5 $\mu s \cdot m^{-1}$,为套管波的慢度.此外,在 350～475 $\mu s \cdot m^{-1}$ 范围内可以看到比较清晰的地层横波慢速.值得注意的是,在套管波与横波慢度之间有一相干性极弱、几乎被套管波屏蔽的变化条带,该信号即为地层纵波信号,但由于该信号的信噪比很低,相干性很差,很难提取地层纵波慢度.

采用本文方法对原始波形进行处理,像对图 5 的理论波形处理那样,首先对波形加窗截取数据前部的套管波和地层纵波部分,对取窗后波形的处理结果在第三、四道中给出,从处理后的波形数据(第三道)可以看出,第一道中直线条状的套管信号被很好地压制,得到了较为清晰的地层信号(图中红线为地层纵波的到时曲线,由以下的慢度分析计算得到).一个明显的现象是处理后的波形的到时和幅度随深度而变化,表明这是受地层岩性变化影响的地层纵波.

图中第四道为处理后的慢度相干图,从处理结果中可以看出地层慢度随深度变化而变化且相干性

相对于原始波形的处理结果(第二道中的纵波)有很大的提升,即使在地层速度较快、纵波信号较弱的井段,也得到了相关性较好的地层纵波信息.为了验证处理结果的正确性,将提取的慢度置于第二道中,可见该曲线与图中微弱的地层信号相互重合,且与横波慢度具有很好的相关性.进一步提取地层横波慢度,并将该慢度与纵波慢度进行对比(第五道).对比可见,二者具有很好的相关性.由提取的纵横波慢度计算可得到地层的纵横波速比,如图中第五道的红线所示,该井段纵横波速比在 1.7 和 1.95 的范围内,均值为 1.80,为该快速地层的典型值,进一步验证了处理结果的可靠性.上述套管井现场数据的处理结果证明了本文方法对实际测井数据应用的有效性.

5　结论

为提高阵列声波测井数据的信噪比,利用声源和接收器的互易原理,对现有的超级虚折射干涉法进行了改进,得到了一种针对测井数据处理的超级混合虚折射干涉方法,弥补了传统方法在近场条件下的缺点,同时可以大大提高有用信号的信噪比,并保证了不同接收器处理效果的一致性.应用本文方法对理论和实际套管测井数据进行了处理:理论数据的处理验证了该方法的正确性和适用性;对现场数据的处理进一步验证了该方法的有效性.处理结果表明:本文方法可以有效地压制套管波,提高地层声波信号的信噪比和相关性,本文的结果为套管井测井数据处理提供了一种新的有效处理方法.

References

Alshuail A, Aldawood A, Hanafy S. 2012. Application of super-virtual seismic refraction interferometry to enhance first arrivals: a case study from Saudi Arabia. *The Leading Edge*, 31(1): 34-39.

Bharadwaj P, Schuster G T, Mallinson I. 2011. Super-virtual refraction interferometry: theory. // 81st Annual Meeting, Society of Exploration Geophysicists. *Expanded Abstracts*, 3809-3813.

Block L V, Cheng C H, Duckworth G L. 1991. Velocity analysis of multi-receiver full waveform acoustic logging data in open and cased holes. *The Log Analyst*, 30: 188-200.

Bose S, Valero H P, Dumont A, 2009. Semblance criterion modification to incorporate signal energy threshold. // 79th Annual International Meeting, Society of Exploration Geophysicists. Expanded Abstracts, 376-380.

Chen X L, Tang X M, Qian Y P. 2013. Simulation of multipole acoustic logging in cracked porous formations. *Geophysics*, 79(1): D1-D10, doi: 10.1190/geo2013-0163.1.

Claerbout J F. 1968. Synthesis of a layered medium from its acoustic transmission response. *Geophysics*, 33(2): 264-269.

Dong S Q, Sheng J M, Schuster J T. 2006. Theory and practice of refraction interferometry. // 76th Annual Meeting, Society of Exploration Geophysicists. Expanded Abstracts, 3021-3025.

Draganov D, Wapenarr K, Thorbecke J. 2006. Seismic interferometry: Reconstructing the earth's reflection response. *Geophysics*, 71(4): SI61-SI70.

Hanafy S M, Ola A, Feras A T. 2011. Super-virtual refraction interferometry: Field data example over a colluvial wedge. // 81st Annual Meeting, Society of Exploration Geophysicists. Expanded Abstracts, 3814-3818.

Hsu K, Baggeroer A B. 1986. Application of the maximum-likelihood method (MLM) for sonic velocity logging. *Geophysics*, 51(3): 780-787.

Jia C Z, Zheng M, Zhang Y F. 2012. Unconventional hydrocarbon resources in China and the prospect of exploration and development. *Petroleum Exploration and Development* (in Chinese), 39(2): 129-136.

Kimball C V, Marzetta T L. 1984. Semblance processing of borehole acoustic array data. *Geophysics*, 49(3): 274 281.

Mallinson I, Bharadwaj P, Schuster G, et al. 2011. Enhanced refractor imaging by supervirtual interferometry. *The Leading Edge*, 30(5): 546-550.

Nakata N, Snieder R, Tsuji T, et al. 2011. Shear wave imaging from traffic noise using seismic interferometry by cross-coherence. *Geophysics*, 76(6): SA97-SA106.

Qiao B P, Guo P, Wang P, et al. 2014. Effectively picking weak seismic signal near the surface based on reverse virtual refraction interferometry. *Chinese J. Geophys.* (in Chinese), 57(6): 1900-1909, doi: 10.6038/cjg20140621.

Schuster G T. 2001. Theory of daylight/interferometric imaging: Tutorial. // 63th Annual EAGE Meeting. Expanded Abstracts, A32.

Schuster G T. 2010. Seismic Interferometry. Cambridge: Cambridge University Press.

Tang X M, Chen X L, Xu X K. 2012. A cracked porous medium elastic wave theory and its application to interpreting acoustic data from tight formations. *Geophysics*, 77(6): D245-D252, doi: 10.1190/geo2012-0091.1.

Tang X M, Patterson D J. 2005. Analyzing and processing acoustic logging data for poorly bonded cased boreholes. // SPWLA 46th Annual Logging Symposium. New Orleans, Louisiana: Society of Petrophysicists and Well-log Analysis..

Tang X M, Qi X, Zhang B, et al. 2015. An interference-based array signal processing technique for cased-hole acoustic logging and applications. *Chinese J. Geophys.* (in Chinese), 58(4): 1447-1457, doi: 10.6038/cjg20150430.

Tang X M, Su Y D, Zhang B. 2016. An advancement in through

casing acoustic logging technology. *Well Logging Technology* (in Chinese), 40(4): 387-391.

Tang X M, Zheng C H. 2004. Quantitative Borehole Acoustic Methods (in Chinese). Beijing: Petroleum Industry Press.

Tubman K M, Cheng C H, Toksöz M N. 1986. Synthetic full waveform acoustic logs in cased boreholes, Ⅱ: Poorly bonded casing. *Geophysics*, 51(4): 902-913.

Valero H P, Skelton O, Almeida C M. 2003. Processing of monopole sonic waveforms through cased hole. // 73th Ann. Internat. Mtg., Soc. Expi. Geophys. Expanded Abstracts, 285-288.

Vasconcelos I, Snieder R. 2008. Interferometry by deconvolution: Part 1 theory for acoustic waves and numerical examples. *Geophysics*, 73(3): S115-S128.

Wapenaar K, Fokkema J. 2006. Green′s function representations for seismic interferometry. *Geophysics*, 71(4): SI33-SI46.

Wapenaar K, Draganov D, Snieder R, et al. 2010. Tutorial on seismic interferometry: Part 1-basic principles and applications. *Geophysics*, 75(5): 75A195-75A209.

Xu S, Su Y D, Chen X L, et al. 2014. Numerical study on the characteristics of multipole acoustic logging while drilling in cracked porous medium. *Chinese J. Geophys.* (in Chinese), 57(6): 1999-2012, doi: 10.6038/cjg20140630.

Zou C N, Yang Z, Zhang G S, et al. 2014. Conventional and unconventional petroleum "orderly accumulation": Concept and practical significance. *Petroleum Exploration and Development* (in Chinese), 41(1): 14-27.

Zou C N, Zhang G S, Yang Z, et al. 2013. Geological concepts, characteristics, resource potential and key techniques of unconventional hydrocarbon: On unconventional petroleum geology. *Petroleum Exploration and Development* (in Chinese), 40(4): 385-399, 454.

附中文参考文献

贾承造，郑民，张永峰. 2012. 中国非常规油气资源与勘探开发前景. 石油勘探与开发，39(2)：129-136.

乔宝平，郭平，王璞等. 2014. 基于逆虚折射干涉法有效提取近地表弱地震信号. 地球物理学报，57(6)：1900-1909，doi：10.6038/cjg20140621.

唐晓明，郑传汉. 2004. 定量测井声学. 北京：石油工业出版社.

唐晓明，祁晓，张博等. 2015. 基于波干涉原理的套管井阵列声波处理方法及其应用. 地球物理学报，58(4)：1447-1457，doi：10.6038/cjg20150430.

唐晓明，苏远大，张博. 2016. 过套管声波测井技术新进展. 测井技术，40(4)：387-391.

许松，苏远大，陈雪莲等. 2014. 含孔隙、裂隙地层随钻多极子声波测井理论. 地球物理学报，57(6)：1999-2012，doi：10.6038/cjg20140630.

邹才能，张国生，杨智等. 2013. 非常规油气概念、特征、潜力及技术——兼论非常规油气地质学. 石油勘探与开发，40(4)：385-399，454.

邹才能，杨智，张国生等. 2014. 常规-非常规油气"有序聚集"理论认识及实践意义. 石油勘探与开发，41(1)：14-27.

（本文编辑　胡素芳）

SCIENCE CHINA
Earth Sciences

•RESEARCH PAPER•

https://doi.org/10.1007/s11430-017-9203-8

An acoustic-wave theory for casing bond evaluation using viscoelastic slip boundary modeling

Xiaoming TANG, Can JIANG, Yuanda SU & Xuelian CHEN*

School of Geosciences, China University of Petroleum, Qingdao 266580, China

Received September 25, 2017; revised March 31, 2018; accepted April 11, 2018; published online May 24, 2018

Abstract Slip boundary condition is commonly utilized to model elastic wave propagation through layered earth media. The same approach is used here to characterize acoustic wave propagation along a cased borehole with various cement bond conditions. By modeling the cement layer between casing and formation as a viscoelastic slip interface with complex coupling rigidity parameters, one can not only reduce the complexity in the classical elastic wave modeling of the problem, but also efficiently model various complicated wave phenomena that are difficult for the existing modeling. More specifically, the new theory can well describe the effect of the cement bond condition change and the location of the change (i.e., whether it is in the first interface between casing and cement, or the second interface between cement and formation) on the acoustic waves, demonstrating the good modeling capability and predicting power. Application of the theory to field data shows that the theory can correctly model the acoustic wave characteristics and interpret the cement bond condition, thus providing a useful fundament theory for casing bond evaluation using acoustic logging.

Keywords Cased borehole, Acoustic logging, Cement evaluation, Viscoelastic slip boundary, Cement bond quality

Citation: Tang X, Jiang C, Su Y, Chen X. 2018. An acoustic-wave theory for casing bond evaluation using viscoelastic slip boundary modeling. Science China Earth Sciences, 61, https://doi.org/10.1007/s11430-017-9203-8

1. Introduction

In modeling the elastic wave propagation through layered structures, the slip boundary and its associated boundary condition can be used to model the effect of a thin layer on the wave propagation when the layer thickness is small compared to wavelength. In this circumstances, the thin layer is treated as an interface or boundary. The boundary condition across the interface is given by (Schoenberg, 1980)

$$\begin{cases} [\sigma] = 0, \\ [u] \neq 0, \end{cases} \tag{1}$$

where the bracket [ ] denotes taking the difference of a physical quantity at the two sides of the boundary; σ and u denote, respectively, the stress and displacement, which can be either normal to the interface, or lying in the plane tangential to the interface. The physical meaning of the boundary condition is that the stress is continuous across the interface while the displacement is not. In other words, the wave motion produces a "slip" across the interface. The amount of the slip is determined by the stress and the coupling rigidity η of the interface (i.e., the thin layer),

$$\sigma = \eta\,[u], \tag{2}$$

where $\eta = M/d$; d is the layer thickness and M is the layer's elastic modulus[1)]. Generally, a complex-valued M can be used in eq. (2) to model the non-elastic coupling of the interface. For example, one can use the Kelvin-Voigt viscoe-

* Corresponding author (email: chenxl@upc.edu.cn)

1) Notice that using rigidity to parameterize the thin layer means M and d can assume arbitrary values as long as their ratio is fixed.

© Science China Press and Springer-Verlag GmbH Germany 2018

lastic model (Fehler, 1982) for the complex modulus M, and the normal and tangential coupling rigidities can be respectively written as (Schoenberg, 1980)

$$\begin{cases} \eta_N = \dfrac{\kappa' + 4\mu'/3 + 4\mathrm{i}\omega\upsilon'/3}{d}, & \text{(Normal)} \\ \eta_T = \dfrac{\mu' + \mathrm{i}\omega\upsilon'}{d}, & \text{(Tangential)} \end{cases} \tag{3}$$

where κ' and μ' are the bulk and shear modulus of the layer medium, respectively; υ' is viscosity; ω is angular frequency of the wave motion. The use of the viscoelastic parameters enhances the modeling capability of the slip boundary theory. For example, using $\mu'=0$ in the tangential rigidity, one can model the viscous coupling of a thin Newtonian fluid layer. The above described viscoelastic slip boundary theory will be used to model acoustic wave propagation along a cased borehole and to characterize the effects of cement bonding on the wave propagation.

Cement bond evaluation of a cased borehole is an important requirement for hydrocarbon development and production in the petroleum industry. The development and application of various evaluation technologies have formed a specialty, in which the acoustic technology is one of the key technologies. The acoustic wave attenuation and amplitude variation along a cased borehole are used to evaluate cement bond integrity and quality between casing and formation rocks. In the field application, however, the technology faces many complexities and uncertainties. The lack of cement bond, non-uniform bonding, unconformity or micro annulus at the bonding interface, etc., all have an impact on the wave amplitude. For the problem of micro annulus alone, it is usually difficult to determine whether it occurs at the first interface between casing and cement, or the second interface between cement and formation. The various cement bond complexities are difficult to characterize using the classic elastic wave theory for layered media.

In the classic elastic wave modeling of cased borehole acoustic logging (Tubman et al., 1984), the casing, cement, and formation are modeled as a cylindrically layered structure, and the micro annulus is modeled as a thin fluid layer of invariant thickness (Tubman et al., 1986). Wave propagation through the layered system is solved using the propagation matrix method (Tang and Cheng, 2004), or the generalized ray theory (Chen et al., 1996). Although the classic theory can model the wave phenomenon for ideal situations (e.g., well bonded casing and free pipe conditions), it is not commonly used for field data inversion for two reasons. First, the layered model consists of many parameters and is computation intensive. Second, it has difficulty modeling the non-elastic coupling effect of the cement layer. In field conditions, an interface micro annulus may be irregularly shaped and has roughness, which in general cannot be modeled as a regular fluid layer of invariant thickness. The interface irregularity, or asperity, causes the two sides of the interface to contact. In passing of an elastic wave through the interface, the friction on the contact areas results in non-elastic attenuation of the passing wave, analogous to the wave energy dissipation in a viscous medium. With regard to the limitation of the classic elastic wave modeling, it is necessary to extend the theory to model the non-elastic coupling effects in the field condition. The afore-described viscoelastic slip boundary theory provides a new approach for this extension, which can be employed to effectively model various elastic and non-elastic cement coupling conditions. The new modeling approach also reduces the complexity in the classic cased borehole acoustic modeling.

2. Theoretical analysis

Let us first analyze requirement and condition for reducing the cement layer in the model of Figure 1a to the slip boundary modeling. For the conventional acoustic logging frequency of 10^4 Hz, the wavelength in the system of Figure 1a is several tens of centimeters. In comparison, the cement layer thickness is generally one to a few centimeters, much smaller than one wavelength and thus satisfying the condition for the slip boundary modeling. One can therefore replace the layered model of Figure 1a with the slip interface model of Figure 1b. In the latter model, the inner and outer radius of the casing is r_0 and r_1, respectively; the radius to formation is r_2. As mentioned before, the thickness of the slip interface (the thick-lined ring area in Figure 1b) can be arbitrarily chosen. One can simply choose the layer thickness as $d=r_2-r_1$.

One can now place a monopole acoustic source in the center of the fluid-filled borehole and actuate the axis-symmetric wave motion in the models of Figure 1. For the cylindrical coordinate (r, z), one defines the displacement-stress vector

$$\mathbf{S} = (u_r, u_z, \sigma_{rr}, \sigma_{rz})^{\mathrm{T}}, \tag{4}$$

where u_r and u_z are the radial and axial displacements, respectively; σ_{rr} and σ_{rz} are the normal and shear stresses for a radial boundary or interface, respectively; T denotes transpose.

At the inner casing boundary r_0, the casing displacement u_r^C and stresses σ_{rr}^C and σ_{rz}^C satisfy the boundary condition,

$$\begin{cases} u_r^f = u_r^C, \\ \sigma_{rr}^f = \sigma_{rr}^C, \quad (r = r_0) \\ 0 = \sigma_{rz}^C. \end{cases} \tag{5}$$

The borehole fluid displacement u_r^f and stress σ_{rr}^f contain two contributions,

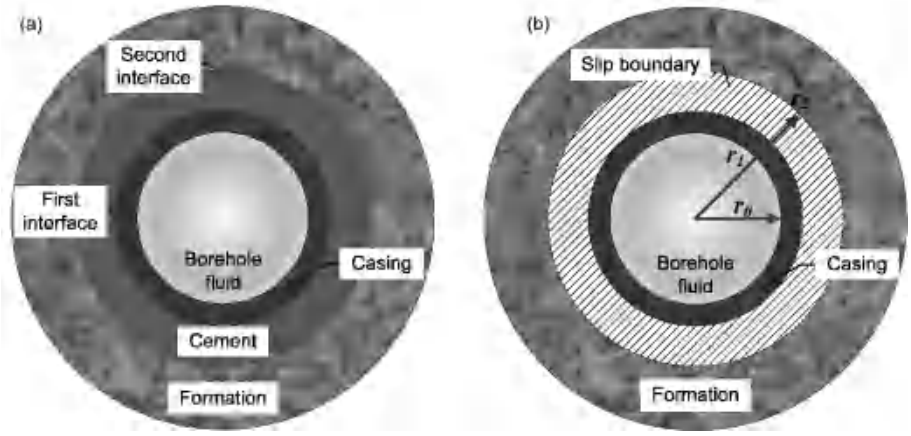


Figure 1 Cased borehole acoustic models. (a) Classic elastic layered model; (b) slip interface model.

$$\begin{cases} u_r^f = u_r^S + u_r^R, \\ \sigma_{rr}^f = \sigma_{rr}^S + \sigma_{rr}^R. \end{cases} \tag{6}$$

One is the direct radiation from the source, u_r^S and σ_{rr}^S, denoted by the superscript "*S*"; the other is the refection from the casing, u_r^R and σ_{rr}^R, denoted by the superscript "*R*".

Applying the slip viscoelastic slip boundary condition to the outer casing boundary r_1 and the formation boundary r_2, one gets

$$\begin{cases} u_r^C = u_r^F + \sigma_r^F / \eta_N, \\ u_z^C = u_z^F + \sigma_{rz}^F / \eta_T, \\ \sigma_{rr}^C = \sigma_{rr}^F, \\ \sigma_{rz}^C = \sigma_{rz}^F, \end{cases} \tag{7}$$

where u_r^F and u_z^F, and σ_{rr}^F and σ_{rz}^F are respectively the normal and shear displacements, and normal and shear stresses of the formation, denoted by the superscript "*F*".

The displacement-stress vector at the casing inner boundary and its counterpart at the outer boundary are connected via the casing propagator matrix **G**, as

$$\mathbf{S}_0 = \mathbf{G}\mathbf{S}_1, \tag{8}$$

where $\mathbf{S}_0$ and $\mathbf{S}_1$ are the vector of eq. (4) evaluated at r_0 and r_1, respectively. The matrix elements of **G** are given in Appendix A (http://link.springer.com). Combining eq. (5) through eq. (8) results in a matrix equation

$$\begin{bmatrix} u_r^R \\ \sigma_{rr}^R \\ 0 \end{bmatrix}_{r=r_0} = \mathbf{G}' \begin{bmatrix} u_r^F + \sigma_{rr}^F / \eta_N \\ u_z^F + \sigma_{rz}^F / \eta_T \\ \sigma_{rr}^F \\ \sigma_{rz}^F \end{bmatrix}_{r=r_1} - \begin{bmatrix} u_r^S \\ \sigma_{rr}^S \\ 0 \end{bmatrix}_{r=r_0}, \tag{9}$$

where **G′** is a 3×4 remainder matrix obtained from the 4×4 matrix **G** by omitting the second row of **G** (because the boundary condition in eq. (5) does not involve the axial displacement u_z). Eq. (9) allows one to model acoustic wave propagation characteristics of the system in Figure 1b.

Removing, form the right hand side of eq. (9), the second term relating to the source radiation results in

$$\begin{bmatrix} u_r^R \\ \sigma_{rr}^R \\ 0 \end{bmatrix}_{r=r_0} = \mathbf{G}' \begin{bmatrix} u_r^F + \sigma_{rr}^F / \eta_N \\ u_z^F + \sigma_{rz}^F / \eta_T \\ \sigma_{rr}^F \\ \sigma_{rz}^F \end{bmatrix}_{r=r_1}. \tag{10}$$

With eq. (10), one can calculate various "eigen" vibration modes of the system. For the axis-symmetric model, the displacement and stress components of borehole fluid at r_0, and those of the formation at r_2, are respectively given below (Tang and Cheng, 2004).

$$\begin{cases} u_r^R = -Af I_1(fr_0) \\ \sigma_{rr}^R = A\rho_f \omega^2 I_0(fr_0) \end{cases}, \text{ (Borehole fluid)}$$

$$\begin{cases} u_r^F = [-p_{fm} K_1(p_{fm} r_2)]B + [-s_{fm} K_1(s_{fm} r_2)]F, \\ u_z^F = [\mathrm{i}kK_0(p_{fm} r_2)]B + [-s_{fm}^2 K_0(s_{fm} r_2)]F, \\ \sigma_{rr}^F = [\rho_{fm}(\beta_{fm}^2 k^2 - \omega^2)K_0(p_{fm} r_2) \\ +\rho_{fm}\beta_{fm}^2 p_{fm} K_1(p_{fm} r_2)/r_2]B \\ +[\rho_{fm}\beta_{fm}^2 s_{fm}^2 K_0(s_{fm} r_2) + s_{fm} K_1(s_{fm} r_2)/r_2]F, \\ \sigma_{rz}^F = [\mathrm{i}k\rho_{fm}\beta_{fm}^2 p_{fm} K_1(p_{fm} r_2)]B \\ +[\rho_{fm}\beta_{fm}^2 (k^2 + s_{fm}^2) s_{fm} K_1(s_{fm} r_2)]F, \end{cases} \text{ (Formation)} \tag{11}$$

where ρ_f is fluid density; $f = \sqrt{k^2 - \omega^2/\alpha_f^2}$ is fluid radial wavenumber; α_f is fluid acoustic velocity; k is axial wavenumber; ρ_{fm} is formation density; $p_{fm} = \sqrt{k^2 - \omega^2/\alpha_{fm}^2}$ and $s_{fm} = \sqrt{k^2 - \omega^2/\beta_{fm}^2}$ are respectively the formation radial compressional and shear wavenumbers; α_{fm} and β_{fm} are respectively the formation compressional and shear velocities;

I_n and K_n (n=0,1) are the modified Bessel function of the first and second, respectively; A is the amplitude coefficient of the borehole acoustic wave, and B and F are the amplitude coefficient of the formation compressional and shear wave, respectively. Substitution of eq. (11) into eq. (10) results in a matrix equation for the coefficients A, B, and F. The non-trivial solution of the coefficients requires that the determinant $D(k, \omega)$ of the matrix be zero, leading to

$$D(k,\omega) = 0. \tag{12}$$

This gives the dispersion equation for the acoustic wave modes of the system. For a given angular frequency ω, the equation is solved to find the wavenumber k for a designated wave mode and calculate its phase velocity dispersion and attenuation. For the axis-symmetric system, the wave modes of eq. (12) include Stoneley, pseudo-Rayleigh, and (for a poorly bonded cased borehole) the casing extensional wave.

Given the source radiation in eq. (9), one can calculate the acoustic waveforms along the borehole. For a monopole source located at r=0 and z=0, its radiated displacement and stress wave spectra at the casing wall are expressed by the following wavenumber integral (Tang and Cheng, 2004).

$$\begin{bmatrix} u_r^S \\ \sigma_{rr}^S \end{bmatrix}_{r=r_0} = \frac{1}{\pi}\int_{-\infty}^{+\infty} S(\omega) \begin{bmatrix} fK_1(fr_0) \\ \rho_f \omega^2 K_0(fr_0) \end{bmatrix} \mathrm{e}^{\mathrm{i}kz}\mathrm{d}k, \tag{13}$$

where $S(\omega)$ is the source wave spectrum. A Gaussian function is usually used, as

$$S(\omega) = \mathrm{e}^{-\left(\frac{\omega-\omega_0}{2\pi f_{bd}}\right)^2}, \tag{14}$$

where ω_0 is the center angular frequency of the source; f_{bd} specifies the bandwidth of the source spectrum. (The following modeling calculations use f_{bd}=2.5 kHz to model the band-limited frequency excitation of an actual logging tool.) Substituting eqs. (11) and (13) into eq. (9) and solving for the acoustic wave amplitude coefficient $A(k, \omega)$, one can calculate the acoustic pressure waveform along the borehole axis using the following wavenumber-frequency integration

$$p(z,t) = \int_{-\infty}^{+\infty} S(\omega)\mathrm{e}^{-\mathrm{i}\omega t}\mathrm{d}\omega \int_{-\infty}^{+\infty} [1 + A(k,\omega)]\mathrm{e}^{\mathrm{i}kz}\mathrm{d}k. \tag{15}$$

Although the above analysis corresponds to the monopole acoustic logging, the slip boundary condition of eqs. (1)–(3) can be applied to describe the coupling condition at any part of the casing. The analysis of eq. (4) though eq. (15) can be extended to the multipole logging situation. Using Fourier synthesis of the multipole mode solutions, the effects of the local coupling condition anomaly can be modeled. For the present monopole logging situation, the effect of the local anomaly can be detected if the azimuthal average of the effect is not zero. The above analysis can be used to quantify the average effect of the anomaly, although the azimuth of the effect can not be resolved.

3. Theoretical modeling

Based on the above theoretical analysis result, one can calculate the borehole acoustic propagation and attenuation characteristics using the model parameters in Tables 1 and 2.

To validate the theoretical analysis, the ideal well bonded and unbonded (i.e., the free-pipe) situations are first modeled. The results are then compared with those modeled using the classic elastic wave theory.

To model the well-boned situation, the shear rigidity of eq. (3) is set to infinity and the normal rigidity is set to 500 GPa m^{-1}. The viscosity parameter is set to zero for this elastic wave modeling. Figure 2 shows the acoustic pressure waveform (lower solid curve) calculated for a receiver 3.65 m away from the source (source center frequency is 8 kHz). In the 0–2.2 ms time range, the first arrival is the formation P wave, instead of the faster casing wave, showing the absence of casing waves for the well bonded condition. This result is in agreement with that of the classic elastic modeling (upper dashed curve). In fact, this result can be derived from the slip boundary condition in eq. (2), which shows that, for a finite and continuous stress, the slip, or the displacement discontinuity, vanishes when the coupling rigidity goes to infinity. In this situation, both the stress and displacement are continuous across the boundary and the slip boundary condition becomes the classic welded boundary condition. For the cased borehole acoustic problem, this means the casing and formation are well coupled by the cement.

For the unbonded free pipe situation, a 0.5 cm fluid layer is inserted between casing and cement in the classic elastic modeling. For the complicated elastic-fluid layered system, the slip boundary model uses an equivalent interface layer of 2 cm thickness and sets the shear rigidity of eq. (3) to zero for modeling the fluid coupling. (Also, for the ideal fluid, the viscosity is set to v'=0, besides setting η_T=0). The fluid coupling is modeled by using η_N=615 GPa m^{-1}. Other modeling parameters are kept the same as Figure 2. The calculated waveforms for a receiver array located from 3.65 to 4.35 m from source are shown in Figure 3. The receiver spacing is 0.1 m.

In the slip boundary modeling result of Figure 3a, the first arriving wave, labeled C, is the casing extensional wave. The formation compressional wave, labeled P, is difficult to discern because of the ringing casing wave. The later arrival, labeled S, is the formation shear wave. The modeled wave phenomena in Figure 3a are very similar to those in Figure 3b modeled using the elastic wave theory, both showing the dominance of the casing wave in the unbonded free-pipe situation as previously modeled by Tubman et al. (1986). Worth mentioning is that the wave phenomena from the complicated casing-fluid-cement-formation model can be modeled using the relatively simpler slip boundary model,

Table 1 Model parameters for borehole fluid, casing, cement, and formation

Medium	Compressional wave velocity (m s^{-1})	Shear wave velocity (m s^{-1})	Density (g cm^{-3})	Radius (m)
Fluid	1500	–	1.0	–
Casing	6098	3354	7.5	0.07
Cement	2823	1729	1.9	0.08
Formation	3500	2000	2.5	0.10

Table 2 Cement parameters for the viscoelastic coupling rigidity

Parameter	Value
Bulk modulus (GPa)	2.25–∞
Shear modulus (GPa)	0.10–∞
Viscosity (Pa s)	10^{-2}–10^{5}
Thickness (m)	2×10^{-2}

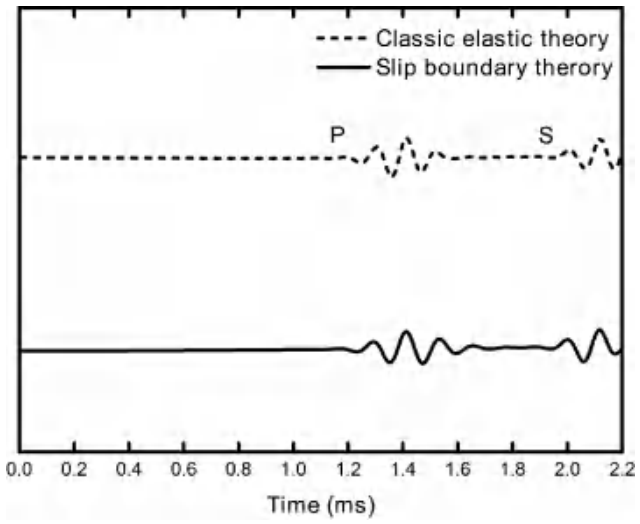


Figure 2 Comparison of modeling results for the slip (lower solid curve) and classic (upper dashed curve) boundary conditions. The labels P and S correspond to formation compressional and shear waves, respectively.

demonstrating the good modeling capability of the latter theory. The following example shows that the theory is particularly suitable for modeling wave attenuations associated with varying cement bonding conditions.

In cement evaluation using acoustic logging, the acoustic wave attenuation and its variation are commonly used to evaluate the quality of cement bonding. The attenuation modeling is rather difficult for the elastic wave theory, because the change of attenuation due to varying cement bond quality cannot be properly modeled by varying the cement and fluid annulus parameters. This modeling is easily handled using the viscoelastic slip boundary condition of eq. (3). Consider the imaginary part of the tangential coupling rigidity η_T, defined as the viscous rigidity $\xi_T=v'/d$. From physical intuition, the "viscosity" of a slip boundary results from the nonelastic friction between the opposite sides of the boundary, which is dominantly a shear motion. One can therefore set in eq. (3) $\eta_N=\infty$ to ignore the contribution of normal coupling to the casing extensional wave. One can thus use the single parameter ξ_T to characterize wave attenuation. Figure 4 shows the synthetic waveforms for three ξ_T values varying from small, medium, to large values (which are respectively $\xi_T=1\times10^4$, 2×10^5, 1×10^6 Pa s m^{-1}). The source-to-receiver distance is 3.65 m and other modeling parameters are the same as Figure 2. The modeling results well simulate the change of attenuation from small to large, as commonly seen from the actual acoustic logging data.

For small ξ_T, the wave phenomenon shown in the bottom waveform is similar to that of the free-pipe situation, showing the dominant first arriving casing wave. With increasing ξ_T, wave attenuation increases and the casing wave amplitude decreases (middle waveform), unmasking the formation P-wave arrival. For large ξ_T, the casing wave is almost completely attenuated and the waveform consists of mostly the formation P and S waves (upper waveform). The situation is very similar to the well bonded situation of Figure 2. The moderate attenuation in the middle waveform, which is difficult to model using the classic elastic modeling, is well modeled by using the viscous rigidity parameter ξ_T. One can therefore use this parameter to characterize the wave attenuation associated with cement bond condition and in turn evaluate the cement bond quality.

One now studies the effect of the real part of η_T (defined as shear rigidity, which is the tangential coupling rigidity evaluated with $v'=0$) on the acoustic waves propagating along casing. Measurements have shown that the value of shear rigidity ranges between 10^8–10^{12} Pa m^{-1} (Pyrak-Nolte et al., 1990; Hsu and Schoenberg, 1993). Using three values in this range (see Table 2) in the calculation gives the three dispersion curves for the casing extension wave in the 0–15 kHz frequency range. A marked characteristic of these curves is the dispersion of the casing wave, with dispersion effect increasing with decreasing frequency. (For comparison, the casing wave velocity for the free-pipe situation is plotted as a dashed line in this figure.) Relative to the free-pipe velocity, the casing wave velocity decreases due to the shear coupling rigidity of the slip interface. The higher the shear rigidity, the larger is the velocity decrease. This modeling result can be used to provide an important basis for evaluating the bonding condition at the first or second in-

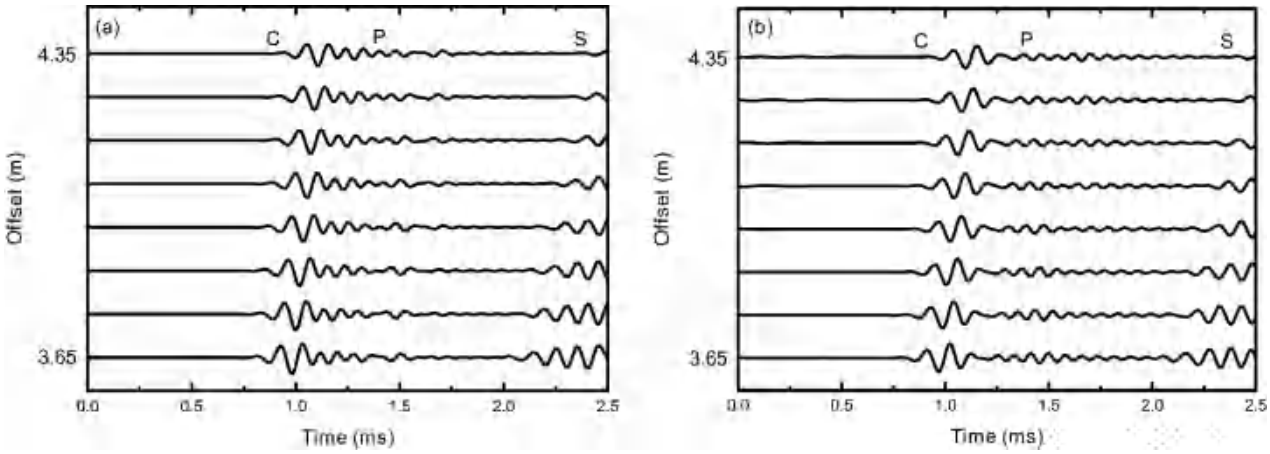


Figure 3 Synthetic array waveform for the unbonded free-pipe situation, respectively calculated using (a) slip boundary condition, and (b) classic elastic wave theory.

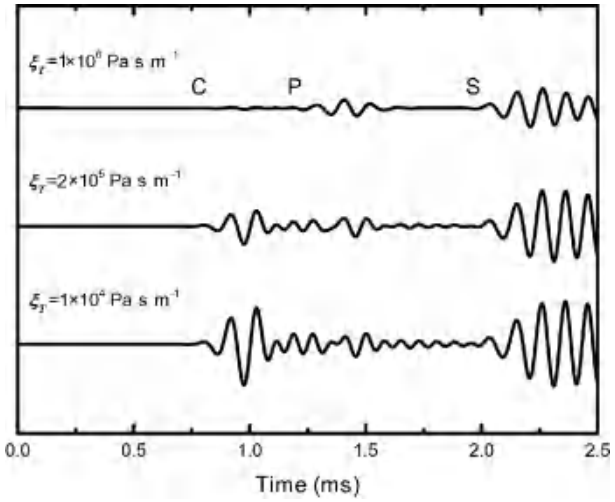


Figure 4 Simulated attenuation variation (weak to strong) using three viscous rigidity values. The label C, P, and S denote casing, formation compressional, and shear waves, respectively.

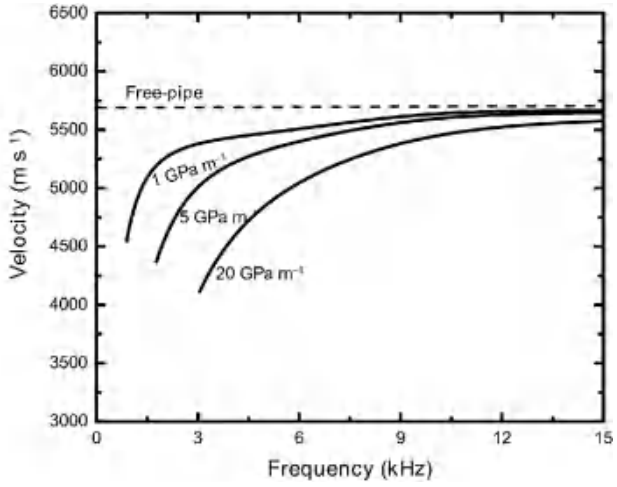


Figure 5 Theoretical dispersion curves of casing extensional wave modeled using three cement shear rigidity values.

terface behind casing. A well-known observation in cased borehole acoustic logging is: when the cement is well coupled with casing but poorly coupled with formation, the casing wave shows a significant velocity decrease (Tao et al., 2004; Zhang et al., 2006). The physical mechanism for the velocity decrease is: the circular casing coupled with cement (the elastic modulus of the latter is much lower than that of the former) behaves like an acoustic wave guide with reduced modulus, resulting in the reduction of the velocity for the extensional wave along casing. According to the modeling result of Figure 5, the condition of the cement attached to casing can be effectively modeled by the effective shear rigidity value. The higher the shear rigidity value, the bigger amount of cement is attached to casing and larger reduction of the casing wave velocity. On the other hand, if there is no cement attachment to casing (i.e., the free-pipe condition), the corresponding shear rigidity value becomes zero.

The above modeling results demonstrate that the viscous and shear rigidity parameters of the viscoelastic slip boundary theory can be used to effectively characterize and evaluate cement bond quality between casing and formation. The value of the viscous rigidity is directly related to the bonding quality, while the value of the shear rigidity is directly related to the amount of cement attached to casing, allowing for evaluating whether the bonding quality issue occurs at the first interface (there is no or little cement attachment to casing), or the second interface (large amount of cement is attached to casing).

4. Application of the theory

The new theory developed here is now applied to the field acoustic data acquired in a cased borehole. By modeling

wave propagation and attenuation characteristics, one can infer and interpret the cement bond condition behind casing. For this 40 year-old cased borehole, the casing has been severely eroded over time. The erosion effect is taken into account by changing the casing inner radius from 0.08 to 0.083 m. The casing outer radius is 0.089 m. Figure 6a shows the array waveforms for a depth along the borehole. The data clearly show the presence of casing (labeled "C") and relatively large-amplitude formation compressional (labeled "P") waves. By applying the Slowness-Time-Coherence (STC) method (Tang and Cheng, 2004) to the array data, a formation P-wave velocity value of 2630 m s^{-1} is determined. By using the Slowness-Frequency-Coherence (SFC) method (Tang and Cheng, 2004) to the same data, one obtains the casing wave dispersion data shown in Figure 6c.

The waveform and the casing wave dispersion characteristics are now modeled using the above theory. For this low-velocity formation, one assumes that the formation shear-wave velocity is twice of the P-wave velocity and the formation density is 2.3 g cm^{-3}. Using a number of viscous and shear rigidity values in the modeling, one finds that η_T= 0.1 GPa m^{-1} and ξ_T=1.5×10^5 Pa s m^{-1} can model the data quite well. Figures 6b and c give the theoretical array waveforms and casing wave dispersion curve, respectively. The waveforms (calculated for a 7 kHz center frequency source) resemble the field data (Figure 6a) quite well, showing small amplitude (significantly attenuated) casing wave followed by a large amplitude formation P-wave. In the frequency range of 5–12 kHz where the dispersion data scatter is relatively small, both theory and data agree well, showing a slight deceasing trend with decreasing frequency, although this trend in the data is not significant. Based on the high viscous rigidity value (ξ_T=1.5×10^5 Pa s m^{-1}) and significant attenuation of the casing wave, one can infer that there is fairly good bonding between casing and formation. However, the presence of the casing wave of measureable amplitude indicates that there is still an issue with the bond quality. For the low shear rigidity value (0.1 GPa m^{-1}) from the modeling, one can determine that quality issue is from the first interface between casing and cement.

Figure 7a shows the array wave data for another depth from the cased borehole. The data shows strong casing waves (labeled "C") overlapping with the later formation compressional waves (labeled "P"). The formation P wave velocity calculated from data is 3034 m s^{-1}; the casing wave dispersion data from the waveforms are shown in Figure 7c. Following the same procedure as Figure 6, the theoretical modeling results for η_T=6 GPa m^{-1} and ξ_T=1×10^4 Pa s m^{-1} are shown in Figure 7b (waveforms) and Figure 7c (dispersion curve), respectively. The theoretical waveform characteristics compare with the field data characteristics quite well, both showing the (almost) non-attenuating (compared to Figure 6a), strong casing wave, with an amplitude comparable to that of the formation P wave. Especially, both the

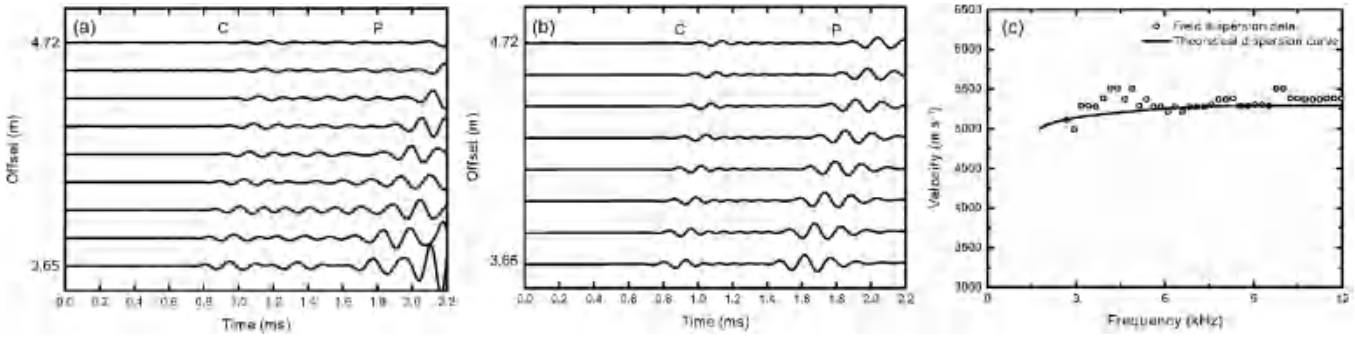


Figure 6 Theoretical modeling of cased borehole acoustic data for the poorly-bonded first interface. (a) Field array wave data; (b) modeled array wave data; (c) theoretical dispersion curve and field dispersion data.

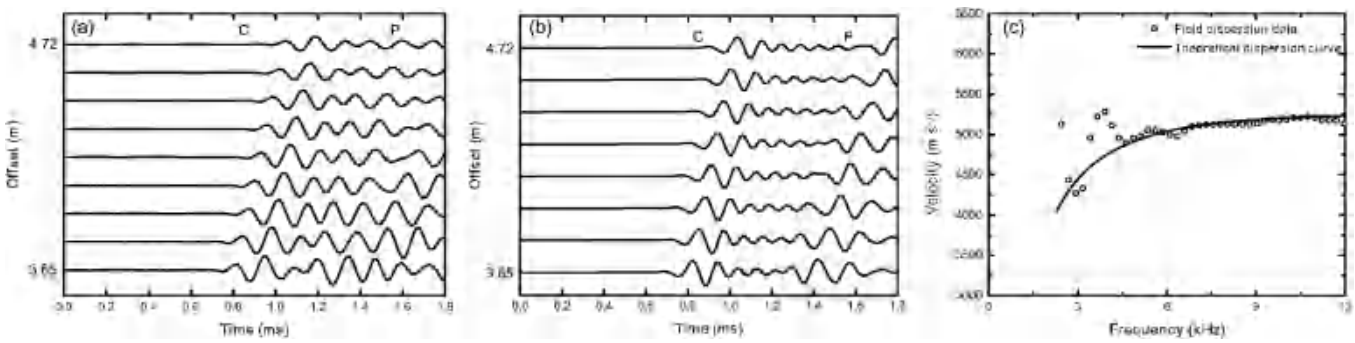


Figure 7 Theoretical modeling of cased borehole acoustic data for the poorly-bonded second interface. (a) Field acoustic data; (b) modeled acoustic data; (c) theoretical dispersion curve and field dispersion data.

theoretical and field dispersion data show the similar dispersion trend, with the velocity decreasing with decreasing frequency. Moreover, for the entire frequency band, the casing wave velocity is significantly lower than its counterpart in Figure 6c. The small ξ_T value (1×10^4 Pa s m^{-1}) of the model and low attenuation in the casing wave data indicate the poor cement bond behind casing. The significant casing velocity reduction and the high η_T value (6 GPa m^{-1}) of the model indicate that a large amount of cement mass is attached to the casing. One can therefore infer that the bonding quality issue is from the second interface between cement and formation.

5. Conclusion

The cement bond condition of a cased borehole can have two major impacts on the acoustic propagation along the borehole. One is that the variation of the bonding quality causes various degrees of wave attenuation and amplitude changes; the other is that, for a poorly bonded second interface, the amount of cement mass attached to casing produces measurable dispersion and velocity reduction of the casing wave. By modeling the cement behind casing as a viscoelastic slip interface, an acoustic wave theory has been developed to effectively model and characterize the wave phenomenon associated with the cement bond condition. Using the viscous and shear rigidity parameters, the theory can well describe the variations of wave amplitude attenuation and velocity dispersion, as has been demonstrated using field data modeling. Compared with the classic elastic modeling of layered media, the new theory has a broader application scope in cement evaluation using cased borehole acoustic logging.

Acknowledgements *The authors thank the reviewers for their valuable comments and suggestions that helped improve the manuscript. This work was supported by the National Natural Science Foundation of China (Grant No. 41774141).*

References

Chen X, Quan Y, Harris J M. 1996. Seismogram synthesis for radially layered media using the generalized reflection/transmission coefficients method: Theory and applications to acoustic logging. Geophysics, 61: 1150–1159

Fehler M. 1982. Interaction of seismic waves with a viscous liquid layer. Bull Seismol Soc Amer, 72: 55–72

Hsu C J, Schoenberg M. 1993. Elastic waves through a simulated fractured medium. Geophysics, 58: 964–977

Pyrak-Nolte L J, Myer L R, Cook N G W. 1990. Transmission of seismic waves across single natural fractures. J Geophys Res, 95: 8617–8638

Schoenberg M. 1980. Elastic wave behavior across linear slip interfaces. J Acoust Soc Am, 68: 1516–1521

Tang X M, Cheng C H. 2004. Quantitative Borehole Acoustic Methods. Amsterdam: Elsevier

Tao H, Zhang H, Hou C, Zhang Y. 2004. Developing cementing quality control technology to meet the requirement of oilfield exploration (in Chinese). Well Logging Technology, 28: 9–12

Tubman K M, Cheng C H, Toksöz M N. 1984. Synthetic full waveform acoustic logs in cased boreholes. Geophysics, 49: 1051–1059

Tubman K M, Cheng C H, Cole S P, Toksöz M N. 1986. Synthetic full-waveform acoustic logs in cased boreholes, II—Poorly bonded casing. Geophysics, 51: 902–913

Zhang H, Huang B, Tao H, Shang Z, Ma J, Wang K. 2006. Detecting cementing quality of secondary interface by using acoustic variable density logging. J Hohai Univ-Nat Sci, 34: 552–556

(Responsible editor: Xingyao YIN)

GEOPHYSICS, VOL. 84, NO. 4 (JULY-AUGUST 2019); P. D161–D169, 7 FIGS., 1 TABLE.
10.1190/GEO2018-0798.1

Cased borehole acoustic-wave propagation with varying bonding conditions: Theoretical and experimental modeling

Can Jiang[1], Xue-Lian Chen[1], Yuan-Da Su[1], and Xiao-Ming Tang[1]

ABSTRACT

Acoustic measurements in cased boreholes are important for cement-bond evaluation behind the casing. In conjunction with a recently developed acoustic-wave theory using slip-boundary modeling, we carried out an experimental study for different cement-bond conditions. Four different cased-hole models were constructed, where the interface between the casing and the cement, and that between the cement and the formation, are decoupled or partially bonded to simulate the different cement bond conditions. An acoustic system is placed in the borehole to measure extensional casing waves along the borehole. By extracting the attenuation and velocity of casing waves from the experimental data, the bonding conditions were analyzed and compared with the theoretical modeling. The results indicate that, compared with the free-pipe situation, the casing waves are attenuated when there is some degree of bonding (good or poor) between the casing and the formation. However, when the poor bonding occurs at the cement-formation interface, the casing wave indicates significant velocity reduction and dispersion, the degree of the velocity change varying with the bonding condition. This wave phenomenon is predicted by the slip-boundary modeling. By adjusting the slip-boundary parameters in the modeling, the experimental results can be quantitatively modeled. These results are also confirmed by cased-hole acoustic logging data examples. The theoretical model can therefore be used to interpret cased-borehole acoustic-wave measurements.

INTRODUCTION

Cement-bond evaluation of a cased borehole is an indispensable step for well completion, which is closely related to well integrity and production safety. Current evaluation by acoustic logging mainly uses the amplitude variation and attenuation of casing waves to evaluate the bond condition. In field applications, however, this technology faces many complexities and uncertainties. For example, the lack of cement, nonuniform bonding, unconformity or micro fluid annulus, all have an impact on the wave amplitude. For the bonding quality issue alone, the bonding conditions at the first interface (between the casing and the cement) and the second interface (between the cement and the formation) can affect the amplitude and attenuation of the casing waves. In many cases, the current technology cannot distinguish at which interface the bonding problem occurs.

In cased-borehole wavefield modeling (Tubman et al., 1984; Wang et al., 2016; Wang and Fehler, 2018) using the classic elastic wave theory for layered media, the casing and cement are modeled as cylindrical layers between the borehole and the formation. A fluid layer is added between the casing and the cement (or the cement and the formation) to simulate the poor bonding condition (Tubman et al., 1986). This method is only available for ideal situations, such as a good bond, free pipe, and bond to casing only (i.e., cement debonded with the formation), etc. However, in most cases, such as with interface roughness and irregularity contact, lack of a cement bond, nonuniform bonding, unconformity, microannulus, etc., are common in the downhole measurements, which may not be satisfactorily modeled using the existing theoretical modeling. Using scaled laboratory borehole models, acoustic wave propagation characteristics in a cased borehole have also been experimentally studied (Schoenberg et al., 1981; Chang and Everhart, 1983). As with the above theoretical models, however, these experiments mainly studied the bonded and unbonded conditions between the casing and the formation. The bonding condition between the cement and the formation were not analyzed.

Manuscript received by the Editor 19 November 2018; revised manuscript received 30 January 2019; published ahead of production 27 March 2019; published online 27 May 2019.
[1]China University of Petroleum, Qingdao, China. E-mail: jiangcan_upc@sina.com; chenxl@upc.edu.cn; syuanda@sina.com; tangxiam@aliyun.com (corresponding author).
© 2019 Society of Exploration Geophysicists. All rights reserved.

Downloaded from pubs.geoscienceworld.org/seg/geophysics/article-pdf/84/4/D161/4806203/geo-2018-0798.1.pdf by Univ of Petroleum (Beijing) - Library user on 09 October 2026

Tang et al. (2018) recently develop an acoustic-wave theory for casing bond evaluation, in which the cement layer between the casing and the formation is modeled as a viscoelastic slip interface with complex coupling stiffness parameters. In a simplistic manner, the slip-boundary condition can be expressed (Schoenberg, 1980; Fehler, 1982) as

$$\begin{cases} [\sigma] = 0; \\ [\mathrm{u}] = \sigma/\eta; \end{cases} \quad (1)$$

where the bracket [ ] denotes taking the difference of a physical quantity at both sides of an interface; σ and u represent, respectively, the normal and shear stresses and displacements; and η denotes the complex coupling stiffness of the interface. Through the stiffness parameters, this boundary condition can model various wave-propagation characteristics along the borehole. The implementation of the boundary condition in a cased borehole is described in Appendix A. In addition to modeling the well-bonded and free-pipe conditions, the new theory can model the waveform variations (i.e., wave attenuation and dispersion) between the above two conditions, allowing for extracting cement-quality information from the acoustic data. In particular, the theory predicts a significant casing-wave dispersion phenomenon associated with the bonding condition variation at the second interface. With these new developments, it is worth carrying out an experimental study on acoustic-wave propagation in the cased borehole with varying bonding conditions. Our experiments include four full-scale cased borehole models: (1) free pipe, (2) poor bond of the first interface, (3) poor bond of the second interface model, and (4) debonded second interface model. Array acoustic waveform data were acquired using a laboratory analog logging device.

In this paper, we first describe the experimental model fabrication. Afterward, we analyze the experimental measurement data. The frequency-velocity coherence (FVC) method (Tang and Cheng, 2004) is used to obtain the dispersion data of the casing waves. We also compare the dispersion and attenuation characteristics of the casing waves with the theoretical modeling results.

EXPERIMENTAL MODELS AND MEASUREMENTS

Fabrication of the cased borehole models

Figure 1 illustrates the four cased-borehole models in our experiments. As Chen (1982) points out, the models should be large enough to capture acoustic signals of interest along the borehole before the model boundary reflection waves. This consideration is also taken into account for our model and measurement. The casing pipe in our model is made of a standard 7 in steel pipe. Before the casing installation, the open-hole formation acoustic parameters were measured by an acoustic logging tool. The cement materials for the models are also sampled, and their acoustic parameters are measured. The parameters from both measurements compare quite well. The model parameters are summarized in Table 1.

Model (a) represents the typical free-pipe condition of a cased borehole, where the formation (formation 1 in Table 1) is made of a mixture of cement and sand. The casing pipe is centered in the borehole, and the annulus between the pipe and formation is filled with water. Unlike model (a), the formation of model (b) is a limestone, whose P-wave velocity is faster than the casing-wave velocity. As shown in Figure 1b, a 1.6 m long section of the casing is wrapped with a 5 mm thick rubber layer. The acoustic property of the rubber is given in Table 1. The rubber is used to simulate the poor bonding condition between the casing and the cement. The casing with the rubber layer is cemented with a class G cement.

The formation of model (c) (formation 2 in Table 1) is a slow formation made of a mixture of cement and soft microspheres, the resulting shear velocity being slower than acoustic velocity of water. Model (c) has a 7 in casing pipe bonded with a class

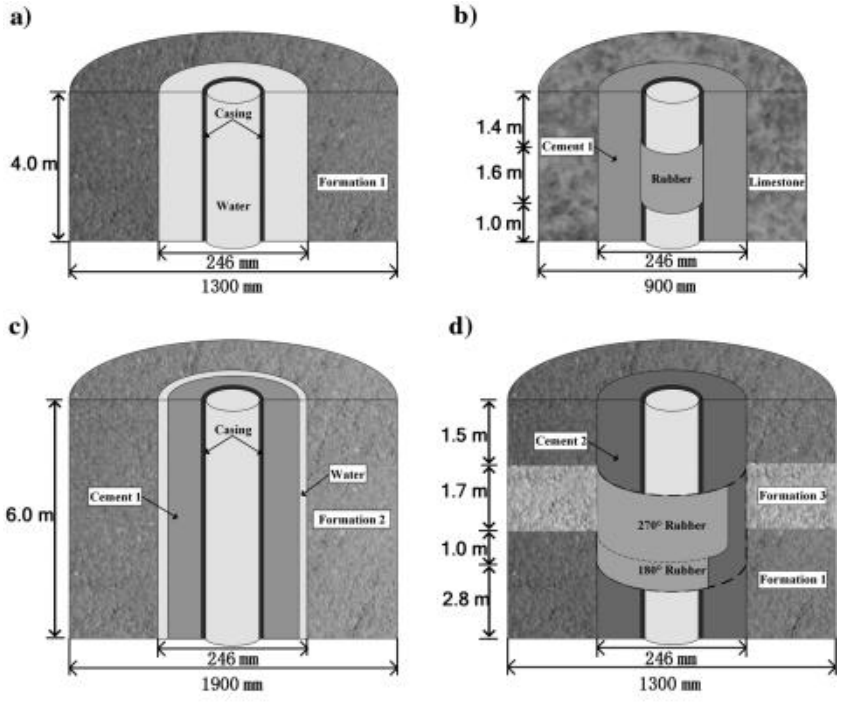


Figure 1. Experimental cased-borehole models. (a) Free-pipe model, (b) rubber layer coupled-casing and cement to simulate the poorly bonded first interface, (c) fluid annulus between the cement and the formation to simulate the decoupled second interface, and (d) the 270° and 180° rubber-coupled-azimuthal sectors between the cement and the formation to simulate the partially bonded second interface. The model parameters are listed in Table 1.

Downloaded from pubs.geoscienceworld.org/seg/geophysics/article-pdf/84/4/D161/4806203/geo-2018-0798.1.pdf by Univ of Petroleum (Beijing) - Library user on 09 October 2026

G cement (cement 1 in Table 1) cylinder. Between the cylinder and the formation is a fluid annulus filled with water.

The formation of model (d) consists of three zones. The upper and lower zones have the same formation property (formation 1, Table 1). The middle zone with 1.7 m height is a slow formation (formation 3, Table 1). There is a 5 mm thick rubber layer between the cement and formation, covering a 270° azimuthal sector. For the remaining 90° sector, the cement is well-bonded to the formation. The same fabrication is made in the lower formation zone with 1.0 m height, where the rubber layer spans only a 180° azimuthal sector, and the remaining 180° sector is well-bonded to the formation. Note that the cement of model (d) is a mixture of cement and sand (cement 2, Table 1).

Experimental system

Figure 2 shows the laboratory measurement system models. Two piezoelectric transducers made of a piezoelectric cylinder of 70 mm diameter and 50 mm height are placed in the borehole. They are mounted on a thin Polivinyl chloride (PVC) pipe, with S and R denoting the source and receiver, respectively. The source is connected to a signal generator to actuate acoustic wave signals. The receiver is connected to an acquisition system. The signal generation and data acquisition are controlled by a computer. In the measurement process, the source and receiver are centered to mitigate the effect of multipole wave signals caused by eccentricity (Kurkjian and Chang, 1986). For a fixed source position, the receiver moves up and down along the PVC pipe. The waveforms are recorded for 10 consecutive receiver positions. The source to first receiver distance is 1.0 m, and the receiver spacing is 0.05 m. The source function is a single-period sine wave, and its center frequency is adjustable in the 3–10 kHz range, which is the frequency range of interest to this study. The recorded waveforms consist of 1024 samples with an increment of 4 μs.

EXPERIMENTAL RESULTS AND ANALYSIS

The experimental array waveform analysis for the above four cased-borehole models is presented in this section. The velocity dispersion of the casing waves is obtained using an FVC processing method (Tang and Cheng, 2004, Chap. 3). The results will be compared with those from the theoretical modeling using slip-boundary theory (Tang et al., 2018).

Table 1. Parameters of the four cased-borehole models.

Medium	P-wave velocity (m/s)	S-wave velocity (m/s)	Density (g/cm^3)	Inner radius (m)
Fluid	1470	—	1.0	0
Casing	5860	3150	7.5	0.080
Cement 1	2846	1654	1.8	0.089
Cement 2	4079	2235	2.4	0.089
Limestone	5988	3040	2.5	0.123
Formation 1	3642	2165	2.3	0.123
Formation 2	2655	1379	1.5	0.123
Formation 3	2353	1238	1.4	0.123
Rubber	1550	50	1.0	—

Free pipe and poorly bonded casing-cement model

Figure 3 shows the measured array waveform data and the corresponding FVC processing results for the free pipe (model a in Figure 1) and the poorly bonded casing and cement (model b in Figure 1) cases, respectively. The array waveforms in Figure 3a (model a) and 3c (model b) span a source-receiver distance from 1.00 to 1.45 m, with a receiver increment of 0.05 m. For the model (b), the waveforms acquired are only from the poor bonding section (see Figure 1b). From Figure 3a, two wave arrivals can be clearly identified, that is, the casing wave labeled as C and the Stoneley wave labeled as ST. The formation arrival is masked by the casing wave and cannot be distinguished. For the poor bonding case of Figure 3c, the waveforms are similar to those of the free-pipe case (Figure 3a). The first arrival (labeled C) is the casing wave instead of the formation P-wave. This is because, compared to the ringing casing wave, the amplitude of the formation P-wave is very small and beyond the recognition capacity of the lab logging tool. Compared to Figure 3a, the casing wave in Figure 3c shows lower amplitude. The last-receiver casing wave amplitude spectra of the two cases are displayed in Figure 3b and 3d (the light curves), respectively. This shows that the rubber coupling between the casing and the cement causes some attenuation of the casing wave relative to the free-pipe scenario. Using the RMS amplitudes of the casing-wave data across the array, we can calculate the average casing-wave attenuation over the array and the average attenuation of Figure 3a and 3c is 4.31 and 7.79 dB/m, respectively. The small but measurable attenuation of the free-pipe wave data is presumably caused by the PVC pipe between the source and receiver, which has a very low quality factor for the extensional wave (Tang, 1992).

Figure 3b and 3d shows the dispersion analysis results using the FVC method. The FVC data as a function of frequency and velocity are displayed by a variable-density image, with the peak values (dots) of the image delineating the velocity of the casing wave at each frequency. Despite some fluctuation, the velocity data show little variation with frequency, both averaging approximately

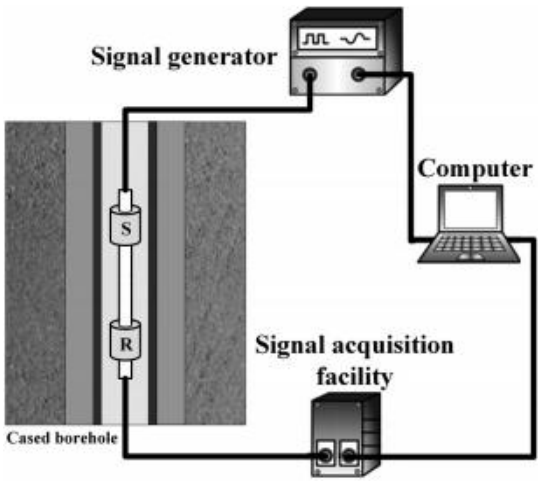


Figure 2. The schematic for the laboratory measurement system.

Downloaded from pubs.geoscienceworld.org/seg/geophysics/article-pdf/84/4/D161/4806203/geo-2018-0798.1.pdf by Univ of Petroleum (Beijing) - Library user on 09 October 2026

5360 m/s, which is very close to the extensional-wave velocity of the steel pipe. This result can also be described by the theory of Tang et al. (2018) using slip-boundary coupling, which shows that, for a casing poorly bonded with cement, the casing wave is a dispersion-free wave propagating at the casing extensional-wave velocity.

Decoupled cement-formation model

Next, we study the effects of decoupling at the second interface (the model c of Figure 1). In this model, the interface is well-bonded and there is a 10 mm water annulus between the cement and formation. The formation is a slow formation whose P- and S-wave velocities are 2655 and 1379 m/s, respectively. To measure wave characteristics of less than 10 kHz, a lower source frequency (approximately 7 kHz) was used. The array waveforms recorded in the borehole are shown in Figure 4a, with a source-receiver distance of 1.20 m and consecutive 13 receiver positions incremented at 0.05 m. In this case, the casing wave (labeled C) is significantly delayed relative to the free-pipe case in Figure 3a. There is an increase in attenuation relative to the free-pipe case. The calculated attenuation across array is approximately 6.58 dB/m. To show the attenuated casing wave, the amplitude of the later Stoneley wave (labeled ST) is clipped in the display.

The dispersion analysis results, using the FVC method, are displayed in Figure 4b. The velocity dispersion data (dots) from picking the peak values of the FVC image shows little variation with frequency, especially in the frequency range of 4–11 kHz, where the wave amplitude spectrum is significantly above its low-amplitude baseline. However, the average value of the velocities is only 4198 m/s, significantly reduced from its free-pipe counterpart of 5360 m/s. This phenomenon is consistent with the field observation in cased borehole acoustic logging. That is, when there is poor or no bonding between the cement and the formation, the measured casing-wave velocity is slower compared to the free-pipe situation. This happens because the casing-cement system, when not or

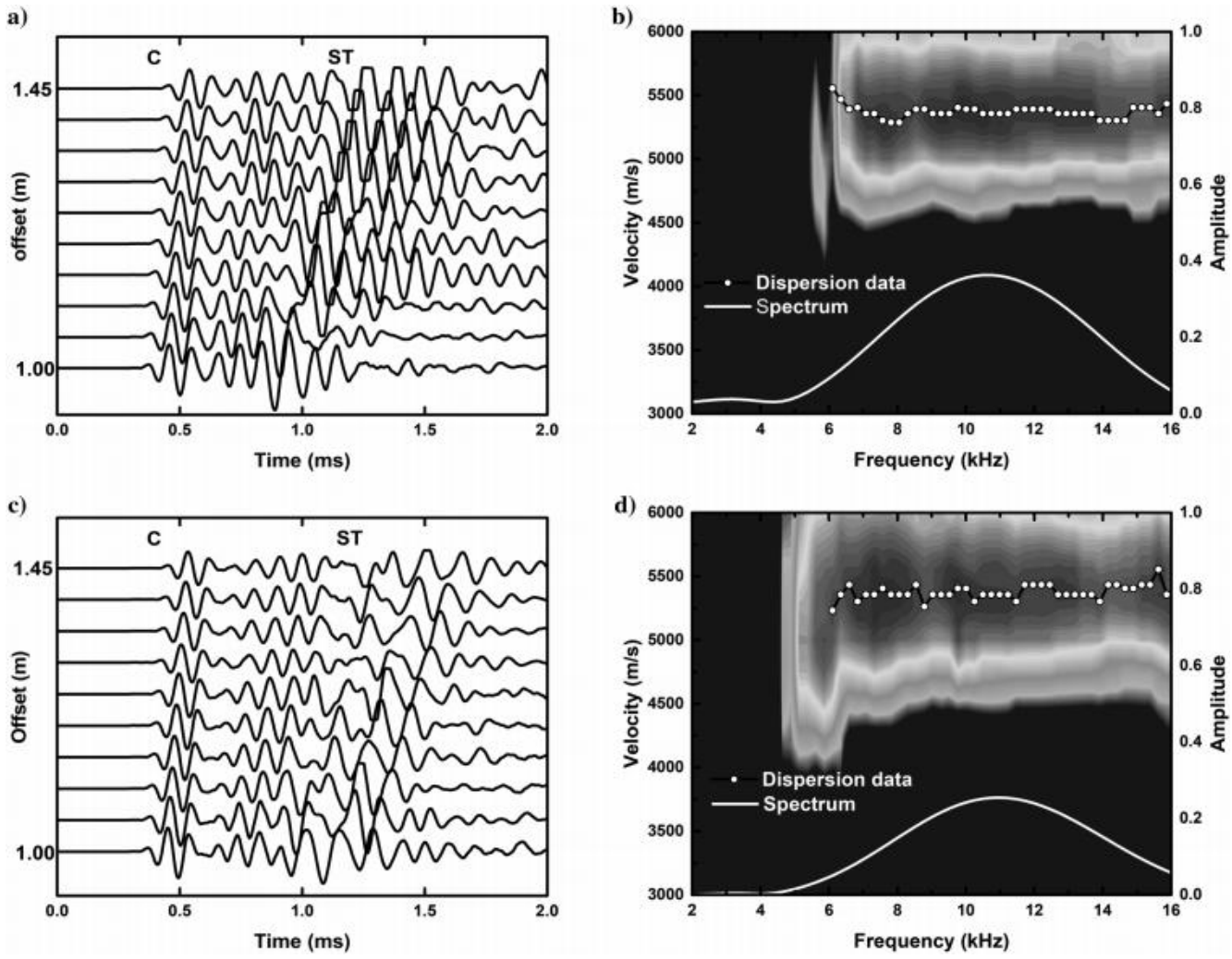


Figure 3. Experimental waveform data for (a) the free-pipe model (model a) and (c) the poorly bonded first interface model (model b). The labels C and ST denote the casing and the Stoneley waves, respectively. The processing results (the dots in b and d) for model (a) and model (b) show that the velocity of the casing waves is almost invariant with the frequency. The amplitude spectrum (the light line) of the casing waves in model (b) is lower than that of model (a).

Downloaded from pubs.geoscienceworld.org/seg/geophysics/article-pdf/84/4/D161/4806203/geo-2018-0798.1.pdf by Univ of Petroleum (Beijing) - Library user on 09 October 2026

poorly bonded with the formation, behaves like an equivalent acoustic waveguide, in which the extensional-wave velocity is slower than that in the steel casing.

Poor bonding between the cement and formation

Using the above decoupled cement-formation model as a reference, we present the measurement and analysis results for the poorly bonded model (model d in Figure 1). In this model, we use a thin rubber layer of different azimuthal coverage to vary the bonding condition, for which the degree of poor bonding is conveniently defined as the R, which is the ratio of the azimuthal angle of the rubber layer (i.e., the decoupled sector) over the entire 360° angle range (Grosmangin et al., 1961). For this azimuthal boundary condition variation, multipole wave constituents will be induced in the model. The contribution of R to each wave constituent is given by Xu et al. (2018) using the multipole mode expansion theory, as

$$C_n = \frac{1}{2\pi}\int_0^{2\pi} R(\theta)\cos(n\theta)d\theta \quad n = 0;1;2:::; \qquad (2)$$

with $n = 0;1;2:::$ denoting the monopole, dipole, and quadrupole, etc. The casing extensional wave of our measurement is an axisymmetric wave $(n = 0)$ corresponding to $C_0 = (1/2\pi)\int_0^{2\pi} R(\theta)d\theta$. Thus, by adjusting the azimuthal coverage of $R(\theta)$, various degrees of bonding quality and its impact on the monopole extensional wave can be simulated.

Figure 5a and 5c shows, respectively, the measured array waveforms for the 270° and 180° decoupled sectors of model (d). When taking the measurement across the two zones, a 0.45 m aperture array was placed in the center part of each zone, with the source being 1.0 m above the array (see Figure 2). For the two different bonding conditions, the casing wave (labeled C) shows quite different attenuation values across the array, being 9.47 (270° decoupling) and 21.2 dB/m (180° decoupling), respectively, causing wave-amplitude attenuation, as shown by the light curves in Figure 5b and 5d. For measuring the attenuated casing waves, the large-amplitude latter arrivals (e.g., Stoneley waves) were clipped. The clipping of the slow-traveling waves does not affect the dispersion analysis of the fast-traveling casing waves because the two waves are well-separated in the velocity-frequency domain.

From the FVC dispersion analysis results given in Figure 5b and 5d, the casing wave velocity values, as well as those shown in Figure 4, are significantly reduced from the casing wave velocity of the free-pipe situation. More interestingly, both data show the trend of decreasing velocity with decreasing frequency. Moreover, the variation is more significant for the 180° decoupling than the 270°. The experimental results will be theoretically modeled using the slip-boundary theory in the following.

Theoretical modeling and discussion

Tang et al.'s (2018) theory based on viscoelastic slip-boundary modeling, as briefly described in Appendix A, uses complex normal and shear stiffness parameters η_N and η_T to model acoustic wave propagation along a cased borehole, where η_N is used to describe the fluid coupling, as in the free-pipe scenario, and η_T is used to model shear coupling, as in the poorly bonded interfaces. For the viscoelastic coupling theory, η_T is given by $\eta_T = \eta_S + i\omega\xi_S$, where the imaginary part of η_T is governed by the viscous shear stiffness ξ_S. This parameter controls the wave attenuation along the borehole. By adjusting the value of ξ_S, the attenuation values in the measured data can effectively be modeled. The real part of η_T, the shear stiffness η_S, describes the overall coupling of the casing-cement system to the formation, and it can be used to model the velocity dispersion of the casing wave (Tang et al., 2018). In the following examples, the value of the stiffness parameters is determined from data fitting, or inversion. For example, by fitting the attenuation and dispersion of the casing wave, the values of ξ_S and η_S can be determined. We now use the theory to model the velocity dispersion using the modeling parameters listed in Table 1.

Figure 6 shows the casing-wave dispersion data for the free-pipe (Figure 3b) and the poor cement-to-formation bonding cases (Figure 5b and 5d). The free-pipe data can be accurately modeled by setting $\eta_T = 0$ and using $\eta_N = 1 \times 10^6$ Gpa · m^{-1}. The modeling of the dispersion data for the poorly bonded cases consists of

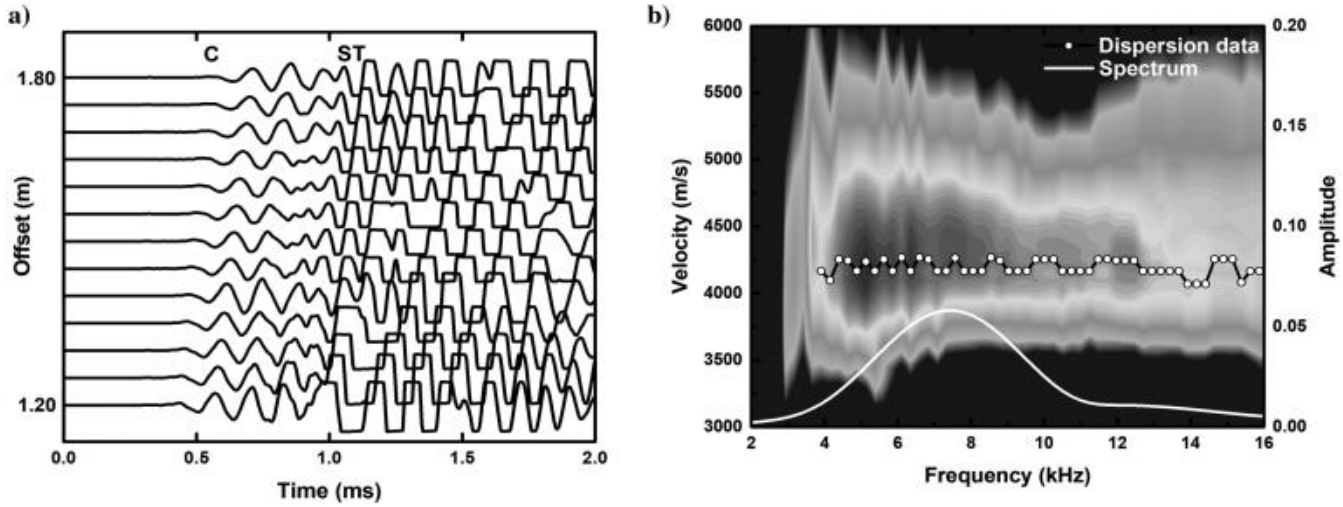


Figure 4. (a) Waveform data and (b) processing result for the decoupled second interface model (model c). The dispersion data (dots) of the casing waves are almost invariant with frequency.

Downloaded from pubs.geoscienceworld.org/seg/geophysics/article-pdf/84/4/D161/4806203/geo-2018-0798.1.pdf by Univ of Petroleum (Beijing) - Library user on 09 October 2026

two steps. The first is to model the velocity variation due to the effective casing-cement waveguide. Using the long-wavelength approximation, the elastic property of the waveguide can be obtained using Voight (1910) averaging, as

$$\frac{1}{M_e} = \frac{S_{cs}}{M_{cs}} + \frac{S_{cm}}{M_{cm}}; \quad \rho_e = S_{cs} \cdot \rho_{cs} + S_{cm} \cdot \rho_{cm}; \qquad (3)$$

where S_{cs} and S_{cm} are the cross-sectional area ratios of the casing and cement over the sum of the two areas, respectively, and M_{cs} and M_{cm} are the elastic moduli (either the bulk or shear modulus) of the casing and cement, respectively, and ρ_{cs} and ρ_{cm} denote the densities of the casing and cement, respectively. With the above averaging scheme for the elastic properties of the effective waveguide, the second step is to use the slip-boundary condition to model the coupling of the waveguide to the formation. According to the model theory (Tang et al., 2018), the most sensitive parameter that controls the casing-wave dispersion characteristics is η_S, the interface shear stiffness. Using the effective waveguide and the respective formation

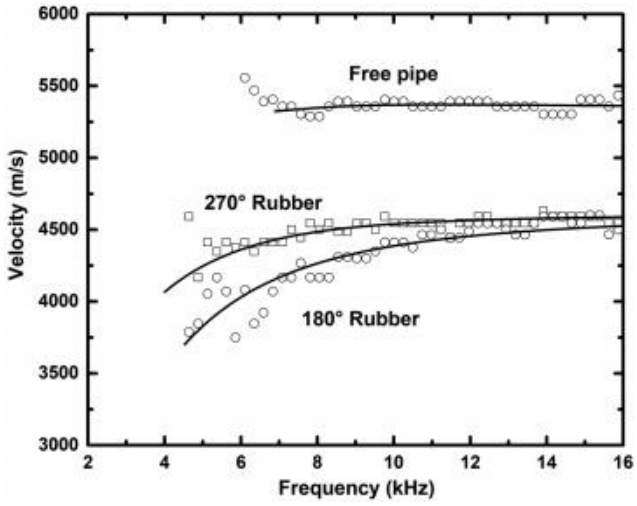


Figure 6. Theoretical modeling (curves) of the casing-wave dispersion data (markers) for model (a) and (d).

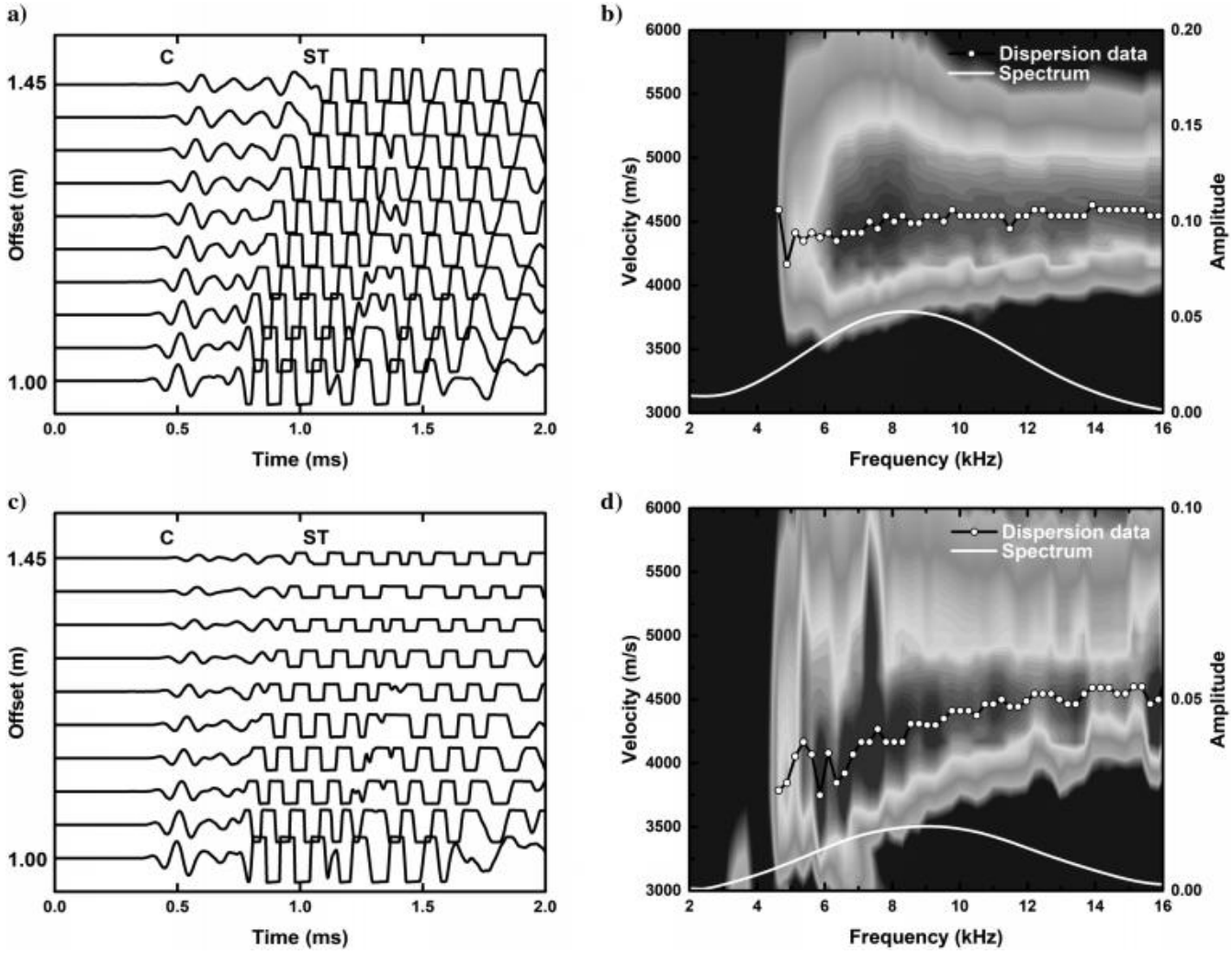


Figure 5. Experimental waveform data and processing results for the two second interface coupling conditions of model (d). Data in (a and c) are, respectively, recorded for the 270° and 180° rubber-coupled-azimuthal sectors. The processing results of (a and c) are, respectively, plotted in (b and d). The velocities of the 270° and 180° sectors are significantly reduced from the free-pipe velocity and exhibit significant dispersion, especially in the 180° sector case.

Downloaded from pubs.geoscienceworld.org/seg/geophysics/article-pdf/84/4/D161/4806203/geo-2018-0798.1.pdf by Univ of Petroleum (Beijing) - Library user on 09 October 2026

properties in Table 1, the shear stiffness values required to fit the dispersion data of the 270° and 180° decoupling sectors are 5 and 13 $Gpa \cdot m^{-1}$, respectively. As shown in Figure 6, the theoretical dispersion curves fit their respective dispersion data very well. The experiment results therefore provide a validation of the theoretical modeling approach, showing that the shear stiffness parameter can be effectively used to describe the overall coupling of the casing-cement system to the formation. For the 270° decoupled sector, only a quarter of the cement circumference is bonded to the formation. This causes some leakage of the wave energy from the casing-cement waveguide into the formation, resulting in wave attenuation and dispersion in the borehole propagation. Correspondingly, a moderate value of the shear stiffness can model the wave characteristics. The attenuation and dispersion become quite severe when half of the cement circumference is bonded to the formation in the 180° sector case. In this situation, a significantly larger stiffness value (for both the real and imaginary parts) is needed to model the wave characteristics. For the extreme case in which the entire cement is well-bonded to formation, the casing wave disappears because the waveguide ceases to exist. Thus, the severe attenuation and dispersion (wave slow down or retardation) of the 180° sector case are the prelude of the vanishing casing waves with the increasing cement bond to the formation.

To further support our experiment and modeling results, we present a field-data example from a cased well. Figure 7a and 7b shows the array wave data from two depth points of the well. The data are plotted in the 0–2.2 ms range to show the first-arriving casing wave across the receiver array. The casing-wave dispersion data for the two depths are shown in Figure 7c (the markers). The two data sets exhibit significantly different values and variation trends. The dispersion data (the circular markers in Figure 7c) for

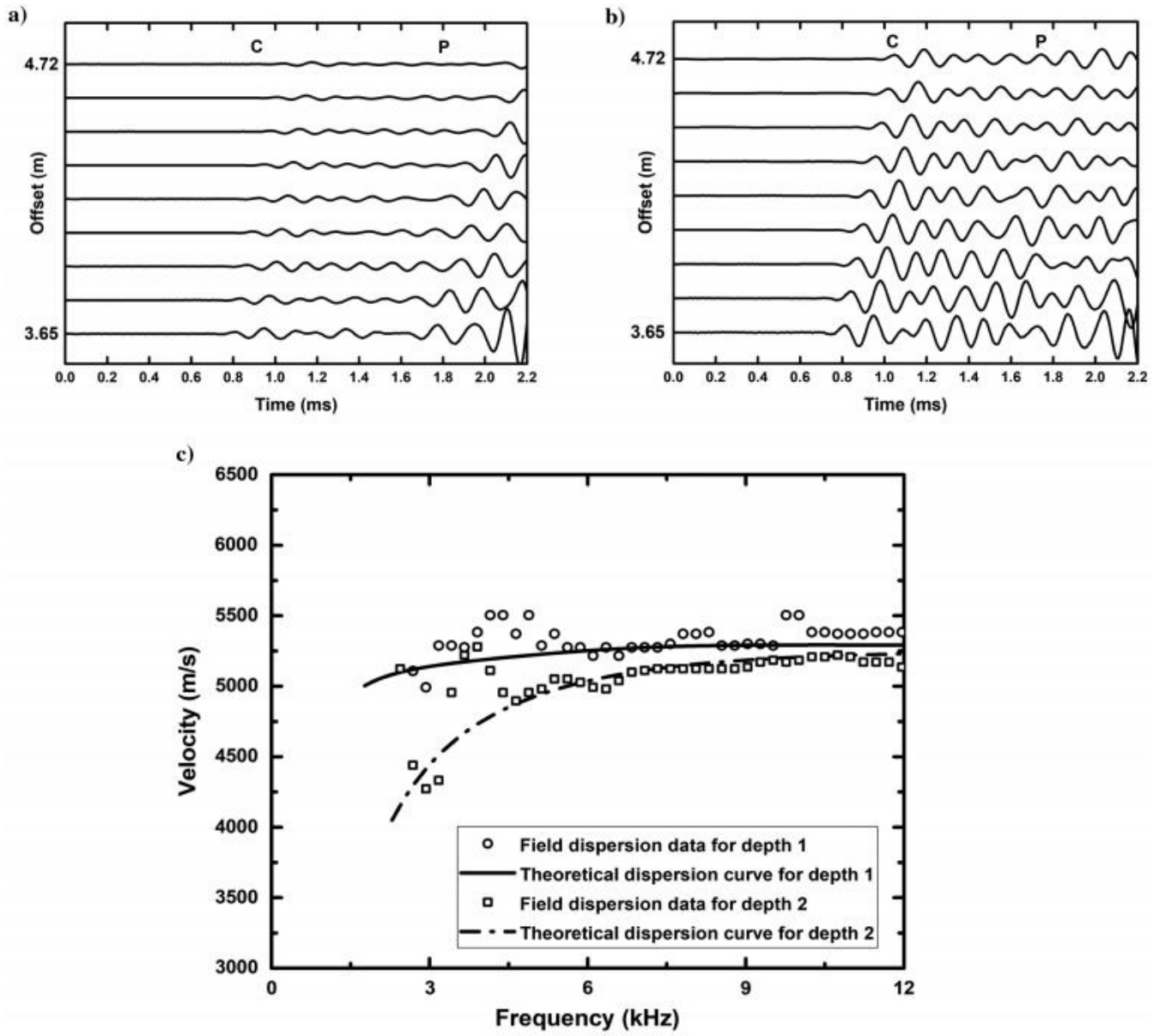


Figure 7. Cased borehole acoustic data with different bonding conditions (a and b) and (c) dispersion analysis and theoretical modeling suggest that the bonding issue for (a) is from the casing-cement interface and that for (b) is from the cement-formation interface.

Downloaded from pubs.geoscienceworld.org/seg/geophysics/article-pdf/84/4/D161/4806203/geo-2018-0798.1.pdf by Univ of Petroleum (Beijing) - Library user on 09 October 2026

Figure 7a are close to the free-pipe velocity value and show only a slight velocity decrease with the decreasing frequency. The dispersion data (the square markers in Figure 7c) for Figure 7b, however, are significantly less than the data of Figure 7a and show a marked decrease of velocity with the decreasing frequency, similar to the dispersion trend of our experimental data (see Figure 6). The two field dispersion data sets are theoretically fitted as shown in Figure 7c. The complex shear stiffness values for the fitting are $\eta_T = 0.1$ Gpa $\cdot$ m^{-1}, $\xi_T = 1.5 \times 10^5$ pa $\cdot$ s $\cdot$ m^{-1} (the upper curve) and $\eta_T = 6$ Gpa $\cdot$ m^{-1}, $\xi_T = 1.0 \times 10^4$ pa $\cdot$ s $\cdot$ m^{-1} (the lower curve), respectively. The theory fits the data quite well. For the data of Figure 7a, the significant attenuation (the large ξ_S value) means that the cement bond quality is fair. However, the presence of the casing wave of measurable amplitude means that there is still some issue with the bond quality. Because of the small deviation (and dispersion) of the casing wave velocity from the casing extensional velocity value, the bond quality issue is from the first interface between the casing and the cement. For the data of Figure 7b, the significant casing wave amplitude and moderate attenuation (moderate ξ_S value) suggest that there is poor bonding behind the casing. The significant dispersion and velocity reduction (large η_S value) indicates that the bonding issue occurs at the second interface between the cement and the formation.

CONCLUSION

Cased borehole acoustic propagation with varying bonding conditions was studied using laboratory experiment and theoretical modeling. The theory and experiment show that the casing-wave velocity variation and attenuation provide an important characteristic to distinguish bonding issues occurring at the casing-cement and the cement-formation interfaces. For issues occurring at the first interface, the wave velocity is close to the free-pipe velocity and shows little dispersion. In comparison, for issues occurring at the second interface, there is a significant velocity reduction from the free-pipe value. On the basis of the velocity reduction, the velocity dispersion and wave attenuation can be used to diagnose the bonding quality of the interface, with increasing dispersion and attenuation indicating increasing bonding quality. Comparison of the measurement data with theory shows that the wave phenomena, especially the observed dispersion characteristics, can be effectively modeled using the slip-boundary modeling approach. The theory can therefore be used to provide a method for interpreting the cased borehole acoustic logging data.

ACKNOWLEDGMENTS

This work is supported by the National Natural Science Foundation of China (grant no. 41774141) and the Fundamental Research Funds for the Central Universities (grant no. 17CX06035).

APPENDIX A

CASING WAVE MODELING USING SLIP-BOUNDARY THEORY

Using the slip-boundary modeling of Tang et al. (2018), the boundary condition between the outer interface of the casing (or the equivalent casing-cement waveguide) and formation can be written as

$$\begin{cases} u_r^C = u_r^F + \sigma_r^F/\eta_N; \\ u_z^C = u_z^F + \sigma_{rz}^F/\eta_T; \\ \sigma_{rr}^C = \sigma_{rr}^F; \\ \sigma_{rz}^C = \sigma_{rz}^F; \end{cases} \tag{A-1}$$

where u_r and u_z, and σ_{rr} and σ_{rz} are, respectively, the normal and shear displacements and the normal and shear stresses of the medium (the casing waveguide or formation). The superscripts "C" and "F" denote the casing waveguide and formation, respectively; η_N and η_T are, respectively, the normal and shear stiffness of the boundary, which vary with the bonding condition and/or cement quality. The imaginary part of η_T is defined as the viscous stiffness, which has a significant influence on the casing wave attenuation.

At the inner casing boundary, the displacement u_r^C and stresses σ_{rr}^C and σ_{rz}^C satisfy the classic solid-fluid boundary condition:

$$\begin{cases} u_r^f = u_r^C; \\ \sigma_{rr}^f = \sigma_{rr}^C; \\ 0 = \sigma_{rz}^C; \end{cases} \tag{A-2}$$

where u_r^f and σ_{rr}^f are, respectively, the displacement and stress of the borehole fluid. Using the Thomson-Hanskell propagator matrix method (Tang and Cheng, 2004) and the boundary condition between the casing waveguide inner and outer boundaries, we combine equations A-1 and A-2 and obtain the dispersion equation for the cased borehole with the viscoelastic slip-boundary coupling

$$D(k; \omega; C; B; F; \eta_N; \eta_T) = 0; \tag{A-3}$$

where k is the axial wavenumber; ω is the angular frequency; C denotes the casing pipe parameters (density, P- and S-velocities, and inner and outer radii); F represents the formation parameters (density, P- and S-velocities, and radii); B is the borehole filled with a fluid parameterized by fluid P-velocity and density; and D is the determinant of a 3×3 matrix whose elements are given in Tang et al. (2018). For a given angular frequency range, we solve the dispersion equation A-3 to find the wavenumber k of a designated wave mode (e.g., casing wave). The theoretical phase-velocity dispersion curves $V_{phase(\omega)}$ can be calculated using $V_{phase(\omega)} = \omega/k$.

REFERENCES

Chang, S. K., and A. H. Everhart, 1983, A study of sonic logging in a cased borehole: Journal of Petroleum Technology, 35, 1745–1750, doi: 10.2118/11034-PA.

Chen, S. T., 1982, The full acoustic wave train in a laboratory model of a borehole: Geophysics, 47, 1512–1520, doi: 10.1190/1.1441301.

Fehler, M., 1982, Interaction of seismic waves with a viscous liquid layer: Bulletin of the Seismological Society of America, 72, 55–72.

Grosmangin, M., P. P. Kokesh, and P. Majani, 1961, A sonic method for analyzing the quality of cementation of borehole casings: Society of Petroleum Engineers, 13, 165–171, doi: 10.2118/1512-G-PA.

Kurkjian, A. L., and S. K. Chang, 1986, Acoustic multipole sources in fluid-filled boreholes: Geophysics, 51, 148–163, doi: 10.1190/1.1442028.

Schoenberg, M., 1980, Elastic wave behavior across linear slip interfaces: The Journal of the Acoustical Society of America, 68, 1516–1521, doi: 10.1121/1.385077.

Schoenberg, M., T. Marzetta, J. Aron, and R. P. Porter, 1981, Space-time dependence of acoustic waves in a borehole: The Journal of the Acoustical Society of America, 70, 1496–1507, doi: 10.1121/1.387107.

Tang, X. M., 1992, A waveform inversion technique for measuring elastic wave attenuation in cylindrical bars: Geophysics, 57, 854–859, doi: 10.1190/1.1443299.

Downloaded from pubs.geoscienceworld.org/seg/geophysics/article-pdf/84/4/D161/4806203/geo-2018-0798.1.pdf by Univ of Petroleum (Beijing) - Library user on 09 October 2026

Tang, X. M., and C. H. Cheng, 2004, Quantitative borehole acoustic methods: Elsevier Science Publishing Co.
Tang, X. M., C. Jiang, Y. D. Su, and X. L. Chen, 2018, An acoustic-wave theory for casing bond evaluation using viscoelastic slip boundary modeling: Science China Earth Sciences, 61, 1057–1064, doi: 10.1007/s11430-017-9203-8.
Tubman, K. M., C. H. Cheng, S. P. Cole, and M. N. Toksöz, 1986, Synthetic full-waveform acoustic logs in cased boreholes, II: Poorly bonded casing: Geophysics, 51, 902–913, doi: 10.1190/1.1442148.
Tubman, K. M., C. H. Cheng, and M. N. Toksöz, 1984, Synthetic full waveform acoustic logs in cased boreholes: Geophysics, 49, 1051–1059, doi: 10.1190/1.1441720.
Voight, W., 1910, Lehrbuch der Kristallphysik: Teubner-Verlag.
Wang, H., and M. C. Fehler, 2018, The wavefield of acoustic logging in a cased-hole with a single casing-Part I: A monopole tool: Geophysical Journal International, 212, 612–626, doi: 10.1093/gji/ggx475.
Wang, H., G. Tao, and X. F. Shang, 2016, Understanding acoustic methods for cement bond logging: The Journal of the Acoustical Society of America, 139, 2407–2416, doi: 10.1121/1.4947511.
Xu, S., C. X. Zhuang, Y. D. Su, Y. K. Liu, Z. P. Zhang, S. J. Guo, and X. M. Tang, 2018, Acoustic source characterization for a logging while drilling tool: Theoretical and experimental modeling: The Journal of the Acoustical Society of America, 144, EL178–EL184, doi: 10.1121/1.5053105.

Downloaded from pubs.geoscienceworld.org/seg/geophysics/article-pdf/84/4/D161/4806203/geo-2018-0798.1.pdf by Univ of Petroleum (Beijing) - Library user on 09 October 2026

纪玉磊, 苏远大, 李盛清等. 2025. 过油管偶极声波测井固井质量评价方法研究. 地球物理学报, 68(10): 4077-4087, doi: 10.6038/cjg2024S0232.

Ji Y L, Su Y D, Li S Q, et al. 2025. Evaluating the cementing quality of cased well through tubing by dipole acoustic logging method. *Chinese J. Geophys.* (in Chinese), 68(10): 4077-4087, doi: 10.6038/cjg2024S0232.

过油管偶极声波测井固井质量评价方法研究

纪玉磊[1,2], 苏远大[1,2,3*], 李盛清[1,2], 陈雪莲[1,2], 唐晓明[1,2,3]

1 中国石油大学 (华东) 深层油气全国重点实验室, 青岛 266580
2 中国石油大学 (华东) 地球科学与技术学院, 青岛 266580
3 青岛海洋科学与技术试点国家实验室, 青岛 266071

摘要 过油管固井质量评价在海上油气井的弃置作业中有广泛需求, 研究双层套管井的固井质量评价方法具有重要意义. 针对 CBL 和 VDL 等现有高频声波技术径向穿透小, 无法透过钢介质油管进行固井质量评价的缺陷, 本文开展了低频偶极声波测井理论与实验研究, 首先理论分析了偶极源下双层套管井的频散曲线, 发现外层套管胶结不好时存在额外的高阶套管弯曲模式, 在此基础上将该模式从波形中提取出来并形成偶极固井质量评价方法, 最后依托实验室模型井开展了双层套管井固井质量评价实验研究, 进一步验证了该方法的有效性和可靠性. 理论与实验的结果表明额外的高阶套管弯曲波可以反应外层套管的水泥胶结情况, 为双层套管井的固井质量评价提供了可行的方法.

关键词 双层套管井; 偶极声源; 固井质量评价; 套管弯曲波

中图分类号 P631 **收稿日期** 2024-04-08, 2024-09-14 收修定稿

DOI: 10.6038/cjg2024S0232 **CSTR:** 32084.14.cjg2024S0232

Evaluating the cementing quality of cased well through tubing by dipole acoustic logging method

JI YuLei[1,2], SU YuanDa[1,2,3*], LI ShengQing[1,2], CHEN XueLian[1,2], TANG XiaoMing[1,2,3]

1 *State Key Laboratory of Deep Oil and Gas, China University of Petroleum (East China), Qingdao* 266580, *China*
2 *School of Geosciences, China University of petroleum, Qingdao* 266580, *China*
3 *Qingdao National Laboratory for Marine Science and Technology, Qingdao* 266071, *China*

Abstract The evaluation of cementing quality through tubing is widely needed in the abandonment of offshore oil and gas well, so it is of great significance to study the evaluation method of cementing quality in double casing well. Aiming at the defect that the high frequency acoustic wave method such as Cement Bond Logging (CBL) and Variable Density Logging (VDL) have small radial penetration and cannot be used to evaluate the cementing quality through steel tubing, this paper has carried out theoretical and experimental research on low frequency dipole acoustic logging. Firstly, the dispersion curve of double casing well under dipole source is analyzed theoretically, and it is found that there are additional high order casing flexural modes when the outer casing is poorly cemented. On this basis, the high order casing flexural modes is extracted from the waveform and a dipole cementing quality evaluation method is formed. Finally, the experimental research on cementing

基金项目 崂山国家实验室科技创新项目 (LSKJ202203407), 国家自然科学基金 (42074137, 41821002, 42174145), 山东省自然科学基金 (ZR201911120382), 中石油重大科技项目 (ZD2019-183-004), 深层油气全国重点实验室课题 (SKLDOG2024-ZYTS-04), 和中央高校基本科研业务费专项 (23CX10001A) 联合资助.

第一作者简介 纪玉磊, 男, 1998 年生, 博士研究生, 主要从事声波测井理论与方法研究. E-mail: 1215532670@qq.com

*** 通讯作者** 苏远大, 男, 1978 年生, 博士, 教授, 主要从事声波测井理论、方法及处理研究. E-mail: syuanda@sina.com

quality evaluation of double casing well is carried out based on the laboratory model well, which further verifies the validity and reliability of this method. The theoretical and experimental results show that the extra high order casing flexural modes can reflect the cement bonding condition of the outer casing, which provides a feasible method for the evaluation of cementing quality of double casing well.

Keywords Double casing well; Dipole acoustic source; Cementing quality evaluation; Casing flexural wave

0 引言

基于声波测井的套管井固井质量评价一直是油气勘探开发领域备受关注的课题，是保障油田安全生产和油气高效开发的关键环节 (Tubman et al., 1986; 唐晓明等, 2018; 林剑松等, 2021). 老旧油气井的封堵和弃置 (plug and abandonment) 是生产井生命周期中的标准操作，为了防止地下流体不受控制地向地层或地表泄漏，在弃井作业之前需要对井筒的完整性进行评估，以确保套管外的水泥环胶结良好，实现油气井长效封堵 (Zeroug et al., 2007, 2016). 传统的生产井固井质量评价作业需要在测井之前移除生产油管，这极大地增加了作业成本，因此过油管的声波测井固井质量评价方法亟待发展 (Bose et al., 2021; Zeroug and Bose, 2018).

多极子阵列声波测井方法由于其频率低 (约 10kHz)、穿透深的特点，在固井质量评价方面相对于超声波测井 (约 250kHz) 具有一定的优势 (陈雪莲和唐晓明, 2021; 孙志峰等, 2023). 为了研究多极子声源在单层套管井中的响应特征，国内外学者针对单层套管井的声场模拟开展了大量研究 (Tubman et al., 1986; Everhart and Chang, 1985; Schmitt, 1993). 在套管井声场模拟的过程中，经典的井孔弹性边界理论通常在套管和水泥环之间增加一个较薄的流体层以模拟不胶结的情况 (张海澜等, 2004; 唐晓明和郑传汉, 2004). 由于流体层完全阻断套管和水泥环之间的剪切耦合，经典的井孔弹性边界理论仅能模拟套管井完全不胶结的情况，近年来，有的研究提出用滑移界面理论表征套管与水泥环部分胶结的情况 (唐晓明等, 2018; Jiang et al., 2019; 潘金林等, 2023). 由于不同的胶结情况会对套管井的声场响应造成显著差异，因此套管井中各模式波的频散分析对反演井孔参数及固井质量评价具有重要意义 (Zhang et al., 2016; 李刚等, 2018; 陈雪莲和唐晓明, 2021; Wang and Fehler, 2018).

在井孔波导模型中，含油管的套管井结构等同于内层环空充填流体的双层套管井. 近年来，国内外学者针对双层套管井的固井质量评价开展了一系列研究工作. Liu 等 (2017) 利用扫频有限元的方法研究了双层套管井中单极、偶极和四极声源下的频散特征，并对比了外层环空为自由套管和胶结良好情况下的频散曲线. 陈雪莲等 (2020) 研究了双层套管井中的单极声波测井响应，指出可以利用套管波幅度和斯通利波的频散特征评价外层环空的胶结情况. Bose 等 (2021) 提出了对双层套管井外层环空的综合评价方法并进行了实验验证. 陈雪莲和唐晓明 (2021) 使用有限差分和实轴积分相结合的方法分析了偶极源下双层套管中不同胶结情况对套管弯曲波的影响，指出了一阶套管弯曲波对外层环空的胶结情况敏感，验证了使用偶极子在双层套管井中进行固井质量评价的可行性. 而偶极声源在胶结不好的套管井中除了会激发一阶套管弯曲波之外，还可以激发高阶套管弯曲波，但是国内外学者对于高阶套管弯曲波的研究较少 (Zeroug and Bose, 2018)，且研究方向多为声源频率对高阶套管弯曲波的影响 (Everhart and Chang, 1985; Wang and Fehler, 2018)，针对双层套管井模型中高阶套管弯曲波的理论模拟与实验研究未见报道.

本文在前人的研究基础上，利用井孔的弹性波动理论计算了双层套管井的波形和频散曲线，提出了使用偶极声源的高阶套管弯曲模式波进行双层套管井固井质量评价的方法，并依托实验室 1∶1 模型井群开展了双层套管井实验研究，理论与实验相结合验证了该方法的可行性，为偶极阵列声波测井在过油管固井质量评价中的应用奠定了基础.

1 油管-套管井模型的井孔弹性波动理论

在海上油气井弃置作业过程中，生产油管与固井套管之间通常没有固井水泥，图 1 显示了双层套管井的模型示意图和井孔截面图，在内层环空始终为流体层的情况下，外层环空胶结良好和自由套管的情况分别如图 1b、c 所示.

在井孔声场的研究中，可以将套管、环空和地

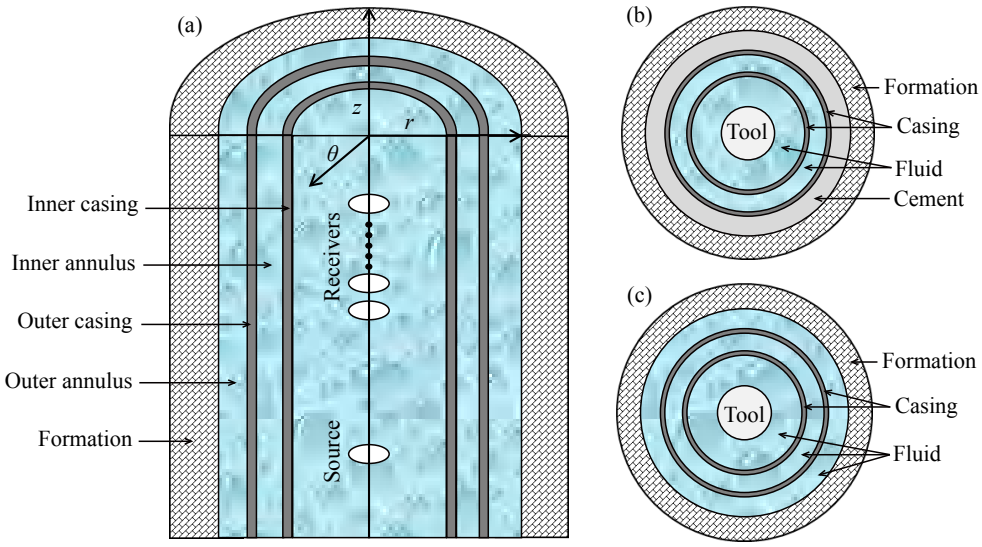


图 1　双层套管井的模型示意图和井孔截面图

Fig. 1　Model schematic diagram and borehole cross section of double casing well

层看作由内向外的同心圆柱层, 在柱坐标系中, 固体层弹性介质的位移和应力矢量由径向、环向和垂直向的位移及其应力组成, 根据弹性介质的波动方程及相应位移势的解, 其可以表示为一个6×6的矩阵$\boldsymbol{T}_{\mathrm{Solid}}$与振幅系数向量$\boldsymbol{X}_{\mathrm{Solid}}$相乘的形式 (唐晓明和郑传汉, 2004), 即:

$$\boldsymbol{S}_{\mathrm{Solid}}=\boldsymbol{T}_{\mathrm{Solid}}\times\boldsymbol{X}_{\mathrm{Solid}},\quad \boldsymbol{X}_{\mathrm{Solid}}=(A,B,C,D,E,F)^{\mathrm{T}}, \tag{1}$$

式中的系数 A, C, E 分别表示在径向, 环向和垂直向上由外向内传播的波, 系数 B, D, F 表示在径向, 环向和垂直向上由内向外传播的波, 其上标 T 表示向量的转置, 矩阵$\boldsymbol{T}_{\mathrm{Solid}}$可由波动方程推导得出, 其具体表达式见附录 A.

与固体层不同的是, 流体层中只存在径向位移和径向应力, 其系数向量$\boldsymbol{X}_{\mathrm{Fluid}}$中只存在与波径向传播有关的系数 A 和系数 B, 此时流体层的位移应力矢量$\boldsymbol{S}_{\mathrm{Fluid}}$可表示为

$$\boldsymbol{S}_{\mathrm{Fluid}}=\boldsymbol{T}_{\mathrm{Fluid}}\times\boldsymbol{X}_{\mathrm{Fluid}},\ \boldsymbol{X}_{\mathrm{Fluid}}=(A,B)^{\mathrm{T}}. \tag{2}$$

模拟井孔的声场时, 地层通常被设置为无限大的边界, 因此, 地层作为特殊的固体层, 只存在由内向外传播的波, 固体层矩阵$\boldsymbol{T}_{\mathrm{Solid}}$中与系数$A,C,E$有关的列不需要考虑, 其矩阵$\boldsymbol{T}_{\mathrm{Formation}}$将由$\boldsymbol{T}_{\mathrm{Solid}}$回退为 6 × 3 的矩阵, 因此地层的位移应力矢量可以表示为

$$\boldsymbol{S}_{\mathrm{Formation}}=\boldsymbol{T}_{\mathrm{Formation}}\times\boldsymbol{X}_{\mathrm{Formation}},\quad \boldsymbol{X}_{\mathrm{Formation}}=(B,D,F)^{\mathrm{T}}. \tag{3}$$

利用井内各圆柱层之间的边界条件, 可以将套管、环空和地层等介质连接起来, 当井内相邻的两个圆柱层均为固体时, 其边界处的六个位移和应力向量都应该连续, 假设井内 L 和 $L+1$ 层均为固体, 则两界面处的边界方程可表示为

$$\boldsymbol{T}^{L}_{\mathrm{Solid}}\times(A^{L},B^{L},C^{L},D^{L},E^{L},F^{L})^{\mathrm{T}}=\boldsymbol{T}^{L+1}_{\mathrm{Solid}}\times(A^{L+1},B^{L+1},C^{L+1},D^{L+1},E^{L+1},F^{L+1})^{\mathrm{T}}. \tag{4}$$

当井内相邻的两个圆柱层为固体和流体时, 其边界处的径向位移和径向应力连续, 环向应力和垂直向应力为零, 环向位移和垂直向位移不考虑, 此时固体层的矩阵$\boldsymbol{T}_{\mathrm{Solid}}$中也应去掉与环向位移和垂直向位移有关的元素, 从而回退为一个4×6的矩阵$\boldsymbol{T}_{\mathrm{Solid}*}$, 此时两界面处的边界方程可表示为

$$\boldsymbol{T}^{L}_{\mathrm{Fluid}}\times(A^{L},B^{L})^{\mathrm{T}}=\boldsymbol{T}^{L+1}_{\mathrm{Solid}*}\times(A^{L+1},B^{L+1},C^{L+1},D^{L+1},E^{L+1},F^{L+1})^{\mathrm{T}}. \tag{5}$$

模拟套管井内的声场时, 井孔流体作为特殊的流体层, 只存在由外向内传播的波, 流体层矩阵$\boldsymbol{T}_{\mathrm{Fluid}}$中由内向外传播的波不需要考虑, 因此, 在井孔流体处矩阵$\boldsymbol{T}_{\mathrm{Fluid}}$降阶为一个 2 × 1 的矩阵$\boldsymbol{T}_{\mathrm{Mud}}$, $\boldsymbol{X}_{\mathrm{Mud}}$表示由外向内传播的波的系数, 此时, 井孔流体的位移应力矢量如式 (6) 所示:

$$\boldsymbol{S}_{\mathrm{Mud}}=\boldsymbol{T}_{\mathrm{Mud}}\times\boldsymbol{X}_{\mathrm{Mud}}. \tag{6}$$

根据位移应力关系及边界条件, 可以模拟以套管井为例的任意多层柱状系统, 以双层套管井外层环空为自由套管的情况为例, 井孔内共存在 5 个边界, 每个边界处的方程都满足式 (5) 中的固体和流体的边界条件, 将这 5 个边界方程联立起来就组成了一个方程组, 即:

$$\begin{pmatrix} -\boldsymbol{T}^1_{\mathrm{Mud}} & \boldsymbol{T}^2_{\mathrm{Solid}*} & \boldsymbol{O}_{4\times2} & \boldsymbol{O}_{4\times6} & \boldsymbol{O}_{4\times2} & \boldsymbol{O}_{4\times3} \\ \boldsymbol{O}_{4\times1} & \boldsymbol{T}^2_{\mathrm{Solid}*} & -\boldsymbol{T}^3_{\mathrm{Fluid}} & \boldsymbol{O}_{4\times6} & \boldsymbol{O}_{4\times2} & \boldsymbol{O}_{4\times3} \\ \boldsymbol{O}_{4\times1} & \boldsymbol{O}_{4\times6} & -\boldsymbol{T}^3_{\mathrm{Fluid}} & \boldsymbol{T}^4_{\mathrm{Solid}*} & \boldsymbol{O}_{4\times2} & \boldsymbol{O}_{4\times3} \\ \boldsymbol{O}_{4\times1} & \boldsymbol{O}_{4\times6} & \boldsymbol{O}_{4\times2} & \boldsymbol{T}^4_{\mathrm{Solid}*} & -\boldsymbol{T}^5_{\mathrm{Fluid}} & \boldsymbol{O}_{4\times3} \\ \boldsymbol{O}_{4\times1} & \boldsymbol{O}_{4\times6} & \boldsymbol{O}_{4\times2} & \boldsymbol{O}_{4\times6} & -\boldsymbol{T}^5_{\mathrm{Fluid}} & \boldsymbol{T}^6_{\mathrm{Formation}} \end{pmatrix} \times \begin{pmatrix} \boldsymbol{X}^1_{\mathrm{Mud}} \\ \boldsymbol{X}^2_{\mathrm{Solid}} \\ \boldsymbol{X}^3_{\mathrm{Fluid}} \\ \boldsymbol{X}^4_{\mathrm{Solid}} \\ \boldsymbol{X}^5_{\mathrm{Fluid}} \\ \boldsymbol{X}^6_{\mathrm{Formation}} \end{pmatrix} = \begin{pmatrix} \mu^{\mathrm{d}}_{\mathrm{f}}, \\ \sigma^{\mathrm{d}}_{\mathrm{rrf}} \\ \boldsymbol{O}_{6\times1} \\ \boldsymbol{O}_{6\times1} \\ \boldsymbol{O}_{6\times1} \end{pmatrix}, \tag{7}$$

式中左侧系数矩阵 $\boldsymbol{M}$ 为一个20×20的方阵，其是角频率和波数的函数，$\boldsymbol{M}$ 中各元素的上标表示井内圆柱层的序号，$\boldsymbol{O}$ 表示零矩阵，其下标表示零矩阵中零元素的行数和列数，向量 $\boldsymbol{X}$ 为套管井内各圆柱层的振幅系数. 等式右侧的径向位移 $\mu^{\mathrm{d}}_{\mathrm{f}}$ 和径向应力 $\sigma^{\mathrm{d}}_{\mathrm{rrf}}$ 为声源辐射直达波的贡献，其表达式分别对应于流体层矩阵 $\boldsymbol{T}_{\mathrm{Fluid}}$ 中与直达波有关的元素.

井内各模式波的频散曲线只受波动方程和边界条件影响，与声源无关，因此求解频散曲线时，式(7)中等式右边的向量均为零，此时式(7)变为齐次方程组，要使该方程组有非零解，其系数矩阵 $\boldsymbol{M}$ 的行列式必须为零，即：

$$\det(\boldsymbol{M}(\omega,k)) = 0, \tag{8}$$

式中 $k=\omega/v$，v 为井内各模式波的相速度，因此，利用牛顿迭代法求解该频散方程即可得到井内各模式波的相速度频散曲线. 本文中模式波的激发强度为井中接收声压信号的强度，其表达式为

$$I(z,\omega) = \mathrm{i}\rho\omega^2 \frac{\det(\boldsymbol{M}(\omega,k))}{\partial[\det(\boldsymbol{M}(\omega,k))]/\partial k}\exp(\mathrm{i}kz). \tag{9}$$

使用实轴积分法即可计算井内的全波波形，求解井内振幅系数向量 $\boldsymbol{X}$ 时则需要考虑声源的影响，当声源为偶极声源时，井轴上的全波波形可表示为

$$P(z,t) = \int_{-\infty}^{+\infty} \boldsymbol{S}(\omega)\boldsymbol{D}(\omega)\mathrm{e}^{-\mathrm{i}\omega t}\mathrm{d}\omega + \frac{r_0}{4}\int_{-\infty}^{+\infty}\int_{-\infty}^{+\infty} f^2\boldsymbol{X}^1_{\mathrm{Mud}}(k,\omega)\boldsymbol{S}(\omega)\mathrm{e}^{\mathrm{i}kz-\mathrm{i}\omega t}\mathrm{d}k\mathrm{d}\omega, \tag{10}$$

式中，$\boldsymbol{D}(\omega)$ 为声源辐射的贡献，r_0 为偶极距，f 为径向波数，$\boldsymbol{X}^1_{\mathrm{Mud}}$ 为式(7)中求解的振幅系数，表示来自井壁处的反射波，$\boldsymbol{S}(\omega)$ 表示声源的频谱. 本文声源选用了主频为3 kHz的余弦包络脉冲.

2 油管-套管井理论计算结果及分析

2.1 油管-套管井的偶极声波测井响应

偶极子在套管井中的传播较为复杂，Rose (2004) 指出，偶极子在空心钢管中会激发非轴对称的弯曲波 $F(n, m)$，其中 n 为环向方位序数，在偶极声源下其值为1，m 表示弯曲波的阶数，在频率轴上其存在无穷多值. 前人的研究 (Wang and Fehler, 2018) 表明，当套管外水泥环胶结不好时，由于流体层阻断了套管中剪切波的传播，套管中也可激发与空心钢管类似的偶极套管弯曲波，除此之外，由于地层的影响，偶极声源还会在套管井中激发地层弯曲波.

图2计算了双层套管井的偶极声波测井响应，其中图2a、b显示了胶结良好和自由套管时的波形，其中绿色实线为首波放大十倍后的波形，图2c、d显示了胶结良好和自由套管时的频散曲线，黑色实线为理论计算的结果，蓝色圆点为理论波形中提取得到的频散曲线，图2e、f显示了胶结良好和自由套管时模式波的激发强度，计算所需的井孔和地层参数在表1中给出.

表1 模型参数

Table 1 Model parameters

介质参数	纵波速度 /(m·s^{-1})	横波速度 /(m·s^{-1})	密度 /(kg·m^{-3})	外径 /mm
井孔流体	1500	–	1000	78.54
内层套管	6098	3354	7500	88.9
流体	1500	–	1000	112.25
外层套管	6098	3354	7500	122.25
水泥/流体	2823/1500	1729/–	1920/1000	145.6/145.6
地层	4000	2300	2500	∞

从模拟的结果可以看出，在0～10 kHz范围内，偶极子在双层套管井中主要激发套管弯曲 (Casing Flexural，以下简称为CF) 模式和地层弯曲 (Formation Flexural，以下简称为FF) 模式，这两种模式在频率轴上均存在无穷多个阶数，其中各阶地层弯曲模式 (FF1，FF2等) 具有相似的特征，即均存在截止频率

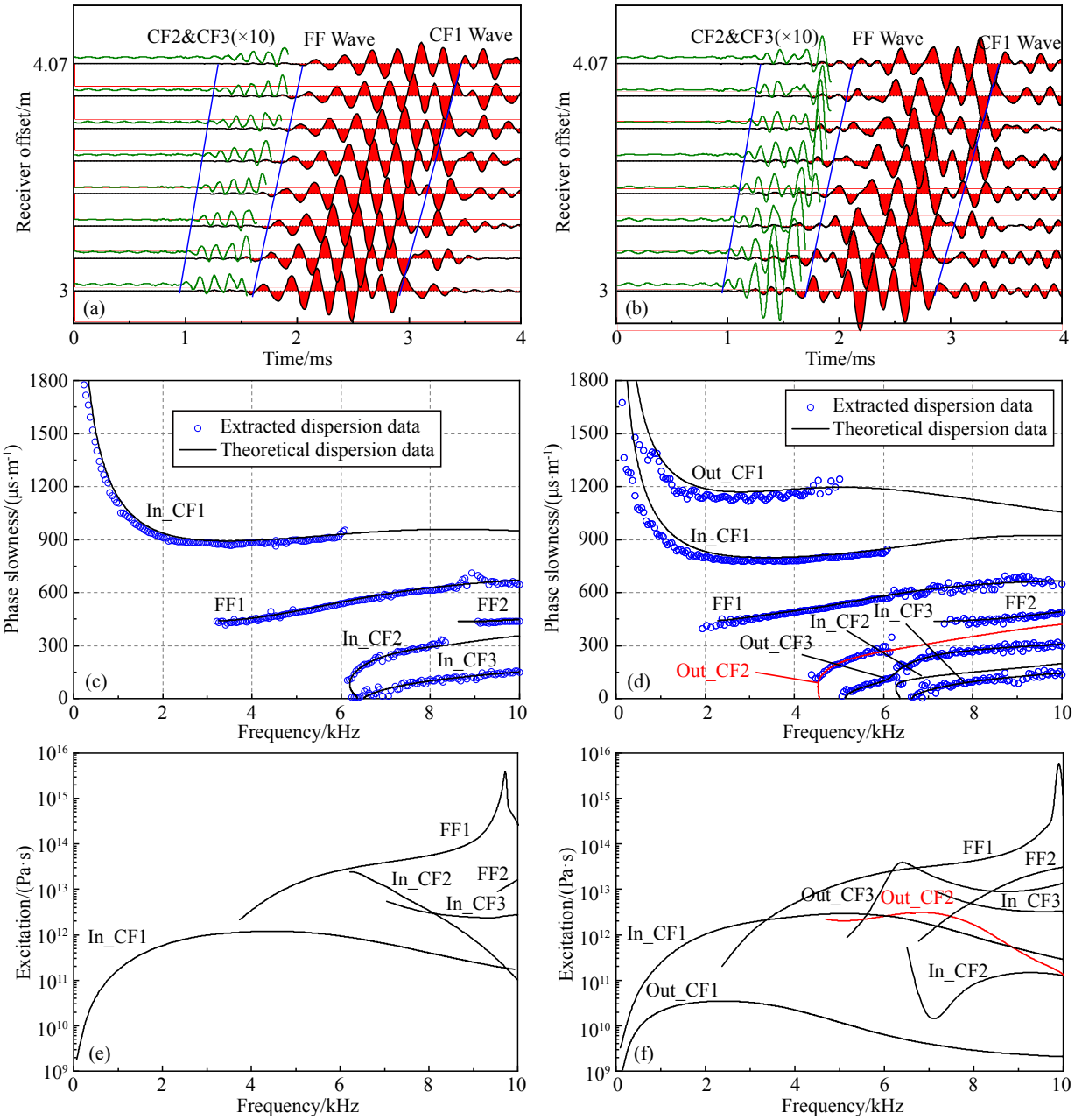


图 2　双层套管井的偶极声波测井响应

(a) 胶结良好时的波形; (b) 自由套管时的波形; (c) 胶结良好时的频散曲线; (d) 自由套管时的频散曲线; (e) 胶结良好时模式波激发强度; (f) 自由套管时模式波激发强度.

Fig. 2　Acoustic logging response of double casing well with dipole source

(a) Waveform with well bonded cased borehole; (b) Waveform with free pipe cased borehole; (c) Dispersion curve with well bonded cased borehole; (d) Dispersion curve with free pipe cased borehole. (e) Excitation spectrum curves of waves with well bonded cased borehole; (f) Excitation spectrum curves of waves with free pipe cased borehole.

并在地层横波速度处截止, 受井孔环境的影响, FF 模式频散曲线的截止频率会产生一定的变化, 但是其截止频率处的慢度值始终为地层的横波速度. 与地层弯曲模式不同的是, 一阶套管弯曲模式 (CF1) 存在于整个频率轴上, 不存在截止频率, 在频率趋近于 0 的过程中, 其慢度值趋近于无穷大, 在外层环空由胶结良好变为流体层的过程中, 其频散曲线的慢度值会随之降低. 高阶套管弯曲模式 (CF2, CF3) 慢度很低, 并在慢度为零处截止. 对比模式波的全波波形与频散曲线可以发现, 全波波形中首先到达的是 CF2 和 CF3 模式, 这些模式波混叠在一起, 幅度最小, 具有很强的频散; 其次到达的是 FF 模式, 这些模式幅度较大, 其慢度值介于一阶套管弯曲模式和高阶套管弯曲模式之间; 最后到达的是 CF1 模式, 这些模式波幅度与 FF 模式相当, 速度最慢, 与 FF 模式混叠在一起, 可以利用信号处理的方法从理论波形中提取这些模式.

对比两种胶结情况下的频散曲线和激发强度可知, 胶结良好时, 井内仅激发地层模式和内层套管模式 In_CF, 自由套管时, 除了 In_CF 模式, 外层

环空中的流体层还激发了额外的套管弯曲模式 Out_CF, 这一现象为双层套管井的固井质量评价提供了一定的可行性. 图 2d 的结果表明, 在外层套管产生的的诸多弯曲模式中, Out_CF1 模式的慢度值高于 In_CF1 模式, 在所有模式波中其激发强度最小, 从现场资料中提取该模式波的难度较大; Out_CF3 模式在所有高阶套管弯曲模式波中激发强度最高, 但是其激发频率较高, 容易受到内层套管模式的干扰, 影响固井质量评价结果; Out_CF2 模式的频散曲线和激发强度在图 2d、f 中以红色实线标出, 其在所有的高阶套管弯曲模式中截止频率最低, 容易从频域中将其分离出来, 且具有较强的激发强度, 因此可以首选该模式波进行固井质量评价.

2.2 油管-套管井的偶极固井质量评价方法

双层套管井的理论计算结果表明, 偶极声源会在外层套管胶结不好时激发额外的高阶套管弯曲模式波, 因此可以使用额外的高阶套管弯曲模式 (Out_CF2) 进行双层套管井的固井质量评价. 图 3 显示了利用 Out_CF2 模式的频散曲线获得偶极固井质量评价指数的方法, 图中粉色实线为理论计算的 Out_CF2 模式的频散曲线, 蓝色圆圈为波列中提取的频散曲线, 由于 Out_CF2 模式仅存在于自由套管的情况下, 因此可以利用波列中提取的频散曲线与理论频散曲线的相似程度判断胶结情况, 而相似程度的公式可表示为

$$n = \sum_{f\in F,\, s\in S} \text{if } (\rho_{\max} > \rho_{\mathrm{t}} \wedge s_{\Delta} < s_{\mathrm{t}}), \tag{11}$$

其中 n 表示相似点的个数, ρ 表示频率-慢度相干图中计算得到的相关系数, f 表示频率范围, s 表示慢度范围, 统计相似点的个数 n 时, 首先需要确定频率-慢度相干图中相关系数的提取阈值 ρ_{t}. 当某一频率下相关系数大于该阈值且为该频率下最大值 $\rho_{\max}$ 时, 该频散点才可以被记录, 即图中蓝色圆圈所示. 然后确定慢度值绝对误差的范围阈值 S_{t}, 图中绿色划线显示了 S_{t} 为正负 25 μs·m^{-1} 的误差范围, 当提取慢度值与理论慢度值的绝对误差 S_{Δ} 小于该阈值时, 该记录点即可视为统计点, 记录频率范围内的所有统计点即可确定相似点数 n. 图 3a 中胶结良好时理论频散曲线误差范围内没有统计点, 相似点数 n 为 0, 图 3b 中自由套管时理论频散曲线误差范围内蓝色记录点的数量即为 n 值, 因此 n 值的大小即可反应外层套管处的胶结情况, 仪器在井内连续测量时, 可以根据井段内所有记录点的相似点数 n 进行归一化处理, 归一化后的值即为偶极固井质量评价的胶结指数 index, 其胶结指数的计算方式为

$$\text{index} = \frac{n - n_{\min}}{n_{\max} - n_{\min}}. \tag{12}$$

3 油管-套管井中偶极阵列声波测井实验

3.1 实验方案

为了进一步验证利用上述高阶套管弯曲模式进行固井质量评价的可行性, 在双层套管模型井中开展了偶极阵列声波测井实验. 图 4a 给出了实验测量原理图, 实验在一口具有不同胶结情况的模型井中开展, 模型井深度 10 m, 上方 5 m 为一界面胶结不好的井段, 下方 5 m 为胶结良好的井段, 将偶极阵列声波测井仪器置于模型井中, 发射换能器与阵列接收换能器均通过电路与信号发生-接收器 (Signal generator and receiver) 连接, 使用上位机 (Upper computer) 下发指令控制信号的产生与数据接收. 图 4b 给出了与实验原理图相对应的实物图, 使用起重机将声波测井仪器置于井孔, 控制仪器在井内不同深度处移动

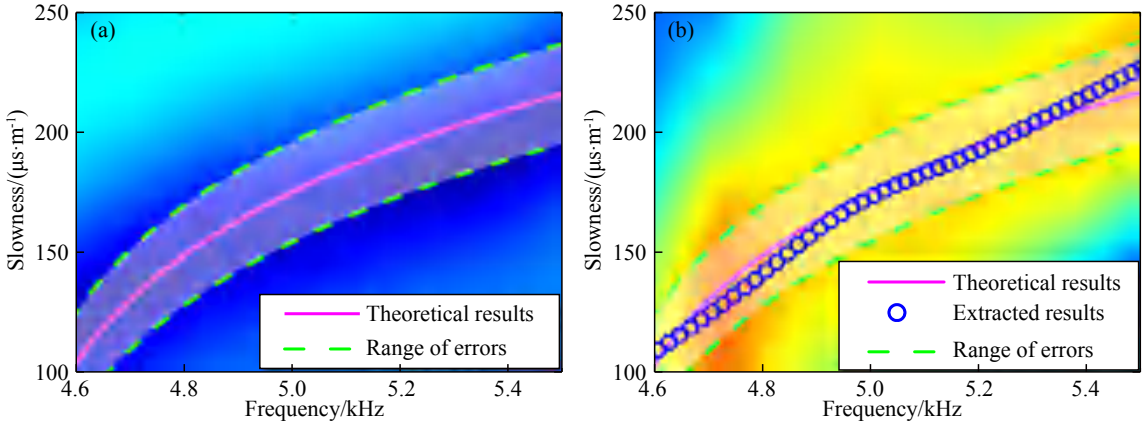


图 3 胶结良好 (a) 和自由套管 (b) 时胶结指数的计算方法

Fig. 3 Calculation of index for well bonded cased borehole (a) and free pipe cased borehole (b)

并记录阵列声波测井数据, 仪器为具有 8 × 4 方位阵列接收功能, 可以通过电路与信号发生-接收器进行实时数据传输, 偶极声波波形采样间隔为 40 μs. 由于内层环空始终为流体层, 因此内层套管在整个井段中均为自由套管, 其中, 内层套管尺寸为 7 in, 外层套管尺寸为 8.6 in. 井中内层套管和外层套管示意图如图 4c 所示, 内层自由套管可以从井中取出, 外层套管固定在井中.

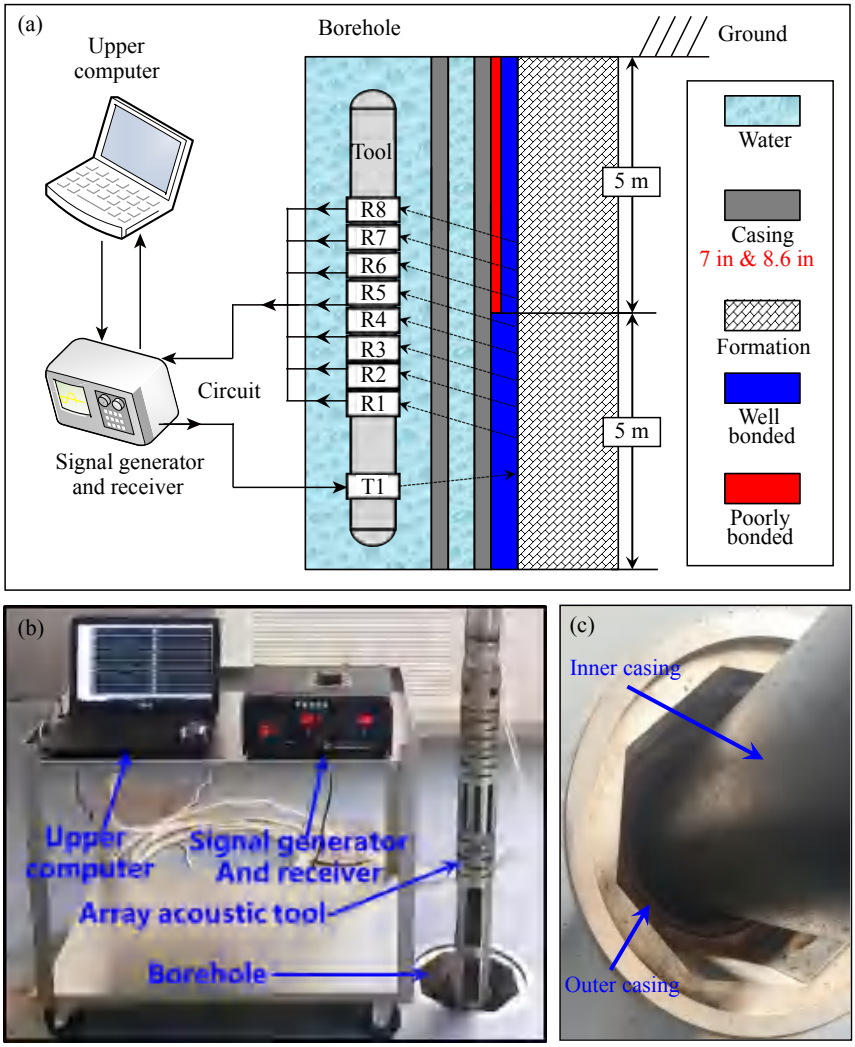


图 4　实验测量系统原理图及实验测量实物图

Fig. 4　Schematic diagram of experimental system and experimental object diagram

3.2　实验测量结果分析

图 5 显示了双层套管模型井中偶极声波测井实验的测量结果, 从波形 (图 5a 胶结良好和图 5b 一界面不胶结) 中可以看到最先到达的是高阶套管弯曲模式 CF2 和 CF3, 其次是地层弯曲模式 FF, 由于内层环空始终为流体层, 两种情况下均存在高阶套管弯曲模式, 因此仅通过波形难以进行固井质量评价. 图 5c、d 分别显示了图 5a、b 实测波形的频率-慢度相干图及频散曲线, 其中黑色实线为理论模拟的结果, 蓝色圆点为实测结果, 可以看出理论与实验的结果具有较好地一致性, 一界面不胶结时相对于胶结良好的情况出现了更多的套管弯曲模式, 其中胶结良好时内层套管产生的 In_CF2 和 In_CF3 模式均可分辨, 而一界面不胶结时 Out_CF2 和 Out_CF3 模在 7 kHz 处发生耦合, 这是因为模拟的套管尺寸和实验的套管尺寸不完全相同, 理论模拟的双层套管尺寸为 17.78 cm 和 24.4475 cm, 而实验室双层套管的尺寸为 17.78 cm 和 21.844 cm, 实验中两层套管的尺寸差异较小, 因此其高阶套管弯曲模式波的频散曲线十分接近. 同样的, In_CF2 和 In_CF3 模式在 9kHz 处发生耦合, 尽管一界面不胶结时高阶套管弯曲模式波的数量相比理论情况下有所减少, 但是 Out_CF2 模式仍较为清晰, 因此, 利用胶结不好时额外的 Out_CF2 模式判断双层套管井的固井质量是可行的.

理论和实验结果表明, 由于双层套管井胶结不好时存在额外的高阶套管弯曲模式波, 因此使用偶极高阶套管弯曲模式进行双层套管井的固井质量评

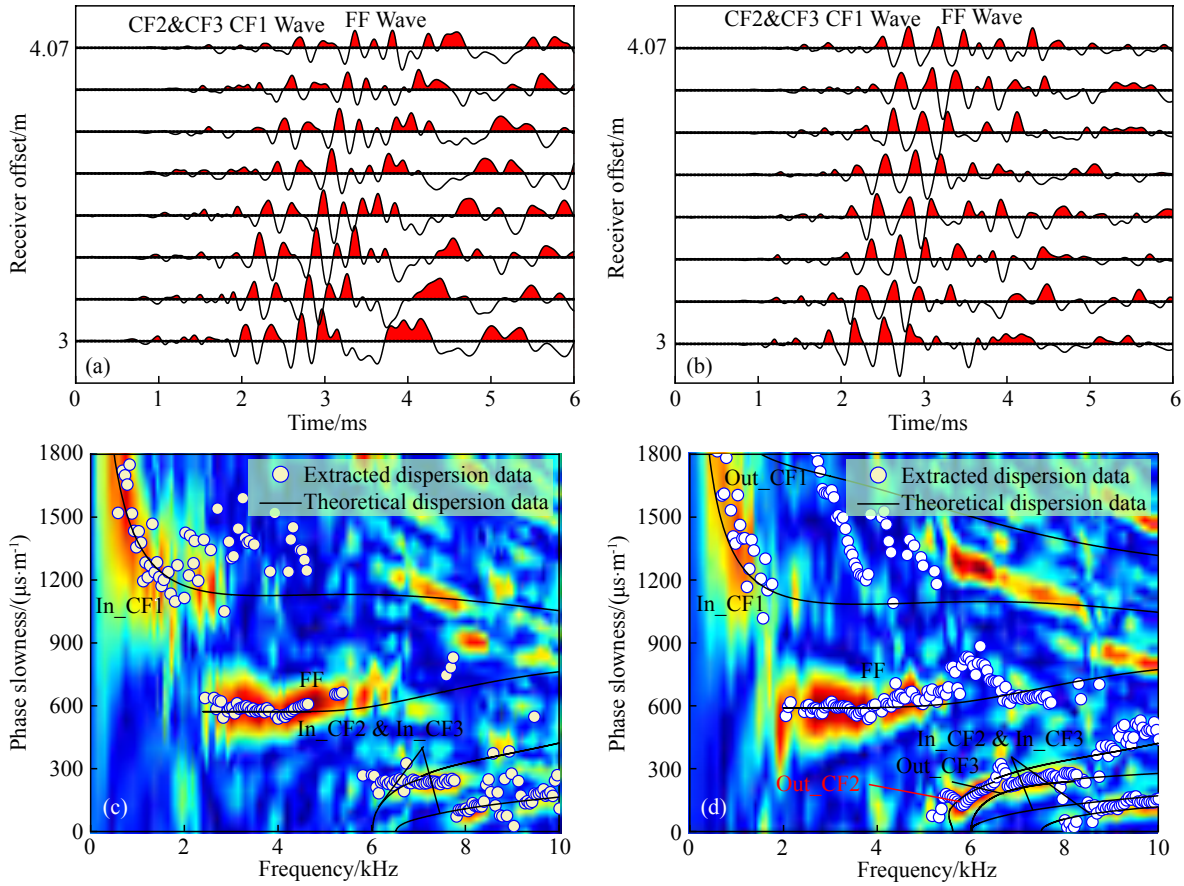


图 5 双层套管井的偶极声波测井响应实验结果

(a) 胶结良好时的波形; (b) 一界面不胶结时的波形; (c) 胶结良好时的频散曲线; (d) 一界面不胶结时的频散曲线.

Fig. 5 Experimental results of dipole acoustic logging response of double casing well

(a) Waveform with well bonded cased borehole; (b) Waveform with the first interface unbonded cased borehole; (c) Dispersion curve with well bonded cased borehole; (d) Dispersion curve with the first interface unbonded cased borehole.

价是可行的, 图 6 显示了一界面不胶结时偶极固井质量评价指数计算的实测结果, 在本文实验井的套管尺寸下, 一界面不胶结时 Out_CF2 模式的频率范围如图 6 所示, 其理论频散曲线以图中粉色实线表示, 在实际测井环境中, 受仪器尺寸, 换能器性能, 套管偏心以及信号处理算法等因素的影响, 实测结果与理论值会存在一定的误差, 图 6b 中红色线段即为式 (11) 中绝对误差$S\Delta$的大小, 当部分实验数据超过给定绝对误差大小时, 即认为此时的频散不是由外层套管外不胶结造成的, 在处理过程中不参与胶结指数的计算. 图 6 的结果表明实测结果与理论具有较好的一致性, 根据计算的胶结指数即可确定偶极声波测井的固井质量评价曲线.

3.3 井段测量实例

本文实验中阵列声波测井仪器的间距为 0.1524 m, 接受阵列长度为 1.07 m, 图 7 显示了实验井井段处理结果, 第 1 道为深度段, 上半段为一界面不胶结井段, 下半段为胶结良好井段, 仪器从胶结良好的井

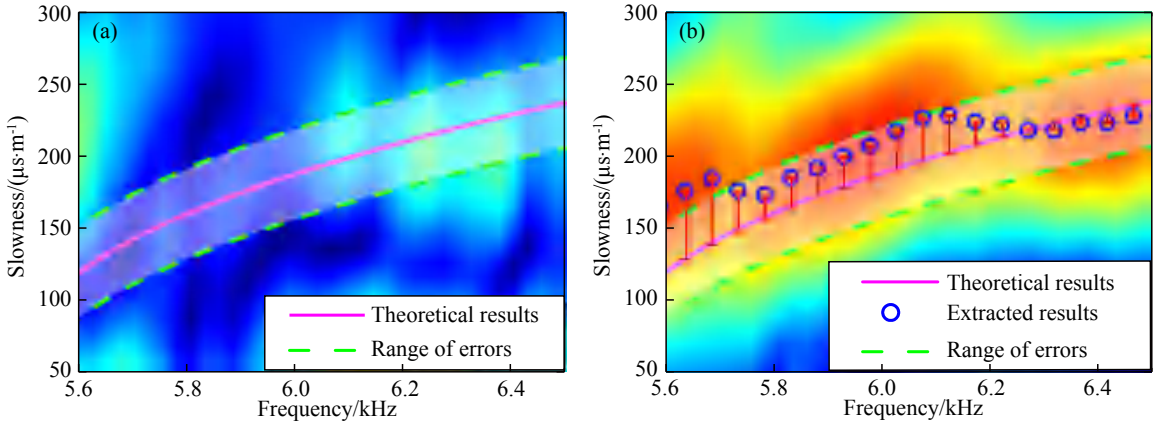


图 6 模型井胶结良好 (a) 和一界面不胶结 (b) 时胶结指数的计算方法

Fig. 6 Calculation of index with well bonded cased borehole (a) and the first interface unbonded cased borehole (b)

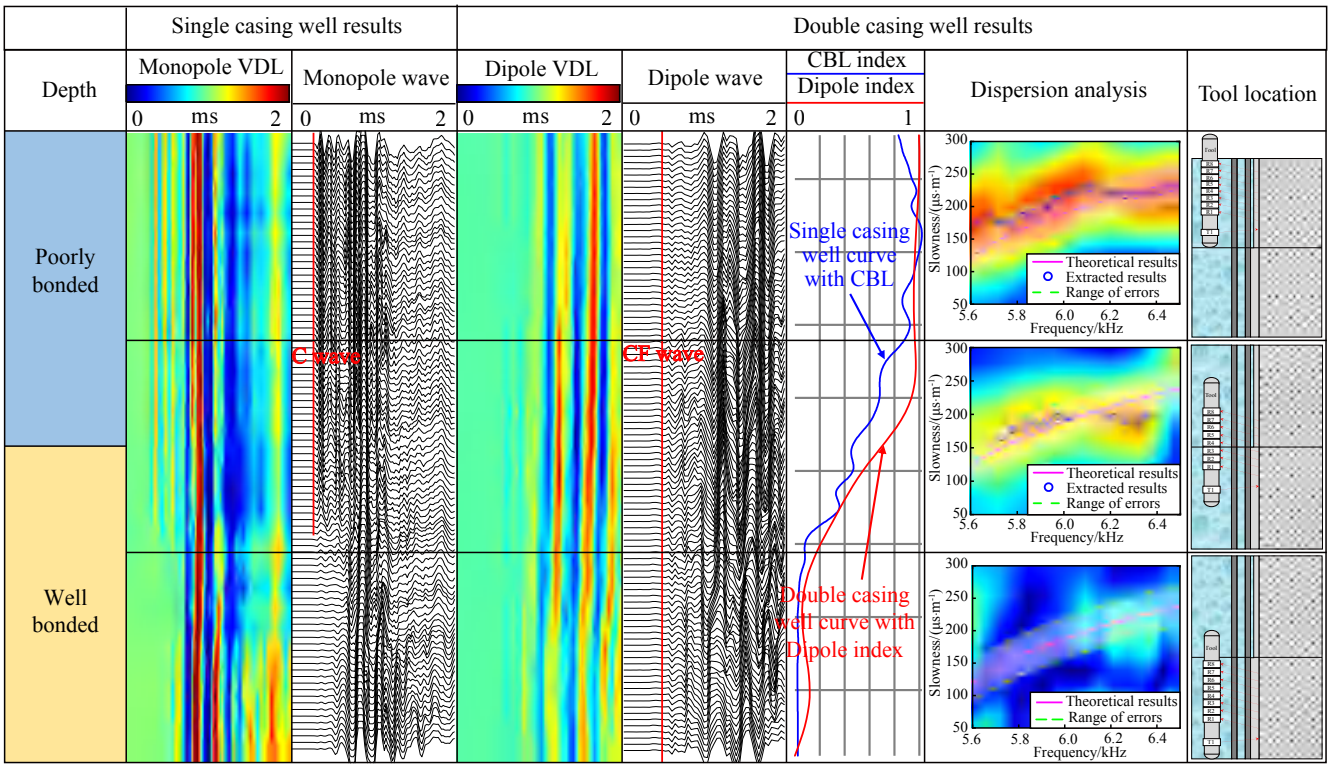


图 7　实验井井段固井质量评价结果

Fig. 7　Evaluation results of cementing quality in experimental well

段上升至一界面不胶结井段的过程中, 由于接受阵列存在一定长度, 因此测量结果存在一个部分胶结的井段. 第 2 道显示了传统单极子变密度测井图的测量结果, 该结果是在移除内层套管后对单层套管的测量结果, 第 3 道显示了与第 2 道相对应的记录点波形图, 从单层套管测量结果可以看出, 套管波会随着仪器上升逐渐出现, 说明井段下方套管胶结良好, 井段上方套管一界面处不胶结, 与模型井的实际情况相对应, 单层套管井的 CBL 测井曲线在第 6 道中用红色实线表示, 第 4 道和第 5 道中显示了偶极子在双层套管井中的测量结果, 可以看出井段中始终存在高阶套管弯曲模式波, 仅通过波形难以进行固井质量评价, 第 6 道中的蓝色实线则显示了图 6 中固井质量评价方法的计算结果, 可以看出基于偶极子的双层套管井固井质量评价结果与单层套管时 CBL 测井的评价结果具有较好的一致性, 并与实际情况相符, 第 7 道显示了仪器在胶结良好、部分胶结和一界面不胶结时某一深度点的 Out_CF2 模式频散处理的结果, 粉色实线为理论频散曲线, 蓝色圆圈为实验提取的频散曲线, 可以看出随着胶结质量变差, Out_CF2 模式逐渐变强, 相应的其评价指数也逐渐变大, 这与第 6 道中的结果相吻合, 第 8 道中显示了不同井段时仪器所处位置的示意图, 与第 7 道中显示的结果相对应.

4　结论

本文使用经典的井孔弹性边界理论模拟了双层套管井不同胶结情况下的偶极声场, 通过理论与实验相结合的方式验证了双层套管井的固井质量评价方法, 得到以下几点认识:

(1) 利用弹性波动理论计算了双层套管井的波形和频散曲线, 发现胶结不好的套管井中存在额外的高阶套管弯曲模式波, 为双层套管井的固井质量评价方法研究提供了理论基础, 验证了海上油气井弃置过程中使用偶极声源过油管固井质量评价的可行性.

(2) 从理论波形中提取了双层套管井的频散曲线并与理论模拟的结果进行对比, 通过设置相关系数的阈值和理论频散曲线的取值范围, 确定了偶极固井质量评价指数的计算原理, 形成了基于偶极声波测井的双层套管井固井质量评价方法.

(3) 通过双层套管井实验验证了使用高阶套管弯曲模式进行固井质量评价的可行性, 使用偶极固井质量评价指数形成了测井曲线并与单层套管井时单极子 CBL 测井的结果进行了对比, 发现了二者具有很好的一致性, 进一步验证了该方法的准确性与可行性, 本文的工作为双层套管井的固井质量评价提供了理论与实验支撑.

附录 A

本文中余弦包络脉冲表达式为

$$S(\omega)=\frac{\mathrm{e}^{\frac{\mathrm{i}\omega T_c}{2}}}{2}\left(\begin{array}{l}\frac{\sin[T_c(\omega+\omega_0)/2]}{\omega+\omega_0}+\frac{\sin[T_c(\omega-\omega_0)/2]}{\omega-\omega_0}+\frac{\sin\left[T_c\left(\omega+\omega_0+\frac{2\pi}{T_c}\right)/2\right]}{2\left(\omega+\omega_0+\frac{2\pi}{T_c}\right)}+\\ \frac{\sin\left[T_c\left(\omega-\omega_0-\frac{2\pi}{T_c}\right)/2\right]}{2\left(\omega-\omega_0-\frac{2\pi}{T_c}\right)}+\frac{\sin\left[T_c\left(\omega+\omega_0-\frac{2\pi}{T_c}\right)/2\right]}{2\left(\omega+\omega_0-\frac{2\pi}{T_c}\right)}+\frac{\sin\left[T_c\left(\omega-\omega_0+\frac{2\pi}{T_c}\right)/2\right]}{2\left(\omega-\omega_0+\frac{2\pi}{T_c}\right)}\end{array}\right),\tag{A1}$$

其中T_c为声源脉冲的长度，ω_0为声源的中心圆频率. 矩阵$\boldsymbol{T}_{\mathrm{Solid}}$为 6 × 6 的矩阵 (以下简写为$\boldsymbol{T}$), 由于矩阵中各元素都有一个共同因子$(fr_0/2)^n\cos[n(\theta-\phi)]\exp(\mathrm{i}kz)/n!$, 所以在表达式中将其省略, $\boldsymbol{T}$矩阵中各元素的表达式为

$$\begin{aligned}
&T_{11}=nI_n(pR)/R+pI_{n+1}(pR),\ T_{12}=nK_n(pR)/R-pK_{n+1}(pR),\ T_{13}=nI_n(sR)/R,\\
&T_{14}=nK_n(sR)/R,\ T_{15}=nikI_n(sR)/R+iksI_{n+1}(sR),\ T_{16}=nikK_n(sR)/R-iksK_{n+1}(sR),\\
&T_{21}=-nI_n(pR)/R,\ T_{22}=-nK_n(pR)/R,\ T_{23}=-nI_n(sR)/R-sI_{n+1}(sR),\\
&T_{24}=-nK_n(sR)/R+sK_{n+1}(sR),\ T_{25}=-nikI_n(sR)/R,\ T_{26}=-nikK_n(sR)/R,\\
&T_{31}=ikI_n(pR),\ T_{32}=ikK_n(pR),\ T_{33}=0,\ T_{34}=0,\ T_{35}=-s^2I_n(sR),\ T_{36}=-s^2K_n(sR),\\
&T_{41}=\rho\left(2k^2\beta^2-\omega^2\right)I_n(pR)+2n(n-1)\rho\beta^2I_n(pR)/R^2-2p\rho\beta^2I_{n+1}(pR)/R,\\
&T_{42}=\rho\left(2k^2\beta^2-\omega^2\right)K_n(pR)+2n(n-1)\rho\beta^2K_n(pR)/R^2+2p\rho\beta^2K_{n+1}(pR)/R,\\
&T_{43}=2n(n-1)\rho\beta^2I_n(sR)/R^2+2ns\rho\beta^2I_{n+1}(sR)/R,\\
&T_{44}=2n(n-1)\rho\beta^2K_n(sR)/R^2-2ns\rho\beta^2K_{n+1}(sR)/R,\\
&T_{45}=2iks^2\rho\beta^2I_n(sR)+2n(n-1)ik\rho\beta^2I_n(sR)/R^2-2iks\rho\beta^2I_{n+1}(sR)/R,\\
&T_{46}=2iks^2\rho\beta^2K_n(sR)+2n(n-1)ik\rho\beta^2K_n(sR)/R^2+2iks\rho\beta^2K_{n+1}(sR)/R,
\end{aligned}\tag{A2}$$

$$\begin{aligned}
&T_{51}=-2n(n-1)\rho\beta^2I_n(pR)/R^2-2np\rho\beta^2I_{n+1}(pR)/R,\\
&T_{52}=-2n(n-1)\rho\beta^2K_n(pR)/R^2+2np\rho\beta^2K_{n+1}(pR)/R,\\
&T_{53}=-2n(n-1)\rho\beta^2I_n(sR)/R^2-s^2\rho\beta^2I_n(sR)+2s\rho\beta^2I_{n+1}(sR)/R,\\
&T_{54}=-2n(n-1)\rho\beta^2K_n(sR)/R^2-s^2\rho\beta^2K_n(sR)-2s\rho\beta^2K_{n+1}(sR)/R,\\
&T_{55}=-2n(n-1)ik\rho\beta^2I_n(sR)/R^2-2niks\rho\beta^2I_{n+1}(sR)/R,\\
&T_{56}=-2n(n-1)ik\rho\beta^2K_n(sR)/R^2+2niks\rho\beta^2K_{n+1}(sR)/R,\\
&T_{61}=2nik\rho\beta^2I_n(pR)/R+2ikp\rho\beta^2I_{n+1}(pR),\\
&T_{62}=2nik\rho\beta^2K_n(pR)/R-2ikp\rho\beta^2K_{n+1}(pR),\\
&T_{63}=nik\rho\beta^2I_n(sR)/R,\ T_{64}=nik\rho\beta^2K_n(sR)/R,\\
&T_{65}=-n\left(k^2+s^2\right)\rho\beta^2I_n(sR)/R-\left(k^2+s^2\right)s\rho\beta^2I_{n+1}(sR),\\
&T_{66}=-n\left(k^2+s^2\right)\rho\beta^2K_n(sR)/R+\left(k^2+s^2\right)s\rho\beta^2K_{n+1}(sR).
\end{aligned}\tag{A3}$$

References

Bose S, Zhu L C, Zeroug S, et al. 2021. Acoustic evaluation of annulus b barriers through tubing for plug and abandonment job planning. //Offshore Technology Conference. Virtual and Houston, Texas: OTC.

Chen X L, Jiang C, Zhang C X, et al. 2020. Response characteristics of monopole sonic log in double casing strings. *Chinese Journal of Geophysics* (in Chinese), 63(11): 4268-4276, doi: 10.6038/cjg2020O0016.

Chen X L, Tang X M. 2021. The wavefield characteristics of dipole acoustic logging in a double-casing well. *Chinese Journal of Geophysics* (in Chinese), 64(1): 363-371, doi: 10.6038/cjg2021O0155.

Everhart A H, Chang S K. 1985. A theoretical study of dipole shear logging in cased holes. //SEG Technical Program Expanded Abstracts 1985. Society of Exploration Geophysicists, 72-74.

Jiang C, Chen X L, Su Y D, et al. 2019. Cased borehole acoustic-wave propagation with varying bonding conditions: Theoretical and experimental modeling. *Geophysics*, 84(4): D161-D169.

Li G, Lü W G, Cui Z W, et al. 2018. Characteristics of dipole flexural wave dispersion shift to the high-frequency in cased hole. *Chinese Journal of Geophysics* (in Chinese), 61(1): 379-388, doi: 10.6038/cjg2018K0248.

Lin J S, Li S Q, Liu Z H, et al. 2021. Numerical simulation and experimental

research of through casing sonic logging with redressing LWD acquisition mode. *Progress in Geophysics* (in Chinese), 36(6): 2496-2502, doi: 10.6038/pg2021EE0477.

Liu Y, D'Angelo R M, Sinha B K, et al. 2017. Theoretical and experimental investigations of acoustic waves in embedded fluid-solid multi-string structures. *Applied Physics Letters*, 110(10): 101906, doi: 10.1063/1.4977937.

Pan J L, Chen X L, Tang X M. 2023. Theoretical calculation of casing well sound field represented by slip interface. *Chinese Journal of Geophysics* (in Chinese), 66(1): 442-453, doi: 10.6038/cjg2022P0832.

Rose J L. 2004. Ultrasonic Waves in Solid Media (in Chinese). He C F, Wu B, Wang X Y Trans. Beijing: Science Press, 49-65.

Schmitt D P. 1993. Dipole logging in cased boreholes. *The Journal of the Acoustical Society of America*, 93(2): 640-657.

Sun Z F, Luo B, Li J, et al. 2023. Study on the wave field of LWD quadrupole acoustic logging tool in a fluid-filled trough. *Progress in Geophysics* (in Chinese), 38(4): 1874-1884, doi: 10.6038/pg2023GG0081.

Tang X M, Jiang C, Su Y D, et al. 2018. An acoustic-wave theory for casing bond evaluation using viscoelastic slip boundary modeling. *Science China Earth Sciences*, 61(8): 1057-1064.

Tang X M, Zheng C H. 2004. Quantitative Borehole Acoustic Methods (in Chinese). Zhao X M Trans. Beijing: Petroleum Industry Press, 20-50.

Tubman K M, Cheng C H, Cole S P, et al. 1986. Synthetic full-waveform acoustic logs in cased boreholes, II—Poorly bonded casing. *Geophysics*, 51(4): 902-913.

Wang H, Fehler M. 2018. The wavefield of acoustic logging in a cased hole with a single casing— Part II: A dipole tool. *Geophysical Journal International*, 212(2): 1412-1428.

Zeroug S, Bounoua N, Lounissi R. 2007. Well Integrity-cement evaluation. //Sonatrach-Schlumberger Well Evaluation Conference, Algeria: 5.32-5.45.

Zeroug S, Bose S, Sinha B, et al. 2016. Sonic and ultrasonic measurement applications for cased oil wells. *Insight-Non-Destructive Testing and Condition Monitoring*, 58(8): 423-430.

Zeroug S, Bose S. 2018. Recent advances in the use of acoustics across the frequency spectrum in the oil and gas industry. *AIP Conference Proceedings*, 1949(1): 020014, doi: 10.1063/1.5031511.

Zhang H L, Wang X M, Zhang B X. 2004. Acoustic Field and Wave in Borehole (in Chinese). Beijing: Sciences Press, 46-60.

Zhang X M, Wang X M, Zhang H L. 2016. Leaky modes and the first arrivals in cased boreholes with poorly bonded conditions. *Science China Physics, Mechanics & Astronomy*, 59(2): 624301, doi: 10.1007/s11433-015-5756-6.

附中文参考文献

陈雪莲, 江灿, 庄春喜等. 2020. 双层套管井中单极子声波测井的响应特征. 地球物理学报, 63(11): 4268-4276, doi: 10.6038/cjg2020O0016.

陈雪莲, 唐晓明. 2021. 偶极子声波测井在双层套管井中激发的声场特征. 地球物理学报, 64(1): 363-371, doi: 10.6038/cjg2021O0155.

李刚, 吕伟国, 崔志文等. 2018. 套管井偶极弯曲波频散向高频偏移的特性. 地球物理学报, 61(1): 379-388, doi: 10.6038/cjg2018K0248.

林剑松, 李盛清, 刘忠华等. 2021. 随钻划眼采集模式的过套管声波测井数值模拟与实验研究. 地球物理学进展, 36(6): 2496-2502, doi: 10.6038/pg2021EE0477.

罗斯 J L. 2004. 固体中的超声波. 何存富, 吴斌, 王秀彦译. 北京: 科学出版社, 49-65.

潘金林, 陈雪莲, 唐晓明. 2023. 滑移界面表征的套管井声场的理论计算. 地球物理学报, 66(1): 442-453, doi: 10.6038/cjg2022P0832.

孙志峰, 罗博, 李杰等. 2023. 随钻四极子声波测井仪在充液圆槽中的波场研究. 地球物理学进展, 38(4): 1874-1884, doi: 10.6038/pg2023GG0081.

唐晓明, 江灿, 苏远大等. 2018. 用黏弹滑移界面表征的固井声波测井理论. 中国科学: 地球科学, 48(8): 1045-1052.

唐晓明, 郑传汉. 2004. 定量测井声学. 赵晓敏译. 北京: 石油工业出版社, 20-50.

张海澜, 王秀明, 张碧星. 2004. 井孔的声场和波. 北京: 科学出版社, 46-60.

（本文编辑　张正峰）

李盛清，林剑松，江灿等. 2020. 随钻声波测井固井质量评价理论与数值模拟研究. 地球物理学报，63(7)：2762-2773，doi：10.6038/cjg2020N0086.

Li S Q, Lin J S, Jiang C, et al. 2020. Theoretical and numerical simulation of LWD acoustic cement logging. *Chinese J. Geophys.* (in Chinese), 63(7): 2762-2773, doi: 10.6038/cjg2020N0086.

随钻声波测井固井质量评价理论与数值模拟研究

李盛清[1,2]，林剑松[1,2]，江灿[1,2]，苏远大[1,2]，唐晓明[1,2]

1 中国石油大学(华东)地球科学与技术学院，青岛 266580

2 中国石油大学(华东)深层油气重点实验室，青岛 266580

摘要 大斜度井、水平井的固井质量评价需求，推动了基于随钻测井仪器的固井质量评价技术的发展. 本文基于弹性波传播理论，建立柱状分层介质的套管井随钻测井模型，模拟了不同水泥胶结情况的随钻声场响应，特别是其波形特征. 结果表明，套管井中随钻与电缆波形特征最大的区别在于随钻波列中存在隔声衰减后的钻铤波. 特别是当水泥胶结较好时，钻铤波与套管波幅度大小相近，甚至钻铤波幅度更大，而时间域上两者波形重叠，该特点使得常规电缆声波(声幅/变密度)固井质量评价方法不适用于随钻测井环境. 本文考察了不同水泥胶结程度下随钻波列中套管波幅度和衰减与胶结指数的关系，形成一种同时利用幅度和衰减的随钻声波胶结指数计算方法，为随钻声波固井质量评价提供理论指导.

关键词 随钻声波测井；固井质量评价；套管波；钻铤波；胶结指数

doi：10.6038/cjg2020N0086 **中图分类号** P631 **收稿日期** 2019-03-06，2020-03-16 收修定稿

Theoretical and numerical simulation of LWD acoustic cement logging

LI ShengQing[1,2], LIN JianSong[1,2], JIANG Can[1,2], SU YuanDa[1,2], TANG XiaoMing[1,2]

1 *School of Geosciences, China University of petroleum, Qingdao* 266580, *China*

2 *Key Laboratory of Deep Oil and Gas, China University of petroleum, Qingdao* 266580, *China*

Abstract The demand for cementing quality evaluation of high-angle and horizontal wells have promoted the development of cementing quality inspection technology based on Logging-While-Drilling (LWD)acoustic tools. Based on the propagation theory of elastic waves, we established a cased LWD model of radially layered media. The acoustic responses of various cementing situations in the LWD environment, mainly the waveforms, are numerically simulated. The results show that the collar waves still exist even after acoustic isolation, which is greatly different from the wireline response. Especially when cement is bonded well, the amplitude of collar waves can compare to or even be larger than that of casing waves. The collar waves and the casing waves overlap in the time domain, leading to that conventional cementing quality evaluation methods of wireline logging (CBL/VDL) is unsuitable for the LWD environment. We also investigated the relationship between casing wave amplitude (or attenuation) and cement bond index in the LWD condition. The calculation method of the LWD hybrid bond index using both amplitude and attenuation was formed, providing theoretical guidance for the cementing

基金项目 国家自然科学基金(41804124，41821002)，国家重点研发计划(2019YFC0605504)，山东省自然科学基金(ZR2019BD039)，山东省博士后创新项目(201901011)，中国博士后科学基金(2019T120615，2018M632745)，中国石油重大科技项目(ZD2019-183-004)，中国科学院战略性先导科技专项 (XDA14020304，XDA14020202) 和中央高校基本科研业务费专项资金资助(18CX02065A)联合资助.

第一作者简介 李盛清，男，1988 年生，博士后，主要从事声波测井理论、方法及处理研究. E-mail：shidalishengqing@yeah.net

quality evaluation based on acoustic logging while drilling.

Keywords　Acoustic logging while drilling; Cementing quality evaluation; Casing wave; Collar wave; Hybrid bond index

0　引言

石油工业中固井质量评价是油气开发和生产的一个重要环节,声波检测是最主要的技术之一.套管井声场特性研究是固井质量评价的理论基础,许多学者就电缆环境的套管井声波响应做了大量的理论分析、数值模拟和实验工作(Tubman et al.,1984;周吟秋等,2007;张宏兵等,2009;Song et al.,2012;He et al.,2014;陈雪莲和唐晓明,2019).目前,基于电缆声波测井的固井质量评价,如声幅测井、声波变密度测井等技术已发展成熟,国内外测井公司也都制定了定性或定量的评价标准.

深水、深层钻探存在电缆测井成本高,难度大并大量占用井架时间的问题,同时大斜度(大位移)井和水平井,由于井斜大轨迹深,电缆测井难以有效测量.随钻测井可在下放或上提仪器时进行滑眼测量,既保证测井数据质量,又能降本增效,适合深水、深层环境;随钻测井仪器亦可弥补大斜度井和水平井中电缆测井爬行器无法深入测量的不足.近年来随钻声波测井技术已经开始广泛使用,对此国内外专家也进行了大量研究工作(Tang et al.,2002;崔志文,2004;苏远大等,2011;王华等,2009;王军等,2019).这些工作都是在裸眼井中进行的,但套管井随钻声场特征研究还鲜有发表.Market 等(2004)模拟了套管井中随钻声波仪器响应,但未考虑固井质量评价方面的应用价值.目前主要有斯伦贝谢公司开展了随钻声波测井在套管井水泥检测方面的研究.Blyth 等(2013)开展了随钻声波固井质量评价的新用途研究.Kinoshita 等(2013)、Pistre 等(2014)进行了随钻声波定量评价固井质量的可行性探索.国内东海平湖油气田也采用了随钻声波测井仪器进行固井质量评价(许风光和白玉洪,2016).在这些固井质量评价实例中,随钻声波都取得了良好的应用效果.Izuhara 等(2017)提出一种基于幅度和衰减联合的评价方法,实现了随钻声波胶结指数的划分.然而这些研究进展仍是参照常规电缆声波评价方法去阐述实际应用效果,并未从理论上深入分析套管井随钻声波测井响应特征.

本文建立柱状分层介质的套管井随钻测井模型,导出了充液井孔声场表达式.根据弹性波传播理论,利用实轴积分法进行了套管井随钻声场模拟,分析了不同水泥胶结情况的随钻声波测井响应特征,主要包括频散特性和理论波形.此外考察了不同水泥胶结程度下随钻波列中套管波幅度和衰减与胶结指数的关系,并与电缆测井情况对比.形成一种同时利用幅度和衰减的随钻声波胶结指数计算方法,进一步通过现场测井实例验证,为随钻声波固井质量评价提供理论指导.

1　套管井随钻声波测井理论

建立柱状分层介质的套管井随钻测井模型,考察套管井内和井外空间的声场特征.图 1 给出该模型示意图,随钻仪器居中放置于井中,钻铤占据井内流体大部分.环状声源贴钻铤外壁激发声场,套管井中的接收器阵列记录随钻声波波形.介质空间在径向上依次被划分为钻铤内流体、钻铤、钻铤外流体、套管、水泥环和无限大地层(各介质为均匀弹性介质).

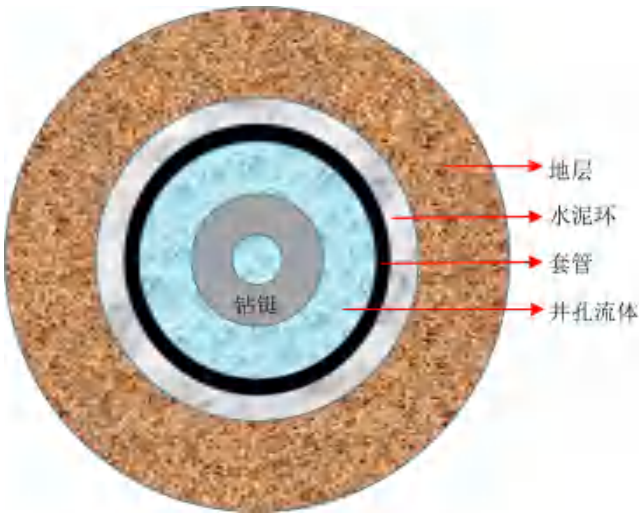


图 1　套管井随钻声波测井模型

Fig. 1　Acoustic logging while drilling model for cased well

1.1　钻铤和钻铤内外流体的声场

根据井孔声场理论(Tang and Cheng,2004),柱坐标系(r,θ,z)中钻铤内流体位移势Φ'的表达式为

$$\Phi'(k,\omega,r,\theta)=A'_nI_n(fr)\cos[n(\theta-\phi)]e^{ikz},\quad(1)$$

由式(1)位移势得到钻铤内流体的径向位移u'_f和应力σ'_{rrf}:

$$\begin{cases} u'_{\mathrm{f}}(k,\omega,r,\theta) = \dfrac{\partial \Phi'}{\partial r} = A'_n\left[\dfrac{n}{r}I_n(fr) + fI_{n+1}(fr)\right]\cos[n(\theta-\phi)]\mathrm{e}^{\mathrm{i}kz}, \\ \sigma'_{\mathrm{rrf}}(k,\omega,r,\theta) = -\rho_{\mathrm{f}}\omega^2\Phi' = -\rho_{\mathrm{f}}\omega^2 A'_n I_n(fr)\cos[n(\theta-\phi)]\mathrm{e}^{\mathrm{i}kz}, \end{cases} \tag{2}$$

(1)、(2)式中 k 是轴向波数，ω 是圆频率，A'_n 是钻铤内流体的入射波振幅系数，I_n 表示第一类贝塞尔函数，n 是多极子阶数，$f=(k^2-k_{\mathrm{f}}^2)^{1/2}$ 是流体径向波数，ρ_{f} 是流体密度.

钻铤既有由外向内的入射波，又有由内向外的出射波，则钻铤纵波、SH 横波和 SV 横波的位移势 Φ^{tool}、χ^{tool} 和 Γ^{tool} 分别为

$$\begin{cases} \Phi^{\mathrm{tool}}(k,\omega,r,\theta) = [A_n^{\mathrm{tool}}I_n(p_{\mathrm{tool}}r) \\ \qquad + B_n^{\mathrm{tool}}K_n(p_{\mathrm{tool}}r)]\cos[n(\theta-\varphi)]\mathrm{e}^{\mathrm{i}kz}, \\ \chi^{\mathrm{tool}}(k,\omega,r,\theta) = [C_n^{\mathrm{tool}}I_n(s_{\mathrm{tool}}r) \\ \qquad + D_n^{\mathrm{tool}}K_n(s_{\mathrm{tool}}r)]\sin[n(\theta-\phi)]\mathrm{e}^{\mathrm{i}kz}, \\ \Gamma^{\mathrm{tool}}(k,\omega,r,\theta) = [E_n^{\mathrm{tool}}I_n(s_{\mathrm{tool}}r) \\ \qquad + F_n^{\mathrm{tool}}K_n(s_{\mathrm{tool}}r)]\cos[n(\theta-\phi)]\mathrm{e}^{\mathrm{i}kz}, \end{cases} \tag{3}$$

式中 $p_{\mathrm{tool}}=(k^2-k_{\mathrm{p}}^2)^{1/2}$ 和 $s_{\mathrm{tool}}=(k^2-k_{\mathrm{s}}^2)^{1/2}$ 分别表示钻铤纵波和钻铤横波的径向波数；$k_{\mathrm{p}}=\omega/v^{\mathrm{tool}}{}_{\mathrm{p}}$ 和 $k_{\mathrm{s}}=\omega/v_{\mathrm{s}}^{\mathrm{tool}}$ 分别表示纵波和横波波数，$v_{\mathrm{p}}^{\mathrm{tool}}$、$v_{\mathrm{s}}^{\mathrm{tool}}$ 分别表示钻铤纵波和横波速度. K_n 表示第二类贝塞尔函数. $A_n^{\mathrm{tool}}(B_n^{\mathrm{tool}})$、$C_n^{\mathrm{tool}}(D_n^{\mathrm{tool}})$、$E_n^{\mathrm{tool}}(F_n^{\mathrm{tool}})$ 分别是钻铤中入射(出射)纵波、SH 横波和 SV 横波的振幅系数.

钻铤外的流体声场包含入射波和出射波，则钻铤外流体的位移势 Φ 表示为

$$\Phi(k,\omega,r,\theta) = [A_nI_n(fr)+B_nK_n(fr)]\cos[n(\theta-\phi)]\mathrm{e}^{\mathrm{i}kz}, \tag{4}$$

得到钻铤外流体径向位移 u_{f} 和应力 σ_{rrf}：

$$\begin{cases} u_{\mathrm{f}}(k,\omega,r,\theta) = \left\{A_n\left[\dfrac{n}{r}I_n(fr)+fI_{n+1}(fr)\right]+ \right. \\ \left. B_n\left[\dfrac{n}{r}K_n(fr)-fK_{n+1}(fr)\right]\right\}\cos[n(\theta-\phi)]\mathrm{e}^{\mathrm{i}kz}, \\ \sigma_{\mathrm{rrf}}(k,\omega,r,\theta) = -\rho_{\mathrm{f}}\omega^2[A_nI_n(fr)+B_nK_n(fr)] \\ \qquad \times\cos[n(\theta-\phi)]\mathrm{e}^{\mathrm{i}kz}, \end{cases} \tag{5}$$

式中 A_n、B_n 分别是钻铤外流体的入射波和出射波振幅系数.

1.2 套管和套管外各介质层的声场

图 1 模型为水泥胶结良好的情况，套管、水泥环和地层组成了圆柱形层状固体介质. 套管和水泥环的声场与钻铤声场类似，包含入射波和出射波. 对于无限大地层，只有向外辐射的波. 套管、水泥环与地层之间的声场由汤姆森-哈斯克传播矩阵 $\boldsymbol{G}$ 连接(Tang and Cheng, 2004)，胶结良好时套管内界面的径向位移 u^{ca} 及应力 $\sigma_{rr}^{\mathrm{ca}}$、$\sigma_{r\theta}^{\mathrm{ca}}$、$\sigma_{rz}^{\mathrm{ca}}$ 与最外层地层声场之间的传递可表示为

$$(u^{\mathrm{ca}},\sigma_{rr}^{\mathrm{ca}},\sigma_{rz}^{\mathrm{ca}},\sigma_{r\theta}^{\mathrm{ca}})^{\mathrm{T}} = \boldsymbol{G}(B_n^{\mathrm{fm}},D_n^{\mathrm{fm}},F_n^{\mathrm{fm}})^{\mathrm{T}}, \tag{6}$$

式中 B_n^{fm}、D_n^{fm}、F_n^{fm} 表示地层出射波的振幅系数. 水泥胶结不好的情况，可在套管与水泥环之间加一流体层来模拟，或将水泥环全部替换成流体(自由套管). 由于固-固和固-液界面的边界条件不同，所以要对流体层的边界单独处理(类似钻铤与钻铤内外流体的边界关系)，再利用汤姆森-哈斯克传播矩阵 $\boldsymbol{G}$ 连接固体介质层之间的声场.

1.3 套管井随钻声波测井边界条件

套管井内流体波动与井外介质层波动可通过套管内壁边界条件衔接. 固-液界面的边界条件是径向位移和径向正应力连续，切应力为零(若是固-固界面，位移和应力的每一个分量都连续)，则钻铤内流体与钻铤界面的边界条件表示为

$$\begin{cases} \boldsymbol{u}'_{\mathrm{f}} = \boldsymbol{u}^{\mathrm{tool}}, \\ \sigma'_{rr\mathrm{f}} = \sigma_{rr}^{\mathrm{tool}}, \\ 0 = \sigma_{rz}^{\mathrm{tool}}, \\ 0 = \sigma_{r\theta}^{\mathrm{tool}}, \end{cases} \quad (r=r_1), \tag{7}$$

钻铤与钻铤外流体界面的边界条件为

$$\begin{cases} \boldsymbol{u}^{\mathrm{tool}} = \boldsymbol{u}_{\mathrm{f}} + \boldsymbol{u}^{\mathrm{s}}, \\ \sigma_{rr}^{\mathrm{tool}} = \sigma_{rr\mathrm{f}}, \\ \sigma_{rz}^{\mathrm{tool}} = 0, \\ \sigma_{r\theta}^{\mathrm{tool}} = 0, \end{cases} \quad (r=r_2), \tag{8}$$

(7)、(8)式中 $\boldsymbol{u}^{\mathrm{tool}}$ 和 $\sigma_{rr}^{\mathrm{tool}}$、$\sigma_{rz}^{\mathrm{tool}}$、$\sigma_{r\theta}^{\mathrm{tool}}$ 分别表示钻铤径向位移和应力分量，r_1、r_2 分别是钻铤内、外径.

钻铤外壁的环状声源采用体积膨胀源的加载方式，即在原有井内流体位移的基础上加上环状声源的位移 $\boldsymbol{u}^{\mathrm{s}}$. 该位移具体表达式为

$$\boldsymbol{u}^{\mathrm{s}} = \varepsilon_n\left[\frac{n}{r}K_n(fr)-fK_{n+1}(fr)\right]I_n(fr)\cos \times[n(\theta-\phi)]\mathrm{e}^{\mathrm{i}kz}, \tag{9}$$

其中多极子阶数 $n=0$ 时 $\varepsilon_n=1$，$n>0$ 时 $\varepsilon_n=2$. 钻铤外流体与套管界面的边界条件为

$$\begin{cases} \boldsymbol{u}_{\mathrm{f}} = \boldsymbol{u}^{\mathrm{ca}}, \\ \sigma_{rr\mathrm{f}} = \sigma_{rr}^{\mathrm{ca}}, \\ 0 = \sigma_{rz}^{\mathrm{ca}}, \\ 0 = \sigma_{r\theta}^{\mathrm{ca}}, \end{cases} (r = r_3), \tag{10}$$

其中 r_3 为套管内径.

以上各部分声场的应力和位移都利用边界条件及汤姆森-哈斯克传播矩阵 $\boldsymbol{G}$ 连接(如(6)式),得到矩阵方程:

$$\boldsymbol{HO} = \boldsymbol{b}, \tag{11}$$

当水泥胶结差时,$\boldsymbol{H}$ 为 20×20 阶的矩阵,其中:$\boldsymbol{O} = [A_n', A_n^{\mathrm{tool}}, B_n^{\mathrm{tool}}, C_n^{\mathrm{tool}}, D_n^{\mathrm{tool}}, E_n^{\mathrm{tool}}, F_n^{\mathrm{tool}}, A_n, B_n, A_n^{\mathrm{ca}}, B_n^{\mathrm{ca}}, C_n^{\mathrm{ca}}, D_n^{\mathrm{ca}}, E_n^{\mathrm{ca}}, F_n^{\mathrm{ca}}, A_n'', B_n'', B_n^{\mathrm{fm}}, D_n^{\mathrm{fm}}, F_n^{\mathrm{fm}}]$, $\boldsymbol{b} = [0, 0,0,0,u^{\mathrm{s}},0,0,0,0,0,0,0,0,0,0,0,0,0,0,0]$. 式中 $A_n^{\mathrm{ca}}(B_n^{\mathrm{ca}})$、$C_n^{\mathrm{ca}}(D_n^{\mathrm{ca}})$、$E_n^{\mathrm{ca}}(F_n^{\mathrm{ca}})$ 分别是套管入射(出射)波、SH 横波和 SV 横波的振幅系数. A_n'' 和 B_n'' 表示套管和水泥层之间的水环振幅系数. 自由套管的情况与水泥胶结差时类似,而胶结良好时,从套管层到地层之间的声场可通过汤姆森-哈斯克传播矩阵 $\boldsymbol{G}$ 连接,因此 $\boldsymbol{H}$ 降为 12×12 阶的矩阵,其中:$\boldsymbol{O} = [A_n', A_n^{\mathrm{tool}}, B_n^{\mathrm{tool}}, C_n^{\mathrm{tool}}, D_n^{\mathrm{tool}}, E_n^{\mathrm{tool}}, F_n^{\mathrm{tool}}, A_n, B_n, B_n^{\mathrm{fm}}, D_n^{\mathrm{fm}}, F_n^{\mathrm{fm}}]$, $\boldsymbol{b} = [0,0,0,0,u^{\mathrm{s}},0,0,0,0,0,0,0]$. $\boldsymbol{H}$ 矩阵各元素表达式在附录中给出.

解方程(11)得系数 A_n 和 B_n,计算钻铤外壁的环状声源在井内环状流体中产生的声波场:

$$P(z,t) = \int_{-\infty}^{+\infty} \rho_{\mathrm{f}} \omega^2 S(\omega) \mathrm{e}^{-\mathrm{i}\omega t} \mathrm{d}\omega \int_{-\infty}^{+\infty} [A_n I_n(fr) + B_n K_n(fr)] \mathrm{e}^{\mathrm{i}kz} \mathrm{d}k, \tag{12}$$

式中 $S(\omega)$ 为声源频谱,可采用瑞克子波或高斯声源.

2　数值计算结果及分析

依照上述理论方法,数值模拟了不同水泥胶结情况的套管井随钻声波测井响应,主要包括频散特性和波形特征,并与电缆情况对比(电缆声波情况的套管井数值模拟方法见 Tubam 等(1984)、Tang 和 Cheng(2004)的文献). 表 1 给出计算所用的钻铤内流体、钻铤、钻铤外流体、套管、水泥环和地层的声学/尺寸参数.

2.1　套管井随钻声波频散特性

水泥完全胶结和自由套管是套管胶结质量的极端情况,考察套管波与一阶钻铤波的频散特性,以此说明钻铤波的影响. 测井响应函数中包含一些极点,对应着沿井轴方向传播的导波或模式波,在给定频率下导波的轴向波数由式(13)确定:

表 1　模型的声学/尺寸参数

Table 1　Acoustic/dimension parameters of the model

介质参数	纵波速度 /(m·s^{-1})	横波速度 /(m·s^{-1})	密度 /(kg·m^{-3})	外径 /m
钻铤内流体	1500	—	1000	0.127
钻铤	5860	3130	7850	0.090
钻铤外流体	1500	—	1000	0.117
套管	6098	3354	7500	0.027
水泥	2823	1729	1920	0.147
地层	3942	2455	2320	∞

$$D_n(k,\omega) = \det(\boldsymbol{H}) = 0, \tag{13}$$

该方程即为频散方程,决定了导波的频散特征,其中 $\det(\boldsymbol{H})$ 表示待求声场矩阵的行列式. 图 2 给出套管井中电缆和随钻单极子模式波的相速度频散二维谱,其中图 2a、b 分别为胶结良好时电缆和随钻的结果. 因套管-水泥-地层耦合较好,套管波衰减大,在 0～20 kHz频段内皆无套管模式波;图 2b 的随钻声波测井出现钻铤模式波,从频散曲线(实心圆点)可以看出钻铤波频散效应明显,无截止频率,在单极子声波测井常用频段(8～13 kHz)内,相速度低于 5000 m·s^{-1}. 图 2c、d 分别为自由套管(流体层厚度为 0.02 m)时电缆和随钻的结果. 由于套管与流体环声阻抗差异大,套管成为波导,大部分声源能量无法进入地层,在套管中激发沿着套管传播的导波—套管模式波. 由图 2c 的频散曲线看出在较低频段套管波速度保持在 5450 m·s^{-1} 左右,基本不频散,大约在 10 kHz 以后迅速下降;图 2d 的随钻声波测井同样有钻铤模式波出现,在较低频段内还能区分钻铤波与套管波,此时套管波速度略大于钻铤波速度(实际测井中套管波慢度大约为 187 μs·m^{-1}). 而在随钻仪器的声源工作频段(图 2d 的矩形框内)钻铤波与套管波相互耦合,在传播速度上难以区分,钻铤波的存在干扰着套管波.

2.2　套管井随钻声波波形响应

常规电缆声波固井质量评价方法基于波列中套管波和地层波的到时和幅度特征,不同水泥胶结情况的电缆声波波形特征为:自由套管时首波波至为高振幅的套管波,地层波被套管波覆盖;水泥胶结良好时套管波受水泥和地层阻尼的影响,幅度衰减大,地层波凸显,首波波至为地层纵波;介于这两种胶结程度时,整体波列为较强的套管波和较弱的地层波. 因此借鉴电缆声波测井方法,模拟了套管井随钻声波测井响应,分析其特征并应用于指导随钻声波固井质量评价.

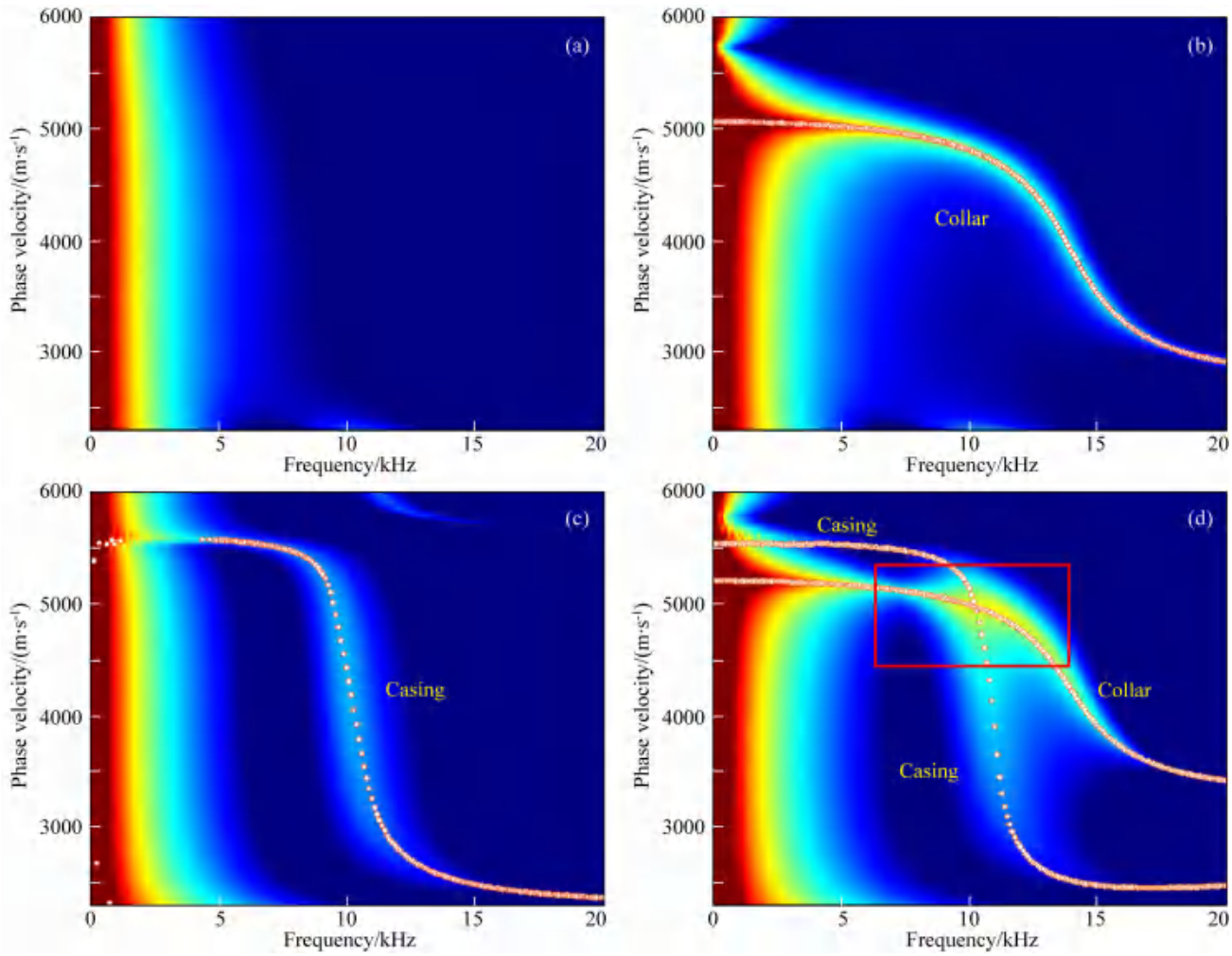


图 2 套管井中电缆和随钻单极子模式波的相速度频散二维谱

(a) 胶结良好二维谱(电缆测井);(b) 胶结良好二维谱(随钻测井);(c) 自由套管二维谱(电缆测井);(d) 自由套管二维谱(随钻测井).

Fig. 2 Two-dimensional spectrum of phase velocity dispersion of wireline and LWD in casing well

(a) Good cementation (wireline); (b) Good cementation (LWD); (c) Free pipe cementation (wireline); (d) Free pipe cementation (LWD).

图 3 给出了随钻测井条件下固井质量良好(水泥与套管和地层都充分胶结)的声波响应. 图 3a 为快速地层中单极子声源激发、井中接收的随钻阵列全波波形,声源中心频率为10 kHz,接收阵列距离声源3.0～4.4 m,接收器间距为 0.2 m(下文的声源和接收参数与此一致). 通过时间-慢度相关法(STC, Kimball and Marzetta,1984)处理波形数据,得到各模式波的时间-慢度相关图(如图 3b). 结合波形和 STC 图可以明显看到初至波振幅较大,慢度约为 210 $\mu s \cdot m^{-1}$,略大于套管波的慢度,参照计算参数可判断为钻铤波(Collar 波),地层纵波被钻铤波所淹没而无法识别. 后续依次到达地层横波(S 波)和斯通利波(ST 波). 图 3c、d 结果与随钻环境不同的是:电缆声波测井中没有钻铤波,地层纵波(P 波)显现(为使小振幅的 P 波可以被看到,整个波列经过放大处理),到时清晰,其慢度约为 250 $\mu s \cdot m^{-1}$. 上述结果表明水泥胶结良好时,随钻波列首波中套管波能量微弱,而幅度较强、速度较快的钻铤波占据主导地位,淹没了地层信号,也难以提取微弱的套管波.

图 4 给出了随钻测井条件下固井质量差(水泥与套管胶结差,水泥与地层充分胶结,即Ⅰ界面胶结差)的声波响应. 图 4a 为随钻阵列全波波形,结合图 4b 可以看出初至波为振幅强的套管波(Casing 波),慢度大约是 180 $\mu s \cdot m^{-1}$,速度接近钢套管的纵波速度,这与胶结差时电缆情况相似(图 4c);不同的是套管波后紧跟速度略小的钻铤波(Collar 波),受套管和地层的影响其慢度约为 220 $\mu s \cdot m^{-1}$,套管波和钻铤波在时域难以分离,但此时套管波振幅远大于钻铤波振幅. 后续仍是地层横波(S 波)和斯通利波(ST 波),地层纵波被套管波和钻铤波共同覆盖. 电缆环境下的 STC 图中无钻铤波(如图 4d),套管波后有相关系数小的地层纵波(P 波)出现,其慢度约为 250 $\mu s \cdot m^{-1}$. 上述结果表明水泥胶结差时,随钻波列中套管波的速度和幅度都大于钻铤波,钻铤波的干扰对提取套管波幅度影响甚微.

图 5 给出了随钻测井条件下自由套管(套管和

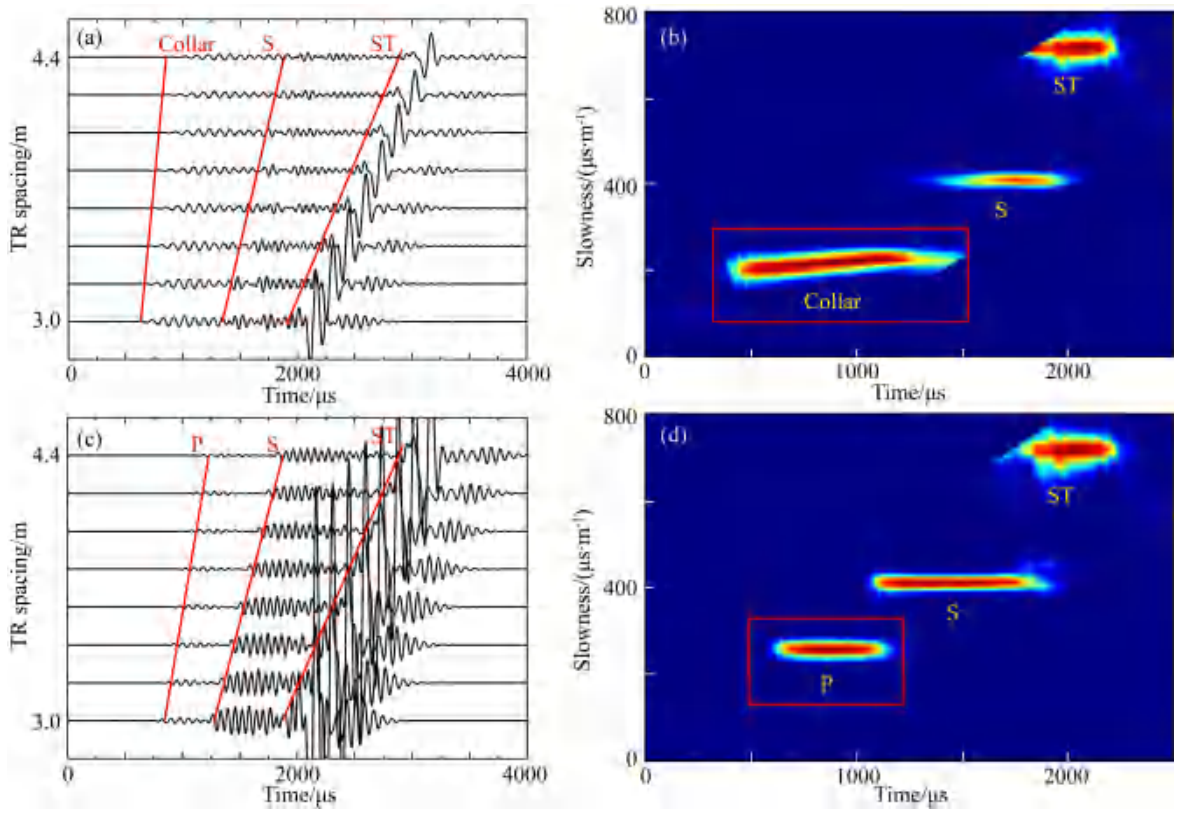


图 3　水泥胶结良好时电缆和随钻声波测井响应

(a) 全波波形图(随钻测井);(b) 时间-慢度相关图(随钻测井);(c) 全波波形图(电缆测井);(d) 时间-慢度相关图(电缆测井).

Fig. 3　Acoustic response of wireline and LWD with good cementation

(a) Simulated array waveform (LWD); (b) Time-Slowness correlogram (LWD);
(c) Simulated array waveform(wireline); (d) Time-Slowness correlogram (wireline).

地层之间为水环)的声波响应. 图 5a 为随钻阵列全波波形,结合图 5b 可以看出波列初至波仍是强套管波(Casing 波),甚至比胶结差时的套管波幅度更大(图 4a),其慢度大约是 180 $\mu s \cdot m^{-1}$,速度接近套管的纵波速度;套管波后是速度略小于套管波速度的钻铤波(Collar 波),其慢度值约为 210 $\mu s \cdot m^{-1}$,相比之下钻铤波振幅远小于套管波振幅. 地层初至纵波被套管波完全覆盖. 图 5c、d 的电缆声波测井中无钻铤波,套管波能量强,STC 图中地层纵波无相关性. 上述结果表明自由套管时随钻波列中套管波振幅更强烈,套管波成分占首波主导地位.

3　随钻环境套管波幅度和衰减规律

3.1　套管波幅度和衰减与胶结指数的关系

套管波幅度和衰减与水泥胶结程度的关系是声波固井质量评价的关键. 为了能完整刻画各胶结程度的波形特征,将流体层和水泥环整体等效为软介质,通过改变其剪切模量,实现胶结程度从 0 到 1 的波形变化表征. 图 6a、b 分别为水泥胶结程度渐变的电缆和随钻波形(波形自上而下由充分胶结到自由套管过渡),并在时窗内提取幅度和衰减. 随着胶结质量逐渐变好套管波幅度由大变小,随钻波列首波中钻铤波的影响不可忽略,特别是在胶结良好时套管波幅度与钻铤波幅度大小相近甚至更小,而两者速度相近使得钻铤波重叠在套管波中,所以此时首波等效为套管波和钻铤波的叠加. 利用图 6a、b 的模拟数据,考察首波幅度和衰减与胶结指数的关系(图 6c、d),其中衰减定义为,

$$ATT = \frac{20}{L}\log\frac{A_{\text{casing}}}{A_{\max}}, \tag{14}$$

式中 L 为源距,A_{casing} 为目的层段的套管波幅度;$A_{\max}$ 为自由套管井段的套管波幅度(套管波幅度通过窗内平均能量计算). 随钻波列首波是套管波和钻铤波的叠加效果,需考虑钻铤波的影响.

图 6c、d 分别给出电缆和随钻声波测井首波幅度和衰减与胶结指数的关系曲线. 黑色实线为电缆测井的结果:图 6c 中套管波幅度(对数刻度)与胶结指数呈线性递减趋势;图 6d 中套管波衰减与胶结指数呈线性递增趋势. 该结果说明电缆波列首波幅度和衰减只有套管波成分的贡献,可实现 0～1 的胶结程度划分. 然而随钻声波仪器的隔声设计无法完全消除钻铤波,钻铤波与套管波在时间域上重叠使得首波幅度和衰减与胶结指数无法保持线性关系,此

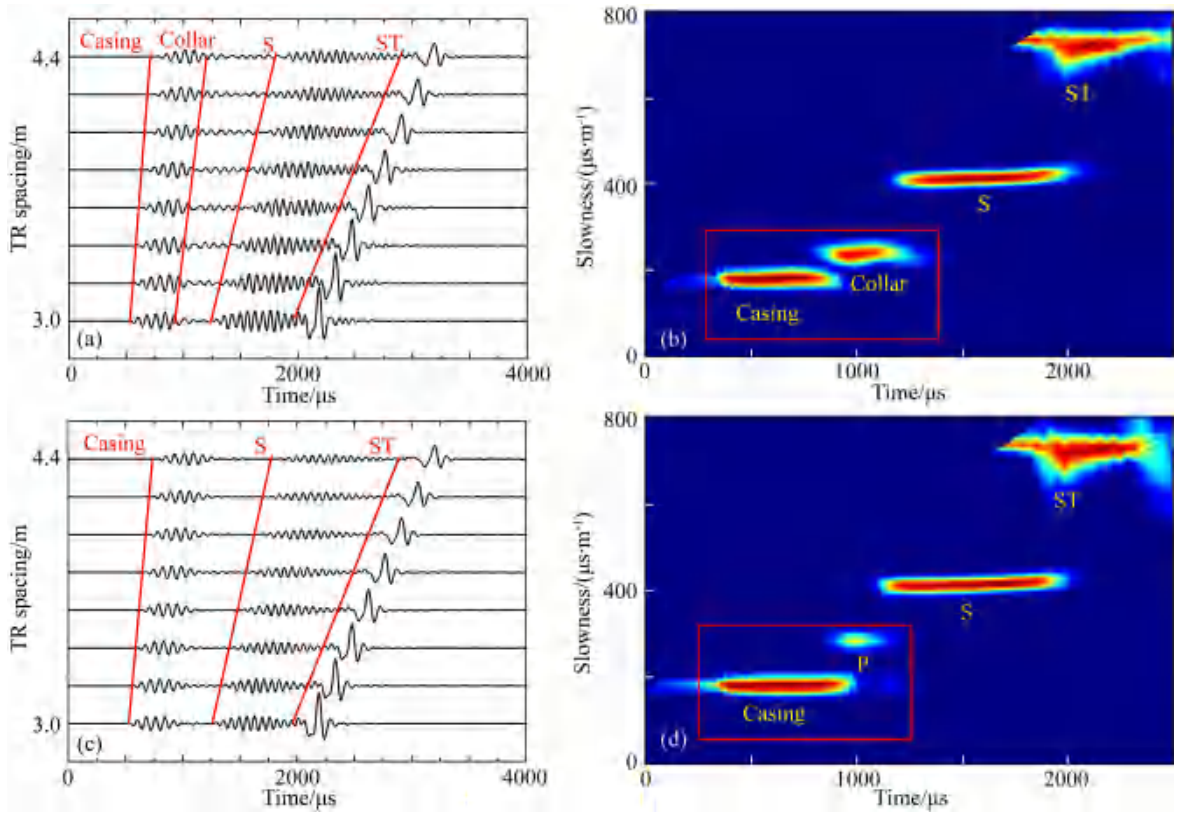


图 4 水泥胶结差时电缆和随钻声波测井响应

(a) 全波波形图(随钻测井);(b) 时间-慢度相关图(随钻测井);(c) 全波波形图(电缆测井);(d) 时间-慢度相关图(电缆测井).

Fig. 4 Acoustic response of wireline and LWD with poor cementation

(a) Simulated array waveform (LWD); (b) Time-Slowness correlogram (LWD); (c) Simulated array waveform (wireline); (d) Time-Slowness correlogram (wireline).

时首波为套管波与钻铤波的总和. 如图 6c、d 中红色实线的随钻测井结果:图 6c 中幅度曲线在较低胶结指数范围内(大约 0～0.5)仍保持线性关系,因为此时套管波幅度远大于钻铤波幅度,而在较高胶结指数范围(大约 0.5～1)线性趋势发生明显偏差,曲线趋于平缓,因为此时套管波幅度与钻铤波幅度大小相近甚至更小. 图 6d 中也有类似现象,随着胶结程度变好随钻环境下的衰减曲线出现偏差,形状变得扁平,甚至在较高胶结指数范围内随着胶结指数增加而呈下降趋势,这与电缆情况衰减随胶结指数增加而增加的趋势相反.

上述结果表明随钻声波测井环境下,由于钻铤波干扰,幅度和衰减随胶结质量出现非线性变化关系,因此利用幅度法或衰减法都不能准确评价固井质量. 但可根据两曲线的特点:0～0.5 的低指数范围内的幅度线性趋势保持良好,0.5～1 较高指数范围内的衰减出现反转趋势(随着胶结指数增大而减小),形成一种随钻声波胶结指数计算方法:将胶结指数范围大致分为两个区域,当胶结指数低于 0.5 时,采用幅度法计算的结果;当胶结指数高于 0.5 时,采用衰减法计算的结果(利用反转趋势进行评价). 该方法从理论上表明了随钻声波固井质量评价的可行性,可用于指导实际资料处理与解释. 需要指出的是,胶结指数的分界点因套管尺寸、水泥类型以及井中流体的性质而变化.

3.2 实例验证

为验证理论图版的正确性,图 7 给出套管井中随钻声波测井实际数据分析(引自 Kinoshitaet al., 2013;Pistre et al., 2014;Izuhara et al., 2015, 2017). 图 7a 第 2 道为波形变密度图,第 3、4 道分别为首波幅度和视衰减. 根据第 5、6 道电缆声波水泥胶结指数曲线(蓝色虚线,图中标识为 Wireline BI),第 7 道的固井评价结果:X165 m～X190 m 深度段为胶结好,X190 m～X212 m 深度段为胶结中,X210 m～X240 m 深度段为胶结差. 由第 5 道中基于幅度法的随钻声波水泥胶结指数曲线(红色实线,图中标识为 LWD A-BI)可以看出在胶结差的深度,随钻与电缆结果吻合良好;在胶结好的深度,随钻与电缆结果有明显差别,同时随钻胶结指数值保持在 0.5 左右,说明胶结较好时基于幅度法的随钻水泥评价失去灵敏度,无法指示固井质量. 从第 2 和 5 道随钻声波测井的水泥胶结指数曲线和幅度中取点,投影至根据上文计算的理论

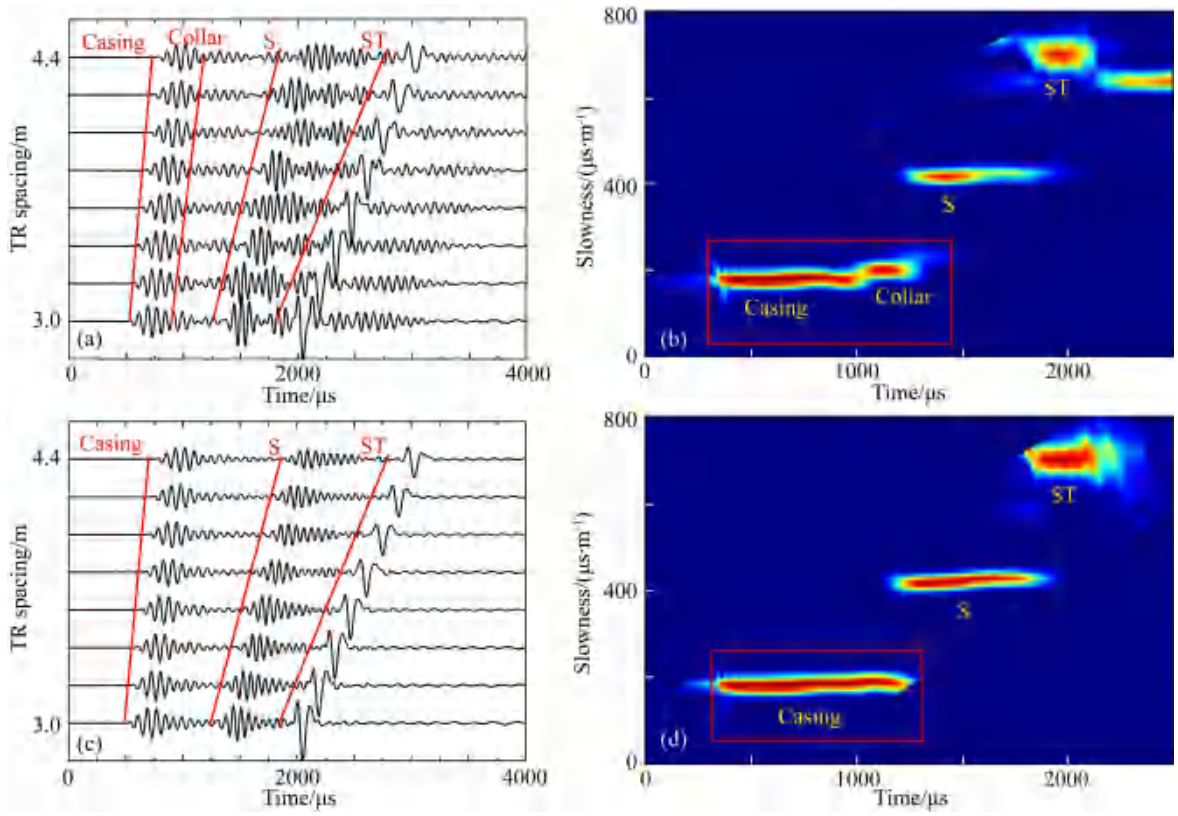


图 5　自由套管时电缆和随钻声波测井响应

(a) 全波波形图(随钻测井);(b) 时间-慢度相关图(随钻测井);(c) 全波波形图(电缆测井);(d) 时间-慢度相关图(电缆测井).

Fig. 5　Acoustic response of wireline and LWD with free pipe

(a) Simulated array waveform (LWD); (b) Time-Slowness correlogram (LWD);
(c) Simulated array waveform(wireline); (d) Time-Slowness correlogram (wireline).

图版中,归一化结果展示在图 7b(蓝色圆圈). 对比发现实际资料的套管波幅度与理论计算的曲线吻合较好:随着胶结指数增大,幅度曲线上翘并趋于平稳. 第 6 道中基于衰减法的随钻声波水泥胶结指数曲线(红色实线,图中标识为 LWD ATT-BI)是利用衰减反转规律评价得到,其结果准确指示胶结质量较好(0.4～1)的深度段(X165 m～X210 m). 说明幅度法处理的较低指数段(0～0.5)和衰减法处理的较高指数段(0.5～1)联合,可得到整个井段的随钻胶结指数曲线. 图 7b 采用式(14)得到图 7c 衰减值(蓝色圆圈),也与理论模拟的衰减规律一致. 该实例表明随钻声波测井在低胶结区域利用幅度线性趋势及高胶结区域利用衰减反转趋势可划分各种胶结程度,验证了理论计算的正确性及实际资料处理的良好应用效果.

4　结论

本文建立了套管井中随钻声波理论,数值模拟了不同水泥胶结情况的套管井随钻声波测井响应,分析了首波幅度和衰减与水泥胶结指数的关系,形成了一种随钻声波测井水泥胶结指数评价方法,实现了随钻条件下固井质量的划分,并通过测井实例验证了方法有效性. 主要得到以下结论:

(1) 水泥胶结程度较差或自由套管时,随钻环境与电缆环境的声波波形都有强振幅的套管初至波,地层纵波能量微弱或被覆盖. 不同的是由于钻铤的存在,随钻环境会产生速度较快、能量较大且沿仪器传播的钻铤波,使得首波波形发生变化. 但此时套管波的速度和幅度都大于钻铤波,套管波占首波主导地位.

(2) 水泥胶结较好时,与电缆情况最大的不同是:随钻波列中幅度较强、速度较快的钻铤波成为首波的主要成分,套管波能量微弱. 钻铤波的干扰使得在高胶结指数时固井质量检测灵敏度下降.

(3) 单独采用幅度法或衰减法难以进行随钻声波固井质量评价,应同时利用幅度在较低指数范围内的线性趋势及衰减在较高指数范围内的反转趋势划分随钻胶结指数,形成一种计算随钻声波测井水泥胶结指数新方法. 数值模拟结果和现场实例表明,随钻声波能扩展传统的电缆声波固井质量评价技术.

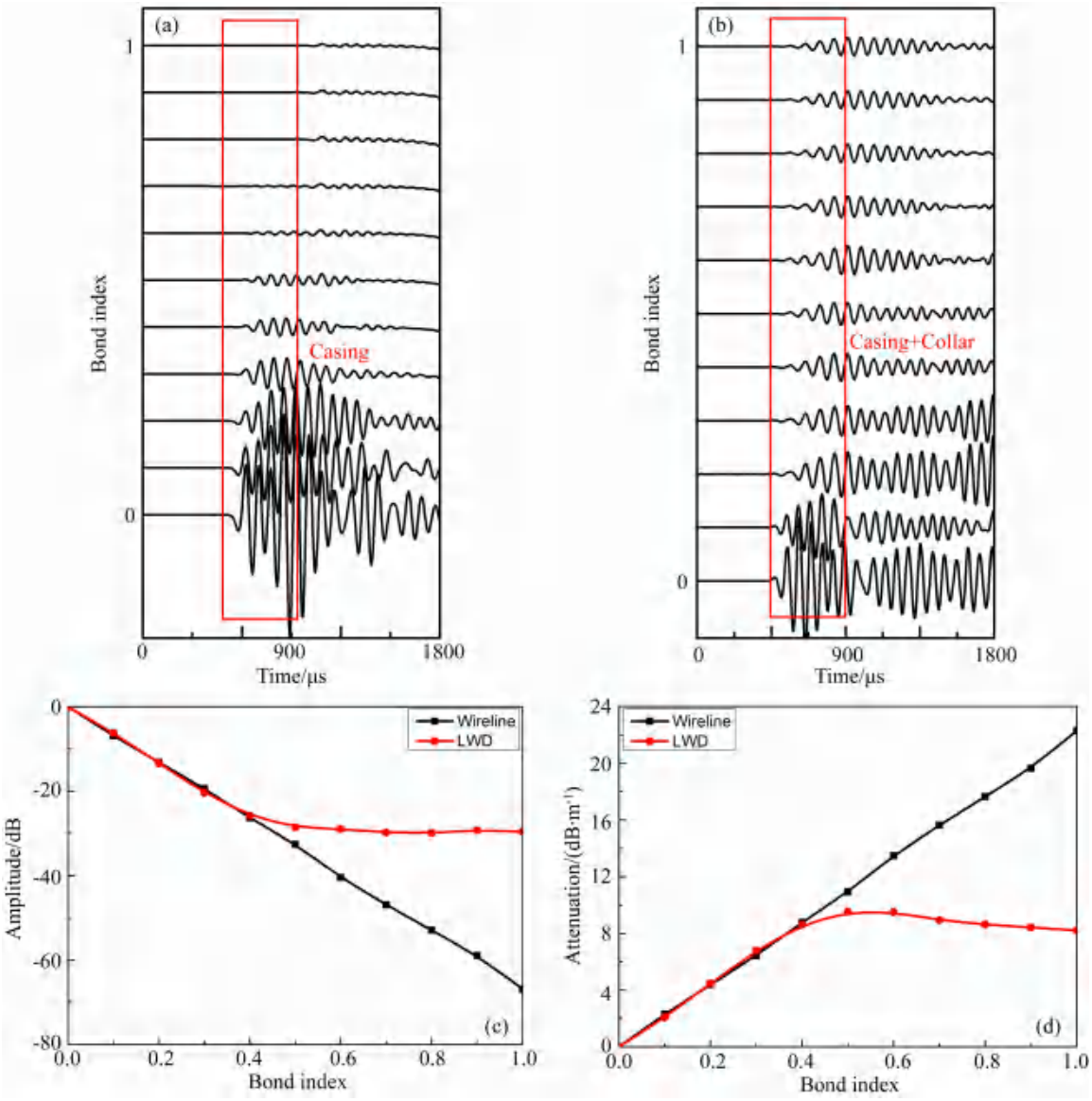


图 6 套管井中电缆和随钻声波测井首波幅度和衰减与胶结指数关系

(a) 胶结程度递增的波形(电缆);(b) 胶结程度递增的波形(随钻);(c) 幅度与胶结指数关系;(d) 衰减与胶结指数关系.

Fig. 6 Relation between the head wave amplitude and attenuation with cementation index of wireline and LWD

(a) Waveform of different cement bond index(wireline); (b) Waveform of different cement bond index(LWD); (c) Relationship of wave amplitude and bond index; (d) Relationship of wave attenuation and bond index.

附录

随钻环境套管井 $\boldsymbol{H}$ 矩阵可用电缆环境裸眼井 $\boldsymbol{M}$ 矩阵、电缆环境套管井 $\boldsymbol{T}$ 矩阵和汤姆森-哈斯克传递矩阵 $\boldsymbol{G}$ 表示($\boldsymbol{M}$ 矩阵、$\boldsymbol{T}$ 矩阵和 $\boldsymbol{G}$ 矩阵元素的计算方法详见 Tang and Cheng,2004 的专著).

$\boldsymbol{M}$ 矩阵部分元素为

$$M_{11} = -n/rI_n(fr) - fI_{n+1}(fr),$$

$$M_{21} = \rho_f\omega^2 I_n(fr),\ M_{31} = 0,\ M_{41} = 0,$$

$\boldsymbol{T}$ 矩阵元素为

$$T_{11} = n/rI_n(pr) + pI_{n+1}(pr),$$

$$T_{12} = n/rK_n(pr) - pK_{n+1}(pr),\ T_{13} = n/rI_n(sr),$$

$$T_{14} = n/rK_n(sr),\ T_{15} = \mathrm{i}k(n/rI_n(sr) + sI_{n+1}(sr)),$$

$$T_{16} = \mathrm{i}k(n/rK_n(sr) - sK_{n+1}(sr)),$$

$$T_{21} = -n/rI_n(pr),\ T_{22} = -n/rK_n(pr),$$

$$T_{23} = -n/rI_n(sr) - sI_{n+1}(sr),$$

$$T_{24} = -n/rK_n(sr) + sK_{n+1}(sr),$$

$$T_{25} = -\mathrm{i}kn/rI_n(sr),\ T_{26} = -\mathrm{i}kn/rK_n(sr),$$

$$T_{31} = \mathrm{i}kI_n(pr),\ T_{32} = \mathrm{i}kK_n(pr),\ T_{33} = 0,$$

$$T_{34} = 0,\ T_{35} = -s^2 I_n(sr),\ T_{36} = -s^2 K_n(sr),$$

$$T_{41} = \rho\beta^2((2n(n-1)/r^2 + 2k^2 - k_s^2)I_n(pr) - 2p/rI_{n+1}(pr)),$$

$$T_{42} = \rho\beta^2((2n(n-1)/r^2 + 2k^2 - k_s^2)K_n(pr) + 2p/rK_{n+1}(pr)),$$

$$T_{43} = 2\rho\beta^2(n(n-1)/r^2 I_n(sr) + ns/rI_{n+1}(sr)),$$

$$T_{44} = 2\rho\beta^2(n(n-1)/r^2 K_n(sr) - ns/rK_{n+1}(sr)),$$

$$T_{45} = 2\rho\beta^2\mathrm{i}k((n(n-1)/r^2 + s^2)I_n(sr) - s/rI_{n+1}(sr)),$$

$$T_{46} = 2\rho\beta^2\mathrm{i}k((n(n-1)/r^2 + s^2)K_n(sr) + s/rK_{n+1}(sr)),$$

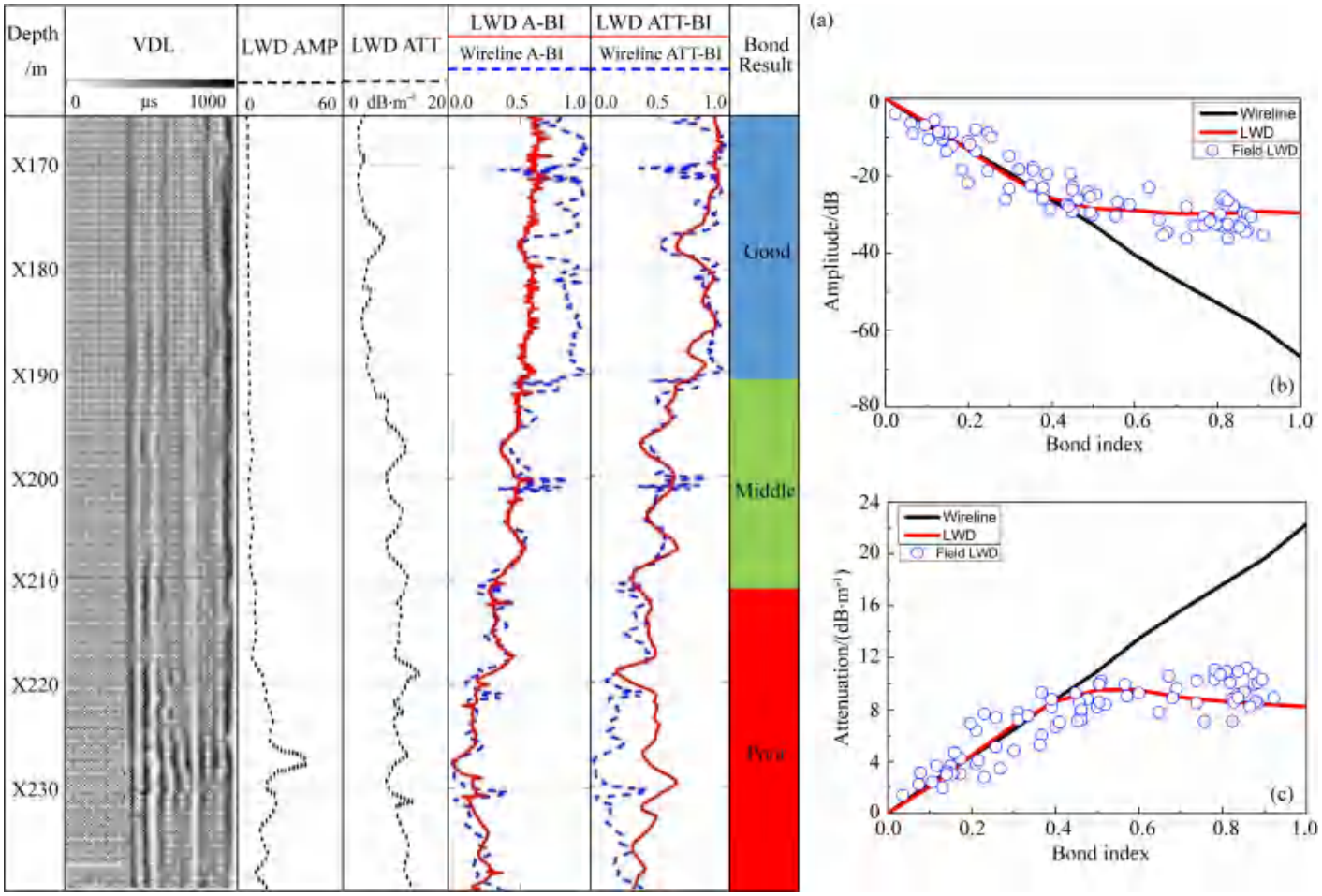


图 7　随钻声波测井实际数据与模拟数据的对比

Fig. 7　Comparison of real and numerical data of acoustic LWD

$T_{51}=2\rho\beta^2(n(1-n)/r^2I_n(pr)-np/rI_{n+1}(pr))$,

$T_{52}=2\rho\beta^2(n(1-n)/r^2K_n(pr)+np/rK_{n+1}(pr))$,

$T_{53}=2\rho\beta^2(n(1-n)/r^2-s^2)I_n(sr)+s/rI_{n+1}(sr))$,

$T_{54}=2\rho\beta^2(n(1-n)/r^2-s^2)K_n(sr)-s/rK_{n+1}(sr))$,

$T_{55}=2\rho\beta^2\mathrm{i}k(n(1-n)/r^2I_n(sr)-ns/rI_{n+1}(sr))$,

$T_{56}=2\rho\beta^2\mathrm{i}k(n(1-n)/r^2K_n(sr)+ns/rK_{n+1}(sr))$,

$T_{61}=2\rho\beta^2\mathrm{i}k(n/rI_n(pr)+pI_{n+1}(pr))$,

$T_{62}=2\rho\beta^2\mathrm{i}k(n/rK_n(pr)-pK_{n+1}(pr))$,

$T_{63}=\rho\beta^2\mathrm{i}kn/rI_n(sr)$, $T_{64}=\rho\beta^2\mathrm{i}kn/rK_n(pr)$,

$T_{65}=\rho\beta^2(2k^2-k_s^2)(-sI_{n+1}(sr)-n/rI_n(sr))$,

$T_{66}=\rho\beta^2(2k^2-k_s^2)(sK_{n+1}(sr)-n/rK_n(sr))$,

其中，k 是轴向波数；ω 是圆频率；n 是声源极性；i 是虚数单位；I_n 是第一类 n 阶贝塞尔函数；K_n 是第二类 n 阶贝塞尔函数；r 是介质层界面到井轴半径；ρ_f 是流体密度；ρ 是介质层密度；$f=(k^2-\omega^2/v_f^2)^{1/2}$ 是流体径向波数，v_f 是流体纵波速度；$p=(k^2-\omega^2/\alpha^2)^{1/2}$ 是介质层纵波径向波数，α 是介质层纵波速度；$s=(k^2-\omega^2/\beta^2)^{1/2}$ 介质层横波径向波数，β 是介质层横波速度，$k_s=\omega/\beta$ 是介质层横波波数.

(1) 随钻环境套管井胶结良好时，$\boldsymbol{H}$ 矩阵(12×12 阶)元素为

$H_{11}=M_{11}^{1i}$, $H(1,2:7)=T^{1i}(1,1:6)$, $H_{21}=M_{21}^{1i}$, $H(2,2:7)=T^{1i}(4,1:6)$, $H_{31}=M_{31}^{1i}$, $H(3,2:7)=T^{1i}(5,1:6)$, $H_{41}=M_{41}^{1i}$, $H(4,2:7)=T^{1i}(6,1:6)$, $H(5,2:7)=T^{1t}(1,1:6)$, $H_{58}=-n/r_{1t}I_n(fr_{1t})-fI_{n+1}(fr_{1t})$, $H_{59}=-n/r_{1t}K_n(fr_{1t})+fK_{n+1}(fr_{1t})$, $H(6,2:7)=T^{1t}(4,1:6)$, $H_{68}=\rho_f\omega^2I_n(fr_{1t})$, $H_{69}=\rho_f\omega^2K_n(fr_{1t})$, $H(7,2:7)=T^{1t}(5,1:6)$, $H(8,2:7)=T^{1t}(6,1:6)$, $H_{98}=-n/r_{2i}I_n(fr_{2i})-fI_{n+1}(fr_{2i})$, $H_{99}=-n/r_{2i}K_n(fr_{2i})+fK_{n+1}(fr_{2i})$, $H(9,10:12)=G(1,2:2:6)$, $H_{10,8}=\rho_f\omega^2I_n(fr_{2i})$, $H_{10,9}=\rho_f\omega^2K_n(fr_{2i})$, $H(10,10:12)=G(4,2:2:6)$, $H(11,10:12)=G(5,2:2:6)$, $H(12,10:12)=G(6,2:2:6)$.

此时 $\boldsymbol{G}$ 矩阵为套管、水泥环和地层之间的传递矩阵.

(2) 随钻环境套管井胶结差时，$\boldsymbol{H}$ 矩阵(20×20 阶)元素与胶结良好时 $\boldsymbol{H}$ 矩阵相同元素为 $H(1,1:7)$, $H(2,1:7)$, $H(3,1:7)$, $H(4,1:7)$, $H(5,2:9)$, $H(6,2:9)$, $H(7,2:7)$, $H(8,2:7)$, $H(9,8:9)$, $H(10,8:9)$.

剩余元素为

$$H(9,10:15)=T^{2i}(1,1:6),$$
$$H(10,10:15)=T^{2i}(4,1:6),$$
$$H(11,10:15)=T^{2i}(5,1:6),$$
$$H(12,10:15)=T^{2i}(6,1:6),$$
$$H(13,10:15)=T^{2t}(1,1:6),$$
$$H_{13,16}=-n/r_{2t}I_n(fr_{2t})-fI_{n+1}(fr_{2t}),$$
$$H_{13,17}=-n/r_{2t}K_n(fr_{2t})+fK_{n+1}(fr_{2t}),$$
$$H(14,10:15)=T^{2t}(4,1:6),$$
$$H_{14,16}=\rho_f\omega^2 I_n(fr_{2t}),$$
$$H_{14,17}=\rho_f\omega^2 K_n(fr_{2t}),$$
$$H(15,10:15)=T^{2t}(5,1:6),$$
$$H(16,10:15)=T^{2t}(6,1:6),$$
$$H_{17,16}=-n/r_{3i}I_n(fr_{3i})-fI_{n+1}(fr_{3i}),$$
$$H_{17,17}=-n/r_{3i}K_n(fr_{3i})+fK_{n+1}(fr_{3i}),$$
$$H(17,18:20)=G(1,2:2:6),$$
$$H_{18,16}=\rho_f\omega^2 I_n(fr_{3i}),$$
$$H_{18,17}=\rho_f\omega^2 K_n(fr_{3i}),$$
$$H(18,18:20)=G(4,2:2:6),$$
$$H(19,18:20)=G(5,2:2:6),$$
$$H(20,18:20)=G(6,2:2:6).$$

此时 $\boldsymbol{G}$ 矩阵为套管、水泥环和地层之间的传递矩阵.

(3) 随钻环境自由套管时，$\boldsymbol{H}$ 矩阵(20×20 阶)元素与胶结差时 $\boldsymbol{H}$ 矩阵相同元素为

$H(1,1:7),H(2,1:7),H(3,1:7),H(4,1:7),H(5,2:9),H(6,2:9),H(7,2:7),H(8,2:7),H(9,8:15),H(10,8:15),H(11,10:15),H(12,10:15),H(13,10:17),H(14,10:17),H(15,10:15),H(16,10:15).$

剩余元素为

$$H_{17,16}=-n/r_{4i}I_n(fr_{4i})-fI_{n+1}(fr_{4i}),$$
$$H_{17,17}=-n/r_{4i}K_n(fr_{4i})+fK_{n+1}(fr_{4i}),$$
$$H(17,18:20)=T^{4i}(1,2:2:6),$$
$$H_{18,16}=\rho_f\omega^2 I_n(fr_{4i}),$$
$$H_{18,17}=\rho_f\omega^2 K_n(fr_{4i}),$$
$$H(18,18:20)=T^{4i}(4,2:2:6),$$
$$H(19,18:20)=T^{4i}(5,2:2:6),$$
$$H(20,18:20)=T^{4i}(6,2:2:6).$$

(1)、(2)和(3)的 $\boldsymbol{H}$ 矩阵中未列出的元素取值为 0. M、T 右上角的数字或 r 右下角的数字表示介质层序号(钻铤、套管、水泥环和地层序号分别是 1、2、3、4)，字母 i 表示在层的内半径处取值，t 表示在层的外半径处取值.

References

Blyth M, Hupp D, Whyte I, et al. 2013. LWD sonic cement logging: benefits, applicability, and novel uses for assessing well integrity. //83rd Ann. Internat Mtg., Soc. Expi. Geophys.. Expanded Abstracts.

Chen X L, Tang X M. 2019. Study on three mode-wave sensitivities to material acoustic property behind casing in a cased well. *Chinese Journal of Geophysics* (in Chinese), 62(4): 1565-1572, doi: 10.6038/cjg2019L0765.

Cui Z W. 2004. Theoretical and numerical study of modified Biot's models, acoustoelectric well logging and acoustic logging while drilling excited by multipole acoustic sources [Ph. D. thesis] (in Chinese). Changchun: Jilin University.

He X, Chen H, Wang X M. 2014. Ultrasonic leaky flexural waves in multilayered media: Cement bond detection for cased wellbores. *Geophysics*, 79(2): A7-A11.

Izuhara W, Hori H, Pistre V, et al. 2015. Method and system of quantitative cement evaluation using logging while drilling. US Patent, 20150168581.

Izuhara W, Yamamoto H, Blyth M, et al. 2017. Full-range quantitative cement bond evaluation with LWD sonic: the right way of approach using a hybrid of amplitude and attenuation. //87th Ann. Internat Mtg., Soc. Expi. Geophys.. Expanded Abstracts.

Kimball C, Marzetta T. 1984. Semblance processing of borehole acoustic array data. *Geophysics*, 49(3): 274-281.

Kinoshita T, Izuhara W, Valero H P, et al. 2013. Feasibility and challenge of quantitative cement evaluation with LWD sonic. //83rd Ann. Internat Mtg., Soc. Expi. Geophys.. Expanded Abstracts.

Market J, Schmitt D P, Deady R. 2004. LWD sonic logging in cased holes. //74th Ann. Internat Mtg., Soc. Expi. Geophys.. Expanded Abstracts.

Pistre V, Kinoshita T, Blyth M, et al. 2014. Attenuation-based quantitative cement bond index with lwd sonic: a novel approach applicable to all casing and cement cases. //84th Ann. Internat Mtg., Soc. Expi. Geophys.. Expanded Abstracts.

Song R L, Liu J X, Hou C H, et al. 2012. Numerical simulation of Sector Bond log and improved cement bond image. *Geophysics*, 77(4): D95-D104.

Su Y D, Zhuang C X, Tang X M. 2011. LWD acoustic color mode wave attenuation character research and isolator design. *Chinese Journal of Geophysics* (in Chinese), 54(9): 2419-2428, doi: 10.3969/j.issn.0001-5733.2011.09.026.

Tang X M, Cheng C H. 2004. Quantitative Borehole Acoustic Methods. San Diego: Elsevier Science Publishing Co. Inc.

Tang X M, Wang T, Patterson D. 2002. Multipole acoustic logging-while-drilling. //72nd Ann. Internat Mtg., Soc. Expi. Geophys.. Expanded Abstracts, 364-368.

Tubman K M, Cheng C H, Toksöz M N. 1984. Synthetic full waveform acoustic logs in cased boreholes. *Geophysics*, 49(7): 1051-1059.

Wang H, Tao G, Wang B, et al. 2009. Wave field simulation and data acquisition scheme analysis for LWD acoustic tool. *Chinese Journal of Geophysics* (in Chinese), 52(9): 2402-2409, doi:

10.3969/j.issn.0001-5733.2009.09.027.

Wang J, Li H Y, Guan W, et al. 2019. Experimental studies on the mechanism of monopole acoustic collar wave. *Chinese Journal of Geophysics* (in Chinese), 62(4): 1541-1553, doi: 10.6038/cjg2019M0042.

Xu F G, Bai Y H. 2016. Application of acoustic LWD to evaluation of well cementing quality of extended reach well-taking Pinghu oil and gas field in East China Sea as an example. *Offshore Oil* (in Chinese), 36(4): 76-80.

Zhang H B, Qin Z G, Sang Z P, et al. 2009. Amplitude features of formation wave in acoustic full waveform of casing wells. *Progress in Geophysics* (in Chinese), 24(3): 1006-1012.

Zhou Y Q, Wang X M, Chen D H. 2007. Study of numerical simulation on amplitude attenuation of first arrivals in cased-hole acoustic logging. *Well Logging Technology* (in Chinese), 31(4): 321-326.

附中文参考文献

陈雪莲,唐晓明. 2019. 套后介质声学性质对套管中三种模式波影响的对比分析. 地球物理学报, 62(4): 1565-1572, doi: 10.6038/cjg2019L0765.

崔志文. 2004. 多孔介质声学模型与多极源声电效应测井和多极随钻声测井的理论与数值研究[博士论文]. 长春: 吉林大学.

苏远大, 庄春喜, 唐晓明. 2011. 随钻声波测井钻铤模式波衰减规律研究与隔声体设计. 地球物理学报, 54(9): 2419-2428, doi: 10.3969/j.issn.0001-5733.2011.09.026.

王华, 陶果, 王兵等. 2009. 多极子随钻声波测井波场模拟与采集模式分析. 地球物理学报, 52(9): 2402-2409, doi: 10.3969/j.issn.0001-5733.2009.09.027.

王军, 李红一, 关威等. 2019. 单极源钻铤波传播机制的实验研究. 地球物理学报, 62(4): 1541-1553, doi: 10.6038/cjg2019M0042.

许风光, 白玉洪. 2016. 随钻声波测井在大位移井固井评价中的应用——以东海平湖油气田为例. 海洋石油, 36(4): 76-80.

张宏兵, 秦正贵, 尚作萍等. 2009. 套管井声波全波列中地层波的幅度特性. 地球物理学进展, 24(3): 1006-1012.

周吟秋, 王秀明, 陈德华. 2007. 套管井声波测井中首波幅度衰减研究. 测井技术, 31(4): 321-326.

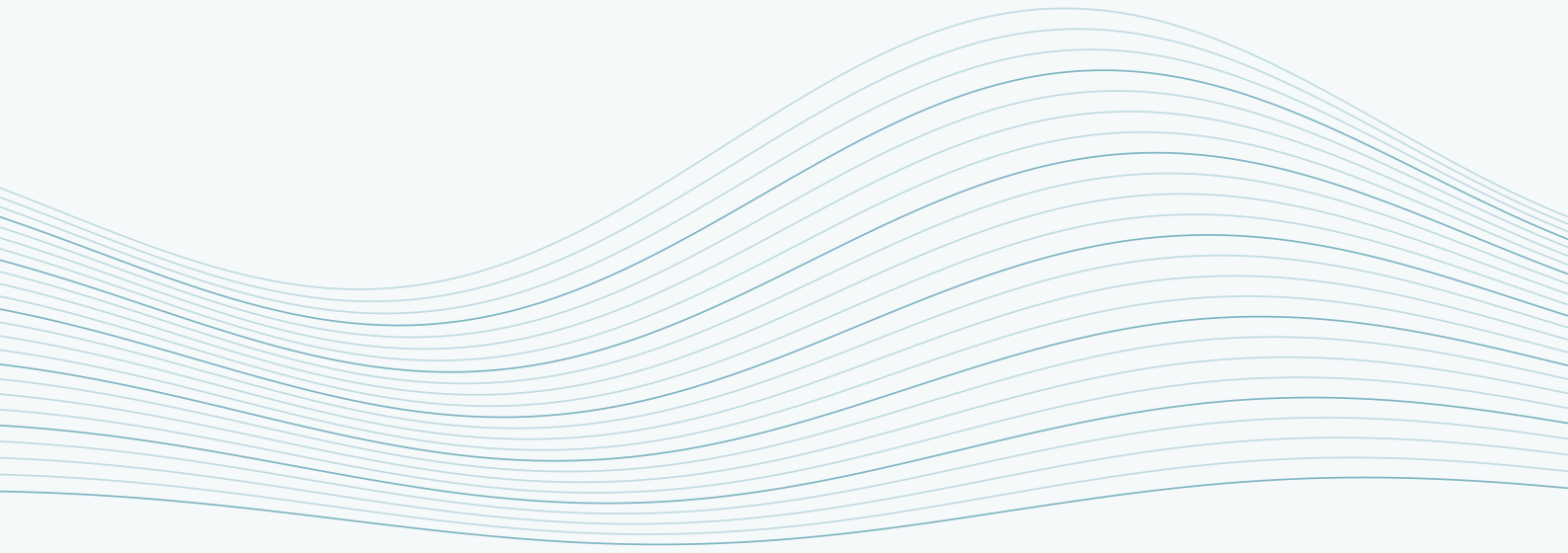
(本文编辑　张正峰)

04

专 题 / 04

声波测井处理方法及现场应用

PROCESSING METHODS AND FIELD APPLICATIONS OF ACOUSTIC LOGGING



收录 10 篇论文

GEOPHYSICS, VOL. 83, NO. 1 (JANUARY-FEBRUARY 2018); P. D1–D8, 6 FIGS., 1 TABLE.
10.1190/GEO2017-0054.1

Elastic-wave evaluation of downhole hydraulic fracturing: Modeling and field applications

Yuan-Da Su[1], Zhen Li[1], Song Xu[1], Chun-Xi Zhuang[1], and Xiao-Ming Tang[1]

ABSTRACT

We numerically simulate elastic-wave propagation along a fluid-filled borehole with a hydraulically fractured formation. The numerical model is based on the results of hydraulic fracturing on laboratory specimens. Two typical models are simulated: a main fracture crossing the borehole and a fracture network extending from the borehole. In addition, both models contain small, secondary fractures surrounding the borehole. Our result indicates that wave propagation in the main-fracture model is characterized by significant S-wave anisotropy for polarization along and normal to the fracture orientation, with the magnitude of anisotropy depending on the fracture aperture and filling material. In contrast, no significant anisotropy is observed for the fracture network model. In both models, wave propagation is significantly affected by small-fracture-induced near-borehole velocity variation. Our modeling results provide a theoretical foundation for evaluating hydraulic fracturing using the borehole acoustic logging. The hydraulic fracture-induced S-wave anisotropy can be evaluated with the cross-dipole S-wave logging, and the fracturing-induced velocity change can be detected by acoustic traveltime tomography. We used field data examples to demonstrate the effectiveness and practicality of using the borehole acoustic techniques for hydraulic fracturing evaluation.

INTRODUCTION

Hydraulic fracturing is the key technology to increase hydrocarbon production in tight reservoirs with low porosity and low permeability (e.g., the unconventional shale-gas reservoirs). For downhole geomechanics applications, this technique is also used in downhole test to determine the magnitude and orientation of the tectonic stress field (Hayashi and Haimson, 1991). It is also used for geothermal production and CO_2 sequestration related application (Legarth et al., 2005; Chiaramonte et al., 2007). Because of the cost associated with the operation, it is very important to evaluate the result of hydraulic fracturing (an example is the wide use of postfracturing microseismic monitoring of the fracturing-induced seismicity; Maxwell et al., 2010; Tary et al., 2014). If the fracturing induces a single major fracture extending along and away from the borehole, an apparent anisotropy is produced along and normal to the fracture orientation, and a downhole acoustic technique, the cross-dipole anisotropy measurement, can be used to detect the fracture-induced anisotropy and evaluate fracture migration along the borehole (Tang et al., 2001; Boness and Zoback, 2006; Schmitt et al., 2012). The cross-dipole tool acquires a four-component wave data set (xx, xy, yx, yy), in which, for Cartesian coordinates x and y, the first (second) letter refers to the dipole source (receiver) orientation. For example, xy is the wave data acquired by the receiver oriented along the y-axis when the source oriented along the x-axis is activated. By finding the two principal components, i.e., the fast and slow S-waves from the 4C data, the anisotropy magnitude and orientation can be determined (Alford, 1986; Tang and Chunduru, 1999). In fracturing an unconventional reservoir, however, a fracture network, rather than a single major fracture, is often desired (Fisher et al., 2002).

A fracture network consists of many, or a swarm of, small fractures with no specific orientation or preferred alignment. The system will not produce an apparent anisotropy around the borehole. Therefore, in case of a fracture network, the anisotropy effect is insignificant and the cross-dipole technique becomes ineffective; other measurement techniques need to be developed to evaluate the result of fracturing. In this regard, a realistic simulation of downhole wave propagation with a hydraulically fractured formation can help us find acoustic signatures that can be used for the evaluation. The main part of this study is the modeling of wave propagation

Manuscript received by the Editor 24 January 2017; revised manuscript received 20 July 2017; published ahead of production 11 September 2017; published online 13 November 2017.
[1]China University of Petroleum, School of Geosciences, Qingdao, China. E-mail: syuanda@sina.com; lizhen9099@hotmail.com; xusongupc@sina.com; zhuangchunxi@sina.com; tangxiam@aliyun.com.
© 2018 Society of Exploration Geophysicists. All rights reserved.

Downloaded from pubs.geoscienceworld.org/seg/geophysics/article-pdf/83/1/D1/4065724/geo-2017-0054.1.pdf by Univ of Petroleum (Beijing) - Library user on 08 October 2026

characteristics in conjunction with downhole hydraulic fracturing. The modeling results are then used to provide a method for evaluating hydraulic fractures.

Because of the importance of hydraulic fracture evaluation, many researchers have numerically modeled the effects of a fracture on the borehole acoustic-wave propagation. For example, Tang and Cheng (1988) and Tang et al. (1991) model the effects of a vertical fracture crossing the vertical borehole on the Stoneley wave attenuation. For the same type of configuration, Xu and Parra (2003) model the fracture-induced S-wave azimuthal anisotropy around the borehole; Ge and Chen (2007) and Zheng et al. (2009) model the effects of the fracture on various borehole guided wave modes. All previous modeling studies assume a planar fracture of finite or infinite extent, crossing the borehole diametrically. The results are valid only for the simple fracture model, and they may fail to capture some useful acoustic-wave signatures present in the field data.

An important distinction of our work from previous modeling efforts is the fracture model used for the modeling. We construct our fracture model based on the results of hydraulic fracturing simulation on laboratory specimens (Holder et al., 1993; Zhou et al., 2010; Guo et al., 2015; Lee et al., 2015). Therefore, our modeling results not only predict the anisotropy induced by a single major fracture but also reveal significant acoustic traveltime changes caused by small fractures around the borehole. This new result provides a new approach for hydraulic fracture evaluation using the acoustic traveltime tomography technique.

With the abundance of field acoustic logging data before and after hydraulic fracturing, our results are readily applied to field data for evaluating hydraulic fractures. By combining the anisotropy and tomography techniques for the evaluation, we can not only assess the effectiveness of fracturing but also determine whether a single major fracture or a fracture network is induced. Field data examples will be used to demonstrate the effectiveness and practicality of the evaluation techniques.

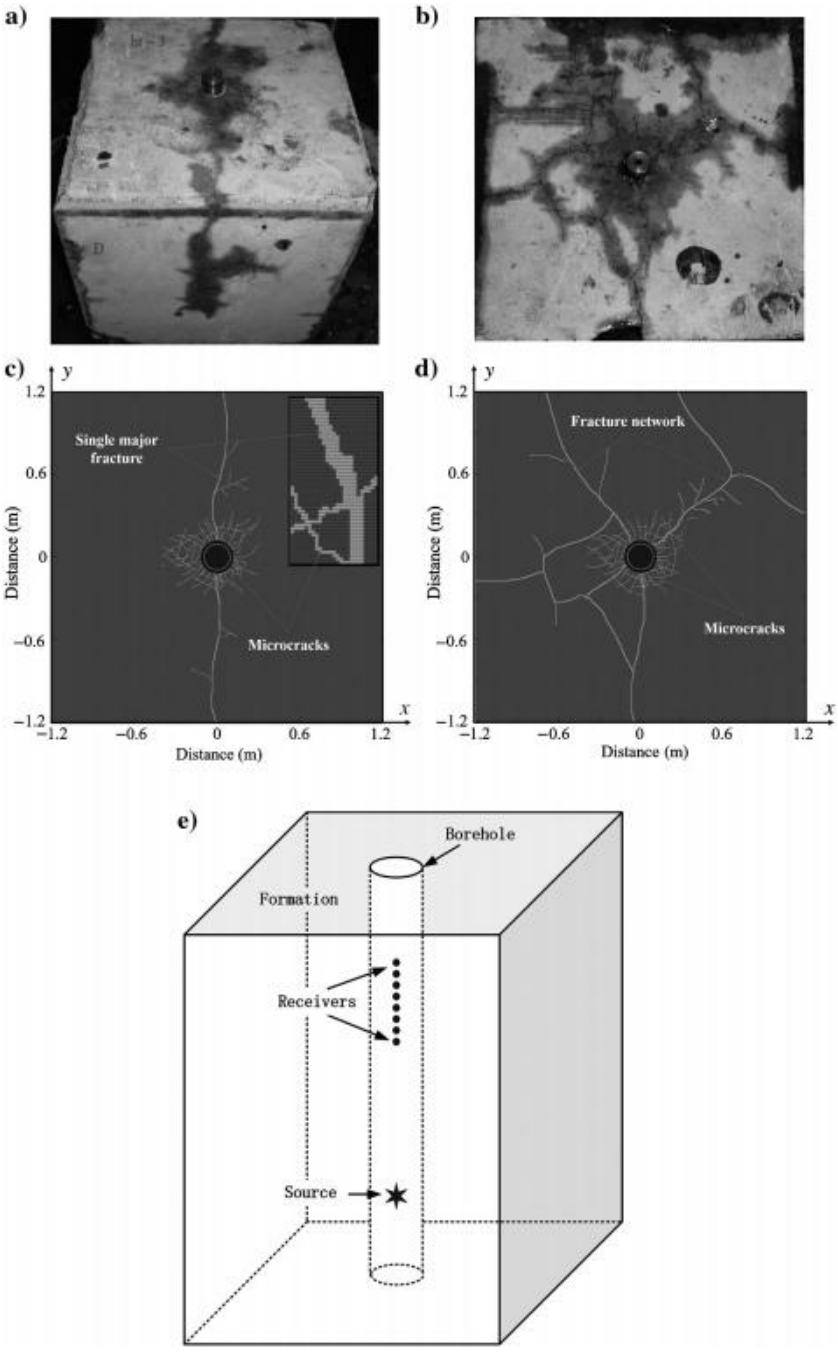


Figure 1. Laboratory hydraulic fracturing results on two specimens: (a) single major fracture, (b) fracture network, and (c and d) numerical simulation models, respectively, constructed from the experiment result in panels (a and b). The source-receiver configuration is shown in panel (e), in which the source-to-receiver distance and the receiver spacing are 2.5 and 0.1 m, respectively, and the borehole diameter is 0.24 m.

HYDRAULIC FRACTURE MODEL AND MODELING RESULTS

To realistically model hydraulic fractures, we construct our model based on laboratory hydraulic fracturing experiments. Zhou et al. (2010) and Guo et al. (2015) have conducted a series of such experiments on laboratory specimens. These researchers used concrete to construct laboratory specimens and, after thermal treatment, created microcracks in them. The specimens were drilled and cased on top. The lower openhole section was used for hydraulic fracturing. The specimens were then loaded internally inside the borehole and externally on the outer sides for the hydraulic fracturing experiment. The external stresses on the outer sides were varied to create different fracturing results. Their results show that, by controlling the stress/pressure loading condition of the experiment, two typical fracture patterns can be stimulated: One is a single major fracture extending from the borehole (Figure 1a), and the other is a fracture network surrounding and extending away from the borehole (Figure 1b). The migration of the fracture/fracture network is visualized by the

Downloaded from pubs.geoscienceworld.org/seg/geophysics/article-pdf/83/1/D1/4065724/geo-2017-0054.1.pdf by Univ of Petroleum (Beijing) - Library user on 08 October 2026

seepage of hydraulic fluid (oil) on the surface of the specimens (Figure 1). An interesting and very important phenomenon for both models is the existence of a zone of small fractures surrounding the borehole. The proximity of the small fractures to the borehole suggests that, regardless of the fracture pattern, single major fracture, or fracture network, a near-borehole fracture zone is formed prior to the extension of the fracture/fracture network into the formation. Therefore, the near-borehole fracture zone should be included for a realistic modeling of the effects of hydraulic fracturing on borehole acoustic-wave propagation.

Based on laboratory fracturing results, we construct our fracture model by mimicking the trace of fractures shown in Figure 1. For modeling field conditions, we first construct a 0.24 m diameter cased borehole with an elastic formation (see parameters in Table 1). The fracture traces in Figure 1 are rescaled and mapped onto a cross section of the borehole-formation model. Assuming that the fracture dimension in the borehole direction is large compared with the wave propagation distance along the borehole (the distance is 4 m in our modeling), the model is invariant in the borehole axial direction. We use a 3D finite-difference elastic-wave modeling technique (Chouet, 1986; Cheng et al., 1995; Wei and Tang, 2012) to simulate acoustic-wave propagation along the borehole, for which the grid size is 1 mm and the model dimension is 4 m along, and 2.4 m perpendicular to, the borehole (see Figure 1e). With the small grid size for the large model, the fracture model can be incorporated. The aperture of the small fractures around the borehole is 2 mm, and the aperture of the fracture/fractures extending away from the borehole is 5 mm. The millimeter-size fracture apertures are used to simulate the filling of proppant in the fracturing process (the commonly used proppant material contains sand or ceramic grains ranging from 0.1 to 2 mm). The fractures from laboratory testing (Figure 1) do not have proppant; only their shape and distribution are used in our model building. The configuration for the single major fracture model and the fracture network model, respectively, is given in Figure 1c and 1d.

For simulating wave propagation along the borehole, a multipole (monopole and dipole) acoustic source is placed at the center of the borehole (see the configuration in Figure 1e). The monopole source generates axisymmetric wave motion in the borehole. In contrast, the dipole-induced wave motion is directional. An array of receivers 2.5 m away from the source is placed along the axis of the borehole to record the acoustic waves. The monopole receiver measures fluid pressure, and the dipole receiver measures fluid particle displacement along the receiver orientation. For the dipole measurement, the source and receiver orientations are aligned. We first present the modeling results for the single major fracture model of Figure 1c. As shown in previous studies (Xu and Parra, 2003; Tang and Cheng, 2004; Zheng et al., 2009), a prominent effect of the single fracture model is the S-wave anisotropy along and perpendicular to the fracture's azimuthal orientation, which can be determined using the borehole cross-dipole acoustic measurement. For modeling the single fracture model in Figure 2a, we align the borehole dipole source and receiver array orientation, respectively, along and perpendicular to the fracture orientation. We use a 3 kHz Ricker wavelet source to actuate the wave propagation. Figure 2a compares the modeled array waveforms for dipole orientations along (solid line) and perpendicular (dashed line) to the fracture, which shows a well-defined S-wave splitting phenomenon (note that the dipole wave behaves like a shear body wave, especially at low frequencies). The dipole S-waves polarizing along the fracture strike direction are significantly faster than the waves polarizing perpendicular to the fracture strike, giving rise to an anisotropy value of approximately 6%. To investigate the effect of fracture aperture and its filling material on the S-wave anisotropy, we vary the aperture from 0 to 10 mm. The fracture filling material is usually made of proppant, a mixture

Table 1. Model parameters.

Parameters	P-wave velocity (m/s)	S-wave velocity (m/s)	Density (kg/m^3)	Outer radius(m)
Fluid	1500	—	1000	0.09
Casing	6098	3354	7500	0.099
Cement	2823	1729	1920	0.12
Formation	4600	2500	2500	∞
Fracture	1800	0–500	1200	—

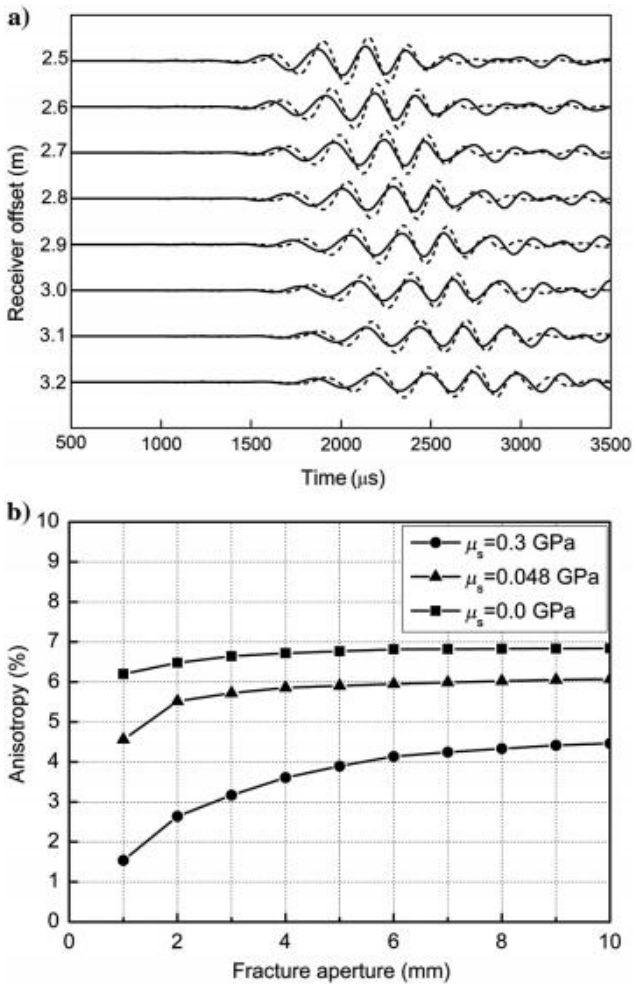


Figure 2. Borehole flexural-wave simulation results for the fracture model of Figure 1c. The array wave data in panel (a) show significant S-wave splitting for waves polarizing along (solid line) and perpendicular to (dashed line) the fracture. (b) The S-wave anisotropy versus fracture aperture for three fracture materials with quite different shear modulus values.

Downloaded from pubs.geoscienceworld.org/seg/geophysics/article-pdf/83/1/D1/4065724/geo-2017-0054.1.pdf by Univ of Petroleum (Beijing) - Library user on 08 October 2026

of fine grains (e.g., sands) and water. The solid grains keep the fracture from closing. Thus, depending on the contact stress exerted on the grains by the fracture surfaces, the proppant material may behave like a solid material. Therefore, we model the proppant as a soft elastic material with a small shear modulus. Figure 2b shows the S-wave anisotropy, as measured from the splitting of fast and slow S-waves (e.g., Figure 2a), as a function of the fracture aperture for three proppant shear modulus values. The modeling results show that, for a fracture material of finite shear modulus, the anisotropy increases with increasing fracture aperture. When the fracture material is pure fluid without shear rigidity, the anisotropy is almost invariant with the fracture aperture. The result is very similar to that of a planar fracture filled with water (Xu and Parra, 2003). Thus, it is clear from the above modeling that the proppant with certain shear rigidity changes the "shear compliance" of the fracture (Schoenberg and Sayers, 1995). The resulting S-wave anisotropy is jointly determined by the fracture shear compliance and the shear modulus of the surrounding rock (Tang and Cheng, 2004). The modeling result provides a basis for evaluating hydraulic fracturing using the S-wave anisotropy measurement (Tang et al., 2001). However, if the fracturing produces a fracture network, instead of a single major fracture, the anisotropy measurement becomes ineffective, as will be shown in the following. In the downhole fracturing operation, the fracture network would normally be generated if the principal stresses normal to the borehole are not significantly different.

Figure 3 shows the dipole array waveforms for two orthogonal orientations (along the x- and y-axis) in the fracture network model. The modeling parameters are the same as those used for the single fracture model. Very much as expected, because the extension of the fractures does not have a preferential direction, the dipole waveforms for the orthogonal direction do not show a measurable anisotropy. Therefore, other techniques need to be developed for evaluating the fracture network. For example, the traveltime tomography technique discussed below can be used. For this technique, the small fractures around the borehole (see Figure 1), which also result from fracturing, play an important role for the evaluation.

We use P-waves generated by a borehole monopole source to probe the near-borehole fracture zone of the fracture network model.

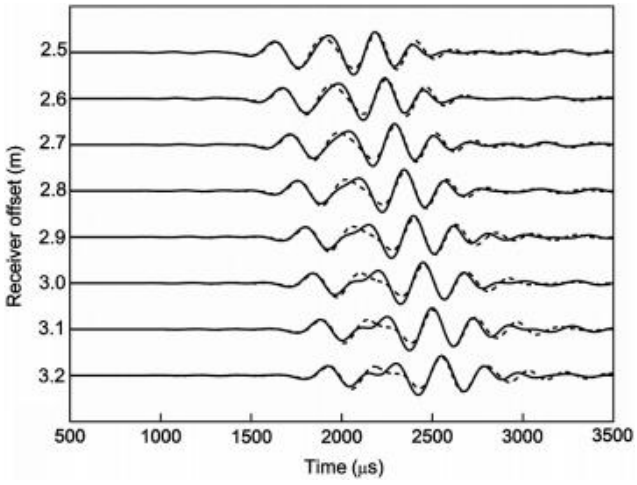


Figure 3. Borehole flexural wave simulation for the fracture network model of Figure 1d. The results show no measurable anisotropy between the two sets of array waveforms for two orthogonal polarization directions x (solid line) and y (dashed line).

The wave center frequency of 8 kHz, as commonly used in monopole acoustic logging, is used for the modeling. For comparison, we also compute the compressional waveforms without fracturing. Figure 4a shows the array P-waves before (solid line) and after (dashed line) fracturing. A prominent feature is that the waves after fracturing are significantly delayed relative to their counterparts before fracturing, indicating the near-borehole velocity change caused by the fractures. Su et al. (2013) show that the wave propagation for the near-borehole velocity change can be modeled by an exponentially varying velocity profile. To demonstrate the equivalence between the fracture zone model and the velocity change model, we use the exponential velocity profile (Figure 4b) to compute the array waveforms for the velocity change model. The computed waveforms (the thick gray line in Figure 4a) overlay with the fracture zone model results very well. Note that the far-borehole velocity of the fracture network model is lower than the formation velocity before fracturing, which is caused by fracture extension into the formation. In fact, the far-borehole velocity change relative to its before-fracturing value is reflected

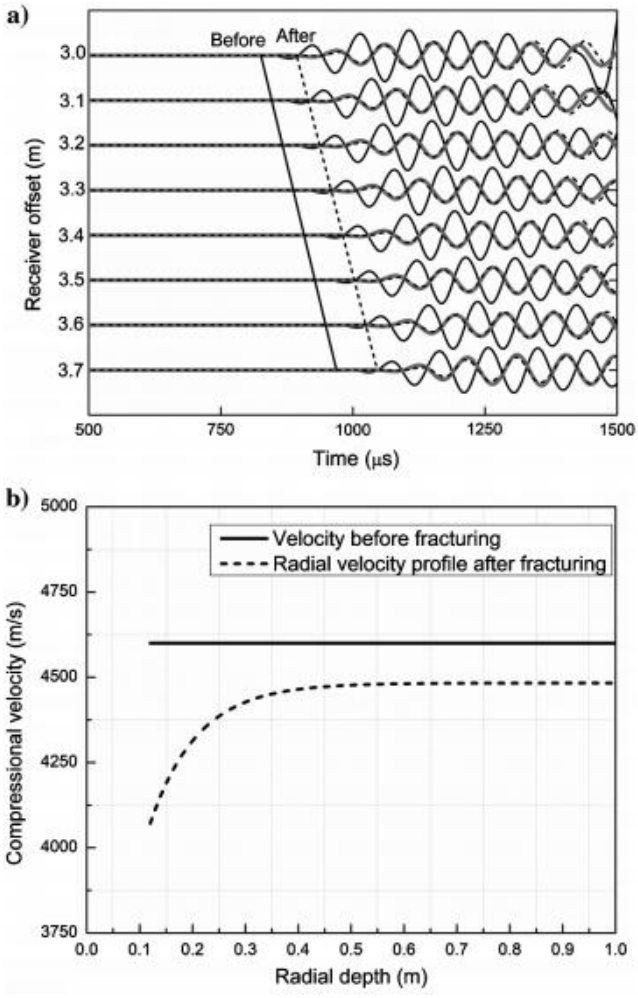


Figure 4. (a) Effect of a near-borehole fracture zone on P-waves (dashed line, from the model of Figure 1d) along the borehole. The wave arrival time after fracturing (dashed line across array) is significantly delayed compared with the arrival time before fracturing (solid line across array). This phenomenon can be modeled by the waveforms (thick gray line) computed using the varying near-borehole velocity profile in (b).

Downloaded from pubs.geoscienceworld.org/seg/geophysics/article-pdf/83/1/D1/4065724/geo-2017-0054.1.pdf by Univ of Petroleum (Beijing) - Library user on 08 October 2026

by the change in the slope of the wave moveout across array before (solid line) versus after (dashed line) fracturing, which is approximately 2.5%. In comparison, the change of the arrival time before versus after fracturing, which is approximately 7%, is quite large. Therefore, this significant traveltime delay is largely caused by the fracturing-induced low-velocity zone in the near-borehole region (see Figure 1b). According to the well-known seismic ray theory (Aki and Richards, 1980), the low-velocity zone bends the acoustic ray into the formation, and the wave is delayed twice while penetrating into, and emerging from, the low-velocity zone. The same modeling result, i.e., the significant arrival-time difference between before- and after-fracturing P-waves, is also true for the single-major fracture model (Figure 1c) because the model also contains a near-borehole fracture zone.

The above modeling results based on realistic fracture models (Figure 1a and 1b) show that the fracture-induced near-borehole velocity change produces significant changes on the borehole wave traveltime, which in turn can be used to determine the velocity change around the borehole. This provides a method for the hydraulic fracturing evaluation. In this regard, an acoustic traveltime tomography technique (Hornby, 1993; Balland and Renaud, 2009) can be used to compute the near-borehole velocity profile from the

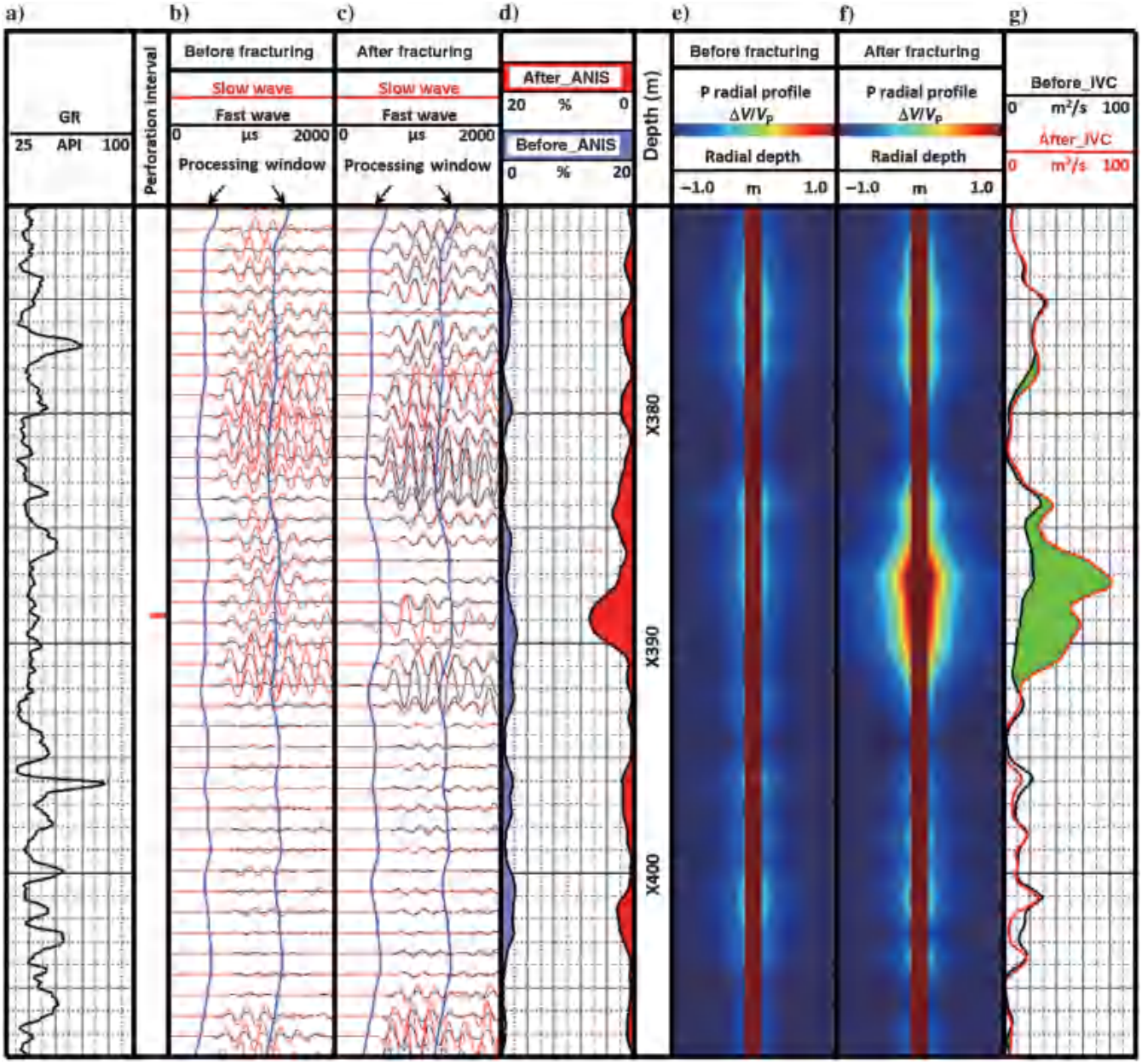


Figure 5. Evaluating result of hydraulic fracturing of a sand reservoir (see the gamma ray log curve in [a]) using before- and after-fracturing S-wave anisotropy (b-d) and P-wave tomography (e-g) techniques. The substantial changes of the after-fracturing anisotropy (d) and velocity tomogram (f and g) relative to their respective before-fracturing counterparts indicate that the fracturing operation is effective, and a single major fracture is formed.

Downloaded from pubs.geoscienceworld.org/seg/geophysics/article-pdf/83/1/D1/4065724/geo-2017-0054.1.pdf by Univ of Petroleum (Beijing) - Library user on 08 October 2026

measured traveltime data from acoustic logging. The technique calculates the acoustic traveltime from a 2D velocity model, in which the P- or S-wave velocity varies along the borehole radial and axial directions. The difference between the calculated and measured traveltime data is minimized to find the best velocity distribution that fits the measured data.

FIELD DATA APPLICATION

We show field data examples of using the borehole elastic-wave measurement for hydraulic fracturing evaluation and demonstrate the application of our modeling result for the evaluation. The first example is hydraulic fracturing in a tight sandstone formation, in which we compare the results of the S-wave anisotropy and P-wave tomogram before and after fracturing. The velocity tomogram is the relative difference between the variable velocity profile and the virgin formation velocity. The tomogram is shown as a variable density image, axisymmetrically displayed with the borehole in the center.

Figure 5a shows the gamma-ray log curve across the formation interval. The gamma-ray log is a measure of natural radioactivity of formation rocks, which is usually high in shale and low in sandstone. Hydraulic fracturing was done for the reservoir interval approximately X389 m. Before fracturing, an acoustic logging pass was made through the interval. The data contained the monopole data set for P-wave tomography analysis (Hornby, 1993; Su et al., 2015) and a 4C cross-dipole data set for the S-wave anisotropy measurement (Tang and Chunduru, 1999). The same logging pass was repeated after fracturing and the before- and after-fracturing results are compared in Figure 5. Figure 5b and 5c shows, respectively, the fast (black) and slow (red) S-waves from the cross-dipole data before (Figure 5b) and after (Figure 5c) fracturing. The S-wave anisotropy before (blue shaded curve, left to right) and after (red shaded curve, right to left) is, respectively, shown in Figure 5d.

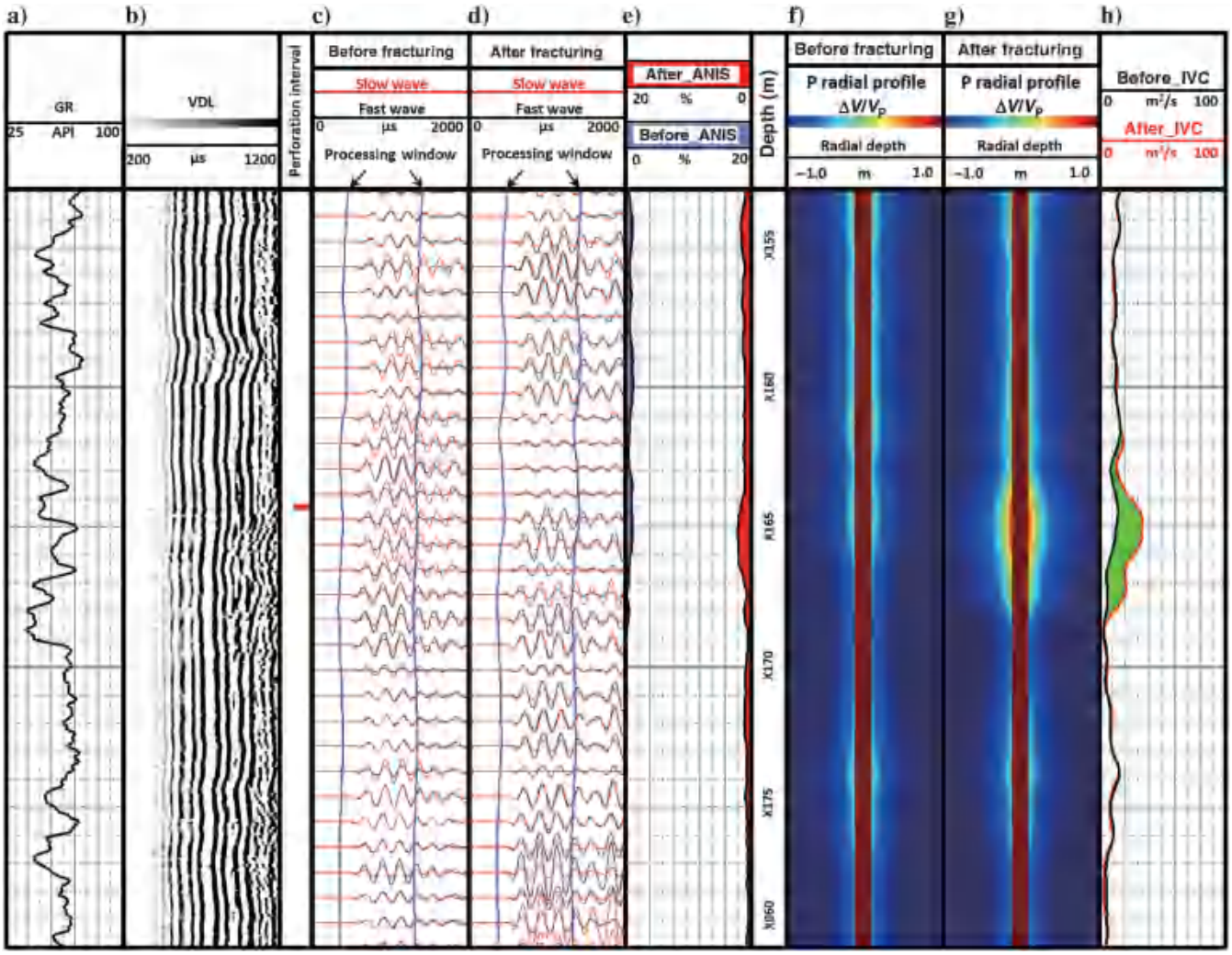


Figure 6. Evaluating result of hydraulic fracturing of a sand-shale sequence (see the gamma-ray log curve in [a]) using before- and after-fracturing S-wave anisotropy (c-e) and P-wave tomography (f-h) techniques in a cased borehole. The variable density log (VDL) waveform display is shown in [b], which indicates a good cement-bond quality. By using the VDL display, small variation features can be clearly visualized. For good bonding, acoustic waves can log through casing and the first-arrival time varies with the formation velocity, as is evident from (b). The minimal change of the shear anisotropy (e) and the significant change of the velocity tomogram (g and h) suggest that the fracturing operation is effective and produces a fracture network around the borehole.

Downloaded from pubs.geoscienceworld.org/seg/geophysics/article-pdf/83/1/D1/4065724/geo-2017-0054.1.pdf by Univ of Petroleum (Beijing) - Library user on 08 October 2026

Compared with the before-fracturing value, the fracturing interval shows a significant increase of the anisotropy value, which, according our modeling result (Figures 1a and 2), is interpreted as the formation of a single major fracture in the fractured interval. This interpretation is consistent with the regional stress condition, in which the substantial difference between maximum and minimum stresses tends to create vertical, tensile fractures along the borehole (Zoback et al., 1985). The fracture growth along the borehole is also supported by the P-wave tomography results in Figure 5e–5g. The acoustic velocity tomogram before (Figure 5e) and after (Figure 5f) shows substantial changes after fracturing. Before fracturing, the tomogram shows some minimal velocity decrease around the borehole, presumably caused by drilling-induced microcracks around the borehole. After fracturing, there is a large decrease of the velocity value in the fracturing interval (the tomogram is shown as the percentage difference of the radial velocity profile at a depth relative to its virgin formation value. The color scale from red to blue indicates a 20% decrease). The overall near-borehole velocity change can be characterized by the magnitude of the change and its area of influence, which can be conveniently assessed by integrating the velocity tomogram along the radial direction. The integrated velocity change curve (IVC curve in Figure 5g) indicates the overall radial velocity change along the borehole. The large difference (shaded area) between the IVC curves before (black) and after (red) fracturing indicates the good fracturing result across the fractured interval, which resulted in 50 tons/day oil production after fracturing.

The second example shows the effectiveness of acoustic tomography when the S-wave anisotropy measurement is ineffective. For a cased borehole across a tight sand-shale formation (see the gamma-ray log curve in Figure 6a), a plan was made to fracture the reservoir consisting of a sand-shale sequence. The variable density logging display of the compressional waveform logging data (Figure 6b) shows good cement-bond quality for the reservoir interval, allowing for the accurate determination of the P-wave traveltime from the data.

Cross-dipole S-wave anisotropy measurements were made before (see the fast and slow S-waves in Figure 6c) and after (see the fast and slow S-waves in Figure 6d). However, the measured anisotropy values before (shaded blue curve, left to right) and after (shaded red curve, right to left) fracturing, as well as their difference, are very small. Therefore, it is difficult to evaluate the effectiveness of the fracturing operation based on the anisotropy measurement. In contrast, the before- (Figure 6f) and after- (Figure 6g) fracturing velocity tomograms and the integrated velocity change curves (Figure 6h) show substantial difference in the fractured interval. This measurement result, i.e., significant near-borehole velocity change but insignificant anisotropy after fracturing, is consistent with our fracture network modeling (Figures 3 and 4), which implies that the fracturing operation produces mainly a fracture network around the borehole, rather than a major fracture extending away from the borehole. The positive evaluation result is confirmed by after-fracturing oil production of 15 tons/day from the fractured interval.

CONCLUSION

Downhole hydraulic fracturing produces two typical results: a single major fracture and a fracture network in the formation surrounding the borehole. In both situations, there is a zone of small, secondary fractures around the borehole. Downhole elastic-wave simulation with a realistic hydraulically fractured formation model demonstrates two important wave propagation characteristics that can be used for evaluating the result of hydraulic fracturing: One is S-wave anisotropy corresponding to the single major fracture model, and the other is the near-borehole velocity change associated with small fractures around the borehole. By measuring the change of anisotropy before and after fracturing, we can assess whether a major fracture is generated. If the anisotropy change is insignificant, we can determine the near-borehole velocity change after fracturing and use the velocity change to assess whether fracturing produces a near-borehole fracture zone, and consequently, an effective fracture network around the borehole. Our modeling results provide new insights for applying the borehole acoustic logging to downhole hydraulic evaluation. These applications are becoming a common practice in the acoustic logging community.

ACKNOWLEDGMENT

This work is supported by the China Natural Science Foundation (grant nos. 41474101 and 41474092).

REFERENCES

Aki, K., and P. G. Richards, 1980, Quantitative seismology: Theory and methods: W. H. Freeman and Co.

Alford, R., 1986, Shear data in the presence of azimuthal anisotropy, Dilley, Texas: 56th Annual International Meeting, SEG, Expanded Abstracts, 476–479.

Balland, C., and V. Renaud, 2009, High-resolution velocity field imaging around a borehole: Excavation-damaged zone characterization: Geophysics, 74, no. 6, E223–E232, doi: 10.1190/1.3237115.

Boness, N., and M. Zoback, 2006, A multiscale study of the mechanisms controlling shear velocity anisotropy in the San Andreas Fault Observatory at Depth: Geophysics, 71, no. 5, F131–F146, doi: 10.1190/1.2231107.

Cheng, N., C. H. Cheng, and M. N. Toksöz, 1995, Borehole wave propagation in three dimensions: Journal of the Acoustical Society of America, 97, 3483–3493, doi: 10.1121/1.412996.

Chiaramonte, L., M. D. Zoback, J. Friedmann, and V. Stamp, 2007, Seal integrity and feasibility of CO_2 sequestration in the Teapot Dome EOR pilot: Geomechanical site characterization: Environmental Geology, 54, 1667–1675, doi: 10.1007/s00254-007-0948-7.

Chouet, B., 1986, Dynamics of a fluid-driven crack in three dimensions by the finite difference method: Journal of Geophysical Research: Solid Earth, 91, 13967–13992, doi: 10.1029/JB091iB14p13967.

Fisher, M. K., C. A. Wright, B. M. Davidson, A. K. Goodwin, E. O. Fielder, W. S. Buckler, and N. P. Steinsberger, 2002, Integrating fracture mapping technologies to optimize stimulations in the Barnett shale: Presented at the SPE Annual Technical Conference and Exhibition.

Ge, Z., and X. Chen, 2007, Boundary element with wavenumber integration simulation of wave propagation in a fluid-filled borehole with arbitrary shape: Theory and preliminary results: 77th Annual International Meeting, SEG, Expanded Abstracts, 338–342.

Guo, T., S. Zhang, H. Ge, X. Wang, X. Lei, and B. Xiao, 2015, A new method for evaluation of fracture network formation capacity of rock: Fuel, 140, 778–787, doi: 10.1016/j.fuel.2014.10.017.

Hayashi, K., and B. C. Haimson, 1991, Characteristics of shut-in curves in hydraulic fracturing stress measurements and determination of in situ minimum compressive stress: Journal of Geophysical Research: Solid Earth, 96, 18311–18321, doi: 10.1029/91JB01867.

Holder, J., N. Morita, A. J. Kenrick, S. Thallak, and K. E. Gray, 1993, Measurements of effective fracture toughness values for hydraulic fracture: Dependence on pressure and fluid rheology: Presented at the SPE Annual Technical Conference and Exhibition.

Hornby, B. E., 1993, Tomographic reconstruction of near-borehole slowness using refracted borehole sonic arrivals: Geophysics, 58, 1726–1738, doi: 10.1190/1.1443387.

Lee, H., T. Moon, and B. C. Haimson, 2015, Borehole breakouts induced in Arkosic sandstones and a discrete element analysis: Rock Mechanics and Rock Engineering, 49, 1369–1388, doi: 10.1007/s00603-015-0812-0.

Legarth, B., E. Huenges, and G. Zimmermann, 2005, Hydraulic fracturing in a sedimentary geothermal reservoir: Results and implications: Interna-

Downloaded from pubs.geoscienceworld.org/seg/geophysics/article-pdf/83/1/D1/4065724/geo-2017-0054.1.pdf by Univ of Petroleum (Beijing) - Library user on 08 October 2026

tional Journal of Rock Mechanics and Mining Sciences, 42, 1028–1041, doi: 10.1016/j.ijrmms.2005.05.014.
Maxwell, S. C., J. Rutledge, R. Jones, and M. Fehler, 2010, Petroleum reservoir characterization using downhole microseismic monitoring: Geophysics, 75, no. 5, 75A129–75A137, doi: 10.1190/1.3477966.
Schmitt, D. R., C. A. Currie, and L. Zhang, 2012, Crustal stress determination from boreholes and rock cores: Fundamental principles: Tectonophysics, 580, 1–26, doi: 10.1016/j.tecto.2012.08.029.
Schoenberg, M., and C. Sayers, 1995, Seismic anisotropy of fractured rock: Geophysics, 60, 204–211, doi: 10.1190/1.1443748.
Su, Y., X. Tang, C. Zhuang, S. Xu, and L. Zhao, 2013, Mapping formation shear-velocity variation by inverting logging-while-drilling quadrupole-wave dispersion data: Geophysics, 78, no. 6, D491–D498, doi: 10.1190/geo2013-0136.1.
Su, Y. D., X. M. Tang, S. Xu, and C. X. Zhuang, 2015, Evaluating rock brittleness from radial P-wave velocity variation in the LWD condition: 77th Annual International Conference and Exhibition, EAGE, Extended Abstracts, doi: 10.3997/2214-4609.201412854.
Tang, X. M., and C. H. Cheng, 1988, Wave propagation in a fluid-filled fracture — An experimental study: Geophysical Research Letters, 15, 1463–1466, doi: 10.1029/GL015i013p01463.
Tang, X. M., and C. H. Cheng, 2004, Quantitative borehole acoustic methods: Elsevier Science Publishing Inc.
Tang, X. M., C. H. Cheng, and M. Toksöz, 1991, Stoneley-wave propagation in a fluid-filled borehole with a vertical fracture: Geophysics, 56,447–460, doi: 10.1190/1.1443062.
Tang, X. M., and R. K. Chunduru, 1999, Simultaneous inversion of formation shear-wave anisotropy parameters from cross-dipole acoustic-array waveform data: Geophysics, 64, 1502–1511, doi: 10.1190/1.1444654.
Tang, X. M., D. Patterson, and M. Hinds, 2001, Evaluating hydraulic fracturing in cased holes with cross-dipole acoustic technology: Presented at the SPE Annual Technical Conference and Exhibition.
Tary, J. B., M. van der Baan, and D. W. Eaton, 2014, Interpretation of resonance frequencies recorded during hydraulic fracturing treatments: Journal of Geophysical Research: Solid Earth, 119, 1295–1315, doi: 10.1002/2013JB010904.
Wei, Z. T., and X. M. Tang, 2012, Numerical simulation of radiation, reflection, and reception of elastic waves from a borehole dipole source: Geophysics, 77, no. 6, D253–D261, doi: 10.1190/geo2012-0061.1.
Xu, P., and J. Parra, 2003, Effects of single vertical fluid-filled fractures on full waveform dipole sonic logs: Geophysics, 68, 487–496, doi: 10.1190/1.1567216.
Zheng, Y., X. Tang, and D. J. Patterson, 2009, Borehole acoustic dipole response with drilling-induced vertical fractures: 79th Annual International Meeting, SEG, Expanded Abstracts, 356–360, doi: 10.1190/1.3255607.
Zhou, J., Y. Jin, and M. Chen, 2010, Experimental investigation of hydraulic fracturing in random naturally fractured blocks: International Journal of Rock Mechanics and Mining Sciences, 47, 1193–1199, doi: 10.1016/j.ijrmms.2010.07.005.
Zoback, M. D., D. Moos, L. Mastin, and R. N. Anderson, 1985, Well bore breakouts and in situ stress: Journal of Geophysical Research: Solid Earth, 90, 5523–5530, doi: 10.1029/JB090iB07p05523.

Downloaded from pubs.geoscienceworld.org/seg/geophysics/article-pdf/83/1/D1/4065724/geo-2017-0054.1.pdf by Univ of Petroleum (Beijing) - Library user on 08 October 2026

APPLIED GEOPHYSICS, Vol.8, No.1 (March 2011), P. 69 - 78, 12 Figures.
DOI: 10.1007/s11770-011-0272-6

An equivalent-tool theory for acoustic logging and applications*

Su Yuan-Da[1], Tang Xiao-Ming[1], Hei Chuang[1], and Zhuang Chun-Xi[1]

Abstract: The influence of an acoustic logging tool on borehole guided wave propagation should be considered in the processing and inversion of the guided waves for formation acoustic property estimation. This study introduces an equivalent-tool theory that models the tool response using an elastic rod with an effective modulus and applies the theory to multipole acoustic logging for both wireline and logging while drilling (LWD) conditions. The theory can be derived by matching the tool's acoustic impedance/conductance to that of the multipole acoustic wavefield around the tool, assuming that tool radius is small compared to wavelength. We have validated the effectiveness and accuracy of the theory using numerical modeling and its practicality using field data. In field data applications, one can calibrate the tool parameters by fitting the theoretical dispersion curve to field data without having to consider the actual tool's structure and composition. We use a dispersion correction example to demonstrate an application of the simple theory to field data processing and the validity of the processing result.
Keywords: Equivalent theory, acoustic tool modeling, impedance match, guided wave

Introduction

Recent years have witnessed growing importance of inverting guided wave dispersion characteristics for formation acoustic parameter estimation, such as inversion of Stoneley wave for TI (transverse isotrop) estimation (Tang, 2003), inversion of dipole-flexural wave dispersion data for mapping formation radial shear velocity profile (Tang and Patterson, 2010; Sinha et al., 2005), and inversion of LWD quadrupole-wave dispersion data for formation shear velocity estimation (Zheng et al., 2006), etc. In the inversion and interpretation of guided wave data from acoustic logging, the effect of an acoustic tool and its interaction with guided wave propagation have long been an important subject because of its theoretical significance and relevance to practical applications.

An actual acoustic tool is rather complex, consisting of electronics and a number of transducers and sensors. In addition, the tool body may be slotted to enhance acoustic coupling with borehole fluid and isolate tool waves traveling along the tool. Various theories have been developed to describe acoustic response of an acoustic tool. For example, White (1983), Cheng et al.(1981), and Tang and Cheng (1993) model the tool as a rigid rod. Chen (1984) models a tool as viscoelastic rod, and Sinha et al. (2009) model the tool as a heavy fluid column. These examples suggest that, for given physical conditions and frequency range, we can develop an equivalent-tool theory to accurately describe the tool response to acoustic excitation of a multipole source.

Manuscript received by the Editor December 17, 2010; revised manuscript received February 22, 2011.
*This work is supported by the Fundamental Research Funds for the Central Universities and the National Hi-tech Research and Development Program of China (863 Program) (Grant No. 2007AA06Z232).
1. China University of Petroleum (East China), Qingdao 266555, China.

Tang and Cheng (2004) have demonstrated the validity of the equivalent-tool theory for Stoneley waves in wireline monopole logging. In the work to be described, we will extend the theory to multipole acoustic logging and verify its validity for both wireline and LWD conditions. Further, we will apply the theory to model tool effects in field data processing. In the field data application, the simplicity of the model makes it possible to effectively process field data of large volume.

Equivalent tool theory

Approximating an acoustic tool of arbitrary internal structure as a cylindrical rod, we want to derive a theory to model the acoustic response of the tool and prove the validity of this approach in the long wavelength scenario. In this scenario, one can use an effective elastic modulus to model the multi-parameter elasticity of the tool. The mathematical analysis of this theory is described in the following.

Consider a multipole acoustic logging tool of radius a centered in a fluid-filled borehole of radius R surrounded by an elastic formation. Acoustic wave propagation in the fluid annulus between the tool and formation is represented by fluid particle displacement u and pressure disturbance p. For a multipole acoustic wavefield, u and p are expressed as (Schmitt, 1988; Tang and Cheng, 2004):

$$\begin{aligned} u &= \left\{ A_n[\frac{n}{r} I_n(fr) + fI_{n+1}(fr)] + B_n[\frac{n}{r} K_n(fr) - fK_{n+1}(fr)] \right\} \cos[n(\theta-\phi)] \\ p &= \left\{ A_n[\rho_f \omega^2 I_n(fr)] + B_n[\rho_f \omega^2 K_n(fr)] \right\} \cos[n(\theta-\phi)] \end{aligned} \quad (a < r < R), \tag{1}$$

where A_n and B_n are the incoming and outgoing wave amplitude coefficient, respectively, the order of the multipole is n, with $n = 0, 1, 2$ representing monopole, dipole, and quadrupole, respectively, ω is angular frequency, $\theta - \phi$ is the multipole alignment azimuth relative to a reference angle ϕ, I_n and K_n are the first and second modified Bessel function of order n, respectively. $f = \sqrt{k^2 - \frac{\omega^2}{V_f^2}}$ is the radial fluid wavenumber. V_f and ρ_f are fluid acoustic velocity and density, respectively. k is the axial wavenumber for the guided multipole wave mode of interest (Tang and Cheng, 2004).

At a fluid-solid boundary (i.e., the interface between borehole fluid and an acoustic tool), the boundary condition for an elastic wave can be adequately specified by matching the acoustic conductance (defined as: u/p) of the fluid to that of the solid. In the long wavelength scenario, the tool can be equivalently modeled as a cylindrical elastic rod. Norris (1990) used this conductance match method to model the effect of a tool on the low-frequency monopole Stoneley wave in the fluid annulus between borehole and the tool, as given below:

$$\left(\frac{u}{p}\right)_{r=a} = -\frac{a}{M_T}, \tag{2}$$

where M_T is tool modulus. We now further assume that: 1) the above low-frequency result is still valid for multipole guided waves as along as tool radius is small compared to wavelength, and 2), the multi-parameter elasticity of a multipole acoustic tool can be modeled by an effective modulus M_T, regardless of the internal structure of the tool. For this multipole wave extension, we can use equation (1) to get the acoustic conductance u/p and use it to match the conductance of the tool at the tool-fluid interface, as in equation (2). From the conductance match, we obtain the following equation to relate the two unknown coefficients A_n and B_n.

$$\begin{aligned} E_{tool} &= \frac{B_n}{A_n} = - \\ &= -\frac{(M_T/a)[n/a\, I_n(fa) + fI_{n+1}(fa)] + \rho_f \omega^2 I_n(fa)}{(M_T/a)[n/a\, K_n(fa) - fK_{n+1}(fa)] + \rho_f \omega^2 K_n(fa)}, \end{aligned} \tag{3}$$

where E_{tool} is the ratio of B_n to A_n consisting of Bessel function combinations and tool's elastic modulus M_T. Thus only one unknown, A_n or B_n, needs to be determined from the boundary condition at the fluid-formation interface. Referring to the derivation procedure given in the reference (Tang and Cheng,

2004), we get the multipole wave dispersion equation for a centered tool in a fluid-filled borehole.

$$D(k,\omega,V_p,V_s,\rho,V_f,\rho_f,R,M_T,a)=0, \qquad (4)$$

where V_p, V_s and ρ are the formation compressional (or *P*) and shear (S) velocity and density, respectively. Specifically, the function *D* represents the determinant of a coefficient matrix, D = det‖*M*‖; the elements of *M* are given (Tang and Cheng, 2004). To get *D* in equation (4), we need only to modify two related elements in the original matrix without tool. The modifications consist of adding a tool-related term to the original elements M_{11} and M_{21}, as shown below

$$\begin{cases} M_{11}: \dfrac{n}{R}I_n(fR)+fI_{n+1}(fR)\rightarrow[\dfrac{n}{R}I_n(fR)+fI_{n+1}(fR)] \quad E \\ \qquad\qquad +E_{tool}[\dfrac{n}{R}K_n(fR)-fK_{n+1}(fR)]. \quad (5) \\ M_{21}: I_n(fR)\rightarrow I_n(fR)+E_{tool}K_n(fR) \end{cases}$$

$$K \quad fR \quad fK \quad fR$$

The symbol "→" in the above expressions denotes replacing the left hand side of the symbol with the expression on the right hand side. Making similar modifications, one can include the tool effect in the dispersion equation for a TI formation and for a porous formation (Tang and Cheng, 2004). Searching the root of equation (4) for the wavenumber *k* of the multipole wave mode in a given frequency range, we get the wave' s phase velocity dispersion curve.

$$V_{ph}=\omega/k. \qquad (6)$$

The dispersion curve computed from equation (6) includes the effect of an acoustic tool. Considering the multi-parameter nature of an actual tool's elasticity, our equivalent tool theory is truly a drastically simplified model. Consequently, one needs to verify whether such a model can adequately describe the acoustic tool response for different excitation mode and for wireline and LWD configurations. For this reason, we verify our tool theory using numerical simulation and field acoustic logging data.

Validating the equivalent tool theory

Tang and Cheng (2004) have studied the influence of an acoustic tool on the monopole Stoneley wave propagation, in which the exact solution for a cylindrical steel shell model is used to verify the validity and accuracy of the equivalent-tool theory. In this study, we will further validate the applicability of the theory to wireline dipole flexural wave, LWD quadrupole wave, and the LWD leaky-P wave mode for an ultra slow formation. (Such a formation is characterized not only by its low velocity, but also by its abnormally high V_p/V_s ratio, which is usually greater than 3.) For the parameter values listed in Table 1, we calculate the exact solution for the given tool parameters; the resulting theoretical dispersion curve will then be compared with the curve calculated using the equivalent tool.

Table 1 Borehole fluid, acoustic tool, and formation parameters used in modeling

Materials	P-velocity (m/s)	S-velocity (m/s)	Density (kg/m^3)	Inner radius (m)	Outer radius (m)
Borehole fluid	1500	—	1000	0	0.12
Drill collar (steel tool)	5860	3130	7850	0.027	0.089
Heavy fluid column (compliant tool)	950	—	7850	0.01	0.045
Fast formation 1	4500	2500	2500	0.12	∞
Fast formation 2	4000	2000	2300	0.12	∞
Ultra slow formation	2080	650	1900	0.12	∞

Verificating the equivalent-tool model using exact solution for cylindrical tool models

We use the heavy fluid cylinder model (Sinha et al., 2009)for a wireline dipole logging tool and a steel shell model for an LWD quadrupole logging tool (Hsu and Sinha, 1998). For these models, the wave dispersion curve can be found exactly. Comparing the curve with corresponding curve calculated using the equivalent-tool theory allows us to assess the validity and accuracy of the simplified model theory.

Figure 1 shows the dispersion curve computed with our equivalent-tool model (red) and with the exact solution for the heavy-fluid model (blue) for the Fast

formation 1 of Table 1. (With the heavy density in the latter model, the fluid velocity may be arbitrarily chosen in a range around the borehole fluid (Sinha et al., 2009)) The dispersion curve without tool (black) is also plotted. The tool radius a for both models is 0.045 m, and the M_T value for the equivalent tool is 35 GPa. Both models give almost the same result in the frequency range of 2-12 kHz, showing only minor difference around the Airy phase frequency about 4 kHz. More importantly, the result indicates that in the frequency range above the cut-off frequency the presence of a tool shifts the entire dispersion curve toward low frequencies, demonstrating the necessity of including the tool effect in the processing and application of flexural-wave dispersion data.

Figure 2 shows the quadrupole-wave dispersion curve with the equivalent-tool model (red, computed with a = 0.089 m and M_T = 269 GPa) and with the exact solution for the drill-collar model (blue) of Table 1, as well as the curve without tool (black). The overall agreement between the two models is quite good, although there is a minor difference in the lower frequency range. However, this difference is quite small compared to the error range in the actual LWD quadrupole measurement. The modeling results shows that our equivalent-tool theory is sufficiently accurate even for the modeling of the LWD quadrupole wave. In the LWD situation, the tool occupies a large portion of the borehole and greatly affects the dispersion characteristics of the quadrupole wave. Compared with the curve without tool, the entire curve with the tool is shifted toward the low-frequency range.

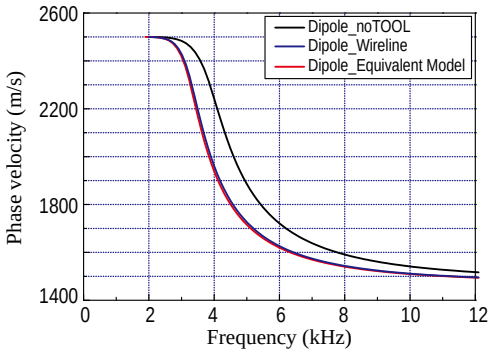


Fig. 1 Dipole flexural-wave dispersion curves with and without a wireline tool.

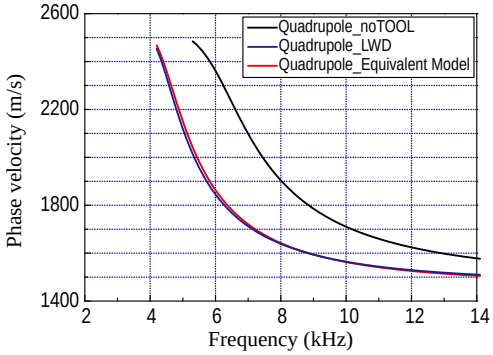


Fig. 2 Quadrupole-wave dispersion curves with and without an LWD tool.

Verification using finite-difference waveform simulation with a slotted LWD tool model

Compared to a wireline acoustic tool, an LWD tool made with a drill collar is relatively simple. Acoustic isolation for an LWD tool is usually achieved by cutting periodic slots on the collar (Figure 3). We use a finite difference technique (Wang and Tang, 2003) to simulate the response of the slotted tool to the multipole acoustic wave propagation along the model. Figure 3 shows an LWD acoustic tool made on the drill collar. The tool is centered in the borehole, with an acoustic source transducer and receiver array placed at the rim of the tool, and the acoustic isolation slots between the source and receivers. The acoustic model uses the Fast formation 2 of Table 1. The model has an outer radius of 1m and height of 8m. Source-to-receiver distance is 3 m, and receiver spacing is 0.2 m. The finite difference modeling uses a time step of 0.1 us and grid size of 2.5 mm.

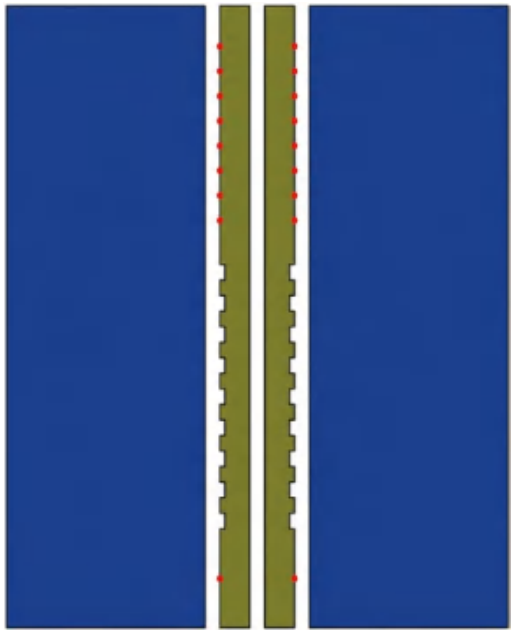


Fig. 3 Diagram illustrating an LWD acoustic model.

Figure 4a shows the simulated array waveform data for a monopole source. The source wavelet is a Ricker wave of 13 kHz center frequency. The large amplitude event in the data is the Stoneley wave mode. Figure 4b shows the dispersion data (dots) extracted from the Stoneley wave data and the dispersion curve computed using the equivalent-tool theory (red curve, with a = 0.089 m and M_T = 130 GPa), as well as the dispersion curve without tool (black). The curve modeled with the tool agrees with the finite difference result very well in the frequency range of 2.5-8 kHz, showing that the presence of an LWD tool substantially reduces the Stoneley velocity relative to the curve without tool.

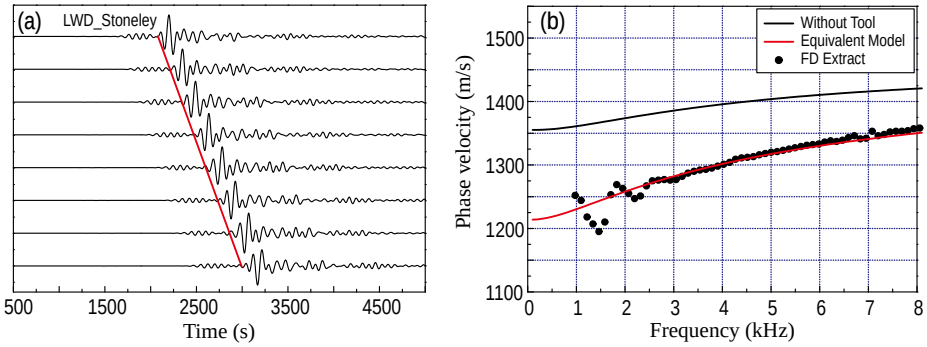


Fig. 4 Finite difference simulation of LWD monopole waves and comparing analytical and extracted Stoneley-wave dispersion data.

Figure 5a shows the finite difference modeling of the LWD quadrupole waveforms. The center frequency of the Ricker wavelet used for the source is 4 kHz. For this low-frequency source, tool quadrupole wave is not excited (Tang and Cheng, 2004) and the data shows only the formation quadrupole wave. Figure 5b shows the dispersion data (dots) extracted from the waveform data and the dispersion curve computed using the equivalent-tool theory (red, same parameters as in Figure 4), together with the dispersion curve without tool (black). The overall agreement between the analytical curve and extracted dispersion data is quite good. The discrepancy near the cut-off frequency is caused by the inaccurate extraction of the dispersion data near the cut-off, where the simulated waveform (the first arriving portion) has very low amplitude.

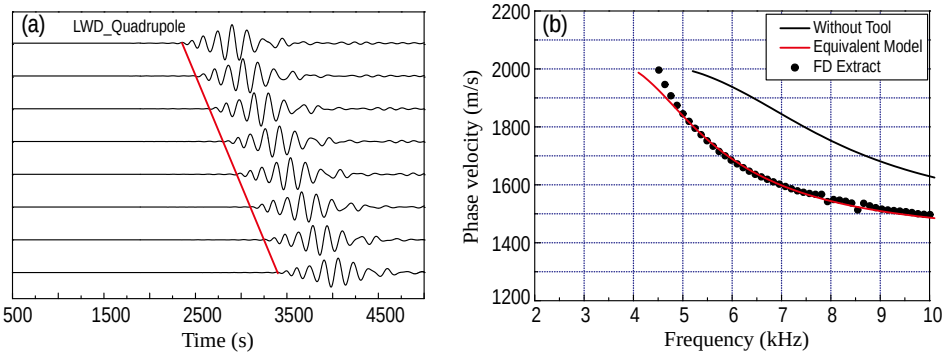


Fig. 5 Finite difference simulation of LWD quadrupole wave and comparing analytical and extracted dispersion data.

The above numerical results validate the equivalent-tool theory for guided waves that are primarily sensitive to formation shear-wave velocity, e.g., Stoneley wave, flexural wave, and quadrupole wave. The next example shows that the theory is also valid for wave modes that are sensitive to formation P-wave velocity, such as leaky-P wave mode. Figure 6a shows the simulated LWD leaky-P wave for the ultra-slow formation of Table 1. For this formation, the waveform data is dominated by a dispersive leaky-P wave. Figure 6b shows the dispersion data (dots) extracted from the waveform data and the dispersion curve (red) computed using the equivalent-tool theory. The dispersion curve for the open hole without tool is also plotted (black). The comparison shows very good agreement between the theoretical and extracted dispersion data, except for the discrepancy

toward low frequencies. The cause of this discrepancy is the same as have been discussed for the quadrupole case (Figure 5). The tool modeling result also shows that the presence of an LWD tool shifts the leaky-P wave dispersion curve toward high frequencies, in contrast to the trend for the flexural and quadrupole wave modes (see Figures 1, 2, and 5). This trend difference is obviously due to the different types of wave modes being discussed. Flexural and quadrupole wave modes are categorized as shear normal modes because they are primarily controlled by shear velocity, whereas the leaky-P wave is mostly controlled by formation P-wave velocity, causing the respective dispersion curves to shift to opposite directions in the presence of an LWD tool.

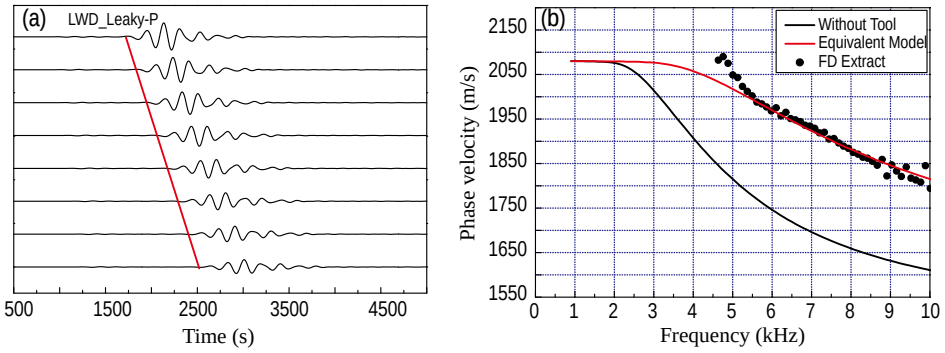


Fig. 6 Finite difference simulation of low-frequency leaky-P wave and comparing analytical and extracted dispersion data.

Tool parameter calibration: An illustration using wireline dipole dispersion data

Method for tool parameter calibration

Tang and Cheng (2004) describe the sensitivity analysis that uses the phase velocity dispersion curve of a guided wave to define the wave's sensitivity to each model parameter. Figure 7 shows, for the Fast formation 1 of Table 1, the sensitivity of dipole-flexural wave to the equivalent-tool model parameters, where the black curve denotes the modulus sensitivity and the red curve is the tool radius sensitivity. The results show that increasing tool radius significantly decreases the flexural-wave velocity, while increasing tool modulus tends to increase the velocity. The result shows that flexural wave is very sensitive to tool radius and moderately sensitive to tool modulus. The sensitivity analysis result indicates that the tool parameters can be adjusted or calibrated to realistically model the effect of an acoustic tool on guided wave propagation.

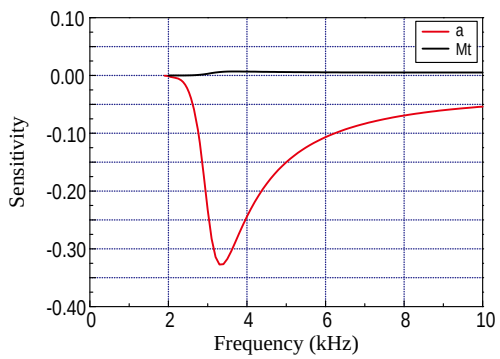


Fig. 7 Sensitivity curves for tool radius and modulus.

When applying the equivalent-tool theory to field data processing and interpretation, the tool parameters can be calibrated by choosing a homogeneous, isotropic interval. Adjusting parameter values to make the theoretical dispersion curve match that of the actual data determines appropriate values of M_T and a, which are then used in the data processing for the depth zone of interest. Figure 8 shows an example of the calibration. The theoretical dispersion curve (red), after calibration to the actual dispersion data (dots), matches the data very well, while the dispersion curve (black) without tool deviates significantly from the field data. This calibration gives M_T = 35 Gpa and a = 0.045 m. These parameter values can then be used in the later processing of the entire depth zone of interest. The actual calibration procedure is described below:

1) Obtain formation P-wave velocity, density, and borehole fluid velocity and density.

2) Extract field dispersion data; obtain formation S-wave velocity from low-frequency portion of the dispersion data.

3) Compute theoretical dispersion curve for the equivalent-tool model and adjust the tool parameters M_T and a to minimize the difference between the field data

and the dispersion curve (red) for the given frequency range. Retain the calibrated parameter values for later use.

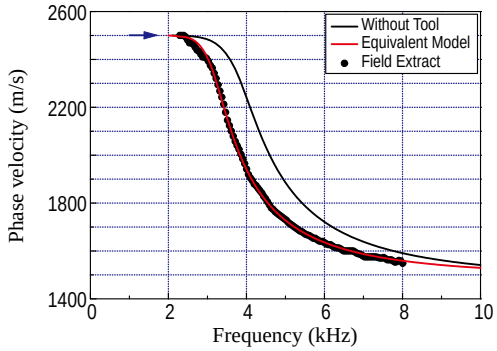


Fig. 8 Diagram illustrating the calibration of tool modulus and radius.

Effect of tool for different formation and borehole parameters

Figure 9a shows a typical field dipole acousitc array waveform data for a fast formation interval. Figure 9b shows the dispersion data (dots) extracted from the waveform data, together with the theoretical dispersion curve computed with (red) and without (black) tool. The blue curve is the relative difference between the two curves, indicating the error that might be incurred if tool effect is not considered in handling the dispersion effect. The error curve shows that for the fast formation situation a maximum error of about 10 % and an average error of 5 % might be encountered in the frequency range below 20 kHz.

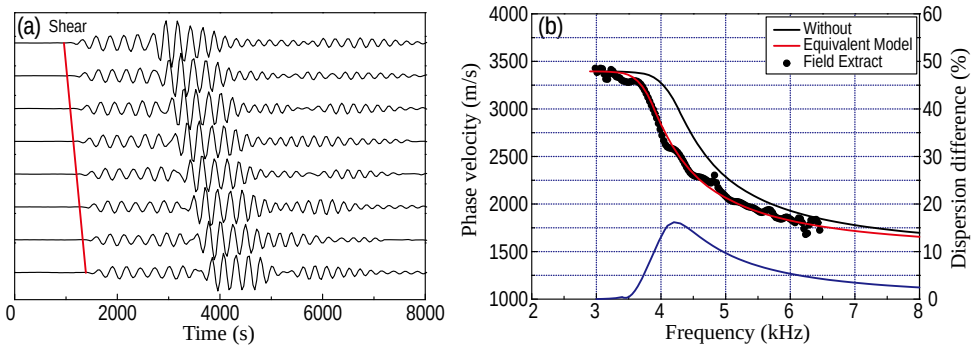


Fig. 9 Typical waveform data for a fast formation and the extracted dispersion data fitted with (red) and without (black) tool.

Figure 10a shows a typical dipole array waveform data from a homogeneous, isotropic slow formation. Figure 10b shows the dispersion data (dots) and the theoretical dispersion curve with (red) and without (black) tool. The dispersion is the relative error between the two curves, which shows that in the slow formation case the maximum error is only about 1% and the average error is about 0.5%.

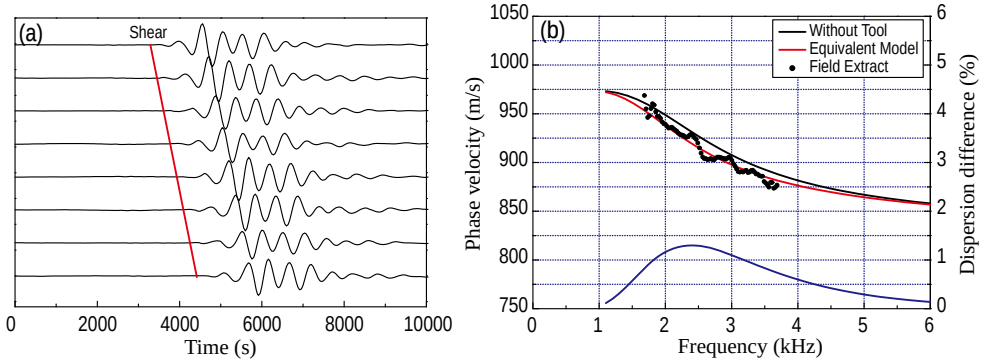


Fig. 10 Typical waveform data for a slow formation and the extracted dispersion data fitted with (red) and without (black) tool.

Comparing the fast (Figure 9) and slow (Figure 10) formation results shows that the tool effect on the flexural-wave dispersion is much more significant in the fast formation than in the slow formation. Figure 11 shows the effect of the equivalent tool on flexural-wave dispersion for different formation shear velocity and

borehole radius values. Horizontal axis is shear velocity and vertical axis is the average relative error between the dispersion curves with and without tool, where the black, red, and green curves correspond to borehole radius of 10 cm, 12 cm, and 15 cm, respectively. For a given tool radius, the tool effect decreases with decreasing shear velocity. For a given shear velocity, the tool effect decreases with increasing borehole radius. The theoretical results are consistent with the field data trend in Figures 9 and 10. Similar trend can also be obtained for LWD quadrupole and leaky-P waves. The modeling results suggest that in calibrating tool parameters to field data, a fast formation with smaller borehole radius should be used to effectively determine the tool parameters.

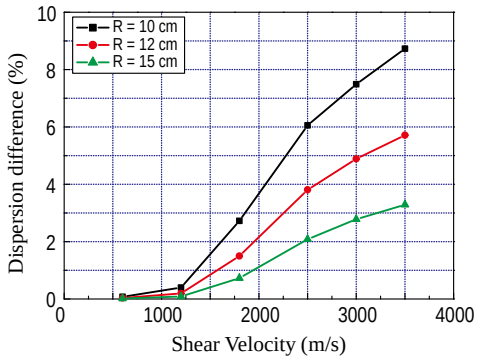


Fig. 11 Tool effect on flexural-wave dispersion for different formation shear velocity and borehole radius values.

A field data application example

Previous modeling examples show that the presence of a tool can significantly affect the propagation of multipole waves for both wireline and LWD conditions.

We now use a field wireline dipole acoustic data set to demonstrate the validity and accuracy of the equivalent-tool model. Kimball (1998) developed a dispersion correction method to extract formation shear velocity from dispersive flexural data. For this method a theoretical dispersion curve must be used. Therefore, whether a tool is included in the theoretical modeling can significantly affect the processing result, as will be shown by the following field example.

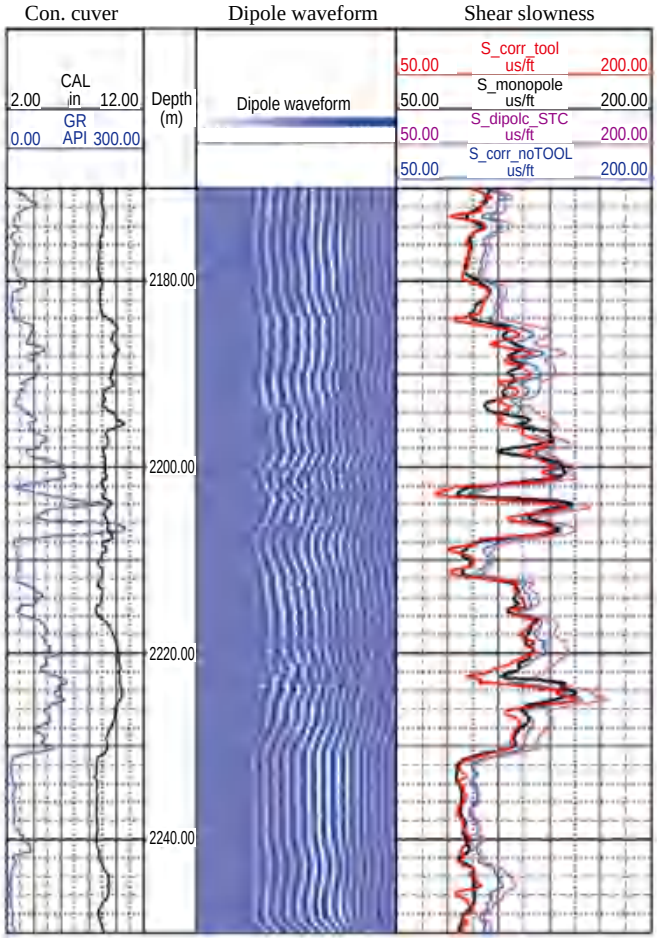


Fig. 12 Example of flexural-wave dispersion correction for a field data set.

Figure 12 shows a field data example of dipole-flexural wave dispersion correction. Calibrating the tool parameters for a limestone interval around 2240 m results in $M_T = 30$ Gpa and $a = 0.025$ m. The first panel plots gamma-ray and borehole caliper log curves. The second panel plots the dipole acoustic waveform using a variable density display. The third panel plots various slowness curves from processing the waveform data, with magenta, blue, and red (double thickness) corresponding to no-dispersion correction (e. g., using the method of kimball (1984)), correction without tool, and correction with the tool, respectively. For comparison, the shear slowness curve obtained from monopole logging is also plotted (thick black curve, the monopole shear slowness is usually dispersion free and regarded as true formation shear slowness). Compared to the curve corrected with tool, the slowness corrected without tool is consistently higher and deviates significantly from the true formation slowness. In contrast, the slowness curve corrected with the equivalent-tool theory is very close to the true slowness, as can be seen from the agreement between the thick red and black curves. In addition, one may notice that the slowness curves corrected with and without tool are quite close to the true shear slowness curve in the sandstone interval between 2200-2228m. In this interval the borehole diameter is significantly enlarged. This borehole enlargement reduces the flexural-wave sensitivity to tool effects, as confirmed by the modeling result in Figure 11.

This case example suggests that one needs to consider the tool effect when processing dispersive dipole acoustic data for shear slowness estimation. In this regard, the simple equivalent-tool theory has important application potential for dispersive acoustic data processing and interpretation.

Conclusions

Numerical modeling and field data processing results of this study show that the presence of a tool can significantly affect multipole acoustic wave propagation and should therefore be considered. The equivalent-tool theory developed in this paper can accurately and efficiently model the multipole acoustic response of the tool in a quite broad frequency range. This study has validated the effectiveness and accuracy of this simple theory for modeling Stoneley, dipole-flexural, quadrupole, and leaky-P waves under both wireline and LWD conditions. By calibrating tool parameters using field data, the theory can be applied to efficiently process field acoustic data with sufficient accuracy, as demonstrated by a field dipole data dispersion correction example. The result shows the important application potential of this simple equivalent-tool theory.

References

Chen, S. T., and Willen, D. E., 1984, Shear wave logging in slow formations: SPWLA 25th Annual Logging Symposium transactions, 10 – 13 June, New Orleans, USA , Paper DD.

Cheng, C. H., and Toksoz, M. N., 1981, Elastic wave propagation in a fluid-filled borehole and synthetic acoustic logs: Geophysics, **46**(7), 1042 – 1053.

Hsu, C. J., and Sinha, B. K., 1998, Mandrel effects on the dipole flexural mode in a borehole: J. Acoust. Soc. Am., **104**(4), 2025 – 2039.

Kimball, C. V., 1998, Shear slowness measurement by dispersive processing of borehole flexural mode: Geophysics, **63**(2), 337 – 344.

Kimball, C. V., and Marzetta, T. L., 1984, Semblance processing of borehole acoustic array data: Geophysics, **49**(3), 274 – 281.

Norris, A. N., 1990, The speed of a tube wave: J. Acoust. Soc. Am., **87**(1), 414 – 417.

Schmitt, D. P., 1988, Shear-wave logging in elastic formations: J. Acoust. Soc. Am., **84**(6), 2215 – 2229.

Sinha, B., Ikegami, T., Johnson, D. L. and Pabon, J., 2009, Use of an effective tool model in sonic logging data processing: U. S. Patent 7529152.

Sinha, B., Vissapragada, B., Kisra, S., Sunaga, S., Yamamoto H., Endo T., and Valero H. P., 2005, Optimal well completions using radial profiling of formation shear slownesses: SPE Annual Technical Conference and Exhibition, 9 – 12 October, Dallas, USA, **SPE95837**, 1 – 13.

Tang, X. M., and Cheng, C. H., 993, Effects of a logging tool on Stoneley waves in elastic and porous boreholes: The Log Analyst, **134**, 46 – 56.

Tang, X. M., 2003, Determining formation sheat-wave transverse isotropy from borehole Stoneley-wave measurements: Geophysics, **68**(1), 118 – 126.

Tang, X. M., and Cheng, A., 2004, Quantitative borehole acoustic methods, Handbook of Geophysical Exploration: Seismic Exploration: Elsevier. Amsterdam, Netherlands.

Tang, X. M., and Patterson, D. J., 2010, Mapping formation radial shear-wave velocity variation by a constrained inversion of borehole flexural-wave dispersion data: Geophysics, **75**(6), E183 – E190.

Wang, T., and Tang, X. M., 2003, Finite-difference modeling of elastic wave propagation: A nonsplitting perfectly matched layer approach: Geophysics, **68**(5),1749 – 1755.

White, J. E., 1983, Underground sound: Elsevier, Amsterdam, Netherlands.

Zheng, Y., Huang, X., Tang, X. M., and Patterson, D., 2006, Application of a new data-driven processing method to LWD and Wireline dispersive compressional and shear waveform data: SPE Annual Technical Conference and Exhibition, 24 – 27 September, San Antonio, USA, **SPE 103328**, 1 – 10.

Su Yuan-Da graduated from China University of Petroleum (East China) with a Master of Science degree in geo-resources exploration and information Technology in 2004. He has been conducting teaching and research in acoustic logging theory and applications. He is a member of Acoustic Society of China.



Petroleum Science xxx (xxxx) xxx

Contents lists available at ScienceDirect

Petroleum Science

journal homepage: www.keaipublishing.com/en/journals/petroleum-science



Original Paper

Fast inversion of formation slowness from LWD acoustic wave modes using deep learning

Kai-Yin Zheng [a,b], Yuan-Da Su [a,b,c,*], Xi-Hao Gu [d], Sheng-Qing Li [a,b,c], Chun-Xi Zhuang [a,b,c], Xiao-Ming Tang [a,b,c]

[a] School of Geosciences, China University of Petroleum (East China), Qingdao, 266580, Shandong, China
[b] National Key Laboratory of Deep Oil and Gas, Qingdao, 266071, Shandong, China
[c] Qingdao National Laboratory for Marine Science and Technology, Qingdao, 266071, Shandong, China
[d] College of Geophysics, Chengdu University of Technology, Chengdu, 610059, Sichuan, China

ARTICLE INFO

Article history:
Received 28 February 2026
Received in revised form
24 May 2026
Accepted 15 June 2026
Available online xxx

Edited by Jie Hao

Keywords:
Acoustic logging-while-drilling
Dispersion
Deep learning
Slowness inversion

ABSTRACT

Developing an effective and efficient method for extracting slowness from logging-while-drilling (LWD) dispersive guided-wave data has always been challenging. Conventional physics-driven methods estimate slowness by fitting theoretical dispersion curves to dispersion data extracted from waveforms. However, this approach is hampered by the inherent computational inefficiency of forward modeling and the instability arising from the extracted dispersion data quality. An efficient processing workflow addresses these limitations by employing a deep learning surrogate model for dispersion curve mapping, coupled with clustering and optimization modules, to determine LWD multipole slowness. The deep learning model employs a ResNet-LSTM architecture, where the residual network (ResNet) module extracts hierarchical features from formation parameters, and the long short-term memory (LSTM) layer models the sequential mapping to predict the dispersion curve. Subsequently, density clustering techniques ensure the quality and validity of the extracted dispersion data, while an optimization algorithm reduces the number of required forward calculations, thereby enhancing inversion efficiency. Comprehensive evaluations on synthetic and field data demonstrate that the workflow provides reliable slowness inversion results with enhanced computational efficiency in both single and joint inversion.
© 2026 Publishing services by Elsevier B.V. on behalf of KeAi Communications Co. Ltd. This is an open access article under the CC BY-NC-ND license (http://creativecommons.org/licenses/by-nc-nd/4.0/).

1. Introduction

Acoustic logging-while-drilling (ALWD) technology has been developed to meet the growing demands of high-angle wells, horizontal wells, and offshore exploration. A key innovation is the quadrupole source, which was designed to estimate formation shear (S) wave slowness while mitigating the interference of the drill-collar wave on the arrival of received waveforms (Tang et al., 2002). However, as a guided wave in the cylindrical borehole waveguide, the quadrupole wave exhibits strong dispersion due to the presence of the drill collar. The phase velocity of the wave varies with frequency and approaches the Scholte wave velocity at high frequencies and the formation S-wave velocity at low frequencies (Tang and Cheng, 2004). Due to the broadband nature of the acoustic source, different frequency components of the wave propagate at different velocities. As a result, the slowness extracted by the non-dispersive slowness-time-coherence (STC) technique (Kimball and Marzetta, 1984; Tang and Cheng, 2004) deviates from the actual formation slowness. This effect is a common influence on borehole-guided waves. For example, the leaky-compressional (P) wave from a monopole tool also becomes dispersive in unconsolidated slow (i.e., ultra-slow) formations. Therefore, the dispersive-wave slowness obtained from the STC processing must be further processed (Cheng, 2015).

The extraction of accurate guided-wave slowness unaffected by dispersion, a process known as dispersion correction from dispersion data generally follows two avenues: data-driven and physics-driven (or model-based) approaches. The data-driven method projects the dispersion data onto the slowness axis and estimates the formation slowness by detecting the low-frequency edge of the projected histogram data (Huang and Yin, 2005; Tang et al., 2010). However, its accuracy is compromised by missing data or a low signal-to-noise ratio (SNR) in the low-frequency range (Lee et al., 2016). The physics-driven method enables the inversion

* Corresponding author.
E-mail address: syuanda@sina.com (Y.-D. Su).
Peer review under the responsibility of China University of Petroleum (Beijing).

https://doi.org/10.1016/j.petsci.2026.06.026
1995-8226/© 2026 Publishing services by Elsevier B.V. on behalf of KeAi Communications Co. Ltd. This is an open access article under the CC BY-NC-ND license (http://creativecommons.org/licenses/by-nc-nd/4.0/).

Please cite this article as: K.-Y. Zheng, Y.-D. Su, X.-H. Gu *et al.*, Fast inversion of formation slowness from LWD acoustic wave modes using deep learning, Petroleum Science, https://doi.org/10.1016/j.petsci.2026.06.026

of formation slowness by fitting the theoretical dispersion curve from a borehole-formation model to the waveforms dispersion data (Xu et al., 2017; Li et al., 2020, 2023; Qi et al., 2024). The key to this approach lies in developing a physical model that accurately simulates dispersion characteristics of guided waves. Given the non-negligible influence of the logging tools on wave propagation, several theoretical models have been proposed (Chen and Willen, 1984; Hsu and Sinha, 1998). Su et al. (2011) extended the equivalent-tool theory to ALWD applications, which not only can simulate tool influence but also reduce the parameters of the physical model. However, the high computational demands of both forward modeling and inversion in physics-driven methods still limit their widespread application.

To improve the efficiency of forward modeling, using a multilayer regression network to substitute for numerical calculations has been demonstrated to be practical in many applications (Assous et al., 2018; Wang et al., 2024). Liang and Lei (2021) developed a fully connected (FC) network to enable the rapid prediction of dispersion curves. However, FC networks require a dense dataset and lengthy training to achieve a good fit in this task, which hinders the efficient development and deployment of diverse formation models. With the development of the network technology, deep learning framework has significantly advanced borehole geophysical applications through its powerful feature extraction capabilities, including well-log reconstruction (Jiang et al., 2022; Lin et al., 2023; Zhang et al., 2024b), reservoir porosity prediction (Yang et al., 2023; Tao et al., 2024), data-driven dispersive processing (Kong et al., 2025) and radial velocity profile inversion (Li et al., 2024), etc. Among various network modules, the convolutional neural network (CNN) is effective at extracting local features, and ResNet can be used to mitigate the vanishing gradient problem associated with deep stacks, which enable efficient feature reuse across layers (He et al., 2016; Zhang et al., 2024a). Meanwhile, LSTM captures global and sequential dependencies within data (Hochreiter and Schmidhuber, 1997), making it particularly well-suited for predicting theoretical dispersion curves. Combining these modules into a ResNet-LSTM hybrid architecture to boost the overall feature capture capacity of the network, allowing it to uncover complex patterns of dispersion curves even with lightweight datasets.

In this study, we construct a dataset based on the principles of physics-driven forward modeling and train a DL model with a ResNet-LSTM architecture designated as the dispersion-curve forward modeling network (DFMNet), to replace the process of numerical forward modeling. The advantage of the method lies in its improved representational capability from local feature extraction and sequential modeling, while the physically simulated dataset enforces meaningful mappings between model inputs and predicted outputs. To enable the application of DFMNet to field data processing, we propose a dispersion correction workflow. First, target dispersion data are extracted from dispersion analysis results (e.g., Prony (Lang et al., 1987), weighted spectral coherence (Tang and Cheng, 2004), or matrix pencil (Ekströzm, 1996) methods), using a density-based clustering technique. Subsequently, DFMNet outputs a theoretical curve fitted to the target dispersion data. Based on the gradient direction of the mismatch error, an optimization method is employed to iteratively invert for the formation slowness that minimizes the error. Finally, we apply the DL-based inversion workflow to both synthetic and field logging-while-drilling acoustic data from diverse formation types, demonstrating that the proposed workflow is capable of performing efficient and robust formation slowness inversion.

2. Dispersion-curve forward modeling network

2.1. Dispersion-curve modeling and dataset construction

The quality of the theoretical dispersion curve dataset is fundamental to model training. In this work, wellbore and formation parameters are treated as sample features, while the corresponding theoretical dispersion curves serve as sample labels. The key to this approach is a reliable numerical model that accurately maps the input parameters to their respective dispersion curves. Fig. 1 shows the model of acoustic logging of an elastic formation with an ALWD tool in the fluid-filled borehole. We employ the equivalent-tool theory (Su et al., 2011) to model the complex ALWD tool as an elastic rod of radius a, and an effective tool modulus M_T, thus eliminating the need to account for the effects of surface isolators and internal circuits on the actual tool. The dispersion equation for an equivalent tool model is given by

$$D\left(\omega, k, v_p, v_s, \rho, v_f, \rho_f, R, a, M_T\right) = \det \boldsymbol{H}(\omega, k) = 0, \tag{1}$$

where ω is the angular frequency, k is the axial wavenumber, v_p, v_s, and ρ are the formation P-, S-wave velocities, and density, respectively; v_f and ρ_f are the mud velocity and density, respectively; R is the borehole radius. Detailed elements of matrix $\boldsymbol{H}$ are detailed in Appendix A. The phase velocity dispersion curve v_{phase} is obtained by solving Eq. (1) for the wavenumber-frequency relationship over the frequency range of interest:

$$v_{phase} = \frac{k}{\omega} \tag{2}$$

Defining the parameter ranges and sampling strategy for the dataset presents another critical challenge. Based on the equivalent-tool model and the related sensitivity analysis in Appendix A, we establish dataset features by integrating the sensitivity analysis results with in situ geological constraints. This approach ensures sample features are sufficiently adaptive to capture dispersion characteristics while avoiding data redundancy. While larger sampling steps are adopted for low-sensitivity parameters (e.g., formation density ρ and mud density ρ_f) to reduce data redundancy, finer intervals are employed for high-sensitivity parameters (e.g., S-wave velocity v_s for the slow formation). To

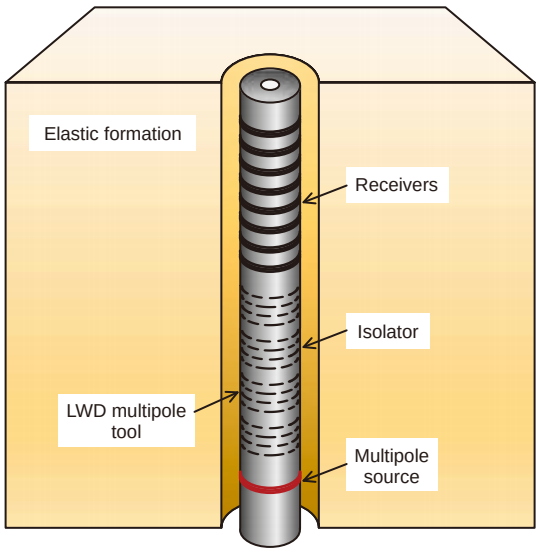


Fig. 1. Model for logging in an elastic formation with an ALWD multipole tool.

ensure the geological plausibility of sample features, we impose parameter bounds conditioned according to the formation type. For example, in the case of a slow formation, we reduce upper bounds on both formation density ρ and S-wave velocity v_s, while for a fast formation, these bounds are extended. Meanwhile, the S-wave velocity upper bound in the slow formation dataset can be somewhat higher than the normal mud velocity to allow for parameter adjustment in the inversion.

Based on the above-described procedure, Tables 1 and 2 give the feature space of monopole P- and quadrupole S-wave dispersion curves dataset, while Eq. (1) maps each sample feature (i.e., parameter combination) to its corresponding label (i.e., dispersion curve). The sizes of the monopole P- and quadrupole S-wave datasets are 386100 and 799920, respectively. This amount of data does not require prohibitive time for label generation using forward modeling. It should be noted that because the network is designed for theoretical forward modeling rather than inversion, data augmentation techniques such as noise injection were not employed. To standardize dimensions, phase velocities below the cutoff frequency are padded with the cutoff-frequency velocity, and each curve is sampled at 0.2 kHz intervals from 0 to 10 kHz for consistent network training.

2.2. DFMNet architecture

In this study, we address the task of forward modeling of theoretical dispersion curves via a ResNet-LSTM architecture (Fig. 2), which involves mapping low-dimensional spatial feature inputs $\mathbf{X} \in \mathbb{R}^{S_{in}}$ to high-dimensional temporal feature outputs $\widehat{\mathbf{Y}} \in \mathbb{R}^{S_{out}}$. Let S_{in} and S_{out} denote the lengths of the input sequence and output sequence, respectively. The mapping can be represented by

$$\widehat{\mathbf{Y}} = \mathrm{f}(\mathbf{X}; \Theta), \tag{3}$$

where f is the network function parameterized by Θ (i.e., weights and biases). The function f is realized by the ResNet-LSTM architecture, which we now describe in detail.

The local feature extraction in the encoder is built upon multiple ResNet modules, which enables the network to capture fine-grained details in dispersion curves, such as the cutoff frequency in the low-frequency band and the rapid slowness variations with frequency in the mid-frequency range. Each module is designed to progressively transform the input sequence through a series of 1D convolutional, batch normalization (BN), and activation function (AF) layers. The BN layers (Ioffe and Szegedy, 2015) are strategically placed after each convolution to mitigate internal covariate shift and enhance training stability. This is followed by AF layers, which employ the rectified linear unit (ReLU) function to introduce non-linearities, essential for approximating complex mappings (Ertuğ;rul, 2018). To ensure efficiency and stability during this dimensional transformation, we incorporate skip connections, which implement a residual learning framework. Given a convolutional stacking block's transformation Conv1D(x), the final output of a residual block Res(x) is expressed as:

$$\mathrm{Res}(x) = \mathrm{Conv1D}(x) + x \tag{4}$$

where x denotes the input to the block. This mechanism facilitates feature reuse from shallow layers, effectively reducing the number of redundant parameters while ensuring the preservation of both fine-grained details and broader trends throughout the network, which is essential for accurately modeling dispersion curves.

The global feature extraction in the encoder begins by applying positional encoding to the local feature outputs, providing the model with dispersion curve sequence order information. These encoded features are first projected into a higher-dimensional space via a FC layer with AF layer. Subsequently, an LSTM layer processes the projected sequence to capture global temporal dependencies. The ability of LSTM to capture long-range patterns relies on its gating mechanism, which selectively updates and propagates information through a cell state C_t. As shown in Fig. 3, the forget gate F_t and input gate I_t determine what historical information to discard and what new information to store:

$$F_t = \sigma(W_F \cdot [h_{t-1}, x_t] + b_F) \tag{5}$$

$$I_t = \sigma(W_I \cdot [h_{t-1}, x_t] + b_I) \tag{6}$$

A candidate cell state $\tilde{C}t$ is then generated based on the current input:

$$\tilde{C}_t = \tanh(W_C \cdot [h_{t-1}, x_t] + b_C) \tag{7}$$

The cell state C_t is updated by combining the previous state with the new candidate values, regulated by the gates:

$$C_t = F_t * C_{t-1} + I_t * \tilde{C}_t \tag{8}$$

The output gate O_t controls the influence of the cell state on the hidden state h_t:

$$O_t = \sigma(W_O \cdot [h_{t-1}, x_t] + b_O) \tag{9}$$

$$h_t = O_t * \tanh(C_t) \tag{10}$$

where σ is the sigmoid function; x_t is the input at time t; h_{t-1} is the previous hidden state; and W_* and b_* are the corresponding

Table 1
Sample features and coverage of monopole P-wave dispersion curves dataset.

Medium	Range	v_p/v_s	v_s, m/s	ρ, kg/m^3	v_f, m/s	ρ_f, kg/m^3	R, m
Slow formation	Lower bound	1.5	400	1500	900	900	0.02 + a
	Upper bound	3.6	1600	2700	1900	2100	0.1 + a
	Step	0.1	100	300	200	300	0.01

Table 2
Sample features and coverage of quadrupole S-wave dispersion curves dataset.

Medium	Range	v_p/v_s	v_s, m/s	ρ, kg/m^3	v_f, m/s	ρ_f, kg/m^3	R, m
Slow formation	Lower bound	1.5	400	1500	900	900	0.02 + a
	Upper bound	3.6	2000	2700	1900	2100	0.1 + a
	Step	0.3	50	300	200	300	0.01
Fast formation	Lower bound	1.5	2000	1700	900	900	0.02 + a
	Upper bound	3.6	3500	3500	1900	2100	0.1 + a
	Step	0.3	100	300	100	300	0.01

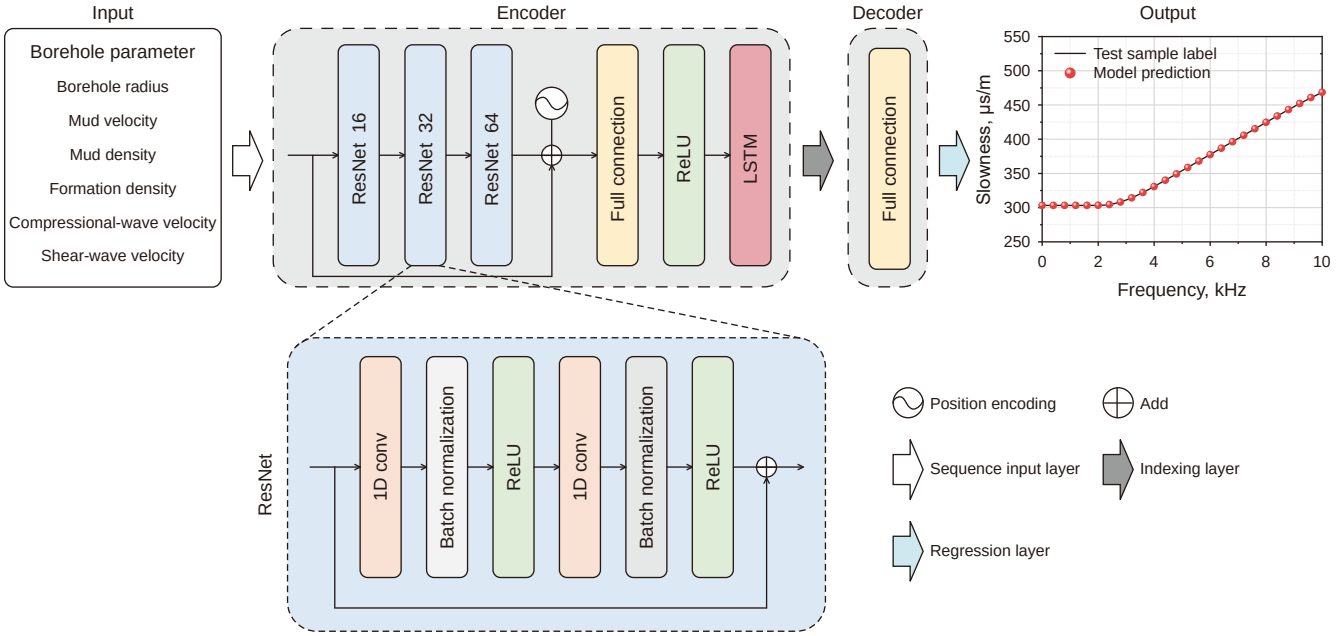


Fig. 2. The architecture of DFMNet. The network mainly contains two parts: the encoder and the decoder. The kernel size in all 1D Conv is 3, and the number of filters in ResNet increases layer-wise to 16, 32, and 64. The channel of the LSTM layer is 128.

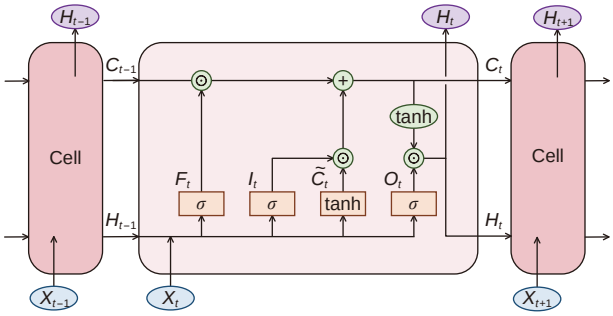


Fig. 3. Schematic diagram of LSTM cell architecture and its operational mechanism. The x_t and h_t are the input and output values, respectively. The long- and short-term memory function of the LSTM layer is cooperatively regulated by four gating structures: the forget gate F_t, input gate I_t, output gate O_t, and candidate memory cell $\tilde{C}t$.

weights and biases. Persistent cell state flow and synergistic gating allow the network to learn the underlying patterns of dispersion curve, holistically modeling the curve morphology across the entire frequency band. Lastly, the output features of LSTM layer are passed through an indexing layer to the decoder, where a final FC layer maps them to the predicted dispersion curve.

2.3. Training results

Model training and performance assessment are conducted using two distinct metrics. The Mean Squared Error (MSE) serves as the loss function during training due to its strong convexity and differentiability, which penalizes large prediction errors and facilitates stable gradient-based optimization. The Mean Relative Error (MRE) is adopted as the evaluation metric to quantify the prediction performance of DFMNet. The two metrics are defined as follows:

$$\mathscr{L}_{\mathrm{MSE}} = \frac{1}{N}\sum_{i=1}^{N}(y_i - \hat{y}_i)^2, \tag{11}$$

$$\mathscr{L}_{\mathrm{MRE}} = \frac{1}{N}\sum_{i=1}^{N}\left|\frac{y_i - \hat{y}_i}{y_i}\right|, \tag{12}$$

where y_i and $\hat{y}i$ are the i-th point of the label curve $\mathbf{Y}$ and the prediction curve $\hat{\mathbf{Y}}$, respectively; N is the total number of curve points. During training, we employ the Adam optimizer (Kingma and Ba, 2014) to minimize $\mathscr{L}_{\mathrm{MSE}}$, leveraging its adaptive learning rate and momentum mechanisms to accelerate convergence. For performance evaluation, $\mathscr{L}_{\mathrm{MRE}}$ is computed on the test set consisting of data not used in training, thereby illustrating the generalization capability of DFMNet.

The DFMNet model were trained using a standardized 9:1 train-test split over 200 epochs with a batch size of 128. Through systematic hyperparameter tuning, the initial learning rate was established at 0.005 with a decay factor of 0.7 applied every 10 epochs. Under this configuration, the ResNet-LSTM architecture demonstrated superior performance compared to the multilayer perceptron (MLP) composed of FC layers in predicting both monopole and quadrupole dispersion curves, as illustrated in Fig. 4. The presented results focus on ultra-slow formation dispersion models, though consistent performance trends were observed across all formation types in our experimental evaluation. For the monopole wave model (Fig. 4(a) and (b)), the ResNet-LSTM architecture achieved a training loss one order of magnitude lower than the MLP counterpart. On the test set, the ResNet-LSTM attained a mean error of 0.00025 with a maximum error of 0.0022, outperforming the MLP which exhibited a mean error of 0.0019 and maximum error of 0.0147 (Table 3). This performance advantage was consistently maintained in the quadrupole wave modeling task (Fig. 4(c) and (d)), where the ResNet-LSTM achieved mean and maximum errors of 0.00014 and 0.0016 respectively, compared to the MLP's 0.0010 and 0.011 (Table 3). While the MLP model can achieve improved performance through data encryption and increased training epochs, ResNet-LSTM architecture

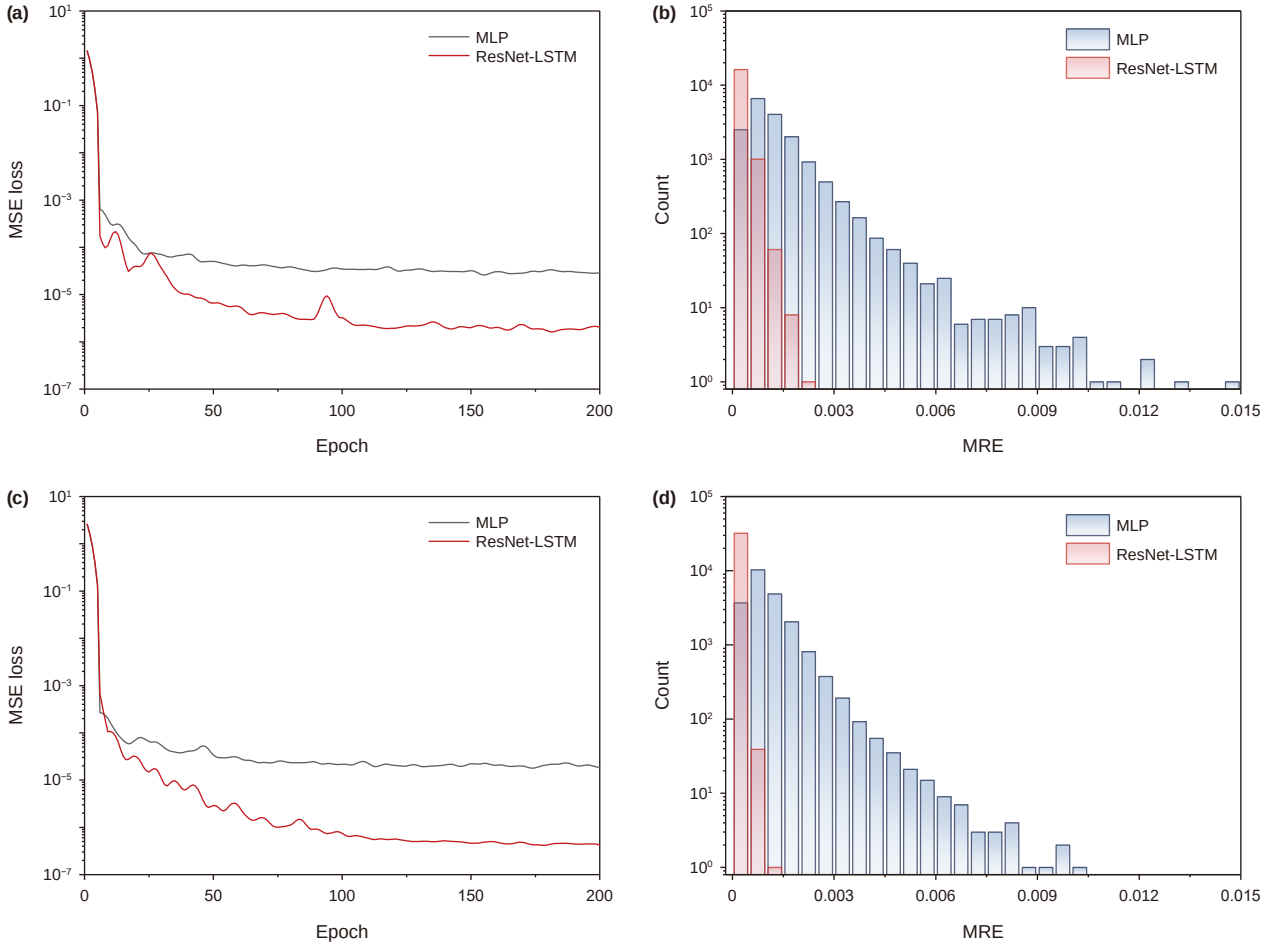


Fig. 4. Evolution of model training loss MSE and test error MRE. **(a)** Training loss for monopole P-wave model. **(b)** Test error for monopole P-wave model. **(c)** Training loss for quadrupole S-wave model. **(d)** Test error for quadrupole S-wave model.

Table 3
Comparison of forward prediction accuracy and computational time across different model architectures.

Method	Monopole P-wave dispersion curve			Quadrupole S-wave dispersion curve		
	Mean error	Max error	1000 curves processing time, s	Mean error	Max error	1000 curves processing time, s
Numerical simulation	–	–	718.489	–	–	310.139
MLP	0.0019	0.0147	0.016	0.0010	0.011	0.018
ResNet-LSTM	0.00025	0.0022	0.022	0.00014	0.0016	0.025

exhibits superior feature extraction capabilities and generalization ability on lightweight datasets. In terms of computational efficiency, the ResNet-LSTM model requires marginally more time than the MLP when processing 1000 dispersion curves, owing to its more complex architectural modules and deeper network structure. Nevertheless, it still represents a substantial improvement over the conventional physics-driven numerical simulation method (Table 3). Considering the trade-off between prediction accuracy and computational cost, the ResNet-LSTM architecture emerges as the more cost-effective choice. The CPU configuration used for the above computational time comparison is the 13th Gen Intel(R) Core(TM) i7-13700.

Fig. 5 further assesses the generalization capability of the ResNet-LSTM architecture by presenting its predictions under unseen formation slowness conditions (within the training set's parameter range) for both monopole and quadrupole waves. The prediction curves (red circle; data thinned for clarity) show a very good agreement with the numerical solution of the dispersion equation (black curve). The consistency of both results is a prerequisite for reliable inversion computations.

3. Slowness inversion workflow

Fig. 6 illustrates the overall workflow for LWD multipole slowness inversion using DFMNet. The main steps are given as follows:

Step I) Dispersion data preprocessing: Initially, the matrix pencil (MP) method is employed to extract dispersion data from waveforms, a process that inherently includes noise and multimode waves. A density-based clustering method is subsequently applied to segregate the dispersion data of different modes. The target dispersion data are then picked by defining cluster boundaries.

Step II) Inversion optimizer iteratively searches for the optimal solution: Once sufficiently trained, DFMNet is deployed to output theoretical dispersion curves. The inversion process is initialized using the formation slowness extracted by STC processing. This initial slowness is fed into DFMNet to generate the corresponding

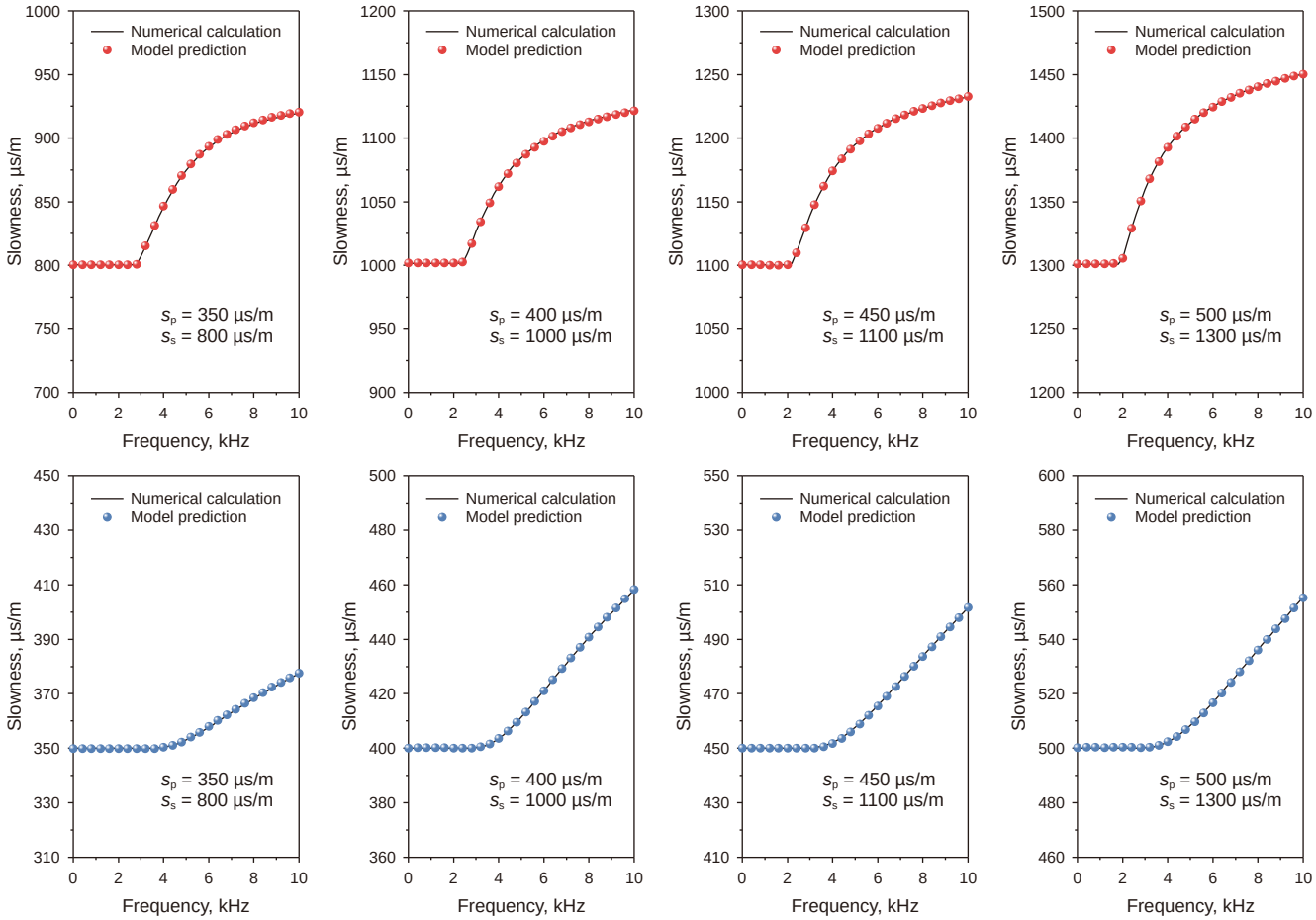


Fig. 5. Comparison of the model prediction and numerical calculation curves under different formation slowness conditions. The upper plots are the comparison for quadrupole S-waves (red). The lower plots are the comparison for the monopole P-wave counterparts in respective formations.

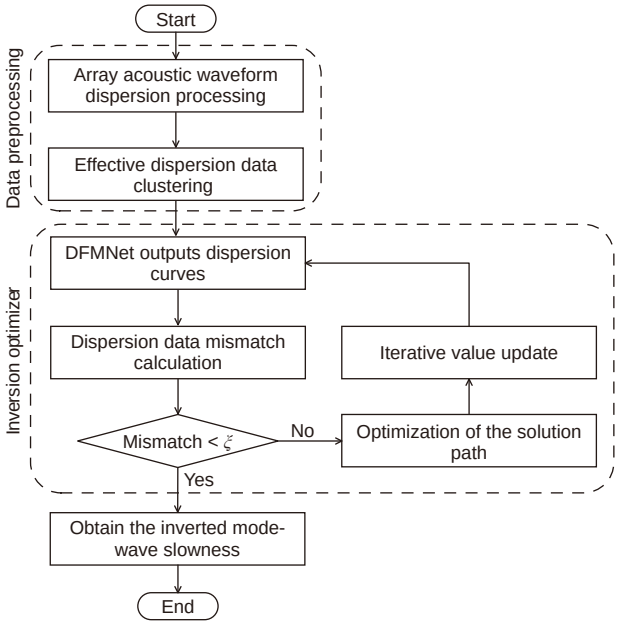


Fig. 6. ALWD slowness inversion workflow diagram. The procedure is divided into (1) data preprocessing to extract robust dispersion data points from waveforms, and (2) an inversion optimizer to iteratively determine the optimal slowness.

theoretical dispersion curve. Subsequently, an objective function computes the mismatch between the predicted curve and the measured dispersion data from Step I. If the mismatch exceeds a predefined threshold ξ, the formation slowness values are updated for the next iteration based on the gradient of the error. This updated slowness is fed back into DFMNet, and the loop continues iteratively until the mismatch between the theoretical and measured dispersion data falls below the threshold ξ. The formation slowness that satisfies this convergence criterion is taken as the final inversion result.

3.1. Target dispersion data clustering

Dispersion data extracted from acoustic logging waveforms are often degraded by noise and, in the case of methods like MP, by mode-mixing effects. In routine processing, this contamination necessitates manual intervention to select the reliable target data for inversion. In this study, we use density-based spatial clustering of applications with noise (DBSCAN) (Ester et al., 1996) to extract valid dispersion data across long well intervals. DBSCAN identifies high-density regions as clusters through two key parameters: the neighborhood radius ε and the minimum number of points (MinPts). Fig. 7(a) shows the clustering process performed by DBSCAN. The algorithm executes clustering through the following steps: (1) A point is designated as a core point (red) if its

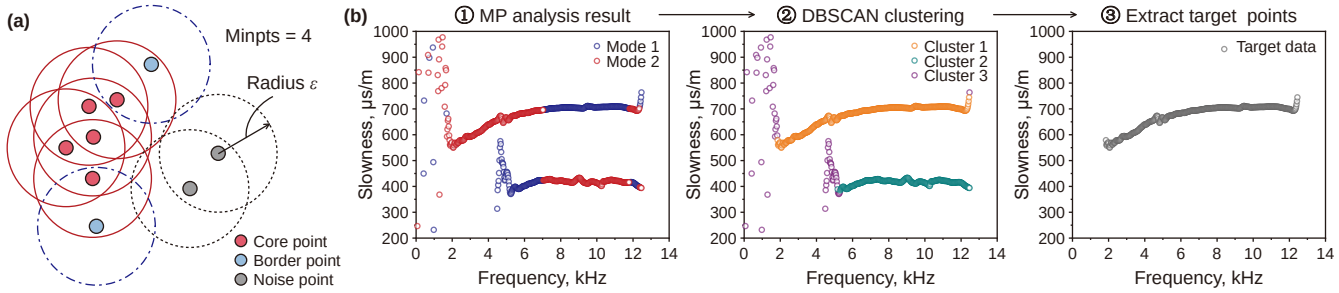


Fig. 7. The principle and the application of the DBSCAN. **(a)** Schematic diagram of the DBSCAN (Minpts = 4) for clustering from discrete points; **(b)** Implementation workflow of DBSCAN for labeling target dispersion data.

ε-neighborhood contains at least MinPts points; (2) Starting from core points, recursively aggregates all density-reachable points to form clusters; (3) Border points (blue) located within the ε-neighborhood of core points are incorporated into the corresponding clusters; (4) Points not assigned to any cluster are classified as noise points (gray).

Fig. 7(b) uses dispersion data derived from MP analysis to demonstrate the workflow for labeling and extracting target dispersion points. The extracted dispersion results exhibit mode aliasing and low-frequency noise. Following normalization of frequency-slowness data points, DBSCAN classification segregates propagating wave modes into Cluster 1 and Cluster 2, with noise categorized as Cluster 3. Finally, by setting the slowness and frequency bounds and extracting the clusters excluding noise within the border, the high SNR data are obtained for the inversion. It is noteworthy that during well-log processing, a predefined set of radius ε and MinPts parameters must be determined based on the point density of dispersion extraction. These parameters should first be debugged at a single depth point to ensure the rationality of clustering results. If the same method is adopted for dispersion data extraction, this predefined parameter set can be transferred and reused for other dispersion data labeling tasks.

3.2. Optimization inversion

The slowness inversion involves fitting theoretical dispersion curves with measured-dispersion data, requiring utilization of high-sensitivity bands of formation velocities to mitigate solution uncertainties (Su et al., 2016). Taking ultra-slow formations as an example, both monopole compressional (MC) and quadrupole shear (QS) waves exhibit significant dispersion effects. As shown in Fig. A2, both monopole P-wave slowness s_P and quadrupole S-wave slowness s_S exhibit high sensitivity within the low-frequency range. The objective function E for the inversion is defined as:

$$E(s_P, s_S) = \lambda \int_{\Omega_1} \left| S_E^{MC}(\omega) - S_T^{MC}(\omega, s_P, s_S) \right|^2 d\omega + (1-\lambda) \int_{\Omega_2} \left| S_E^{QS}(\omega) - S_T^{QS}(\omega, s_P, s_S) \right|^2 d\omega, \quad (13)$$

where S_E and S_T denoted the extracted dispersion data and theoretical dispersion curves, respectively; Ω_1 and Ω_2 represent processing frequency ranges for the monopole and quadrupole waves, respectively; λ serves as a weighting factor to balance the contributions of the two terms in Eq. (13). By appropriately tuning this parameter, the inherent non-uniqueness of the inversion can be effectively mitigated (Su et al., 2016; Li et al., 2020). The objective function retains the theoretical foundation of the conventional physics-driven method but differentiates itself by its implementation strategy. It replaces the numerical forward solver with DFMNet. This strategic substitution dramatically accelerates the output of theoretical dispersion curves while maintaining physical consistency. It should be noted that the dispersion curves predicted by DFMNet are relatively sparse in the frequency domain. Interpolation is applied to align the prediction with the frequency of the dispersion data, thereby enabling a frequency-matched evaluation within the objective function.

To minimize the data misfit defined in Eq. (13), we employ a momentum gradient descent method (Polyak, 1964) to enhance the efficiency and stability of inversion. This optimizer utilizes not only the current gradient $\nabla E(\theta_n)$ but also incorporates a momentum term, which accumulates a velocity vector from past gradients. Governed by a momentum coefficient γ, this term amplifies consistent descent directions and dampens oscillations, allowing for larger effective step sizes and smoother convergence. The update rule is given by:

$$v_n = \gamma \cdot v_{n-1} + \eta \cdot \nabla E(\theta_n), \quad (14)$$

$$\theta_{n+1} = \theta_n - v_n, \quad (15)$$

where n denotes the iteration step; v_n serves as a velocity vector (momentum term) that accumulates historical update information at iteration n, assists in the update of parameters; θ_n denotes the value of the optimization variable at iteration n; η denotes the learning rate. The method is controlled by the learning rate η and the momentum coefficient γ. Analogous to the parameter tuning in density clustering, the two parameters are debugged on a single depth point to ensure reasonable convergence behavior.

3.3. Synthetic data example

To evaluate the inversion performance and the time consumption of the proposed workflow, we use synthetic waveforms of the ultra-slow formation for testing. We first generate LWD monopole and quadrupole array waveforms using the parameters listed in Table A1, with the drill collar wave suppressed to isolate the formation leaky-P and screw wave (Fig. 8(a) and (c)). The dispersion effect on the waveform morphology becomes increasingly evident with larger receiver offsets, which accounts for the inaccuracies in the STC processing method. As shown in Fig. 8(b) and (d), the formation slowness extracted by STC processing (DTP and DTS, corresponding to the high coherence in the figures) exceeds the theoretical parameter values employed in the waveform simulation (TDTP and TDTS).

To achieve reliable slowness estimation, we need to employ inversion. The physics-driven method serves as a benchmark for performance comparison. Here, dispersion analysis is performed

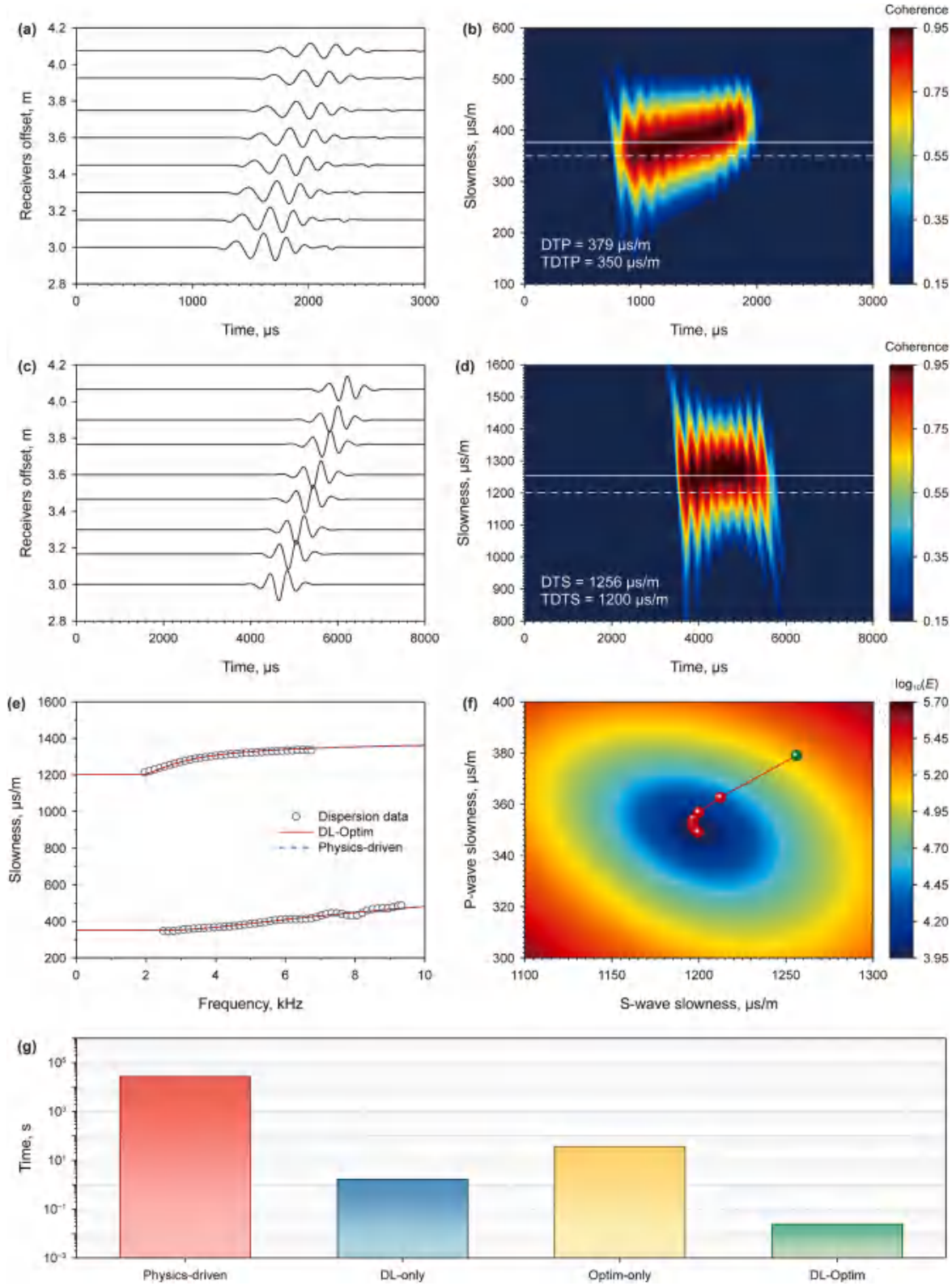


Fig. 8. Performance evaluation of the inversion workflow using synthetic ultra-slow formation data. **(a)** and **(c)** Monopole and quadrupole array waveforms. **(b)** and **(d)** Comparison of STC-processed slowness (DTP and DTS, white solid line) with the theoretical formation slowness (TDTP and TDTS, white dashed line). **(e)** Comparison of inverted dispersion curve from different inversion methods. **(f)** Solution paths of interpolation and optimization inversion. **(g)** The computational costs of different inversion methods.

on the waveforms prior to inversion. As the waveforms are synthetically generated, the extracted dispersion data exhibits a high SNR (without the need for clustering), thereby providing a reliable basis for evaluating the effectiveness of the inversion methods. As shown in Fig. 8(e), both inversion methods yield consistent slowness estimates that closely fit the measured dispersion data. The inverted slowness, determined by the low cutoff-frequency, agrees with the corresponding theoretical values. However, the underlying inversion processes differ significantly (Fig. 8(f)). The conventional physics-driven method evaluates all possible parameter combinations across the predefined slowness range and identifies the optimal set by minimizing the mismatch, with each theoretical dispersion curve computed via numerical iterative calculation. In contrast, the proposed workflow employs gradient-based optimization to iteratively update the slowness values, drastically reducing the number of parameter combinations required. Owing to the low non-uniqueness of the inversion problem, the optimization converges rapidly and is insensitive to the initial slowness value. Moreover, it replaces the numerical solver with DFMNet, accelerating the forward modeling step. These synergistic improvements ultimately result in a reduction in computation time. To isolate the contribution of each architectural component, Fig. 8(g) reports the exact computational costs for the DFMNet-only configuration (1.664 s), the optimization-only baseline (36.293 s), and the conventional physics-driven method (27102.326 s). While each module independently reduces processing time relative to the conventional approach, their integrated architecture produces a synergistic effect that drastically enhances computational efficiency, achieving an inference time of merely 0.024 s per depth point.

4. Field data application

4.1. Moderately fast formation example

Using the proposed inversion workflow, Fig. 9 shows the processing results for a moderately fast formation interval of 500 m. Panel 1 shows the original well-log data. The first trace is the gamma ray and borehole caliper curves. The second and third traces are variable-density plots of monopole and quadrupole full-waveforms, respectively. The P- and S-wave slowness obtained from monopole (blue) and quadrupole (black) waveforms by STC processing are shown in panels 2 and 3. The S-wave slowness extracted from the quadrupole waveforms is higher than that from the monopole waveforms due to the quadrupole screw wave dispersion effect. Since the dispersion effect of P-waves is negligible in a moderately fast formation, only the quadrupole S-wave

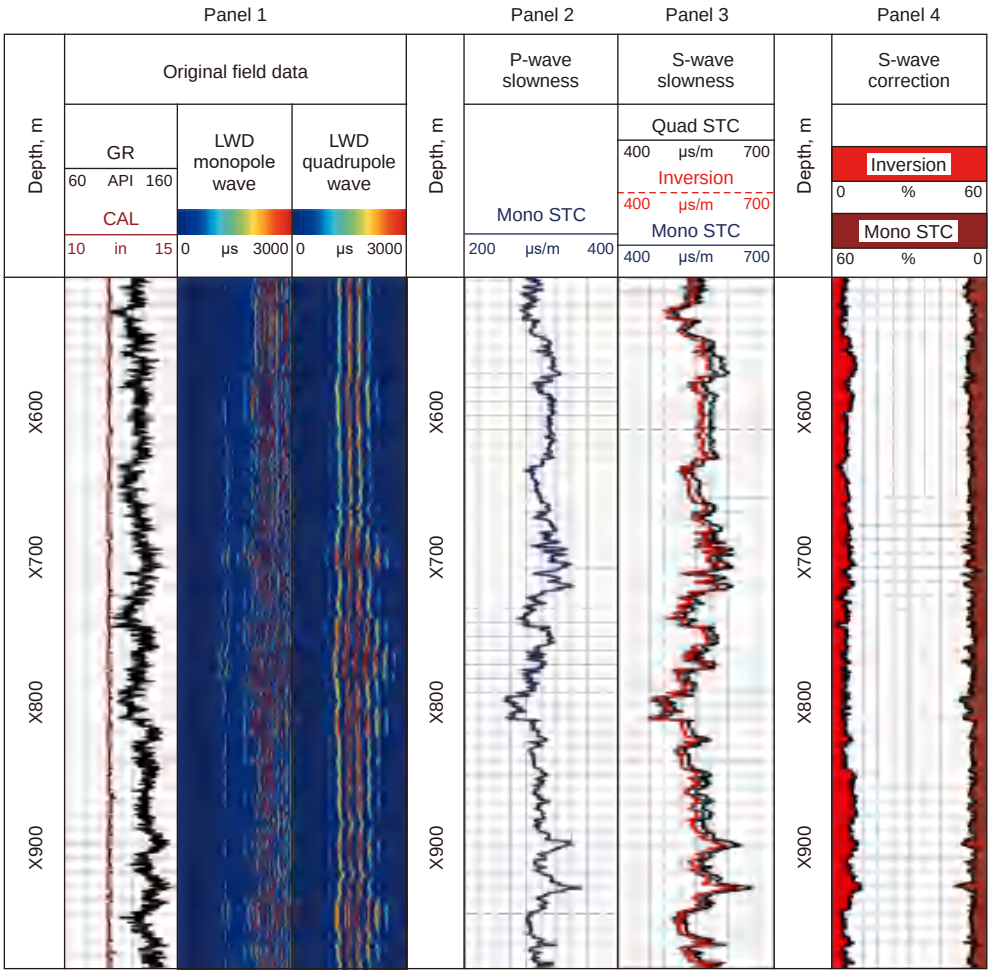


Fig. 9. The application of the inversion workflow to estimate the S-wave slowness of a fast formation. Panel 1 shows the monopole- and quadrupole-wave raw data and conventional log curves. Panel 2 shows the STC result of the monopole P-wave. Panel 3 shows the S-wave slowness results from different methods: the STC (black) and the inversion (red) of quadrupole S-wave slowness; the latter overlays with the monopole S-wave slowness (blue) very well. Panel 4 compares the percentage corrections of the latter two S-wave slowness curves relative to the first curve.

slowness is inverted in this formation interval. The objective function simplifies to the first term in Eq. (13):

$$E(s_S) = \int_{\Omega_1} \left| S_E^{QS}(\omega) - S_T^{QS}(\omega, s_S) \right|^2 d\omega. \quad (16)$$

As S-wave slowness extracted from monopole waveforms using STC processing is less sensitive to dispersion effects, it provides a reliable reference used to verify the accuracy of the S-wave slowness inversion in this test example. The inverted quadrupole S-wave slowness curve (red) closely matches the monopole S-wave slowness curve (blue) in panel 3, with a relative error of approximately 1–6% between the two curves. Using the STC-extracted quadrupole S-wave slowness as the reference, panel 4 further shows that the percentage difference between the inverted S-wave slowness and the reference (plotted left to right) and that of the monopole S-wave slowness (plotted right to left) is quite consistent with each other. The excellent agreement demonstrates the validity of the proposed method in fast formations. Additionally, a primary advantage of this inversion workflow is the high computational efficiency. By leveraging dispersion data extracted directly from waveforms and accelerated with parallel computing across 8 CPU cores, the method processes a 500 m well section in just 7.5 s (at 65 m/s).

4.2. Ultra-slow formation example

The ultra-slow formation example (Fig. 10) further demonstrates the advantage of the proposed joint inversion method. Panel 1 shows the original well-log data. The first trace is the gamma ray and borehole caliper curves of the formation interval. The second and third traces are variable-density plots of monopole and quadrupole full-waveforms, respectively. In ultra-slow formations, both the measured monopole and quadrupole waves exhibit dispersion, necessitating corrections to STC-extracted results. This study utilizes joint inversion results from the physics-driven method from Su et al. (2016) as a benchmark reference to validate the proposed method. The monopole P- and quadrupole S-wave slowness inversion results (red) in panels 2 and 3, respectively, closely match the reference curves (blue), exhibiting relative errors of 1–8% across the full well section, while their deviation from the STC-extracted results (black) quantifies the required dispersion correction. The percentage corrections of the monopole P- (quadrupole S-) wave slowness for the DL-based and physics-driven inversion methods are shown in panel 4 (panel 5), denoted by the red- and coffee-shaded curves, respectively. The agreement between the two results validates the proposed inversion workflow. Meanwhile, the proposed method offers superior computational efficiency compared to the physics-driven method. It processes a 600 m well section in merely 15 s, yielding a processing speed of 40 m/s. Although the joint inversion in the ultra-slow formation incurs a higher computational load and thus runs slower than in the moderately fast formation, its speed remains notable. Simultaneously, the integration of the density-based clustering method enhances the SNR of the formation dispersion data used for inversion. This advancement reduces the need for manual intervention, thereby significantly promoting the streamline of the slowness inversion.

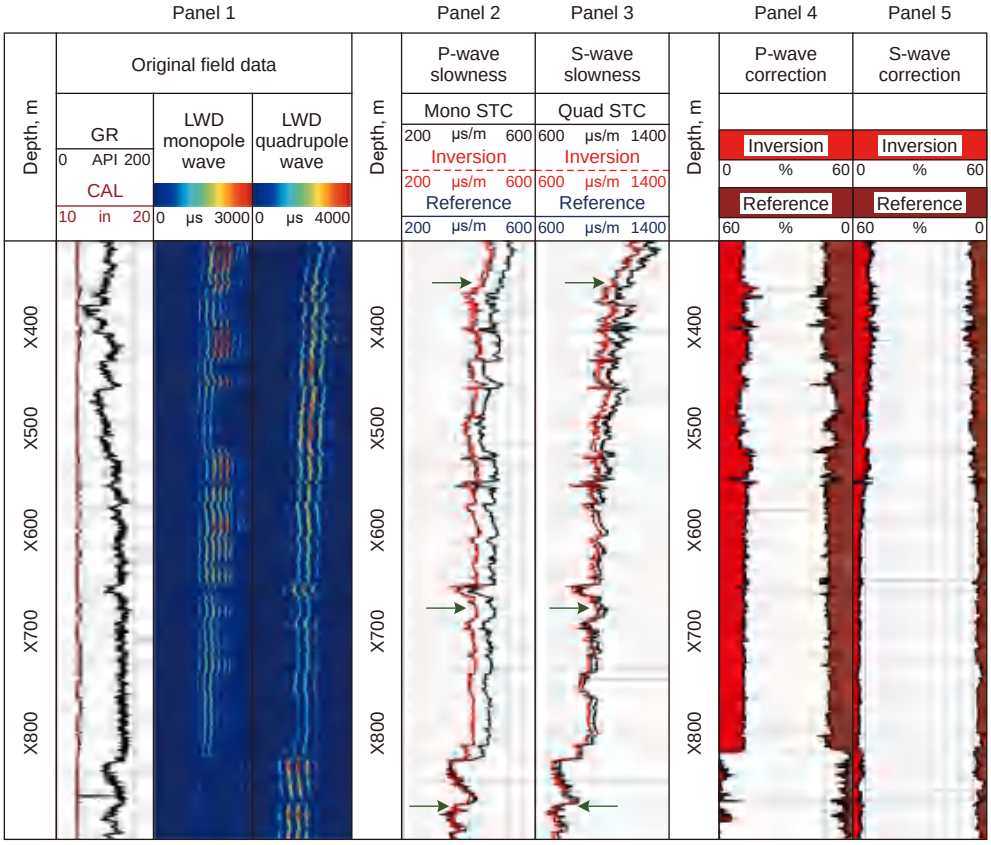


Fig. 10. The application of the proposed workflow to invert P- and S-wave slowness of ultra-slow formation. Panel 1 shows the monopole- and quadrupole-wave raw data and conventional log curves. Panels 2 and 3 show, respectively, the P- and S-wave slowness results from STC-extracted (black), the DL-based (red), and the physics-driven (blue) inversion. Panels 4 and 5 compare the percentage corrections of DL-based (red shading) and physics-driven (coffee shading) methods for monopole and quadrupole wave data, respectively.

To further demonstrate the effectiveness of the density-based clustering and optimization methods for inversion, Fig. 11 illustrates the key features of the inversion procedure using three depth points of Fig. 10 (pointed by arrows) with different formation slowness values. In Fig. 11(a)–(c), and (e), orange and black circles denote dispersion data points of the target mode waves before and after applying DBSCAN, respectively. Compared to conventional methods that select short segments of high-SNR dispersion data for inversion, the DBSCAN method allows for the utilization of all valid dispersion data while filtering out scattered data points. Blue and red curves denote the theoretical dispersion curves before and after inversion, respectively. The post-inversion curve exhibits excellent agreement with the target dispersion data. The objective function plots in Fig. 11(b)–(d), and (f) illustrate the gradient-guided trajectory of the inversion iteration. Using the momentum gradient descent method, the global minimum of the objective function can be quickly located in just a few iterations. For the three chosen depths, P-wave dispersion decreases with decreasing slowness, while S-wave dispersion correction is still quite significant. As shown in Fig. 10 (panels 4 and 5), P-wave

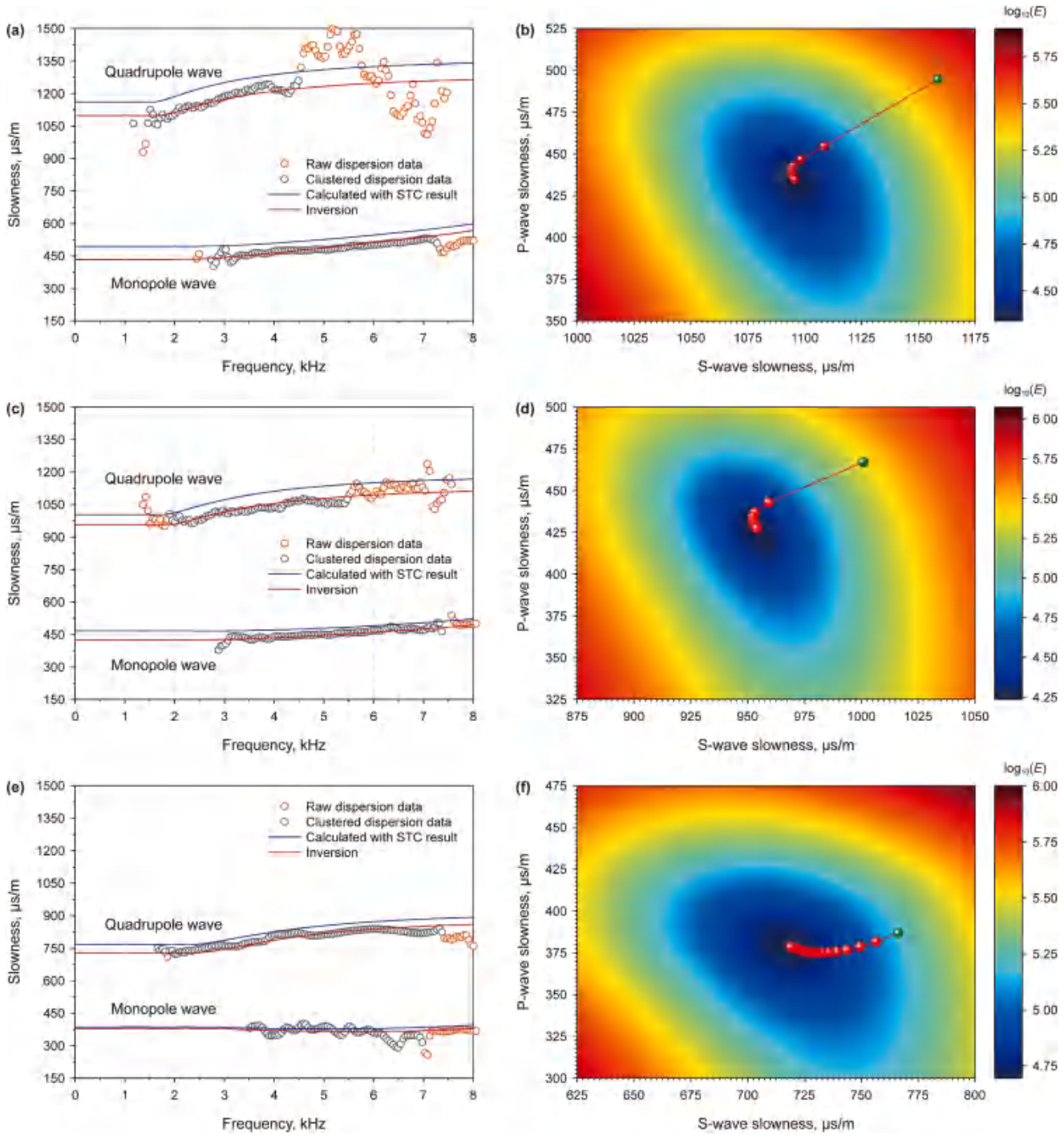


Fig. 11. Key features of the inversion at three selected depth points from Fig. 10 **(a)**, **(c)**, and **(e)** show details of the dispersion data fitting: the inversion-fitted dispersion curve (red) overlays the data (markers), while the curve without inversion (black) deviates from the data. **(b)**, **(d)**, and **(f)** illustrate the inversion optimization process, where the optimization follows a steeply descending trajectory toward the minimum of the objective function.

corrections average 12% in the upper formation but decrease to less than 6% in the lower formation. In contrast, S-wave corrections maintain consistent values between 6 and 8% throughout the entire well section, consistent with the individual analysis results of Fig. 11. The above application examples and result analyses show that the DL-based inversion workflow can be applied to diverse formations to obtain accurate formation guided-wave slowness from ALWD data. The inversion procedure is both efficient and robust, offering an effective and economic tool for ALWD applications.

5. Conclusions

The dispersion effect in the LWD multipole acoustic data significantly affects the accuracy of the slowness determination, and its correction is computationally expensive. A DL-based inversion workflow has been developed to greatly improve the correction efficiency while maintaining accuracy, thereby optimizing the existing mainstream paradigm. We develop a dispersion curve dataset based on equivalent-tool theory, along with a ResNet-LSTM architecture termed DFMNet. Error analysis confirms the generalization and feature extraction capabilities of DFMNet, demonstrating that model prediction can be achieved even when trained on lightweight datasets. Furthermore, we employ an adaptive clustering method for labeling of target dispersion data via the DBSCAN and utilize the momentum gradient descent method to optimize the inversion. Combining these methods with DFMNet forms a stable and efficient inversion workflow for ALWD data processing. The workflow has been applied to ALWD data acquired in diverse formations. The results, compared with those from the existing physics-driven method, further support the accuracy, robustness, and, most importantly, efficiency of the new DL-based workflow. While a key limitation of physics-driven dispersion curve is that the curves become inaccurate when the assumed physical model deviates from the actual formation, both the DFMNet architecture and the dataset generation strategy are extendable to other LWD acoustic modes (e.g., dipole flexural waves) or other complex formations (e.g., heterogeneous and anisotropic formations), offering a scalable and promising tool for ALWD data processing.

CRediT authorship contribution statement

Kai-Yin Zheng: Writing – original draft, Visualization, Validation. **Yuan-Da Su:** Writing – review & editing, Funding acquisition, Data curation. **Xi-Hao Gu:** Methodology, Investigation. **Sheng-Qing Li:** Supervision, Funding acquisition. **Chun-Xi Zhuang:** Software. **Xiao-Ming Tang:** Supervision, Resources.

Declaration of competing interests

The authors declare that they have no known competing financial interests or personal relationships that could have appeared to influence the work reported in this paper.

Acknowledgments

This study was supported by the National Natural Science Foundation of China (Grant No. 42574180, 42574150) and the Shandong Provincial Natural Science Foundation (Grant No. ZR2024YQ062).

Appendix A. LWD multipole wave dispersion equation and the related sensitivity analysis based on equivalent-tool theory

Matrix **H** of the multipole wave dispersion Eq. (1) for an elastic formation surrounding a fluid-filled borehole with an LWD tool at its center is given by:

$$\begin{cases} H_{11} = -\left[\frac{n}{R}I_n(fR) + fI_{n+1}(fR)\right] - E_{\text{tool}}\left[\frac{n}{R}K_n(fR) - fK_{n+1}(fR)\right] \\ H_{12} = \left[\frac{n}{R}K_n(pR) - pK_{n+1}(pR)\right] \\ H_{13} = \frac{n}{R}K_n(sR) \\ H_{14} = \mathrm{i}k\left[\frac{n}{R}K_n(sR) - sK_{n+1}(sR)\right] \end{cases}, \tag{A-1}$$

$$\begin{cases} H_{21} = \rho_{\text{f}}\omega^2[I_n(fR) + E_{\text{tool}}K_n(fR)] \\ H_{22} = 2\rho v_{\text{s}}^2\left[\left(\frac{n^2-n}{R^2} + k^2\right)K_n(pR) + \frac{p}{R}K_{n+1}(pR)\right] - \rho\omega^2 K_n(pR) \\ H_{23} = 2\rho v_{\text{s}}^2\left[\frac{n^2-n}{R^2}K_n(sR) - \frac{ns}{R}K_{n+1}(sR)\right] \\ H_{24} = 2\mathrm{i}k\rho v_{\text{s}}^2\left[\left(\frac{n^2-n}{R^2} + s^2\right)K_n(sR) + \frac{s}{R}K_{n+1}(sR)\right] \end{cases}, \tag{A-2}$$

$$\begin{cases} H_{31} = 0 \\ H_{32} = 2\rho v_{\text{s}}^2\left[\frac{n^2-n}{R^2}K_n(pR) + \frac{np}{R}K_{n+1}(pR)\right] \\ H_{33} = 2\rho v_{\text{s}}^2\left[\left(\frac{n^2-n}{R^2} - \frac{s^2}{2}\right)K_n(sR) - \frac{s}{R}K_{n+1}(sR)\right] \\ H_{34} = 2\mathrm{i}k\rho v_{\text{s}}^2\left[\frac{n^2-n}{R^2}K_n(sR) + \frac{ns}{R}K_{n+1}(sR)\right] \end{cases}, \tag{A-3}$$

and

$$\begin{cases} H_{41} = 0 \\ H_{42} = 2ik\rho v_{\text{s}}^2\left[\frac{n}{R}K_n(pR) - pK_{n+1}(pR)\right] \\ H_{43} = \frac{ikn\rho v_{\text{s}}^2}{R}K_n(sR) \\ H_{44} = -\left(k^2 + s^2\right)\rho v_{\text{s}}^2\left[\frac{n}{R}K_n(sR) - sK_{n+1}(sR)\right] \end{cases}, \tag{A-4}$$

where I_n and K_n (n = 0, 1, 2) denote the first- and second-kind modified Bessel functions of the nth order, respectively. The radial wavenumbers for the borehole fluid and formation P and S waves are given by:

$$\begin{cases} f = \sqrt{k^2 + \left(\omega/v_{\text{f}}\right)^2} \\ p = \sqrt{k^2 + \left(\omega/v_{\text{p}}\right)^2} \\ s = \sqrt{k^2 + \left(\omega/v_{\text{s}}\right)^2} \end{cases}. \tag{A-5}$$

Appearing in D_{11} and D_{21} of Eqs. (A-1) and (A-2) is the coefficient E_{tool}, which is obtained by matching the instrument's

acoustic admittance at its surface with the fluid's acoustic admittance, and involves a combination of Bessel functions related to the elasticity of logging tools (Tang and Cheng, 2004; Su et al., 2011):

$$E_{\text{tool}} = \frac{B_n}{A_n} = -\frac{\frac{n}{a}I_n(fa) + fI_{n+1}(fa) - Y\rho_f\omega^2 I_n(fa)}{\frac{n}{a}K_n(fa) - fK_{n+1}(fa) - Y\rho_f\omega^2 K_n(fa)}, \quad \text{(A-6)}$$

where a and M_T are the tool radius and modulus to simulate the effect of logging tools.

Fig. A1 shows the dispersion curve calculated using the equivalent-tool theory (red) for the slow formation. It agrees closely with the conventional cylindrical shell model (blue) and exhibits a deviation from the no-tool model (black). The minor discrepancy with the cylindrical shell model is far smaller than the interference from noise in field data and does not affect subsequent dataset construction and inversion. In addition to maintaining high accuracy, the equivalent-tool model reduces computation time by approximately 68% relative to the conventional cylindrical shell model. As exemplified in Fig. A1 case, the simulation times are 0.20 s (no-tool), 0.97 s (conventional), and 0.31 s (equivalent-tool). The efficiency gains significantly reduce the computational overhead of training dataset generation.

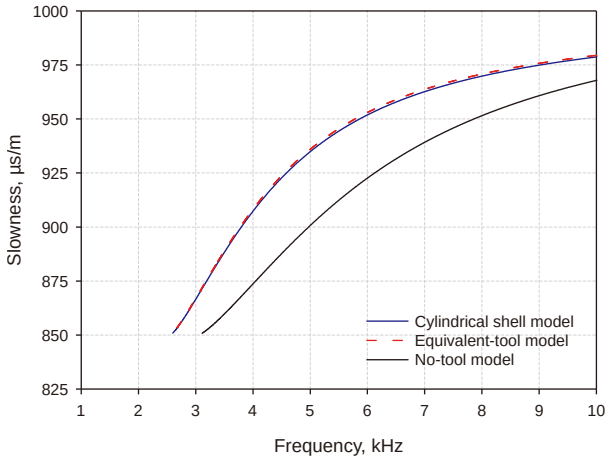


Fig. A1. The comparison of quadrupole S-wave dispersion curves of the cylindrical shell (solid blue), equivalent-tool (dashed red), and no-tool (black solid) models. The formation parameters are listed in Table A1 (slow formation).

The sensitivity of dispersion curves to wellbore and formation parameters across different frequency bands can be quantified using the following equation (Cheng et al., 1982):

$$\text{SN}(\omega, p) = \frac{p}{v_{\text{phase}}(\omega, p)} \cdot \frac{\partial v_{\text{phase}}(\omega, p)}{\partial p}, \quad \text{(A-7)}$$

where $\text{SN}(\omega, p)$ refers to the sensitivity of the dispersion curve to model parameter p listed in Table A1. The sensitivity analysis in Fig. A2 reveals distinct parameter influences across formations. For fast formations, quadrupole wave dispersion shows high sensitivity to S-wave velocity at low frequencies and even higher sensitivity to mud velocity at higher frequencies, while the sensitivity of the remaining parameters across the full frequency band falls within the range of −0.4 to 0.4. For slow and ultra-slow formations, S-wave velocity dominates across the entire frequency spectrum, with the sensitivity of the other parameters lying within −0.2 to 0.2. In ultra-slow formations, monopole P-wave dispersion is primarily controlled by P- and S-wave velocities together with borehole radius, and the sensitivity of the remaining parameters stays within −0.4 to 0.4. Based on the above analysis, we distinguish high-sensitivity from low-sensitivity parameters by whether the absolute value of sensitivity exceeds 0.4. The classification according to this criterion serves as an important guide in dataset construction.

Table A1
Parameters of drill collar and formation for simulating the LWD multipole waves.

Medium	P-wave slowness, μs/m	S-wave slowness, μs/m	Density, kg/m^3	Inner radius, m	Outside radius, m
Drill collar	171	319	7850	0.027	0.089
Borehole fluid	700	—	1200	0	0.12
Fast formation	250	400	2500	0.12	∞
Slow formation	400	850	2500	0.12	∞
Ultra-slow formation	350	1200	2000	0.12	∞

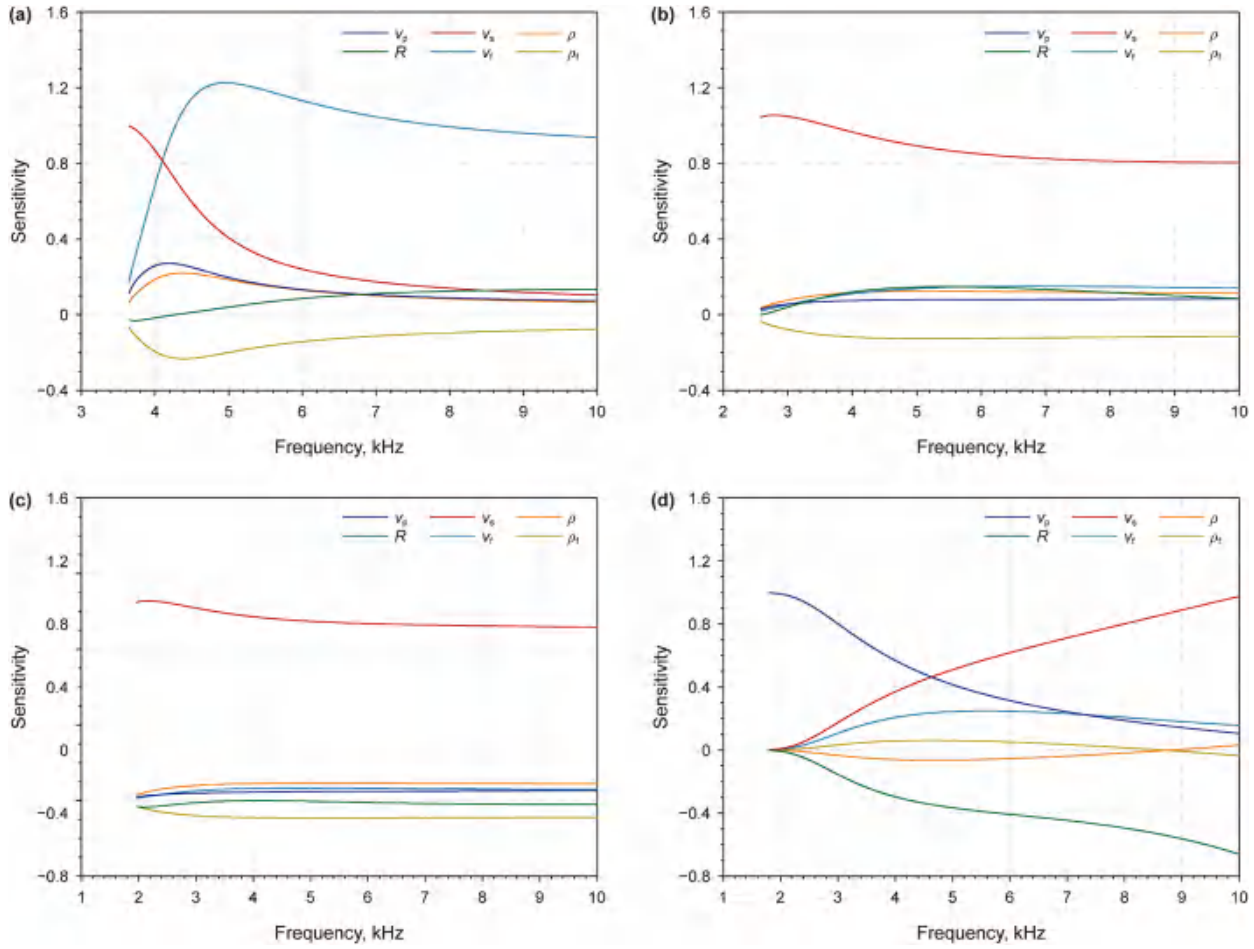


Fig. A2. Sensitivity analysis for the quadrupole S- and monopole P-wave modes. **(a)** Quadrupole S-wave mode in fast formation. **(b)** Quadrupole S-wave mode in slow formation. **(c)** Quadrupole S-wave mode in ultra-slow formation. **(d)** Monopole P-wave mode in ultra-slow formation.

References

Assous, S., Tudge, J., Whetton, J., Elkington, P., 2018. Dispersive mode processing of borehole acoustic logs using fast slowness-frequency inversion. In: Abu Dhabi International Petroleum Exhibition & Conference.

Chen, S., Willen, D., 1984. Shear wave logging in slow formations. In: 25th Annual Logging Symposium, SPWLA. Extended Abstracts.

Cheng, C.H., 2015. Can we ever trust the shear-wave log? Lead. Edge 34, 278–284. https://doi.org/10.1190/tle34030278.1.

Cheng, C.H., Toksöz, M.N., Willis, M.E., 1982. Determination of in situ attenuation from full waveform acoustic logs. J. Geophys. Res. Solid Earth 87, 5477–5484. https://doi.org/10.1029/JB087iB07p05477.

Ekströzm, M.P., 1996. Dispersion estimation from borehole acoustic arrays using a modified matrix pencil algorithm. In: Conference Record of the 29th Asilomar Conference on Signals, Systems and Computers, pp. 449–453.

Ertuğrul, Ö.F., 2018. A novel type of activation function in artificial neural networks: trained activation function. Neural Netw. 99, 148–157. https://doi.org/10.1016/j.neunet.2018.01.007.

Ester, M., Kriegel, H., Sander, J., Xu, X., 1996. A density-based algorithm for discovering clusters in large spatial databases with noise. In: Proceedings of 2nd International Conference on Knowledge Discovery and Data Mining, pp. 226–231.

He, K.M., Zhang, X.Y., Ren, S.Q., Sun, J., 2016. Deep residual learning for image recognition. In: IEEE Conference on Computer Vision and Pattern Recognition, pp. 770–778.

Hochreiter, S., Schmidhuber, J., 1997. Long short-term memory. Neural Comput. 9 (8), 1735–1780. https://doi.org/10.1162/neco.1997.9.8.1735.

Hsu, C.J., Sinha, B.K., 1998. Mandrel effects on the dipole flexural mode in a borehole. J. Acoust. Soc. Am. 104, 2025–2039. https://doi.org/10.1121/1.423767.

Huang, X., Yin, H., 2005. A data-driven approach to extract shear and compressional slowness from dispersive waveform data. In: SEG Technical Program Expanded Abstracts, pp. 384–387.

Ioffe, S., Szegedy, C., 2015. Batch normalization: accelerating deep network training by reducing internal covariate shift. In: 32nd International Conference on Machine Learning, pp. 448–456.

Jiang, C.B., Zhang, D.X., Chen, S.F., 2022. Handling missing data in well-log curves with a gated graph neural network. Geophysics 88 (1), D13–D30. https://doi.org/10.1190/geo2022-0028.1.

Kimball, C.V., Marzetta, T.L., 1984. Semblance processing of borehole acoustic array data. Geophysics 49 (3), 274–281. https://doi.org/10.1190/1.1441659.

Kingma, D.P., Ba, J., 2014. Adam: a Method for Stochastic Optimization arXiv: 1412.6980.

Kong, F.T., Liu, Y.X., Zhang, B.Q., et al., 2025. A dispersive processing of borehole guided wave data using multitask physics-informed deep learning. IEEE Trans. Geosci. Rem. Sens. 63, 1–13. https://doi.org/10.1109/tgrs.2025.3642437.

Lang, S., Kurkjian, A., McClellan, J., et al., 1987. Estimating slowness dispersion from arrays of sonic logging waveforms. Geophysics 52, 530–544. https://doi.org/10.1190/1.1442322.

Lee, S.Q., Tang, X.M., Su, Y.D., Zhuang, C.X., 2016. Model-based dispersive processing of borehole dipole wave data using an equivalent-tool theory. Geophysics 81 (1), D35–D43. https://doi.org/10.1190/geo2015-0210.1.

Li, J.C., He, X., Chen, H., et al., 2024. Inversion of radial shear velocity profile for acoustic logging using CNN-LSTM network. IEEE Trans. Geosci. Rem. Sens. 62, 1–10. https://doi.org/10.1109/tgrs.2024.3370106.

Li, J.C., He, X., Zhao, A.S., Jiang, C., 2023. Joint inversion of formation radial shear-velocity profiles by dipole acoustic logging while drilling. Geophysics 88 (4), D295–D305. https://doi.org/10.1190/geo2022-0426.1.

Li, Y.H., Xu, S., Jiang, C., et al., 2020. Joint inversion of logging-while-drilling multipole acoustic data to determine formation shear-wave transverse isotropy. Geophysics 85 (4), D121–D132. https://doi.org/10.1190/geo2019-0611.1.

Lin, L., Wei, H., Wu, T.T., et al., 2023. Missing well-log reconstruction using a sequence self-attention deep-learning framework. Geophysics 88 (6), D391–D410. https://doi.org/10.1190/geo2022-0757.1.

Liang, L., Lei, T., 2021. Machine-learning-enabled automatic sonic shear processing. Petrophysics 62, 282–295. https://doi.org/10.30632/pjv62n3-2021a3.

Polyak, B.T., 1964. Some methods of speeding up the convergence of iteration methods. USSR Comput. Math. Math. Phys. 4 (5), 1–17.

Qi, Q.M., Xue, Y.J., Cao, J.X., Wang, X.J., 2024. Inversion of shear wave slowness and attenuation from dipole acoustic logging data based on an equivalent tool theory. Geophysics 89 (4), D255–D265. https://doi.org/10.1190/geo2023-0587.1.

Su, Y.D., Jiang, C., Zhuang, C.X., et al., 2016. Joint inversion of logging-while-drilling multipole acoustic data to determine P- and S-wave velocities in unconsolidated slow formations. Geophysics 81 (5), D553–D560. https://doi.org/10.1190/geo2016-0133.1.

Su, Y.D., Tang, X.M., Hei, C., Zhuang, C.X., 2011. An equivalent tool theory for acoustic logging and applications. Appl. Geophys. 8, 69–78. https://doi.org/10.1007/s11770-011-0272-6.

Tang, X.M., Cheng, C.H., 2004. Quantitative Borehole Acoustic Methods. Elsevier Science Publishing Co.

Tang, X.M., Dubinsky, V., Wang, T., et al., 2002. Shear-velocity measurement in the logging-while-drilling environment: modeling and field evaluations. In: SPWLA 43rd Annual Logging Symposium.

Tang, X.M., Li, C., Patterson, D., 2010. A curve-fitting technique for determining dispersion characteristics of guided elastic waves. Geophysics 75 (3), E153–E160. https://doi.org/10.1190/1.3420736.

Tao, B.C., Liu, X.Y., Zhou, H.L., et al., 2024. Porosity prediction based on a structural modeling deep-learning method. Geophysics 89 (6), M197–M210. https://doi.org/10.1190/geo2024-0035.1.

Wang, L., Han, Y.Y., Li, Z.Q., et al., 2024. The joint physics and data-driven geometrical factor of array laterolog in layered formations. Geophysics 90 (1), D11–D25. https://doi.org/10.1190/geo2024-0112.1.

Xu, S., Tang, X.M., Su, Y.D., et al., 2017. Determining formation S-wave transverse isotropy from borehole flexural-wave dispersion data. Geophysics 82 (2), D47–D55. https://doi.org/10.1190/geo2016-0223.1.

Yang, L.Q., Fomel, S., Wang, S.D., et al., 2023. Porosity and permeability prediction using a transformer and periodic long short-term network. Geophysics 88 (1), WA293–WA308. https://doi.org/10.1190/geo2022-0150.1.

Zhang, H.Y., Wu, W.S., Song, X.Y., 2024a. Well logs reconstruction based on deep learning technology. IEEE Geosci. Remote Sens. Lett. 21, 1–5. https://doi.org/10.1109/lgrs.2024.3354210.

Zhang, H.J., Sun, Z., Li, X., et al., 2024b. Deep learning approach to inverting flexural wave dispersion. In: Fourth International Meeting for Applied Geoscience & Energy, pp. 439–443.

Petroleum Science xxx (xxxx) xxx

Contents lists available at ScienceDirect

Petroleum Science

journal homepage: www.keaipublishing.com/en/journals/petroleum-science



Original Paper

Inversion of S-wave transverse isotropy from acoustic logging-while-drilling data using a CNN-LSTM network

Ou-Yang Xu [a,b], Yuan-Da Su [a,b,c,*], Bo Rao [a,b,c], Wen-Hao Wang [a,b], Sheng-Qing Li [a,b,c], Xiao-Ming Tang [a,b,c]

[a] School of Geosciences, China University of Petroleum (East China), Qingdao, 266580, Shandong, China
[b] National Key Laboratory of Deep Oil and Gas, Qingdao, 266071, Shandong, China
[c] Qingdao National Laboratory for Marine Science and Technology, Qingdao, 266071, Shandong, China

ARTICLE INFO

Article history:
Received 16 April 2026
Received in revised form
4 June 2026
Accepted 17 July 2026
Available online xxx

Edited by Jie Hao

Keywords:
Acoustic logging-while-drilling
Deep learning
S-wave transverse isotropy
Joint inversion

ABSTRACT

Acoustic logging-while-drilling (ALWD) has been widely used in recent years. This study demonstrates that the ALWD data can be used to estimate formation S-wave anisotropy, providing important information for the exploration and development of unconventional reservoirs. The inversion of the S-wave anisotropy is jointly done using the monopole Stoneley- and quadrupole-wave data, which, when applied in the ALWD condition, is hampered by the high cost of forward modeling and drilling noise. To achieve fast and stable inversion, a multi-component system which contains CNN-LSTM network, gradient-descent optimization, and joint inversion strategy is developed. It not only enhances the forward modeling accuracy and improves inversion efficiency but also reduces the nonuniqueness of the estimated anisotropy parameters. For the construction of this system, we first analyze the sensitivity of key parameters in transversely isotropic formations and construct a multipole LWD dispersion dataset. Then, a CNN-LSTM model is designed to build a nonlinear mapping between formation parameters and dispersion curves, which greatly enhances the forward modeling efficiency. The trained model is then introduced into the joint inversion objective function. A gradient-descent algorithm is further used to optimize the inversion process, attaining convergence in only a few dozen iterations. The efficient inversion method is applied to field ALWD data. The results show that the method is six orders of magnitude faster than conventional methods and the accuracy and robustness of the results are also improved, thus providing a fast and effective method for the ALWD applications.

© 2026 Publishing services by Elsevier B.V. on behalf of KeAi Communications Co. Ltd. This is an open access article under the CC BY-NC-ND license (http://creativecommons.org/licenses/by-nc-nd/4.0/).

1. Introduction

Many unconventional reservoirs, such as shales, exhibit anisotropic properties (White and Tongtaow, 1981). Accurate determination of formation anisotropy is crucial in hydrocarbon reservoir exploration and development, allowing for estimating formation stresses and mechanical properties (Tang and Cheng, 2004). For cases where the symmetry axis of a TI medium is normal to the borehole axis (referred to as an HTI formation when it is perpendicular), dipole sonic logging can be used to exploit shear-wave splitting in the borehole and invert formation anisotropy by matching the fast and slow shear-wave waveforms (Ellefsen K. J. et al., 1990; Esmersoy C. et al., 1994; Tang and Cheng, 2004; Wang et al., 2025). When the TI symmetry axis is parallel to the borehole axis, i.e., in a VTI formation, analytical solutions are available to describe borehole acoustic-wave propagation (Chan and Tsang, 1983; Hu and He, 2009; He and Hu, 2010; Lee et al., 2013; Rao et al., 2022; Tongtaow C, 1982; White and Tongtaow, 1981).

For wireline acoustic logging, VTI anisotropy has traditionally been estimated using Stoneley-wave inversion techniques (Tang, 2003), but these methods are mainly applicable to slow formations. To address this limitation, Xu et al. (2017) proposed an anisotropy-inversion approach based on dipole flexural waves, enabling application to fast formations. In recent years, logging-while-drilling (LWD) acoustic logging has been developing rapidly, enabling real-time measurement of formation P- and S-wave velocities during drilling and providing critical technical

* Corresponding author.
E-mail address: syuanda@sina.com (Y.-D. Su).

Peer review under the responsibility of China University of Petroleum (Beijing).

https://doi.org/10.1016/j.petsci.2026.07.034

1995-8226/© 2026 Publishing services by Elsevier B.V. on behalf of KeAi Communications Co. Ltd. This is an open access article under the CC BY-NC-ND license (http://creativecommons.org/licenses/by-nc-nd/4.0/).

Please cite this article as: O.-Y. Xu, Y.-D. Su, B. Rao *et al.*, Inversion of S-wave transverse isotropy from acoustic logging-while-drilling data using a CNN-LSTM network, Petroleum Science, https://doi.org/10.1016/j.petsci.2026.07.034

support for safe drilling and geosteering (Briggs, 2006; Cui, 2004; Sinha et al., 2009; Tang et al., 2003, 2006; Tang et al., 2006; Wang and Tao, 2011). Li et al. (2020) were the first to invert VTI formation anisotropy using ALWD monopole Stoneley- and quadrupole-wave data. By fitting theoretical dispersion curves to measured dispersion data (derived from array waveforms using various methods; Ekstrom, 1996; Lang S. W. et al., 1987; Nolte B. et al., 1997), dispersion effects in quadrupole LWD slow-shear slowness estimation are corrected, and accurate formation shear-wave anisotropy is obtained simultaneously. Then, Li et al. (2022) used ALWD monopole Stoneley and quadrupole wave data to invert VTI formation anisotropy, and this method offers novel application values for ALWD dipole sources. On the other hand, dispersion data can also be used for permeability inversion (Tang and Cheng, 1996; Zhuang et al., 2019), and for evaluating hydraulic-fracturing performance by comparing radial velocity profiles before and after stimulation (Burridge and Sinha, 1996; Li et al., 2022), and for formation slowness estimation (Lee et al., 2016; Su et al., 2016). However, the above dispersion data inversion processes are usually performed iteratively and are time-consuming, severely limiting their practical applications.

The inversion efficiency is more important for LWD applications, where timely answers are needed for decision making and safe drilling operations. To improve inversion efficiency, Collins (2013) built a theoretical dispersion dataset in advance and then used interpolation for variable-parameter fitting. However, this method requires the guided-wave modes to vary monotonically with the target inversion parameters within the inversion frequency band. Assous et al. (2018) used a fully connected multilayer perceptron (MLP) to train a theoretical dispersion dataset and achieved fast calculation of dispersion curves. Liang et al. (2021a, 2021b, 2021c) further applied this approach to dipole flexural-wave dispersion correction in open holes, cased holes, and even to LWD conditions. In this framework, machine learning was used to replace the tedious solution of the dispersion equation in the inversion process. However, the inversion accuracy becomes insufficient for parameters near the edge of the dataset (Zhang et al., 2024). This limitation is mainly because the MLP lacks constraints on the spatial characteristics of the data set. As a result, local features of dispersion curves cannot be extracted stably from a limited dataset. In addition, when dealing with large datasets, the training speed of the MLP shallow network is severely limited.

Building on the above studies, this work combines theoretical modeling, inversion method optimization, and field data testing to construct an integrated system for real-time inversion of VTI formation anisotropy from ALWD data. By analyzing velocity dispersion and parameter sensitivity for LWD monopole Stoneley and quadrupole, an appropriate parameter step size is selected to construct a theoretical dispersion dataset for ALWD waves. A hybrid network architecture couples a convolutional neural network with a long short-term memory network (CNN–LSTM; Li et al., 2024; Zhang et al., 2022) and can therefore handle the spatial and sequential characteristics of dispersion data. This network, when used to train on this dataset, can perform high-quality computation of guided-wave dispersion curves and effectively improve both the accuracy and speed of dispersion-curve estimation. In addition, by integrating a gradient-descent algorithm (Haji and Abdulazeez, 2021), the number of inversion iterations is reduced, further enhancing inversion efficiency. Therefore, the novelty of this work lies in the integrated combination of fast CNN-LSTM-based forward model, efficient gradient-descent optimization, and multipole-wave joint inversion for ALWD field application. Processing results from field ALWD data also validate the accuracy of the proposed method, demonstrating its superior performance over traditional inversion methods.

2. Preparation for the inversion work

Fig. 1 shows the physical model of ALWD logging with a multipole source in a VTI formation, where the direction of S-wave propagation denotes the symmetry-axis direction of the VTI medium and is parallel to the borehole z-axis. According to previous studies (Lee et al., 2013; Li et al., 2020; Tang and Cheng, 2004), the dispersion equation for this case can be written as:

$$D(n,k,\omega,C_{11},C_{13},C_{33},C_{44},C_{66},B,C,F)=\det\left[\left(\mathbf{H}_{ij}\right)_{12\times12}\right]=0, \tag{1}$$

where n = 0, 1, 2 denote a monopole, dipole, and quadrupole source, respectively; k denotes the wavenumber on z-axis; these five elastic constants (C_{11}, C_{13}, C_{33}, C_{44}, C_{66}) can describe the elastic properties of the VTI formation (Crampin, 1984); B represents the borehole fluid parameters, including the fluid velocity, density, and radius of the borehole fluid ring; C and F denote the parameters about the collar and the formation, respectively; the nonzero elements of matrix $(\mathbf{H}_{ij})_{12\times12}$ that describe ALWD wavefields are detailed in Appendix A.

Following the works of Xu et al. (2017) and Li et al. (2020), we use the ANNIE approximation (Schoenberg et al., 1996) in our analysis, for which the elastic coefficients C_{13} and C_{11} are expressed by $\begin{cases} C_{13}=C_{33}-2C_{44} \\ C_{11}=C_{33}+2(C_{66}-C_{44}) \end{cases}$. The other elastic coefficients can be expressed in terms of wave propagation velocities (i.e. $C_{33}=\rho V_P^2$ related to the P-wave velocity, $C_{44}=\rho V_{SV}^2$ related to the vertical S-wave velocity and $C_{66}=\rho V_{SH}^2$ related to the horizontal S-wave velocity, where ρ is the formation density). Of the five elastic parameters, only the P- and the S-wave velocities can be directly determined from the logging measurements (Xu et al., 2017). In addition, the Thomsen (1986) S-wave anisotropy parameter γ (defined by $\gamma=(C_{66}-C_{44})/2C_{44}$) is needed to fully characterize a VTI formation, which is precisely the object of the work described in the following.

Solving the dispersion equation (Eq. (1)) numerically, the phase velocity (V_{ST} and V_{QD}) dispersion curves of the Stoneley and the quadrupole waves are calculated as:

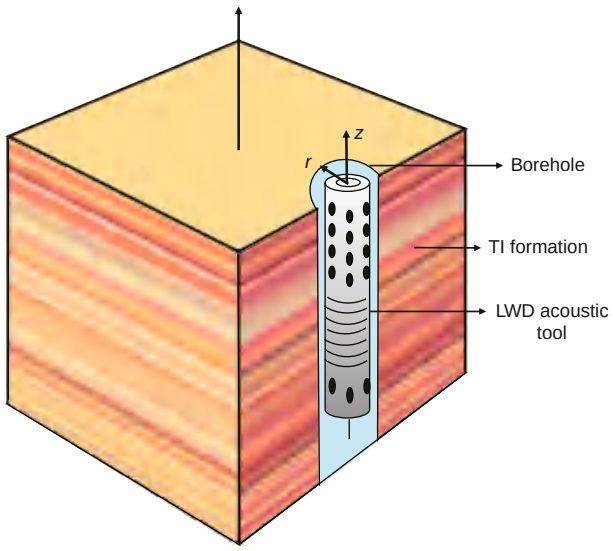


Fig. 1. Model for the ALWD tool in a VTI formation with a multipole source.

$$\begin{cases} V_{ST} = \omega / k_{ST} \\ V_{QD} = \omega / k_{QD} \end{cases}, \tag{2}$$

where k_{ST} and k_{QD} are wavenumbers of ALWD Stoneley and quadrupole waves, respectively. The upper part of Figs. 2–3 shows the dispersion curves of the Stoneley wave (Figs. 2(a) and 3(a)) and quadrupole wave (Figs. 2(b) and 3(b)) in fast and slow formations (parameters are given in Table 1). As frequency increases, the velocity variations of these two guided waves differ between anisotropic and isotropic formations, reflecting the effect of anisotropy.

Existing work on geophysical inversion shows that sufficient training data can significantly enhance the generalization ability of the model (e.g., Chen et al., 2022; Hu et al., 2020; Luo et al., 2025; Meng et al., 2023; Onalo et al., 2019). Therefore, dataset preparation is a critical prerequisite for network training. Before constructing the dispersion dataset, it is necessary to analyze the sensitivity [$Sen(p)$] of a model parameters "P" to quantitatively evaluate their influence on the dispersion curve (Cheng et al., 1982):

$$Sen_{ST\ or\ QD}(p) = \frac{p}{V_{ST\ or\ QD}} \cdot \frac{\partial V_{ST\ or\ QD}}{\partial p}. \tag{3}$$

As shown in the lower part of Figs. 2–3, the S-wave velocities V_{SV} and V_{SH} are directly related to anisotropy. For the fast formation (Fig. 2), the Stoneley wave sensitivity to V_{SH} is high at low frequencies (Fig. 2(a)), and the quadrupole wave sensitivity to V_{SV} (Fig. 2(b)) remains high near the cutoff frequency (4.4–6 kHz). For the slow formation (Fig. 3), the Stoneley wave sensitivity to V_{SH} is high at low frequencies and to V_{SV} is high at high frequencies (Fig. 3(a)), and the quadrupole wave sensitivity maintains high sensitivity to V_{SV} over the entire frequency band (Fig. 3(b)). These complementary features of quadrupole and Stoneley waves to S-wave velocity (V_{SV} and V_{SH}) provide strong support for the subsequent joint inversion of S-wave anisotropy using these two waves, as also shown by Li et al. (2020). Additionally, we also investigated the sensitivities to borehole radius (r), formation P wave velocity (V_p), formation density, borehole fluid velocity (V_f), and fluid density (ρ_f). Among those parameters, the sensitivity to V_f is high. Then, the sampling density of each parameter (see Table 2) is chosen according to the principle of "dense steps for high sensitivity and sparse steps for low sensitivity." As the number of parameters increases, the dataset size also grows substantially (Fig. 4). After computing the dispersion curves of the Stoneley and quadrupole waves corresponding to these combinations of formation parameters, they are used as the dataset for subsequent deep-learning training.

3. Network traing methods and results

3.1. Modeling parameters

Unlike conventional iterative, computation intensive inversion methods, deep learning constrained by a physical model can directly build a nonlinear mapping between formation parameters and dispersion curves. This direct mapping property enables the CNN-LSTM network designed in this study to accelerate the forward prediction of LWD multipole acoustic dispersion curves (Fig. 5). The network has four parts: input, local feature learning, global information learning, and output. The input is a set of formation-parameter combinations, and the output is the corresponding dispersion curve.

At the beginning of the network, the formation-parameter combinations are fed into the local feature learning module as a one-dimensional vector. This module contains two local feature learning blocks (LFLBs). In the deeper part of the network, the numbers of channels in the one-dimensional convolutional layers are set to 64 and 128, respectively. The main function of the LFLB is

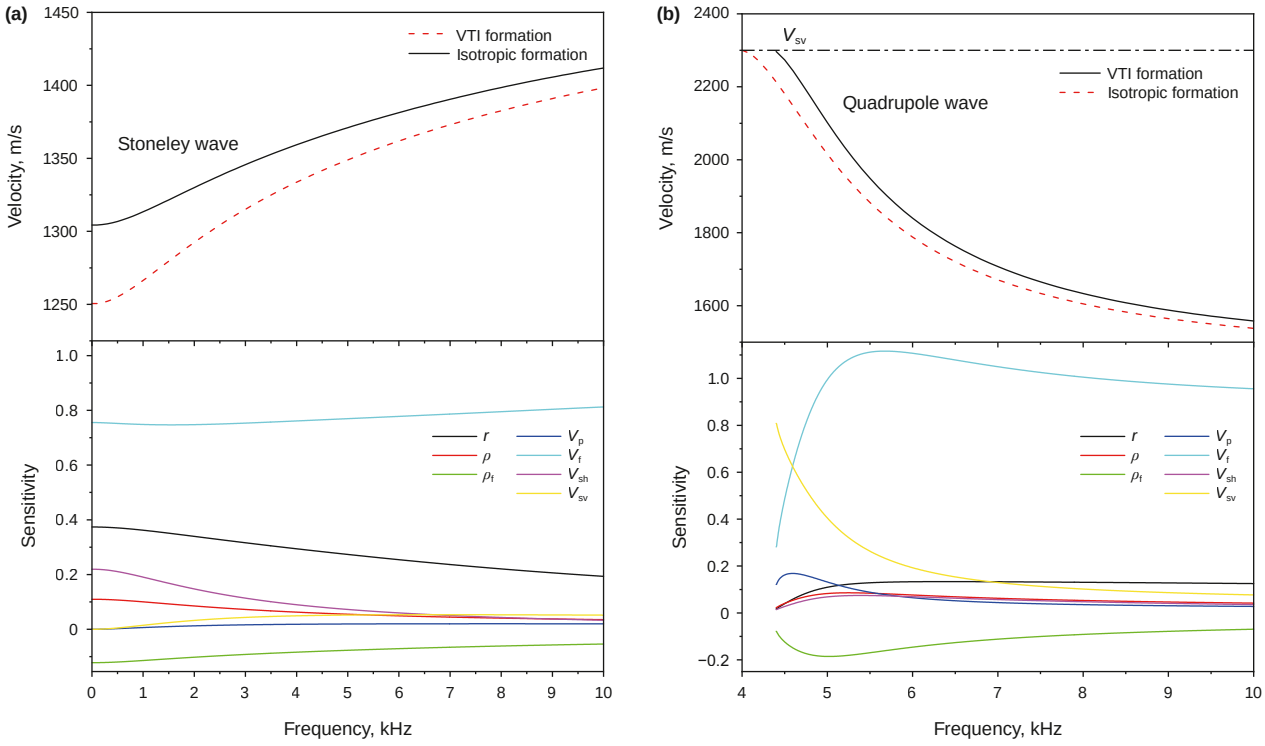


Fig. 2. ALWD Stoneley **(a)** and quadrupole **(b)** wave dispersion curves (the upper part), sensitivity curves (the lower part) for the fast VTI formation.

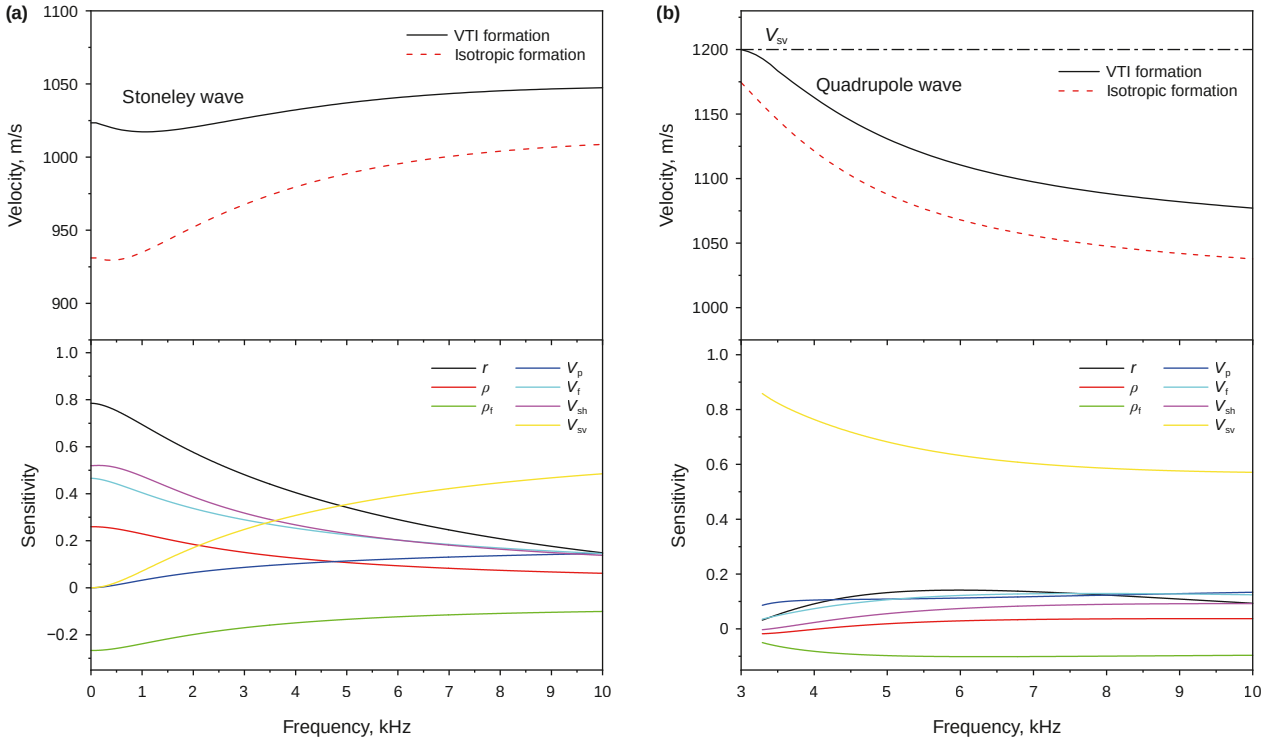


Fig. 3. ALWD Stoneley **(a)** and quadrupole **(b)** wave curves (the upper part), sensitivity curves (the lower part) for the slow VTI formation.

Table 1
Parameters of the VTI formation and the borehole.

Medium	P-wave velocity, m/s	S-wave velocity, m/s	S-wave anisotropy	Density, kg/m^3	Outer, m
Inner fluid	1500	-	-	1000	0.027
Drill collar	5860	3130	-	7850	0.090
Outer fluid	1500	-	-	1000	0.117
Fast formation	4800	2300	0.2	2550	∞
Slow formation	2100	1200	0.2	2450	∞

Table 2
Parameter combination of dataset.

Parameter	Unit	Low Bound	High Bound	Step
r	m	0.10	0.18	0.01
ρ_f	kg/m^3	800	1600	200
ρ	kg/m^3	1750	3000	250
V_f	m/s	1200	2000	100
V_{sv}	m/s	1200	3000	100
pr	-	0.1	0.4	0.1
γ	-	0	0.5	0.1

to extract local features from the dispersion curves, such as inflection points and slope changes in specific frequency bands. Each LFLB includes two one-dimensional convolutional layers named CNN (Krizhevsky et al., 2012), two batch-normalization (BN) layers, two rectified linear unit (ReLU) activation layers, and one max-pooling layer. Convolution and pooling are the key operations in the LFLB. Through weight sharing and local connectivity, the convolutional layers learn the nonlinear mapping between formation parameters and dispersion curves. The max-pooling layer divides the input features into nonoverlapping regions and keeps

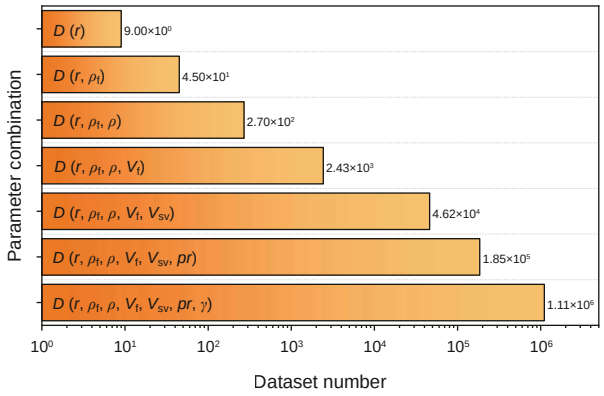


Fig. 4. Dataset size of different parameter combinations.

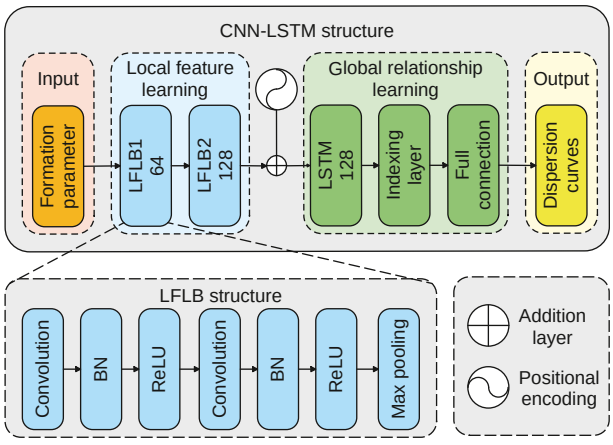


Fig. 5. 1D CNN-LSTM network structure.

the most important features. This helps reduce noise and improve model robustness (Zhang et al., 2021).

Long short-term memory (LSTM) is a type of recurrent neural network that is designed to learn global dependencies in sequential data (Schmidhuber and Hochreiter, 1997). Dispersion curves can also be treated as frequency sequences (Kong et al., 2017). Therefore, an LSTM module is added after the LFLB, so that the extracted local-feature sequence can be further used to learn global information. The LSTM structure has four main components: an input gate, an output gate, a forget gate, and a memory cell with self-recurrent connections (Fig. 6). The state update at each time step is described by the following equations:

$$\begin{aligned} f_t &= \sigma\left(\mathbf{W}_f[h_{t-1}, x_t] + \mathbf{b}_f\right), \\ i_t &= \sigma(\mathbf{W}_i[h_{t-1}, x_t] + \mathbf{b}_i), \\ o_t &= \sigma(\mathbf{W}_o[h_{t-1}, x_t] + \mathbf{b}_o), \\ \tilde{C}_t &= \tanh(\mathbf{W}_c[h_{t-1}, x_t] + \mathbf{b}_c), \\ C_t &= f_t \otimes C_{t-1} + i_t \otimes \tilde{C}_t, \\ x_t &= o_t \otimes \sigma C_t, \\ h_t &= o_t \otimes \tanh(C_t), \end{aligned} \tag{4}$$

where f_t, i_t, and o_t denote the forget gate, input gate, and output gate, respectively. C_t is the updated memory-state value at the current time step; x_t and h_t are the input and output values, respectively; $\mathbf{W}$ and $\mathbf{b}$ denote the weight matrix and bias vector, respectively; σ and tanh represent the sigmoid function and the hyperbolic tangent function, respectively; $\oplus$ and $\otimes$ denote element-wise addition and the Hadamard product, respectively.

At the end of the network, the indexing layer extracts the required sequential information from the LSTM module. The extracted features are then dimension-adjusted and combined through fully connected layers, and generate the final forward modeling dispersion curves. It should be noted that although the LSTM is designed for sequential data and can learn some long-term dependencies, it is still essentially an autoregressive model, because its memory mechanism emphasizes state information rather than positional information. In other words, the LSTM has limited ability to learn the absolute order of adjacent frequency points along a dispersion curve. To address this issue, positional encoding (Vaswani et al., 2017) is added before the LSTM module. This helps the model predict physically plausible and smooth dispersion curves, instead of producing nonphysical oscillations or jumps. The positional encoding is defined as follows:

$$\mathbf{PE}(pos, j) = \begin{cases} \sin\left(\dfrac{pos}{10000^{2i/d}}\right) & , \quad j = 2i \\ \cos\left(\dfrac{pos}{10000^{2i/d}}\right) & , \quad j = 2i+1 \end{cases} \tag{5}$$

where d is the dimension of the embedding vector, j is the index of the current dimension, and pos is the index of the frequency point. **PE** denotes the positional encoding, which is added through an addition layer between the CNN module and the LSTM module.

3.2. Training and testing dataset results

Using the method described earlier and the parameter combinations listed in Table 2, a total of 1,108,080 samples were constructed. Then, these data were divided into three subsets: 90% for training, 5% for validation, and 5% for testing. Each data pair consists of seven formation parameters as input, and a dispersion curve sequence of 101 points as output, with the frequency predefined in the range 0-10 kHz at a step size of 0.1 kHz. For the training process (100 epochs), the initial learning rate is set to 0.01, the loss function is the mean squared error (MSE, as given in Eq. (6)), the optimization uses the Adam algorithm, and the batch size is 512. Fig. 7 shows the loss of the dispersion data for both guided waves under the employed deep-learning model, which decreases simultaneously for both the training and validation sets without underfitting, indicating that the model is well trained.

$$Loss = \frac{1}{N}\sum_{i=1}^{N}\left(V_{th}^{i} - V_{nn}^{i}\right)^{2} \tag{6}$$

where N is the number of points in the frequency sequence; V_{th} is the theoretical dispersion curve in the dataset; and V_{nn} is the dispersion curve predicted by the network.

To evaluate the performance of the training network, we computed the mean relative error MRE ($MRE = \mathrm{E}(|V_{ma} - V_{nn}|)/\mathrm{E}(V_{ma}) \times 100\%$) of the predicted dispersion curves for the testing dataset as shown in the histogram of Fig. 8. For both quadrupole and Stoneley waves, the maximum mean relative error does not exceed 0.8%, with vast majority being within 0.1%. In addition, we selected results with different error magnitudes for illustration, as shown in Fig. 9. Fig. 9a–f indicate that the predicted dispersion curves closely match the theoretical dispersion curves. Under the same computational environment, the cost of computing a single dispersion curve was reduced from 1.2 s to 0.02 ms. This demonstrates that deep-learning-based dispersion prediction is both highly accurate and extremely fast, making it suitable for incorporation into the subsequent inversion workflow.

However, formation in complex or special work areas are indeed not taken into account, mainly for two reasons: first, such formation conditions are relatively rare, and their dispersion curves differ significantly from those of conventional formation, requiring in-depth discussion regarding theory and instrument

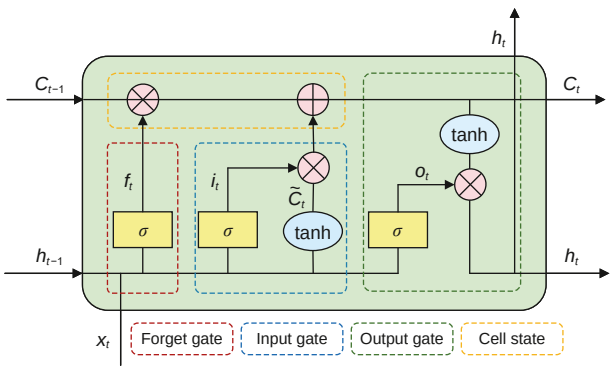


Fig. 6. The LSTM unit structure diagram.

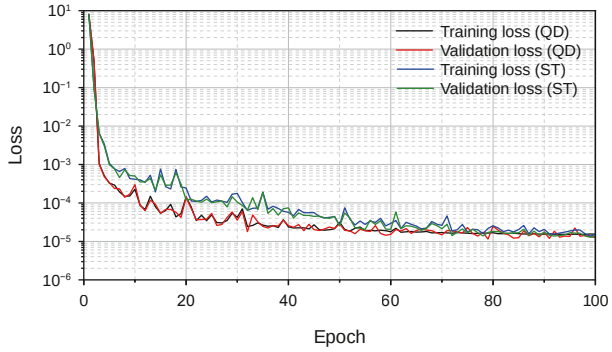


Fig. 7. Training and validation loss of LWD quadrupole and Stoneley wave dispersion data.

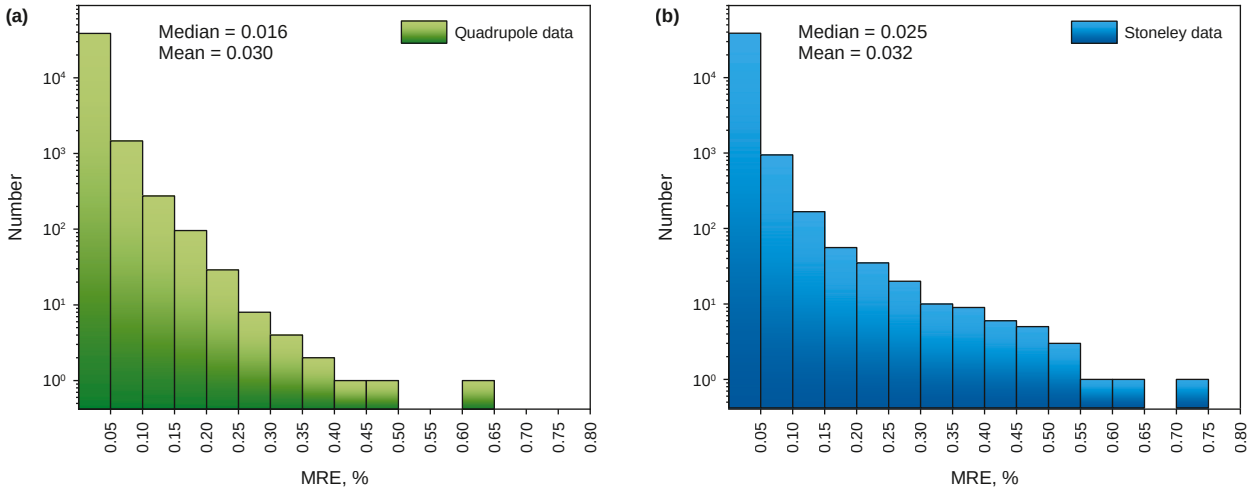


Fig. 8. Histograms of the mean relative error for the test datasets of LWD quadrupole **(a)** and Stoneley **(b)** wave.

applicability; second, the parameter combinations that cover all types of conditions require a large dataset, which is difficult to achieve in a single attempt due to limited computational resources. Nevertheless, it is worth noting that near the boundary parameters, the CNN-LSTM network can still stably compute the dispersion curves, as shown in Fig. 9 (the parameters marked in red are the boundary parameters.). The selected parameter combinations in Table 2 can reconstruct common formation conditions and meet the needs of most field data.

3.3. Inversion method based on deep learning

In practice, joint processing of ALWD monopole Stoneley and quadrupole wave data maximizes data utilization and reduces inversion non-uniqueness (Li et al., 2020). The objection function for the joint inversion is written as

$$E(V_{SV},\gamma)=\left\{\begin{array}{l}(1-\lambda)\sum\limits_{\Omega_{ST}}P_{ST}(\omega)\left[V_{nn}^{ST}(V_{SV},\gamma;\omega)-V_{d}^{ST}(\omega)\right]^{2}+\\ \lambda\sum\limits_{\Omega_{QD}}P_{ST}(\omega)\left[V_{nn}^{QD}(V_{SV},\gamma;\omega)-V_{d}^{QD}(\omega)\right]^{2}\end{array}\right\} \tag{7}$$

where ω denotes the angular frequency; V_{nn} and V_d denote the predicted and the measured phase velocity dispersion curves, respectively; Ω_{ST} and Ω_{QD} denote the processing frequency ranges of the Stoneley and the quadrupole waves, respectively; P_{ST} and P_{QD} are the power spectra for the Stoneley and quadrupole waves, respectively; λ is a weighting factor, and the value range of λ is between 0 and 0.5 (see the specific calculation method in Appendix B).

To further evaluate the performance of the network in inversion, we use synthetic waveforms (the array waveforms of Stoneley and quadrupole wave are shown in Fig. 10(a) and (b), respectively.) to validate the deep learning method for evaluating formation anisotropy. The parameters used for the synthetic data are shown in Table 1. First, the synthetic waveforms were processed using the velocity-frequency cohenrence method (Tang and Cheng, 2004), obtaining the quadrupole and Stoneley wave dispersion data, as shown in Fig. 10(a) (black circles). Next, the deep-learning-predicted theoretical dispersion curves were used to fit the data of each wave mode (red solid lines). For comparison, the theoretical isotropic dispersion curves (blue dashed lines) were also plotted. The fitted dispersion curves correspond to the solution minimum of the objective function of the joint inversion (Eq. (7)). Compared with single wave mode inversion (Li et al., 2020), the joint inversion combines the sensitivity of the two wave modes to respective inversion parameters, thereby reducing the non-uniqueness of the inversion results. Fig. 10(b) shows the variable-density plot of the objective function for the joint inversion method, where the minimum of the objective function over the two-dimensional domain (V_{SV}, γ) obtains the optimal solution point (V_{SV} = 1200 m/s, γ = 0.2). The inversion results match well with the parameters listed in Table 1, confirming the accuracy of performing joint inversion using the deep learning approach. The noise tests (the details in Appendix B) is added to make the synthetic data more similar to the actual data. It show that the inversion remains stable under low-level noise, although the uncertainty increases as the noise level increases. When noise is at a high level, it is necessary to adopt certain noise reduction techniques to improve the stability of inversion results, such as median filtering and cluster analysis.

In the inversion process, however, each point in the two-dimensional parameter space corresponds to a network-predicted dispersion curve, and the total number of such curves increases rapidly as the inversion iterates to approach accurate results. To optimize the inversion process, a gradient-descent algorithm is introduced (Haji and Abdulazeez, 2021), as shown in Fig. 11(a). This algorithm computes the gradient of the loss function with respect to the model parameters and updates the parameters in the opposite direction of the gradient, that is, along the steepest descent direction, until the optimal solution is reached. In this study, the objective function E is used as the loss function, and the inversion parameters are treated as the iterative variables. After the learning rate is properly adjusted (from 0.1 to 0.001), convergence to the optimal solution can be achieved in only a few iterations, as shown in Fig. 11(b). In addition, the initial value V_{SV} is estimated from the conventional slowness-processing result, whereas the initial value γ was selected within the physically reasonable range of the training dataset. The learning rate was determined through trial tests (from 0.1 to 0.001) by considering both convergence speed and stability. The iteration is terminated when the relative change of the objective function became smaller than a prescribed threshold (ΔV_{SV} <1 m/s and $\Delta\gamma$<0.002) or when the maximum

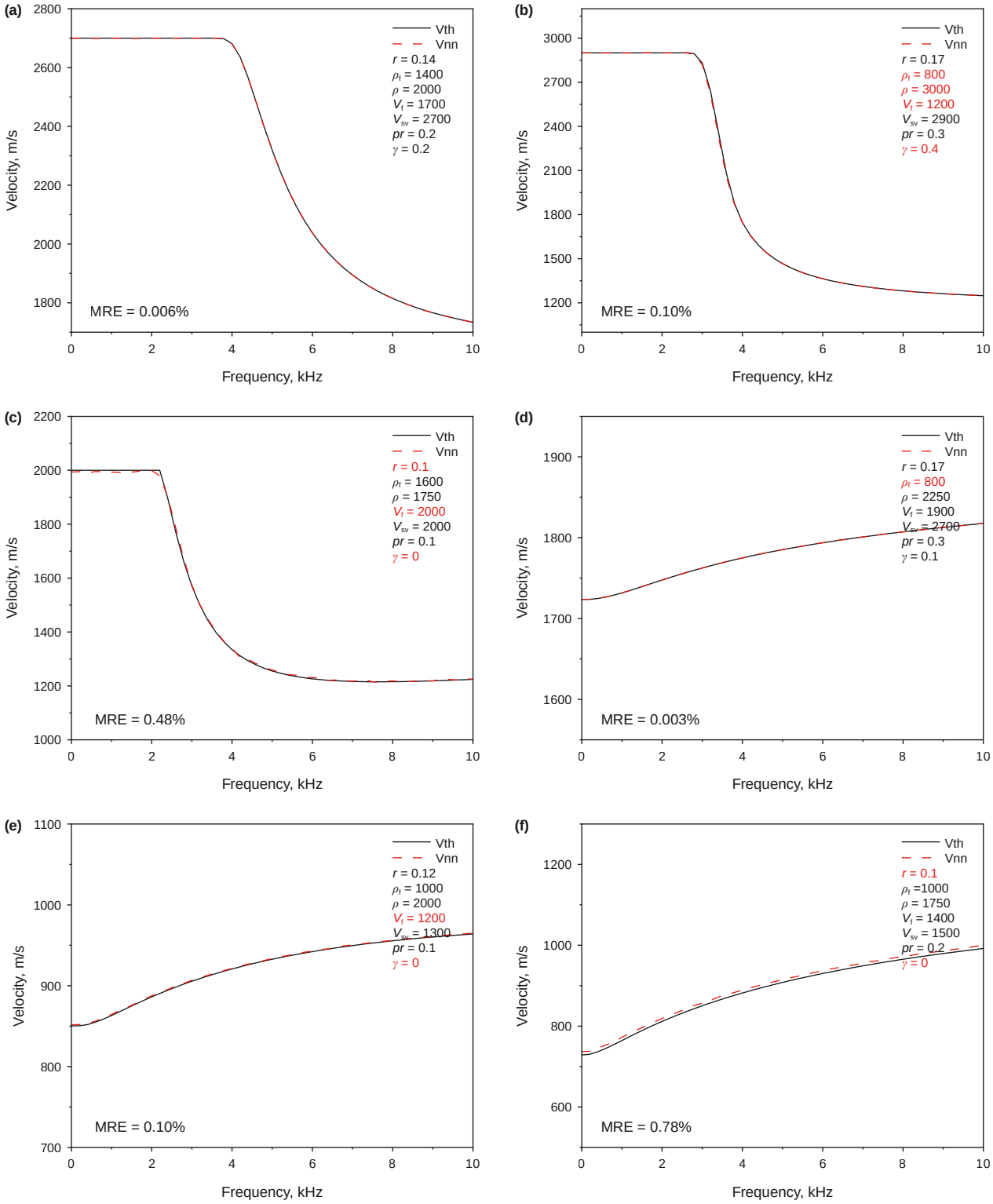


Fig. 9. Compare V_{th} with V_{nn} on the testing dataset.

number of iterations (set to 30 times) was reached. To evaluate the dependence on the initial model, several inversions were also performed using different initial values of V_{SV} and γ. The results in Fig. 12 show that the inversion converges to nearly the same solution for reasonable initial models, indicating good convergence stability of the proposed method.

4. Field application

We apply the new method to process a field ALWD data set. Fig. 13 shows the processing results. The first panel in Fig. 13 is the natural gamma curve, with the subsequent panels depicting the LWD monopole and quadrupole variable-density waveform

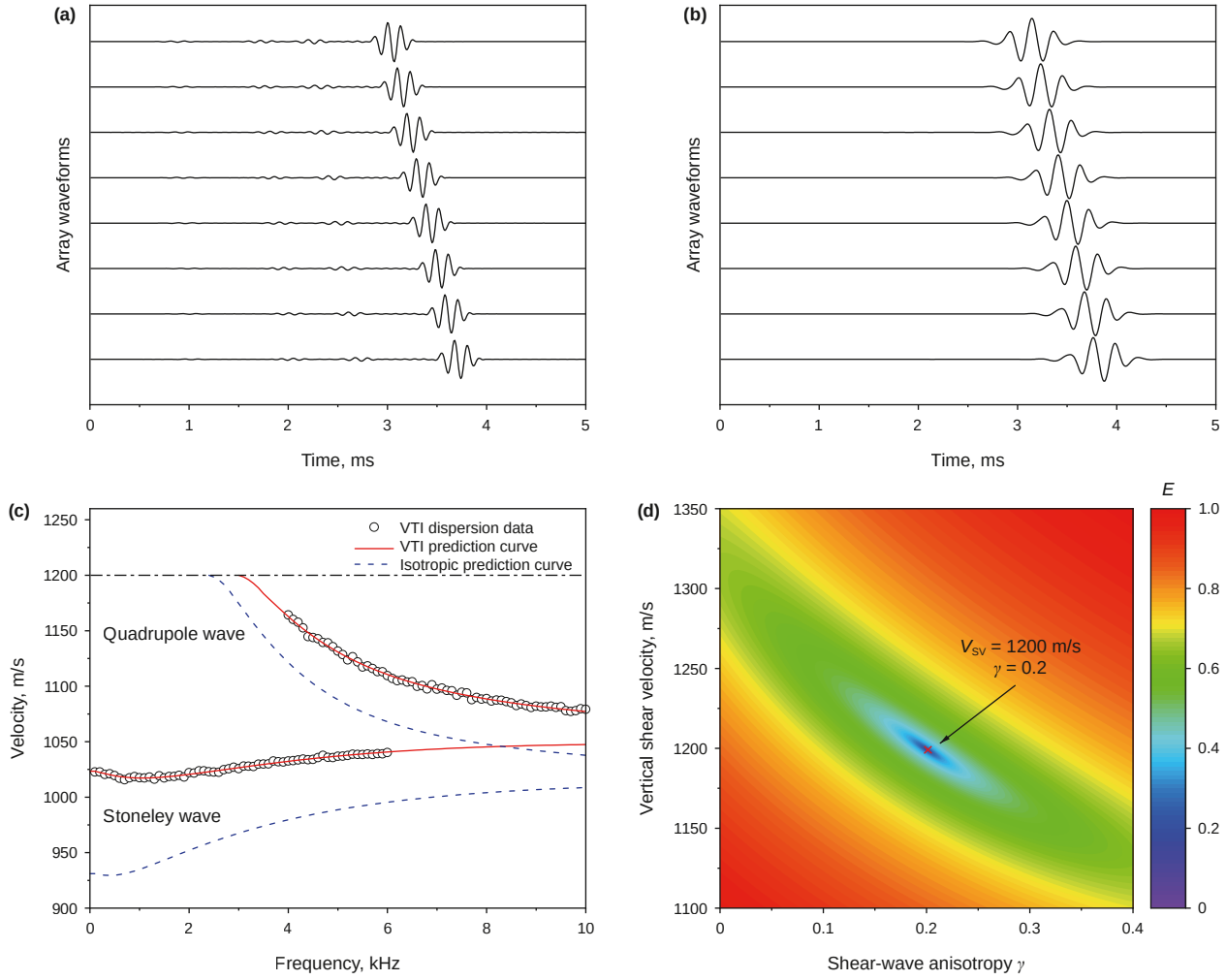


Fig. 10. Inversion results of deep learning by using synthetic wave data: the LWD array synthetic waveforms of Stoneley wave **(a)** and quadrupole wave **(b)**; **(c)** theoretical dispersion curves predicted by the network for Stoneley- and quadrupole-wave (solid lines) versus the dispersion data extracted from the waveforms; **(d)** the variable-density display of the objective function for the joint inversion.

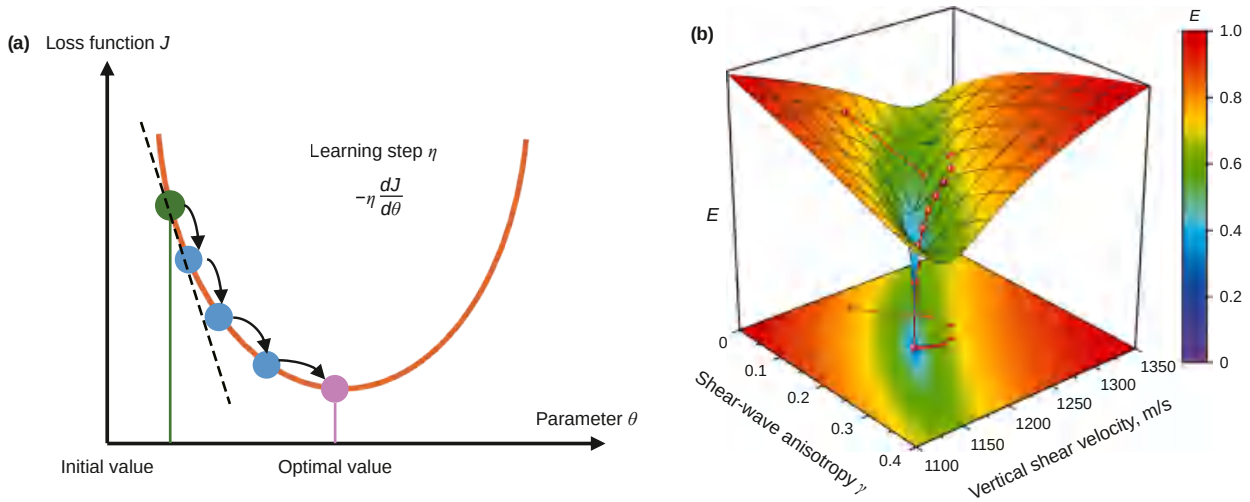


Fig. 11. Principle of the gradient descent **(a)** and its application in inversion **(b)**.

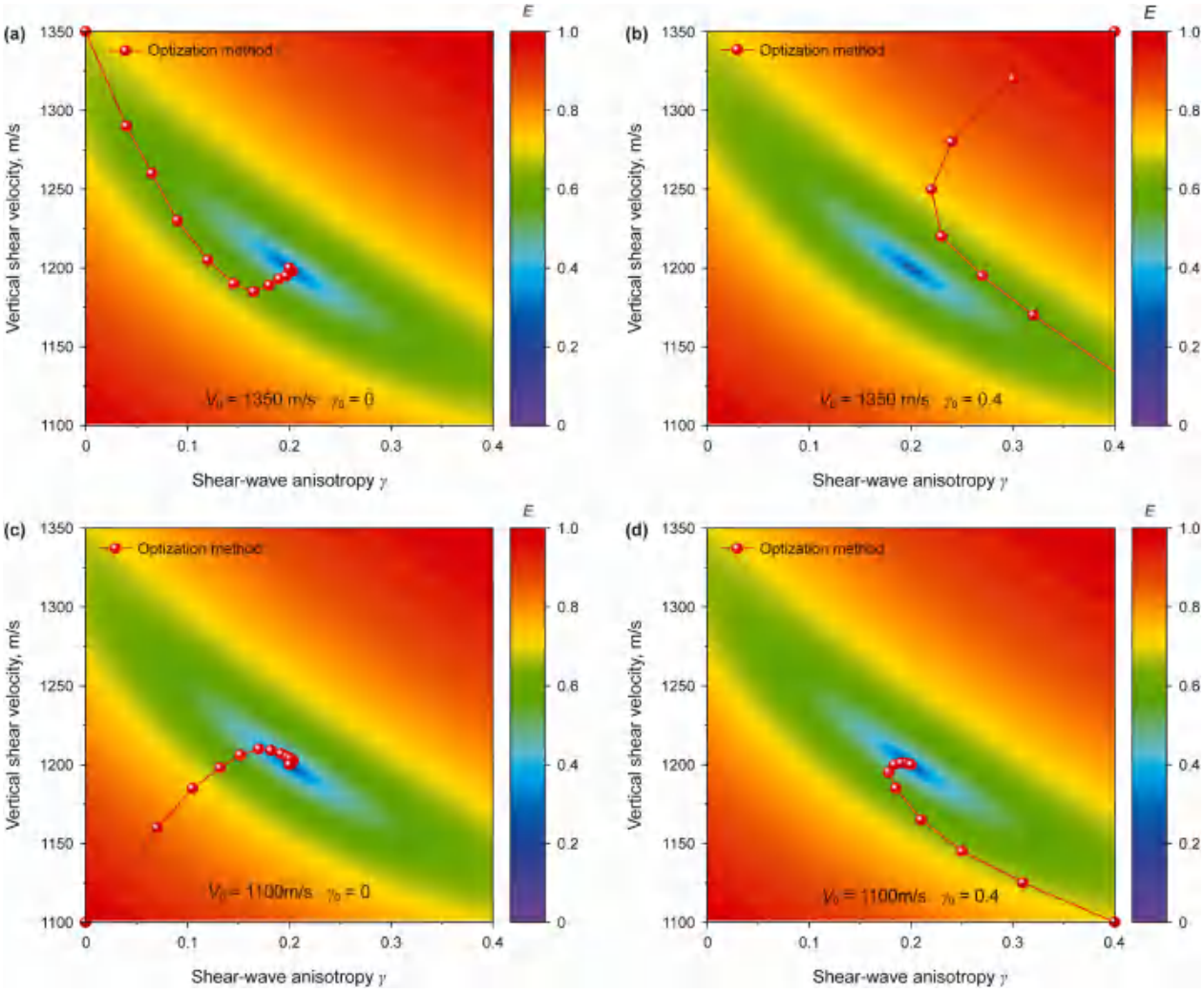


Fig. 12. The inversion results of the gradient-descent optimization under different initial values.

data, respectively. The fourth panel shows the acoustic slowness of the shear wave (blue dotted line) and Stoneley wave (black line) extracted from the waveform data, and the shear wave slowness obtained through joint inversion method (red line). The fifth (sixth) panel displays the dispersion data (black circles) obtained from the LWD Stoneley (quadrupole) waveforms versus at equally spaced frequency, along with the dispersion curve predicted by the CNN-LSTM-based inversion (red line). The seventh panel compares the anisotropy parameter γ obtained from both the new and traditional method (Li et al., 2020). The final panel is the absolute error AE and relative error RE of the anisotropy parameter γ obtained by the two methods in seventh panel. The result of Fig. 13 shows that the collected waveform data is of good quality, and the dispersion curves obtained from the inversion fit well with the dispersion data from the waveforms. Especially, the anisotropy parameters obtained by the new inversion are relatively close to those obtained by the traditional inversion. Their absolute error (AE) is less than 2%, and their relative error (RE) is less than 6%, thereby demonstrating the reliability of the new inversion method.

To further verify the accuracy of the inversion results, two representative depth points, one anisotropic and one isotropic, were selected from the entire section for display (see Figs. 14 and 15). Fig. 14(a) and (b) show the LWD Stoneley and quadrupole array waveforms at the depth of X004 m, while Fig. 14(c) and (d) show the detailed inversion result for the anisotropic formation. The dispersion data (circles) extracted from the array waveforms fit well with the dispersion curve (red line) predicted by the CNN-LSTM network. The objective function's variable-density display exhibits an optimal value within the two-dimensional parameter domain, with the optimization path landed on an anisotropy value of 0.235. Concurrently, the shear wave velocity is determined to be 1667 m/s, which is more accurate than the velocity obtained by STC method (which is affected by the dispersion effect). For comparison, Fig. 15(a) and (b) present the LWD Stoneley and quadrupole array waveforms for the isotropic formation at the depth of X037 m. Fig. 15(c) and (d) demonstrate the inversion result, where the dispersion curve predicted by the CNN-LSTM network fits well with the dispersion data. The optimization path converges to the minimum value when the anisotropy is zero and the shear wave velocity is 2000 m/s. The above results show that the new method not only can invert anisotropy accurately but also corrects the dispersion effect in the shear wave velocity estimation.

Finally, a statistical analysis of the processing speed for the above ALWD data set was carried out, with Fig. 16 showing the result. Under the same computational environment, we use both the proposed method and the traditional method to process the

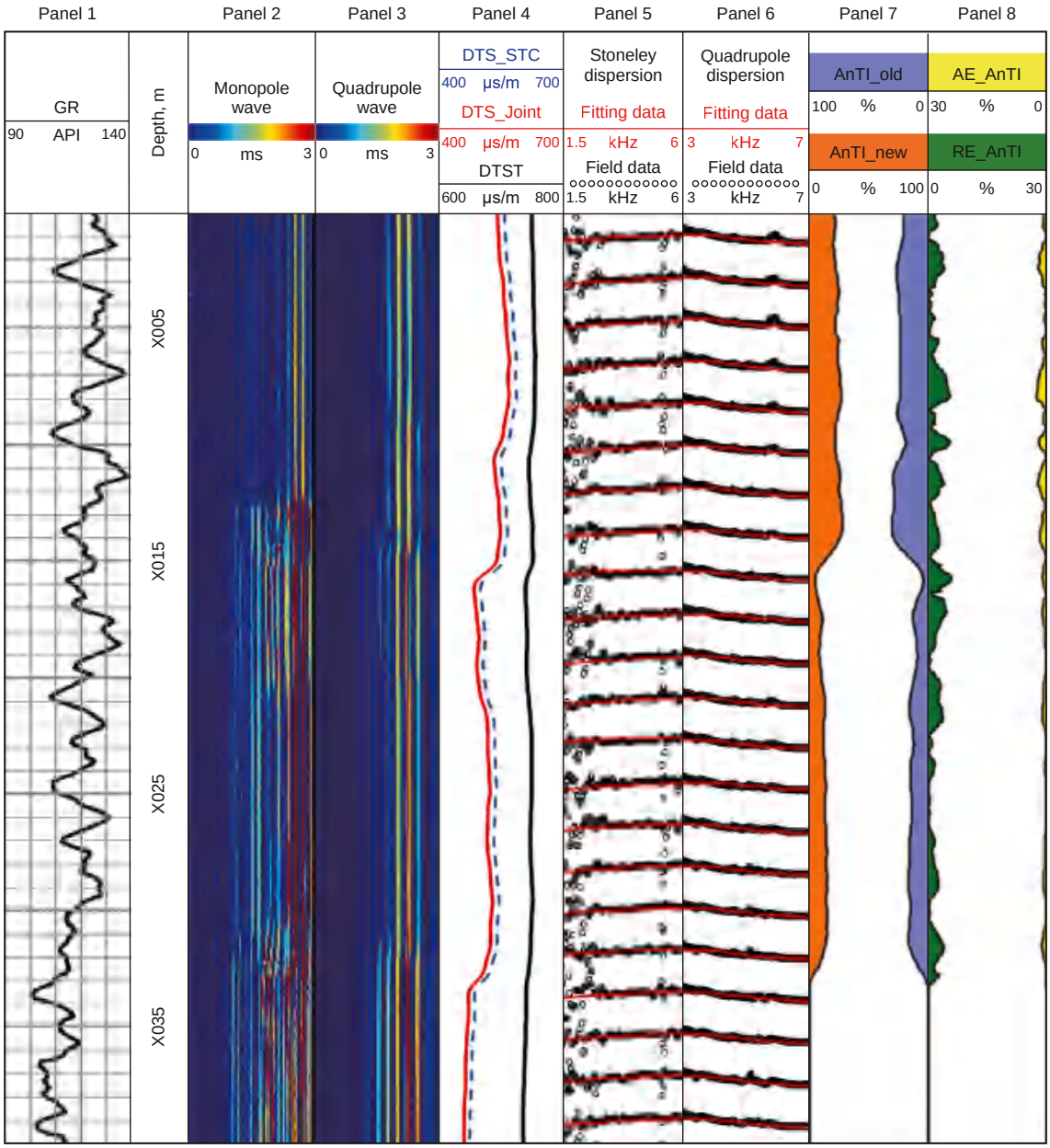


Fig. 13. An example of the new inversion method for sandstone shale formation, including a comparison with traditional method in seventh and final panel.

same well section (including the same input parameters, processing units, and inversion task), and the former is six orders of magnitude faster than the latter. This makes the proposed method a very efficient tool for field ALWD data processing.

5. Conclusion

Real-time estimation of formation anisotropy from ALWD data requires efficient inversion method for the data processing, for which two main issues must be solved. The first is the slow forward solution of the dispersion equation. The second is the large number of forward simulations required during inversion. To address the first issue, a CNN-LSTM deep learning model is introduced, and a multipole LWD dispersion-curve dataset is constructed based on sensitivity analysis, which, after training, the model can accurately predict dispersion curves. Because the CNN and LSTM modules in this model learn local features and global dependencies of the dispersion curves, respectively, allowing for maintaining. This maintains prediction accuracy and greatly reduces the computational cost. To address the second issue, a gradient-descent algorithm is used to optimize the inversion. This reduces the number of forward simulations from thousands to only a few dozen. Applying the new method to the joint ALWD data inversion obtains accurate estimates of formation anisotropy and shear-wave slowness. Compared with the traditional method, the processing speed is greatly enhanced, making the new method a very efficient tool for ALWD data processing.

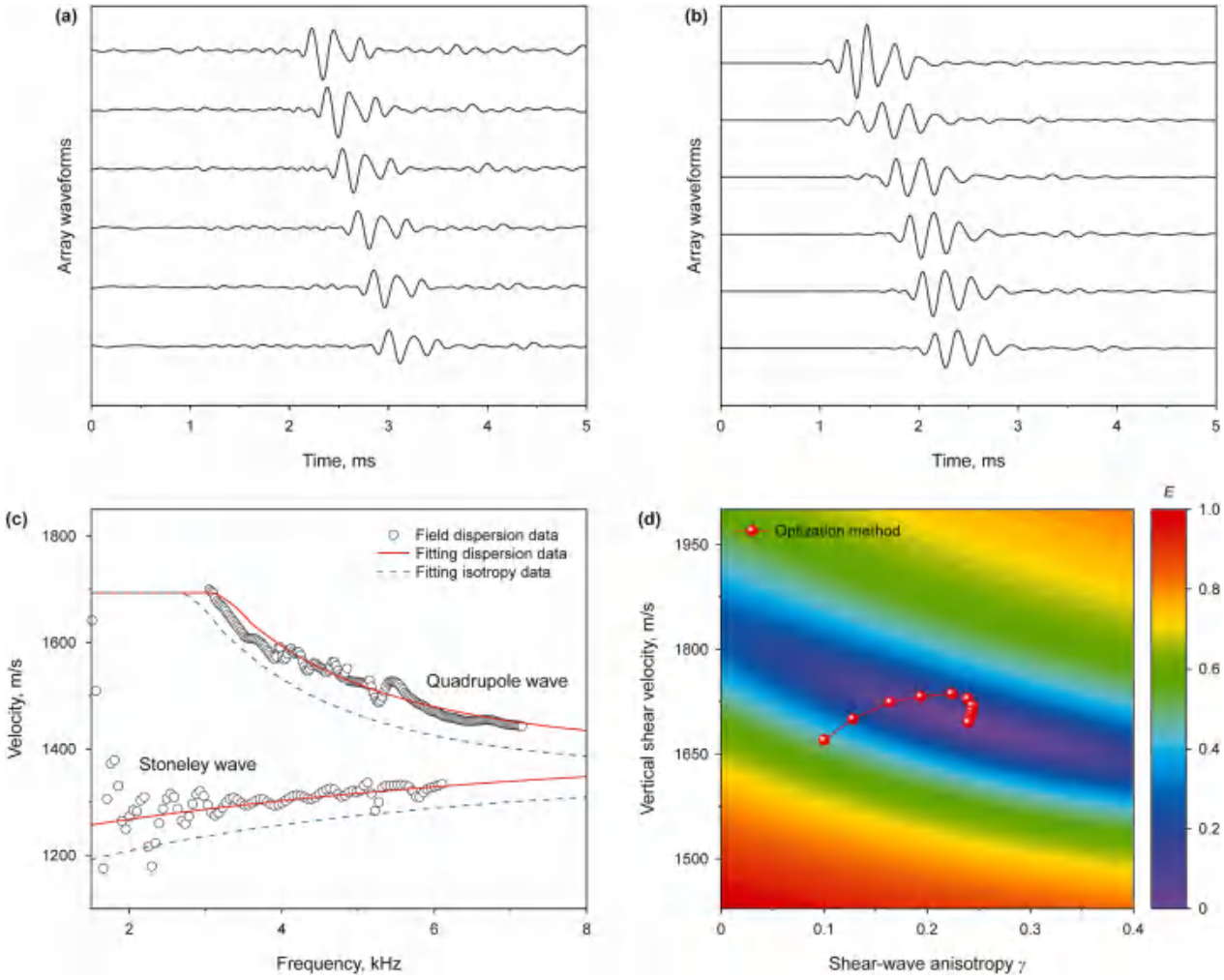


Fig. 14. Detailed inversion results of new method at an anisotropic formation depth (X004 m): the LWD array measurements of Stoneley wave **(a)** and quadrupole wave **(b)**; **(c)** predicted dispersion curves (solid lines) versus the dispersion data (circles) extracted from the waveforms; **(d)** the optimization path for the minimum solution.

CRediT authorship contribution statement

Ou-Yang Xu: Writing – original draft, Visualization, Validation, Methodology, Investigation, Formal analysis, Data curation. **Yuan-Da Su:** Writing – review & editing, Validation, Software, Resources, Funding acquisition, Conceptualization. **Bo Rao:** Writing – review & editing, Software, Resources, Formal analysis. **Wen-Hao Wang:** Writing – review & editing, Validation, Supervision. **Sheng-Qing Li:** Supervision, Funding acquisition. **Xiao-Ming Tang:** Writing – review & editing, Methodology.

Conflict of interest

The authors declare that they have no known competing financial interests or personal relationships that could have appeared to influence the work reported in this paper.

Acknowledgments

This study was supported by the National Natural Science Foundation of China (Grant No. 42574180, 42574150) and the Shandong Provincial Natural Science Foundation (Grant No. ZR2024YQ062).

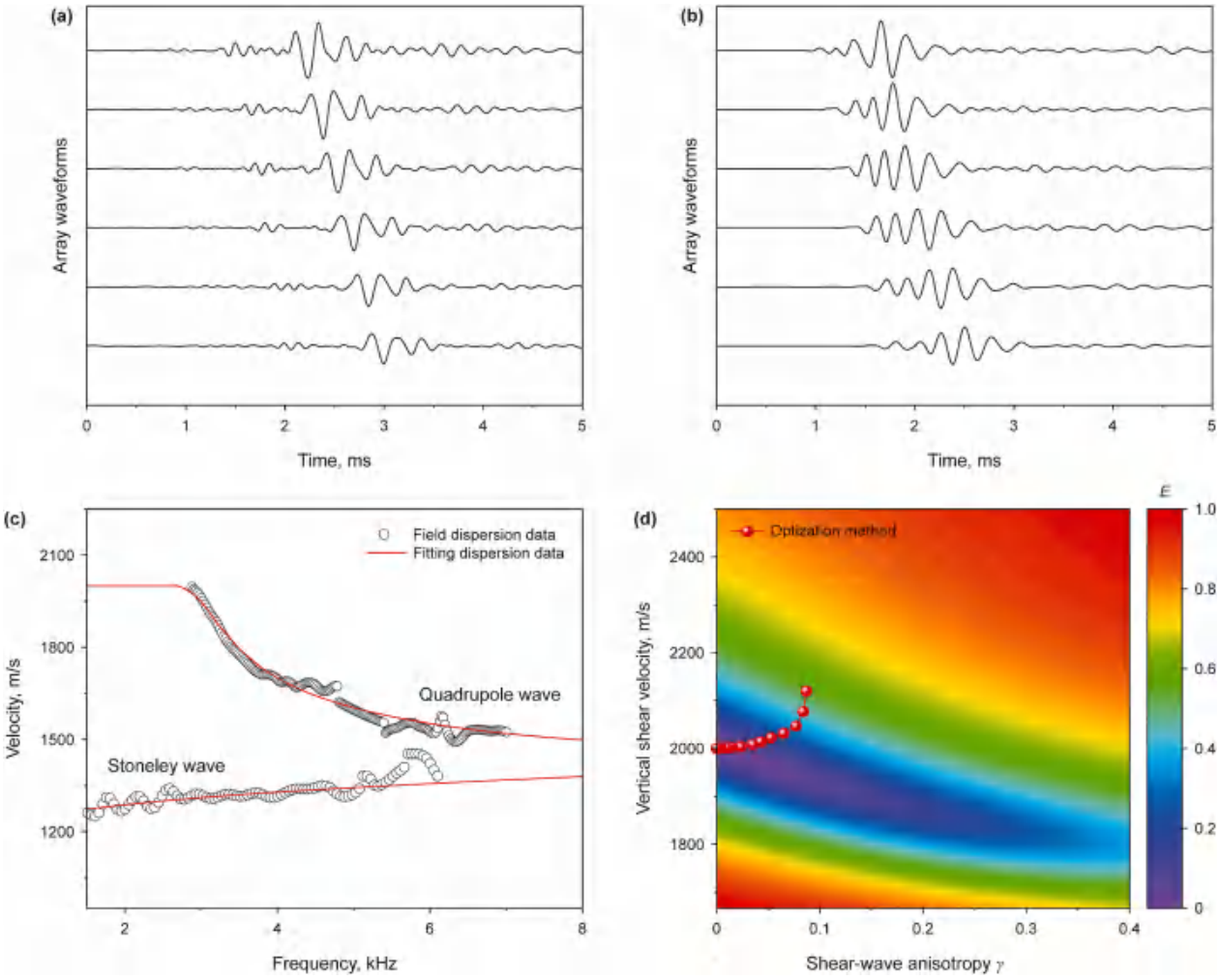


Fig. 15. Detailed inversion results of new method at an isotropic formation depth (X037 m): the LWD array measurements of Stoneley wave **(a)** and quadrupole wave **(b)**; **(c)** predicted dispersion curves (solid lines) versus the dispersion data (circles) extracted from the waveforms; **(d)** the optimization path for the minimum solution.

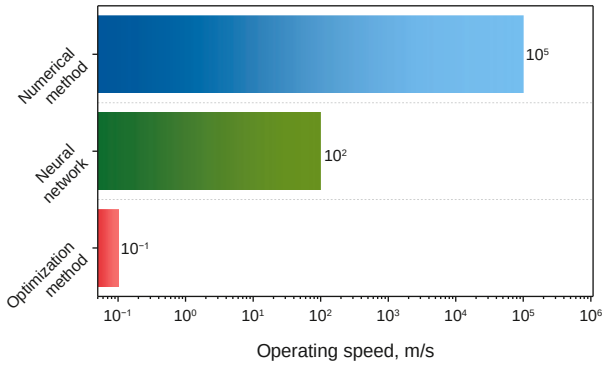


Fig. 16. Comparison of processing speed for the well section inversion.

Appendix A. Nonzero elements of global matrix H

As defined in Eq. (1), the global matrix **H** is a 12×12 matrix comprising nonzero elements, detailed as below:

$$\mathbf{H}_{1,1}=-fX_1(fr_0),\mathbf{H}_{1,2}=pX_1(pr_0),\mathbf{H}_{1,3}=pY_1(pr_0),\mathbf{H}_{1,4}=\frac{n}{r_0}I_n(sr_0),$$

$$\begin{aligned}
\mathbf{H}_{1,5}&=\frac{n}{r_0}K_n(sr_0),\mathbf{H}_{1,6}=iks\mathbf{X}_1(sr_0),\mathbf{H}_{1,7}=iks\mathbf{Y}_1(sr_0),\mathbf{H}_{2,1}=\rho_f\omega^2I_n(fr_0),\mathbf{H}_{2,2}=\mu^t\left[2k^2-\left(k_s^t\right)^2\right]I_n(pr_0)+\frac{2p\mu^t}{r_0}\mathbf{X}_2(pr_0),\mathbf{H}_{2,3}\\
&=\mu^t\left[2k^2-\left(k_s^t\right)^2\right]K_n(pr_0)+\frac{2p\mu^t}{r_0}\mathbf{Y}_2(pr_0),\mathbf{H}_{2,4}=-\frac{2\mu^tns}{r_0}\mathbf{X}_3(sr_0),\mathbf{H}_{2,5}=-\frac{2\mu^tns}{r_0}\mathbf{Y}_3(sr_0),\mathbf{H}_{2,6}=2ik\mu^ts\left[sI_n(sr_0)+\frac{1}{r_0}\mathbf{X}_2(sr_0)\right],\mathbf{H}_{2,7}\\
&=2ik\mu^ts\left[sK_n(sr_0)+\frac{1}{r_0}\mathbf{Y}_2(sr_0)\right],\mathbf{H}_{3,2}=\frac{2pn\mu^t}{r_0}\mathbf{X}_3(pr_0),\mathbf{H}_{3,3}=\frac{2pn\mu^t}{r_0}\mathbf{Y}_3(pr_0),\mathbf{H}_{3,4}=-s^2\mu^t\mathbf{X}_4(sr_0),\mathbf{H}_{3,5}=-s^2\mu^t\mathbf{Y}_4(sr_0),\mathbf{H}_{3,6}\\
&=\frac{2iksn\mu^t}{r_0}\mathbf{X}_3(sr_0),\mathbf{H}_{3,7}=\frac{2iksn\mu^t}{r_0}\mathbf{Y}_3(sr_0),\mathbf{H}_{4,2}=2ikp\mu^t\mathbf{X}_1(pr_0),\mathbf{H}_{4,3}=2ikp\mu^t\mathbf{Y}_1(pr_0),\mathbf{H}_{4,4}=\frac{ikn\mu^t}{r_0}I_n(sr_0),\mathbf{H}_{4,5}\\
&=\frac{ikn\mu^t}{r_0}K_n(sr_0),\mathbf{H}_{4,6}=-\left(k^2+s^2\right)s\mu^t\mathbf{X}_1(sr_0),\mathbf{H}_{4,7}=-\left(k^2+s^2\right)s\mu^t\mathbf{Y}_1(sr_0),\mathbf{H}_{5,2}=pX_1(pr_1),\mathbf{H}_{5,3}=p\mathbf{Y}_1(pr_1),\mathbf{H}_{5,4}\\
&=\frac{n}{r_0}I_n(sr_1),\mathbf{H}_{5,5}=\frac{n}{r_0}K_n(sr_1),\mathbf{H}_{5,6}=iks\mathbf{X}_1(sr_1),\mathbf{H}_{5,7}=iks\mathbf{Y}_1(sr_1),\mathbf{H}_{5,8}=-f\mathbf{X}_1(fr_1),\mathbf{H}_{5,9}=-fY_1(fr_1),\mathbf{H}_{6,2}\\
&=\mu^t\left[2k^2-\left(k_s^t\right)^2\right]I_n(pr_1)+\frac{2p\mu^t}{r_1}\mathbf{X}_2(pr_1),\mathbf{H}_{6,3}=\mu^t\left[2k^2-\left(k_s^t\right)^2\right]K_n(pr_1)+\frac{2p\mu^t}{r_1}\mathbf{Y}_2(pr_1),\mathbf{H}_{6,4}=-\frac{2\mu^tns}{r_0}\mathbf{X}_3(sr_1),\mathbf{H}_{6,5}\\
&=-\frac{2\mu^tns}{r_0}\mathbf{Y}_3(sr_1),\mathbf{H}_{6,6}=2ik\mu^ts\left[sI_n(sr_1)+\frac{1}{r_1}\mathbf{X}_2(sr_1)\right],\mathbf{H}_{6,7}=2ik\mu^ts\left[sK_n(sr_1)+\frac{1}{r_1}\mathbf{Y}_2(sr_1)\right],\mathbf{H}_{6,8}=\rho_f\omega^2I_n(fr_1),\mathbf{H}_{6,9}\\
&=\rho_f\omega^2K_n(fr_1),\mathbf{H}_{7,2}=\frac{2pn\mu^t}{r_1}\mathbf{X}_3(pr_1),\mathbf{H}_{7,3}=\frac{2pn\mu^t}{r_1}\mathbf{Y}_3(pr_1),\mathbf{H}_{7,4}=-s^2\mu^t\mathbf{X}_4(sr_1),\mathbf{H}_{7,5}=-s^2\mu^t\mathbf{Y}_4(sr_1),\mathbf{H}_{7,6}=\frac{2iksn\mu^t}{r_1}\mathbf{X}_3(sr_1),\mathbf{H}_{7,7}\\
&=\frac{2iksn\mu^t}{r_1}\mathbf{Y}_3(sr_1),\mathbf{H}_{8,2}=2ikp\mu^t\mathbf{X}_1(pr_1),\mathbf{H}_{8,3}=2ikp\mu^t\mathbf{Y}_1(pr_1),\mathbf{H}_{8,4}=\frac{ikn\mu^t}{r_1}I_n(sr_1),\mathbf{H}_{8,5}=\frac{ikn\mu^t}{r_1}K_n(sr_1),\mathbf{H}_{8,6}\\
&=-\left(k^2+s^2\right)s\mu^t\mathbf{X}_1(sr_1),\mathbf{H}_{8,7}=-\left(k^2+s^2\right)s\mu^tY_1(sr_1),\mathbf{H}_{9,8}=-fX_1(fr_2),\mathbf{H}_{9,9}=-f\mathbf{Y}_1(fr_2),\mathbf{H}_{9,10}=(1+ika')q_P\mathbf{Y}_1(q_Pr_2),\mathbf{H}_{9,11}\\
&=\frac{n}{r_2}K_n(q_{SH}r_2),\mathbf{H}_{9,12}=(b'+ik)q_{SV}\mathbf{Y}_1(q_{SV}r_2),\mathbf{H}_{10,8}=\rho_f\omega^2I_n(fr_2),\mathbf{H}_{10,9}=\rho_f\omega^2K_n(fr_2),\mathbf{H}_{10,10}\\
&=\left[C_{11}q_P^2-C_{13}k^2+(C_{11}-C_{13})ika'q_P^2\right]K_n(q_Pr_2)+\frac{2C_{66}q_P}{r_2}(1+ika')\mathbf{Y}_2(q_Pr_2),\mathbf{H}_{10,11}=-\frac{2C_{66}nq_{SH}}{r_2}\mathbf{Y}_3(q_{SH}r_2),\mathbf{H}_{10,12}\\
&=\left[\left(C_{11}q_{SV}^2-C_{13}k^2\right)b'+(C_{11}-C_{13})ikq_{SV}^2\right]K_n(q_{SV}r_2)+\frac{2C_{66}q_{SV}}{r_2}(ik+b')\mathbf{Y}_2(q_{SV}r_2),\mathbf{H}_{11,10}=\frac{2C_{66}nq_P}{r_2}(1+ika')\mathbf{Y}_3(q_Pr_2)\mathbf{H}_{11,11}\\
&=-C_{66}q_{SH}^2\mathbf{Y}_4(q_{SH}r_2),\mathbf{H}_{11,12}=\frac{2C_{66}nq_{SV}}{r_2}(b'+ik)\mathbf{Y}_3(q_{SV}r_2),\mathbf{H}_{12,10}=C_{44}q_P\left[2ik-a'\left(k^2+q_P^2\right)\right]\mathbf{Y}_1(q_Pr_2),\mathbf{H}_{12,11}\\
&=\frac{iknC_{44}}{r_2}K_n(q_{SH}r_2),\mathbf{H}_{12,12}=-C_{44}q_{SV}\left[\left(k^2+q_{SV}^2\right)-2ikb'\right]\mathbf{Y}_1(q_{SV}r_2)
\end{aligned}\tag{A-1}$$

where, *In* and *Kn* (n = 0, 1, 2) denote the first- and second-kind modified Bessel functions of the nth order, respectively; $\mu^t=\rho_t\cdot(v_s^t)^2$ and ρ_t denote the shear modulus and density of the drill collar; v_f, v_p, v_s are the fluid velocity, the P- and Swave velocities of the drill collar, respectively; the corresponding wavenumbers (k_f, k_p, k_s) and radial wavenumbers (f, p, s) are given by:

$$\begin{cases}k_f=\omega/v_f\\k_p=\omega/v_p\\k_s=\omega/v_s\end{cases},\tag{A-2}$$

$$\begin{cases} f = \sqrt{k^2 - k_f^2} \\ p = \sqrt{k^2 - k_p^2} \\ s = \sqrt{k^2 - k_s^2} \end{cases}, \tag{A-3}$$

The radial wavenumbers for the formation quasi-P- and quasi-S-waves are given by:

$$\begin{cases} q_P = \omega\sqrt{\dfrac{-V + \sqrt{V^2 - 4UW}}{2U}} \\ q_{SV} = \omega\sqrt{\dfrac{-V - \sqrt{V^2 - 4UW}}{2U}} \\ q_{SH} = \sqrt{\dfrac{c_{44}k^2 - \rho\omega^2}{C_{66}}} \end{cases}, \tag{A-4}$$

with the symbols U, V, and W defined by:

$$\begin{cases} U = C_{11}C_{44} \\ V = \rho(C_{11} + C_{44}) - \left(C_{11}C_{33} - C_{13}^2 - 2C_{13}C_{44}\right)\left(k^2 \middle/ \omega^2\right) \\ W = C_{33}C_{44}\left(\rho \middle/ C_{44} - k^2 \middle/ \omega^2\right)\left(\rho \middle/ C_{33} - k^2 \middle/ \omega^2\right) \end{cases}, \tag{A-5}$$

The coefficients a' and b' denoting the shear coupling to the quasi-P wave and the compressional coupling to the quasi-S wave are given by:

$$\begin{cases} a' = -\dfrac{1}{ik}\dfrac{(C_{13} + 2C_{44})k^2 - C_{11}q_P^2 - \rho\omega^2}{C_{44}k^2 - (C_{11} - C_{13} - C_{44})q_P^2 - \rho\omega^2} \\ b' = -ik\dfrac{C_{44}k^2 - (C_{11} - C_{13} - C_{44})q_{SV}^2 - \rho\omega^2}{(C_{13} + 2C_{44})k^2 - C_{11}q_{SV}^2 - \rho\omega^2} \end{cases}, \tag{A-6}$$

In the above equation, **X** and **Y** are combinations of Bessel functions, detailed as below:

$$\begin{cases} \mathbf{X}_1(x) = \dfrac{n}{x}I_n(x) + I_{n+1}(x) \\ \mathbf{X}_2(x) = \dfrac{n(n-1)}{x}I_n(x) - I_{n+1}(x) \\ \mathbf{X}_3(x) = \dfrac{1-n}{x}I_n(x) - I_{n+1}(x) \\ \mathbf{X}_4(x) = \left[1 + \dfrac{2n(n-1)}{x^2}\right]I_n(x) - \dfrac{2}{x}I_{n+1}(x) \end{cases}, \tag{A-7}$$

$$\begin{cases} \mathbf{Y}_1(x) = \dfrac{n}{x}K_n(x) - K_{n+1}(x) \\ \mathbf{Y}_2(x) = \dfrac{n(n-1)}{x}K_n(x) + K_{n+1}(x) \\ \mathbf{Y}_3(x) = \dfrac{1-n}{x}K_n(x) + K_{n+1}(x) \\ \mathbf{Y}_4(x) = \left[1 + \dfrac{2n(n-1)}{x^2}\right]K_n(x) + \dfrac{2}{x}K_{n+1}(x) \end{cases}, \tag{A-8}$$

Furthermore, the dispersion equation is obtained by setting the determinant in Eq. (A-1) equal to zero. For a given angular frequency ω, the corresponding wavenumbers k are then determined through numerical methods.

Appendix B. The tests in inversion process

The weight coefficient λ is obtained by calculating the median or mean of the mode-wave objective functions. This method offers two advantages: first, it ensures that the contributions of the two mode waves are in the same order of magnitude, thereby reducing inversion errors. Second, it enables rapid adjustment of the weight coefficient at different depth points during well-segment processing, allowing better adaptation to field data applications. Using this method, the weight factor λ from the synthetic waveform data in Fig. 10 is 0.3. Based on field data processing, it is shown that the value of λ in engineering practice ranges from 0 to 0.5. In addition, the sensitivity experiment on λ (Li et al., 2023) is conducted, as follows:

$$\lambda_{ST/QD} = \sum_j \left(\sum_{\Omega_{ST/QD}} Sensitivity_{ST/QD}^{p_j}\right) \Big/ \sum_j \left(\sum_{\Omega_{ST}} Sensitivity_{ST}^{p_j} + \sum_{\Omega_{QD}} Sensitivity_{QD}^{p_j}\right) \tag{B-1}$$

where $\sum_{\Omega_{ST/QD}} Sensitivity_{ST/QD}^{p}$ is the Stoneley- or quadrupole-wave sensitivity to the parameter p, respectively. And j is the number of inversion parameter. For joint inversion, we choose to calculate the weighting factor λ by summing the sensitivity to the shear velocity V_{SV} and the anisotropy γ. Substituting the data from Fig. 10 into Eq. (B-1), the calculation result ($\lambda = 0.32$) is similar to those obtained using our approach for calculating the median. The sensitivity experiment on λ verified the feasibility of our initial calculation method. Based on field data processing, it is shown that the value of λ in engineering practice ranges from 0 to 0.5.

To evaluate the robustness of the proposed inversion method under noisy ALWD conditions, Gaussian noise and discrete noise were added to the Stoneley- and quadrupole-wave dispersion data at different levels, as shown in Figs. B1(a)-(b) and B2(a)-(b). For each noise level, the inverted V_{SV} and γ were calculated. The purpose of this test was to examine whether the proposed method could still recover stable anisotropy estimates when the measured dispersion data were contaminated by noise. The results indicate that the proposed method maintains stable inversion results under low noise levels (as shown in Figs. B1(c) and B2(c)), while the uncertainty of the inverted parameters increases under high noise conditions (as shown in Figs. B1(d) and B2(d)). When noise is at a high level, it is necessary to adopt certain noise reduction techniques to improve the stability of inversion results, such as median filtering and cluster analysis.

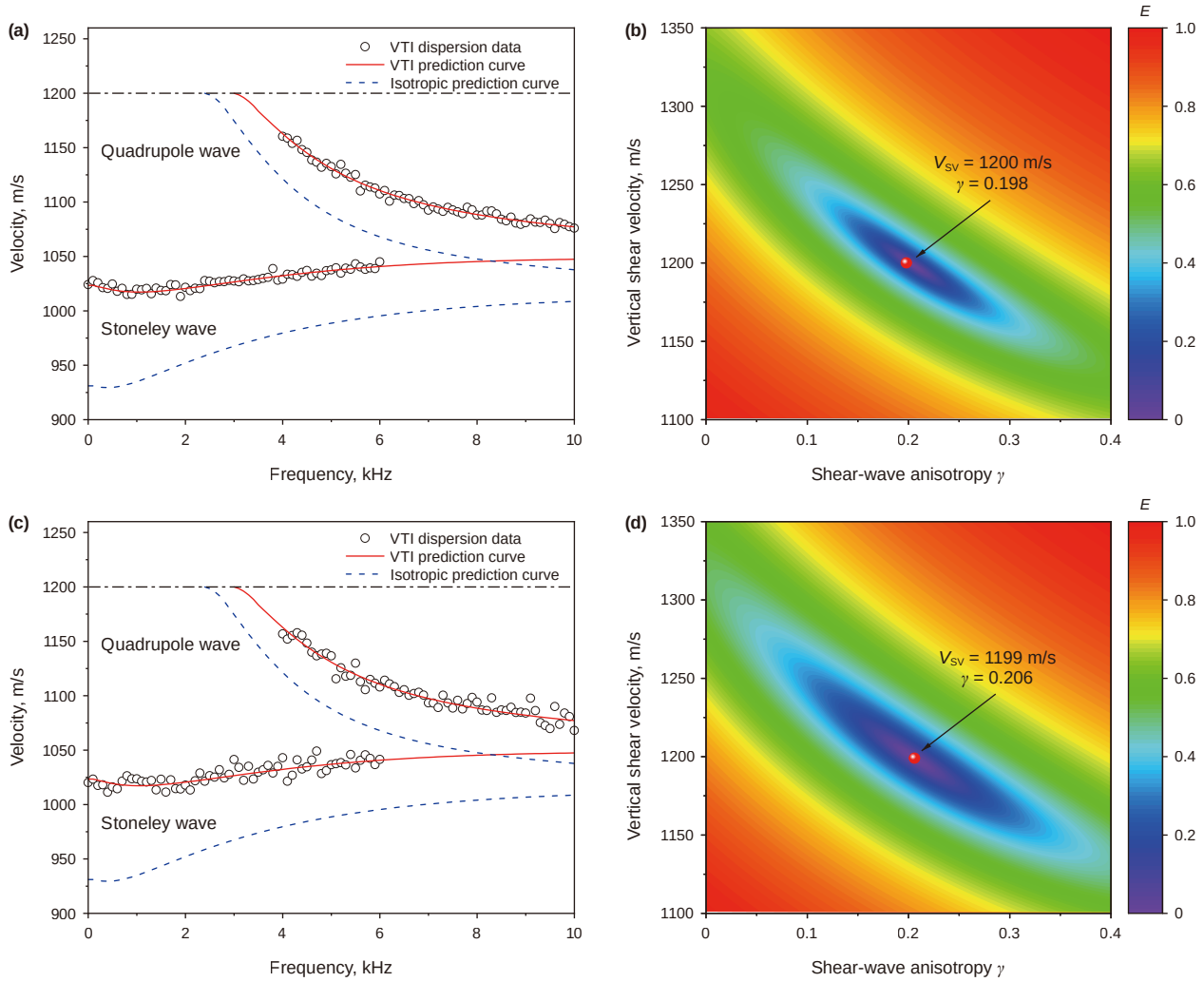


Fig. B1. Inversion results contain synthetic Gaussian noise data: **(a)** the dispersion data of low-level Gaussian noise; **(b)** the inversion results of low-level Gaussian noise; **(c)** the dispersion data of high-level Gaussian noise; **(d)** the inversion results of high-level Gaussian noise.

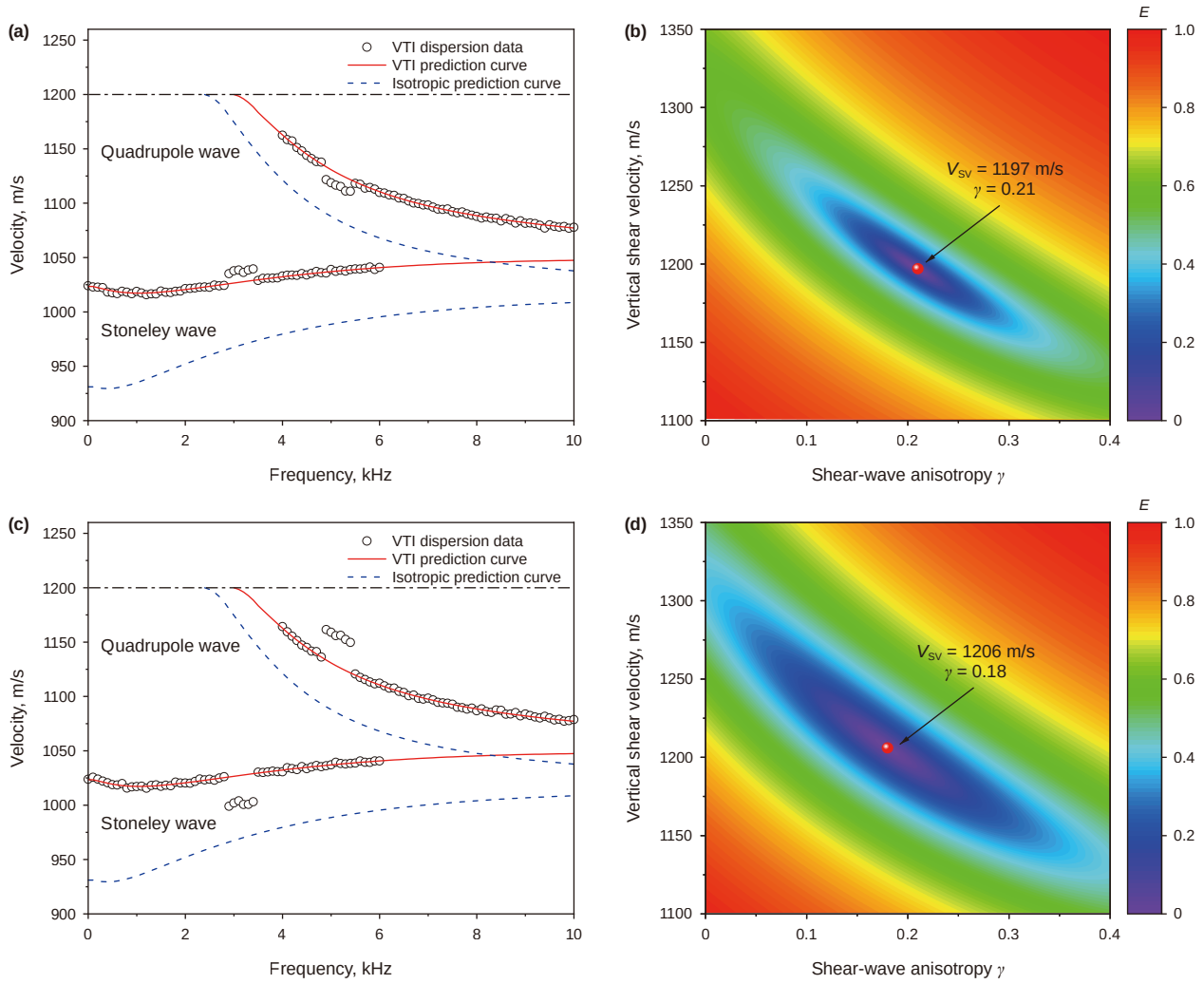


Fig. B2. Inversion results contain synthetic discrete noise data: **(a)** the dispersion data of low-level discrete noise; **(b)** the inversion results of low-level discrete noise; **(c)** the dispersion data of high-level discrete noise; **(d)** the inversion results of high-level discrete noise.

References

Assous, S., Tudge, J., Whetton, J., Elkington, P., 2018. Dispersive mode processing of borehole acoustic logs using fast slowness-frequency inversion. In: Abu Dhabi International Petroleum Exhibition and Conference. SPE. https://doi.org/10.2118/192767-MS.

Briggs, V.A., 2006. A Comparison of Logging While Drilling (Lwd) and Wireline Acoustic Measurements. Massachusetts Institute of Technology.

Burridge, R., Sinha, B.K., 1996. Inversion for formation shear modulus and radial depth of investigation using borehole flexural waves. SEG Tech. Progr. Expand. Abstr. 15 (1), 158–161. https://doi.org/10.1190/1.1826426.

Chan, A.K., Tsang, L., 1983. Propagation of acoustic waves in a fluid-filled borehole surrounded by a concentrically layered transversely isotropic formation. SEG Tech. Progr. Expand. Abstr. 74 (5), 1605–1616. https://doi.org/10.1190/1.1893773.

Chen, X., Xia, J., Pang, J., et al., 2022. Deep learning inversion of rayleigh-wave dispersion curves with geological constraints for near-surface investigations. Geophys. J. Int. 231 (1), 1–14. https://doi.org/10.1093/gji/ggac171.

Cheng, C.H., Toksöz, M.N., Willis, M.E., 1982. Determination of *in situ* attenuation from full waveform acoustic logs. J. Geophys. Res. 87 (B7), 5477–5484. https://doi.org/10.1029/jb087ib07p05477.

Collins, M., 2013. Joint VTI and mud slowness inversion using multiple modes and adaptive weighting. In: Global Meeting Abstracts. Society of Exploration Geophysicists, pp. 2548–2555. https://doi.org/10.1190/urtec2013-265.

Crampin, S., 1984. Effective anisotropic elastic constants for wave propagation through cracked solids. Geophys. J. Int. 76, 135–145. https://doi.org/10.1111/J.1365-246X.1984.TB05029.X.

Cui, Z.W., 2004. Theoretical and Numerical Study of Modified Biot's Models, Acoustoelectric Well Logging and Acoustic Logging While Drilling Excited by Multipole Acoustic Sources. Jilin University, Changchun [Ph. D. thesis] (in Chinese).

Ekstrom, M.P., 1996. Dispersion estimation from borehole acoustic arrays using a modified matrix pencil algorithm. In: Conference Record of the twenty-ninth Asilomar Conference on Signals, Systems and Computers, vol. 1. IEEE, pp. 449–453. https://doi.org/10.1109/ACSSC.1995.540589.

Ellefsen, K.J., Cheng, C.H., Toksöz, M.N., 1990. Cylindrical waves in transversely isotropic media. J. Acoust. Soc. Am. 70 (4), 1147–1155. https://doi.org/10.1121/1.386946.

Esmersoy, C., Koster, K., Williams, M., et al., 1994. Dipole Shear Anisotropy Logging. Seg Technical Program Expanded Abstracts, pp. 1139–1142. https://doi.org/10.1190/1.1822720.

Haji, S.H., Abdulazeez, A.M., 2021. Comparison of optimization techniques based on gradient descent algorithm: a review. PalArch's J. Archaeol. Egypt/Egyptol. 18 (4), 2715–2743.

He, X., Hu, H.S., 2010. Single-valued definition of the multivalued function for borehole acoustic waves in transversely isotropic formations. Sci. China Phys. Mech. Astron. 53 (8), 1419–1426. https://doi.org/10.1007/s11433-010-4037-7.

Hu, H.S., He, X., 2009. The low-frequency asymptotic velocity of pseudo-rayleigh, flexural, and screw waves in a transversely isotropic formation. Chin. J. Geophys. 52 (7), 1873–1880. https://doi.org/10.3969/j.issn.0001-5733.2009.07.022.

Hu, Y., Guo, R., Jin, Y., et al., 2020. A supervised descent learning technique for solving directional electromagnetic logging-while-drilling inverse problems. IEEE Trans. Geosci. Rem. Sens. 99, 1–13. https://doi.org/10.1109/TGRS.2020.2986000.

Kong, W., Dong, Z.Y., Jia, Y., et al., 2017. Short-term residential load forecasting based on lstm recurrent neural network. IEEE Trans. Smart Grid 10 (1), 841–851. https://doi.org/10.1109/TSG.2017.2753802.

Krizhevsky, A., Sutskever, I., Hinton, G.E., 2012. Imagenet Classification with Deep Convolutional Neural Networks, vol. 25. NIPS.Curran Associates Inc. https://doi.org/10.1145/3065386.

Lang, S.W., Kurkjian, A.,L., McClellan, J.H., et al., 1987. Estimating slowness dispersion from arrays of sonic logging waveforms. Geophysics 52 (4), 530–544. https://doi.org/10.1190/1.1442322.
Lee, X.Q., Chen, H., He, X., Wang, X.M., et al., 2013. Analyses on mode waves of acoustic logging while drilling in transversely isotropic formations. Chin. J. Geophys. 56 (9), 3212–3222. https://doi.org/10.6038/cjg20130933.
Lee, S.Q., Tang, X.M., Su, Y.D., et al., 2016. Model-based dispersive processing of borehole dipole wave data using an equivalent-tool theory. Geophysics 81 (1), D35–D39. https://doi.org/10.1190/geo2015-0210.1.
Li, Y.H., Xu, S., Jiang, C., Su, Y.D., Tang, X.M., 2020. Joint inversion of logging-while-drilling multipole acoustic data to determine formation shear-wave transverse isotropy. Geophysics 85 (4), 1–43. https://doi.org/10.1190/geo2019-0611.1.
Li, J.C., He, X., Zhao, A.S., et al., 2023. Joint inversion of formation radial shear-velocity profiles by dipole acoustic logging while drilling. Geophysics 88 (4), D295–D305, 10.11902Fgeo2022-0426.1.
Li, H.R., Tang, X.M., Li, S.Q., et al., 2022. Dynamic fluid transport property of hydraulic fractures and its evaluation using acoustic logging. Petrol. Explor. Dev. 49 (1), 194–202. https://doi.org/10.11698/PED.2022.01.18.
Li, J.C., He, X., Jiang, C., 2022. Joint inversion method of formation shear-wave anisotropy from logging-while-drilling acoustic data. Appl. Geophys.: Bull. Chin. Geophys. Soc. 19 (4). https://doi.org/10.1007/s11770-022-0947-1.
Li, J.C., He, X., Chen, H., Jiang, C., Wang, W., 2024. Inversion of radial shear velocity profile for acoustic logging using CNN-LSTM network. IEEE Trans. Geosci. Rem. Sens. 62, 1–10. https://doi.org/10.1109/TGRS.2024.3370106.
Liang, L., Lei, T., 2021. Machine-learning-enabled automatic sonic shear processing. Petrophysics 62 (3), 14. https://doi.org/10.30632/PJV62N3-2021a3.
Liang, L., Lei, T., Blyth, M., 2021b. Automatic logging-while-drilling dipole sonic shear processing enabled by physics-driven machine learning. In: SPWLA 62nd Annual Logging Symposium. OnePetro. https://doi.org/10.30632/SPWLA-2021-0059.
Liang, L., Lei, T., Donald, A., et al., 2021c. Physics-driven machine-learning-based borehole sonic interpretation in the presence of casing and drillpipe. SPE Reservoir Eval. Eng 24 (2), 15. https://doi.org/10.2118/201542-PA.
Luo, C., Grana, D., Wen, X., et al., 2025. Adaptive Markov Chain Monte Carlo with sparse constraints for nonlinear seismic inversion. Geophysics 90 (6), M289–M302. https://doi.org/10.1190/geo2024-0923.1.
Meng, Q., Chen, Y., Sha, F., et al., 2023. Inversion of rayleigh wave dispersion curve extracting from ambient noise based on dnn architecture. Appl. Sci. 13 (18), 2076–3417. https://doi.org/10.3390/app131810194.
Nolte, B., Rao, R., Huang, X., 1997. Dispersion Analysis of Split Flexural Waves. Massachusetts Institute of Technology. Earth Resources Laboratory.
Onalo, D., Oloruntobi, O., Adedigba, S., et al., 2019. Dynamic data driven sonic well log model for formation evaluation. J. Petrol. Sci. Eng. 175, 1049–1062, Apr. https://doi.org/10.1016/j.petrol.2019.01.042.
Rao, B., Tang, X.M., Su, Y.D., 2022. Theoretical calculation and mechanism analysis for component waves of acoustic logging while drilling in transversely isotropic formations, Chinese J. Geophys 65 (8), 3198–3212. https://doi.org/10.6038/cjg2022O0423 in Chinese.
Schmidhuber, J., Hochreiter, S., 1997. Long short-term memory. Neural Comput 9 (8), 1735–1780. https://doi.org/10.1162/neco.1997.9.8.1735.
Schoenberg, M., Muir, F., Sayers, C.M., 1996. Introducing annie: a simple three parameters anisotropic velocity model for shales. J. Seismic Explor. 5, 35–49.
Sinha, B.K., Simsek, E., Asvadurov, S., 2009. Influence of a pipe tool on borehole modes. Geophysics 74 (3), E111–E123. https://doi.org/10.1190/1.3085644.
Su, Y.D., Jiang, C., Zhuang, C.X., et al., 2016. Joint inversion of logging-while-drilling multipole acoustic data to determine p- and s-wave velocities in unconsolidated slow formations. Geophysics 81 (5), 795–799. https://doi.org/10.1190/geo2016-0133.1.
Tang, X.M., 2003. Determining formation shear-wave transverse isotropy from borehole stoneley-wave measurements. Geophysics 68 (1), 118–126. https://doi.org/10.1190/1.1543199.
Tang, X., Cheng, C.H., 1996. Fast inversion of formation permeability from stoneley wave logs using a simplified biot-rosenbaum model. Geophysics 61 (3), 639–645. https://doi.org/10.1190/1.1443993.
Tang, X.M., Cheng, C.H., 2004. Quantitative Borehole Acoustic Methods. Elsevier Science Publishing Company Inc.
Tang, X.M., Dubinsky, V., Patterson, D.J., 2006. Development of a low frequency LWD quadrupole shear-wave technology to improve quality of formation shear velocity measurement. In: Annual Technical Conference and Exhibition. SPE, Extended Abstracts. https://doi.org/10.2118/102335-MS.
Tang, X.M., Dubinsky, V., Wang, T., et al., 2003. Shear-velocity measurement in the logging-while-drilling environment: modeling and field evaluations. Petrophysics 44 (2), 79–90.
Thomsen, L., 1986. Weak elastic anisotropy. Geophysics 51, 1954–1966. https://doi.org/10.1190/1.1442051.
Tongtaow, C., 1982. Wave Propagation Along a Cylindrical Borehole in a Transversely Isotropic Medium. Colorado School of Mines.
Vaswani, A., Shazeer, N., Parmar, N., et al., 2017. Attention is all you need. Adv. Neural Inf. Process. Syst. 30. https://doi.org/10.48550/arXiv.1706.03762.
Wang, H., Tao, G., 2011. Wavefield simulation and data-acquisition-scheme analysis for lwd acoustic tools in very slow formations. Geophysics 76 (3), E59–E68. https://doi.org/10.1190/1.3552929.
Wang, W.H., Li, S.Q., Zhuang, C.X., et al., 2025. Dynamic seismic s-wave anisotropy in vertically fractured rocks: modeling and field application. Geophysics 90 (5), A31–A35. https://doi.org/10.1190/geo2024-0908.1.
White, J.E., Tongtaow, C., 1981. Cylindrical waves in transversely isotropic media. J. Acoust. Soc. Am. 70, 1147–1155. https://doi.org/10.1121/1.386017.
Xu, S., Tang, X.M., Su, Y.D., Lee, S.Q., Zhuang, C.X., 2017. Determining formation s-wave transverse isotropy from borehole flexural-wave dispersion data. Geophysics 82 (2), D47–D55. https://doi.org/10.1190/geo2016-0223.1.
Zhang, Z.H., Lu, R.Q., Liao, X.L., et al., 2021. Inversion of magnetic anomaly and magnetic gradient anomaly based on fully convolution network. Progress in Geophysics 36 (1), 325–337. https://doi.org/10.1029/JC084iC12p07899.
Zhang, Z.H., Shi, Z.Y., Ma, N., et al., 2022. Deep learning inversion of Rayleigh dispersion curves. Chin. J. Geophys. 65 (6), 2244–2259. https://doi.org/10.6038/cjg2022P0446 in Chinese.
Zhang, H., Sun, Z., Li, X., et al., 2024. Deep Learning Approach to Inverting Flexural Wave Dispersion. In: Fourth International Meeting for Applied Geoscience & Energy, pp. 439–443. https://doi.org/10.1190/image2024-4089186.1.
Zhuang, C.X., Li, Y.H., Kong, F.T., et al., 2019. Formation permeability estimation using Stoneley waves from logging while drilling: theory, method, and application. Chin. J. Geophys. 62 (11), 4482–4492. https://doi.org/10.6038/cjg2019N0122 in Chinese.

GEOPHYSICS, VOL. 90, NO. 6 (NOVEMBER-DECEMBER 2025); P. D125–D136, 11 FIGS., 1 TABLE.
10.1190/GEO2024-0675.1

Ultraslow formation shear slowness estimation in a large borehole using an eccentric dipole tool

Bo Rao[1], Yuan-Da Su[1], Jing-Qi Lin[2], Yang Liu[1], Sheng-Qing Li[1], and Xiao-Ming Tang[1]

ABSTRACT

Obtaining accurate shallow ultraslow formation S-wave (shear) slowness is crucial for seismic exploration and hydrocarbon reserve assessment. Dipole acoustic logging is an effective method for estimating slow formation shear slowness. However, for the large borehole and unconsolidated soft sediments of the shallow marine environment, conventional dipole logging is often ineffective. To address this issue, we develop tool eccentricity for dipole S-wave logging. This study provides the theoretical justification of our method. The dipole acoustic wavefield of an eccentric tool is studied using a dual-cylindrical coordinate system in connection with the translational addition theorem for cylindrical Bessel functions, which provide analytical solutions to analyze the effects of tool eccentricity and formation elastic property. The results indicate that tool eccentricity in such an environment can substantially increase the dipole-wave amplitude for estimating the formation shear slowness. The S-wave logging can even be conducted by positioning the dipole tool against the borehole wall. This logging configuration is tested in a shallow test well with an oversized borehole. The measurement results are compared with their centralized counterparts. The measured data indicate that compared with the centralized tool measurement, eccentering the dipole tool can greatly enhance the measured S-wave amplitude and improve the accuracy of the formation shear slowness measurement, thereby providing an effective method for obtaining formation shear slowness in shallow soft sediments.

INTRODUCTION

Soft unconsolidated sediments are often encountered onshore and in shallow marine environments. Obtaining the shear slowness from these formations has been an important topic in dipole acoustic logging (Sinha et al., 1994; Tang and Patterson, 2001; Cao et al., 2003; Li et al., 2013, 2019; Jiang et al., 2019).

Dipole logging in the ultraslow formation has been used to obtain the formation P-wave (compressional) slowness (Tichelaar and Luik, 1995). Zhang et al. (2009) theoretically analyze the physical mechanism of the dipole leaky P wave in a slow formation and study the effect of the leaky mode on the compressional head wave. Chen et al. (2009) analyze the amplitude variation of the dipole leaky P wave in ultraslow formation with respect to the formation velocity, borehole diameter, and other related parameters and validate the use of the leaky mode to extract the formation compressional slowness.

Despite the success in dipole compressional slowness estimation, measuring ultraslow formation shear slowness has encountered difficulties. The first is the large size of the borehole in shallow soft sediments. Conventional (centralized) dipole logging in the oversized borehole condition often fails to obtain the shear slowness. As a result, logging with the eccentric tool has been proposed. Leslie and Randall (1990) analyze the acoustic wavefield excited by an eccentric dipole source using theoretical and experimental methods and discuss the variation in the flexural wave velocity and amplitude with the tool eccentricity distance and direction. Zhang et al. (1996) study the nonaxisymmetric wavefield generated by an eccentric monopole source and attempt to extract the S-wave component by subtracting the waveforms of the inline receivers. Pardo et al. (2011) develop a high-order polynomial adaptive finite-element method for modeling the acoustic wavefield with an eccentric monopole tool and show that the wavefield contains

Manuscript received by the Editor 20 September 2024; revised manuscript received 27 April 2025; published ahead of production 24 June 2025; published online 20 August 2025.
[1]China University of Petroleum (East China), National Key Laboratory of Deep Oil and Gas, Qingdao, China and China University of Petroleum (East China), School of Geosciences, Qingdao, China. E-mail: raob0801@foxmail.com; syuanda@sina.com (corresponding author); 1759775844@qq.com; shidalishengqing@yeah.net; tangxiam@aliyun.com.
[2]China National Logging Corporation, Xinjiang Branch, Karamay, China. E-mail: cjlinjq@cnpc.com.cn
© 2025 Society of Exploration Geophysicists. All rights reserved.

Downloaded from pubs.geoscienceworld.org/seg/geophysics/article-pdf/90/6/D125/7330891/geo-2024-0675.1.pdf by Univ of Petroleum (Beijing) - Library user on 08 October 2026

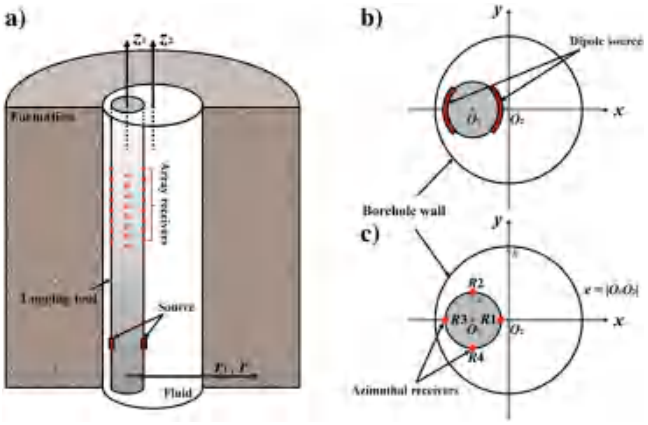


Figure 1. (a) Schematic diagram of the dipole wireline logging model with an eccentric tool, (b) configuration of the dipole source, and (c) configuration of the azimuthal receivers.

Table 1. Acoustic parameters of the theoretical model.

Medium	Compressional slowness ($\mu s \cdot m^{-1}$)	Shear slowness ($\mu s \cdot m^{-1}$)	Density ($kg \cdot m^{-3}$)	Inner radius (m)
Tool	170.65	319.45	7850	0
Borehole fluid	666.67	—	1000	0.05
Fast formation	222.22	377.36	2400	0.1
Slow formation	434.78	1000.00	2000	0.1
Ultraslow formation	630.12	1700.68	2000	0.4

the flexural wave constituents. Muga et al. (2015) develop a semi-analytical method to simulate the borehole acoustic wavefield excited by an eccentric multipole source. Xu and Hu (2019, 2020) calculate the reflected (radiated) acoustic wavefield inside (outside) the borehole excited by an eccentric point source. Whereas the existing studies were not focused on the oversized borehole condition, the present study focuses on this condition and demonstrates the dramatic effect of eccentric dipole logging in this condition. Undeniably, the difficulty also can be solved by applying some advanced data processing algorithms for high-quality measurement data in the centered case (Sollie, 1999; Tagbor et al., 2005; Xia et al., 2024).

In this paper, we use the analytical solutions in a dual-cylindrical coordinate system (Ji et al., 2021; Rao et al., 2023a, 2023b) to analyze the acoustic field of an eccentric dipole tool in a large borehole with an ultraslow formation. The results show that eccentering the dipole tool can greatly increase the dipole-wave amplitude for measuring the ultraslow formation shear slowness, thereby substantially improving the results of S-wave logging in such an environment. The theoretical analysis results are validated by field testing in a shallow oversized well.

MODEL AND SIMULATION

Figure 1 shows a theoretical dipole acoustic logging model with an eccentered tool. The tool is considered to be a rigid rod, as described by Tang and Cheng (1993) and Su et al. (2011). Looking outward from the tool axis, the three layers represent the logging tool, borehole fluid, and formation, respectively. The dual-cylindrical coordinate system with coordinates $(r_1; \varphi_1; z_1)$ and $(r_2; \varphi_2; z_2)$ is used for the analysis, as shown in Figure 1a, with the radii r_1 and r_2 originating from the center of the tool and borehole, respectively.

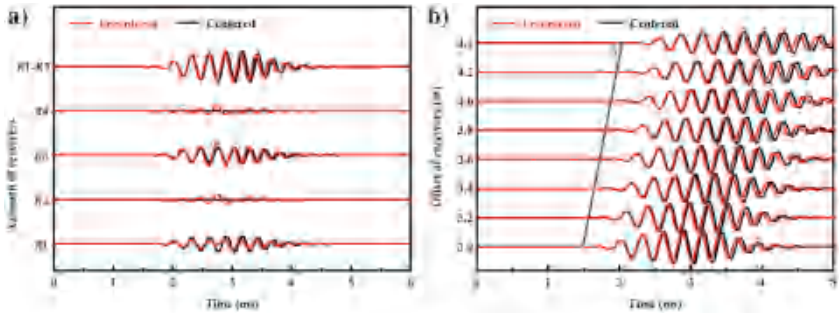


Figure 2. Modeling of dipole logging in a fast formation. (a) Azimuthal receiver response at 3 m distance from source for the centered (black) and eccentered (red) cases. The x-dipole acquisition result R1–R3 also is shown. (b) The calculated array waveform data for the centered (black) and eccentered (red) cases.

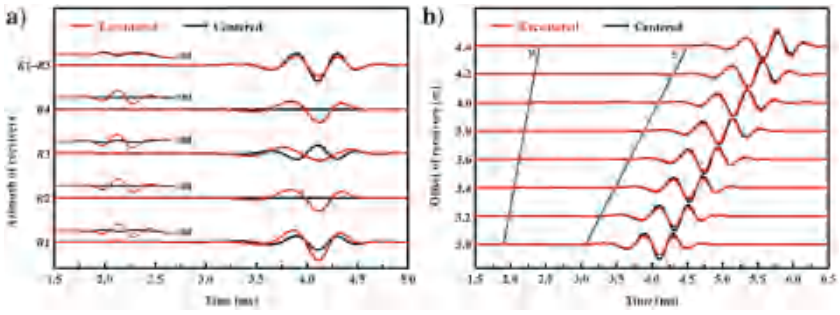


Figure 3. Modeling of dipole logging in a slow formation. (a) Azimuthal receiver response at 3 m distance from source for the centered (black) and eccentered (red) cases. The x-dipole acquisition result R1–R3 also is shown. (b) The calculated array waveform data for the centered (black) and eccentered (red) cases.

Downloaded from pubs.geoscienceworld.org/seg/geophysics/article-pdf/90/6/D125/7330891/geo-2024-0675.1.pdf by Univ of Petroleum (Beijing) - Library user on 08 October 2026

The tool and borehole are assumed parallel to each other such that z_1 and z_2 can be represented by one common variable z. A ring dipole source is placed on the surface of the logging tool (Tang and Cheng, 2004), as shown in Figure 1b. The dipole source consists of two oppositely mounted subsources, which can generate radial forces with equal amplitudes but opposite polarities. A four-receiver array is circumferentially placed at the outer surface of the tool with a 90° azimuthal increment (R1–R4 in Figure 1c). The receiver spacing in array is 0.2 m. The minimum offset, i.e., the distance between the source and first receiver, is 3.0 m. The labels a and b represent the radius of the tool and borehole, respectively. Here, O_1 and O_2 denote the origin of the tool and borehole, respectively; and $e = |O_1O_2|; (0 \le e \le b - a)$; is the tool offset. To quantitatively describe the extent of tool eccentricity from the borehole axis, we define a normalized eccentricity coefficient $ECC = e/(b - a)$. Detailed theoretical derivations are provided in Appendix A.

In dipole acoustic logging, the formation shear slowness is estimated from the low-frequency end (also called the cut-off frequency) of the dipole-generated flexural-wave dispersion curve. We first use a 2 kHz Ricker wavelet to actuate the x-dipole source in a common borehole with fast and slow formation, respectively, as a reference for subsequent large borehole with an ultraslow formation case. Using equation A-11 (see Appendix A), we investigate the acoustic wavefield of an eccentric tool versus the centered tool scenario. The acoustic parameters of the theoretical model of Figure 1 are provided in Table 1. Note a small quality factor (Q) on the tool P- and S-wave velocities has been introduced to simulate the acoustic isolation of the tool. In Figure 1, the logging tool is positioned eccentrically, with an eccentricity of 45 mm toward 180°. The radius of the borehole is 10 cm, and the tool is 5 cm, i.e., ECC = 90%.

Figures 2 and 3 show the fast and slow formation acoustic wavefield, respectively, of an eccentric dipole tool versus its centralized counterpart. Figures 2a and 3a show the waveforms at different azimuthal receivers and the output waveform at 3 m. Figures 2b and 3b show the calculated array output waveforms from 3 to 4.4 m. The black and red curves represent the waveforms for the centralized and eccentered cases, respectively. In the fast formation, the waveforms at inline receivers (R1 and R3) have small difference in the amplitude and phase from those of the centralized tool case. The difference becomes larger in the slow formation case, but it can be eliminated by subtracting the waveforms of the inline receivers. A clearer comparison is shown in Figures 2b and 3b, indicating that the tool eccentricity does not affect the estimation of formation shear slowness in this condition. Notably, the waveforms at the crossline receivers (R2 and R4) are not zero as in the centralized case and are identical because the crossline receivers are symmetric relative to the borehole center. Note the crossline and inline

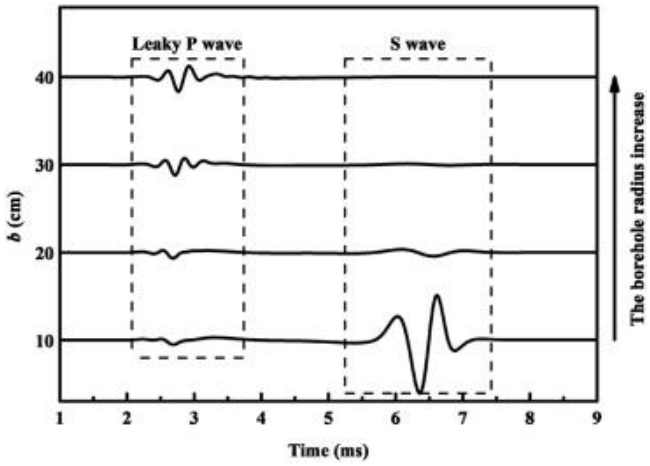


Figure 4. Modeling of centered dipole logging in an ultraslow formation with different borehole radius.

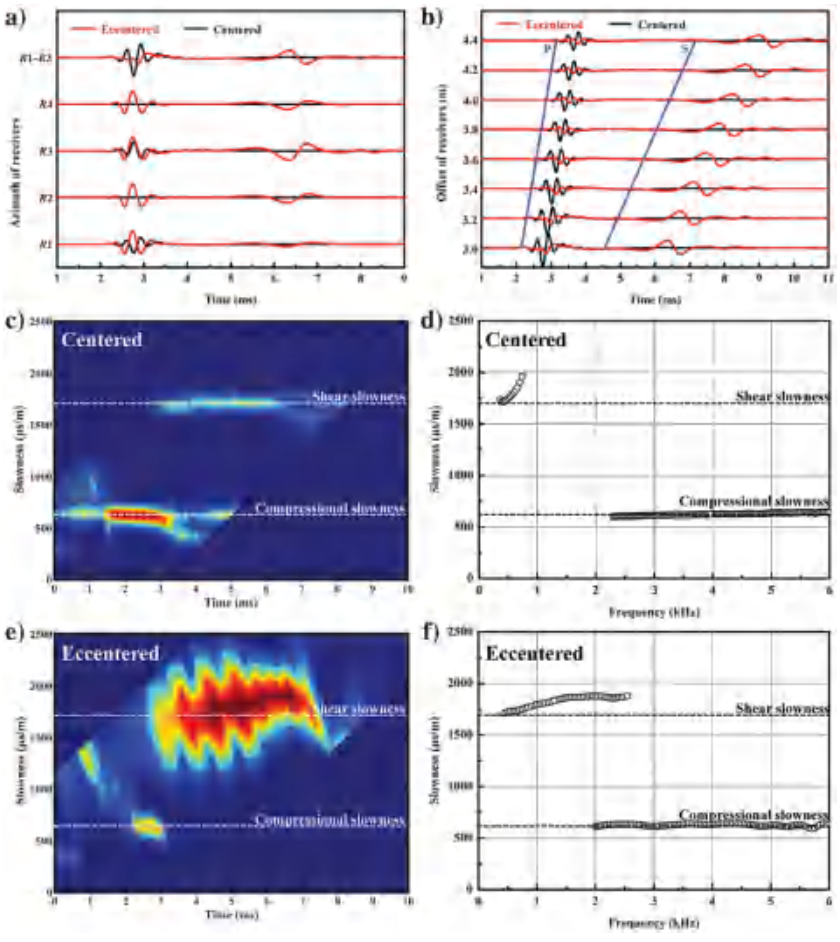


Figure 5. Modeling of dipole logging in an ultraslow formation with a large borehole. (a) Azimuthal receiver response at 3 m distance from source for the centered (black) and eccentered (red) cases with the x-dipole acquisition result R1–R3 also shown. (b) The calculated array waveform data for the centered (black) and eccentered (red) cases. (c and d) The STC correlogram and the dispersion data obtained from processing the array waveform for the centered tool case, respectively. (e and f) The STC correlogram and the dispersion data obtained from processing the array waveform for the eccentered tool case, respectively.

Downloaded from pubs.geoscienceworld.org/seg/geophysics/article-pdf/90/6/D125/7330891/geo-2024-0675.1.pdf by Univ of Petroleum (Beijing) - Library user on 08 October 2026

wave amplitudes are of the same order of magnitude. In addition, the amplitude of the leaky P wave excited in the case of tool eccentricity is much larger, between 1.5 and 2.7 ms, as shown in Figure 3a (the wave amplitude has been amplified by a factor of 80), which is beneficial for estimating slow formation compressional slowness.

Onshore shallow formations and seabed sediment layers typically exhibit ultralow acoustic velocities and ultrahigh wave attenuation.

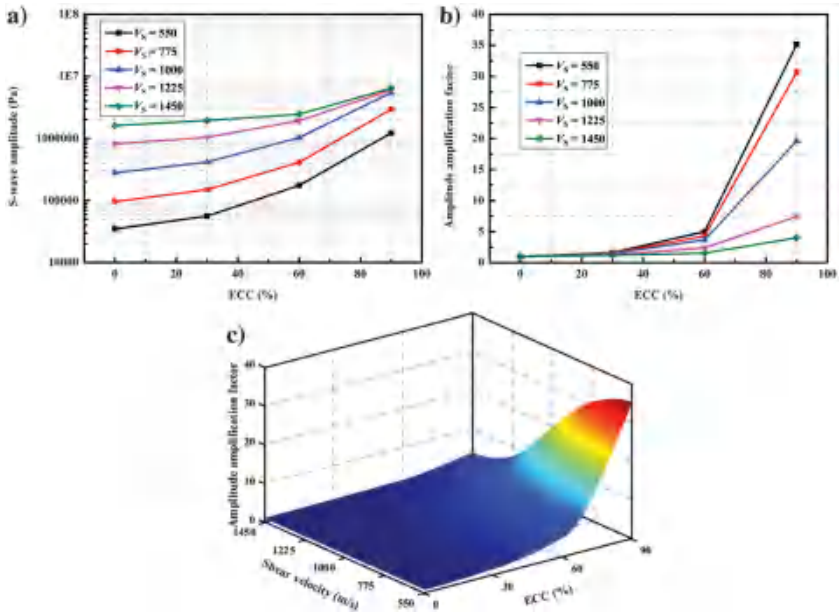


Figure 6. (a) The S-wave amplitude and (b) amplification factor versus tool eccentricity for shear velocity values ranging from slow to ultraslow formations. (c) The amplitude variation trend for the two parameters is shown as a surface plot. Note the dramatic amplitude increase in the high-eccentricity and low-velocity situation.

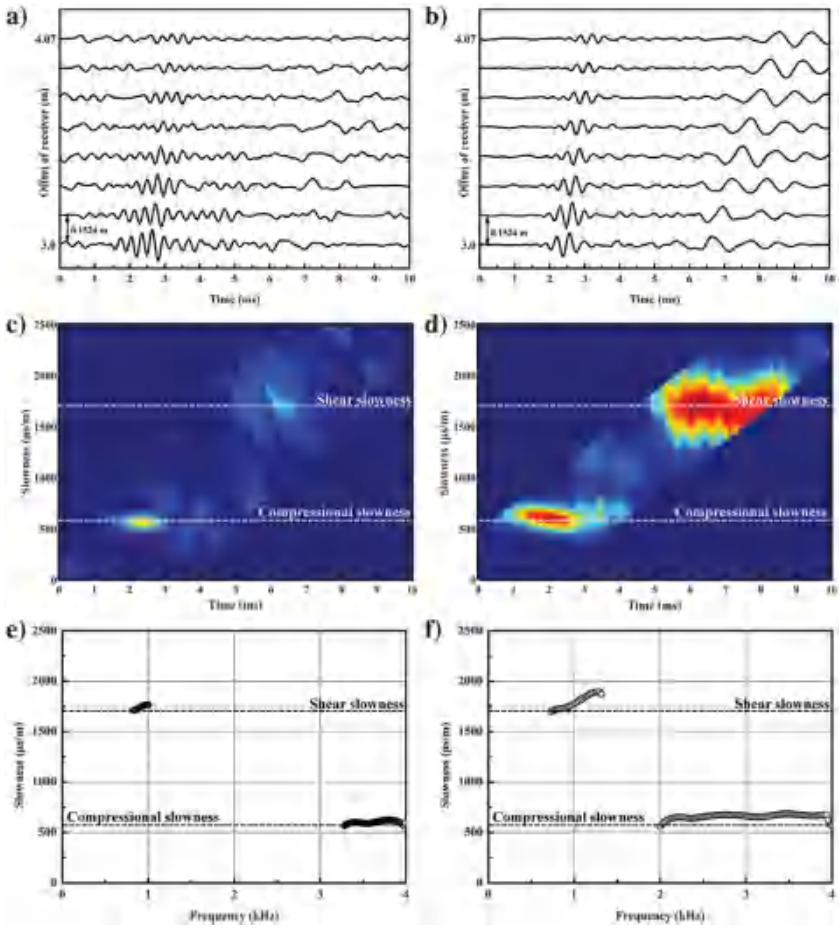


Figure 7. (a and b) Measured array waveform data and (c–f) the STC (SFC) processing result at a shallow depth in the test well for the (a, c, and e) centered-tool and (b, d, and f) eccentered-tool cases, respectively.

Downloaded from pubs.geoscienceworld.org/seg/geophysics/article-pdf/90/6/D125/7330891/geo-2024-0675.1.pdf by Univ of Petroleum (Beijing) - Library user on 08 October 2026

In addition, the lack of consolidation in the ultraslow formation causes borehole enlargement while drilling, up to 32 in (approximately equal to 80 cm) in diameter. Conventional (centralized) dipole logging often fails to obtain the S wave with sufficient amplitude due to the oversized borehole. As shown in Figure 4, when modeling centered dipole logging in an ultraslow formation with different borehole radius, the larger the borehole radius, the smaller the measured S-wave amplitude. In particular, when the borehole radius reaches 40 cm, the S-wave amplitude becomes extremely low. Note that the leaky P-wave amplitude increases with increasing borehole radius.

We now model the dipole logging in an ultraslow formation with a large borehole. The acoustic parameters of the theoretical model of Figure 1 are provided in Table 1. In Figure 1, the logging tool is positioned eccentrically, with an eccentricity of 31.5 cm toward 180°. The radius of the borehole is 40 cm, and the tool is 5 cm (i.e., ECC = 90%). Using equation A-11 (see Appendix A), we investigate the acoustic wavefield of an eccentric dipole tool versus the centered tool scenario. As shown in Figure 5a and 5b, the S waves (arriving at approximately 4.5 ms) of the eccentered tool have much higher amplitude than their centered counterparts, with the S wave at R3, which is closest to the borehole wall, having the highest amplitude.

To show the impact of the centered and eccentered waves on the array slowness analysis, the slowness-time coherence (STC) method and the slowness-frequency coherence (SFC) method are applied, respectively, to the data (Tang and Cheng, 2004). Note that a band-pass filter with a passband of approximately 0.7–4.3 kHz is used for STC processing. In the centralized case, a strong coherence is observed for the P wave, as indicated by the coherence peak at the formation compressional slowness in Figure 5c and the leaky P wave dispersion data in Figure 5d. The horizontal dashed lines in Figure 5 indicate the formation shear slowness and compressional slowness, respectively. Note that there is little dipole-generated flexural wave dispersion data. In addition, the coherence for the S wave is quite low in Figure 5c, which, in the field condition with noises, makes it difficult to extract the formation shear slowness from the STC and SFC processing results. In contrast, the STC and SFC results for the eccentered case (Figure 5e and 5f, respectively) show strong coherence for P and S waves (note that the flexural wave dispersion data now appear integral), from which the formation compressional and shear slowness values can be correctly extracted, although the coherence for the P wave is lower than those in the centralized case. This modeling example shows that eccentering the dipole tool in a large borehole can greatly increase the formation S-wave amplitude, which, in the field condition with noises, enhances signal-to-noise ratio (S/N) and improves the accuracy of shear slowness estimation in ultraslow formations.

Using equation A-11 (see Appendix A), we repeat the preceding modeling for a range of formation shear velocity and tool eccentricity parameters. The eccentricity coefficient (ECC) ranges from 0% to 90%, and the formation shear velocity (V_S) varies from 550 to 1450 m/s. Here, $V_P = 2 \cdot V_S$, where V_P is the formation compressional velocity, from which the formation density ρ^F is calculated using the empirical relation for the soft sediment, $\rho^F = 0.414 \cdot V_P^{0.214}$. Figure 6a and 6b shows, respectively, the S-wave amplitude and the amplitude amplification factor (i.e., amplitude ratio between the centered and the eccentered results) versus tool eccentricity for slow to ultraslow shear velocity values. The variation trend can be seen more clearly in Figure 6c, where the amplitude amplification factor is shown as a surface plot versus the shear velocity and eccentricity. The results show that the S-wave amplitude increases dramatically with increasing tool eccentricity, especially for the ultraslow formation scenario (black curve). For large eccentricity values (i.e., ECC > 60%), the S-wave amplitude can even have an order of magnitude increase for moderate to ultraslow formations. This explains why placing the dipole tool against the (oversized) borehole can obtain good shear slowness logs in the shallow soft sediments.

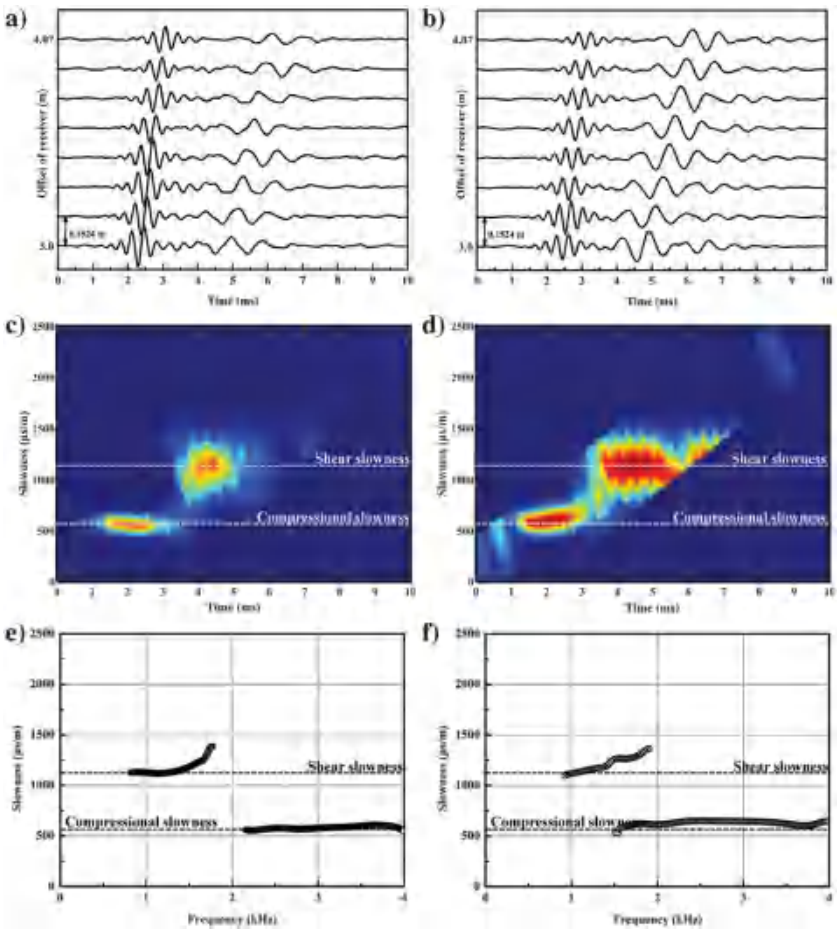


Figure 8. (a and b) Measured array waveform data and (c–f) the STC (SFC) processing result at a deep depth in the test well for the (a, c, and e) centered-tool and (b, d, and f) eccentered-tool cases, respectively.

Downloaded from pubs.geoscienceworld.org/seg/geophysics/article-pdf/90/6/D125/7330891/geo-2024-0675.1.pdf by Univ of Petroleum (Beijing) - Library user on 08 October 2026

FIELD DATA EXAMPLE FOR A LARGE BOREHOLE WITH AN ULTRASLOW FORMATION

To validate our theoretical analysis result and demonstrate the advantage of tool eccentering in logging an ultraslow formation with a large borehole, we carried out a field experiment in a test well in western China. The well was drilled into soft sediments. Due to the unconsolidated formation, the borehole was washed out, and the enlarged borehole had a diameter of 32 in. In the upper 100 m section of the well, the formation shear slowness varied from approximately 840 to 1650 μs/m. The borehole and formation condition of the test well fit well with the intended experiment.

The experiment was conducted in two stages. In the first stage, the logging was conducted with a customized leaf-spring stabilizer with four arms to maintain tool centralization, in which the maximum off-axis distance of a single arm was up to 20 inches. In the second stage, the stabilizer was removed partly such that the tool was placed close to the borehole wall. Here, the tool eccentricity coefficient reached approximately 90%–95%. The two logging runs produced quite different results. For the shallow enlarged part of the well, the typical data characteristics of the two results are shown in Figure 7, which displays array waveform data (Figure 7a and 7b) and the associated STC (SFC) processing result (Figure 7c–7f) for the centered and eccentered cases, respectively. Note that a bandpass filter with a passband of approximately 0.8–4.0 kHz was used for STC processing. The field data and results resembled their theoretical counterparts of Figure 5 very well, both showing that for the large hole and ultraslow condition, the centered (eccentered) dipole tool obtains weak, low-coherence (strong, high-coherence) S-wave signals and inaccurate (accurate) shear slowness values.

In the deeper part of the well, the hole size is still quite large (>20 in), but the formation shear slowness decreases. The deeper well counterpart of Figure 7 is shown in Figure 8. Because of the decrease in formation shear slowness, the centered-tool data (Figure 8c and 8e) show S-wave signals with improved quality and coherence. In comparison, the eccentered tool results (Figure 8d and 8f) are still significantly better than the centered results, which is consistent with the theoretical modeling result of Figure 6.

Figure 9 summarizes the processing results for the centered and eccentered dipole logging data from the test well. The bit size, gamma ray, and caliper log curves are shown in track 1. The caliper log curves clearly indicate significant borehole enlargement, with an average diameter of approximately 29 in, indicating the extremely large borehole condition. Tracks 2 and 3 display the waveform data (only the data from the first receiver of an eight-receiver tool are displayed) and the STC correlogram for the centered-tool logging case, respectively. In a deeper interval, the waveform data exhibit reasonable quality and good coherence. However, in the shallower interval above X70 m, the formation S-wave amplitude weakens, and the signal coherence degrades. As a result, slowness picking from the STC correlogram obtains scattered unreliable values (blue circles in track 6). In this case, often only the formation compressional slowness can be measured due to the lack of formation S-wave coherence. For comparison, the monopole compressional slowness is displayed in track 6 (black curve). The eccentered-tool logging substantially improves the S-wave processing result. Tracks 4 and 5 display the waveform data and the STC correlogram for the eccentered case, respectively. It is undeniable that the P-wave coherence is lower than in the centralized case, which is consistent with the theoretical analysis shown in Figure 5. Throughout the depth section, the S-wave data exhibit good S/N and high coherence. In particular, the waveform quality in the shallow interval above X70 m is significantly improved compared with the centered-tool case. STC processing of the data obtains a continuous and reliable shear slowness log curve (red curve in track 6) that correlates well with the compressional slowness log curve. A more detailed comparison is shown in Figure 10. The corresponding P-to-S velocity ratio versus compressional slowness crossplot is shown in Figure 11. Moreover, in the interval below X70 m, where the formation becomes faster, the shear slowness curves obtained from both data sets agree quite well, indicating reliable measurements and valid processing results in the eccentric case.

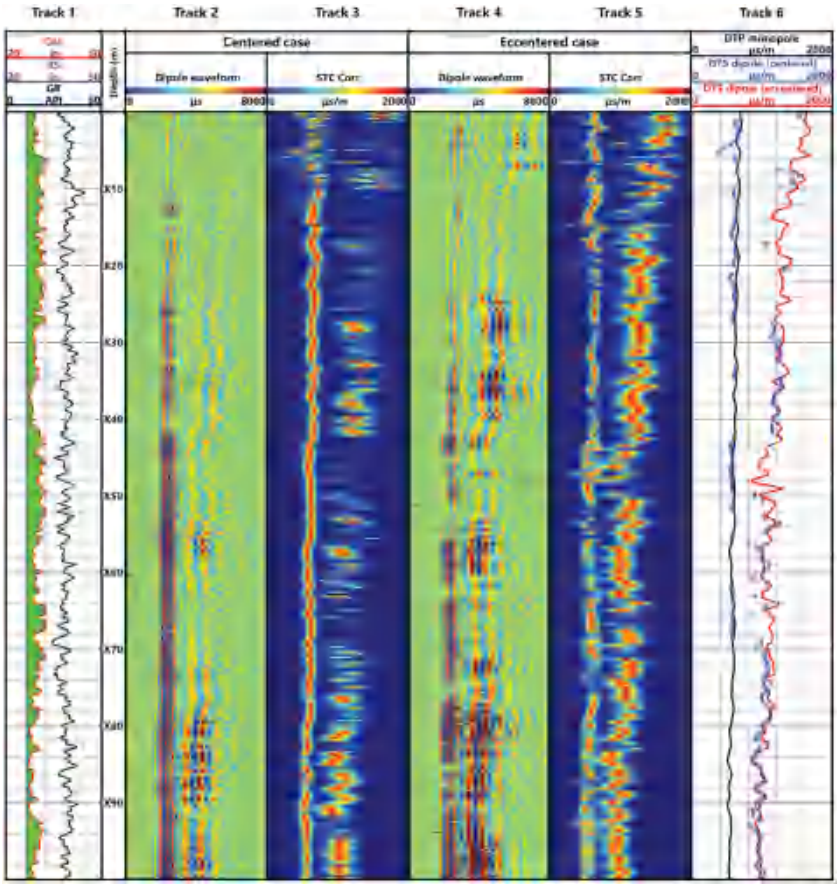


Figure 9. Experiment data and results for a test well with oversized borehole (track 1) and ultraslow formation. Tracks 2 and 3 show the waveform data and the associated STC correlogram for the centered-tool logging runs, respectively; and tracks 4 and 5 show the waveform data and the associated STC correlogram for the eccentered-tool logging runs, respectively. The compressional and shear slowness results from the two logging runs are compared in track 6 (see text for details).

Downloaded from pubs.geoscienceworld.org/seg/geophysics/article-pdf/90/6/D125/7330891/geo-2024-0675.1.pdf by Univ of Petroleum (Beijing) - Library user on 08 October 2026

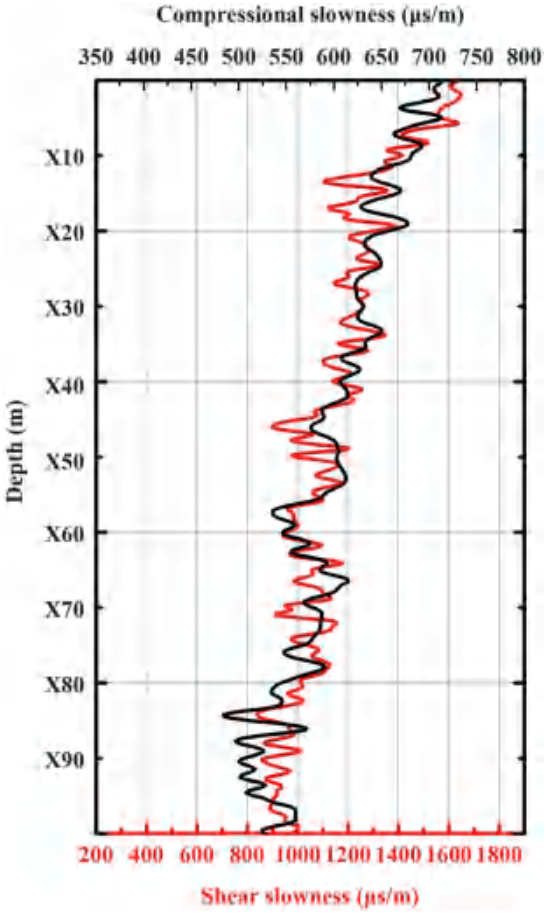


Figure 10. Comparison of the compressional (black) and shear (red) slowness log curves. Note that the compressional slowness is displayed in the range of 350–800 μs/m, and the shear slowness is displayed in the range of 200–1900 μs/m.

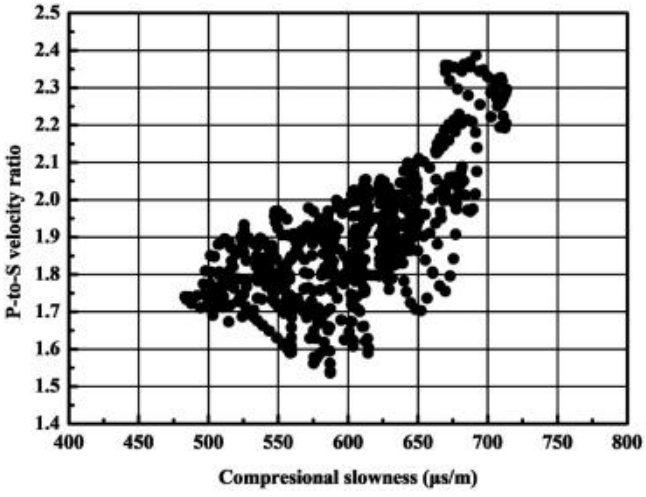


Figure 11. The P-to-S velocity ratio versus compressional slowness crossplot.

CONCLUSION

This study presents the analysis results for dipole shear slowness estimation in a large borehole with an ultraslow formation, emphasizing the effect of tool eccentering. The theoretical formulation uses a nonaxisymmetric borehole model and a dual-cylindrical coordinate system, for which the solution is found by using translational addition theorem for cylindrical Bessel functions. Our modeling results show that the formation S-wave amplitudes increase with increasing tool eccentricity, especially in the ultraslow formation, indicating that eccentrically positioning the dipole tool against the borehole wall will yield the reliable measurement result. The effectiveness of the eccentered-tool logging scheme has been validated by the field test results from a shallow oversized well, making it a viable method for dipole S-wave logging in shallow soft sediments. Undeniably, it will weaken the P-wave coherence compared with the centralized case.

ACKNOWLEDGMENTS

This work was supported by the Shandong Provincial Natural Science Foundation (grant no. ZR2024YQ062), the National Natural Science Foundation of China (grant nos. U21B2064 and 42174145), the State Key Laboratory of Deep Oil and Gas (grant no. SKLDOG2024-ZYTS-04), and the Fundamental Research Funds for the Central Universities (grant no. 24CX02006A).

DATA AND MATERIALS AVAILABILITY

Data associated with this research are confidential and cannot be released.

APPENDIX A

ANALYTICAL SOLUTIONS OF BOREHOLE DIPOLE ACOUSTIC WAVEFIELDS IN THE CASE OF TOOL ECCENTRICITY

For the theoretical analysis using the dual coordinates in Figure 1, the wavefield in the tool and borehole fluid is represented in the first coordinate centered around O_1, and the wavefield in the formation is represented in the second coordinate centered around O_2.

Based on the theory of acoustic wavefield in radially layered media (Cui, 2004; Tang and Cheng, 2004), we derive the general solution for the wave displacement potential within the logging tool, borehole fluid, and formation in the frequency-wavenumber domain as follows.

In the tool coordinates, the P- and S-wave potentials in the tool (ϕ^{tool}; χ^{tool}; and Γ^{tool}) and the P-wave potential in the borehole fluid (ϕ^{out}) are given by, respectively,

$$\begin{cases} \phi^{tool}(k;\omega;r_1;\varphi_1) = \sum_{n=-\infty}^{\infty} A_n^{tool} I_n(\eta_P^{tool} r_1)\cos(n\varphi_1)e^{ikz} \\ \chi^{tool}(k;\omega;r_1;\varphi_1) = \sum_{n=-\infty}^{\infty} C_n^{tool} I_n(\eta_S^{tool} r_1)\sin(n\varphi_1)e^{ikz} \\ \Gamma^{tool}(k;\omega;r_1;\varphi_1) = \sum_{n=-\infty}^{\infty} E_n^{tool} I_n(\eta_S^{tool} r_1)\cos(n\varphi_1)e^{ikz} \\ \phi^{out}(k;\omega;r_1;\varphi_1) = \sum_{n=-\infty}^{\infty} [A_n^{out} I_n(\eta_f r_1) + B_n^{out} K_n(\eta_f r_1)]\cos(n\varphi_1)e^{ikz} \end{cases}; \quad \text{(A-1)}$$

where k is the axial wavenumber; ω is the angular frequency; I_n and K_n are the first and second kind of nth-order modified Bessel functions, respectively; n denotes the azimuthal number in the tool coordinate; $\eta_P^{tool} = (k^2 - k_{pc}^2)^{1=2}$ and $\eta_S^{tool} = (k^2 - k_{sc}^2)^{1=2}$ are the radial wavenumbers for the tool P and S waves, respectively; $k_{pc} = \omega=V_P^{tool}$ and $k_{sc} = \omega=V_S^{tool}$ are the axial wavenumbers for the tool P and S waves, respectively; V_P^{tool} and V_S^{tool} are the tool

Downloaded from pubs.geoscienceworld.org/seg/geophysics/article-pdf/90/6/D125/7330891/geo-2024-0675.1.pdf by Univ of Petroleum (Beijing) - Library user on 08 October 2026

P- and S-wave velocities, respectively; $\eta_f = (k^2 - k_f^2)^{1=2}$ is the radial wavenumber for the borehole fluid; $k_f = \omega/v_f$ is the axial wavenumber for the borehole fluid; and v_f is the fluid P-wave velocity.

In the borehole coordinates, the P- and S-wave potentials in the formation ($\phi^F; \chi^F; \Gamma^F$) are given by, respectively,

$$\begin{cases} \phi^F(k;\omega;r_2;\varphi_2) = \sum_{u=-\infty}^{\infty} B_u^F K_u(\eta_P^F r_2)\cos(u\varphi_2)e^{ikz} \\ \chi^F(k;\omega;r_2;\varphi_2) = \sum_{u=-\infty}^{\infty} D_u^F K_u(\eta_S^F r_2)\sin(u\varphi_2)e^{ikz} \\ \Gamma^F(k;\omega;r_2;\varphi_2) = \sum_{u=-\infty}^{\infty} F_u^F K_u(\eta_S^F r_2)\cos(u\varphi_2)e^{ikz} \end{cases}; \tag{A-2}$$

where u denotes the azimuthal number in the borehole coordinate; $\eta_P^F = (k^2 - k_{pt}^2)^{1=2}$ and $\eta_S^F = (k^2 - k_{st}^2)^{1=2}$ are the radial wavenumbers for the formation P and S waves, respectively; $k_{pt} = \omega/V_P^F$ and $k_{st} = \omega/V_S^F$ are the axial wavenumbers for the formation P and S waves, respectively; and V_P^F and V_S^F are the formation P- and S-wave velocities, respectively.

The wave amplitude coefficients in equations A-1 and A-2 (i.e., from A_n^{tool} to F_u^F) are determined by the fluid-solid boundary conditions at the outer tool interface and the borehole wall, which require the continuity of the displacement and stress in the normal direction (u_r and σ_{rr}, respectively), and vanishing of the shear stresses in the tangential direction (σ_{rz} and $\sigma_{r\varphi}$, respectively), of the interfaces. For the dual-coordinate system, the boundary conditions at the outer tool interface are specified in the tool coordinates, and those at the borehole wall are specified in the borehole coordinates as follows.

At the outer tool interface ($r_1 = a$):

$$\begin{cases} u_r^{tool}(a^-) = u_r^{out}(a^+) \\ \sigma_{rr}^{tool}(a^-) = \sigma_{rr}^{out}(a^+) + \sigma_n^s(a^+) \\ \sigma_{rz}^{tool}(a^-) = 0 \\ \sigma_{r\varphi}^{tool}(a^-) = 0 \end{cases}; \tag{A-3}$$

At the borehole-formation interface ($r_2 = b$):

$$\begin{cases} u_r^{out}(b^-) = u_r^F(b^+) \\ \sigma_{rr}^{out}(b^-) = \sigma_{rr}^F(b^+) \\ 0 = \sigma_{rz}^F(b^+) \\ 0 = \sigma_{r\varphi}^F(b^+) \end{cases}; \tag{A-4}$$

where the superscripts tool, out, and F denote the wavefield in the eccentric tool, borehole fluid, and formation, respectively.

The symbol σ_n^s in equation A-3 denotes the normal stress exerted by the dipole source at the rim of the logging tool. Assuming that the distribution of the excitation amplitude is a cosine function along the height (Fu and Gou, 2022), the expression of the dipole source in the tool coordinate can be expressed as

$$\sigma_n^s(\varphi_1;k;\omega) = p_0 S(\omega)\frac{2z_0}{\pi^2 - 4z_0^2k^2}\cos(kz_0) \cdot \frac{4}{\pi}\sum_{m=0}^{\infty}\frac{\sin(2m+1)\frac{\pi}{2}}{2m+1}\cos(2m+1)\varphi_1; \tag{A-5}$$

where p_0 is a constant used to describe the strength of the source, which is set to 10^5 Pa in the simulation; $S(\omega)$ is the source function; and z_0 represents the half-height of the source.

From equation A-5, it can be seen that the dipole mode consists of dipole ($m = 0$), sextupole ($m = 1$), and higher-order multipoles ($m > 1$). However, the contribution of each order to the dipole mode is weighted by the term $\sin(2m+1)\pi=2=(2m+1)$, showing that the higher the source order, the lower the contribution to the wavefield amplitude.

We now transform the wavefield solution of the dual-coordinate system into the one-coordinate system solution. The transformation uses the classic form of the translational addition theorem for cylindrical Bessel functions (Ji et al., 2021; Rao et al., 2023a, 2023b) as follows:

$$\begin{cases} I_n(\eta_f r_1)\begin{Bmatrix}\cos(n\varphi_1)\\ \sin(n\varphi_1)\end{Bmatrix} = \sum_{u=-\infty}^{\infty} I_{n-u}(\eta_f e) I_u(\eta_f r_2)\begin{Bmatrix}\cos(u\varphi_2)\\ \sin(u\varphi_2)\end{Bmatrix} \\ K_n(\eta_f r_1)\begin{Bmatrix}\cos(n\varphi_1)\\ \sin(n\varphi_1)\end{Bmatrix} = \sum_{u=-\infty}^{\infty}(-1)^{n-u} I_{n-u}(\eta_f e) K_u(\eta_f r_2)\begin{Bmatrix}\cos(u\varphi_2)\\ \sin(u\varphi_2)\end{Bmatrix} \end{cases}. \tag{A-6}$$

Substituting equation A-6 into $\phi^{out}(k;\omega;r_1;\varphi_1)$ in equation A-1, the potential function of the borehole fluid is now expressed by the borehole coordinate variables:

$$\phi^{out}(k;\omega;r_2;\varphi_2) = \sum_{u=-\infty}^{\infty}\left[\begin{matrix}\sum_{n=-\infty}^{\infty} A_n^{out} I_{n-u}(\eta_f e) I_u(\eta_f r_2) \\ +\sum_{n=-\infty}^{\infty} B_n^{out}(-1)^{n-u} I_{n-u}(\eta_f e) K_u(\eta_f r_2)\end{matrix}\right]\cos(u\varphi_2)e^{ikz}. \tag{A-7}$$

With the transformation, the boundary conditions at the borehole wall (equation A-4) can be solved precisely in the borehole coordinate system. The displacement and stresses of the elastic waves are first calculated using Helmholtz decomposition theory and Hooke's law and then substituted into the boundary conditions (equations A-3 and A-4), which, after truncating the series summation of the displacement and stresses at a sufficiently larger number N, that is, $n; u = 0; \pm 1; \cdots; \pm N$, yields a matrix equation for determining the unknown amplitude coefficients in equations A-1 and A-2:

$$D_{(16N+8)\cdot(16N+8)} X_{(16N+8)\cdot 1} = Q_{(16N+8)\cdot 1}; \tag{A-8}$$

where D is a (16N + 8) × (16N + 8) square matrix. In practice, waveform calculations with N = 5 yield results with sufficient accuracy and X and Q are (16N + 8) × 1 vectors given by

$$X_{(16N+8)\cdot 1} = \begin{bmatrix} A_{-N}^{tool}; A_{-N+1}^{tool}; \cdots; A_{N-1}^{tool}; A_N^{tool}; C_{-N}^{tool}; C_{-N+1}^{tool}; \cdots; C_{N-1}^{tool}; C_N^{tool}; \\ E_{-N}^{tool}; E_{-N+1}^{tool}; \cdots; E_{N-1}^{tool}; E_N^{tool}; A_{-N}^{out}; A_{-N+1}^{out}; \cdots; A_{N-1}^{out}; A_N^{out}; \\ B_{-N}^{out}; B_{-N+1}^{out}; \cdots; B_{N-1}^{out}; B_N^{out}; B_{-N}^F; B_{-N+1}^F; \cdots; B_{N-1}^F; B_N^F; \\ D_{-N}^F; D_{-N+1}^F; \cdots; D_{N-1}^F; D_N^F; F_{-N}^F; F_{-N+1}^F; \cdots; F_{N-1}^F; F_N^F \end{bmatrix}^T; \tag{A-9}$$

$$Q_{(16N+8)\cdot 1} = (0; \cdots; 0; \sigma_1^s; 0; \sigma_3^s; 0; \cdots; \sigma_{2m+1}^s; 0; \cdots; 0)^T. \tag{A-10}$$

In equation A-10, the source strength σ_n^s has nonzero contributions only at odd order, with σ_1^s corresponding to the contribution of the pure dipole, relating to the (3N + 3)th term in the column vector.

Downloaded from pubs.geoscienceworld.org/seg/geophysics/article-pdf/90/6/D125/7330891/geo-2024-0675.1.pdf by Univ of Petroleum (Beijing) - Library user on 08 October 2026

By solving equation A-8 to find the amplitude coefficients in equation A-9, the wavefields inside and outside the borehole can be fully determined. Especially, the fluid pressure in the borehole fluid is calculated in the tool coordinate system using $p(k;\omega;r_1;\varphi_1) = \rho_f\omega^2\phi^{out}(k;\omega;r_1;\varphi_1)$ as follows:

$$p(z;t;r_1;\varphi_1) = \int_{-\infty}^{+\infty}\frac{\rho_f\omega^2}{2\pi}S(\omega)e^{-i\omega t} \times \int_{-\infty}^{+\infty}\sum_{n=-N}^{N}\begin{bmatrix}A_n^{out}I_n(\eta_f a)\\ +B_n^{out}K_n(\eta_f a)\end{bmatrix}\cos(n\varphi_1)e^{ikz}dkd\omega; \quad (A\text{-}11)$$

where ρ_f is the borehole fluid density and $\varphi_1 = 0^o$, 90°, 180°, and 270° indicate the receiver azimuths in the tool coordinate system corresponding to R1–R4 in Figure 1c, respectively. The output waveforms of the dipole tool (pointing to the x-axis) are generated by subtracting the waveforms of the inline receivers R1–R3.

The elements of the matrix D in equation A-8 are given as follows (all unlisted elements are zero):

$$\begin{pmatrix}D_{1;1}\\ D_{2;2}\\ \cdots\\ D_{2N+1;2N+1}\end{pmatrix} = \left[\frac{n}{a}I_n(\eta_p^{tool}a) + \eta_p^{tool}I_{n+1}(\eta_p^{tool}a)\right];$$

$$\begin{pmatrix}D_{1;2N+2}\\ D_{2;2N+3}\\ \cdots\\ D_{2N+1;4N+2}\end{pmatrix} = \frac{n}{a}I_n(\eta_s^{tool}a);$$

$$\begin{pmatrix}D_{1;4N+3}\\ D_{2;4N+4}\\ \cdots\\ D_{2N+1;6N+3}\end{pmatrix} = ik\left[\frac{n}{a}I_n(\eta_s^{tool}a) + \eta_s^{tool}I_{n+1}(\eta_s^{tool}a)\right];$$

$$\begin{pmatrix}D_{1;6N+4}\\ D_{2;6N+5}\\ \cdots\\ D_{2N+1;8N+4}\end{pmatrix} = -\left[\frac{n}{a}I_n(\eta_f a) + \eta_f I_{n+1}(\eta_f a)\right];$$

$$\begin{pmatrix}D_{1;8N+5}\\ D_{2;8N+6}\\ \cdots\\ D_{2N+1;10N+5}\end{pmatrix} = -\left[\frac{n}{a}K_n(\eta_f a) - \eta_f K_{n+1}(\eta_f a)\right];$$

$$\begin{pmatrix}D_{2N+2;1}\\ D_{2N+3;2}\\ \cdots\\ D_{4N+2;2N+1}\end{pmatrix} = \mu^{tool}\left[\left(\frac{2n(n-1)}{a^2} + 2k^2 - k_{sc}^2\right)I_n(\eta_p^{tool}a) - \left(\frac{2\eta_p^{tool}}{a}I_{n+1}(\eta_p^{tool}a)\right)\right];$$

$$\begin{pmatrix}D_{2N+2;2N+2}\\ D_{2N+3;2N+3}\\ \cdots\\ D_{4N+2;4N+2}\end{pmatrix} = 2\mu^{tool}\left[\frac{n(n-1)}{a^2}I_n(\eta_s^{tool}a) + \frac{n}{a}\eta_s^{tool}I_{n+1}(\eta_s^{tool}a)\right];$$

$$\begin{pmatrix}D_{2N+2;4N+3}\\ D_{2N+3;4N+4}\\ \cdots\\ D_{4N+2;6N+3}\end{pmatrix} = 2\mu^{tool}ik\left[\left(\frac{n(n-1)}{a^2} + (\eta_s^{tool})^2\right)I_n(\eta_s^{tool}a) - \frac{\eta_s^{tool}}{a}I_{n+1}(\eta_s^{tool}a)\right];$$

$$\begin{pmatrix}D_{2N+2;6N+4}\\ D_{2N+3;6N+5}\\ \cdots\\ D_{4N+2;8N+4}\end{pmatrix} = \rho_f\omega^2 I_n(\eta_f a);$$

$$\begin{pmatrix}D_{2N+2;8N+5}\\ D_{2N+3;8N+6}\\ \cdots\\ D_{4N+2;10N+5}\end{pmatrix} = \rho_f\omega^2 K_n(\eta_f a);$$

$$\begin{pmatrix}D_{4N+3;1}\\ D_{4N+4;2}\\ \cdots\\ D_{6N+3;2N+1}\end{pmatrix} = 2ik\mu^{tool}\left[\frac{n}{a}I_n(\eta_p^{tool}a) + \eta_p^{tool}I_{n+1}(\eta_p^{tool}a)\right];$$

$$\begin{pmatrix}D_{4N+3;2N+2}\\ D_{4N+4;2N+3}\\ \cdots\\ D_{6N+3;4N+2}\end{pmatrix} = ik\mu^{tool}\frac{n}{a}I_n(\eta_s^{tool}a);$$

Downloaded from pubs.geoscienceworld.org/seg/geophysics/article-pdf/90/6/D125/7330891/geo-2024-0675.1.pdf by Univ of Petroleum (Beijing) - Library user on 08 October 2026

$$\begin{pmatrix} D_{4N+3;4N+3} \\ D_{4N+4;4N+4} \\ \cdots \\ D_{6N+3;6N+3} \end{pmatrix} = \mu^{tool}(k_{sc}^2 - 2k^2) \times \left[\left(\frac{n}{a} I_n(\eta_s^{tool} a) + \eta_s^{tool} I_{n+1}(\eta_s^{tool} a) \right) \right];$$

$$\begin{pmatrix} D_{8N+5;8N+5} & D_{8N+5;8N+6} & \cdots & D_{8N+5;10N+5} \\ D_{8N+6;8N+5} & D_{8N+6;8N+6} & \cdots & D_{8N+6;10N+5} \\ \cdots & \cdots & \cdots & \cdots \\ D_{10N+5;8N+5} & D_{10N+5;8N+6} & \cdots & D_{10N+5;10N+5} \end{pmatrix} = \begin{pmatrix} -\left[\frac{-N}{b} K_{-N}(\eta_f b) - \eta_f K_{-N+1}(\eta_f b) \right] (-1)^{n+N} I_{n+N}(\eta_f e) \\ -\left[\frac{-N+1}{b} K_{-N+1}(\eta_f b) - \eta_f K_{-N+2}(\eta_f b) \right] (-1)^{n+N-1} I_{n+N-1}(\eta_f e) \\ \cdots \\ -\left[\frac{N}{b} K_N(\eta_f b) - \eta_f K_{N+1}(\eta_f b) \right] (-1)^{n-N} I_{n-N}(\eta_f e) \end{pmatrix};$$

$$\begin{pmatrix} D_{6N+4;1} \\ D_{6N+5;2} \\ \cdots \\ D_{8N+4;2N+1} \end{pmatrix} = 2\frac{n\mu^{tool}}{a} \left[\frac{(1-n)}{a} I_n(\eta_p^{tool} a) - \eta_p^{tool} I_{n+1}(\eta_p^{tool} a) \right];$$

$$\begin{pmatrix} D_{8N+5;10N+6} \\ D_{8N+6;10N+7} \\ \cdots \\ D_{10N+5;12N+6} \end{pmatrix} = \frac{n}{b} K_n(\eta_p^F b) - \eta_p^F K_{n+1}(\eta_p^F b);$$

$$\begin{pmatrix} D_{8N+5;12N+7} \\ D_{8N+6;12N+8} \\ \cdots \\ D_{10N+5;14N+7} \end{pmatrix} = \frac{n}{b} K_n(\eta_s^F b);$$

$$\begin{pmatrix} D_{6N+4;2N+2} \\ D_{6N+5;2N+3} \\ \cdots \\ D_{8N+4;4N+2} \end{pmatrix} = \mu^{tool} \left[\left(\frac{2n(1-n)}{a^2} - (\eta_s^{tool})^2 \right) I_n(\eta_s^{tool} a) + 2\frac{\eta_s^{tool}}{a} I_{n+1}(\eta_s^{tool} a) \right];$$

$$\begin{pmatrix} D_{8N+5;14N+8} \\ D_{8N+6;14N+9} \\ \cdots \\ D_{10N+5;16N+8} \end{pmatrix} = ik \left[\frac{n}{b} K_n(\eta_s^F b) - \eta_s^F K_{n+1}(\eta_s^F b) \right];$$

$$\begin{pmatrix} D_{6N+4;4N+3} \\ D_{6N+5;4N+4} \\ \cdots \\ D_{8N+4;6N+3} \end{pmatrix} = 2ik\mu^{tool} \frac{n}{a} \left[\frac{(1-n)}{a} I_n(\eta_s^{tool} a) - \eta_s^{tool} I_{n+1}(\eta_s^{tool} a) \right];$$

$$\begin{pmatrix} D_{10N+6;6N+4} & D_{10N+6;6N+5} & \cdots & D_{10N+6;8N+4} \\ D_{10N+7;6N+4} & D_{10N+7;6N+5} & \cdots & D_{10N+7;8N+4} \\ \cdots & \cdots & \cdots & \cdots \\ D_{12N+6;6N+4} & D_{12N+6;6N+5} & \cdots & D_{12N+6;8N+4} \end{pmatrix} = \begin{pmatrix} \rho_f \omega^2 I_{-N}(\eta_f b) I_{n+N}(\eta_f e) \\ \rho_f \omega^2 I_{-N+1}(\eta_f b) I_{n+N-1}(\eta_f e) \\ \cdots \\ \rho_f \omega^2 I_N(\eta_f b) I_{n-N}(\eta_f e) \end{pmatrix};$$

$$\begin{pmatrix} D_{8N+5;6N+4} & D_{8N+5;6N+5} & \cdots & D_{8N+5;8N+4} \\ D_{8N+6;6N+4} & D_{8N+6;6N+5} & \cdots & D_{8N+6;8N+4} \\ \cdots & \cdots & \cdots & \cdots \\ D_{10N+5;6N+4} & D_{10N+5;6N+5} & \cdots & D_{10N+5;8N+4} \end{pmatrix} = \begin{pmatrix} -\left[\frac{-N}{b} I_{-N}(\eta_f b) + \eta_f I_{-N+1}(\eta_f b) \right] I_{n+N}(\eta_f e) \\ -\left[\frac{-N+1}{b} I_{-N+1}(\eta_f b) + \eta_f I_{-N+2}(\eta_f b) \right] I_{n+N-1}(\eta_f e) \\ \cdots \\ -\left[\frac{N}{b} I_N(\eta_f b) + \eta_f I_{N+1}(\eta_f b) \right] I_{n-N}(\eta_f e) \end{pmatrix};$$

$$\begin{pmatrix} D_{10N+6;8N+5} & D_{10N+6;8N+6} & \cdots & D_{10N+6;10N+5} \\ D_{10N+7;8N+5} & D_{10N+7;8N+6} & \cdots & D_{10N+7;10N+5} \\ \cdots & \cdots & \cdots & \cdots \\ D_{12N+6;8N+5} & D_{12N+6;8N+6} & \cdots & D_{12N+6;10N+5} \end{pmatrix} = \begin{pmatrix} \rho_f \omega^2 K_{-N}(\eta_f b)(-1)^{n+N} I_{n+N}(\eta_f e) \\ \rho_f \omega^2 K_{-N+1}(\eta_f b)(-1)^{n+N-1} I_{n+N-1}(\eta_f e) \\ \cdots \\ \rho_f \omega^2 K_N(\eta_f b)(-1)^{n-N} I_{n-N}(\eta_f e) \end{pmatrix};$$

Downloaded from pubs.geoscienceworld.org/seg/geophysics/article-pdf/90/6/D125/7330891/geo-2024-0675.1.pdf by Univ of Petroleum (Beijing) - Library user on 08 October 2026

$$\begin{pmatrix} D_{10N+6;10N+6} \\ D_{10N+7;10N+7} \\ \cdots \\ D_{12N+6;12N+6} \end{pmatrix} = \mu^F \left[\left(\frac{2n(n-1)}{b^2} + 2k^2 - k_{st}^2 \right) K_n(\eta_p^F b) + \left(\frac{2\eta_p^F}{b} K_{n+1}(\eta_p^F b) \right) \right];$$

$$\begin{pmatrix} D_{10N+6;12N+7} \\ D_{10N+7;12N+8} \\ \cdots \\ D_{12N+6;14N+7} \end{pmatrix} = 2\mu^F \left[\frac{n(n-1)}{b^2} K_n(\eta_s^F b) - \frac{n}{b} \eta_s^F K_{n+1}(\eta_s^F b) \right];$$

$$\begin{pmatrix} D_{10N+6;14N+8} \\ D_{10N+7;14N+9} \\ \cdots \\ D_{12N+6;16N+8} \end{pmatrix} = 2\mu^F ik \left[\left(\frac{n(n-1)}{b^2} + (\eta_s^F)^2 \right) K_n(\eta_s^F b) + \frac{\eta_s^F}{b} K_{n+1}(\eta_s^F b) \right];$$

$$\begin{pmatrix} D_{12N+7;10N+6} \\ D_{12N+8;10N+7} \\ \cdots \\ D_{14N+7;12N+6} \end{pmatrix} = 2ik\mu^F \left[\frac{n}{b} K_n(\eta_p^F b) - \eta_p^F K_{n+1}(\eta_p^F b) \right];$$

$$\begin{pmatrix} D_{12N+7;12N+7} \\ D_{12N+8;12N+8} \\ \cdots \\ D_{14N+7;14N+7} \end{pmatrix} = ik\mu^F \frac{n}{b} K_n(\eta_s^F b);$$

$$\begin{pmatrix} D_{12N+7;14N+8} \\ D_{12N+8;14N+9} \\ \cdots \\ D_{14N+7;16N+8} \end{pmatrix} = \mu^F (k_{st}^2 - 2k^2) \left[\left(\frac{n}{b} K_n(\eta_s^F b) - \eta_s^F K_{n+1}(\eta_s^F b) \right) \right];$$

$$\begin{pmatrix} D_{14N+8;10N+6} \\ D_{14N+9;10N+7} \\ \cdots \\ D_{16N+8;12N+6} \end{pmatrix} = 2\frac{n\mu^F}{b} \left[\frac{(1-n)}{b} K_n(\eta_p^F b) + \eta_p^F K_{n+1}(\eta_p^F b) \right];$$

$$\begin{pmatrix} D_{14N+8;12N+7} \\ D_{14N+9;12N+8} \\ \cdots \\ D_{16N+8;14N+7} \end{pmatrix} = \mu^F \left[\left(\frac{2n(1-n)}{b^2} - (\eta_s^F)^2 \right) K_n(\eta_s^F b) - 2\frac{\eta_s^F}{b} K_{n+1}(\eta_s^F b) \right];$$

$$\begin{pmatrix} D_{14N+8;14N+8} \\ D_{14N+9;14N+9} \\ \cdots \\ D_{16N+8;16N+8} \end{pmatrix} = 2ik\mu^F \frac{n}{b} \left[\frac{(1-n)}{b} K_n(\eta_s^F b) + \eta_s^F K_{n+1}(\eta_s^F b) \right]; \quad \text{(A-12)}$$

where $\mu^{tool} = \rho^{tool}(V_S^{tool})^2$ is the shear modulus of the tool, ρ^{tool} is the density of the tool, $\mu^F = \rho^F(V_S^F)^2$ is the shear modulus of the formation outside the borehole, ρ^F is the density of the formation, and $n = (-N; -N+1; \cdots; N-1; N)$ is the vector of circumferential periodic numbers.

REFERENCES

Cao, Z. L., K. X. Wang, G. Li, R. H. Xie, J. S. Liu, and X. M. Lv, 2003, Dipole flexural waves splitting induced by borehole pressurization and formation stress concentration: Chinese Journal of Geophysics, 46, 712–724, doi: 10.1002/cjg2.3391.

Chen, X. L., Y. R. Fan, and X. K. Xu, 2009, Propagation characteristics of mode waves in the borehole with ultra soft formations: Computing Techniques for Geophysical and Geochemical Exploration, 31, 460–465.

Cui, Z. W., 2004, Theoretical and numerical study of modified Biot's models, acoustoelectric well logging and acoustic logging while drilling excited by multipole acoustic sources: Ph.D. dissertation, Jilin University.

Fu, X., and Y. Gou, 2022, An analysis for unipole acoustic logging while drilling wavefields with varying eccentered collar positions: Journal of Geophysics and Engineering, 19, 475–493, doi: 10.1093/jge/gxac026.

Ji, Y. J., X. He, H. Chen, X. M. Wang, and H. L. Zhang, 2021, Acoustic fields for monopole logging while drilling with an eccentric collar: Geophysics, 86, no. 2, D43–D63, doi: 10.1190/geo2019-0744.1.

Jiang, C., C. X. Zhuang, S. Q. Li, Y. D. Su, and X. M. Tang, 2019, Joint inversion for compressional and shear wave slowness using multipole acoustic array logging data: Chinese Journal of Geophysics, 62, 2294–2302, doi: 10.6038/cjg2019L0714.

Leslie, H. D., and C. J. Randall, 1990, Eccentric dipole sources in fluid-filled boreholes: Numerical and experimental results: The Journal of the Acoustical Society of America, 87, 2405–2421, doi: 10.1121/1.399086.

Li, H. B., J. J. Zhang, S. J. Cai, and H. J. Pan, 2019, 3D rock physics template for reservoirs with complex pore structure: Chinese Journal of Geophysics, 62, 2711–2723, doi: 10.6038/cjg2019K0672.

Li, H. B., J. J. Zhang, and F. C. Yao, 2013, Inversion of effective pore aspect ratios for porous rocks and its applications: Chinese Journal of Geophysics, 56, 608–615, doi: 10.6038/cjg20130224.

Muga, I., D. Pardo, P. J. Matuszyk, and C. Torres-Verdín, 2015, Semi-analytical response of acoustic logging measurements in frequency domain:

Downloaded from pubs.geoscienceworld.org/seg/geophysics/article-pdf/90/6/D125/7330891/geo-2024-0675.1.pdf by Univ of Petroleum (Beijing) - Library user on 08 October 2026

Computers & Mathematics with Applications, 70, 314–329, doi: 10.1016/j.camwa.2015.03.028.
Pardo, D., P. J. Matuszyk, I. Muga, C. Torres-Verdín, A. Mora, and V. M. Calo, 2011, Simulation of wireline sonic logging measurements acquired with borehole–eccentered tools using a high-order adaptive finite-element method: Journal of Computational Physics, 230, 6320–6333, doi: 10.1016/j.jcp.2011.04.028.
Rao, B., Y. D. Su, S. Q. Li, Y. T. Sun, W. X. Chen, and X. M. Tang, 2023a, Influence of drill collar eccentricity on quadrupole shear-wave logging while drilling: Theory and field case: Chinese Journal of Geophysics, 66, 111–121, doi: 10.6038/cjg2022Q0477.
Rao, B., Y. D. Su, S. Q. Li, and X. M. Tang, 2023b, Effects of collar eccentricity on azimuthal response characteristics for acoustic reflection measurement while drilling: Geophysics, 88, no. 5, D325–D337, doi: 10.1190/geo2022-0756.1.
Sinha, B. K., A. N. Norris, and S. K. Chang, 1994, Borehole flexural modes in anisotropic formations: Geophysics, 59, 1037–1052, doi: 10.1190/1.1443660.
Sollie, F. O., 1999, WL and LWD sonic logging of soft formations — A case study from a deep-water, frontier-area field: Presented at the 40th Annual Logging Symposium, SPWLA, Extended Abstracts.
Su, Y. D., X. M. Tang, C. Hei, and C. X. Zhuang, 2011, An equivalent-tool theory for acoustic logging and applications: Applied Geophysics, 8, 69–78, doi: 10.1007/s11770-011-0272-6.
Tagbor, K., T. Plona, H. Yamamoto, G. De, and J. Walsh, 2005, Acoustic characterization of an extremely slow formation in California: Presented at the 46th Annual Logging Symposium, SPWLA, Extended Abstracts.
Tang, X. M., and C. H. Cheng, 1993, Effects of a logging tool on the stoneley waves in elastic and porous boreholes: The Log Analyst, 134, 46–56.
Tang, X. M., and C. H. Cheng, 2004, Quantitative borehole acoustic methods: Elsevier Science Publishing Inc.
Tang, X. M., and D. Patterson, 2001, Shear wave anisotropy measurement using cross-dipole acoustic logging: An overview: Petrophysics, 42, 107–117.
Tichelaar, B., and K. W. Luik, 1995, Sonic logging of compressional-wave velocities in a very slow formation: Geophysics, 60, 1627–1633, doi: 10.1190/1.1443895.
Xia, L. D., T. Nagano, K. Suzuki, and M. Satoh, 2024, Customized wireline acoustic data acquisition and processing at unconsolidated formation: Presented at the 29th Annual Logging Symposium, SPWLA, Extended Abstracts.
Xu, F. L., and H. S. Hu, 2019, A semianalytical approach to calculate the reflected wave of an eccentric source in a borehole: Geophysics, 84, no. 1, D1–D9, doi: 10.1190/geo2017-0660.1.
Xu, J. Q., and H. S. Hu, 2020, Study on the radiation and reception of the wave field in a single-well imaging system with an eccentric source: Chinese Journal of Geophysics, 63, 3545–3561, doi: 10.6038/cjg2020N0015.
Zhang, B. X., K. X. Wang, and Q. D. Dong, 1996, Nonaxisymmetric acoustic field excited by a cylindrical tool placed off a borehole axis and extraction of shear wave: The Journal of the Acoustical Society of America, 99, 682–690, doi: 10.1121/1.414645.
Zhang, X. M., H. L. Zhang, and X. M. Wang, 2009, Leaky modes and their contributions to the compressional head wave in a borehole excited by a dipole source: Science in China Series G: Physics, Mechanics & Astronomy, 52, 676–684, doi: 10.1007/s11433-009-0085-2.

Biographies and photographs of the authors are not available.

Downloaded from pubs.geoscienceworld.org/seg/geophysics/article-pdf/90/6/D125/7330891/geo-2024-0675.1.pdf by Univ of Petroleum (Beijing) - Library user on 08 October 2026

GEOPHYSICS, VOL. 81, NO. 1 (JANUARY-FEBRUARY 2016); P. D35–D43, 4 FIGS., 1 TABLE.
10.1190/GEO2015-0210.1

Model-based dispersive processing of borehole dipole wave data using an equivalent-tool theory

Sheng-Qing Lee[1], Xiao-Ming Tang[1], Yuan-da Su[1], and Chun-Xi Zhuang[1]

ABSTRACT

We have developed a model-based processing technique for borehole dipole S-wave logging data to estimate formation shear slowness from the data. During dipole acoustic logging, the presence of the logging tool can significantly affect the dispersion characteristics of flexural waves. Therefore, modeling the effects of the tool is essential for model-based processing. We have determined that an equivalent-tool theory using only two parameters, tool radius, and modulus, can adequately model the flexural-wave-dispersion characteristics. We used this theory, together with a calibration procedure, to determine the tool parameters to formulate an inversion method for the logging data processing. Our use of the equivalent tool theory played an important role in fitting the theoretical dispersion curve to the actual flexural-wave-dispersion data, enabling fast processing of the field acoustic data. An advantage of this model-based method is its prediction power, which, in the absence of low-frequency dispersion data, allows for predicting formation shear slowness from the low-frequency limit of the model-fitted dispersion curve. We have also developed an application procedure of the method for field-data processing and demonstrated its effectiveness in the dispersion correction using field acoustic data from fast and slow formations.

INTRODUCTION

One important task in borehole acoustic logging is to provide compressional (P) and shear (S)-wave velocity profiles for geophysical exploration and petroleum engineering applications. However, the accuracy of the velocity measurement is often impaired by the dispersion of borehole-guided waves. For example, the pseudo-Rayleigh waves in monopole logging (Cheng and Toksöz, 1981), flexural waves in dipole logging (Schmitt, 1988), screw waves in quadrupole logging (Tang et al., 2002), and even the leaky P-waves excited by multipole logging in a slow formation (Hornby and Pasternark, 2000; Tang et al., 2005) are all dispersive. Geerits and Tang (2003) show that, in the presence of dispersion, the slowness obtained from dipole-flexural wave data using the conventional nondispersive processing technique, e.g., the slowness time coherence (STC) method (Kimball and Marzetta, 1984), is larger than the true formation S-slowness. As summarized in a recent review (Cheng, 2015), despite three decades of S-wave logging, slowness data from the measurements need to be corrected for dispersion.

Various dispersion-correction methods have been developed to get the formation slowness from dispersive borehole guided waves (Tang et al., 1995; Kimball, 1998; Geerits and Tang, 2003). These methods, because they handle the dispersion effects of the waveform data, are called dispersive processing methods. In contrast, methods that do not consider the dispersion effects are called nondispersive processing methods, such as the STC method (Kimball and Marzetta, 1984) and the waveform inversion method (Tang and Cheng, 2004). A primary application of the dispersive methods is the estimation of formation S-slowness from dipole logging, which is the key technology for borehole acoustic logging, especially in slow formations (Tang and Cheng, 2004). Because of the dispersion, the dipole-flexural wave detected by a logging tool lags behind the true formation S-wave arrival time and the flexural-wave slowness needs to be compensated, or corrected, for the dispersion effect to estimate the S-wave slowness. Dispersion correction methods may be categorized as data-driven and model-based.

The data-driven method uses the fact that the phase slowness of a guided wave approaches the formation slowness toward low frequencies (see Huang et al., 2005; Zheng et al., 2006). This method projects the frequency dispersion data onto the slowness axis and finds the formation slowness from the projected data. The method requires that a "flat" portion exists in the low-frequency range of the data and that portion of the data is close to the formation slow-

Manuscript received by the Editor 2 April 2015; revised manuscript received 18 August 2015; published online 16 November 2015.
[1]China University of Petroleum (East), School of Geosciences, Qingdao, China. E-mail: shidalishengqing@yeah.net; tangxiam@aliyun.com; syuanda@sina.com; zhuangchunxi@sina.com.
© 2015 Society of Exploration Geophysicists. All rights reserved.

Downloaded from pubs.geoscienceworld.org/seg/geophysics/article-pdf/81/1/D35/3247663/geo2015-0210.pdf by Univ of Petroleum (Beijing) - Library user on 08 October 2026

ness. The method becomes invalid if the low-frequency data are missing due to noise contamination or insufficient excitation of the tool's acoustic source. Tang et al. (2010) propose a curve-fitting method, which is also a data-driven method, to handle data scatter in the low-frequency range. However, like Huang et al.'s (2005) method, that method is also impaired by the missing low-frequency data because the fitting curve is constructed from the actual data.

The model-based methods are basically curve-fitting methods using theoretical modeling, which compute a theoretical dispersion curve to fit the actual dispersion data. A challenge, however, is how to accurately and effectively model the effect of the logging tool on the borehole guided-wave propagation. In the early methods of Tang et al. (1995), Kimball (1998), and Geerits and Tang (2003), the tool effect is not included, and the result of dispersion correction could be significantly biased. The main objective of this paper is to solve the tool-effect modeling problem for the model-based method.

Some theoretical models have been used to describe the effect of a logging tool on borehole acoustic wave propagation, especially on the dispersion characteristics of guided waves (Cheng and Toksöz, 1981; White, 1983; Chen and Willen, 1984; Tang and Cheng, 1993; Sinha et al., 2009; Su et al., 2011). Of these models, the equivalent-tool theory, which is originally proposed by Tang and Cheng (2004) for a monopole and is later developed by Su et al. (2011) for a multipole, is found to be quite suited for dispersion modeling. The theory can adequately model the tool effect on wave dispersion with a minimum number of model parameters, and it can thus be used for computing the model dispersion curve for the data fitting. The advantage of the model-based curve-fitting method, as compared with the data-driven method, is the "prediction power" of the model theory, which allows for predicting the formation slowness value from the low-frequency limit of the model dispersion curve. This is very important for slow-formation data processing. In the slow formation, the flexural-wave-dispersion curve reaches the formation slowness at very low frequencies, sometimes even at less than 1 kHz. This requires the excitation of low-frequency flexural-wave energy for the shear measurement. Consequently, data acquired by tools that do not have adequate low-frequency excitation may not reach the formation slowness. In this situation, a dispersion correction method that has the prediction power to extrapolate the data to the low-frequency limit is badly needed.

In the following text, we first briefly describe the equivalent-tool theory and test its validity using synthetic modeling. We then use the theory to formulate a curve-fitting dispersive processing method to obtain formulation slowness from measured dispersion data. Finally, we demonstrate the effectiveness and validity of the method using dipole flexural-wave data logged in fast and slow formations.

EQUIVALENT-TOOL THEORY FOR ACOUSTIC LOGGING

The foundation of model-based curve fitting is the calculation of the theoretical dispersion curve using the guided-wave theory. For a fluid-filled borehole containing a logging tool in an elastic formation, the effects of the tool need to be included to properly model the wave dispersion in the actual data. As shown by many existing publications (e.g., Cheng and Toksöz, 1981; Chen and Willen, 1984; Tang and Cheng, 1993; Sinha et al., 2009; Su et al., 2011), the presence of the tool affects different types of guided waves in different ways. For shear-normal modes controlled by formation S-wave velocity, the dispersion curve will shift toward a low frequency relative to its counterpart without the tool; however, for the leaky modes controlled by formation P-wave velocity, the dispersion curve will shift to a higher frequency, exhibiting an opposite trend to that of the shear-normal mode. For processing a large volume of field data, one needs to find a way to effectively and efficiently model the logging tool. The actual logging tool can be quite complicated, consisting of a cylindrical housing for electronics and sensors, etc. Therefore, finding an effective model to adequately describe the tool effects is essential for dispersion curve modeling.

The equivalent-tool theory provides an effective method for modeling the acoustic logging tool. Using only two parameters, tool radius and modulus, this theory can adequately model the tool effects on multipole wave propagation and dispersion (Su et al., 2011). The dispersion equation for an equivalent tool centered in the borehole surrounded by an elastic formation is given as

$$D(k;\omega;F;B;M_T;a) = 0; \tag{1}$$

where k is the axial wavenumber, ω is the angular frequency, F represents the elastic formation and the associated parameters such as P and S slowness and density, and B stands for the borehole waveguide containing borehole fluid. The logging tool is characterized by two parameters a and M_T, respectively, denoting the radius and effective modulus of the tool; D is the determinant of a 4×4 matrix, $H_{ij}(i;j = 1;2;3;4)$, modified from its counterpart without the tool. The latter matrix, i.e., the matrix without the tool, is given in Appendix A. For the equivalent-tool theory, the modification is done by replacing the elements H_{11} and H_{21} in Appendix A, which are related to the borehole acoustic wavefield, with the following expressions:

$$\begin{aligned} H_{11} &= -\left[\frac{n}{R}I_n(fR) + fI_{n+1}(fR)\right] \\ &\quad - E_{tool}\left[\frac{n}{R}K_n(fR) - fK_{n+1}(fR)\right] \\ H_{21} &= \rho_f\omega^2[I_n(fR) + E_{tool}K_n(fR)]; \end{aligned} \tag{2}$$

where ρ_f is the fluid density; I_n and K_n are the first and second kind modified Bessel functions of order n, respectively; n is the order of multipole with $n = 0;1;2$ denoting the monopole, dipole, and quadrupole, respectively; $f = \sqrt{k^2 - \omega^2/\alpha_f^2}$ is the radial fluid wavenumber; and α_f and R are the borehole fluid velocity and radius, respectively. The tool coefficient E_{tool} is given by the ratio of the Bessel function combinations related to tool elasticity as

$$E_{tool} = -\frac{\frac{M_T}{a}\left[\frac{n}{a}I_n(fa) + fI_{n+1}(fa)\right] + \rho_f\omega^2 I_n(fa)}{\frac{M_T}{a}\left[\frac{n}{a}K_n(fa) - fK_{n+1}(fa)\right] + \rho_f\omega^2 K_n(fa)}; \tag{3}$$

The above formula is derived by matching the impedance of the tool to the ratio of the acoustic pressure over the displacement at the tool surface using the long-wavelength approximation (Tang and Cheng, 2004). This simple modification uses only two parameters a and M_T to model the tool effect. By solving dispersion

Downloaded from pubs.geoscienceworld.org/seg/geophysics/article-pdf/81/1/D35/3247663/geo2015-0210.pdf by Univ of Petroleum (Beijing) - Library user on 08 October 2026

equation 1 in the frequency range of interest to find the wavenumber k for a given multipole order n, the theoretical phase slowness dispersion curve $S(\omega)$ containing the tool effect is calculated using

$$S(\omega) = \frac{k}{\omega}: \tag{4}$$

We use a dipole-flexural-wave ($n = 1$) example to show the validity and effectiveness of the equivalent-tool theory, and we demonstrate the effect of a logging tool on the flexural-wave dispersion. In this example, the tool is modeled as a fluid-filled elastic cylindrical shell concentric with the borehole (Table 1). This cylindrical layer model can be solved exactly (Tang and Cheng, 2004) to find the formation flexural-wave-dispersion curve, which is then used to compare with its equivalent-tool counterpart calculated using equations 1–4.

Figure 1 compares the phase slowness dispersion curve from the cylindrical shell modeling (dashed curve) and from the equivalent-tool theory (upper solid curve). The latter curve is calculated with $a = 0.035$ m and $M_T = 28.6$ GPa. For reference, the dispersion curve without the tool is also plotted (lower solid curve). As shown in the figure, relative to the curve without the tool, the dispersion curves with a tool have higher slowness and are shifted toward a lower frequency in the higher frequency range. Despite the tool effect, the low-frequency limit of the curves approaches the formation shear slowness of 435 μs/m. More importantly, the dispersion curves for the two very different tool models agree very well, showing only minor differences in the medium-frequency range where the dispersion curve changes rapidly. This minor difference is insignificant in field-data modeling because it is small compared with the error caused by the data noise. This comparison shows that the simple equivalent tool and the more complicated cylindrical shell tool have a similar effect on the calculated flexural-wave-dispersion curve. (The underlying physics is that when the tool size is small compared with wavelength, the wave senses the overall elasticity and is insensitive to the detailed structure of the tool.) The advantage of the equivalent-tool theory is that it represents an adequate simplification of the complicated logging tool and is computationally efficient. Thus, the theory is well-suited for field-data processing and inversion.

DISPERSION CORRECTION BASED ON EQUIVALENT-TOOL THEORY

The field dipole waveforms are first processed to obtain the flexural-wave-dispersion data as a function of frequency. For an acoustic array of N equally spaced receivers, the waveform data are Fourier transformed into the frequency domain, yielding the wave-spectral array $X_m(\omega)$; $(m = 1;2:::;N)$. A slowness-frequency coherence function is then computed from the spectral data (Tang and Cheng, 2004) as

$$\rho(\omega; s) = \frac{\left|\sum_{m=1}^{N} X_m^*(\omega) e^{-i\omega(m-1)sd}\right|}{\sqrt{N \sum_{m=1}^{N} X_m^*(\omega) X_m(\omega)}}; \tag{5}$$

where * donates the complex conjugate and d is the receiver spacing. For each frequency ω, the slowness value s that maximizes $\rho(\omega; s)$ gives the dispersion relation $S_d(\omega) = s$, which provides the data for the formation S-slowness estimation.

Inversion formulation

Field dispersion data, as computed from the above method, often suffer from insufficient low-frequency excitation and noise interference, causing scatter in the low-frequency data and making it difficult to get formation slowness from the data. When this happens, fitting the data with a curve is a better solution. Curve fitting can fit the flat portion of the data, if it exists, as well as the dispersive part in a broader frequency range, and it can thus effectively handle the effects caused by noise. The low-frequency limit of the fitted theoretical curve, when the curve fits the flat portion of the data, directly gives the formation slowness. If, however, the flat portion is missing and the low-frequency end of the dispersion data does not reach the formation slowness, the curve's low-frequency limit gives a prediction of the formation slowness. We now describe how to implement our curve-fitting method to field-data processing. According to the borehole elastic-wave theory, a shear-normal mode such as a dipole-flexural wave is primarily controlled by formation S-slowness (Tang and Cheng, 2004). In other words, the flexural-wave mode has the highest sensitivity to formation S-velocity and is much less sensitive to P-slowness. Therefore, in our inversion method, we let the highly sensitive S-slowness be the parameter to be estimated, and we treat other less sensitive parameters, such as P-slowness, density, etc., as the known parameters, which are conventional curves from borehole log measurements. The latter parameters are from the log curves and are fixed during the inversion process. This single-parameter inversion scheme eliminates the nonuniqueness of the inversion and greatly improves the processing efficiency.

The inversion minimizes, in a least-squares sense, the difference between the model dispersion curve and the actual dispersion data $S_d(\omega)$ as

$$E(s) = \int_{\Omega} |S_m(\omega; s) - S_d(\omega)|^2 d\omega: \tag{6}$$

We parameterize the model dispersion curve $S_m(\omega; s)$ with the formation S-slowness s, and the P-slowness, density, borehole diameter, etc., are input from borehole log measurements. The objective function $E(s)$ is calculated over Ω, the frequency band that includes the most reliable portion of the dispersion data $S_d(\omega)$. The borehole fluid density and fluid slowness can be estimated from the type of drilling mud used. The equivalent-tool parameters

Table 1. Cylindrical layer model parameters.

Medium	P-velocity (m/s)	S-velocity (m/s)	Density (kg/m^3)	Inner radius (m)	Outer radius (m)
Fluid	1500	—	1000	0	0.12
Cylindrical shell	5860	3130	7850	0.035	0.045
Formation	4000	2300	2500	0.117	∞

Downloaded from pubs.geoscienceworld.org/seg/geophysics/article-pdf/81/1/D35/3247663/geo2015-0210.pdf by Univ of Petroleum (Beijing) - Library user on 08 October 2026

can be estimated using a calibration method to be described. By iteratively adjusting the formation slowness s in equation 6, the s value that minimizes $E(s)$ is taken as the formation S-slowness. The iteration can start from the initially processed slowness data obtained using, e.g., the STC method (e.g., Kimball and Marzetta, 1984; Tang and Cheng, 2004). Because the STC slowness is close to the true formation slowness, the iteration converges very fast, allowing for efficient processing of the field logging data. The uncertainty estimation of the processing result will be discussed in the "Quality control" subsection.

Tool-parameter calibration

We use a calibration procedure to determine the tool parameters a and M_T for the field-data processing. We first choose a depth interval with known formation slowness. This interval can be easily identified by inspecting the dispersion data to look for a flat portion of the data, from which the formation slowness can be easily determined. Then, by fitting the theoretical dispersion curve with the dispersion data using an objective function parameterized by a and M_T, the tool parameters can be obtained by minimizing the objective function:

$$E(M_T; a) = \int_\Omega |S_m(\omega; M_T; a) - S_d(\omega)|^2 d\omega: \qquad (7)$$

The above is a two-parameter optimization problem, which can be performed effectively using a very fast simulated annealing algorithm (Ingber, 1989). In a similar manner, the borehole fluid density and slowness, if they are unknown, can be determined using the calibration method. The result of calibration can be assessed by the fit of the theoretical curve with the data. The calibration is regarded to be successful when the curve fits the data in the chosen frequency range.

The use of the equivalent-tool theory realistically models the effects of the logging tool on the dispersion of borehole guided waves, enabling the theoretical dispersion curve to fit the actual dispersion data well. This theory, combined with the single-parameter inversion using equation 6, provides a fast processing method to extract formation S-slowness from dispersive dipole acoustic waveform data.

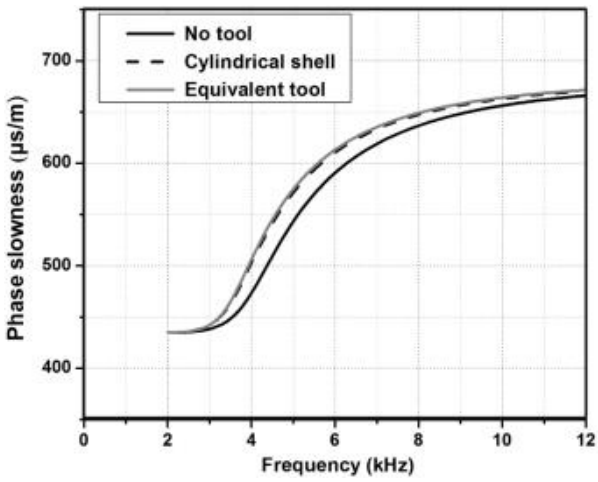


Figure 1. Flexural-wave-dispersion curves from two tool models (upper curves) compared with the curve without a tool (lower curve).

Quality control

After estimating the formation slowness, it is important to provide a quality control for assessing the uncertainty of the result (Kimball and Marzetta, 1984; Plona and Alford, 2005). A slowness-probability density (SPD) function (Tang et al., 2010) can be used to provide an effective quality measure. The SPD function is defined as

$$\mathrm{SPD}(s) = \frac{1}{\omega_H - \omega_L} \int_\Omega \exp\left\{ -\left[\frac{s - S_d(\omega)}{\sigma_s} \right]^2 \right\} d\omega; \qquad (8)$$

where Ω is the frequency range; ω_H and ω_L are the high and low limits of the measured frequency, respectively; and σ_s is standard deviation of $S_d(\omega)$ on Ω. In general, when the wave slowness approaches the formation slowness toward low frequencies, the low-frequency portion of $S_d(\omega)$ varies more slowly than the dispersive, higher frequency portion. This means that the slowness data will have a higher probability of occurrence near the formation slowness in the low-frequency range, corresponding to a peak in the associated SPD function. This is why the data-driven method of Huang et al. (2005) determines the formation slowness by tracking the edge of the SPD function (i.e., the slowness probability histogram in their paper). For quality controlling our estimated slowness result, we display the slowness curve together with the variable density (VD) image of the SPD function (see the field-data processing examples in the next section, "Test example"). The result is considered "good" if the slowness curve tracks the edge of the SPD image and "no good" if such tracking could not be obtained.

Test example

We use the field flexural-wave data from a depth point to demonstrate the dispersion correction method and result. Figure 2a shows the array (the receiver spacing is 0.1524 m) dipole-flexural-waveform data logged in a slow formation. The STC correlogram, obtained by a low-pass, 2-kHz filter to the data, is shown in Figure 2b, which gives a slowness value of 692.7 μs/m. The dispersion data (circles) are computed from the data in Figure 2a using equation 4. The low-frequency portion of the dispersion data (solid circles) tends to flatten and reaches a slowness value (presumably the formation S-slowness) of 665 μs/m. The STC-processed slowness value significantly deviates from this low-frequency value. This deviation can be explained by the weighted average slowness theorem, as proven by Tang and Cheng (2004). According to this theorem, the slowness value from a nondispersive processing method, such as STC, is an average of the frequency-varying slowness data weighted by the power spectrum of the wave data in the measurement frequency range. Because most of the dispersion data are very dispersive and the wave spectral energy (computed from the data of Figure 2a) is mostly in the dispersive frequency range, the weighted average of the dispersion data with the wave spectrum gives a slowness value that is significantly slower than the low-frequency end value of the dispersion data.

The dispersion data are inverted to estimate the formation S-slowness. To test the prediction power of the inversion method, we pur-

Downloaded from pubs.geoscienceworld.org/seg/geophysics/article-pdf/81/1/D35/3247663/geo2015-0210.pdf by Univ of Petroleum (Beijing) - Library user on 08 October 2026

posely leave out the low-frequency portion of the data and use only the dispersive part (open circles). In the inversion, the formation P-slowness and density, borehole fluid density and slowness, and borehole radius, as from logging data, are 343.01 μs/m, 2.17 g/cm^3, 1.33 g/cm^3, 806.31 μs/m, and 0.162 m, respectively. The equivalent-tool parameters, obtained by calibration from a different depth interval using equation A-1, are $a = 0.058$ m and $M_T = 56.9$ GPa, respectively. Using the STC slowness as the initial value, the inversion adjusts the formation S-slowness value to fit the dispersion data (open circles) by minimizing the objective function in equation 7, yielding an S-slowness value of 665 μs/m, a correction amount of 4% relative to the STC result. Using the S-slowness value from the inversion, the calculated theoretical dispersion curve fits very well with the entire dispersion data, including the data (solid circles) that are not used in the inversion. The inversion result shows the ability of the technique to predict the formation S-slowness when the low-frequency data are missing. The result also shows the importance of the equivalent tool in the data fitting. If the same data were inverted using the model dispersion curve without the tool (the dashed curve in Figure 2c), it would have been very difficult to fit the data. Because the presence of the tool shifts the whole model dispersion curve toward low frequencies (see also Figure 1), the dispersion curve without the tool, which varies in a higher frequency range, would not fit the data regardless of how the model parameters are adjusted.

FIELD-DATA APPLICATION AND EXAMPLES

In the following, we apply our method to field-data processing to demonstrate the efficiency and effectiveness of the method. The field dipole-flexural data processing procedure is summarized as follows:

1) Input the array wave data and compute dispersion data using equation 5.
2) Obtain the P-slowness, density, caliper log data, and borehole mud density and velocity for theoretical dispersion curve calculation.
3) Find a proper formation depth interval with a known or easily obtainable S-slowness, and calibrate the tool radius and modulus using equation 7.
4) Process the data using STC and use the result as the initial value in equation 6, adjust a trial slowness to minimize the objective function in this equation, and obtain the S-slowness from the minimization.
5) Use equation 8 to calculate the SPD function.
6) Repeat steps 1–5 for the depth interval of interest, and plot the resulting S-slowness curve with SPD image for quality control.

Fast-formation example

A fast-formation example from the above processing procedure is shown in Figure 3a for a 180-m depth interval. Panel 1 shows the gamma ray, borehole caliper, and spontaneous potential log curves. Panel 2 shows the VD display of the STC correlogram and the processed slowness curve tracking the peak of the STC image. Panel 4 is the VD image of the flexural-wave data for receiver 1. The effect of dispersion is quite significant because the large-amplitude event lagging behind is the dispersive Airy phase, and the first-arrival portion of the waveform has a very

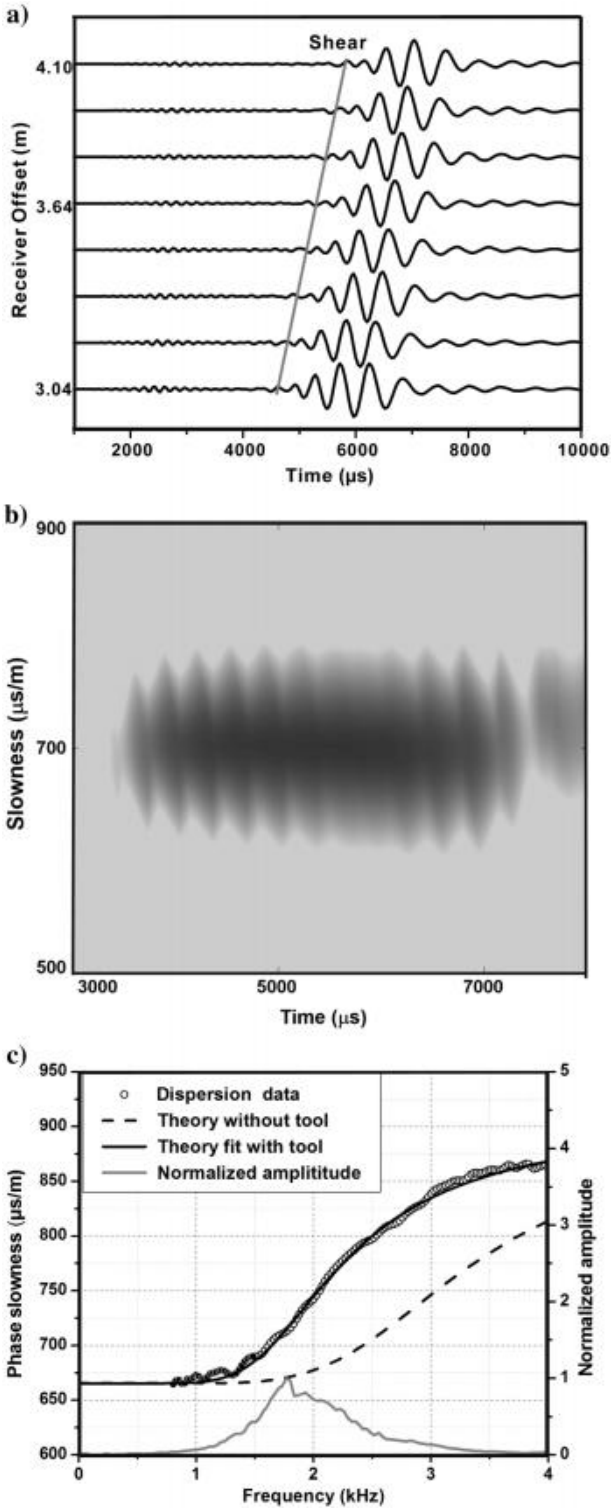


Figure 2. (a) Field array flexural-wave data, (b) STC correlogram for the data in panel (a), and (c) dispersion data (circles) and theoretical fitting (solid curve) of the data (open circles are used in fitting). For comparison, the wave spectrum (bottom curve) and theoretical dispersion curve without the tool (dashed curve) are also plotted. The latter curve varies in a higher frequency range and therefore cannot fit the data.

Downloaded from pubs.geoscienceworld.org/seg/geophysics/article-pdf/81/1/D35/3247663/geo2015-0210.pdf by Univ of Petroleum (Beijing) - Library user on 08 October 2026

small amplitude. To reduce the effect of dispersion, the wave data were low-pass filtered at less than 3.5 kHz before the STC processing. Panel 3 plots the dispersive processing slowness curve (red) and the STC-processed slowness (blue), together with the S-slowness curve from monopole data (black). For quality controlling the slowness results, the SPD VD image calculated using equation A-1 is displayed in green in the background. Because of the low-pass filtering for the STC processing, the slowness before and after the dispersive processing is not significantly different. Figure 3b is an example of dispersion data fitting for the depth of ×230 m. The slowness data show a small flat portion approaching the formation S-slowness, and the model dispersion curve fits all of the slowness data quite well. Figure 3c shows the distribution histogram for the dispersion correction over the displayed depth interval, in which the correction is defined as the percentage difference between the STC and the dispersive processing slowness curves. The distribution is peaked at approximately 2.5%, reaching 7% for some intervals. A fairly significant amount of correction, approximately 4%, is noticed in the ×088 – ×103 m depth interval (see panel 3 of Figure 3a, in which the interval is pointed out by a blue arrow), whose validity and significance are discussed in the following.

The validity of our dispersive processing method can be assessed in two ways. First, there is an overall agreement of the estimated S-slowness with the monopole S-slowness. The latter slowness is almost dispersion free and should be regarded as the true formation S-slowness. Second, there is an overall tracking of the slowness curve with the edge of the SPD image. As mentioned earlier, detecting the edge of the SPD function gives the formation S-slowness for the data-driven dispersive processing method (Huang et al., 2005; Zheng et al., 2006). For this example, our method and the existing method should give similar results. As a final check, we use the slowness estimated from our dispersive processing method to calculate an S-wave traveltime, which we overlay on the wave data VD image in panel 4. This traveltime curve traces the first-arriving part of the wave very well. Therefore, the comparison,

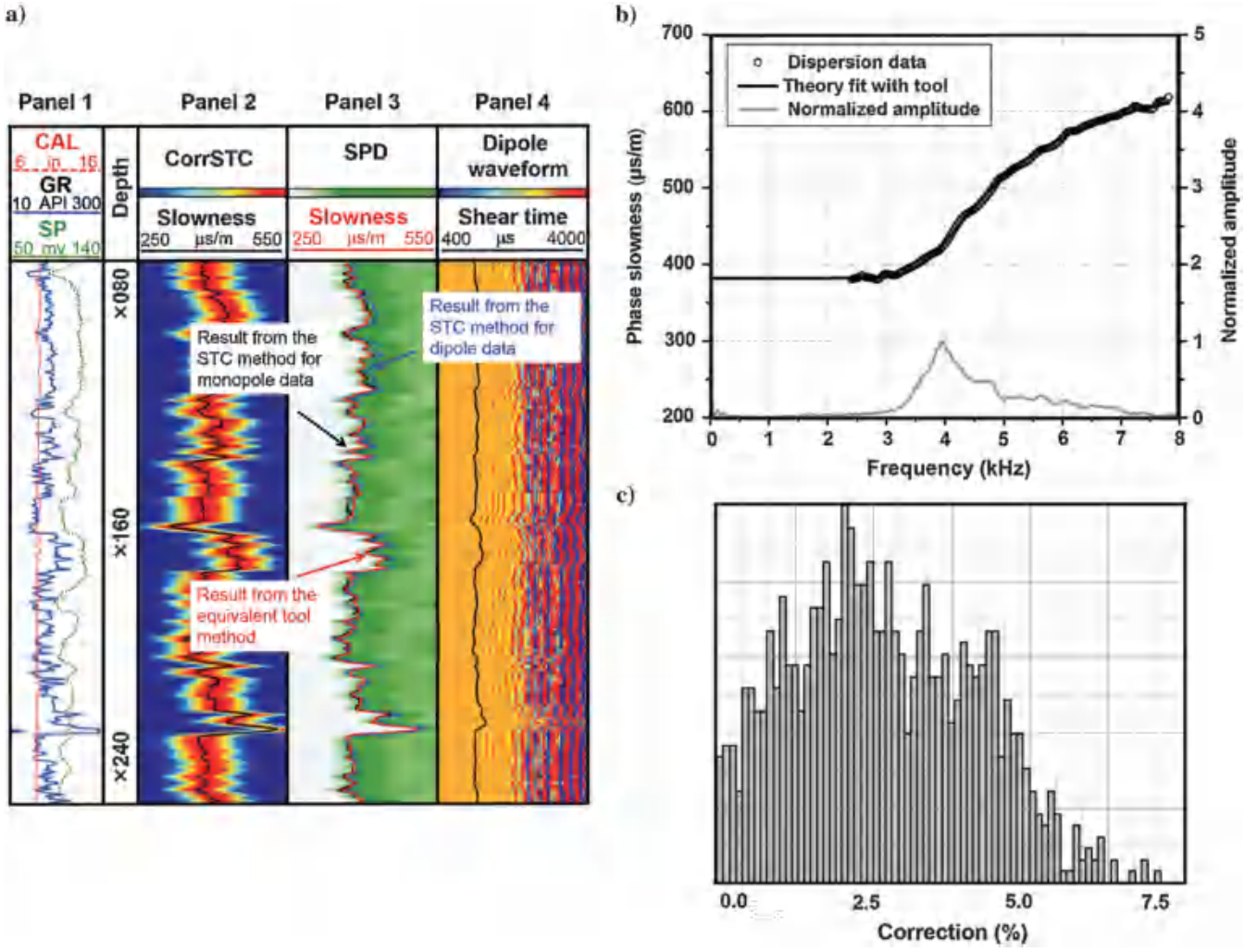


Figure 3. (a) Example of flexural-wave-dispersion correction for a fast formation. Panel 1 shows the conventional log curves, panel 2 shows the STC correlogram (CorrSTC) image and the obtained slowness from processing the waveform data in panel 4, and panel 3 is the comparison of different slowness results with the SPD image (in green). (b) Fitting the dispersion data with the theory for the depth of ×230 m. (c) Histogram of the correction (in percent) for the processing interval.

Downloaded from pubs.geoscienceworld.org/seg/geophysics/article-pdf/81/1/D35/3247663/geo2015-0210.pdf by Univ of Petroleum (Beijing) - Library user on 08 October 2026

as shown in panels 3 and 4, supports the validity and accuracy of our dispersive processing result.

Slow-formation example

We now discuss the flexural-wave-dispersive processing in a slow formation and compare the processing result with the slowness for a logging while drilling (LWD) shear measurement. In a slow formation, the S-wave cannot be directly measured from monopole logging. This is the major reason for the development of wireline dipole and LWD quadrupole acoustic technologies (Tang and Cheng, 2004; Tang et al., 2006; Cheng, 2015). The main advantage of the LWD quadrupole wave measurement is that the quadruple wave when operating in the low-frequency range does not produce a drill-collar quadrupole wave and reaches the formation S-slowness toward low frequencies.

In practice, dipole-flexural-wave-dispersion correction is more important and demanding for slow formations than for fast formations. In the slow formation situation in which the flexural-wave-dispersion curve reaches the formation slowness at very low frequencies, the slowness data measured by tools that do not have adequate low-frequency excitation energy may suffer seriously from the dispersion effect. In this situation, the prediction power of the model-based method can extrapolate the data to the low-frequency limit. This is shown in the following example.

The dipole data for this example are from an unconsolidated slow formation. Figure 4a shows the data and dispersive processing results for a 180-m depth interval. Panel 1 displays the gamma-ray and caliper log curves. Because of the (0.3-m or 12-in.) large borehole and quite-slow formation velocity, the flexural-wave data (panel 3; only receiver 1 data are displayed) are very dispersive. There are some leaky-P-waves present in the data, which is typical for a slow formation and can be suppressed by the low-pass filtering of lower than 2.5 kHz. The STC correlogram and the picked slowness from the filtered data are displayed in panel 2. The quality of the data and the STC processing results are quite good. However,

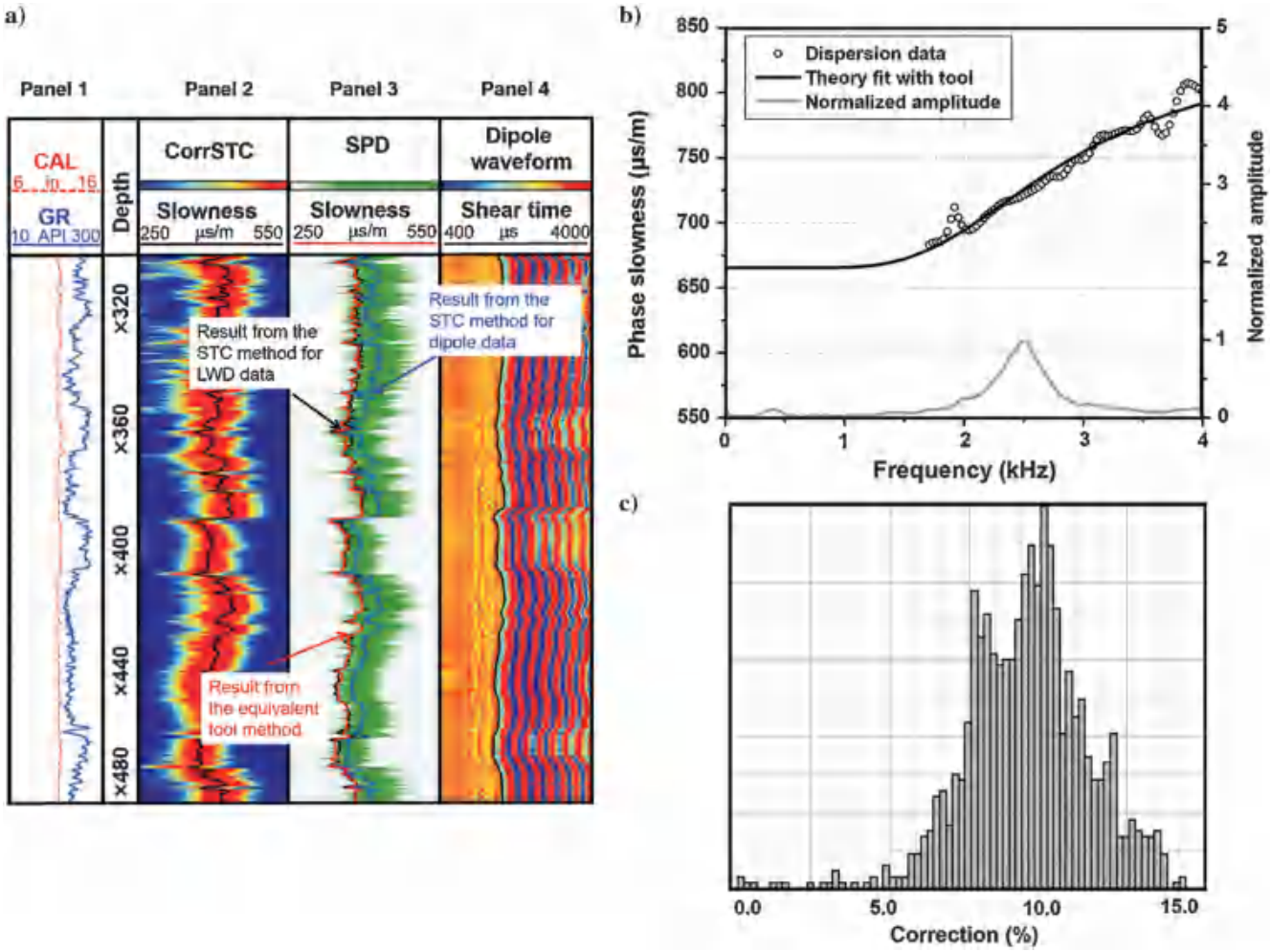


Figure 4. (a) Example of a flexural-wave-dispersion correction for a slow formation. Panel 1 shows the conventional log curves, panel 2 shows the STC correlogram (CorrSTC) image and the obtained slowness from processing the waveform data in panel 4, and panel 3 is the comparison of different slowness results with the SPD image (in green). (b) Fitting dispersion data and predicting S-slowness from the low-frequency limit of the fitted theoretical dispersion curve for the depth of ×408 m. (c) Histogram of the dispersion correction (in percent) for the processing interval.

Downloaded from pubs.geoscienceworld.org/seg/geophysics/article-pdf/81/1/D35/3247663/geo2015-0210.pdf by Univ of Petroleum (Beijing) - Library user on 08 October 2026

the frequency content of the waveform data (see the wave spectrum in Figure 4b), even after the low-pass filtering, is still high for measuring S-slowness for this large hole and slow formation situation. As a result, the STC slowness is strongly biased by the dispersion effect. The slowness curve (blue) is compared with the SPD image in panel 3, and the dispersion effect is clearly revealed. The slowness curve, instead of tracking the edge of the SPD image as it should, tracks close to the peak of the image, indicating that the slowness value is significantly slower than the true formation S-slowness.

The inversion using equation 6 is applied to "predict" the formation S-slowness. Figure 4b shows an example of dispersion correction for the missing low-frequency data. (The data are taken from the depth of ×408 m.) We call this correction a prediction because the formation slowness is obtained from the low-frequency limit of the theoretical dispersion curve (<1 kHz) that is fit to the measured data by our inversion method. Note that the estimated model dispersion curve extends beyond the low-frequency range of the measured data. The predicted slowness (red) is compared with the S-slowness curve obtained from the LWD quadrupole measurement (black). There is excellent agreement between the two results. Considering that the respective result is obtained from very different measurements and processing methods, the agreement is remarkable. Note also that both curves track slightly off the edge of the SPD image compared with the fast formation example in Figure 3a, in which the dispersive processing result tracks the edge of the SPD image. This is not surprising because, in the absence of low-frequency content of the data, the edge of the SPD function does not reach the true S-slowness value. A distribution histogram for the dispersion correction of the displayed interval is shown in Figure 4c. The distribution is bell shaped, ranging from 5% to 15% and averaging approximately 10%. The distribution data is missing in the less than 5% range, which again indicates that the wave slowness is significantly off the formation S-slowness and that dispersion correction is indeed needed.

CONCLUSIONS

Guided waves (e.g., dipole S-waves) in borehole acoustic logging can be strongly dispersive. Correcting for dispersion is an important procedure to obtain accurate formation slowness from the data. Model-based dispersion correction needs to consider the presence of a logging tool in theoretical modeling. We have demonstrated that the two-parameter equivalent-tool theory can realistically and adequately model the effects of the tool on the flexural-wave-dispersion data. Fitting the theoretical dispersion curve to the dispersive slowness data in the measurement frequency range gives a fast and effective dispersive-wave processing method. We have demonstrated the validity of our method by applying it to a fast and a slow formation field-data set. The latter data example shows an advantage of the prediction power of the method, which allows for obtaining formation slowness beyond the measurement frequency range.

ACKNOWLEDGMENTS

The authors thank Y. Zheng and the anonymous reviewers for their comments and suggestions that helped improve the manuscript. This work is supported by the China Natural Science Foundation (grant no. 41474101) and by the Fundamental Research and Development Program (2014CB239006).

APPENDIX A

DETAILS OF MATRIX H WITHOUT THE TOOL

The elements of matrix H for a fluid-filled borehole without the tool are given as follows:

$$
\begin{aligned}
H_{11} &= -\frac{nI_n(fR)}{R} - fI_{n+1}(fR);\\
H_{21} &= \rho_f\omega^2 I_n(fR);\\
H_{31} &= 0;\\
H_{41} &= 0;\\
H_{12} &= \frac{nK_n(pR)}{R} - pK_{n+1}(pR);\\
H_{22} &= \frac{2\rho\beta^2 n(n-1)K_n(pR)}{R^2} + \rho(2\,k^2\beta^2 - \omega^2)K_n(pa)R\\
&\quad + \frac{2p\rho\beta^2 K_{n+1}(pR)}{R};\\
H_{32} &= \frac{2n\rho\beta^2}{R}\left[pK_{n+1}(pR) - \frac{(n-1)K_n(pR)}{R}\right];\\
H_{42} &= 2ik\rho\beta^2\left[\frac{nK_n(pR)}{R} - pK_{n+1}(pR)\right];\\
H_{13} &= \frac{nK_n(sR)}{R};\\
H_{23} &= \frac{2\rho\beta^2 n(n-1)K_n(sR)}{R^2} - \frac{2n\rho s\beta^2 K_{n+1}(sR)}{R};\\
H_{33} &= -\rho\beta^2\left\{\left[s^2 + \frac{2n(n-1)}{R^2}\right]K_n(sR) + \frac{2\,sK_{n+1}(sR)}{R}\right\};\\
H_{43} &= \frac{ikn\rho\beta^2 K_n}{R};\\
H_{14} &= \frac{iknK_n(sR)}{R} - iksK_{n+1}(sR);\\
H_{24} &= 2ik\rho\beta^2\left[\frac{n(n-1)}{R^2} + s^2\right]K_n(sR) + \frac{2iks\rho\beta^2 K_{n+1}(sR)}{R};\\
H_{34} &= 2ikn\rho\beta^2\left[\frac{sK_{n+1}(sR)}{R} - \frac{(n-1)K_n(sR)}{R^2}\right];\ \text{and}\\
H_{44} &= (k^2+s^2)\rho\beta^2\left[sK_{n+1}(sR) - \frac{nK_n(sR)}{R}\right].
\end{aligned}
\tag{A-1}
$$

In the above expressions, I_n and K_n are the modified Bessel functions of the first and second order, respectively, and n is the order of the multipole with $n = 0;1;2$ denoting the monopole, dipole, and quadrupole, respectively; R is the borehole radius; ρ and ρ_f are the solid and fluid densities; α, β, and α_f are the formation P-, S-wave velocity, and borehole fluid velocity, respectively; and $p = (k^2 - \omega^2/\alpha^2)^{1/2}$, $s = (k^2 - \omega^2/\beta^2)^{1/2}$, and $f = (k^2 - \omega^2/\alpha_f^2)^{1/2}$ are the compressional, shear, and borehole acoustic radial wave-

Downloaded from pubs.geoscienceworld.org/seg/geophysics/article-pdf/81/1/D35/3247663/geo2015-0210.pdf by Univ of Petroleum (Beijing) - Library user on 08 October 2026

number, respectively. The derivation of the equation and expressions can be found in Tang and Cheng (2004).

REFERENCES

Chen, S. T., and D. E. Willen, 1984, Shear wave logging in slow formations: Presented at the SPWLA 25th Annual Logging Symposium, DD.

Cheng, C. H., 2015, Can we ever trust the shear-wave log?: The Leading Edge, 34, 278–284, doi: 10.1190/tle34030278.1.

Cheng, C. H., and M. N. Toksöz, 1981, Elastic wave propagation in a fluid-filled borehole and synthetic acoustic logs: Geophysics, 46, 1042–1053, doi: 10.1190/1.1441242.

Geerits, T., and X. M. Tang, 2003, Centroid phase slowness as a tool for dispersion correction of dipole acoustic logging data: Geophysics, 68, 101–107, doi: 10.1190/1.1543197.

Hornby, B. E., and E. S. Pasternark, 2000, Analysis of full-waveform sonic data acquired in unconsolidated gas sands: Petrophysics, 41, 363–374.

Huang, X., and H. Yin, 2005, A data-driven approach to extract shear and compressional slowness from dispersive waveform data: 75th Annual International Meeting, SEG, Expanded Abstracts, 384–387.

Ingber, L., 1989, Very fast simulated reannealing: Mathematical and Computer Modelling, 12, 967–973, doi: 10.1016/0895-7177(89)90202-1.

Kimball, C. V., 1998, Shear slowness measurement by dispersive processing of borehole flexural mode: Geophysics, 63, 337–344, doi: 10.1190/1.1444333.

Kimball, C. V., and T. L. Marzetta, 1984, Semblance processing of borehole acoustic array data: Geophysics, 49, 274–281, doi: 10.1190/1.1441659.

Plona, T., and M. J. Alford, 2005, Slowness-frequency projection logs, a new QC method for accurate sonic slowness evaluation: Presented at the SPWLA 46th Annual Logging Symposium, T.

Schmitt, D. P., 1988, Shear-wave logging in elastic formations: Journal of the Acoustical Society of America, 84, 2215–2229, doi: 10.1121/1.397015.

Sinha, B., T. Ikegami, D. L. Johnson, and J. Pabon, 2009, Use of an effective tool model in sonic logging data processing: U.S. Patent 7,529,152.

Su, Y. D., X. M. Tang, C. H. Hei, and C.-X. Zhuang, 2011, An equivalent-tool theory for acoustic logging and applications: Applied Geophysics, 8, 69–78, doi: 10.1007/s11770-011-0272-6.

Tang, X. M., and C. H. Cheng, 1993, Effects of a logging tool on Stoneley waves in elastic and porous boreholes: The Log Analyst, 34, 46–56.

Tang, X. M., and C. H. Cheng, 2004, Quantitative borehole acoustic methods: Elsevier Science Publishing Co.

Tang, X. M., Y. Zheng, and V. Dubinsky, 2005, Logging while drilling acoustic measurement in unconsolidated slow formations: Presented at the 46th Annual Logging Symposium, SPWLA.

Tang, X. M., V. Dubinsky, and D. Patterson, 2006, Development of a low-frequency LWD quadrupole shear-wave technology to improve quality of formation shear velocity measurement: Presented at the Annual Technical Conference and Exhibition, SPE, 102335.

Tang, X. M., C. Li, and D. Patterson, 2010, A curve-fitting technique for determining dispersion characteristics of guided elastic waves: Geophysics, 75, no. 3, E153–E160, doi: 10.1190/1.3420736.

Tang, X. M., E. C. Reiter, and D. R. Burns, 1995, A dispersive-wave processing technique for estimating formation shear velocity from dipole and Stoneley waveforms: Geophysics, 60, 19–28, doi: 10.1190/1.1443747.

Tang, X. T., T. Wang, and D. Patterson, 2002, Multipole acoustic logging-while-drilling: 72nd Annual International Meeting, SEG, Expanded Abstracts, 364–367.

White, J. E., 1983, Underground sound: Elsevier Science Publishing Co.

Zheng, Y., X. Huang, X. M. Tang, D. Patterson, and H. Yin, 2006, Application of a new data-driven dispersive processing method to LWD compressional and shear waveform data: Presented at the Annual Technical Conference and Exhibition, SPE, 103328.

Downloaded from pubs.geoscienceworld.org/seg/geophysics/article-pdf/81/1/D35/3247663/geo2015-0210.pdf by Univ of Petroleum (Beijing) - Library user on 08 October 2026

GEOPHYSICS, VOL. 82, NO. 2 (MARCH-APRIL 2017); P. D47–D55, 9 FIGS., 1 TABLE.
10.1190/GEO2016-0223.1

Determining formation S-wave transverse isotropy from borehole flexural-wave dispersion data

Song Xu[1], Xiao-Ming Tang[1], Yuan-Da Su[1], Sheng-Qing Lee[1], and Chun-Xi Zhuang[1]

ABSTRACT

Many earth formations are characterized as transversely isotropic (TI) media. In acoustic logging through a vertical borehole, the S-wave TI property has traditionally been determined from borehole monopole Stoneley-wave measurements, but the feasibility of shear-TI estimation from dipole flexural waves has not been fully investigated. We have developed a methodology to determine the TI parameters from borehole dipole-flexural wave data. Our analysis shows that the Stoneley wave is sensitive to the TI property mainly in an acoustically slow formation, and the sensitivity diminishes when the formation becomes faster. The advantage of the flexural wave over the Stoneley wave is that the former wave is sensitive to the TI property in the slow and fast formations, provided the wave measurement is made in a broad frequency range in which the flexural-wave dispersion characteristics from low to high frequencies can be used. By calculating the theoretical flexural-wave dispersion curve for the TI formation and using it to fit the measured wave dispersion data, we can simultaneously determine the vertical and horizontal S-wave velocities, from which the S-wave TI parameter is obtained. Application of our methodology to field data processing shows that the TI parameter estimated from the flexural wave is almost identical to that from the Stoneley wave for a slow formation. For a fast formation, the flexural-wave result is more accurate and reliable compared with the Stoneley-wave result. Our study, thus, introduces a novel application of dipole acoustic logging.

INTRODUCTION

In the exploration and production of hydrocarbon reservoirs in sedimentary rocks, a very common scenario is the anisotropy in many sedimentary layered formations, especially in shales. The anisotropy is commonly modeled as transverse isotropy ([TI] or vertical TI [VTI] for the horizontally layered sediments with a vertical symmetric axis). A TI formation is described by five elastic constants:

$$[c_{11}; c_{13}; c_{33}; c_{44}; c_{66}]: \quad (1)$$

For a VTI formation with a vertical borehole, c_{11} and c_{33} relate to the horizontal and vertical P-wave velocities, respectively. The last two constants c_{44} and c_{66} relate to the vertical and horizontal S-wave velocities, respectively. This study focuses on how to determine c_{44} and c_{66} from borehole acoustic logging measurements.

Acoustic logging in a vertical borehole surrounded by a VTI formation (see Figure 1) has been studied by, among others, White and Tongtaow (1981) and Tongtaow (1982) for monopole logging and Ellefsen (1990) and Schmitt (1989) for multipole (monopole, dipole, and quadrupole) logging. The general conclusion is that only the vertical wave propagation velocities (i.e., $V_P = \sqrt{c_{33}/\rho}$ for the P-wave and $V_{sv} = \sqrt{c_{44}/\rho}$ for the S-wave, where ρ is the formation density) can be directly determined from the logging measurements, regardless of whether a monopole, dipole, or quadrupole tool is used. As for the horizontal wave propagation velocities, only the horizontal S-wave velocity $V_{sh} = \sqrt{c_{66}/\rho}$ can be derived from the logging. It is generally believed that the monopole Stoneley-wave inversion is the best way for the horizontal shear derivation (Tang, 2003; Tang and Cheng, 2004), although theoretical modeling shows that the flexural wave from dipole logging has sensitivity to the horizontal shear at high frequencies (Tang and Cheng, 2004).

The Stoneley-wave inversion technique has traditionally been used for the shear-anisotropy estimation (Tang, 2003), especially

Manuscript received by the Editor 26 April 2016; revised manuscript received 13 October 2016; published online 24 January 2017.
[1]China University of Petroleum (EAST), School of Geosciences and Technology, Qingdao, China. E-mail: xusongupc@sina.com; tangxiam@aliyun.com; syuanda@sina.com; shidalishengqing@yeah.net; zhuangchunxi@sina.com.
© 2017 Society of Exploration Geophysicists. All rights reserved.

Downloaded from pubs.geoscienceworld.org/seg/geophysics/article-pdf/82/2/D47/4052662/geo-2016-0223.1.pdf by Univ of Petroleum (Beijing) - Library user on 08 October 2026

in estimating anisotropy for unconventional shale gas or oil reservoirs (Norris and Sinha, 1993; Sinha et al., 2014). It is easy to demonstrate the sensitivity of the Stoneley wave to the shear anisotropy using the wave's velocity in the low-frequency limit (White and Tongtaow, 1981):

$$V_{ST}|_{\omega\to 0} = V_f/\sqrt{1+K_f/c_{66}}; \quad (K_f = \rho_f V_f^2); \quad (2)$$

where ω is the angular frequency and ρ_f and V_f are the borehole fluid density and velocity, respectively. This simple formula shows that, at low frequencies, the sensitivity of the Stoneley wave to the formation S-wave TI is controlled largely by the velocity of the horizontally rather than by the vertically propagating S-wave. On the other hand, the same formula that supports the Stoneley-wave technique can also be used to show its drawback in fast formations. A fast formation is characterized by much higher shear rigidity compared with the fluid modulus K_f, resulting in $c_{66} \gg K_f$ in equation 2. Consequently, the Stoneley velocity is controlled mostly by the fluid velocity V_f, causing a decrease in the sensitivity to c_{66} and an increase in the uncertainty in the estimated TI parameter.

To overcome the drawback of the Stoneley-wave technique in fast formations, some work has been done to investigate the use of flexural waves from dipole logging for the S-wave anisotropy estimation. The early development of dipole logging focused on getting low-frequency flexural-wave data to minimize the dispersion effect in the shear velocity measurement (Zemanek et al., 1984). With the development of the technology, modern dipole tools can now obtain the flexural-wave dispersion data in a broad frequency range (Tang and Patterson, 2010; Sinha et al., 2014; Walker et al., 2015; Lee et al., 2016), allowing for analyzing the anisotropy effect from the data. For example, Sunaga et al. (2009) and Valero et al. (2009) show the influence of the anisotropy at high frequencies on the flexural dispersion data; Fang et al. (2013) even propose to estimate the anisotropy from the flexural-wave dispersion data. Using the perturbation of VTI constants relative to an isotropic elastic model, Sinha et al. (2014) and Sinha and Walsh (2015) develop an inversion algorithm to estimate the VTI constants from the dipole and Stoneley dispersion data. Following this development trend, we use the exact solution of the VTI model to provide a comprehensive theoretical analysis and we develop an inversion technique to estimate the shear anisotropy from the borehole acoustic logging data.

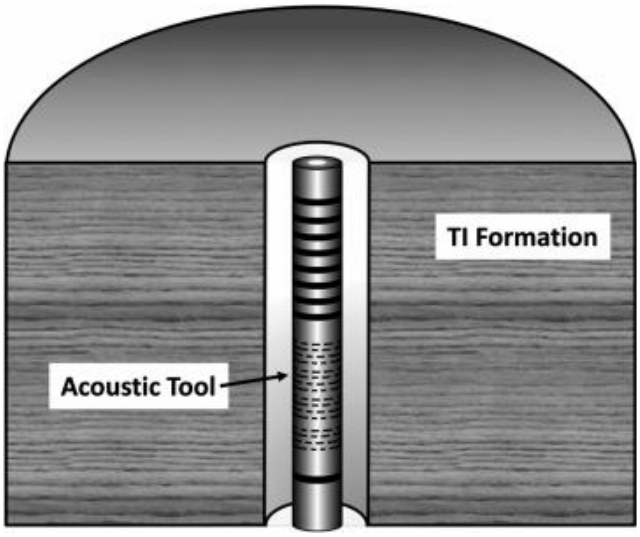


Figure 1. Model for logging in a VTI formation with a multipole acoustic tool.

In the following sections, we first describe the acoustic theory for borehole multipole-wave propagation with a VTI formation and we perform a sensitivity analysis of the multipole (monopole and dipole) wave to the TI parameter. We then develop the inversion method to extract the anisotropy parameter from field data. Finally, we apply the method to field data processing. We will compare the result from the new method with the result from the traditional Stoneley-wave method for a fast and a slow formation and discuss the similarities and differences between the two results.

THEORETICAL ANALYSIS

Figure 1 depicts acoustic logging of a TI formation with a multipole acoustic tool in the fluid-filled borehole. We include the tool in our analysis because it affects the wave propagation characteristics and must be properly modeled in the field data analysis. In the analysis of Stoneley-wave propagation in a VTI formation, Tang (2003) introduces an equivalent-tool theory. Recent work of Lee et al. (2016) shows that the theory can adequately model the flexural-wave propagation in an isotropic formation. In this paper, we extend the previous work and use the equivalent tool theory to model the flexural-wave propagation in a VTI formation.

The analysis of multipole wave propagation with a TI medium and the formulation of the equivalent-tool theory have been published in the literature (e.g., see Tang, 2003; Tang and Cheng, 2004; Su et al., 2011; Lee et al., 2016). We put the theoretical result and equations related to the current work in Appendix A for reference. The analysis results in a wave dispersion equation for computing the multipole wave propagation for the model of Figure 1:

$$D(k;\omega;c_{66};c_{44};M_T;r;a;\rho;V_f;\rho_f;c_{11};c_{13};c_{33}) = 0; \quad (3)$$

where k is the wavenumber, ω is the angular frequency, r is borehole radius, and ρ is the formation density; ρ_f and V_f are the borehole fluid density and velocity, respectively. The equivalent tool is modeled by tool modulus M_T and tool radius a. The parameters in the above dispersion equation are ordered by their importance and relevance to the present problem.

By solving the above dispersion equation in the frequency range of interest to find the root values of k for the monopole Stoneley wave (denoted by k_{ST}) and for the dipole flexural wave (denoted by k_{FL}), the phase velocity (or slowness) dispersion curve for these waves is obtained:

$$\begin{cases} V_{ST} = \omega/k_{ST} \\ V_{FL} = \omega/k_{FL} \end{cases} \text{or} \quad \begin{cases} S_{ST} = k_{ST}/\omega \\ S_{FL} = k_{FL}/\omega \end{cases}. \quad (4)$$

After the dispersion curve calculation, a sensitivity analysis can be used to assess the importance of the anisotropy parameter in affecting the wave propagation characteristics. The sensitivity is defined as the partial derivative of the normalized phase velocity (slowness) with respect to a model parameter (Tang and Cheng, 2004). For example, the sensitivity to the horizontal V_{sh} and vertical V_{sv} shear velocity is, respectively,

Downloaded from pubs.geoscienceworld.org/seg/geophysics/article-pdf/82/2/D47/4052662/geo-2016-0223.1.pdf by Univ of Petroleum (Beijing) - Library user on 08 October 2026

$$\begin{cases} \text{Sens}^{SV} = \frac{V_{sv}}{V(\omega)} \cdot \frac{\partial V(\omega)}{\partial V_{sv}} \\ \text{Sens}^{SH} = \frac{V_{sh}}{V(\omega)} \cdot \frac{\partial V(\omega)}{\partial V_{sh}} \end{cases}, \quad (5)$$

where $V(\omega)$ is the phase velocity of the Stoneley or flexural wave. The sensitivity defined above is also called the partition coefficient (Cheng et al., 1982) because it describes the partitioning of a fraction of the total strain energy of the wave vibration to a designated model parameter. Because of the conservation of energy, the sum of the coefficients for all parameters must be equal to one. Therefore, if the sensitivity to a model parameter is high, it means that the parameter can be estimated with high confidence or low uncertainty.

Using equations 4 and 5, we conduct the dispersion and sensitivity analyses for the fast and slow TI formation and the equivalent tool parameters in Table 1. (The parameters of Table 1, together with a simple three-parameter model, the ANNIE model to be discussed, give the complete set of VTI parameters.) Figure 2 shows the Stoneley- and flexural-wave phase velocity dispersion curves for the fast (Figure 2a) and slow formations (Figure 2b). For comparison, the anisotropic (solid) and isotropic (dashed, assuming $c_{44} = c_{66}$) dispersion curves are calculated. In the slow formation scenario, the anisotropic Stoneley velocity is significantly faster than the isotropic velocity because the wave is mostly sensitive to c_{66} and $c_{66} > c_{44}$. However, for the fast formation, the difference is much reduced because the wave is more sensitive to borehole fluid and less sensitive to c_{66}. For fast and slow formations, the flexural-wave velocities approach the vertical shear velocity $V_{sv} = \sqrt{c_{44}/\rho}$, showing that low-frequency dipole logging allows estimation of only V_{sv}. With increasing frequency, the anisotropic velocity becomes faster than the isotropic velocity. This shows that it is possible to measure the anisotropy from the high-frequency part of the flexural-wave dispersion curve.

Figure 3a and 3b shows the Stoneley- and flexural-wave sensitivity, respectively, to vertical (V_{sv}, solid curves) and horizontal (V_{sh}, dashed curves) shear velocity for the fast (red) and slow (black) formation models. The Stoneley sensitivity is dominated by V_{sh} at low frequencies, as can be anticipated from equation 2. With increasing frequency, the wave's sensitivity to V_{sv} increases. It is important to notice the sensitivity difference between the fast and slow formations. In the fast formation case, the sensitivity is much reduced relative to the slow formation case, as is also explained using equation 2. The reduced sensitivity causes the TI estimation from the Stoneley wave to have large uncertainties. It is interesting to study the flexural-wave sensitivities for the fast (red) and slow (black) formations. There is no doubt that the wave's sensitivity to the TI anisotropy is dominated by V_{sv} toward low frequencies. With the increasing frequency, the sensitivity to V_{sv} decreases significantly and the sensitivity to V_{sh} increases. Examining frequencies greater than 4 kHz for the slow formation, we find a V_{sh} sensitivity larger than 20%. For the fast formation, although the sensitivity decreases at high frequencies, the sensitivity curve reaches a peak value of approximately 25% less than 4 kHz. In fact, the sensitivity peak corresponds to the "Airy phase" of the flexural wave (Tang and Cheng, 2004), which is quite common in fast formation dipole logging. Given sufficient bandwidth, the large sensitivity (approximately 20%) of flexural waves to the horizontal shear velocity makes it possible to determine the S-wave TI from the dipole logging data. In the following, we formulate an inversion procedure for the S-wave TI determination.

THE INVERSION METHOD

The goal for the shear TI inversion is to determine the c_{44} and c_{66} parameters in equation 1. The model theory of equations 3 and 4 is used to do forward modeling for the inversion. However, the theory

Table 1. Acoustic properties for model of Figure 1.

Materials constituents	V_P (m/s)	V_S (m/s)	Density (kg/m^3)	Thomsen γ	Radius (m)	Modulus (GPa)
Borehole fluid	1500	—	1000	—	0.100	—
Equivalent tool	—	—	—	—	0.045	130
Fast formation	4000	2500	2650	0.20	∞	—
Slow formation	3000	1250	2000	0.20	∞	—

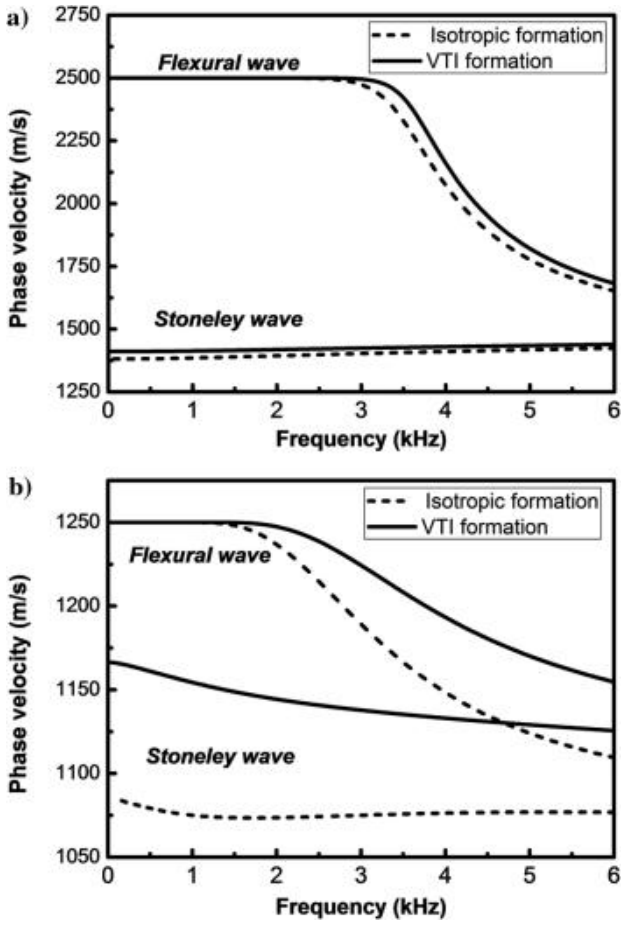


Figure 2. Flexural- and Stoneley-wave dispersion curves (solid) in (a) fast and (b) slow VTI formations. For comparison, each curve's isotropic counterpart (dashed) is also plotted.

Downloaded from pubs.geoscienceworld.org/seg/geophysics/article-pdf/82/2/D47/4052662/geo-2016-0223.1.pdf by Univ of Petroleum (Beijing) - Library user on 08 October 2026

needs all five elastic constants of equation 1 for the modeling calculation. Therefore, our strategy is to use an approximate relationship to relate two of the five parameters to the rest of parameters, which are either known (i.e., $c_{33} = \rho V_P^2$ where the V_P is obtained from logging) or to be inverted (i.e., c_{44} and c_{66}). The relationship is the ANNIE approximation commonly used in the logging community (Schoenberg et al., 1996), as given below:

$$c_{13} = c_{33} - 2c_{44} \tag{6}$$

$$c_{11} = c_{33} + 2(c_{66} - c_{44}): \tag{7}$$

We will discuss the accuracy of the approximation below. However, we note that the impact on our inversion will be minimal because the borehole Stoneley and flexural waves are not sensitive to these parameters (Ellefsen, 1990; Tang and Cheng, 2004). We test the approximation of equations 6 and 7 using the published core measurement data compiled by Thomsen (1986) in his well-known paper on seismic anisotropy. The test results are plotted in Figure 4. Figure 4a shows the c_{33} from equation 6 versus the measured c_{33}, and Figure 4b shows the c_{11} from equation 7 versus the measured c_{11}. Apart from a few outliers, most data fall onto the (45°) diagonal line. To further test the accuracy of the approximation, we calculate the correlation coefficient between Thomsen's measurements and predicted results. The correlation coefficients are 0.9357 and 0.9847, respectively, validating the approximation.

The S-wave TI estimation uses the sensitivity of the flexural wave to the vertical shear velocity V_{sv} at low frequencies and the wave's sensitivity to the horizontal shear velocity V_{sh} at medium to high frequencies to formulate an inversion method. The inversion simultaneously obtains the two parameters from the flexural-wave dispersion data. For the inversion method to be described in the following text, we will use slowness (inverse velocity), instead of velocity, to follow the convention used in the logging community.

The phase slowness dispersion in the frequency range of interest is extracted from the waveform data using the slowness-frequency-coherence (SFC) (Tang and Cheng, 2004; Lee et al., 2016). Then, the theoretical dispersion curve is calculated using equations 3 and 4 to fit the dispersion data. The inversion is done by minimizing the following objective function constructed as the root-mean-square misfit error between the theoretical curve and the dispersion data for the processing frequency range Ω:

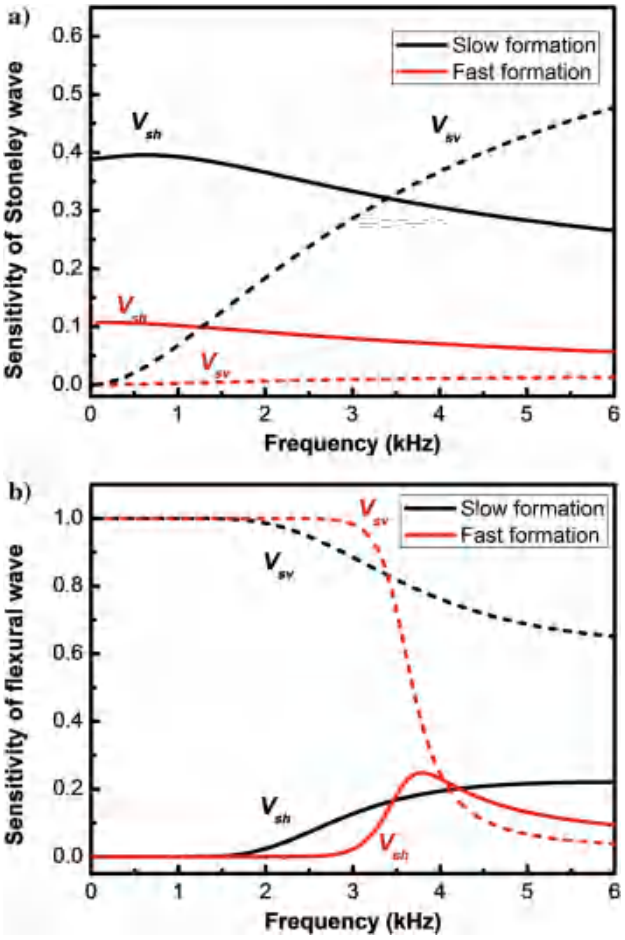


Figure 3. (a) Stoneley- and (b) flexural-wave sensitivity to vertical (dashed, V_{sv}) and horizontal (solid, V_{sh}) shear velocities for the fast (red) and slow (black) VTI formations. Note that the fast flexural-wave sensitivity to V_{sh} has a peak in the medium frequency range.

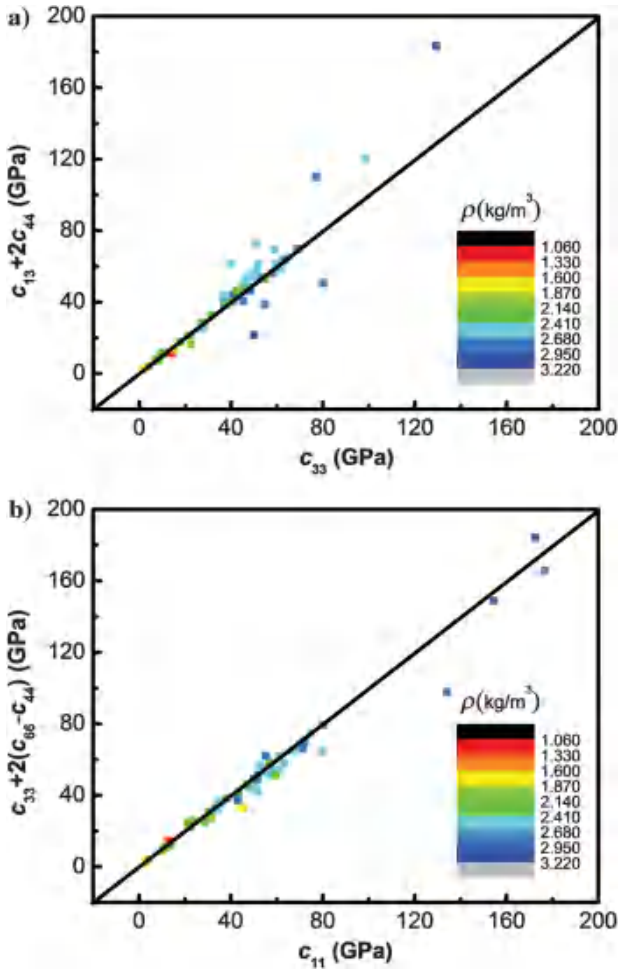


Figure 4. A test of the ANNIE approximation using the core measurement data of Thomsen (1986): (a) the ANNIE-calculated c_{33} versus measured c_{33} and (b) the ANNIE-calculated c_{11} versus measured c_{11}. The data are color coded by the density of each core sample. Most data fall onto the (45°) diagonal line, validating the ANNIE approximation.

Downloaded from pubs.geoscienceworld.org/seg/geophysics/article-pdf/82/2/D47/4052662/geo-2016-0223.1.pdf by Univ of Petroleum (Beijing) - Library user on 08 October 2026

$$E(S_{sv};\gamma) = \int_{\Omega} |S_m(\omega;S_{sv};\gamma) - S_d(\omega)|^2 d\omega; \quad (8)$$

where S_m and S_d denote the calculated slowness dispersion curve and the processed dispersion data, respectively, S_{sv} is the vertical shear slowness, and γ is Thomsen's S-wave TI parameter defined by

$$\gamma = \frac{c_{66} - c_{44}}{2c_{44}}: \quad (9)$$

For simultaneously inverting the two parameters S_{sv} and γ, the data frequency band should span the low, medium, and, preferably, medium- to high-frequency ranges, so that the sensitivity to both parameters is effectively captured, as shown by the sensitivity curves in Figure 3. For the Stoneley-wave inversion, the vertical shear slowness S_{sv} is assumed known and only the γ parameter is inverted for the low-frequency Stoneley-wave measurement band Ω. The reason for this is also explained in the sensitivity analysis of Figure 3.

We use the synthetic flexural-wave dispersion data to test the validity and effectiveness of the inversion using equation 8. In Figure 5b, the dispersion data (circles) are computed using an SFC method (e.g., Lee et al., 2016) from the synthetic array waveform data calculated using the slow formation parameters in Table 1. The frequency band used for the inversion is 1–8 kHz. The inversion can start with an isotropic model ($\gamma = 0$) and an initial slowness value for S_{sv}. In actual data processing, this slowness can be obtained by applying the standard slowness-time-coherence (STC) method to the array waveform data (Kimball and Marzetta, 1984). The inversion then iterates the S_{sv} and γ parameters until the objective function in equation 8 is minimized. This gives the estimated parameter values of $S_{sv} = 800\ \mu s/m$ ($V_{sv} = 1250\ m/s$) and $\gamma = 0.20$, in agreement with the respective parameter values in Table 1. To verify the uniqueness of the solution, Figure 5a displays the variable density (VD) image of the objective function in the 2D parameter domain of $780\ \mu s/m < S_{sv} < 820\ \mu s/m$ and $0 < \gamma < 0.4$. A unique minimum exists at the inverted solution point, demonstrating that the inversion using the broadband data can indeed determine the S-wave TI parameters. The model slowness-dispersion curve (black solid line) calculated with the inverted parameter values fit the input data (open circles). For comparison, the isotropic formation dispersion curve (dashed) calculated using the inverted S_{sv} is also plotted to show the substantial difference between the two scenarios.

APPLICATION TO FIELD DATA

S-wave TI parameters are increasingly used in geophysical and geomechanical applications, especially in conjunction with unconventional shale gas or oil reservoirs (Sayers, 2005; Sinha et al., 2014). In the following, we apply our inversion method to field data processing and demonstrate the validity and effectiveness of the method. Two data sets will be used: One is the data from a slow formation, and the other is the data from a fast formation. The anisotropy result from our new method will be compared with that from the traditional Stoneley-wave method to demonstrate the advantage of the new method.

Slow formation example

Using the above inversion for field data processing, a slow formation example is shown for a 32 m depth interval (Figure 6). Panel 1 displays the gamma ray and borehole caliper log curves, showing that the formation consists mainly of a sand-shale sequence. Panels 2 and 3 show the VD display of the monopole and dipole flexural waveform data. The monopole and dipole data were, respectively, processed to obtain the P- (blue curve) and S- (black curve) slowness log curves in panel 6 using the standard STC processing method. Dispersion data were also extracted from the monopole Stoneley and dipole flexural waves. For illustration purposes, the flexural dispersion data are shown in panel 4 (dotted curve in this panel l; for brevity, the Stoneley dispersion is not shown). Because of the high attenuation of the slow formation, the dispersion data quality is a little poor, especially at high frequencies (3.5–4.0 kHz). With the P- and S-slowness logs as input, we invert the Stoneley and flexural dispersion data separately to obtain the respective anisotropy parameter γ in panel 5 (the left shaded curve is from flexural data, and the right shaded curve is from Stoneley data). The two γ results are almost identical. Considering that the

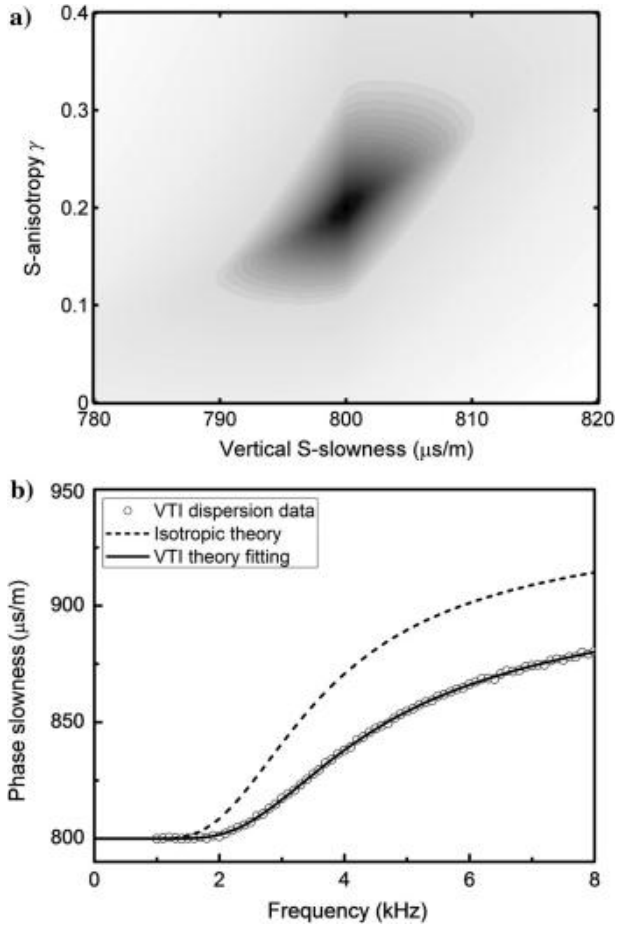


Figure 5. Inversion method testing using the synthetic flexural-wave dispersion data (markers in box plot [b]). The objective function (VD image [in box plot [a]) has a unique solution minimum over the 2D parameter domain. The resulting dispersion curve (black solid curve in [b]) fits that data very well. For comparison, the isotropic dispersion curve (dashed) is also plotted.

Downloaded from pubs.geoscienceworld.org/seg/geophysics/article-pdf/82/2/D47/4052662/geo-2016-0223.1.pdf by Univ of Petroleum (Beijing) - Library user on 08 October 2026

results are from two different measurements, the agreement is good. To further validate the flexural-wave inversion results, we overlay the inversion-fitted dispersion curve calculated with the TI parameters with the dispersion data (dots). The theory fits the data very well, especially at low frequencies. To test the validity of the inverted vertical shear slowness S_{sv}, we plot it (red curve) in panel 6 on the background of the slowness probability density (SPD) image. The SPD method is used for quality controlling the slowness result from processing the dispersive flexural wave (Huang and Yin, 2005; Lee et al., 2016). If the result is close to the true vertical formation shear slowness, it should track the edge of the SPD image. As shown in panel 6, the inverted S_{sv} curve is significantly faster than the STC-processed slowness (black) and tracks the edge of the SPD image. To explain why the Stoneley and flexural inversions can get valid results, we plot the respective average sensitivity curve in panel 7. The average curve is the γ-sensitivity curve in Figure 3 averaged in the respective processing frequency. For the Stoneley, the frequency range is 0–3 kHz; for the flexural wave, the frequency range is 0.55–4.3 kHz. For the processing interval, the sensitivity is approximately 0.3 for the Stoneley and approximately 0.25 for the flexural wave. The significant sensitivity values allow the anisotropy parameter γ to be reliably estimated from both data sets.

Fast formation example

The fast formation example (Figure 7) demonstrates the advantage of the flexural wave over the Stoneley wave for the shear-TI inversion. Panel 1 shows the caliper and gamma-ray log curves for a 35 m formation interval consisting of sand, shaly sand, and some shale streaks. Panels 2 and 3 show the monopole and dipole waveform data, respectively. For the fast formation, P- and S-wave slowness log curves can be directly obtained by STC processing of the monopole data, as given in panel 6. The dispersion data (dotted curve in panel 4) from the dipole data processing cover a broad frequency range of 2–9 kHz. The inversion using the monopole Stoneley data in the frequency range of 0–3 kHz obtains the S-wave γ parameter curve in panel 5 (right shaded curve). Because of the strong jitter at high frequencies (7.5–9.0 kHz), the inversion using the flexural-wave dispersion data in the frequency range of 2–7 kHz obtains the γ curve in panel 5 (left shaded curve) and the vertical shear slowness curve in panel 6 (red curve). The validity of the

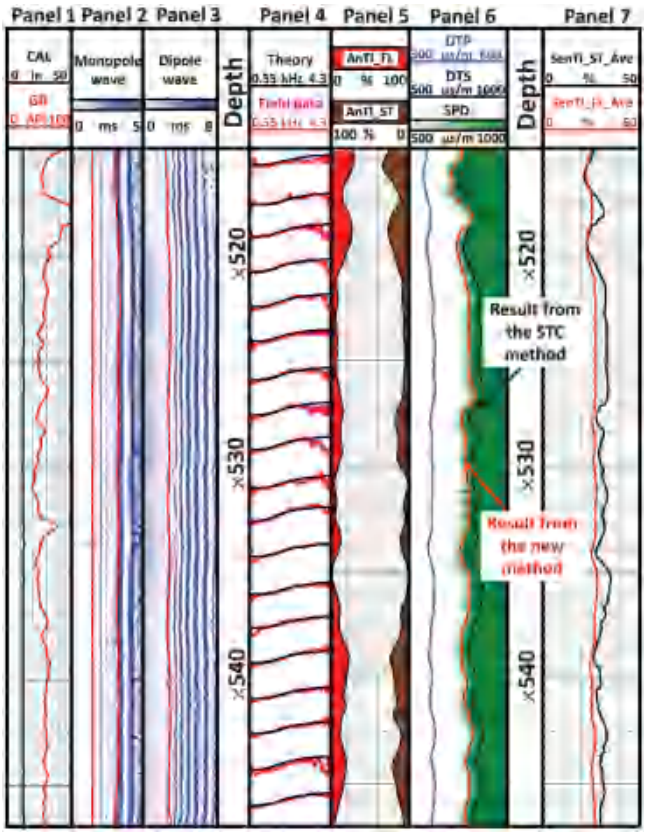


Figure 6. S-wave TI inversion for a sand-shale formation (see gamma-ray curve GR in panel 1), using the (panel 2) monopole Stoneley and (panel 3) dipole flexural-wave data, respectively. Because both waves have a significant sensitivity to the (panel 7) TI anisotropy, their (panel 5) inversion results are in good agreement. For quality controlling the flexural-wave inversion, panel 4 displays the dispersion data fitting and panel 6 shows the SPD edge tracking by the inverted vertical S-slowness curve DTS (red). For comparison, the P-slowness curve DTP is also plotted in panel 6.

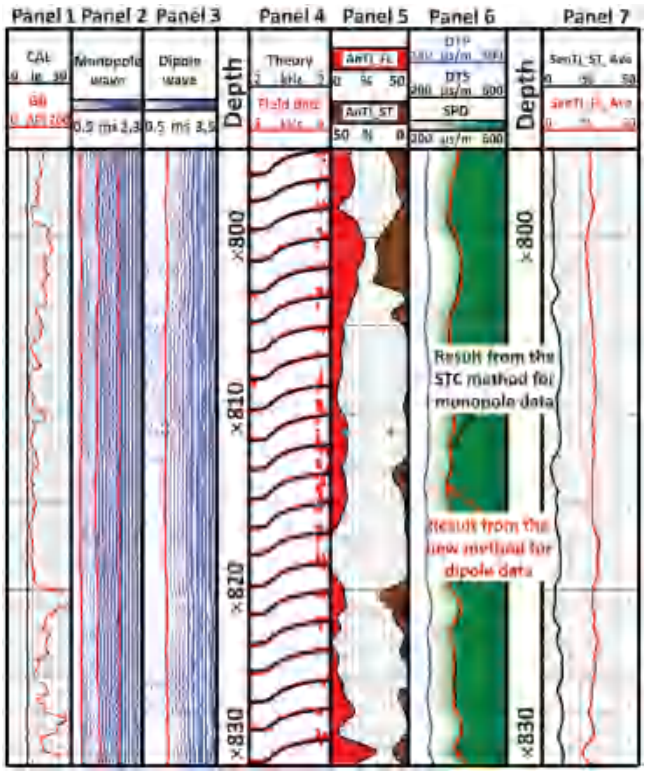


Figure 7. S-wave TI inversion for a fast sand-shale formation (see the gamma-ray curve GR in panel 1) using the monopole Stoneley data in panel 2 and the dipole-flexural wave data in panel 3, respectively. Because the flexural-wave sensitivity to TI is higher than the Stoneley wave's (panel 7), the anisotropy form the flexural wave is more accurate and reliable. Panel 5 also shows the corresponding estimate based on core measurements. For quality controlling the flexural-wave inversion, panel 4 displays the dispersion data fitting and panel 6 shows the SPD tracking by the inversion result, in which the monopole S-slowness DTS and P-slowness DTP are also shown (black and blue curves in panel 6).

Downloaded from pubs.geoscienceworld.org/seg/geophysics/article-pdf/82/2/D47/4052662/geo-2016-0223.1.pdf by Univ of Petroleum (Beijing) - Library user on 08 October 2026

inverted slowness curve is supported by its tracking along the edge of the SPD image and by its close agreement with the monopole shear slowness (black curve). The two different methods allow independent estimates of the γ curves. The curves differ in the middle sand interval, but they agree in the upper and lower shale streaks. These two anisotropy curves and their validity are further examined below.

The validity of the curves is checked by the core measurement result. A core sample was taken from the middle sand interval and was measured in the laboratory to determine its TI parameters. The

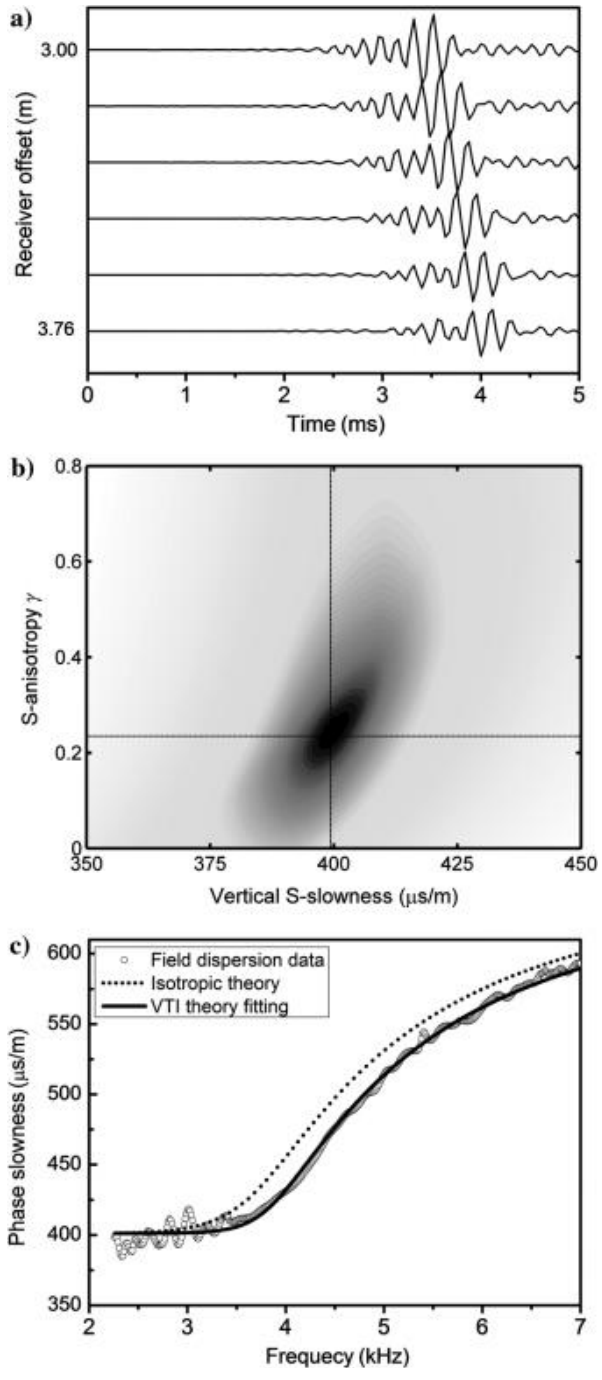


Figure 8. Detailed inversion results for an anisotropic formation depth (×800 m). (a) The array waveform data are used to obtain the dispersion data (markers in box plot [c]). (b) The solution minimum of the objective function corresponds to the inversion-fitted dispersion curve (black solid curve in box plot [c]). The dispersion curve computed with an isotropic formation (back dashed curve in box plot [c]) cannot fit the data.

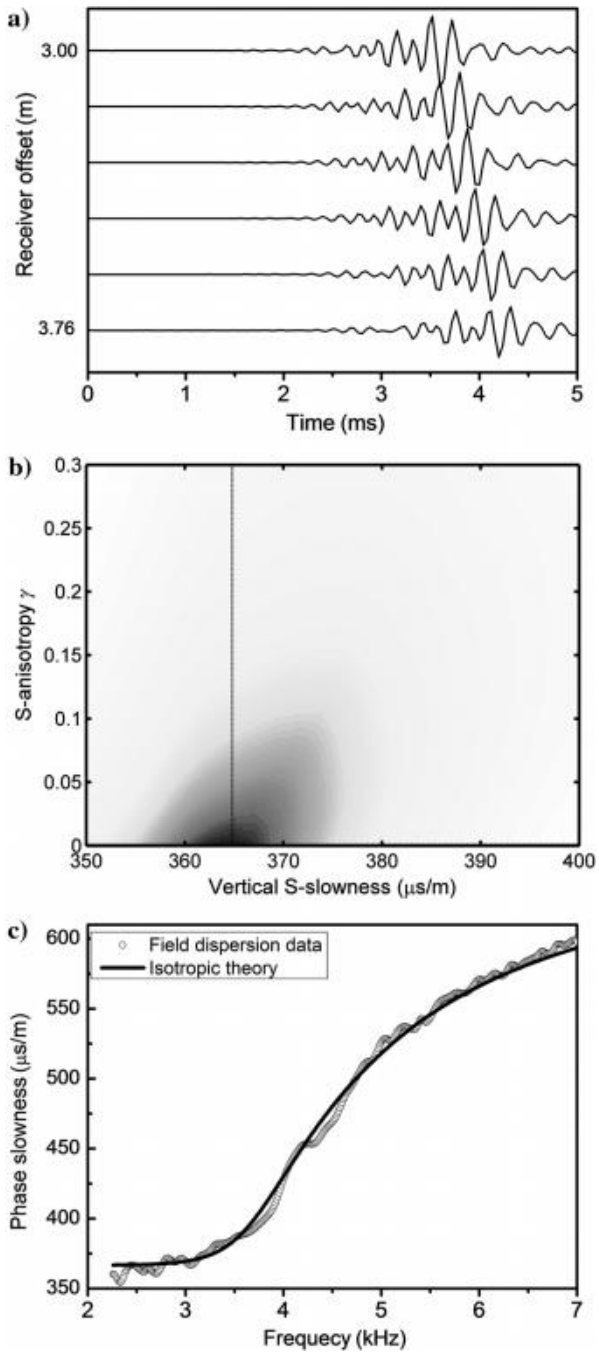


Figure 9. Detailed inversion results for an isotropic formation depth (×818 m). (a) The array waveform data are used to obtain the dispersion data (markers in box plot [c]). (b) The solution minimum of the objective function is at zero anisotropy. Correspondingly, the dispersion data can be fitted with an isotropic dispersion curve (solid curve in box plot [c]).

Downloaded from pubs.geoscienceworld.org/seg/geophysics/article-pdf/82/2/D47/4052662/geo-2016-0223.1.pdf by Univ of Petroleum (Beijing) - Library user on 08 October 2026

measured γ value of 0.12 is plotted twice in panel 6; once from left to right to compare with the flexural γ and the other from right to left to compare with the Stoneley γ. The measured γ falls on to the γ curve from the flexural wave. In comparison, the γ curve from the Stoneley wave shows an almost zero value for this interval. For further examination, the detailed inversion analysis and results are shown in Figure 8 for the depth of ×800 m. Figure 8 shows the array flexural waveform data (Figure 8a) and its processed dispersion (Figure 8c). The VD image of the objective function (equation 8) clearly shows a well-defined minimum over the 2D S_{sv} and γ domain, for which the inverted value is 0.225, as is the value for the γ curve at this depth. The detailed dispersion data fitting is shown in Figure 8c, where the isotropic theory (black dashed line) does not fit the data but the anisotropic theory (black solid line) fits the data very well. For comparison to this anisotropic depth, Figure 9 shows the results of the same analysis for an isotropic depth at ×818 m. Compared with the anisotropic counterpart of Figure 8, one can see that the solution on the VD image occurs at $\gamma = 0$. The dispersion data (Figure 8c) can be well-fitted by the isotropic theory. Therefore, the above analyses and results, together with the core measurement, indicate that the shear anisotropy from the flexural-wave inversion is more accurate and reliable than that from the Stoneley-wave inversion.

To explain the root cause of the difference between the flexural- and Stoneley-wave inversion results, plane 7 plots the average sensitivity curves for the two wave modes. For the Stoneley, the sensitivity is averaged in the 0–3 kHz range, whereas for the flexural wave, the averaging range is 2–7 kHz. In this formation interval, the average Stoneley sensitivity is less than 0.1, not even half the value of its flexural-wave counterpart (which is greater than 0.2). The sensitivity comparison further supports that the flexural-wave inversion result is more accurate and reliable for the fast formation situation.

CONCLUSION

Flexural waves from dipole acoustic logging in a VTI formation are sensitive to the formation S-wave TI property, especially in the medium- to high-frequency range. The flexural-wave dispersion data can therefore be used to quantify the S-wave TI parameters. Compared with the traditional S-wave TI estimation using Stoneley waves, the flexural-wave method has two advantages: (1) It can simultaneously determine the vertical and horizontal shear velocities, whereas the Stoneley can only determine the latter, and (2) the flexural wave has higher sensitivity to the TI property than does the Stoneley wave in a fast formation and can thus be used in the fast and slow formations. Based on flexural-wave analysis and its advantages, we have developed an inversion method to simultaneously determine the horizontal and vertical S-wave velocity profiles from the data. Field data examples support the validity and effectiveness of the method.

ACKNOWLEDGMENTS

We thank the reviewers and the associate editor for their careful reviews that helped improve the manuscript. This work is supported by the Fundamental Research and Development Program (grant no. 2014CB239006), the China Natural Science Foundation (nos. 41474101 and 41474092), and the Fundamental Research Funds for the Central Universities (no. 16CX06040A).

APPENDIX A

MULTIPOLE WAVE DISPERSION EQUATION FOR A FLUID-FILLED BOREHOLE CENTERED BY A LOGGING TOOL AND SURROUND BY A VTI FORMATION

The multipole wave dispersion equation 3 for a TI formation surrounding a fluid-filled borehole with a logging tool at its center is given by

$$D(k;\omega) = \det\begin{pmatrix} T_{11} & T_{12} & T_{13} & T_{14} \\ T_{21} & T_{22} & T_{23} & T_{24} \\ T_{31} & T_{32} & T_{33} & T_{34} \\ T_{41} & T_{42} & T_{43} & T_{44} \end{pmatrix} = 0; \qquad \text{(A-1)}$$

where "det" denotes taking the determinant of the matrix (T_{ij}) for the TI formation, and whose elements are

$$\begin{cases} T_{11} = -\left[\frac{n}{R} I_n(fr) + f I_{n+1}(fr)\right] - E_{tool}\left[\frac{n}{R} K_n(fr) - f K_{n+1}(fr)\right] \\ T_{12} = (1 + ika')\left[\frac{n}{r} K_n(q_p r) - q_p K_{n+1}(q_p r)\right] \\ T_{13} = \frac{n}{r} K_n(q_{SH} r) \\ T_{14} = (b' + ik)\left[\frac{n}{r} K_n(q_{SV} r) - q_{SV} K_{n+1}(q_{SV} r)\right] \end{cases}; \qquad \text{(A-2)}$$

$$\begin{cases} T_{21} = \rho_f \omega^2 [I_n(fr) + E_{tool} K_n(fr)] \\ T_{22} = [c_{11}(1 + ika')q_p^2 + c_{13}(-k^2 - ika' q_p^2)] K_n(q_p r) \\ \quad + \frac{2c_{66}}{r}(1 + ika')\left[\frac{n(n-1)}{r} K_n(q_p r) + q_p K_{n+1}(q_p r)\right] \\ T_{23} = \frac{2nc_{66}}{r}\left[\frac{(n-1)}{r} K_n(q_{SH} r) - q_{SH} K_{n+1}(q_{SH} r)\right] \\ T_{24} = [c_{11}(b' + ik)q_{SV}^2 + c_{13}(-k^2 b' - ikq_{SV}^2)] K_n(q_{SV} r) \\ \quad + \frac{2c_{66}}{r}(b' + ik)\left[\frac{n(n-1)}{r} K_n(q_{SV} r) + q_{SV} K_{n+1}(q_{SV} r)\right] \end{cases}; \qquad \text{(A-3)}$$

$$\begin{cases} T_{31} = 0 \\ T_{32} = \frac{2c_{66}n}{r}(1 + ika')\left[\frac{(1-n)}{r} K_n(q_p r) + q_p K_{n+1}(q_p r)\right] \\ T_{33} = -c_{66}\left\{\left[\frac{2n(n-1)}{r^2} + q_{SH}^2\right] K_n(q_{SH} r) + \frac{2q_{SH}}{r} K_{n+1}(q_{SH} r)\right\} \\ T_{34} = \frac{2c_{66}n}{r}(b' + ik)\left[\frac{(1-n)}{r} K_n(q_{SV} r) + q_{SV} K_{n+1}(q_{SV} r)\right] \end{cases}; \qquad \text{(A-4)}$$

and

$$\begin{cases} T_{41} = 0 \\ T_{42} = c_{44}[2ik - a'(k^2 + q_p^2)]\left[\frac{n}{r} K_n(q_p r) - q_p K_{n+1}(q_p r)\right] \\ T_{43} = \frac{iknc_{44}}{r} K_n(q_{SH} r) \\ T_{44} = c_{44}[2ikb' - (k^2 + q_{SV}^2)]\left[\frac{n}{r} K_n(q_{SV} r) - q_{SV} K_{n+1}(q_{SV} r)\right] \end{cases}; \qquad \text{(A-5)}$$

Downloaded from pubs.geoscienceworld.org/seg/geophysics/article-pdf/82/2/D47/4052662/geo-2016-0223.1.pdf by Univ of Petroleum (Beijing) - Library user on 08 October 2026

where I_n and K_n ($n = 0, 1, 2$) denote the first- and second-kind modified Bessel functions of the nth order, respectively. The radial wavenumbers for the borehole fluid and formation quasi-P and quasi-S waves are given by

$$\begin{cases} f = \left(k^2 - \frac{\omega^2}{V_f^2}\right)^{1/2} \\ q_p = \omega\sqrt{\frac{-V+\sqrt{V^2-4UW}}{2U}} \\ q_{SV} = \omega\sqrt{\frac{-V-\sqrt{V^2-4UW}}{2U}} \\ q_{SH} = \sqrt{\frac{c_{44}k^2-\rho\omega^2}{c_{66}}} \end{cases}; \quad \text{(A-6)}$$

with the symbols U, V, and W given by

$$\begin{cases} U = c_{11}c_{44} \\ V = \rho(c_{11}+c_{44}) - (c_{11}c_{33} - c_{13}^2 - 2c_{13}c_{44})(k^2/\omega^2): \\ W = c_{33}c_{44}(\rho/c_{44} - k^2/\omega^2)(\rho/c_{33} - k^2/\omega^2) \end{cases} \quad \text{(A-7)}$$

The shear coupling to the quasi-P wave a' and the compressional coupling to the quasi-S wave b' coefficients appearing in equations A-2–A-5 are given by

$$\begin{cases} a' = -\frac{1}{ik}\frac{(c_{13}+2c_{44})k^2 - c_{11}q_p^2 - \rho\omega^2}{c_{44}k^2 - (c_{11}-c_{13}-c_{44})q_p^2 - \rho\omega^2} \\ b' = -ik\frac{c_{44}k^2 - (c_{11}-c_{13}-c_{44})q_{SV}^2 - \rho\omega^2}{(c_{13}+2c_{44})k^2 - c_{11}q_{SV}^2 - \rho\omega^2} \end{cases}: \quad \text{(A-8)}$$

Appearing in T_{11} and T_{21} of equations A-2 and A-3 is the coefficient E_{tool}, which models the effect of a compliant acoustic logging tool on the wave propagation. This coefficient (Tang and Cheng, 2004; Su et al., 2011) is given below:

$$E_{tool} = -\frac{\frac{n}{a}I_n(fa) + fI_{n+1}(fa) + \frac{a}{M_T}\rho_f\omega^2 I_n(fa)}{\frac{n}{a}K_n(fa) - fK_{n+1}(fa) + \frac{a}{M_T}\rho_f\omega^2 K_n(fa)}; \quad \text{(A-9)}$$

where a and M_T denote the radius and elastic modulus of the tool, respectively.

By setting the determinant in equation A-1 to zero, the resulting equation is called the dispersion equation. The wavenumbers k satisfying the dispersion equation are found numerically for each given angular frequency ω.

REFERENCES

Cheng, C. H., M. N Toksöz, and M. E. Willis, 1982, Determination of in situ attenuation from full waveform acoustic logs: Journal of Geophysical Research, 87, 5477–5484, doi: 10.1029/JB087iB07p05477.

Ellefsen, K. J., 1990, Elastic wave propagation along a borehole in an anisotropic medium: Ph.D. thesis, Massachusetts Institute of Technology.

Fang, X. D., C. Chang, and A. Cheng, 2013, System and method for determining shear wave anisotropy in a vertically transversely isotropic formation: U.S. Patent 2,013,022,421.

Huang, X., and H. Yin, 2005, A data-driven approach to extract shear and compressional slowness from dispersive waveform data: 75th Annual International Meeting, SEG, Expanded Abstracts, 384–387.

Kimball, C. V., and T. L. Marzetta, 1984, Semblance processing of borehole acoustic array data: Geophysics, 49, 274–281, doi: 10.1190/1.1441659.

Lee, S. Q., X. M Tang, Y. D. Su, and C. X. Zhuang, 2016, Model-based dispersive processing of borehole dipole wave data using an equivalent-tool theory: Geophysics, 81, no. 1, D35–D43, doi: 10.1190/geo2015-0210.1.

Norris, A. N., and B. K. Sinha, 1993, Weak elastic anisotropy and the tube wave: Geophysics, 58, 1091–1098, doi: 10.1190/1.1443493.

Sayers, C. M., 2005, Seismic anisotropy of shales: Geophysical Prospecting, 53, 667–676, doi: 10.1111/j.1365-2478.2005.00495.x.

Schmitt, D. P., 1989, Acoustic multipole logging in transversely isotropic poroelastic formations: The Journal of Acoustical Society of America, 86, 2397–2421, doi: 10.1121/1.398448.

Schoenberg, M., F. Muir, and C. M. Sayers, 1996, Introducing ANNIE: A simple three-parameter anisotropic velocity model for shales: Journal of Seismic Exploration, 5, 35–49.

Sinha, B. K., A. Donald, J. Walsh, and T. Lei, 2014, Anisotropic elastic constants from dipole flexural dispersions in unconventional shale-gas reservoirs: 84th Annual International Meeting, SEG, Expanded Abstracts, 596–600.

Sinha, B. K., and J. Walsh, 2015, Orthorhombic elastic constants and mechanical properties for optimal completion of unconventional gas-shale reservoirs: 85th Annual International Meeting, SEG, Expanded Abstracts, 684–688.

Su, Y. D., X. M. Tang, C. Hei, and C. X. Zhuang, 2011, An equivalent-tool theory for acoustic logging and applications: Applied Geophysics, 8, 69–78, doi: 10.1007/s11770-011-0272-6.

Sunaga, S., B. K. Sinha, T. Endo, and J. Walsh, 2009, Radial profiling of shear slownesses in TIV formations: 79th Annual International Meeting, SEG, Expanded Abstracts, 3481–3485.

Tang, X. M., 2003, Determining formation shear-wave transverse isotropy from borehole Stoneley-wave measurements: Geophysics, 68, 118–126, doi: 10.1190/1.1543199.

Tang, X. M., and C. H. Cheng, 2004, Quantitative borehole acoustic methods: Elsevier Science Publishing Company Inc.

Tang, X. M., and D. J. Patterson, 2010, Mapping formation radial shear-wave velocity variation by a constrained inversion of borehole flexural-wave dispersion data: Geophysics, 75, no. 6, E183–E190, doi: 10.1190/1.3502664.

Thomsen, L., 1986, Weak elastic anisotropy: Geophysics, 51, 1954–1966, doi: 10.1190/1.1442051.

Tongtaow, C., 1982, Wave propagation along a cylindrical borehole in a transversely isotropic medium: Ph.D. thesis, Colorado School of Mines.

Valero, H. P., T. Ikegami, B. Sinha, S. Bose, and T. Plona, 2009, Sonic dispersion curves identify TIV anisotropy in vertical wells: 79th Annual International Meeting, SEG, Expanded Abstracts, 381–385.

Walker, K., J. Granville, G. Kainer, and A. Cheng, 2015, Logging services: Towards the 3D measurement of formation properties in high-resolution with a continuous depth of investigation: Presented at the Annual Technical Conference and Exhibition, SPE-175093–MS.

White, J. E., and C. Tongtaow, 1981, Cylindrical waves in transversely isotropic media: The Journal of Acoustical Society of America, 70, 1147–1155, doi: 10.1121/1.386946.

Zemanek, J., F. A. Angona, D. M. Williams, and R. L. Caldwell, 1984, Continuous acoustic shear wave logging: Presented at the SPWLA 25th Annual Logging Symposium.

Downloaded from pubs.geoscienceworld.org/seg/geophysics/article-pdf/82/2/D47/4052662/geo-2016-0223.1.pdf by Univ of Petroleum (Beijing) - Library user on 08 October 2026

文章编号：1000-0747(2016)03-0417-08 DOI: 10.11698/PED.2016.03.12

基于弹性波速径向变化的岩石脆裂性定量评价

唐晓明，许松，庄春喜，苏远大，陈雪莲

（中国石油大学（华东）地球科学与技术学院）

基金项目：国家重点基础研究发展计划（973）项目（2014CB239006）；国家自然科学基金（41474101，41474092）；中央高校基本科研业务费专项资金（14CX05010A，16CX06040A）；山东省自然科学基金（ZR2014DL009）

摘要：岩石的脆性和可压裂性是非常规油气储集层体积压裂重要的岩石力学参数，为获得地层岩石的脆性和可压裂性指标，基于声波测井得到的井壁地层纵、横波速度的径向变化，求得地层的脆裂指数，指导储集层压裂改造作业。钻井过程中岩石破坏时在井壁地层中产生微裂缝，导致弹性波速度降低，波速在径向上发生由小到大的变化。采用测井纵波速度的层析成像和偶极弯曲波频散特征反演获得井壁周围地层纵、横波速度径向剖面，将两个剖面沿井径方向积分，得到纵、横波脆裂指数。脆裂指数与脆性指数、可压裂指数相关性较好，验证了用脆裂指数评估岩石脆裂性质的有效性；实际对测井数据的处理和分析亦证明了这种方法的可行性和有效性，结果对于储集层压裂优选层位和压裂改造实施有指导意义。图 7 表 1 参 17

关键词：岩石脆裂性；脆裂指数；声波速度径向变化；声波测井；弹性波速

中图分类号：P618 **文献标识码：**A

Quantitative evaluation of rock brittleness and fracability based on elastic-wave velocity variation around borehole

TANG Xiaoming, XU Song, ZHUANG Chunxi, SU Yuanda, CHEN Xuelian

(*School of Geosciences & Technology, China University of Petroleum, Qingdao* 266555, *China*)

Abstract: Brittleness and fracability are two important rock properties in hydraulic fracturing of unconventional reservoirs. Based on the variation of compressional and shear velocity around borehole using acoustic measurement, an effective technique is developed to estimate these parameters to guide reservoir-fracturing. During drilling, when the rock is broken, a significant amount of drilling induced cracks will occur in the formation around the borehole, resulting in the drop of radial elastic wave velocity and the wave velocity variation from low to high in radial direction. The radial variation of compressional and shear velocities of formation rocks surrounding a borehole were respectively obtained from P-wave travel time tomography and dipole shear-wave dispersion inversion. By integrating the two variation profiles along the radial direction, the brittleness-fracability index is obtained to estimate the brittleness and fracability of formation rocks. The index shows fairly good consistency and correlation with rock brittleness and fracability, which demonstrates the practicability and effectiveness of the proposed approach. Well log data analysis examples are presented to demonstrate the effectiveness of our technique.

Key words: rock brittleness-fracability; brittleness-fracability index; radial acoustic velocity variation; acoustic well logging; elastic-wave velocity

1 岩石脆裂性评价原理

非常规油气压裂开采的实践证明，地层岩石的脆性和可压裂性是影响压裂效果的关键因素。在脆性好的岩石中，当外加载荷超过岩石的破裂强度时，岩石随即起裂且裂缝的扩展不需要外加能量。反之，脆性差的岩石则会发生塑性屈服，裂缝起裂需要继续外加能量。因此，岩石的脆性是一个重要参数。但是，岩石的脆性并不等于岩石的可压裂性，如很多脆性很高的岩石，如花岗岩、白云岩等，其脆性非常高，但其强度也很高，难以压裂。因此，岩石的脆性和可压裂性共同决定要达到一定压裂效果所需的载荷大小和能量多少。这两项参数的获取亦是目前非常规油气地球物理勘探的重要内容。

目前对岩石脆性的计算一般采用矿物成分分析和弹性参数测量两种方法。在矿物成分分析法中，利用岩石中的脆性矿物，如石英、长石和方解石等所占比例得出岩石脆性指标，矿物成分数据往往通过元素俘获测井方法获得[1-3]。弹性参数测量法则通过测量地层岩石的弹性模量和泊松比定义岩石的脆性指标[4]：

$$B_{\mathrm{r}}=\frac{E_{\mathrm{N}}+\nu_{\mathrm{N}}}{2} \tag{1}$$

(C)1994-2022 China Academic Journal Electronic Publishing House. All rights reserved. http://www.cnki.net

其中 $E_N=\frac{E-E_{min}}{E_{max}-E_{min}}$；$\nu_N=\frac{\nu_{max}-\nu}{\nu_{max}-\nu_{min}}$

岩石可压裂性的估算目前尚无成熟方法，前述分析指出该参数与岩石的强度有关，具体而言，与岩石起裂所要克服的断裂韧性有关[5]。孙建孟等人[6]提出了一种利用岩石脆性指数 B_r 与断裂韧性 K_C 指标估计地层岩石可压裂性的方法：

$$F_r \equiv B_{rN}K_{CN} \tag{2}$$

其中 $B_{rN}=\frac{B_r-B_{r\,min}}{B_{r\,max}-B_{r\,min}}$；$K_{CN}=\frac{K_{Cmax}-K_C}{K_{Cmax}-K_{Cmin}}$

但地层岩石的断裂韧性 K_C 值比弹性参数测量难度大，因此该方法只能作为参考。

本文提出利用钻井过程导致的井壁附近岩石波速变化来综合评估岩石脆裂性的方法。钻井的难易程度和效率与地层岩石的力学性质密切相关，岩石“可钻性”的一般定义如下：

$$DB \equiv \sigma_c/\sigma_t \tag{3}$$

该定义说明钻头必须要克服岩石的机械强度使其碎裂后才能在地层中钻进，因此，钻井过程本身就是对地层岩石所做的破坏性力学试验。而岩石破碎的难易程度和所需能量大小又与岩石的脆裂性质直接相关。破碎的结果是在井壁附近产生数目可观的微裂隙或裂缝。

从岩石力学角度对井壁岩石微裂隙产生的机理加以说明：钻井过程中，井内岩石碎裂后被带走，而井外岩石尚未被破坏，因此井壁岩石在钻井过程中处于破裂临界状态。对于脆性岩石而言，达此临界状态时的一个普遍岩石力学现象是岩石体积膨胀或扩容，这源于应力作用下岩石中微裂缝的产生和扩展，表现之一是岩石弹性波速（包括纵波和横波）明显降低[7]。可压裂性好的岩石容易起裂，脆性高的岩石起裂后产生的裂缝多，造成的波速降低愈明显。将此脆性岩石的扩容机理应用于扩容后的井壁岩石，不难看出岩石的脆裂性质与井壁附近波速变化的对应关系，相应地，测量这种变化及其影响范围即可评估岩石的脆裂性。钻井对井壁附近声波速度的影响已为实验室测量所验证[8]，在实际测井资料处理中也有大量实例[9]。

井壁岩石的波速降低取决于岩石中裂缝密度的大小[10-11]。但是，钻井造成的岩石变化是局部的，只发生在井筒周围，离井较远距离的原状地层却不受影响，从井壁到地层深处地层波速度呈现出由低到高的径向变化。通过求取地层波速的径向变化，可以得到井壁附近的裂隙密度及钻井影响范围，这种由钻井产生的影响大小及范围信息直接反映了钻井时岩石所体现出的脆裂性质。

2 纵、横波速度径向剖面的求取

井壁周围地层纵、横波速径向剖面的求取分别通过测井纵波速度的层析成像和偶极弯曲波频散特征的反演来获得，本文着重于方法的应用，详细原理可参见文献[9]、[12-13]。

2.1 纵波速度的层析成像

如图 1 所示，阵列式声波测井仪器激发的声波在波速径向增加的地层中传播，地层速度的变化使得不同接收器接收声波的径向穿透时间有所不同，这样波的走时就含有地层变化的信息，从而可以用来确定地层速度的径向变化。

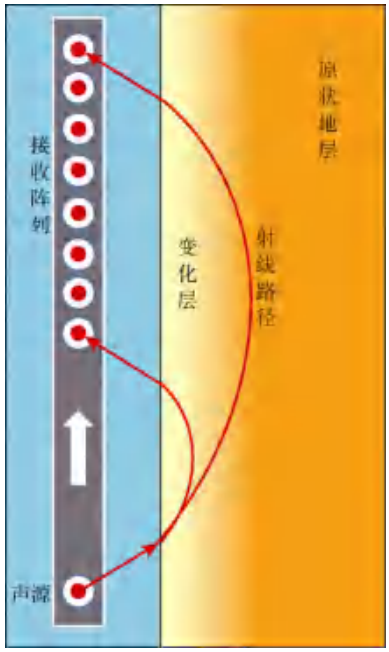


图 1 速度径向变化地层中的声波射线路径示意图

Hornby[9]利用走时层析成像技术获得了井壁附近地层沿轴向和径向的二维速度剖面，即选取二维速度剖面函数 $v(r,z)$，对其用射线追踪的方法计算得到声波走时 t：

$$t=\int_{s(v)}\frac{\mathrm{d}s}{v(r,z)} \tag{4}$$

然后使计算和实测的走时之差达到最小，得到与实测数据符合最好的速度分布模型，该分布模型便描述了波速沿井轴向 z 和径向 r 的变化。

在获得地层的层析成像之前，可用一种直观有效的方法来判断目的层是否存在声波速度由低到高的径向变化。如图 1 所示的径向变化地层，声波射线从声

(C)1994-2022 China Academic Journal Electronic Publishing House. All rights reserved. http://www.cnki.net

源出发穿入地层后在阵列中出射，根据本多夫定理[14]，波在射线出射处沿井轴方向的视速度等于波在其最大穿透深度处的地层速度，该视速度即为波在阵列中传播的平均速度，可用阵列相关的方法[14]提取。笔者用此速度来计算声波传播到第 1 个接收器的走时，并将其定义为参考走时 TT_{ref}，公式如下：

$$TT_{\mathrm{ref}}=\int_{z_s}^{z_{r1}}\frac{\mathrm{d}z}{v(z)}+TT_{\mathrm{f}} \tag{5}$$

将公式（5）中的参考走时与实测走时比较，对于声速无径向变化的地层，参考走时与实测一致。当声速沿径向增加时，射线由浅到深进入地层后再折射回来，由于公式（5）中的 v 为声波所能达到的最大速度，因此由该公式计算出的参考走时比实测走时要小，实测走时滞后于参考走时。由此，通过比较实测与参考走时，即使不通过层析成像处理，也能判断地层声速是否发生了径向变化。

图 2 为利用上述两种方法判断地层声速有无径向变化的实例，图中第 2 道给出了由公式（5）计算出的

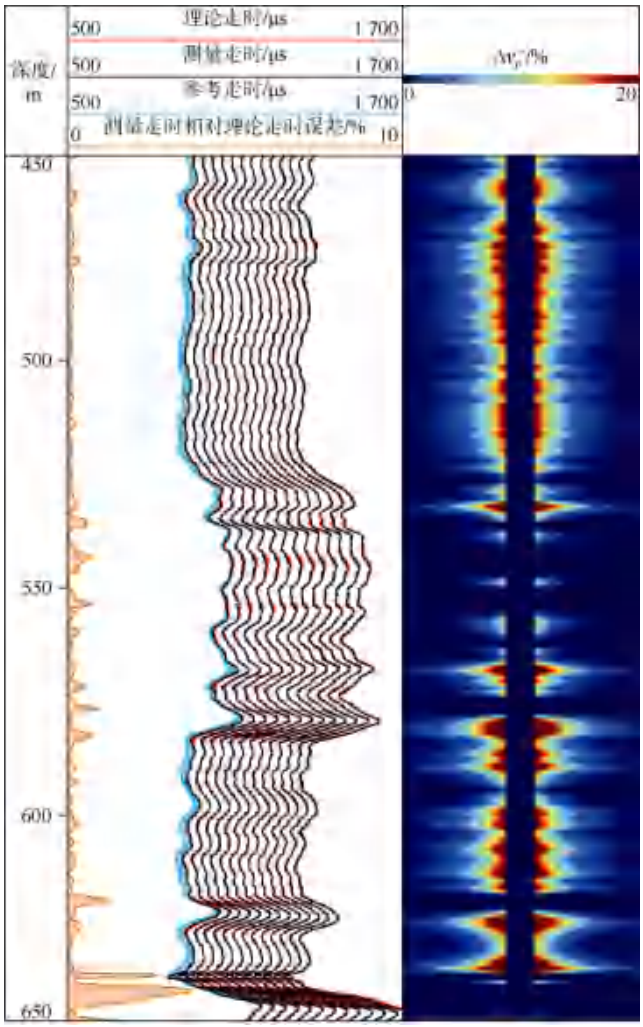


图 2　地层声速径向变化判定图

第 1 个接收器上的参考走时曲线，以及 13 个接收器上实测的走时曲线，对比第 1 个接收器上的参考走时和测量走时可以发现，后者明显滞后于前者，特别是在 455～525 m、580～620 m 深度段。由此可以判定这些深度段的地层发生了明显的径向速度变化。图 2 第 3 道给出了用层析成像技术反演得到的声速变化的层析成像图，$\Delta v_{\mathrm{P}}'$为径向深度上纵波速度与原状地层纵波速度的相对差别的百分比：

$$\Delta v_{\mathrm{P}}'=(v_{\mathrm{pi}}-v_{\mathrm{pw}})/v_{\mathrm{pi}}\times 100\% \tag{6}$$

同理有：

$$\Delta v_{\mathrm{S}}'=(v_{\mathrm{si}}-v_{\mathrm{sw}})/v_{\mathrm{si}}\times 100\% \tag{7}$$

速度变化剖面的正确与否可由图 2 第 2 道曲线验证：①该速度剖面计算出的理论走时曲线（红色）是否与实测走时曲线（黑色）吻合；②实测走时相对于参考走时的滞后是否对应于速度变化剖面。图 2 第 2 道还给出了理论走时与实测走时的拟合误差曲线。当理论走时与实测走时吻合时，速度剖面的误差小，反之误差大。由图 2 可以看出，走时滞后明显的地带，速度剖面的变化也大，且径向影响深度明显加深。

2.2 横波速度剖面的反演

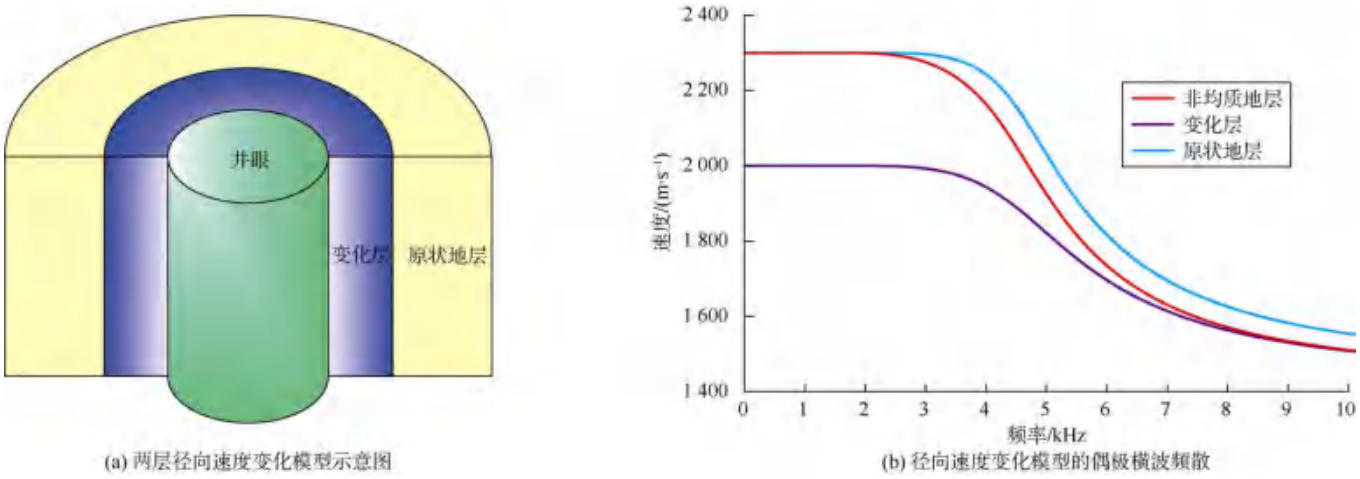
偶极横波测井通过产生沿井筒传播的弯曲波来测量地层的横波速度。研究发现，地层横波速度的径向变化会明显影响弯曲波的频散特征[15]。图 3a 给出了一个简单的两层径向变化模型，图 3b 给出了对应的弯曲波频散曲线（红线），同时还分别给出了以原状地层（蓝线）和变化层（紫线）横波速度计算出的两条均匀地层的频散曲线。对比可见，在波穿透较深的低频部分，地层的频散曲线与均匀原状地层对应的曲线一致。随着频率增加波长变短，穿透深度变浅，频散曲线又趋向于由变化层速度计算的均匀地层频散曲线。根据频散曲线的上述变化特征，得出了求取地层横波速度径向变化的约束反演方法[12-13,16]，即通过将以下目标函数极小化来实现：

$$E_{\mathrm{OBJ}}(\Delta v,\Delta r)=\sum\nolimits_{\Omega}\left[v_{\mathrm{t}}(\omega,\Delta v,\Delta r)-v_{\mathrm{d}}(\omega)\right]^2+\lambda\sum\nolimits_{\Omega'}\left[v_{\mathrm{t}}(\omega,\Delta v,\Delta r)-v_{\mathrm{h}}(\omega)\right]^2 \tag{8}$$

上式中的反演目标函数既要求理论与实测数据在测井频段Ω中符合，又要求理论曲线 v_{t} 与 v_{h} 在高频区间 Ω'趋于一致。后一个条件即为约束条件，通过调节权重因子λ来实现。该条件很好地消除了反演中存在的不唯一性[16]。

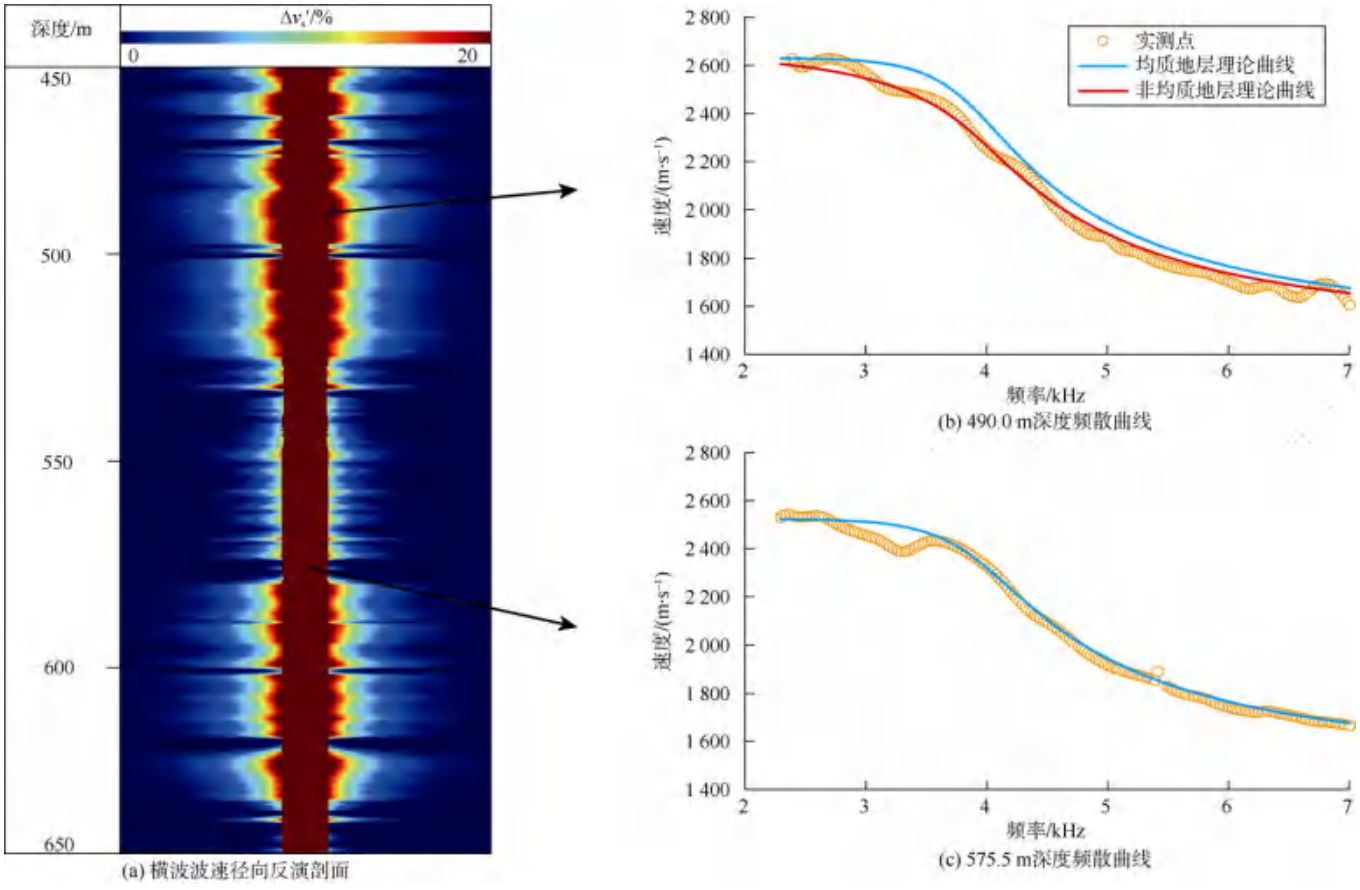
图 4 是横波波速径向反演剖面的实例，图 4a 为径向深度上横波速度与原状地层横波速度差别的相对百分数。为验证该速度变化剖面，对 490.0 m、583.9 m 深

(C)1994-2022 China Academic Journal Electronic Publishing House. All rights reserved.　http://www.cnki.net



(a) 两层径向速度变化模型示意图　(b) 径向速度变化模型的偶极横波频散

图 3　两层地层模型及其弯曲波频散曲线



(a) 横波波速径向反演剖面　(b) 490.0 m深度频散曲线　(c) 575.5 m深度频散曲线

图 4　横波波速径向反演剖面及频散曲线

度处的频散曲线进行分析。在 575.5 m 处，横波速度径向剖面变化甚微，计算出的理论频散曲线与实测数据拟合很好。但在横波速度径向变化明显的 490.0 m 深度处，实测数据明显低于均匀地层的频散曲线（蓝线），这时须采用变化地层模型，计算出的频散曲线（红线）方能与实测数据符合，由此验证了横波速度剖面的正确性。

3 纵、横波速剖面与岩石脆性指标

图 2 和图 4 中的纵、横波速度径向剖面为同一地层深度区间的结果，为了对纵、横波速度径向剖面进行定量化比较，对纵、横波速度剖面 $\Delta v_p(r)$ 和 $\Delta v_s(r)$ 沿井径方向积分，即：

$$\begin{cases} BF_{vp} = \dfrac{1}{R}\displaystyle\int_{r=R}^{\infty} \Delta v_p(r)/v_p \,\mathrm{d}r \\ BF_{vs} = \dfrac{1}{R}\displaystyle\int_{r=R}^{\infty} \Delta v_s(r)/v_s \,\mathrm{d}r \end{cases} \tag{9}$$

该积分值即为岩石的脆裂指数（BF_{vp} 和 BF_{vs}，见图 5），反映了纵、横波速度变化及影响区域的大小，是

(C)1994-2022 China Academic Journal Electronic Publishing House. All rights reserved. http://www.cnki.net

速度剖面变化的综合体现。图 5 还给出了由公式（1）和公式（2）计算的岩石脆性指数和可压裂指数曲线。对钻井时造成的岩石破裂，一般认为以剪切型破坏为主，故公式（2）中的 K_c 取为岩石的Ⅱ型断裂韧性 $K_{\mathrm{II C}}$（$K_{\mathrm{II C}}$ 的计算参见文献[5]）。由图 5 可见，纵、横波速度的径向变化剖面存在很好的一致性，两者在变化的强弱及范围上对应得很好。纵、横波脆裂指数曲线（图 5 第 5、第 6 道）之间也有很好的对应性和相关性。

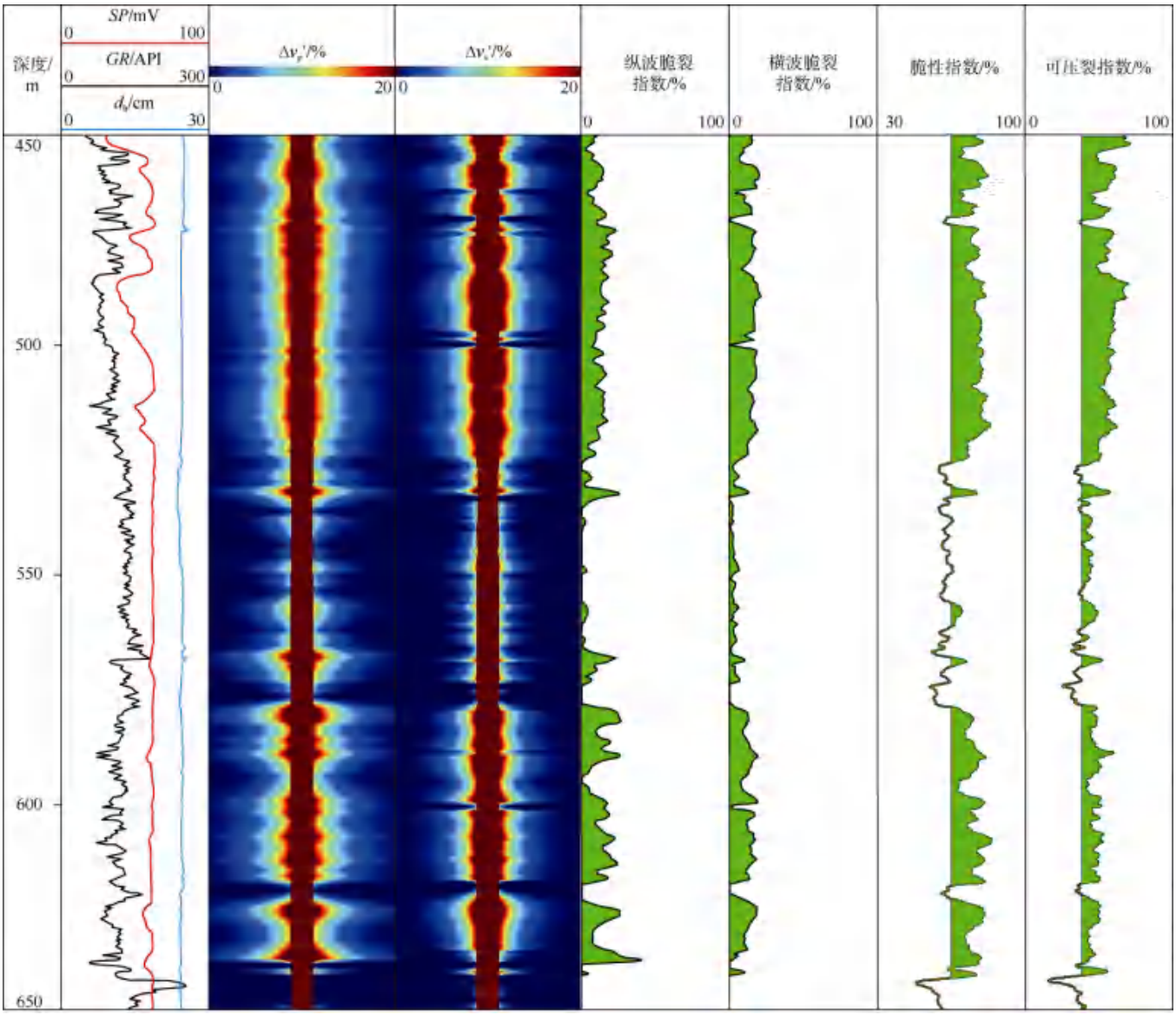


图 5　纵、横波速度变化剖面与岩石脆裂性指数对比（*GR*—自然伽马；*SP*—自然电位；d_h—井径）

纵、横波脆裂指数具相关性说明钻井过程破坏井壁岩石的同时造成了纵波和横波速度的下降。这种现象可以从孔裂隙弹性波理论[17]得到很好的解释。根据该理论，当岩石中产生了微裂隙时，岩石的体积模量和剪切模量同时改变，从而影响纵、横波的速度。因此可以认为，图中纵、横波速的径向变化是钻井过程在井壁上产生的微裂缝所致。

将纵、横波速的径向变化剖面与常规计算的脆性指数曲线（图 5 第 7 道）和可压裂指数（第 8 道）比较，可以看出波速径向变化的大小与脆性指数、可压裂指数的高低有很好的相关性。对于该砂、泥岩地层（见图 5 第 2 道 *GR*、*SP* 曲线），上部（450～525 m）的砂体较下部（580～640 m）多，故上部的脆性指数、可压裂指数总体比下部要高，对应的纵、横波速度变化也是上部比下部大；中部（525～580 m）泥岩段脆性指数、可压裂指数最小，径向剖面变化也很小。这种波速变化与脆性指数、可压裂指数相关的实质是岩石中存在裂缝。

(C)1994-2022 China Academic Journal Electronic Publishing House. All rights reserved.　http://www.cnki.net

为进一步验证上述定义的纵、横波脆裂指数的合理性和有效性，分别将纵、横波脆裂指数与岩石脆性指数、可压裂指数进行相关性分析，由图 6 可以看出，纵、横波脆裂指数与岩石的脆性指数、可压裂指数具有较好的相关性，平均相关系数在 0.76 左右；其中，横波脆裂指数与岩石脆性指数相关性最好，相关系数达 0.90，表明该地层横波脆裂指数对岩石脆性最为敏感；脆裂指数与岩石可压裂指数相关性略差，相关系数约为 0.60～0.70，这也说明公式（2）计算的岩石可压裂指数不够准确，仅作参考。通过对以上数据的相关性对比，说明纵、横波脆裂指数可以同时指示岩石的脆、裂性质。

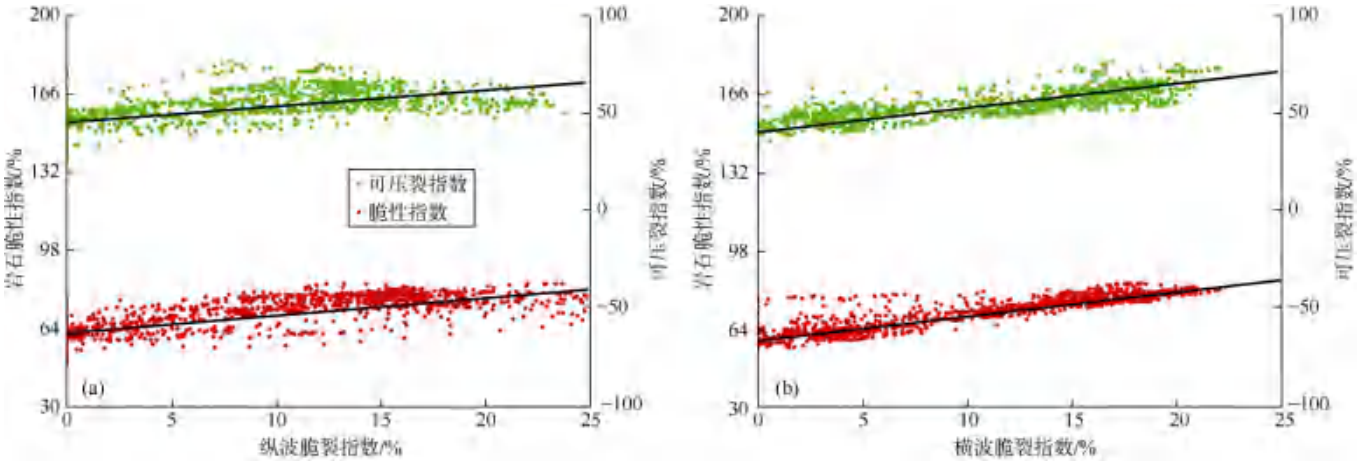


图 6 纵、横波脆裂指数与岩石脆性指数及可压裂指数交会图

为进一步验证本文方法的有效性，以横波脆裂指数为例，针对同一地区 10 口井进行了相关性的统计（见表 1），结果表明该地区横波速度的径向变化与岩石的脆裂性质有较好的相关性，从统计意义上进一步验证了用波速径向变化剖面评估岩石脆裂性质的有效性。

表 1 某一地区岩石横波脆裂指数与岩石脆性指数、可压裂指数的相关性统计

井号	BF_{vs} 与岩石脆性指数相关系数	BF_{vs} 与岩石可压裂指数相关系数
S1	0.79	0.69
S2	0.73	0.75
S3	0.82	0.84
S4	0.85	0.81
S5	0.82	0.78
S6	0.75	0.70
S7	0.64	0.69
S8	0.87	0.66
S9	0.96	0.91
S10	0.61	0.57
平均	0.78	0.74

需要指出的是，本文定义的脆裂指数并不等同于常规方法得到的脆性与可压裂性。如公式（1）的脆性指数，根据声波测井原理，弹性参数法中计算弹性模量和泊松比时所用弹性波速是穿过径向变化区域以外的原状地层速度，与速度变化区无关。公式（1）的脆性指数与岩石基质有关，而公式（9）考虑速度变化计算的脆裂指数与基质破坏产生的裂缝有关，两者并不等同，它们之间的相关性是由于外力作用后基质中产生裂缝引起的。

4 脆裂指数在指导压裂改造中的应用

图 7 为利用脆裂指数指导致密储集层压裂改造的综合应用实例，由图中自然伽马曲线可知该井 947～977 m 段为（致密）砂岩；图中第 3 道为偶极波形变密度图，可以看出声波波形在储集层段的波形质量较好；第 4 道为利用偶极横波反演的径向距离 1 m 范围内的横波速度变化剖面，可以看出，在 947～977 m 井段附近，地层横波速度径向变化特征较明显，变化带横波速度明显小于原状地层横波速度。图 7 中第 5 道是由该剖面积分计算出的横波脆裂指数曲线，该指数可以用来综合评估岩石脆性和可压裂性。

综上所述，947～977 m 储集层段径向横波速度变化较大，岩石更易破碎，同时储集层顶部脆裂指数变化相对底部要小，说明顶部岩石相对底部可压裂性较差且破裂压力偏大。因此，为了将整个储集层压开，应选择在顶部进行压裂施工，这样在压裂顶部的同时也会把脆裂性较好的底部井段压开。第 6 道是压裂后测得的正交偶极快、慢横波波形，两波之间的明显分异说明该井段存在较大的各向异性[15]。第 7 道为压裂

(C)1994-2022 China Academic Journal Electronic Publishing House. All rights reserved. http://www.cnki.net

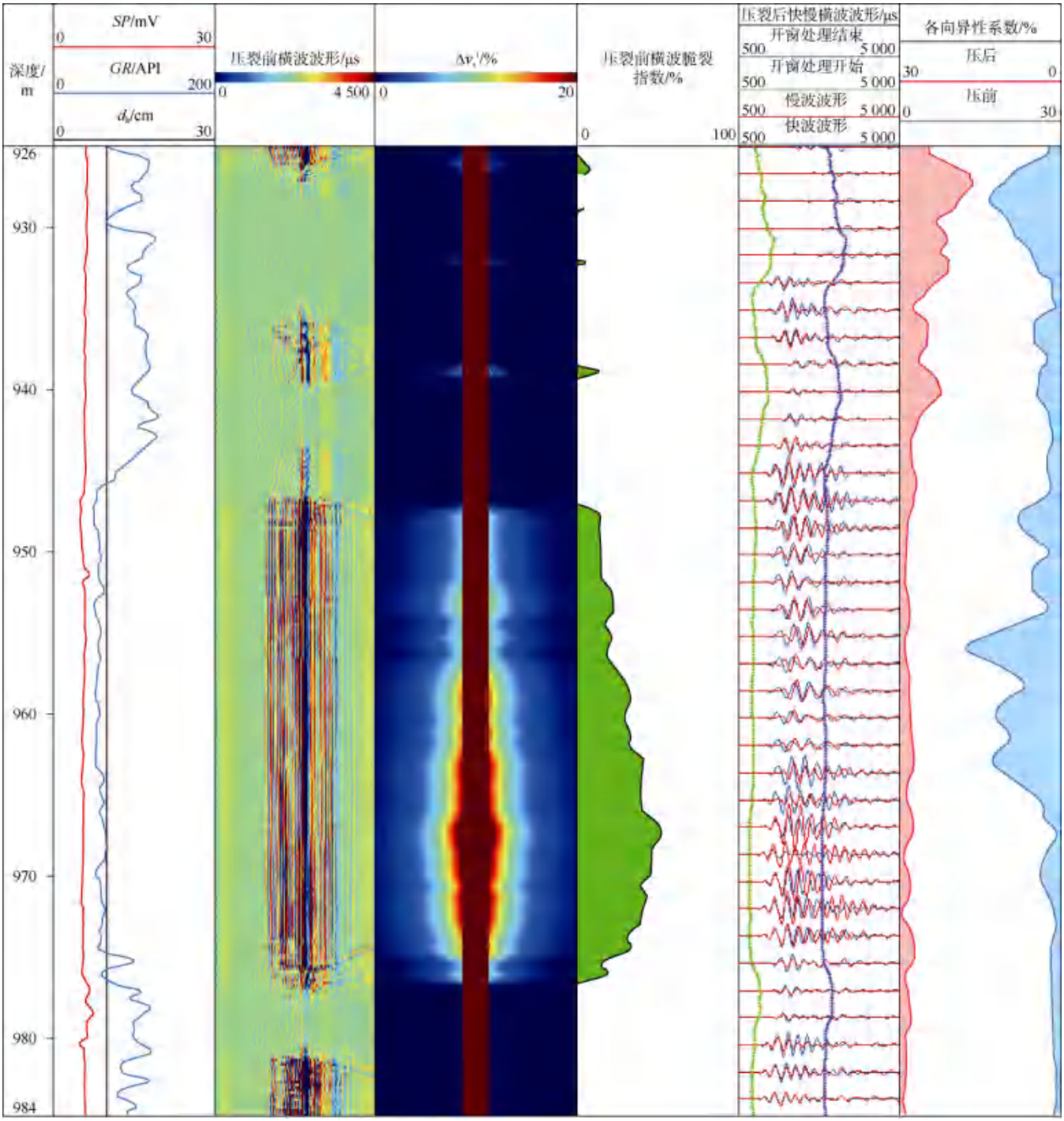


图 7　致密储集层横波速度剖面与多种测井结果对比图

前、压裂后横波各向异性。该储集层上方地层各向异性在压裂前、后无大的变化，但储集层部位压后各向异性较压前明显增大，说明储集层被压开，并且开始产气，压裂效果理想。这一实例说明了本文方法得到的脆裂指数在指导地层压裂改造应用中的有效性。

5 结语

钻井过程会导致井壁岩石扩容，在岩石中产生微裂缝。裂缝数目的多少、影响区域的大小与岩石的脆裂性——脆性和可压裂性密切相关，而裂缝的存在会同时造成纵、横波速的径向变化。通过求取井壁岩石波速的径向变化，可以有效评估地层岩石的脆裂性。这种有效性已为大量数据所证实。本文方法可指导非常规油气储集层压裂改造作业。

符号注释：

BF_{vp}——纵波脆裂指数，无因次；BF_{vs}——横波脆裂指

(C)1994-2022 China Academic Journal Electronic Publishing House. All rights reserved.　http://www.cnki.net

数，无因次；B_r——岩石的脆性指数，无因次；DB——岩石可钻性，无因次；E——地层弹性模量，GPa；E_{OBJ}——约束反演方法目标函数，m^2/s^2；F_r——地层可压裂指数，无因次；K_C——岩石断裂韧性，$MPa \cdot m^{1/2}$；r——径向位置，m；Δr——波速变化区域大小，m；R——井眼半径大小，m；s——声波传播的最短路径，m；t——声波走时，s；TT_f——声波在井筒流体中的传播时间，s；TT_{ref}——参考走时，s；v——地层速度，m/s；Δv——波速变化大小，m/s；$v(z)$——阵列处理提取的地层声速函数，m/s；v_d——阵列弯曲波提取的频散曲线函数，m/s；v_h——井壁地层横波速度计算的均匀地层频散曲线函数，m/s；v_{pi}——原状地层纵波波速，m/s；v_{pw}——钻后实际地层纵波波速，m/s；v_{si}——原状地层横波波速，m/s；v_{sw}——钻后实际地层横波波速，m/s；v_t——径向变化模型理论频散曲线函数，m/s；Δv_P——纵波波速变化，m/s；$\Delta v_P'$——纵波波速变化率，%；$\Delta v_s'$——横波波速变化率，%；Δv_s——横波波速变化，m/s；z——声波波形数据采集的深度，m；z_{r1}——第 1 个接收器深度，m；z_s——声源深度，m；λ——权重因子，无因次；ω——角频率，Hz；ν——地层泊松比，无因次；Ω——测井频段，Hz；Ω'——高频处理频段，Hz；σ_c——岩石单轴抗压强度，MPa；σ_t——岩石单轴抗拉强度，MPa。下标：max——最大值；min——最小值；N——归一化值。

参考文献：

[1] PEREZ A R, MARFURT K. Mineralogy-based brittleness prediction from surface seismic data: Application to the Barnett Shale[J]. Interpretation, 2014, 2(4): T255-T271.

[2] 刘绪纲，孙建孟，郭云峰. 元素俘获谱测井在储层综合评价中的应用[J]. 测井技术, 2005, 29(3): 236-239.
LIU Xugang, SUN Jianmeng, GUO Yunfeng. Application of elemental capture spectroscopy to reservoir evaluation[J]. Well Logging Technology, 2005, 29(3): 236-239.

[3] WU H L, LI N, LAN C L, et al. Standard spectrum measurement and simulation of elemental capture spectroscopy log[J]. Applied Geophysics, 2013, 10(1): 109-116.

[4] RICKMAN R, MULLEN M, PETER E, et al. A practical use of shale petrophysics for stimulation design optimization: All shale plays are not clones of the Barnett Shale[R]. SPE 115258-MS, 2008.

[5] 袁俊亮，邓金根，张定宇，等. 页岩气储层可裂性评价技术[J]. 石油学报, 2013, 34(3): 523-527.
YUAN Junliang, DENG Jin'gen, ZHANG Dingyu, et al. Fracability evaluation of shale-gas reservoirs[J]. Acta Petrolei Sinica, 2013, 34(3): 523-527.

[6] 孙建孟，韩志磊，秦瑞宝，等. 致密气储集层可压裂性测井评价方法[J]. 石油学报, 2015, 36(1): 74-80.
SUN Jianmeng, HAN Zhilei, QIN Ruibao, et al. Log evaluation method of fracturing performance in tight gas reservoir[J]. Acta Petrolei Sinica, 2015, 36(1): 74-80.

[7] 陈颙，黄庭芳，刘恩儒. 岩石物理学[M]. 合肥：中国科技大学出版社, 2004.
CHEN Yong, HUANG Tingfang, LIU Enru. Rock physics[M]. Hefei: China University of Science and Technology Press, 2004.

[8] WINKLER K W. Borehole damage indicator from stress-induced velocity variations[J]. Geophysics, 2005, 70(10): F11-F16.

[9] HORNBY B E. Tomographic reconstruction of near-borehole slowness using refracted borehole sonic arrivals[J]. Geophysics, 1993, 58(12): 1726-1738.

[10] THOMSEN L. Biot-consistent elastic moduli of porous rocks: Low-frequency limit[J]. Geophysics, 1985, 50(12): 2797-2807.

[11] TANG Xiaoming, CHEN Xuelian, XU Xiaokai. A cracked porous medium elastic wave theory and its application to interpreting acoustic data from tight formations[J]. Geophysics, 2012, 77(6): D245-D252.

[12] TANG X M, PATTERSON D J. Mapping formation radial shear-wave velocity variation by a constrained inversion of borehole flexural-wave dispersion data[J]. Geophysics, 2010, 75(6): E183-E190.

[13] SU Y D, TANG X M, ZHUANG C X, et al. Mapping formation shear-velocity variation by inverting logging-while-drilling quadrupole-wave dispersion data[J]. Geophysics, 2013, 78(6): D491-D498.

[14] 徐果明，周蕙兰. 地震学原理[M]. 北京：科学出版社, 1982.
XU Guoming, ZHOU Huilan. Principle of seismology[M]. Beijing: Science Press, 1982.

[15] 唐晓明，郑传汉. 定量测井声学[M]. 北京：石油工业出版社, 2004.
TANG Xiaoming, ZHENG Chuanhan. Quantitative acoustic well logging[M]. Beijing: Petroleum Industry Press, 2004.

[16] 赵龙，唐晓明，苏远大，等. 横波速度径向层析成像方法及应用研究[J]. 应用声学, 2014, 33(1): 9-15.
ZHAO Long, TANG Xiaoming, SU Yuanda, et al. Research on radial shear-wave velocity tomography[J]. Journal of Applied Acoustics, 2014, 33(1): 9-15.

[17] 唐晓明. 含孔隙、裂隙介质弹性波动的统一理论-Biot 理论的推广[J]. 中国科学：地球科学, 2011, 41(6): 784-795.
TANG Xiaoming. A unified theory for elastic wave propagation through porous media containing cracks: An extension of Biot's poroelastic wave theory[J]. SCIENCE CHINA Earth Sciences, 2011, 54(9): 1441-1452.

第一作者简介：唐晓明（1955-），男，四川雅安人，博士，中国石油大学（华东）教授，主要从事地球物理（声波）测井、岩石物理学、地震波传播及测量等方面的研究和技术开发工作。地址：山东省青岛市黄岛区长江西路 66 号，中国石油大学地球科学与技术学院，邮政编码：266580。E-mail: tangxiam@aliyun.com

联系作者：陈雪莲（1976-），女，河北衡水人，博士，中国石油大学（华东）副教授，主要从事声波测井方法及岩石物理学方面的教学和科研工作。地址：山东省青岛市黄岛区长江西路 66 号，中国石油大学地球科学与技术学院，邮政编码：266580。E-mail: chenxl@upc.edu.cn

收稿日期：2015-03-05 **修回日期**：2016-03-29

（编辑 黄昌武）

(C)1994-2022 China Academic Journal Electronic Publishing House. All rights reserved. http://www.cnki.net

GEOPHYSICS, VOL. 85, NO. 1 (JANUARY-FEBRUARY 2020); P. D37–D43, 11 FIGS., 2 TABLES.
10.1190/GEO2019-0028.1

Effect of perforation on borehole acoustic wave logging: Modeling and application

Huan-Ran Li[1], Xi-Hao Gu[1], Cong-Hui Zhang[2], Yuan-Da Su[1], and Xiao-Ming Tang[1]

ABSTRACT

In hydraulic-fracturing design and oil-recovery efficiency prediction, quantitative evaluation of perforation and its penetration depth is often desired, for which an effective method needs to be developed. We have developed a perforated cased-borehole model for the field test configuration and simulated the elastic wave propagation in the model excited by a borehole monopole source using the finite-difference method. After a multivariate regression analysis, the simulation results yield a relationship for the perforation penetration depth versus the induced P-wave traveltime change and formation slowness. For field application purposes, borehole array acoustic logging with a perforated borehole model is simulated. The calculated waveform data, in conjunction with the above-mentioned relationship, yield an accurate estimate of the perforation penetration depth. A field perforation test is used to develop application of our method.

INTRODUCTION

Perforation is a commonly used operation in well completion, which penetrates through a cased borehole and creates tunnels in the formation to facilitate the flow of reservoir fluid into the wellbore. Given the size of the perforation bullet, the penetration depth, that is, the length of the tunnels, directly influences the outcome flow efficiency. On the basis of the perforation operation, hydraulic fracturing can be further applied to enhance production of low-porosity and low-permeability reservoirs (e.g., unconventional shale-gas reservoirs) (Su et al., 2017). Thus, the perforated tunnel length is also an important parameter for hydraulic fracturing design. Therefore, for oil and gas recovery efficiency and hydraulic-fracturing design, evaluating the perforation result in terms of its penetration depth becomes an important task in field operation. However, quantitative evaluation methods have not yet been developed because the effects of perforation on various borehole measurements, for example acoustic logging, are not yet fully understood.

Currently, perforation evaluation mainly depends on non-well-logging methods (Seibi et al., 2008). Early attempts tried to establish the relationship between perforation penetration depth and well measurements, such as acoustic velocity (Li et al., 2010) and ultrasonic resonance attenuation (Qiao and Du, 2000), but follow-up of these efforts has not been reported. A later effort reported by Brooks (2006) provides an empirical formula to calculate the perforation penetration depth using the resonance frequency determined from a frequency sweep measurement. This study investigates a direct evaluation method using acoustic logging through the perforated borehole interval.

The borehole acoustic traveltime tomography technique (Aki and Richards, 1980; Hornby, 1993; Tang and Cheng, 2004; Cerveny, 2005) has been used to map the velocity variation in the formation surrounding the borehole, which has yielded several important applications, such as formation alteration identification, brittleness estimation (Tang et al., 2016), and hydraulic fracturing evaluation (Su et al., 2017). Because perforation actually alters near-well formation, its aftermath effects can also be detected and evaluated by the perforation-induced traveltime changes. However, the sensitivity of the acoustic measurement to the perforation-related changes needs to be evaluated first.

In the following, the acoustic/elastic model for a cased borehole with various perforation tunnels is first constructed. Acoustic propagation in the model is simulated using a 3D finite-difference method in the time domain (3D FDTD) (Cheng et al., 1995) method to investigate the relationship between the induced traveltime change and preformation tunnel parameters. The dependence of the time change on formation slowness will also be analyzed. The perforation model is simplified as a cased-borehole model with cylindrical perforating tunnels. We then simulate acoustic wave propagation

Manuscript received by the Editor 14 January 2019; revised manuscript received 13 July 2019; published ahead of production 28 October 2019; published online 28 November 2019.
[1]China University of Petroleum, School of Geosciences, Qingdao, China. E-mail: kestrel2012@live.com; guxih@sina.com; syuanda@sina.com; tangxiam@aliyun.com.
[2]China Oilfield Services Limited WellTech, Sanhe, China. E-mail: zhangch@cosl.com.cn.
© 2020 Society of Exploration Geophysicists. All rights reserved.

Downloaded from pubs.geoscienceworld.org/seg/geophysics/article-pdf/85/1/D37/4927925/geo-2019-0028.1.pdf by Univ of Petroleum (Beijing) - Library user on 08 October 2026

through this model with different tunnel lengths by a 3D FDTD method to investigate the relation between the preformation-induced traveltime change and the length of the perforation tunnels. Thereafter, acoustic logging along the perforated borehole is simulated, and the data are used for the perforation penetration depth estimation. The result will be used to provide a method for processing and interpreting the data from a field perforation test example.

MODEL CONSTRUCTION AND NUMERICAL MODELING

For the model construction, we first describe the relevant borehole completion and perforation processes. For completing a borehole drilled to the target formation, metal pipes, or casing, are set into the borehole and then bonded to the formation by a layer of cement. The cased borehole is then perforated by shooting a bullet to the target formation. The passage behind the bullet, referred to as perforation tunnel, facilitates the flow of oil and gas from the reservoir into the wellbore, avoiding the complexities caused by drilling and mud filtration around the borehole. The perforation tunnel length is an important factor controlling the perforation efficiency. A cement target test is commonly performed at the surface to test the perforation device (i.e., the perforation gun). For the surface condition, such tests often create meter-long tunnels (see Figure 1). For downhole conditions, however, an American Petroleum Institute (API) test is usually recommended. In such a test, the (rock) sample is loaded with appropriate pore pressure, borehole pressure, and confining pressure. In this case, the perforation tunnel length is much reduced. For example, the same device and same amount of perforation charge that would produce a nominal tunnel length of 1.5 m in the cement target test produced only a 0.3 m long tunnel on a sandstone specimen in the API test (see Figure 2; data are provided by the China Offshore Logging Co.). Therefore, for modeling the field condition, the tunnel length in our model varies between 0 and 0.4 m. For perforation efficiency and fluid flow optimization, these perforation tunnels are arranged in specific patterns, which we adopt in our model construction. An example of one such pattern is shown in Figure 3. In this pattern, the perforation tunnel is modeled as a fluid cylinder, whose radius can be eliminated from the cement target test (Figure 1) or from the API test (Figure 2). The tunnels are aligned along the borehole to form tunnel arrays. These arrays are evenly distributed around the borehole azimuth. We use four parameters, shot density (shots per meter), tunnel radius, penetration depth, and azimuthal angle between tunnel arrays, to describe the perforation model. The default model in this paper uses 40 holes/m of shot density, 0.02 m of tunnel radius, 0.4 m long tunnel length, and 60° of tunnel array separation angle. As shown in Figure 3, there are 80 perforated tunnels in total, covering a length of 2 m along the borehole direction and the distance between the acoustic source and the beginning of the perforation tunnels is 0.5 m.



Figure 1. An example of a cement target test.

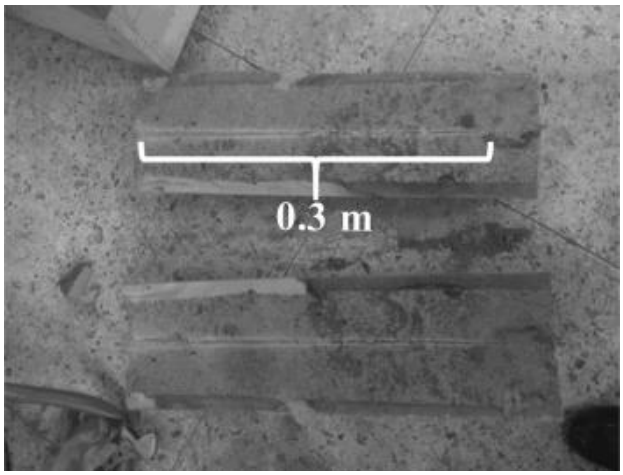


Figure 2. An example of an API test (purple sandstone).

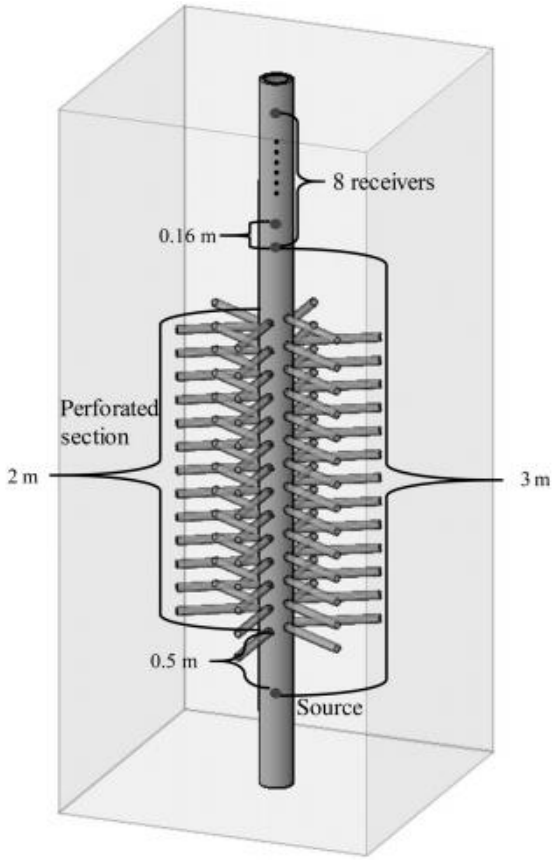


Figure 3. Diagram of the default perforated model.

Downloaded from pubs.geoscienceworld.org/seg/geophysics/article-pdf/85/1/D37/4927925/geo-2019-0028.1.pdf by Univ of Petroleum (Beijing) - Library user on 08 October 2026

NUMERICAL SIMULATION

We give a brief description of the 3D FDTD method used in our numerical simulation. The velocity-stress formulation (Cheng et al., 1995; Liu et al., 1996) is used to represent the elastic wave equation. A staggered finite-difference technique (Cheng, 1994; Cheng et al., 1995) is used to solve the elastic wave equation (see the algorithm implementation described by Wei and Tang, 2012).

A cased borehole model in Table 1 is used to verify the accuracy of the 3D FDTD modeling algorithm. The acoustic wave propagation along the cased borehole with a homogeneous elastic formation is calculated, respectively, using the 3D FDTD method and the real-axis-integration (RAI) method (Tang and Cheng, 2004). An 8 kHz center frequency monopole source is placed at the center of the borehole, and the receiver array spans from 3.0 to 4.12 m along the borehole axis at an increment of 0.16 m. The grid size for the 3D model is $\Delta x = \Delta y = \Delta z = 2$ mm, and the iteration time step is 0.1 μs. Figure 4 compares the simulated waveforms (the solid line) and those from the RAI method (the dashed line). Because the P-wave arrival is the main interest of our study, only the head wave portion of the data is plotted. The two results agree quite well, supporting the validity and accuracy of our 3D FDTD algorithm.

The perforations surrounding the cased borehole reduce the formation acoustic wave velocity and cause the delay of the acoustic wave traveltime. The 3D FDTD difference method is used to model the acoustic wave propagation in conjunction with the perforated casing-formation model. To visualize this wave propagation, wavefield snapshots of the unperforated cased-borehole model and the default perforated borehole model are compared in Figure 5 for two time instants after source actuation. The snapshots at 0.5 ms (Figure 5a and 5b) show the weak P-wavefront followed by the strong S-wavefront. The wavefield entering into the perforated zone (shaded box) begins to show appreciable changes (Figure 5b) compared to its unperforated counterpart (Figure 5a). In the snapshots at 1.0 ms (Figure 5c and 5d), the P- and S-wavefronts have passed through the perforated zone. The wavefield trailing the S-wavefront

Table 1. Default cased-borehole model parameters.

Medium	Parameter			
	V_P (m/s)	V_S (m/s)	Density (kg/m^3)	Outer radius (m)
Wellbore fluid	1500	0	1000	0.07
Casing tube	6098	3354	7500	0.08
Cement	2823	1729	1920	0.1
Formation	4000	2300	2500	∞

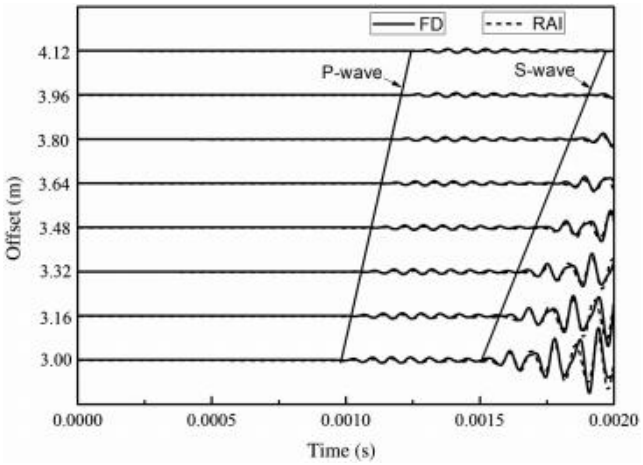


Figure 4. Waveform comparison between FDTD (the solid curve) and the RAI (the dashed curve) for a cased-borehole model.

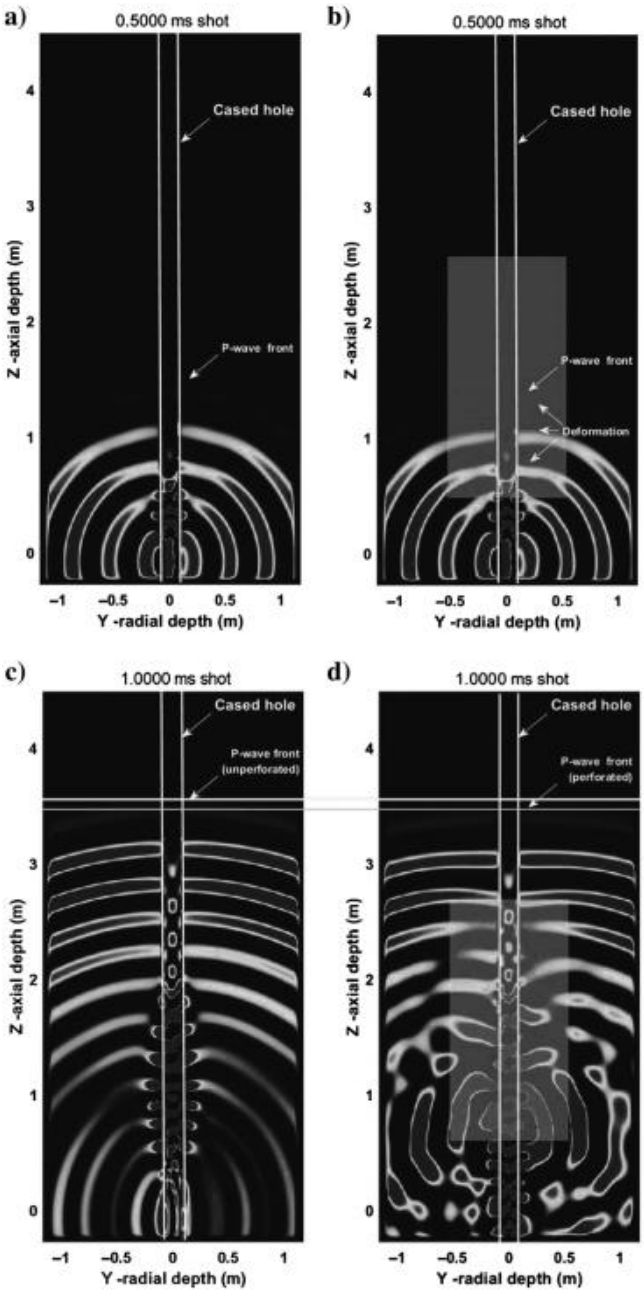


Figure 5. Wavefield snapshots for the (a and c) unperforated and (b and d) perforated models. For the two models, the snapshots are taken at (a and b) 0.5 ms and (c and d) 1.0 ms from the source firing, respectively. Shadow in (b and d) is the perforated zone.

Downloaded from pubs.geoscienceworld.org/seg/geophysics/article-pdf/85/1/D37/4927925/geo-2019-0028.1.pdf by Univ of Petroleum (Beijing) - Library user on 08 October 2026

is severely distorted or scattered by the perforated zone (Figure 5d) compared with its unperforated counterpart (Figure 5c). More importantly, the P-wavefront at the borehole for the perforated model (thin line) is evidently delayed relative to its unperforated counterpart (thick line). Compared with the S-wave information, the P-wave arrival time can be more accurately determined and is more straightforward to use for evaluating the perforation result. Figure 6 shows the simulated array waveforms from the perforated (dashed) and unperforated (solid) models in the P-wave time window of 0.8–1.8 ms. Complementary to the wavefront delay seen in the snapshots, the perforation-induced P-wave delay can now be seen more clearly across the entire array.

We now investigate the effect of penetration depth on the P-wave traveltime for a fixed receiver position (e.g., the first receiver). Starting with the unperforated model, seven different models, with penetration depths of 1, 3, 6, 10, 20, 30, and 40 cm, are successively calculated. A time window is placed on the P-wave arrival data,

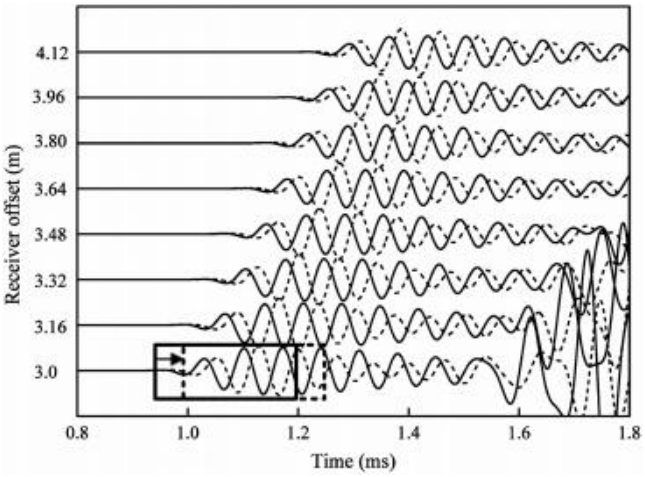


Figure 6. The P-wave delay of the original casedborehole model (the solid line) and the default perforation model (the dashed line) on the array waveforms.

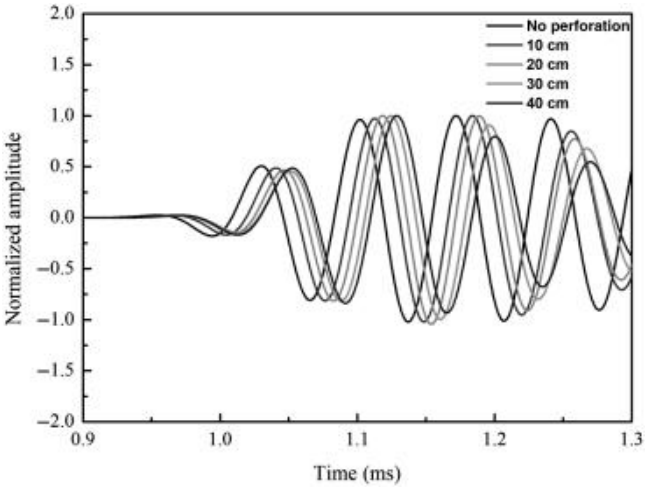


Figure 7. The P-wave portion of the simulated data, showing the successive delay of the wave with the increasing penetration depth values.

containing about four cycles (see Figure 6). The resulting waveforms in the window are displayed in Figure 7 for the 10–40 cm models, showing that the waves are successively delayed with increasing perforation depth. The arrival times of the waves can be easily determined. More conveniently, the arrival time difference, or delay, between the perforated and unperforated models can be obtained by cross-correlating their corresponding waveforms in the window. The determined time delay versus perforation depth is shown in Figure 8. The data trend shows that the time delay is almost linearly proportional to the perforation depth. However, the fitted line has a nonzero delay value when the penetration depth into the formation is zero, which is caused by the perforated casing and cement. In fact, as will be shown below, the delay caused by the perforated casing and cement varies strongly with the slowness of the surrounding formation.

To investigate the effects of formation slowness on the P-wave time delay, the P-wave slowness/velocity values are varied (see Table 2) in the simulation. These values are based on Han et al. (1986) for very hard to moderately soft formation rocks. For the range of slowness values, the 1D display of Figure 8 becomes a 2D display of the calculated time delay versus penetration depth and formation P-wave slowness, as shown in Figure 9a. For each slow-

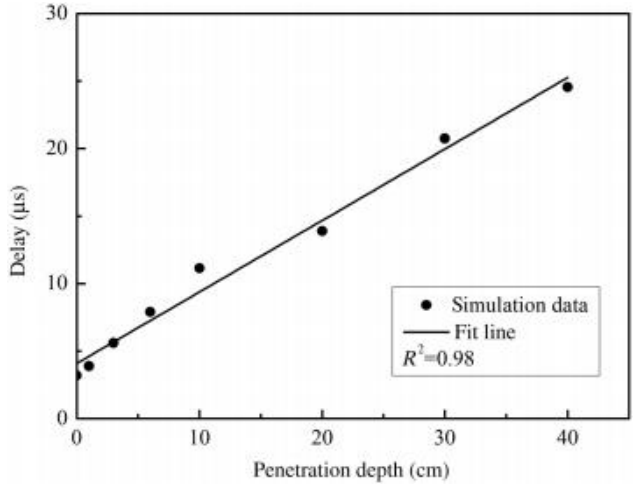


Figure 8. Relation between the P-wave delay and the penetration depth (default model of Table 1).

Table 2. Seven sets of formation parameters for the simulation.

Medium	Parameter		
	V_P (m/s)	V_S (m/s)	Density (kg/m^3)
Formation 1 (default)	4000	2300	2500
Formation 2	3000	1800	2000
Formation 3	3610	2090	2250
Formation 4	4660	2910	2660
Formation 5	5230	3090	2570
Formation 6	5520	3600	2530
Formation 7	6800	3560	2700

Downloaded from pubs.geoscienceworld.org/seg/geophysics/article-pdf/85/1/D37/4927925/geo-2019-0028.1.pdf by Univ of Petroleum (Beijing) - Library user on 08 October 2026

ness value, the time delay is almost linearly proportional to the perforation depth, similar to the trend of Figure 8. However, for each penetration depth, the variation trend with slowness appears more complicated. To reduce the complexity, we analyze the variation trend at the zero penetration length, focusing on the effect of the perforated casing and cement.

Figure 9b shows the time delay of the perforated casing and cement relative to the unperforated situation as a function of formation slowness sl. The zero-length data (markers) fitted by an analytical slowness function (curve),

$$\text{delay}_0 = a(\text{sl} - \text{sl}_0)e^{-b(\text{sl}-\text{sl}_0)} \quad \text{with } a = 0.75;$$
$$b = 0.03\ \text{m}/\mu\text{s}; \quad \text{and} \quad \text{sl}_0 = 147.05\ \mu\text{s}/\text{m}; \tag{1}$$

shows a drastic increase with formation slowness (the delay_0 curve peak [at approximately 9 μs] occurs at approximately 180 μs/m, which is larger than the casing P-wave slowness [163 μs/m]; thereafter, the curve decreases with the increasing formation slowness). This variation trend can be theoretically explained using a layered formation model, for which the perforated casing-cement system is treated as a near-borehole layer whose velocity is slower than that of the intact casing. When the formation is faster than the layer, the energy-trapping effect of the slower layer causes the delay effect. The effect starts to diminish when the formation becomes slower than the layer. This explains why the delay_0 data show a peak at approximately 180 μs/m, which is approximately the overall slowness of the perforated casing/cement layer. After subtracting the effect due to the perforated casing and cement, the data appear better behaved, as shown in Figure 9c, in which a multivariate regression of the data using

$$\text{delay-delay}_0 = c + d \cdot \text{pd} + e \cdot \text{sl} + f \cdot \text{pd} \cdot \text{sl} + g \cdot \text{sl}^2$$
$$\text{with: } c = -18.67\ \mu\text{s}; \quad d = 0.03\ \mu\text{s}/\text{m}; \quad e = 0.165\ \text{m};$$
$$f = 0.0019; \quad g = -3.4 \times 10^{-4}\ \text{m}^2/\mu\text{s} \tag{2}$$

fits the data quite well. The result clearly shows that in the formation beyond casing and cement, the P-wave traveltime delay increases almost linearly with penetration depth and quadratically with formation slowness. Equation 2 can be rewritten as

$$\text{pd} = \frac{\text{delay} - \text{delay}_0 - c - e \cdot \text{sl} - g \cdot \text{sl}^2}{d + f \cdot \text{sl}} \tag{3}$$

from which the perforation penetration depth pd can be directly calculated from the measured arrival time-delay and formation P-wave slowness data.

The above simulation results (equations 1–3) are obtained with a 2 m long perforation zone along the borehole. With a small modification, the results can be applied to a zone of different length. Noe that the time delay is the integration of the perforation-induced change along the perforated borehole and, for the perforation configuration in Figure 3, the change is almost invariant along the borehole. Therefore, the delay value should be proportional to the length of the wave travel path, if the path is within the zone, or to the length of the zone, if the zone is within the travel path. Thus, the delay data measured along a perforation zone of length L can be equated to the data delay^0 for the 2 m length zone using the following scaling relation:

$$\frac{2}{L^0}\text{delay} \rightarrow \text{delay}^0; \quad L^0 = \begin{cases} L & (L < L_{sr}) \\ L_{sr} & (L \geq L_{sr}) \end{cases}; \tag{4}$$

where L_{sr} is the length of the wavepath along borehole. For an array tool, L_{sr} can be taken as the distance from the source to the middle

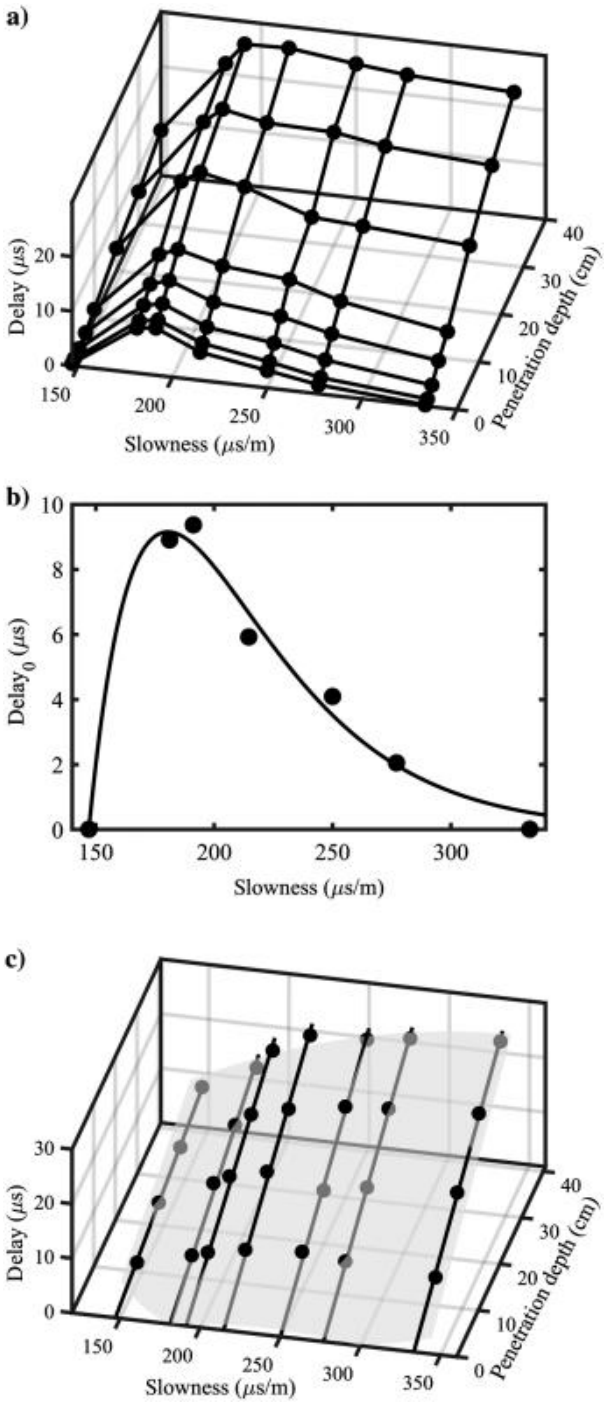


Figure 9. (a) Simulated time delay data versus perforation penetration depth and formation slowness. (b) Simulated time delay data versus formation slowness for the perforated casing and cement only. (c) Multivariate regression of the data after subtracting the zero perforation length data in (b).

Downloaded from pubs.geoscienceworld.org/seg/geophysics/article-pdf/85/1/D37/4927925/geo-2019-0028.1.pdf by Univ of Petroleum (Beijing) - Library user on 08 October 2026

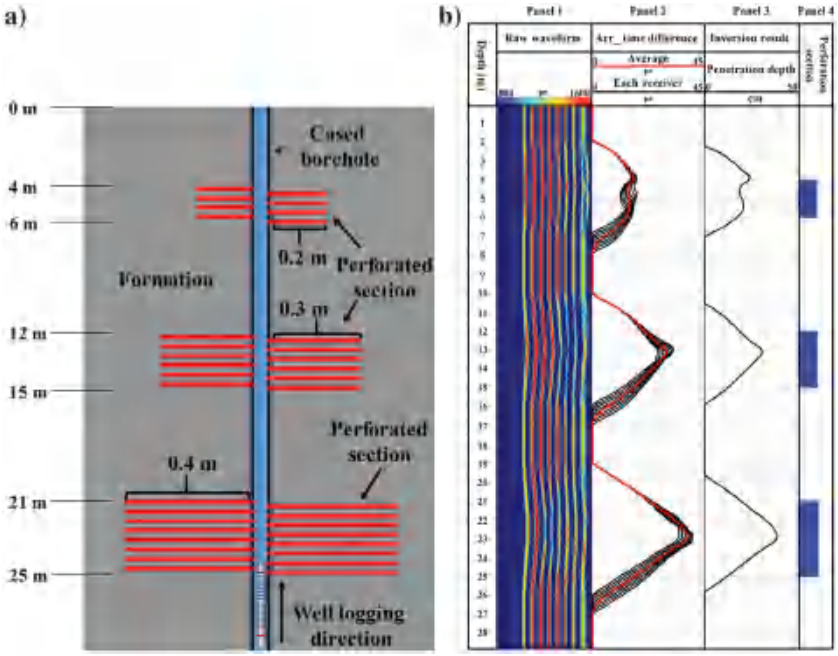


Figure 10. (a) Diagram of the logging model including three perforated zones. (b) P-wave traveltime delay data (panel 1, on receiver 1 of the eight-receiver array) from the model simulation and penetration depth estimation result (panel 3). The P-wave arrival time delay curves (the black curves in panel 2) are calculated for all receivers of the array relative to their unperforated counterpart. The red curve is their average.

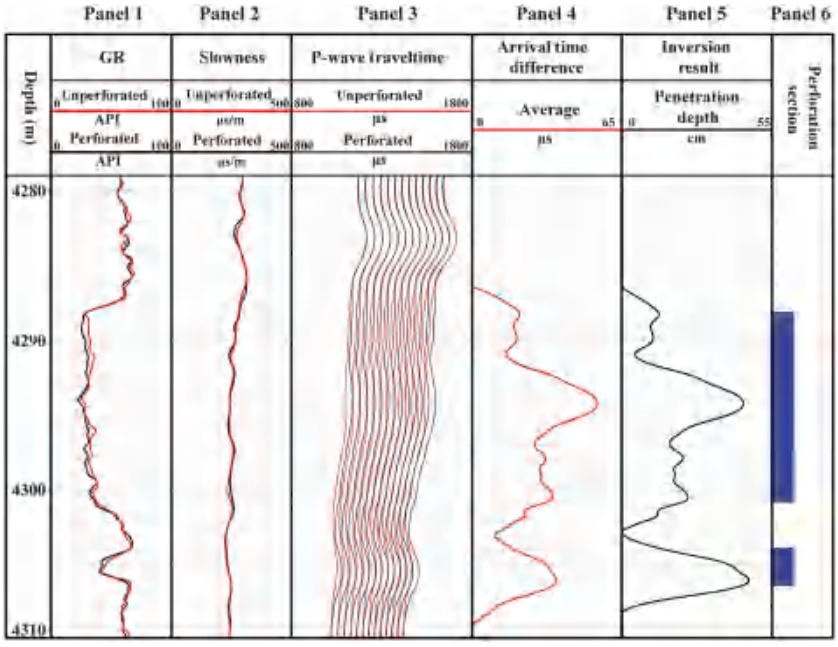


Figure 11. Perforation penetration depth evaluation method applied in a field example. Panels 1 and 2 are the GR and P-wave slowness curves of the formation before (red) and after (black) the perforation, respectively. Panel 3 displays the P-wave traveltime curves picked from all 13 receivers of the array acoustic data before (red) and after (black) the perforation. The average time delay between the perforated and unperforated traveltime data is shown in panel 4. The estimated perforation depth curve is shown in panel 5, which correlates with the designed perforation zones (the shaded rectangles in panel 6).

of the receiver array. Note the delay_0 curve of equation 1, which is obtained for a zone length of 2 m, also needs to be scaled accordingly. With the above modification, the scaled $\text{delay}_0^{\prime}$ and $\text{delay}_0^{\prime\prime}$ data can be used in equation 3 to estimate the penetration depth for the perforation zone of given length L.

We now test the applicability of the above penetration depth estimation scheme by simulating the continuous acoustic logging across perforated zones of different lengths and penetration depths. Figure 10a illustrates the model of a cased borehole and a formation (see the parameters in Table 1) with three perforated zones for the acoustic logging simulation. The tool's source and receiver configuration and source frequency are the same as those used in Figure 3. The tool is pulled from bottom to top at a 0.1 m increment. The upper, middle, and lower perforation zones are located at the intervals of 4–6, 12–15, and 21–25 m of the model, respectively; the perforation depths for each zone are 20, 30, and 40 cm, respectively. The simulated acoustic waveform is displayed in panel 1 of Figure 10b (only data from the first receiver of an eight-receiver array are shown). The traveltime delay on the first arriving P-wave can be clearly identified across the three perforated zones. The difference of the curves relative to their respective counterpart without perforation is the time delay caused by the perforation. The data curves for all eight receivers (panel 2) show a similar anomaly feature around the perforated zone, although the anomaly width for each receiver varies a little due to the source-receiver spacing change within the array. The average of the data is also plotted in panel 2 (the red curve) to represent the overall effect of the perforation on the array acoustic data. This average curve is first scaled using equation 4. The scaled curve, together with the formation P-wave slowness (Table 1), is used in equation 3 to yield the estimated perforation depth curve in panel 3. The three humps on the curve correspond to the three perforation zones. The curve values taken from the center of the zones are 19, 30, and 38 cm, respectively, in good agreement with the model in Figure 9a. Considering the complexity of the model and the simplicity of our approach, the agreement is quite satisfactory.

FIELD DATA APPLICATION

After validating the relationship of the time delay with penetration depth and formation slowness (equations 1–3), we apply it to the field acoustic logging data for a perforated tight sandstone formation along a cased borehole. The perforating scheme used for the operation is illustrated in Figure 3. Figure 11 shows the gamma ray (GR curves

Downloaded from pubs.geoscienceworld.org/seg/geophysics/article-pdf/85/1/D37/4927925/geo-2019-0028.1.pdf by Univ of Petroleum (Beijing) - Library user on 08 October 2026

in panel 1) and P-wave slowness (panel 2) of the formation before (red) and after (black) the perforation. The slowness, as obtained from a long spacing array acoustic tool, shows few changes before and after perforation, whereas the GR logs, which have a shallow depth of investigation, show appreciable changes in the sandstone interval (zones with low GR values). The different behaviors on the two types of data suggest that the perforation-induced formation changes mainly occur in the near-borehole region. The P-wave traveltime curves (panel 3) picked from all 13 receivers of the array acoustic data before (red) and after (black) perforation highlight changes in the perforated section (shaded depths in panel 6). The average time difference, or delay, between the perforated and unperforated traveltime data, is plotted in panel 4, in the same manner as shown in Figure 10b. This curve, together with the formation P-wave slowness (panel 2), is used in equations 1–4 to yield the estimated perforation penetration depth curve in panel 5. The penetration depth curve correlates well with the perforation zones (4289–4302 and 4305–4307 m), as marked in panel 6. The penetration depth varies in the zones, approximately 12 cm at 4290 m, 23 cm at 4298 m, 44 cm at 4293 m, and reaches the highest value of 48 cm at 4306 m. Thus, this field data example demonstrates a simple and effective application of the above simulation result.

CONCLUSION

A quantitative acoustic method for evaluating the result of downhole perforation operation has been developed, using the relationship between the perforation penetration depth and the perforation-induced acoustic traveltime delay for a designated configuration. By simulating acoustic wave propagation through a borehole and formation model with the perforation configuration, such a relationship can be quantified. The simulation result shows that, for a commonly used long spacing acoustic tool with an 8 kHz operation frequency, the perforation-induced P-wave traveltime delay is almost linearly related to the penetration depth. The dependence of the time delay on the formation slowness can be divided into two parts. The first is the slowness dependence of the delay caused by perforated casing and cement; the second is the dependence of the delay on the slowness of the formation: The slower the formation, the longer the time delay. A relationship based on a multivariate regression technique satisfactorily fits the simulated time delay data versus the penetration depth and formation P-wave slowness parameters. The relationship has been validated using simulated acoustic logging data across perforated formation intervals. As shown in the field application example, this relationship can be effectively applied to estimate the perforation penetration depth using the traveltime and slowness data from acoustic logging measurements.

ACKNOWLEDGMENTS

The authors thank the anonymous reviewers for their comments and suggestions that helped improve the manuscript. The authors also thank the China Offshore Logging Co. for providing the field data. This work is supported by the Fundamental Research Funds for the Central Universities (YCX2019001)and by Shandong Provincial Natural Science Foundation (ZR2019BD039).

DATA AND MATERIALS AVAILABILITY

Data associated with this research are confidential and cannot be released.

REFERENCES

Aki, K., and P. Richards, 1980, Quantitative seismology: Theory and methods: W. H. Freeman and Co.
Brooks, J., 2006, Tool for measuring perforation tunnel depth: U.S. Patent Application 11/160, 998.
Cerveny, V., 2005, Seismic ray theory: Cambridge University Press.
Cheng, N., 1994, Borehole wave propagation in isotropic and anisotropic media: Three-dimensional finite difference approach: Ph.D. dissertation, Massachusetts Institute of Technology.
Cheng, N., C. H. Cheng, and M. N. Toksöz, 1995, Borehole wave propagation in three dimensions: Journal of the Acoustical Society of America, 97, 3483–3493, doi: 10.1121/1.412996.
Han, D. H., A. Nur, and D. Morgan, 1986, Effects of porosity and clay content on wave velocities in sandstones: Geophysics, 51, 2093–2107, doi: 10.1190/1.1442062.
Hornby, B. E., 1993, Tomographic reconstruction of near-borehole slowness using refracted borehole sonic arrivals: Geophysics, 58, 1726–1738, doi: 10.1190/1.1443387.
Li, J., S. Bi, G. Liu, and D. Li, 2010, Study on the formation penetration test of shaped charges: Well Logging Technology, 34, 613–617, doi: 10.3969/j.issn.1004-1338.2010.06.023.
Liu, Q. H., E. Schoen, F. Daube, C. Randall, H. L. Liu, and P. Lee, 1996, A three-dimensional finite difference simulation of sonic logging: Journal of the Acoustical Society of America, 100, 72–79, doi: 10.1121/1.415869.
Qiao, W. X., and G. S. Du 2000, FEM simulation of ultrasonic pulse scattered by fluid-filled perforation: Well Logging Technology, 25, 96–100, doi: 10.3969/j.issn.1004-1338.2001.02.003.
Seibi, A. C., F. H. Boukadi, S. Salmi, and A. Bemani, 2008, Mathematical model for estimating perforation penetration depth: Petroleum Science and Technology, 26, 1786–1795, doi: 10.1080/10916460701677690.
Su, Y. D., Z. Li, S. Xu, C. X. Zhuang, and X. M. Tang, 2017, Elastic-wave evaluation of downhole hydraulic fracturing: Modeling and field applications: Geophysics, 83, no. 1, D1–D8, doi: 10.1190/geo2017-0054.1.
Tang, X. M., and C. H. Cheng, 2004, Quantitative borehole acoustic methods: Elsevier Science Publishing Inc.
Tang, X. M., S. Xu, C. X. Zhuang, Y. D. Su, and X. L. Chen, 2016, Assessing rock brittleness and fracability from radial variation of elastic wave velocities from borehole acoustic logging: Rock brittleness and fracability: Geophysical Prospecting, 64, 958–966, doi: 10.1111/1365-2478.12377.
Wei, Z. T., and X. M. Tang, 2012, Numerical simulation of radiation, reflection, and reception of elastic waves from a borehole dipole source: Geophysics, 77, no. 6, D253–D261, doi: 10.1190/geo2012-0061.1.

Downloaded from pubs.geoscienceworld.org/seg/geophysics/article-pdf/85/1/D37/4927925/geo-2019-0028.1.pdf by Univ of Petroleum (Beijing) - Library user on 08 October 2026

Azimuthal shear-wave anisotropy measurement in a borehole: Physical modeling and dipole acoustic verification

Chunxi Zhuang, Song Xu,[a] Huanran Li, Yuanda Su, and Xiaoming Tang
School of Geosciences, China University of Petroleum (East China), Qingdao, China
zhuangchx_upc@upc.edu.cn, xusongupc@sina.com, kestrel2012@live.com, syuanda@sina.com, tangxiam@aliyun.com

Abstract: An anisotropic physical model is constructed to evaluate the anisotropy measurement. The model consists of a series of equally spaced thin limestone slab sheets cemented with concrete, resulting in a transversely isotropic medium. For the anisotropy measurement evaluation, the borehole model is tested by a standard multipole acoustic tool. The measurement finds an S-wave anisotropy magnitude about 20% and determines the fast S-wave polarization along the alignment direction of the slab sheets. The results of the work not only validate the borehole measurement technology, but also provide a testing facility for calibrating the measurement acoustic tool.

© 2019 Acoustical Society of America
[CCC]
Date Received: May 23, 2019 Date Accepted: July 18, 2019

1. Introduction

Seismic azimuthal anisotropy is an important property for shallow crustal rocks. The anisotropy is often associated with the alignment of fractures, geological beddings, and unbalanced tectonic stresses (Esmersoy et al., 1995; Tang and Cheng, 2004). A rock with this anisotropy is characterized as a TI (transversely isotropic) medium with five independent elastic constants (C_{11}, C_{12}, C_{22}, C_{44}, C_{55}). The TI medium has a symmetry axis such that the compressional (P) and shear (S) wave velocities along and normal to this axis are $\sqrt{C_{11}/q}$ and $\sqrt{C_{22}/q}$ (q is medium density), and $\sqrt{C_{55}/q}$ and $\sqrt{C_{44}/q}$, respectively (Mavko et al., 2009). For a vertical borehole penetrating the TI medium, the medium is called the VTI medium if its symmetry is along the borehole, and the HTI if its symmetry axis is in the horizontal plane normal to the borehole.

For measuring the earth formation rock anisotropy in a borehole, a four-component (4C) cross-dipole acoustic tool is commonly used (Alford, 1986). With two orthogonal dipole source-receiver systems X and Y, this tool acquires a 4C data set (xx, xy, yx, yy), where the first (second) letter refers to the dipole source (receiver) orientation. From the 4C data, the formation HTI anisotropy magnitude and its symmetry axis orientation can both be determined (e.g., Alford, 1986; Tang and Chunduru, 1999).

Although the measurement methodology has been theoretically validated and the technology has been widely used for decades (e.g., Tang and Cheng, 2004; Miller et al., 2012; Su et al., 2017; Oshima et al., 2018; Xu et al., 2018), an experimental evaluation of the measurement results under controlled laboratory conditions has not been reported. Such an evaluation is also missing in the tool engineering and manufacturing process. As a result, many manufacturing-related problems are reported from field applications, which are found to be frequently associated with misalignment, miswiring, or unbalance of the X dipole and Y dipole source and receiver systems. To minimize these problems in the manufacturing process, it is desired to build an experiment facility with an HTI physical borehole model for the tool testing and calibration. The main objective of this paper is to demonstrate that such a physical model can be effectively and efficiently constructed and used for the evaluation and testing application.

2. HTI model construction

Because the HTI, or azimuthal anisotropy, is often associated with the alignment of geological structures in field conditions, we built our model using a series of aligned

[a]Author to whom correspondence should be addressed.

08 October 2026 09:02:51

thin limestone slab sheets. These slab sheets are equally spaced and cemented with a class G cement to build a 5 m height and 3.5 m diameter cylinder block with a borehole of 11 cm diameter in the center [see Fig. 1(a)]. The acoustic properties and thicknesses of the limestone and cement materials are listed in Table 1.

For comparison purposes, an isotropic model of the same dimensions was also built using the cement material. The anisotropic block is placed on top of the isotropic block to construct a test borehole model of 10 m height [see Fig. 1(a)]. For measuring the acoustic properties of the model [see Fig. 1(b)], eight small boreholes of 4 cm diameter were drilled close to the outside of the model. From the center of the main borehole, the radial distance to each borehole is 1.5 m and the azimuthal angle between two small holes is 45°.

From the given model parameters, the anisotropic elastic property of the model can be theoretically calculated. Since we will measure the anisotropy along and perpendicular to the slab alignment direction, the Reuse and Voigt average methods (Reuss, 1929; Mavko et al., 2009) can be used to compute the effective elastic properties for the two directions. The appropriateness of the methods will later be tested by comparing their calculated theoretical result with the measurement data from the physical model. Using the averaging methods, the Young's and shear moduli along and perpendicular to the slab alignment direction are calculated, respectively, as

$$\begin{aligned} E_{\parallel} &= a_1 E_1 + a_2 E_2, \\ l_{\parallel} &= a_1 l_1 + a_2 l_2, \end{aligned} \tag{1}$$

and

$$\begin{aligned} \frac{1}{E_{\perp}} &= \frac{a_1}{E_1} + \frac{a_2}{E_2}, \\ \frac{1}{l_{\perp}} &= \frac{a_1}{l_1} + \frac{a_2}{l_2}, \end{aligned} \tag{2}$$

where $a_1 = d_1/(d_1 + d_2)$ and $a_2 = d_2/(d_1 + d_2)$ are the volume fraction of the limestone (denoted by subscript 1) and cement (denoted by subscript 2), respectively. From a_1 and a_2, the average density q of the model can be calculated,

$$q = a_1 q_1 + a_2 q_2. \tag{3}$$

The Young's and shear moduli of the limestone and cement materials are calculated from the measured acoustic parameters in Table 1 using

$$\begin{aligned} E_1 &= \frac{q_1 v_{s1}^2 (3v_{p1}^2 - 4v_{s1}^2)}{v_{p1}^2 - v_{s1}^2}, \\ E_2 &= \frac{q_2 v_{s2}^2 (3v_{p2}^2 - 4v_{s2}^2)}{v_{p2}^2 - v_{s2}^2}, \\ l_1 &= q_1 v_{s1}^2, \\ l_2 &= q_2 v_{s2}^2. \end{aligned} \tag{4}$$

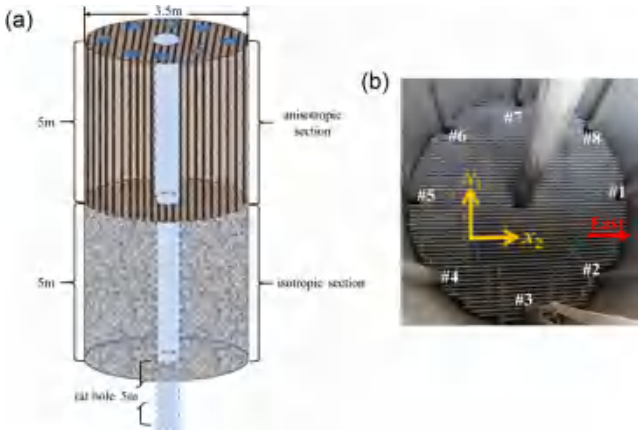


Fig. 1. (Color online) (a) Test borehole model. The upper anisotropic part consists of regularly cemented limestone slab sheets and the lower isotropic part is mode of concrete. The rat hole below the model is for acoustic tool logging from below the model. (b) Picture showing the model construction.

08 October 2026 09:02:51

Table 1. Physical parameters of the model materials.

	V_p (m/s)	V_s (m/s)	Density/(kg/m^3)	Thickness (cm)
Limestone	6524	3473	2705	2
Cement	3483	1901	2185	3

With Young's and shear moduli of Eqs. (1) and (2) along and perpendicular to the axis of symmetry, four of the five elastic constants can be determined (Mavko et al., 2009, Table 2.1.1),

$$\begin{aligned} C_{11} &= l_{\perp}\frac{4l_{\perp}-E_{\perp}}{3l_{\perp}-E_{\perp}}, \\ C_{22} &= l_{\parallel}\frac{4l_{\parallel}-E_{\parallel}}{3l_{\parallel}-E_{\parallel}}, \\ C_{44} &= l_{\parallel}, \\ C_{55} &= l_{\perp}. \end{aligned} \tag{5}$$

The remaining C_{12} can be calculated using the ANNIE approximation (Shoenberg, 1996) as

$$C_{12} = C_{11} - 2C_{55}. \tag{6}$$

With the known elastic constants, the P- and S-wave anisotropy value can be defined as

$$\begin{aligned} \mathrm{Ani}^{P} &= \frac{C_{22}-C_{11}}{2C_{11}}, \\ \mathrm{Ani}^{S} &= \frac{C_{44}-C_{55}}{2C_{55}}. \end{aligned} \tag{7}$$

3. Experiment testing

The physical model of Fig. 1 was acoustically tested in the acoustic logging frequency range of 20 kHz. A monopole acoustic logging tool is placed in the main borehole at the center of the model to generate wave propagation away from the borehole. The waves are measured at each small borehole near the rim of the model using a hydrophone transducer. The measured waveform data from the lower (cement) and upper (limestone and cement composite) parts of the model are shown in Figs. 2(a) and 2(b), respectively.

The first arrival of the wave data in Fig. 2(a) is the P-wave through the cement model. The arrival time for the azimuthally distributed boreholes is approximately constant except for borehole #6, where the wave is appreciably delayed, which may have been caused by inhomogeneous curing of the cement in the model construction. Despite this data outlier, the cement model can be regarded as approximately isotropic and homogeneous.

Compared to Fig. 2(a), the wave data of Fig. 2(b) for the anisotropic model show substantial azimuthal variations, the wave arrival perpendicular to the slab alignment direction (waveforms 3 and 7) is substantially delayed compared to the arrival along the alignment direction (waveform 1), indicating the effect of azimuthal anisotropy (HTI). Figures 2(c) and 2(d) show the correlation processing results of the isotropic and anisotropic models in Fig. 1(a), respectively. The P- and S-wave data at two adjacent boreholes are windowed. The windowed data are cross-correlated to find the arrival time difference between the boreholes from the peak of the correlogram for the respective P- and S-waves, giving the respective P- and S-wave arrival times as shown in Figs. 2(a) and 2(b).

From the data of Figs. 2(c) and 2(d), the P- and S-wave velocities are calculated for each azimuthal direction. For comparison, the theoretical counterparts of the velocities from the TI model are also calculated using the anisotropic elastic constant determined from Eqs. (1)–(6). The results are plotted in Fig. 2(c) (cement) and 2(d) (limestone and cement composite).

Figure 2(e) shows that the cement model velocity is almost invariant with azimuth, except at hole 6. The cause of this data outlier was discussed before. In comparison, the elliptically shaped azimuthal variation of the theoretical curve shown in

08 October 2026 09:02:51

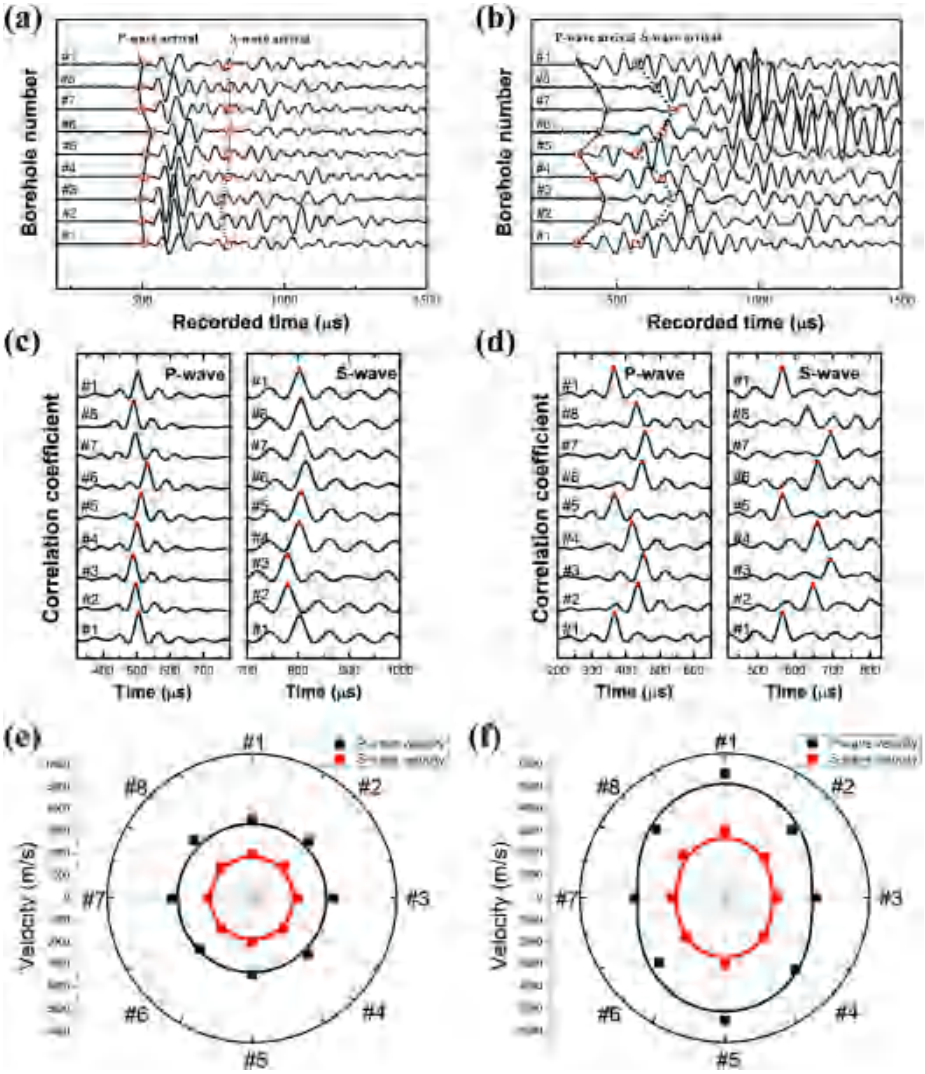


Fig. 2. (Color online) Acoustic waveforms measured at the eight small holes around the model for the isotropic (a) and anisotropic (b) part of the model. (c) and (d) show the P- and S-wave correlation processing results of the isotropic and anisotropic models. The measured P-wave and S-wave velocities (markers) as a function of azimuth are compared with the theoretical modeling result (curves) for the isotropic (e) and anisotropic (f) cases.

Fig. 2(f) exhibits a typical HTI characteristic. The theoretical velocity as a function of azimuth angle is calculated by solving Christoffel equation (Musgrave, 1970) for the TI parameters from Eqs. (1)–(6). The theoretically calculated P-wave and S-wave anisotropy values are 27% and 22%, respectively, which agree with their respective experimental counterpart of 32% and 25%. In addition, the theoretical and experimental values at the 45° azimuth angle (holes 2, 4, 6, and 8) also agree with each other. The comparison in Fig. 2 shows that the model in Fig. 1 and its theoretical description [Eqs. (1)–(6)] provide an effective anisotropic medium that can be adequately used to test the performance of the cross-dipole anisotropy measurement tool.

The model of Fig. 1, after filling with water, was logged with a 4C cross dipole acoustic tool. The source excitation center frequency is 2 kHz. The receiver array on the tool spans from 3.4 m to 4.2668 m, with a 0.1524-m spacing [Fig. 3(a)]. The logging was done from bottom to top at a 0.1524 m increment. Rotating the 4C data with the azimuth gives slow (fast) shear wave that polarizes along (perpendicular to) the TI-axis of symmetry (Tang and Cheng, 2004).

The upper and lower figures of Fig. 3(b) show the typical fast (red) and slow (black) waves across the receiver array for the cement (lower) and limestone and cement composite (upper) part of the model, respectively. Because of the isotropy of the cement model, the fast and slow waves are almost identical to each other (especially the first arrival portion), showing no splitting between the waves. However, there is substantial shear-wave splitting for the anisotropic model data. Using a time-domain anisotropy processing method (Tang and Chundura, 1999), the fast and slow shear

08 October 2026 09:02:51

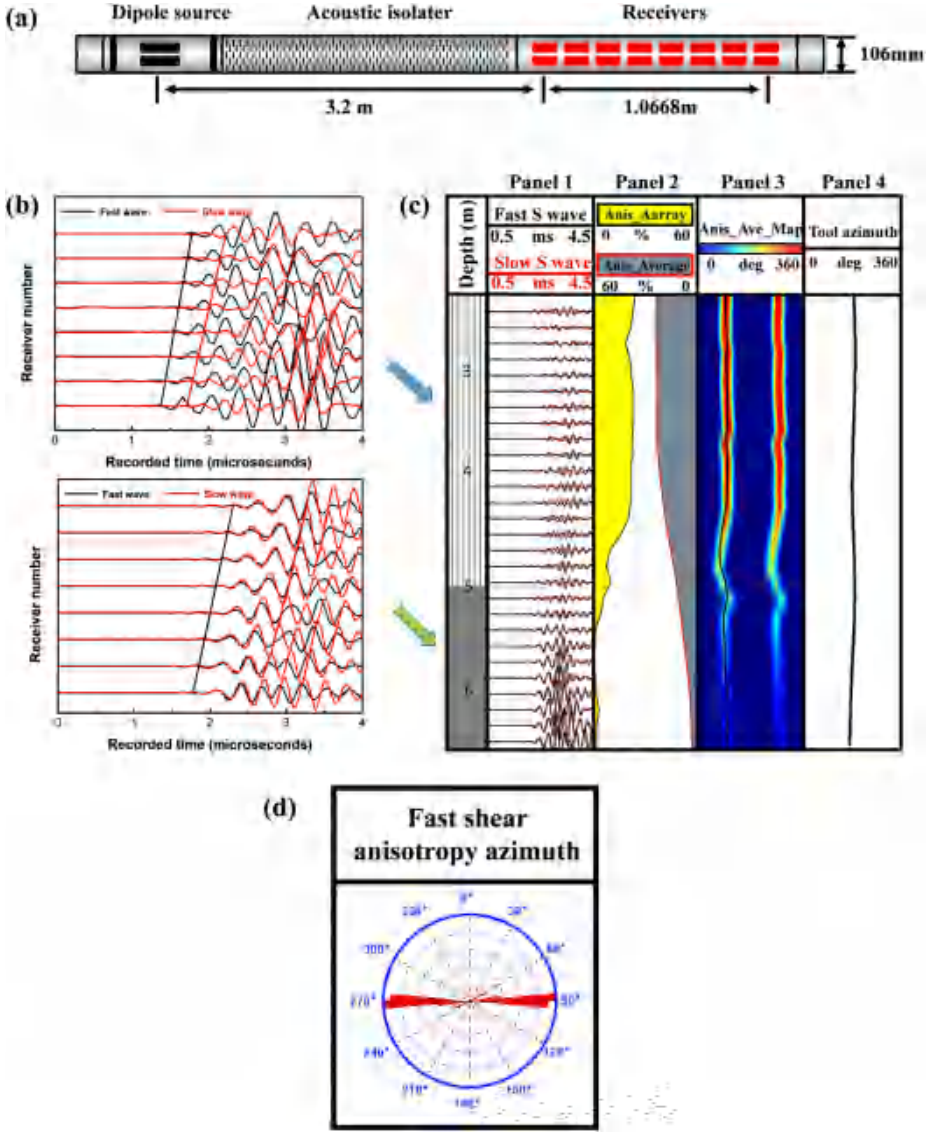


Fig. 3. (Color online) (a) Configuration of the tool used for the anisotropy measurement. (b) Typical fast (red) and slow (black) array waveform data for the isotropic (lower figure) and anisotropic (upper figure) part of the model. (c) Fast and slow shear waves (panel 1), shear-wave anisotropy (panel 2), tool azimuth (panel 4) and anisotropy image display (panel 3), whose average fast shear azimuth is summarized by the rose diagram in (d), for a 5 m section of the model. The arrows indicate where the array data in (a) are taken from.

velocity values from the anisotropy data analysis are 2577 and 2066 m/s, respectively, as indicated by moveout slope of the black (fast wave) and red (slow wave) lines, respectively. The anisotropy determined from the dipole acoustic measurement is 21.5%, in agreement with the S-wave anisotropy measurement results of Figs. 2(b) and 2(f).

Figure 3(c) shows the waveform data (panel 1) and anisotropy results (panels 2 and 3) for a 5 m section of the model (3 m in the upper anisotropic part and 2 m in the lower isotropic part; data near the upper and lower ends of the model are omitted due to boundary reflection contamination). The waveforms in panel 1 are the fast (red) and slow (black) waves of the first receiver for the entire 5 m section, showing again the merge of the waves in the isotropic (cement) section and the wave splitting in the upper anisotropic section. Panel 2 shows the anisotropy values of this interval for two resolutions (Tang and Chunduru, 1999). One is the anisotropy across the receiver array (left-to-right). The other is the average anisotropy from source to receiver (right-to-left). The very small anisotropy in the lower section is attributed to model inhomogeneity and model end reflection. The large anisotropy (~22%) in the upper section corresponds to the anisotropy of the composite model. Panel 3 is a variable density image display of anisotropy combining its magnitude and azimuth (Tang and Cheng, 2004). The tool azimuth curve in panel 4 shows that the tool was barely spinning during data

08 October 2026 09:02:51

acquisition. As expected, the anisotropy azimuth (fast shear wave polarization direction), as shown by a rose diagram [see Fig. 3(d)] coincides with the EW alignment of the slab sheets [see Fig. 1(b)] very well. The performance of the cross dipole anisotropy measurement tool is thus verified.

4. Conclusion

An effective medium borehole model was constructed to test the performance of the borehole cross-dipole shear-wave anisotropy measurement tool. The model consists of aligned and regularly cemented slab sheets to generate substantial anisotropy between the directions along and normal to the alignment. The anisotropy can be theoretically calculated using the Reuse and Voigt average methods and the results compare with those of the experiment measurement. More importantly, the anisotropic medium, when used to construct a borehole model, provides an effective test of the cross-dipole acoustic logging tool before releasing the tool to field applications.

Acknowledgments

The authors thank the associate editor and reviewers for their comments and suggestions that helped to improve the manuscript. This work was supported by the China Natural Science Foundation (Grant Nos. 41604109 and 41774138), and China Academy of Sciences Strategic Leading Science and Technology Project (Grant Nos. XDA14020304 and XDA14020302). The authors thank Dr. Yukai Liu, Dr. Can Jiang, Shangjing Guo, and Xilong Yang for their efforts to this work.

References and links

Alford, R. M. (1986). "Shear data in the presence of azimuthal anisotropy: Dilley, Texas," in 1986 SEG Annual Meeting, Society of Exploration Geophysicists (November).

Esmersoy, C., Kane, M., Boyd, A., and Denoo, S. (1995). "Fracture and stress evaluation using dipole-shear anisotropy logs," in SPWLA 36th Annual Logging Symposium, Society of Petrophysicists and Well-Log Analysts (January).

Mavko, G., Mukerji, T., and Dvorkin, J. (2009). The Rock Physics Handbook: Tools for Seismic Analysis of Porous Media (Cambridge University Press, Cambridge).

Miller, D. E., Horne, S. A., and Walsh, J. (2012). "Precise inversion of logged slownesses for elastic parameters in a gas shale formation," Geophysics 77(4), B197–B206.

Musgrave, M. J. (1970). Crystal Acoustics: Introduction to the Study of Elastic Waves and Vibrations in Crystals (Holden-Day, San Francisco).

Oshima, A., Syresin, D., Blyth, M., and Schmitt, D. P. (2018). "Advanced dipole shear measurements with a new logging while drilling sonic tool," in SPWLA 59th Annual Logging Symposium, Society of Petrophysicists and Well-Log Analysts (June).

Reuss, A. (1929). "Berechnung der fließgrenze von mischkristallen auf grund der plastizitätsbedingung für einkristalle" ("Calculation of the flow limit of mixed crystals on the basis of plasticity condition for single crystals"), Z. Ang. Math. Mech. 9, 49–58.

Schoenberg, M. (1996). "Introducing ANNIE: A simple three parameter anisotropic velocity model for shales," J. Seism. Explor. 5, 35–49.

Su, Y. D., Li, Z., Xu, S., Zhuang, C. X., and Tang, X. M. (2017). "Elastic wave evaluation of downhole hydraulic fracturing: Modeling and field applications," Geophysics 83(1), D1–D8.

Tang, X. M., and Cheng, C. H. A. (2004). Quantitative Borehole Acoustic Methods (Elsevier Science Publishing, Amsterdam, the Netherlands).

Tang, X. M., and Chunduru, R. K. (1999). "Simultaneous inversion of formation shear-wave anisotropy parameters from cross-dipole acoustic-array waveform data," Geophysics 64(5), 1502–1511.

Xu, S., Tang, X. M., Torres-Verdín, C., and Su, Y. D. (2018). "Seismic shear wave anisotropy in cracked rocks and an application to hydraulic fracturing," Geophys. Res. Lett. 45(11), 5390–5397, https://doi.org/10.1029/2018GL077931.

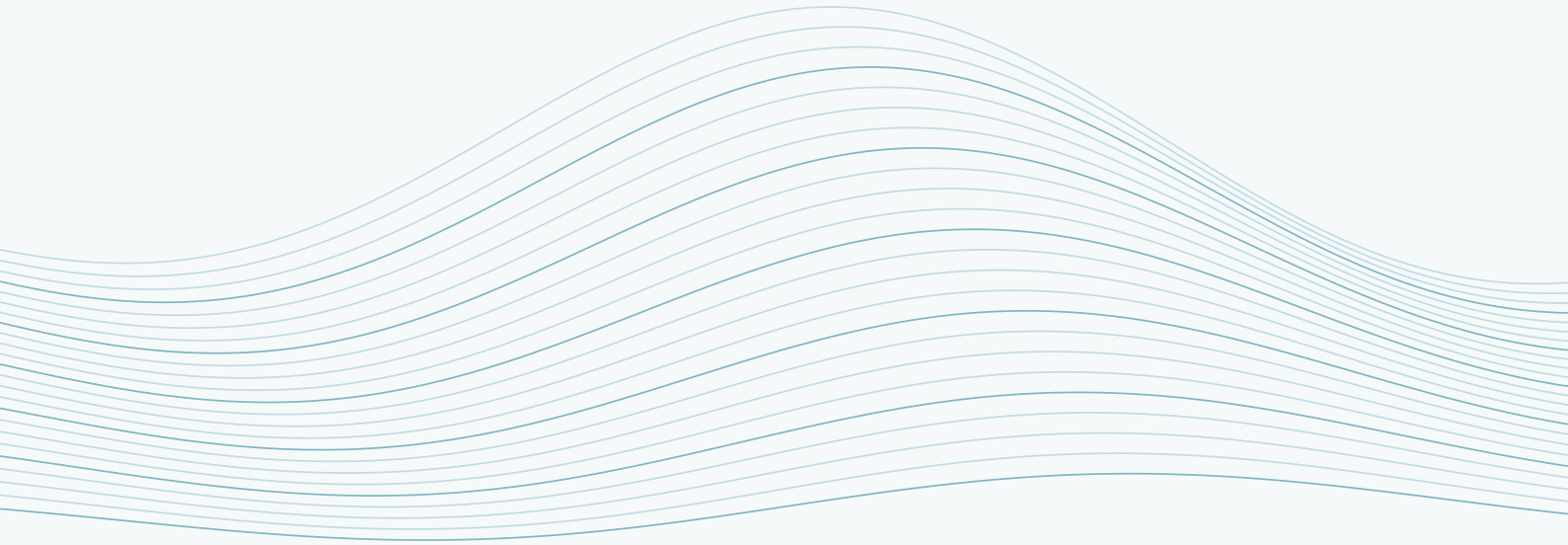
08 October 2026 09:02:51

05

专 题 / 05

其他

OTHER STUDIES



收录 5 篇论文

DOI：10.16489/j.issn.1004-1338.2003.05.004

一种提取声波测井频散波相慢度的方法*

苏远大 乔文孝
（石油大学地球资源与信息学院·山东）

摘 要

苏远大，乔文孝·一种提取声波测井频散波相慢度的方法，测井技术·2003，27(5)：364～368

在声波测井中，单极子声源激发的斯通利波和偶极子声源激发的弯曲波都是频散波。严格来讲，传统的相似法只适于处理非频散波，不适于处理频散波。只有从频散的斯通利波和弯曲波中提取出相慢度，才有可能进一步求准地层渗透率和横波慢度等参数。提出一种简便、快捷的方法从声波测井的频散波中提取相慢度。该方法从离散傅立叶变换的圆周时移性质出发，分别将2道频散波在幅度最大位置劈开做圆周时移，对圆周时移后的波形做快速傅立叶变换进而得到2道连续的相位谱，再由2道波形的相位差和接收探头间距可以计算出相慢度。给出了用该方法处理理论计算的偶极子波和现场声波测井资料的例子。

关键词： 相慢度 频散波 相位谱 圆周时移 幅度谱

ABSTRACT

Su Yuanda，Qiao Wenxiao·A Method to Extract Phase Slowness of Dispersive Wave from Sonic Logging Data·WLT，2003，27(5)：364－368

In sonic well logging，Stoneley wave generated by a monopole source and flexural wave generated by a dipole source are both dispersive waves. Strictly speaking，conventional semblance method is not adaptable to dispersive waves processing but only to nondispersive waves processing. Only when phase slowness is extracted from the Stoneley wave and the flexural wave，can the parameters of formation be obtained exactly，such as permeability and shear slowness. This paper presents a simple and quick processing method to extract the phase showness from dispersive waves provided by sonic logging. According to the circularly-shifting character of DFT，two dispersive waveforms are split at the position of maximal amplitude and shifted circularly，thus two continuous phase spectrums are gained by doing FFT of the shifted waveforms，then the phase slowness can be calculated with the phase difference and the transceiver spacing. As examples，the method is employed to process both theoretical dipole wave and field sonic logging data in this paper.

Subjects：phase slowness dispersive wave phase spectrum circularly-shifting amplitude spectrum

引 言

声波测井仪在充液井孔中激发并记录声波，记录到的波形包括非频散波(纵波与横波首波)和频散波(单极子声源激发的斯通利波[1]和偶极声源激发的弯曲波[2])。非频散波的相慢度不随频率的变化而变化，而频散波的相慢度是随频率变化而变化的。严格来讲传统的相似法只适用于处理非频散波，不适用于处理频散波。只有从频散的斯通利波和弯曲波中提取出相慢度，才有可能进一步求准地层渗透率和横波慢度等参数。因此国内外学者一直在研究如何从频散波中准确地提取相慢度。S·W·Lang 等人用 Prony 法、K·Hsu 等人用参数估算法可以从阵列声波测井资料中提取不同模式波的相慢度[3,4]，但要求不少于8道等间距测量信号，而且计算速度比较慢；乔文孝等人用相位展开法提取2道信号中频散波的相速度[5]，该方法具有原理简单、计算

*CNPC 测井重点实验室资助项目

(C)1994-2023 China Academic Journal Electronic Publishing House. All rights reserved. http://www.cnki.net

速度较快等优点，但在相位展开过程中会带来一些不确定性误差；李鹤升等人用矢量点乘法可以从多道频散波中提取相慢度[6]，该方法数学原理清楚，计算简单、速度较快，但在处理过程中将实际非常复杂的地层理想化。

本文利用离散傅立叶变换的圆周时移性，将两道频散波在幅度最大位置劈开做圆周时移，然后对其做快速傅立叶变换进而得到 2 道连续的相位谱，再由 2 道波形的相位差和接收探头间距计算出相慢度；最后给出了理论计算偶极子波的校验例子和现场声波测井资料的处理例子。现场资料的初步处理过程显示出该方法具有简便、快捷、可靠等优点。

方法介绍

对声波测井波形作频谱分析时，通常是直接对时域波形做快速傅立叶变换来获得幅度谱和相位谱。如图 1(a)给出的时域波形，图 1(b)和 1(c)分别给出了对波形直接做快速傅立叶变换得到的幅度谱和相位谱。从图 1(c)中可看出，在幅角主值(－π，＋π)范围内相位谱是不连续的，呈锯齿形。由于相位谱不连续，就不能进一步得到准确的相位差。

Fitting，Dale W 等人介绍了一种从时域波形中获得连续相位谱的简便、有效的方法[7]。将时域波形在质心位置劈开做一定的圆周时移后，再对移动后的波形做快速傅立叶变换就可以在幅角范围内得到连续的相位谱。该方法在无损检测和超声测量实验中已经得到广泛的应用[8,9]。图 1(d)给出了将图 1(a)中的波形在幅度最大的位置劈开做圆周时移得到的波形，图 1(e)和图 1(f)中分别给出了对圆周时移后的波形做快速傅立叶变换得到的幅度谱和相位谱。从图 1(f)中可以看出，波形作圆周时移后得到的相位谱在幅角主值(－π，＋π)范围内是连续的。

将波形在幅度最大位置(t_0)劈开做圆周时移前、后获得的幅度谱是一致的，而在幅角主值范围内的相位谱发生了变化，圆周时移后可以在幅角主值范围内得到连续的相位谱；根据离散傅立叶变换的圆周时移特性[10]，移动前的相位谱 $\theta(f)$ 与移动后的相位谱 $\varphi(f)$ 相差 ωt_0，即

$$\theta(f) = \varphi(f) \pm \omega t_0 \qquad (1)$$

那么，通过圆周时移处理就可以直接得到确定的、连续的相位谱。

从频散波中提取相慢度的具体步骤如下。

首先，选取 2 道频散波，将这 2 道波形分别在幅度

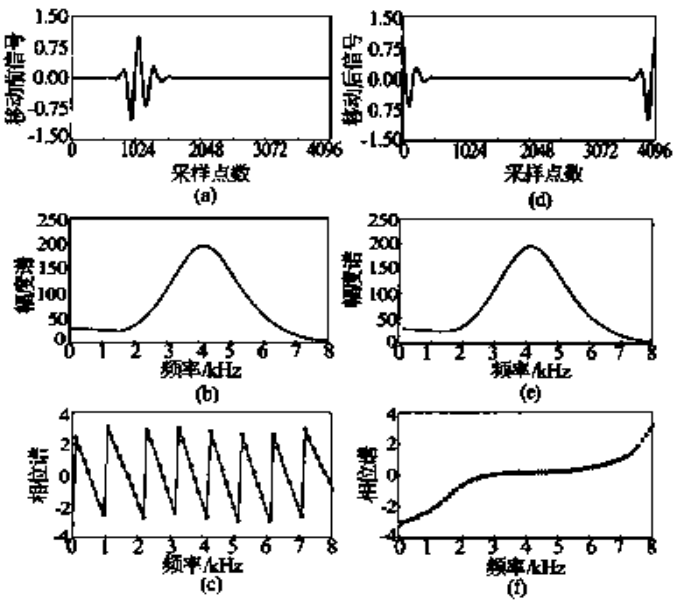


图 1　移动前、后的波形及其幅度谱和相位谱

最大的位置劈开作圆周时移，再对圆周时移后的波形做快速傅立叶变换，得到幅角主值范围内的连续相位谱；然后，根据离散傅立叶变换的圆周时移特性，获得 2 道频散波的连续相位谱；最后，由 2 道波形的连续相位谱计算出相位差 $\Delta\varphi$，进而求得延迟时间 Δt_d，即

$$\Delta t_d = \frac{\Delta\varphi}{\omega} \qquad (2)$$

由 2 个接收器的间距 Δl 与延迟时间 Δt_d 求出频散波的相慢度 $S_p(\omega)$，即

$$S_p(\omega) = \frac{\Delta t_d}{\Delta l} = \frac{\Delta\varphi}{\Delta l \cdot \omega} \qquad (3)$$

理论偶极子波形的校验举例

将上述方法首先用理论计算的偶极子波形进行校验。根据多极子声源在无限大、均匀的弹性地层充液井孔中的声场理论[2]，数值计算硬、软地层充液井孔中偶极子波的频散曲线和接收波形。数值计算时所选的参数见表 1。

表 1　软、硬地层的参数

参数名称	硬地层	软地层
地层纵波声速/m·s^{-1}	4600	2500
地层横波声速/m·s^{-1}	2700	1000
流体声速/m·s^{-1}	1524	1524
地层密度/g·cm^{-3}	2.5	2.3
流体密度/g·cm^{-3}	1.0	1.0
井眼半径/m	0.1	0.1
声源主频/kHz	2.5	2.5

(C)1994-2023 China Academic Journal Electronic Publishing House. All rights reserved.　http://www.cnki.net

图 2(a)和图 3(a)分别给出了理论计算的不同接收源距的硬地层和软地层偶极子波形。用本文所述方法从图 2(a)和图 3(a)的偶极子波形中提取的相慢度与理论计算的相慢度频散曲线进行对比，图 2(b)和图 3(b)分别给出了从理论计算的硬、软地层偶极子波形中提取的相慢度与理论计算的频散曲线的对比结果。图中小圆圈是用本文所述方法从波形中提取出的相慢度，实线是理论计算的频散曲线。从图 2(b)和图 3(b)中可以看出，用本文所述方法从波形中提取的相慢度与理论计算的相慢度频散曲线吻合的相当好。初步验证表明，该方法适用于从频散波中提取相慢度。

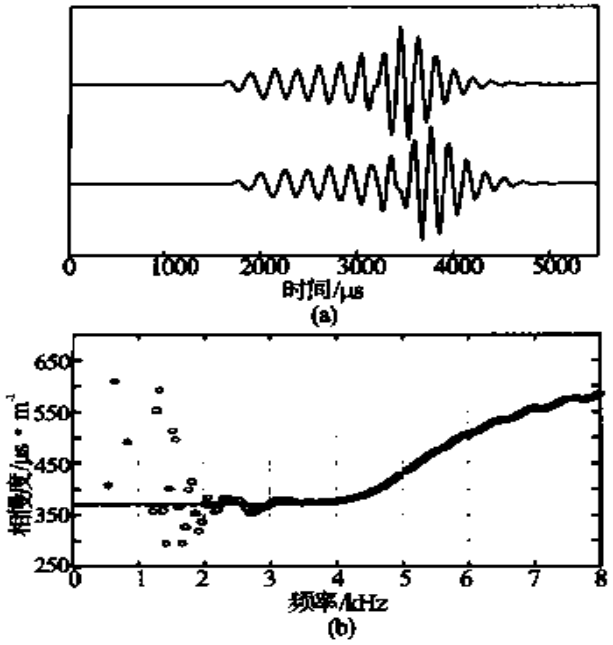


图 2 硬地层偶极子波的接收波形和相慢度

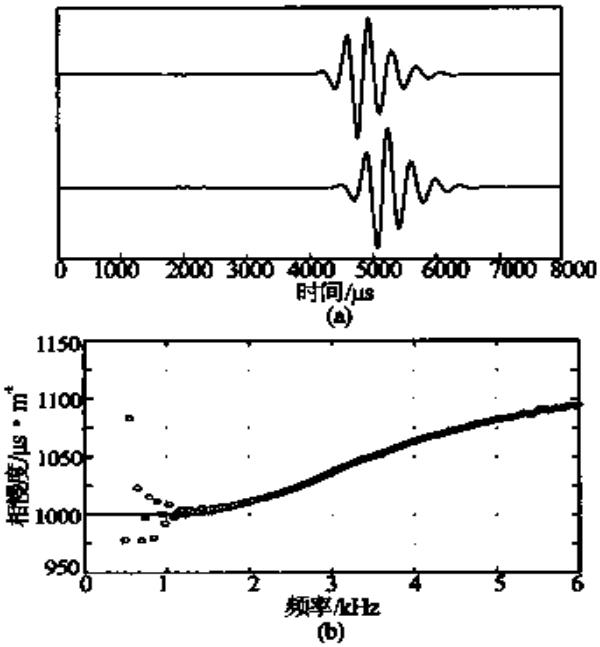


图 3 软地层偶极子波的接收波形和相慢度

现场资料的处理举例

在实际声全波测井中，单极子声源激发的斯通利波和偶极声源激发的弯曲波都是频散波。用本文所述的方法可以从现场的斯通利波和偶极子波中提取相慢度，本文分别给出了某个深度点和某一深度段的现场资料的处理结果。

1. 现场偶极子波的处理结果

图 4(a)给出了某一深度点的 2 道现场偶极子波形，图 4(b)给出了用本文所述方法从 2 道现场偶极子波形中提取的相慢度频散曲线。该地层为软地层，地层横波慢度约为 666 $\mu s/m$，从现场偶极波形中提取的相慢度的趋势与理论的频散曲线有较好的一致性。

利用本文所述的方法处理了某井的现场偶极子波形资料，图 5(a)给出了某一深度段测得的偶极子波形，图 5(b)给出了从图 5(a)的偶极子波形中提取的相慢度。图 5(b)的结果不是对记录的整个波形处理得到的相慢度，而是选取偶极子波的主要能量部分进行处理得到的偶极子波相慢度。

2. 现场斯通利波的处理结果

图 6(a)给出了偶极横波成像测井仪(DSI)的单极子低频模式在某一深度点获得的 2 道斯通利波波形，图 6(b)给出了从 2 道斯通利波波形中提取的相慢度频散曲线，处理结果与文献[6]的结果有较好的一致性。

利用本文所述的方法处理了某井的现场斯通利波

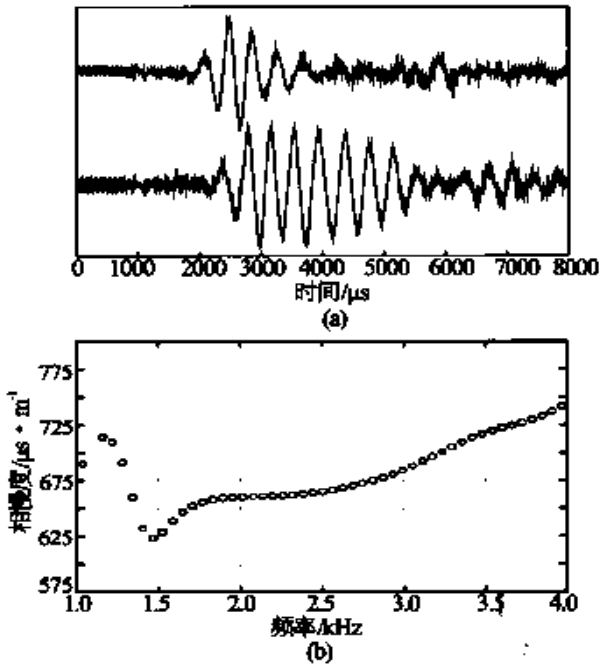


图 4 现场的偶极子波波形和处理结果

(C)1994-2023 China Academic Journal Electronic Publishing House. All rights reserved. http://www.cnki.net

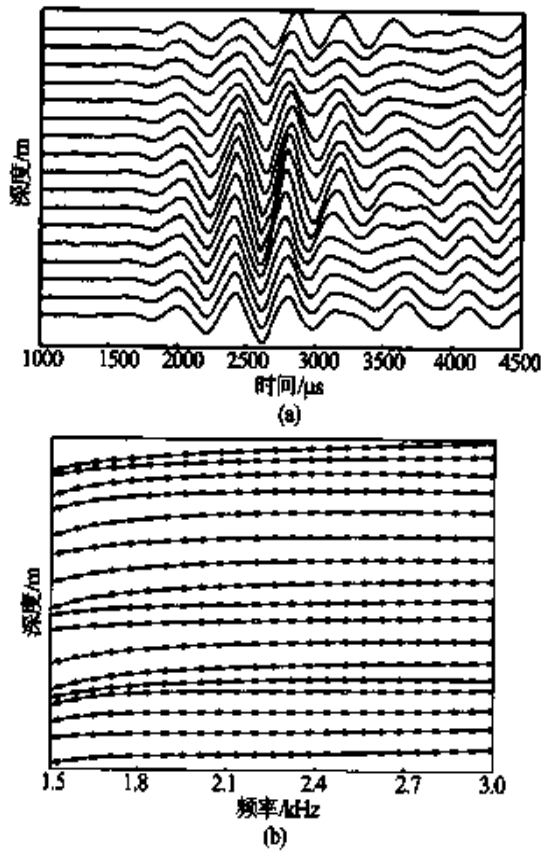


图 5　某一深度段的现场偶极波形和相慢度处理结果

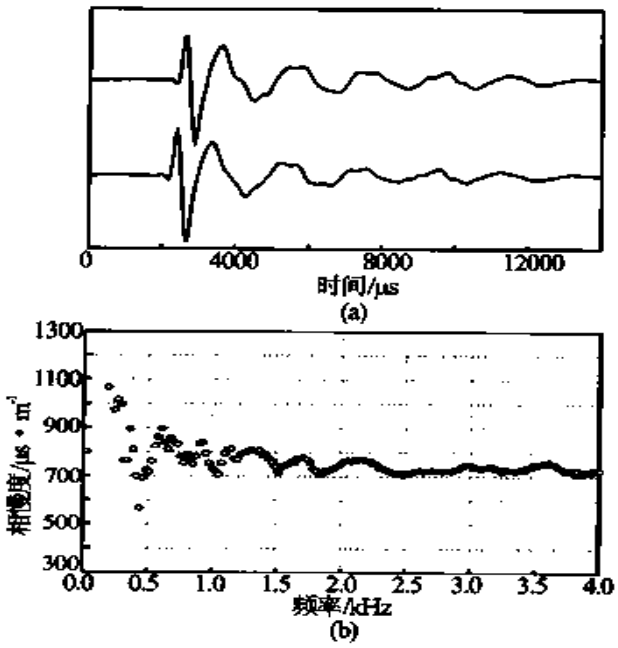


图 6　现场的斯通利波波形和处理结果

波形资料,图 7(a)给出了某一深度段的现场斯通利波波形,图 7(b)给出了从图 7(a)的斯通利波波形中提取的相慢度。图 7(b)的结果是选取斯通利波的主要能量部分进行处理得到的斯通利波相慢度。

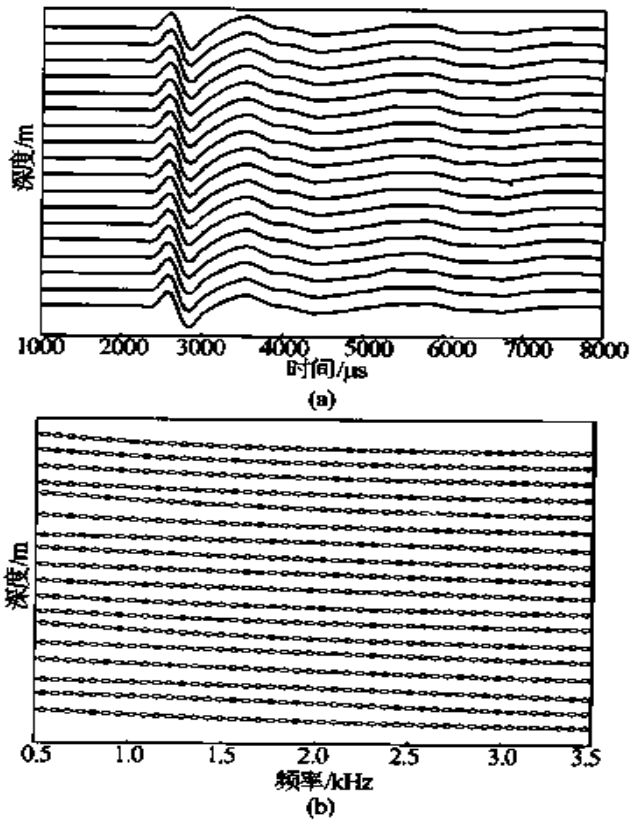


图 7　某一深度段的现场斯通利波波形和相慢度处理结果

讨　论

1. 质心位置选取对相位谱的影响

图 8(a)表示同一道波形分别在 3 个不同位置劈开后的波形,小圆圈表示在最大幅度位置劈开的波形,小方块和小三角分别表示在最大幅度前、后的某一位置劈开的波形,其对应的相位谱如图 8(b)所示。从图 8(b)中可以看出,质心位置选取不同时对应的相位谱有所不同,将最大幅度位置视为质心时对应的相位谱在 8 kHz 处出现不连续点,最大幅度前的位置视为质心时对应的相位谱没有出现不连续点,最大幅度后的位置视为质心时对应的相位谱在 7 kHz 处出现不连续点。图 8(b)中的实线是波形的幅度谱,从幅度谱中可以看出感兴趣的频率范围为 0～7 kHz。从图 8(b)中可看出,在最大幅度位置附近选取不同质心时,对感应趣的频率范围内的相位谱几乎没有影响,这也充分体现出该方法的适应性较强。因此,本文为便于处理将最大幅度位置视为质心位置。

2. 由弯曲波相慢度反演地层横波慢度

偶极声源在充液井孔中激发的弯曲波可以实现任意地层的横波测井,弯曲波只有在频率较低(小于截止频率)时的相慢度才等于地层横波慢度。在此能从弯曲

(C)1994-2023 China Academic Journal Electronic Publishing House. All rights reserved.　http://www.cnki.net

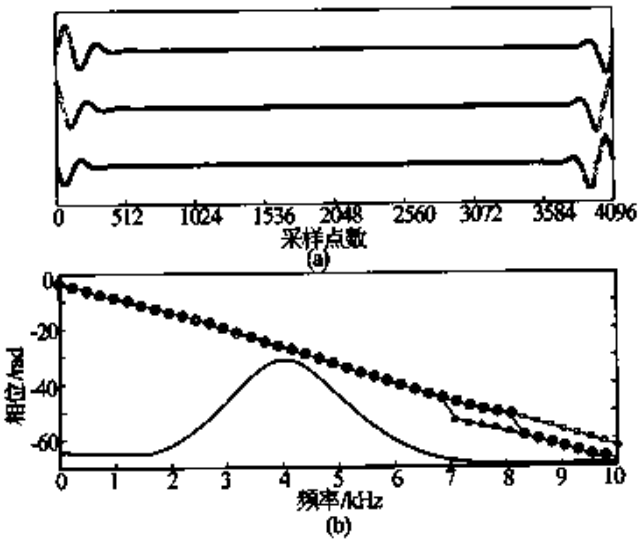


图 8 不同质心位置的波形及相位谱

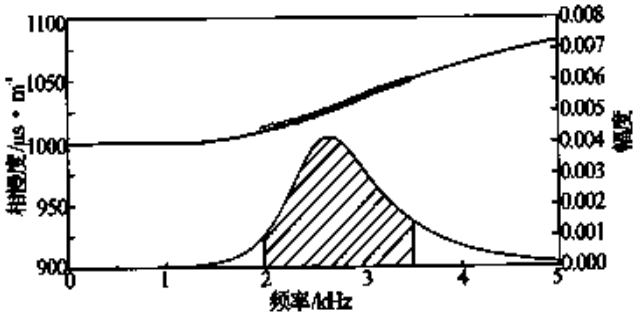


图 9 由提取的弯曲波相慢度反演地层横波慢度

波中获得准确的地层横波慢度是非常有意义的。

用本文所述方法处理现场偶极声波资料时，由于噪声和探头频带等因素的影响，在频率较低处的弯曲波相慢度很难求准，但可在主频附近获得准确的相慢度。通过在一定范围内调整横波慢度数值计算弯曲波频散曲线，将计算的频散曲线与提取的主频附近的相慢度进行对比，当两者相差最小时，可以反演出准确的地层横波慢度，同时获得整个频率范围内的弯曲波相慢度。图 9 中小圆圈是用本文的方法在阴影频率范围内提取的弯曲波相慢度。在一定范围内调整地层横波慢度数值计算频散曲线(如图 9 中虚线所示)，当提取的相慢度与数值计算的相慢度相差最小时，得到地层横波慢度以及整个频率范围内的 弯曲波相慢度，如图 9 中实线所示。同理，用该方法也可以从斯通利波的相慢度中反演地层横波慢度。

结 论

本文介绍了一种提取声波测井中频散波相慢度的方法，该方法是将 2 道频散波分别在幅度最大的位置劈开作圆周时移，对圆周时移后的波形做快速傅立叶变换，进而得到 2 道连续的相位谱，再由 2 道波形的相位差和接收探头间距计算出相慢度。通过对理论的偶极子波形处理表明，利用该方法从频散波中提取的相慢度与理论的相慢度频散曲线基本一致。

该方法可用于处理现场声波测井资料，在处理现场斯通利波和偶极子波资料的过程中其优越性得以体现。这种方法最大的优点是原理清晰易懂、计算速度相当快，可以从现场声波测井资料中准确地获得主频附近的相慢度。同时，在最大幅度附近选取不同质心位置时，对感兴趣频率范围内的相位谱影响不大，使得该方法有较强的适应性。用该方法从现场偶极子波和斯通利波中提取出主频附近的相慢度，然后对其进行频散校正，可以较准确地反演出地层的横波慢度。

参 考 文 献

[1] Cheng C H and Toksoz M· Elastic Wave Propagation in a Fluid-filled Borehole and Synthetic Acoustic Logs· *Geophysics*, 1981, 46(7): 1042－1053

[2] Kurkjian A L and Chang S K· Acoustic Multipole Sources in Fluid-filled Boreholes· *Geophysics*, 1986, 51(1): 148－163

[3] Lang S W and Kurkjian A L, *et al*·· Estimating Slowness Dispersion From Arrays of Sonic Logging Waveforms· *Geophysics*, 1987, 52(4): 530－544

[4] Hsu K and Esmersoy C· Parametric Estimation of Phase and Group Slowness from Sonic Logging Waveforms· *Geophysics*, 1992, 57(8): 978－985

[5] 乔文孝，阎树汶·用相位展开法提取相速度·声学学报，1993, 20(2): 135～137

[6] 李鹤升等·从矢量点乘引出的频散处理方法·测井技术，2001, 25(5): 335～341

[7] Fitting D W and Ader L· Ultrasonic Spectral Analysis for Non-destructive Evaluation· New York: A Division of Plemun Publishing Corporation· 1981: 78－81

[8] Rokhlin S I and Lewis K F, *et al*·· Real-time Study of Frequency Dependence of Attenuation and Velocity of Ultrasonic Waves During the Curing Reaction of Epoxy Resin· *J· Acoust· Soc· Am*·, 1986, 79(6): 1786－1793

[9] He P and Zheng J· Acoustic Dispersion and Attenuation Measurement Using Both Transmitted and Reflected Pulses· *Ultrasonics*, 2001, 39(1): 27－32

[10] 姜建国等编著·信号与系统分析基础·北京：清华大学出版社，1994: 103～105

(修改稿收稿日期：2003 04 16 本文编辑 高宝善)

(C)1994-2023 China Academic Journal Electronic Publishing House. All rights reserved. http://www.cnki.net

作　者　简　介

柯式镇　副教授，1967 年生。1999 年获石油大学(华东)应用地球物理学博士学位。(地址：北京市昌平区水库路石油大学资源与信息学院测井研究室　邮编：102200　电话：010　89733317)

严蓬蓬　1970 年生。现在清华大学物理系就读。(地址：北京市清华大学物理系，邮编：100084　电话：013611254109　E　mail：yanpp00@mails·tsinghua·edu·cn)

何峰江　在读博士生，1970 年生。主要研究声波测井。(地址：北京昌平石油大学岩石物理实验室　邮编：102249)

苏远大　1978 年生。现在石油大学(华东)攻读地球探测与信息技术专业硕士学位。(地址：山东东营石油大学地球资源与信息学院　邮编：257061　电话：0546-8395629(H)　E　mail：Syuanda@sina·com)

吴文圣　1972 年生。现在清华大学工程物理系做博士后研究。从事核测井方法、数值模拟、数据处理和测井综合解释研究。(地址：北京市清华大学工程物理系 3　8 信箱　邮编：100084　电话：010　62772496　E　mail：wwslog@hotmail·com)

姚绪刚　高级工程师，1960 年生。1982 年毕业于华东石油学院测井专业。长期从事测井技术研究和质量管理。现任中国石油集团测井有限公司长庆事业部经理。(地址：陕西西安高陵泾河工业园区泾渭东路方元大厦　邮编：710201　电话：029　6029811)

柴满州　高级工程师，1963 年生。1983 年毕业于武汉工业大学，1993 年获西南石油学院工学硕士学位。(地址：河南省濮阳市中原路 109 号　邮编：457001　电话：0393　4890974)

王新东　助理工程师，1972 年生。2000 年函授毕业于石油大学油藏工程专业。从事油气田地质与开发管理工作。(地址：山东省监邑县临盘采油厂地质研究所　邮编：251507　电话：0546　8869112　Email：lpwxd@slof·com·cn)

张宪生　高级工程师，1969 年生。1991 年毕业于大庆石油学院勘探系。主要从事测井解释方法及应用软件研究。(地址：黑龙江省大庆市测井公司研发中心　邮编：163412　电话：0459　5681886)

王　青　工程师，1968 年生。1990 年毕业于大庆石油学院测井专业。现从事测井处理、解释和测井地质研究工作。(地址：河北省廊坊市万庄 44 信箱　邮编：065007　E　mail：wangq6667@sina·com　电话：010　69213604)

罗　利　高级工程师，1971 年生，1991 年毕业于江汉石油学院测井专业。从事测井解释及数字处理方法研究工作。(地址：重庆市江北区大石坝四川石油管理局测井公司研究所方法室　邮编：400021　电话：023　67406032　E　mail：luoli3988@163·com)

王树松　工程师，1968 年生。1990 年毕业于西南石油学院测井专业。现从事生产管理工作。(地址：山东省东营市胜利测井四分公司　邮编：257096　电话：0546　8761394　E　mail：wshs@slof·com)

李淑英　工程师，1970 年生。1992 年西安石油学院计算机专业毕业，现从事计算机系统管理与维护工作。(地址：河南省濮阳市中原油田测井公司解释计算中心　邮编：457001　电话：0393　4824426)

李振苓　工程师。1992 年毕业于石油大学矿场地球物理专业，一直从事测井资料综合解释研究。(地址：河北省任丘市华北石油测井公司解释计算中心　邮编：062552　电话：0317　2783492/2701044/2701114)

王　建　1973 年生。2000 年在北京航空航天大学机械工程及自动化学院攻读硕士学位，研究方向计算机图形学及科学计算可视化。(地址：北京北四环中路 229 号海泰大厦 1111 室　邮编：100083)

金　燕　1967 年生。1993 年在成都理工学院获硕士学位，从事测井地质应用研究工作。(地址：四川省成都市府青路一段 1 号　邮编：610051　电话：028　86015634)

侯雨庭　1971 年生。现就读于西北大学在职研究生班。从事测井解释及方法研究。(地址：陕西省西安市长庆兴隆园小区研究院　邮编：710021)

杨景强　工程师，1972 年生。1999 年毕业于大庆石油学院，获应用地球物理专业硕士学位。现从事水淹层解释研究工作。(地址：黑龙江省大庆市让湖路区大庆油田有限责任公司勘探开发研究院地球物理测井研究室　邮编：163712　电话：0459　5508417)

谭增驹　高级工程师。1982 年毕业于江汉石油学院测井专业。现任中国石油集团测井有限公司吐哈事业部副经理。(地址：新疆鄯善中国石油集团测井有限公司吐哈事业部　邮编：838202　电话：0995　8372429)

李　勇　高级工程师，1962 年生。1982 年毕业于北京大学无线电电子学系声学专业。长期从事测井技术工作。(地址：河南省南阳市河南石油勘探局测井公司技术科　邮编：473132　电话：0377　3839413)

王兴之　工程师，1969 年生。1990 年毕业于西安电子科技大学计算机及应用专业。现从事 CSU 仪修工作。(地址：河南省濮阳市中原油田测井公司引进中心　邮编：457001　E　mail：xingzhiw@shou·com)

补　福　1989 年毕业于石油大学测井专业。现从事生产技术工作。(地址：重庆市江北区大石坝四川石油管理局测井公司　邮编：400021　电话：023　67352185)

刘河秀　高级工程师，1968 年生。1991 年毕业于大庆石油学院物探专业，现从事射孔工艺技术研究工作。(地址：黑龙江省大庆市大庆油田有限责任公司试油试采分公司研究所　邮编：163412　E　mail：liuhexiu@petrochina·com·cn　电话：0459　5685226)

杨健弟　工程师，1956 年生。1983 年西安石油职工大学测井专业毕业。从事测井仪研发工作。(地址：陕西省西安市红专南路 10 号西安石油勘探仪器总厂　邮编：710061　电话：029　6583254)

(C)1994-2023 China Academic Journal Electronic Publishing House. All rights reserved.　http://www.cnki.net

DOI :特方特特特特f·issn·特特特特

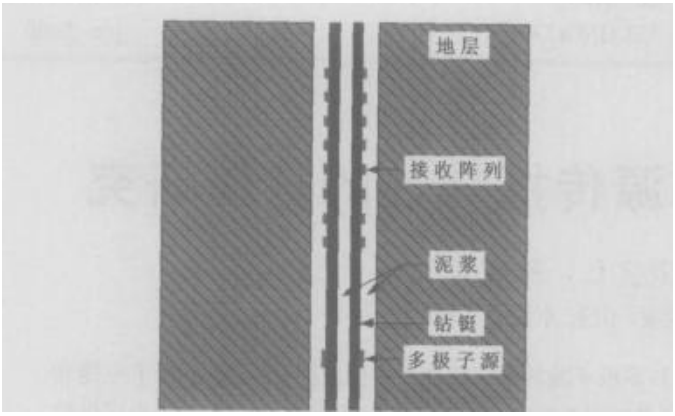


图 1 多极子随钻声波测井理论模型

波模式，则频散方程为 $|D_n(\omega, k)|=0$，其中 $n=0, 1, 2$ 时分别对应单极、偶极和四极子模式。

2 数值计算结果及分析

利用实轴积分法和牛顿迭代法数值考察了软地层随钻测井情况的单极子、偶极子和四极子声源的传播特性。其中地层、钻铤和井内泥浆的声学参数见表 1。

表 1 钻铤、井内泥浆和地层声学参数

	纵波速度 / (m·s^{-1})	纵波品质因数	横波速度 / (m·s^{-1})	横波品质因数	密度 / (kg·m^{-3})	半径 / m
钻铤内外泥浆	1470	100	—	—	1000	0.027
钻铤	5860	30	3130	40	7800	0.090
软地层	2742	50	1067	60	2320	∞

2.1 多极子模式波频散特性

图 2给出了软地层随钻测井单极子、偶极子和四极子声源激发的各种模式波的相速度频散曲线。从图 2(a)可看出随钻单极子声源激发钻铤模式波（弱实线）、内斯通利波（虚线）和外斯通利波（实线）模式。其中，钻铤模式波低频时速度约为钻铤纵波速度的 0.85 倍，且在 12 kHz以下的整个频段存在；内斯通利波的频散很弱，其相速度略微低于井内流体声速；外斯通利波与电缆测井斯通利模式波相对应，反映地层信息，但软地层情况随钻单极子测井的外斯通利波是正频散的，即群速度大于相速度。从图 2（b）可看出随钻偶极子声源激发钻铤模式弯曲波（虚线）和地层模式弯曲波（实线）。其中，钻铤模式弯曲波频散非常严重，速度小于钻铤横波速度；地层模式弯曲波无截止频率，且在任何频率下都明显低于地层横波速度。随钻偶极声源除了在频率很低时，钻铤和地层模式弯曲波几乎在整个频率范围内都同时存在。从图 2(c)可看出随钻四极子声源激发钻铤模式四极子波（虚线）和地层模式四极子波（实线）。钻铤模式四极子波的速度较高，在 10 kHz左右存在截止频率，低于截止频率时不存在钻铤模式的四极子波；地层模式四极子波在 2.5 kHz附近存在截止频率，且在截止频率处以地层横波速度传播。从频散图 2中可看出，在 0～10 kHz(四极子声源的实际工作频段）的频段只存在地层模式四极子波。

2.2 多极子声源声全波波形

图 3给出软地层情况随钻单极子、偶极子和四极子声源激发的阵列波形。图 3(a)给出随钻单极子声源激发的声全波波形，声源中心频率为 8 kHz。从图 3(a)中可看出，随钻单极子声全波波形中存在幅度较大的钻铤

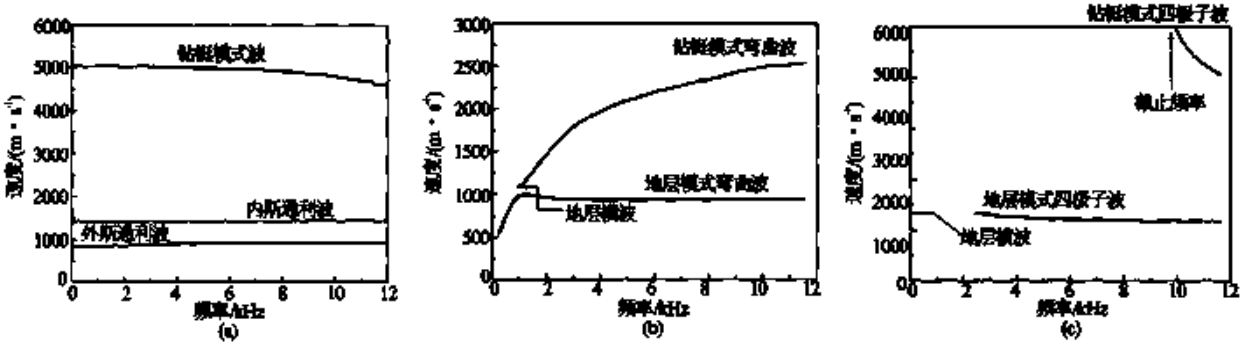


图 2 软地层随钻多极子声源的模式波频散曲线

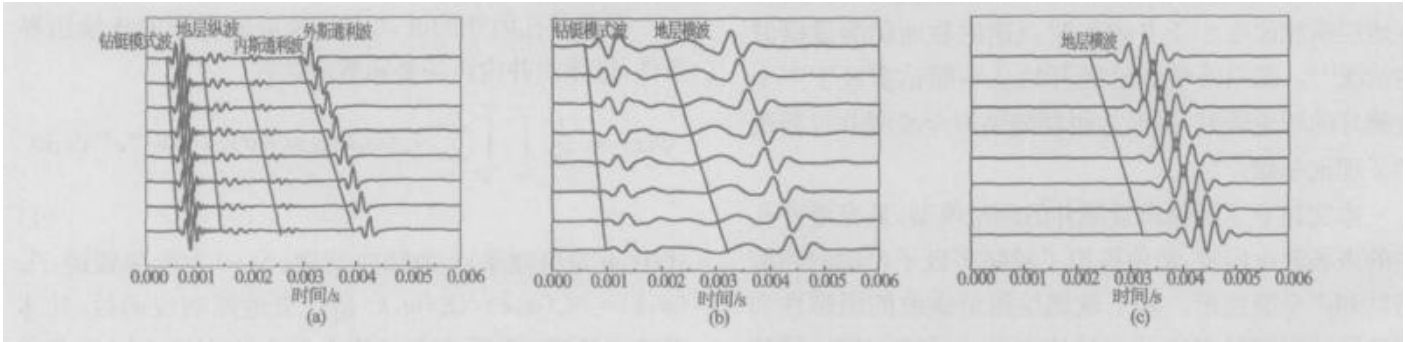


图 3 软地层随钻多极子声源的阵列波形

(C)1994-2023 China Academic Journal Electronic Publishing House. All rights reserved. http://www.cnki.net

模式波,接着是地层纵波,而后 2个是存在于钻铤内外界面的斯通利波,其中钻铤模式波严重干扰地层纵波,尤其地层纵波速度与钻铤模式波速度接近情况。图 3(b)给出偶极子声源激发的声全波波形,声源中心频率为 2 kHz。最先到达的是速度较快的钻铤模式弯曲波,而后是地层模式弯曲波。地层模式波到时比地层横波到时晚了许多,而且受钻铤模式波影响严重,没有清晰的波至。图 3(c)给出四极子声源激发的声全波波形,声源中心频率为 2 kHz。可看出,全波中只存在地层模式的四极子波,基本以地层的横波速度传播。在钻铤模式波截止频率以下激励四极子声源,可以使钻铤模式波对测量地层横波的干扰降低到最小甚至没有。

2.3 与电缆测井对比分析

将电缆测井和随钻测井在软地层中单极、偶极和四极子声源分别激发的斯通利波、弯曲波和四极子波的相速度频散曲线进行对比(见图 4)。

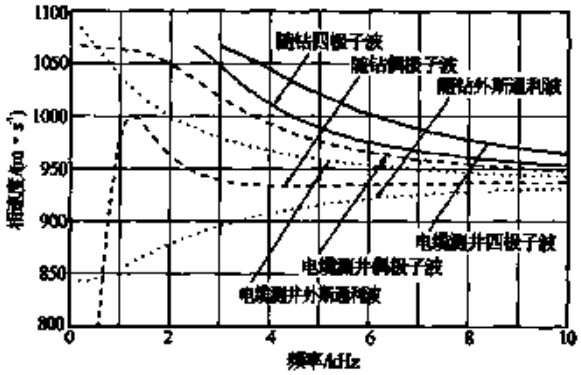


图 4 软地层情况电缆测井与随钻测井多极子波频散特性对比

由图 4可看出,电缆测井单极斯通利波无截止频率,而偶极弯曲波和四极子波均存在截止频率,且在截止频率附近均以地层横波速度传播;随钻测井环境下,整个频段单极斯通利波和地层模式弯曲波的相速度明显地低于地层横波速度,而且与电缆测井相比频散曲线趋势都发生了较大变化甚至趋势相反。四极子波的频散特性与电缆测井情况基本一致,截止频率处以地层横波速度传播。对比结果表明,与电缆多极子声波测井不同,随钻测井环境下用单极和偶极声源测量软地层的横波速度是不合适的,而利用四极子声源测量软地层的横波速度是最佳选择。

3 结 论

(1)由于钻铤的存在使其与地层发生了耦合作用,随钻多极子声源的传播特性与传统的电缆测井存在较大的差别。

(2)随钻测井环境下,单极和偶极子声源均激发幅度很强的钻铤模式波,严重干扰地层纵波或横波的测量,而四极子声源在低频时(10 kHz以下)不激发钻铤模式波,只激发地层模式波。

(3)随钻偶极子声源激发的地层模式波无截止频率,且低频时不以地层横波速度传播,而四极子声源激发的地层模式波在截止频率附近以地层横波速度传播。

四极子声源最适合于随钻测井环境下测量地层的横波速度。由于实际钻井过程仪器无法保证居中,特别是水平井和大斜度井。因此,多极子声源偏心情况对随钻声波测井响应的影响有待进一步深入研究。

参考文献:

[1] 时鹏程. 随钻测井技术在我国石油勘探开发中的应用[J]. 测井技术, 2002, 26(6): 441—445.

[2] Hsu C J and Sinha B K. Mandrel Effects on the Dipole Flexural Mode in a Borehole [J]. J. Acoust. Soc. Am., 1998, 104(4): 2025—2039.

[3] Tang X M, Dubinsky V, Wang T, Bolshakov A and Patterson D. Shear-velocity Measurement in the Logging-While-Drilling Environment: Modeling and Field Evaluations [A], SPWLA 43rd Annual Logging Symposium Transactions [C]. Paper RR, 2002.

[4] Tang X M, Wang T, Patterson D. Multipole Acoustic Logging-While-Drilling [A]. 72nd Ann. Internat. Mtg., Soc. Explor. Geophys., Expanded Abstracts [C]. 2002: 364—368.

[5] 崔志文,王克协,等. 多极源随钻声波测井的理论与数值研究 [A]. 中国地球物理年会 [C]. 2003: 76.

[6] Wang T, Tang X M. Finite-difference Modeling of Elastic Wave Propagation: A Nonsplitting Perfectly Matched Layer Approach [J]. Geophysics, 2003, 68(5): 1749—1755.

(收稿日期: 2006-02-21 本文编辑 余 迎)

(C)1994-2023 China Academic Journal Electronic Publishing House. All rights reserved. http://www.cnki.net

文章编号:1000-1441(2005)04-0409-04

正交偶极声波测井资料在评价地层各向异性中的应用

苏远大[1],乔文孝[2],孙建孟[1],陈雪莲[1]

(1. 石油大学(华东)地球资源与信息学院,山东东营 257061;2. 石油大学(北京)地球资源与信息学院,北京 102249)

摘要:裂缝和不均衡地应力等均可引起地层的各向异性,利用正交偶极子测量的 4 组波形可在井孔内评价地层的各向异性。其方法原理是,根据各向异性地层中偶极声源激发的快、慢弯曲波具有波形相似的特征,对所有接收阵列的快、慢弯曲波进行波形匹配,并构造目标函数,然后反演出地层的各向异性参数。用该方法处理了裂缝性和存在不均衡地应力地层中多口井的正交偶极资料,处理结果与成像资料基本吻合,表明各向异性系数和快横波方位能够用来指示地层的裂缝和地应力信息。

关键词:各向异性;快横波方位;波形匹配;横波分裂;正交偶极声波测井

中图分类号:P631.4　　**文献标识码**:A

正交偶极横波测井技术可以在井孔中测量地层横波各向异性,其分辨率远远高于地震测量的结果[1,2]。正交偶极测量的各向异性可以用来确定地应力的大小和方位以及裂缝的强度和取向等[3]。因此,如何从正交偶极资料中获得准确的地层各向异性参数至关重要[4~6]。传统的方法是旋转 4 组正交偶极波形获得快、慢横波波形后,分别处理得到快、慢横波慢度[1,5],该方法的主要缺点是方位具有不确定性。Tang 等介绍了一种由正交偶极资料同时反演出可靠的地层横波各向异性参数的方法[4]。

1　方法介绍

1.1　测量原理

方位各向异性地层中存在相互正交的快横波面和慢横波面,当一束横波信号入射到各向异性地层时,就分裂成沿快、慢波面传播的快、慢横波。正交偶极声波测井仪器(XMAC)能够在井孔中测量地层横波各向异性,该仪器由 2 组相互正交的偶极发射和接收探头组成,一次测量中记录 4 组波形(图 1),

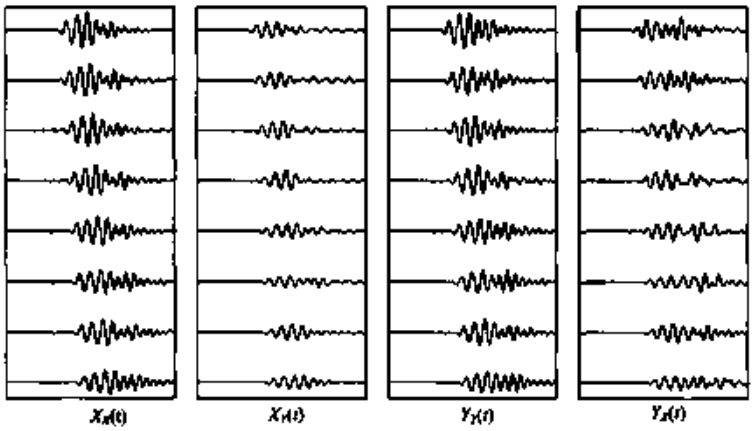


图 1　XMAC 测量的正交偶极波形

2 组平行分量的波形(X_X, Y_Y)和 2 组交叉分量的波形(X_Y, Y_X),其中前一个字母代表发射探头的偏振方向,脚标代表接收探头的偏振方向。

当偶极发射探头的偏振方向与地层快慢横波面重合时,记录的 2 组平行分量波形分别为快、慢弯曲波波形。实际测量中偶极发射探头的偏振方向一般不与快慢横波面重合,即 X 方向与快横波

收稿日期:2004-10-17;改回日期:2004-12-26。

作者简介:苏远大(1978—),男,硕士,主要从事声波测井方法和资料处理的教学和科研工作。

(C)1994-2023 China Academic Journal Electronic Publishing House. All rights reserved.　http://www.cnki.net

面有一夹角 θ(图 2)。此时可通过对记录的 4 组波形旋转 θ 角后获得快、慢弯曲波波形(P_F 和 P_S)[4],分别为:

$$P_F(t)=\cos^2\theta X_X(t)+\sin\theta\cos\theta[X_Y(t)+Y_X(t)]+\sin^2\theta Y_Y(t) \quad (1)$$

$$P_S(t)=\sin^2\theta X_X(t)-\sin\theta\cos\theta[X_Y(t)+Y_X(t)]+\cos^2\theta Y_Y(t) \quad (2)$$

对 P_F 和 P_S 关于 θ 求导可以获得 2 组次级波 P_F^θ 和 P_S^θ。

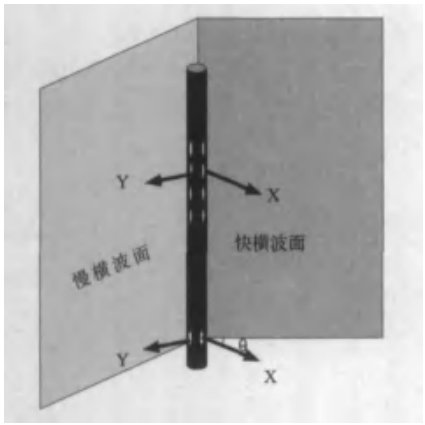


图 2 各向异性地层中正交偶极测井示意图

1.2 构造目标函数

数值研究表明快慢横波的波形具有相似性[7]。因此慢横波在时域内适当的向前移动将与快横波充分匹配,即两道波的相关性最强。将任意一接收器 n 的慢横波向前移动 $s_2(m-n)\delta z+\delta sz_m$ 后将与接收器 m 的快横波充分匹配,其中 $\delta s=s_2-s_1$,s_2 是慢横波慢度,s_1 是快横波慢度,z_m 是声源到接收器 m 的距离,δz 是接收间距。通过对所有接收阵列($N=8$)的波形在时窗 T 内进行相似匹配可构造出反演各向异性参数的目标函数 $E(s_2,\delta s,\theta)$,即

$$E(s_2,\delta s,\theta)=2-\frac{1}{2N^2}\sum_{m,n=1}^{N}\left\{\left(\int_T\left|P_{Sn}(t-s_2(m-n)\delta z+\delta sz_m)+P_{Fm}(t)\right|^2\mathrm{d}t\right)\Big/\left(\int_T\left|P_{Sn}(t-s_2(m-n)\delta z+\delta sz_m\right|^2\mathrm{d}t+\int_T\left|P_{Fm}(t)\right|^2\mathrm{d}t\right)+\left(\int_T\left|P_{Sn}^\theta(t-s_2(m-n)\delta z+\delta sz_m)+P_{Fm}^\theta(t)\right|^2\mathrm{d}t\right)\Big/\left(\int_T\left|P_{Sn}^\theta(t-s_2(m-n)\delta z+\delta sz_m)\right|^2\mathrm{d}t+\int_T\left|P_{Fm}^\theta(t)\right|^2\mathrm{d}t\right)\right\} \quad (3)$$

方程(3)中,包括了由 N 个接收器组成的阵列中快、慢横波匹配的所有可能情况,可以有效地抑制和消除不连续因素的影响。当目标函数达到最小时,可反演出可靠的各向异性参数。用公式(3)可得到关于各向异性系数和快横波方位的目标函数。图 3 和图 4 分别给出各向同性和各向异性地层的目标函数。各向同性地层的目标函数在 0°和 90°的位置出现 2 个基本相等的极小值且各向异性系数接近于零;而各向异性地层中目标函数在方位上相差 90°的 2 个位置上出现极小值,这 2 个极小值分别对应快、慢横波,其中快横波对应全局极小值,而慢横波只是对应一个局部极小值。

用模拟退火法从目标函数中确定全局极小值,进而可以快速反演出可靠的各向异性系数和确定快横波方位。

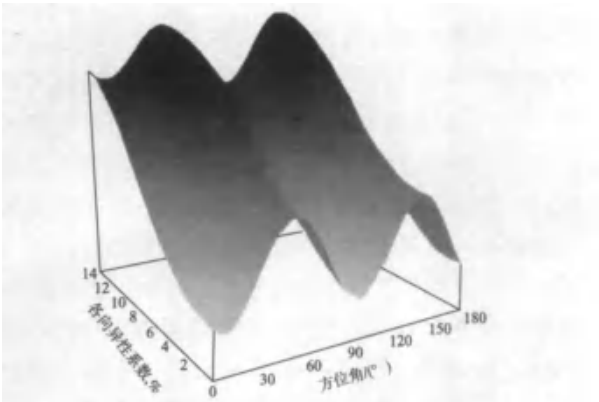


图 3 各向同性地层的目标函数

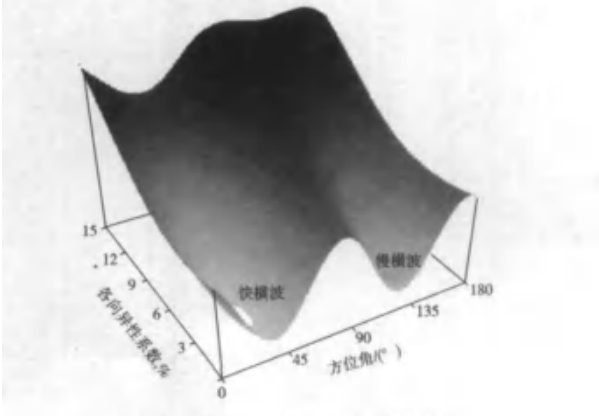


图 4 各向异性地层的目标函数

2 现场资料处理实例

地层中的裂缝特征和地应力场分析是油气勘探中的 2 个重要环节。理论研究表明[3,8],裂缝性

(C)1994-2023 China Academic Journal Electronic Publishing House. All rights reserved. http://www.cnki.net

地层和存在不均衡地应力的地层中均表现为横波各向异性。因此，可以通过正交偶极资料确定各向异性参数，进一步获得裂缝的发育度和走向以及地应力大小和方位。

2.1　裂缝性地层的各向异性评价

裂缝性地层中，在与裂缝走向平行的方向上偏振的横波对应的地层弹性模量较高，因而传播较快；而在裂缝开裂方向（即垂直裂缝表面的方向）上偏振的横波对应的弹性模量较低，因而传播速度较慢。这就导致了横波在 2 个偏振方向上的各向异性。图 5 给出了裂缝性碳酸盐岩地层中正交偶极资料的各向异性评价结果，图中电成像资料显示在 3 327～3 330 m 存在天然裂缝。图中第 4 道给出 2 种分辨率的各向异性曲线，分别是发射器到接收器阵列中点间的平均各向异性（$\overline{\eta}$）和接收器阵列间的各向异性曲线（η_{mn}），可看出在 3 327～3 330 m 各向异性较大，为 8%左右，与成像资料吻合较好，其中各向异性的大小可以反映裂缝的强度；第 2 道给出了从正交偶极资料获得的快横波慢度（S_F）和慢横波慢度（S_S）曲线以及声波时差（Δt）曲线，处理得到的快、慢横波慢度与测量的声波时差的趋势有很好的一致性；第 3 道给出快、慢弯曲波波形和由平行分量的弯曲波慢度确定的处理时窗曲线，如果快、慢弯曲波波列包含在处理时窗内，那么就说明获得的快、慢弯曲波波形数据是准确的。而快、慢横波波形的分离程度反映各向异性的大小，与第 4 道中各向异性曲线有较好的对应性；第 5 道显示的是仪器方位（θ_T）和快横波方位（θ_F）曲线。如果快横波方位较稳定，不随仪器旋转，则说明计算的各向异性是正确的以及快横波方位是可靠的，此时的快横波方位代表裂缝的走向；图中第 1 道给出了自然伽马和井径曲线。

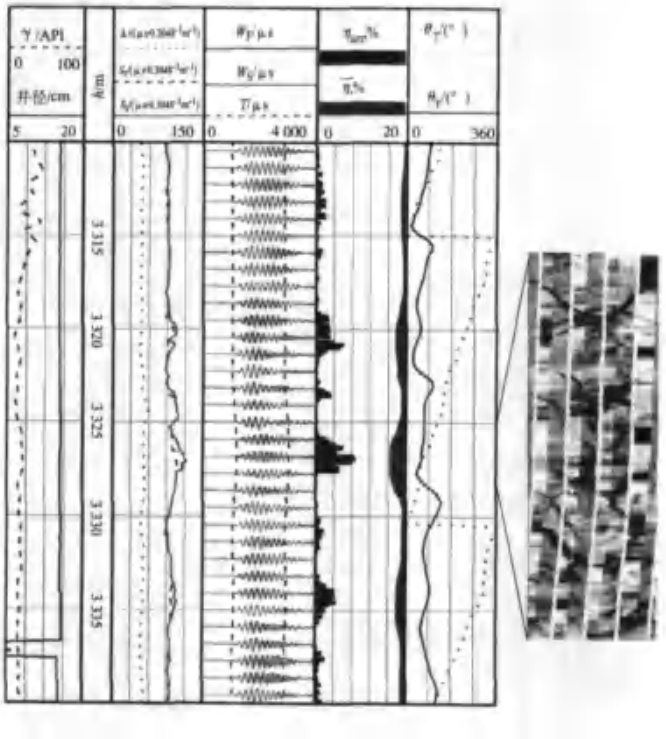


图 5　裂缝性地层正交偶极资料的各向异性评价结果

2.2　存在不均衡地应力地层的各向异性评价

存在不均衡应力的地层中，最大、最小水平地应力和井孔静水压力的作用导致井孔内应力集中，使得沿着最大水平应力方向偏振的横波比垂直与该方向偏振的横波传播速度快，进而产生横波各向异性。

图 6 给出了存在不均衡地应力的砂岩地层中正交偶极资料的各向异性评价结果，图中声成像资料显示在 795～812 m 裂缝不发育，有明显的椭圆井眼崩落现象，这说明该井段存在不均衡的地应力。图中各道曲线与图 5 一致，从各向异性曲线可看出纯砂岩井段（795～812 m）存在相对较小的各向异性，为 2%左右；在砂泥岩薄互层存在固有各向异性，相对较大，约 5%左右。

(C)1994-2023 China Academic Journal Electronic Publishing House. All rights reserved.　http://www.cnki.net

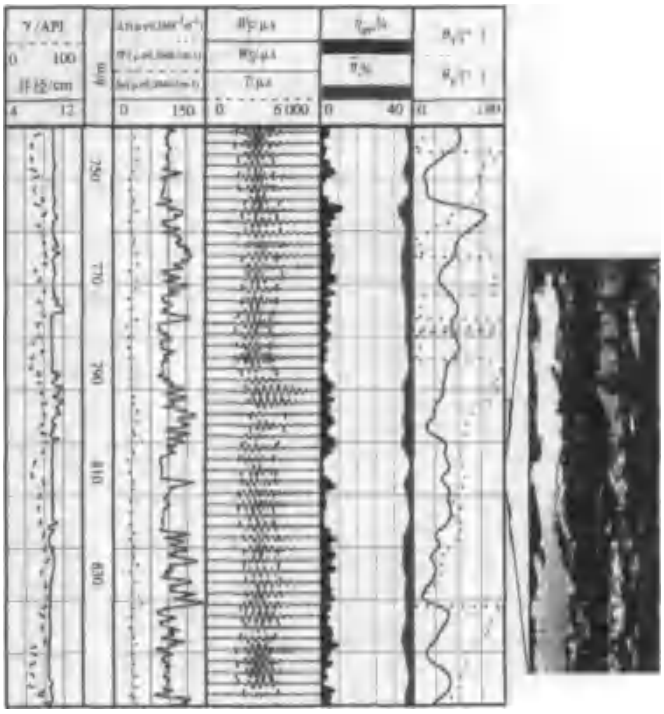


图 6 存在不均衡地应力地层中正交偶极资料的各向异性评价结果

3 结束语

本文介绍了一种由正交偶极测井资料确定地层横波各向异性参数的方法。该方法以快、慢弯曲波波形具有相似性为基础，对所有接收阵列的波形进行相似匹配，构造出目标函数进而反演地层横波各向异性参数。通过对裂缝性和存在不均衡地应力地层中正交偶极资料的处理，结果表明各向异性系数和快横波方位能用来指示地层的裂缝和不均衡地应力信息。该方法充分地利用了现场资料的信息，有效地抑制噪音等不连续因素的影响，但不足之处是没有考虑弯曲波的频散和衰减等因素的影响。

参 考 文 献

1 Alford R M. Shear data in presence of azimuthal anisotropy [J]. Expanded Abstracts of 62th Annual international SEG Mtg, 1986, 476～479

2 Mueller M C, Boyd A J, Esmersoy C. Case studies of the dipole shear anisotropy log [J]. Expanded Abstracts of 70th Annual international SEG Mtg, 1994, 1 143～1 146

3 Esmersoy C, Kane M, Boyd A, et al. Fracture and stress evaluation using dipole-shear anisotropy logs[J]. SPWLA 36th Annual Logging Symposium, 1995, 1～12

4 Tang X M, Chunduru R K. Simultaneous inversion of formation shear-wave anisotropy parameters from cross-dipole acoustic-array waveform data [J]. Geophysics, 1999, 64(5): 1 502～1 511

5 李维意，李永胜，汪中浩，等. 利用偶极横波成像测井资料评价地层的各向异性[J]. 江汉石油学院学报，1999, 21(4): 36～38

6 陶果，Cheng C H, Toksoz M N. 应用正交偶极子测井资料测量 EDA 地层的横波各向异性[J]. 地球物理学报，1999, 42(2): 277～286

7 Cheng N Y, Cheng C H. Decompostion and particle motion of acoustic dipole log in anisotropy formation [J]. Expanded Abstracts of 71th Annual international SEG Mtg, 1995, 1～4

8 秦绪英，陈有明，陆黄生. 井中应力场的计算及其应用研究[J]. 石油物探，2003, 42(2): 271～275

（本文编辑：朱文杰）

(C)1994-2023 China Academic Journal Electronic Publishing House. All rights reserved. http://www.cnki.net

文章编号:1673-5005(2006)04-0038-04

裸眼时差与变密度测井地层波能量相结合改进固井Ⅱ界面评价

苏远大,孙建孟,李召成,张振城,陈雪莲

(中国石油大学 地球资源与信息学院,山东 东营 257061)

摘要:固井Ⅱ界面胶结情况直接影响生产井中油、水层的窜通,是固井质量检测的重要环节。利用裸眼井声波时差资料计算出变密度波列中的地层波波至,结合现场变密度资料在频域内对地层波能量进行了准确求取,并对固井Ⅱ界面进行了评价。结果表明,固井Ⅰ、Ⅱ界面水泥完全胶结时,地层波能量和声波时差存在一定的指数关系。在此基础上考虑地层声速参数对地层波能量的影响,特别是快、慢地层对Ⅱ界面评价的影响,给出了一种新的主要反映水泥胶结质量的Ⅱ界面胶结指数的定义。评价结果表明,新的胶结指数曲线在固井Ⅱ界面胶结良好井段相对较平滑且数值接近于 1,基本能够消除地层声速对Ⅱ界面胶结质量的影响,进而改进了固井Ⅱ界面的评价质量。

关键词:Ⅱ界面胶结指数;声波时差;变密度测井;地层波能量;固井质量

中图分类号:P 631.84 **文献标识码**:A

Improved second interface cementing evaluation using open hole slowness and formation wave energy of variable density log

SU Yuan-da, SUN Jian-meng, LI Zhao-cheng, ZHANG Zhen-cheng, CHEN Xue-lian

(*Faculty of Geo-Resource and Information in China University of Petroleum, Dongying* 257061, *Shandong Province, China*)

Abstract: As an important link for cementing quality measurement, the bond of second interface has direct effect on the connection between oil and water bearing zones in the producing well. The arrival time of the formation wave of variable density log (VDL) waveform was derived from the open hole acoustic data and the formation wave energy was calculated accurately in frequency domain. By the method, field VDL data were processed. The results show that, when the cement of first and second interface bonds well, there exists exponential relationship between the formation wave energy and slowness. Considering the effects of formation slowness on formation wave energy, especially the effect of fast or slow formation on the evaluation of second interface, a new bond index of second interface that mainly reflects the cement bond quality was provided. The processed results show that the new bond index curve is relatively smooth and the value is close to one in the well-bonded second interface, which can basically eliminate the influence of the formation velocity on the bond quality of second interface and can improve the evaluation quality of second interface.

Key words: bond index of second interface; slowness; variable density log; formation wave energy; cementing quality

固井Ⅱ界面胶结情况直接影响生产井中油、水层的窜通,是固井质量检测的重要环节。目前,固井质量定量评价大多集中在Ⅰ界面,对Ⅱ界面胶结质量的评价方法研究还不够完善。最初,Brown 等[1]利用声波变密度资料对固井Ⅰ,Ⅱ界面胶结情况进行了定性分析;针对套管井中的不同胶结情况,Tubman 等[2]从理论上进行了深入研究;胡文祥等[3]通过实验研究获得了不同胶结情况的声波全波列波形,理论与实验波形具有很好的一致性;官波和王天波等[4-5]分别在时域和频域内计算了地层波能量,并用地层波归一化能量定量评价了Ⅱ界面胶结质量。以上方法均没有考虑地层声学特性对地层波能量的影响,定义的胶结指数不够合理。刘继生等[6]综合利用声波变密度、伽马密度和自然伽马测井资料评价固井Ⅱ界面胶结质量,克服了仅利用地层波的能量评价固井Ⅱ界面胶结质量的单一性,但只是将声衰减作为参考,没有实现定量化。胡文祥等[7]数值模拟了不同地层水泥完全胶结时的声波

收稿日期:2005-10-12

作者简介:苏远大(1978-),男(汉族),吉林榆树人,助教,硕士,从事声波测井方法及资料处理的教学与科研工作。

(C)1994-2023 China Academic Journal Electronic Publishing House. All rights reserved. http://www.cnki.net

全波列波形，发现水泥完全胶结时地层波能量与地层声速有关，且中速地层的地层波能量明显大于高速地层。笔者结合现场声波时差和变密度资料研究固井Ⅱ界面水泥完全胶结时地层波能量与声波时差的关系，在此基础上给出一种新的主要反映水泥胶结质量的Ⅱ界面胶结指数的定义，用于对现场变密度资料的处理。

1　地层波波至时和能量的确定

1.1　地层波波至时的确定

利用裸眼井的声波时差和井径资料可以确定变密度资料中地层波的到达时间。由于裸眼井的声波时差是消除了井内液体和井径变化等因素影响后的补偿时差，而套管井中的变密度波形的传播路径包括了井内液体、套管、水泥环和地层等，因此利用声波时差确定变密度资料中地层波的波至时必须进行校正。变密度资料中地层波的到达时间 t 的表达式[8] 为

$$t = t_{m-s} + t_c + t_f. \tag{1}$$

式中，t_{m-s} 为地层波在钻井液和套管中的传播时间，μs；t_c 为地层波在水泥环中的传播时间，μs；t_f 为地层波在地层中的传播时间，μs。

图 1 中第 3 道给出的是声波变密度波列和用式(1) 计算的地层波到达的时间。可以看出计算的地层波到达时间在水泥胶结良好井段(1 880 m 以上)与波列吻合很好；在水泥胶结中等或偏差井段(1 880 m 以下)，由于变密度波列中地层波不清晰，可能导致到达时间曲线与波列吻合较模糊。

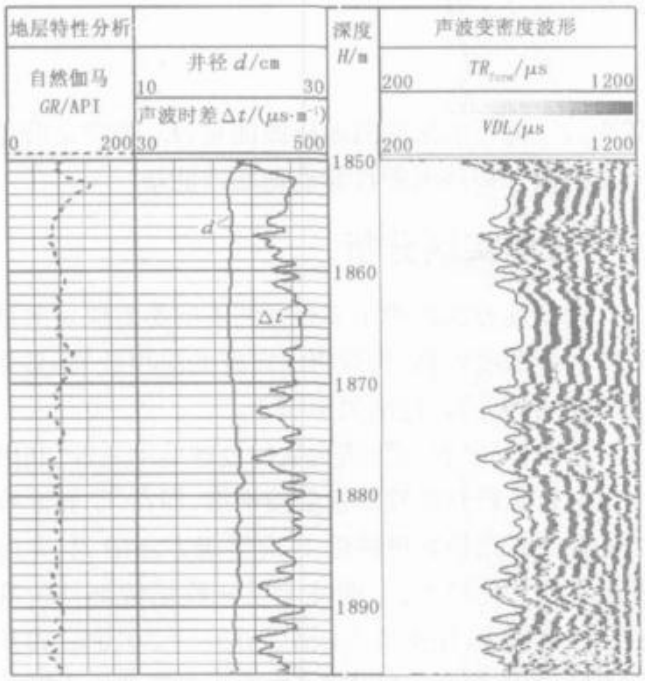


图 1　地层波波至时确定成果图

1.2　地层波能量的计算

由于地层波受高频套管波和噪音等因素影响，尽管准确地确定了地层波波至时，但直接在时域内计算地层波能量也是不准确的。图 2(a) 给出了套管井中接收的典型波形，图中时窗内的波形为地层波；图 2(b) 给出了整个波列(虚线) 以及时窗内地层波(实线) 的幅度谱，其中阴影部分的能量为真正的地层波能量。从图 2 中可以看出，在时域内无法彻底消除套管波对地层波的影响，只有在频域内才可以消除高频套管波的影响。

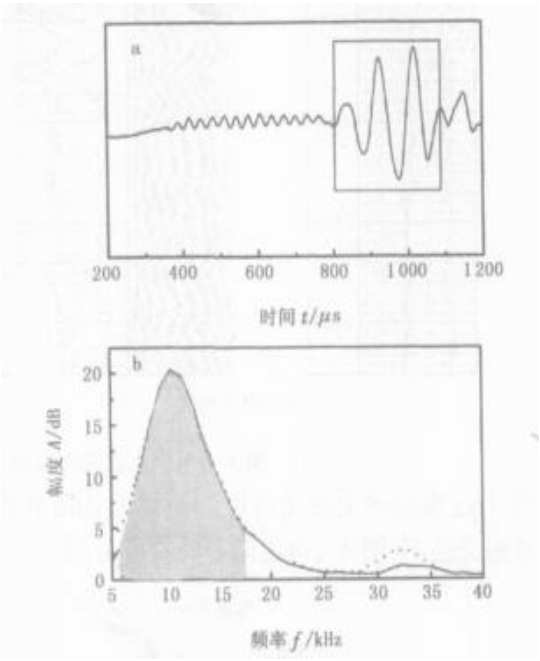


图 2　套管井中的典型波形及幅度谱

计算地层波能量的步骤如下：

(1) 在时域内以式(1) 确定的地层波到达时间起开窗，确保能够完全包括地层波信息；

(2) 对时窗内的波形作快速傅里叶变换得到幅度谱 $A(f)$，并确定地层波主频值；

(3) 在频域内计算主频附近的地层波能量 E，其计算式为

$$E = \int_{f_1}^{f_2} A(f)\mathrm{d}f. \tag{2}$$

式中，f_1 和 f_2 分别为地层波的起始和终止频率，kHz。

2　固井Ⅱ界面胶结指数的定义

2.1　地层波能量与声波时差的关系

结合现场变密度资料，利用上述方法计算了完全胶结井段的地层波能量，并与裸眼井的声波时差进行了对比。图 3 给出了两个完全胶结井段的地层波能量和声波时差对比结果。从图中的变密度波形

(C)1994-2023 China Academic Journal Electronic Publishing House. All rights reserved.　http://www.cnki.net

看出两个井段的套管波幅度很小，出现了清晰的地层波且幅度较大，定性评价为 Ⅰ，Ⅱ 界面均胶结良好。从第 3 道给出的声波时差和地层波能量曲线发现，两者的趋势有很好的一致性，即在水泥胶结良好井段地层的声波时差越大，对应的套管井声波全波列中地层波的能量也越强。

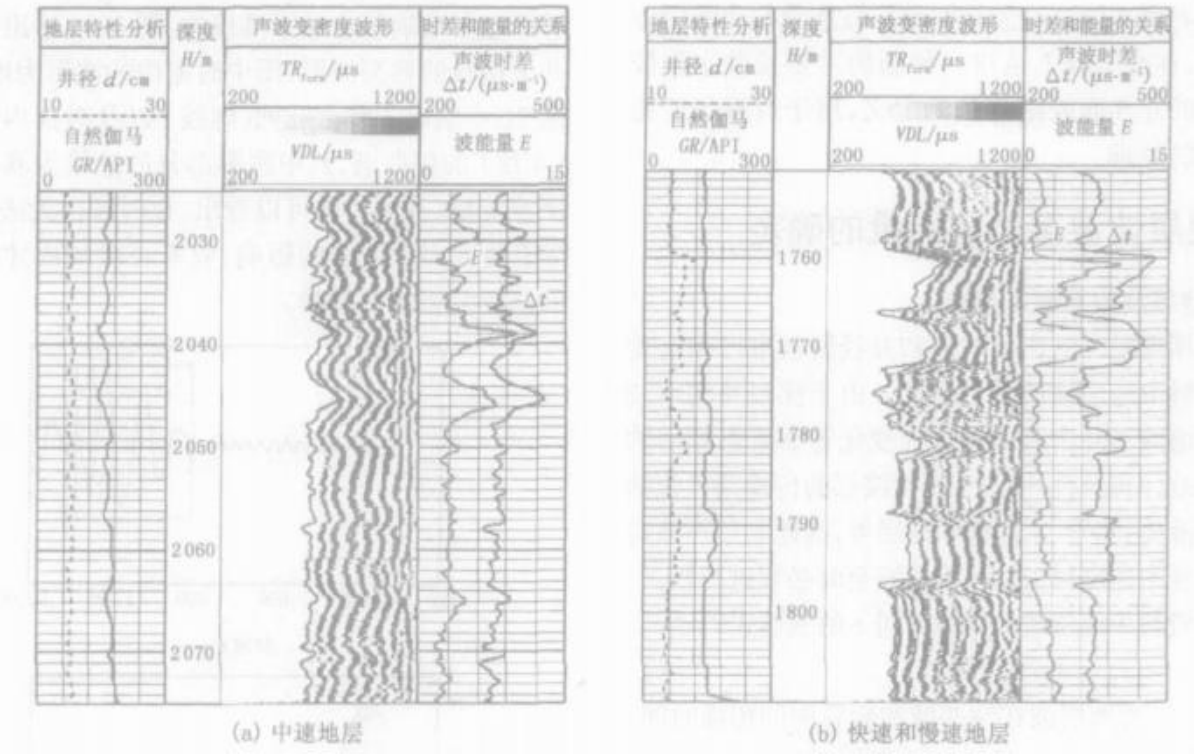


图 3　两个水泥完全胶结井段地层波能量和声波时差的对比

将上述水泥完全胶结井段的地层波能量和声波时差做交会图(图 4)，得出两者的对应关系。

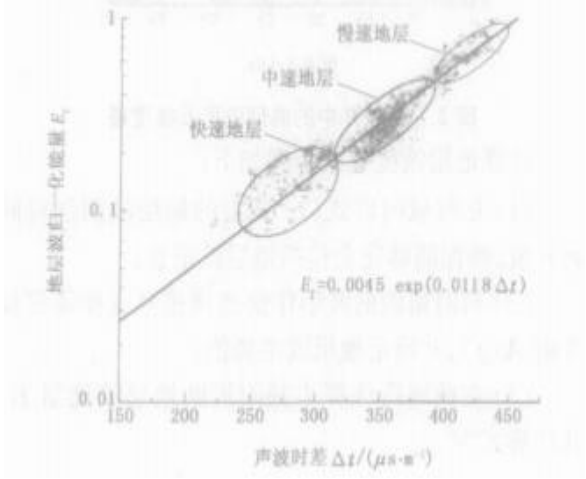


图 4　水泥完全胶结井段地层波能量和声波时差交会图

对所有地层情况下的地层波能量与声波时差进行拟合(图 4 中实线所示) 发现，Ⅰ，Ⅱ 界面水泥完全胶结时地层波能量和声波时差存在指数关系。图 4 中还存在一些较明显的离散点，其主要原因是套管接箍、仪器偏心等因素的影响，而不是地层声波时差的影响。

2.2　固井 Ⅱ 界面胶结指数

在声波变密度资料中，地层波能量反映固井 Ⅱ 界面胶结情况的同时，也受到地层声波时差的严重影响。因此，单纯用地层波能量来评价固井 Ⅱ 界面胶结质量的传统方法是不准确的，必须结合地层声波时差定义给出合理的 Ⅱ 界面胶结指数定义。

根据 Ⅰ，Ⅱ 界面水泥完全胶结时地层波能量和声波时差的关系，定义评价水泥胶结质量的 Ⅱ 界面胶结指数 I_{B2} 为

$$I_{B2}=\frac{E_d}{E_v}. \tag{3}$$

式中，E_d 为当前深度的地层波能量；E_v 为完全胶结时由裸眼井声波时差计算的地层波能量。

3　应用实例分析

用上述方法处理了多口井的不同类型仪器测量的声波变密度资料，均取得了良好的应用效果，某井段的 Ⅱ 界面的处理结果见图 5。

从两种 Ⅱ 界面胶结指数的处理结果发现，利用本文中方法得到的胶结指数较平滑，即在 Ⅱ 界面胶结良好时胶结指数更接近 1；而传统方法的 Ⅱ 界面胶结指数变化较大，不能完全反映胶结情况且很难制定评价标准。用本文方法对 2 000 ～ 2 010 m 的井段评价为 Ⅱ 界面胶结中等，而传统方法评价为胶结较差，对该层进行开采发现，该井段正常产油，日产

(C)1994-2023 China Academic Journal Electronic Publishing House. All rights reserved. http://www.cnki.net

油 10 t，不产水。另外，用本文方法对 2010～2100 m 的整个井段评价为 Ⅱ 界面胶结良好，但由于受地层声波时差变化的影响，传统方法对该井段中较硬地层的评价结果不准确。

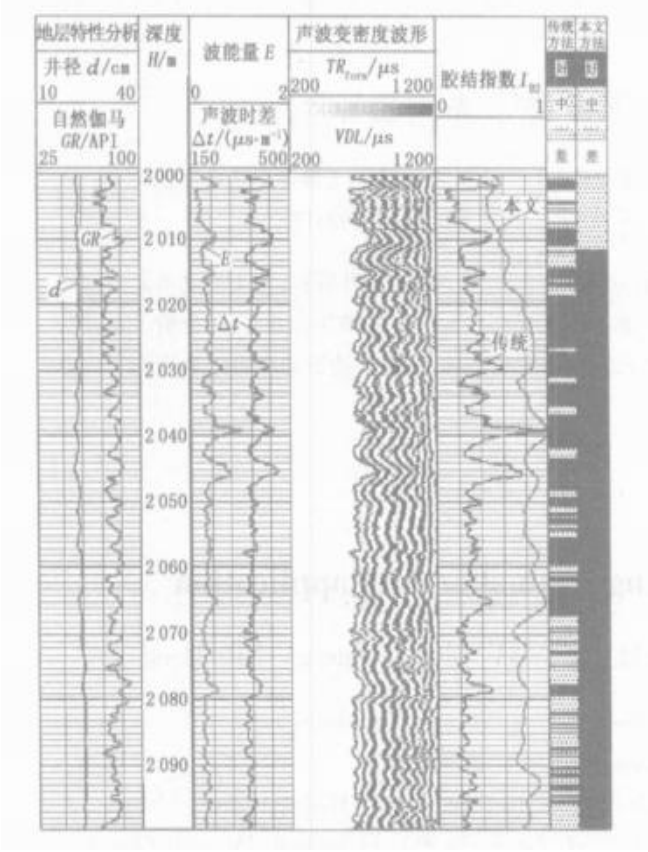


图 5　某井段声波变密度资料的 Ⅱ 界面处理成果

4　结　论

(1) 利用裸眼井声波时差和井径确定地层波到达时间后在频域内求地层波能量，可消除高频套管波干扰。

(2) Ⅰ、Ⅱ 界面水泥完全胶结时，声波变密度资料中地层波能量反映 Ⅱ 界面胶结情况的同时受地层声波时差的影响较大，即与声波时差存在一定的指数关系。

(3) 本文方法基本消除了地层声波时差对固井 Ⅱ 界面胶结指数的影响，明显地改进了 Ⅱ 界面的评价质量。

参考文献：

[1] BROWN H D. New developments in sonic wave train display and analysis in cased holes[R]. SPWLA 11th Annual Logging Symp, 1970.

[2] TUBMAN K M, CHENG C H, COLE S P, et al. Synthetic full-waveform acoustic logs in cased borehole, Ⅱ-poorly bonded casing[J], Geophysics, 1986, 51(4): 902-913.

[3] 胡文祥，刘银斌，周继宏，等. 套管井水泥胶结测井实验模拟[J]. 江汉石油学院学报，1997，19(3)：51-55.
HU Wen-xiang, LIU Yin-bin, ZHOU Ji-hong, et al. Experimental modelling for cement bond logging in cased wells[J]. Journal of Jianghan Petroleum Institute, 1997, 19(3): 51-55.

[4] 官波，薛桂玉，赵彦军，等. 用声波全波列测井资料定量评价固井质量的方法[J]. 测井技术，2002，26(5)：383-386.
GUAN Bo, XUE Gui-yu, ZHAO Yan-jun, et al. A method for cementing quality evaluation with full-wave acoustilog data[J]. Well Logging Technology, 2002, 26(5): 383-386.

[5] 王天波，刘正锋，张宇晓，等. 声幅变密度测井定量评价固井质量的研究[J]. 测井技术，2002，26(1)：55-59.
WANG Tian-bo, LIU Zheng-feng, ZHANG Yu-xiao, et al. Quantitative evaluation of cementing quality with AC VDL logs[J]. Well Logging Technology, 2002, 26(1): 55-59.

[6] 刘继生，王克协，吕秀梅，等. 水泥-地层界面胶结状况综合解释方法及应用[J]. 测井技术，2000，24(5)：340-344.
LIU Ji-sheng, WANG Ke-xie, LÜ Xiu-mei, et al. A comprehensive evaluating method for the cement-formation interface and its application[J]. Well Logging Technology, 2000, 24(5): 340-344.

[7] 胡文祥，钱梦马录. 套管井声场合成波形及其时频特征分析[J]. 声学学报，2002，27(3)：223-228.
HU Wen-xiang, QIAN Meng-lu. Synthetic waveforms of the acoustic field in cased boreholes and their time-frequency distribution[J]. Chinese Journal of Acoustics, 2002, 27(3): 223-228.

[8] 孙建孟，苏远大，李召成，等. 定量评价固井Ⅱ界面胶结质量的方法研究[J]. 测井技术，2004，28(3)：199-202.
SUN Jian-meng, SU Yuan-da, LI Zhao-cheng, et al. On quantitative evaluation of second interface cementing quality[J]. Well Logging Technology, 2004, 28(3): 199-202.

（编辑　刘艳荣）

(C)1994-2023 China Academic Journal Electronic Publishing House. All rights reserved.　http://www.cnki.net

◀固井与泥浆▶

地层声速对固井质量评价的影响及消除方法

苏远大[1]　孙建孟[1]　施振飞[2]　唐振欢[2]

(1. 中国石油大学(华东)地球资源与信息学院·山东东营　257061; 2. 江苏石油勘探局地质测井处·江苏扬州　225009)

摘　要：分析研究表明，快速地层水泥完全胶结时的地层波与套管波的主频差别较大，套管波主频明显偏高。通过在频域内计算套管波能量，可有效消除快速地层对固井Ⅰ界面胶结质量评价的影响。另外，结合现场变密度测井资料研究发现，地层波能量不仅反映固井Ⅱ界面胶结情况且受地层声速的严重影响，Ⅰ、Ⅱ界面水泥完全胶结时地层波能量和声波时差存在一定的指数关系。考虑地层声速的影响，可定义出主要反映水泥胶结质量的Ⅱ界面胶结指数。给出了快速地层和复杂岩性地层的现场变密度资料的处理实例，处理结果表明，通过计算套管波能量和定义Ⅱ界面胶结指数基本消除了地层声速对固井Ⅰ、Ⅱ界面胶结质量评价的影响。

关键词：固井质量；声波时差；声波全波列测井

中图分类号：TE151；TE26　　**文献标识码**：A　　**文章编号**：1001-0890(2005)04-0039-03

引　言

固井是油、水井建井过程中的重要环节，固井质量好坏直接影响井的使用寿命以及整个注、采期间能否顺利生产[1]，而套管与水泥环(Ⅰ界面)、水泥环与地层(Ⅱ界面)交界面的水泥胶结质量是评价固井质量的主要指标[2]。目前，声波变密度测井是同时评价Ⅰ、Ⅱ界面胶结质量的有效方法，但常规的处理技术对快速地层(地层声速接近钢套管声速)的Ⅰ界面和复杂岩性地层的Ⅱ界面固井质量评价通常不准确[3-5]。笔者分析了快速、慢速地层的地层波与套管波的频率特性，发现套管波主频比快速地层中地层波主频明显偏高。在频域内计算套管波能量能有效消除快速地层对固井Ⅰ界面评价的影响。针对复杂岩性地层的Ⅱ界面固井质量评价，结合现场变密度测井资料研究发现，地层波能量不仅反映固井Ⅱ界面胶结情况且受地层声速的严重影响，即Ⅰ、Ⅱ界面水泥完全胶结时地层波能量和声波时差存在一定的指数关系。地层波能量和声波时差的关系，可作为定性评价Ⅱ界面固井质量的参考；同时也可根据该关系定义出只反映水泥胶结质量的Ⅱ界面胶结指数。

1　快速地层对Ⅰ界面评价的影响

快速地层套管井中，水泥完全胶结的地层波与Ⅰ界面胶结差的套管波到时基本一致，如图 1 所示。图中第 3 道是Ⅰ界面胶结差的套管波，其中虚线是套管波到时曲线；第 4 道是快速地层水泥完全胶结时的地层波，虚线是套管波到时曲线，实线是地层波到时曲线；第 1 道是自然伽马和井径曲线；第 2 道是裸眼井声波时差曲线。由于这两种情况在时域内很难区分，快速地层中容易将地层波误认为是套管波，使得对固井Ⅰ界面胶结质量评价错误。

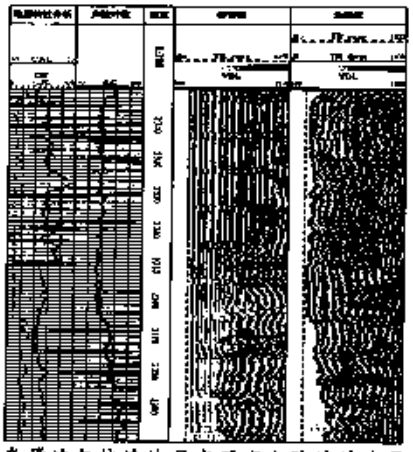


图 1　套管波与快速地层水泥完全胶结的地层波对比

图 2(a)给出Ⅰ界面胶结差的套管波(曲线 1)、快速地层完全胶结情况的地层波(曲线 2)和慢速地层完全胶结情况的地层波(曲线 3)。从图中以可看出，套管波和快速地层的地层波到时基本一致，波形特征相似，而慢速地层中地层波到时较晚很容易与套管波区分。将以上 3 种情况的时域波形作频谱分析，图 2(b)给出对应的幅度谱。发现 3 种情况的频率

收稿日期：2004-11-18；**改回日期**：2005-04-15

作者简介：苏远大(1978—)，男，2004 年获石油大学(华东)地球探测与信息技术专业硕士学位，助教。

联系电话：(0546) 8391703

中国知网　https://www.cnki.net

特性差别较大，套管波主频较高，接近 20kHz，快速地层的地层波主频偏低，17kHz 左右，而慢速地层的主频最低达到 14kHz。这样，在频域内可以区分套管波到达时间出现的波形是Ⅰ界面胶结差的套管波，还是快速地层完全胶结情况的地层波。

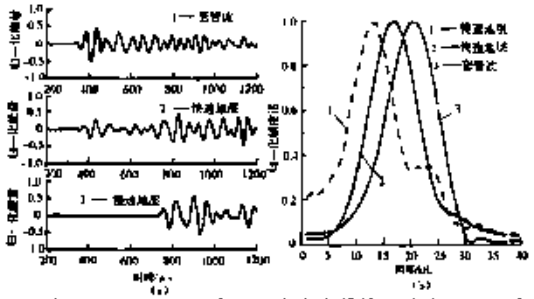


图 2 快速、慢速地层胶结良好和自由套管情况的波形及频谱对比

在套管波主频（20kHz）附近计算套管波的能量，可以有效地消除快速地层的影响，进而准确评价Ⅰ界面胶结情况。套管波能量的计算公式为：

$$E = \int_{f_1}^{f_2} A(f)\mathrm{d}f \tag{1}$$

式中，$A(f)$ 为套管波幅度谱；f_1 为套管波的起始频率，f_2 为套管波的终止频率。

图 3 是快速地层Ⅰ界面固井质量评价成果图，图中第 1 道是自然伽马和井径曲线；第 2 道是裸眼井声波时差曲线；第 3 道是变密度波形以及套管波和地层波到达时间，快速地层中地层波和套管波到时非常接近，从变密度波形可看出该井段出现了清晰的地层波，定性评价为Ⅰ、Ⅱ界面均胶结良好；第 4 道是时域和频域内计算的套管波能量得到的Ⅰ界面胶结指数，其中实线是频域的胶结指数，虚线是时域的胶结指数，时域内得到的胶结指数明显受快速地层波的影响，数值偏小且变化较大，而频域内得到的胶结指数均在 96%以上且数值稳定，能够真实地反映Ⅰ界面的胶结质量；第 5 道是频域滤波后的套管波，从滤波后的波形发现地层波的干扰已经被消除；第 6、7 道分别是时域和频域法的Ⅰ界面综合评价结果。SBT 资料显示，该井段Ⅰ界面胶结良好，传统的时域法对一些井段的评价结果明显出现错误，而在频域内计算套管波能量的评价结果准确可靠。

2 地层声速对 II 界面评价的影响

结合现场变密度测井资料计算了完全胶结井段的地层波能量，并与裸眼井的声波时差对比。图 4 给出了复杂岩性地层中水泥完全胶结井段的地层波能量和声波时差对比结果。图中第 1 道是自然伽马和井径曲线；第 2 道是变密度波形和地层波到达时间；第 3 道

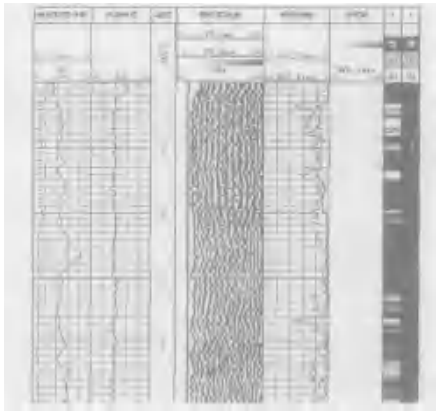


图 3 快速地层Ⅰ界面固井质量评价成果

是裸眼井声波时差和计算的地层波能量曲线，其中实线为地层波能量、虚线为声波时差。从图中的变密度波形看出该井段的套管波幅度很小，出现了清晰的地层波且幅度较大，定性评价为Ⅰ、Ⅱ界面均胶结良好。从第 3 道的声波时差和地层波能量曲线发现，两者的趋势有很好的一致性，即在水泥完全胶结井段地层的声波时差越大对应的套管井声全波中地层波的能量也越强。

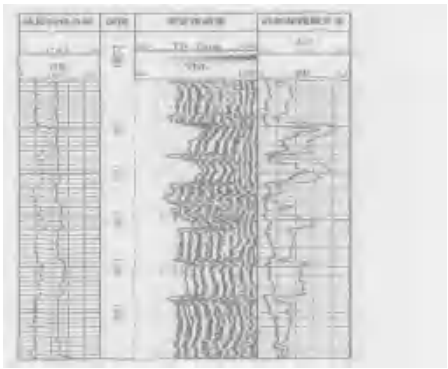


图 4 水泥完全胶结井段地层波能量和声波时差的对比

将上述水泥完全胶结井段的地层波能量和声波时差做交会图，得出两者的对应关系。图 5 给出了地层波能量和声波时差的交会图，其中“*”表示慢速地层，“×”表示中速地层，“+”表示快速地层。对所有地层情况的地层波能量与声波时差进行拟合发现，Ⅰ、Ⅱ界面水泥完全胶结时，地层波能量和声波时差存在一定的指数关系。

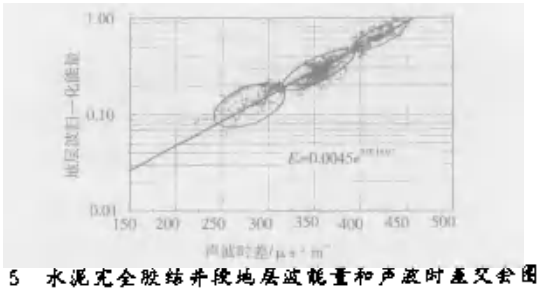


图 5 水泥完全胶结井段地层波能量和声波时差交会图

中国知网 https://www.cnki.net

变密度声波资料中，地层波能量反映Ⅱ界面胶结情况的同时，也受到地层声速的严重影响。因此，单纯用地层波能量的大小来评价Ⅱ界面胶结质量的传统方法是不准确的，必须结合地层声波时差定义出合理的Ⅱ界面胶结指数。

3　结　论

1）套管波的主频比快速地层水泥完全胶结时地层波的主频明显偏高。

2）在频域内计算套管波能量，能够消除快速地层对Ⅰ界面胶结质量评价的影响。

3）地层波能量不仅反映Ⅱ界面胶结质量，而且受地层声波时差的影响，即Ⅰ、Ⅱ界面水泥完全胶结时地层波能量与声波时差存在一定的指数关系。

参　考　文　献

[1] 杜汇．提高水泥环第二界面胶结质量的固井技术 [J]．石油钻探技术，1999，27 (1)：35-36.

[2] Brown H D New developments in sonic wave train display and analysis in cased holes [A]．SPWLA 11th annual logging symp，1970-5.

[3] 姬钢芝，刘正锋，王子荣．固井声幅—变密度测井的影响因素分析 [J]．测井技术，2002，26 (6)：486-489.

[4] 刘继生，王克协，吕秀梅，等．水泥-地层界面胶结状况综合解释方法及应用 [J]．测井技术，2000，24 (5)：340-344.

[5] 王天波，刘正锋，张宇晓，等．声幅变密度测井定量评价固井质量的研究 [J]．测井技术，2002，26 (1)：55-59.

[审稿　郭小阳]

Effects of Formation Velocity on Cementing Evaluation and Its Elimination

Su Yuanda[1]　**Sun Jianmeng**[1]　**Shi Zhenfei**[2]　**Tang Zhenhuan**[3]

(1. *College of Geo-resources and Information, China University of Petroleum (Huadong), Dongying, Shandong, 257061, China*; 2. *Geology Logging Department, Jiangsu Petroleum Exploration Bureau, Yangzhou, Jiangsu, 225009, China*)

Abstract: The results obtained indicate that the center frequency of cased wave is obviously higher than that of formation wave in fast formation. The effects of fast formation on first interface evaluation can be effectively eliminated by calculating cased wave energy in frequency domain. In addition, based on field VDL data, it is found that formation wave energy that actually reflects the cement quality of second interface is affected by formation velocity. When the cement of first and second interface bonds well, there exists exponential relationship between formation wave energy and slowness. Considering the effects of formation velocity on formation wave energy, a bond index of second interface that mainly reflects the cement bond quality is defined. Examples of processing fast formation and complicated lithology formation with field VDL data are offered in this paper. The processed results show that basically the influence of formation velocity on the bond quality of first and second interface is eliminated.

Key words: cementing quality; interval transit time; full wavetrain acoustic logging

河南油田研制成功四相分离器

河南油田稠油区块具有浅、薄、散和小等特点，采出液物性较差，胶质沥青质含量高、密度高、粘度大、携砂量大，脱水一直非常困难，而且容易造成设备堵塞。常规的地面集输处理工艺采用多段流程，首先大罐沉降除去部分油砂，然后再掺稀油多段脱水。这种工艺存在系统运行能耗大、效率低、集输系统不密闭、设备运行不平稳、油气损耗大等问题。

河南油田在三相分离器基础上，通过吸收和进一步研究三相分离的预脱气、水洗破乳、整流和界面控制等技术，研制出了新型四相分离器，克服了含砂稠油填料堵塞，以及稠油脱水不能用填料的问题，并新增了旋流进口预脱气、水出口隔板式排水、槽式负压除砂等多项新功能。其性能在两方面得到明显提高，一是明显提高设备脱水效率；二是具有设备不停产除砂功能。另外，三相分离器为油水共同加热，热耗很大，而新型四相高效分离器将加热盘管设在油层区，只加热油层不加热水层，以保证乳状液的有效加热，实现了稠油高含水原油一段脱气脱水合格，简化了流程，减少了工程投资，降低了能耗。

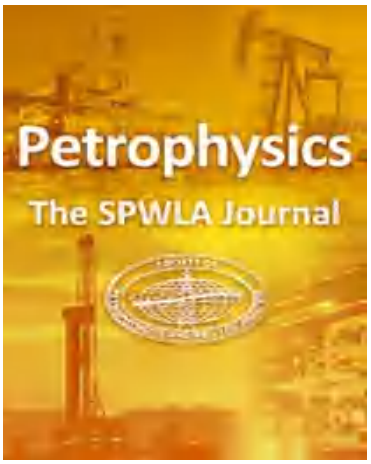
新一代四相高效分离器还具有处理能力大、设备有效利用率高、自动化程度高等特点，其单位体积处理能力为传统设备的 6～8 倍。现场试用后，效果良好。

中国知网　https://www.cnki.net


GEOPHYSICS
SEG

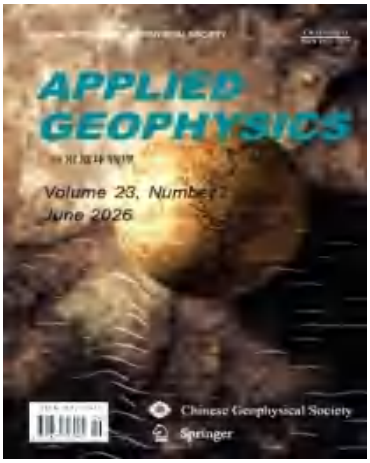

SCIENCE CHINA
Earth Sciences

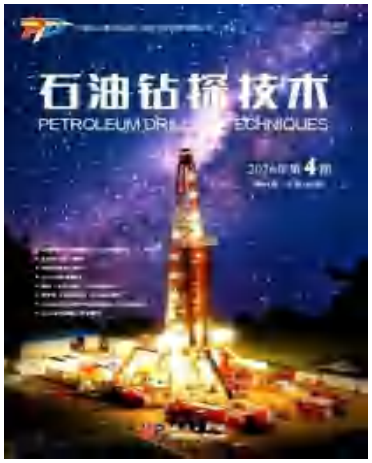

JASA

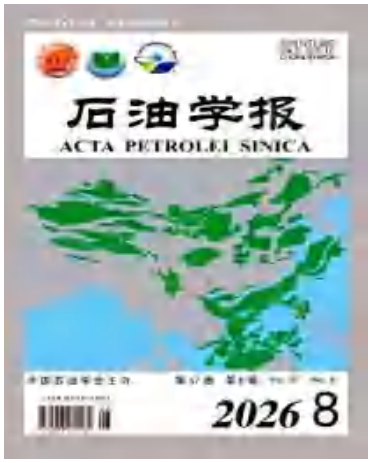

Petrophysics
The SPWLA Journal


Petroleum Science
KeAi


JOURNAL OF GEOPHYSICS AND ENGINEERING
OXFORD


APPLIED GEOPHYSICS
Volume 23, Number 2
June 2026
Chinese Geophysical Society
Springer


石油钻探技术
PETROLEUM DRILLING TECHNIQUES


石油学报
ACTA PETROLEI SINICA
2026 8


声学学报
ACTA ACUSTICA
5
2026


Royal Astronomical Society
Geophysical Journal International
academic.oup.com/gji


测井技术
4


石油物探
GEOPHYSICAL PROSPECTING FOR PETROLEUM
5
2026


地球物理学报
CHINESE JOURNAL OF GEOPHYSICS
2026

苏远大 教授 / 博士生导师

中国石油大学（华东）地球科学与技术学院

系属：测井系　　**学位：**博士

专业：地球物理测井　　**职称：**教授

电子邮箱：syuanda@sina.com

联系电话：18678969916

通讯地址：山东省青岛市长江西路66号工科楼C座533



◎个人概况

吉林榆树人，教授，博士生导师，现任地球科学与技术学院学院副院长。山东省青年科技奖、山东省优秀研究生导师、傅承义青年科技奖等获得者；兼任中国地球物理学会井孔地球物理专业委员会副主任、常务副秘书长，中国海洋石油集团测井与定向井重点实验室声学测井分室主任等。长期致力于声波测井理论方法、仪器装备与处理软件研发。主持国家级、省部级和油田企业合作等科研项目30余项，在中国科学：地球科学、Geophysics等国内外知名期刊发表论文100余篇，授权发明专利40多项，登记软件著作权16项，获省部级科研奖励10余项，指导硕博研究生80余人。

◎研究方向

主要研究方向为地球物理测井（特别是声波测井），在深地深海复杂井况、复杂地层声波测井理论方法与仪器装备研发等方面形成研究特色。先后主持国家自然科学基金、国家863计划课题、国家重点研发计划子课题、国家油气重大专项任务、中科院A类先导专项、企事业合作项目等课题30余项。

◎教育经历

2011-09至2014-07，中国石油大学（华东）地质资源与地质工程，博士

2001-09至2004-07，中国石油大学（华东）地球探测与信息技术，硕士

1997-09至2001-07，中国石油大学（华东）应用地球物理，学士

◎工作经历

2018.01-至今，中国石油大学（华东），教授，博士生导师

2016.10-2017.10，香港中文大学，访问学者

2011.12-2018.01，中国石油大学（华东），副教授

2006.07-2011.12，中国石油大学（华东），讲师

2004.07-2006.07，中国石油大学（华东），助教

◎学术兼职

1. 中国地球物理学会井孔地球物理专业委员会 副主任（2025.12-）

2. 中国海洋石油集团测井与定向井重点实验室声学测井分室 主任（2022.11-）

3. 中国地球物理学会井孔地球物理专业委员会 常务副秘书长（2018.1-2025.12）

4. 中国声学学会检测声学委员会 委员（2022.04-）

5. 中国仪器仪表学会声学仪器专业委员会 委员（2026.07-）

6. 山东省地球物理学会 理事（2020.05-）

7. 山东声学学会 常务理事（2018.05-）

8. SPWLA（国际岩石物理学家与测井分析家协会）、SEG（美国勘探地球物理学家协会）、EAGE（欧洲地球物理学会）会员

9.《测井技术》、《石油物探》期刊编委

◎主讲课程

本科生课程：《测井方法与原理（声波）》、《测井方法及综合解释》、《声波测井》、《地球物理测井》、《非电法测井》

研究生课程：《地球物理测井技术前沿》、《测井技术进展》、《定量测井声学》

◎指导研究生及博士后

合作博士后

2025年：饶博（博士后，中国石油大学（华东））

指导研究生

2026届：郑志成（硕士，中国石油集团测井有限公司）；魏立智（硕士，自主择业）

2025届：饶博（博士，校优秀博士论文、校首届“工程十佳”，中国石油大学（华东）博士后）；吴兴能（博士，中国石油塔里木油田）；张雯棋（硕士，中海油田服务股份有限公司）；王世爽（硕士，中国石油集团测井有限公司）；徐朝阳（硕士，中国石油集团长庆油田）；赵岳（硕士，中国石油大学（华东）硕博连读）；戴阳（硕士，中国石油大学（华东）硕博连读）

2024届：凌子晨（硕士，中海油田服务股份有限公司）；王怡宁（硕士，中国石油集团测井有限公司）；邓旭（硕士，中石化经纬有限公司）；纪玉磊（硕士，天津大学攻读博士）；陈声远（硕士，中国石油大学（华东）攻读博士）

2023届：柳泽旭（硕士，中国海洋石油集团有限公司海南分公司）；张恒建（硕士，中海油田服务股份有限公司）；张翰林（硕士，中石化西南勘探分公司）；刘杨（硕士，中国石化集团华东石油局）；窦响（硕士，烟台市委组织部）

2022届：孔令文（硕士，中石化石油勘探开发研究院无锡石油地质研究所）；周金鹏（硕士，中国石化集团上海海洋石油局有限公司）

2021届：崔新豪（硕士，中国石油集团测井有限公司）

2020届：刘汇鑫（硕士，中海油田服务股份有限公司）

2019届：张正鹏（硕士，上海勘察设计研究院青岛分公司）；伍文杰（硕士，襄阳华润燃气有限公司）

2018届：郭尚静（硕士，中海油田服务股份有限公司）

2017届：江灿（硕士，中国石油大学（华东）攻读博士）

2016届：杨喜龙（硕士，微梦创科网络科技有限公司）

协助指导博士研究生

2024届：古希浩（研究员，成都理工大学）；王鹤鸣（Postodoctoral Researcher， Paris-Saclay University）

2023届：李杨虎（高工，中石油新疆油田勘探开发研究院）

2022届：李焕然（高工，中海油天津分公司勘探开发研究院）

2021届：孔凡童（教授，长江大学）

2020届：江灿（博士后，中科院声学研究所）

2019届：许松（副教授，中国海洋大学）；李振（副教授，成都理工大学）

2018届：刘玉凯（Research Scientist，Eindhoven University of Technology）

2017届：李盛清（教授、山东省优青，中国石油大学（华东））；曹景记（高工、副主任，中海油研究总院）

2016届：黑创（教授、副院长，长江大学）；张博（高级工程师，光科芯图（北京）科技有限公司）

招生专业（学术学位/专业学位）：地质资源与地质工程、资源与环境（地质工程）

欢迎具有勘查技术与工程、地球物理学、测井、声学、计算机、信号处理、智能算法、物理、数学、力学等相关专业背景的学生报考博士/硕士研究生！

◎承担项目

先后承担的国家/省部级项目

国家自然科学基金面上项目：南海超深水超浅部弱固结含气储层随钻声波测井理论与方法研究，主持

国家自然科学基金面上项目：过套管方位远探测声波成像测井理论与方法研究，主持

国家自然科学基金面上项目：钻井附近地层随钻三维声速成像测井理论与方法研究，主持

国家自然科学基金委青年基金项目：随钻声波测井仪器声系最优化设计理论和方法研究，主持

国家自然科学基金企业创新联合基金重点项目：随钻声波远探测成像测井理论与实验方法，第二

国家“863”计划子课题：随钻声波测井关键技术，主持

国家重点研发计划子课题：声波远探测井旁裂缝带预测方法与研发，主持

国家油气重大专项任务：基于高分辨率阵列超声波速度成像岩石力学性能测量技术研究，主持

中国科学院攻坚专项子课题：随钻方位声波成像降噪处理软件研制及模块集成，主持

中国科学院A类战略先导专项子课题：随钻方位声波成像测井技术—随钻声波隔声体研制，主持

崂山实验室“十四五”重大项目课题：南海高温高压条件下测井响应机理与油气评价，主持

山东省自然科学基金面上项目：过套管偶极横波远探测成像测井理论与方法研究，主持

国家油气重大专项子课题：随钻声波测井仪器声系及隔声体方法研究，第二

中国石油天然气集团公司重大科技项目课题：声波远探测测井技术研究，第二

中国科学院重点部署项目子课题：随钻方位声波成像关键技术—隔声体设计与数据处理，第二

先后主持的油田企业合作项目

中海油企业合作项目：低频阵列声波测井仪器的储层评价技术研究

中海油企业合作项目：随钻声波高强度隔声体仿真及测试评价

中海油企业合作项目：随钻旋转多扇区偶极横波远探测成像处理方法研究

中海油企业合作项目：胶结差的套后阵列声波时差提取方法及水泥环厚度反演方法研究

中海油企业合作项目：邻井井眼反射波成像理论模拟及定量计算方法研究

中海油企业合作项目：随钻四极子数据处理方法及软件研制

中海油企业合作项目：长源距声波固井质量评价及过套管声波时差提取方法研究

中海油企业合作项目：随钻四极子横波测井关键技术研究

中海油企业合作项目：声波远探测与过套管裂缝检测数值模拟与实验研究

中海油企业合作项目：随钻多极子声波测井并仪径隔声体研制

中海油企业合作项目：三维声波隔声体仿真模拟软件

中海油企业合作项目：随钻声波测井隔声技术和信号处理方法研究

中石油企业合作项目：远探测声波井下仪器研制与现场应用

中石油企业合作项目：纵横波径向信息检测

中石油企业合作项目：致密储层水平横波速度提取方法测试

中石化企业合作项目：过套管声波测井技术研究

中石化企业合作项目：声波远探测测井技术在超深碳酸盐岩储层评价中的应用研究

中石化企业合作项目：深层缝洞型储层声特征响应机理研究

◎获奖情况

科研成果奖

1. 2025，中国专利优秀奖，1/4
2. 2025，教育部工程技术奖，二等奖，1/18
3. 2016，中国石油和化学工业联合会技术发明奖，一等奖，1/10
4. 2024，日内瓦国际发明展，金奖，1/7
5. 2020，中国发明协会发明创新奖，一等奖，1/6
6. 2022，中国发明协会发明创业成果奖，一等奖，1/6
7. 2017，中国海洋工程咨询协会技术发明奖，二等奖，1/9
8. 2019，山东省科技进步奖，二等奖，2/9
9. 2020，中国海洋工程咨询协会技术发明奖，一等奖，2/15
10. 2020，中国地球物理学会科技进步奖，一等奖，2/15

教学成果奖

1. 2025，山东省教学成果奖，一等奖，3/15
2. 2024，中国石油大学（华东）教学成果奖，特等奖，2/15
3. 2024，中国石油大学（华东）十佳研究生导学团队

◎荣誉称号

1. 山东省青年科技奖
2. 傅承义青年科技奖
3. 中国石油和化学工业联合会青年科技突出贡献奖
4. 山东省优秀研究生导师

5. 中华总工会“全国工人先锋号”成员

6. 中国石油大学（华东）青年骨干教师

7. 中国石油大学（华东）青年五四奖章

◎代表性期刊论文

2026年

[96] Zheng Kaiyin, **Su Yuanda***, Gu Xihao, Li Shengqing, Zhuang Chunxi, Tang Xiaoming. (2026). Fast inversion of formation slowness from LWD acoustic wave modes using deep learning. Petroleum Science, Online publication.

[95] Xu Ouyang, **Su Yuanda***, Rao Bo, Wang Wenhao, Li Shengqing, Tang Xiaoming. (2026). Inversion of S-wave transverse isotropy from acoustic logging-while-drilling data using a CNN-LSTM network. Petroleum Science, Online publication.

[94] Chen Shengyuan, **Su Yuanda***, Gu Xihao, Li Shengqing, Tang Xiaoming. (2026). SH wavefield simulation of dipole acoustic reflection survey for multi-fracture system. Geophysics, 91(1), D49–D60. https://doi.org/10.1190/geo-2025-0152

[93] 赵岳，**苏远大***，饶博，郭尚静，周建文，李盛清，唐晓明. (2026). 过套管声波测井的双源反激参数优化实验研究. 地球物理学报, 69(9), 4321–4334.

[92] Wang Wenhao, Li Shengqing*, **Su Yuanda**, Tang Xiaoming. (2026). A unified model for characterizing wave propagation in a microcracked porous background with intersecting fractures. Geophysical Journal International. Online publication.

[91] Zhao Fangfang, Chen Xuelian*, Pan Jinlin, **Su Yuanda**, Tang Xiaoming. (2026). The influence of casing curvature and thickness on the attenuation of circumferential SH-waves. Journal of Geophysics and Engineering, 23(1), 21–30.

[90] 古希浩，唐晓明，**苏远大**，李盛清*，黄建平. (2026). 井中多极声源在渗透孔隙地层中的辐射特征. 地球物理学报, 69(4), 1–16.

[89] 潘金林，陈雪莲*，**苏远大**，唐晓明. (2026). 沿套管周向传播的准弯曲型Lamb波频散与衰减特征研究. 地球物理学报, 69(1), 426–436.

2025年

[88] **苏远大**，饶博，庄春喜，李盛清，谭宝海，唐晓明*. (2025). 井中偶极横波远探测方位180°不确定性问题的求解:理论、方法和实验. 中国科学: 地球科学, 55(7), 2210–2225.

Su Yuanda, Rao Bo, Zhuang Chunxi, Li Shengqing, Tan Baohai, Tang Xiaoming*. (2025). Solving the azimuthal 180°-ambiguity problem in borehole dipole shear wave reflection imaging: Theory, method and experiment. Science China Earth Sciences, 68(7), 2138–2153.

[87] Rao Bo, **Su Yuanda***, Lin Jingqi, Liu Yang, Li Shengqing, Tang Xiaoming. (2025). Ultraslow formation shear slowness estimation in a large borehole using an eccentric dipole tool. Geophysics, 90(6), D111–D122.

[86] 纪玉磊，**苏远大***，李盛清，陈雪莲，唐晓明. (2025). 过油管偶极声波测井固井质量评价方法研究. 地球物理学报, 68(10), 4077–4087.

[85] 陈声远，**苏远大***，段文星，李盛清，唐晓明. (2025). 基于角谱法的偶极SH横波远探测声场模拟方法. 地球物理学报, 68(6), 2404–2415.

[84] 沈永进，**苏远大***. (2025). 用声波测井Stoneley波的衰减系数谱识别连通裂缝. 地球物理学报, 68(9), 3651–3663.

[83] Wang Wenhao, Li Shengqing*, Zhuang Chunxi, **Su Yuanda**, Tang Xiaoming. (2025). Dynamic seismic shear wave anisotropy in vertically fractured rocks: Modeling and field application. Geophysics, 90(5), A31–A35.

[82] Wang Wenhao, Li Shengqing*, Guo Junxin, Zhang Chengsen, Wu Xingneng, **Su Yuanda**, Tang Xiaoming. (2025). Pressure effect on wave propagation in saturated porous rocks with aligned fractures. Geophysics, 90(3), MR207–MR225.

[81] Wang Wenhao, Li Shengqing*, Guo Junxin, **Su Yuanda**, Tang Xiaoming. (2025). Pressure-dependent dynamic elastic properties and wave velocities in saturated porous rocks with aligned fractures. Geophysical Journal International, 240(3), 1732–1754.

[80] Gu Xihao, Tang Xiaoming*, **Su Yuanda**, Li Shengqing. (2025). Acoustic ranging of multiple nearby wells using dipole acoustic logging. Geophysics, 90(2), A15–A19.

[79] Pan Jinlin, Chen Xuelian*, **Su Yuanda**, Tang Xiaoming. (2025). Application of Slip Interface Theory in the Evaluation of Casing Well Cementing Quality. Petrophysics, 66(5), 872–885.

[78] Zhang Kai*, Li Shengqing, **Su Yuanda**, Tan Baohai. (2025). Subdivision gain control signal collection technology for remote acoustic logging. Journal of Geophysics and Engineering, 22(3), 847–853.

[77] 程凤，陈雪莲*，**苏远大**，唐晓明. (2025). 弯曲型Lamb波在非均匀套管中的散射特征研究. 地球物理学报, 68(12), 4868–4880.

2024年

[76] **苏远大**，饶博，孔令文，李盛清*，谭宝海，庄春喜，唐晓明. (2024). 井中方位纵波远探测：理论、实验与现场应用. 地球物理学报, 67(2), 630–640.

[75] Wu Xingneng*, **Su Yuanda**, Zhang Chengsen, Xin Yi, Chen Xu, Li Nan, Huang Ruokun, Tang Baoyong, Zhao Xinjian. (2024). A novel evaluation method of dolomite reservoir using electrical image logs: The Cambrian dolomites in Tarim Basin, China. Geoenergy Science and Engineering, 233, 212509.

[74] Shen Yongjin*, **Su Yuanda**. (2024). Experimental study on transient electromagnetic conductivity logging in cased well. Applied Geophysics, 22(2), 422–431.

[73] Gu Xihao, Kong Fantong, **Su Yuanda**, Tang Xiaoming*. (2024). Radiation efficiency and energy distribution from a borehole dipole source in the vertical transverse isotropic formation. Petroleum Science, 21(6), 4034–4051.

[72] Li Shengqing, Wang Wenhao, **Su Yuanda**, Guo Junxin*, Tang Xiaoming. (2024). P-and SV-wave dispersion and attenuation in saturated microcracked porous rock with aligned penny-shaped fractures. Petroleum Science, 21(1), 143–161.

[71] Wang Wenhao, Li Shengqing*, Guo Junxin, Zhao Long, Guo Shangjing, **Su Yuanda**, Tang Xiaoming. (2024). Dispersion and attenuation characteristics of obliquely incident SV wave in a fluid-saturated porous rock containing aligned penny-shaped fractures. Geophysics, 89(3), MR125–MR136.

[70] Wang Wenhao, Li Shengqing*, Guo Junxin, Zhang Chengsen, Duan Wenxing, **Su Yuanda**, Tang Xiaoming. (2024). Frequency-dependent elastic properties of fracture-induced VTI rocks in a fluid-saturated porous and microcracked background. Geophysics, 89(3), MR137–MR153.

[69] 王文浩，李盛清*，陈鸣，毛锐，**苏远大**，唐晓明. (2024). 海域天然气水合物地层的弹性波特征及井孔多频数据研究. 地球物理学报, 67(11), 4417–4431.

2023年

[68] Rao Bo, **Su Yuanda**, Li Shengqing, Tang Xiaoming*. (2023). Effects of collar eccentricity on azimuthal response characteristics for acoustic reflection measurement while drilling. Geophysics, 88(5), D325–D337.

[67] 饶博，**苏远大***，李盛清，孙云涛，陈文轩，唐晓明. (2023). 钻铤偏心对随钻四极子横波测井影响: 理论与实例分析. 地球物理学报, 66(1), 111–121.

[66] Gu Xihao, Tang Xiaoming*, **Su Yuanda**, Li Shengqing. (2023). Elastic wave radiation and reception of a borehole dipole source in a vertically transverse isotropic formation. Geophysics, 88(2), D177–D191.

[65] Li Shengqing, Wang Wenhao, **Su Yuanda**, Guo Junxin*. (2023). Effective elastic properties and S-wave anisotropy for rocks containing any oriented penny-shaped cracks in transversely isotropic background. Geophysics, 88(3), MR65–MR81.

2022年

[64] 饶博，唐晓明，**苏远大***. (2022). 横向各向同性地层随钻多极子测井声场的分波分析与特性研究. 地球物理学报, 65(8), 3198–3212.

[63] Li Yanghu, Tang Xiaoming*, **Su Yuanda**. (2022). Borehole radiation and reception responses for azimuthal shear-wave reflection imaging with an off-centred dipole acoustic tool. Journal of Geophysics and Engineering, 19(5), 1180–1195.

[62] Tan Baohai, Zhang Kai*, **Su Yuanda**, Li Shengqing, Zhang Lijun. (2022). Research on acoustic logging while drilling transmitting technologies. Journal of Geophysics and Engineering, 19(3), 511–520.

[61] Li Zhen, Li Shengqing*, Qi Qiaomu, **Su Yuanda**, Wang Xingjian. (2022). Investigation of through-casing borehole acoustic reflection imaging with a dipole source: Modeling and field application. Journal of Natural Gas Science and Engineering, 105, 104715.

[60] Li Huanran, Tang Xiaoming*, Li Shengqing, **Su Yuanda**. (2022). Dynamic fluid transport property of hydraulic fractures and its evaluation using acoustic logging. Petroleum Exploration and Development, 49(1), 223–232.

[59] 古希浩，唐晓明*，**苏远大**. (2022). 井中偶极声源在横向各向同性地层中的辐射波场. 地球物理学报, 65(4), 1494–1507.

[58] 李杨虎，唐晓明*，**苏远大**. (2022). 偶极横波远探测在裸眼井及套管井中接收波场的方位响应特征. 地球物理学报, 65(10), 4122–4140.

[57] 夏飞月，**苏远大**，唐晓明*. (2022). 斯通利波在渗透地层和裂缝带的反射及透射: 解析和数值方法模拟对比. 地球物理学报, 65(4), 1508–1518.

2021年

[56] 唐晓明，古希浩，李杨虎，**苏远大***. (2021). 井孔与弹性波的相互作用:理论,方法和应用. 地球物理学报, 64(12), 4227–4238.

[55] Gu Xihao, Tang Xiaoming*, **Su Yuanda**. (2021). Delineating a cased borehole in unconsolidated formations using dipole acoustic data from a nearby well. Geophysics, 86(5), D139–D147.

[54] Xu Song, Tang Xiaoming*, Torres-Verdín Carlos, Li Zhen, **Su Yuanda**. (2021). Evaluation of 3D shear-wave anisotropy based on elastic-wave velocity variations around the borehole. Geophysics, 86(3), D103–D112.

[53] Xu Song, Tang Xiaoming*, Chen Ming, **Su Yuanda**, Qian Yuping, Sun Dianqiang, Torres-Verdín Carlos. (2021). Estimation of directional crack density and fluid properties from well logs in vertical wells. Geophysics, 86(4), D113–D124.

2020年

[52] **Su Yuanda**, Fang Xinding, Tang Xiaoming*. (2020). Measurement of the shear slowness of slow formations from monopole logging-while-drilling sonic logs. Geophysics, 85(1), D45–D52.

[51] Li Yanghu, Xu Song, Jiang Can, **Su Yuanda***, Tang Xiaoming. (2020). Joint inversion of logging-while-drilling multipole acoustic data to determine formation shear-wave transverse isotropy. Geophysics, 85(4), D121–D132.

[50] Xu Song, **Su Yuanda***, Tang Xiaoming. (2020). Elastic properties of transversely isotropic rocks containing aligned cracks and application to anisotropy measurement. Applied Geophysics, 17(2), 182–191.

[49] 李盛清，**苏远大***，唐晓明. (2020). 基于四分量偶极横波远探测的井周构造走向快速反演方法研究. 地球物理学报, 63(6), 2478–2487.

[48] Xu Song, Tang Xiaoming*, **Su Yuanda**, Torres-Verdín Carlos. (2020). Crack‐Induced Shear‐Wave Orthorhombic Anisotropy: Modeling and Inversion of Shear‐Wave Borehole Measurements. Journal of Geophysical Research: Solid Earth, 125(3), e2019JB018741.

[47] Xu Song, Tang Xiaoming*, **Su Yuanda**, Zhuang Chunxi. (2020). Seismic shear wave anisotropy of an anisotropic rock containing aligned cracks: theory and applications to experiment and field data. Geophysical Journal International, 220(1), 404–414.

[46] Kong Fantong, Jiang Can, **Su Yuanda**, Tang Xiaoming*. (2020). A multiple filtering and correlation array signal processing technique for cased-hole acoustic logging and applications. Interpretation, 8(3), SL1–SL8.

[45] Li Huanran, Gu Xihao, Zhang Conghui, **Su Yuanda**, Tang Xiaoming*. (2020). Effect of perforation on borehole acoustic wave logging: Modeling and application. Geophysics, 85(1), D37–D43.

[44] 李盛清*，林剑松，江灿，**苏远大**，唐晓明. (2020). 随钻声波测井固井质量评价理论与数值模拟研究. 地球物理学报, 63(7), 2762–2773.

2019年

[43] Tang Xiaoming*, **Su Yuanda**, Zhuang Bo. (2019). A THROUGH-CASING ACOUSTIC LOGGING TOOL USING DUAL-SOURCE TRANSMITTERS. Petrophysics, 60(5), 631–639.

[42] Li Shengqing, Tang Xiaoming*, **Su Yuanda**. (2019). Shear wave imaging to determine near-borehole faults for ocean drilling exploration. Geophysical Journal International, 217(1), 288–293.

[41] Xu Song, Tang Xiaoming*, **Su Yuanda**. (2019). A sphere-equivalency approach for calculating the elastic property of an isotropic solid containing aligned inclusions: Modeling and experiment data verification. Geophysics, 84(5), C239–C249.

[40] Jiang Can, Chen Xuelian, **Su Yuanda**, Tang Xiaoming*. (2019). Cased borehole acoustic-wave propagation with varying bonding conditions: Theoretical and experimental modeling. Geophysics, 84(4), D161–D169.

[39] Zhuang Chunxi, Xu Song*, Li Huanran, **Su Yuanda**, Tang Xiaoming. (2019). Azimuthal shear-wave anisotropy measurement in a borehole: Physical modeling and dipole acoustic verification. The Journal of the Acoustical Society of America, 146(2), EL129–EL134.

[38] Li Shengqing, Chen Ming, Gu Xihao, **Su Yuanda**, Tang Xiaoming*. (2019). Application of four-component dipole shear reflection imaging to interpret the geological structure around a deviated well. Applied Geophysics, 16(3), 291–301.

[37] 庄春喜，李杨虎，孔凡童，陈鸣*，张聪慧，**苏远大**，唐晓明. (2019). 随钻斯通利波测井反演地层渗透率的理论、方法及应用. 地球物理学报, 62(11), 4482–4492.

[36] 江灿，庄春喜*，李盛清，**苏远大**，唐晓明. (2019). 多极子阵列声波测井数据的纵横波慢度联合反演方法. 地球物理学报, 62(6), 2294–2302.

[35] 唐晓明*，古希浩，**苏远大**. (2019). 过套管偶极横波远探测理论与应用. 中国石油大学学报：自然科学版, 43(5), 65–72.

2018年

[34] **Su Yuanda**, Li Zhen, Xu Song, Zhuang Chunxi, Tang Xiaoming*. (2018). Elastic-wave evaluation of downhole hydraulic fracturing: Modeling and field applications. Geophysics, 83(1), D1–D8.

[33] Li Zhen, **Su Yuanda**, Tang Xiaoming, Li Huanran, Liu Qing Huo*. (2018). A hybrid method to simulate elastic wave scattering of three-dimensional objects. The Journal of the Acoustical Society of America, 144(4), EL268–EL274.

[32] Liu Yukai, Smeulders David, **Su Yuanda**, Tang Xiaoming*. (2018). Seismoelectric interface electromagnetic wave characteristics for the finite offset Vertical Seismoelectric Profiling configuration: Theoretical modeling and experiment verification. The Journal of the Acoustical Society of America, 143(1), EL13–EL18.

[31] Xu Song, Tang Xiaoming*, Torres-Verdín Carlos, **Su Yuanda**. (2018). Seismic Shear Wave Anisotropy in Cracked Rocks and an Application to Hydraulic Fracturing. Geophysical Research Letters, 45(11), 5390–5397.

[30] Tang Xiaoming*, Jiang Can, **Su Yuanda**, Chen Xuelian. (2018). An acoustic-wave theory for casing bond evaluation using viscoelastic slip boundary modeling. Science China Earth Sciences, 61(8), 1057–1064.

[29] Xu Song, Zhuang Chunxi*, **Su Yuanda**, Liu Yukai, Zhang Zhengpeng, Guo Shangjing, Tang Xiaoming. (2018). Acoustic source characterization for a logging while drilling tool: Theoretical and experimental modeling. The Journal of the Acoustical Society of America, 144(3), EL178–EL184.

[28] 许松，唐晓明，**苏远大**，庄春喜*. (2018). 斯通利波和弯曲波联合反演地层VTI各向异性的阵列声波处理方法. 地球物理学报, 61(12), 5105–5114.

2017年

[27] **苏远大***，许松，江灿，唐晓明. (2017). 随钻四极子横波测井钻铤尺寸优化设计的理论研究. 地球物理学报, 60(4), 1606–1615.

[26] Xu Song, Tang Xiaoming*, **Su Yuanda**, Li Shengqing, Zhuang Chunxi. (2017). Determining formation S-wave transverse isotropy from borehole flexural-wave dispersion data. Geophysics, 82(2), D47–D55.

[25] 许松，**苏远大**，唐晓明*. (2017). 基于超级混合虚折射干涉法的阵列声波处理方法及其在套管井中的应用. 地球物理学报, 60(7), 2904–2912.

[24] 孔凡童，庄春喜，**苏远大**，唐晓明*. (2017). 随钻四极横波测量的数据驱动频散处理方法. 地球物理学报, 60(12), 4938–4944.

2016年

[23] **Su Yuanda**, Jiang Can, Zhuang Chunxi, Xu Song, Tang Xiaoming*. (2016). Joint inversion of logging-while-drilling multipole acoustic data to determine P- and S-wave velocities in unconsolidated slow formations. Geophysics, 81(5), D553–D560.

[22] **苏远大**，庄春喜，唐晓明*，黑创，许松，李振，杨喜龙. (2016). 一种刻槽式随钻声波测井隔声体的理论与实验研究. 地球物理学报, 59(12), 4521–4528.

[21] 刘玉凯，唐晓明，**苏远大***. (2016). 随钻条件下井旁界面声电效应的辐射电磁波响应特征. 地球物理学报, 59(5), 1898–1908.

[20] Li Shengqing, Tang Xiaoming*, **Su Yuanda**, Zhuang Chunxi. (2016). Model-based dispersive processing of borehole dipole wave data using an equivalent-tool theory. Geophysics, 81(1), D35–D43.

[19] Tang Xiaoming*, Xu Song, Zhuang Chunxi, **Su Yuanda**, Chen Xuelian. (2016). Assessing rock brittleness and fracability from radial variation of elastic wave velocities from borehole acoustic logging: Rock brittleness and fracability. Geophysical Prospecting, 64(4), 958–966.

[18] Tang Xiaoming*, Li Zhen, Hei Chuang, **Su Yuanda**. (2016). Elastic wave scattering to characterize heterogeneities in the borehole environment. Geophysical Journal International, 205(1), 594–603.

[17] Tang Xiaoming*, Cao Jingji, Li Zhen, **Su Yuanda**. (2016). Detecting a fluid-filled borehole using elastic waves from a remote borehole. The Journal of the Acoustical Society of America, 140(2), EL211–EL217.

[16] 唐晓明*，许松，庄春喜，**苏远大**，陈雪莲. (2016). 基于弹性波速径向变化的岩石脆裂性定量评价. 石油勘探与开发, 43(3), 417–424.

[15] 曹景记，唐晓明*，**苏远大**，魏周拓，庄春喜. (2016). 随钻偶极远探测声场的辐射特性. 地球物理学报, 59(9), 3503–3513.

[14] 张博，唐晓明*，**苏远大**，祁晓. (2016). 一种利用双源反激的随钻声波测井方法. 地球物理学报, 59(3), 1151–1160.

2015年

[13] **Su Yuanda**, Tang Xiaoming*, Xu Song, Zhuang Chunxi. (2015). Acoustic isolation of a monopole logging while drilling tool by combining natural stopbands of pipe extensional waves. Geophysical Journal International, 202(1), 439–445.

[12] **Su Yuanda**, Tang Xiaoming*, Liu Yukai, Xu Song, Zhuang Chunxi. (2015). Extensional-wave stopband broadening across the joint of pipes of different thickness. The Journal of the Acoustical Society of America, 138(5), EL447–EL451.

[11] 许松，唐晓明，**苏远大***. (2015). 横向各向同性固体材料中含定向非均匀体的有效弹性模量研究. 物理学报, 64(20), 314–322.

[10] 唐晓明*，祁晓，张博，李盛清，**苏远大**. (2015). 基于波干涉原理的套管井阵列声波处理方法及其应用. 地球物理学报, 58(4), 1447–1457.

2014年

[9] 许松，**苏远大***，陈雪莲，唐晓明. (2014). 含孔隙、裂隙地层随钻多极子声波测井理论. 地球物理学报, 57(6), 1999–2012.

[8] 陈雪莲，唐晓明*，钱玉萍，**苏远大**. (2014). 含孔隙、裂隙致密介质中多极子声波的传播特征. 地球物理学报, 57(9), 2961–2970.

2013年

[7] **Su Yuanda**, Tang Xiaoming*, Zhuang Chunxi, Xu Song, Zhao Long. (2013). Mapping formation shear-velocity variation by inverting logging-while-drilling quadrupole-wave dispersion data. Geophysics, 78(6), D491–D498.

[6] 魏周拓，唐晓明，**苏远大**，谭宝海. (2013). 利用井中低频偶极横波进行声波远探测的新方法. 地球物理学报, 56(10), 3572–3580.

2012年

[5] Tang Xiaoming, Chen Xuelian, Xu Xiaokai, **Su Yuanda**. (2012). A cracked porous medium elastic wave theory and its application to interpreting acoustic data from tight formations. Geophysics, 77(6), D245–D252.

[4] 唐晓明*，魏周拓，**苏远大**. (2012). 利用井中偶极声源远场辐射特性的远探测测井. 地球物理学报, 55(8), 2798–2807.

[3] 陈雪莲，唐晓明*，**苏远大**. (2012). 孔,裂隙并存地层中的声波测井理论及多极子声场特征. 地球物理学报, 55(6), 2129–2140.

2011年

[2] **Su Yuanda**, Tang Xiaoming, Hei Chuang, Zhuang Chunxi. (2011). An equivalent-tool theory for acoustic logging and applications. Applied Geophysics, 8(1), 69–78.

[1] **苏远大***，庄春喜，唐晓明. (2011). 随钻声波测井钻铤模式波衰减规律研究与隔声体设计. 地球物理学报, 54(9), 2419–2428.

2010年之前

[1] **苏远大**，孙建孟，李召成，张振城，陈雪莲. 裸眼时差与变密度测井地层波能量相结合改进固井II界面评价[J]. 中国石油大学学报(自然科学版), 2006, 30(4): 38-41.

[2] **苏远大**，孙建孟，范宜仁，陈雪莲.基于软地层随钻多极子声源传播特性的数值研究[J]. 测井技术, 2006, 30(3): 205-207.

[3] **苏远大**，孙建孟，施振飞，唐振欢. 地层声速对固井质量评价的影响及消除方法[J]. 石油钻探技术, 2005, 33(4): 39-41.

[4] **苏远大**，乔文孝，孙建孟，陈雪莲. 正交偶极声波测井资料在评价地层各向异性中的应用[J]. 石油物探, 2005, 44(4): 409-412.

[5] **苏远大**，乔文孝. 一种提取声波测井频散波相慢度的方法[J]. 测井技术, 2003, 27(5): 364-368, 445.

◎学术交流

[1] **Su Yuanda**, Liu Xien Zhuang Chunxi Sun Zhifeng Hei Chuang. Estimating radial variation of unconsolidated formations using borehole leaky-p wave dispersion, 2011, SPWLA Logging Symposium, Houston, USA.

[2] **Su Yuanda**, Tang Xiaoming Tan Baohai. Acoustic isolation by combining natural stopbands of pipe extensional waves, 2012, JASA Acoustic HK, Hong Kong, China.

[3] **Su Yuanda**, Tang Xiaoming, Xu Song, Zhuang Chunxi. Evaluating Rock Brittleness from Radial P-wave Velocity Variation in the LWD Condition, 2015, 77th EAGE Conference and Exhibition, Madrid, Spain.

[4] **Su Yuanda**, Jiang Can, Zhuang Chunxi, Xu Song, Tang Xiaoming. Joint inversion of logging while drilling multipole acoustic data to determine P- and S-wave velocities in unconsolidated slow formations, 2016, SEG Annual Meeting, Dallas, Texas, USA.

[5] Rao Bo, **Su Yuanda**, Li Shengqing, Tang Xiaoming. Response characteristics of multipole sonic log in double casing strings, 2022, 49th Annual Review of Progress in Quantitative Nondestructive Evaluation.

[6] Rao Bo, **Su Yuanda**, Li Shengqing, Tang Xiaoming. Azimuthal reflected P-wave imaging: experiment and field application, 2024, 85th EAGE Annual Conference & Exhibition.

[7] 饶博，**苏远大**，李盛清，唐晓明. 钻铤偏心对随钻远探测声场的影响研究，2023，中国地球科学联合学术年会. (优秀学生报告)

[8] 凌子晨，**苏远大**，李盛清，唐晓明. 随钻阵列超声波速度测井数值模拟与实验研究，2023，中国地球科学联合学术年会.

[9] 赵岳，**苏远大**，李盛清，唐晓明. 过套管声波测井理论与实验研究，2024，中国地球科学联合学术年会. (优秀学生报告)

[10] 饶博，**苏远大**，李盛清，唐晓明. 井中随钻方位纵波远探测：理论与实验研究，2025，中国地球科学联合学术年会.

[11] 徐欧阳，**苏远大**，郑凯尹，李盛清，唐晓明. 基于神经网络的随钻多极声波数据联合反演地层各向异性，2025，中国地球科学联合学术年会. (优秀学生报告)

[12] 郑志成，**苏远大**，王子阳，李盛清，唐晓明. 基于激光测振技术的高温高压声波测井换能器实验研究，2025，中国地球科学联合学术年会.

[13] 王文浩，**苏远大**，李盛清，庄春喜，谭宝海，唐晓明. 深层油气声波远探测技术与装备及储层反射“亮点”技术应用，2026，中国地球物理学会地球物理技术委员会第十三届学术会议. (优秀学生报告)

[14] **苏远大**. 随钻声波井旁远探测技术进展与钻头前探新思路，2026，中国地球物理学会地球物理技术委员会第十三届学术会议，邀请报告.

[15] **苏远大**. 高温高压声波测井换能器性能在线测试装置及其应用，2025，中国地球物理年会“井孔地球物理学及深部钻测技术”专题，邀请报告.

[16] **苏远大**. 声学测井技术最新研究进展，2024、2025、2026，中海油田服务股份有限公司，邀请报告

[17] **苏远大**. 随钻声波测井技术进展，2023，中国石油集团测井有限公司，邀请报告.

[18] **苏远大**. 声波测井技术研究进展，2022、2026，中石化经纬公司，邀请报告.

[19] **苏远大**. 方位远探测声波测井技术研究进展，2026，中科院地质与地球物理所“青促会论坛”，邀请报告.

[20] **苏远大**. 井孔声学测井技术研究进展，2016，香港大学、香港中文大学、南方科技大学，邀请报告.

◎发明专利

[1] **苏远大**，凌子晨，李盛清. 一种近钻头随钻阵列超声速度成像测井装置及方法.

[2] **苏远大**，纪玉磊，李盛清，唐晓明，陈雪莲. 偶极声波测井套管井质量反演方法、装置、设备和介质.

[3] **苏远大**，郑凯尹，李盛清，唐晓明，庄春喜，古希浩，饶博，王文浩，陈声远. 一种随钻测井横波速度处理方法、装置、设备和存储介质.

[4] **苏远大**，张雯棋，李盛清，赵岳，郑凯尹. 一种基于神经网络的地层各向异性成因分类方法及设备.

[5] **苏远大**，李杨虎，唐晓明，许松，江灿. 一种随钻声波测井评价地层各向异性的方法.

[6] **苏远大**，李焕然，唐晓明. 一种定量评价射孔穿透深度的声学测井方法.

[7] **苏远大**，唐晓明，刘西恩，谭宝海，李刚，刘玉凯. 一种变径隔声结构的随钻声波测井装置.

[8] **苏远大**，唐晓明，庄春喜，黑创. 随钻声波测井钻铤变径声系隔声体的最优化设计方法.

[9] **苏远大**，唐晓明，庄春喜，赵龙，许松. 一种反演地层横波速度径向剖面的方法.

[10] **苏远大**，秦瑞宝，孙建孟，邓启才，陈雪莲，汤丽娜，庄春喜． 一种泄露模式波反演软地层横波速度的方法.

[11] 李盛清，**苏远大**，庄春喜，唐晓明. 一种声学测井的声波远探测成像方法、设备、介质及产品.

[12] 李盛清，**苏远大**，唐晓明，周军，张波，陈文辉，张晋言. 一种井中三维探测的多分量声波测井装置.

[13] 唐晓明，**苏远大**，庄春喜. 井周地质反射体环向扫描成像的探测方法.

[14] 唐晓明，**苏远大**，谭宝海，李刚. 一种在钻铤上变径隔声的随钻声波测井方法及装置.

[15] 唐晓明，**苏远大**，魏周拓，谭宝海. 在井中发射并接收偶极横波的探测方法.

[16] 程凤，**苏远大**，陈雪莲，谭宝海，李盛清，周雅丽. 一种基于超声Lamb波套管井非均匀性测量方法.

[17] 李盛清，沈钦宇，**苏远大**，唐晓明，张翰林，庄春喜. 一种测井预测产能的方法和处理装置.

[18] 唐晓明，李杨虎，**苏远大**，庄春喜，孔凡童. 一种随钻声波测井评价地层渗透率的方法.

[19] 许松，唐晓明，**苏远大**，庄春喜，陈雪莲. 一种基于裂缝交汇图版的储层压裂效果评价方法.

[20] 陈雪莲，江灿，**苏远大**，李盛清，饶博，唐晓明. 从套管井声波测井中获取套管与水泥界面剪切耦合刚度的方法.

[21] 唐晓明，王鹤鸣，**苏远大**，陈雪莲. 一种利用孔隙、裂隙介质弹性波理论反演岩石孔隙分布特征方法.

[22] 唐晓明，古希浩，**苏远大**. 一种基于井孔与弹性波相互作用理论的邻井探测方法.

[23] 许松，唐晓明，**苏远大**，庄春喜，谭宝海. 一种评价井周横波三维各向异性的方法.

[24] 唐晓明，孔凡童，**苏远大**. 一种提取套管井地层声波速度的方法.

[25] 黑创，唐晓明，**苏远大**，庄春喜，罗明璋，李修权，张磊，陈伟国. 一种井周岩石非均匀各向异性的识别方法及系统.

[26] 唐晓明，张博，**苏远大**. 一种基于双源反激技术的随钻声波测井方法及装置.

[27] 唐晓明，张博，**苏远大**，谭宝海. 一种双源反激过套管声波测井方法及装置.

[28] 唐晓明，祁晓，**苏远大**，李盛清. 一种利用管波与地层声波干涉原理提取地层声速的方法.

[29] 李盛清，刘晓阳，张恒建，**苏远大**，张凯，唐晓明. 一种声波远探测数据质量检测方法.

[30] 李盛清，张广栋，张淼鹤，**苏远大**，唐晓明. 一种阵列声波测井评价固井质量的方法及处理装置.

[31] 李盛清，张广栋，张淼鹤，**苏远大**，唐晓明. 一种随钻声波固井质量评价方法及处理装置.

[32] 陈雪莲，唐晓明，庄妍，**苏远大**，谭宝海，李盛清，庄春喜，张凯. 使用SH模式波和A0模式波识别套管井水泥环胶结状况的方法.

[33] 李盛清，张淼鹤，张广栋，**苏远大**，唐晓明. 一种阵列声波测井评价固井二界面胶结质量方法及装置.

[34] 许松，申富豪，唐晓明，**苏远大**，陈雪莲. 一种评价井外不同方位下裂缝发育程度的方法.

[35] 唐晓明，李思亦，许松，**苏远大**，刘颖宇，孙福亭. 一种基于声波远探测和岩石力学的裂缝有效性评价方法.

[36] 黑创，张磊，唐晓明，**苏远大**，吴爱平. 一种定量评价地层非均匀性的方法及装置.

[37] 黑创，唐晓明，庄春喜，**苏远大**，李振，李修权. 一种多参数联合反演计算岩石散射衰减的方法.

[38] 谭宝海，张博，郝仲田，**苏远大**，唐晓明. 一种用于随钻声波测井的声源激励装置.

[39] 陈雪莲，韩旺，张聪慧，郭辛阳，**苏远大**，王文梁，谭宝海，庄春喜，张凯，李盛清. 一种利用贴井壁声系实时监测水泥窜槽的实验方法.

[40] 陈雪莲，唐晓明，李盛清，庄春喜，**苏远大**，谭宝海，许松. 一种识别双层套管井外层套管与地层之间胶结状况的方法.

[41] 郭辛阳，陈雪莲，步玉环，高乾浩，**苏远大**，韩旺，郭胜来，柳华杰，张锐，王成文. 全尺寸高温高压水泥环水力封隔性评价装置.

[42] 唐晓明，陈雪莲，许松，庄春喜，**苏远大**. 从井中弹性波速的径向变化获取地层岩石脆裂性质的方法.

[43] 唐晓明，陈雪莲，程凤，庄春喜，**苏远大**，李盛清. 一种套管井水泥环第二界面反射位成像和水泥环空介质属性反演的方法.

[44] 李杰，罗瑜林，刘西恩，李辉，孙志峰，**苏远大**. 一种随钻声波隔声结构.

◎软件著作权

[1] 声波远探测测井反射波成像处理软件，登记号：2012SR049453

[2] 正交偶极远探测反射声波成像处理软件，登记号：2013SR026687

[3] 声波远探测成像测井数值模拟软件，登记号：2020SR1713552

[4] 声波远探测成像增强软件，登记号：2020SR1732595

[5] 阵列声波时差提取处理软件，登记号：2013SR160939

[6] 阵列声波高分辨率时差处理软件，登记号：2016SR364525

[7] 阵列声波纵波速度径向剖面反演软件，登记号：2015SR118187

[8] 阵列声波多道波至提取处理软件，登记号：2014SR206121

[9] 阵列声测井数据的频率-波数（f-k）滤波处理软件，登记号：2012SR049457

[10] 声波测井孔隙、裂隙参数反演处理软件，登记号：2015SR268553

[11] 偶极子横波径向速度剖面反演软件，登记号：2015SR137120

[12] 偶极横波时差的频散校正处理软件，登记号：2012SR049437

[13] 横波各向异性（横向各向同性TI）的声测井数据反演软件，登记号：2012SR049291

[14] 随钻和电缆阵列声波数据速度和频散分析软件，登记号：2013SR161296

[15] 声波测井仿真实验软件，登记号：2016SR375966

[16] 三维井孔声场有限差分数值模拟软件，登记号：2015SR268555